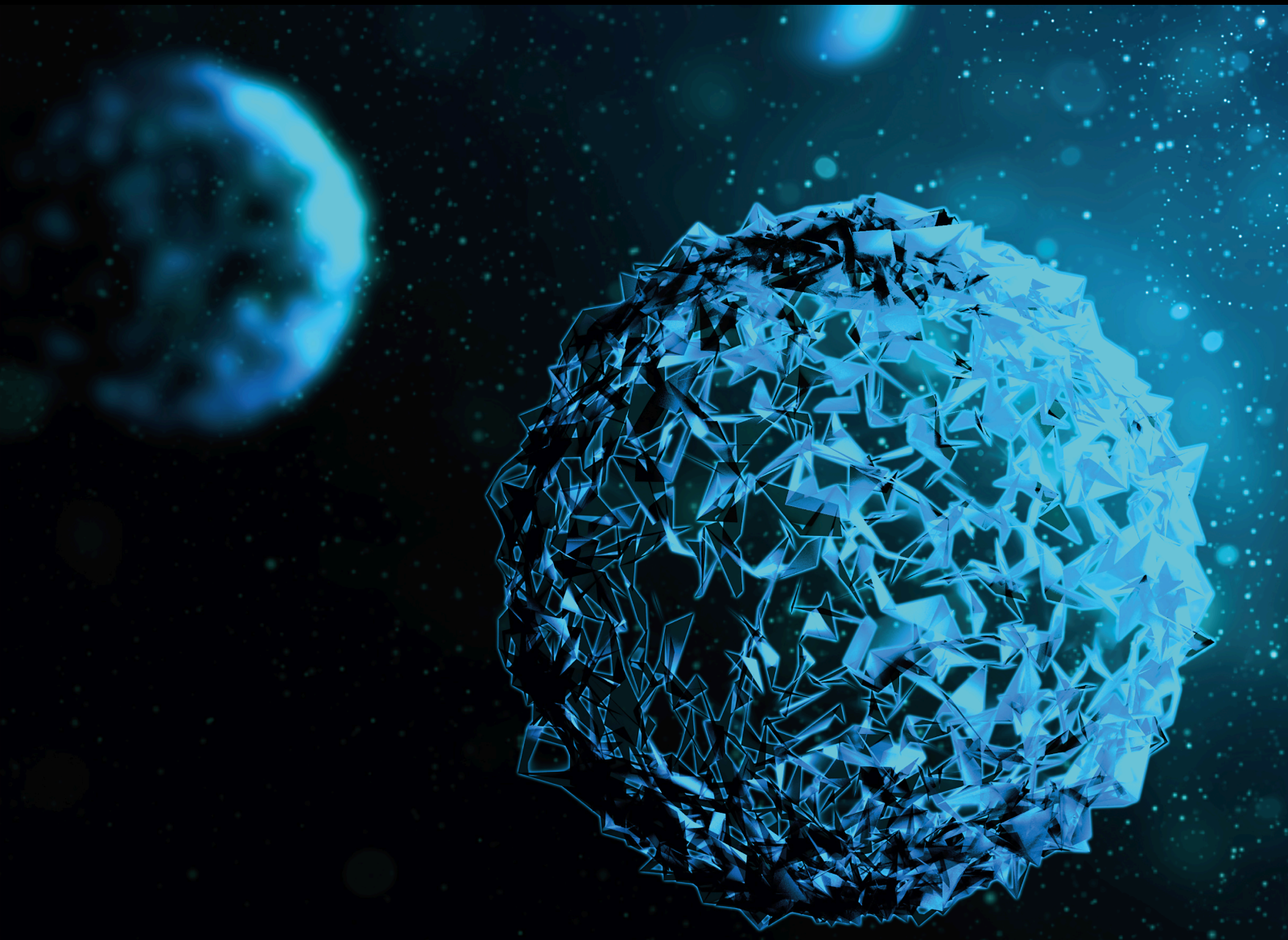


# Computer-Aided Diagnosis of Pleural Mesothelioma: Recent Trends and Future Research Perspectives

Lead Guest Editor: Gaganpreet Kaur

Guest Editors: Abolfazl Mehbodniya, Fawaz Al-Mufti, and Mukesh Soni





---

# **Computer-Aided Diagnosis of Pleural Mesothelioma: Recent Trends and Future Research Perspectives**

BioMed Research International

---

# **Computer-Aided Diagnosis of Pleural Mesothelioma: Recent Trends and Future Research Perspectives**

Lead Guest Editor: Gaganpreet Kaur

Guest Editors: Abolfazl Mehbodniya, Fawaz Al-Mufti, and Mukesh Soni



Copyright © 2024 Hindawi Limited. All rights reserved.

This is a special issue published in "BioMed Research International." All articles are open access articles distributed under the Creative Commons Attribution License, which permits unrestricted use, distribution, and reproduction in any medium, provided the original work is properly cited.

## Section Editors

Penny A. Asbell, USA  
David Bernardo , Spain  
Gerald Brandacher, USA  
Kim Bridle , Australia  
Laura Chronopoulou , Italy  
Gerald A. Colvin , USA  
Aaron S. Dumont, USA  
Pierfrancesco Franco , Italy  
Raj P. Kandpal , USA  
Fabrizio Montecucco , Italy  
Mangesh S. Pednekar , India  
Letterio S. Politi , USA  
Jinsong Ren , China  
William B. Rodgers, USA  
Harry W. Schroeder , USA  
Andrea Scribante , Italy  
Germán Vicente-Rodríguez , Spain  
Momiao Xiong , USA  
Hui Zhang , China

## Academic Editors

## Bioinformatics

# Contents

---

**Retracted: Dynamic Data Infrastructure Security for Interoperable e-Healthcare Systems: A Semantic Feature-Driven NoSQL Intrusion Attack Detection Model**

BioMed Research International

Retraction (1 page), Article ID 9804280, Volume 2024 (2024)

**Retracted: The Optos 200Tx Scanning Laser Ophthalmoscope Application in Retinoblastoma Patients' Follow-Up**

BioMed Research International

Retraction (1 page), Article ID 9820545, Volume 2024 (2024)

**Retracted: Deep Learning-Based Real-Time Discriminate Correlation Analysis for Breast Cancer Detection**

BioMed Research International

Retraction (1 page), Article ID 9829340, Volume 2024 (2024)

**Retracted: Effects of Sacubitril/Valsartan on the Expression of CaMKII/Ca<sub>v</sub>1.2 in Atrial Fibrillation Stimulation Rabbit Model**

BioMed Research International

Retraction (1 page), Article ID 9890209, Volume 2024 (2024)

**Retracted: Ant Colony Optimization-Enabled CNN Deep Learning Technique for Accurate Detection of Cervical Cancer**

BioMed Research International

Retraction (1 page), Article ID 9878397, Volume 2024 (2024)

**Retracted: Diagnosis of Prostate Cancer Using GLCM Enabled KNN Technique by Analyzing MRI Images**

BioMed Research International

Retraction (1 page), Article ID 9875401, Volume 2024 (2024)

**Retracted: PSO-Based Evolutionary Approach to Optimize Head and Neck Biomedical Image to Detect Mesothelioma Cancer**

BioMed Research International

Retraction (1 page), Article ID 9870105, Volume 2024 (2024)

**Retracted: Classification and Detection of Mesothelioma Cancer Using Feature Selection-Enabled Machine Learning Technique**

BioMed Research International

Retraction (1 page), Article ID 9868791, Volume 2024 (2024)

**Retracted: Detection of Pancreatic Cancer in CT Scan Images Using PSO SVM and Image Processing**

BioMed Research International

Retraction (1 page), Article ID 9862575, Volume 2024 (2024)

**Retracted: Appropriate Supervised Machine Learning Techniques for Mesothelioma Detection and Cure**  
BioMed Research International  
Retraction (1 page), Article ID 9861926, Volume 2024 (2024)

**Retracted: Applications of Neural Network-Based Plan-Cancer Method for Primary Diagnosis of Mesothelioma Cancer**  
BioMed Research International  
Retraction (1 page), Article ID 9861895, Volume 2024 (2024)

**Retracted: Heterogeneous Network-Based Inductive Matrix Methods for Predicting Biomedical Gene Disease**  
BioMed Research International  
Retraction (1 page), Article ID 9856095, Volume 2024 (2024)

**Retracted: Developing an Efficient Cancer Detection and Prediction Tool Using Convolution Neural Network Integrated with Neural Pattern Recognition**  
BioMed Research International  
Retraction (1 page), Article ID 9853939, Volume 2024 (2024)

**Retracted: Lung Cancer Classification and Prediction Using Machine Learning and Image Processing**  
BioMed Research International  
Retraction (1 page), Article ID 9851527, Volume 2024 (2024)

**Retracted: CNN-Based Cross-Modal Residual Network for Image Synthesis**  
BioMed Research International  
Retraction (1 page), Article ID 9851230, Volume 2024 (2024)

**Retracted: Effect of Evodiamine on Collagen-Induced Platelet Activation and Thrombosis**  
BioMed Research International  
Retraction (1 page), Article ID 9850671, Volume 2024 (2024)

**Retracted: Diagnostic Significance of 3D Automated Breast Volume Scanner in a Combination with Contrast-Enhanced Ultrasound for Breast Cancer**  
BioMed Research International  
Retraction (1 page), Article ID 9846951, Volume 2024 (2024)

**Retracted: ML-Based Texture and Wavelet Features Extraction Technique to Predict Gastric Mesothelioma Cancer**  
BioMed Research International  
Retraction (1 page), Article ID 9842416, Volume 2024 (2024)

**Retracted: Multiresolution-Based Singular Value Decomposition Approach for Breast Cancer Image Classification**  
BioMed Research International  
Retraction (1 page), Article ID 9836827, Volume 2024 (2024)

# Contents

---

**Retracted: Multidimensional CNN-Based Deep Segmentation Method for Tumor Identification**

BioMed Research International

Retraction (1 page), Article ID 9836130, Volume 2024 (2024)

**Retracted: Principal Component and Path Analysis for Trait Selection Based on the Assessment of Diverse Lentil Populations Developed by Gamma-Irradiated Physical Mutation**

BioMed Research International

Retraction (1 page), Article ID 9835247, Volume 2024 (2024)

**Retracted: Prognostic Diagnosis for Breast Cancer Patients Using Probabilistic Bayesian Classification**

BioMed Research International

Retraction (1 page), Article ID 9834396, Volume 2024 (2024)

**Retracted: Attention Layer-Based Multidimensional Feature Extraction for Diagnosis of Lung Cancer**

BioMed Research International

Retraction (1 page), Article ID 9832129, Volume 2024 (2024)

**Retracted: Metaheuristic Optimization-Driven Novel Deep Learning Approach for Brain Tumor Segmentation**

BioMed Research International

Retraction (1 page), Article ID 9793501, Volume 2024 (2024)

**Retracted: Image Super-Resolution Reconstruction Method for Lung Cancer CT-Scanned Images Based on Neural Network**

BioMed Research International

Retraction (1 page), Article ID 9791081, Volume 2024 (2024)

**Retracted: Correlation-Based Mutual Information Model for Analysis of Lung Cancer CT Image**

BioMed Research International

Retraction (1 page), Article ID 9781059, Volume 2024 (2024)

**Retracted: Groundwater Suitability Evaluation Using Entropy Weightage Quality Index (EWQI) Model and Human Health Cancer Risk Assessment of Heavy Metal in Eastern India**

BioMed Research International

Retraction (1 page), Article ID 9768197, Volume 2024 (2024)

**Retracted: A Multi-Thresholding-Based Discriminative Neural Classifier for Detection of Retinoblastoma Using CNN Models**

BioMed Research International

Retraction (1 page), Article ID 9760632, Volume 2024 (2024)

**Retracted: Cyclic GAN Model to Classify Breast Cancer Data for Pathological Healthcare Task**

BioMed Research International

Retraction (1 page), Article ID 9759054, Volume 2024 (2024)



**Retracted: An Effective Machine Learning-Based Model for an Early Heart Disease Prediction**

BioMed Research International

Retraction (1 page), Article ID 9754362, Volume 2024 (2024)

**Retracted: Image Processing and Machine Learning-Based Classification and Detection of Liver Tumor**

BioMed Research International

Retraction (1 page), Article ID 9865170, Volume 2023 (2023)

**Retracted: Structural Modifications and Strategies for Native Starch for Applications in Advanced Drug Delivery**

BioMed Research International

Retraction (1 page), Article ID 9862042, Volume 2023 (2023)

**Retracted: Identification and Classification of Prostate Cancer Identification and Classification Based on Improved Convolution Neural Network**

BioMed Research International





Retraction (1 page), Article ID 9804727, Volume 2023 (2023)

**Retracted: Prediction Performance of Deep Learning for Colon Cancer Survival Prediction on SEER Data**

BioMed Research International







Retraction (1 page), Article ID 9867970, Volume 2023 (2023)

**[Retracted] An Effective Machine Learning-Based Model for an Early Heart Disease Prediction**

Pierre Claver Bizimana , Zuping Zhang , Muhammad Asim , and Ahmed A. Abd El-Latif 








Research Article (11 pages), Article ID 3531420, Volume 2023 (2023)

**[Retracted] Heterogeneous Network-Based Inductive Matrix Methods for Predicting Biomedical Gene Disease**

Pranjit Das , Loveleen Kumar , Sheshang Degadwala , Md. Nasre Alam , Vikash Jakhmola , and C. Rohith Bhat 

Research Article (13 pages), Article ID 7121514, Volume 2023 (2023)

**[Retracted] Ant Colony Optimization-Enabled CNN Deep Learning Technique for Accurate Detection of Cervical Cancer**

R. Kavitha , D. Kiruba Jothi , K. Saravanan , Mahendra Pratap Swain , José Luis Arias Gonzáles , Rakhi Joshi Bhardwaj , and Elijah Adomako 

Research Article (9 pages), Article ID 1742891, Volume 2023 (2023)








**[Retracted] A Multi-Thresholding-Based Discriminative Neural Classifier for Detection of Retinoblastoma Using CNN Models**

Parmod Kumar , D. Suganthi , K. Valarmathi , Mahendra Pratap Swain , Piyush Vashistha , Dharam Buddhi , and Emmanuel Sey 







Research Article (9 pages), Article ID 5803661, Volume 2023 (2023)

## Contents





**[Retracted] Applications of Neural Network-Based Plan-Cancer Method for Primary Diagnosis of Mesothelioma Cancer**

Dhiraj Kapila , Sarika Panwar , M. K. Mohan Maruga Raja , Tamal Mondal , Shaik Mohammad Rafi , Suryabhan Pratap Singh , and Bhupendra Kumar   
Research Article (10 pages), Article ID 3164166, Volume 2023 (2023)

**[Retracted] Developing an Efficient Cancer Detection and Prediction Tool Using Convolution Neural Network Integrated with Neural Pattern Recognition**

Roshan Gangurde , Vishal Jagota, Mohammad Shahbaz Khan , Viji Siva Sakthi , Udaya Mouni Boppana , Bernard Osei , and Kakarla Hari Kishore   
Research Article (11 pages), Article ID 6970256, Volume 2023 (2023)





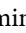

**[Retracted] Diagnosis of Prostate Cancer Using GLCM Enabled KNN Technique by Analyzing MRI Images**

L. Anand , Shivalal Mewada , WameedDeyah Shamsi , Mahyudin Ritonga , Noza Aflisia , Prakash KumarSarangi , and Moses NdoleArthur   
Research Article (7 pages), Article ID 3913351, Volume 2023 (2023)

**[Retracted] Lung Cancer Classification and Prediction Using Machine Learning and Image Processing**

Sharmila Nageswaran , G. Arunkumar , Anil Kumar Bisht , Shivalal Mewada , J. N. V. R. Swarup Kumar , Malik Jawarneh , and Evans Asenso   
Research Article (8 pages), Article ID 1755460, Volume 2022 (2022)








**[Retracted] Multidimensional CNN-Based Deep Segmentation Method for Tumor Identification**

R. John Martin , Uttam Sharma , Kiranjeet Kaur , Noor Mohammed Kadhim , Madonna Lamin , and Collins Sam Ayipeh   
Research Article (11 pages), Article ID 5061112, Volume 2022 (2022)


**[Retracted] Metaheuristic Optimization-Driven Novel Deep Learning Approach for Brain Tumor Segmentation**

R. Kalpana , M. Anto Bennet , and Abdul Wahab Rahmani   
Research Article (15 pages), Article ID 2980691, Volume 2022 (2022)







**[Retracted] Multiresolution-Based Singular Value Decomposition Approach for Breast Cancer Image Classification**

Suman Mann , Amit Kumar Bindal , Archana Balyan , Vijay Shukla , Zatin Gupta , Vivek Tomar , and Shahajan Miah   
Research Article (11 pages), Article ID 6392206, Volume 2022 (2022)









**[Retracted] The Optos 200Tx Scanning Laser Ophthalmoscope Application in Retinoblastoma Patients' Follow-Up**

Xuehao Cui, Xunda Ji, Yan Shao, Peiquan Zhao, and Xiaorong Li   
Research Article (5 pages), Article ID 5422360, Volume 2022 (2022)

**[Retracted] CNN-Based Cross-Modal Residual Network for Image Synthesis**

Rajeev Kumar , Vaibhav Bhatnagar , Amit Jain , Mahesh Singh , Z. H. Kareem , and R. Sugumar   
Research Article (9 pages), Article ID 6399730, Volume 2022 (2022)








**[Retracted] Structural Modifications and Strategies for Native Starch for Applications in Advanced Drug Delivery**

Pankaj Bhatt , Vipin Kumar , Richa Goel , Somesh Kumar Sharma , Shikha Kaushik , Shivani Sharma , Alankar Shrivastava , and Mulugeta Tesema   
Research Article (14 pages), Article ID 2188940, Volume 2022 (2022)







**[Retracted] PSO-Based Evolutionary Approach to Optimize Head and Neck Biomedical Image to Detect Mesothelioma Cancer**

Sheeba Praveen , Neha Tyagi , Bhagwant Singh , Girija Rani Karetla , Meenakshi Anurag Thalor , Kapil Joshi , and Melkamu Tsegaye   
Research Article (12 pages), Article ID 3618197, Volume 2022 (2022)


**[Retracted] Diagnostic Significance of 3D Automated Breast Volume Scanner in a Combination with Contrast-Enhanced Ultrasound for Breast Cancer**

Quan Yuan , Canxu Song , Yan Tian , Nan Chen , Xing He , Ying Wang , and Pihua Han   
Research Article (8 pages), Article ID 3199884, Volume 2022 (2022)






**[Retracted] Correlation-Based Mutual Information Model for Analysis of Lung Cancer CT Image**

N. Shanmuga Vadivu , Gauri Gupta , Quadri Noorulhasan Naveed , Tariq Rasheed , Sitesh Kumar Singh , and Dharmesh Dhabliya   
Research Article (12 pages), Article ID 6451770, Volume 2022 (2022)

**[Retracted] Effects of Sacubitril/Valsartan on the Expression of CaMKII/Ca<sub>v</sub>1.2 in Atrial Fibrillation Stimulation Rabbit Model**

Qi Lou, Lu-yi-fei Li, Guang-zhong Liu, Cheng-chuang Zhan, Li Zhang, Yan-xiang Zang, and Wei-min Li   
Research Article (8 pages), Article ID 5832543, Volume 2022 (2022)

**[Retracted] Classification and Detection of Mesothelioma Cancer Using Feature Selection-Enabled Machine Learning Technique**

M. Shobana , V. R. Balasraswathi , R. Radhika , Ahmed Kareem Oleiwi , Sushovan Chaudhury , Ajay S. Ladkat , Mohd Naved , and Abdul Wahab Rahmani   
Research Article (6 pages), Article ID 9900668, Volume 2022 (2022)

**[Retracted] Effect of Evodiamine on Collagen-Induced Platelet Activation and Thrombosis**









Xiaona Yang, Min Leng, Lihong Yang, Yunzhu Peng, Jing Wang , Qian Wang, Kun Wu, Junhua Zou, Wen Wan, Longjun Li, Yujia Ye , and Zhaohui Meng   
Research Article (10 pages), Article ID 4893859, Volume 2022 (2022)

## Contents







**[Retracted] Image Processing and Machine Learning-Based Classification and Detection of Liver Tumor**

V. Durga Prasad Jasti , Enagandula Prasad , Manish Sawale , Shivilal Mewada , Manoj L. Bangare , Pushpa M. Bangare , Sunil L. Bangare , and F. Sammy   
Research Article (7 pages), Article ID 3398156, Volume 2022 (2022)







**[Retracted] Detection of Pancreatic Cancer in CT Scan Images Using PSO SVM and Image Processing**

Arshiya S. Ansari , Abu Sarwar Zamani , Mohammad Sajid Mohammadi , Meenakshi , Mahyudin Ritonga , Syed Sohail Ahmed , Devabalan Pounraj , and Karthikeyan Kaliyaperumal   
Research Article (7 pages), Article ID 8544337, Volume 2022 (2022)









**[Retracted] Prognostic Diagnosis for Breast Cancer Patients Using Probabilistic Bayesian Classification**

N. Junath , Alok Bharadwaj , Sachin Tyagi , Kalpana Sengar , Mohammad Najmus Saquib Hasan , and M. Jayasudha   
Research Article (10 pages), Article ID 1859222, Volume 2022 (2022)







**[Retracted] Cyclic GAN Model to Classify Breast Cancer Data for Pathological Healthcare Task**

Pooja Chopra , N. Junath , Sitesh Kumar Singh , Shakir Khan , R. Sugumar , and Mithun Bhowmick   
Research Article (12 pages), Article ID 6336700, Volume 2022 (2022)

**[Retracted] Principal Component and Path Analysis for Trait Selection Based on the Assessment of Diverse Lentil Populations Developed by Gamma-Irradiated Physical Mutation**

Sandip Debnath , Abhik Sarkar , Kahkashan Perveen , Najat A. Bukhari , Kavindra Kumar Kesari , Amit Verma , Nihar Ranjan Chakraborty , and Mulugeta Tesema   
Research Article (14 pages), Article ID 9679181, Volume 2022 (2022)







**[Retracted] Identification and Classification of Prostate Cancer Identification and Classification Based on Improved Convolution Neural Network**








Shobha Tyagi , Neha Tyagi , Amarendranath Choudhury , Gauri Gupta , Musaddak Maher Abdul Zahra , and Saima Ahmed Rahin   
Research Article (10 pages), Article ID 9112587, Volume 2022 (2022)







**[Retracted] Image Super-Resolution Reconstruction Method for Lung Cancer CT-Scanned Images Based on Neural Network**







Jianming Xu , Weichun Liu, Yang Qin, and Guangrong Xu  
Research Article (10 pages), Article ID 3543531, Volume 2022 (2022)







**[Retracted] Groundwater Suitability Evaluation Using Entropy Weightage Quality Index (EWQI) Model and Human Health Cancer Risk Assessment of Heavy Metal in Eastern India**







Shivam Saw , Prasoon Kumar Singh , Jaydev Kumar Mahato , Rohit Patel , Deepak Naresh Dhopte , and Evans Asenso   
Research Article (14 pages), Article ID 2476126, Volume 2022 (2022)


**[Retracted] Appropriate Supervised Machine Learning Techniques for Mesothelioma Detection and Cure**  
Komal Saxena , Abu Sarwar Zamani , R. Bhavani , K. V. Daya Sagar , Pushpa M. Bangare , S. Ashwini , and Saima Ahmed Rahin   
Research Article (11 pages), Article ID 2318101, Volume 2022 (2022)

**[Retracted] ML-Based Texture and Wavelet Features Extraction Technique to Predict Gastric Mesothelioma Cancer**  
Neeraj Garg , Divyanshu Sinha , Babita Yadav , Bhoomi Gupta , Sachin Gupta , and Shahajan Miah   
Research Article (9 pages), Article ID 1012684, Volume 2022 (2022)

**[Retracted] Attention Layer-Based Multidimensional Feature Extraction for Diagnosis of Lung Cancer**  
Manisha Bhende , Anuradha Thakare , V. Saravanan , K. Anbazhagan , Hemant N. Patel , and Ashok Kumar   
Research Article (11 pages), Article ID 3947434, Volume 2022 (2022)

**[Retracted] Deep Learning-Based Real-Time Discriminate Correlation Analysis for Breast Cancer Detection**  
Manisha Bhende , Anuradha Thakare , Bhasker Pant , Piyush Singhal , Swati Shinde , and V. Saravanan   
Research Article (12 pages), Article ID 4609625, Volume 2022 (2022)

**[Retracted] Prediction Performance of Deep Learning for Colon Cancer Survival Prediction on SEER Data**  
Surbhi Gupta , S. Kalaivani , Archana Rajasundaram , Gaurav Kumar Ameta , Ahmed Kareem Oleiwi , and Betty Nokobi Dugbakie   
Research Article (12 pages), Article ID 1467070, Volume 2022 (2022)

**[Retracted] Dynamic Data Infrastructure Security for Interoperable e-Healthcare Systems: A Semantic Feature-Driven NoSQL Intrusion Attack Detection Model**  
R. Sreejith  and S. Senthil  
Research Article (26 pages), Article ID 4080199, Volume 2022 (2022)

## *Retraction*

# **Retracted: Dynamic Data Infrastructure Security for Interoperable e-Healthcare Systems: A Semantic Feature-Driven NoSQL Intrusion Attack Detection Model**

### **BioMed Research International**

Received 8 January 2024; Accepted 8 January 2024; Published 12 February 2024

Copyright © 2024 BioMed Research International. This is an open access article distributed under the Creative Commons Attribution License, which permits unrestricted use, distribution, and reproduction in any medium, provided the original work is properly cited.

This article has been retracted by Hindawi following an investigation undertaken by the publisher [1]. This investigation has uncovered evidence of one or more of the following indicators of systematic manipulation of the publication process:

- (1) Discrepancies in scope
- (2) Discrepancies in the description of the research reported
- (3) Discrepancies between the availability of data and the research described
- (4) Inappropriate citations
- (5) Incoherent, meaningless and/or irrelevant content included in the article
- (6) Manipulated or compromised peer review

The presence of these indicators undermines our confidence in the integrity of the article's content and we cannot, therefore, vouch for its reliability. Please note that this notice is intended solely to alert readers that the content of this article is unreliable. We have not investigated whether authors were aware of or involved in the systematic manipulation of the publication process.

Wiley and Hindawi regrets that the usual quality checks did not identify these issues before publication and have since put additional measures in place to safeguard research integrity.

We wish to credit our own Research Integrity and Research Publishing teams and anonymous and named external researchers and research integrity experts for contributing to this investigation.

The corresponding author, as the representative of all authors, has been given the opportunity to register their agreement or disagreement to this retraction. We have kept a record of any response received.

### **References**

- [1] R. Sreejith and S. Senthil, "Dynamic Data Infrastructure Security for Interoperable e-Healthcare Systems: A Semantic Feature-Driven NoSQL Intrusion Attack Detection Model," *BioMed Research International*, vol. 2022, Article ID 4080199, 26 pages, 2022.

## Retraction

# Retracted: The Optos 200Tx Scanning Laser Ophthalmoscope Application in Retinoblastoma Patients' Follow-Up

### BioMed Research International

Received 8 January 2024; Accepted 8 January 2024; Published 9 January 2024

Copyright © 2024 BioMed Research International. This is an open access article distributed under the Creative Commons Attribution License, which permits unrestricted use, distribution, and reproduction in any medium, provided the original work is properly cited.

This article has been retracted by Hindawi following an investigation undertaken by the publisher [1]. This investigation has uncovered evidence of one or more of the following indicators of systematic manipulation of the publication process:

- (1) Discrepancies in scope
- (2) Discrepancies in the description of the research reported
- (3) Discrepancies between the availability of data and the research described
- (4) Inappropriate citations
- (5) Incoherent, meaningless and/or irrelevant content included in the article
- (6) Manipulated or compromised peer review

The presence of these indicators undermines our confidence in the integrity of the article's content and we cannot, therefore, vouch for its reliability. Please note that this notice is intended solely to alert readers that the content of this article is unreliable. We have not investigated whether authors were aware of or involved in the systematic manipulation of the publication process.

Wiley and Hindawi regrets that the usual quality checks did not identify these issues before publication and have since put additional measures in place to safeguard research integrity.

We wish to credit our own Research Integrity and Research Publishing teams and anonymous and named external researchers and research integrity experts for contributing to this investigation.

The corresponding author, as the representative of all authors, has been given the opportunity to register their agreement or disagreement to this retraction. We have kept a record of any response received.

### References

- [1] X. Cui, X. Ji, Y. Shao, P. Zhao, and X. Li, "The Optos 200Tx Scanning Laser Ophthalmoscope Application in Retinoblastoma Patients' Follow-Up," *BioMed Research International*, vol. 2022, Article ID 5422360, 5 pages, 2022.

## Retraction

# Retracted: Deep Learning-Based Real-Time Discriminate Correlation Analysis for Breast Cancer Detection

### BioMed Research International

Received 8 January 2024; Accepted 8 January 2024; Published 9 January 2024

Copyright © 2024 BioMed Research International. This is an open access article distributed under the Creative Commons Attribution License, which permits unrestricted use, distribution, and reproduction in any medium, provided the original work is properly cited.

This article has been retracted by Hindawi following an investigation undertaken by the publisher [1]. This investigation has uncovered evidence of one or more of the following indicators of systematic manipulation of the publication process:

- (1) Discrepancies in scope
- (2) Discrepancies in the description of the research reported
- (3) Discrepancies between the availability of data and the research described
- (4) Inappropriate citations
- (5) Incoherent, meaningless and/or irrelevant content included in the article
- (6) Manipulated or compromised peer review

The presence of these indicators undermines our confidence in the integrity of the article's content and we cannot, therefore, vouch for its reliability. Please note that this notice is intended solely to alert readers that the content of this article is unreliable. We have not investigated whether authors were aware of or involved in the systematic manipulation of the publication process.

Wiley and Hindawi regrets that the usual quality checks did not identify these issues before publication and have since put additional measures in place to safeguard research integrity.

We wish to credit our own Research Integrity and Research Publishing teams and anonymous and named external researchers and research integrity experts for contributing to this investigation.

The corresponding author, as the representative of all authors, has been given the opportunity to register their agreement or disagreement to this retraction. We have kept a record of any response received.

### References

- [1] M. Bhende, A. Thakare, B. Pant, P. Singhal, S. Shinde, and V. Saravanan, "Deep Learning-Based Real-Time Discriminate Correlation Analysis for Breast Cancer Detection," *BioMed Research International*, vol. 2022, Article ID 4609625, 12 pages, 2022.



## Retraction

# Retracted: Effects of Sacubitril/Valsartan on the Expression of CaMKII/Ca<sub>v</sub>1.2 in Atrial Fibrillation Stimulation Rabbit Model

### BioMed Research International

Received 8 January 2024; Accepted 8 January 2024; Published 9 January 2024

Copyright © 2024 BioMed Research International. This is an open access article distributed under the Creative Commons Attribution License, which permits unrestricted use, distribution, and reproduction in any medium, provided the original work is properly cited.

This article has been retracted by Hindawi following an investigation undertaken by the publisher [1]. This investigation has uncovered evidence of one or more of the following indicators of systematic manipulation of the publication process:

- (1) Discrepancies in scope
- (2) Discrepancies in the description of the research reported
- (3) Discrepancies between the availability of data and the research described
- (4) Inappropriate citations
- (5) Incoherent, meaningless and/or irrelevant content included in the article
- (6) Manipulated or compromised peer review

The presence of these indicators undermines our confidence in the integrity of the article's content and we cannot, therefore, vouch for its reliability. Please note that this notice is intended solely to alert readers that the content of this article is unreliable. We have not investigated whether authors were aware of or involved in the systematic manipulation of the publication process.

Wiley and Hindawi regrets that the usual quality checks did not identify these issues before publication and have since put additional measures in place to safeguard research integrity.

We wish to credit our own Research Integrity and Research Publishing teams and anonymous and named external researchers and research integrity experts for contributing to this investigation.

The corresponding author, as the representative of all authors, has been given the opportunity to register their agreement or disagreement to this retraction. We have kept a record of any response received.

### References

- [1] Q. Lou, L.-y.-f. Li, G.-z. Liu et al., "Effects of Sacubitril/Valsartan on the Expression of CaMKII/Ca<sub>v</sub>1.2 in Atrial Fibrillation Stimulation Rabbit Model," *BioMed Research International*, vol. 2022, Article ID 5832543, 8 pages, 2022.

## Retraction

# Retracted: Ant Colony Optimization-Enabled CNN Deep Learning Technique for Accurate Detection of Cervical Cancer

### BioMed Research International

Received 8 January 2024; Accepted 8 January 2024; Published 9 January 2024

Copyright © 2024 BioMed Research International. This is an open access article distributed under the Creative Commons Attribution License, which permits unrestricted use, distribution, and reproduction in any medium, provided the original work is properly cited.

This article has been retracted by Hindawi following an investigation undertaken by the publisher [1]. This investigation has uncovered evidence of one or more of the following indicators of systematic manipulation of the publication process:

- (1) Discrepancies in scope
- (2) Discrepancies in the description of the research reported
- (3) Discrepancies between the availability of data and the research described
- (4) Inappropriate citations
- (5) Incoherent, meaningless and/or irrelevant content included in the article
- (6) Manipulated or compromised peer review

The presence of these indicators undermines our confidence in the integrity of the article's content and we cannot, therefore, vouch for its reliability. Please note that this notice is intended solely to alert readers that the content of this article is unreliable. We have not investigated whether authors were aware of or involved in the systematic manipulation of the publication process.

Wiley and Hindawi regrets that the usual quality checks did not identify these issues before publication and have since put additional measures in place to safeguard research integrity.

We wish to credit our own Research Integrity and Research Publishing teams and anonymous and named external researchers and research integrity experts for contributing to this investigation.

The corresponding author, as the representative of all authors, has been given the opportunity to register their agreement or disagreement to this retraction. We have kept a record of any response received.

### References

- [1] R. Kavitha, D. K. Jothi, K. Saravanan et al., "Ant Colony Optimization-Enabled CNN Deep Learning Technique for Accurate Detection of Cervical Cancer," *BioMed Research International*, vol. 2023, Article ID 1742891, 9 pages, 2023.

## Retraction

# Retracted: Diagnosis of Prostate Cancer Using GLCM Enabled KNN Technique by Analyzing MRI Images

### BioMed Research International

Received 8 January 2024; Accepted 8 January 2024; Published 9 January 2024

Copyright © 2024 BioMed Research International. This is an open access article distributed under the Creative Commons Attribution License, which permits unrestricted use, distribution, and reproduction in any medium, provided the original work is properly cited.

This article has been retracted by Hindawi following an investigation undertaken by the publisher [1]. This investigation has uncovered evidence of one or more of the following indicators of systematic manipulation of the publication process:

- (1) Discrepancies in scope
- (2) Discrepancies in the description of the research reported
- (3) Discrepancies between the availability of data and the research described
- (4) Inappropriate citations
- (5) Incoherent, meaningless and/or irrelevant content included in the article
- (6) Manipulated or compromised peer review

The presence of these indicators undermines our confidence in the integrity of the article's content and we cannot, therefore, vouch for its reliability. Please note that this notice is intended solely to alert readers that the content of this article is unreliable. We have not investigated whether authors were aware of or involved in the systematic manipulation of the publication process.

Wiley and Hindawi regrets that the usual quality checks did not identify these issues before publication and have since put additional measures in place to safeguard research integrity.

We wish to credit our own Research Integrity and Research Publishing teams and anonymous and named external researchers and research integrity experts for contributing to this investigation.

The corresponding author, as the representative of all authors, has been given the opportunity to register their agreement or disagreement to this retraction. We have kept a record of any response received.

### References

- [1] L. Anand, S. Mewada, W. Shamsi et al., "Diagnosis of Prostate Cancer Using GLCM Enabled KNN Technique by Analyzing MRI Images," *BioMed Research International*, vol. 2023, Article ID 3913351, 7 pages, 2023.

## Retraction

# Retracted: PSO-Based Evolutionary Approach to Optimize Head and Neck Biomedical Image to Detect Mesothelioma Cancer

### BioMed Research International

Received 8 January 2024; Accepted 8 January 2024; Published 9 January 2024

Copyright © 2024 BioMed Research International. This is an open access article distributed under the Creative Commons Attribution License, which permits unrestricted use, distribution, and reproduction in any medium, provided the original work is properly cited.

This article has been retracted by Hindawi following an investigation undertaken by the publisher [1]. This investigation has uncovered evidence of one or more of the following indicators of systematic manipulation of the publication process:

- (1) Discrepancies in scope
- (2) Discrepancies in the description of the research reported
- (3) Discrepancies between the availability of data and the research described
- (4) Inappropriate citations
- (5) Incoherent, meaningless and/or irrelevant content included in the article
- (6) Manipulated or compromised peer review

The presence of these indicators undermines our confidence in the integrity of the article's content and we cannot, therefore, vouch for its reliability. Please note that this notice is intended solely to alert readers that the content of this article is unreliable. We have not investigated whether authors were aware of or involved in the systematic manipulation of the publication process.

Wiley and Hindawi regrets that the usual quality checks did not identify these issues before publication and have since put additional measures in place to safeguard research integrity.

We wish to credit our own Research Integrity and Research Publishing teams and anonymous and named external researchers and research integrity experts for contributing to this investigation.

The corresponding author, as the representative of all authors, has been given the opportunity to register their agreement or disagreement to this retraction. We have kept a record of any response received.

### References

- [1] S. Praveen, N. Tyagi, B. Singh et al., "PSO-Based Evolutionary Approach to Optimize Head and Neck Biomedical Image to Detect Mesothelioma Cancer," *BioMed Research International*, vol. 2022, Article ID 3618197, 12 pages, 2022.

## *Retraction*

# **Retracted: Classification and Detection of Mesothelioma Cancer Using Feature Selection-Enabled Machine Learning Technique**

### **BioMed Research International**

Received 8 January 2024; Accepted 8 January 2024; Published 9 January 2024

Copyright © 2024 BioMed Research International. This is an open access article distributed under the Creative Commons Attribution License, which permits unrestricted use, distribution, and reproduction in any medium, provided the original work is properly cited.

This article has been retracted by Hindawi, as publisher, following an investigation undertaken by the publisher [1]. This investigation has uncovered evidence of systematic manipulation of the publication and peer-review process. We cannot, therefore, vouch for the reliability or integrity of this article.

Please note that this notice is intended solely to alert readers that the peer-review process of this article has been compromised.

Wiley and Hindawi regret that the usual quality checks did not identify these issues before publication and have since put additional measures in place to safeguard research integrity.

We wish to credit our Research Integrity and Research Publishing teams and anonymous and named external researchers and research integrity experts for contributing to this investigation.

The corresponding author, as the representative of all authors, has been given the opportunity to register their agreement or disagreement to this retraction. We have kept a record of any response received.

### **References**

- [1] M. Shobana, V. R. Balasrswathi, R. Radhika et al., "Classification and Detection of Mesothelioma Cancer Using Feature Selection-Enabled Machine Learning Technique," *BioMed Research International*, vol. 2022, Article ID 9900668, 6 pages, 2022.

## Retraction

# Retracted: Detection of Pancreatic Cancer in CT Scan Images Using PSO SVM and Image Processing

### BioMed Research International

Received 8 January 2024; Accepted 8 January 2024; Published 9 January 2024

Copyright © 2024 BioMed Research International. This is an open access article distributed under the Creative Commons Attribution License, which permits unrestricted use, distribution, and reproduction in any medium, provided the original work is properly cited.

This article has been retracted by Hindawi following an investigation undertaken by the publisher [1]. This investigation has uncovered evidence of one or more of the following indicators of systematic manipulation of the publication process:

- (1) Discrepancies in scope
- (2) Discrepancies in the description of the research reported
- (3) Discrepancies between the availability of data and the research described
- (4) Inappropriate citations
- (5) Incoherent, meaningless and/or irrelevant content included in the article
- (6) Manipulated or compromised peer review

The presence of these indicators undermines our confidence in the integrity of the article's content and we cannot, therefore, vouch for its reliability. Please note that this notice is intended solely to alert readers that the content of this article is unreliable. We have not investigated whether authors were aware of or involved in the systematic manipulation of the publication process.

Wiley and Hindawi regrets that the usual quality checks did not identify these issues before publication and have since put additional measures in place to safeguard research integrity.

We wish to credit our own Research Integrity and Research Publishing teams and anonymous and named external researchers and research integrity experts for contributing to this investigation.

The corresponding author, as the representative of all authors, has been given the opportunity to register their agreement or disagreement to this retraction. We have kept a record of any response received.

### References

- [1] A. S. Ansari, A. S. Zamani, M. S. Mohammadi et al., "Detection of Pancreatic Cancer in CT Scan Images Using PSO SVM and Image Processing," *BioMed Research International*, vol. 2022, Article ID 8544337, 7 pages, 2022.

## *Retraction*

# **Retracted: Appropriate Supervised Machine Learning Techniques for Mesothelioma Detection and Cure**

### **BioMed Research International**

Received 8 January 2024; Accepted 8 January 2024; Published 9 January 2024

Copyright © 2024 BioMed Research International. This is an open access article distributed under the Creative Commons Attribution License, which permits unrestricted use, distribution, and reproduction in any medium, provided the original work is properly cited.

This article has been retracted by Hindawi, as publisher, following an investigation undertaken by the publisher [1]. This investigation has uncovered evidence of systematic manipulation of the publication and peer-review process. We cannot, therefore, vouch for the reliability or integrity of this article.

Please note that this notice is intended solely to alert readers that the peer-review process of this article has been compromised.

Wiley and Hindawi regret that the usual quality checks did not identify these issues before publication and have since put additional measures in place to safeguard research integrity.

We wish to credit our Research Integrity and Research Publishing teams and anonymous and named external researchers and research integrity experts for contributing to this investigation.

The corresponding author, as the representative of all authors, has been given the opportunity to register their agreement or disagreement to this retraction. We have kept a record of any response received.

### **References**

- [1] K. Saxena, A. S. Zamani, R. Bhavani et al., "Appropriate Supervised Machine Learning Techniques for Mesothelioma Detection and Cure," *BioMed Research International*, vol. 2022, Article ID 2318101, 11 pages, 2022.

## *Retraction*

# **Retracted: Applications of Neural Network-Based Plan-Cancer Method for Primary Diagnosis of Mesothelioma Cancer**

### **BioMed Research International**

Received 8 January 2024; Accepted 8 January 2024; Published 9 January 2024

Copyright © 2024 BioMed Research International. This is an open access article distributed under the Creative Commons Attribution License, which permits unrestricted use, distribution, and reproduction in any medium, provided the original work is properly cited.

This article has been retracted by Hindawi, as publisher, following an investigation undertaken by the publisher [1]. This investigation has uncovered evidence of systematic manipulation of the publication and peer-review process. We cannot, therefore, vouch for the reliability or integrity of this article.

Please note that this notice is intended solely to alert readers that the peer-review process of this article has been compromised.

Wiley and Hindawi regret that the usual quality checks did not identify these issues before publication and have since put additional measures in place to safeguard research integrity.

We wish to credit our Research Integrity and Research Publishing teams and anonymous and named external researchers and research integrity experts for contributing to this investigation.

The corresponding author, as the representative of all authors, has been given the opportunity to register their agreement or disagreement to this retraction. We have kept a record of any response received.

### **References**

- [1] D. Kapila, S. Panwar, M. K. M. M. Raja et al., “Applications of Neural Network-Based Plan-Cancer Method for Primary Diagnosis of Mesothelioma Cancer,” *BioMed Research International*, vol. 2023, Article ID 3164166, 10 pages, 2023.



## Retraction

# Retracted: Heterogeneous Network-Based Inductive Matrix Methods for Predicting Biomedical Gene Disease

### BioMed Research International

Received 8 January 2024; Accepted 8 January 2024; Published 9 January 2024

Copyright © 2024 BioMed Research International. This is an open access article distributed under the Creative Commons Attribution License, which permits unrestricted use, distribution, and reproduction in any medium, provided the original work is properly cited.

This article has been retracted by Hindawi following an investigation undertaken by the publisher [1]. This investigation has uncovered evidence of one or more of the following indicators of systematic manipulation of the publication process:

- (1) Discrepancies in scope
- (2) Discrepancies in the description of the research reported
- (3) Discrepancies between the availability of data and the research described
- (4) Inappropriate citations
- (5) Incoherent, meaningless and/or irrelevant content included in the article
- (6) Manipulated or compromised peer review

The presence of these indicators undermines our confidence in the integrity of the article's content and we cannot, therefore, vouch for its reliability. Please note that this notice is intended solely to alert readers that the content of this article is unreliable. We have not investigated whether authors were aware of or involved in the systematic manipulation of the publication process.

Wiley and Hindawi regrets that the usual quality checks did not identify these issues before publication and have since put additional measures in place to safeguard research integrity.

We wish to credit our own Research Integrity and Research Publishing teams and anonymous and named external researchers and research integrity experts for contributing to this investigation.

The corresponding author, as the representative of all authors, has been given the opportunity to register their agreement or disagreement to this retraction. We have kept a record of any response received.

### References

- [1] P. Das, L. Kumar, S. Degadwala, M. N. Alam, V. Jakhmola, and C. R. Bhat, "Heterogeneous Network-Based Inductive Matrix Methods for Predicting Biomedical Gene Disease," *BioMed Research International*, vol. 2023, Article ID 7121514, 13 pages, 2023.

## *Retraction*

# **Retracted: Developing an Efficient Cancer Detection and Prediction Tool Using Convolution Neural Network Integrated with Neural Pattern Recognition**

### **BioMed Research International**

Received 8 January 2024; Accepted 8 January 2024; Published 9 January 2024

Copyright © 2024 BioMed Research International. This is an open access article distributed under the Creative Commons Attribution License, which permits unrestricted use, distribution, and reproduction in any medium, provided the original work is properly cited.

This article has been retracted by Hindawi following an investigation undertaken by the publisher [1]. This investigation has uncovered evidence of one or more of the following indicators of systematic manipulation of the publication process:

- (1) Discrepancies in scope
- (2) Discrepancies in the description of the research reported
- (3) Discrepancies between the availability of data and the research described
- (4) Inappropriate citations
- (5) Incoherent, meaningless and/or irrelevant content included in the article
- (6) Manipulated or compromised peer review

The presence of these indicators undermines our confidence in the integrity of the article's content and we cannot, therefore, vouch for its reliability. Please note that this notice is intended solely to alert readers that the content of this article is unreliable. We have not investigated whether authors were aware of or involved in the systematic manipulation of the publication process.

Wiley and Hindawi regrets that the usual quality checks did not identify these issues before publication and have since put additional measures in place to safeguard research integrity.

We wish to credit our own Research Integrity and Research Publishing teams and anonymous and named external researchers and research integrity experts for contributing to this investigation.

The corresponding author, as the representative of all authors, has been given the opportunity to register their agreement or disagreement to this retraction. We have kept a record of any response received.

### **References**

- [1] R. Gangurde, V. Jagota, M. S. Khan et al., "Developing an Efficient Cancer Detection and Prediction Tool Using Convolution Neural Network Integrated with Neural Pattern Recognition," *BioMed Research International*, vol. 2023, Article ID 6970256, 11 pages, 2023.

## *Retraction*

# **Retracted: Lung Cancer Classification and Prediction Using Machine Learning and Image Processing**

### **BioMed Research International**

Received 8 January 2024; Accepted 8 January 2024; Published 9 January 2024

Copyright © 2024 BioMed Research International. This is an open access article distributed under the Creative Commons Attribution License, which permits unrestricted use, distribution, and reproduction in any medium, provided the original work is properly cited.

This article has been retracted by Hindawi, as publisher, following an investigation undertaken by the publisher [1]. This investigation has uncovered evidence of systematic manipulation of the publication and peer-review process. We cannot, therefore, vouch for the reliability or integrity of this article.

Please note that this notice is intended solely to alert readers that the peer-review process of this article has been compromised.

Wiley and Hindawi regret that the usual quality checks did not identify these issues before publication and have since put additional measures in place to safeguard research integrity.

We wish to credit our Research Integrity and Research Publishing teams and anonymous and named external researchers and research integrity experts for contributing to this investigation.

The corresponding author, as the representative of all authors, has been given the opportunity to register their agreement or disagreement to this retraction. We have kept a record of any response received.

### **References**

- [1] S. Nageswaran, G. Arunkumar, A. K. Bisht et al., “Lung Cancer Classification and Prediction Using Machine Learning and Image Processing,” *BioMed Research International*, vol. 2022, Article ID 1755460, 8 pages, 2022.

## *Retraction*

# **Retracted: CNN-Based Cross-Modal Residual Network for Image Synthesis**

### **BioMed Research International**

Received 8 January 2024; Accepted 8 January 2024; Published 9 January 2024

Copyright © 2024 BioMed Research International. This is an open access article distributed under the Creative Commons Attribution License, which permits unrestricted use, distribution, and reproduction in any medium, provided the original work is properly cited.

This article has been retracted by Hindawi, as publisher, following an investigation undertaken by the publisher [1]. This investigation has uncovered evidence of systematic manipulation of the publication and peer-review process. We cannot, therefore, vouch for the reliability or integrity of this article.

Please note that this notice is intended solely to alert readers that the peer-review process of this article has been compromised.

Wiley and Hindawi regret that the usual quality checks did not identify these issues before publication and have since put additional measures in place to safeguard research integrity.

We wish to credit our Research Integrity and Research Publishing teams and anonymous and named external researchers and research integrity experts for contributing to this investigation.

The corresponding author, as the representative of all authors, has been given the opportunity to register their agreement or disagreement to this retraction. We have kept a record of any response received.

### **References**

- [1] R. Kumar, V. Bhatnagar, A. Jain, M. Singh, Z. H. Kareem, and R. Sugumar, "CNN-Based Cross-Modal Residual Network for Image Synthesis," *BioMed Research International*, vol. 2022, Article ID 6399730, 9 pages, 2022.

## Retraction

# Retracted: Effect of Evodiamine on Collagen-Induced Platelet Activation and Thrombosis

### BioMed Research International

Received 8 January 2024; Accepted 8 January 2024; Published 9 January 2024

Copyright © 2024 BioMed Research International. This is an open access article distributed under the Creative Commons Attribution License, which permits unrestricted use, distribution, and reproduction in any medium, provided the original work is properly cited.

This article has been retracted by Hindawi following an investigation undertaken by the publisher [1]. This investigation has uncovered evidence of one or more of the following indicators of systematic manipulation of the publication process:

- (1) Discrepancies in scope
- (2) Discrepancies in the description of the research reported
- (3) Discrepancies between the availability of data and the research described
- (4) Inappropriate citations
- (5) Incoherent, meaningless and/or irrelevant content included in the article
- (6) Manipulated or compromised peer review

The presence of these indicators undermines our confidence in the integrity of the article's content and we cannot, therefore, vouch for its reliability. Please note that this notice is intended solely to alert readers that the content of this article is unreliable. We have not investigated whether authors were aware of or involved in the systematic manipulation of the publication process.

Wiley and Hindawi regrets that the usual quality checks did not identify these issues before publication and have since put additional measures in place to safeguard research integrity.

We wish to credit our own Research Integrity and Research Publishing teams and anonymous and named external researchers and research integrity experts for contributing to this investigation.

The corresponding author, as the representative of all authors, has been given the opportunity to register their agreement or disagreement to this retraction. We have kept a record of any response received.

### References

- [1] X. Yang, M. Leng, L. Yang et al., "Effect of Evodiamine on Collagen-Induced Platelet Activation and Thrombosis," *BioMed Research International*, vol. 2022, Article ID 4893859, 10 pages, 2022.

## *Retraction*

# **Retracted: Diagnostic Significance of 3D Automated Breast Volume Scanner in a Combination with Contrast-Enhanced Ultrasound for Breast Cancer**

### **BioMed Research International**

Received 8 January 2024; Accepted 8 January 2024; Published 9 January 2024

Copyright © 2024 BioMed Research International. This is an open access article distributed under the Creative Commons Attribution License, which permits unrestricted use, distribution, and reproduction in any medium, provided the original work is properly cited.

This article has been retracted by Hindawi following an investigation undertaken by the publisher [1]. This investigation has uncovered evidence of one or more of the following indicators of systematic manipulation of the publication process:

- (1) Discrepancies in scope
- (2) Discrepancies in the description of the research reported
- (3) Discrepancies between the availability of data and the research described
- (4) Inappropriate citations
- (5) Incoherent, meaningless and/or irrelevant content included in the article
- (6) Manipulated or compromised peer review

The presence of these indicators undermines our confidence in the integrity of the article's content and we cannot, therefore, vouch for its reliability. Please note that this notice is intended solely to alert readers that the content of this article is unreliable. We have not investigated whether authors were aware of or involved in the systematic manipulation of the publication process.

Wiley and Hindawi regrets that the usual quality checks did not identify these issues before publication and have since put additional measures in place to safeguard research integrity.

We wish to credit our own Research Integrity and Research Publishing teams and anonymous and named external researchers and research integrity experts for contributing to this investigation.

The corresponding author, as the representative of all authors, has been given the opportunity to register their agreement or disagreement to this retraction. We have kept a record of any response received.

### **References**

- [1] Q. Yuan, C. Song, Y. Tian et al., "Diagnostic Significance of 3D Automated Breast Volume Scanner in a Combination with Contrast-Enhanced Ultrasound for Breast Cancer," *BioMed Research International*, vol. 2022, Article ID 3199884, 8 pages, 2022.

## *Retraction*

# **Retracted: ML-Based Texture and Wavelet Features Extraction Technique to Predict Gastric Mesothelioma Cancer**

### **BioMed Research International**

Received 8 January 2024; Accepted 8 January 2024; Published 9 January 2024

Copyright © 2024 BioMed Research International. This is an open access article distributed under the Creative Commons Attribution License, which permits unrestricted use, distribution, and reproduction in any medium, provided the original work is properly cited.

This article has been retracted by Hindawi, as publisher, following an investigation undertaken by the publisher [1]. This investigation has uncovered evidence of systematic manipulation of the publication and peer-review process. We cannot, therefore, vouch for the reliability or integrity of this article.

Please note that this notice is intended solely to alert readers that the peer-review process of this article has been compromised.

Wiley and Hindawi regret that the usual quality checks did not identify these issues before publication and have since put additional measures in place to safeguard research integrity.

We wish to credit our Research Integrity and Research Publishing teams and anonymous and named external researchers and research integrity experts for contributing to this investigation.

The corresponding author, as the representative of all authors, has been given the opportunity to register their agreement or disagreement to this retraction. We have kept a record of any response received.

### **References**

- [1] N. Garg, D. Sinha, B. Yadav, B. Gupta, S. Gupta, and S. Miah, "ML-Based Texture and Wavelet Features Extraction Technique to Predict Gastric Mesothelioma Cancer," *BioMed Research International*, vol. 2022, Article ID 1012684, 9 pages, 2022.

## Retraction

# Retracted: Multiresolution-Based Singular Value Decomposition Approach for Breast Cancer Image Classification

### BioMed Research International

Received 8 January 2024; Accepted 8 January 2024; Published 9 January 2024

Copyright © 2024 BioMed Research International. This is an open access article distributed under the Creative Commons Attribution License, which permits unrestricted use, distribution, and reproduction in any medium, provided the original work is properly cited.

This article has been retracted by Hindawi following an investigation undertaken by the publisher [1]. This investigation has uncovered evidence of one or more of the following indicators of systematic manipulation of the publication process:

- (1) Discrepancies in scope
- (2) Discrepancies in the description of the research reported
- (3) Discrepancies between the availability of data and the research described
- (4) Inappropriate citations
- (5) Incoherent, meaningless and/or irrelevant content included in the article
- (6) Manipulated or compromised peer review

The presence of these indicators undermines our confidence in the integrity of the article's content and we cannot, therefore, vouch for its reliability. Please note that this notice is intended solely to alert readers that the content of this article is unreliable. We have not investigated whether authors were aware of or involved in the systematic manipulation of the publication process.

Wiley and Hindawi regrets that the usual quality checks did not identify these issues before publication and have since put additional measures in place to safeguard research integrity.

We wish to credit our own Research Integrity and Research Publishing teams and anonymous and named external researchers and research integrity experts for contributing to this investigation.

The corresponding author, as the representative of all authors, has been given the opportunity to register their agreement or disagreement to this retraction. We have kept a record of any response received.

### References

- [1] S. Mann, A. K. Bindal, A. Balyan et al., "Multiresolution-Based Singular Value Decomposition Approach for Breast Cancer Image Classification," *BioMed Research International*, vol. 2022, Article ID 6392206, 11 pages, 2022.



## Retraction

# Retracted: Multidimensional CNN-Based Deep Segmentation Method for Tumor Identification

### BioMed Research International

Received 8 January 2024; Accepted 8 January 2024; Published 9 January 2024

Copyright © 2024 BioMed Research International. This is an open access article distributed under the Creative Commons Attribution License, which permits unrestricted use, distribution, and reproduction in any medium, provided the original work is properly cited.

This article has been retracted by Hindawi following an investigation undertaken by the publisher [1]. This investigation has uncovered evidence of one or more of the following indicators of systematic manipulation of the publication process:

- (1) Discrepancies in scope
- (2) Discrepancies in the description of the research reported
- (3) Discrepancies between the availability of data and the research described
- (4) Inappropriate citations
- (5) Incoherent, meaningless and/or irrelevant content included in the article
- (6) Manipulated or compromised peer review

The presence of these indicators undermines our confidence in the integrity of the article's content and we cannot, therefore, vouch for its reliability. Please note that this notice is intended solely to alert readers that the content of this article is unreliable. We have not investigated whether authors were aware of or involved in the systematic manipulation of the publication process.

Wiley and Hindawi regrets that the usual quality checks did not identify these issues before publication and have since put additional measures in place to safeguard research integrity.

We wish to credit our own Research Integrity and Research Publishing teams and anonymous and named external researchers and research integrity experts for contributing to this investigation.

The corresponding author, as the representative of all authors, has been given the opportunity to register their agreement or disagreement to this retraction. We have kept a record of any response received.

### References

- [1] R. J. Martin, U. Sharma, K. Kaur, N. M. Kadhim, M. Lamin, and C. S. Ayipeh, "Multidimensional CNN-Based Deep Segmentation Method for Tumor Identification," *BioMed Research International*, vol. 2022, Article ID 5061112, 11 pages, 2022.

## *Retraction*

# **Retracted: Principal Component and Path Analysis for Trait Selection Based on the Assessment of Diverse Lentil Populations Developed by Gamma-Irradiated Physical Mutation**

### **BioMed Research International**

Received 8 January 2024; Accepted 8 January 2024; Published 9 January 2024

Copyright © 2024 BioMed Research International. This is an open access article distributed under the Creative Commons Attribution License, which permits unrestricted use, distribution, and reproduction in any medium, provided the original work is properly cited.

This article has been retracted by Hindawi following an investigation undertaken by the publisher [1]. This investigation has uncovered evidence of one or more of the following indicators of systematic manipulation of the publication process:

- (1) Discrepancies in scope
- (2) Discrepancies in the description of the research reported
- (3) Discrepancies between the availability of data and the research described
- (4) Inappropriate citations
- (5) Incoherent, meaningless and/or irrelevant content included in the article
- (6) Manipulated or compromised peer review

The presence of these indicators undermines our confidence in the integrity of the article's content and we cannot, therefore, vouch for its reliability. Please note that this notice is intended solely to alert readers that the content of this article is unreliable. We have not investigated whether authors were aware of or involved in the systematic manipulation of the publication process.

Wiley and Hindawi regrets that the usual quality checks did not identify these issues before publication and have since put additional measures in place to safeguard research integrity.

We wish to credit our own Research Integrity and Research Publishing teams and anonymous and named external researchers and research integrity experts for contributing to this investigation.

The corresponding author, as the representative of all authors, has been given the opportunity to register their agreement or disagreement to this retraction. We have kept a record of any response received.

### **References**

- [1] S. Debnath, A. Sarkar, K. Perveen et al., "Principal Component and Path Analysis for Trait Selection Based on the Assessment of Diverse Lentil Populations Developed by Gamma-Irradiated Physical Mutation," *BioMed Research International*, vol. 2022, Article ID 9679181, 14 pages, 2022.

## Retraction

# Retracted: Prognostic Diagnosis for Breast Cancer Patients Using Probabilistic Bayesian Classification

### BioMed Research International

Received 8 January 2024; Accepted 8 January 2024; Published 9 January 2024

Copyright © 2024 BioMed Research International. This is an open access article distributed under the Creative Commons Attribution License, which permits unrestricted use, distribution, and reproduction in any medium, provided the original work is properly cited.

This article has been retracted by Hindawi following an investigation undertaken by the publisher [1]. This investigation has uncovered evidence of one or more of the following indicators of systematic manipulation of the publication process:

- (1) Discrepancies in scope
- (2) Discrepancies in the description of the research reported
- (3) Discrepancies between the availability of data and the research described
- (4) Inappropriate citations
- (5) Incoherent, meaningless and/or irrelevant content included in the article
- (6) Manipulated or compromised peer review

The presence of these indicators undermines our confidence in the integrity of the article's content and we cannot, therefore, vouch for its reliability. Please note that this notice is intended solely to alert readers that the content of this article is unreliable. We have not investigated whether authors were aware of or involved in the systematic manipulation of the publication process.

Wiley and Hindawi regrets that the usual quality checks did not identify these issues before publication and have since put additional measures in place to safeguard research integrity.

We wish to credit our own Research Integrity and Research Publishing teams and anonymous and named external researchers and research integrity experts for contributing to this investigation.

The corresponding author, as the representative of all authors, has been given the opportunity to register their agreement or disagreement to this retraction. We have kept a record of any response received.

### References

- [1] N. Junath, A. Bharadwaj, S. Tyagi, K. Sengar, M. N. S. Hasan, and M. Jayasudha, "Prognostic Diagnosis for Breast Cancer Patients Using Probabilistic Bayesian Classification," *BioMed Research International*, vol. 2022, Article ID 1859222, 10 pages, 2022.

## *Retraction*

# **Retracted: Attention Layer-Based Multidimensional Feature Extraction for Diagnosis of Lung Cancer**

### **BioMed Research International**

Received 8 January 2024; Accepted 8 January 2024; Published 9 January 2024

Copyright © 2024 BioMed Research International. This is an open access article distributed under the Creative Commons Attribution License, which permits unrestricted use, distribution, and reproduction in any medium, provided the original work is properly cited.

This article has been retracted by Hindawi, as publisher, following an investigation undertaken by the publisher [1]. This investigation has uncovered evidence of systematic manipulation of the publication and peer-review process. We cannot, therefore, vouch for the reliability or integrity of this article.

Please note that this notice is intended solely to alert readers that the peer-review process of this article has been compromised.

Wiley and Hindawi regret that the usual quality checks did not identify these issues before publication and have since put additional measures in place to safeguard research integrity.

We wish to credit our Research Integrity and Research Publishing teams and anonymous and named external researchers and research integrity experts for contributing to this investigation.

The corresponding author, as the representative of all authors, has been given the opportunity to register their agreement or disagreement to this retraction. We have kept a record of any response received.

### **References**

- [1] M. Bhende, A. Thakare, V. Saravanan, K. Anbazhagan, H. N. Patel, and A. Kumar, "Attention Layer-Based Multidimensional Feature Extraction for Diagnosis of Lung Cancer," *BioMed Research International*, vol. 2022, Article ID 3947434, 11 pages, 2022.

## Retraction

# Retracted: Metaheuristic Optimization-Driven Novel Deep Learning Approach for Brain Tumor Segmentation

### BioMed Research International

Received 8 January 2024; Accepted 8 January 2024; Published 9 January 2024

Copyright © 2024 BioMed Research International. This is an open access article distributed under the Creative Commons Attribution License, which permits unrestricted use, distribution, and reproduction in any medium, provided the original work is properly cited.

This article has been retracted by Hindawi following an investigation undertaken by the publisher [1]. This investigation has uncovered evidence of one or more of the following indicators of systematic manipulation of the publication process:

- (1) Discrepancies in scope
- (2) Discrepancies in the description of the research reported
- (3) Discrepancies between the availability of data and the research described
- (4) Inappropriate citations
- (5) Incoherent, meaningless and/or irrelevant content included in the article
- (6) Manipulated or compromised peer review

The presence of these indicators undermines our confidence in the integrity of the article's content and we cannot, therefore, vouch for its reliability. Please note that this notice is intended solely to alert readers that the content of this article is unreliable. We have not investigated whether authors were aware of or involved in the systematic manipulation of the publication process.

Wiley and Hindawi regrets that the usual quality checks did not identify these issues before publication and have since put additional measures in place to safeguard research integrity.

We wish to credit our own Research Integrity and Research Publishing teams and anonymous and named external researchers and research integrity experts for contributing to this investigation.

The corresponding author, as the representative of all authors, has been given the opportunity to register their agreement or disagreement to this retraction. We have kept a record of any response received.

### References

- [1] R. Kalpana, M. A. Bennet, and A. W. Rahmani, "Metaheuristic Optimization-Driven Novel Deep Learning Approach for Brain Tumor Segmentation," *BioMed Research International*, vol. 2022, Article ID 2980691, 15 pages, 2022.

## *Retraction*

# **Retracted: Image Super-Resolution Reconstruction Method for Lung Cancer CT-Scanned Images Based on Neural Network**

### **BioMed Research International**

Received 8 January 2024; Accepted 8 January 2024; Published 9 January 2024

Copyright © 2024 BioMed Research International. This is an open access article distributed under the Creative Commons Attribution License, which permits unrestricted use, distribution, and reproduction in any medium, provided the original work is properly cited.

This article has been retracted by Hindawi, as publisher, following an investigation undertaken by the publisher [1]. This investigation has uncovered evidence of systematic manipulation of the publication and peer-review process. We cannot, therefore, vouch for the reliability or integrity of this article.

Please note that this notice is intended solely to alert readers that the peer-review process of this article has been compromised.

Wiley and Hindawi regret that the usual quality checks did not identify these issues before publication and have since put additional measures in place to safeguard research integrity.

We wish to credit our Research Integrity and Research Publishing teams and anonymous and named external researchers and research integrity experts for contributing to this investigation.

The corresponding author, as the representative of all authors, has been given the opportunity to register their agreement or disagreement to this retraction. We have kept a record of any response received.

### **References**

- [1] J. Xu, W. Liu, Y. Qin, and G. Xu, "Image Super-Resolution Reconstruction Method for Lung Cancer CT-Scanned Images Based on Neural Network," *BioMed Research International*, vol. 2022, Article ID 3543531, 10 pages, 2022.

## *Retraction*

# **Retracted: Correlation-Based Mutual Information Model for Analysis of Lung Cancer CT Image**

### **BioMed Research International**

Received 8 January 2024; Accepted 8 January 2024; Published 9 January 2024

Copyright © 2024 BioMed Research International. This is an open access article distributed under the Creative Commons Attribution License, which permits unrestricted use, distribution, and reproduction in any medium, provided the original work is properly cited.

This article has been retracted by Hindawi, as publisher, following an investigation undertaken by the publisher [1]. This investigation has uncovered evidence of systematic manipulation of the publication and peer-review process. We cannot, therefore, vouch for the reliability or integrity of this article.

Please note that this notice is intended solely to alert readers that the peer-review process of this article has been compromised.

Wiley and Hindawi regret that the usual quality checks did not identify these issues before publication and have since put additional measures in place to safeguard research integrity.

We wish to credit our Research Integrity and Research Publishing teams and anonymous and named external researchers and research integrity experts for contributing to this investigation.

The corresponding author, as the representative of all authors, has been given the opportunity to register their agreement or disagreement to this retraction. We have kept a record of any response received.

### **References**

- [1] N. S. Vadivu, G. Gupta, Q. N. Naveed, T. Rasheed, S. K. Singh, and D. Dhabliya, "Correlation-Based Mutual Information Model for Analysis of Lung Cancer CT Image," *BioMed Research International*, vol. 2022, Article ID 6451770, 12 pages, 2022.

## Retraction

# Retracted: Groundwater Suitability Evaluation Using Entropy Weightage Quality Index (EWQI) Model and Human Health Cancer Risk Assessment of Heavy Metal in Eastern India

### BioMed Research International

Received 8 January 2024; Accepted 8 January 2024; Published 9 January 2024

Copyright © 2024 BioMed Research International. This is an open access article distributed under the Creative Commons Attribution License, which permits unrestricted use, distribution, and reproduction in any medium, provided the original work is properly cited.

This article has been retracted by Hindawi following an investigation undertaken by the publisher [1]. This investigation has uncovered evidence of one or more of the following indicators of systematic manipulation of the publication process:

- (1) Discrepancies in scope
- (2) Discrepancies in the description of the research reported
- (3) Discrepancies between the availability of data and the research described
- (4) Inappropriate citations
- (5) Incoherent, meaningless and/or irrelevant content included in the article
- (6) Manipulated or compromised peer review

The presence of these indicators undermines our confidence in the integrity of the article's content and we cannot, therefore, vouch for its reliability. Please note that this notice is intended solely to alert readers that the content of this article is unreliable. We have not investigated whether authors were aware of or involved in the systematic manipulation of the publication process.

Wiley and Hindawi regrets that the usual quality checks did not identify these issues before publication and have since put additional measures in place to safeguard research integrity.

We wish to credit our own Research Integrity and Research Publishing teams and anonymous and named external researchers and research integrity experts for contributing to this investigation.

The corresponding author, as the representative of all authors, has been given the opportunity to register their agreement or disagreement to this retraction. We have kept a record of any response received.

### References

- [1] S. Saw, P. K. Singh, J. K. Mahato, R. Patel, D. N. Dhopte, and E. Asenso, "Groundwater Suitability Evaluation Using Entropy Weightage Quality Index (EWQI) Model and Human Health Cancer Risk Assessment of Heavy Metal in Eastern India," *BioMed Research International*, vol. 2022, Article ID 2476126, 14 pages, 2022.



## Retraction

# Retracted: A Multi-Thresholding-Based Discriminative Neural Classifier for Detection of Retinoblastoma Using CNN Models

### BioMed Research International

Received 8 January 2024; Accepted 8 January 2024; Published 9 January 2024

Copyright © 2024 BioMed Research International. This is an open access article distributed under the Creative Commons Attribution License, which permits unrestricted use, distribution, and reproduction in any medium, provided the original work is properly cited.

This article has been retracted by Hindawi following an investigation undertaken by the publisher [1]. This investigation has uncovered evidence of one or more of the following indicators of systematic manipulation of the publication process:

- (1) Discrepancies in scope
- (2) Discrepancies in the description of the research reported
- (3) Discrepancies between the availability of data and the research described
- (4) Inappropriate citations
- (5) Incoherent, meaningless and/or irrelevant content included in the article
- (6) Manipulated or compromised peer review

The presence of these indicators undermines our confidence in the integrity of the article's content and we cannot, therefore, vouch for its reliability. Please note that this notice is intended solely to alert readers that the content of this article is unreliable. We have not investigated whether authors were aware of or involved in the systematic manipulation of the publication process.

Wiley and Hindawi regrets that the usual quality checks did not identify these issues before publication and have since put additional measures in place to safeguard research integrity.

We wish to credit our own Research Integrity and Research Publishing teams and anonymous and named external researchers and research integrity experts for contributing to this investigation.

The corresponding author, as the representative of all authors, has been given the opportunity to register their agreement or disagreement to this retraction. We have kept a record of any response received.

### References

- [1] P. Kumar, D. Suganthi, K. Valarmathi et al., "A Multi-Thresholding-Based Discriminative Neural Classifier for Detection of Retinoblastoma Using CNN Models," *BioMed Research International*, vol. 2023, Article ID 5803661, 9 pages, 2023.

## Retraction

# Retracted: Cyclic GAN Model to Classify Breast Cancer Data for Pathological Healthcare Task

### BioMed Research International

Received 8 January 2024; Accepted 8 January 2024; Published 9 January 2024

Copyright © 2024 BioMed Research International. This is an open access article distributed under the Creative Commons Attribution License, which permits unrestricted use, distribution, and reproduction in any medium, provided the original work is properly cited.

This article has been retracted by Hindawi following an investigation undertaken by the publisher [1]. This investigation has uncovered evidence of one or more of the following indicators of systematic manipulation of the publication process:

- (1) Discrepancies in scope
- (2) Discrepancies in the description of the research reported
- (3) Discrepancies between the availability of data and the research described
- (4) Inappropriate citations
- (5) Incoherent, meaningless and/or irrelevant content included in the article
- (6) Manipulated or compromised peer review

The presence of these indicators undermines our confidence in the integrity of the article's content and we cannot, therefore, vouch for its reliability. Please note that this notice is intended solely to alert readers that the content of this article is unreliable. We have not investigated whether authors were aware of or involved in the systematic manipulation of the publication process.

Wiley and Hindawi regrets that the usual quality checks did not identify these issues before publication and have since put additional measures in place to safeguard research integrity.

We wish to credit our own Research Integrity and Research Publishing teams and anonymous and named external researchers and research integrity experts for contributing to this investigation.

The corresponding author, as the representative of all authors, has been given the opportunity to register their agreement or disagreement to this retraction. We have kept a record of any response received.

### References

- [1] P. Chopra, N. Junath, S. K. Singh, S. Khan, R. Sugumar, and M. Bhowmick, "Cyclic GAN Model to Classify Breast Cancer Data for Pathological Healthcare Task," *BioMed Research International*, vol. 2022, Article ID 6336700, 12 pages, 2022.

## Retraction

# Retracted: An Effective Machine Learning-Based Model for an Early Heart Disease Prediction

### BioMed Research International

Received 8 January 2024; Accepted 8 January 2024; Published 9 January 2024

Copyright © 2024 BioMed Research International. This is an open access article distributed under the Creative Commons Attribution License, which permits unrestricted use, distribution, and reproduction in any medium, provided the original work is properly cited.

This article has been retracted by Hindawi following an investigation undertaken by the publisher [1]. This investigation has uncovered evidence of one or more of the following indicators of systematic manipulation of the publication process:

- (1) Discrepancies in scope
- (2) Discrepancies in the description of the research reported
- (3) Discrepancies between the availability of data and the research described
- (4) Inappropriate citations
- (5) Incoherent, meaningless and/or irrelevant content included in the article
- (6) Manipulated or compromised peer review

The presence of these indicators undermines our confidence in the integrity of the article's content and we cannot, therefore, vouch for its reliability. Please note that this notice is intended solely to alert readers that the content of this article is unreliable. We have not investigated whether authors were aware of or involved in the systematic manipulation of the publication process.

Wiley and Hindawi regrets that the usual quality checks did not identify these issues before publication and have since put additional measures in place to safeguard research integrity.

We wish to credit our own Research Integrity and Research Publishing teams and anonymous and named external researchers and research integrity experts for contributing to this investigation.

The corresponding author, as the representative of all authors, has been given the opportunity to register their agreement or disagreement to this retraction. We have kept a record of any response received.

### References

- [1] P. C. Bizimana, Z. Zhang, M. Asim, and A. A. Abd El-Latif, "An Effective Machine Learning-Based Model for an Early Heart Disease Prediction," *BioMed Research International*, vol. 2023, Article ID 3531420, 11 pages, 2023.

## *Retraction*

# **Retracted: Image Processing and Machine Learning-Based Classification and Detection of Liver Tumor**

### **BioMed Research International**

Received 12 December 2023; Accepted 12 December 2023; Published 13 December 2023

Copyright © 2023 BioMed Research International. This is an open access article distributed under the Creative Commons Attribution License, which permits unrestricted use, distribution, and reproduction in any medium, provided the original work is properly cited.

This article has been retracted by Hindawi, as publisher, following an investigation undertaken by the publisher [1]. This investigation has uncovered evidence of systematic manipulation of the publication and peer-review process. We cannot, therefore, vouch for the reliability or integrity of this article.

Please note that this notice is intended solely to alert readers that the peer-review process of this article has been compromised.

Wiley and Hindawi regret that the usual quality checks did not identify these issues before publication and have since put additional measures in place to safeguard research integrity.

We wish to credit our Research Integrity and Research Publishing teams and anonymous and named external researchers and research integrity experts for contributing to this investigation.

The corresponding author, as the representative of all authors, has been given the opportunity to register their agreement or disagreement to this retraction. We have kept a record of any response received.

### **References**

- [1] V. D. P. Jasti, E. Prasad, M. Sawale et al., "Image Processing and Machine Learning-Based Classification and Detection of Liver Tumor," *BioMed Research International*, vol. 2022, Article ID 3398156, 7 pages, 2022.

## *Retraction*

# **Retracted: Structural Modifications and Strategies for Native Starch for Applications in Advanced Drug Delivery**

### **BioMed Research International**

Received 12 December 2023; Accepted 12 December 2023; Published 13 December 2023

Copyright © 2023 BioMed Research International. This is an open access article distributed under the Creative Commons Attribution License, which permits unrestricted use, distribution, and reproduction in any medium, provided the original work is properly cited.

This article has been retracted by Hindawi, as publisher, following an investigation undertaken by the publisher [1]. This investigation has uncovered evidence of systematic manipulation of the publication and peer-review process. We cannot, therefore, vouch for the reliability or integrity of this article.

Please note that this notice is intended solely to alert readers that the peer-review process of this article has been compromised.

Wiley and Hindawi regret that the usual quality checks did not identify these issues before publication and have since put additional measures in place to safeguard research integrity.

We wish to credit our Research Integrity and Research Publishing teams and anonymous and named external researchers and research integrity experts for contributing to this investigation.

The corresponding author, as the representative of all authors, has been given the opportunity to register their agreement or disagreement to this retraction. We have kept a record of any response received.

### **References**

- [1] P. Bhatt, V. Kumar, R. Goel et al., "Structural Modifications and Strategies for Native Starch for Applications in Advanced Drug Delivery," *BioMed Research International*, vol. 2022, Article ID 2188940, 14 pages, 2022.

## *Retraction*

# **Retracted: Identification and Classification of Prostate Cancer Identification and Classification Based on Improved Convolution Neural Network**

### **BioMed Research International**

Received 26 September 2023; Accepted 26 September 2023; Published 27 September 2023

Copyright © 2023 BioMed Research International. This is an open access article distributed under the Creative Commons Attribution License, which permits unrestricted use, distribution, and reproduction in any medium, provided the original work is properly cited.

This article has been retracted by Hindawi following an investigation undertaken by the publisher [1]. This investigation has uncovered evidence of one or more of the following indicators of systematic manipulation of the publication process:

- (1) Discrepancies in scope
- (2) Discrepancies in the description of the research reported
- (3) Discrepancies between the availability of data and the research described
- (4) Inappropriate citations
- (5) Incoherent, meaningless and/or irrelevant content included in the article
- (6) Peer-review manipulation

The presence of these indicators undermines our confidence in the integrity of the article's content and we cannot, therefore, vouch for its reliability. Please note that this notice is intended solely to alert readers that the content of this article is unreliable. We have not investigated whether authors were aware of or involved in the systematic manipulation of the publication process.

Wiley and Hindawi regrets that the usual quality checks did not identify these issues before publication and have since put additional measures in place to safeguard research integrity.

We wish to credit our own Research Integrity and Research Publishing teams and anonymous and named external researchers and research integrity experts for contributing to this investigation.

The corresponding author, as the representative of all authors, has been given the opportunity to register their agreement or disagreement to this retraction. We have kept a record of any response received.

### **References**

- [1] S. Tyagi, N. Tyagi, A. Choudhury, G. Gupta, M. M. A. Zahra, and S. A. Rahin, "Identification and Classification of Prostate Cancer Identification and Classification Based on Improved Convolution Neural Network," *Bio Med Research International*, vol. 2022, Article ID 9112587, 10 pages, 2022.

## Retraction

# Retracted: Prediction Performance of Deep Learning for Colon Cancer Survival Prediction on SEER Data

### BioMed Research International

Received 1 August 2023; Accepted 1 August 2023; Published 2 August 2023

Copyright © 2023 BioMed Research International. This is an open access article distributed under the Creative Commons Attribution License, which permits unrestricted use, distribution, and reproduction in any medium, provided the original work is properly cited.

This article has been retracted by Hindawi following an investigation undertaken by the publisher [1]. This investigation has uncovered evidence of one or more of the following indicators of systematic manipulation of the publication process:

- (1) Discrepancies in scope
- (2) Discrepancies in the description of the research reported
- (3) Discrepancies between the availability of data and the research described
- (4) Inappropriate citations
- (5) Incoherent, meaningless and/or irrelevant content included in the article
- (6) Peer-review manipulation

The presence of these indicators undermines our confidence in the integrity of the article's content and we cannot, therefore, vouch for its reliability. Please note that this notice is intended solely to alert readers that the content of this article is unreliable. We have not investigated whether authors were aware of or involved in the systematic manipulation of the publication process.

In addition, our investigation has also shown that one or more of the following human-subject reporting requirements has not been met in this article: ethical approval by an Institutional Review Board (IRB) committee or equivalent, patient/participant consent to participate, and/or agreement to publish patient/participant details (where relevant).

Wiley and Hindawi regrets that the usual quality checks did not identify these issues before publication

and have since put additional measures in place to safeguard research integrity.

We wish to credit our own Research Integrity and Research Publishing teams and anonymous and named external researchers and research integrity experts for contributing to this investigation.

The corresponding author, as the representative of all authors, has been given the opportunity to register their agreement or disagreement to this retraction. We have kept a record of any response received.

### References

- [1] S. Gupta, S. Kalaivani, A. Rajasundaram, G. K. Ameta, A. K. Oleiwi, and B. N. Dugbokie, "Prediction Performance of Deep Learning for Colon Cancer Survival Prediction on SEER Data," *BioMed Research International*, vol. 2022, Article ID 1467070, 12 pages, 2022.

## Retraction

# Retracted: An Effective Machine Learning-Based Model for an Early Heart Disease Prediction

### BioMed Research International

Received 8 January 2024; Accepted 8 January 2024; Published 9 January 2024

Copyright © 2024 BioMed Research International. This is an open access article distributed under the Creative Commons Attribution License, which permits unrestricted use, distribution, and reproduction in any medium, provided the original work is properly cited.

This article has been retracted by Hindawi following an investigation undertaken by the publisher [1]. This investigation has uncovered evidence of one or more of the following indicators of systematic manipulation of the publication process:

- (1) Discrepancies in scope
- (2) Discrepancies in the description of the research reported
- (3) Discrepancies between the availability of data and the research described
- (4) Inappropriate citations
- (5) Incoherent, meaningless and/or irrelevant content included in the article
- (6) Manipulated or compromised peer review

The presence of these indicators undermines our confidence in the integrity of the article's content and we cannot, therefore, vouch for its reliability. Please note that this notice is intended solely to alert readers that the content of this article is unreliable. We have not investigated whether authors were aware of or involved in the systematic manipulation of the publication process.

Wiley and Hindawi regrets that the usual quality checks did not identify these issues before publication and have since put additional measures in place to safeguard research integrity.

We wish to credit our own Research Integrity and Research Publishing teams and anonymous and named external researchers and research integrity experts for contributing to this investigation.

The corresponding author, as the representative of all authors, has been given the opportunity to register their agreement or disagreement to this retraction. We have kept a record of any response received.

### References

- [1] P. C. Bizimana, Z. Zhang, M. Asim, and A. A. Abd El-Latif, "An Effective Machine Learning-Based Model for an Early Heart Disease Prediction," *BioMed Research International*, vol. 2023, Article ID 3531420, 11 pages, 2023.



## Research Article

# An Effective Machine Learning-Based Model for an Early Heart Disease Prediction

Pierre Claver Bizimana <sup>1</sup>, Zuping Zhang <sup>1</sup>, Muhammad Asim <sup>2,3</sup>,  
and Ahmed A. Abd El-Latif <sup>2,4</sup>

<sup>1</sup>School of Computer Science and Engineering, Central South University, Changsha 410083, China

<sup>2</sup>EIAS Data Science Lab, College of Computer and Information Sciences, Prince Sultan University, Riyadh 11586, Saudi Arabia

<sup>3</sup>School of Computer Science and Technology, Guangdong University of Technology, Guangzhou 510006, China

<sup>4</sup>Department of Mathematics and Computer Science, Faculty of Science, Menoufia University, Shebin El-Kom 32511, Egypt

Correspondence should be addressed to Zuping Zhang; [zpzhang@csu.edu.cn](mailto:zpzhang@csu.edu.cn), Muhammad Asim; [asimpk@csu.edu.cn](mailto:asimpk@csu.edu.cn), and Ahmed A. Abd El-Latif; [a.rahiem@gmail.com](mailto:a.rahiem@gmail.com)

Received 22 May 2022; Revised 28 June 2022; Accepted 18 July 2022; Published 29 April 2023

Academic Editor: Abolfazl Mehbodniya

Copyright © 2023 Pierre Claver Bizimana et al. This is an open access article distributed under the Creative Commons Attribution License, which permits unrestricted use, distribution, and reproduction in any medium, provided the original work is properly cited.

Heart disease (HD) has become a dangerous problem and one of the most significant mortality factors worldwide, which requires an expensive and sophisticated detection process. Most people are affected due to the failure of the heart which seriously threatens their lives due to high morbidity and mortality. Therefore, accurate prediction and diagnosis are needed for early prevention, detection, and treatment to reduce the death threats to human life. However, an early and accurate prediction of HD is still a challenging task to be addressed. In this work, we propose a machine learning-based prediction model (MLbPM) that exploits a combination of the data scaling methods, the split ratios, the best parameters, and the machine learning algorithms for predicting HD. The performance of the proposed model is tested by performing experiments on a University of California Irvine HD dataset to indicate the presence or absence of HD. The results show that the proposed MLbPM provides an accuracy of 96.7% when logistic regression, robust scaler, best parameter, and 70:30 as a split ratio of the dataset are considered. In addition, MLbPM outperforms other compared works in terms of accuracy.

## 1. Introduction

Heart disease (HD) occupies the top place as a cause of death across the globe. According to the World Health Organization, almost 17.9 million deaths occur every year due to HD, estimated to be 31% of deaths globally [1]. HD describes any condition affecting the heart. The current generation is continuously very busy in everyday life due to the technological developments. This situation causes nervousness, restlessness, and stress, leading to HD. Early detection and classification could help to decide whether a patient has HD or not, and this prediction may prevent deaths. Electrocardiography and blood tests are often required for patients with HD symptoms to evaluate the disease appropriately [2, 3]. Medical diagnosis is a complicated and vital task, and various factors make it hard for physicians to assess and

detect the type of HD. The prediction of HD, when done early, has shown its benefit, such as allowing people to save their money, gain health, and not waste time [4–8]. To this end, an automated prediction system could be advantageous as it would be utilized by nonmedical personnel too.

Machine learning (ML) is an artificial intelligence branch that operates by analyzing data and recognizing patterns with minimum human intervention. In order to forecast new output values, ML algorithms use historical data as input. The successful use of ML provides options that can grant benefits in a rural area where doctors and expensive equipment are limited. Different studies have made it feasible to develop a decision support system using data information and ML approaches and improve HD prediction [9, 10]. ML algorithms are expanding, and they have shown promising results in different applications, for example,

online learning [11], scheduling [12], multiobjective optimization [13], and vehicle routing [14]. ML approaches are often preferred because they allow low computational cost and reasonable memory consumption. They are also useful when they are applied to efficient models, and their quality also depends on the quality of the data. Crucial data preprocessing steps such as data cleaning, feature selection, and data scaling are often required to get standard data. While most of the studies have been interested in the ML algorithm-based approach with the use of feature selection [3, 9], a minimum number of them paid attention to the impact of the combined split ratio, best parameter, and scaling methods' influence on the model performance [10, 15, 16]. It is so challenging to decide at the same time which split ratios, best parameters, and scaling methods are suitable for the best model when the dataset often contains features that vary in degrees of magnitude, range, and units.

To address the abovementioned challenges, this work proposes an ML-based prediction model (MLbPM) which uses the best data scaling method, the split ratio, and the best parameter and evaluates classifiers by measuring the classification accuracy of various ML algorithms to predict HD. Specifically, this work combines four ML algorithms and three data scaling methods, with the default or best parameters and the split ratios to find the best match for HD prediction. More specifically, we use ML algorithms such as logistic regression (LR), Naive Bayes (NB), support vector machine (SVM), and  $K$ -nearest neighbors (KNN), the involvement of the default or best parameter, the split ratio, and three data scaling methods such as standard scaler (SS), min-max scaler (MS), and robust scaler (RS).

The main contributions of this work are given as follows:

- (1) We propose a model called MLbPM, which focuses on split ratios, parameter tuning, and data scaling methods
- (2) We improve the HD prediction accuracy, reduce the false predictions, and compare the default and the best parameter in a matter of what is the best to use
- (3) We identify an appropriate prediction algorithm among the four ML algorithms in order to classify the given University of California Irvine (UCI) HD dataset, accurately
- (4) We validate the model performance using metrics like accuracy,  $F1$  score, precision, recall, and a receiver operating characteristic (ROC) curve. The experimental results show the superiority of the proposed model

The organization of the remaining parts of the work is as follows. Section 2 discusses related works. Section 3 explains the methodologies and the proposed system model. Section 4 carries out the analysis of the experimental results. Finally, Section 5 concludes the work and shows the possibility of the future work.

## 2. Related Works

Most of the works consulted on HD prediction presented their outcomes in terms of accuracy according to the used

ML algorithms. Then, the performance differs from study to study due to different ML algorithms. For example, Tu et al. [17] obtained an accuracy of 81.14% after using bagging and 78.9% after using a decision tree (DT). An accuracy of 84.14% was reached when Srinivas et al. [18] applied a naive approach and were able to correctly identify patients with HD. Classification and regression trees (CART) and DT have been used by Chaurasia and Pal [19], and their experiment showed an accuracy of 83.49% for CART and 82.50% for DT. Hari Ganesh and Gajenthiran [20] applied an NB approach and carried out an accuracy of 83.40%. SVM (linear and sigmoid) is used by Takçi [10] and got an accuracy of 84.81% and 84.44% when identifying HD patients. In addition, other works used the standard ML algorithms to predict HD, especially SVM with an accuracy of 84.85%, LR with 82.56%, and DT with 82.22% in [9], LR with 85.86% and Vote 87.4% in [16], SVM with 85% in [21], 84.12% in [22], and 83.6% and KNN with an accuracy of 78% [23]. Kavitha et al. [24] proposed a novel ML approach, and experimental results show an accuracy level of 88.7% with the hybrid model. Malavika et al. tested and compared various ML methods to predict HD where LR obtained 86.88% as accuracy [25].

Data scaling is one of the important techniques in order to scale and normalize data. Several techniques for data scaling are available; however, choosing appropriate scaling methods for ML algorithms is a challenging task to be considered. Some works mention the influence of data scaling practices on different ML algorithms. Ahsan et al. [15] tested different ML algorithms before and after scaling methods where LR obtained 84% accuracy. Shahriyari [26] showed that normalization significantly affected the performance of different ML algorithms. SVM had a maximum accuracy of 78%, compared to the other supervised algorithms. However, their work also showed that NB had the best precision and the lowest time. There is another work conducted by Ambarwari et al. [27], which showed that data scaling methods such as normalization and min-max normalization also significantly affect data analysis. Balabaeva and Kovalchuk [28] examined the effect of different scaling methods on the datasets from patients with heart failure. Various scaling methods, SS, MS, max Abs scaler, RS, and quantile transformer, have been used with LR, random forest, DT, and Xgboost.

The train/test split ratio could affect the outcome of the models and thus the prediction performance itself. However, only a few works considered the split ratio; for example, Rácz et al. [29] evaluated the effect of the train/test split ratios on the ML algorithm's performance. They tested and compared several combinations of dataset sizes and split ratios. They applied them to five different ML algorithms to find the dissimilarities or resemblances. They noticed clearly that the distinctions depended not only on the applied ML algorithms but also on the dataset sizes, which may extend to the train/test split ratios.

From the abovementioned introduction and related works, one can notice that the work on the simultaneous use of ML algorithms, scaling methods, split ratio, parameter tuning, etc. has rarely been available in the current literature.

Despite the utilization of data scaling methods in some works and the split ratios in others, according to the concerned work, the research work on the impact and interaction between the scaling methods, the train/test split ratios, and the best parameters combined is still missing in the current literature. This proposed work considers the combined impact of split ratio, parameter tuning, and scaling methods on the four ML algorithms (i.e., KNN, LR, NB, and SVM) for HD prediction.

### 3. The Proposed System Model

**3.1. Dataset Description.** In this work, we consider one of the frequently used UCI HD datasets, which can be found on Kaggle [30]. This dataset contains 14 attributes that include one target attribute and has 303 instances. The details of the dataset are presented in Table 1. This table comprises six numerical and eight categorical attributes.

According to the attributes, patients aged between 29 and 79 have been selected in this dataset and are considered for the experimental study. The gender value 1 has been assigned to male patients and 0 to female patients. There are four types of chest pain indicating HD. First of all, a kind named typical angina is caused by reduced blood flow to the heart muscles because of narrowed coronary arteries. The second one is called atypical angina, and it is a chest pain that occurs during mental or emotional stress. The third one, nonangina chest pain, may be caused due to various reasons. The last type is an asymptomatic type which may not be a symptom of HD. Trestbps reads the resting blood pressure. Chol informs about cholesterol level. Fbs is the fasting blood sugar level, and its assigned value is 1 if the fasting blood sugar is above 120 mg/dl and 0 if it is below. Restecg is known as a resting electrocardiographic result, while Thalch is the maximum rate of the heart. Indeed, Exang is exercise-induced angina. Oldpeak informs about ST depression. Slope informs about the pitch of the peak exercise ST. Ca tells the number of significant vessels colored by fluoroscopy. Thal is the exercise test duration in minutes, and Num is the target attribute. The presence or absence of HD is the target attribute which comprises binary values. The value 0 represents normal, and 1 signifies that the patient is confirmed with HD.

**3.2. Data Preprocessing.** The dataset used in this work does not have any null values. It has nominal attributes and numerical attributes. The dataset used is a medical dataset taken from Kaggle.

The attribute values of Age, Trestbps, Chol, Fbs, Thalch, and Oldpeak are numeric. They do not need any encoding. Sex, with the attribute value 2, Cp 4, Restecg 3, Exang 2, Slope 3, Ca 4, Thal 4, and Num 2 are nominal. These nominal features have to be encoded. Nominal and numeric attributes are visible in Table 1. For this work, we used 14 variables from the Cleveland UCI HD dataset. The most important considerations of preprocessing were to do encoding on nominal features. These nominal features have been encoded using a one-hot encoding function.

The data scaling action for numerical features is handled, as various ML algorithms require data scaling methods to produce the best results. We used three scaling methods: the first is SS which standardizes features with a zero mean and a standard deviation, and it makes the distribution become standardized. The second is MS which scales features in a given range [0, 1]. If there are negative values in the dataset, the range is [-1, 1]. During the data scaling action, the shape of the original distribution is not changed. The third is RS, and it removes outliers and facilitates using SS or MS if needed. RS works with the quantile range.

**3.3. ML Algorithms.** In the medical domain, ML has one of the essential tasks to predict the correct classification. Usually, trained physicians and other medical professionals can perform interpretation. However, with the massive amount of data generated every day, it is very challenging to carry out the classification of data. Different ML algorithms can support physicians in clinical applications. They can reduce the working load of medical experts and clinicians in the procedures of prediction, diagnosis, or prognosis. Various ML algorithms can cope with prediction tasks, among many others. The following subsections provide a comprehensive understanding of some of the ML algorithms.

**3.3.1. KNN.** KNN is a supervised ML algorithm that is used to classify label datasets. It classifies objects according to the nearest neighbor. KNN calculates the distance of an attribute from its neighbors. When the data points are continuous attributes, this algorithm employs Euclidean distance (ED) given by equation (1) or Manhattan distance (MD) defined in equation (2) for measuring the distance between the data points. The hamming distance (HD) is defined in equation (3), which can be used when the attributes are categorical.

$$ED = \left( \sum_{i=1}^k (x_i - y_i)^2 \right)^{1/2}, \quad (1)$$

$$MD = \sum_{i=1}^k |(x_i - y_i)|, \quad (2)$$

$$HD = \sum_{i=0}^k |(x_i - y_i)|. \quad (3)$$

KNN considers all features of equal weight. It is a technique of choice for a classification problem when the dataset does not have numerous variables. This is the case of the present dataset used in this work. In case the features are too many, the best way is to make a feature selection.

**3.3.2. LR.** LR is a supervised ML algorithm that allows a mapping between a response variable and predictor variables. LR establishes relationships between variables and predicts a particular outcome. Assume that LR is ready to predict  $y$ , the mathematical formula is as follows:

$$y^* = w[0] * x[0] + w[1] * x[1] + \dots + w[p] * x[p] + b > 0, \quad (4)$$

TABLE 1: Feature information of Cleveland UCI HD dataset.

Attribute	Data type	Range	Description
Age	Numeric	29–77	The age is displayed in years.
Sex	Nominal	0 or 1	1 stands for male, and 0 stands for female.
Cp	Nominal	1–4	The chest pain types are represented by 4 values.
Trestbps	Numeric	94–200	The resting blood pressure is measured in mm Hg on admission to the hospitals.
Chol	Numeric	126–564	The serum cholesterol is measured in mg/dl.
Fbs	Nominal	0 or 1	The fasting blood sugar must be $\geq 120$ mg/dl; it is represented by 1 for true and 0 for false.
Restecg	Nominal	0–2	This is the resting electrocardiographic results.
Thalach	Numeric	71–202	This is the maximum heart rate achieved.
Exang	Nominal	0 or 1	This is exercise-induced angina (1 = yes; 0 = no).
Oldpeak	Numeric	0–62	This is the ST depression induced by exercise when a patient is at rest.
Slope	Nominal	1–3	This the slope of the peak exercise ST segment.
Ca	Numeric	0–3	The number of major vessels (0–3) colored by fluoroscopy.
Thal	Nominal	3–7	This stands for thallium stress result; 1 = normal, 2 = fixed defect, 3 = reversible defect.
Num	Nominal	0–4	It is the outcome; 0 = no disease and 1 = disease.

where  $w[i]$  and  $b$  are coefficients learned from the training set and  $x[i]$  are the input variables.

**3.3.3. NB.** NB is a supervised ML algorithm that cooperates with Bayes' theorem. It is a probability-oriented classifier. It works by considering all variables in the dataset conditionally independent. This means that there is no correlation between the variables, and it is often useful for a sparse dataset. Here, the Bayes theorem is given:

$$P(X|P) = \frac{P(Y|X) \cdot P(X)}{P(Y)}, \quad (5)$$

where  $P$  stands for probability.  $P(A)$  is calculated for a given element  $X$  and its probability of occurrence, where  $P(X)$  is the probability of occurrence of element  $X$ ,  $P(Y)$  is the probability of occurrence of element  $Y$ , and  $P(X|Y)$  is the conditional probability of element  $X$  given element  $Y$  occurs, and this theorem will be used to perform the classification. The aforementioned theorem would do a direct multiplication of the probability of each feature occurring for independent features.

**3.3.4. SVM.** SVM is a supervised ML that is used for binary classification problems in various fields, especially in the medicine field. In SVM, the calculation of the support vector is done across the decision boundary instead of calculating according to the distance across each data point. This support vector is a good tool, which is used to classify a given dataset.

**3.4. The Proposed MLbPM.** A model named MLbPM is proposed as given in Figure 1 and Algorithm 1. It utilizes LR, the split ratios, the best parameters, and the scaling methods. Let us consider the dataset  $D$ , which contains  $n$  feature variables,  $m$  classifications, and a  $P$  number of patient records. Let us consider a classification problem where sample  $X$  is assigned to one of the potential classification classes  $m$

( $C_1, C_2, \dots, C_m$ ) in the applied dataset. In our work, the dataset outcome is divided into two groups: normal or healthy people and abnormal patients. Let us name it class  $C_1$  for normal (value 0) and class  $C_2$  for abnormal (value 1).

After loading the HD dataset, we do preprocess our data and split the dataset  $D$  into two subsets, one for training data and another one for testing data. The formula followed for splitting our dataset is

$$\text{Dataset} = \text{training data} + \text{testing data}. \quad (6)$$

It is normal for the training data to be superior to the testing data, and the sum of the training data and the testing data makes the whole dataset considered for an experiment as given in equation (6). Our dataset is divided into two split ratios SR1 and SR2 known as 80:20 and 70:30, respectively, where 80 and 70 ratios show the training data while 20 and 30 represent the testing data. We also use the scaling methods SS, MS, and RS, and four base classifiers are trained on training samples. The hyperparameters of base classifiers are tuned to improve the predictive accuracy, and the trained model is tested for evaluation.

The experiments follow two options: one without scaling methods and another one with scaling methods. The first option is done, on the one hand, considering the 80:20 split ratio with the default or best parameter on each ML algorithm such as KNN, LR, NB, and SVM. These ML algorithms are considered as base classifiers for training, and the models created are used for the test. The parameters of KNN, LR, NB, and SVM are tuned using the hyperparameter optimization technique grid search cross-validation in order to get the best parameters. On the other hand, the 70:30 split ratio is used by repeating the same procedures as applied on 80:20 split ratio. The LR model is the performant model even when both split ratios and best parameters are considered. The work in hand of LR, 70:30 as a split ratio, and the best parameter produce good accuracy.

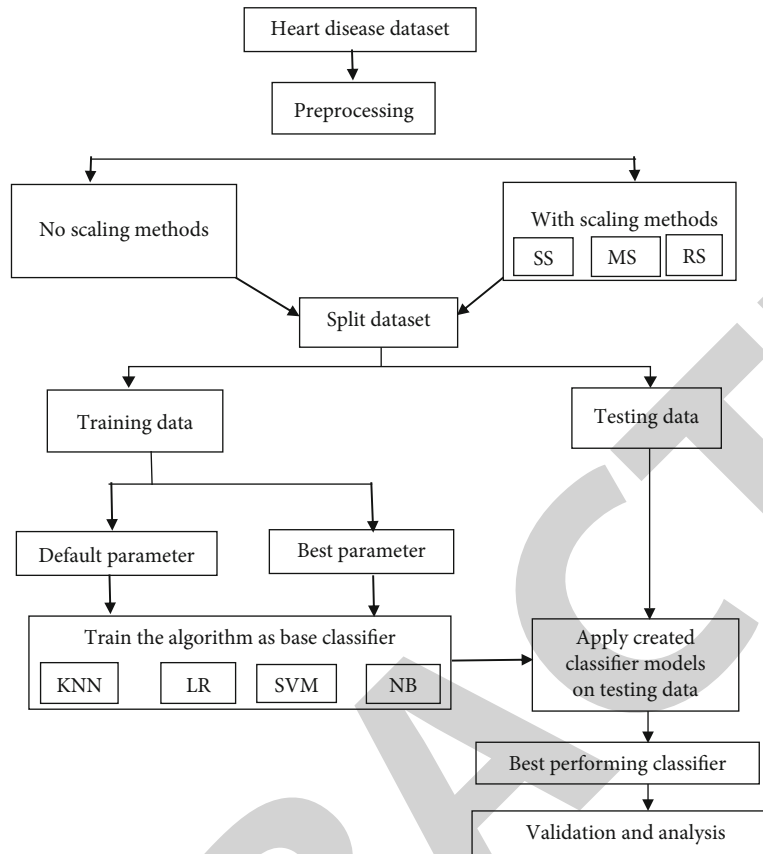


FIGURE 1: Framework of the approach followed for the MLbPM.

The other option concerns using the data scaling methods: SS, MS, and RS are applied to the input attributes. Each scaling method is used with each split ratio and the default or best parameter. The same previous classifiers are tested, and the LR classifier is the effective classifier at any time when both split ratios, best parameters, and RS are considered. The LR, the 70:30 split ratio, the best parameter, and RS make a proposed MLbPM more accurate than the standard ML algorithms.

As shown in Algorithm 1, first dataset  $D$  is loaded, and then, all nominal features (denoted by NF) are identified. After that, each nominal feature is encoded (lines 1 to 9), and  $D1$  is divided into two sets, one for training and another for testing (line 10).  $M$  base classifiers are selected (line 11) for classifying HD. Subsequently, predictions are made according to each classifier and a chosen split ratio (lines 12 to 15). After that, the hyperparameter is tuned to improve the result of each base classifier (line 16). The performance evaluation is executed, and the results are saved (line 20). In addition, the numeric features are identified and scaled using scaling methods (lines 23 to 28). After that, the previous actions are repeated from lines 10 to 17 (line 29). Subsequently, all classifiers' performances are evaluated (line 31), and the results are saved again (line 32). Finally, after comparing the results of all classifiers, the best model is selected and validated (line 34).

## 4. Experimental Results

An experimental work with various classification algorithms on the Cleveland UCI HD dataset has been done. Some algorithms showed good accuracy, whereas others performed poorly. This work has used three types of scaling methods such as SS, MS, and RS to improve the performances of four different ML algorithms like LR, KNN, NB, and SVM. A train/test split function with the number five as a random state is applied to divide the dataset into training and testing data. The split ratios of 80:20 and 70:30 are used for each experiment.

**4.1. Metrics Used.** Distinguished performance indices are considered to validate the integrity of our research results. They are accuracy,  $F1$  score, precision, and recall. Those indices are calculated using true positive (TP), true negative (TN), false positive (FP), and false negative (FN). The performance metrics are given as follows:

- (1) Accuracy: it is a metric for evaluating classification models. It is the fraction of predictions that the model got right as it is shown in equation (7) and helps to measure how well the model works. The formula is as follows:

```

1: Load the HD dataset  $D$ 
2: Identify  $P$  total number of patient records PR in  $D$ 
3: Find out  $N$  nominal features NF in  $D$ 
4: for  $i = 1 : P$  do
5:   for  $j = 1 : N$  do
6:     Apply one-hot encoding on each NF
7:   end for
8:   Return  $D_1$ 
9: end for
10: Partition  $D_1$  into two sets: training TR and testing TS data
11: Select  $M$  base classifier algorithms CA
12: for  $i = 1 : M$  do
13:   Consider split ratio 80:20 SR1 and 70:30 SR2
14:   Predict the result of  $CA_i$  on TR with R1
15:   Predict the result of  $CA_i$  on TR with SR2
16:   Tune the hyperparameter of  $CA_i$  and go to step 12
17: end for
18: for  $i = 1 : M$  do
19:   Evaluate the performance of  $CA_i$  on TS
20:   Predict the result of  $CA_i$  on TS, save the results
21: end for
22: Get  $D_1$  in step 8 and go to step 23
23: Identify  $K$  numeric features NC in  $D_1$ 
24: for  $i = 1 : K$  do
25:   Identify scaling methods SM
26:   Scale each NC with a SM
27:   Return  $D_2$ 
28: end for
29: Execute steps 10 to 17 for  $D_2$ , then go to step 30
30: for  $i = 1 : M$  do
31:   Evaluate the performance of each classifier on TS
32:   Predict the result of each classifier on TS, save the results
33: end for
34: Select and validate the best model

```

ALGORITHM 1:Pseudocode of the proposed MLbPM.

$$\text{Accuracy} = \frac{TP + TN}{TP + TN + FP + FN}. \quad (7)$$

- (2) *F1* score: it is a weighted average of precision and recall, and it conveys the balance between precision and recall. Equation (8) clarifies the *F1* score formula. The following is the mathematical formula of *F1* score:

$$F1 \text{ score} = \frac{2TP}{2TP + FP + FN}. \quad (8)$$

- (3) Precision: it is a metric that quantifies the number of correct positive predictions made as it is in equation (9). It is used to measure how many of the samples predicted as positive are actually positive. Its formula is as follows:

$$\text{Precision} = \frac{TP}{TP + FP}. \quad (9)$$

- (4) Recall: it is a metric that quantifies the number of correct positive predictions made out of all positive predictions that could have been made. It helps to measure how many of the positive samples are captured by the positive predictions as shown in equation (10). The formula is as follows:

$$\text{Recall} = \frac{TP}{TP + FN}. \quad (10)$$

TP is known as true positive and represents the number of persons correctly predicted with HDs. TN signifies true negative and represents the persons tested accurately as negative. FP is false positive and refers to those persons that are wrongly tested as positive. FN is known as false negative and indicates the persons incorrectly predicted as negative.

4.2. *The Impact of Split Ratio and Best Parameter on ML Algorithms.* Table 2 presents the overall accuracy, *F1* score, precision, and recall for all the four used ML algorithms without scaling methods. These algorithms are used with

TABLE 2: The results based on accuracy, *F1* score, precision, and recall for LR, KNN, SVM, and NB.

Algorithm	Accuracy	<i>F1</i> score	Precision		Recall	
			0	1	0	1
KNN	64.83	68.62	65	65	56	73
LR	94.2	94.67	95	92	91	96
SVM	91.20	91.66	91	92	91	92
NB	87.91	88.17	85	91	91	85

two types of parameters, such as the default and best parameters, respectively. The results presented in Table 2 are done according to the split ratio of 70 : 30 and the best parameters that provided good results.

With the split ratio of 70 : 30 and the best parameter, LR shows the highest accuracy of 94.2%, compared to the other three ML algorithms. LR uses the best parameters such as *C*, maxiter, penalty, and solver with 0.0001, 5000, none, and sag as values, respectively. On the other hand, KNN reveals the lowest performance with 64.83% of accuracy. LR also produces the highest *F1* score of 94.67%, while KNN has the lowest *F1* score of 68.62%.

With the same split ratio and best parameter above, the LR shows the highest precision of 95% for class 0 and 92% for class 1. On the other hand, KNN gives the lowest precision of 65% for 0 and 65% for 1. LR offers the highest recall, 91% for 0 and 96% for 1, while KNN has the most inadequate recall, 56% for 0 and 73% for 1. To further validate our results, we applied an ROC curve as demonstrated in Figure 2. LR performs better than KNN, NB, and SVM.

**4.3. The Impact of the Split Ratio on LR.** Table 3 presents the impact of the split ratio on the model’s results. Practically, LR gained 2.4% additional accuracy when used with a split ratio of 70 : 30 and the best parameter than a split ratio of 80 : 20 and with the default parameter. With 80 : 20 as a split ratio, LR obtained an accuracy of 91.8%, 92.06% for *F1* score, a precision of 93% for class 0 and 91% for 1, and a recall of 90% for class 0 and 94% for 1. However, LR obtains an accuracy of 94.2%, 94.67% for *F1* score, a precision of 95% for class 0 and 92% for 1, and a recall of 91% for class 0 and 96% for 1, when used with a split ratio of 70 : 30. The 70 : 30 split ratio provides better results than the 80 : 20 split ratio.

This ROC curve is used to validate the performance of obtained results, according to 70 : 30 and 80 : 20 split ratio. Considering the performant LR, it is shown that the 70 : 30 split ratio provided the good results compared to 80 : 20, as shown in Figure 3.

**4.4. The Impact of the Best Parameter on LR.** Table 4 presents the effectiveness of the best parameters on the results. When LR is used with the default parameter, the accuracy is 93.4%, 93.75% for *F1* score, a precision of 93% for class 0 and 94% for 1, and a recall of 93% for class 0 and 94% for 1. However, LR obtains an accuracy of 94.2%, 94.67% for *F1* score, a precision of 95% for class 0 and 92% for 1, and a recall of 91% for class 0 and 96% for 1, when it is used with the best parameter.

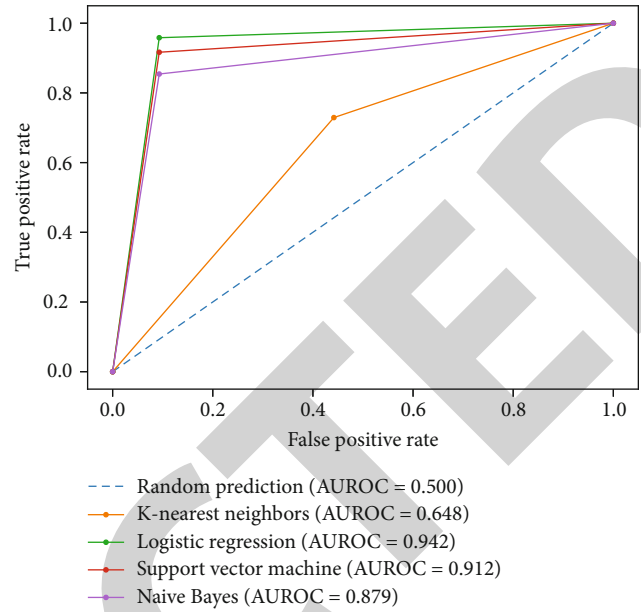


FIGURE 2: ROC curve of classifiers used with 70% training and 30% testing ratio and BP.

TABLE 3: The impact of the split ratio on LR results.

Split ratio	Accuracy	<i>F1</i> score	Precision		Recall	
			0	1	0	1
70 : 30	94.2	94.67	95	92	91	96
80 : 20	91.8	92.06	93	91	90	94

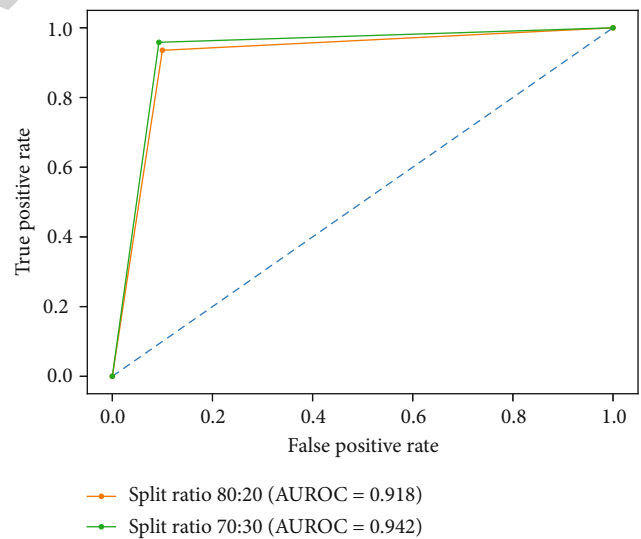


FIGURE 3: ROC curve that evaluates the impact of the split ratio on LR.

According to LR, default, and the best parameter, we applied a ROC curve to validate the results further. LR, with the best parameter, remains with good performance than with the default parameter as shown in Figure 4.

**4.5. Impact of the Scaling Methods.** Table 5 presents accuracy, *F1* score, precision, and recall for LR as an effective

TABLE 4: Impact of the best parameter on LR.

Parameter type	Accuracy	F1 score	Precision		Recall	
			0	1	0	1
Default	93.4	93.75	93	94	93	94
Best	94.2	94.67	95	92	91	96

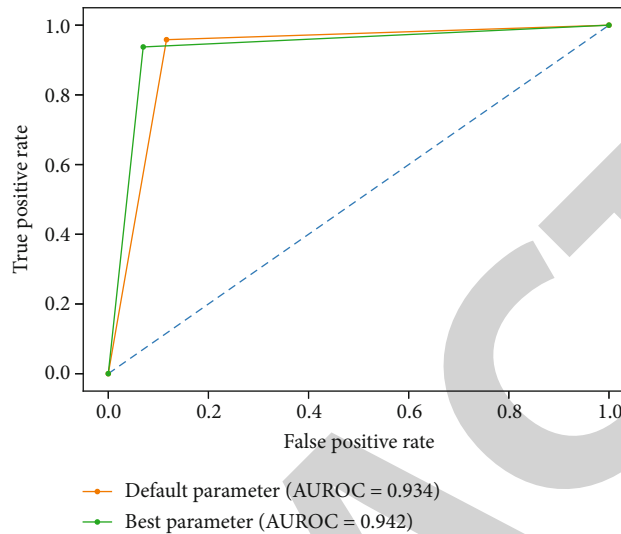


FIGURE 4: ROC comparative curve for the default and the best parameter.

TABLE 5: Result of LR as the performant algorithm with the best parameters, the scaling methods, and the split ratio of 70 : 30.

ALGO	Moment	Scaling method	Accuracy	F1 score	Precision	Recall		
LR	Before scaling	....	94.20	94.67	95	92	91	96
		SS	96.50	96.75	95	96	93	94
	After scaling	MS	87.91	88.42	88	88	86	89
		RS	96.7	96.75	95	96	93	94

algorithm with the best parameter and the split ratio of 70:30 and with the scaling methods such as SS, MS, and RS. With the scaling methods, LR algorithm shows the best results. It shows the highest accuracy of 96.7% when applied with RS and uses C, maxiter, penalty, and solver as the best parameters with 0.08858668, 100, l2, and lbfgs as values, respectively. In terms of F1 score, LR obtains an F1 score of 96.75% and shows the highest precision of 95% for class 0 and 96% for 1 with RS. LR has the highest recall of 93% for class 0 and 94% for 1, when used with RS.

As can be seen in Table 5, the accuracy obtained before scaling and after scaling (using RS) is 94.2% and 96.7%, respectively, which shows that the accuracy improves up to 2.5% after applying the scaling methods. Thus, scaling methods have great impact on the performance of the proposed model/algorithm.

To further validate our model’s results, we applied the ROC curve as demonstrated in Figure 5, and our findings demonstrate that the results after scaling methods are better than before scaling, according to our model.

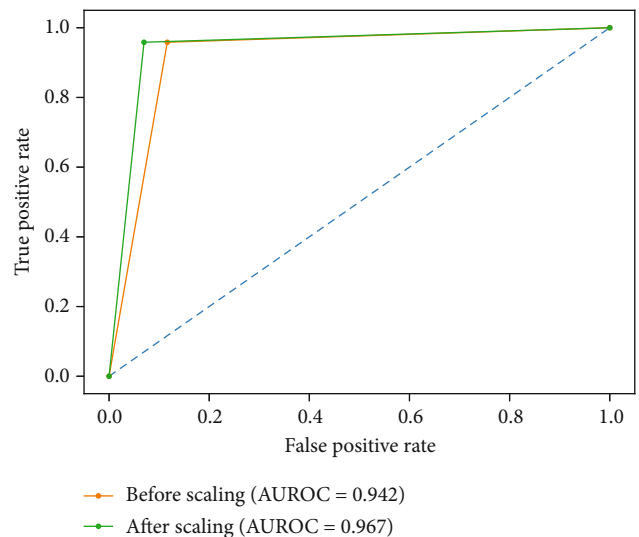


FIGURE 5: ROC comparison curve of LR results before and after scaling.



TABLE 6: Comparison of our results based on LR with the other studies.

Studies	Accuracy with 80 : 20 SR		
	Before scaling	Max	Min
Amin et al. [16]	85.86%	...	...
Bashir et al. [9]	82.56%	...	...
Balabaeva and Kovalchuk [28]	80.8%	82.2% (SS)	80.9%
Ahsan et al. [15]	84%	84% (SS, MM, RS)	68% (NR)
MLbPM	91.8%	92.8% (RS)	86.88% (MS)

**4.6. Comparison with Other Studies.** As discussed in the related work section, Amin et al. [16] and Bashir et al. [9] tested standard ML algorithms without applying scaling methods. In contrast, Balabaeva and Kovalchuk [28] and Ahsan et al. [15] tested and evaluated the standard ML algorithms before and after scaling. They did not mention default and best parameters, but they all used 80:20 as a split ratio. To compare our results with those available in the related works, we used only the 80:20 split ratio without and with scaling methods for a fair comparison, because the other authors do not use the 70:30 split ratio. The comparison results are shown in Table 6: column 2 presents the accuracy of the proposed method compared with other works, and they clarify that our proposed MLbPM based on LR is more performant than the models proposed in [9, 15, 16, 28] without considering scaling methods. In column 3, the results of Amin et al. and Bashir et al. are missing because they did not use scaling methods. As it is shown in Table 6, our model's results are still the best than in [15, 28] after having used SS, MS, and RS as scaling methods on LR.

To further prove the effectiveness of the proposed MLbPM, we present the evaluation of accuracy compared with others works in Figures 6 and 7. Figure 6 presents the evaluation of accuracy of MLbPM with other compared works before scaling. In contrast, Figure 7 shows the comparison of the evaluation of accuracy obtained by the proposed MLbPM compared with other works after scaling. Figures 6 and 7 show that our proposed model performs better than all the compared works and provides more promising results than them before and after scaling.

**4.7. Discussion.** In this work, the performances of four different ML algorithms (i.e., KNN, LR, NB, and SVM) were analyzed by considering the split ratios, the parameter tuning, and the data scaling approaches. We evaluated the above-mentioned ML algorithms with the 80:20 and 70:30 split ratios, the default and best parameters, and different scaling methods such as SS, MS, and RS. As results, we noticed that among the four mentioned ML algorithms, LR provides better results.

According to the results, we remarked that the 70:30 split ratio is the best split ratio which has given the best result as it is shown in Table 3. By testing the default and best parameter for LR, we concluded that the best parameter provided better results compared to the default parameter as it is given in Table 4.

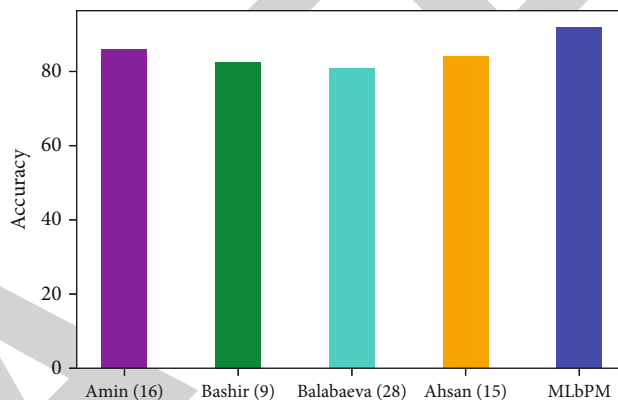


FIGURE 6: Evaluation of MLbPM with other works before scaling.

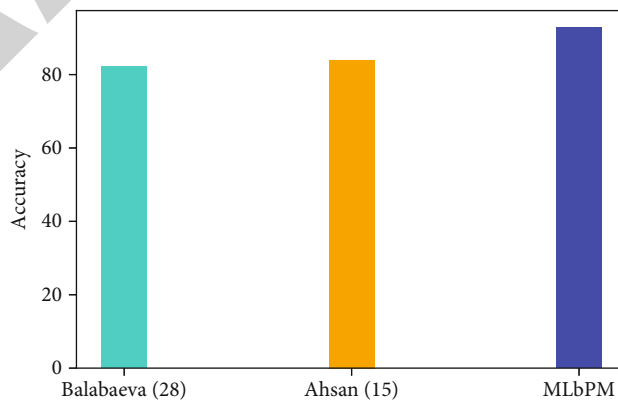


FIGURE 7: Evaluation of MLbPM with other works after scaling.

We tested different scaling methods and evaluated the proposed MLbPM model, before scaling and after scaling. We concluded that, after scaling, the proposed model provides better results than others and achieved an accuracy of 96.7% as given in Table 5. In addition, we tested different scaling methods and noticed that, among the scaling methods, RS is the best scaling method as shown in Tables 5 and 6 and has a great impact on the results.

## 5. Conclusion

This work evaluated four ML algorithms (i.e., KNN, LR, NB, and SVM) and three distinct data scaling methods to detect

patients with HD using the UCI HD dataset. We proposed a model called the ML-based prediction model (MLbPM) which is the combination of the split ratio, the best parameters, the data scaling methods, and the ML algorithms. The proposed MLbPM was evaluated by performing various experiments using the UCI HD dataset. According to the results, the split ratio, the parameter tuning, and the data scaling methods influence the algorithm's performance. The experimental results show that the proposed MLbPM provides better accuracy of 96.7% by using the LR algorithm with a split ratio of 70:30, best parameter, and scaling method robust scalar. In addition, as it can be seen in experimental results, MLbPM outperforms other compared works in terms of accuracy. We believe that this proposed MLbPM will guide the researchers or practitioners performing their HD medical tasks. In the future, we plan to design some fast and low-complexity algorithms based on artificial intelligence keeping in view the demand for real-time HD prediction in the smart E-health care system.

### Data Availability

The datasets generated during and analyzed during the current study are available from the corresponding authors upon reasonable request.

### Conflicts of Interest

The authors declare that they have no conflicts of interest.

### Acknowledgments

This research was funded by the Hunan Key Laboratory for Internet of Things in Electricity (Grant No. 2019TP1016), the National Natural Science Foundation of China (Grant No. 72061147004), the National Natural Science Foundation of Hunan Province (Grant No. 2021JJ30055), and the project about research on key technologies of power knowledge graph (Grant No. 5216A6200037) and was also supported by the EIAS Data Science Lab, College of Computer and Information Sciences, Prince Sultan University, Riyadh, Saudi Arabia.

### References

- [1] WHO World Health Organization, *Cardiovascular diseases (cvds)-key facts*, 2021.
- [2] E. E. Tripoliti, T. G. Papadopoulos, G. S. Karanasiou, K. K. Naka, and D. I. Fotiadis, "Heart failure: diagnosis, severity estimation and prediction of adverse events through machine learning techniques," *Computational and Structural Biotechnology Journal*, vol. 15, pp. 26–47, 2017.
- [3] A. P. Pawlovsky, "An ensemble based on distances for a KNN method for heart disease diagnosis," in *2018 International Conference on Electronics, Information, and Communication (ICEIC)*, Honolulu, HI, USA, 2018.
- [4] W. P. Lord and D. C. Wiggins, "Medical decision support systems," in *Advances in Health Care Technology Care Shaping the Future of Medical*, pp. 403–419, Springer, Berlin/Heidelberg, 2006.
- [5] M. Hammad, A. A. Abd El-Latif, A. Hussain et al., "Deep learning models for arrhythmia detection in IoT healthcare applications," *Computers and Electrical Engineering*, vol. 100, p. 108011, 2022.
- [6] A. Sedik, M. Hammad, A. A. Abd El-Latif et al., "Deep learning modalities for biometric alteration detection in 5g networks-based secure smart cities," *IEEE Access*, vol. 9, pp. 94780–94788, 2021.
- [7] M. Hammad, M. H. Alkinani, B. B. Gupta, A. El-Latif, and A. Ahmed, "Myocardial infarction detection based on deep neural network on imbalanced data," *Multimedia Systems*, pp. 1–13, 2021.
- [8] M. Bukhari, S. Yasmin, S. Sammad, A. El-Latif, and A. Ahmed, "A deep learning framework for leukemia cancer detection in microscopic blood samples using squeeze and excitation learning," *Mathematical Problems in Engineering*, vol. 2022, Article ID 2801227, 18 pages, 2022.
- [9] S. Bashir, Z. S. Khan, F. H. Khan, A. Anjum, and K. Bashir, "Improving heart disease prediction using feature selection approaches," in *2019 16th International Bhurban Conference on Applied Sciences and Technology (IBCAST)*, pp. 619–623, Islamabad, Pakistan, 2019.
- [10] H. Takçi, "Improvement of heart attack prediction by the feature selection methods," *Turkish Journal of Electrical Engineering and Computer Sciences*, vol. 26, pp. 1–10, 2018.
- [11] Y. Luo, X. Han, and C. Zhang, "Prediction of learning outcomes with a machine learning algorithm based on online learning behavior data in blended courses," *Asia Pacific Education Review*, 2022.
- [12] M. Frye, D. Gyulai, J. Bergmann, and R. H. Schmitt, "Adaptive scheduling through machine learning-based process parameter prediction," *MM Science Journal*, vol. 2019, no. 4, pp. 3060–3066, 2019.
- [13] S. Mahjoubi, R. Barhemat, P. Guo, W. Meng, and Y. Bao, "Prediction and multi-objective optimization of mechanical, economical, and environmental properties for strain-hardening cementitious composites (SHCC) based on automated machine learning and metaheuristic algorithms," *Journal of Cleaner Production*, vol. 329, p. 129665, 2021.
- [14] R. Bai, X. Chen, Z. L. Chen et al., "Analytics and machine learning in vehicle routing research," *International Journal of Production Research*, vol. 61, no. 1, pp. 4–30, 2021.
- [15] M. M. Ahsan, M. A. Parvez Mahmud, P. K. Saha, K. D. Gupta, and Z. Siddique, "Effect of data scaling methods on machine learning algorithms and model performance," *Technologies*, vol. 9, no. 3, p. 52, 2021.
- [16] M. S. Amin, Y. K. Chiam, and K. D. Varathan, "Identification of significant features and data mining techniques in predicting heart disease," *Telematics and Informatics*, vol. 36, pp. 82–93, 2019.
- [17] T. My Chau, D. Shin, and D. K. Shin, "Effective diagnosis of heart disease through bagging approach," in *2009 2nd International Conference on Biomedical Engineering and Informatics*, Tianjin, China, 2009.
- [18] B. Konda Srinivas, K. Rani, and A. Govrdhan, "Applications of data mining techniques in healthcare and prediction of heart attacks," *International Journal on Computer Science and Engineering*, vol. 2, no. 2, pp. 250–255, 2010.
- [19] V. Chaurasia and S. Pal, "Early prediction of heart diseases using data mining techniques," *Caribbean Journal of Science and Technology*, vol. 1, pp. 208–217, 2013.

## Retraction

# Retracted: Heterogeneous Network-Based Inductive Matrix Methods for Predicting Biomedical Gene Disease

### BioMed Research International

Received 8 January 2024; Accepted 8 January 2024; Published 9 January 2024

Copyright © 2024 BioMed Research International. This is an open access article distributed under the Creative Commons Attribution License, which permits unrestricted use, distribution, and reproduction in any medium, provided the original work is properly cited.

This article has been retracted by Hindawi following an investigation undertaken by the publisher [1]. This investigation has uncovered evidence of one or more of the following indicators of systematic manipulation of the publication process:

- (1) Discrepancies in scope
- (2) Discrepancies in the description of the research reported
- (3) Discrepancies between the availability of data and the research described
- (4) Inappropriate citations
- (5) Incoherent, meaningless and/or irrelevant content included in the article
- (6) Manipulated or compromised peer review

The presence of these indicators undermines our confidence in the integrity of the article's content and we cannot, therefore, vouch for its reliability. Please note that this notice is intended solely to alert readers that the content of this article is unreliable. We have not investigated whether authors were aware of or involved in the systematic manipulation of the publication process.

Wiley and Hindawi regrets that the usual quality checks did not identify these issues before publication and have since put additional measures in place to safeguard research integrity.

We wish to credit our own Research Integrity and Research Publishing teams and anonymous and named external researchers and research integrity experts for contributing to this investigation.

The corresponding author, as the representative of all authors, has been given the opportunity to register their agreement or disagreement to this retraction. We have kept a record of any response received.

### References

- [1] P. Das, L. Kumar, S. Degadwala, M. N. Alam, V. Jakhmola, and C. R. Bhat, "Heterogeneous Network-Based Inductive Matrix Methods for Predicting Biomedical Gene Disease," *BioMed Research International*, vol. 2023, Article ID 7121514, 13 pages, 2023.

## Research Article

# Heterogeneous Network-Based Inductive Matrix Methods for Predicting Biomedical Gene Disease

Pranjit Das <sup>1</sup>, Loveleen Kumar <sup>2</sup>, Sheshang Degadwala <sup>3</sup>, Md. Nasre Alam <sup>4</sup>,  
Vikash Jakhmola <sup>5</sup> and C. Rohith Bhat <sup>6</sup>

<sup>1</sup>Department of Computer Science and Engineering, Koneru Lakshmaiah Education Foundation (K L University), Vaddeswaram, India

<sup>2</sup>Department of Computer Science & Engineering, Swami Keshvanand Institute of Technology, Management & Gramothan, Jaipur, Rajasthan, India

<sup>3</sup>Department of Computer Engineering, Sigma Institute of Engineering, Vadodara, Gujarat, India

<sup>4</sup>Woldia University, Woldia, Ethiopia

<sup>5</sup>Uttaranchal Institute Pharmaceutical Sciences, Uttaranchal University, Dehradun, India

<sup>6</sup>Department of Computer Science and Engineering, Saveetha School of Engineering (SIMATS), Chennai, Tamilnadu, India

Correspondence should be addressed to Md. Nasre Alam; [nasarhi@wldu.edu.et](mailto:nasarhi@wldu.edu.et)

Received 22 July 2022; Revised 19 November 2022; Accepted 7 April 2023; Published 24 April 2023

Academic Editor: Abolfazl Mehbodniya

Copyright © 2023 Pranjit Das et al. This is an open access article distributed under the Creative Commons Attribution License, which permits unrestricted use, distribution, and reproduction in any medium, provided the original work is properly cited.

Prediction of gene-disease associations has grown in popularity in recent biomedical research. However, positive and unlabeled (PU) issues and limited gene-disease association data are common concerns with present association prediction algorithms. A gene-disease association prediction approach based on Katz-enhanced inductive matrix completion is suggested in light of the abovementioned flaws. Preestimate based on the Katz technique and refined estimation based on the inductive matrix completion approach makes the model. The Katz technique is utilized to preestimate the gene-disease association on the basis of gene-disease heterogeneous network to mitigate the effects of association data-sparse and PU issues. The Katz technique, however, necessarily introduces some noise when predicting gene-disease connections due to the similarity network's quality limitations. Therefore, the elastic net regularization approach is utilized to increase the resilience of the conventional inductive matrix completion model. As a result, the prediction effect of gene-disease connections is increased using robustness and a better inductive matrix completion model. The experimental findings demonstrate that the proposed model has dramatically increased recall and precision compared to widely used gene-disease association prediction approaches. It can also resolve the typical cold-start issue in association prediction. The proposed KIMC method may consider integrating more diverse biological data sources in the future and also aid in the effective extraction of the feature data of genes and diseases with higher correlation from this biological data to improve the prediction effect.

## 1. Introduction

Diseases are related to many factors, such as heredity and living environment, and many diseases are closely associated with specific genes. For example, common cancers in life [1–3], Alzheimer's disease [4], and diabetes [5], are all infections caused by a variety of gene defects. Therefore, the exploration of disease-causing genes is very crucial in understanding the causes of diseases, clinical diagnosis of conditions, and early preventive treatment. It

is also a key objective for human genome research and has major implications for science and society. Moreover, the initial identification of disease-related pathogenic genes is crucial for the development of disease treatment strategies and medications.

Early gene-disease association studies were carried out based on clinical and biological experimental methods usually that consume a lot of workforces and material resources. This limits the potential researches on pathogenic gene and seriously affects the related public datasets—data quality.

For example, genetic association databases [6] and the widely used OMIM [7] dataset both record only a small number of established gene-disease associations. It is not known whether there is an association relationship between most genes and diseases, which on the one hand, leads to highly sparse known association data between genes and conditions in the dataset and, on the other hand, leads to severe data skew problems in the dataset. That is, these datasets only contain certain gene-disease relationships (referred to as positive relationships in this paper) and do not contain any determining nonassociated relationships between genes and diseases (referred to as negative relationships in this paper). For those unknown gene-disease associations (referred to in this paper as unlabeled relationships), it is necessary to predict whether there is an association between them. This kind of problem is usually called a positive and unlabeled (PU) learning problem in machine learning. Existing research has shown that the lack of negative relationships will seriously affect the learning effect of PU learning problems [8].

In recent years, through high-throughput sequencing, biomedical text mining, and other means, valuable biological information (i.e., intrinsic gene characteristics, intergene similarity information, gene array information, and disease similarity information) can be obtained. The emergence of such details also allows one to study new forecasting methods to alleviate the above shortcomings. Firstly, the Katz technique was developed which constructed a gene-disease heterogeneous network by integrating intergene similarity information, interdisease similarity information, and gene-disease association information prediction to alleviate the drawback of data sparsity. However, this method cannot effectively predict nodes that are not connected to the network and will be affected by the quality of the constructed network [9, 10]. Literature [11] turned to the popular inductive matrix completion (IMC) method in machine learning to predict gene-disease associations, effectively overcoming the cold start problem. However, this method suffers from data sparsity and the PU problem. In view of the aforementioned shortcomings, a gene-disease association prediction method based on Katz-enhanced inductive matrix completion is recommended. The model is created by preestimating using the Katz technique and fine-tuning estimation using the inductive matrix completion approach. In order to lessen the effects of association data-scarcity and PU problems, the Katz technique is used to preestimate the gene-disease association based on the gene-disease heterogeneous network.

In response to the above problems, this paper proposes a Katz-boosted inductive matrix completion for gene-disease association prediction (KIMC) model based on Katz-enabled inductive matrix completion. The motivation of this model is to use the traditional Katz method to optimize the newly proposed inductive matrix completion method, which is essentially a step-by-step gene-disease prediction paradigm, including Katz method-based preestimation and inductive matrix completion method. The refinement of the estimate mainly consists of two steps. Specifically, the Katz method was first used to predict the association of unlabeled relationships for all gene-disease

pairs based on the constructed gene-disease heterogeneous network. Since data is close to 1 in the estimated association score, data can be regarded as positive association information, and data comparable to 0 can be regarded as negative association information. Katz's preestimation not only alleviates the data sparsity defect but also alleviates the PU problem implications for subsequent inductive matrix completion methods. However, limited by the quality of the constructed gene-disease heterogeneous network, the predicted gene-disease association information based on the Katz method inevitably contains a certain degree of noise. To overcome the influence of these noises on the inductive matrix completion method, this paper introduces the elastic net regularization [12] into the newly proposed inductive matrix completion method to enhance its robustness, then uses the improved elastic net regularization to induce the type matrix completion model to refine gene-disease association prediction effects. Experiments on the OMIM dataset show that the KIMC method proposed in this paper not only significantly improves recall and precision compared with several other competing approaches but also solves the typical cold start in gene-disease association prediction.

The main contributions of this paper are as follows:

- (1) A gene-disease association prediction model based on Katz-enhanced inductive matrix completion is proposed. The model not only combines the advantages of the Katz method and the inductive matrix completion method but also enhances the noise-tolerant performance of the model by introducing an elastic net regularization mechanism, which can effectively alleviate the data sparsity and PU problems that traditional methods are susceptible to
- (2) An efficient elastic net regularization inductive matrix completion optimization algorithm is designed using the nearest neighbor forward-backward splitting technique, and the algorithm's convergence is proved theoretically
- (3) Multiple sets of experimental results on the OMIM dataset show that the proposed KIMC model can achieve better prediction results than existing prediction methods and solve the cold-start problem of effectively predicting new diseases or new genes

## 2. Related Works

Many disease-causing gene prediction algorithms based on different gene-disease datasets have been proposed in the past decade. These algorithms are mainly divided into methods based on network similarity measurement and techniques based on machine learning.

Literature [13] proposed the correlating protein interaction network and phenotype network to predict disease genes (CIPHER) method which hypothesized that two genes closer to the interaction network might lead to more similar diseases. Disease similarity can be explained in terms of genetic similarity, using the entire disease similarity network

and PPI (protein-protein interaction) network calculation to get a score; this score measures how likely a gene is to cause a particular disease. Literature [14] improved the random walk method and proposed a random walk with restart on the heterogeneous network (RWRH) model. In this model, the gene-disease heterogeneous network is constructed using intergene similarity information, interdisease similarity information, and gene-disease association information. This method fully considers the global knowledge of the whole network. A random walk particle is used to diffuse along network connections to capture the similarity between nodes to calculate the relationship between genes and diseases. Literature [15] introduced the Katz method based on the gene-disease heterogeneous network which is widely used in social network analysis. Katz method uses the number of walk paths with different lengths between two nodes on the heterogeneous network and calculates the similarity between nodes to predict the association between genes and diseases. Literature [9] and literature [10] conducted a detailed analysis and comparison of the above methods based on network similarity measures. These methods predict genes by calculating the similarity between candidate genes and disease nodes in the network. These methods can integrate different types of gene similarity information and disease similarity information into the gene-disease heterogeneous network to enhance the amount of data information; its shortcomings are also apparent for those not connected to the heterogeneous network. Moreover, gene and disease nodes cannot be effectively predicted while relying on constructing high-quality biological network models. Based on functional gene associations and gene-phenotype connections in model organisms, two techniques for predicting gene-disease associations, the first approach, the Katz measure, is driven by its success in predicting social network links and is closely related to several of the new approaches put forth for inferring gene-disease associations. The second approach, known as CATAPULT (Combining dATA Across species using Positive-Unlabeled Learning Techniques), is a supervised machine learning approach that makes use of a biased support vector machine and features produced from walks in a heterogeneous gene-trait network. OMIM phenotypes and drug-target interactions are two different datasets that were used to evaluate the performance of the suggested methods and related state-of-the-art methodologies.

Based on the limitations of the above methods, some researchers have proposed methods based on machine learning. For example, literature [15] proposed combining data across species using positive-unlabeled learning techniques (CATAPULT) which can mine disease-causing genes by training a biased support vector machine (SVM) classifier to classify gene-phenotype associations. Since the first illness gene was discovered in 1949, thousands of other genes have been shown to be connected to various diseases [16]. The most common kind of evidence for the prediction of disease-gene connections is protein-protein interaction (PPI) networks, which have been employed in a variety of studies [17]. Prior methods attempted to predict disease-gene correlations by directly utilizing PPI networks' topological structure. However, as they only use universal PPI net-

works retrieved from web databases, which include a lot of false positives, the prediction accuracy cannot be increased. In order to anticipate disease-gene connections, researchers frequently integrate PPI networks with additional forms of data. Combining PPI networks with clinical data that distinguishes between patients (cases) and average people is one tactic (control) [18].

A method for predicting gene-disease associations based on Katz-enhanced inductive matrix completeness is proposed. The model is created by preestimating using the Katz technique and fine-tuning estimation using the inductive matrix completion approach. In order to lessen the effects of association data scarcity and PU problems, the Katz technique is used to preestimate the gene-disease association based on the gene-disease heterogeneous network.

microRNA-disease association (MDA) predictions have been applied since the issue was raised in the late 2000s based on the data fusion paradigm. Integrating many data sources broadens the scope of research and makes it more difficult to create algorithms that produce accurate, succinct, and consistent representations of the combined data [19]. Accurate discovery of miRNA-disease associations (MDAs), a requirement for developing successful miRNA therapies, has drawn significant scientific attention over the past 15 years, as seen by the more than 55 000 related articles that are currently available on PubMed [20]. lncRNAs have received a great deal of attention in recent years from academics all around the world. In the past several years, tens of thousands of lncRNA have been discovered in eukaryotic creatures ranging from worms to humans thanks to the rapid advancements in experimental equipment and computer prediction algorithms [21]. A family of single-stranded, covalently closed RNA molecules known as circular RNAs (circRNAs) perform a range of biological tasks. The discovery of circRNA-disease connections will aid in the diagnosis and treatment of diseases as research has shown that circRNAs are engaged in a wide range of biological processes and are crucial in the emergence of numerous complicated disorders [22].

Given a disease phenotype in question, a gene is not connected to the phenotype in question. Researchers often report positive correlations between genes and phenotypes, but negative correlations are far less common. The unlabeled gene-disease phenotype pairings function as adverse associations in the CATAPULT technique. Only the positive relationships and a significant number of unlabeled gene-disease phenotype pairings are known as negative associations, which is a peculiarity of the dataset. CATAPULT's central tenet is that the instances are not often considered evil. False negatives are severely punished, whereas false positives are not severely punished.

CATAPULT classifies the human gene-phenotype pairings with only one training session using a biased SVM. With this method, a classifier is trained to categorize the bootstrap samples as negatives alongside the positive data by selecting a random bootstrap sample of a few unlabeled examples from the set of all unlabeled examples. Positive and unlabeled samples are used by CATAPULT to create an aggregate classifier using the bagging approach.

Literature [11] proposed the IMC method, which can extract gene features from gene microarray data, gene function interaction data, and homologous gene-phenotype data of different species, from disease similarity networks and clinical manifestations of diseases. The disease characteristics are obtained from a large number of medical literatures and integrated into this method to make up for the limitation that the standard matrix completion (MC) can only rely on the existing observable associations to make predictions. It can predict new genes and diseases and solve the cold start problem encountered by the MC method. The prediction effect has been greatly improved compared to the previously proposed method. Tang et al. [23] used case studies, global and local leave-one-out cross-validation (LOOCV), and the human miRNA-disease correlation dataset derived from the HMDDv2.0 database to assess the effectiveness of DLRMC. As an outcome, the AUCs of DLRMC in global LOOCV and local LOOCV, respectively, are 0.9174 and 0.8289, which significantly beat a number of prior techniques. microRNAs (miRNAs) have been linked in numerous scientific studies to the occurrence and progression of numerous human disorders. The connection between miRNAs and human diseases has recently been the subject of an increasing amount of research. Nevertheless, the recognized connections are frequently few, and it is difficult to reliably estimate the possible associations between miRNA and diseases from vast amounts of biomedical information [24].

Identification of in silico miRNA targets is a critical step in considering that the miRNA interactome has largely not even for the most part been sufficiently mapped model creatures that were studied. There have been initiatives to promote the need for computational to support the experimental identification, and analyses are needed. This has contributed to the emergence of several miRNA target prediction methods [25], which are currently regarded as essential for the design of applicable experiments. These programmes recognize in silico miRNA targets as potential research subjects in the future or for computing tasks like target enrichment analysis. Predictions made with the current computational from relevant interaction databases or web servers and algorithms can be obtained [26].

### 3. Preliminary Knowledge

This section mainly introduces several different gene-disease association prediction methods available. The main goal of this paper is to predict the underlying causative genes of diseases, and the gene and disease datasets used today often have only a small number of known gene-disease associations. Usually, a known gene-disease association matrix  $PR^{N_g \times N_d}$  is constructed as follows:

$$P = \begin{bmatrix} 1 & 0 & \cdots & 0 & 0 \\ 0 & 0 & \cdots & 0 & 1 \\ \vdots & \vdots & \vdots & \vdots & \vdots \\ 0 & 1 & \cdots & 0 & 1 \\ 0 & 0 & \cdots & 0 & 0 \end{bmatrix}. \quad (1)$$

Rows and columns correspond to genes and diseases, respectively,  $N_g$  refers to the total number of genes,  $N_d$  refers to the total number of conditions,  $P_{ij} = 1$  means there is an association between gene  $i$  and disease  $j$ , and  $P_{ij} = 0$  denotes that the association between gene  $i$  and disease  $j$  is unknown (there may be an association or may not exist). The constructed gene-disease association matrix is highly sparse as it contains many strange associations. Moreover, there are only positive association data; therefore, the problem is referred to as a typical PU learning problem. The main task is to design effective methods to predict unknown associations to predict disease-causing genes.

**3.1. Katz Method.** The Katz method is similar to algorithms such as CIPHER [13] and RWRH [14], and the essence of these methods is based on the network similarity measure. Specifically, the Katz method calculates the similarity score between genes and diseases based on the gene-disease relationship network and sorts the genes corresponding to the disorders according to the similarity scores to select suitable candidate disease-causing genes. The Katz method successfully applies to social network relationship prediction [15]. It uses the number of walk paths between two nodes with different lengths to calculate the similarity between nodes. The gene and disease relationship networks are also the same. The method calculates the similarity score between nodes. Here, a gene-disease relationship heterogeneous network is constructed using the gene-gene similarity network, gene-disease association network, and disease-disease similarity network. An essential objective in bioinformatics has long been making accurate predictions of novel gene-disease correlations. The so-called guilt-by-association (GBA) approach, in which novel candidate genes are discovered through their relationship with genes previously known to be involved in the condition under study, has shown to be a particularly effective method. Direct protein-protein connections, such as those maintained by the Human Reference Protein Database (HPRD) [27], are one of the most widely used types of connection. CIPHER [28], GeneWalker [16], Prince [17] are just a few of the techniques that have been developed in recent years that have expanded the association from simply direct protein interactions to further links in various ways.

Then, the Katz method is used to predict gene-disease association in the heterogeneous network. The heterogeneous network structure is shown in Figure 1. The adjacency matrix of the illustrated heterogeneous network is expressed as

$$C = \begin{bmatrix} G & P \\ P^T & D \end{bmatrix}. \quad (2)$$

Among them,  $G$  refers to the gene-gene similarity network;  $D$  refers to the disease-disease similarity network;  $P$  refers to the gene-disease association network. Since there are not many direct associations between gene  $G_i$  and disease  $D_j$  in the network, it is necessary to express the association between genes and diseases by calculating the number of paths of different lengths between nodes.

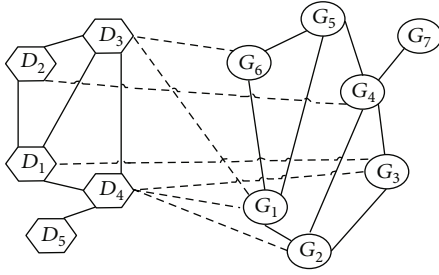


FIGURE 1: Structure of heterogeneous networks.

Let  $(C^l)_{ij}$  represents a path of length  $l$  between gene  $G_i$  and disease  $D_j$  quantity. The internode similarity is defined on  $C$  as follows:

$$S^{\text{Katz}}(C)_{ij} = \sum_{l=1}^k \beta^l (C^l)_{ij}. \quad (3)$$

Among them,  $\beta$  is a nonnegative constant, which is used to control the influence of paths of different lengths, and the value range of  $\beta$  is  $(0, \min\{1, 1/\|C\|_2\})$ . Converting Equation (3) into matrix form, the corresponding correlation score matrix can be expressed as follows:

$$S^{\text{Katz}}(C) = \sum_{l \geq 1} \beta^l C^l = (I - \beta C)^{-1} - I. \quad (4)$$

However, in the Katz method, it is not necessary to consider the number of paths of all lengths because paths with shorter path lengths convey more similar information between nodes. In contrast, nodes with farther distances communicate less information, so only the sum of finite path lengths needs to be considered. An earlier study [29] found that the smaller values of  $k$  (usually  $k=3$  or  $k=4$ ) usually show better performance. In the experiment, taking  $k=3$  and taking out the corresponding gene-disease similarity Katz score matrix can be expressed as

$$S_{G-D}^{\text{Katz}} = \beta P + \beta^2 (GP + PD) + \beta^3 (PP^T P + G^2 P + GPD + PD^2). \quad (5)$$

Use Equation (5) to find the score between genes and diseases. The method integrates auxiliary information (i.e., gene-gene similarity network and disease-disease similarity network) into the gene-disease heterogeneous network, effectively improving the prediction effect. The flowchart of method implementation is presented in Figure 2.

**3.2. Standard Matrix Completion (MC).** Due to the apparent shortcomings of the network-based association prediction method, Katz proposed to use the matrix completion theory for gene-disease association prediction. Initially, gene-

disease associations were predicted using the MC method, which decomposes the target matrix into two low-rank matrices  $W \in R^{N_g \times k}$  and the product of  $H \in R^{N_d \times k}$  where  $k \ll N_g, N_d$ . Therefore, predicting genetic disease associations can be written to solve the following optimization problem:

$$\min_{W, H} \sum_{(i,j) \in \Omega} (P_{ij} - W_i H_j^T)^2 + \frac{\lambda}{2} (\|W\|_F^2 + \|H\|_F^2), \quad (6)$$

where  $\Omega$  is the set of positions of observed elements,  $\lambda$  is the regularization parameter, and  $W_i$  and  $H_j$  represent the latent features of the  $i$ th gene and the  $j$ th disease, respectively, minimizing  $\lambda/2(\|W\|_F^2 + \|H\|_F^2)$ , equivalent to reducing the nuclear norm of  $WH^T$ .

The gene-disease association matrix  $P$  constructed using existing biological datasets is very sparse. For instance, the OMIM database datasets show that the majority of diseases have only one gene known to be associated with them, and the majority of genes do not have any conditions that are related to them. Here, standard matrix completion cannot predict those rows and columns in the correlation matrix with no elements, i.e., suffer from the cold-start problem.

**3.3. Inductive Matrix Completion (IMC).** Since standard matrix completion is used to predict gene-disease associations, a single type of data (only known gene-disease associations are used), such as biomedical literature, functional annotations, protein-protein interactions, homology tables of different species, and much biometric information such as gene microarrays, cannot be effectively used. There will be a cold start problem when forecasting, and the forecasting effect is not ideal. Given the above issues, finding characteristic information that can effectively utilize such genes and diseases is necessary. The multilabel learning problem formulated in literature [30] can make good use of such feature information. In multilabel learning problem, a low-rank linear model  $Z \in R^{d \times l}$  needs to be learned, in which each gene is expressed with the aid of  $d$  features and  $L$  labels. When  $x \in R^d$  represents the eigenvector of the gene, the prediction for  $j$  of illness can be described as  $x^T Z_j$ , where  $Z_j$  represents the  $j$ th column of matrix  $Z$ .

Applying the IMC [31] model to the gene-disease association prediction problem, IMC presumes that an association matrix is constructed by using the eigenvectors w.r.t., its row, and column entities to  $Z \in R^{f_g \times f_d}$  (where  $Z$  is a low-rank matrix), with the observed in  $P$  element to restore  $Z$ . Let  $x_i \in R^{f_g}$ ,  $y_j \in R^{f_d}$  denote the eigenvectors of gene  $i$  and disease  $j$ , respectively;  $X \in R^{N_g \times f_g}$  refers to  $N_g$  genes, the training feature matrix, each row of which represents the eigenvector of a gene;  $Y \in R^{N_d \times f_d}$  represents a feature training matrix of  $N_d$  diseases, where each row represents a feature vector for one condition. The IMC will be modelled as  $P_{ij} = x_i^T Z y_j$ , and the low-rank matrix  $Z$  needs to be recovered, i.e.,  $Z = WH^T$  where  $W \in R^{f_g \times k}$ ,  $H \in R^{f_d \times k}$ ,  $k \ll f_g, f_d$ .



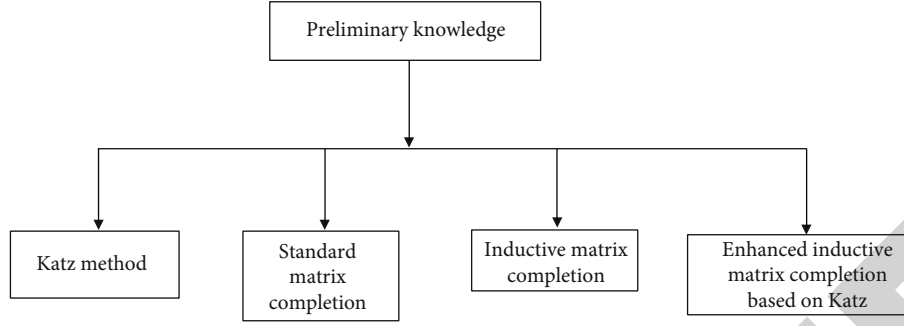


FIGURE 2: Flowchart of method implementation.

Therefore, gene-disease associations predictive modelling addresses the following problems:

$$\min_{W,H} \sum_{(i,j \in \Omega)} \left( P_{ij} - x_i^T W H^T y_j \right)^2 + \frac{\lambda}{2} (\|W\|_F^2 + \|H\|_F^2). \quad (7)$$

For disease  $j$ , which does not exist in the training data, if it has its feature vector  $y_j$ , then for all genes  $i$ , all its associations  $P_{ij}$  can be calculated. The same is true for a new gene and can effectively solve the cold-start problem encountered by the MC method. When the count of features is large,  $k$  is set to a lower value, and the count of parameters to be learned is lesser than  $f_g \times f_d$ . In typical matrix completion, the number of parameters to be known is  $(N_g \times N_d) \times k$ . It is not difficult to discover that the parameters required for IMC learning depend simply on the number of features associated with genes and diseases rather than the number of genes and diseases.

The MC problem can be regarded as a particular case of the IMC problem when the feature matrix  $X$  of genes is a unit matrix of size  $N_g$ , and the feature matrix  $Y$  of diseases is a unit matrix of size  $N_d$ . Here, Equation (7) is solved using alternating minimization (i.e., fixed  $W$  to find  $H$  or fixed  $H$  to find  $W$ , alternating iterative solution); when any one ( $W$  or  $H$ ) is selected, the answer has only one variable ( $H$  or  $W$ ), and then, it can be solved by conjugate gradient descent.

**3.4. Enhanced Inductive Matrix Completion Based on Katz.** Due to the extreme sparseness of existing gene-disease data and the most gene-disease databases that only record identified associations, existing methods suffer from data sparsity and PU issues. Therefore, it is necessary to seek a more stable way that can alleviate the influence of the sparse problem of gene-disease association data and the power of the PU problem. Therefore, a KIMC method is proposed, which integrates the Katz method for association prediction on the gene-disease heterogeneous network and inductive matrix completion model. First, when constructing a heterogeneous network, the proven gene-gene similarity information and disease-disease similarity information can be obtained from databases widely recognized in the industry. Together with the gene-disease association information, a heterogeneous

network can be formed. This type of information used by the Katz method can convey gene-disease-related information more directly than feature information. To integrate the IMC method to enhance the prediction effect without losing its inductive character, model the problem as

$$P = S_{G-D}^{\text{Katz}}(C) + \alpha XYZ^T, \quad (8)$$

where  $X \in R^{N_g \times f_g}$  represents the feature matrix of  $N_g$  genes,  $Y \in R^{N_d \times f_d}$  represents the feature matrix of  $N_d$  diseases, and  $Z \in R^{f_g \times f_d}$  represents the low-rank matrix that needs to be recovered. The parameter  $\alpha$  adjusts the prediction weight using feature information, where  $\alpha = 1$ . Using Equation (7) to calculate  $S_{G-D}^{\text{Katz}}(C)$ , the generated score data between genes and diseases, the part with a high score is regarded as positive association information, and the part with a low score is considered as negative association information.

It makes up for the shortcomings of traditional methods that can only use known gene-disease associations and can effectively alleviate the PU problem and the data sparseness problem encountered when using gene-disease association data directly. Integrate inductive matrix completion methods for residual matrix  $R = P - S_{G-D}^{\text{Katz}}(C)$  are solved to enhance its prediction effect. Therefore, we will use an inductive matrix complement, and the complete method solution residual  $R$  is modelled as

$$\min_{Z \in R^{f_g \times f_d}} \|Z\|_* \text{ s.t. } P_{\Omega}(XYZ^T) = P_{\Omega}(R). \quad (9)$$

Due to the influence of the quality of the constructed network, the introduction of the residual matrix  $R$  will bring some noise, and the direct use of the inductive matrix completion solution will affect the prediction effect and stability. Therefore, the matrix elastic net regularization [12] is introduced to alleviate this problem. Model the solution residual  $R$  as

$$\min_{Z \in R^{f_g \times f_d}} \|Z\|_* + \frac{\lambda}{2} \|Z\|_F^2 \text{ s.t. } P_{\Omega}(XYZ^T) = P_{\Omega}(R), \quad (10)$$

**Inputs:** Gene and disease feature matrices  $X, Y$ , association matrix  $P$ , set of sampling subscripts  $\Omega$ , gene similarity matrix  $G$ , disease similarity matrix  $D$ , parameters  $\beta, \delta, \rho, \lambda$ , and the number of iterations  $\text{Max}_{\text{iter}}$

**Output:** Predicted correlation matrix  $S_{G-D}^{\text{Katz}}(C) + XZY^T$

1. Calculate  $S_{G-D}^{\text{Katz}}(C)$  according to equation (5)
2. Calculate the residual matrix  $R$
3. Initialize  $Z_0 = 0$
4. For  $k= 0$  to  $\text{Max}_{\text{iter}}$
5. Update  $Z$  according to equation (17)
6. End for
7. Return  $S_{G-D}^{\text{Katz}}(C) + XZY^T$

ALGORITHM 1: Enhanced inductive matrix completion based on Katz.

TABLE 1: Recall vs.  $r$ .

Recall	Top- $r$	MC	Katz	IMC	KIMC1	KIMC2
0	0	0	0	0	0	0
0.1	20	0.05	0.1	0.2	0.15	0.25
0.2	40	0.07	0.12	0.22	0.17	0.27
0.3	60	0.06	0.11	0.21	0.16	0.26
0.4	80	0.07	0.12	0.22	0.17	0.27
0.5	100	0.08	0.13	0.23	0.18	0.28

Further, problem (10) can be transformed into an equivalent penalty function.

$$\min_{Z \in \mathbb{R}^{f_g \times f_d}} \|Z\|_* + \frac{\lambda}{2} \|Z\|_F^2 + \frac{\rho}{2} \|P_\Omega(XYZ^T - R)\|_F^2. \quad (11)$$

This paper intends to use the nearest neighbor forward-backward splitting (PFBS) [32] technique to optimize the solution to the problem (11). May wish to order

$$\begin{aligned} F_1(Z) &= \|Z\|_*, \\ F_2(Z) &= \frac{\lambda}{2} \|Z\|_F^2 + \frac{\rho}{2} \|P_\Omega(XYZ^T - R)\|_F^2. \end{aligned} \quad (12)$$

Then, problem (11) can be formalized in the general form as follows:

$$\min_{Z \in \mathbb{R}^{f_g \times f_d}} F_1(Z) + F_2(Z). \quad (13)$$

According to the PFBS rules,  $Z$  can be solved iteratively as follows:

$$Z^{k+1} = \arg \min_{Z \in \mathbb{R}^{f_g \times f_d}} \left\{ \delta \|Z\|_* + \frac{1}{2} \left\| Z - \left( Z^k - \delta \nabla F_2(Z^k) \right) \right\|_F^2 \right\}, \quad (14)$$

where  $\delta$  is the updated step size, and

$$\nabla F_2(Z) = \lambda Z + \rho(X^T X Z Y^T Y - X^T R Y). \quad (15)$$

According to [32], for a matrix  $B \in \mathbb{R}^{f_g \times f_d}$  and a constant  $\tau > 0$ , we have

$$D_\tau(B) = \operatorname{argmin}_{A \in \mathbb{R}^{f_g \times f_d}} \tau \|A\|_* + \frac{1}{2} \|A - B\|_F^2. \quad (16)$$

Therefore, an iterative update of  $Z$  can be transformed into

$$Z^{k+1} = D_\delta \left( Z^k - \delta \nabla F_2(Z^k) \right). \quad (17)$$

Further, Theorem 3.4 of Reference [33] shows that if the minimum of the optimization problem (13) exists and  $0 < \delta < 2/L_f$ , then for any initial parameter  $Z_0$ , the solution sequence (14) converges to the minimum value of Equation (13), where  $L_f$  is the Lipschitz of the function  $F_2(Z)$  continuous gradient, that is, for a convex function  $F(X)$ ,  $\exists L_f > 0$ ; for  $\forall X_1, X_2$ , the following inequality holds

$$\|\nabla F(X_2) - \nabla F(X_1)\|_F \leq L_f \|X_2 - X_1\|_F. \quad (18)$$

According to Proposition 1, if one can find a constant  $L_f > 0$  and if  $F_2(Z)$  satisfies Equation (18), then, the solution sequence (14) converges, and then, KIMC calculates the method combines, according to the Reference [33], Lemma 1, it is proved that

$$\begin{aligned} \|\nabla F(X_2) - \nabla F(X_1)\|_F^2 &= \|\lambda \Delta Z + \rho(X^T X \Delta Z Y^T Y)\|_F^2 \\ &\leq 2\|\lambda \Delta Z\|_F^2 + 2\|\rho X^T X \Delta Z Y^T Y\|_F^2 \\ &\leq 2\lambda^2 \|\Delta Z\|_F^2 + 2\rho^2 \|\rho X^T X \Delta Z Y^T Y\|_F^2 \\ &\leq 2\lambda^2 \|\Delta Z\|_F^2 + 2\rho^2 \sigma_{\max}^2(X^T X) \sigma_{\max}^2(Y^T Y) \|\Delta Z\|_F^2 \\ &\leq 2\lambda^2 + 2\rho^2 \sigma_{\max}^2(X^T X) \sigma_{\max}^2(Y^T Y) \|\Delta Z\|_F^2. \end{aligned} \quad (19)$$

Therefore, the Lipschitz constant is

$$L_f = \sqrt{2\lambda^2 + 2\rho^2 \sigma_{\max}^2(X^T X) \sigma_{\max}^2(Y^T Y)}. \quad (20)$$

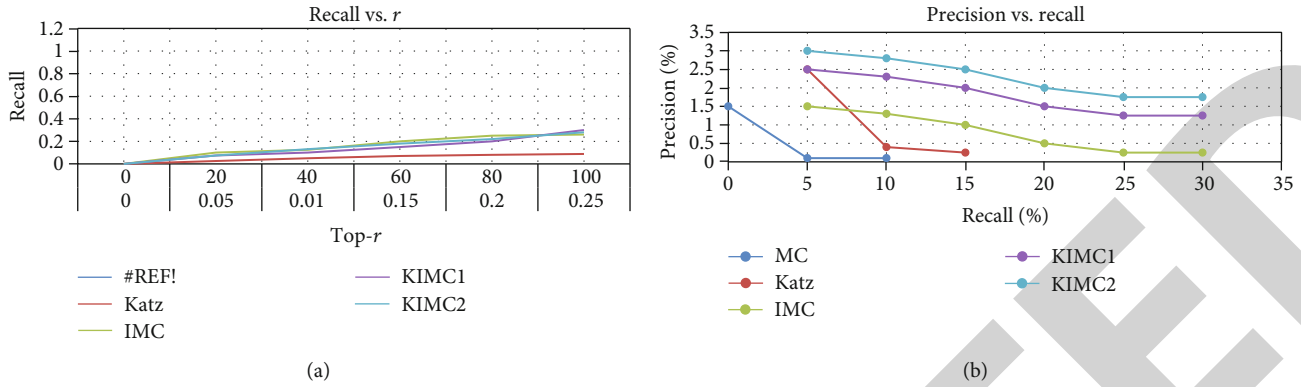


FIGURE 3: (a) Overall performance w.r.t. various thresholds. (b) Overall performance w.r.t. various thresholds.

TABLE 2: Precision vs. recall %.

Precision %	Recall %	MC	Katz	IMC	KIMC1	KIMC2
0	0	1.5				
0.5	5	0.1	2.5	1.5	2.5	3
1	10	0.1	0.4	1.3	2.3	2.8
1.5	15		0.25	1	2	2.5
2	20			0.5	1.5	2
2.5	25			0.25	1.25	1.75
3	30			0.25	1.25	1.75

TABLE 3: Recall vs.  $r$  for new gene.

Recall	Top- $r$	Katz	IMC	KIMC1	KIMC2
0	0	0	0	0	0
0.05	20	0.025	0.1	0.075	0.135
0.01	40	0.05	0.125	0.1	0.16
0.15	60	0.65	0.725	0.7	0.76
0.2	80	0.85	0.925	0.9	0.96
0.25	100	0.85	0.92	0.9	0.96

In this paper, the KIMC model with and without the regularization term of the elastic net is denoted as KIMC1 and KIMC2, respectively, and the solution process of KIMC2 is shown in Algorithm 1.

Katz status calculations are made possible for very large networks by an algorithm, although it should be noted that the metric has limited application. The Katz score is a modification of degree centrality, where distant players are taken into consideration through additional geometric series iterations. In fact, the Katz score frequently has a strong correlation with degree, offering a local gauge of centrality (based more on a node's immediate surroundings than its position across the larger network). So, even though other shortest-path or eigenvector centrality metrics offer a more comprehensive perspective, Katz scores never-

theless allow for the differentiation of actors of the same degree.

## 4. Experimental Results and Analysis

In this section, the gene-disease datasets and the sources of gene and disease characteristics used in the experiments are introduced, and the general evaluation criteria for gene-disease association prediction and the experimental results are analyzed in detail. Finally, the performance of several methods is compared.

**4.1. Datasets and Features.** The gene and disease information used in this study comes from the OMIM database, which not only includes relevant information on all monogenic diseases inherited in Mendelian fashion but also includes information on chromosomal diseases, polygenic diseases, and mitochondrial diseases, covering various conditions. Additionally, it gives details on information on the chromosomal location, linkage relationship, structure, and function of known pathogenic genes and describes the clinical knowledge of various genetic diseases. The data is updated in a timely and authoritative manner. The experiment uses the gene-disease dataset provided by the literature [15], which includes the gene-disease associations collected via OMIM dataset, including 12331 and 3209 genes and diseases, respectively, and a total of 3954 known genes-disease associations and gene-gene similarity information for 12331 genes and phenotype-phenotype similarity data (i.e., disease-disease similarity data) for 3209 diseases. In addition, the gene and disease signatures required in this study can be extracted from different types of biological data from other sources. For example, gene signatures are removed from gene microarray data, gene function interaction data, homologous gene-phenotype data of different species, disease similarity networks, clinical manifestation data of diseases, and analysis of a large number of medical literature data. Disease characteristics were obtained from the data. Faced with such complex data, principal component analysis (PCA) is usually utilized for dimensionality reduction to extract the main features of genes and diseases.

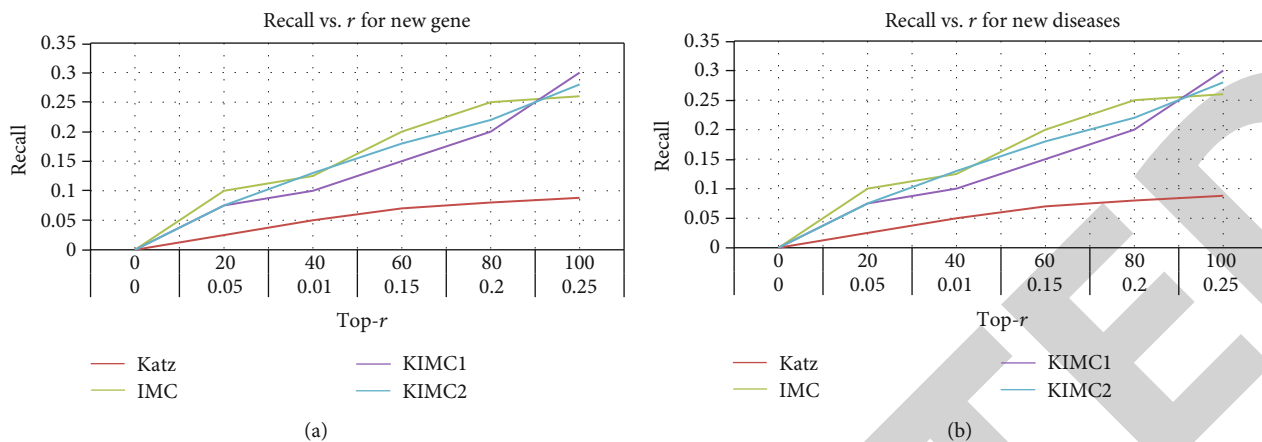


FIGURE 4: (a) Recall w.r.t. various threshold  $r$ . (b) Recall w.r.t. various threshold  $r$ .

TABLE 4: Recall vs.  $r$  for new diseases.

Recall	Top- $r$	Katz	IMC	KIMC1	KIMC2
0	0	0	0	0	0
0.05	20	0.025	0.1	0.075	0.075
0.01	40	0.05	0.125	0.1	0.13
0.15	60	0.07	0.2	0.15	0.18
0.2	80	0.08	0.25	0.2	0.22
0.25	100	0.088	0.26	0.3	0.28

However, this experiment uses the genes and disease features provided by the literature [11].

In multivariate data analysis, principal component analysis (PCA) is frequently employed to minimize the dimension of the data, facilitate further analysis, and enable efficient data summarization. It is now a helpful tool for analyzing microarray data. It is sometimes challenging to assess the overall gene expression differences between data from various groups or to categorize based on a very high number of genes for a specific microarray dataset. This study provides a gene selection technique based on Krzanowski’s plan. Using data on cancer gene expression, we show how successful this method is and contrast it with several different gene selection methods. The optimal gene subset for maintaining the original data structure is chosen using the suggested strategy.

**4.2. Evaluation Indicators and Methods.** As with the Katz [15], MC [11], and IMC [11] methods mentioned above, the experiments are evaluated using 3-fold cross-validation. When considering the prediction performance, the top- $r$  sorting method is used (that is, the gene score value corresponding to each disease column in the prediction result is sorted from large to small, and first  $r$  genes are taken as the candidate pathogenic genes of the respective disease and the other few gene-disease association prediction methods. When evaluating the performance in different ways, take the disease-related causative genes corresponding

to different thresholds  $r$ , compare the known associations recorded in the test set, and compare each method’s recall. They are calculated as follows:

$$\text{Recall} = \frac{TP}{TP + FN}. \tag{21}$$

At the same time, the accuracy of the experimental results needs to be analyzed. It is calculated as follows:

$$\text{Precision} = \frac{TP}{TP + FP}. \tag{22}$$

Among them,  $TP$  represents the number of correctly identified associations in the known gene-disease associations in the test set,  $FN$  represents the number of associations that are not accurately determined in the known gene-disease associations in the test set, and  $FP$  represents the unknown gene-disease associations determined as associated quantities. In the current field of biological research, it is hoped to get a better prediction effect in a low threshold range, usually  $r \leq 100$ . Second, while evaluating the global performance of prediction methods, researchers pay more attention to new genes and diseases with research gaps than some widely studied genes and diseases, hoping to continuously discover valuable new genes and disease associations to promote the development of medical research. Therefore, various methods are also concerned here for novel genes that have only one known association but no association at training time and new diseases that have only one available association but not at training time. At the same time, to verify the effectiveness of the proposed method, the top 10 candidate genes of 8 common diseases were selected and compared with the database and literature reports.

**4.3. Global Performance.** Some recently proposed gene-disease association prediction methods were undertaken for comparison during experimentation, namely, MC, IMC, and Katz. The recall results of 3-fold cross-validation are shown in Figure 2 and Table 1, where the abscissa

TABLE 5: Prediction of top 10 candidates.

Leukemia MIM : 601626	Alzheimer's disease MIM : 104300	Insulin resistance MIM : 125853	Prostate cancer MIM : 176807
TP53 (7157) [11]	PSEN1 (5563) [4]	SHH (6469)	SHH (6469) [1]
PAX6 (5080)	PSEN2 (5564) [4]	FGFR2 (2263)	BMP2 (650) [18]
PITX2 (5308)	LFNG (3955)	STAR (6770)	IHH (3549)
PTEN (5728) [15]	MESP2 (145873)	DLK1 (8788)	DHH (50846)
RUNX2 (860)	DLL3 (10683)	FGF10 (2255)	SOX2 (6657)
FGFR3 (2261)	TCF15 (6939)	CYP11A1 (1583)	LMNA (4000)
FOXE3 (2301)	CIT (11113)	CYP11B1 (1584)	AKT1 (207) [16]
SPI1 (6688)	NKX3-2 (579)	CYP17A1 (1586)	SIX1 (6495)
TGFB2 (7042)	CHUK (1147)	LBX1 (10660)	IGF1R (3480)
CREBBP(1387)	ROR2 (4920)	HSD3B2 (3284)	STAT3 (6774) [7]
Schizophrenia MIM : 181500	Breast cancer MIM : 114480	Gastric cancer MIM : 137215	Colorectal cancer MIM : 114500
PSEN1 (5663)	TP53 (7157)	TP53 (7157)	TP53 (7157)
WNT4 (54361)	APC (324)	APC (324)	APC (324)
FGFR3 (2261)	CTNNB1 (1499)	AXIN1 (8312)	CTNNB1 (1499)
PITX2 (5038)	AXIN1 (8312)	KIT (3815)	AXIN1 (8312)
PAX3(5077)	FGFR3(2261)	KRAS (3845) [3]	BMPRIA (657)
MSX2(4488)	MSH2(4436)	MSH2 (4436)	FGFR3 (2261)
PAX2(5076)	CDKN2A(1029)	CTNNB1 (1499) [13]	BMPRI1B (658)
PTEN(5728)	BRCA1(672) [2]	MSH6 (2956)	PTEN (5728)
TBX3(6929)	RAD51(5888) [2]	RAD51 (5888)	MSH2 (4436)
IHH(3549)	KRAS(3845)	BRCA1 (672)	SMAD4 (4089)

represents the value of different thresholds  $r$ , and the ordinate represents the recall. The performance of the proposed KIMC1 method and KIMC2 method is better than several other comparison methods when taking different threshold  $r$ . When the threshold is set to  $r = 100$ , the recall rates of several methods are 6.7% for the MC method, 11.3% for the Katz method, 23.2% for the IMC method, 26.5% for the KIMC1 method, and 27.6% for the KIMC2 method. The KIMC2 method with elastic net regularization has a specific improvement compared with the previously proposed IMC method of integrating genetic disease features. The proposed method combines the advantages of the Katz method and the inductive matrix completion method simultaneously, and the overall performance has been improved further. At the same time, it can be seen from the figure that adding elastic net regularization can effectively alleviate the influence of data noise and enhance prediction: effect and stability. Secondly, the precision-recall curves of the experimental results are also given here. As shown in Figure 3(b) and Table 2, the abscissa is the recall, and the ordinate is the precision. It can be observed from the figure that when the recall rate is greater than 4%, under the same precision rate, the recall rates of KIMC1 and KIMC2 are improved compared with the other three methods. The curves under different thresholds with and without elastic net regularization are also compared here. It can be found that the precision rate of KIMC2 after adding elastic net regularization is also significantly improved compared with KIMC1.

**4.4. Prediction of New Genes and New Diseases.** In gene-disease association prediction, there is often a problem that is easily overlooked; most of the genes and diseases recorded in the existing databases are genes and conditions with high recognition and association, and only a few are associated with a single gene; therefore, in the experimental evaluation, such genes and diseases with higher credit and association are often more likely to be predicted, while in reality, researchers pay more attention to those genes and conditions that are in the blank of research. Therefore, we only focus on those genes and needs that are known to be associated with a single association and hide these known associations during training to show the predictive power of different methods for new genes and diseases.

Within the range of the threshold  $r \leq 100$ , the recall rate of new genes is shown in Figure 3(a) and Table 3, the abscissa represents different thresholds, and the ordinate represents the recall rate of new genes. When the threshold range is  $0 < r \leq 45$ , the Katz method predicts better than IMC when using the gene-gene similarity network and disease-disease similarity network as auxiliary information. Because in a heterogeneous network, such data can more directly reflect the association between genes and diseases. However, using different gene and disease data extraction features, IMC performed poorly within this threshold range. When  $r > 45$ , the prediction effect of the IMC method is significantly improved, and the advantage of using feature information for prediction is reflected. The proposed

KIMC1 method and KIMC2 method integrate the benefits of the Katz and IMC methods, making the prediction performance more stable in different threshold ranges while improving the prediction efficiency. When  $r = 100$ , the new gene recall rate of the KIMC2 method was 17.4%. The recall rate of new diseases is shown in Figure 4(b) and Table 4, where the abscissa represents the threshold, and the ordinate represents the recall rate of new diseases. It can be found from the figure that the predictive ability of the KIMC1 method and KIMC2 for new illnesses is also better than several other comparison methods.

**4.5. Prediction of Top 10 Causative Genes for Some Common Diseases.** The above analysis of the predictive power of new genes is only verified on the known gene-disease association datasets in the OMIM database, and some disease-causing genes that are not recorded in the database cannot be evaluated and verified the overall effect will be low. Simultaneous association between genes also cannot be analyzed. Here, the top 10 pathogenic gene prediction results of several common diseases in real life are selected for analysis, and the effect of the proposed method is further explained. Eight common diseases are chosen here, namely, leukemia, Alzheimer's disease, insulin resistance, prostate cancer, schizophrenia, breast cancer, stomach cancer (gastric cancer), and colon cancer (colorectal cancer). During the experiment, all the relevant pathogenic gene information of these 8 diseases in the training data was hidden (that is, the columns corresponding to these 8 common diseases were all set to "0"), and the top 10 candidate pathogenic genes of the predicted diseases were shown in Table 5. In the table, the number after the infection (such as MIM:601626) represents its corresponding number in the OMIM database, and the number after the gene (such as PAX6 (5080)) represents the corresponding number of the gene in the NCBI database. The gene order in the table is arranged in descending order of the prediction score. Through the analysis of the candidate disease-causing genes in the table, it can be found that the disease-causing genes predicted by this method are not limited to the genes recorded in the gene-disease relationship dataset but also predict some disease-related genes discovered in later studies. For example, the genes associated with Alzheimer's disease include PSEN1 and PSEN2 [4]. These confirmed disease-related genes are shown in the table.

Secondly, it can be found from the table that there is a high degree of overlap between the top 10 predicted genes of these 8 diseases, and some genes are shared in the 8 diseases, such as TP53, KRAS, and RAD51, which have been confirmed to be associated with multiple cancers. They are closely related, so this is solid evidence to support the idea that these common genes represent etiological relationships between various diseases. That is, such shared genes can lead to a variety of conditions. Through the analysis of such shared genes, it is further verified that the prediction results of the KIMC method can show some commonalities of genes. Therefore, the KIMC method can provide a valuable reference for researchers to discover disease-causing genes and study the association between disease-causing genes.

The Cancer Genome Atlas (TCGA) has changed our understanding of cancer, established the significance of cancer genomics, and even started to alter how the disease is handled in clinical settings. The effects extend even deeper, touching computational biology, health and scientific technology, and other study areas. Over a 12-year span, the Cancer Genome Atlas (TCGA) acquired, identified, and examined cancer samples from over 11,000 people. The procedure was intricate and continuously altering to take into account new technologies, the subtle differences between various cancer forms, and other shifting elements. In order to overcome the problem of data sparsity, the Katz technique was created, which built a gene-disease heterogeneous network by integrating information on intergene similarity, information on interdisease similarity, and information on gene-disease association information prediction. However, this approach cannot reliably forecast.

## 5. Conclusion

This paper proposes an enhanced inductive matrix completion based on the Katz gene-disease association prediction algorithm for the (KIMC) model. The algorithm combines the advantages of the Katz and IMC methods, which can effectively alleviate the impact of the PU problem encountered. First, in the face of highly sparse gene-disease association data, it can effectively help the data sparsity problem encountered by existing methods. Secondly, by introducing elastic net regularization, the influence of data noise is alleviated, and the noise tolerance of the algorithm is enhanced while improving the prediction effect. Compared with the existing prediction methods, the prediction effect of the KIMC method is significantly improved. It can also effectively predict new genes and diseases that researchers are more concerned about. This method is of great significance for reducing research costs and helping researchers deeply study different diseases' causative genes and gene correlations. Based on the KIMC method proposed in this paper, future studies might take into account combining more diverse biological data sources, and they might investigate how to effectively extract from this biological data the features of genes and diseases with stronger association to help improve the prediction effect.

## Data Availability

The data shall be made available on request.

## Conflicts of Interest

The authors declare that they have no conflict of interest.

## Acknowledgments

This research work is self-funded.

## References

- [1] J. Xu, L. Chen, H. Wu, and S. Zha, "One-step multi-view inductive matrix completion for gene-disease associations prediction," in *2021 IEEE International Conference on Systems, Man, and Cybernetics (SMC)*, pp. 914–920, Melbourne, Australia, October 2021.
- [2] H. Wang, Y. Wei, M. Cao, M. Xu, W. Wu, and E. P. Xing, "Deep inductive matrix completion for biomedical interaction prediction," in *2019 IEEE International Conference on Bioinformatics and Biomedicine (BIBM)*, pp. 520–527, San Diego, CA, USA, November 2019.
- [3] X. Zeng, Y. Lin, Y. He, L. Lv, X. Min, and A. Rodríguez-Patón, "Deep collaborative filtering for prediction of disease genes," *IEEE/ACM Transactions on Computational Biology and Bioinformatics*, vol. 17, no. 5, pp. 1639–1647, 2020.
- [4] X. Wang, Y. Gong, J. Yi, and W. Zhang, "Predicting gene-disease associations from the heterogeneous network using graph embedding," in *2019 IEEE International Conference on Bioinformatics and Biomedicine (BIBM)*, pp. 504–511, San Diego, CA, USA, November 2019.
- [5] Y. Hu, A. Sharma, G. Dhiman, and M. Shabaz, "The identification nanoparticle sensor using back propagation neural network optimized by genetic algorithm," *Journal of Sensors*, vol. 2021, Article ID 7548329, 12 pages, 2021.
- [6] R. Al-Dalky, K. Taha, D. Al Homouz, and M. Qasaimeh, "Applying Monte Carlo simulation to biomedical literature to approximate genetic network," *IEEE/ACM Transactions on Computational Biology and Bioinformatics*, vol. 13, no. 3, pp. 494–504, 2016.
- [7] X. Zeng, N. Ding, and Q. Zou, "Latent factor model with heterogeneous similarity regularization for predicting gene-disease associations," in *2016 IEEE International Conference on Bioinformatics and Biomedicine (BIBM)*, pp. 682–687, Shenzhen, China, December 2016.
- [8] P. Mitra, T. Pijnenburg, and V. Sazonau, "Discovering gene-disease associations with biomedical word embeddings," in *2020 19th IEEE International Conference on Machine Learning and Applications (ICMLA)*, pp. 163–170, Miami, FL, USA, December 2020.
- [9] J. W. Luo, Y. Liu, P. Liu, Z. Lai, and H. Wu, "Data integration using tensor decomposition for the prediction of miRNA-disease associations," *IEEE Journal of Biomedical and Health Informatics*, vol. 26, no. 5, pp. 2370–2378, 2022.
- [10] J.-Y. Shi, "The need of accelerators in analyzing biological networks," in *2016 IEEE International Conference on Bioinformatics and Biomedicine (BIBM)*, pp. 1436–1436, Shenzhen, China, December 2016.
- [11] R. Li, Y. Dong, Q. Kuang et al., "Inductive matrix completion for predicting adverse drug reactions (ADRs) integrating drug-target interactions," *Chemometrics and Intelligent Laboratory Systems*, vol. 144, pp. 71–79, 2015.
- [12] T. Thakur, I. Batra, M. Luthra et al., "Gene expression-assisted cancer prediction techniques," *Journal of Healthcare Engineering*, vol. 2021, Article ID 4242646, 9 pages, 2021.
- [13] S. Sreekala and K. A. A. Nazeer, "A literature search tool for identifying disease-associated genes using hidden Markov model," in *2014 First International Conference on Computational Systems and Communications (ICCSC)*, pp. 90–94, Trivandrum, India, December 2014.
- [14] C. H. Lee, O. Koyejo, and J. Ghosh, "Identifying candidate disease genes using a trace norm constrained bipartite raking model," in *2013 35th Annual International Conference of the IEEE Engineering in Medicine and Biology Society (EMBC)*, pp. 3459–3462, Osaka, Japan, July 2013.
- [15] C. Fan, X. Lei, and F. X. Wu, "Prediction of CircRNA-disease associations using KATZ model based on heterogeneous networks," *International Journal of Biological Sciences*, vol. 14, no. 14, pp. 1950–1959, 2018.
- [16] S. Köhler, S. Bauer, D. Horn, and P. N. Robinson, "Walking the interactome for prioritization of candidate disease genes," *American Journal of Human Genetics*, vol. 82, no. 4, pp. 949–958, 2008.
- [17] O. Vanunu, O. Magger, E. Ruppim, T. Shlomi, and R. Sharan, "Associating genes and protein complexes with disease via network propagation," *PLoS Computational Biology*, vol. 6, no. 1, article e1000641, 2010.
- [18] P. Jia, S. Zheng, J. Long, W. Zheng, and Z. Zhao, "dmGWAS: dense module searching for genome-wide association studies in protein-protein interaction networks," *Bioinformatics*, vol. 27, no. 1, pp. 95–102, 2011.
- [19] L. Huang, L. Zhang, and X. Chen, "Updated review of advances in microRNAs and complex diseases: taxonomy, trends and challenges of computational models," *Briefings in Bioinformatics*, vol. 23, no. 5, 2022.
- [20] L. Huang, L. Zhang, and X. Chen, "Updated review of advances in microRNAs and complex diseases: experimental results, databases, webservers and data fusion," *Briefings in Bioinformatics*, vol. 23, no. 6, article bbac397, 2022.
- [21] X. Chen, C. C. Yan, X. Zhang, and Z. H. You, "Long non-coding RNAs and complex diseases: from experimental results to computational models," *Briefings in Bioinformatics*, vol. 18, no. 4, pp. 558–576, 2017.
- [22] C. C. Wang, C. D. Han, Q. Zhao, and X. Chen, "Circular RNAs and complex diseases: from experimental results to computational models," *Briefings in Bioinformatics*, vol. 22, no. 6, article bbab286, 2021.
- [23] C. Tang, H. Zhou, X. Zheng, Y. Zhang, and X. Sha, "Dual Laplacian regularized matrix completion for microRNA-disease associations prediction," *RNA Biology*, vol. 16, no. 5, pp. 601–611, 2019.
- [24] X. Zheng, C. Zhang, and C. Wan, "miRNA-disease association prediction via non-negative matrix factorization based matrix completion," *Signal Processing*, vol. 190, article 108312, 2022.
- [25] P. Alexiou, M. Maragkakis, G. L. Papadopoulos, M. Reczko, and A. G. Hatzigeorgiou, "Lost in translation: an assessment and perspective for computational microRNA target identification," *Bioinformatics*, vol. 25, no. 23, pp. 3049–3055, 2009.
- [26] T. M. Witkos, E. Koscianska, and W. J. Krzyzosiak, "Practical aspects of microRNA target prediction," *Current Molecular Medicine*, vol. 11, no. 2, pp. 93–109, 2011.
- [27] Human Protein Reaction Database, HPRDAugust 2012, <http://www.hprd.org>.
- [28] X. Wu, R. Jiang, M. Q. Zhang, and S. Li, "Network-based global inference of human disease genes," *Molecular Systems Biology*, vol. 4, no. 1, p. 189, 2008.
- [29] C. Deng, C.-X. Lin, and H.-D. Li, "Improving the prediction of disease-associated genes by integrating annotated gene sets," in *2021 IEEE International Conference on Bioinformatics and Biomedicine (BIBM)*, pp. 386–391, Houston, TX, USA, December 2021.

## Retraction

# Retracted: Ant Colony Optimization-Enabled CNN Deep Learning Technique for Accurate Detection of Cervical Cancer

### BioMed Research International

Received 8 January 2024; Accepted 8 January 2024; Published 9 January 2024

Copyright © 2024 BioMed Research International. This is an open access article distributed under the Creative Commons Attribution License, which permits unrestricted use, distribution, and reproduction in any medium, provided the original work is properly cited.

This article has been retracted by Hindawi following an investigation undertaken by the publisher [1]. This investigation has uncovered evidence of one or more of the following indicators of systematic manipulation of the publication process:

- (1) Discrepancies in scope
- (2) Discrepancies in the description of the research reported
- (3) Discrepancies between the availability of data and the research described
- (4) Inappropriate citations
- (5) Incoherent, meaningless and/or irrelevant content included in the article
- (6) Manipulated or compromised peer review

The presence of these indicators undermines our confidence in the integrity of the article's content and we cannot, therefore, vouch for its reliability. Please note that this notice is intended solely to alert readers that the content of this article is unreliable. We have not investigated whether authors were aware of or involved in the systematic manipulation of the publication process.

Wiley and Hindawi regrets that the usual quality checks did not identify these issues before publication and have since put additional measures in place to safeguard research integrity.

We wish to credit our own Research Integrity and Research Publishing teams and anonymous and named external researchers and research integrity experts for contributing to this investigation.

The corresponding author, as the representative of all authors, has been given the opportunity to register their agreement or disagreement to this retraction. We have kept a record of any response received.

### References

- [1] R. Kavitha, D. K. Jothi, K. Saravanan et al., "Ant Colony Optimization-Enabled CNN Deep Learning Technique for Accurate Detection of Cervical Cancer," *BioMed Research International*, vol. 2023, Article ID 1742891, 9 pages, 2023.



## Research Article

# Ant Colony Optimization-Enabled CNN Deep Learning Technique for Accurate Detection of Cervical Cancer

R. Kavitha <sup>1</sup>, D. Kiruba Jothi <sup>2</sup>, K. Saravanan <sup>3</sup>, Mahendra Pratap Swain <sup>4</sup>,  
José Luis Arias Gonzáles <sup>5</sup>, Rakhi Joshi Bhardwaj <sup>6</sup>, and Elijah Adomako <sup>7</sup>

<sup>1</sup>Sri Ram Nallamani Yadava Arts and Science College, Manonmaniam Sundaranar University, Tirunelveli, India

<sup>2</sup>Department of Information Technology, Sri Ram Nallamani Yadava college of Arts and Science, Manonmaniam Sundaranar University, Tirunelveli, India

<sup>3</sup>Department of Information Technology, R.M.D. Engineering College, Chennai, India

<sup>4</sup>Department of Pharmaceutical Sciences and Technology, Birla Institute of Technology, Mesra, Ranchi, India

<sup>5</sup>Pontificia Universidad Católica del Perú, Peru

<sup>6</sup>Department of Computer Engineering, Vishwakarma Institute of Technology, Savitribai Phule Pune University, Pune, India

<sup>7</sup>University of Ghana, Accra, Ghana

Correspondence should be addressed to Elijah Adomako; eadomako011@st.ug.edu.gh

Received 7 August 2022; Revised 3 October 2022; Accepted 7 February 2023; Published 21 February 2023

Academic Editor: Gaganpreet Kaur

Copyright © 2023 R. Kavitha et al. This is an open access article distributed under the Creative Commons Attribution License, which permits unrestricted use, distribution, and reproduction in any medium, provided the original work is properly cited.

Cancer is characterized by abnormal cell growth and proliferation, which are both diagnostic indicators of the disease. When cancerous cells enter one organ, there is a risk that they may spread to adjacent tissues and eventually to other organs. Cancer of the cervix of the uterus often initially manifests itself in the uterine cervix, which is located at the very bottom of the uterus. Both the growth and death of cervical cells are characteristic features of this condition. False-negative results provide a significant moral dilemma since they may cause women to get an incorrect diagnosis of cancer, which in turn can result in the woman's premature death from the disease. False-positive results do not raise any significant ethical concerns; but they do require a patient to go through an expensive and time-consuming treatment process, and they also cause the patient to experience tension and anxiety that is not warranted. In order to detect cervical cancer in its earliest stages in women, a screening procedure known as a Pap test is often performed. This article describes a technique for improving images using Brightness Preserving Dynamic Fuzzy Histogram Equalization. To individual components and find the right area of interest, the fuzzy c-means approach is applied. The images are segmented using the fuzzy c-means method to find the right area of interest. The feature selection algorithm is the ACO algorithm. Following that, categorization is carried out utilizing the CNN, MLP, and ANN algorithms.

## 1. Introduction

Cancer is a disease that is characterized by abnormal cell growth and proliferation. A malignant cell that has invaded an organ has the potential to spread to neighboring tissues and, ultimately, to other organs. Any aberrant cell proliferation, whether benign or malignant, is referred to as a tumor. A benign tumor, like a typical skin wart, remains in its former destination and does not move to other parts of the body or invade neighboring normal tissue. A cancerous tumor, on the other hand, has the ability to both spread

throughout the body via the circulatory or lymphatic systems and infiltrate neighboring healthy cells (metastasis). Only malignant tumors are appropriately referred to as cancers, and the danger of cancer stems from its propensity to infiltrate and spread. Cervical cancer first manifests itself in the tissue of the uterine cervix, which is located at the very bottom of the uterus. The infection is characterized by cervical cell growth that is out of control as well as cell death. In about 90 percent of instances of cervical cancer, squamous cell carcinomas are found in the exocervix, which is the region outside of the cervix. Because it is a slow-growing

disease that has not yet spread to other regions of the body, cervical cancer in its early stages does not produce any symptoms. Early identification and treatment are both completely curative and preventive when it comes to this condition since it has a prolonged premalignant phase. According to the National Cancer Institute in the United States, cervical cancer is the fourth most frequent illness found in women and is one of the most common causes of cancer death in women worldwide. Cervical cancer is also one of the most common causes of cancer mortality in males [1]. The development of abnormal cells in the cervix's lining is known as cervical cancer. Squamous cell carcinoma is the most typical type of cervical cancer. Cervical cancer symptoms include bleeding after intercourse, in between cycles, or during menopause; watery, red, possibly thick, and foul-smelling vaginal discharge; and pain in the pelvis or during sexual activity. Numerous illnesses were linked to cervical instances. The most common cervical illness among symptomatic southern Ethiopian women was cervical carcinoma. When compared to other cervical cases, the high prevalence of cervical cancer was seen in postmenopausal women. The incidence of cervical cancer [2] and the mortality rate have both decreased in industrialized countries because to the increased use of frequent and mandated screening. On the other hand, cancer is more prevalent in countries with low and moderate incomes, where resources are few and people are not properly educated about the hazards posed by the illness. More women die from cancer in these countries. There are a number of problems associated with automatic screening methods. Particles from the surfaces and surrounding areas of the cervix are carefully extracted during a Pap smear procedure so that they may be inspected under a microscope for cervical cancer or cell changes that could lead to the disease. With a Pap smear, other issues like infections or inflammatory disorders may be found. It is frequently done simultaneously with a pelvic examination and may also be done simultaneously with a test for particular types of human papillomavirus (HPV). These downsides include a decreased sensitivity, uncertainty surrounding cost efficiency, and the inability to detect cases of early abnormalities. It is shown in Figure 1.

The question of whether or not to utilize an automated screening system as opposed to a manual screening method has been hotly contested for decades, and the issue has not been addressed to anyone's satisfaction. They look for early sickness detection, first before indications emerge. This has the advantage of allowing for much early medical intervention for the illness. A problem should only be treated early if doing so leads to a better health outcome than delaying treatment. It has been passionately debated for decades whether to use an automated screening system instead of a manual screening technique, and the problem has not been resolved to everyone's satisfaction. Pathologists are required to examine each subimage on a separate slide under a microscope in the event of manually screening of Pap smear pictures in order to make a medical diagnosis. In the case of manual screening of Pap smear photos, pathologists are required to inspect each subimage on a separate slide under a microscope in order to arrive at a diagnosis of sickness.

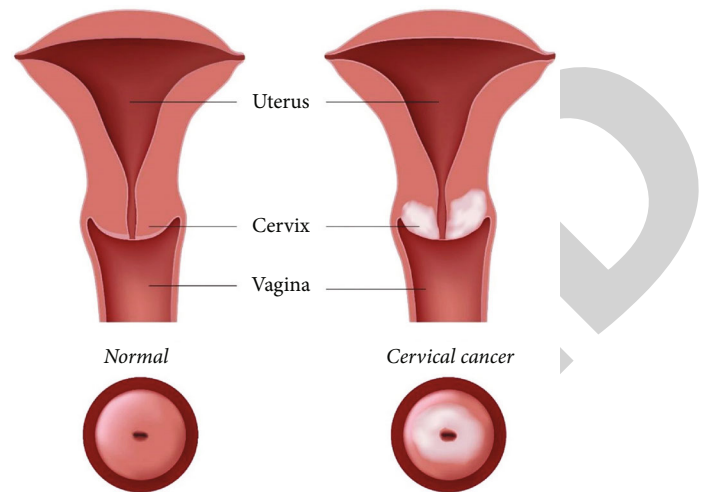


FIGURE 1: Cervical cancer symptoms.

During mass screening operations, a large number of samples need to be analyzed, which requires more cytotechnicians with higher expertise as well as additional time. The quality of medical photographs has significantly increased because of the developments in medical imaging technology, which has made it possible to diagnose sickness at an earlier stage [3, 4].

Screening may be performed by an automated diagnostic tool without the introduction of observer bias if healthy samples are correctly classified as normal and those with sickness are correctly classified as abnormal. In the event that a patient is given an incorrect diagnosis during screening, they may be subjected to unnecessary follow-up and treatment even when they do not really have the condition. If a test has a false-negative or false-positive result, the one who has the ailment will interpret the result as normal, whereas the individual who does not have the illness would interpret the result as abnormal. Negative smear tests were examined to assess the diagnostic accuracy of recurrence. A total of 122 negative smear results were obtained from women who did not have cervix disease, and 61 of them came from 41 women whose negative smear results were reported within 5.5 years of their CC diagnosis (used as control group). At review, it was discovered that every test from a woman without cervical cancer came back negative. On the other hand, 27.1% of cancer cases from cytologists were recorded as positive. As a direct consequence of this, patients often report feeling of anxiety and depression [5, 6]. Figure 2 shows the different stages of cervical cancer that can be seen in the patients.

Patients who have precancerous lesions will get treatment as quickly as feasible utilizing computer-assisted screening technologies. These approaches have the potential to discover abnormal Pap smear results in patients. The success of an automated screening product is limited by the high cost of the screening equipment, the price of screening activities, and the challenge of achieving high accuracy while simultaneously minimizing the number of false-negative samples produced. It is necessary to develop classification strategies that are both effective and trustworthy if

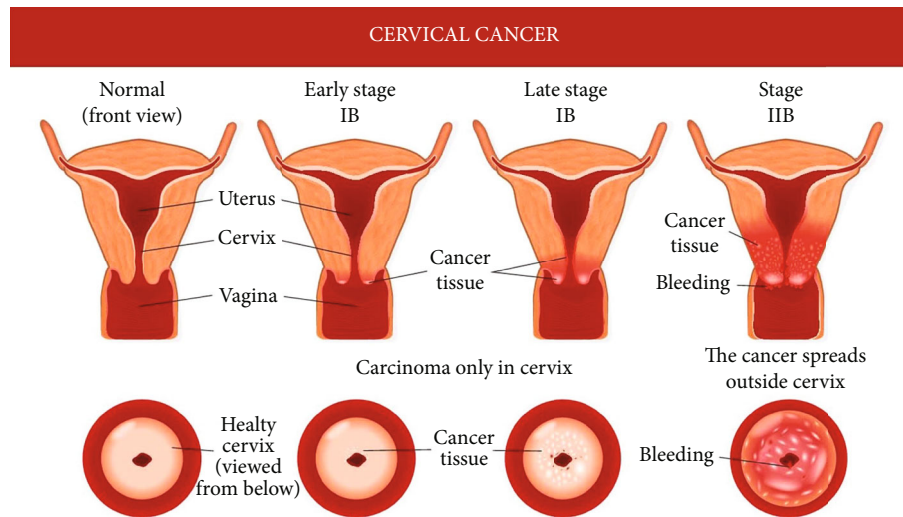


FIGURE 2: Stages of cervical cancer.

automated systems are to be capable of correctly distinguishing between diseased and healthy samples. Screening samples may now be done more quickly, consistently, and accurately than ever before with the use of machine learning algorithms and medical image processing techniques, all at a cheaper cost than traditional visual screening methods [7]. The precancer stages of cervical cancer are shown in Figure 3.

Image collection, noise reduction, segmentation of regions of interest, feature extraction, and classification are among the major procedures that comprise a Pap smear screening system. The key steps is the Pap smear screening technique. There may be further processes as well. There are several stages to the design process, and each one must be completed successfully for the classification and diagnosis of illness to be done appropriately. False-negative test results are a significant ethical consideration since they can result in a wrong diagnosis of female cancer, which could cause the patient to pass away from the condition. Untrue tests do not provide a severe ethical dilemma, but they do subject the patient to an expensive treatment method and undue anxiety. Other steps may also be included. The process of design consists of multiple steps, and the successful completion of each stage is essential for correctly classifying and diagnosing sickness. False-negative test results are a major ethical concern since they may lead to the incorrect diagnosis of cancer in women, which can then result in the patient's death from the disease. False-positive results do not raise a serious ethical issue; but they do require a patient to undergo an expensive therapeutic process which causes the patient to experience unnecessary worry. It is of the utmost importance to develop a computer-aided diagnosis approach for cervical cancer treatment, in particular in developing countries and poorer nations, where the incidence and fatality rates of the disease are much greater than in wealthy nations.

Researchers are increasingly turning to machine learning (ML), a research approach that is in the process of undergoing fast development. Their goal is to improve cancer detection and treatment. It falls under the umbrella of "artificial

intelligence." Software applications are capable of predicting events more correctly without specific guidelines thanks to machine learning (ML), a type of artificial intelligence (AI). Machine learning algorithms take previous information as input and estimate future accurate output. Medical experts may quickly gain a new viewpoint thanks to the ML categorization of cancer. In reality, the use of machine learning methods may broaden the tumor prognosis window. The ML classification of cancer might provide medical professionals a different perspective in a very short amount of time. The use of machine learning algorithms may, in fact, broaden the scope of cancer prediction [8].

The classification power of ML is most beneficial in biological applications when it is employed in combination with genomic and proteomic data. Because of the growing amount of data available on cancer, machine learning is often used in the process of identifying and diagnosing cancer. The ML approach is reflective of the rising trend toward personalized and predictive medicine in medicine generally.

This article contains a methodology that uses Brightness Preserving Dynamic Fuzzy Histogram. For improving image contrast, fuzzy logic-based histogram equalization (FHE) is suggested. As opposed to conventional crisp histograms, fuzzy histograms are built using fuzzy set theory in order to more effectively handle the ambiguity of grey level data. The fuzzy distribution is divided into two subhistograms based on the median value of the original image in the second stage, and each subhistogram is then separately balanced to preserve contrast enhancement. Two well-known metrics utilized to assess the both qualitative and quantitative assessments of the proposed FHE approach are average information contents (AIC) and natural image quality evaluator (NIQE) index for different pictures. Equalization for image enhancement. Images are segmented to detect correct region of interest using the fuzzy c-means technique. In this method, the author transformed the colour image to grayscale and applied a median filter to lessen the level of noise and improve the representation of the image before using the fuzzy c-means clustering algorithm. Clusters and

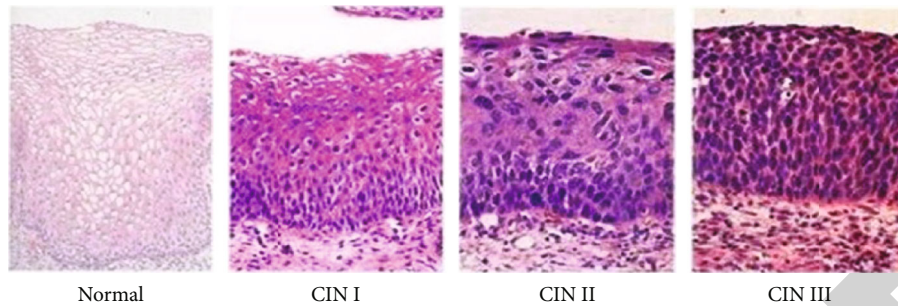


FIGURE 3: Cervical precancer stages.

classification are the third and fourth steps of this process, respectfully. The centre value may be calculated thanks to the patch-based sorting. A data collection is divided into  $N$  clusters using the fuzzy  $c$ -means (FCM) data clustering method, with each data point in the dataset to some extent belonging to each cluster. A data point will have a high degree of membership in a cluster, for instance, if it is near to the cluster's center. ACO algorithm is used for feature selection. Then, classification is performed using CNN, MLP, and ANN algorithms. Accuracy of ACO-CNN is highest among all classifiers used in this experimental study.

Both aberrant cell growth and reproduction, which are both diagnostic indications of the illness, are characteristics of cancer. The membrane of the uterine cervix, which is found at the base of the uterus, is where cervical cancer first shows symptoms. Cell death and uncontrollable cervical cell proliferation are symptoms of the illness. The fourth most prevalent disease in women and one of the leading causes of cancer-related deaths in women globally is cervical cancer.

The remainder of this paper is organized as follows: Section 2 covers the literature survey. Section 3 covers the methodologies, and the results are analyzed in Section 4. Section 5 contains concluding remarks as well as future scope of the research.

## 2. Literature Survey

The augmentation of a photograph is done with the intention of calling attention to certain aspects in order to facilitate future research. A machine learning-based programme called automated visual assessment (AVE) scans digital images of the cervix for indications of cancer or precancer. An AVE-positive result indicates the existence of troubling lesions that are either suggestive of cancer or enhance the possibility that cancer will develop in the near future. An AVE-negative outcome, on the other hand, indicates a cervix that is not at higher risk for cancer. The methodologies may be broken down into two primary categories: the spatial domain and the frequency domain. The values of a picture's pixels are inputted directly into mathematical calculations that are performed in the spatial domain. The picture is transformed using a Fourier transformation in the frequency domain first, and then, the inverse of the image that was converted using the Fourier transform is used to create the

final image. Filtering is one component of image enhancement, and its purposes include reducing distracting noise and bringing attention to certain aspects of an image.

The authors Lu et al. [8] offered a comparative analysis of a variety of techniques for improving the quality of the pictures. Approaches from the spatial domain, the frequency domain, and the fuzzy domain were all used throughout the investigation. Approaches based on histograms and fuzzy logic have both been shown to be effective. The author of the research believes that the evaluation of the fuzzy-based enhancement's  $K$  factor might perhaps be automated by employing ant colony optimization to provide a more accurate representation of the image.

According to the author, the Poisson noise is introduced into cell images as a result of the noneven distribution of photons. According to the findings of the study, an adaptive Wiener filter has the potential to effectively minimize the Poisson noise. Even if the picture qualities change from one location to another, it is still feasible to denoise photographs by using an adaptive Wiener filter [9].

Bihistogram equalization is a method that was created by Tang and Isa [10] with the purpose of increasing the quality of grayscale pictures. The input histogram is used to generate not one but two subhistograms. The picture's oversaturation was brought under control by clipping the histogram, and then, the output that was generated was equalized and mixed to make the finished product. In general, the performance of the authors' technique is superior to that of existing histogram-based improvement algorithms, as shown by a comparison with those algorithms.

It was found by Kumbhar et al. [11] that the main attributes of an image may be retrieved for enhanced diagnosis if the features of medial photos are increased. The images were run through filters before any sharpening or noise reduction methods were applied to them. In addition to that, an effect called "Adaptive Histogram Equalization and Average Filter" was added to the photo in order to make it seem better.

In the Herlev dataset, Chankong et al. [12] segregated the nucleus from the cytoplasm by using a patch-based version of the fuzzy  $c$ -means clustering algorithm. In this method, the author converted the colour image to grayscale and used a median filter to reduce the amount of noise and smooth out the appearance of the picture. The third and fourth processes in this process are called clustering and segmentation, respectively. The patch-based sorting allowed for the calculation of the central value.

According to Sharma and Mangat [13], an additional improvement was made to the work, and the author improved the “fuzzy c-means (FCM)” clustering technique by working with various numbers of clusters rather of just one. This was done in order to reinforce the clustering of the data. The author recommended combining techniques to segmentation with methods for locating areas of interest in order to improve the accuracy of the segmentation process. There is a possibility that the present accuracy of the Herlev dataset may be improved using a variety of feature variations, improved noise reduction techniques, and segmentation methods (93.7 percent).

Saha et al. [14] introduced a circularly shaped function that put a restriction on the form of the cluster in order to enhance the border of the nucleus. This was done in order to make the nucleus seem more complete.

A categorization system that is based on texture and was created by Mariarpatham and Stephen [15] is used to categorize smear photographs into a total of seven separate groups. In terms of the accuracy of classification, it was shown that SVM had a precision of 97.38 percent for normal squamous, 93.89 percent for intermediate squamous, 87.33 percent for mild dysplasia, and 58.52 percent for severe dysplasia. The RBF, linear, and quadratic SVM kernels were used in the classification process.

A wide range of neural network architectures were put to the test by Devi et al. [16] for the purpose of disease diagnosis. ANN designs such as the multilayered perceptron may be helpful when it comes to the acceleration of the detection process. Both a feedforward network and a knowledge-based neural network were utilized in order to map the input pictures with the rules and extract the features that are necessary for classification. As a result, the classification results exhibited by the network were superior, and it had a decent accuracy rate. The results of the classification carried out using the artificial neural network (ANN) method are better and have a high rate of accuracy.

Athinarayanan et al. [17] developed a categorization system for cervical disease by analyzing images obtained from Pap smears. In order to improve the rough set text on co-occurrence matrix, we made use of the ERSTCM and CABS descriptors as well as the concatenated feature extraction approach (CFE). Using a classifier, it is possible to measure the performance of the extracted features by comparing them to statistical criteria such as sensitivity, specificity, and accuracy. This can be done with the help of a classification algorithm (FL-HKSVM). The performance of the concatenated feature extraction method was superior than that of the other two classifiers. Feature extraction is the process of converting raw data into manageable quantitative properties while conserving the original dataset’s characteristics. It yields superior results when compared to utilizing machine learning on the raw data directly. Since CNNs can automatically generate features from time series information and frequency represented images, they are most frequently employed in healthcare applications. After that, a classifier network uses these features to do classification and regression. A neural network that has hundreds of hidden layers is referred to as a deep learning network. This kind of net-

work is able to capture the nonlinear link that exists between intricate patterns and make accurate predictions. For the purposes of picture recognition and analysis, deep neural network topologies such as the convolution neural network (CNN) are often used [18]. A system will automatically learn features at many different levels of abstraction in order for it to be able to learn every conceivable characteristic. This is necessary for the system to be able to learn everything.

The precision of the cell segmentation is a crucial component in the overall success of the traditional machine learning approaches. Taha et al. [19] proposed a technique for categorizing cells without the need for segmentation. Their approach included the use of a deep feature learning convolution neural network. They were successful in assigning categories to the Herlev dataset with a rate of accuracy of 98 percent, which is an admirable achievement.

Hyeon et al. [20] trained a model that can differentiate between healthy and sick cervical cells by using a convolutional neural network (CNN) and retrieving feature vectors from images of cervical cells. These collected characteristics were trained with the use of an SVM classifier, which resulted in a success rate of 78 percent overall. The study presented here proposes a classification model for prostate cancer that makes use of deep learning methods and achieves an accuracy of 80.1% on training sets and 78.1% on testing sets, respectively.

Devi et al. [16] investigated a variety of neural network architectures, convolutional neural network architecture, and feedforward network architecture. According to the results, the performance of ANN might be enhanced by including a learning capacity that assists in the improvement of its efficiency through the evaluation of exceptional performance.

### 3. Methodology

This article contains a methodology that uses Brightness Preserving Dynamic Fuzzy Histogram Equalization for image enhancement. Images are segmented to detect correct region of interest using the fuzzy c-means technique. ACO algorithm is used for feature selection. Then, classification is performed using CNN, MLP, and ANN algorithms. Accuracy of ACO-CNN is highest among all classifiers used in this experimental study. Interstrategies modelled after ants are referred to as “ants.” Biological ants’ pheromone-based communication is frequently the dominating paradigm. For many optimization projects requiring some kind of graph, local search algorithms combined with artificial ants have emerged as the preferred approach. This framework is shown in Figure 4.

By using the technique for fuzzy histogram equalization, the method known as “Brightness Preserving Dynamic Fuzzy Histogram Equalization” has been updated in order to increase both its brightness and its contrast. It was chosen to first use a Gaussian kernel to smooth out the image histogram and then to segment the troughs for dynamic equalization. This was done after the decision was made. Histograms are processed using crisp histograms so that the contrast may be made better. Brightness Preserving Dynamic Fuzzy

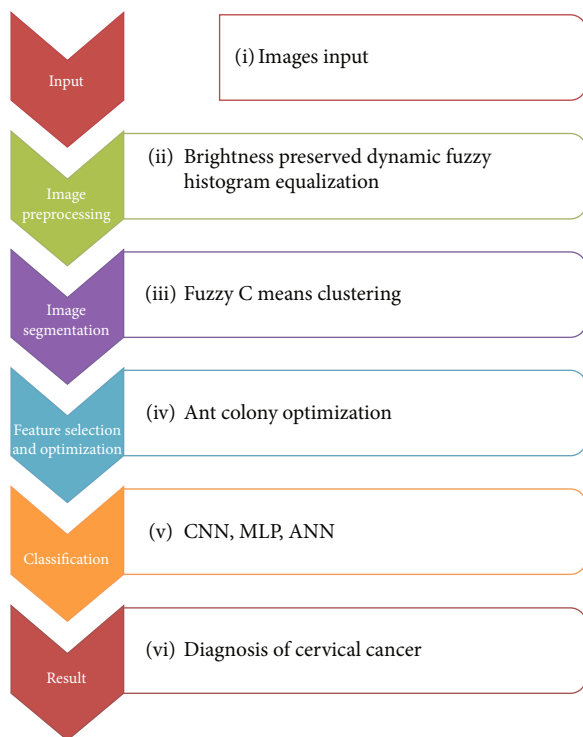


FIGURE 4: Ant colony optimization-enabled CNN deep learning technique for accurate detection of cervical cancer.

Histogram Equalization [21] is a modified method that was developed as a result of the authors' use of fuzzy statistics in the original methodology. As a result, the authors were able to efficiently keep the mean image brightness.

The fuzzy *c*-means clustering approach combines pixels and groups together according to the similarity criteria that they share with one another. Because the nucleus and cytoplasm both have consistent pixel values, this method was successful when applied to Pap smear photographs. When an algorithm uses fuzzy *c*, it indicates that it does not definitively decide on the absolute membership value of a certain cluster. Because it takes into consideration the degree of membership and then utilizes that value to identify the cluster, it is possible to accomplish an accurate segmentation using this method. In order to do medical image analysis, one of the most important steps is to cut the image into a number of smaller, more manageable pieces. Because of its accuracy and ease of use, the fuzzy *c*-means method is a popular choice for clustering data in the field of medical image analysis [22].

The selection strategy is used to both increase the dimensionality of the input and recover the prominent aspects of the sign representation. Within this part, ant colony optimization, often known as ACO, is used as a tool to assist in the process of feature selection. Finding good pathways throughout graphs is a computer challenge that can be solved using the probability ant colony optimization algorithm (ACO). Multiagent techniques influenced by the behavior of actual ants are represented by artificial ants. Biological ants' pheromone-based communication is frequently the dominating paradigm. Combinations of artificial ants

and local search algorithms have become the standard method for several optimization tasks that involve networks, such as route choice and internet routing. According to ACO, which is one of the most recent approaches to approximation optimization, actual ants, which use the chemical signaling agent known as pheromone to communicate with one another, may use to find the shortest pathways between their nest and food sources. Pheromones are used by ants to communicate with one another [23].

The efficacy of machine learning methods is severely limited when they are used to enormous datasets because of challenges such as underfitting, model complexity, and a lack of resource optimization. These challenges make it difficult for the approaches to be effective. Deep learning networks may be applied to massive amounts of data in order to discover new information, make predictions about the future based on that knowledge, and put that knowledge to use. The machine models are able to learn directly from photographs, videos, and text thanks to a technique called deep learning. As the amount of data available increases, several deep learning architectures have been implemented in order to obtain an outstanding level of performance in comparison to previous machine learning methods. The approach known as "Brightness Preserving Dynamic Fuzzy Histogram Equalization" has been revised to increase both brightness and contrast utilizing the fuzzy histogram equalization technique. The fuzzy *c*-means clustering method groups and mixes pixels in accordance with the similarity criteria they share. This technique worked well with Pap smear images since the nucleus and cytoplasm both have constant pixel values.

The convolutional neural network is a deep neural network that is extensively used in computer vision. It is constructed by assembling deep neural network design. CNN is built on many different layers, including convolutional, pooling, activation, and linked convolutional layers. A deep convolutional neural network (CNN) is an end-to-end architecture that, as the name indicates, is composed of a number of convolutional layers. The filters that are used in the convolutional layer are the most essential component there. At the convolutional layer, just a small number of the input picture's pixels—let us say  $3 \times 3$ —are allowed to get through the filter [24].

The values of the pixels are subjected to a "dot" operation, and the filter uses a predetermined weight to determine how much of an impact this operation will have on the final result. As a direct consequence of this procedure, the convolutional layer will provide an image with a more compact matrix containing the data points. The activation layer takes the shape of a matrix and is responsible for supplying the network with nonlinearity as well as back propagation. Pooling decreases the number of layers in samples, in addition to lowering the size of the filter matrix. The selection of a single feature from each group by the pooling layer gives rise to the name "max layer," which describes this selection. The max layers are linked to provide a list of probabilities for a variety of probable labels for the image that is being analyzed. When making a decision on how to classify anything, the label that seems to fit best is the one that is chosen.

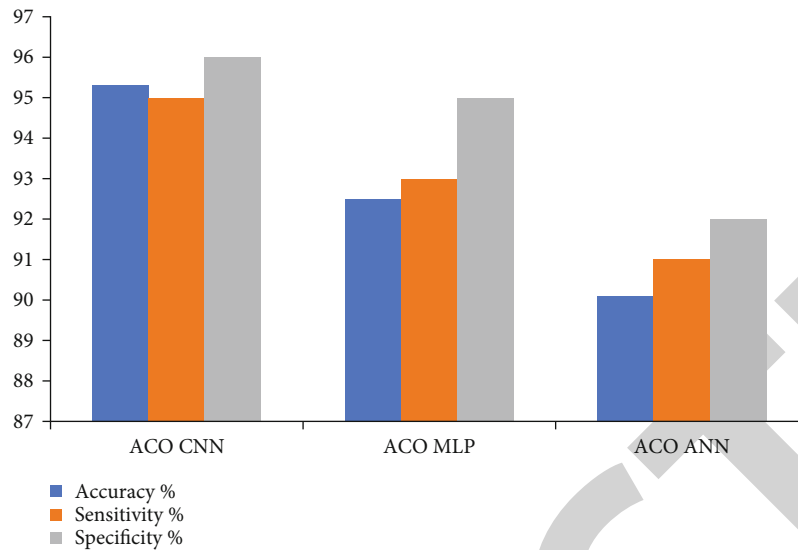


FIGURE 5: Accuracy, sensitivity, and specificity of machine learning techniques for diagnosis of cervical cancer on the Herlev dataset.

It was Professors Bernard Widrow and Ted Hoff, back in 1960, who created a mathematical model. Information may be processed in an analogous manner to the way the human brain works. Using this strategy, researchers were able to classify and forecast chronic illnesses like breast cancer. ANN [25] is a powerful tool for revealing BC's simple connections. An ML process was used to create and construct this algorithm for a specific purpose, such as pattern cataloging. Edges of the ANN model refer to the connections made between layers. Input, intermediate, and output layers are formed by the arrangement of neurons. Edges link the neurons, and each side has a vertex, which is termed "wait" in this context. The underlying concept of ANN is that of a network of neurons.

An MLP algorithm is a kind of machine learning algorithm that recreates the decision-making and learning processes of a natural artificial neural network (ANN) by using several fully connected layers. MLP used three different layers for its nodes: (A) the initial layer, also known as the input layer; (B) the intermediate layer, also known as the hidden layer; and (C) the output layer. The back propagation method is used in order to affect an update to the weight of the MLP. MLP allows for the recognition of non-linear datasets that are separable [26].

#### 4. Result Analysis

The Herlev dataset consists of 242 normal cells, 650 images are used to train the model, and the remaining 267 images were used to test the model [27]. A model's performance can be gauged by its sensitivity and specificity. In contrast to specificity, which measures how well the model predicts real negatives, sensitivity measures how well the model predicts true positives. The results are shown in Figure 5.

Brightness Preserving Dynamic Fuzzy Histogram Equalization is used for image enhancement. Images are segmented to detect correct region of interest using the fuzzy

c-means technique. ACO algorithm is used for feature selection. Then, classification is performed using CNN, MLP, and ANN algorithms. Accuracy of ACO-CNN is highest among all classifiers used in this experimental study. Various authors have investigated similar studies in their results. The result trend of the current study is similar to the findings of various researchers. A deep learning method for cervical cancer detection using Pap smear images is proposed by Taha et al. [19]. They use the Herlev public database for single cell Pap smears to demonstrate the effectiveness of this novel approach, and the results of the experiments show that our suggested system works noticeably better than other cutting edge techniques.

#### 5. Conclusion

Since abnormal cell growth and multiplication are diagnostic signs of cancer, this condition is regarded as its distinguishing feature. Once malignant cells have invaded an organ, it is possible that they will spread to the tissues nearby before eventually reaching other organs. The uterus cervix, which is located at the very bottom of the uterus, is frequently where uterine cervical cancer first manifests itself. Both the growth and death of cervical cells are hallmarks of this condition. Both of these procedures are signs. False-negative results pose a huge ethical problem since they may result in women being given the wrong cancer diagnosis, which may cause the woman to pass away from the disease too soon. In this sense, erroneous negative outcomes might be to blame for the early demise of females. False-positive results do not lead to any significant ethical issues, but they do make a patient undergo an expensive and time-consuming treatment process, as well as put them through unneeded stress and concern. Women are frequently subjected to a monitoring procedure called a Pap test in an effort to find cervical cancer in its earliest stages, when it is most curable. By using the procedures described in this

article, which make use of a method called Brightness Preserving Dynamic Fuzzy Histogram Equalization, image quality can be enhanced. Images are segmented using the fuzzy c-means technique to determine the proper area of interest. The ACO algorithm is used to select the characteristics. Then, classification is performed with the aid of the CNN, MLP, and ANN algorithms. Of all the classifiers used in this experimental inquiry, the ACO-CNN classifier had the highest accuracy.

## Data Availability

The corresponding author will provide data on request.

## Conflicts of Interest

There is no conflict of interest.

## References

- [1] R. Shafabakhsh, R. J. Reiter, H. Mirzaei, S. N. Teymoordash, and Z. Asemi, "Melatonin: a new inhibitor agent for cervical cancer treatment," *Journal of Cellular Physiology*, vol. 234, no. 12, pp. 21670–21682, 2019.
- [2] US Preventive Services Task Force, S. J. Curry, A. H. Krist et al., "Screening for cervical cancer," *Journal of the American Medical Association*, vol. 320, no. 7, pp. 674–686, 2018.
- [3] S. Pankaj, S. Nazneen, S. Kumari et al., "Comparison of conventional Pap smear and liquid-based cytology: a study of cervical cancer screening at a tertiary care center in Bihar," *Indian Journal of Cancer*, vol. 55, no. 1, pp. 80–83, 2018.
- [4] A. S. Zamani, L. Anand, K. P. Rane et al., "Performance of machine learning and image processing in plant leaf disease detection," *Journal of Food Quality*, vol. 2022, Article ID 1598796, 7 pages, 2022.
- [5] N. Dong, L. Zhao, C. H. Wu, and J. F. Chang, "Inception v3 based cervical cell classification combined with artificially extracted features," *Applied Soft Computing*, vol. 93, article 106311, 2020.
- [6] R. Veluri, I. Patra, M. Naved et al., "Learning analytics using deep learning techniques for efficiently managing educational institutes," *Materials Today: Proceedings*, vol. 51, pp. 2317–2320, 2022.
- [7] T. Zhang, Y. M. Luo, P. Li et al., "Cervical precancerous lesions classification using pre-trained densely connected convolutional networks with colposcopy images," *Biomedical Signal Processing and Control*, vol. 55, article 101566, 2020.
- [8] J. Lu, E. Song, A. Ghoneim, and M. Alrashoud, "Machine learning for assisting cervical cancer diagnosis: an ensemble approach," *Future Generation Computer Systems*, vol. 106, pp. 199–205, 2020.
- [9] T. Deepa and A. N. Rao, "A study on denoising of poisson noise in Pap smear microscopic image," *Indian Journal of Science and Technology*, vol. 9, no. 45, 2016.
- [10] J. R. Tang and N. A. M. Isa, "Adaptive image enhancement based on bi-histogram equalization with a clipping limit," *Computers & Electrical Engineering*, vol. 40, no. 8, pp. 86–103, 2014.
- [11] U. Kumbhar, V. Patil, and S. Rudrakshi, "Enhancement of medical images using image processing in matlab," *International Journal of Engineering Research and Technology*, vol. 2, no. 4, pp. 2359–2364, 2013.
- [12] T. Chankong, N. Theera-Umpon, and S. Auephanwiriyakul, "Automatic cervical cell segmentation and classification in Pap smears," *Computer Methods and Programs in Biomedicine*, vol. 113, no. 2, pp. 539–556, 2014.
- [13] B. Sharma and K. K. Mangat, "Various techniques for classification and segmentation of cervical cell images—a review," *International Journal of Computer Applications*, vol. 147, no. 9, pp. 16–20, 2016.
- [14] R. Saha, M. Bajger, and G. Lee, "Spatial shape constrained fuzzy c-means (fcm) clustering for nucleus segmentation in Pap smear images," in *2016 International conference on digital image computing: techniques and applications (DICTA)*, pp. 1–8, Gold Coast, QLD, Australia, 2016.
- [15] E. J. Mariarputham and A. Stephen, "Nominated texture based cervical cancer classification," *Computational and Mathematical Methods in Medicine*, vol. 2015, Article ID 586928, 10 pages, 2015.
- [16] M. A. Devi, S. Ravi, J. Vaishnavi, and S. Punitha, "Classification of cervical cancer using artificial neural networks," *Procedia Computer Science*, vol. 89, pp. 465–472, 2016.
- [17] S. Athinarayanan, M. Srinath, and R. Kavitha, "Computer aided diagnosis for detection and stage identification of cervical cancer by using Pap smear screening test images," *ICTACT Journal on Image & Video Processing*, vol. 6, no. 4, 2016.
- [18] L. Zhang, L. Lu, I. Noguez, R. M. Summers, S. Liu, and J. Yao, "DeepPap: deep convolutional networks for cervical cell classification," *IEEE Journal of Biomedical and Health Informatics*, vol. 21, no. 6, pp. 1633–1643, 2017.
- [19] B. Taha, J. Dias, and N. Werghe, "Classification of cervical-cancer using Pap-smear images: a convolutional neural network approach," in *Annual Conference on Medical Image Understanding and Analysis*, pp. 261–272, Cham, 2017.
- [20] J. Hyeon, H.-J. Choi, K. N. Lee, and B. D. Lee, "Automating papanicolaou test using deep convolutional activation feature," in *2017 18th IEEE International Conference on Mobile Data Management (MDM)*, pp. 382–385, Daejeon, Korea (South), 2017.
- [21] D. Sheet, H. Garud, A. Suveer, M. Mahadevappa, and J. Chatterjee, "Brightness preserving dynamic fuzzy histogram equalization," *IEEE Transactions on Consumer Electronics*, vol. 56, no. 4, pp. 2475–2480, 2010.
- [22] J. R. Tang, N. A. Mat Isa, and E. S. Ch'ng, "A fuzzy-c-means-clustering approach: quantifying chromatin pattern of non-neoplastic cervical squamous cells," *PLoS One*, vol. 10, no. 11, article e0142830, 2015.
- [23] S. Singh and R. R. Janghel, "Early diagnosis of Alzheimer's disease using ACO optimized deep CNN classifier," in *Ubiquitous Intelligent Systems. Smart Innovation, Systems and Technologies*, P. Karuppusamy, I. Perikos, and F. P. García Márquez, Eds., vol. 243, Springer, Singapore, 2022.
- [24] A. Ghoneim, G. Muhammad, and M. S. Hossain, "Cervical cancer classification using convolutional neural networks and extreme learning machines," *Future Generation Computer Systems*, vol. 102, pp. 643–649, 2020.
- [25] J. Zhang, C. Li, Y. Yin, J. Zhang, and M. Grzegorzec, "Applications of artificial neural networks in microorganism image analysis: a comprehensive review from conventional



## Retraction

# Retracted: A Multi-Thresholding-Based Discriminative Neural Classifier for Detection of Retinoblastoma Using CNN Models

### BioMed Research International

Received 8 January 2024; Accepted 8 January 2024; Published 9 January 2024

Copyright © 2024 BioMed Research International. This is an open access article distributed under the Creative Commons Attribution License, which permits unrestricted use, distribution, and reproduction in any medium, provided the original work is properly cited.

This article has been retracted by Hindawi following an investigation undertaken by the publisher [1]. This investigation has uncovered evidence of one or more of the following indicators of systematic manipulation of the publication process:

- (1) Discrepancies in scope
- (2) Discrepancies in the description of the research reported
- (3) Discrepancies between the availability of data and the research described
- (4) Inappropriate citations
- (5) Incoherent, meaningless and/or irrelevant content included in the article
- (6) Manipulated or compromised peer review

The presence of these indicators undermines our confidence in the integrity of the article's content and we cannot, therefore, vouch for its reliability. Please note that this notice is intended solely to alert readers that the content of this article is unreliable. We have not investigated whether authors were aware of or involved in the systematic manipulation of the publication process.

Wiley and Hindawi regrets that the usual quality checks did not identify these issues before publication and have since put additional measures in place to safeguard research integrity.

We wish to credit our own Research Integrity and Research Publishing teams and anonymous and named external researchers and research integrity experts for contributing to this investigation.

The corresponding author, as the representative of all authors, has been given the opportunity to register their agreement or disagreement to this retraction. We have kept a record of any response received.

### References

- [1] P. Kumar, D. Suganthi, K. Valarmathi et al., "A Multi-Thresholding-Based Discriminative Neural Classifier for Detection of Retinoblastoma Using CNN Models," *BioMed Research International*, vol. 2023, Article ID 5803661, 9 pages, 2023.

## Research Article

# A Multi-Thresholding-Based Discriminative Neural Classifier for Detection of Retinoblastoma Using CNN Models

Parmod Kumar <sup>1</sup>, D. Suganthi <sup>2</sup>, K. Valarmathi <sup>3</sup>, Mahendra Pratap Swain <sup>4</sup>,  
Piyush Vashistha <sup>5</sup>, Dharam Buddhi <sup>6</sup>, and Emmanuel Sey <sup>7</sup>

<sup>1</sup>Department of Electronics and Information Engineering, Jiangxi University of Engineering, Xinyu City, Jiangxi, China

<sup>2</sup>Department of Computer Science, Saveetha College of Liberal Arts and Sciences, SIMATS, Chennai, India

<sup>3</sup>Department of Computer Science and Engineering, Panimalar Engineering College, Chennai, India

<sup>4</sup>Department of Pharmaceutical Sciences and Technology, Birla Institute of Technology, Mesra, Ranchi, India

<sup>5</sup>Department of Computer Engineering & Applications, GLA University, Mathura, Uttar Pradesh, India

<sup>6</sup>Division of Research & Innovation, Uttarakhand University, Dehradun, Uttarakhand, India

<sup>7</sup>Kwame Nkrumah University of Science and Technology, Kumasi, Ghana

Correspondence should be addressed to Emmanuel Sey; [ese5@st.knust.edu.gh](mailto:ese5@st.knust.edu.gh)

Received 6 August 2022; Accepted 25 November 2022; Published 6 February 2023

Academic Editor: Gaganpreet Kaur

Copyright © 2023 Parmod Kumar et al. This is an open access article distributed under the Creative Commons Attribution License, which permits unrestricted use, distribution, and reproduction in any medium, provided the original work is properly cited.

Cancer is one of the vital diseases which lead to the uncontrollable growth of the cell, and it affects the body tissue. A type of cancer that affects the children below five years and adults in a rare case is called retinoblastoma. It affects the retina in the eye and the surrounding region of eye like the eyelid, and sometimes, it leads to vision loss if it is not diagnosed at the early stage. MRI and CT are widely used scanning procedures to identify the cancerous region in the eye. Current screening methods for cancer region identification needs the clinicians' support to spot the affected regions. Modern healthcare systems develop an easy way to diagnose the disease. Discriminative architectures in deep learning can be viewed as supervised deep learning algorithms which use classification/regression techniques to predict the output. A convolutional neural network (CNN) is a part of the discriminative architecture which helps to process both image and text data. This work suggests the CNN-based classifier which classifies the tumor and nontumor regions in retinoblastoma. The tumor-like region (TLR) in retinoblastoma is identified using the automated thresholding method. After that, ResNet and AlexNet algorithms are used to classify the cancerous region along with classifiers. In addition, the comparison of discriminative algorithm along with its variants is experimented to produce the better image analysis method without the intervention of clinicians. The experimental study reveals that ResNet50 and AlexNet yield better results compared to other learning modules.

## 1. Introduction

Ophthalmology is a branch of medicine, and surgeries that focuses on the diagnosis and treating a wide variety of conditions that affect the eyes are needed. The eye is the organ that takes in light and transmits information about what it sees to the brain, which then forms a picture. Several structures are seen in someone's eyes. The pupil lets light enter the eye. A brilliantly pigmented round muscle, the iris, gives us eye color. A transparent cornea covers the pupil and iris. Together with the crystalline lens, it produces a sharp vision

at the retinal receptor level. The globe, the orbit (sometimes known as the eye socket), and the adnexa are the three primary components of the eye. Tumors of the eye can be either benign or malignant. Eye tumors, also known as ocular tumors, can originate in any part of the eye. When healthy cells in or around the eye undergo malignant changes, they begin to multiply uncontrollably and spread to other parts of the body, which ultimately results in the production of malignant cells. Ocular tumors are another name for eye tumors. A mass of cells that develops erratically is called a tumor. It might be malignant or not. Malignant is the

medical term for cancerous tumors. Benign tumors are those that are not cancerous. The tissues around the eyeball are impacted by orbital malignancies. The orbit is the name for this. Additionally, the eyeball's moving muscles and its associated nerves may be impacted. The tear ducts and eyelids may also be impacted. Adnexal tumors are cancers that affect these structures. Commonly, benign moles develop into malignant melanomas. A benign tumor will grow in size but will not spread to other organs. Benign tumor cells are noncancerous tumors which cause inflammation around the eye. A malignancy that originates in the eyeball is referred to as an intraocular tumor, which literally means "inside the eye." Primary intraocular malignancies and secondary intraocular cancers are the two distinct subtypes of intraocular tumors that can manifest in the eye. Primary intraocular cancers start inside the eye. Melanoma is the most common primary eye cancer in adults [1]. Retinoblastoma (RB) is the most common intraocular malignancy in children. Secondary intraocular malignancies originate on the surface of the globe and then spread into its interior. Retinoblastoma is a kind of cancer that seldom affects adults and children under the age of five. If it is not identified at an early stage, it can sometimes result in vision loss. It affects the retina in the eye as well as the area around the eye, such as the eyelid. To locate the malignant spot in the eye, MRI and CT scans are frequently performed. The clinicians' assistance is required for the current cancer region identification screening procedures to identify the affected areas. Modern healthcare systems create a quick method of disease diagnosis. Retinoblasts make up retinoblastoma (basophilic cells with hyperchromatic nuclei and scanty cytoplasm). The majority of retinoblastomas are undifferentiated; however, variable levels of differentiation are evident because rosettes occur. Although they are not technically "eye tumors," their incidence is much higher than that of primary intraocular malignancies. Malignancies of the breast and lung are the most prevalent primary tumors that can spread to the eye and cause secondary cancers. The uvea is where the vast majority of these malignancies have metastasized and migrated to the eyeball. The thin layer of light-sensitive tissue that covers the back of the eye is called the retina. It is the reason why we are able to see because when a light signal is received by the eye, it is sent to the brain via the retinal nerve fiber layer. Retinoblastoma can affect either one eye or both eyeballs, depending on which eye is initially infected. As a result, the child's eye has the appearance of a cat's eye. Retinoblastoma's genetic abnormality causes immature eye cells. These retinal cancer cells spread. This spread might harm the spine and brain. A biopsy is used to diagnose most malignancies. During a biopsy, the doctor takes a sample of the tumor for microscopic analysis. Due to two factors, biopsies are infrequently utilized to diagnose retinoblastoma. A biopsy from an eye tumor can spread cancerous cells outside the eye and is challenging to perform. Experienced doctors can frequently identify retinoblastoma without doing a biopsy, and it seldom goes undiagnosed in youngsters with other eye conditions. Robots with artificial intelligence mimic human cognition. Any system that uses machine learning is capable of picking up different patterns and char-

acteristics without human interaction. Imaging tests can be used (1) to determine if an eye tumor is retinoblastoma, (2) to determine tumor size and spread, and (3) to evaluate treatment. Image diagnosis of retinoblastoma includes different methods like ultrasound imaging, magnetic resonance imaging (MRI), and computed tomography (CT) scan [2]. The imaging techniques show the position of the retina in the eye, and the photographs also allow clinicians to investigate a patient's retina, diagnose retinal mutations, and analyze retinal findings. Machine learning is a pattern segmentation procedure that includes a learning approach to understand what distinguishes underlying patterns. Deep learning is the fastest-growing machine learning technology. DL simulates human brain functioning using artificial neural networks. Ophthalmology is about to revolutionize eye screening, diagnosis, and treatment. Deep learning technology could alter ophthalmology treatment. Ophthalmology diagnostic tools provide a computerized picture of eye components. Ophthalmology is a good fit for DL algorithms. DL algorithms in ophthalmology will revolutionize ophthalmologists' work. In the coming years, intelligent technology will aid in eye cancer screening and detection. As DL technology advances, it will be further incorporated into ophthalmic care, freeing practitioners from repetitious duties. Ophthalmologists can improve patient care and interactions. The proposed work is about development of discriminative deep learning model for detection of retinoblastoma using convolutional neural network (CNN) variants with automated multithresholding method.

## 2. Related Works

Retinoblastoma seems to be the most common type of cancerous tumor in kids' eyes. It makes up about 2–3% of all cancers in kids. Leukocoria and strabismus are indeed the two most frequent signs of retinoblastoma. Leukocoria is the most typical early indication of retinoblastoma (a cloudy white pupil). The pupil might seem silvery or yellow under strong light. Other indications include the following: eyes that are not aligned properly, squinted eyes, a larger-than-average pupil, and a murky iris (the colored part of the eye) bad vision. An overview of retinoblastoma, its characteristics, prior discoveries, and research is reviewed in relation to this paper. Allam et al. study the comparison of different artificial intelligence (AI) techniques used to detect the retinoblastoma. This study used AI to classify ocular cancers. Most researches used a two-step strategy to classify eye tumor; they are preprocessing to eliminate noise and classifier. Classifiers employ computer vision techniques, artificial neural networks, and machine learning. Back propagation neural network and image processing yield better performance compared to different AI techniques [3]. Anand et al. report the deep learning technique that allows ophthalmologists towards early prediction and diagnosis of retinoblastoma. LPDMF filter can be used for preprocessing, and the preprocessed images are then segmented using the convolutional neural network (CNN). In retinoblastoma, CNN can be utilized to accurately segment the tumor and the ocular anatomy. The preprocessed images are segmented

using a convolutional neural network (CNN) with an architecture known as U-Net to separate the foreground tumor cells from the background's segments of retinoblastoma. The network uses data augmentation techniques to increase the number of training samples while using fewer filters. The seven-layer U-Net architecture has a geometrically increasing number of feature maps at each level and concludes that the suggested model is better than supervised learning algorithms, but still, the quality of the output is not compromised; it requires manual screening to verify the predictive model [4]. Henning et al. proposed a CNN method for detecting leukocoria, which is one of the main symptoms to cause retinoblastoma in the eye. Leukocoria can cause damage to the lens (such as a cataract), vitreous (such as a haemorrhage), or retina (such as retinoblastoma). It may be the first sign of a variety of systemic and intraocular disease processes. The symptom of leukocoria is the light-sensing layer in the back of the eye, typically absorbing the majority of light entering the eye through the pupil. The pupil, however, reflects a little portion of light back out. Due of the reflected reddish orange tint, this is referred to as a red reflex. Red eye is a common effect that flash photography can capture. However, in situations with leukocoria, the pupil of one or both eyes may appear white, yellow, or just pale. 832 eye images are collected from affected children and Flickr, and then, the input images are trained using a traditional three-layer CNN; the model reports a minimum accuracy with small amount of dataset [5]. They studied the mutation of retinoblastic gene in bladder cancer using machine learning algorithms. The study included CTU scans from 18 patients with RB1 mutation and 54 without. A wrapper-based sequencing feature extraction approach and Pearson's correlation analysis were used for feature selection. Models were created using XGBoost, random forest (RF), and KNN [6]. Priya proposed a CNN-based retinoblastoma detection methods with some segmentation techniques of image processing and calculates the regression of tumors using convex polygon and convex area with the accuracy of 87% [7]. Healthcare has been altered by diagnostic health imaging technology, which now enables earlier diagnosis of medical disorders, lessens the need for pointless invasive exploratory procedures, and improves patient outcomes. The MRA can sometimes gather information that CT scans, ultrasounds, or X-rays cannot by using radio wave energy pulses and a magnetic field. MRA exams are frequently used to gather data on the health of blood flow and blood vessel walls in the legs, neck, brain, and kidneys. MRAs are also used by medical professionals to scan blood arteries for calcium deposits, aneurysms, and clots. In rare circumstances, they might ask for a contrast dye to give the images of the blood vessels in the scan more detail. Strijbis et al. proposed a segmentation method for retinoblastoma using Multiview CNN. The dataset includes 23 patients (17 healthy and 27 RB eyes.). The performance of Multiview CNN can be evaluated using  $k$ -fold cross validation methods, and it concludes that the proposed method gives better results for segmenting the retinoblastic image [8].

### 3. Proposed Methodology

Retinoblastoma is perhaps the most frequent pediatric ocular malignancy. In developed countries, retinoblastoma survival rates are 90–99% with current medical treatment. To obtain these survival percentages, retinoblastoma patients must be often evaluated under anesthesia before age 5 for early discovery of new or recurrent tumors, as well as medication and diagnosis of complications. Unlike retinoblastoma, retinoma does not grow or diminish over time. Fundus and OCT images (Figure 1) are used to record the condition of the inner surface of the retina, with the goal of recording the presence of abnormalities and tracking how they evolve over time. OCT is not an eye examination. An eye examination examines eyesight and vision. An OCT scan helps an optometrist to look deeper inside the eyes and their structures than digital retinal imaging. An OCT scan helps an ophthalmologist to assess individual eyesight. A fundus camera, also known as a retinal camera, is a specialized type of low-power microscope that has a camera mounted to it. Its purpose is to take photographs of the internal surface of the eye, such as the retinal, retinal vasculature, optic nerves, macular, and posterior pole [9]. In this study, an image processing approach to classify the cancerous and noncancerous regions in eye images by utilizing Otsu cluster and automated multithresholding was proposed. For accurate categorization, a good image processing approach might be manually chosen. This region selection method can become laborious with more photographs.

A system that analyzes photos and finds suitable places may be more useful. To facilitate image categorization, an appropriate image processing approach is proposed. Segmentation is an essential stage in fundus and OCT image processing. Image segmentation divides an image into distinct sections. Utilizing the properties of a picture's pixels, similarity can be assessed. Segmentation is a pixel categorization method that divides an image into sections with similar content. There are three types of image segmentation: methods for object boundaries based on edges. Closed object regions were created using pixel-based categorization, which uses techniques built from image histogram statistics and region-based approach where regions are created by rapidly evaluating pixels in a region-growing process. To obtain the best threshold value, background removal is the first step. We use an automatic multithresholding at this point to take both dark and light photos of the eye to spot any tumor-like tissue. In the process of processing OCT and fundus images, segmentation is a crucial step. The initial step is background removal in order to get an optimal threshold value. At this stage, use an automatic multithresholding to perform both dark and light images of the eye to identify tumor-like region. Thresholding is a crucial method for segmenting images. In comparison to a gray-level image with 256 levels, the segmented image produced by thresholding has the advantages of smaller storage volume, quick processing, and ease of manipulation. This has made thresholding techniques quite popular in recent years. A successful segmentation will distinguish between pixels with similar values to improve contrast and separate objects from the background.

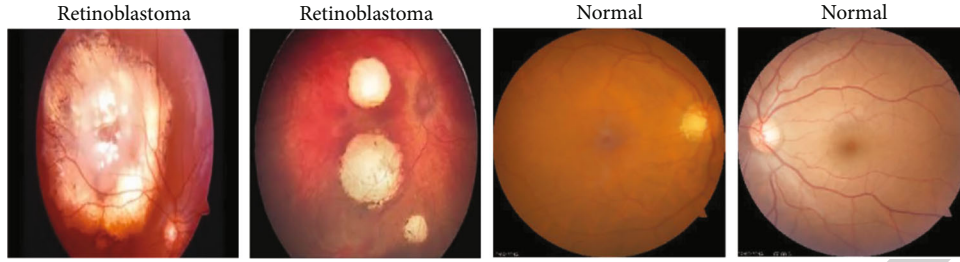


FIGURE 1: Fundus images of patients with and without RB.

In many image processing applications, image regions are anticipated to have uniform properties (such as hue or gray level), indicating that they are parts of the same object or its facets and suggesting the prospect of effective segmentation. There are two categories of thresholding techniques: bilevel and multilevel. First, get a histogram from the image with the background removed by moving the  $x$  axis of the histogram. Then, the  $y$  axis of the histogram, which shows the number of pixels, goes from the highest number, i.e., maximum point to the lowest number, i.e., minimum point. This maximum point ( $ma$ ) and minimum point ( $mi$ ) show a smooth status; on clearer region of the tumor cells, its histogram is quickly going down. From the falling curve (Figure 2), we can figure out the smooth rate; the smooth rate can be expressed in

$$SR = \frac{\sqrt{\sum_{j=ma}^{mi} ((j, 1) - (j + 1, 1))}}{ma - mi} \quad (1)$$

If the curves in the histogram gradually decrease in slope from its maximum point to its minimum point, this indicates that the image is dark and that its smooth rate is high. It indicates that the sharpness is low and that there are many dark pixels in the image. If the curve in the histogram drops off suddenly from its maximum point to its minimum point, this indicates that the image is bright and that its smooth rate is low. It indicates that there is a higher contrast, as well as a high quantity of pixels that are bright. When we reach a steady rate, the value of the threshold for the subsequent stage will be calculated on its own automatically. The histogram of each division is utilized to calculate thresholds, and each pixel's grayscale value is compared to the threshold to classify it. When image  $g(a, b)$  classes employ threshold  $t$ , it can be expressed as

$$g(a, b) = \begin{cases} 1 & \text{if } g(a, b) \text{ greater than threshold value,} \\ 0 & \text{if } g(a, b) \text{ greater than or equal to threshold value.} \end{cases} \quad (2)$$

Multithresholding gathers similar data based on the features in a single group of clusters and dissimilar ones in separate clusters. The following steps shows the steps of automatic multithresholding:

- (1) Apply Otsu multithresholding technique and get a threshold value ( $G1, G2$ )
- (2) Apply Otsu multithresholding algorithm to separate  $G1$  into two groups ( $G1a, G1b$ ) and  $G2$  into two groups ( $G2a, G2b$ ) ( $G2a, G2b$ )
- (3) Third, apply Otsu multithresholding method to divide  $G1a, G1b, G2a,$  and  $G2b$  into  $G1a+, G1a, G1b+, G1b, G2a+, G2a, G2b+,$  and  $G2b$

Automatic multithresholding method groups a tumor-like region (TLR) into a single cluster [10]. Once the TLR is identified (Figure 3), the cancerous cell and noncancerous cells are needed to be differentiated, because not all the tumors lead to retinoblastoma. The next step is to classify the retinoblastomatic cell and nonretinoblastomatic cell; this classification is carried out using AlexNet and ResNet50 algorithms.

**3.1. ResNet50.** An existing deep learning framework for classifying photos is called ResNet50. It is based on the convolutional neural network (CNN, or Conv Net), a deep neural network type typically employed for image analysis. A million photos from a thousand different categories were used to train ResNet50, which contains 50 layers. A convolution block and an identity block are included in each of the ResNet50 model's five stages. Each identity block has the same amount of identity blocks, and each convolution block has three levels of convolution. Additionally, the model has more than 23 million trainable parameters, demonstrating its deep architecture and ability to recognize images more accurately.

Residual networks are made up of several successive residual modules, which are ResNet's basic building blocks [11]. As the network learns deeper, it gets harder to train people. In most cases, the input feature map is followed by a convolutional filter, a nonlinear activation function, and a pooling operation. The next layer is then the output. This is where the back propagation algorithm is put into action. As the network gets bigger, it gets harder and harder to bring everything together. ResNet50 is built in four stages. The size of the image when it comes in is  $224 \times 224 \times 3$ . Every ResNet structure does the first convolution and max pooling differently, using kernel sizes of  $7 \times 7$  and  $3 \times 3$ , respectively. Next, the first stage of the network begins. It is made up of 3 residual blocks, each of which has 3 layers. The kernels used to do the convolution operation with all three layers of the first

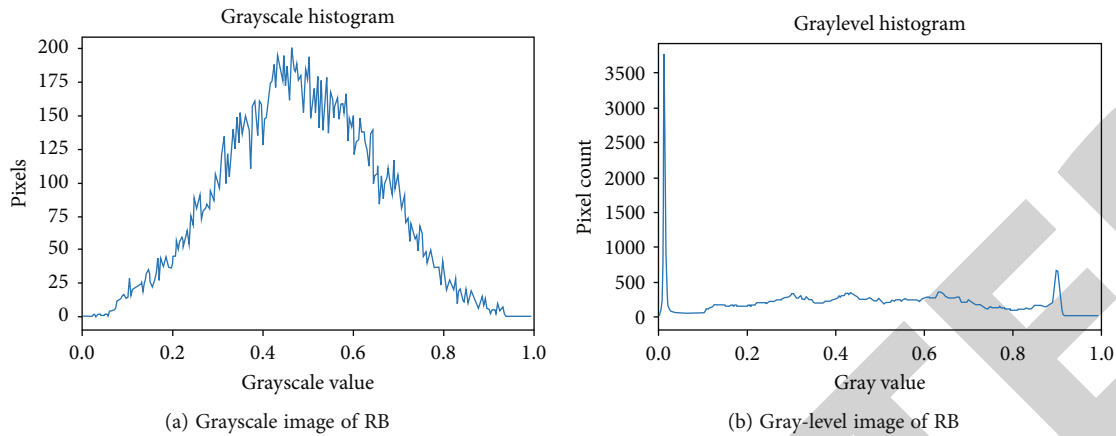


FIGURE 2: Histogram representation for RB image.

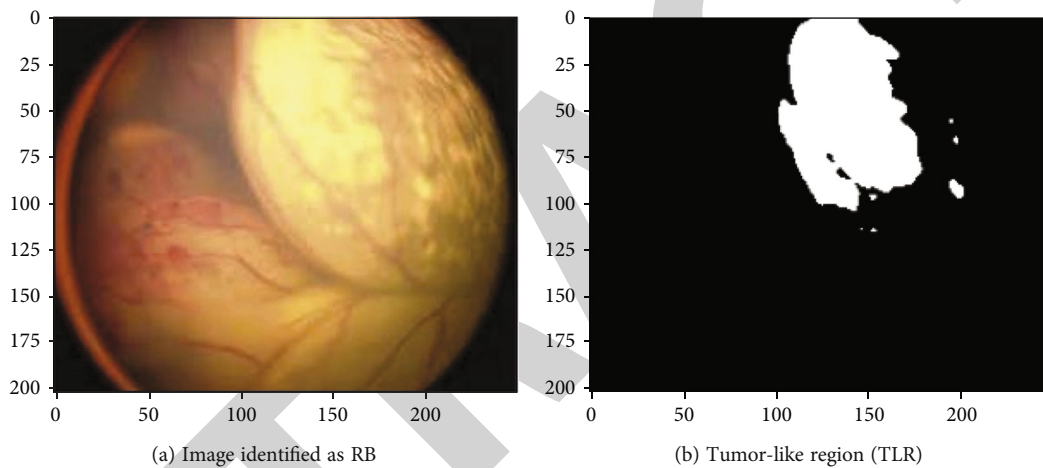


FIGURE 3: RB image with TLR.

stage block are 64, 64, and 128 bits in size, respectively. The wavy arrows show that the relationship is clear. The dashed arrow shows that the process of bending in the residual block is done with stride 2. This means that the height and width of the input will be cut in half, but the width of the channel will be doubled. As we move from one moment to the next, the width of the channel is doubled and the length of the input is cut in half. Constriction pattern is used for large networks like ResNet50 and ResNet152. For every extra process  $F$ , three layers are moved on top of each other. The three layers are made up of  $1 \times 1$ ,  $3 \times 3$ , and  $1 \times 1$  convolution. The  $1 \times 1$  convolution layers are in charge of making the dimensions smaller and then changing them. With less input and output dimensions, the  $3 \times 3$  layer is still a bottleneck. Lastly, the network has an average pooling layer followed by a layer with 1000 neurons that are connected to each other [12].

3.2. AlexNet. AlexNet [13] outperformed conventional deep learning algorithms. It was a revolution in deep learning for visual recognition and classification. The first convolutional layer uses 96  $11 \times 11$  receptive filters, with normali-

zation of local response (LRN). With a 2-step stride,  $3 \times 3$  filters are used in max pooling. Five-by-five filters are employed in the second layer. Three-by-three filters with 384, 384, and 296 feature maps are used in the third, fourth, and fifth convolutional layers. Following are two FC dropout layers, followed by a Softmax layer. This approach uses the same number of feature maps to train two networks that are identical. Dropout and LRN are introduced by this network. LRN can be applied to single channels or to feature maps, which normalize a  $N \times N$  patch depending on neighborhood values. Second, LRN functions across feature maps or channels.

Figure 4 illustrates the architecture of the proposed methodology where the input image is given into autothresholding method to identify the tumor-like region (TLR). The TLR is identified by using the OTSU autothresholding method, where it applies clustering technique to group the similar set of images based on equations (1) and (2). In this work, the performance of the two variants of convolutional neural network (CNN) algorithms, ResNet and AlexNet, is compared. Automated thresholding method identifies TLR but not all the tumors are malignant.

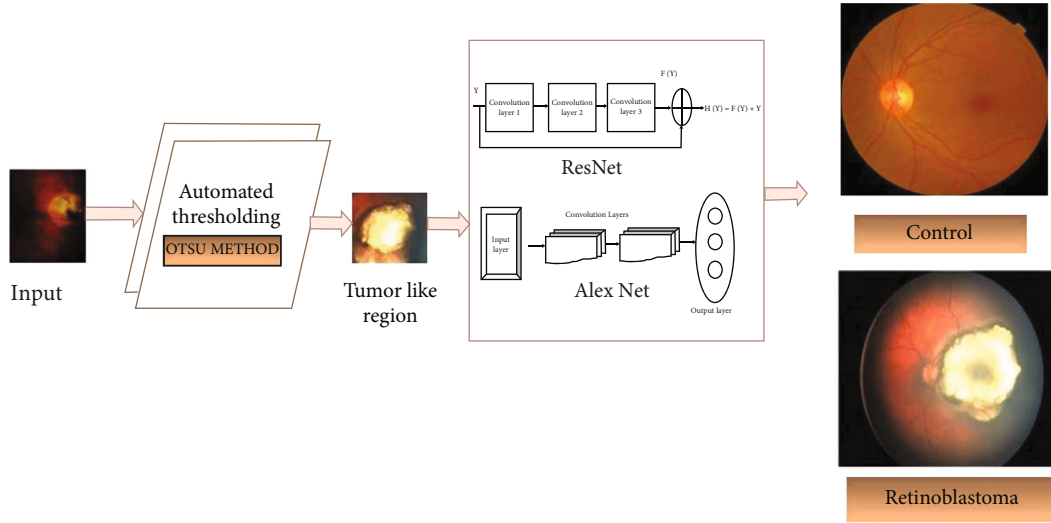


FIGURE 4: Architecture of the proposed methodology.

Step 1: Input image

Step 2: Image segmentation and clustering

2.1. Automated multithresholding to predict dark and light images of the eye to identify the TLR

2.2. Get the histogram of an image with  $x$  and  $y$  axis. Identify smooth rate (SR) using maximum (ma) and minimum point (mi).

$$SR = \sqrt[2]{\sum_{j=ma}^{mi} ((j, 1) - (j + 1, 1)) / ma - mi}$$

Step 3: Apply CNN variants (ResNet and AlexNet) to find the cancerous tumors and classify the control and case image of an eye

Step 4: Classified output image

#### ALGORITHM I.

Tumors that are cancerous or malignant have the potential to metastasize to adjacent tissue, glands, and other body organs. Metastases are the new tumors (mets). After treatment, cancerous tumors may return (cancer recurrence). It may be fatal to have these tumors.

- (i) Nonmalignant: benign tumors are rarely life-threatening and are not cancerous. They are localized, which means that they frequently do not spread to other areas of the body or impact neighboring tissue. Treatment is not necessary for many benign tumors. On the other hand, certain benign tumors press against other bodily parts and require medical attention
- (ii) Precancerous: if left untreated, these noncancerous tumors may develop into malignancy. The CNN variants are used to identify the cancerous region and classify the images

## 4. Dataset and Implementation

MathWorks [14] is the source of our dataset, which aims to construct a model for detecting degenerative disease (DR). The MRI, CT, and fundus procedures are utilized to examine the eyeballs. MRI images demonstrate the ligamentous engagement in the extraocular extension highlighted in this

TABLE 1: Classes of retinoblastoma.

Category	Degree	Number
I	No RB	35
II	Weak RB	64
III	Substantial RB	74
IV	Extreme RB	68
V	Proliferate RB	37

scan. Retinoblastoma might show up as both hyper- and hyporeflective on an MRI scan. The calcified area is obvious on the CT image, and the eye is nucleated by the huge tumor. Patients' fundus images are captured using the Retcam pediatric camera. Patients between the ages of 12 and 20 are targeted for this study. According to Table 1 and Figure 5, the dataset contains high-resolution eye pictures that have been rated by skilled specialists into five classes (I-V). Each picture is rated on a scale of I to V, where I represents no retinoblastoma, II represents weak retinoblastoma, III represents substantial retinoblastoma, IV represents extreme retinoblastoma, and V represents proliferating retinoblastoma. In the proposed implementation, 128 patches are created for each of the  $1024 \times 1024$  pixel input images. The data from each patch is then further reformed: they are turned counterclockwise by 90, 180, 270, and 360 degrees, and each one is inverted

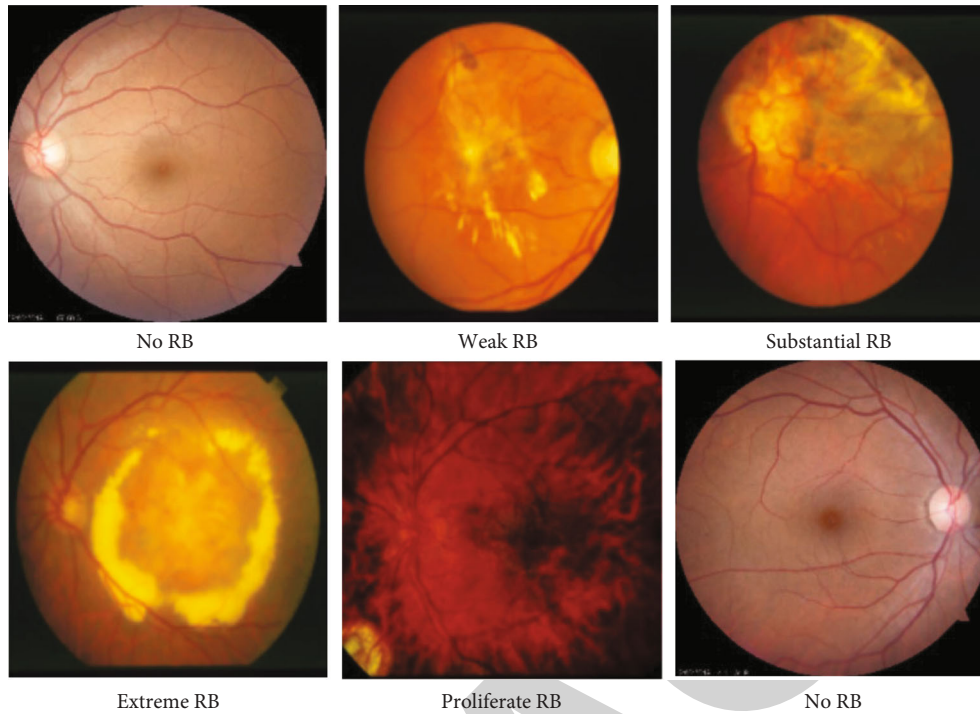


FIGURE 5: Different stages of retinoblastoma.

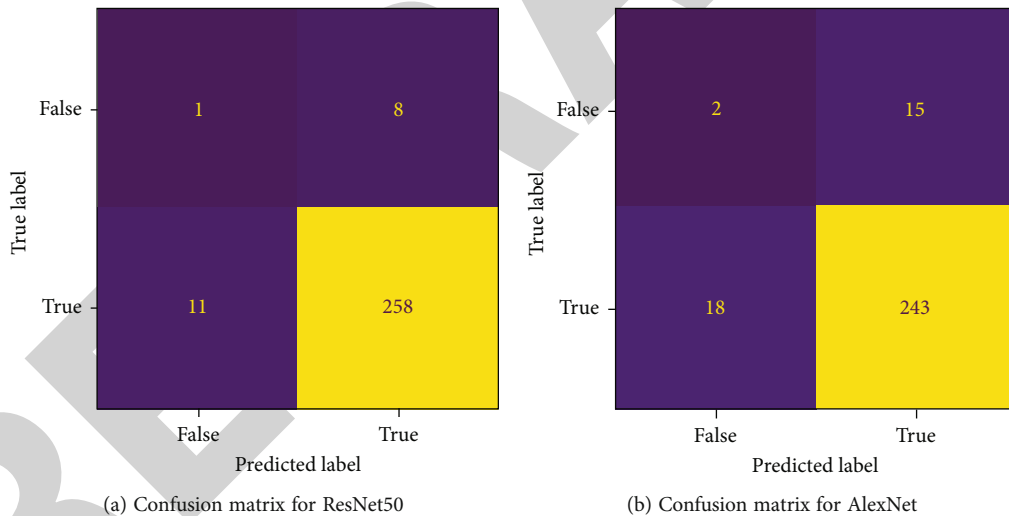


FIGURE 6: Confusion matrix for CNN models.

horizontally afterward. In this way, eight alternative patches are generated for each source patches, resulting in 1024 training parameters for the proposed system performance analysis. A total of 183,747 trainable parameters are built using the dataset for performance analysis.

The proposed methodology was implemented in a system with a configuration of i7 11th generation GPU and 16 GB of RAM. Programming language used for the implementation is Python 3.10.5 with Keras and TensorFlow as the backend structure. From the dataset (278), 70% (194) of the image set is utilized for training and 30% (84) of the dataset is used for testing. The number of epochs attempted in this implementa-

tion is 10 which was sufficient for the performance converge. The ReLU and Softmax optimizer are used as the activation function and the assumed learning rate is 0.0001.

### 5. Results and Discussion

A retinoblastoma model is proposed, and its performance is evaluated using metrics including accuracy, precision, recall, and *F1* score. To demonstrate the effectiveness of the suggested algorithm, the existing techniques XGBoost, random forest, CNN, and KNN are compared with RB-AlexNet and RB-ResNet.





FIGURE 7: Classified images with and without RB.

TABLE 2: Performance comparison of the proposed vs. existing models.

Framework	Accuracy	Precision	Recall	F1 score
XGBoost [6]	82	87	86	86
Random forest [6]	85	90	89	88
KNN [6]	84	88	89	88
CNN [7]	87	92	93	92
AlexNet	88.12	93.10	94.18	93.64
ResNet50	93.16	95.91	96.99	96.44

The performance metrics is analyzed using the following equations:

$$\begin{aligned}
 \text{Accuracy} &= \frac{TP + TN}{TP + TN + FP + FN}, \\
 \text{Precision} &= \frac{TP}{TP + FP}, \\
 \text{Recall} &= \frac{TP}{TP + FN}, \\
 \text{F1 score} &= 2 * \frac{\text{Precision} * \text{recall}}{\text{Precision} + \text{recall}}.
 \end{aligned} \tag{3}$$

The ResNet50 result includes the following: from a total of 278 images, 258 images are true positives (TP), i.e., correctly classified RB images; 11 images are false positives (FP), i.e., incorrectly classified as RB images; 8 images are false negative (FN), i.e., incorrectly classified as normal images; and 1 image is true negative (TN), i.e., correctly classified as normal image. The AlexNet result includes the following: from a total of 278 images, 243 images are TP, 18 images are FP, 15 images are FN, and 2 images are TN. Figure 6 depicts the confusion matrix for the proposed algorithm with ResNet50 and AlexNet architecture. An analysis of the confusion matrix for a convolutional neural network (CNN) reveals which classes the model predicts properly

## *Retraction*

# **Retracted: Applications of Neural Network-Based Plan-Cancer Method for Primary Diagnosis of Mesothelioma Cancer**

### **BioMed Research International**

Received 8 January 2024; Accepted 8 January 2024; Published 9 January 2024

Copyright © 2024 BioMed Research International. This is an open access article distributed under the Creative Commons Attribution License, which permits unrestricted use, distribution, and reproduction in any medium, provided the original work is properly cited.

This article has been retracted by Hindawi, as publisher, following an investigation undertaken by the publisher [1]. This investigation has uncovered evidence of systematic manipulation of the publication and peer-review process. We cannot, therefore, vouch for the reliability or integrity of this article.

Please note that this notice is intended solely to alert readers that the peer-review process of this article has been compromised.

Wiley and Hindawi regret that the usual quality checks did not identify these issues before publication and have since put additional measures in place to safeguard research integrity.

We wish to credit our Research Integrity and Research Publishing teams and anonymous and named external researchers and research integrity experts for contributing to this investigation.

The corresponding author, as the representative of all authors, has been given the opportunity to register their agreement or disagreement to this retraction. We have kept a record of any response received.

### **References**

- [1] D. Kapila, S. Panwar, M. K. M. M. Raja et al., “Applications of Neural Network-Based Plan-Cancer Method for Primary Diagnosis of Mesothelioma Cancer,” *BioMed Research International*, vol. 2023, Article ID 3164166, 10 pages, 2023.

## Research Article

# Applications of Neural Network-Based Plan-Cancer Method for Primary Diagnosis of Mesothelioma Cancer

Dhiraj Kapila <sup>1</sup>, Sarika Panwar <sup>2</sup>, M. K. Mohan Maruga Raja <sup>3</sup>, Tamal Mondal <sup>4</sup>,  
Shaik Mohammad Rafi <sup>5</sup>, Suryabhan Pratap Singh <sup>6</sup> and Bhupendra Kumar <sup>7</sup>

<sup>1</sup>Department of Computer Science & Engineering, Lovely Professional University, Phagwara, Punjab, India

<sup>2</sup>Department of Electronics and Telecommunication Engineering, AISSMS's Institute of Information Technology, Pune, India

<sup>3</sup>Parul Institute of Pharmacy & Research, Parul University, Vadodara, Gujarat, India

<sup>4</sup>Department of Botany, Hiralal Mazumdar Memorial College for Women, Dakshineswar, Kolkata 700035, India

<sup>5</sup>Department of Computer Science and Engineering, Sri Mittapalli College of Engineering, Guntur, Andhra Pradesh, India

<sup>6</sup>Information Technology, Institute of Engineering and Technology, Deen Dayal Upadhyaya Gorakhpur University, Gorakhpur, India

<sup>7</sup>Debre Tabor University, Debre Tabor, Ethiopia

Correspondence should be addressed to Bhupendra Kumar; drbkumar@dtu.edu.et

Received 26 July 2022; Revised 23 September 2022; Accepted 24 November 2022; Published 4 February 2023

Academic Editor: Gaganpreet Kaur

Copyright © 2023 Dhiraj Kapila et al. This is an open access article distributed under the Creative Commons Attribution License, which permits unrestricted use, distribution, and reproduction in any medium, provided the original work is properly cited.

“Malignant mesothelioma (MM)” is an uncommon although fatal form of cancer. The proper MM diagnosis is crucial for efficient therapy and has significant medicolegal implications. Asbestos is a carcinogenic material that poses a health risk to humans. One of the most severe types of cancer induced by asbestos is “malignant mesothelioma.” Prolonged shortness of breath and continuous pain are the most typical symptoms of the condition. The importance of early treatment and diagnosis cannot be overstated. The combination “epithelial/mesenchymal appearance of MM,” however, makes a definite diagnosis difficult. This study is aimed at developing a deep learning system for medical diagnosis MM automatically. Otherwise, the sickness might cause patients to succumb to death in a short amount of time. Various forms of artificial intelligence algorithms for successful “Malignant Mesothelioma illness” identification are explored in this research. In relation to the concept of traditional machine learning, the techniques support “Vector Machine, Neural Network, and Decision Tree” are chosen. SPSS has been used to analyze the result regarding the applications of Neural Network helps to diagnose MM.

## 1. Introduction

After the widespread usage of asbestos throughout World War II and subsequently, a significant increase in age-standardized mesothelioma occurrence and fatality rates occurred in the 1960s. The pervasive use of asbestos persisted in high-resource nations (the United States, Europe, and Australia) until the late 1970s and early 1980s when regulatory measures were enacted to limit and prohibit the advertising use of six of the approximately 400 inorganic mineral fibres found in nature “(amphiboles fibres (crocidolite, actinolite, tremolite, anthophyllite, and amosite) and serpentine fibres (chrysotile))”. These six fibres were gener-

ally referred to as “asbestos” for legal reasons. The remaining 400 mineral fibres are unregulated, and may be used openly, even though many of them are carcinogenic, and have been linked to mesothelioma. Furthermore, germline mutations in the BRCA1-associated protein 1 (BAP1) and other tumour suppressor genes have been causally related to mesothelioma, sometimes in combination with asbestos or other carcinogenic fibres (gene-environment interaction (GxE)). In addition, therapeutic ionising radiation to the chest, which is typically used to treat lymphomas, has indeed been related to mesothelioma (and sarcomas) in young children [1]. Being exposed to asbestos is the main risk factor for mesothelioma. Up to 80% of all instances can be attributed

to it. Asbestos fibres can transfer on skin and clothing, thus living with someone who works with it may raise a person's risk of developing mesothelioma. Some toxins alter a cell's DNA to produce cancer. Others cause cancer indirectly, without directly affecting DNA. For instance, they may speed up cell division, which could enhance the likelihood that DNA modifications will take place. Despite extensive diagnostic workup, the tumour is not a known primary tumour (CUP) metastatic tumour where the primary tumour cannot be identified. CUP represents 1% to 2% of all metastatic tumours and presents a diagnostic and therapeutic challenge. Indirect "platinum-based chemotherapy" is a common first-line treatment, with a response rate of 30% and a "median survival of 9 to 12 months," respectively. No grading method exists for cancer with an unknown primary (CUP). This is due to cancer already has progressed and the location of the primary cancer's genesis is unknown. CUP can typically be divided into groups by the type of cell that gave rise to it. The aim may be to temporarily reduce the size of the cancer in an effort to alleviate symptoms and lengthen your life because CUP is too developed to be cured. So, the goal of this treatment is to alleviate symptoms like pain rather than to treat the illness, it is referred to as palliative care or supportive care. In recent decades, great efforts have been devoted to identifying the genetic and transcriptional structure of CUP to identify and characterize major molecular changes and gene expression patterns for specific cell-based therapy. Previously, microarray data have been used for DNA and RNA sequencing (RNA-seq), DNA methylation, and whole genome sequencing, with varying degrees of efficiency [2]. Due to issues of distribution, cost, and lack of standardization, such systems are not yet widely integrated into the current CUP analysis workflow.

Therefore, current guidelines for treating CUP still rely on clinical chemistry and immunosuppressive properties to identify the source tissue, although many cases remain undiagnosed and are often treated with therapeutic agents. The use of gene expression data to assess progenitor cells has been extensively studied in the past and RNA-seq methods are more powerful than microarrays in terms of tumour characteristics and diagnostic accuracy. However, due to the large amount of information generated during whole transcript sequencing, it is difficult to develop appropriate analytical methods. Artificial intelligence and machine learning technologies have recently made it possible to analyze large amounts of high-resolution molecular data. Pleural mesothelioma involves "two lung tissues, the viscera of the thorax and the pleura," accounting for approximately 75% of all mesotheliomas. It develops in the thin membrane that lines the chest cavity and lungs, the pleura. This generally occurs when asbestos fibres get lodged in this lining leading to scarring and inflammation, and subsequently the disease. Pericardial mesothelioma is a type of mesothelioma that involves the mucosa of the pericardium and the mucous membrane that surrounds the heart. It has only been diagnosed in fewer than 200 people in history and this is difficult to research on. The tumours in this cancer form in the lining of the heart, pericardium, and generally results from the metastasis of cancer from another part of the body. Pericar-

dial mesothelioma is often misdiagnosed before autopsy [3]. "Mesothelioma" is always a tumour, but some people may have symptoms of mesothelioma and pleural effusion from mesothelioma. "Severe pain, shortness of breath," "cough," "painful and dry cough," "pleural effusion," "chest pain," and "shoulder pain" were common diagnostic symptoms. Other symptoms that may occur in the final stage are weakness, fever, vomiting, high blood pressure (low oxygen in the blood), dysphagia (difficulty in swallowing), fever, night sweats, and weight loss. Clinical characteristics, associated with symptoms, provide measurable information to facilitate assessment. Clinical characteristics such as "histological substructure," "time to diagnosis," "platelet count," "haemoglobin," and disease levels are used to evaluate survival outcomes according to current methods. In the case of mesothelioma, the industrial history can be very important because it indicates prior asbestos exposure. The risk of developing mesothelioma increases with continued asbestos exposure. Thrombocytopenia can be identified by imaging and diagnostic equipment, including X-ray, MRI, and positron emission tomography (PET). To detect mesothelioma, routine blood tests are necessary [4]. The area that is impacted by MM can be seen on a PET-CT scan. It can also demonstrate whether MM has migrated to the neighbourhood lymph nodes. In rural places, medical imaging technology is pricy and scarce, if it is even accurate and useful. Additionally, a clinical diagnosis like lymphoma is challenging and unsuitable for people. Researchers have used machine learning techniques to solve health information classification problems to speed up diagnosis and simplify testing. "Machine learning" algorithms can collect, process, and analyze medical data in seconds or minutes. X-rays are used in computed tomography (CT) examinations. Magnets and radio waves are used in magnetic resonance imaging (MRI) scans. Both generate static photos of bodily parts and organs. A radioactive tracer is used in PET scans to demonstrate how an organ is operating in real time. The internal organs and tissues of your body are depicted in great detail by a CT scan. A PET scan can be more precise than other imaging procedures and can detect aberrant activity. Additionally, it can cause your body to alter sooner. PET-CT scans are used by doctors to reveal more details about the cancer.

People with "non-mesothelioma" mesothelioma have symptoms similar to mesothelioma, such as pleura. However, these patients were not diagnosed with mesothelioma by their doctors. Clinically it can be difficult to distinguish between "mesothelioma" and "asbestos" patients with pleural effusion and clinical signs suggestive of "mesothelioma" but without the disease. This process can cause breast epithelium, "pleural effusion," and "other radiological changes" similar to "mesothelioma." Technical methods for predicting cancer are well known in scientific research. The mesothelioma data used here comes from previous experiments using the probiotic nervous system (PNN) to diagnose mesothelioma. Probabilistic neural networks have also been used to predict responses to chemotherapy and identify future cancer patients. Scientists began their research on simulating probabilistic neural networks, by comparing various

“machine learning” algorithms such as “random neural networks,” “random trees,” “decision trees,” and “uniform rules” reproductive power. The design has been written using original databases. These methods were chosen because they are particularly suitable for databases that have been developed by researchers and have previously been shown to be effective and efficient in solving similar health information problems [5]. For example, systems “artificial neural networks” have been used to detect microscopic images of breast cancer and identify specific sequences of “DNA-binding” and “RNA-binding proteins.” Random trees have also found many uses in bioinformatics and psychoanalysis, such as data classification. Researchers have also utilised the random forest to sort data from various malignancies, including lung and renal cell carcinoma. Despite the fact that many mechanical engineering specialists advice beginning with basic mechanical engineering techniques like systematic regress, scientists avoid this since it can be erroneous even when it can be utilised successfully in close settings [6]. The mesothelioma database includes nearly identical datasets derived from similar clinical trials. The researchers used a random tree to extract these features and classify them to identify patient symptoms and clinical predictors of mesothelioma.

Overall, this research presents an argument for the utility of Artificial Intelligence and Machine Learning applications in increasing the accuracy of the early diagnosis of mesothelioma. Such applications will reduce the time taken to analyze the bulk data generated during the mesothelioma diagnosis tests and act in a supportive role to the medical professions. A literature review followed by the use of algorithms to analyze data and a discussion of the generated results comprises the research.

The remainder of this paper is organised as follows. Section 2 presents a literature review, the methodologies are presented in Section 3, and the results are analyzed in Section 4. Section 5 contains a discussion of the current work’s findings, and Section 6 contains concluding remarks as well as future research directions for the research effort described in this article.

## 2. Literature Review

Malignant mesothelioma (MM) is a malignancy that is rare yet deadly. The number of patients with MM is identified at an elevated level, and the disease is unresponsive to existing treatment methods such as chemotherapy, surgeries, radiation, and immunotherapy. Following a diagnosis of advanced MM, the expected median overall survival is one year. MM has a significant link to asbestos exposure, a material that was widely utilised in the 1970s and 1980s all over the world. Even though asbestos usage was outlawed in the twenty-first, throughout the twentieth century, the “estimated incidence of MM” has consistently climbed due to the disease’s long latency period.

Histopathology along with clinical and radiological findings are used to diagnose MM. “Correct diagnosis of MM” is an important step towards successful treatment and has important “medical and legal implications” due to the

“problems of profitability” associated with this diagnosis. However, making a clear “MM diagnosis” can be difficult, especially in the early stages. This is often due to symptoms of other malignancies (mainly adenocarcinoma) or the presence of benign/aggressive actions. While the prevalence of MM is decreasing, the goal of early cancer diagnosis is to identify symptomatic individuals as soon as possible to provide them with the greatest chance of obtaining a successful course of treatment. A reduced chance of survival, more treatment-related issues, and higher cost of care are all consequences of delayed or inadequate cancer therapy. A precise diagnosis to avoid complications and speedy deterioration, early detection of diseases to enable speedier intervention and save precious time. All dementia illnesses do not develop in the same way, therefore an accurate diagnosis is helpful in determining the patient’s best course of treatment. The use of diagnostic systems (DSS) has increased rapidly over the past two decades. “DSS for MM” allows the “pathologist” to quickly see “medical information.” Most importantly, it can reduce pathological differences [7]. Previous research on “computer-aided MM detection” focused mainly on the development of “automated imaging tools” such as statistical algorithms to identify “pleural projections in breast CT images” and its four numbers. Furthermore, since “pleural thickening” does not always indicate. Until recently, there were not many diagnostic options for MM. For DSS to be more accurate, multidimensional data such as clinical, biological, and radiological aspects of MM should be integrated. Multiple myeloma can be diagnosed using a lot of information. Using a Probabilistic Neural Network (PNN), the researchers achieved a classification rate of 96.30%. On the other hand, comparison agents cannot help in the analysis of MM [8]. Techniques for selecting feature can be used to eliminate features from the “basic feature set” that are pointless or useless allowing the analysis model to focus on more diverse features, thereby improving accuracy and reducing learning time [9]. Classification is important for DSS because the analysis is the main classification problem. In the past various machine learning techniques, such as conveyor belts, “excessive learning machines (ELM),” and deep learning, have been used as classification tools to help analyze “(DL; also called advanced learning). DL makes it easy to create “data views” and different stages of extraction, using algorithms, with many features. Finite Boltzmann machines, automatic coding, “deep belief networks,” and “oscillation neural networks” are all part of this set of DL algorithms [10]. Sound recognition, object recognition, and visual fields are greatly enhanced by these tasks. It has been noted that neural networking-based models that use AI and machine learning are matching or exceeding the accuracy and expectations of results from traditional methods of diagnosis of MM. Thus, it can be said that shifting toward this method is a viable path in the future.

## 3. Methodology

Firstly, the researcher of this paper used MATLAB software to feed the input variables and determined the encoding length. ReliefF and (Genetic Algorithm) GA were used in

the MATLAB software to understand how the training and assessment data help the algorithms to become developed. The justification for using the ReliefF method is the efficiency it shows when working with regression problems that have bulk data and improves the result. The implementation of GA will further enhance the quality of solutions to the research problems and optimize the results. Due to the focus on the accuracy of results, these two models were selected for analysis. A total of 70% of the training dataset and 30% of assessment datasets were utilized to develop the diagnostic algorithm for the disease. In this aspect, interpretivist research philosophy was followed to draw the discussion based on the interest of the researcher. Although part research was analyzed, however, the cross-validation folds, number of generations, encoding length, and iterations were selected only by the researcher.

A total of 15 experiments were performed using the two algorithms. GA optimization helped to collect the genetic data of the selected population, and contrarily, it helped to collect the fitness data as well. A ReliefF algorithm was used to select the feature of the disease. The filtering method was used to extract the subsets. The crossover rate of the method was 2 and a significant number of cross-validation folds, iteration numbers, population size, encoding length, number of generations, and number of samples was considered for the experiment.

The accuracy of the current model was obtained 15 times as the experiment was conducted 15 times by changing the number of cross-validation folds, generation number, encoding length, number of runs, and iterations. After that, the set of 15 findings was stored in a Microsoft Excel. Graphical representations were made using the Excel tool and further data analysis was done using “Statistical Package for Social Sciences” or IBM SPSS version 26 software. Descriptive Statistical analysis and multiple regression analysis were carried out with a 95% confidence level. The independent and dependent variables for multiple regression analysis are as follows: *independent variables*: encoding length/number of input variables, cross-validation folds, number of generations, number of iterations, and number of runs. On the other hand, the *dependent variable* is model accuracy. The model accuracy of the technique will help to understand the reliability and the findings of the primary method will be discussed using the recently available journal articles.

#### 4. Findings and Analysis through SPSS

The data representation in Table 1 shows the descriptive statistics output where it can be observed that a total of 15 experiments were performed and none of those is missing.

The maximum and minimum numbers of input variables/encoding lengths are 34 and 2, respectively. A maximum of 14 cross-validation folds, 323 iterations, 8 runs, and 100 generations were selected to observe the change in accuracy. It can be observed that the current machine-learning model consisting of the two algorithms is 99.78% accurate (maximum).

Table 2 shows the regression analysis at a 95% confidence level and according to the data, the significance value for “number of encoding variables and coding length” and “model accuracy” has been observed at 0.013 which shows a statistical significance ( $p < 0.05$ ). Again, the value of cross-validation folds and “model accuracy” has been observed at 0.007, which shows a high statistical significance value. The value between the number of generations and model accuracy is 0.013, which shows statistical significance. The significance value between iterations and model accuracy is 0.032, which again shows a high statistical significance. However, the significance value between the number of runs and total model accuracy has been observed at 0.292 which shows a low “statistical significance” or statistically not significant ( $p > 0.05$ ).

This shows that as the number of input variables and encoding length, cross-validation folds, iterations, and the number of generations increases, the overall model accuracy also increases. On the other side, as the number of runs increases, the model accuracy decreases.

Table 3 shows the value of ANOVA regression analysis, and according to the results, the  $F$  statistics value has been observed at 52.312, which is a high value. Again, the statistical value has been observed at 0.000, which shows a high statistical significance. Thus, the ANOVA regression analysis has shown that the model accuracy has a statistically significant relationship with all the independent variables including the number of runs. This shows that the statistical significance between model accuracy and the number of runs is low statistical significance.

Table 4 shows the model summary of ANOVA regression, and according to the data, the  $R$  value has been observed at 0.983 and the  $R$  square value has been observed at 0.967. The adjusted  $R$  square value has been observed at 0.948. These high values indicate statistical significance. The standard error has been observed at 0.52737.

Figure 1 shows the graphical representation of the relationship between the number of variables and the classification accuracy. According to the data, as the number of input variables increases, the overall classification accuracy also increases.

Figure 2 shows the graphical regression of the relationship between model accuracy and cross-validation folds. According to Figure 2, as the number of cross-validation folds increases, the overall model accuracy also increases.

The regression ANOVA has shown that the cross-validation fold and model accuracy has the highest significance level (0.007). This shows that cross-validation folds have a high degree of relationship with the model accuracy. It can be stated that while implementing “neural networking” for cancer detection, individuals should enhance the number of cross-validation folds. This helps in improving the accuracy level. Thus, medical and healthcare professionals can detect the presence of oncogenic tissues more accurately and rapidly. This on the other hand also would enhance the rapid diagnosis, which will ultimately alleviate the patient’s well-being. Therefore, it can be stated that neural networking and cross-validation folds are essential for the proper detection of oncogenic tissue and cell.

TABLE 1: Output of descriptive statistics.

	N	Critical analysis		Average value	Deviation from mean	SD <sup>2</sup>
		Min.	Mx.			
Experiment ID	15	1	15	8.00	4.472	20.000
Number of input variables and encoding length	15	2	34	18.87	10.921	119.267
Cross-validation folds	15	0	14	7.00	4.472	20.000
Number of generations	15	1	100	46.80	32.070	1028.457
Iterations	15	10	323	185.60	114.765	13171.114
Number of runs	15	1	8	4.27	2.251	5.067
Model accuracy	15	92.30	99.78	97.1547	2.31835	5.375
Valid N (listwise)	15					

TABLE 2: Regression coefficient.

Critical analysis	Coefficients <sup>a</sup>		Number	Key determinant	95%	
	Overall Val Main Val	Coefficient Err Beta			Lower bound	Upper bound
(Constant)	94.477	.561	168.433	.000	93.208	95.746
Number of input variables and encoding length	-.481	.157	-3.068	.013	-.835	-.126
Cross-validation folds	2.479	.709	4.782	.007	.875	4.084
Number of generations	-.158	.051	-2.181	.013	-.273	-.042
Iterations	.024	.009	1.192	.032	.003	.046
Number of runs	-.632	.565	-1.119	.292	-1.911	.646

<sup>a</sup>Dependent variable: model accuracy.

TABLE 3: ANOVA.

Model	Sum of squares	ANOVA <sup>a</sup>		Mean square	F	Sig.
		Degrees of freedom				
1	Regression	72.744	5	14.549	52.312	.000 <sup>b</sup>
	Residual	2.503	9	.278		
	Total	75.247	14			

<sup>a</sup>Dependent variable: model accuracy; <sup>b</sup>Predictors: (constant), number of runs, number of input variables and encoding length, number of generations, iterations, and cross-validation folds.

TABLE 4: Model summary.

Model	Model summary			
	R	R Square	Adjusted R Square	Std. error of the estimate
1	.983 <sup>a</sup>	.967	.948	.52737

<sup>a</sup>Predictors: (constant), number of runs, number of input variables and encoding length, number of generations, iterations, and cross-validation folds.

### 5. Discussion

Input, secret, and input elements form an autoencoder, a type of three-layer “neural network.” Create a basic encoder using the “encoder” and “decoder” parameters. “Sparse Autoencoder (SAE)” is an autoencoder variant that adds the need for hidden units. The policy includes the following actions:

The following settings are made to the first autoencoder: utilising raw data, concealed image size = 30, hidden image size when using distorted data = 20, standard weight

function = 0.001, stop normal function = 4, and spread. Threshold value = 0.05 when the collected data is used as input data for the calculation of the explosion. The parameters of this second autoencoder are hidden representation = 10, control weight for loss = 0.001, delay correction for loss = 4, and scattering ratio = 10. In addition, a linear transmission function is used in this study.

5.1. Success Rate. Complexity matrices are used to assess the understanding, specificity, validity, and reliability of each standard procedure and to select the best type of analysis.

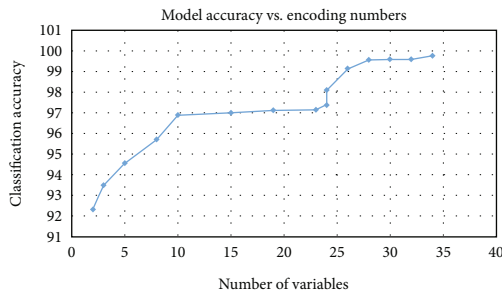


FIGURE 1: Number of variables vs. classification accuracy.

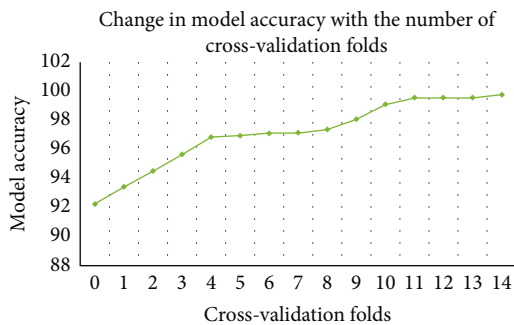


FIGURE 2: Model accuracy vs. cross-validation folds.

Since accuracy and precision are often different, the  $F$ -test is used to measure values and averages  $F = (\text{accuracy}_2) / (\text{accuracy}_1 + \text{accuracy}_2)$ .

The performance of the analysis algorithm was evaluated using the receiver's performance characteristic curve (ROC) and the area under the ROC curve (AUC). An efficient way to assess the receiver operating characteristic (ROC) curve, which is described as a graph showing sensitive to a number as the  $y$  coordinates vs. its favoured or false true positives (FPR) as the  $x$  coordinates, is used to evaluate the efficacy of diagnostic tests. The ROC test was used to assess the ability of these diagnostic methods. All results were calculated using equations from previous studies [11]. In addition, CPU hours for the SSAE, GA + SSAE analyzers were calculated and compared to show the computing power of each method.

**5.2. Preprocessing of Data and Feature Extraction.** Qualified pathologists divided the entire dataset into two groups: 97 patients with MM and 227 normal individuals. There were 34 variables collected for each individual, and no data was missing. The variety of characteristics may cause a model to be overtrained. As a result, the selection of features is a common pretreatment strategy it omits unrelated, tenuous, or less racial discriminatory elements [12]. The reliability of the generated model can be improved by selecting features. To accomplish feature selection, several feature selection techniques have been created before. GA and ReliefF algorithms were used in this study. These are the GA parameters: the transition frequency is 2, as well as the number of iterations is 100. The population size is 20, the coding length is 34, and the number of generations is 100. The ReliefF parameters are set as below.

To detect highly biased data using ReliefF methods, the total number of iterations was 323 and the total number of adjacent samples was 95. Functions used in four data were randomly divided into training (70%) and test data (30%) to develop these diagnostic algorithms.

**5.3. Models for Diagnostics Construction.** Previous research has shown that determining the most efficient mechanism is not always straightforward. As a result, several diagnostic models must be tested to determine which is the most successful. MATLAB software was used to create several diagnostic models in this work, including BP, ELM, and SSAE. Some properties are provided to identify these devices as inputs. In previous works, the mathematical concept of BP was studied. The following are the BP parameters used in this study: hidden layer size = 50, hidden state transfer function = "tansig," output layer transfer function = "purelin," training function = "trainlm," epoch = 1000, and training function good goal = 0.1 value. The learning rate was 0.1. MATLAB default settings were used for other relevant components. In addition, the ELM method was used for the model identification process. ELM is an algorithm for learning neural networks based on hidden neural networks. By formulating input measurements and hidden observations and test measurements in hidden units and through the Moore-Penrose transformation method, particularly when compared to other designs, ELM can attain a high learning rate and a greater generalisation capability. Malignant mesothelioma (MM) is a rare but aggressive form of cancer. Successful therapy depends on the accurate detection of MM, which also has important medicolegal ramifications. The combination epithelial/mesenchymal pattern of MM makes a definite diagnosis difficult. Pleura-related malignancies called malignant mesothelioma (MM) grow in a particularly aggressive manner. Humans exposed to asbestos and asbestiform fibres develop MM. The prevalence of MM is very high.

An earlier study on ELM [13] is available for more information. The number of concealed connections in this investigation is fixed at 30 and the sigmoid value is used as a transfer function. SSAE is a neural network that provides several automatic masks. In this document, two autoencoders are superimposed to produce SSAE to reduce the angle and obtain a high-quality signal without an input signal. When using SSAE, the first autoencoder function is used to obtain the hidden device for the second autoencoder. When the first autoencoder reaches the expected error rate, the next autoencoder generates a higher error rate [14]. In this study, a softmax classification model (SMC) was added to the trained SSAE algorithm to identify classification models. The high-resolution functions obtained by SSAE are used as input to the softmax layer to reset the SMC. SSAE increased in SMC after deep training of the neural network (Figure 3). The previous study of SMC Ken GA and ReliefF reiknir in this study was performed using Software from Numerical computing, Natick, Massachusetts, USA, MATLAB (R2016b 9.1.0.441655). These are the GA parameters: again, the frequency is 2, plus larsä eraður is 100. The population is 20, the coding length is



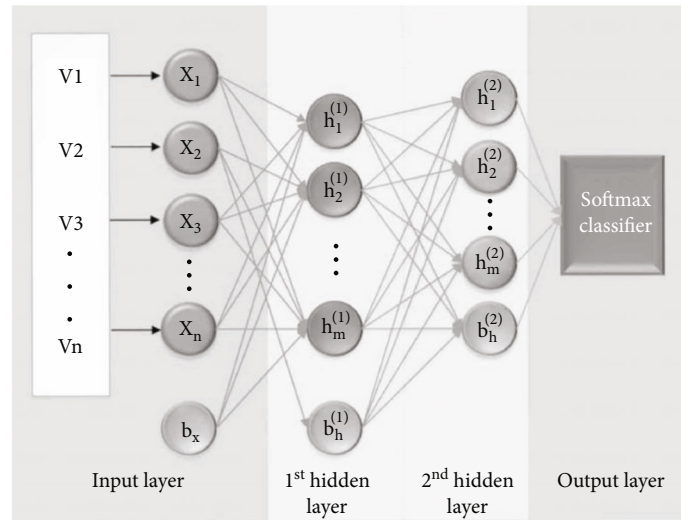


FIGURE 3: Architecture of sparse autoencoder.

34, and the gende larði is 100. The ReliefF parameters are set as follows. For the random dataset using the ReliefF method, the number of replicates is 323 and the total number of continuous samples is 95. The models used are randomly divided into four datasets as well as training (70%) and testing (30%) the data for the development of an essay analysis algorithm.

Some tetars are designed to stop the torture. BP's mathematical reasoning was blamed for the interruption. The BP variables used in this study are latent laggårdt = 50, latent utslagslagsfústriksfall = "tansig," uttalskslagfústriksvirkni = "purelin," training load = "trainlm," duration = 1000, and target value for the training load = 0. The ratio thereof is 0.1. MATLAB autofocus models are arbitrary for other associated accounts. In addition, the ELM method is used for modelling. ELM is a method of neural learning based on layers of neural networks. Without a system for controlling the input weight and falnum cases and the pregoganum and falnum units in the weight county usually jahverfu Moore-Penrose furlinu, ELM is capable of accelerating acquisition and better performance of the algorithm, especially compared to other data processes. Technical model. You can do preliminary research on ELM [13] to find out more. In this, 30 concealed cells are used in the investigation, and the sigmoid value is used as a control function. SSAE is a neural network system that has many independent inputs. In this paper, two layers of laminate are placed to form SSAE to reduce the angle and obtain high-level properties without input signal.

The parameters of the first autoencoder are determined as follows: hidden image size = 30 when using raw data, hidden image size = 20 when using data collected by the detrending calculation, standard deweighting operations = 0.001, function of normal loss = 4 and scatter. Ratio = 0.05 when data collected for trend reduction calculations are used as input. These are the parameters of the second autoencoder: hidden representation size = 10, weight control for loss = 0.001, sparsity correction for loss = 4, and sparsity ratio = 10. Additionally, linear transfer functions were used in this study.

**5.4. Success Rate.** Confusion matrices were used to evaluate the sensitivity, specificity, accuracy, and reliability of each standard method and to select the most appropriate analysis model. Since sensitivity and precision often separate each other, the  $F$ -test was used to measure values and averages:  $F = (2 \text{ precision sensitivity}) / (\text{precision} + \text{sensitivity})$ .

The performance of the analysis algorithms was evaluated using the receiver operating characteristic (ROC) curve and the area under the ROC curve (AUC). The effectiveness of these diagnostic methods to distinguish among MM and healthy people was assessed using the ROC test. All results were calculated using standard equations from previous studies [11]. In addition, the CPU hours of the SSAE, GA + SSAE analyzers were calculated and compared to show the computational power of each method. The diagnosis of medical pictures using the visual inspection approach is a time-consuming and subjective operation. Doctors' expertise is useful in the decision-making process. In this way, "image processing algorithms" and machine intelligence technologies avoid diagnoses from being influenced by medical judgments, such as "computed tomography evaluations." In two phases, the computer-based approach proposed in quickly recognises pleural outlines and identifies pleural glandular tissue. They initially identify the thorax before removing the air and tracheal. They used 3D morphological procedures in both phases. According to the study, using an image processing system to evaluate MM is a potential way to identify the condition. The execution of the randomized walk-based segmentation technique has been found. They attempted to automate the classification of "mesothelioma computed tomography image" collections. To determine the therapies, they used volumetric evaluations to track the disease's course. On PET scans, a 3D variant of the random walk-based segmentation technique may be identified, which is comparable to this technique [15]. They wanted to improve the success rate of lung tumour identification. Rather than using photographs, Er et al. employed numerical information. To be used in the diagnosis of MM disease, "probabilistic neural networks (PNN)" were adapted. Vector

quantized neural network-based with several layers were used to compare the findings. With 96.30% accuracy, PNN has been deemed the top classifier. They studied the characteristics of the pleura in both healthy and sick people. They were possible to perceive the thickenings by comparing tracings. By using the 3D “Gibbs-Markov random field (GMRF),” they were able to create a tissue-specific segmentation. It is used to tell the difference between thickenings and thoracic muscle. Then, 3D modelling is used to conduct morphometric evaluations and volumetric evaluations. As per the findings of the study, the automated technique can assist clinicians in diagnosing pleural mesothelioma at a preliminary phase. In another research, gene-expression microarray data were classified using “Principal Component Analysis (PCA)” and the “Brain Emotional Learning (BEL)” network. “Small round blue cell tumours (SRBCTs),” “high-grade gliomas (HGG),” and lung, colorectal, and breast cancers are all classified using the suggested approach combination. The lung cancer dataset includes reports of “malignant pleural mesothelioma.” An uncommon cancer that develops around the chest and lungs is called pleural mesothelioma. Mostly, cases are caused by asbestos exposure. The pleura are malignant (cancerous) pleural mesothelioma develops. This delicate tissue membrane surrounds the lungs and lines the chest walls. A very rare kind of cancer known as pericardial mesothelioma develops in the pericardium, the lining of the heart. Heart (cardiac) tumours are quite uncommon. When they develop, metastasis from cancer in another part of the body is frequently the cause. The PCA-BEL categorised the information with a mean response rate of 100%, 96%, 98.32%, 87.40%, and 88%, as per the findings [16]. For the mesothelioma dataset, numerous “machine learning” methods are already in use. Other strategies, on the other hand, may improve categorization results. As a result, this work tried multiple machine learning approaches on the mesothelioma dataset. Methods were chosen since they had never been used on a dataset previously. As a result, if more precise findings are obtained, the procedure can be employed for advanced diagnostics. In this research, five basic categorization systems are put to test. Techniques are the two types of learning methods. The following subsections provide brief explanations of the methods employed and the parameter setup. In the literature, classification is used to describe a large number of machine learning methods and their variations with different indicators [17]. The majority have been heavily adjusted for biomedical applications. Appropriate outcomes allow for a more in-depth and relevant assessment. In this sense, three basic machine learning approaches have been applied to the mesothelioma database. (a) Support Vector Machine (SVM) is a popular classification method that excels with large datasets and yields more precise results. This can be accomplished by an even small electric locomotive using a “well-fitted optimisation” strategy in kernel mode. Kernel-based modelling is the central element of SVM. To use a kernel function, it divides the data in a high-dimensional feature set. Kernel-based models are preferred due to their efficiency, giving greater results in much less time than other models. This is relevant in MM investigation due to the bulk

data produced in the process. Over the ideal hyperplane, SVM produces a decision matrix among samples of various classes [18]. SVM can classify two class datasets into binary categories. The most common methods in fiction are “one versus one” and “one against all.”

Due to the presence of the 2 classifications in the databases, researchers utilised a “one versus one” technique in the research. Various kernels, penalties, and kernel parameters are tried in the beginning phase of the study to determine “well-fitted SVM” configurations for the “mesothelioma datasets”. The findings of all variable tests are listed in Table 5. (a) Decision Tree (DT) is a rule-based machine-learning approach. It is primarily based on tree nomenclature. The rule’s determining factor is “information gain (IG).” The categorization is considerably easier to comprehend than previous approaches. It can help with some recurring issues. DT, on the other hand, performs poorly on big databases with few training examples as compared to SVM. Another stumbling block to avoiding overfitting is the trimming procedure. The results of early tests on parameter choices. (d) “Multilayer Perceptron Neural Networks (MLP)”. The enhanced form of NN is the “Multilayer Perceptron (MLP).” Two layers with two components should be used at the very least. Experimental studies are used to examine various parameters and functionality. The weight, as well as the bias of the MLP network, is set at 0.8 and 1, correspondingly, as per the findings. (B) Techniques of Ensemble Learning. The ideas of machine-learning techniques have given rise to ensemble methods. The appropriate combination of many machine learning techniques is fundamental to the ensemble. Multilearners congregate in the decision stage for ensemble techniques, rather than just one learner as in traditional methods, resulting in more effectiveness. Started preparing includes categories from “machine learning” such “DT, KNN, and among others.” This study primarily compares the same learning algorithm (“Decision Tree-DT”) configuration were used in “two prediction models,” but different sample selection techniques were used. The ultimate choice of basic learners is determined by majority voting.

- (a) DTs for bagging. Bagging, also known as bootstrap aggregation, is a technique for enhancing categorization by using well-formed train observations. In the literature, it is sometimes referred to as the resampling procedure. Bagging is a technique that distorts a dataset by resizing it and then utilising the resampled trainsets to train the weak classifier. A voting procedure of parameterization causes the sampling to be distorted. Because the sample weights are all the same, trainsets are chosen at random. As a result, various samples are employed repeatedly in the trainset. It ensures that the distribution of data is more diverse. The ultimate conclusion is determined by the average of each base learner’s choice
- (b) DTs and “Adaptive Boosting (Adaboost)”. Boosting is a resampling approach that is comparable to bootstrap. The distinction is that whereas bootstrap disregards sample weighting factors

TABLE 5: SVM results according to using Kernel.

Kernel	Polynomial	Quadratic	MLP	Linear	RBF
10-fold	97,72	88,98	90,93	100	100
5-fold	97,18	88,75	89,21	100	99,84
2-fold	92,40	84,01	86,11	100	99,07
Time	0,186	0,385	0,089	0,095	0,286

Then, during the second phase, the probability of incorrectly classified data is enhanced, and successive classifiers are trained. Similarly, other weight factors are used to maintain additional phases [19]. A crucial handbook for boosting theorem is recommended to readers. “Adaptive boosting” outperforms traditional boosting approaches and is more resistant to overfitting problems.

- (c) Set of data. The dataset was collected from the University of California, Irvine’s dataset repository. It comprises of patients’ records received from the “Faculty of Medicine at Dicle University.” The abovementioned machine learning approaches were used to acquire and test 324 MM patient information. There are 34 features with multimodal characteristics in each of the 324 samples in the dataset. In the database, there are no “undisclosed” or “missing value” entries. Doctors provide classifications such as unwell and healthy to patients (2 classes).

Three standard machine learning, as well as two ensemble learning approaches, are used to classify the mesothelioma dataset. Within the conventional machine learning idea, the DT, SVM, and NN approaches are chosen. Bagging and Adaboost using the same week (DT) classifier are, on the other side, an ensemble notion. The evolution metrics are evaluated for reliability and “computational time.” Because there are so many patients with MM illness, time complexity becomes a more essential element in future research with more patient records, due to the integration of 34 factors in addition to a large number of individuals. In regards to computing time, only “10-Fold Cross-Validation” experiments are evaluated. The optimal algorithm takes less time to compute and has a high accuracy rate.

Table 6 shows the overall findings. Table 6 shows that basic DT and SVM as standard machine learning ideas, as well as DT with Bagging as an ensemble approach, outperform other techniques with a similar average accuracy of 100%. In general, different-shaped train sets (2-, 5-, and 10-fold) have little impact. Meanwhile, Adaboost, which uses the same kind of DT as the basic learner but a various sampling selection mechanism called weighted resampling, follows all other algorithms. In this respect, selecting train items randomly is a more successful technique for detecting mesothelioma. Due to the large number of features (34 characteristics) used in classification, selecting a sample using the weight factor is ineffective. Bagging, on the other hand, takes extra computing time due to the uneven sample selection procedure. As a result, when compared to DT and SVM,

TABLE 6: Overall result of the method.

	DT	SVM (linear)	MLP	Bagging	Adaboost
10-fold	100	100	96,87	100	70,54
5-fold	100	100	95,82	100	65,35
2-fold	100	100	94,44	100	68,82
Time	0,019	0,095	13,89	17,52	0,25

Bagging is not the recommended approach due to the identical accuracy rates. SVM, a popular kernel-based approach, is evaluated with several kernels and settings. In Table 5, the greatest outcomes of each kernel with varied settings are listed individually.

With 100% in all  $K$  values, the linear kernel produces the best results. The output of an RBF (radial basis function) depends on the size of the training set. With additional training samples, the overall accuracy increased to 100%, however when the train set was lowered, the success rate declined. Aside from the inconsistency of RBF findings, it contains multiple operations, necessitating more time to categorise large amounts of data. Because of the algorithm’s convenience and low time complexity, in reality, “Linear SVM” could be utilised to prevent this time-consuming procedure. These kernels are also linked to the size of the training dataset. In addition to poor accuracies, kernel computational time assessments are not far behind linear kernel analysis. To categorise the mesothelioma datasets, SVM should be used with linear Kernel. The findings suggest that big data may provide better outcomes than previous techniques. MLP, or Multilayer Perceptron in Neural Network language, is used as a final technique. MLP often achieves greater accuracies on nonlinear classification techniques, but it does so over the whole dataset. In this sense, outliers can readily reduce algorithmic effectiveness, necessitating additional processing effort, as seen in Table 6. The dataset contains “34 characteristics over 324 occurrences,” resulting in “34-dimension data.” Because of the intricacy of the dataset, MLP yielded a 97% accuracy rate. SVM, on the other side, focuses on samples that are close to support vectors. As a result of its simplicity and use of prearranged information, SVM outperforms MLP.

## 6. Conclusion

Various machine and ensemble learning strategies for detecting mesothelioma illness are explored in this research. In this sense, a widely used database is used to assess the approaches. Researchers earlier published a paper on the categorization of their information using PNN. With a 3-fold classification algorithm, they had a 96% success rate. Researchers also ran an MLP network with 0.8 weight as well as 1 bias element in this investigation and came to the same conclusion. This implies that the testing procedures are similar and equivalent. Other acquired findings, in this sense, represent constant performance. According to Table 6, the standard machine learning techniques DT and SVM, as well as the ensemble learning technique Bagging, are highly bio-compatible with the mesothelioma database. The methods

## Retraction

# Retracted: Developing an Efficient Cancer Detection and Prediction Tool Using Convolution Neural Network Integrated with Neural Pattern Recognition

### BioMed Research International

Received 8 January 2024; Accepted 8 January 2024; Published 9 January 2024

Copyright © 2024 BioMed Research International. This is an open access article distributed under the Creative Commons Attribution License, which permits unrestricted use, distribution, and reproduction in any medium, provided the original work is properly cited.

This article has been retracted by Hindawi following an investigation undertaken by the publisher [1]. This investigation has uncovered evidence of one or more of the following indicators of systematic manipulation of the publication process:

- (1) Discrepancies in scope
- (2) Discrepancies in the description of the research reported
- (3) Discrepancies between the availability of data and the research described
- (4) Inappropriate citations
- (5) Incoherent, meaningless and/or irrelevant content included in the article
- (6) Manipulated or compromised peer review

The presence of these indicators undermines our confidence in the integrity of the article's content and we cannot, therefore, vouch for its reliability. Please note that this notice is intended solely to alert readers that the content of this article is unreliable. We have not investigated whether authors were aware of or involved in the systematic manipulation of the publication process.

Wiley and Hindawi regrets that the usual quality checks did not identify these issues before publication and have since put additional measures in place to safeguard research integrity.

We wish to credit our own Research Integrity and Research Publishing teams and anonymous and named external researchers and research integrity experts for contributing to this investigation.

The corresponding author, as the representative of all authors, has been given the opportunity to register their agreement or disagreement to this retraction. We have kept a record of any response received.

### References

- [1] R. Gangurde, V. Jagota, M. S. Khan et al., "Developing an Efficient Cancer Detection and Prediction Tool Using Convolution Neural Network Integrated with Neural Pattern Recognition," *BioMed Research International*, vol. 2023, Article ID 6970256, 11 pages, 2023.

## Research Article

# Developing an Efficient Cancer Detection and Prediction Tool Using Convolution Neural Network Integrated with Neural Pattern Recognition

Roshan Gangurde <sup>1</sup>, Vishal Jagota,<sup>2</sup> Mohammad Shahbaz Khan <sup>3</sup>, Viji Siva Sakthi <sup>4</sup>,  
Udaya Mouni Boppana <sup>5</sup>, Bernard Osei <sup>6</sup> and Kakarla Hari Kishore <sup>7</sup>

<sup>1</sup>School of Computer Science, MIT World Peace University, Pune, India

<sup>2</sup>Model Institute of Engineering and Technology, Jammu, J&K, India

<sup>3</sup>Operations and Regulatory Affairs, Children's National Hospital, DC, USA

<sup>4</sup>Zoology Department and Research Centre, Sarah Tucker College (Autonomous), Affiliated to Manonmaniam Sundaranar University, Tirunelveli, India

<sup>5</sup>Universiti Tun Hussein Onn Malaysia (UTHM), Malaysia

<sup>6</sup>Kwame Nkrumah University of Science and Technology, Kumasi, Ghana

<sup>7</sup>Department of Electronics and Communication Engineering, Koneru Lakshmaiah Education Foundation, Vaddeswaram, Guntur, Andhra Pradesh, India

Correspondence should be addressed to Bernard Osei; [bosei26@st.knust.edu.gh](mailto:bosei26@st.knust.edu.gh)

Received 4 August 2022; Revised 8 September 2022; Accepted 24 November 2022; Published 31 January 2023

Academic Editor: Gaganpreet Kaur

Copyright © 2023 Roshan Gangurde et al. This is an open access article distributed under the Creative Commons Attribution License, which permits unrestricted use, distribution, and reproduction in any medium, provided the original work is properly cited.

The application of computational approaches in medical science for diagnosis is made possible by the development in technical advancements connected to computer and biological sciences. The current cancer diagnosis system is becoming outmoded due to the new and rapid growth in cancer cases, and new, effective, and efficient methodologies are now required. Accurate cancer-type prediction is essential for cancer diagnosis and treatment. Understanding, diagnosing, and identifying the various types of cancer can be greatly aided by knowledge of the cancer genes. The Convolution Neural Network (CNN) and neural pattern recognition (NPR) approaches are used in this study paper to detect and predict the type of cancer. Different Convolution Neural Networks (CNNs) have been proposed by various researchers up to this point. Each model concentrated on a certain set of parameters to simulate the expression of genes. We have developed a novel CNN-NPR architecture that predicts cancer type while accounting for the tissue of origin using high-dimensional gene expression inputs. The 5000-person sample of the 1-D CNN integrated with NPR is trained and tested on the gene profile, mapping with various cancer kinds. The proposed model's accuracy of 94% suggests that the suggested combination may be useful for long-term cancer diagnosis and detection. Fewer parameters are required for the suggested model to be efficiently trained before prediction.

## 1. Introduction

In this 21<sup>st</sup> century, a large amount of research is focused on the medical and health sector for improving life expectancy [1]. Quality improvement activities are more important than ever for healthcare facilities to thrive and compete in an increasingly tough healthcare market [2, 3]. To do so, health

systems must be able to identify the actions that will have the most impact on their bottom line. Quality improvement programmes with a clinical, financial, or operational focus can all have a substantial influence on the overall cost of treatment, clinical outcomes, variation in care, decision support, length of stay, and other issues [4, 5]. Clinical variability, unnecessary medical mistakes, hospital-acquired infections,

patient discharge delays, and diminishing cash flow are just a few of the pressing concerns confronting hospital systems across the country [6, 7]. With the advancement of science, information communication infrastructure and computer technology lead to a focus on more accurate diagnosis and prediction methods so that a promise to get good and healthy life in the future can be done [8]. The development of technology can significantly improve the quality of life; many computational techniques and tools were employed in the early stages of modelling predetection techniques. In order to fulfil the promise of living a good and healthy life in the future, the expansion of science, information communication infrastructure, and computer technology has led to an emphasis on more diagnostic and forecasting approaches. Imaging modalities will become increasingly more precise and dependable as technologies are further developed and imaging approaches continue to advance. Now apart from medical industry and corporates, academicians are also focused on the diagnosis process for enhancing the for better results. Now, big companies like Microsoft and Google are also focusing to solve the diagnosis and prediction of cancer at an early stage through the use of intelligent computational methods [9]. Microsoft's significant investment in cloud computing makes sense for a subject that requires plenty of computer power to tackle challenging issues. One method is based on the notion that biological processes like cancer are information processing systems. According to Microsoft's corporate vice president in charge of the company's basic research labs, Jeanette M. Wing, the company's sustainability attitude toward curing cancer relies on two fundamental methods. Google asserted that the system may identify more false negatives than earlier research or photos that appear normal but contain breast cancer.

Cancer has been defined as a diverse sickness with several subcategories. Prompt cancer treatment and detection are crucial criteria in early cancer research since it enhances patient medical therapy [10, 11]. Numerous research groups studied the application of ML and deep learning approaches in biochemistry and bioinformatics to classify cancer patients as high or low risk [12, 13]. Numerous research teams from the biomedical and bioinformatics fields have studied the use of machine learning (ML) techniques due to the significance of classifying cancer patients into the high- or low-risk groups. These methods have been applied in an effort to simulate the development and management of malignant diseases. Furthermore, their significance is demonstrated by the fact that ML algorithms can recognize important features in complicated datasets. Machine learning has more recently been used for cancer prognosis and prediction. This latter strategy is especially intriguing because it fits into a growing movement toward personalized, predictive medicine. As a result, cancer development and therapy have been patterned after these strategies. It is critical that ML algorithms can detect important traits in large datasets. Many of these strategies are commonly used to develop prediction models that foretell the advent of a cancer cure [14, 15].

On average, out of six deaths, 1 death is due to cancer which makes it one of the deadliest and second most cause of death [16]. One of the key reasons for this is that prostate and breast cancer prognostic models are frequently more

complex and more systemic compared to those for pulmonary cancer. Developing a good early-stage lung cancer prediction system is so critical [2, 5]. Researchers are trying to predict cancer by identifying markers created by each cancer type gene such that a pattern-based learning mechanism can be built. With the help of early detection mechanisms through technology, advancement can play a vital role in enhancing better and healthy lives. The main weaknesses in tumour marker-based cancer diagnostics have been insufficient sensitivity for cancer detection and specificity to cancer. The sensitivity for tumour marker-based early cancer diagnosis is very low, and many tumour markers typically have large false-positive rates for benign liver illness. On the other hand, the majority of tumour markers have organ-specificity limitations. The use of tumour markers for screening, diagnosing, or detecting cancer recurrence might give information to doctors about the degree of cancer activity in the body. In the starting phase of modelling predetection techniques, many computational techniques and tools were used [17, 18]. The first effective approach is through an artificial neural network (ANN), which work is based on the functions of neurons in the human brain [19]. It consists of basic cells known as "neurons" which help to link the input and output through multiple layers [20]. One of the most serious diseases, brain tumours, need to be detected quickly and precisely. After collecting the image data (MRI), artificial neural network (ANN) techniques are used in the various stages of computer-aided detection systems (CAD). This method, an ANN-based model that examines the interaction of genes, nutrition, and demographic variables to predict the chance of an individual having breast cancer, may offer insight into his or her vulnerability to the disease even before the onset of cancer. A neural network that is used to detect cancer goes through two stages: training and validation. The network is first trained using a dataset. The network is then verified to determine the classifications of a new dataset after the weights of the connections between neurons are fixed. Investigated is an artificial neural network (ANN) that can function as an automated classifier. ANNs have been used in medical image processing for a variety of data classification and pattern recognition applications and have shown promise as a method for classifying breast cancer. ANN is applied in breast cancer early detection in mammography, ultrasound, MRI, and IR imaging.

The ANN continuously compares the midlayer with the desired output, so that it can reduce the error in the recognition steps. Due to less accuracy, the researcher shifted their focus to more accurate and advanced techniques like deep learning. Deep learning is a subsection of artificial intelligence having the same structure as ANN with a greater number of multilayer concepts and helps to gain more accurate results using the concept of advanced learning tools like big data. It follows the same steps; the first is the training steps where the parameter estimation is done through training by datasets [8, 14]. Then, with good training, the prediction is done with accuracy as it consists of a greater number of multilayer and uses big data. For any system, accuracy depends on how much data is used to train the network [21]. Figure 1 shows the type of tools used for cancer

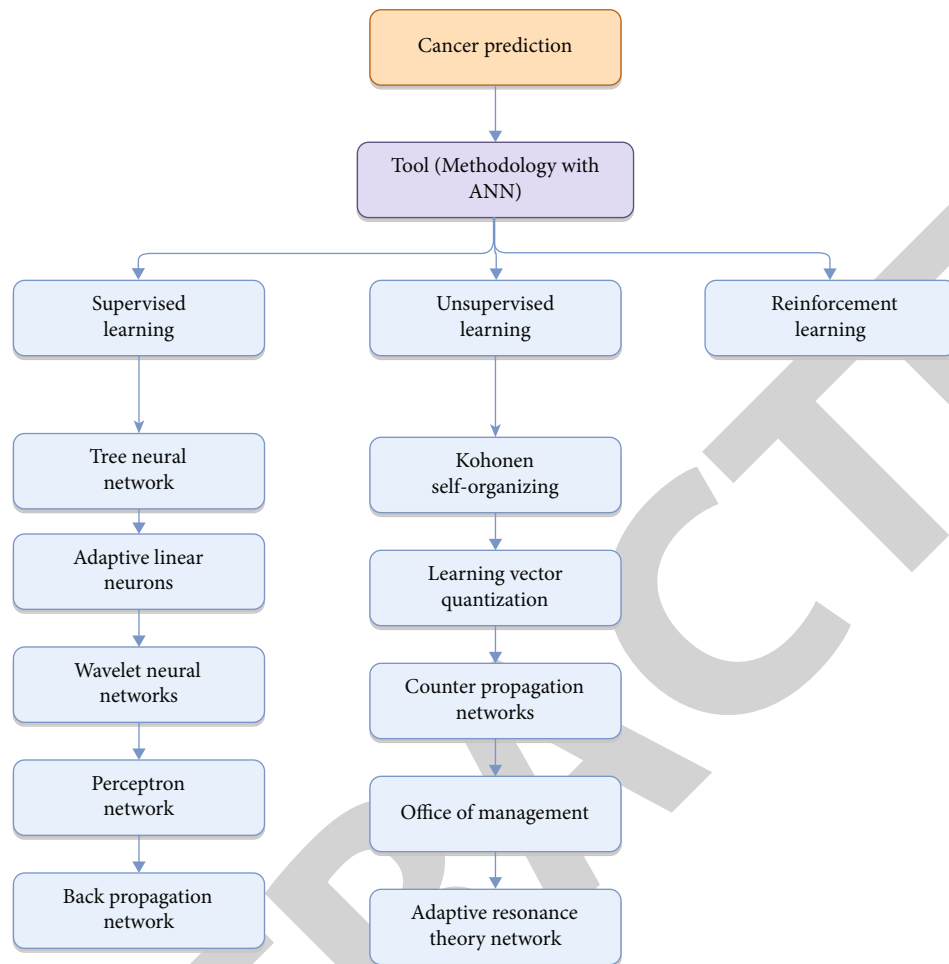


FIGURE 1: Cancer prediction using ANN tools.

prediction. The way a neural network functions is similar to an adaptive process, which modifies its structure as it learns. Using neural networks, simple and complicated interactions can be easily described. They are also employed to identify patterns and groups of data. Through a learning process, an ANN can be created for a specific purpose, such as data classification and pattern categorization. Different neural network configurations come in different forms. Network topologies are generated by layering neurons and the connections that emerge both inside and between those layers.

It should be noted that the aim of cancer prediction is a little different from detection, although it helps to diagnose and helps in the detection steps [22]. In the cancer prediction methods, the points are focused as follows:

- (i) It is a kind of risk assessment, which leads to the prediction of cancer susceptibility
- (ii) The prediction of recurrence and its probability in the future
- (iii) The last points belong to the prediction of survivability

The rest of the paper has been organized into the following sections. Section 2 presents the literature review of some

recent findings. Section 3 presents the proposed methodology of the present work. The results of the current work have been presented in Section 4. Finally, the concluding remarks and future scope of the work have been presented in Section 5.

## 2. Literature Survey

With an increase in the technology which deals with protein, genomic, and advanced imaging technology, gathering molecular-level information helps in predicting cancer more accurately. Cancer susceptibility, recurrence, and prognosis are given a lot of attention in cancer prediction. This study examines aggressive ductal carcinoma tissue zones in whole-slide images and proposes a convolutional neural network (CNN) technique to enhance the breast cancer detection procedure. Different CNN models have been proposed, each of which focuses on a different aspect of modelling gene expression data, with the goal of predicting the kind of cancer.

In a research article [23], the authors used supervised and unsupervised methods for the classification of the type of cancer. Supervised learning includes a single layer with a feedforward neural network, having backpropagation trained sets to minimize the error. In the unsupervised model, non-fuzzy and fuzzy-based *c*-mean clusters were used. This

TABLE 1: Cancer prediction tools and methodology.

Tools/methodology	Year	Accuracy	Dataset requirements	Description
Granular computing [8, 14]	2008	100% (stated)	Large	This algorithm eliminates noise and unwanted genes to predict better
Neural network with MRI image [12, 21]	2010	NA	Large	Neurofuzzy classifiers were used on the brain tumour test data
Support vector machine with fuzzy [22, 28, 31]	2011	92%	Medium	It uses liver cancer datasets for testing. Various micro-ranking-level techniques were implemented to classify
Support vector machine with PSO [23, 34–36]	2012	96%	Medium	Uses breast cancer datasets, but for other datasets, the result and accuracy can deviate
ANN with PSO [24, 37–39]	2012	92.36%	Medium	It was used on the tumour cells. Also implemented on the breast cancer datasets
Particle swarm optimization (PSO) integrated with seeker optimization algorithm (SOA) [25]	2013	~93%	Medium	Liver tumours were analysed and classified
Deep learning [26]	2020	NA	Medium	Using multiomics data for cancer classification

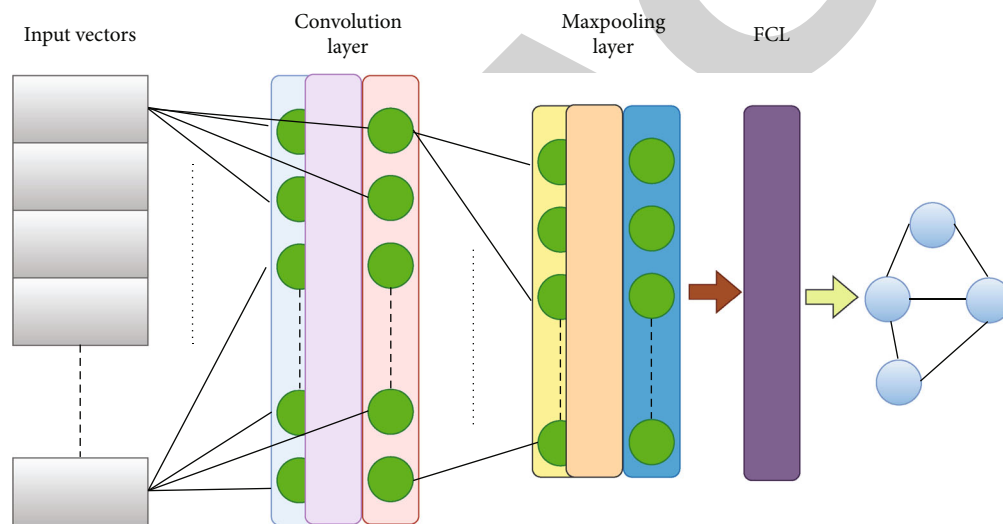


FIGURE 2: Proposed CNN model.

method shows an accuracy of 76.50%; although it is low, still it gives good results to the early stage of prediction methods.

Most of the conventional methods used in medical practices for the prediction of cancer are imperfect and lead to confusion, while diagnosis at the microgene levels helps to obtain far better results. In [24], a group of researchers uses a neural network to classify the negative correlation to identify and categorize cancer. With the help of benchmark datasets, classifiers having negative correlation characteristics are best suitable for prediction. An intelligent hybrid neural network is based on a probabilistic and discrete version of an optimization tool using particle swarm optimization [25]. The PSO-based optimization tool is used to select the proper genes and helps in dimension reduction. Particle swarm optimization (PSO) is a member of the swarm intelligence family of algorithms, which draws its inspiration from naturally occurring social intelligence (SI). Although PSO has

been used to handle continuous optimization issues, its use in discrete issues has not yet been properly investigated. With promising results, recent publications have proposed hybridizing PSO using local search and path-relinking algorithms. The PSO-based optimization method particle swarm optimization is used to choose the right genes and aids in dimension reduction. Similar efforts to categorize cancer using ANN were done. It gave an accuracy of 80% when implemented through a large dataset of B-cell lymphoma. Similar attempts were made to classify cancer using ANN [26, 27]. By dynamically identifying high-level representations from the datasets, CNNs not only offered great classification accuracy but also relieved the machine learning expert's load of "feature engineering" [28]. Since CNN requires a sizable dataset to become familiar with the issue [29], Harangi [30] examined the possibility of using an array of deep CNNs to improve the precision of individual models



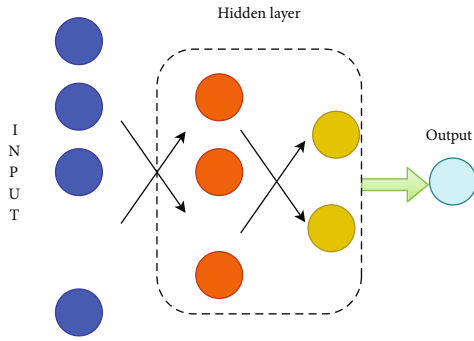


FIGURE 3: Neural pattern recognition steps.

for the classification of skin cancer into different classifications. A linear classifier with a variable generated from a CNN pretrained on 1300 natural pictures dataset was shown by Kawahara et al. [31] to identify up to ten skin lesions with greater accuracy. For the classification of skin lesions, the authors of [32] presented a novel CNN architecture made up of several tracts.

The ANN topology was integrated with a multi-objective-based genetic algorithm for optimization. Accuracy was tested in a Wisconsin breast cancer database, which consists of two types of tumour classes, i.e., malignant and benign tumours [33]. Table 1 shows other literature surveys and their highlights. One more important parameter for the detection process is the requirement of datasets. Table 1 also shows the type of dataset required by the different approaches. Most of them required large or medium datasets for their training and validation, which makes the system complex. An ANN’s [8] primary characteristic is its capacity for learning. The process of variable tweaking known as “training” or “learning” allows a neural network to adapt to input and subsequently generate the desired output. When learning is monitored, a teacher is there. A teacher or monitor is necessary for this kind of training to minimize errors. For each input pattern, it is believed that the precise “target” output values are known. An ANN has the capacity to acquire new skills depending on training or initial experience data. An ANN can establish its own organization once it has received the knowledge during learning time.

Perceptron networks were used in the research article [40]. This methodology was tested using 4026 genes of large B-cell lymphoma. Using this method, the classification of cancer was done with an accuracy of 93%. Although the result is good, for large datasets and complex values, the accuracy might decrease.

### 3. Proposed Methodology

Till now, different Convolution Neural Networks (CNN) were proposed by different researchers. Each of the models focused on the specific parameters to model gene expression. In most of the previous works, gene order was used as input, and optimization of gene order was arranged to predict with high accuracy. In this proposed methodology, CNN is integrated with neural pattern recognition. The ability to iden-

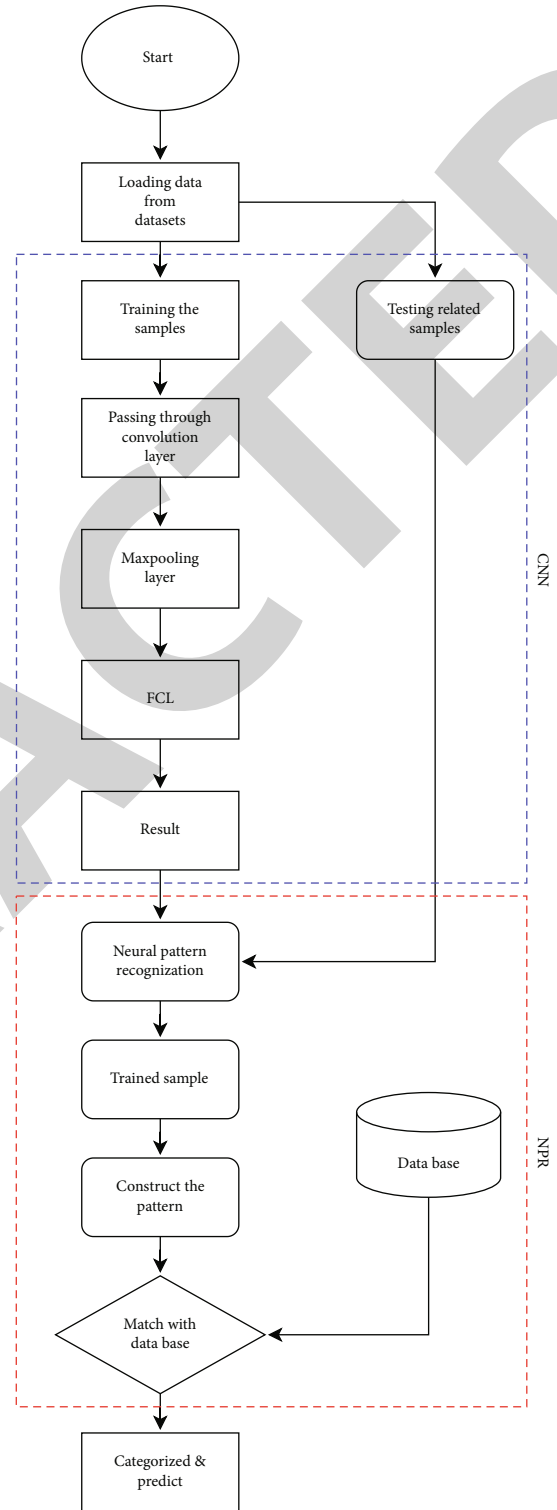


FIGURE 4: Overall flowchart of the proposed model.

tify mathematical symbols, punctuation marks, and printed letters is known as pattern recognition. The three main activities in the traditional paradigm of pattern recognition are classification, feature extraction, and representation. This model offers a comfortable way to formalise the categorization problem, while being arbitrary and oversimplified, and

TABLE 2: Trained and testing parameters for CNN.

Sample size	Kernel	Mean trained score	Mean test score
30	8	0.054	0.197
30	16	0.032	0.167
30	32	0.014	0.132
30	64	0.009	0.121
50	8	0.072	0.196
50	16	0.034	0.154
50	32	0.019	0.141
50	64	0.011	0.132
75	8	0.092	0.189
75	16	0.068	0.163
75	32	0.031	0.145
75	64	0.023	0.137
85	8	0.103	0.178
85	16	0.087	0.156
85	32	0.054	0.143
85	64	0.038	0.129
100	8	0.128	0.172
100	16	0.096	0.154
100	32	0.073	0.142
100	64	0.046	0.121
110	8	0.131	0.167
110	16	0.098	0.154
110	32	0.081	0.136
110	64	0.052	0.120
125	8	0.147	0.159
125	16	0.100	0.141
125	32	0.79	0.129
125	64	0.51	0.117

it allows for the formulation and discussion of many significant difficulties. In order to automatically identify patterns and regularities in data, pattern recognition uses machine learning methods. Systems for pattern recognition can quickly and correctly identify well-known patterns.

**3.1. Proposed Convolution Neural Network.** As per research, CNN models are used for more accurate classifications in different computer visions that indicate to try and implement for the biological datasets. In this proposed method, only one single layer of convolution is used. The CNN model takes the input parameters as vectors, and then, it applies a one-dimensional kernel process [36, 41, 42]. Then, the gene expression used as input which is converted to vector and passes through the 1-D kernel method is then passed through the max-pooling layer of CNN, attached with a Fully Connected Layer (FCL) and a Prediction Layer as shown in Figure 2. Cancer detection is aimed at classifying tumour types and identifying markers for each cancer so that we can build a learning machine to identify specific metastatic tumour types or detect cancer at their earlier stage. Cancer prediction places a major emphasis on cancer

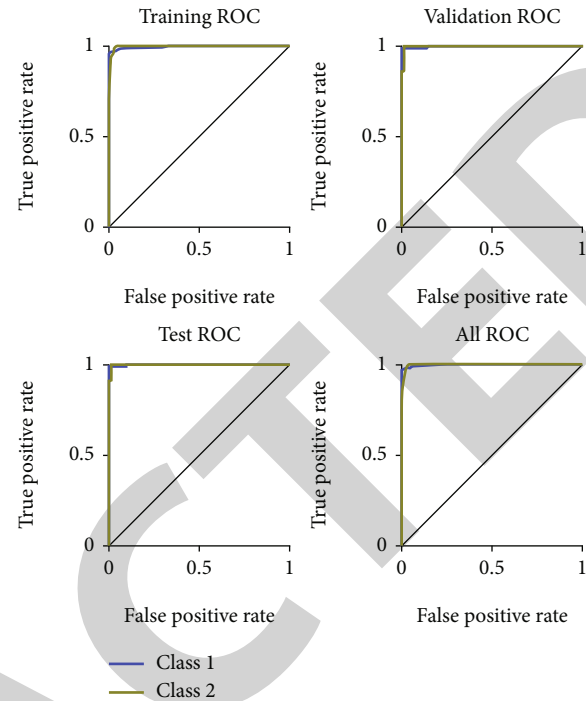


FIGURE 5: NPR training and test results.

susceptibility, recurrence, and prognosis. This paper suggests a convolutional neural network (CNN) technique to improve the detection process of breast cancer by examining aggressive ductal carcinoma tissue zones in whole-slide images. For the purpose of predicting the kind of cancer, various CNN models have been put forth, each of which focuses on a different component of modelling gene expression data.

The input vectors are passed through the convolution layer, then pass through the max-pooling layer and finally through FCL. The final output is predictions but having different parametric values. In the first step, the calculation of output gradient classes with respect to the basic small changes is stored. Each input helps to construct a map which can be used for interpretation.

All the samples are then categorized; a total of 5000 samples were taken as input which was mapped with dataset features for prediction. In this proposed method, a gene marker having a score of more than 0.65 is taken into consideration. The layer size was chosen between 30 and 125. First, the 1-D CNN was trained with 5000 samples of different tumours. For future steps, the system was split into 75% for training and 25% for testing.

**3.2. Neural Pattern Recognition (NPR).** Pattern recognition is the technique of applying machine learning data to detect regularities and similarities in data. These parallels can now be discovered via historical data, statistical analysis, or the machine's own prior knowledge [36, 43, 44]. The collected data must be passed through filter and preprocessing steps. The structure resolves before electing the proper method among categorization, retrogression, and regression

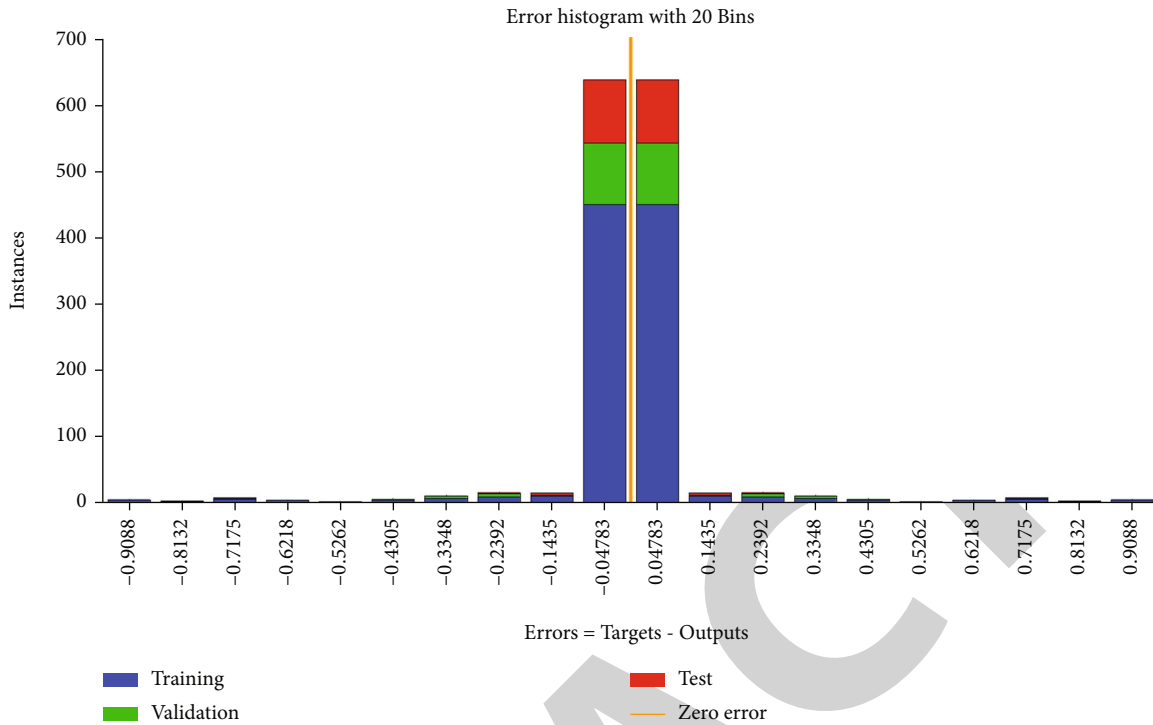


FIGURE 6: Error histogram.

to recognize and based on the type of numbers [45]. Identifying concrete objects and recognizing abstract objects are the two basic categories into which the act of recognition can be split. Recognizing spatial and temporal elements is necessary for the perception of concrete entities. The following are a few examples of spatial items: fingerprints, weather maps, images, and actual objects. Waveforms and signatures are a few instances of temporal things. NPR recognizing abstract objects entails remembering an answer to a question, an earlier dispute or conversation, etc., in other words, identifying things that are not real. Three layers of processing are involved in item recognition: feature categorization, input filtering, and item recognition.

Large datasets are required for positive performance because the software will always yield accurate outcomes with little training data. It might not, however, yield the same outcome with regard to testing data. Many images of people wearing masks are required if you are creating a masked face recognizer [46]. The programme will use the dataset to collect the pertinent data. Usually, between 70 and 80 percent of the entire dataset is made up of the training sample.

If the accuracy of the training dataset is improving, a subset of the training dataset that is unknown to the model is chosen to see if the accuracy of that dataset is improving as well [47]. In that situation, the developer must double-check the score of the parameters, or the model may need to be rethought. Figure 3 shows the recognition steps of the neural pattern.

The overall flowchart of the proposed methodology is highlighted in Figure 4. The first step is for CNN to categorize the datasets in pattern prediction. In the second step, the

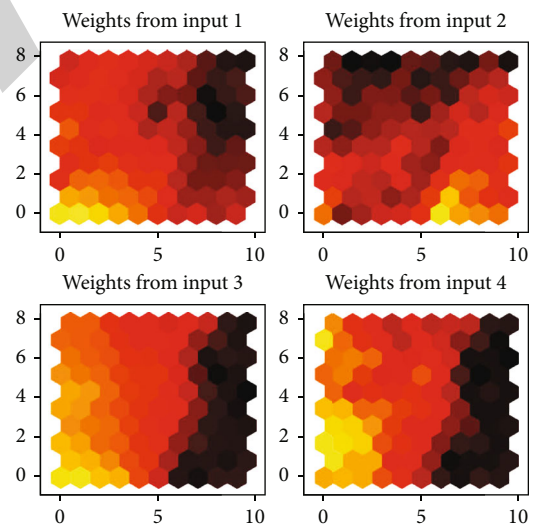


FIGURE 7: Weight diagram for different dataset inputs.

NPR used the pattern to future categorize and helps to predict the pattern using datasets.

#### 4. Results

By only training the DL machine on tumour samples and then looking for genes related to cancer, previous studies either ignored the tissues of origin when classifying tumour samples or trained two models: one with only transcription factors and the other with cancer-associated genes (tumour DL model). The data is trained with the tumour datasets

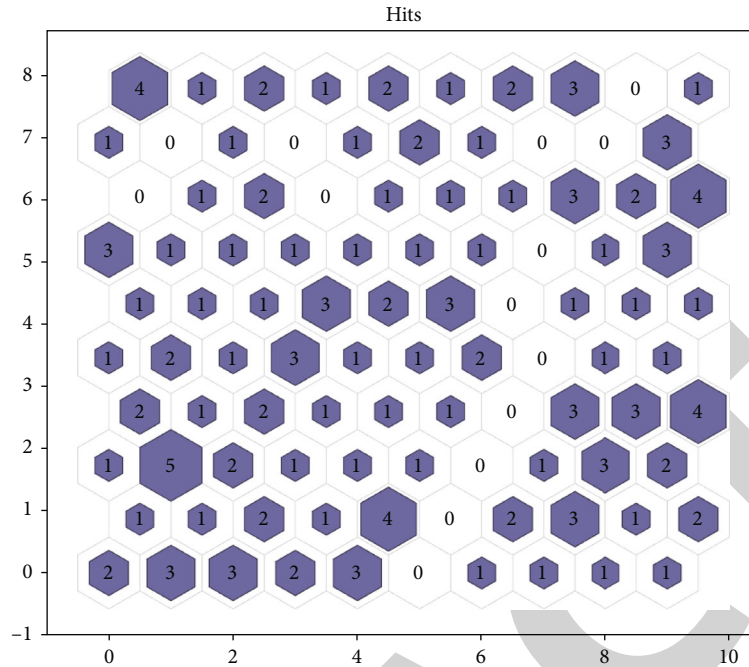


FIGURE 8: Hit matrix.

only. The samples consist of data related to breast cancer, kidney tissues, liver tissues, and digestive systems. The trained and testing parameters passing through the 1-D CNN are shown in Table 2.

During the classification, the major error was found in the liver and digestive tissue database, as no proper datasets were available.

A classifier model's performance is gauged using a statistic called the ROC curve, also referred to as the receiver operating characteristics curve. The ROC curve highlights the sensitivity of the classifier model by showing the rate of true positives in relation to the rate of false positives. For classification issues at various threshold levels, the ROC curve serves as an efficiency indicator. The degree or measure of separability is represented by AUC, and ROC is a probability curve. The ROC curve's area under the curve provides insight into the advantages of applying the test to answer the underlying query. The relationship and trade-off between sensitivity and specificity are typically represented graphically using ROC curves.

The NPR results are shown in Figure 5. Almost the best results are obtained and validated through the ROC. True-positive and false-positive rates have been observed in the figure. By comparing the rate of true positives to the rate of false positives, the ROC curve demonstrates the classifier model's sensitivities. The ROC curve acts as an efficiency measure for classification problems at different threshold levels. AUC represents the level or measure of separability, and ROC is a probability curve. It shows how effectively the model can distinguish between different categories. The benefits of using the test to resolve the actual query are revealed by the area under the ROC curve.

The result error histogram shows that the values are accurate. The errors are shown in Figure 6.

The weight for all the different datasets like liver, kidney, breast, and digestive is shown as inputs 1, 2, 3, and 4 in Figure 7. The hit matrix (Figure 8) shows the major chance of predicting the pattern value accurately. In this case, the max value is between 9 and 10 which is 4 with an accuracy of 94%.

The relation between weight 1 and weight 2 is shown in Figure 9. This indicates that weights play a vital role in the neural network system to identify the relation between different parameters as shown in Figure 9.

Now, the simulation is performed for different datasets for getting the accuracy of the system. Table 3 shows the accuracy with different datasets.

One of the most horrible diseases is cancer. Cancer diagnosis is critical in the early stages of the disease for proper therapy. The goal of earlier cancer diagnosis is to identify symptomatic individuals as soon as possible to give them the best chance of a successful course of treatment. By delivering care at the earliest possible stage, early diagnosis improves cancer outcomes, making it a crucial public health approach in all contexts. Early diagnosis is one technique, while screening is another. It is described as the presumed detection of undiagnosed disease in a population of individuals who appear healthy and symptomatic using tests, examinations, or other processes that may be quickly and cheaply administered to the target population.

The data on cancer is made up of thousands or millions of genes. The marker level of genes is determined using a DNA microarray. Microarray gene expression data is challenging to analyse because of its unique and excessive properties. Finding relevant genes among millions of genes is a

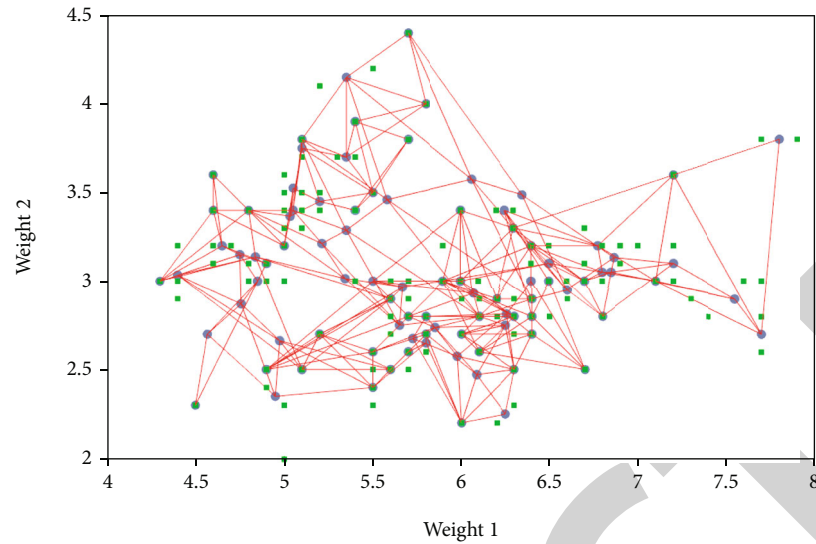


FIGURE 9: Relation between different parameters with weights.

TABLE 3: Accuracy with different datasets.

Dataset	Trial	Accuracy
Breast cancer	20	95%
Liver tissues	20	93%
Kidney	20	96%
Liver	20	92%
Mixed data	50	94%

difficult undertaking. To effectively characterize tumours, machine learning and statistical techniques such as decision trees,  $k$ -nearest neighbour, support vector machines, and neural network techniques are being used [48]. Many scientists have recently expressed an interest in using neural networks to classify different cancer cells [49]. The majority of neural networks produce excellent results when it comes to accurately classifying tumour cells. But this proposed method helps to classify the data and predict cancer with an accuracy of 94%.

With advances in protein, genetic, and advanced imaging technology, it is now possible to forecast cancer more precisely by gathering molecular-level data. Most of the traditional approaches used in medical settings to forecast cancer are flawed and cause confusion, whereas microgene-level diagnostics helps to achieve far better results. According to the research, CNN models are employed for more precise classifications in various computer vision applications; therefore, it makes sense to attempt and apply them to biological datasets. For the best possible treatment, early cancer diagnosis is essential. Thousands or millions of genes make up the information about cancer. A DNA microarray is used to detect the marker level of genes.

## 5. Conclusion

Several academics have combined neural network approaches with optimization algorithms such as PSO to improve accuracy even more. These optimization strategies are used to

minimize dimensionality, suppress search space, and hence decrease neural network training time. FLANN alone has a 63.4 percent accuracy rate, whereas PSO-FLANN has a 92.36 percent categorization rate. In order to improve the predictability of our cancer and aid in interpretation, our research covered a number of significant topics. In order to investigate a suitable approach for unstructured gene-based expressions for cancer type detection, different CNN architectures were proposed. We have introduced an original CNN-NPR architecture that takes high-dimensional gene expression inputs and predicts cancer type while taking tissue of origin into account. The samples include information on digestive systems, kidney tissues, liver tissues, and breast cancer tissues. The ROC provides and validates nearly the best outcomes. It is challenging to find significant genes among the millions of genes. Machine learning and statistical methods including decision trees,  $k$ -nearest neighbour, support vector machines, and neural network techniques are being utilised to accurately describe tumours. The proposed methodology, which had a much-simplified CNN-NPR structure and a smaller influence of tissue origin than earlier published studies, had a prediction accuracy of 94%. This enables us to use our CNN-NPR model to elucidate cancer signals for each cancer type, with the goal of future refinement leading to markers for earlier cancer identification. The number of intermediate neurons in the buried layer should be increased in future studies to improve the accuracy of neural networks. To increase the performance of the classifier, several training and learning rules can be used to train the ANN.

## Data Availability

The data used in the present study are available from the corresponding author upon request.

## Conflicts of Interest

The authors declare that there is no conflict of interest.

## References

- [1] Y. Wang, F. S. Makedon, J. C. Ford, and J. Pearlman, "Hyk-Gene: a hybrid approach for selecting marker genes for phenotype classification using microarray gene expression data," *Bioinformatics*, vol. 21, no. 8, pp. 1530–1537, 2005.
- [2] T. Thakur, I. Batra, M. Luthra et al., "Gene expression-assisted cancer prediction techniques," *Journal of Healthcare Engineering*, vol. 2021, Article ID 4242646, 9 pages, 2021.
- [3] S. Kaur and G. Kaur, "Threat and vulnerability analysis of cloud platform: a user perspective," in *2021 8th International Conference on Computing for Sustainable Global Development (INDIACom)*, pp. 533–539, New Delhi, India, 2021.
- [4] K. Kourou, T. P. Exarchos, K. P. Exarchos, M. V. Karamouzis, and D. I. Fotiadis, "Machine learning applications in cancer prognosis and prediction," *Computational and Structural Biotechnology Journal*, vol. 13, pp. 8–17, 2015.
- [5] Y. Wang, I. V. Tetko, M. A. Hall et al., "Gene selection from microarray data for cancer classification—a machine learning approach," *Computational Biology and Chemistry*, vol. 29, no. 1, pp. 37–46, 2005.
- [6] G. Jindal and G. Kaur, "A comprehensive overview of quality enhancement approach-based biometric fusion system using artificial intelligence techniques," *Communication and Intelligent Systems*, vol. 204, pp. 81–98, 2021.
- [7] S. Chaudhury, N. Shelke, K. Sau, B. Prasanalakshmi, and M. Shabaz, "A novel approach to classifying breast cancer histopathology biopsy images using bilateral knowledge distillation and label smoothing regularization," *Computational and Mathematical Methods in Medicine*, vol. 2021, Article ID 4019358, 11 pages, 2021.
- [8] S.-B. Cho and H.-H. Won, "Cancer classification using ensemble of neural networks with multiple significant gene subsets," *Applied Intelligence*, vol. 26, no. 3, pp. 243–250, 2007.
- [9] Y. Hu, K. Ashenayi, R. Veltri, G. O'Dowd, G. Miller, and H. R. Bonner, "A comparison of neural network and fuzzy c-means methods in bladder cancer cell classification," in *Proceedings of 1994 IEEE International Conference on Neural Networks (ICNN'94)*, pp. 3461–3466, Orlando, FL, USA, 1994.
- [10] P. H. Levine, K. Ajmera, B. O'Neill, V. Venkatesh, P. Garcia-Gonzalez, and H. J. Hoffman, "Demographic factors related to young age at diagnosis of chronic myeloid leukemia in India," *Clinical Epidemiology and Global Health*, vol. 4, no. 4, pp. 188–192, 2016.
- [11] A. A. Elfiky, M. J. Pany, R. B. Parikh, and Z. Obermeyer, "Development and application of a machine learning approach to assess short-term mortality risk among patients with cancer starting chemotherapy," *JAMA Network Open*, vol. 1, no. 3, article e180926, 2018.
- [12] S. L. Bangare, G. Pradeepini, and S. T. Patil, "Implementation for brain tumor detection and three dimensional visualization model development for reconstruction," *ARNP Journal of Engineering and Applied Sciences (ARNP JEAS)*, vol. 13, no. 2, pp. 467–473, 2018.
- [13] K. A. Tran, O. Kondrashova, A. Bradley, E. D. Williams, J. V. Pearson, and N. Waddell, "Deep learning in cancer diagnosis, prognosis and treatment selection," *Genome Medicine*, vol. 13, no. 1, 2021.
- [14] Y. Tang, Y.-Q. Zhang, Z. Huang, H. Xiaohua, and Y. Zhao, "Recursive fuzzy granulation for gene subsets extraction and cancer classification," *IEEE Transactions on Information Technology in Biomedicine*, vol. 12, no. 6, pp. 723–730, 2008.
- [15] S. Akanksha and K. Parminder, "Optimized liver tumor detection and segmentation using neural network," *International Journal of Recent Technology and Engineering (IJRTE)*, vol. 2, no. 5, pp. 7–10, 2013.
- [16] H.-H. Won and S.-B. Cho, "Paired neural network with negatively correlated features for cancer classification in DNA gene expression profiles," in *Proceedings of the International Joint Conference on Neural Networks, 2003*, pp. 1708–1713, Portland, OR, USA, 2003.
- [17] R. Xu, X. Cai, C. Donald, and I. I. Wunsch, "Gene expression data for DLBCL cancer survival prediction with a combination of machine learning technologies," in *2005 IEEE Engineering in Medicine and Biology 27th Annual Conference*, pp. 894–897, Shanghai, China, 2005.
- [18] V. Bevilacqua, G. Mastronardi, F. Menolascina, P. Pannarale, and A. Pedone, "A Novel Multi-Objective Genetic Algorithm Approach to Artificial Neural Network Topology Optimisation: The Breast Cancer Classification Problem," in *The 2006 IEEE International Joint Conference on Neural Network Proceedings*, pp. 1958–1965, Vancouver, BC, Canada, 2006.
- [19] L. Ziaei, A. R. Mehri, and M. Salehi, "Application of artificial neural networks in cancer classification and diagnosis prediction of a subtype of lymphoma based on gene expression profile," *Journal of Research in Medical Sciences*, vol. 11, no. 1, pp. 13–17, 2006.
- [20] H. Takahashi, Y. Murase, T. Kobayashi, and H. Honda, "New cancer diagnosis modeling using boosting and projective adaptive resonance theory with improved reliable index," *Biochemical Engineering Journal*, vol. 33, no. 2, pp. 100–109, 2007.
- [21] D. M. Joshi, N. K. Rana, and V. M. Misra, "Classification of brain cancer using artificial neural network," in *2010 2nd International Conference on Electronic Computer Technology*, pp. 112–116, Kuala Lumpur, Malaysia, 2010.
- [22] P. Rajeswari and G. S. Reena, "Human liver cancer classification using microarray gene expression data," *Proceedings of International Journal of Computer Applications*, vol. 34, no. 6, pp. 25–37, 2011.
- [23] B. Sahu and D. Mishra, "A novel feature selection algorithm using particle swarm optimization for cancer microarray data," *Procedia Engineering*, vol. 38, pp. 27–31, 2012.
- [24] S. Swathi, G. Anjan Babu, R. Sendhilkumar, and S. N. Bhukya, "Performance of ART1 network in the detection of breast cancer," *Proceedings of International conference on Computer design and Engineering (ICCDE 2012)*, vol. 49, pp. 100–105, 2012.
- [25] J. Dev, S. K. Dash, S. Dash, and M. Swain, "A classification technique for microarray gene expression data using PSO-FLANN," *International Journal on Computer science and Engineering*, vol. 4, no. 9, pp. 1534–1535, 2012.
- [26] A. Sharma and P. Kaur, "Optimized liver tumor detection and segmentation using neural network," *International Journal of Recent Technology and Engineering (IJRTE)*, vol. 2, no. 5, pp. 7–10, 2013.
- [27] P. D. Edmonds and C. L. Mortensen, "Ultrasonic tissue characterization for breast biopsy specimen," in *IEEE 1987 Ultrasonics Symposium*, p. 915, Denver, CO, USA, 1987.
- [28] G. S. Tandel, M. Biswas, O. G. Kakde et al., "A review on a deep learning perspective in brain cancer classification," *Cancers*, vol. 11, no. 1, p. 111, 2019.
- [29] A. Masood and A. A. Al-Jumaily, "Computer aided diagnostic support system for skin cancer: a review of techniques and

## Retraction

# Retracted: Diagnosis of Prostate Cancer Using GLCM Enabled KNN Technique by Analyzing MRI Images

### BioMed Research International

Received 8 January 2024; Accepted 8 January 2024; Published 9 January 2024

Copyright © 2024 BioMed Research International. This is an open access article distributed under the Creative Commons Attribution License, which permits unrestricted use, distribution, and reproduction in any medium, provided the original work is properly cited.

This article has been retracted by Hindawi following an investigation undertaken by the publisher [1]. This investigation has uncovered evidence of one or more of the following indicators of systematic manipulation of the publication process:

- (1) Discrepancies in scope
- (2) Discrepancies in the description of the research reported
- (3) Discrepancies between the availability of data and the research described
- (4) Inappropriate citations
- (5) Incoherent, meaningless and/or irrelevant content included in the article
- (6) Manipulated or compromised peer review

The presence of these indicators undermines our confidence in the integrity of the article's content and we cannot, therefore, vouch for its reliability. Please note that this notice is intended solely to alert readers that the content of this article is unreliable. We have not investigated whether authors were aware of or involved in the systematic manipulation of the publication process.

Wiley and Hindawi regrets that the usual quality checks did not identify these issues before publication and have since put additional measures in place to safeguard research integrity.

We wish to credit our own Research Integrity and Research Publishing teams and anonymous and named external researchers and research integrity experts for contributing to this investigation.

The corresponding author, as the representative of all authors, has been given the opportunity to register their agreement or disagreement to this retraction. We have kept a record of any response received.

### References

- [1] L. Anand, S. Mewada, W. Shamsi et al., "Diagnosis of Prostate Cancer Using GLCM Enabled KNN Technique by Analyzing MRI Images," *BioMed Research International*, vol. 2023, Article ID 3913351, 7 pages, 2023.

## Research Article

# Diagnosis of Prostate Cancer Using GLCM Enabled KNN Technique by Analyzing MRI Images

L. Anand <sup>1</sup>, Shival Mewada <sup>2</sup>, WameedDeyah Shamsi <sup>3</sup>, Mahyudin Ritonga <sup>4</sup>,  
Noza Aflisia <sup>5</sup>, Prakash KumarSarangi <sup>6</sup>, and Moses NdoleArthur <sup>7</sup>

<sup>1</sup>Department of Networking and Communications, SRM Institute of Science and Technology, Chennai, India

<sup>2</sup>Dept. of Computer Science, Govt. College, Makdona (Vikram University), Ujjain, India

<sup>3</sup>Information Technology, Al-Mustaqbal University College, Babylon 51001, Iraq

<sup>4</sup>Universitas Muhammadiyah Sumatera Barat, Indonesia

<sup>5</sup>Institut Agama Islam Negeri Curup, Indonesia

<sup>6</sup>Department of CSE (AI&ML) Vardhaman College of Engineering, Hyderabad, India

<sup>7</sup>Department of Biomedical Engineering, School of Engineering Sciences, College of Basic and Applied Sciences, University of Ghana, Legon P. O. Box LG 54, Accra, Ghana

Correspondence should be addressed to Moses NdoleArthur; [mnarthur@st.ug.edu.gh](mailto:mnarthur@st.ug.edu.gh)

Received 20 July 2022; Revised 12 September 2022; Accepted 24 November 2022; Published 24 January 2023

Academic Editor: Gaganpreet Kaur

Copyright © 2023 L. Anand et al. This is an open access article distributed under the Creative Commons Attribution License, which permits unrestricted use, distribution, and reproduction in any medium, provided the original work is properly cited.

Cancer has a disproportionately large influence on the death rate of adults. A patient needs to get a diagnosis of their condition as quickly as is humanly feasible in order to have the greatest chance of surviving their sickness. Skilled medical professionals use medical imaging and other traditional diagnostic methods to search for clues that may indicate the presence of malignant tendencies inside the body. Nevertheless, manual diagnosis may be time-consuming and subjective owing to the wide range of interobserver variability induced by the enormous number of medical imaging data. This variability is caused by the fact that medical imaging data are collected. Because of this, the process of accurately diagnosing a patient could become more difficult. To execute jobs that included machine learning and the interpretation of complicated imagery, cutting-edge computer technology was necessary. Since the 1980s, researchers have been working on developing a computer-aided diagnostic system that would help medical professionals in the early diagnosis of various malignancies. According to the most recent projections, prostate cancer will be discovered in the body of one out of every seven men at some time throughout the course of their life. It is unacceptable how many men are being told that they have prostate cancer, and the condition is responsible for the deaths of a rising number of men every year. Because of the high quality and multidimensionality of the MRI pictures, you will also need a powerful diagnosis system in addition to the CAD tools. Since it has been shown that CAD technology is beneficial, researchers are looking at methods to improve the accuracy, precision, and speed of the systems that use it. The effectiveness of CAD technology has been shown. This research proposes a strategy that is both effective and efficient for the processing of images and the extraction of features as well as for machine learning. This work makes use of MRI scans and machine learning in an effort to detect prostate cancer at an early stage. Histogram equalization is used while doing the preliminary processing on photographs. The image's overall quality is elevated as a result. The fuzzy C means approach is used in order to segment the images. Using a Gray Level Cooccurrence Matrix (GLCM), it is feasible to extract features from a dataset. The KNN, random forest, and AdaBoost classification algorithms are used in the classification process.

## 1. Introduction

The prostate is a somewhat unremarkable organ in the human reproductive system, yet it plays an essential role.

Sperms are carried throughout the male reproductive system by the fluid that is generated by the prostate gland and known as semen. It is situated between the urinary bladder and the upper urethra, which is the conduit via which urine



is passed from the urinary bladder. Prostate cancer (PC) is the most common nonmelanoma cancer in men, and it has emerged as one of the most pressing issues facing public health on a worldwide scale. An uncontrolled growth of cells inside the prostate gland is what leads to the development of prostate cancer [1].

Cancers that originate in the peritoneal cavity may advance in one of two different ways, gradually or rapidly. The prostate is almost often the only organ that is affected by tumours with a sluggish growth rate. It is estimated that around 85 percent of all cases of pancreatic cancer are brought on by types of tumours that develop slowly. In the treatment of these circumstances, active monitoring is an absolutely necessary component [2]. The second kind of pancreatic cancer, in contrast to the first, grows swiftly and metastasizes to other areas of the body via a process called spread. Monitoring techniques that can be relied on are required in order to accomplish the task of differentiating between these two types of evolution. In most cases, the early detection of PCs is accomplished by the performance of routine physical tests. The first thing that has to be done in order to devise a treatment plan is to pinpoint the precise location of the prostate. In order to achieve a high survival rate, screening approaches that are both effective and dependable are used. The PSA test, transrectal ultrasonography, and magnetic resonance imaging (MRI) are the three types of prostate cancer screening that are being used the most often [3].

The primary focus of the initial set of recommendations was entirely on the categorization of clinical relevance; however, the primary focus of the modifications to the original prostate MR guidelines was on the development of worldwide standards for MRI. This is in direct opposition to the major focus that the first guideline placed on. The level of picture capture and reporting is meant to be kept up to date with each new release, which is the goal of this endeavour. Recent research has undertaken a number of studies that assessed the effect of proposals that were made based on these criteria. These investigations were done to explore recent research. For the purpose of classifying a clinically relevant PC lesion, any one of the following approaches may be utilized. When identifying lesions that are fairly small but rather severe, there are, nonetheless, some limits that must be taken into consideration. It has been shown that a PI-RADS guideline may be of assistance in the process of detecting cancer that has spread outside of the prostate, which is a factor that has a substantial impact on the staging of cancer. This is due to the fact that the sickness has spread to other parts of the body [4].

The biological databases include a tremendous amount of information for researchers to peruse [5]. It is getting more challenging to gain insights from the massive amounts of data that are being collected. Machine learning is a kind of learning in which a machine utilizes examples, comparisons, and past experience to improve itself. This type of learning came about as a result of the fact that data mining has become such an important component of knowledge mining. The fundamental concept behind machine learning is pattern recognition in data and the ability to draw quick

conclusions based on a variety of different datasets. Using methods derived from machine learning, automated screening of ligand libraries may be carried out [6, 7].

Histopathology, which is used for the diagnosis and study of illnesses that damage the body's tissues, requires the careful examination of tissues and/or cells using a microscope. Histopathologists provide diagnoses based on the analysis of tissue samples in order to assist other medical professionals in the treatment of patients.

Through the examination of MRI images, the machine learning approaches that are presented in this article may identify prostate cancer. Histogram equalization is used during the preprocessing stage of image creation. It results in a higher overall picture quality. The fuzzy C means algorithm is used to carry out the process of image segmentation. The method known as the Gray Level Cooccurrence Matrix is used in order to extract features. The KNN, random forest, and AdaBoost classification algorithms are used in the process of classification.

## 2. Literature Survey

In order to accomplish the findings that they did, Rampun et al. [8] used a combination of an anisotropic diffusion filter and a median filter. Due to the fact that noise and edges both produce uniform gradients, it is more challenging to remove noise from photographs that have a low signal-to-noise ratio. A noise gradient can be recognized by using a thresholding technique, but the edges of the gradient are smoothed down. Samarasinghe et al. [9] stated that the researchers carried out their work with the use of a three-dimensional sliding Gaussian filter. Because this filtering strategy is unable to eliminate the noise distribution in MPMRI photos, more complex and innovative alternative strategies have been offered as a means of addressing these kinds of problems. MPMRI images make advantage of the sparsity that is provided by the wavelet decomposition, which means that these pictures may gain benefit from the wavelet decomposition and shrinking techniques. One example of an orthogonal transformation that may be seen in action is the wavelet transform. The Rician distribution, on the other hand, maintains the unwanted noise signal even when applied to the wavelet transform domain. As a consequence of this, the wavelet and scaling coefficients have to be adjusted in part due to the distribution of noise in the data. Therefore, in order to filter out the noise in T2W photos, Lopes et al. [10] used the joint detection and estimation approach. In order to calculate the noise-free wavelet coefficient, a maximum a posteriori estimate of the noisy wavelet coefficients is used. After being normalized, each picture was adjusted such that the PZ region had a mean value of one and a standard deviation of zero. After that, the normalized MPMRI pictures were used for the purposes of instruction and evaluation within the study. As a consequence of carrying out this method, the dynamic ranges of the various MPMRI sequence intensities have been brought into alignment, which has led to an increase in the segmentation stability.

Raw images are distorted not only by noise but also by a bias field that is produced by an endorectal coil [11].

Variation in signal intensity may be attributed to the bias field, which can be detected in MRI images. As a consequence of this, the intensity of similar tissues changes greatly depending on where they are located in the image. This causes succeeding stages of the computer-aided design system to be more challenging.

Because there is a learning component involved in both the process of segmentation and the process of classification, training images are necessary. Therefore, in order to make a diagnosis that is correct and can be performed automatically, it is essential to collect signal intensity images from patients whose readings are comparable to those of one another and who are members of the same group (cancerous or noncancerous). There is still some degree of variation in the photographs that are generated, even when all of the patients are examined with the same scanner, using the same technique, and using the same settings. Viswanath et al. [12] used the piecewise linear normalization strategy to normalize T2W photos in order to eliminate the variability across patients and assure repeatability. This was done in order to normalize the images. During the course of this inquiry, piecewise linear normalizing techniques were used in order to locate and extract the original foreground.

Atlas-based segmentation is the method that is employed the most often in medical image analysis. This is due to the fact that it works better with pixel intensities and regions that are poorly defined. When analyzing prostate data obtained from MRI, Tian et al. [13] used the graph cut segmentation strategy with the superpixel notion to get their desired results. Cut-and-paste segmentation is helpful since it reduces the amount of computing and memory resources that are required. Due to the fact that it is only partially automated, the procedure has to be set up manually. Martin et al. [14] separated the prostate from the MRI using an atlas-based deformable model segmentation technique. In order to move the contour closer to the borders of the prostate, an atlas-based technique was used, and a deformable model was used, a probabilistic depiction of the location of the prostate.

A totally automated technique for segmenting the prostate in MRI images was developed by Vincent et al. in paper [15]. This method made use of an active appearance model. Through the use of a multistart optimization process, the model is meticulously matched to the test photographs.

An atlas-based matching strategy was utilized by Klein et al. [16] to automatically segment the prostate. They did this by using a nonrigid registration and comparing the target image to a large number of pre-labeled atlas photographs with hand segmentation. Following the completion of registration, the matching segmentation photographs are concatenated in order to provide an MR image segmentation of the prostate.

In order to accomplish segmentation of the prostate, deformable models make use of both internal and external energies. Internal energy is used to smooth the boundaries of the prostate, while external energy is used to propagate the shape. Chandra et al. [17] developed a method that can swiftly and automatically segment prostate images that were scanned without the use of an endorectal coil. During the

training phase of this case-specific deformable system's initialization process, a patient-specific triangulated surface and image feature system is developed. The initialization surface of the picture may be changed with the help of an image feature system by using the concept of template matching. In recent years, there has been an increase in the use of multiatlas techniques and deformable models to the process of automatic prostate segmentation.

In the research carried out by Yin et al. [18], a prostate segmentation method that is both fully automated and very reliable was used. When a normalized gradient field has been cross-correlated with the prostate, the graph-search approach is used to enhance the prostate mean shape system. This helps to better understand how the prostate develops over time. Deformable models are helpful in situations when noise or sampling irregularities are to blame for the appearance of unwanted prostate boundaries.

The simplest strategy to achieve a comprehensive response while also overcoming challenges with segmentation is to make use of a technique that involves graph cutting. For the purpose of segmenting the prostate, Mahapatra and Buhmann presented the graph cut strategy [19], which makes use of the semantic information that was collected. Random forests were used as part of a super-voxel segmentation strategy in order to provide an estimate of the volume of the prostate as well as its location. The volume of the prostate was further optimized with the help of random forest classifiers that were trained on photos and the signals from its surroundings. In order to optimize the graph cuts used for prostate segmentation, a Markov random field is used.

Puech et al. [20] created a set of rules for predicting test results by making use of the data that was obtained via medical support systems. It is feasible to categorize data by making use of similarity measures and the fundamental method of supervised machine learning known as k-nearest neighbor (k-NN). The k-means clustering technique is an unsupervised algorithm that splits the data into k-numbers of groups in an iterative manner. k is the number of iterations. Every point in the feature space is given an identifier that corresponds to the k-number of centroids that is geographically closest to it. After that step has been completed, a new mean is calculated for each cluster, and the positions of each cluster's centroid are modified so that they are consistent with the new mean. The procedure of assigning and updating centroids will continue until such time as the centroids will no longer undergo any changes. The number of classes that make up a cluster is often denoted by the letter k.

The method of classification known as linear discriminant analysis (LDA) is used in order to establish an ideal linear separation between the two classes. This results in an increase in the difference between the interclasses and a decrease in the difference between the intraclasses. The Naive Bayes classifier is the one that is used most often. It is a probabilistic kind of classification since it is based on the assumption that each dimension of the features being analyzed is independent. Using this method, it is thus feasible to classify photographs with the greatest possible posterior probability.

Another widely used approach to classification is known as adaptive boosting, or AdaBoost for short. AdaBoost is an ensemble learning technique that was created in [21]. Using this approach, many weak learners are merged to produce a single powerful classifier. The AdaBoost (AdB) classifier is superior to the random forest classifier in terms of performance. This classifier gives preference to weak learners such as decision stumps, classification trees, and regression trees. During the course of their research, Lopes et al. used an AdaBoost classifier to complete the classification procedure.

Using Gaussian processes to label classes is one way to do class labelling within the context of an approach to classification that is based on a sparse kernel. This approach is known as the kernel strategy, and it derives its name from the fact that it generates new labels by making use of the whole training dataset. In order to assign a category to an unlabeled image, sparse kernel classification algorithms rely on a restricted number of samples that have been tagged from the dataset that is used for training [22]. The support vector machine (SVM), which is an example of a sparse kernel technique, is used to select the best linear hyperplane to split up into two label classes with the largest margin of error. This is accomplished by comparing the data to determine which linear hyperplane produces the best results. Choosing the most appropriate linear hyperplane on which to categorize the data enables this goal to be realised. Support vector machines are useful classifiers in applications that take place in the real world because they are trustworthy and can be extended. This makes them helpful in applications that take place in the actual world.

### 3. Methodology

This section presents machine-learning techniques for prostate cancer detection by analyzing MRI images. Image preprocessing is done using histogram equalization. It improves image quality. Image segmentation is performed using the fuzzy C means algorithm. Features are extracted using the Gray Level Cooccurrence Matrix algorithm. Classification is performed using the KNN, random forest, and AdaBoost algorithms. Figure 1 shows the machine-learning techniques for prostate cancer detection by analyzing MRI images.

Pictures that are clearer and more detailed may be obtained from medical imaging procedures such as digital X-rays, MRIs, CT scans, and PET scans by using the basic image processing method of histogram equalization. For the purpose of determining the pathology and arriving at a diagnosis based on these pictures, high-definition photographs are required. After all of the processing is done, applying histogram equalization to the image will make any noises that were previously hidden in the picture audible again. This method is often used in the field of medical imaging analysis [23]. After determining the image's gray mapping by the use of gray operations, the approach generates a gray-level histogram that has levels of gray that are perfect, consistent, and smooth.

Clustering is a strategy that groups together patterns that are similar to one another in an effort to find the underlying

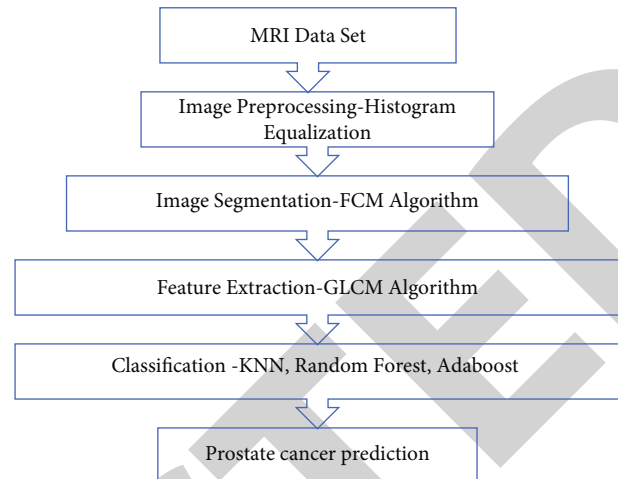


FIGURE 1: Machine-learning techniques for prostate cancer detection by analyzing MRI images.

links that exist between the pixels in a picture. This approach's goal is to uncover the underlying linkages that exist. The word "clustering" refers to the practise of grouping objects into groups based on the fundamental features they share with one another. When using the FCM approach, the data objects are sorted and categorized into groups based on the membership values that they have. During the process of maximising the function of the object, the technique of least squares is used, and the division of the final data is carried out once the computation has been completed [24].

Feature extraction is a method of image processing that may be used to lessen the amount of data stored on a computer by deleting dimensions from a collection of feature subsets that are deemed unnecessary or irrelevant. The GLCM approach is used to recover the properties of the texture and preserve a connection among the pixels. This is accomplished by calculating the cooccurrence values of the gray levels. The general linear model (GLM) is constructed by applying the conditional probability density functions  $p(i, j|d, \varphi)$  and the selected direction of  $\varphi = 0, 45, 90, \text{ or } 135$  degrees, and the distances  $d$  ranging from 1 to 5. The GLCM algorithm is used in order to accomplish this goal. For instance, the probability that two pixels with the same gray level  $I$  and/or  $j$  are spatially connected may be found by using the function  $p(i, j|d, \varphi)$ , and the distance in question is referred to as the intersample distance ( $d$ ). The GLCM places a strong emphasis on contrast, correlation, energy, entropy, and homogeneity among its many significant qualities [25].

KNN is a kind of supervised method that is used particularly for classification purposes. When using this method, the most important thing to remember is that it always produces the same results, even when using the same training data. It is possible to give a class to all of the samples or only one or two of them based on the value that is closest to it in the population. The Euclidean distance is specified in the equation that was just presented as a way to quantify how similar two-pixel places are to one another. Therefore, the

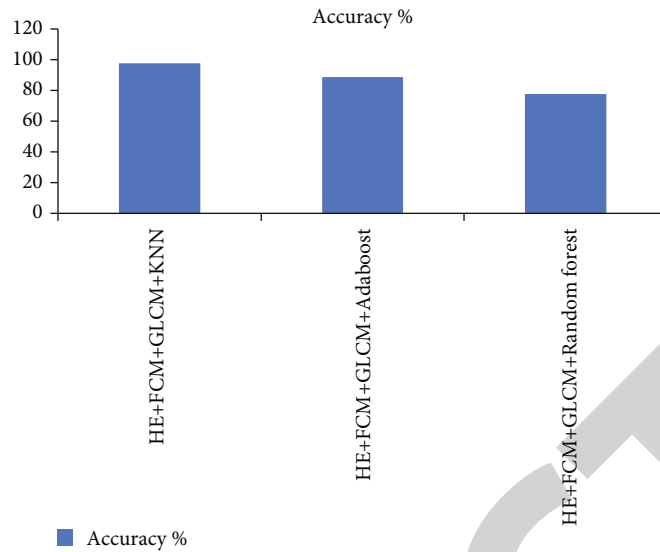


FIGURE 2: Accuracy comparison of classifiers for prostate cancer prediction.

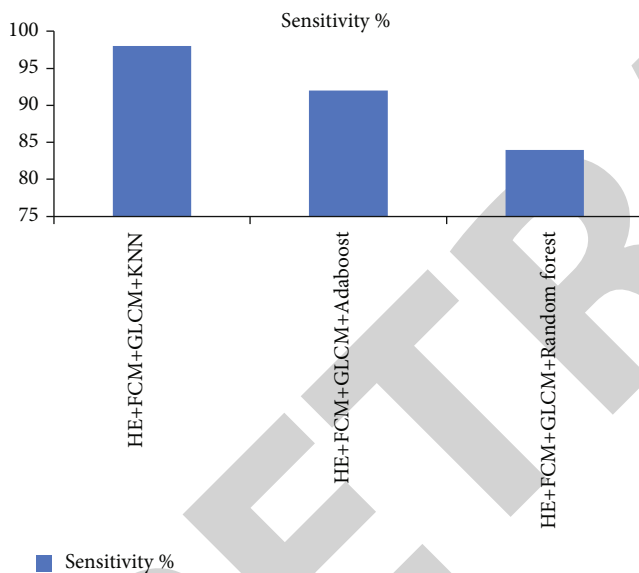


FIGURE 3: Sensitivity comparison of classifiers for prostate cancer prediction.

pixels wind up in the same group, which is where they should have been all along given the odds. In KNN, the letter K represents the neighborhood with the shortest distance between any two neighbors. The number of homes that are located close is the most essential consideration. If there are just two courses, the number of courses will almost always be an odd number. At that stage in the algorithm, the calculation known as the nearest neighbor calculation is  $K = 1$ . This is the simplest of all the conceivable scenarios to take place [26].

The model creates random forests, thus the name “random forest,” and this is precisely what it does. RF stands for “random forest.” With the help of this approach, it is possible to construct a forest of decision trees, each of which is educated in a distinct way. This method was used in the construction of the current forest of trees, which depicts all

of the feasible responses to the questions including multiple choice options. As a direct consequence of this, they were included into the calculations in order to create even more accurate estimations [27].

There is a method known as AdaBoost that may be used to classifiers that are not very effective in order to increase the accuracy with which they classify data. The algorithm AdaBoost will be used to distribute the initial weights for each observation. After a few iterations, observations that have been incorrectly categorized will be given greater weight, while observations that have been successfully classified will be given less weight. The efficacy of the classifier is significantly improved as a result of the weights on the observations being measures of the class to which the observation belongs. This helps to decrease instances of incorrect categorization. When using the strategy of “boosting,” many pupils who are struggling academically are successively fitted in an adjustable manner. In each subsequent model in the series, observations that were given insufficient weight in earlier models are given a greater amount of emphasis in that model [28].

#### 4. Result Analysis

In this experimental set up, PROMISE dataset [29] is used. 80 MRI images are used in the study. 55 images are used in training of model and 25 images are used for testing of model. Image preprocessing is done using histogram equalization. It improves image quality. Image segmentation is performed using the fuzzy C means algorithm. The Gray Level Cooccurrence Matrix technique is used in the process of feature extraction. The KNN, random forest, and AdaBoost classification algorithms are used in the classification process. Accuracy, sensitivity, and specificity are the three characteristics upon which the performance of a variety of distinct algorithms is evaluated and compared during the course of this research. Performance is shown in Figures 2–4. From the figures, it is clear that the accuracy,

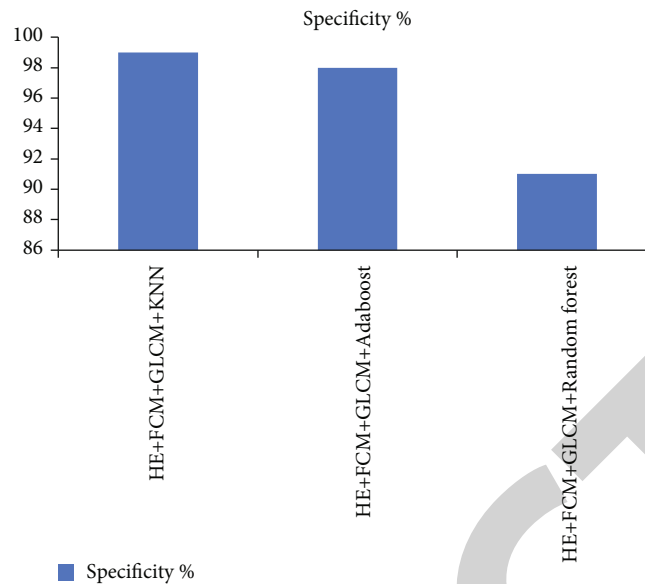


FIGURE 4: Specificity comparison of classifiers for prostate cancer prediction.

sensitivity, and specificity of KNN algorithm is better than AdaBoost decision tree and random forest algorithm. GLCM feature selection results in increasing accuracy of KNN technique.

## 5. Conclusion

Cancer is the leading cause of mortality among those over the age of 65. If a diagnosis of the patient's condition can be made as quickly as possible, it will significantly improve the patient's chances of surviving the illness. Medical imaging, much like traditional diagnosis, is analyzed by skilled specialists who search for any indicators that the body may be expressing malignant tendencies. These professionals seek for any signals that the body may be displaying cancerous tendencies. On the other hand, manual diagnosis may be time-consuming and subjective owing to the wide range of interobserver variability that is caused by the huge quantity of medical imaging data. This variability is a result of the vast amount of data that is included in medical images. Because of this, providing an appropriate diagnosis to a patient might be challenging. In order to accomplish tasks that required the use of machine learning and the processing of intricate pictures, it was necessary to make use of the most cutting-edge computer technology. Since many decades ago, efforts have been made to create a computer-aided diagnostic system with the intention of supporting medical professionals in the early diagnosis of various types of cancer. It is expected that one man in every seven will be diagnosed with prostate cancer at some point throughout their lives. An unacceptably high percentage of men are being told they have prostate cancer, and each year, this illness claims the lives of an increasing number of people. Due to the high quality and the multidimensional nature of MRI pictures, it is necessary to make use of a suitable diagnosis system in conjunction with CAD tools. I am now engaged in the process of developing a project that is based on the goals that we

have in common. Because it has been shown that the computer-aided design (CAD) technology that is already in use is beneficial, researchers are presently focusing their efforts on creating strategies to increase the accuracy, specificity, and speed of these systems. This research presents a model that is effective with regard to the processing of images, the extraction of features, and the acquisition of new skills using machine learning.

## Data Availability

The data shall be made available on request.

## Conflicts of Interest

The authors declare that they have no conflicts of interest.

## References

- [1] J. C. Vilanova, V. Catalá, F. Algaba, and O. Laucirica, Eds., *Atlas of Multiparametric Prostate MRI: With PI-RADS Approach and Anatomic-MRI-Pathological Correlation*, Springer, 2017.
- [2] A. Cameron, F. Khalvati, M. A. Haider, and A. Wong, "MAPS: a quantitative radiomics approach for prostate cancer detection," *IEEE Transactions on Biomedical Engineering*, vol. 63, no. 6, pp. 1145–1156, 2016.
- [3] V. Jasti, A. Zamani, K. Arumugam et al., "Computational technique based on machine learning and image processing for medical image analysis of breast cancer diagnosis," *Security and Communication Networks*, vol. 2022, Article ID 1918379, 7 pages, 2022.
- [4] I. A. Aljarrah, "Effect of image degradation on performance of convolutional neural networks," *International Journal of Communication Networks and Information Security (IJCNIS)*, vol. 13, no. 2, pp. 215–219, 2022.
- [5] S. Chaudhury, A. N. Krishna, S. Gupta et al., "Effective image processing and segmentation-based machine learning

## *Retraction*

# **Retracted: Lung Cancer Classification and Prediction Using Machine Learning and Image Processing**

### **BioMed Research International**

Received 8 January 2024; Accepted 8 January 2024; Published 9 January 2024

Copyright © 2024 BioMed Research International. This is an open access article distributed under the Creative Commons Attribution License, which permits unrestricted use, distribution, and reproduction in any medium, provided the original work is properly cited.

This article has been retracted by Hindawi, as publisher, following an investigation undertaken by the publisher [1]. This investigation has uncovered evidence of systematic manipulation of the publication and peer-review process. We cannot, therefore, vouch for the reliability or integrity of this article.

Please note that this notice is intended solely to alert readers that the peer-review process of this article has been compromised.

Wiley and Hindawi regret that the usual quality checks did not identify these issues before publication and have since put additional measures in place to safeguard research integrity.

We wish to credit our Research Integrity and Research Publishing teams and anonymous and named external researchers and research integrity experts for contributing to this investigation.

The corresponding author, as the representative of all authors, has been given the opportunity to register their agreement or disagreement to this retraction. We have kept a record of any response received.

### **References**

- [1] S. Nageswaran, G. Arunkumar, A. K. Bisht et al., "Lung Cancer Classification and Prediction Using Machine Learning and Image Processing," *BioMed Research International*, vol. 2022, Article ID 1755460, 8 pages, 2022.

## Research Article

# Lung Cancer Classification and Prediction Using Machine Learning and Image Processing

Sharmila Nageswaran <sup>1</sup>, G. Arunkumar <sup>2</sup>, Anil Kumar Bisht <sup>3</sup>, Shivlal Mewada <sup>4</sup>,  
J. N. V. R. Swarup Kumar <sup>5</sup>, Malik Jawarneh <sup>6</sup>, and Evans Asenso <sup>7</sup>

<sup>1</sup>Department of Sensor and Biomedical Technology, School of Electronics Engineering, Vellore Institute of Technology, Tamil Nadu, India

<sup>2</sup>Department of Computer Science and Engineering, Madanapalle Institute of Technology & Science, Madanapalle, Andhra Pradesh, India

<sup>3</sup>Department of CS&IT, MJP Rohilkhand University, Bareilly, U. P., India

<sup>4</sup>Department of Computer Science, Govt. College, Makdona (Vikram University), Ujjain, India

<sup>5</sup>Department of CSE, SR Gudlavalleru Engineering College, Gudlavalleru, India

<sup>6</sup>Faculty of Computing Sciences, Gulf College, Oman

<sup>7</sup>Department of Agricultural Engineering, University of Ghana, Ghana

Correspondence should be addressed to Evans Asenso; [easenso@ug.edu.gh](mailto:easenso@ug.edu.gh)

Received 1 June 2022; Revised 21 July 2022; Accepted 30 July 2022; Published 22 August 2022

Academic Editor: Gaganpreet Kaur

Copyright © 2022 Sharmila Nageswaran et al. This is an open access article distributed under the Creative Commons Attribution License, which permits unrestricted use, distribution, and reproduction in any medium, provided the original work is properly cited.

Lung cancer is a potentially lethal illness. Cancer detection continues to be a challenge for medical professionals. The true cause of cancer and its complete treatment have still not been discovered. Cancer that is caught early enough can be treated. Image processing methods such as noise reduction, feature extraction, identification of damaged regions, and maybe a comparison with data on the medical history of lung cancer are used to locate portions of the lung that have been impacted by cancer. This research shows an accurate classification and prediction of lung cancer using technology that is enabled by machine learning and image processing. To begin, photos need to be gathered. In the experimental investigation, 83 CT scans from 70 distinct patients were utilized as the dataset. The geometric mean filter is used during picture preprocessing. As a consequence, image quality is enhanced. The *K*-means technique is then used to segment the images. The part of the image may be found using this segmentation. Then, classification methods using machine learning are used. For the classification, ANN, KNN, and RF are some of the machine learning techniques that were used. It is found that the ANN model is producing more accurate results for predicting lung cancer.

## 1. Introduction

One of the most lethal types of the disease, lung cancer, is responsible for the passing away of about one million people every year. The current state of affairs in the world of medicine makes it absolutely essential to perform lung nodule identification on chest CT scans. This is due to the fact that lung nodules are becoming increasingly common. As a direct result of this, the deployment of CAD systems is required in order to accomplish the objective of early lung cancer identification [1].

When doing a CT scan, sophisticated X-ray equipment is utilized in order to capture images of the human body from a number of different angles. Following this, the images are fed into a computer, which processes them in such a way as to produce a cross-sectional view of the internal organs and tissues of the body [2].

A CAD approach was trained and assessed in two separate experiments. One research used a computer simulation using ground truth that was generated by computers. In this work, the cardiac-torso (XCAT) digital phantom was used to replicate 300 CT scans. The second research made use of

patient-based ground truth using human subjects and implanted spherical nodules of varied sizes (i.e., 3-10 mm in diameter) at random inside the lung area of the simulated pictures. CT images from the LIDC-IDRI dataset were used to create the CAD technique. 888 CT pictures left for processing after CT scans with a wall thickness of more than 2.5 mm were disregarded. In all investigations, a 10-fold cross-validation approach was used to assess network hyperparameterization and generalization. The detection sensitivities were measured in response to the average false positives (FPs) per picture to assess the overall accuracy of the CAD approach. Using the free-receiver response operating characteristic (FROC) curve, the detection accuracy in the patient research was further evaluated in 9 previously published CAD investigations. The mean and standard error between the anticipated value and ground truth were used to measure the localization and diameter estimate accuracies. In all investigations, the average outcomes throughout the 10 cross-validation folds showed that the CAD approach had a high level of detection accuracy. In the patient trial, the corresponding sensitivities were 90.0 percent and 95.4 percent, showing superiority in the FROC curve analysis over many traditional and CNN-based lung nodule CAD approaches. In both investigations, the nodule localization and diameter estimation errors were fewer than 1 mm. The CAD approach that was created was highly efficient in terms of computing [3].

It is likely that intravenous injection of contrast (X-ray dye) may considerably improve the quality of CT imaging, which can reveal a wide variety of organs and tissues. This is one of the potential benefits of contrast injection. In addition, CT scans can reliably detect kidney or gallstones, as well as abnormal fluid buildup or enlarged lymph nodes in the abdominal region or pelvis. This is in addition to the capacity to detect gallstones and kidney stones. Because the CT scan is unable to provide a precise diagnosis of certain organs, such as the stomach, it can, however, be used to reveal abnormalities in the soft tissues that are positioned nearby, offering an indirect diagnosis of these organs [4, 5].

If lung cancer is detected at an early stage, the American Cancer Society estimates that a patient has a 47 percent chance of surviving the disease. It is quite unlikely that X-ray pictures may accidentally reveal lung cancer in its earlier stages [6]. It is famously difficult to detect lesions that are round and have a diameter of 510 millimeters or less. A CT scan of a patient diagnosed with lung cancer is shown in Figure 1.

The processing of images is an essential activity for a diverse variety of business sectors. It is utilized in X-ray imaging of the lungs in order to find regions that contain cancerous growths. In order to detect areas of the lung that have been affected by cancer, image processing techniques such as noise reduction, feature extraction, identification of damaged regions, and maybe a comparison with data on the medical history of lung cancer are utilized. The majority of the time, digital image processing makes use of a diverse set of methods to merge a number of distinct aspects of a picture into a single coherent entity. This research takes an innovative technique in order to zero down on a particular



FIGURE 1: CT scan image for lung cancer.

aspect of the overall lung image. The split region may be seen in a variety of ways, including from different viewpoints and when illuminated in different ways. When utilizing this method, one of the key benefits is the ability to differentiate between portions of a picture that have been impacted by cancer and sections that have not been affected by cancer by comparing the intensity of the two sets of photos [6, 7].

As a result of the fact that the majority of patients are diagnosed at a more advanced stage, lung cancer is the primary cause of death resulting from cancer. There is currently no chance of a successful treatment being developed. Lung cancer is consistently ranked as one of the most lethal forms of the disease, regardless of whether a country is industrialized or developing. The incidence of lung cancer in developing countries is on the rise as a result of a longer life expectancy, more urbanization, and the adoption of Western lifestyles. The early detection of cancer and the survival of people with the disease are both essential to the control of lung disease [8, 9].

The literature survey section contains a review of various techniques for the classification and detection of cancer using image processing and classification. The methodology section presents accurate classification and prediction of lung cancer using machine learning and image processing-enabled technology. First, images are acquired. Then, images are preprocessed using the geometric mean filter. This results in improving image quality. Then, images are segmented using the *K*-means algorithm. This segmentation helps in the identification of the region of interest. Then, machine learning classification techniques are applied. The result section contains details related to the dataset and results achieved by various techniques.

To reduce the amount of data that has to be broken down, this study illustrates a method to separate the lung tissue from a chest CT. We will likely have a fully automated computation for cutting the lung tissue into sections and for separating the two sides of the lung as well. The threshold shown in the image separates fat from low-thickness tissue (the lungs). Cleaning is done to get rid of the commotion, air, and flight routes. Finally, a combination of morphological operations is used to tame the unexpected limit. The database used for the evaluation was obtained from a book that instructs radiologists. The



current analysis shows that the linked division computation attempts to handle a wide range of different circumstances. The portioned lungs' textural accents were taken off, and it was provided. The neurological system is used to differentiate between the various lung diseases [10].

*1.1. Literature Survey.* Palani and Venkatalakshmi [11] have given predictive modeling of lung cancer illness by continuous monitoring. They did this by using fuzzy cluster-linked augmentation with a categorization. The fuzzy clustering approach is essential to the production of accurate picture segmentation. We instead utilized the fuzzy *C*-means clustering approach in order to accomplish our goal of further disentangling the characteristics of the transitional area from those of the lung cancer image. In this particular investigation, the Otsu thresholding method was applied in order to distinguish the transition area from the lung cancer representation. In addition to this, the right edge picture is utilized in conjunction with the morphological, thinning procedure in order to improve the presentation of the segmentation. The current Association Rule Mining (ARM), the conventional decision tree (DT), and the CNN are combined with a novel incremental classification technique in order to accomplish classification in an incremental fashion. In order to carry out the operations, standard images from the database were utilized, as well as the most recent data on the patient's health collected from IoT devices that were attached to the patient. The culmination of the research indicates that the predictive modeling system has become more accurate.

Deep residual learning was utilized by Bhatia et al. in order to develop a method for determining whether or not a CT picture contains lung cancer. The researchers have devised a preprocessing pipeline by making use of the UNet and ResNet models. This pipeline is intended to highlight and extract features from sections of the lung that are cancerous. An ensemble of XGBoost and random forest classifiers is used to gather predictions about the likelihood that a CT scan is malignant. The results of each classifier's predictions are then pooled, and the final result is used to determine the likelihood that a CT scan is malignant. The LIDC-IRDI has an accuracy that is 84 percent higher than that of typical techniques [12].

Joon et al. [13] segmented lung cancer using an active spline model as their method of analysis. With X-ray photos, through the use of this technique, X-ray images of the lung have been obtained. To begin, it is recommended that a median filter be used for noise detection while the preprocessing stage is being carried out. During the phase devoted to segmentation, further *K*-means and fuzzy *C*-means clustering are utilized for the purpose of feature capture. In this research, the ultimate feature retrieval outcome is reached after the X-ray picture has been segmented. The recommended model was developed by the application of the SVM approach for classification. In order to simulate the findings of the cancer detection system, MATLAB is utilized. The purpose of this study was to detect and categorize lung cancer by making use of images that were both normal and malignant.

Nithila and Kumar [14] have developed an active contouring model, and this model has been deployed. An application of a variation level set function was used for the segmentation of the lungs. It is essential to properly segment the parenchyma in order to arrive at an appropriate diagnosis of lung illness. CT, which stands for computerized tomography, was the first imaging modality to make use of image analysis in this manner. A significant advancement in CT lung image segmentation has been made by the development of the SBGF-new SPF function, which stands for selective binary and Gaussian filtering-new signed pressure force. By taking this strategy, external lung limitations have been identified, and inefficient expansion at the margins has been prevented. Comparisons are being made between the currently under consideration algorithm and four distinct active contour models. The results of the tests demonstrate that the strategy that was provided is reliable and can be computed very quickly [13].

Lakshmanaprabu et al. [15] created OODN (Optimal Deep Neural Network) by lowering the number of characteristics in lung CT scans and comparing it to other classification algorithms. This allowed them to design a more accurate method. The adoption of an automated classification method for lung cancer has cut down on the amount of time needed for human labeling and removed the possibility of mistakes being made by the individual doing the labeling. According to the findings of the researchers, the performance of the machine learning algorithms in terms of accuracy and precision in the detection of normal and abnormal lung photos has significantly increased. According to the findings, the research was successful in classifying lung pictures with a peer specificity of 94.56 percent, a level of accuracy of 96.2 percent, and a level of sensitivity of 94.2 percent. It has been shown that it is feasible to increase the performance of cancer detection in CAT scans [14]. The research has shown that this is the case.

Talukdar and Sarma have placed a strong emphasis on the use of image processing methods for the diagnosis of lung cancer (2018). Deep learning methodologies are being applied to the study of lung cancer. The most prevalent kind of cancer, lung cancer, is taking the lives of an alarmingly high number of individuals. The likelihood of an individual acquiring lung cancer was evaluated with a computed tomography (CT) scan. The growth of precancerous tissue is referred to as "nodules," and their presence is utilized as a general indication of cancer. Educated radiologists are able to detect nodules and often predict their relationship with cancer. However, these radiologists are also capable of producing false positive and false negative findings. Because the patient is under continual stress, a tremendous quantity of data is evaluated, and a decision that is suitable for the patient is made in a timely manner. As a consequence of this, developing a computer-aided detection system that is capable of rapidly detecting features based on the input of radiologists is most likely to be the answer [15].

Yu et al. have obtained histopathology whole-slide slides of lung cancer and squamous cell carcinoma that have been stained with hematoxylin and eosin (2016). Patients' photographs were taken from TCGA (The Cancer Genome Atlas)

and the Stanford TMA (Tissue Microarray Database), plus an additional 294 photos. Even when conducted with the greatest of intentions, an assessment of human pathology cannot properly predict the patient's prognosis. A total of 9,879 quantitative elements of an image were retrieved, and machine learning algorithms were used to select the most important aspects and differentiate between patients who survived for a short period of time and those who survived for a long period of time after being diagnosed with stage I adenocarcinoma or squamous cell carcinoma. The researchers used the TMA cohort to validate the survival rate of the recommended framework (P0.036 for tumor type). According to the findings of this study, the characteristics that are created automatically may be able to forecast the prognosis of a lung cancer patient and, as a consequence, may help in the development of personalized medication. The methodologies that were outlined can be utilized in the analysis of histopathology images of various organs [16].

Pol Cirueda and his colleagues used an aggregation of textures that kept the spatial covariances across features consistent. Mixing the local responses of texture operator pairs is done using traditional aggregation functions like the average; nonetheless, doing so is a vital step in avoiding the problems of traditional aggregation. Pretreatment computed tomography (CT) scans were utilized in order to assist in the prediction of NSCLC nodule recurrence prior to the administration of medication. After that, the recommended methods were put to use in order to compute the kind of NSCLC nodule recurrence according to the manifold regularized sparse classifier. These discoveries, which offer up new study possibilities on how to use morphological, tissue traits to evaluate cancer invasion, need to be confirmed and investigated further. However, this will not be possible without more research. When modeling orthogonal information, the author focused on the textural characteristics of nodular tissue and coupled those characteristics with other variables such as the size and shape of the tumor [17].

The creation of a method for the early detection and accurate diagnosis of lung cancer that makes use of CT, PET, and X-ray images by Manasee Kurkure and Anuradha Thakare in 2016 has garnered a significant amount of attention and enthusiasm. The utilization of a genetic algorithm that permits the early identification of lung cancer nodules by diagnostics allows for the optimization of the findings to be accomplished. It was necessary to employ both Naive Bayes and a genetic algorithm in order to properly and swiftly classify the various stages of cancer images. This was done in order to circumvent the intricacy of the generation process. The categorization has an accuracy rate of up to eighty percent [18].

Sangamithraa and Govindaraju [19] have used a preprocessing strategy in order to eliminate the unwanted unaffected by the use of median and Wiener filters. This was done in order to improve the quality of the data. The  $K$ -means method is used to do the segmentation of the CT images. EK-mean clustering is the method that is used to achieve clustering. To extract contrast, homogeneity, area, correlation, and entropy features from images, fuzzy EK-

mean segmentation is utilized. A back propagation neural network is utilized in order to accomplish the classification [20].

According to Ashwini Kumar Saini et al. (2016), a summary of the types of noise that might cause lung cancer and the strategies for removing them has been provided. Due to the fact that lung cancer is considered to be one of the most life-threatening kinds of cancer, it is essential that it be detected in its earlier stages. If the cancer has a high incidence and mortality rate, this is another indication that it is a particularly dangerous form of the disease. The quality of the digital dental X-ray image analysis must be significantly improved for the study to be successful. A pathology diagnosis in a clinic continues to be the gold standard for detecting lung cancer, despite the fact that one of the primary focuses of research right now is on finding ways to reduce the amount of image noise. X-rays of the chest, cytological examinations of sputum samples, optical fiber investigations of the bronchial airways, and final CT and MRI scans are the diagnostic tools that are utilized most frequently in the detection of lung malignancies (MRI). Despite the availability of screening methods like CT and MRI that are more sensitive and accurate in many parts of the world, chest radiography continues to be the primary and most prevalent kind of surgical treatment. It is routine practice to test for lung cancer in its early stages using chest X-rays and CT scans; however, there are problems associated with the scans' weak sensitivities and specificities [19].

Neural ensemble-based detection is the name given to the automated method of illness diagnosis that was suggested in Kureshi et al.'s research [21] (NED). The approach that was suggested utilized feature extraction, classification, and diagnosis as its three main components. In this experiment, the X-ray chest films that were taken at Bayi Hospital were utilized. This method is recommended because it has a high identification rate for needle biopsies in addition to a decreased number of false negative identifications. As a result, the accuracy is improved automatically, and lives are saved [22].

Kulkarni and Panditrao [23] have created a novel algorithm for early-stage cancer identification that is more accurate than previous methods. The program makes use of a technology that processes images. The amount of time that passes is one of the factors that is considered while looking for anomalies in the target photographs. The position of the tumor can be seen quite clearly in the original photo. In order to get improved outcomes, the techniques of watershed segmentation and Gabor filtering are utilized at the preprocessing stage. The extracted interest zone produces three phases that are helpful in recognizing the various stages of lung cancer: eccentricity, area, and perimeter. These phases may be found in the extracted interest zone. It has been revealed that the tumors come in a variety of dimensions. The proposed method is capable of providing precise measurements of the size of the tumor at an early stage [21].

Westaway et al. [24] used a radiomic approach to identify three-dimensional properties from photos of lung cancer in order to provide prediction information. As is well

known, classifiers are devised to estimate the length of time an organism will be able to continue existing. The Moffitt Cancer Center in Tampa, Florida, served as the location from where these photographs for the experiment's CT scans were obtained. Based on the properties of the pictures produced by CT scans, which may suggest phenotypes, human analysis may be able to generate more accurate predictions. When a decision tree was used to make the survival predictions, it was possible to accurately forecast seventy-five percent [23] of the outcomes.

CT (computed tomography) images of lung cancer have been categorized with the use of a lung cancer detection method that makes use of image processing. This method was described by Chaudhary and Singh [25]. Several other approaches, including segmentation, preprocessing, and the extraction of features, have been investigated thus far. The authors have distinguished segmentation, augmentation, and feature extraction, each in its own unique section. In Stages I, II, and III, the cancer is contained inside the chest and manifests as larger, more invasive tumors. By Stage IV, however, cancer has spread to other parts of the body [24], at which point it is said to be in Stage IV.

## 2. Methodology

This section shows an accurate classification and prediction of lung cancer using technology that is enabled by machine learning and image processing. To begin, photos need to be gathered. After that, a geometric mean filter is used to perform preprocessing on the images. This ultimately leads to an improvement in image quality. After that, the  $K$ -means method is used to segment the images. The identification of the region of interest is facilitated by this segmentation. After that, categorization strategies based on machine learning are utilized. Figure 2 illustrates the classification and prediction of lung cancer utilizing technology that enables machine learning and image processing.

The preprocessing of images plays a significant role in the proper classification of photographs of illnesses. CT scans provide images with a broad variety of artefacts, including noise, which may be seen in these scans. These artefacts may be removed by using image filtering methods. A geometric mean filter is applied to the input pictures in an effort to decrease the amount of noise [25].

This is accomplished by using a method known as linear discriminant analysis (LDA), which cuts down on the amount of space required for the initial data matrix. The PCA and LDA are two examples of parallel transformation algorithms. In contrast to the supervised LDA method, the PCA is an unsupervised analysis method. In contrast to principal component analysis (PCA), latent dynamic analysis (LDA) seeks to identify a feature subspace that maximizes the possibility of class restoration. It is possible to avoid overfitting by placing more importance on the class-reparability of the data rather than the processing costs [26].

The method of segmentation is used in the process of medical image processing. The basic role of a picture is to differentiate between components that are beneficial and those that are harmful. As a consequence of this, it separates

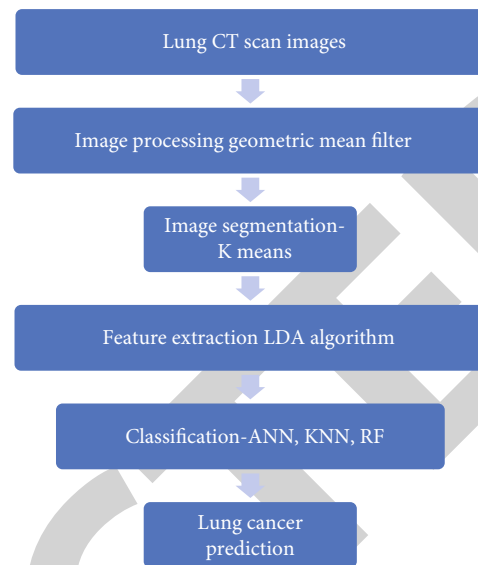


FIGURE 2: Classification and prediction of lung cancer using machine learning and image processing-enabled technology.

a picture into distinct pieces based on the degree to which each component is similar to its surrounding components. This effect may be achieved by manipulating the intensity as well as the texture. An area of interest that has been segmented may be utilized as a diagnostic tool to quickly get information that is pertinent to the issue at hand. When it comes to the process of segmenting medical pictures, the technique known as  $K$ -means clustering is the one that is used most often. During the clustering process, the picture is divided into a number of different groups, also known as clusters, which do not overlap with one another. These clusters are not connected to one another in any way. In this picture, there are a few distinct clusters that can be noticed. Every one of them has its own one-of-a-kind collection of reference points to which each pixel is assigned. To divide the available data into  $k$  separate groups, the  $K$ -means clustering algorithm divides the available information based on  $k$  reference points [27].

Artificial neural networks, also known as ANNs, are used often in the medical industry for the purpose of classifying medical images for the goal of diagnosing illness. In terms of the way it performs its tasks, the ANN is fairly comparable to the human brain. It is feasible to get the knowledge required to make an informed guess about the category that a photograph belongs to by looking at a collection of images that have already been categorized. This may be accomplished by looking at a collection of pictures that have been categorized. A category has already been selected for each of the pictures included in this gallery. An artificial neural network (ANN) is constructed up of artificial neurons, which are programmed to behave in a manner that is analogous to that of their biological counterparts in the human brain. Neurons are able to communicate with one another outside of their bodies through connections. It is possible to assign weights to neurons and edges, and those weights may be changed at any time throughout the process of learning.

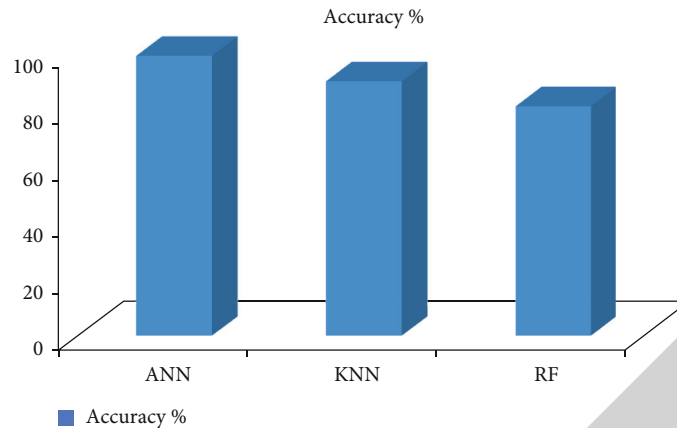


FIGURE 3: Accuracy of machine learning techniques for lung cancer detection.

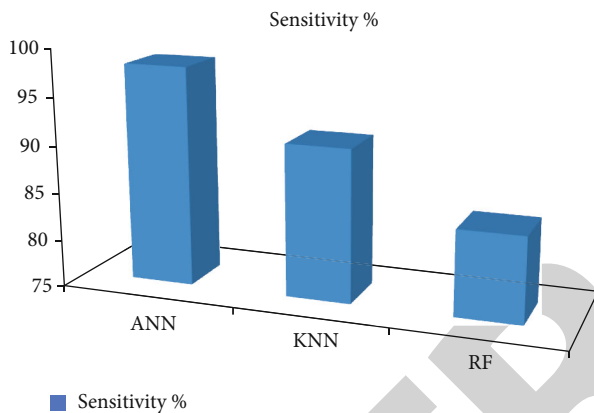


FIGURE 4: Sensitivity of machine learning techniques for lung cancer detection.

The standard structure of an artificial neural network has three layers: an input layer, a hidden layer, and an output layer that is in charge of creating the signal. This is the architecture that is used the most often. The most popular topologies for artificial neural networks include an input layer, a hidden layer, and a final layer; however, there are other possible configurations as well. It is conceivable that there is just one hidden layer, that there are several hidden levels, or that there are no hidden layers at all. Each and every one of these options is not completely out of the question. The weights that need to be adjusted until the desired output is reached are tucked away in a layer that is below the active layer [28]. The iterations are closely related to computing efficiency during the training of the ANN model. Precision will suffer by having too few hidden layer neurons, while too many neurons would lengthen training time.

The KNN approach, which is the method that is used in ML the most commonly, makes it easy to learn about the algorithms that are employed in ML. It is a technique of supervised learning that does not need the use of any parameters. The phase that the  $k$ -training NN goes through is thus significantly quicker than the phase that other classifiers go through. The testing stage, on the other hand, takes longer

and uses more memory as it goes on. In order to use  $k$ -nearest neighbors to categorize new kinds of data points, one needs first to have data that is already organized into many different categories. Because training observations are included in each labeled dataset, the algorithm is able to establish a connection between  $x$  and  $y$  in each training dataset  $(x, y)$ . The typical practice at this location is delaying the processing in order to locate the KNN function. The contributions of neighbors may be weighted in classification models as well as regression models, which can result in a higher average score for those who live in close proximity to one another in comparison to those who live farther away. As the distance between two neighbors increases, an additional weighting of  $1/d$  is applied to each neighbor [29]. Despite producing good precision on the test dataset, KNN is still slower and more expensive to run in terms of both time and memory. To store the whole training dataset for prediction, it needs a lot of memory. Additionally, as Euclidean distance is very reactive to orders of magnitude, features in the dataset with high magnitudes always have a higher weight than those with low magnitudes. Last but not least, we must remember that KNN is not appropriate for large-dimensional datasets.

It is possible to construct predictive models by using the random forest approach, which is used by a lot of people. Only two of the many applications that may be accomplished using RF are regression and classification [30]. It is possible to develop machine learning algorithms that are capable of making predictions with a high degree of accuracy so long as datasets are changed appropriately [31]. This approach is highly user-friendly in comparison to other algorithms, and it has a lot of support from members of the general public. For the purposes of this model, RF is an abbreviation for “random forest,” and true to its moniker, the model creates random forests. With the help of this technique, one may generate an entire grove of decision trees, each of which is trained in a distinct way. This method was used to build the current thicket of trees representing the many possible multiple-choice responses. As a direct consequence of this, they were integrated in order to provide even more accurate projections [22].

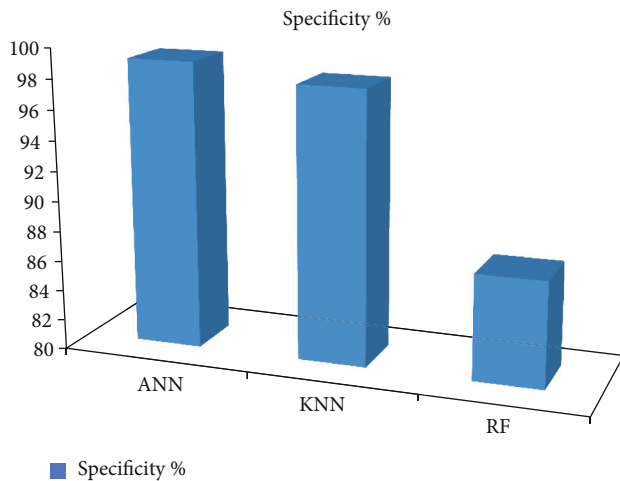


FIGURE 5: Specificity of machine learning techniques for lung cancer detection.

### 3. Result Analysis

A dataset of 83 CT images from 70 different patients was used in the experimental study [x]. Images are preprocessed using the geometric mean filter. This results in improving image quality. Then, images are segmented using the K-means algorithm. This segmentation helps in the identification of the region of interest. Then, machine learning classification techniques are applied.

For performance comparison, three parameters, accuracy, sensitivity, and specificity, are used:

$$\begin{aligned} \text{Accuracy} &= \frac{TP + TN}{TP + TN + FP + FN}, \\ \text{Sensitivity} &= \frac{TP}{TP + FN}, \\ \text{Specificity} &= \frac{TN}{TN + FP}, \end{aligned} \quad (1)$$

where TP is true positive, TN is true negative, FP is false positive, and FN is false negative.

Results of different machine learning predictors are shown in Figures 3–5. The accuracy of ANN is better.

### 4. Conclusion

Lung cancer is one of the deadliest types of the disease, claiming the lives of approximately one million people each year. Given the current state of affairs in medicine, it is critical that lung nodule identification be performed on chest CT scans. As a result, the use of CAD systems is crucial for the early detection of lung cancer. Image processing is a necessary activity that is employed in a wide range of economic domains. It is used in X-ray imaging of the lungs to find areas of the body that have developed malignant growths. Image processing techniques such as noise reduction, feature extraction, identification of damaged regions, and maybe comparison with data on the medical history of

lung cancer are used to locate sections of the lung that have been affected by cancer. This study demonstrates accurate lung cancer classification and prediction using technologies enabled by machine learning and image processing. To begin, photographs must be collected. Following that, the images are preprocessed using a geometric mean filter. This eventually leads to an increase in image quality. The K-means approach is then used to segment the images. This segmentation makes it easier to identify the region of interest. Following that, machine learning-based categorization algorithms are used. ANN predicts lung cancer with more accuracy. This research will help to increase the accuracy of lung cancer detection systems that use strong classification and prediction techniques. This study brings cutting-edge images based on machine learning techniques for implementation purposes.

### Data Availability

The data shall be made available on request.

### Conflicts of Interest

The authors declare that they have no conflict of interest.

### References

- [1] S. Ahmed Medjahed, T. AitSaadi, A. Benyettou, and M. Ouali, "Kernel-based learning and feature selection analysis for cancer diagnosis," *Applied Soft Computing*, vol. 51, pp. 39–48, 2017.
- [2] N. Deepa, B. Prabadevi, P. K. Maddikunta et al., "An AI-based intelligent system for healthcare analysis using Ridge-Adaline Stochastic Gradient Descent Classifier," *The Journal of Supercomputing*, vol. 77, no. 2, pp. 1998–2017, 2021.
- [3] C. Liu, S. C. Hu, C. Wang, K. Lafata, and F. F. Yin, "Automatic detection of pulmonary nodules on CT images with YOLOv3: development and evaluation using simulated and patient data," *Quantitative Imaging in Medicine and Surgery*, vol. 10, no. 10, pp. 1917–1929, 2020.
- [4] V. Jasti, A. S. Zamani, K. Arumugam et al., "Computational technique based on machine learning and image processing for medical image analysis of breast cancer diagnosis," *Security and communication networks*, vol. 2022, Article ID 1918379, 7 pages, 2022.
- [5] B. De Potter, J. Huyskens, B. Hiddinga et al., "Imaging of Urgencies and Emergencies in the Lung Cancer Patient," *Insights into imaging*, vol. 9, no. 4, pp. 463–476, 2018.
- [6] S. Chaudhury, A. N. Krishna, S. Gupta et al., "Effective image processing and segmentation-based machine learning techniques for diagnosis of breast cancer," *Computational and Mathematical Methods in Medicine*, vol. 2022, Article ID 6841334, 6 pages, 2022.
- [7] J. Li, Y. Wang, X. Song, and H. Xiao, "Adaptive multinomial regression with overlapping groups for multi-class classification of lung cancer," *Computers in Biology and Medicine*, vol. 100, pp. 1–9, 2018.
- [8] A. Halder and A. Kumar, "Active learning using Fuzzy-Rough Nearest Neighbor classifier for cancer prediction from microarray gene expression data," *Journal of Biomedical Informatics*, vol. 34, no. 1, p. 2057001, 2020.

## Retraction

# Retracted: Multidimensional CNN-Based Deep Segmentation Method for Tumor Identification

### BioMed Research International

Received 8 January 2024; Accepted 8 January 2024; Published 9 January 2024

Copyright © 2024 BioMed Research International. This is an open access article distributed under the Creative Commons Attribution License, which permits unrestricted use, distribution, and reproduction in any medium, provided the original work is properly cited.

This article has been retracted by Hindawi following an investigation undertaken by the publisher [1]. This investigation has uncovered evidence of one or more of the following indicators of systematic manipulation of the publication process:

- (1) Discrepancies in scope
- (2) Discrepancies in the description of the research reported
- (3) Discrepancies between the availability of data and the research described
- (4) Inappropriate citations
- (5) Incoherent, meaningless and/or irrelevant content included in the article
- (6) Manipulated or compromised peer review

The presence of these indicators undermines our confidence in the integrity of the article's content and we cannot, therefore, vouch for its reliability. Please note that this notice is intended solely to alert readers that the content of this article is unreliable. We have not investigated whether authors were aware of or involved in the systematic manipulation of the publication process.

Wiley and Hindawi regrets that the usual quality checks did not identify these issues before publication and have since put additional measures in place to safeguard research integrity.

We wish to credit our own Research Integrity and Research Publishing teams and anonymous and named external researchers and research integrity experts for contributing to this investigation.

The corresponding author, as the representative of all authors, has been given the opportunity to register their agreement or disagreement to this retraction. We have kept a record of any response received.

### References

- [1] R. J. Martin, U. Sharma, K. Kaur, N. M. Kadhim, M. Lamin, and C. S. Ayipeh, "Multidimensional CNN-Based Deep Segmentation Method for Tumor Identification," *BioMed Research International*, vol. 2022, Article ID 5061112, 11 pages, 2022.

## Research Article

# Multidimensional CNN-Based Deep Segmentation Method for Tumor Identification

**R. John Martin** <sup>1</sup>, **Uttam Sharma** <sup>2</sup>, **Kiranjeet Kaur** <sup>3</sup>, **Noor Mohammed Kadhim** <sup>4</sup>,  
**Madonna Lamin** <sup>5</sup> and **Collins Sam Ayipeh** <sup>6</sup>

<sup>1</sup>Faculty of Computer Science and Information Technology, Jazan University, Saudi Arabia

<sup>2</sup>Department of Computer Science and Engineering, Gautam Buddha University, Greater Noida, India

<sup>3</sup>Department of CSE, University Centre for Research & Development, Chandigarh University, Mohali, Punjab 140413, India

<sup>4</sup>Department of Medical Instruments Engineering Techniques, Al-Farahidi University, Baghdad 10021, Iraq

<sup>5</sup>Computer Science and Engineering, ITM SLS Baroda University, Vadodara, 391510 Gujarat, India

<sup>6</sup>Kwame Nkrumah University of Science and Technology, Kumasi, Ghana

Correspondence should be addressed to Collins Sam Ayipeh; [csayipeh@st.knust.edu.gh](mailto:csayipeh@st.knust.edu.gh)

Received 13 June 2022; Revised 18 July 2022; Accepted 23 July 2022; Published 21 August 2022

Academic Editor: Gaganpreet Kaur

Copyright © 2022 R. John Martin et al. This is an open access article distributed under the Creative Commons Attribution License, which permits unrestricted use, distribution, and reproduction in any medium, provided the original work is properly cited.

Weighted MR images of 421 patients with nasopharyngeal cancer were obtained at the head and neck level, and the tumors in the images were assessed by two expert doctors. 346 patients' multimodal pictures and labels served as training sets, whereas the remaining 75 patients' multimodal images and labels served as independent test sets. Convolutional neural network (CNN) for modal multidimensional information fusion and multimodal multidimensional information fusion (MMMDF) was used. The three models' performance is compared, and the findings reveal that the multimodal multidimensional fusion model performs best, while the two-modal multidimensional information fusion model performs second. The single-modal multidimensional information fusion model has the poorest performance. In MR images of nasopharyngeal cancer, a convolutional network can precisely and efficiently segment tumors.

## 1. Introduction

Nasopharyngeal carcinoma (NPC) is the most common malignant tumor in the human nasopharynx. According to the World Health Organization report, about 80% of NPC patients worldwide are concentrated in China, and most of the remaining patients are found in Southeast Asia and the Middle East and North Africa [1, 2]. According to statistics, the incidence of NPC in Guangzhou is 17.8 per 100,000 people, the incidence rate is rising, and the incidence is younger [3]. However, most patients have missed the most. Therefore, the early diagnosis of NPC is essential to seize the best time for treatment. At present, the treatment of NPC is mainly radiotherapy, and the accurate localization of NPC lesions is a crucial basis for the formulation of radiotherapy plans and implementation of radiotherapy. In radiation

therapy, high-energy X-rays are utilized to destroy cancer cells. A schedule for radiation therapy normally consists of a certain number of sessions spaced out over a defined period of time. The most common form of external beam radiation therapy used to treat NPC sends radiation from a machine outside the body directly at the tumor. With the reduced risk to healthy cells and fewer side effects, intensity-modulated radiation therapy, a kind of external beam radiation therapy, makes it possible to administer larger radiation therapy doses. The ASCO suggests intensity-modulated radiation therapy for all patients with stage II to stage IVA NPC.

NPC segmentation is a difficult procedure since the morphological structure of the nasopharyngeal region is convoluted, the severity of the tumor is equivalent to that of neighboring tissues, and the morphology of the tumor

varies greatly across individuals. Traditional manual tumor contour segmentation, a crucial step in radiotherapy, has become labor- and time-intensive due to the enormous amount of data produced by several patients. As a result, there is an increasing need for automated segmentation algorithms that are trustworthy in order to lighten the workload of radiologists. MR images are often used in diagnosing and localization of NPC due to their high resolution and strong safety. Before making a treatment plan, clinicians usually need to examine each MR image. Whether there is a lesion in the image and manually outline the tumor boundary, due to the complex and changeable shape, size, and location of the tumor between different NPC patients, this process has disadvantages such as heavy workload, high requirements for doctors' experience, and significant subjective influence. Therefore, researchers have sought to delineate the NPC lesion area automatically. The cancer care team will suggest a treatment plan based on the kind, severity, and extent of the nasopharynx cancer as well as its stage and rate of spread. The conventional therapy for these early-stage cancers is radiation therapy focused on the tumor. Although radiotherapy is frequently used to treat the neck's surrounding lymph nodes, cancer has not yet spread to the lymph nodes at this time. Stages II, III, IVA, and IVB patients with varying stages of NPC typically get chemotherapy to the nasopharynx and neck lymph nodes. In addition to the targeted drug cetuximab, chemotherapy is frequently used to treat patients with stage IVC (Erbixitux). Another alternative is immunotherapy.

Traditional image segmentation approaches, such as the threshold method, area growth method, and statistical theory [4, 5], as well as machine learning methods, such as support vector machines and artificial neural networks [6, 7], are used to segment NPC tumors. The threshold is a well-liked method of segmenting images. It aids in separating the backdrop from the foreground. By selecting the proper threshold value  $T$ , the grey level photograph may be converted into a binary image. The binary image should fully expose the elements of interest's orientation and structure (foreground). Getting a binary image from the outset has the advantage of reducing complexity and simplifying the identification and verification procedures.

Deep learning is a crucial diagnostic technology that produces accurate findings by using an organized network with homogeneous portions. Utilizing statistical model automatic segmentation approaches in several essential scenarios, its excellent quality has been shown. Performance measurements demonstrate that deep learning algorithms are significantly more successful at segmenting pictures than a statistical method. For a number of diverse medical image segmentation tasks, the deep learning approach is applied with the highest level of accuracy. The process of segmenting pictures will need the development and comparison of a number of deep learning algorithms in the future.

The SVM model can function by choosing an appropriate margin or hyperplane when there are values in the characteristics of two groups that tend to group around distinct values, such as predicting values associated with a tumor grade or categorizing various tissues with varied attenuation

and textures exhibited. Support vector machines have been used successfully to solve problems with image segmentation and classification. Early image segmentation algorithms were built on digital image processing and optimization approaches.

With the help of methods like region growth and the snake's algorithm, which included creating beginning regions, these early algorithms compared pixel values to get an understanding of the segment map. These methods took a localized view of an image's characteristics by focusing on local gradients and pixel differences. Edge detection, Otsu's algorithm, and clustering algorithms were developed somewhat later among the common image processing techniques. These algorithms viewed the input image from a broad perspective. Such ideas almost always need the inclusion of features. Manual intervention procedures like extraction and dimensionality reduction have drawbacks like model robustness and noise sensitivity. Less time and storage space are required with dimensional reduction. It helps eliminate multicollinearity, improving comprehension of the machine learning model's parameters. It removes those features from the data since including irrelevant features in the data might decrease model accuracy and cause your model to train using irrelevant traits.

As a result, adopting such approaches to create quick automated segmentation of NPCs is difficult. Convolutional neural networks (CNN) and other deep learning (DL) approaches have been extensively employed in medicine. Segmenting an item that may be moved in the image is extremely difficult since the CNN model is not scale- and rotation-invariant. The speed of evaluation is one of the main issues with employing a CNN model in the medical field, as many pharmacological treatments require quick replies to reduce the need for extra investigation and treatment. They can extract characteristics in pictures directly and automatically, from low-level to high-level, abstract to concrete. Image classification, segmentation, and registration are all techniques used in image processing. Literature [8] employed an encoder-decoder fully convolutional neural network to segment CT images of NPC patients and compared it to the VGG network [9] in NPC segmentation. The findings suggest that the network can significantly enhance NPC segmentation.

Literature [10] employed a fully convolutional neural network with an encoder-decoder to segment the MR images of 27 NPC patients and used leave-one-out cross-validation to accomplish NPC segmentation. Literature [11] also employed a convolutional neural network to separate the lesion region of 30 NPC patients' T1W modality MR data. To enhance the segmentation findings, they applied a 3D graph cut technique. The value of the Dice is 0.851. All of the models utilized in the preceding experiments are 2D models. As a result, the association of visual characteristics in 3D space is not taken into account. 2D CNN typically achieves higher Dice scores than its 3D version for three reasons: first, if we opt to work with volumes above slices for a particular data set of 3D pictures, the sample size is less, which may cause convergence issues during network training. Second, we can increase the output of a 2D design



greater than its 3D version for a given set of computer resources. When deep learning architectures are designed for 2D pictures, 3D data offers various challenges, such as less effective volumetric input pipelines. Third, 3D image processing requires extra code since image augmentation libraries were created for 2D pictures. Additionally, working with volumes calls for greater processing power, particularly RAM and VRAM. The network topology is basic, the experimental data is limited, and segmentation is limited to pictures from a single modality. However, since the local knowledge of NPC tumors represented by single-modality imaging data is restricted, the model's resilience must be increased.

Even though the 2D network has fewer parameters and can fit models quickly, it does not properly utilize the topological information between layers. As a consequence, the segmentation results are prone to inaccuracy and irregular borders [12]. The 3D network may compensate for this shortcoming, but it comes with the drawbacks of a large number of parameters and sluggish or even difficult model fitting. As a result, this work integrates 2D and 3D information using the H-DenseUNet model suggested by literature [13]. To assist doctors in the diagnosis and treatment planning of hepatocellular carcinoma, an accurate and computerized liver and tumor segmentation strategy is highly sought in clinical practice. However, 2D convolutions are constrained in their capacity to effectively exploit location data along the third dimension, whereas 3D convolutions suffer from a severe computational expense and GPU memory usage. To address these issues, a brand-new hybrid densely linked UNet (H-DenseUNet) is proposed. It is made up of a 2D DenseUNet for efficiently extracting intraslice characteristics and a 3D counterpart for hierarchically aggregating volumetric contexts, similar to how the auto-context algorithm segments tumors and the liver. Specifically, the 2D network's quick segmentation findings are utilized to drive the 3D model's learning and implementation of segmentation [14]. A new deep segmentation method of multimodal and multidimensional information fusion is proposed using MR images of three modalities, T1W, T2W, and T1C, to establish a multimodal 2D-ResUNet 3D-ResUNet multidimensional feature fusion model to achieve automatic and accurate segmentation of NPC lesions.

## 2. Research Method

**2.1. Network Structure.** Figure 1 depicts the deep convolutional neural network structure, which primarily consists of a multimodal 2D-ResUNet system, 3D-ResUNet structure, and 2D+3D fusion layer. A 3D picture  $I_{R13844384b3}$  is used as the model's input. The batch size, image height ( $h$ ), image width ( $w$ ), image depth ( $b$ ), and numerous picture channels ( $c$ ) of the input network are all represented by the size 1384384b3. The picture modalities T1W, T2W, and T1C are represented by the number of image channels  $c = 3$ .

First, three modalities of 2D pictures are produced if the function defines the process of transforming 3D images into

2D and explains the inverse operation of the transformation; second, the 2D network is defined as after multimodal 2D-ResUNet, the feature map and probability map of the 2D image is as follows:

$$\begin{aligned} F_{2d} &= f_{2d}(I_{2d-T1W}, I_{2d-T2W}, I_{2d-T1C}; \theta_{2d}), F_{2d} \in R^{b*384*384*16}, \\ y_{2d} &= f_{2dcls}(F_{2d}; \theta_{2dcls}), y_{2d} \in R^{b*384*384*2}. \end{aligned} \quad (1)$$

The parameters of the convolutional network and the classification network, respectively, are  $\theta_{2d}$  and  $\theta_{2dcls}$  in the formula.  $F_{2d}$  and  $y_{2d}$  must perform the following inverse transformations to get the relevant 3D feature map to merge the findings of the 2D network with the 3D web:

$$\begin{aligned} \hat{F}_{2d} &= T^{-1}(F_{2d}), \hat{F}_{2d} \in R^{1*384*384*b*16}, \\ \hat{y}_{2d} &= T^{-1}(y_{2d}), \hat{y}_{2d} \in R^{1*384*384*b*2}. \end{aligned} \quad (2)$$

Merge  $\hat{y}_{2d}$  with  $I$  and input them into 3D-ResUNet to get the feature map of the 3D network:

$$F_{3d} = f_{3d}(I, \hat{y}_{2d}; \theta_{3d}), F_{3d} \in R^{1*384*384*b*16}. \quad (3)$$

In the formula,  $\theta_{3d}$  is the parameter of the 3D network. After summing  $\hat{F}_{2d}$ ,  $F_{3d}$  to get  $Z$ , input the 2D+3D fusion layer  $f_{HF}$ , perform convolution calculation to get  $H$ , and then go through the classification layer  $f_{HFcls}$  to get the 3D segmentation result  $y_H$ .

$$\begin{aligned} Z &= \hat{F}_{2d} + F_{3d}, \\ H &= f_{HF}(Z; \theta_{HF}), \\ y_H &= f_{HFcls}(H; \theta_{HFcls}). \end{aligned} \quad (4)$$

The parameters of the convolutional layer  $f_{HF}$  of the fusion layer and the classification layer  $f_{HFcls}$ , respectively, are represented by the formula: HF and HFcls. We are aware that the network aims to recognize the fundamental patterns in each Conv Layer. For instance, the network attempts to learn patterns and edges in the first layer. It tries to comprehend the form, color, and other things in the second layer. The picture is attempted to be classified by a final layer known as the feature layer or fully connected layer. The first fully connected layer, which is a convolutional layer and presents the last challenge in the CNN layer, is unknown in terms of its dimensions. The size of each convolution layer must first be determined, starting with the size of the input picture.

Table 1 shows the network architecture and associated parameters for 2D-ResUNet and 3D-ResUNet. The model is built using the ResUNet with residual structure because the residual design may effectively tackle issues like gradient disappearance [15]. It is employed in activities involving computer vision. It has been shown that the performance of the network is superior to that of a network with convolutional layers stacked on top of each other [16]. The network

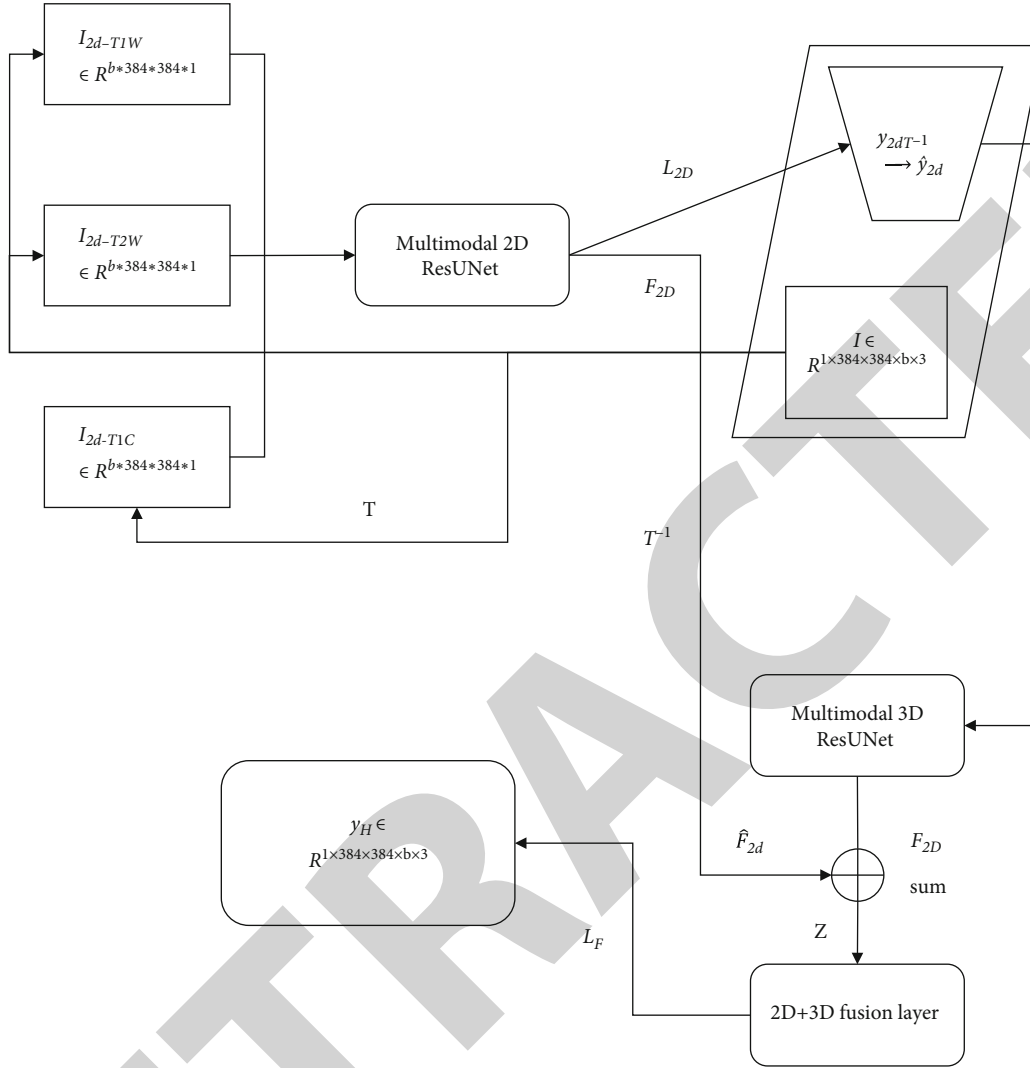


FIGURE 1: Convolution neural network structure with multimodal and multidimensional fusion.

combines the benefits of the 2D network's quick fitting speed with the 3D grid's adequate use of spatial information. It employs the 2D web segmentation findings to drive the fitting of the 3D model, allowing for more efficient model training and testing.

**2.2. Multimodal 2D Convolution.** The multimodal 2D-ResUNet structure is shown in Figure 2, which mainly includes an encoder of three modal images, a multimodal convolution structure, a decoder, and a skip connection structure between the encoder and the decoder. The decoder consists of a convolution block with residual structure and a deconvolution layer. Each pooling layer pools the three modal images in the encoder [17]. And then, perform the convolution operation on the three types of feature maps after pooling to realize the fusion of multimodal 2D features. The specific implementation process is as follows: the three modal images undergo the same level of convolution and pooled feature maps. With the same size, by merging the

three feature maps in the direction of the image depth, a 3D feature map with a depth of 3 can be generated [18]. Then, a convolution kernel of size (1, 1, 3) is used to create a (1, 1, 3). Convolve the feature map for the step size so that the depth of the feature map is converted to 1, and the profound fusion of the three modal features is realized. Finally, the same filter level feature maps are added to reduce the loss of information in the deconvolution process.

**2.3. Multimodal 3D-ResUNet.**  $y_{2d}^{T-1}$  by  $\hat{y}_{2d}$  is shown in Figure 1. The input of the multimodal 3D-ResUNet is the image obtained after the transformation of the segmentation probability map of the multimodal 2D-ResUNet and the original information of the model, so the input size is  $1 \times 384 \times 384 \times b \times 5$ , where "5" means that the network input is 5 channels, which are 3 modal images and the segmentation probability map of tumor and background obtained by the multimodal 2D-ResUNet network. 3D segmentation can be achieved by inputting the 3D-ResUNet network with

TABLE 1: 2D-ResUNet and 3D-ResUNet network structures.

Network layer	2D-ResUNet		3D-ResUNet	
	Feature map size	Network layer size	Feature map size	Network layer size
Input	$384 \times 384$	—	$384 \times 384 \times 8$	—
Residual structure 1	$384 \times 384$	$[3 \times 3, 16] \times 5$	$384 \times 384 \times 8$	$[3 \times 3 \times 3, 16] \times 5$
Max pooling layer 1	$192 \times 192$	$2 \times 2$ max pooling	$192 \times 192 \times 4$	$2 \times 2 \times 2$ max pooling
Residual structure 2	$192 \times 192$	$[3 \times 3, 32] \times 5$	$192 \times 192 \times 4$	$[3 \times 3 \times 3, 32] \times 5$
Max pooling layer 2	$96 \times 96$	$2 \times 2$ max pooling	$96 \times 96 \times 4$	$2 \times 2 \times 1$ max pooling
Residual structure 3	$96 \times 96$	$[3 \times 3, 64] \times 5$	$96 \times 96 \times 4$	$[3 \times 3 \times 3, 64] \times 5$
Max pooling layer 3	$48 \times 48$	$2 \times 2$ max pooling	$48 \times 48 \times 2$	$2 \times 2 \times 2$ max pooling
Residual structure 4	$48 \times 48$	$[3 \times 3, 128] \times 5$	$48 \times 48 \times 2$	$[3 \times 3 \times 1, 128] \times 5$
Max pooling layer 4	$24 \times 24$	$2 \times 2$ max pooling	$24 \times 24 \times 2$	$2 \times 2 \times 1$ max pooling
Residual structure 5	$24 \times 24$	$[3 \times 3, 256] \times 5$	$24 \times 24 \times 2$	$[3 \times 3 \times 1, 256] \times 5$
Deconvolution 1	$48 \times 48$	$3 \times 3, 2 \times 2$ -[residual structure 4]	$48 \times 48 \times 2$	$3 \times 3 \times 1, 2 \times 2 \times 1$ -[residual structure 4]
Deconvolution 2	$96 \times 96$	$3 \times 3, 2 \times 2$ -[residual structure 3]	$96 \times 96 \times 4$	$3 \times 3 \times 3, 2 \times 2 \times 2$ -[residual structure 3]
Deconvolution 3	$192 \times 192$	$3 \times 3, 2 \times 2$ -[residual structure 2]	$192 \times 192 \times 4$	$3 \times 3 \times 1, 2 \times 2 \times 1$ -[residual structure 2]
Deconvolution 4	$384 \times 384$	$3 \times 3, 2 \times 2$ -[residual structure 1]	$384 \times 384 \times 8$	$3 \times 3 \times 3, 2 \times 2 \times 2$ -[residual structure 1]
Convolutional layer	$384 \times 384$	$1 \times 1, 2$	$384 \times 384 \times 8$	$1 \times 1 \times 1, 2$

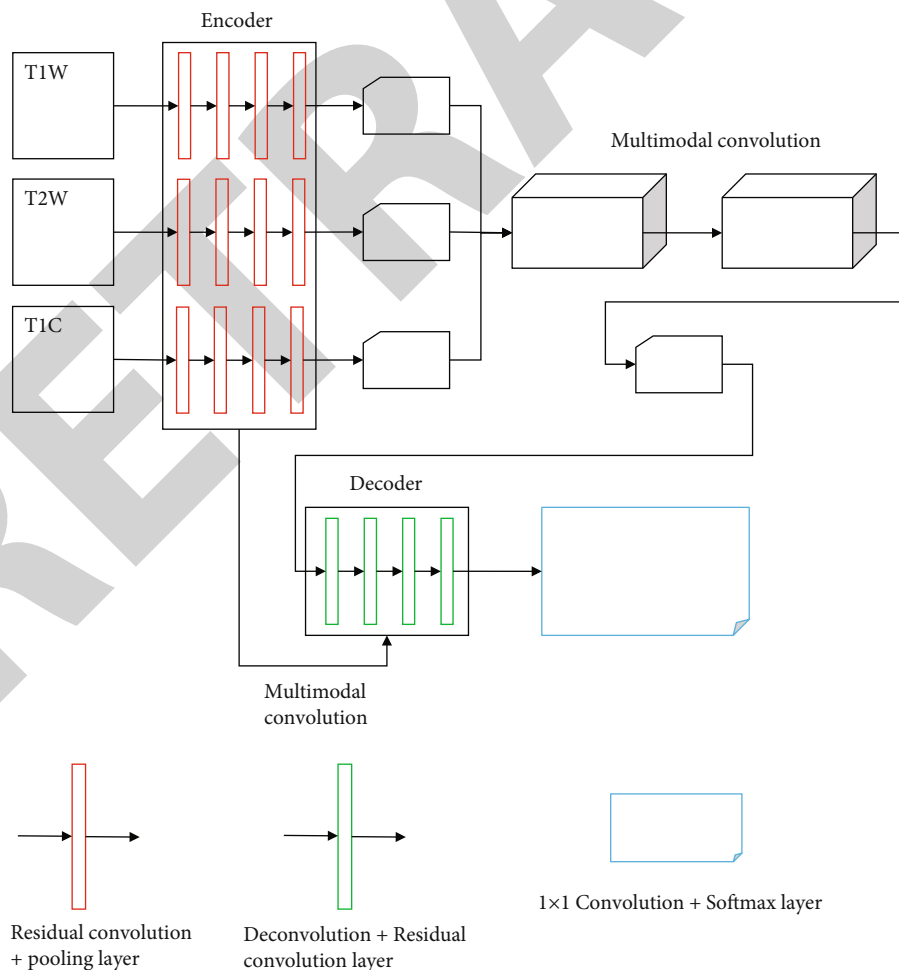


FIGURE 2: Multimodal 2D-ResUNet structures.

skip connections and residual structure [19]. Therefore, the network uses 3 modal images as the three channels of the input image and the multimodal 2D-ResUNet segmentation probability map as input two tracks of the image; thus, using the 2D network fast segmentation results to guide 3D model segmentation.

The suggested MultiRes block is used to replace the series of two convolutional layers in the MultiResUNet model. The 18-layer ResNet CNN is chosen above the other CNNs because it has a greater accuracy and requires fewer compute processes. Figure 2 depicts the algorithm's structure. A  $7 \times 7$  kernel filter with a stride of 2 first filters the input picture to 64 channels.  $3 \times 3$  kernel filters convolute the remaining blocks. The skip connection arrow connects the two blocks to avoid gradients vanishing, which is the ResNet algorithm's fundamental competency.

**2.4. Loss Function Calculation.** The Sorensen-Dice coefficient is a statistic created in the 1940s to assess the similarity between the two samples, which is where Dice loss gets its name. Milletari et al. presented it to the computer vision community in 2016 for 3D medical picture segmentation. The ground truth border pixels and anticipated boundary pixels in boundary detection tasks may be seen as two sets. The two sets are programmed to gradually overlap by using Dice loss. Due to the importance of high accuracy, Dice loss takes into account the loss of data both locally and internationally. In the MR images of nasopharyngeal carcinoma patients in this study, the proportion of the tumor area relative to the entire image is tiny; that is, the size of the tumor area is much smaller than the area of the nontumor site, so the Dice loss [20] is used as the primary loss function, defined as follows:

$$\text{Dice} = \frac{2|P \cap G|}{|P| + |G|}. \quad (5)$$

In the formula,  $P$  is the output result of the model, and  $G$  is the actual label, that is, the manually drawn tumor contour.

Dice loss is defined as

$$L = 1 - \text{Dice}. \quad (6)$$

The total loss of the model consists of two parts: the loss  $L_{2D}$  of 2D-ResUNet and the loss  $L_F$  of the 2D+3D fusion layer. Therefore, the complete loss of the model is the weighted sum of these two losses:

$$L_{\text{Total}} = \alpha L_{2D} + L_F. \quad (7)$$

In the formula,  $\alpha$  is the weight of 2D-ResUNet loss, which is set to 0.5 in this study, indicating that the model pays more attention to the loss of the final output.

### 3. Data Set

421 NPC patients were collected with T1W, T2W, and T1C MR images of three brain structures, and 1.5T GE Medical Systems was used for horizontal scanning. The MR image has  $TE = 8.69$  ms,  $DFOV = 198$  mm, slice thickness 6 mm and total of 31 slices. T1C image parameters are  $TR = 753$  ms,  $TE = 8.69$  ms,  $DFOV = 198$  mm, and slice thickness 6 mm; there are 31 layers in full; the parameters of the T2W image are  $TR = 2900$  ms,  $TE = 83.56$  ms, and  $DFOV = 189$  mm, the layer thickness is 5 mm, there are 32 layers in total, and the resolution of all 3D image horizontal slices is  $512 \times 512$ . An experienced clinician manually delineated the tumor region of the T2W modality images to determine the segmentation labels. The images of 346 patients were randomly selected from all 421 subjects as the training set. The images of the remaining 75 patients were used as the independent test set; the information on the training set and test set is shown in Table 2.

### 4. Experimental Result Analysis

**4.1. Evaluation Indicators.** The Dice coefficient [5], Hausdorff distance (HD) [5], and percentage of area difference (PAD) [6] are used as the evaluation indicators of the model effect. HD and PAD are defined as follows:

$$\text{HD}(P, G) = \max_{a \in P} \left\{ \max_{b \in G} [d(a, b)] \right\}, \quad (8)$$

where  $d(a, b)$  is the Euclidean distance.

$$\text{PAD} = \frac{|P - G|}{G}. \quad (9)$$

The smaller the values of HD and PAD, the closer the model segmentation results are to the manual delineation results, and the better the model performance.

**4.2. Training and Testing.** Firstly, the single-modal multidimensional fusion models of T1W, T2W, and T1C three modal data were constructed by using single-modal 2D-ResUNet and 3D-ResUNet and 2D+3D fusion layers, respectively, which are T1W-MDF, T2W-MDF, T1C-MDF; then, combine T1W, T2W, and T1C in pairs, namely, T1W+T2W, T1W+T1C, and T2W+T1C, a total of three dual-modal images as two channels of the 3D image, respectively, to recombine the 3D image. Then, the 2 modal images are used as the input of each encoder of the multimodal 2D-ResUNet, and the 2D-ResUNet output probability map and the 2 modal 3D input images are merged and then input into 3D-ResUNet and then passed through 2D+3D. The fusion layer constructs two-modal multidimensional information fusion segmentation models, which are T1W+T2W-MDF, T1W+T1C-MDF, and T2W+T1C-MDF; finally, the three modal images of T1W, T2W, and T1C are used as the 3D images, respectively. Three-channel, after the 3D image is reorganized, each modal image is used as the input of each encoder of the multimodal 2D-ResUNet,

TABLE 2: Training set and test set information of nasopharyngeal carcinoma (NPC) segmentation model.

Data set	Number of subjects	Number of people (male/female)	Age (mean $\pm$ SD)
Training set	346	254/92	45.5 $\pm$ 11.9
Test set	75	55/20	44.9 $\pm$ 11.6

TABLE 3: Performance comparison of different NPC segmentation models.

Nasopharyngeal carcinoma segmentation model			Dice rate	HD (mm)	PAD ratio
T1W-MDF		MDF	0.77418	6.6402	20.4
T2W		MDF	0.77826	6.4974	18.258
T1C		MDF	0.76194	6.5382	20.196
T1W	T2W	MDF	0.79662	5.9568	16.83
T1W	T1C	MDF	0.78846	6.1404	17.442
T2W	T1C	MDF	0.7905	6.0486	17.136
Methods1 [20]			0.74052	6.9564	24.276
Methods2 [21]			0.73236	7.0482	25.602
Methods3 [22]			0.74562	6.885	23.154
MMMDF			0.8211	5.6712	15.81

and the output probability map of the mmultimodal2D-ResUNet is combined with the mmultimodal3D input image. After merging, they are input into 3D-ResUNet, and then, a multimodality multidimensional fusion (MMMDF) segmentation model is constructed through a 2D+3D fusion layer.

The TensorFlow [21] software library is used to build the model. The initial learning rate in the training phase is 0.001, and the attenuation is multiplied by 0.9 every 4 rounds. The Adam optimizer is used for optimization. The graphics card is NVIDIA Titan XP GPU, a single-modal multidimensional fusion model, dual-mode. The training time of the multimodal fusion model and the multimodal fusion model was 23 h 37 min, 30 h 24 min, and 34 h 47 min, respectively. The testing time of each patient in the three types of models in the testing phase was about 13, 18, and 18 minutes, respectively—22 s.

Using the same training set and test set, the algorithms in the literature [8, 10, 16] are trained and tested, and the results are compared with the MMMDF method proposed in this paper, as shown in Table 3. For the different models in this paper, the resulting boxplot is shown in Figure 3.

It can be seen from Table 2 and Figure 3 that the segmentation performance of the MMMDF model is better than that of the model with any single modality of T1W, T2W, and T1C as input and better than any two-modal multidimensional fusion segmentation model. The MMMDF segmentation results are compared with 3. A statistical test was carried out on the segmentation results of the two-modal multidimensional fusion. The results showed that the  $P$  values of the Dice coefficient, the area difference ratio, and the Hausdorff distance were all less than 0.05, indicating that the segmentation performance of the MMMDF model

was better than that of any two-modal multidimensional fusion model. Calculating the average Hausdorff distance between the two-point sets is a typical practice evaluation metric. In medical image segmentation, it is utilized to compare actual photos to the segmentations that allow for their ranking. The Dice coefficient and the IoU have many similarities. They are positively correlated, so if one asserts that model A is better at segmenting pictures than model B, the other will do the same. Similar to the IoU, they also have a range from 0 to 1, with 1 being the maximum similarity between predicted and truth. The Dice coefficient should ideally not be higher than 1. A Dice coefficient typically ranges from 0 to 1. If you are obtaining a coefficient greater than 1, perhaps, you should check your implementation. The performance is better and has statistical differences. Using multimodality as the input of 2D-ResUNet, in the process of network convolution, the information of different modalities is fused: in addition, multimodal images are used as the input of 3D-ResUNet, and the communication between other modalities is connected again, so the effect of the fusion model is better than the effect of single-modal intake. In addition, the use of multidimensional models in series combines the fast-fitting speed of 2D models and the characteristics of 3D models. After learning the good advantages, a better segmentation effect is obtained on the test set.

It can be seen from Table 2 that compared with the methods mentioned in other literature, the MMMDF segmentation model proposed in this paper has a significant improvement in the performance of NPC segmentation. This is because the studies in this literature only use a simple 2D encoder-decoder network or fine-tune the network structure based on this while only taking a single modality image.

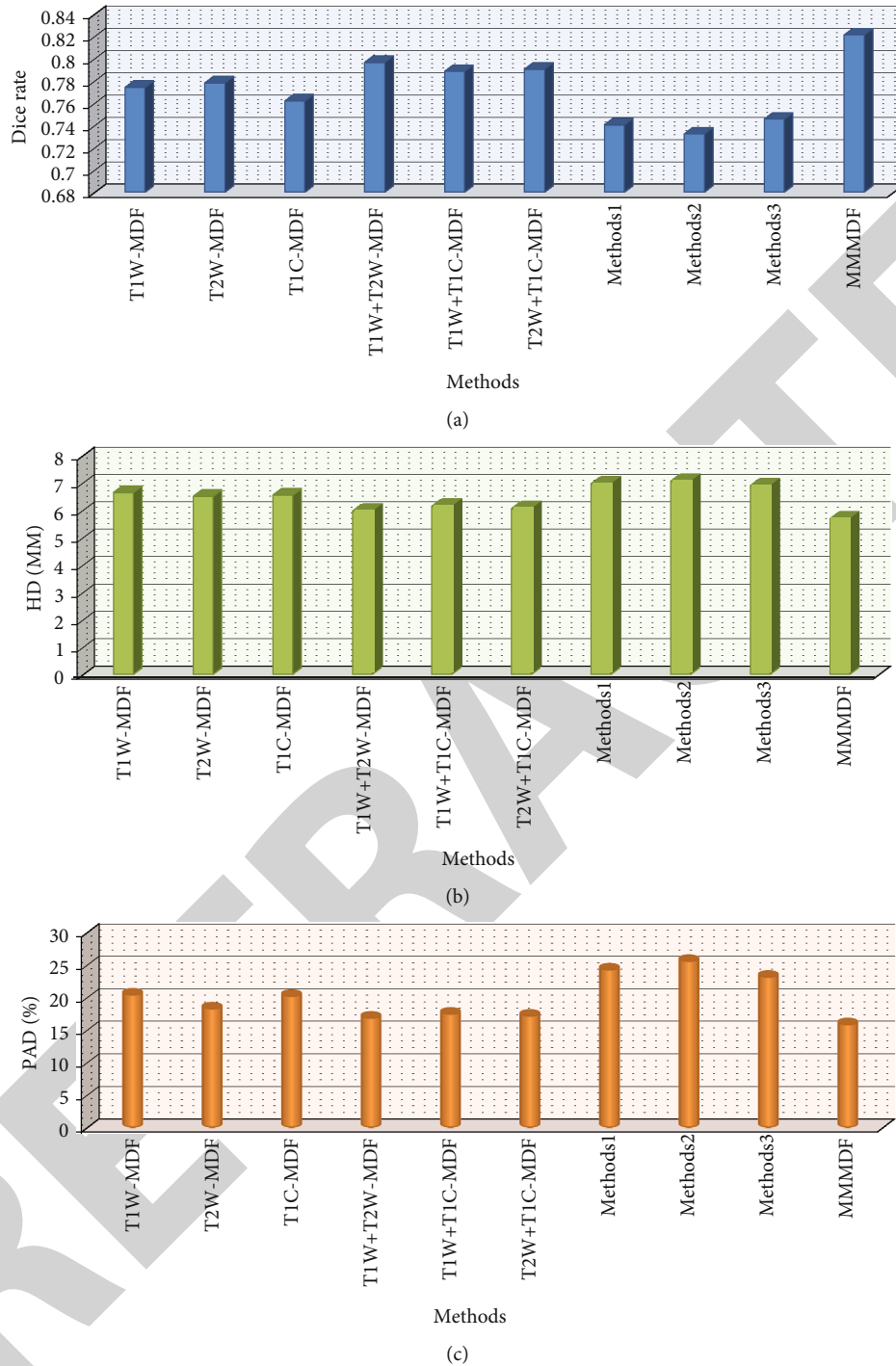


FIGURE 3: Comparison of performance box plots of seven NPC segmentation models.

Figure 4 shows the partial segmentation results obtained by the T1W-MDF, T2W-MDF, T1C-MDF, and MMMDF models. Morphology, volume, and tumors in different regions showed excellent segmentation results. In Figures 4 and 5, each row represents another patient, and the first column represents the input image; the 2~8 columns represent T1W-MDF, T2W, the methods of MDF, T1C-MDF, Methods1 [20], Methods2 [15], and

Methods3 [22], and the results of MMMDF. The first column of Figure 4 is the final image, and the second to eighth columns are the enlarged images of the first column of the window area. Two lines represent the manually delineated tumor region (gold standard) and the model segmentation result. The performance comparison of different NPC segmentation models is shown in Table 3.

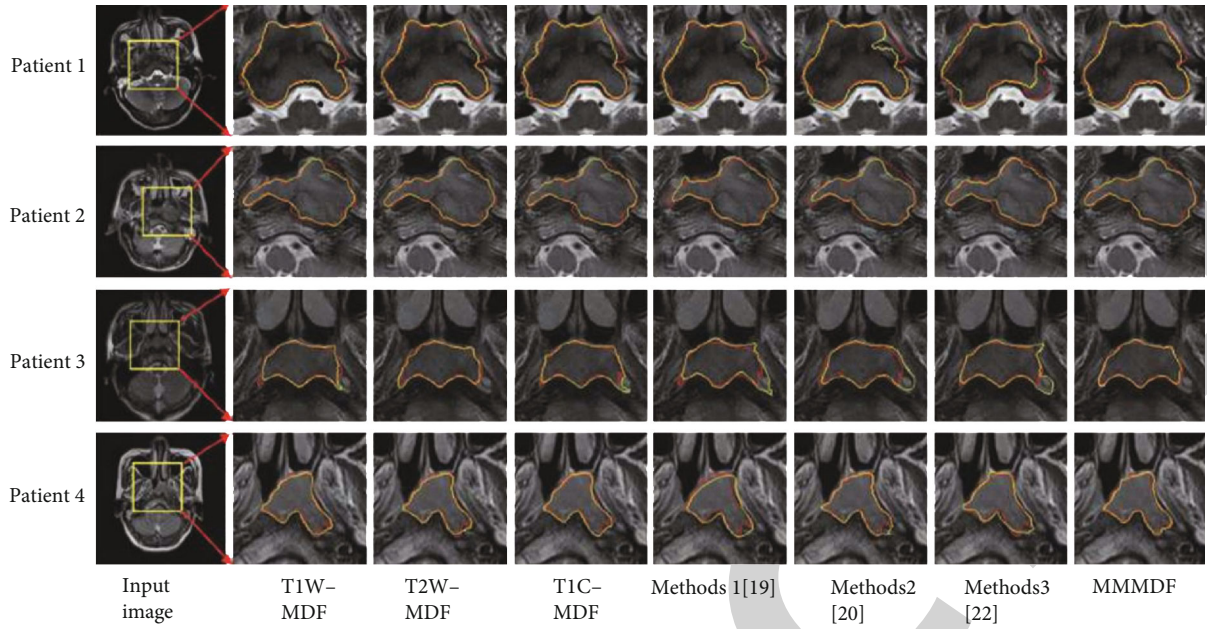


FIGURE 4: Comparison of the 2D segmentation results.

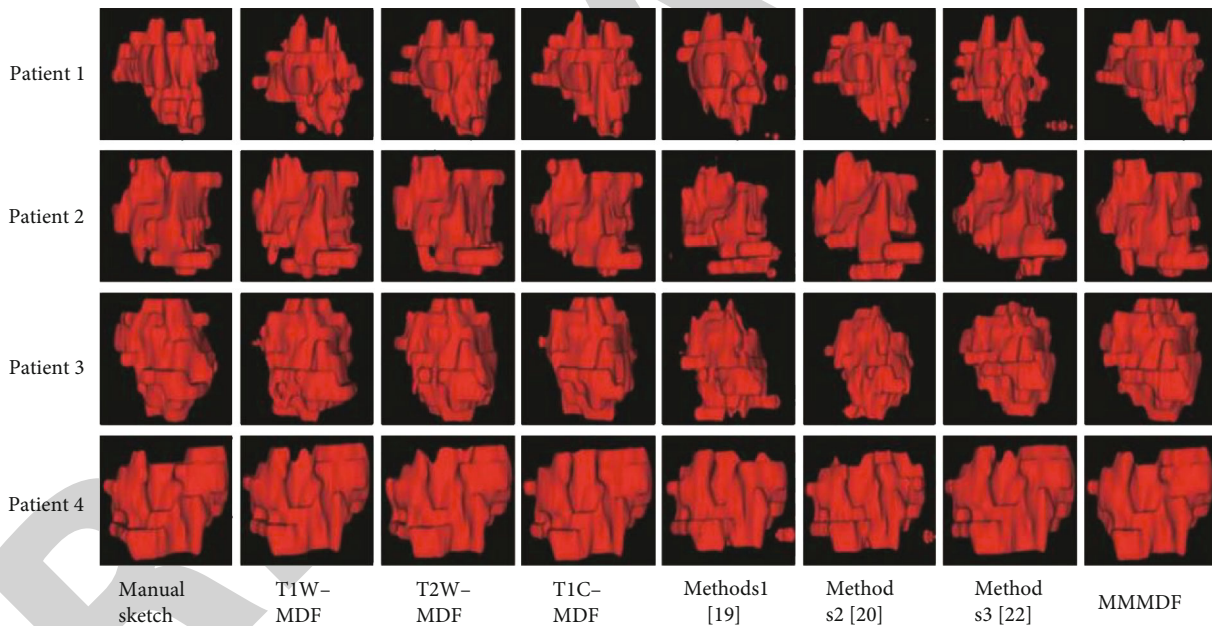


FIGURE 5: Comparison of the 3D segmentation results.

**5. Conclusion**

This work used three modal MR scans of T1W, T2W, and T1C of the head and neck of NPC patients to obtain precise segmentation of lesions in NPC patients. It developed a novel deep learning segmentation model based on multimodal and multidimensional information fusion. In the experiment, the findings reveal that the multimodal multidimensional information fusion model can more correctly detect lesions and enhance the segmentation effect when

compared to the single-modal multidimensional fusion model and other existing approaches for NPC lesion segmentation. The approach suggested in this study may efficiently and accurately localize NPC tumors, offer an objective foundation for NPC diagnosis and therapy, and increase the efficiency and level of diagnosis and treatment. This research contains four major flaws: (1) a total of 421 patients' MR pictures were obtained in three modalities, with a modest number of patient samples. (2) The resolution is poor, the slice thickness is 5 mm, and the spatial structure

information is discontinuous or partly absent; therefore, increasing the sample size will assist in enhancing the segmentation model's generalization capacity. On the one hand, it makes identifying the tumor location in the training sample more challenging. On the other hand, it prevents the 3D segmentation model from making efficient use of the image's layer topological information. (3) The model's segmentation performance is poor in certain tumor locations with a small area, and it is required to concentrate on how to improve the segmentation results by using tumor area information from neighboring layers. (4) Different modal pictures have different positions. Space is guaranteed. The model's dependability and flexibility will benefit from the regular position.

## Data Availability

The data shall be made available on request.

## Conflicts of Interest

The authors declare that they have no conflict of interest.

## References

- [1] Y. Li, T. Dan, H. Li et al., "NPCNet: jointly segment primary nasopharyngeal carcinoma tumors and metastatic lymph nodes in MR images," *IEEE Transactions on Medical Imaging*, vol. 41, no. 7, pp. 1639–1650, 2022.
- [2] G. Tao, H. Li, L. Liu, and H. Cai, "Detection-and-excitation neural network achieves accurate nasopharyngeal carcinoma segmentation in multi-modality MR images," in *2021 IEEE International Conference on Bioinformatics and Biomedicine (BIBM)*, pp. 1063–1068, Houston, TX, USA, 2021.
- [3] Z. Ma, X. Wu, and J. Zhou, "Automatic nasopharyngeal carcinoma segmentation in MR images with convolutional neural networks," in *2017 International Conference on the Frontiers and Advances in Data Science (FADS)*, pp. 147–150, Xi'an, China, 2017.
- [4] G. Chen, H. Hu, R. Chen, and D. Xu, "Statistical classification based on SVM for Raman spectra discrimination of nasopharyngeal carcinoma cell," in *2012 5th International Conference on BioMedical Engineering and Informatics*, pp. 1000–1003, Chongqing, China, 2012.
- [5] J. Zhang, Y. Ge, Y. Chen, and X. Chen, "A study on the positioning accuracy of patient positioning based on Optical Positioning System for nasopharyngeal carcinoma: Compared with conventional method," in *2013 IEEE International Conference on Medical Imaging Physics and Engineering*, pp. 11–13, Shenyang, China, 2013.
- [6] P. Ritthipravat, C. Tatanun, T. Bhongmakapat, and L. Tuntiyatorn, "Automatic segmentation of nasopharyngeal carcinoma from CT images," in *2008 International Conference on BioMedical Engineering and Informatics*, pp. 18–22, Sanya, China, 2008.
- [7] K. -W. Huang, Z. -Y. Zhao, Q. Gong, J. Zha, L. Chen, and R. Yang, "Nasopharyngeal carcinoma segmentation via HMRf-EM with maximum entropy," in *2015 37th Annual International Conference of the IEEE Engineering in Medicine and Biology Society (EMBC)*, pp. 2968–2972, Milan, Italy, 2015.
- [8] L. B. Zhou, S. J. Zhengdong, and D. Wei, "A simple program to calculate normal tissue complication probability in external beam radiotherapy for nasopharyngeal carcinoma," in *2010 International Conference on Computer Application and System Modeling (ICCASM 2010)*, pp. V7-493–V7-496, Taiyuan, 2010.
- [9] M. Shabaz and U. Garg, "Evaluation and categorization of handwriting patterns reflecting sentiments," *International Journal of Recent Technology and Engineering*, vol. 8, no. 2, pp. 2475–2477, 2019.
- [10] O. F. Baker and S. A. Kareem, "ANFIS models for prognostic and survival rate analysis "nasopharyngeal carcinoma"," in *2008 4th IEEE International Conference on Management of Innovation and Technology*, pp. 537–541, Bangkok, Thailand, 2008.
- [11] A. Gupta and L. K. Awasthi, "Peer enterprises: a viable alternative to Cloud computing?," in *2009 IEEE International Conference on Internet Multimedia Services Architecture and Applications (IMSAA)*, Bangalore, India, 2009a.
- [12] G. K. Saini, H. Chouhan, S. Kori et al., "Recognition of human sentiment from image using machine learning," *Annals of the Romanian Society for Cell Biology*, vol. 25, no. 5, pp. 1802–1808, 2021.
- [13] M. Kong and S. E. Hong, "Tumor regression patterns by follow-up duration in patients with nasopharyngeal carcinoma treated with concurrent chemoradiotherapy," *Journal of Radiation Research*, vol. 58, no. 2, pp. 232–237, 2017.
- [14] T. Thakur, I. Batra, M. Luthra et al., "Gene expression-assisted cancer prediction techniques," *Journal of Healthcare Engineering*, vol. 2021, Article ID 4242646, 9 pages, 2021.
- [15] P.-s. Dai, B. Wang, M. Chen, X. Min, Y. Ju, and S. Huang, "Computer simulation of radioactive source delivery process in nasopharyngeal carcinoma brachytherapy," in *2007 1st International Conference on Bioinformatics and Biomedical Engineering*, pp. 671–674, Wuhan, China, 2007.
- [16] S. Chaudhury, N. Shelke, K. Sau, B. Prasanalakshmi, and M. Shabaz, "A novel approach to classifying breast cancer histopathology biopsy images using bilateral knowledge distillation and label smoothing regularization," *Computational and Mathematical Methods in Medicine*, vol. 2021, Article ID 4019358, 2021.
- [17] H. Lu, H. Lin, G. Feng et al., "Interfractional and intrafractional errors assessed by daily cone-beam computed tomography in nasopharyngeal carcinoma treated with intensity-modulated radiation therapy: a prospective study," *Journal of Radiation Research*, vol. 53, no. 6, pp. 954–960, 2012.
- [18] A. Gupta and L. K. Awasthi, "Security issues in cross-organizational peer-to-peer applications and some solutions," in *Contemporary Computing. IC3 2009*, vol. 40 of Communications in Computer and Information Science, Springer, Berlin, Heidelberg, 2009.
- [19] C. Li, H. Niu, M. Shabaz, and K. Kajal, "Design and implementation of intelligent monitoring system for platform security gate based on wireless communication technology using ML," *International Journal of Systems Assurance Engineering and Management*, vol. 13, no. S1, pp. 298–304, 2022.
- [20] W. W. K. Fung, V. W. C. Wu, and P. M. L. Teo, "Developing an adaptive radiation therapy strategy for nasopharyngeal carcinoma," *Journal of Radiation Research*, vol. 55, no. 2, pp. 293–304, 2014.



## Retraction

# Retracted: Metaheuristic Optimization-Driven Novel Deep Learning Approach for Brain Tumor Segmentation

### BioMed Research International

Received 8 January 2024; Accepted 8 January 2024; Published 9 January 2024

Copyright © 2024 BioMed Research International. This is an open access article distributed under the Creative Commons Attribution License, which permits unrestricted use, distribution, and reproduction in any medium, provided the original work is properly cited.

This article has been retracted by Hindawi following an investigation undertaken by the publisher [1]. This investigation has uncovered evidence of one or more of the following indicators of systematic manipulation of the publication process:

- (1) Discrepancies in scope
- (2) Discrepancies in the description of the research reported
- (3) Discrepancies between the availability of data and the research described
- (4) Inappropriate citations
- (5) Incoherent, meaningless and/or irrelevant content included in the article
- (6) Manipulated or compromised peer review

The presence of these indicators undermines our confidence in the integrity of the article's content and we cannot, therefore, vouch for its reliability. Please note that this notice is intended solely to alert readers that the content of this article is unreliable. We have not investigated whether authors were aware of or involved in the systematic manipulation of the publication process.

Wiley and Hindawi regrets that the usual quality checks did not identify these issues before publication and have since put additional measures in place to safeguard research integrity.

We wish to credit our own Research Integrity and Research Publishing teams and anonymous and named external researchers and research integrity experts for contributing to this investigation.

The corresponding author, as the representative of all authors, has been given the opportunity to register their agreement or disagreement to this retraction. We have kept a record of any response received.

### References

- [1] R. Kalpana, M. A. Bennet, and A. W. Rahmani, "Metaheuristic Optimization-Driven Novel Deep Learning Approach for Brain Tumor Segmentation," *BioMed Research International*, vol. 2022, Article ID 2980691, 15 pages, 2022.

## Research Article

# Metaheuristic Optimization-Driven Novel Deep Learning Approach for Brain Tumor Segmentation

R. Kalpana <sup>1</sup>, M. Anto Bennet <sup>1</sup> and Abdul Wahab Rahmani <sup>2</sup>

<sup>1</sup>Department of Electronics and Communication Engineering, VelTech Rangarajan Dr. Sagunthala R&D Institute of Science and Technology, Avadi, Chennai, Tamil Nadu 600062, India

<sup>2</sup>Isteqlal Institute of Higher Education, Kabul, Afghanistan

Correspondence should be addressed to R. Kalpana; [kalpanar.ece25@gmail.com](mailto:kalpanar.ece25@gmail.com) and Abdul Wahab Rahmani; [ab.wahab.professor@isteqlal.edu.af](mailto:ab.wahab.professor@isteqlal.edu.af)

Received 16 June 2022; Revised 21 July 2022; Accepted 27 July 2022; Published 18 August 2022

Academic Editor: Gaganpreet Kaur

Copyright © 2022 R. Kalpana et al. This is an open access article distributed under the Creative Commons Attribution License, which permits unrestricted use, distribution, and reproduction in any medium, provided the original work is properly cited.

Brain tumor has the foremost distinguished etiology of high mortality. Neoplasm, a categorization of brain tumors, is very operative in distinguishing and determining the tumor's exact location in the brain. Magnetic resonance imaging (MRI) is an efficient noninvasive technique for the anatomical examination of brain tumors. Growth tissues have a distinguishable look in MRI pictures in order that they are unit-wide used for brain tumor feature extraction. The existing research algorithms for brain tumors have some limitations such as different qualities, low sensitivity, and diagnosing the tumor at its stages. In this particular piece of research, an innovative method of optimization known as the procedure for lightning attachment algorithm (PLA) is used, and for the purpose of classification, a CNN model known as DenseNet-169 is applied. PLA was used in order to optimize the growth, and a network model known as the DenseNet-169 model was utilized in order to extract the various growth-optimization choices. First, the MR images of the brain were preprocessed to remove any outliers. Next, the Dense Net-169 CNN model was used to extract network choices from the MR images. In addition, it is used to execute the function of a classifier in order to identify the growth as either an aberrant growth or a traditional growth. In addition, the publicly benchmarked datasets that are widely utilized have validated the algorithmic rule that was granted. The planned system demonstrates the satisfactory accuracy in getting ready to on the dataset and outperforms many of the notable current techniques.

## 1. Introduction

Brain tumors are the foremost dreadful cancer among the various kinds of them. One of the most unpleasant types of cancer is a tumour, which has resulted in a massive population die-off [1]. Brain tumor needs precise analysis by the doctor that may categorize the tumor exactly [2]. Solely concerning, some kinds of brain tumors are cancerous, i.e., malignant. The tumor will impair the function of the brain either benign or malignant. It compresses the nerve and blood vessels and also causes many symptoms such as headaches perhaps severe, temperament changes, confusion, balance issues, nausea, difficulty in focusing, coordination, and concentration, numbness, weakness, and complication in sensory like hearing, vision, or speaking and seizures, and

uncommon temporary state, amnesia, stumbling with thinking, speaking, and understanding languages [3].

There are two sorts of tumours: benign and malignant. A tumour is occasionally treatable and is not considered malignant; however, a malignancy is harmful if it is not detected early. Tumors are among the various types of development that can be fatal and affect important brain components such as nerve tissue, white matter (WM), substantia grisea (GM), and liquid body material (CSF). This additionally damages the central nervous system [4]. Primary tumors will develop in the brain extent, and the tumors which develop apart from the brain extent are known as secondary tumors [3]. The tumor cells are also called neoplastic cells where they grow rapidly and divide in multiples more than the usual, or instead, they will not die [5]. One of the foremost

common kinds of brain tumor is glioma. These gliomas emerge by the surrounding and nurture cells of glial cells, which also contain astrocytes, which are found in the brain, oligodendrocytes, and ependymoma cells [6]. The most common CNS tumor is low-grade glioma (LGG) and is categorized as grade-I and grade-II glial tumors, namely, oligodendroglioma and gangliomas pleomorphic xanthoastrocytoma. These were common mostly in pediatrics than adults. The least malignant and most common LGG is a pilocytic astrocytoma; by gross total resection, overall survival can be >90-95% for about 5 years. Figure 1(a) represents the epidemiology of LGG. Many patients have multiple progressions and recurrences depending on location and ability to resect. Then, the most aggressive and malignant glial tumor is high-grade glioma (HGG) which is classified as grade-III and grade-IV, and these were common mostly in adults than in pediatrics. Figure 1(b) represents the epidemiology of HGG. HGG has a penurious survival outcome and is more resistant to therapy compared to LGG. The outcomes of HGG is universally poor showing 5-year overall survival is 15-20%. Nevertheless, recent analysis helps doctors move to victimization growth genetic science to higher classify gliomas. Individuals with a 5-year survival rate with a cancerous brain or system growth is three hundred and sixty-five days. The 10-year survival rate is concerning thirty-first. The 5-year survival rate for individuals younger than age fifteen is over seventy-fifth. For individuals aged fifteen to thirty-nine, the 5-year survival rate is over seventy-two. The 5-year survival rate for individuals aged forty and over is over twenty-first [7].

The use of magnetic resonance imaging (MRI) in medical imaging allows for a good view of the body's soft tissues [5]. The positioning and size of these tumours in a brain magnetic resonance imaging (MRI) picture must be determined for diagnosis and therapy [8]. The most common types of MRI sequences are called T1-weighted and T2-weighted scans. When the TE and TR timings are kept relatively short, the resulting images are T1-weighted. The contrast and brightness of the image are mostly attributable to the characteristics of the T1 tissue. On the other hand, T2-weighted images are produced by employing TE and TR times that are significantly longer. The T2 properties of the tissue are primarily responsible for determining the contrast and brightness of these pictures. In this study, we present procedure for lightning attachment (PLA), a novel optimization approach inspired by lightning occurrences in which large quantities of electrical charges build up within the cloud. Lightning is created when the number of charges within a cloud increase, resulting in an increase in electrical intensity. Lightning can strike at any time, and it will erupt from a variety of locations [9].

This paper uses Dense Net Model as the basic structural unit feature extraction of the tumor and classifies the abnormal brain tumors in the LGG and HGG. When it comes to deep learning, CNNs (convolutional neural networks) are a type of deep neural network that is used to analyse graphical pictures. The dense convolutional network (Dense-Net), introduced in is a convolutional network where the layers are linked to all the further layers in the network. The Dense-Net is used for accurate feature extraction of the

image. In our proposed model, Dense net 169 is used as a feature extractor. The Dense-Net architecture has been proposed in recent years, and work on standard datasets has shown it to be substantially deeper, more accurate, and efficient than most architectures. Its dense interconnections between layers are proposed to encourage feature reuse [10].

### 1.1. Contribution of the Paper

- (i) We use BraTS 2016, 2017, and BraTS 2018 datasets to be used in the training and validation phases
- (ii) The brain tumor features were extracted and classified by utilizing DenseNet-169 for obtaining deeper and more generic features
- (iii) We propose a novel method named lightning attachment procedure algorithm for feature selection
- (iv) The performance measures are evaluated with optimization performance

The remainder of the paper is structured as follows: Section 2 is dedicated to related work. The preprocessing method and the phase of scheme are explained in Section 3. The experimental results of the advanced model is explain in Sections 4 and 5. Finally, in Sections 6, the findings and future work are discussed.

## 2. Related Works

Brain tumor optimization is embraced for tumor detection due to high mortality, and many researchers are floundering to diagnose brain tumors at early stages using several machine learning architectures. The very first step for brain tumor optimization is preprocessing Kumar (2020) [5] developed a deep learning algorithm that has been tuned called Dolphin-SCA correlated with D-CNN for effective classification and segmentation of brain tumor. After preprocessing, the segmentation is passed out by a vague deformable blending model with dolphin-SCA. And on power LDP and statistical characteristics, the feature extraction method is carried out. These features are used in D-CNN for the sorting of brain tumor with D-SCA and were compared with the BraTS and Sim BraTS datasets. However, for effective treatments, the accuracy of the current model should be improved. Brain tumour segmentation approaches based on classical image processing and machine learning are not optimal enough among the currently suggested brain segmentation methods. After preprocessing feature extraction is the vital procedure which is done by Yin et al. (2020) [8], a novel metaheuristic-based technique for brain tumour early detection background removal, feature extraction, and classification using a multilayer perceptron neural network are the three key aspects of the proposed technique. The best selection of features and classification stages is achieved using an updated model of the whale optimization method based on chaos theory and logistic mapping approach. Furthermore, Alagarsamy et al. (2021) [11] used

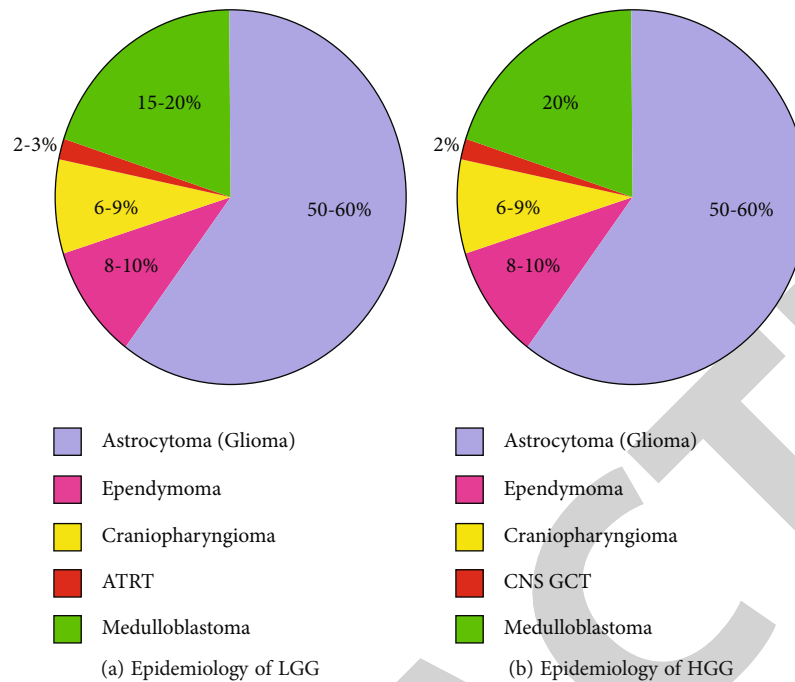


FIGURE 1: Epidemiology of LGG and HGG.

a spatially constrained fish school optimization method (SCFSO) and an interval type-II vague logic system to address brain tumour abnormalities. SCFSO and IT2FLS can intervene and investigate large datasets and complicated cancers. The suggested approach provides a distinct separation of the tumour and nontumor regions, allowing for treatment preplanning. Huge database requirements and high computational time still pose a problem for deep learning. So, a lot of work is done for feature extraction in order to forecast the occurrence of a brain tumour. Deb and Roy (2021) [12] recommended a system to identify picture normalcy and abnormality; we used an adaptive fuzzy deep neural network with frog leap optimization. Classification is done by AFNN, and segmentation is done using adaptive flying squirrel algorithms. The accuracy gained by the proposed system is 99.6%. Additionally, various authors have proposed different feature extraction models to classify brain tumors. For the identification of brain tumours, Sharif et al. (2019) [13] designed a swarm optimization with a blending of characteristics which was used. In the initial stage, the head is taken out by the BSE technique. Then, the image is fed to PSO for segmentation. For feature selection, a genetic algorithm is used to extract LBP and deep features from segmented pictures. At last, the classification of tumor kinds is done using ANN and is compared with the RIDER and BraTS datasets.

Because of the time necessary for the training process, this suggested system has certain disadvantages, including a long processing time and decreased accuracy. Later, Cristin et al. (2021) [14] created an excellent tumour classification algorithm called fractional-chicken swarm optimization (fractional-CSO). To improve the accuracy, chicken swarm is combined with a derivative factor. The MR pictures have been preprocessed, and the features have been retrieved effi-

ciently. The tumour classification security level is achieved utilising deep recurrent neural networks that are trained using the suggested fractional CSO technique and have an accuracy of roughly 93.35 percent. The conventional methods lack accuracy in segmentation due to the complex spatial variation of tumors. Furthermore, Shivhare and Kumar (2021) [4] proposed the MLP (multilayer perceptron) to improve the accuracy of segmentation of brain tumours, to improve the accuracy of segmentation of brain tumours, and to improve the accuracy of segmentation of brain tumours. For this, three metaheuristic optimization algorithms GWO, AEFO, and SMO have been used. Grounded on the voting, a majority three models have been combined. The three brain tumor regions are segmented by different magnetic resonance modalities. The proposed system uses the BraTS dataset and can achieve 92% of DSC. Rammurthy and Mahesh (2020) [2] experimented with an automatic tumor classification model. This paper an optimized Whale Harris Hawks Optimization technique is used. The dissection process is done using cellular automata and rough set theory. Some features like size, LOOP, mean, variance, and kurtosis are extracted from segments. Detection done using D-CNN, wherein the training is done using the proposed model, is designed by WOH and HHO Algorithm. Different strategies for brain tumour classification have been created in the literature and, however, owed to inaccuracy, then inadequate result making the prevailing techniques have failed to give enhanced classification. Besides, Vilas et al. (2020) [10] proposed spontaneous brain tumor dissection using Dense Net. In this project, we recommend a Dense Net architecture for automatic segmentation based on CNN. The performance of Dense Net architecture against that of U-net is utilized, and the drawn analysis is compared with the BraTS dataset.

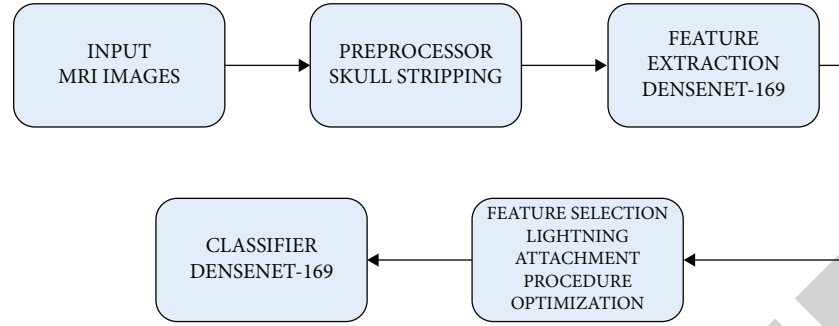


FIGURE 2: Architecture for suggested model.

TABLE 1: Training and validation datasets for the BraTS system.

Dataset	Description
BraTS-2016 [13]	Each has 220 aberrant higher-grade glioma (HGG) photos and 54 normal lower-grade glioma (LGG) images.
BraTS 2017 [1]	There have been a total of 431 examples in total, 285 training cases (210 HGG and 75 LGG) and 146 testing cases (both HGG and LGG) were included in the study.
BraTS 2018 [1]	There has been a total of 476 examples in total, 285 training cases (210 HGG and 75 LGG) and 191 testing cases for both HGG and LGG were included in the study.

### 3. Methodology Proposed

Skull scripting is adopted as a preprocessing in our proposed model, followed by Dense Net-169 for feature extraction and classification. Procedure for lightning attachment has been used to execute a feature selection step prior to categorization (PLA). The above procedures are used in the BraTS datasets from 2016, 2017, and 2018. The architecture for the suggested model is shown in Figure 2.

**3.1. Dataset Description.** For the purpose of training and validation of the architecture that has been proposed, three datasets were used in this study. BraTS 2016, BraTS 2017, and BraTS 2018, respectively, were chosen as the datasets. Each database contains ground-truth photos for four distinct classes, including Flair, T1CE, T1, and T2. The datasets are divided into two distinct modes: LGG and HGG, with each distinct mode containing four stage tumours (T1-weighted, T1CE, T2-weighted, and flair) [15]. To resolve disparities, the data is removed from the skull, aligned to suit an anatomical template, and resampled at  $1\text{ mm}^3$  resolution. A volume (dimension) of  $240 * 240 * 155$  is assigned to each sequence [16]. All photos have anisotropic resolutions that are resampled to become isotropic. The 60% flair and T1CE photos, as well by using this picture, ground truth images are utilised to train a CNN model for the disunion technique. The remaining 40% of photos, from both classes, and 100% of T1 and T2 are used in the testing phase [1]. The BraTS datasets' training validation is shown in Table 1. Figure 3 shows a selection of photos from the BraTS collection.

**3.2. Skull Stripping as Preprocessing.** Skull striping is the process of removing nonbrain structures and undesired picture sections from a scanned image in order to obtain the image

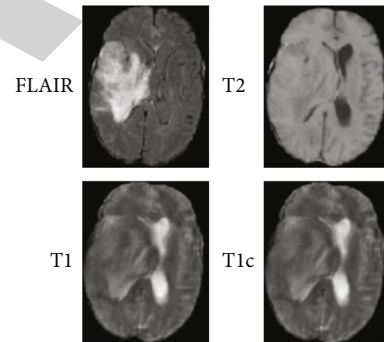


FIGURE 3: A selection of pictures from the Multimodal Brain Dataset (BraTS) [17].

necessary for tumour identification. The brain, scalp, skull, and dura are all visible in the photograph. With the use of a cerebrospinal fluid rim, you can separate the undesired components (CSF). Intensity thresholding and morphological operations can be used to remove the skull and acquire the requisite brain region for tumour identification. Allow the input picture to be epitomised as a collection of pixels with intensity values at relevant locations in the image.

$$\text{Let } I_p = I_{p1}, I_{p2}, I_{pn} = I_{pn} = I_{pn} = I_{pn} = I_{pn} = I_{pn} = I_{pn} = I_{pn} = I_{pn}. \quad (1)$$

In the case of  $I_{p1}$ , the intensity levels of pixels 1 to  $n$  are represented by the integer  $I_{pn}$ . And  $np$  stands for the total number of pixels in a picture. Let us say the intensity threshold is  $T$ , and the circumstance for removing pixels extracted from the picture is that the intensity of those pixels is less

than  $T$ . Pixels that match this requirement are normally used to denote thin connections. The technique meets two conditions. The first is that nonbrain structures should be only weakly connected to the brain. The mask formed by intensity thresholding should also preserve as much brain as possible undamaged. Setting the proper threshold number is critical in this case, since setting it too low might result in the inclusion of garbage, which is undesired. Threshold levels that are too high can assist distinguish between brain and nonbrain structures, but they come at the expense of brain function.

We now have the requisite brain picture, which must be improved to make it suitable for the tumour identification procedure. We employ morphological procedures to do this. It also aids in the elimination of tight connections [18].

**3.3. Feature Extraction.** By directly integrating all layers with the same feature sizes, DenseNet is able to solve the problem of gradient vanishing, which occurs frequently in deep CNN. The multilayer architecture of the DenseNet-169 is seen in Figure 3. The most compelling justification for utilising DenseNet as a feature extractor is due to the fact that as you delve further into the network, you will become aware of an increasing number of general features. The method for the extraction of features was carried out with the assistance of a densely connected convolutional neural network (DenseNet-169) that had been trained in advance. The variant that was used in this work was trained with the use of the ImageNet dataset, which is a large dataset that is accessible to the public.

In order to create the DenseNet169 architecture, one layer of complexity and amalgamation is placed at the beginning, followed by three conversion layers and four dense blocks. The classification layer comes after these previous stages have been completed. The first convolutional layer performs  $7 * 7$  intricacies when stride 2 is used, and this is followed by a maximum pooling of  $3 * 3$  when stride 2 is used. After then, there is a dense block in the network that is surveyed by three sets. Within each set is a conversion layer, and then, there is a dense block. Conversion layers are the names given to the layers that can be found between thick blocks. A batch normalisation layer and a  $1 * 1$  convolutional layer come first in each of the network's conversion layers. Next comes a  $2 * 2$  average pooling layer with a stride of 2 and finally comes a stride of 2.

As previously stated, there are four dense blocks, each of which has two intricacy layers, the first of which is of  $1 * 1$ , and the second of which is of size  $3 * 3$ . The four dense blocks of the DenseNet169 design pretrained on ImageNet are 6, 12, 32, and 32 pixels in size. Following this is the sorting layer, which does overall average pooling of 77% and finally followed by fully connected layer that uses "softmax" as the activation [19].

**3.4. Classifier.** In recent years, CNN has made significant improvement in a number of areas, including picture categorization. This is due to the fact that CNN networks are one of the most accurate technologies currently available for detecting characteristics in input pictures.

Intracacial layers, initiation layers, set normalisation layer, and amalgamating layers are used for feature extraction in Dense Net-169, while dropout layers are utilised for classification.

- (i) Compressed layers, also known as completely linked layers, comprise numerous neurons or units, with the last thick layer has the same number of neurons as the number of categories. The activation layer is placed after each dense layer. The activation function used to the output of the final dense layer differs significantly from the sigmoid or softmax function used in the previous dense layers. In multiclass classification tasks, each category is assigned decimal probabilities using the Softmax function, with the target category having the greatest probability. The following formula is used to calculate the softmax of  $i$ th output unit

$$\hat{y}_i = \frac{e^{x_i}}{\sum_i^N e^{x_i}}, \text{ For } i = 1, 2, 3, \dots, N, \quad (2)$$

where  $x_i$  is the output of the  $i$ th dimension,  $N$  is the no. of dimensions, and  $\hat{y}_i$  is the probability associates with the  $i$ th category.

During forecasting, a sample is assigned to the category with the highest likelihood, as indicated below.

$$\hat{y}_i = \max_{i \in [1, N]} \hat{y}_i. \quad (3)$$

In binary classification problems, the sigmoid function is employed. It accepts any real number between 0 and 1 and returns a result that falls inside that range. The following equation is used to compute it numerically:

$$\text{Sigmoid}(X) = \frac{1}{1 + e^{-x}}. \quad (4)$$

- (ii) Dropout layers are a regularisation method used only during network training to prevent overfitting by temporarily removing a subsection of the inputted neurons and their connections from the thick layer before them. Except the last layer, which yields category-specific probabilities, the dense layers are normally surveyed by a loafer layer

**3.5. Feature Selection: Procedure for Lightning Attachment (PLA).** The suggested algorithm and its source of inspiration are shown in this section. Lightning is caused by an increase the total number of charges stored in the cloud, which results in a surge in electrical intensity. Precipitous will air-strike, and it may hit several times.

The four phases of attachment to precipitous technique are as follows: (1) breakup of air at the cloud's surface, (2) descendant motion of the lightning channel, (3) ascendant leader expansion, and (4) ultimate hit location [9].

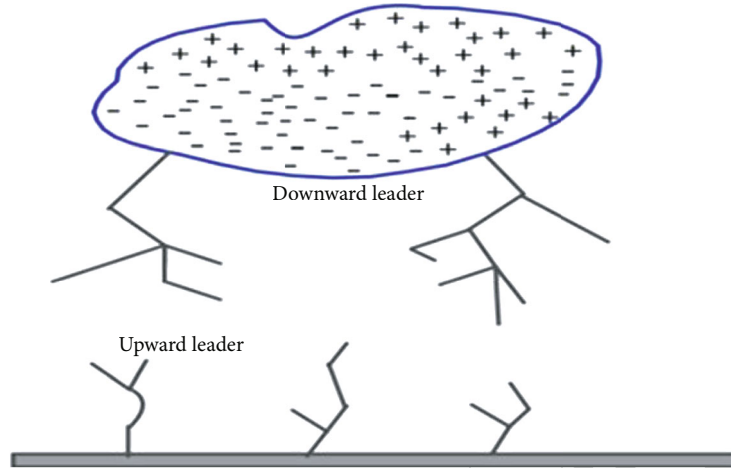


FIGURE 4: The formation of charges in the cloud [9].

3.5.1. *Creativity*. The four processes of lightning attachment are as follows: (1) air disintegration on the cloud surface, (2) descending exodus of the precipitous channel, (3) the formation and spread of rising leaders from the ground earthed objects, and (4) final leap. These steps are detailed in this article.

(1) *Cloud Edge Air Breakdown*. As seen in Figure 4, the cloud's charge may be broken down into three pieces: a large amount of negative charge in the cloud's lower half, a large amount of affirmative charge in the cloud's superior part, and tiny amount of affirmative charge in cloud's bottom portion. The potential between the charge centres grows as the number of these charges grows, and it is possible for the negative charges to separate from the large positive charge section or the little positive charge component. As a result of this breakdown, power gradient near the cloud's edge rises, lightning forms, and a massive amount of electrical energy (mainly negative charge) flows toward the earth. Lightning may originate from several points, as evidenced by high-speed images of genuine lightning strikes [20].

(2) *Effort of the Downhill Leader Headed for the Earth*. The precipitous approaches the ground in an ongoing motion as the air breakdown occurs near the cloud's edge. The precipitous comes to a halt after each stride, then continues in one or more different directions towards the earth. To comprehend this technique, envision a hemisphere underneath the leader tip with the midpoint of the leader tip and the ambit of the next step length after each step. On the surface of this hemisphere, there are several potential jump places to choose from. The next jump point is chosen at random, however, a place, with a greater electrical field value; it is more likely that the line connecting the leader tip and the matching point will be picked.

(3) *Fading Branches*. The charge of the upper most division is allocated into innovative divisions if there are more than

one point for the following lightning jump. The same technique is followed for all new branches, resulting in the formation of new branches. When the charge on a branch falls below critical value (IC), there is no decomposition of air and so no additional movement. As a result, this branch would vanish.

(4) *Propagation of Upward Leaders*. Clouds indicate that there is a massive negative charge above the ground. Positive charges clump together on the earth surface or on an earthed item underneath the cloud as a result of this. The intense electric field produces air breakup in the sharp points; thus, the upward leader begins there and spreads across the air. These upper leads accelerate their approach to the descending leader as it reaches the earth. The ascending leaders likewise go through the branching and branch fading process.

(5) *Final Leap (3.5.1.5) (Striking Point Determination)*. The ultimate jump happens whenever an ascending leader reaches a descending leader, and the striking point is the place where the upward leader began. All other branches vanish in this condition, and the cloud's charge is absorbed through this route [21].

(6) *The PLA Algorithm*.

*Step 1. Trial spots.*

The trial locations indicate the downward leaders' beginning points, which is obtained as follows:

$$X_{ts}^i = X_{min}^i + (X_{max}^i - X_{min}^i) * \text{rand}. \quad (5)$$

The initial trial locations are denoted by  $X_{ts}^i$ . The control variable's lowest value is  $X_{min}^i$ , and its maximum value is  $X_{max}^i$ .  $\text{rand}$  is a random number between 0 and 1. For the first places, the fitness function is determined as follows:

TABLE 2: Discussion of the BraTS 2016 dataset in comparison.

Techniques	Acc (%)	Spec (%)	Sens (%)
Dolphin SCA+ FNB	93.35	93.57	95.94
DWT+DBN	91.38	94	93
Bayesian HSC multi-SVNN	90.98	93.89	92.59
Fine-tuned CNN	90.63	93.25	92.89
Fractional CSO	93.75	94	93
PLA + Dense Net-169	94	95.2	95.9

TABLE 3: Discussion of the BraTS 2017 dataset in comparison.

Techniques	Acc (%)	Spec (%)	Sens (%)
Dolphin SCA+ FNB	94.5	94.9	96.8
DWT+DBN	92.88	95	94
Bayesian HSC multi-SVNN	91.90	94.68	93.95
Fine-tuned CNN	91.56	94.42	93.58
Fractional CSO	92.67	95	94
PLA + Dense Net-169	95	95.7	96.2

$$F_{ts}^i = \text{obj}(X_{ts}^i). \quad (6)$$

*Step 2. Determination of the next leap.*

The fitness values are calculated by averaging all of the original points:

$$\begin{aligned} X_{avr} &= \text{mean}(X_{ts}), \\ F_{avr} &= \text{obj}(X_{avr}). \end{aligned} \quad (7)$$

The average point is denoted by  $X_{avr}$ , and the neutral purpose of the average point is denoted by  $F_{avr}$ . As previously stated, the lightning has multiple paths where it jumps to the next highest optional point. A random solution  $j$  (potential point) is chosen to update the point  $I$  so  $i \neq j$ . The acquired answer is then compared to the possible solution. As a result, the following formula may be used to determine the next jump:

$$\begin{aligned} X_{ts\_new}^i &= X_{ts}^i + \text{rand} * (X_{avr} + X_{PS}^j) \text{IFF } j < F_{avr}, \\ X_{ts\_new}^i &= X_{ts}^i - \text{rand} * (X_{avr} + X_{PS}^j) \text{IFF } j > F_{avr}. \end{aligned} \quad (8)$$

*Step 3. Fading of sections.*

If the critical value is smaller than the electric field of the new test point, the branch will stay continuous; otherwise, it will fade, as shown in the following diagram.

$$X_{ts}^i = X_{ts\_new}^i \text{IFF } F_{ts\_new}^i < F_{ts}^i. \quad (9)$$

In this procedure, test points are run, and the first stage's leftover points are moved down.

*Step 4. Rising march of the leader.*

The ascending leader, which is spread throughout the canal significantly, moves the points up in this operation.

TABLE 4: Discussion of the BraTS 2018 dataset in comparison.

Techniques	Acc	Spec	Sens
Dolphin SCA+ FNB	95.3	95.3	97.7
DWT+DBN	93.20	96	95
Bayesian HSC multi-SVNN	92.56	95.09	94.29
Fine-tuned CNN	92.42	95.04	94.05
Fractional CSO	93.35	96	95
PLA + Dense Net-169	96.8	97	98

As a result, an exponent operator looks like this:

$$S = 1 - \left(\frac{t}{t_{\max}}\right) * \exp\left(-\frac{t}{t_{\max}}\right). \quad (10)$$

If  $t$  is the number of iterations, and  $t_{\max}$  is the maximum number of iterations, and next leap is determined by the channel's charge, the next point is as follows:

$$X_{ts\_new}^i = X_{ts\_new}^i + \text{rand} * s * (X_{\text{best}}^i - X_{\text{worst}}^i), \quad (11)$$

where  $X_{\text{best}}^i$  and  $X_{\text{worst}}^i$  are the best and the worst solutions among the populations.

*Step 5. No returns of lightning.*

When the down and up leaders get together, and the striking spot is assigned, the lightning operation comes to a halt [9].

#### 4. Performance Assessments

To assess the recommended ML model with optimization performance, performance metrics including accuracy, error rate, sensitivity, specificity, and  $F1$ -measure are employed.

True positives (TP) are instances in which the ground truth image's tumour (1) data point is accurately identified as the segmented image's tumour (1) data point.

True negatives (TN) occur when a ground truth image's nontumour (0) data point is accurately tagged as a segmented image's nontumour (0) data point.

False positives (FP) happen when a ground truth image's nontumour (0) data point is incorrectly identified as a segmented image's tumour (1) data point.

False negatives (FN) are when the ground truth image's tumour (1) data point is accurately tagged as the segmented image's nontumour (0) data point.

The number of positive and negative data points divided by the total number of data points is known as accuracy

$$\text{Accuracy} = \frac{(TP + TN)}{(TP + TN + FP + FN)} * 100. \quad (12)$$

The ratio of genuine positives to positive calls is known as precision or specificity. Positive predictive rate (PPR):

$$\text{Specificity} = \frac{TP}{TP + FP}. \quad (13)$$



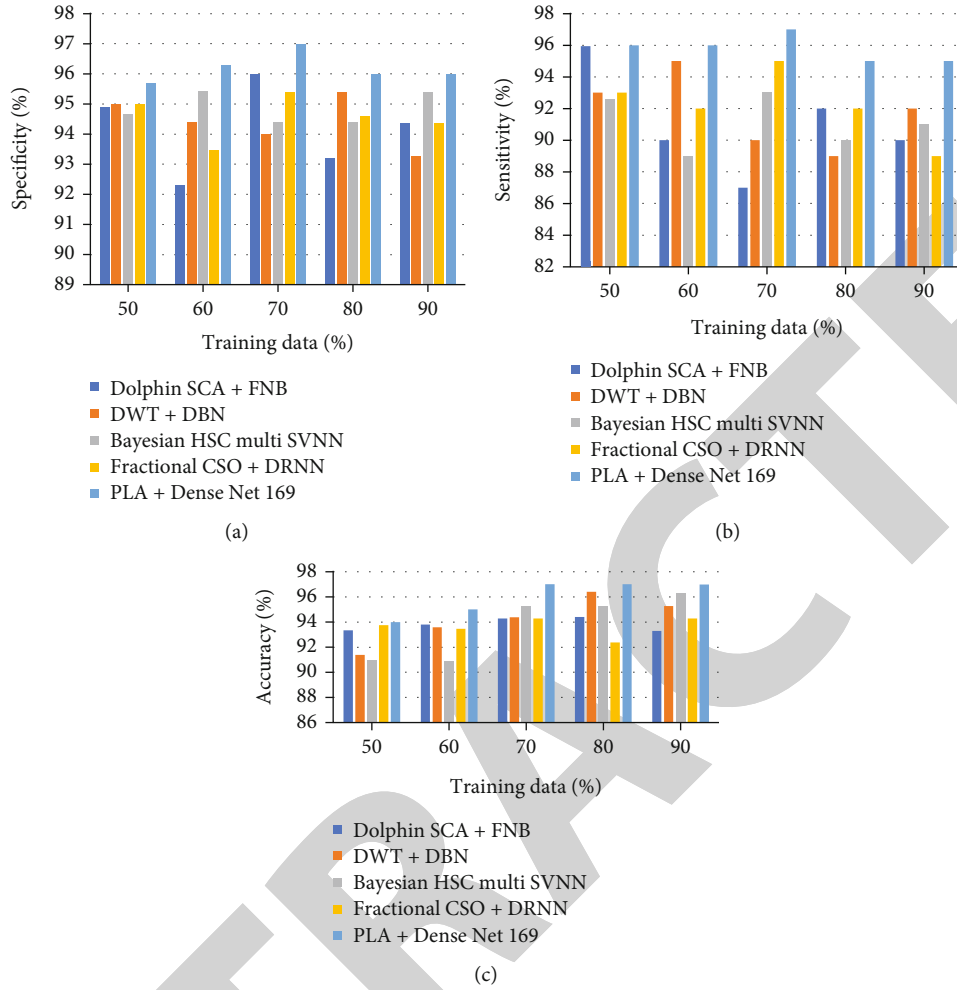


FIGURE 5: Analysis of specificity, sensitivity, and accuracy using the BraTS 2016 database. (a) Specificity, (b) sensitivity, and (c) accuracy.

The chance of a positive test if the patient has a tumour is known as recall or sensitivity. It is also known as the true-positive rate:

$$\text{Sensitivity} = \frac{TP}{TP + FN}. \quad (14)$$

## 5. Result and Discussion

**5.1. Contrast.** The proposed PLA-Deep CNN mechanism is associated to four current techniques: (i) Dolphin Echolocation-based Sine Cosine Algorithm +fuzzy-based Naive Bayes (Dolphin-SCA+FNB) [5], (ii) DWT-deep belief network (DBN) (DWT+DBN) [22], (iii) Bayesian HCS-multi-SVNN [23], and (iv) Fractional—the comparison study for BraTS 2016, 2017, and 2018 data is shown in Tables 2–4.

**5.1.1. Using the BraTS 2016 Information, a Comparative Study Was Conducted**

(i) Variation of data analysis for training

Using the BraTS 2016 database with different training data percentages, the recommended PLA-Deep CNN is

compared to current approaches like Dolphin-SCA + FNB, DWT + DBN, Bayesian HCS-multi-SVNN, and Fractional CSO + DRNN in relations of specificity, precision, and accuracy. The specificity analysis findings for various training data percentages are shown in Figure 5(a). Dolphin-SCA + FNB, DWT +DBN, Bayesian HCS-multi-SVNN, and Fractional CSO +DRNN all have specificity scores of 93.57 percent, 94 percent, 93.89 percent, and 94 percent, respectively, with 90 percent training data. The proposed PLA-based Deep CNN technique has a high specificity, which means it can recognise negatives more accurately. The findings of the sensitivity parameter analysis utilising the BraTS 2016 database are shown in Figure 5(b). When the training data percentage is 70, the relevant sensitivity values measured by Dolphin-SCA + FNB, DWT +DBN, Bayesian HCS-multi-SVNN, Fractional CSO +DRNN, and suggested PLA-based Deep CNN are 95.94 percent, 93 percent, 92.59 percent, 93 percent, and 95.9 percent. Figure 5 depicts the precision parameter analysis by the BraTS 2018 record (c). The precision values assessed by Dolphin-SCA + FNB, DWT +DBN, Bayesian HCS-multi-SVNN, Fractional CSO +DRNN, and the suggested PLA-based Deep CNN are 93.35 percent, 91.38 percent, 90.98 percent, 93.75 percent, and 94 percent, respectively, once the exercise data

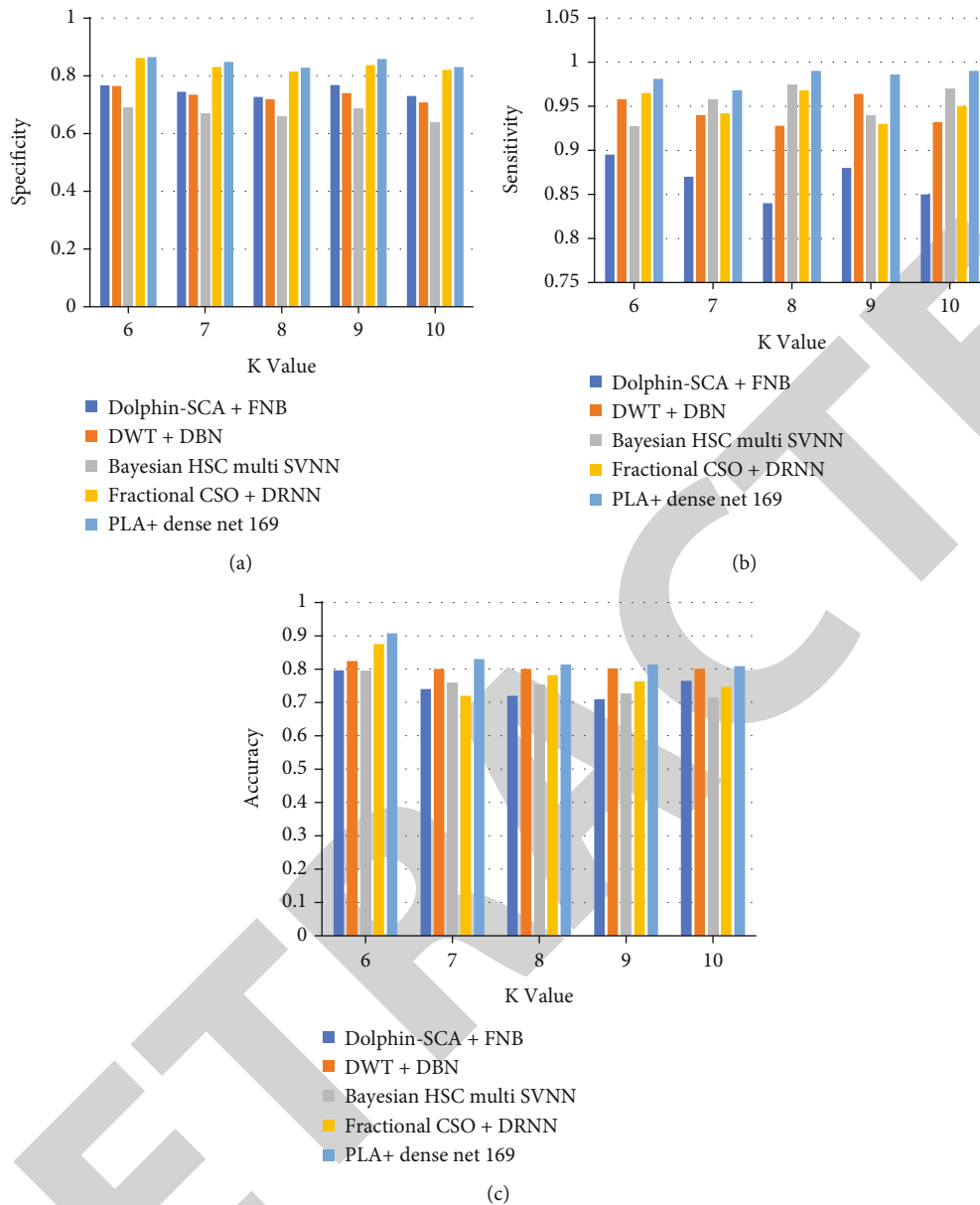


FIGURE 6: Using the BraTS 2016 database, analysis by altering  $K$ -Fold. (a) Specificity, (b) sensitivity, and (c) accuracy.

proportion is 50. Among the existing techniques, the recommended PLA-based Deep CNN has the maximum accuracy, showing that it is capable of reliably recognising the tumorous region.

(ii) Variation of  $K$ -Fold analysis

Figure 5 depicts a qualified analysis plot based on specificity, understanding, and precision metrics by the BraTS 2016 record for different  $K$ -Fold values. Figure 6 depicts the results of a specificity examination for  $K$ -Fold values vacillating from 2 to 6. (a). For  $K$  – Fold = 2, the specificity standards measured by Dolphin-SCA + FNB, DWT +DBN, Bayesian HCS-multi-SVNN, and Fractional CSO +DRNN are 0.767, 0.765, 0.691, 0.702, and 0.863, respectively. Figure 6 depicts the results of the sensitivity parameter analysis using the BraTS database

(b). Dolphin-SCA + FNB, DWT +DBN, Bayesian HCS-multi-SVNN Fine Tuned CNN Fractional CSO +DRNN, and suggested PLA-based Deep CNN exhibit sensitivity values of 0.895, 0.958, 0.927, 0.965, and 0.981 when  $K$  – Fold = 2. Figure 6 depicts the precision parameter analysis using the BraTS record. (c). When  $K$ -Fold is equal to 4, the precision values assessed by Dolphin-SCA + FNB, DWT +DBN, Bayesian HCS-multi-SVNN Fine Tuned CNN Fractional CSO +DRNN, and suggested PLA-based Deep CNN are 0.796, 0.824, 0.795, 0.875, and 0.907.

(iii) ROC analysis

Once FPR is 0.3, the analogous TPR standards restrained by Dolphin-SCA + FNB, DWT +DBN, Bayesian HCS-multi-SVNN, Fractional CSO +DRNN, and projected and

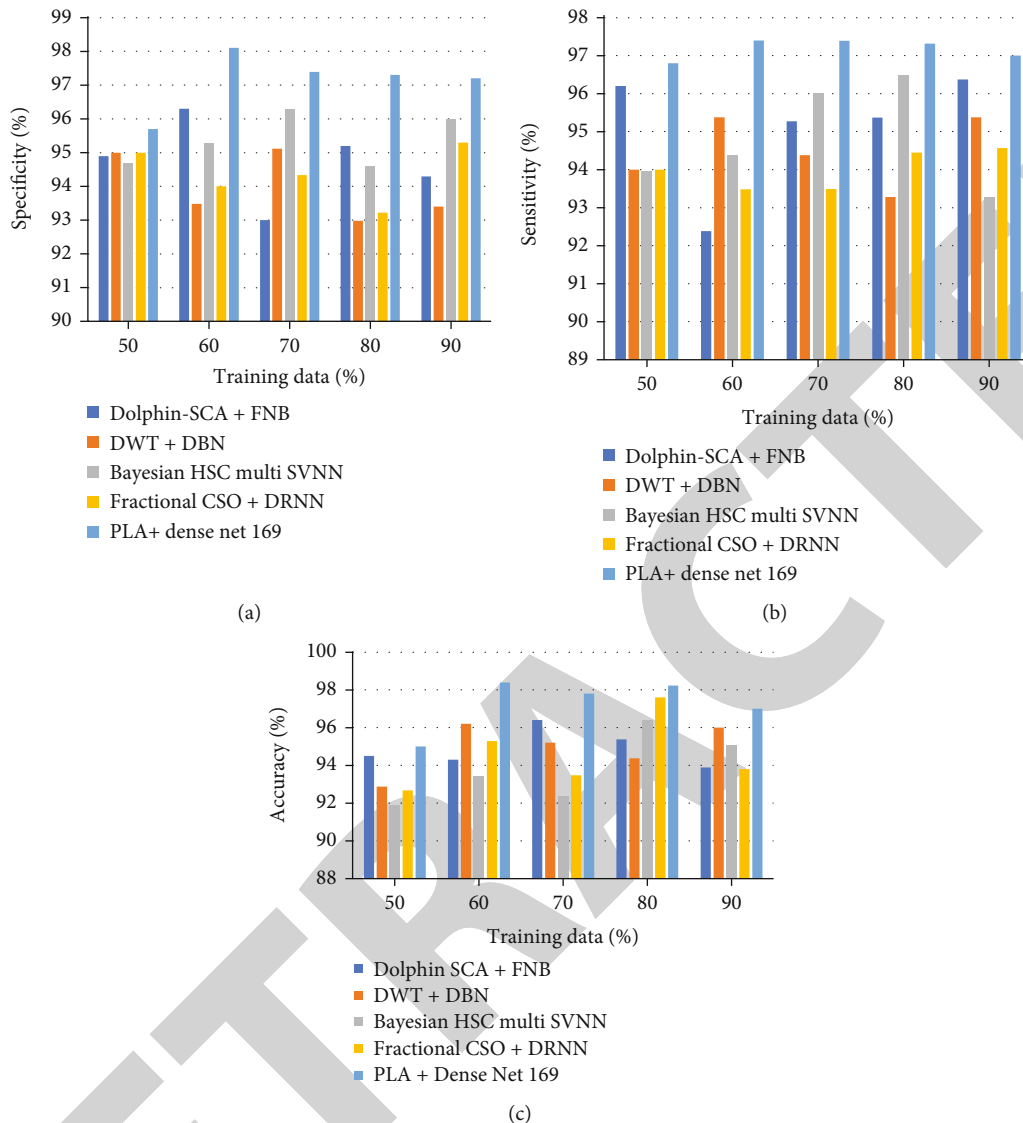


FIGURE 7: Analysis utilising the BraTS 2017 database with different training data. (a) Specificity, (b) sensitivity, and (c) accuracy.

proposed PLA-based Deep CNN are 0.905, 0.742, 0.712, 0.84, and 0.943, respectively. Furthermore, the suggested PLA-based Deep CNN outperforms the FPR = 0.8, 0.9, 1 for identifying tumour and nontumour areas with a TPR of 1.

### 5.1.2. Using the BraTS 2017 Information, a Comparative Study Was Conducted

#### (i) Variation of data analysis for training

The recommended PLA-based Deep CNN is compared to current approaches such as Dolphin-SCA + FNB, DWT +DBN, Bayesian HCS-multi-SVNN, and Fractional CSO +DRNN in terms of specificity, compassion, and precision using the different training data percentages from the BraTS 2017 database. Figure 7 depicts the findings of a research on specificity for different training data percentages (a). Dolphin-SCA + FNB, DWT +DBN, Bayesian HCS-multi-

SVNN, and Fractional CSO +DRNN have specificity values of 94.9 percent, 95 percent, 94.68 percent, and 95 percent, respectively, whereas suggested PLA-based Deep has a specificity of 95.7 percent with 90% training data. The suggested PLA-based Deep CNN approach has a high specificity, and as a result, it has a better capacity to properly recognise negatives. The sensitivity parameter analysis utilising the BraTS 2017 database is shown in Figure 7(b). The sensitivity values determined by Dolphin-SCA + FNB, DWT +DBN, Bayesian HCS-multi-SVNN, Fractional CSO +DRNN, and suggested PLA-based Deep CNN are 96.8%, 94.5 percent, 94.5 percent, and 96.2 percent, respectively, once the physical activity data percentage is 70%. The accuracy parameter analysis utilising the BraTS 2018 database is shown in Figure 7(c). The precision values assessed by Dolphin-SCA + FNB, DWT +DBN, Bayesian HCS-multi-SVNN, Fractional CSO +DRNN, and suggested PLA-based Deep CNN are 94.5 percent, 92.88 percent, 91.90 percent, 92.67 percent, and 95 percent, respectively, when the training data percentage is 50. The

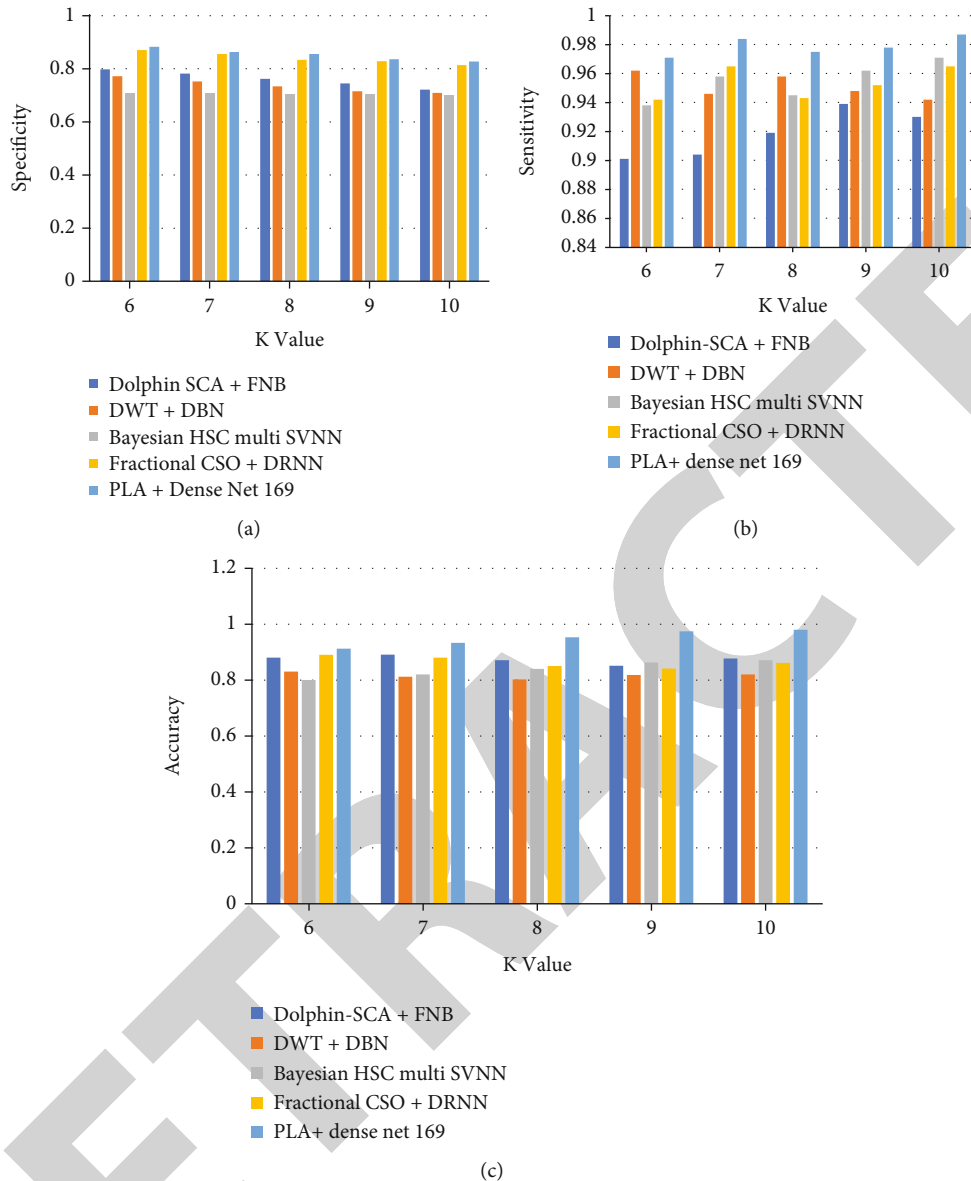


FIGURE 8: Analysis utilising the BraTS 2017 database and adjusting  $K$ -Fold. (a) Specificity, (b) sensitivity, and (c) accuracy.

suggested PLA-based Deep CNN has all the known techniques and has the highest accuracy, indicating that it is capable of accurately identifying the tumorous portion.

(ii) Variation of  $K$ -Fold analysis

For varied  $K$ -Fold values, employing the BraTS 2018 database, Figure 8 depicts a relative analysis plot using specificity, sensitivity, and accuracy measures. Figure 7 shows the results of a specificity study for  $K$ -Fold values ranging from 2 to 6 (a). Dolphin-SCA + FNB, DWT +DBN, Bayesian HCS-multi-SVNN, and Fractional CSO +DRNN have specificity values of 0.798, 0.772, 0.708, 0.691, and 0.871, respectively, while the suggested PLA-based Deep CNN has a specificity of 0.842 for  $K$  - Fold = 2. The results of the sensitivity parameter analysis utilising the BraTS database are shown in Figure 8(b). When  $K$  - Fold = 2, the sensitivity

values of Dolphin-SCA + FNB, DWT +DBN, Bayesian HCS-multi-SVNN, Fractional CSO +DRNN, and suggested PLA-based Deep CNN are 0.901, 0.962, 0.938, 0.942, and 0.971, respectively. Figure 8 shows the results of the accuracy parameter study using the BraTS database (c). When  $K$  - Fold = 4, the accuracy scores of Dolphin-SCA + FNB, DWT +DBN, Bayesian HCS-multi-SVNN, Fractional CSO +DRNN, and the suggested PLA-based Deep CNN are 0.881, 0.831, 0.801, 0.891, and 0.913, respectively.

(iii) ROC-based analysis

TPR values measured by Dolphin-SCA + FNB, DWT +DBN, Bayesian HCS-multi-SVNN, Fractional CSO +DRNN, and proposed PLA-based Deep CNN are 0.912, 0.735, 0.831, 0.85, and 0.951, respectively, when FPR is 0.3. Furthermore, the suggested PLA-based Deep CNN

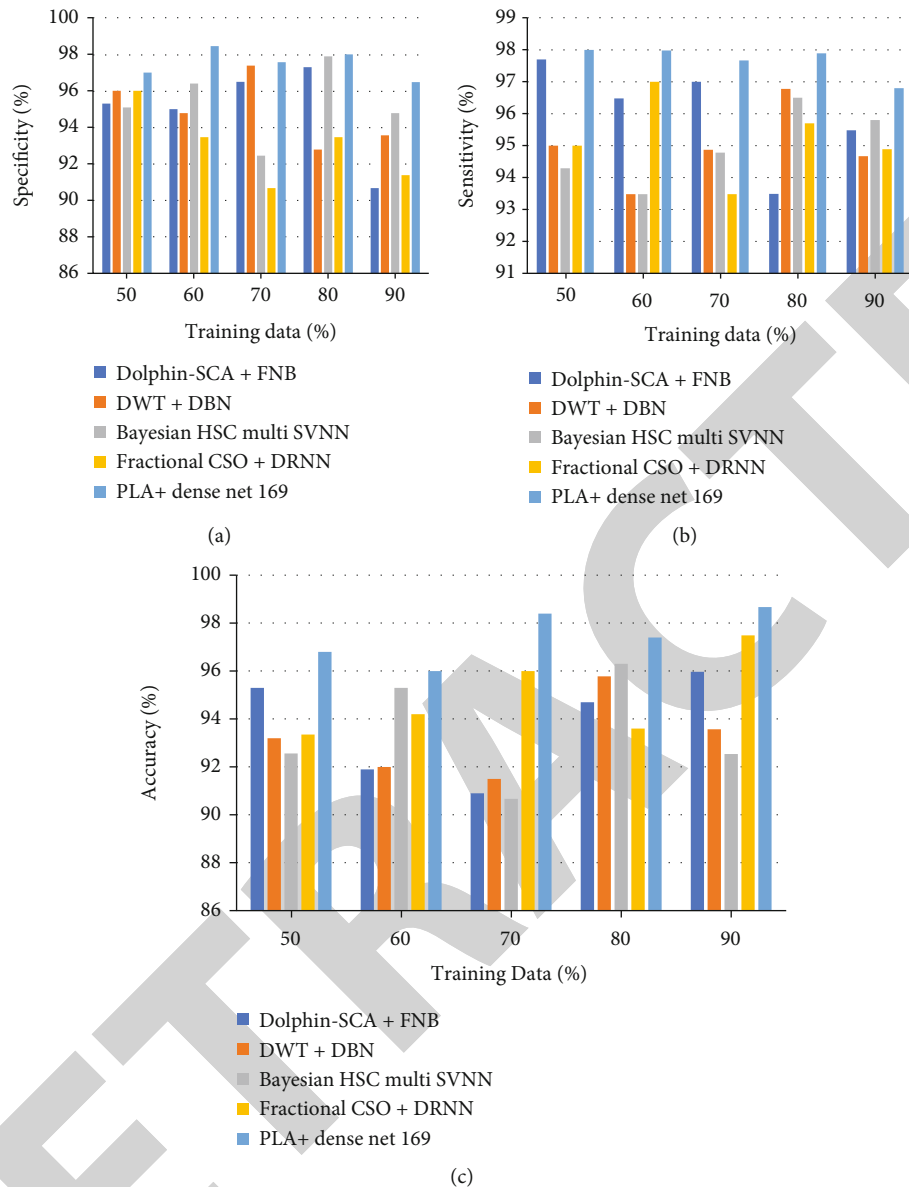


FIGURE 9: Training data analysis utilising the BraTS 2018 database. (a) Specificity, (b) sensitivity, and (c) accuracy.

outperforms the FPR = 0.8, 0.9, and 1 in categorising tumour and nonneoplastic areas with a TPR of 1.

### 5.1.3. Using the BraTS 2018 Information, a Comparative Study Was Conducted

#### (i) Variation of the training data analysis

In Figure 9, the suggested PLA-based Deep CNN is compared to current approaches such as Dolphin-SCA + FNB, DWT +DBN, Bayesian HCS-multi-SVNN, and Fractional CSO+DRNN in terms of specificity, compassion, and precision using the BraTS 2018 database for different training data percentages. Figure 9 shows the specificity analysis for different training data percentages (a). Dolphin-SCA + FNB, DWT +DBN, Bayesian HCS-multi-SVNN, and Fractional CSO +DRNN had specificity values of 95.3 percent,

96 percent, 95.09 percent, and 96 percent, respectively, and recommended PLA-based Deep 97 percent for 90 percent training data. The suggested PLA-based Deep CNN approach has a high specificity, which means it has a better capacity to properly recognise negatives.

Using the BraTS 2018 database, the analysis in terms of the sensitivity parameter is shown in Figure 9(b). When the training data percentage is 70%, the sensitivity values assessed by Dolphin-SCA + FNB, DWT +DBN, Bayesian HCS-multi-SVNN, Fractional CSO +DRNN, and proposed PLA-based Deep CNN are 97.7%, 95.29 percent, 95 percent, and 98 percent, respectively. Using the BraTS 2018 database, the accuracy parameter analysis is shown in Figure 9(c). The equivalent accuracy values measured by Dolphin-SCA + FNB, DWT +DBN, Bayesian HCS-multi-SVNN and Fractional CSO +DRNN and suggested PLA-based Deep CNN are 95.3 percent, 93.20 percent, 92.56 percent, 93.35 percent,

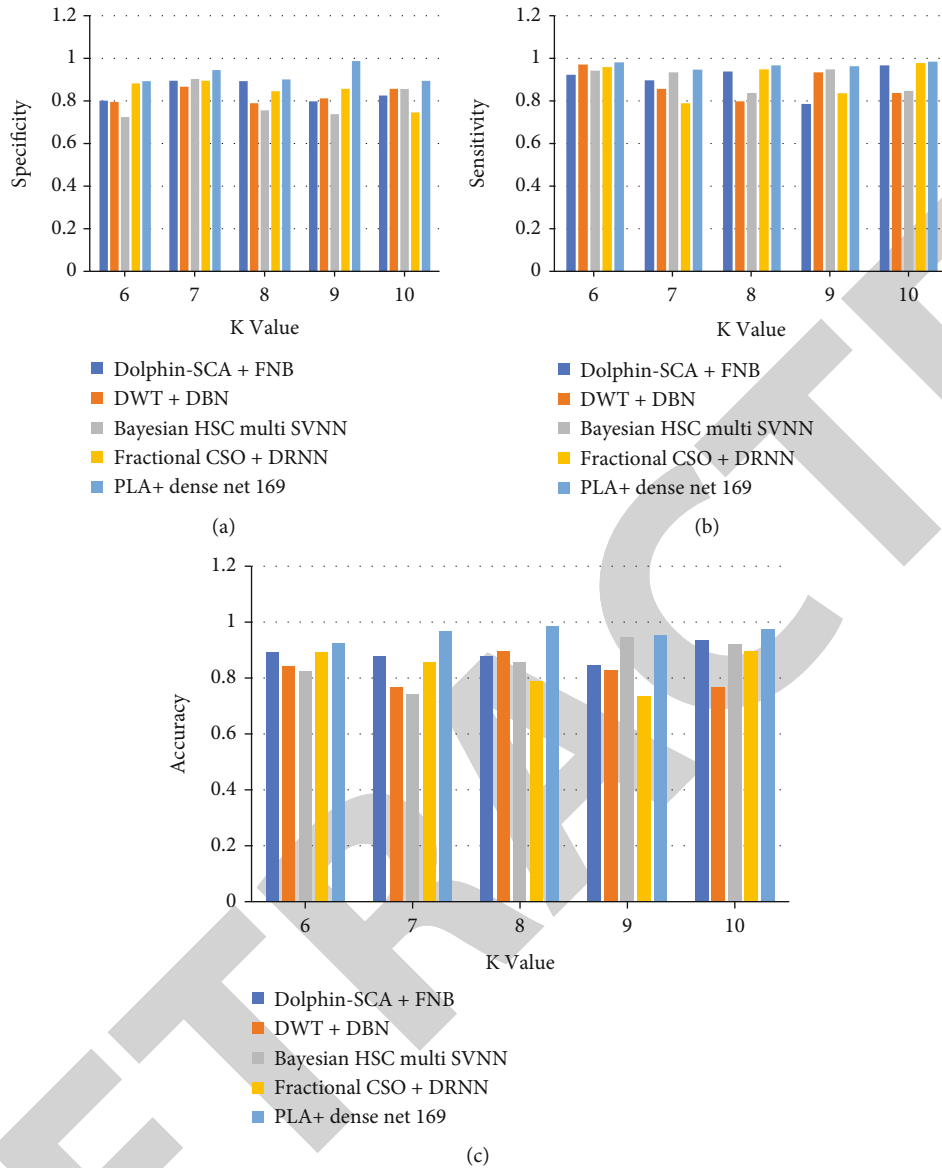


FIGURE 10: Using the BraTS 2018 database, examine the effects of changing K-Fold. (a) Sensitivity, (b) accuracy, and (c) specificity.

and 96.8 percent when the training data percentage is 50. Among the available approaches, the suggested PLA-based Deep CNN has the best accuracy, indicating that it is capable of accurately identifying the tumorous portion.

(ii) Variable K-Fold analysis

Using the BraTS 2018 database, Figure 10 shows a relative investigation plan created on specificity, compassion, and precision characteristics for varied K-Fold values. Figure 10 shows the results of a specificity study for a range of K-Fold values from 2 to 6. (a). Dolphin-SCA + FNB, DWT +DBN, Bayesian HCS-multi-SVNN, and Fractional CSO +DRNN have specificity values of 0.801, 0.795, 0.724, and 0.882, respectively, whereas the suggested PLA-based Deep CNN has a specificity of 0.851 for K – Fold = 2. Using the BraTS database, the examination in relations of the understanding parameter is shown in Figure 10(b).

Dolphin-SCA + FNB, DWT +DBN, Bayesian HCS-multi-SVNN, Fractional CSO +DRNN, and projected PLA-based Deep CNN have sensitivity values of 0.923, 0.971, 0.942, 0.959, and 0.981 when K – Fold = 2. Figure 10 shows the results of the precision parameter study using the BraTS record (c). When K-Fold is equal to 4, the precision values assessed by Dolphin-SCA + FNB, DWT +DBN, Bayesian HCS-multi-SVNN Fine Tuned CNN Fractional CSO +DRNN, and proposed PLA-based Deep CNN are 0.892, 0.843, 0.825, 0.893, and 0.924, respectively.

(iii) ROC-based analysis

After FPR is 0.3, the comparable TPR morals assessed by Dolphin-SCA + FNB, DWT +DBN, Bayesian HCS-multi-SVNN, Fractional CSO +DRNN, and suggested PLA-based Deep CNN are 0.9276, 0.742, 0.845, 0.86, and 0.964. Furthermore, the suggested PLA-based Deep CNN outperforms the

FPR = 0.8, 0.9, and 1 in categorising tumour and nonneoplastic areas with a TPR of 1.

In this paper, a novel enhanced PLA is suggested as a complete technique for brain tumour classification based on optimum feature selection. For the validation of the proposed technique, two BraTS datasets were employed. The preprocessing technology is intended to aid in the categorization of brain tumours in brain imaging. Cristian et al. (2021) presented fractional-chicken swarm optimization (fractional-CSO) as a useful categorization approach. The cancer categorization is carried out once the brain pictures have been preprocessed and the characteristics retrieved efficiently. Using a simulated BraTS dataset, we achieved accuracy, specificity, and sensitivity of 93.35, 96, and 95 percent. For brain tumour diagnosis utilising MR images, Ram-murthy and Mahesh (2020) introduces Whale Harris Hawks Optimization (WHHO), an optimization-driven approach. Maximum accuracy, sensitivity, and specificity for the proposed WHHO-based Deep CNN were 0.816, 0.974, and 0.791, respectively. On a set of benchmark cases, PLA's experimental findings are compared to those of other common optimizers, and the results are confirmed. According to the comparative results in the tables, employing the suggested technique for improving picture feature selection and ML classification produces good results when compared to existing optimization methods.

## 6. Conclusion

In this study, the procedure for lightning attachment (PLA) plus support vector machine (SVM) classifier is proposed as a brain tumour classification method for finding cancer locations from MRI data. Both of these classification methods are combined into one. Both the training and the validation of our proposed architecture made use of the datasets that we acquired, which were referred to as BraTS 2017 and BraTS 2018. Skull stripping, also known as the elimination of nonbrain structure and undesirable aspects of an image obtained from a scanned photograph in order to obtain the necessary imaging for the identification of a tumour, is a technique that is used to remove components that are not requested. In this particular scenario, the preprocessor known as "skull stripping" is utilised. The characteristics are extracted by DenseNet-169, which then produces features that are more general for the deeper network. Following that, the procedure for lightning attachment is used to the feature selection process. This population-based strategy got its start because of the physical phenomena that occur during the lightning attachment technique. These phenomena include air interruption, descending leader movement, ascending leader inception and dispersion, and ultimate leap. Our research utilised a classifier known as a sustainment vector machine (SVM), which brings us to the next stage of the process, which is classification. Because it is a binary classifier that is based on supervised learning, it differentiates between two classes by building a hyperplane in high-dimensional feature space. This allows it to process information in a more efficient manner. The reliability of the system may be improved by increasing the amount of

data points. The process of accurately classifying things may lead to the discovery of other features that are significant in this regard. This computerised method could also be used to categorise other brain diseases in addition to other medical photographs of various pathological situations, types, and states of disease.

## Data Availability

The data shall be made available on request.

## Conflicts of Interest

The authors declare that they have no conflict of interest.

## References

- [1] A. N. Rehman, M. A. Khan, T. Saba et al., "Microscopic brain tumor detection and classification using 3D CNN and feature selection architecture," *Research and Techniques in Microscopy*, vol. 84, no. 1, pp. 133–149, 2021.
- [2] D. Rammurthy and P. K. Mahesh, "Whale Harris Hawks optimization based deep learning classifier for brain tumor detection using MRI images," *Journal of King Saud University - Computer and Information Sciences*, 2022.
- [3] <https://my.clevelandclinic.org/health/diseases/6149-brain-cancer-brain-tumor>.
- [4] S. N. Shivhare and N. Kumar, "Tumor bagging: a novel framework for brain tumor segmentation using metaheuristic optimization algorithms," *Multimedia Tools and Applications*, vol. 80, no. 17, pp. 26969–26995, 2021.
- [5] S. Kumar and D. P. Mankame, "Optimization driven deep convolution neural network for brain tumor classification," *Biocybernetics and Biomedical Engineering*, vol. 40, no. 3, pp. 1190–1204, 2020.
- [6] <https://www.ncbi.nlm.nih.gov/books/NBK441874/>.
- [7] <https://www.cancer.net/cancer-types/brain-tumor/statistics>.
- [8] B. Yin, C. Wang, and F. Abza, "New brain tumor classification method based on an improved version of whale optimization algorithm," *Biomedical Signal Processing and Control*, vol. 56, p. 101728, 2020.
- [9] M. Maha, Y. Abdel-Raheem, K. Salah, and E. Mohamed, "Lightning attachment procedure optimization algorithm for nonlinear non-convex short-term hydrothermal generation scheduling," *Soft Computing*, vol. 24, no. 21, pp. 16225–16248, 2020.
- [10] B. Vilas, A. Narayan, M. Akshatha, P. Tunga, and D. V. Singh, "Automatic brain tumor segmentation using Dense-Net," *International Research Journal of Engineering and Technology (IRJET)*, vol. 7, no. 6, 2020.
- [11] S. Alagarsamy, Y. D. Zhang, V. Govindaraj, M. P. Rajasekaran, and S. Sankaran, "Smart identification of topographically variant anomalies in brain magnetic resonance imaging using a fish school-based fuzzy clustering approach," *IEEE Transactions on Fuzzy Systems*, vol. 29, no. 10, pp. 3165–3177, 2021.
- [12] D. Deb and S. Roy, "Brain tumor detection based on hybrid deep neural network in MRI by adaptive squirrel search optimization," *Multimedia Tools and Applications*, vol. 80, pp. 2621–2645, 2021.
- [13] M. Sharif, J. Amin, M. Raza, M. Yasmin, and S. C. Satapathy, "An integrated design of particle swarm optimization (PSO)

## Retraction

# Retracted: Multiresolution-Based Singular Value Decomposition Approach for Breast Cancer Image Classification

### BioMed Research International

Received 8 January 2024; Accepted 8 January 2024; Published 9 January 2024

Copyright © 2024 BioMed Research International. This is an open access article distributed under the Creative Commons Attribution License, which permits unrestricted use, distribution, and reproduction in any medium, provided the original work is properly cited.

This article has been retracted by Hindawi following an investigation undertaken by the publisher [1]. This investigation has uncovered evidence of one or more of the following indicators of systematic manipulation of the publication process:

- (1) Discrepancies in scope
- (2) Discrepancies in the description of the research reported
- (3) Discrepancies between the availability of data and the research described
- (4) Inappropriate citations
- (5) Incoherent, meaningless and/or irrelevant content included in the article
- (6) Manipulated or compromised peer review

The presence of these indicators undermines our confidence in the integrity of the article's content and we cannot, therefore, vouch for its reliability. Please note that this notice is intended solely to alert readers that the content of this article is unreliable. We have not investigated whether authors were aware of or involved in the systematic manipulation of the publication process.

Wiley and Hindawi regrets that the usual quality checks did not identify these issues before publication and have since put additional measures in place to safeguard research integrity.

We wish to credit our own Research Integrity and Research Publishing teams and anonymous and named external researchers and research integrity experts for contributing to this investigation.

The corresponding author, as the representative of all authors, has been given the opportunity to register their agreement or disagreement to this retraction. We have kept a record of any response received.

### References

- [1] S. Mann, A. K. Bindal, A. Balyan et al., "Multiresolution-Based Singular Value Decomposition Approach for Breast Cancer Image Classification," *BioMed Research International*, vol. 2022, Article ID 6392206, 11 pages, 2022.



## Research Article

# Multiresolution-Based Singular Value Decomposition Approach for Breast Cancer Image Classification

Suman Mann <sup>1</sup>, Amit Kumar Bindal <sup>2</sup>, Archana Balyan <sup>3</sup>, Vijay Shukla <sup>4</sup>,  
Zatin Gupta <sup>5</sup>, Vivek Tomar <sup>6</sup> and Shahajan Miah <sup>7</sup>

<sup>1</sup>Department of Information Technology, Maharaja Surajmal Institute of Technology, New Delhi, India

<sup>2</sup>Department of Computer Science & Engineering, MM Engineering College, MMDU, Mullana, Ambala, India

<sup>3</sup>Department of Electronics and Communication Engineering, Maharaja Surajmal Institute of Technology, New Delhi, India

<sup>4</sup>Department of Computer Science & Engineering, Greater Noida Institute of Technology, Greater Noida, India

<sup>5</sup>School of Computing Science & Engineering, Galgotias University, Greater Noida, Gautam Buddha Nagar, Uttar Pradesh, India

<sup>6</sup>Department of Computer Science & Engineering, KIET Group of Institutions, Delhi-NCR, Ghaziabad, Uttar Pradesh, India

<sup>7</sup>Department of EEE, Bangladesh University of Business and Technology (BUBT), Dhaka, Bangladesh

Correspondence should be addressed to Zatin Gupta; [zatin.gupta2000@gmail.com](mailto:zatin.gupta2000@gmail.com) and Shahajan Miah; [miahbubt@bubt.edu.bd](mailto:miahbubt@bubt.edu.bd)

Received 19 May 2022; Accepted 18 July 2022; Published 11 August 2022

Academic Editor: Gaganpreet Kaur

Copyright © 2022 Suman Mann et al. This is an open access article distributed under the Creative Commons Attribution License, which permits unrestricted use, distribution, and reproduction in any medium, provided the original work is properly cited.

Breast cancer is the most prevalent form of cancer that can strike at any age; the higher the age, the greater the risk. The presence of malignant tissue has become more frequent in women. Although medical therapy has improved breast cancer diagnostic and treatment methods, still the death rate remains high due to failure of diagnosing breast cancer in its early stages. A classification approach for mammography images based on nonsubsampling contourlet transform (NSCT) is proposed in order to investigate it. The proposed method uses multiresolution NSCT decomposition to the region of interest (ROI) of mammography images and then uses Z-moments for extracting features from the NSCT-decomposed images. The matrix is formed by the components that are extracted from the region of interest and are then subjected to singular value decomposition (SVD) in order to remove the essential features that can generalize globally. The method employs a support vector machine (SVM) classification algorithm to categorize mammography pictures into normal, benign, and malignant and to identify and classify the breast lesions. The accuracy of the proposed model is 96.76 percent, and the training time is greatly decreased, as evident from the experiments performed. The paper also focuses on conducting the feature extraction experiments using morphological spectroscopy. The experiment combines 16 different algorithms with 4 classification methods for achieving exceptional accuracy and time efficiency outcomes as compared to other existing state-of-the-art approaches.

## 1. Introduction

Breast cancer is now one of the most common cancers in women. According to the World Health Organization, between 2008 and 2012, breast cancer incidence and mortality have increased by approximately 20% and 14% [1]. Faced with the increasingly severe health situation, technical workers from self-detection activity to medical image-based breast cancer early detection techniques, especially the study of mammograms, manage breast cancer mortality to some extent. However, by X-ray, some of the mammary images obtained by photography will inevitably contain some noise,

such as fatty breast groups that are very close to the gray level of the lesion area organization; it is difficult even for experienced radiologists to accurately identify the type of tumor (benign, malignant, and normal) [2, 3], and in dense breast cases, patients with this type of breast are usually young patients. It can be seen that the research on the classification of adipose breast cancer tumors has strong practical application value and social value.

At present, the classification methods based on mammography images are demonstrated as follows: (1) Feng et al. proposed a method for detecting lesions based on region growth [4]; (2) Hmadian et al. used Z-moments as

the shape which is one of the methods of a shape descriptor [5]; (3) Orel et al. adopted the salient index number to represent the geometry of the lesion boundary [6]; (4) Burriel et al. adopted the strategy of convolutional neural network (CNN) segmentation in the feature extraction stage [7]; and (5) detection and classification by wavelet transform were proposed by researchers and highlight the different methods of mammography.

Because mammograms do not show perfectly the swelling of the outline of the tumor, the first four mentioned above are the most important for classifying the tumor. Both methods require the doctor to manually assign the tumor region to each image. The fifth method proposed by Sidney et al. does not require a manual, but the original breast image is decomposed into a series of subimages with different spatial resolutions and frequency characteristics, reflecting the local variation features of the original breast images. Thus, various feature information can be extracted from different subimages using Z-moments, but the wavelet transform has only three directions of horizontal, vertical, and diagonal detail information and subsamples the original breast image. Therefore, it has a great impact on the contours and linear features of the original breast image. The singularity of the surface is difficult to express well [8].

As an important factor affecting the experimental effect, the classification method chosen should be a good classification method for breast images. Correct classification is the key to the success of the experiment. The obtained experimental data were tested with different classification methods, and the results are compared. It is found that the linear kernel function of support vector machines (SVM) has the best classification effect. But authors did not perform any cleaning work on their data; as a result, the amount of data is large and complex, so choosing a good data cleaning method is also very important.

Because of the mentioned issues, this paper proposes the nonsubsampling contourlet transform (NSCT) method for classifying mammography images. Pretreated lipid NSCT image decomposition of the fatty mammogram is performed to obtain the original breast image. A series of sub images are extracted from the gland image through Z-moments in order to extract features from a large amount of data using the method of value decomposition (singular value decomposition (SVD)) is performed. After cleaning, different classification methods are used to classify them, so it not only reduces the amount of data but also improves the quality of data, making the classification more accurate. Both the accuracy and time efficiency are better than those of the method proposed by previous researchers.

The organization of this paper is as follows: Section 2 is the premap of mammography images which is the preprocessing process; Section 3 introduces the framework of this method; Section 4 is divided into three parts: the first part introduces the nonsubsampling contour transformation method (NSCT) principle and its applications, the second part presents Z-moments, and the third part discusses the classification algorithm of SVM; Section 5 introduces the experimental dataset and presents the experimental results

and analysis; and Section 6 presents the conclusion and scope for future work.

## 2. Preprocessing Process

The following main studies apply mathematical morphology to the mammography image method for preprocessing.

Mathematical morphology is a nonlinear filtering method in image processing. It has four basic operations: dilation, erosion (or invasion eclipse), opening, and closing, which are different in binary and grayscale image features [9–12]. Based on these methods, many mathematical forms can be combined and algorithms can be used to analyze the shape and structure of images for analytical processing, including image segmentation, feature extraction, boundary detection, image filtering, and image enhancement and restoration.

Equations (1) and (2) are corrosion and dilation, respectively, in mathematical expression:

$$\xi_g(f)(u) = \bigcap_{v \in S} f(v) \vee \bar{g}(u - v), \quad (1)$$

$$\xi_g(f)(u) = \bigcup_{v \in S} f(v) \vee g(u - v), \quad (2)$$

where  $f : S \rightarrow [0, 1]$  and  $g : S \rightarrow [0, 1]$  are normalized single spectral images,  $S \subseteq Z^2$ , the symbols  $\bigcup$  and  $\vee$  are associated with the max operation, the symbols  $\bigcap$  and  $\wedge$  are associated with the min operation, and  $\bar{g}(u) = 1 - g(u)$ . For  $\forall u \in S$ ,  $g : S \rightarrow [0, 1]$  are the corresponding erosion and dilation structuring elements [9–12].

Combining the mathematical expressions for erosion and dilation, one can get open. The mathematical expression  $\gamma_g(f)(u)$  uses the original erosion-and-dilation reason. Next, consider the normalized single spectral image  $f : S \rightarrow [0, 1]$  by the structure element  $g : S \rightarrow [0, 1]$ , the remaining area generated by the  $k$ th opening operation. The mathematical expression for ( $k \geq 0$ ) is

$$V(k) = \sum_{v \in S} \gamma_g^k(f)(u). \quad (3)$$

Through the above description of the basic operations of mathematical morphology, expression (4) is obtained (the discrete cumulative density function):

$$E[k] = 1 - \frac{V(k)}{V(0)}. \quad (4)$$

The discrete density function, also known as mode spectrum or morphological spectrum, is described by equation (5) [12]. Learning about its preservation through morphological theory proves that each binary image has a unique representation based on that spectrum because this pattern or morphological spectrum can be used as an exact shape-based feature extractor and the mode spectrum has negligible mammary irregularities at the edges of the mass leading to low-amplitude changes in the morphological spectrum

ability and its ability to function as a tumor regardless of tumor size which is nothing but a unique representation of a shape. This is the reason for the preprocessing method of the adrenal X-ray images. Reflecting the histopathological complexity of adrenal glands, the classification of adrenal lesions may be complex [13–15]. Lesions of the adrenal gland can be roughly classified as either primary or secondary. Primary adrenal lesions, that is, lesions originating from the adrenal gland itself, can be cortical or medullary in origin. Lesions of the adrenal glands can also be classified according to their laterality, that is, as unilateral or bilateral [16]. Additionally, bilateral lesions might develop with syndromes of hormone excess or insufficiency. It complements functional imaging and hormonal analysis in the diagnosis of functioning tumors [17]. The role of adrenal X-ray imaging is to differentiate between benign and malignant lesions and to provide diagnosis wherever possible [18].

$$\xi_g[k] = E[k + 1] - E[k]. \quad (5)$$

To calculate the morphological spectrum of an image, one has to perform equation (5) until the algorithm converges. Different mammograms in the database at different times of iterative calculations are required to obtain the morphological spectral results in order to avoid the problem of different morphological spectrum sizes; 7 systems will be used as metrics to represent these spectra, i.e., mean, standard deviation, mode, median value, kurtosis, min, and max.

### 3. Introduction to the Framework

The following describes the feature extraction and classification framework.

Methods for classifying breast lesions from mammography images are highly dependent on the feature extraction stage. This paper uses a hybrid approach that combines NSCT and Z-moments. The overall framework of the feature extraction method is shown in Figure 1. The combination of multiresolution NSCT and Z-moments can be mixed. Texture and shape features are used to improve image representation in the classification stage.

Mammography is the preferred method for early detection of breast cancer; nevertheless, only a few specialists have difficulties interpreting mammography images [19]. Classification of mammography images to normal, benign, and malignant is highly dependent on the feature extraction stage which is done through the NSCT method [20]. Feature extraction is done in two stages: in the first stage, the region of interest as an input image for subsampled pyramid filter banks (NSPFB) is decomposed into low-pass subband images (LSI) and bandpass subband image (BSI) to achieve multiscale decomposition of the image [21]. Then, the non-subsampled directional filter bank (NSDFB) is used to decompose the BSI into the multidirectional subband image and use the bandpass directional subband image (BDSI), so that the multidirectional decomposition of the image can be realized for mathematical morphology, and the procedure is repeated.

The operation is to obtain a multilayer NSCT of the input image [22] which is a raw breast. The X-ray image is decomposed by the NSPFB to the first scale in order to get the images LSI1 and BSI2. Then, the image is obtained by NSPFB decomposition of the second scale LSI2 and BSI2 and so on.

If  $BSI_n (n \in 1, 2, \dots, n)$  is decomposed in the  $m$ -level direction; that is,  $2m$   $m$ -level BDSIs with the same size as the original image can be obtained, called for BDSIm. The original X-ray image can be decomposed by  $J$ -slice NSCT. Get 1 LSI $J$  and  $\sum_{j=1}^J 2^{m_j}$  BDSIs, where  $m_j$  is the scale  $j$  direction series below.

According to the above description, several concepts can be defined here:

*Definition 1* (low-pass subband image (LSI)).

$$LSI_i = H_0(LSI_{(i-1)}), \quad i \in \{1, 2, \dots\}, \quad (6)$$

where LSI $_i$  represents the LSI decomposed by the  $i$ th scale NSPFB, and when  $i = 1$ , LSI $_0$  represents the original mammogram; the function  $H_0(z)$  is the bandpass decomposition of the two-channel nonsubsampling filter bank (NSPFB) waver.

*Definition 2* (bandpass subband image (BSI)).

$$BSI_i = H_1(LSI_{(i-1)}), \quad i \in \{1, 2, \dots\}, \quad (7)$$

where BSI $_i$  represents the BSI decomposed by the  $i$ th scale NSPFB, and when  $i = 1$ , LSI $_0$  represents the original mammogram; the function  $H_1(z)$  is the bandpass decomposition of the two-channel nonsubsampling filter bank (NSPFB) waver.

According to the above description and previous research results, this multipoint high-resolution image decomposition method can effectively detect breast lesions, suspicious lesions, and breast tissue successfully [22].

The second stage will use the Z-moments obtained in the first stage; the subgraph of the feature extraction method has been widely used in the shape analysis of lesions [6, 23] because the shape is important for determining breast cancer lesions; the degree of malignancy is critical [24]. For every raw milk, 32 high-dimensional subimages are extracted from the decomposition of the gland X-ray image, so a raw mammogram can be extracted to 480 eigenvalues, as shown in Figure 1.

Finally, the extracted 480 eigenvalues are decomposed by SVD for feature reduction to obtain features with smaller dimensions but can generalize the global quality. Because the learning of a classifier is typically a time-consuming process that may entail numerous iterations of training data [25], cross-validation paired with different random beginning conditions and testing of various kernels (learning functions) were carried out, and the more significant the amount of data, the more time-consuming it will be. Therefore, the SVD method is used in this paper to extract

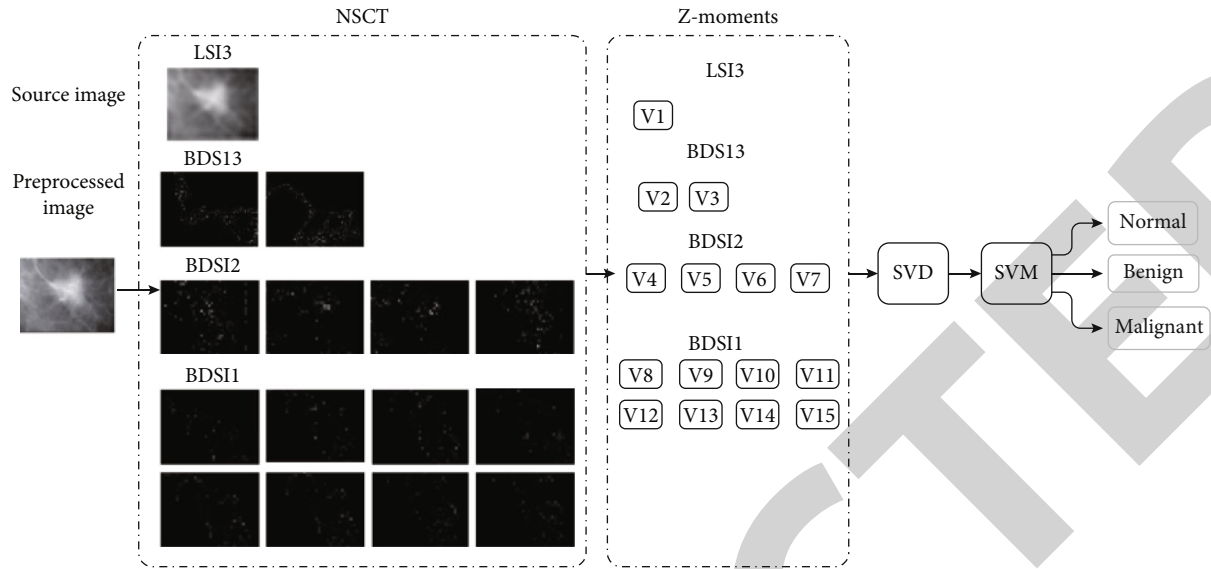


FIGURE 1: Overall frame.

essential features that can generalize globally, thereby reducing the amount of data and time consumption.

The above is an introduction to the framework shown in Figure 1, and compared with the state-of-the-art methods, it achieves both accuracy and time efficiency with remarkable result.

#### 4. Feature Extraction Stage

The process of feature extraction is based on NSCT and the construction of Z-moments and the classification algorithm flow of SVM.

**4.1. Feature Extraction Based on NSCT.** NSCT was proposed by Cunha et al. in 2005. Shift-invariant contour transform [26] is based on NSPFB, and NSDFB transformation of both methods is described in detail below.

**4.2. Nonsubsampling Tower Filters.** The nonsubsampling tower filter (NSPFB) differs from a number proposed by Do and Vetterli that can better represent two-dimensional signals (learning tools—Laplacian pyramid (LP) multiscale analysis in the contour transformation method) [27]. Because of LP multiscale segmentation, both analysis and discrete wavelet transform are used when decomposing the original mammogram. Using downsampling, results in multiscale decomposition of low-frequency images and high-frequency images do not have the size of the original image. The downsampling process will be distorted in the filter, so using LP multiscale, neither the solution nor the discrete wavelet transforms lack translation invariance. While the NSPFB cancels the downsampling operation of the signal during its decomposition, the wave filter performs the corresponding upsampling (interpolation) operation, reducing the original milk distortion of glandular radiographs during multiscale decomposition.

Figure 2 shows the decomposition process of a three-layer NSPFB [27]. As can be seen from Figure 2, each mam-

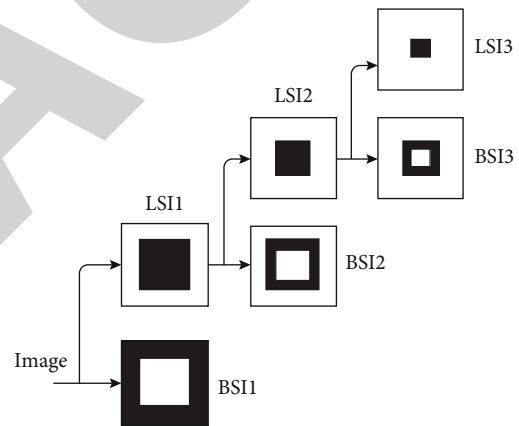


FIGURE 2: NSPFB decomposition process.

mogram is processed by NSPFB. Decompose it into images of different scales. The first scale decomposition gets LSI1 and BSI1, the second scale decomposition gets LSI2 and BSI2, and so on.

**4.2.1. Nonsubsampling Directional Filters.** The nonsubsampling directional filter (NSDFB) is a two-channel filter bank, whose main function is to perform the BSI obtained by NSPFB tree structure decomposition. And if the BSI passes through an  $l$ -ary tree structure decomposition, effectively divide the signal into  $2l$  subbands whose frequency bands are divided into wedges. The discrete wavelet transform can also perform this process, but it is far from scatter wavelet transform which can only extract detail images in horizontal, vertical, and diagonal directions, while NSDFB can extract detail images in multiple directions. Each orientation sub map obtained by NSDFB is larger than the original breast image and is same as all bandpass divisors which is different from the discrete wavelet transform. The sum of the images is equal to the original image.

*Definition 3* (band pass direction subband image (BDSI)).

$$BDSI1 = \{U_0(BSIj) + U_1(BSIj)\}, \quad j = \{1, 2, \dots\}. \quad (8)$$

This means that a 1-level directional decomposition of  $BSI_j$  will result in 2 BDSI1s.

$BSI_j$  represents the BSI decomposed by the  $j$ th scale NSPFB.  $BSI_j$  performs 2-level directional decomposition; then, 4 BDSI2 are obtained, whose expression formula is

$$BDSI2 = \left\{ \begin{array}{l} U_0(U_0(BSIj)) + U_1(U_0(BSIj)) + \\ U_0(U_1(BSIj)) + U_1(U_1(BSIj)) \end{array} \right\}, \quad j \in \{1, 2, \dots\}. \quad (9)$$

The decomposition of  $BSI_j$  in the  $m$ -level direction is carried out and so on.

As shown in Figure 3, it is shown that different methods are used for different scales of BSI, the process of decomposition; because  $BSI1$  is compared with other  $BSI_i$  ( $i \neq 1$ ), in its graph, the structure, outline, and texture of the image are the clearest, and the details of the original image are more clear. It is similar, so it is decomposed in 3-level direction to get 8 BDSI3;  $BSI2$  performs 2-level tree structure decomposition to obtain 4 BDSI2 and  $BSI3$ .

Perform 1-level tree structure decomposition to get 2 BDSI1, and the last LSI3, which is most similar to the original image, does not perform tree-like segmentation solution; the Zernike moment can be directly constructed [27].

**4.3. Constructing Zernike Moments.** LSI3 and all BDSI1 and both BDSI2 and BDSI3 are used to construct Z-moments. Enter an image. Each original image expanded after being decomposed by NSCT has 15 subgraphs, and each subgraph can be constructed with 32 Z-moments of the value. The calculation process of Z-moments consists of 3 steps: calculation of radial polynomial, calculation of Zernike basis functions, and calculation of Z-moments that project images onto Zernike basis functions.

The process of obtaining Z-moments starts at Zernike calculation of radial polynomials. Real-valued one-dimensional radial polynomial  $R_{n,m}$  is defined as

$$R_{n,m} = \sum_{s=0}^{(n-|m|)/2} (-1)^s \frac{(n-s)!}{s!((n-|m|)/2-s)!((n-|m|)/2-s)!} \rho^{n-2s}, \quad (10)$$

where  $n$  is a nonnegative integer;  $m$  is an integer such that  $n - |m| = \text{even number}$  and  $|m| \leq n$ ; and  $\rho$  is the length from the origin to the vector  $(x, y)$ .

According to formula (10), the complex-valued two-dimensional Zernike defined by the unit circle basis function is

$$V_{n,m}(\rho, \theta) = R_{n,m}(\rho)e^{jm\theta}, \quad |\rho| \leq 1. \quad (11)$$

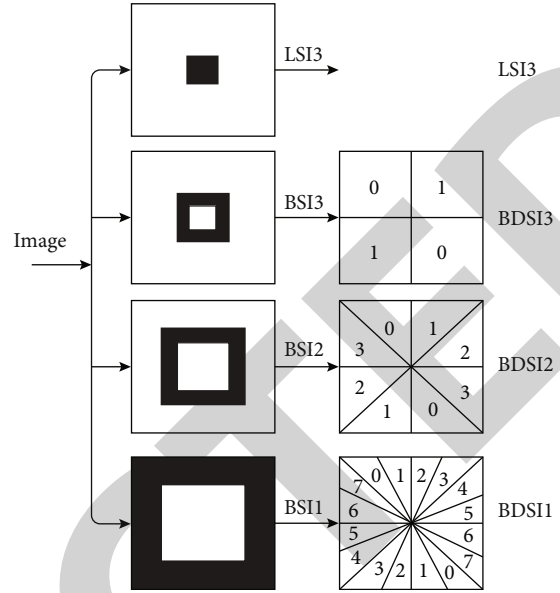


FIGURE 3: NSDFB decomposition process.

The complex-valued two-dimensional Zernike polynomials satisfy the following orthogonal conditions:

$$\int_0^{2\pi} \int_0^1 V_{n,m}^*(\rho, \theta) V_{p,q}(\rho, \theta) \rho d\rho d\theta = \begin{cases} \frac{\pi}{n+1}, & n=p, \quad m=q, \\ 0, & \text{else.} \end{cases} \quad (12)$$

Among them,  $*$  represents a conjugated complex number. As mentioned earlier, orthogonality means that the image information of different moments formed by different  $n$  and  $m$  combinations is nonredundant. The rest are non-overlapping. Using this property, the contribution from every combination is made unique and invariant of the data in the image [28]. In fact, different combinations exist. All features have the same importance. In a composite of  $n, m$  Z-moments are defined as

$$Z_{n,m} = \frac{n+1}{\pi} \int_0^{2\pi} \int_0^1 f(\rho, \theta) V_{n,m}^*(\rho, \theta) \rho d\rho d\theta, \quad (13)$$

where  $f(c, r)$  is the image function, and equation (13) is for digital images. The integral can be exchanged with the summation. Also, the image coordinates must be adjusted to  $[0,1]$  using mapping transformation. Figure 4 depicts the mapping transformation of the original image. Elements do not participate in the calculation of Z-moments.

The discrete formal representation of Z-moments of an image is as follows:

$$\begin{aligned} Z_{n,m} &= \frac{n+1}{\lambda\pi} \sum_{c=0}^{N-1} \sum_{r=0}^{N-1} f(c, r) V_{n,m}^*(c, r) \\ &= \frac{n+1}{\lambda\pi} \sum_{c=0}^{N-1} \sum_{r=0}^{N-1} f(c, r) R_{n,m}(\rho_{c,r}) e^{-jm\theta_{c,r}}, \end{aligned} \quad (14)$$

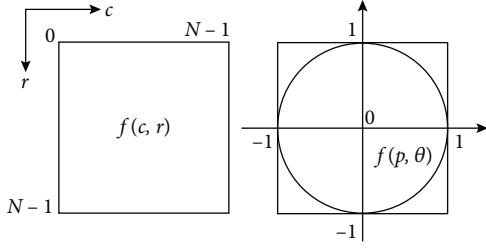


FIGURE 4: Original image normalized map.

where  $0 \leq \rho_{cr} \leq 1$  and  $\lambda\pi$  are normalization factors, in Z-moments. Transform distance  $\rho_{cr}$  and phase  $\theta_{cr}$  at pixel  $(c, r)$  are given by the following formula [27]. Note that  $c$  and  $r$  represent the number of columns and rows.

$$\begin{cases} \rho_{cr} = \frac{\sqrt{(2c - N + 1)^2 + (2r - N + 1)^2}}{N}, \\ \theta_{cr} = \tan^{-1}\left(\frac{N - 1 - 2r}{2c - N + 1}\right). \end{cases} \quad (15)$$

Using equations (14) and (15), we get only  $c$ ,  $r$ ,  $m$  and  $n$  in the final equation of the function. In fact, if the image ROI (region of interest) area has an odd number of rows and columns, it will have focal points as follows:

$$(c, r) = \left(\frac{N-1}{2}, \frac{N-1}{2}\right). \quad (16)$$

Combining equations (15) and (16), the following initial values can be obtained:

$$\begin{cases} \rho_{cr} = 0, \\ \theta_{cr} = \tan^{-1}\left(\frac{0}{0}\right) = \text{Nan}. \end{cases} \quad (17)$$

This paper chooses high-order Z-moments, although compared to low-order Z-moments, higher-order Z-moments not only have higher computational complexity degrees but also higher sensitivity to noise, so if there is no precise selection, system performance may degrade. However, due to the fact that high-order Z-moments describe shapes better than lower-order Z-moments and edge features, in order to more accurately analyze the contour of the image, this paper selects high-order Z-moments.

By the values of  $n$  and  $m$  given in Table 1, it can be obtained from each low-frequency map, Z-moments consisting of 32 values are obtained from images or high-frequency images.

**4.4. Classification of Support Vector Machines.** There are many classification algorithms; this paper uses a support vector machine (SVM) classification method, because through experimental analysis, the classification effect of using SVM is the most. And through the feature extraction process of Z-moments, each original features are considered. The original mammogram has  $32 \times 15 = 480$  features, but not all

TABLE 1: Higher-order Z-moment values of  $n$  and  $m$ .

$n$	$m$	Z-moment quantity
10	2,6,10	32
11	3,7,11	
12	0,6,8,10	
13	1,5,7,13	
14	2,6,8,16	
15	3,7,9,15	
16	0,2,4,14,16	
17	1,5,9,15,17	

features are useful for image classification, so use the SVD method to reduce features and extract features that can represent more than 95% of the population. The top  $K$  values of the image information were obtained. This reduces the amount of data and shortens the classification training time, and the classification accuracy is improved. The idea of SVM is to map the input vector to a high-dimensional feature space, and then, the optimal classification surface is constructed in this high-dimensional space, which is originally linear and inseparable. The problem is transformed into a linearly separable one in high-dimensional space. At the same time, to avoid the ‘‘curse of dimensionality’’ from occurring, the kernel function  $K(x_i, x_j) = \phi(x_i)\phi(x_j)$  generation substitutes the inner product operation.

SVM cleverly solves high-dimensional and nonlinear problems and has good generalization, and there is a unique solution. Algorithm 1 is the algorithm flow of SVM.

## 5. Experimental Setup and Result Analysis

**5.1. Dataset.** This article uses the 255 IRMA database of fatty breast tissue images, including 233 normal cases (no lesions), 72 benign cases, and 83 malignant cases [10]. The IRMA dataset documentation not only is detailed but also introduces the scanning methods for each mammography imaging and whether the imaging direction is the right breast or the left breast; the breast lesions are determined according to the standard classification of BIRADS: benign, malignant, and normal [24]. However, artifacts are often present in mammograms, such as by finger common grooves and grease caused by striations, which will make the image processing difficult. The IRMA database is selected through the use of specialized clinical knowledge; select a region of interest (ROI) to avoid these situations. Figure 5 shows the 8 original breast images in IRMA with left and right sides and a comparison chart in the same direction. The IRMA medical image database also provides mammograms for calcifications, structural distortions, and asymmetries [29]. However, this paper only deals with mammograms that deal with fatty breast tissue picture. Additionally, using the IRMA database for classification applications, the dataset must also be balanced, so this experiment also synthesized 161 good sex cases and 150 malignant instances. The synthetic method is based on real graphs.

Input: The feature dataset  $Fc = \{zm1, zm2, \dots, zmn\}$  obtained after preprocessing, feature extraction and SVD decomposition of mammography images.  
 Output: category of mammogram (normal, benign, malignant); training time (Train-time), prediction time (Test-time), prediction accuracy.  
 (Test-rate).  
 1. For ( $i = 1; i < n; i++$ )  
 2. Read ( $zmi$ )  
 3. Split ( $Fc$ ) is the training set (Train  $Fc$ ) and the test set (Test  $Fc$ )  
 4. For Train  $Fc$ , let it be used as the input data of the SVM model.  
 Train, calculate Train-time and output  
 5. Based on the trained SVM model, take Test  $Fc$  as input, and input  
 Find out the category to which these Test  $Fc$ s should belong, calculate and output Test-time  
 6. Output the Test-rate between the predicted class and the true class.

ALGORITHM 1: SVM-based classification method.

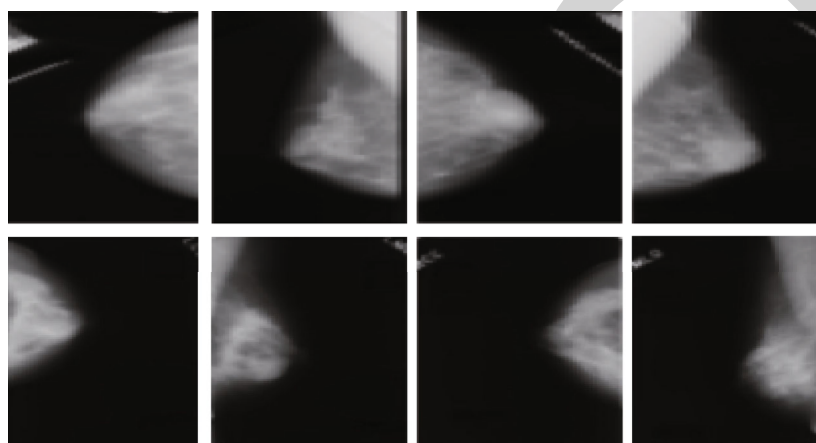


FIGURE 5: Original breast image.

Cancer develops when healthy breast cells change and expand uncontrollably, forming a mass or sheet of cells known as a tumor. A tumor may be cancerous or benign. A malignant tumor is one that can grow and spread to other areas of the body. A benign tumor is one that is able to develop but has not spread. This covers both noninvasive breast cancer (stage 0) and locally progressed and early-stage invasive breast cancer (stages I, II, and III) [21]. The breast cancer stage describes the size and spread of the tumor. Although breast cancer typically spreads to nearby lymph nodes, in which case it is still considered a local or regional disease, it can also move through the blood arteries and/or lymph nodes to the bones, lungs, liver, and brain. This is the most advanced stage of breast cancer, defined as stage IV or metastatic illness. However, lymph node involvement alone is often insufficient to diagnose breast cancer at stage IV [30].

**5.2. Experimental Results and Analysis.** To validate the classification method of NSCT-based mammography images, this paper mainly compares the experimental results of authors. Therefore, the experiment uses different classifiers or the same classification with different kernel functions of the processor, combining various processing processes to form a ratio that is more experimental.

Table 2 lists various experimental methods. Among them, the experimental formula and black method is the combination method proposed in this paper; there are 4 kinds in total, and the next will be based on these 4 types that are used to analyze experimental results.

**5.2.1. Analysis of Test Set Accuracy.** Based on the 16 experimental schemes in Table 2, this paper first considers the accuracy of the test set classification results, which can also intuitively explain that this paper method outperforms other methods.

As can be seen from Figure 6, for the kernel function of SVM, whether it is using linear, polynomial, RBF, or decision trees, the accuracy of the methodology is higher. For Sidney's 3 different discrete wavelet transforms, choosing the effect of Symlet8 waves is best among various classification methods. In addition, for this experiment, the kernel function of SVM has better performance when choosing linear and polynomial. Experimental results are good, and the experimental results of the linear kernel function are better. Table 3 shows the accuracy of the test set.

**5.2.2. Temporal Analysis of the Training Set.** While focusing on experimental accuracy, time efficiency is also an ignored metric. A good classification method needs to

TABLE 2: Experimental methods.

Method name	Classification	Feature extraction	Image decomposition
SVM11	SVM linear	Higher-order Zernike moments, SVD	NSCT
SVM12	SVM linear	Low-order Zernike moments	Biorthogonals3.8
SVM13	SVM linear	Low-order Zernike moments	Daubechies9
SVM14	SVM linear	Low-order Zernike moments	Symlet9
SVMp5	SVM polynomial	Higher-order Zernike moments, SVD	NSCT
SVMp6	SVM polynomial	Low-order Zernike moments	Biorthogonals3.8
SVMp7	SVM polynomial	Low-order Zernike moments	Daubechies9
SVMp8	SVM polynomial	Low-order Zernike moments	Symlet9
SVMR9	SVM RFB	Higher-order Zernike moments, SVD	NSCT
SVMR10	SVM RFB	Low-order Zernike moments	Biorthogonals3.8
SVMR11	SVM RFB	Low-order Zernike moments	Daubechies9
SVMR12	SVM RFB	Low-order Zernike moments	Symlet9
DT13	Decision tree	Higher-order Zernike moments, SVD	NSCT
DT14	Decision tree	Low-order Zernike moments	Biorthogonals3.8
DT15	Decision tree	Low-order Zernike moments	Daubechies9
DT16	Decision tree	Low-order Zernike moments	Symlet9

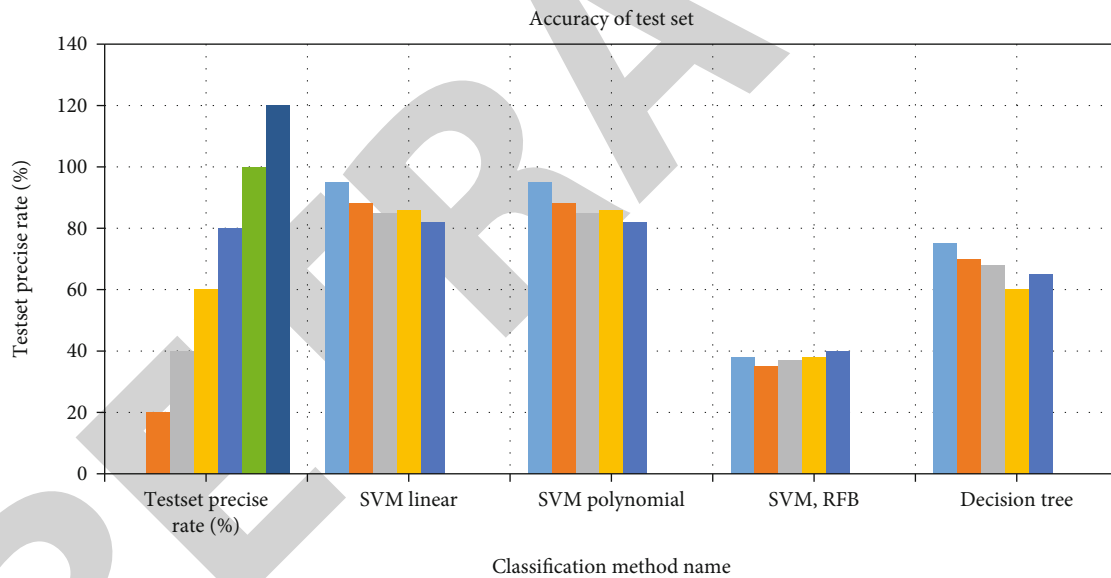


FIGURE 6: Graphical analysis of accuracy of the test set.

TABLE 3: Accuracy of the test set.

Test set precise rate (%)	SVM linear	SVM polynomial	SVM RFB	Decision tree
0	95	95	38	75
20	88	88	35	70
40	85	85	37	68
60	86	86	38	60
80	82	82	40	65

comprehensively consider accurate rate and time efficiency, balancing the two indicators to maximize the classification effect. It is more likely to be applied in practice if it is excellent. Figure 7 and Table 4 give training time for various classification methods. It can be seen from Figure 7 that no matter which kind of classification method is adopted in this paper (class methods), the training time required for the training set is significantly lower than that of Sidney et al. who proposed 3 types of wavelet transforms. The reason is that unlike the method proposed by Sidney et al., the method in this paper performed first the singular value decomposition of the data, instead of directly using the resulting data as input to various classifiers, thereby reducing the



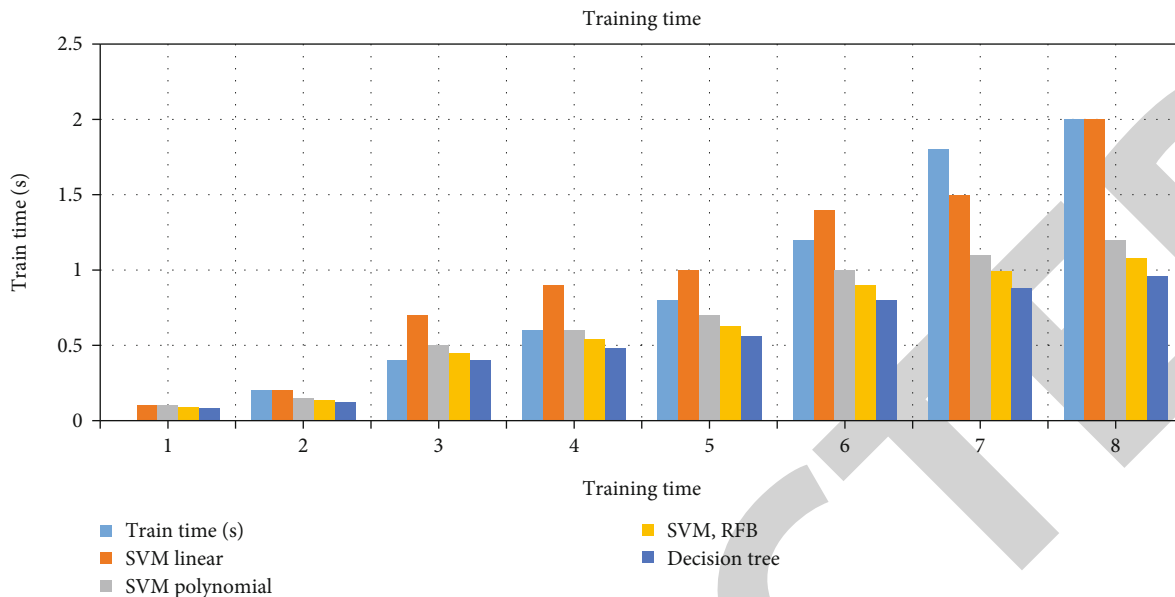


FIGURE 7: Graphical analysis of training time.

TABLE 4: Training time.

Train time (s)	SVM linear	SVM polynomial	SVM RFB	Decision tree
0	0.1	0.1	0.09	0.08
0.2	0.2	0.15	0.135	0.12
0.4	0.7	0.5	0.45	0.4
0.6	0.9	0.6	0.54	0.48
0.8	1	0.7	0.63	0.56
1.2	1.4	1	0.9	0.8
1.8	1.5	1.1	0.99	0.88
2	2	1.2	1.08	0.96

dimension of the data and improving the efficiency of training time. Therefore, the method in this paper is to a certain extent practical.

In conclusion, 16 experimental methods of 4 types are implemented in this paper in the method, whether it is the experimental method proposed in this paper or literature. The proposed experimental method, the linear kernel function method of SVM, has achieved the best classification effect. And for the exploit proposed by literature, discrete wavelet transform decomposes images and also does a small comparative experiment of wave transform, and the experimental effect is expressed; Sidney et al. proposed the Symlet8-type discrete wavelet transform which has the best experimental results, but it is not as good as the NSCT method proposed in this paper. It is mainly due to the high-order Zernike moments which are used in the feature extraction stage, which are better than those of the authors. The low-order Zernike moments used by humans can extract more representative milk features of glandular X-ray images and be decomposed by SVD to make the

features more representative, the amount of data is greatly reduced, and the time efficiency is also greatly improved.

The proposed algorithm has been compared with the current state-of-the-art techniques. The methods include Biorthogonals3.8, Daubechies9, and Symlet9. The classification techniques used are SVM linear, SVM polynomial, SVM RFB, and decision tree. The accuracy of the proposed methodology is higher, i.e., 96.76%. It is also evident from the results obtained that the kernel function of SVM has better performance when choosing linear and polynomial.

## 6. Conclusion

This paper presents a classification method of mammography images based on NSCT. The method first decomposes the region of interest of the mammography image into multiresolution submaps through NSCT decomposition and then uses the Nick moment to extract the features in the subgraph, and in the data preprocessing stage, singular value decomposition is selected to reduce the features, so as to extract important features that can generalize globally. The method in this paper combines texture and shape features and uses an SVM-based classification algorithm to classify mammography images into normal, benign, and malignant and realizes the detection and classification of breast lesions. Taking into account the BIRADS criteria, this paper defines the categories of interest as normal (undamaged breast tissue), benign, and malignant lesions. Through the theoretical basis of mathematical morphology, it is proven that the mode spectrum is the ideal and unique shape representation of the binary image. And this paper also conducts feature extraction experiments using morphological spectroscopy and evaluates them. The experimental procedure combines 16 different algorithms of 4 types of classification methods.

More difficult mammography images such as dense, extremely dense, and fibroglandular breast tissue can be processed to a large extent based on the ideas of the method in this paper. With future improvements, it can also be applied to other forms of cancer diagnosis or other related biomedical image classification problems, such as brain magnetic resonance imaging, immunohistochemical images, and other complex image analysis problems where both morphology and texture are essential. The overall accuracy of the classification method in this paper is high, and the training time is relatively low, which is convenient for rapid promotion and helps doctors accurately diagnose the disease.

## Data Availability

The data shall be made available on request.

## Conflicts of Interest

The authors declare that they have no conflict of interest.

## References

- [1] F. Pak, H. R. Kanan, and A. Alikhassi, "Improvement of benign and malignant probability detection based on non-subsample contourlet transform and super-resolution," in *2014 22nd International Conference on Pattern Recognition*, pp. 895–899, Stockholm, Sweden, August 2014.
- [2] X. Jia, W. Meng, S. Li, Z. Tong, and Y. Jia, "A rare case of intracystic Her-2 positive young breast cancer," in *2021 IEEE International Conference on Bioinformatics and Biomedicine (BIBM)*, pp. 2598–2602, Houston, TX, USA, December 2021.
- [3] S. Ghoul, D. M. K. Nashawati, M. A. Hamaly, S. Mutlaq, A. Mansour, and A. Nofal, "Streamlining the interventional breast imaging workflow by lean methodology implementation," in *2018 1st International Conference on Cancer Care Informatics (CCI)*, pp. 41–46, Amman, Jordan, November 2018.
- [4] X. Feng, L. Song, S. Wang et al., "Accurate prediction of neoadjuvant chemotherapy pathological complete remission (pCR) for the four sub-types of breast cancer," *IEEE Access*, vol. 7, pp. 134697–134706, 2019.
- [5] A. A. Hmaidan, E. Boutou, K. Jamal, and A. Al-Omari, "Availability and usability of the hospital-based cancer registry data for measuring the quality outcome indicators of healthcare provided to breast and colorectal cancer patients at King Hussein Cancer Center," in *2018 1st International Conference on Cancer Care Informatics (CCI)*, pp. 195–204, Amman, Jordan, November 2018.
- [6] V. E. Orel, O. Rykhalskyi, L. Syvak et al., "Computer-assisted inductive moderate hyperthermia planning for breast cancer patients," in *2020 IEEE 40th International Conference on Electronics and Nanotechnology (ELNANO)*, pp. 474–477, Kyiv, Ukraine, April 2020.
- [7] V. Burriel, O. Pastor, M. Peña-Chilet, M. T. Martínez, and G. Ribas, "Conceptual schema of miRNA's expression: using efficient information systems practices to manage and analyse data about miRNA expression studies in breast cancer," in *2016 IEEE Tenth International Conference on Research Challenges in Information Science (RCIS)*, pp. 1–2, Grenoble, France, June 2016.
- [8] B. Bilgiç, "Comparison of breast cancer and skin cancer diagnoses using deep learning method," in *2021 29th Signal Processing and Communications Applications Conference (SIU)*, pp. 1–4, Istanbul, Turkey, June 2021.
- [9] A. Easson, A. Pandya, J. Pasternak, N. Mohammed, and A. Douplik, "Improving the patient cancer experience: multi-spectral (white light/autofluorescence/Raman) needle endoscopy for cancer diagnostics in breast and thyroid," in *2020 Photonics North*, pp. 1–2, Niagara Falls, ON, Canada, May 2020.
- [10] M. Mahrooghy, A. B. Ashraf, D. Daye et al., "Pharmacokinetic tumor heterogeneity as a prognostic biomarker for classifying breast cancer recurrence risk," *IEEE Transactions on Biomedical Engineering*, vol. 62, no. 6, pp. 1585–1594, 2015.
- [11] A. Tripathi and K. Misra, "Stilbene analogues as inhibitors of breast cancer stem cells through P-glycoprotein efflux; a 3D quantitative structure-activity relationship study (inhibitory activity of stilbenes analogues on breast cancer stem cells)," in *2016 International Conference on Bioinformatics and Systems Biology (BSB)*, pp. 1–4, Allahabad, India, March 2016.
- [12] C. Keatmanee, S. S. Makhanov, K. Kotani, W. Lohitvisate, and S. S. Thongvigitmanee, "Automatic initialization for active contour model in breast cancer detection utilizing conventional ultrasound and color Doppler," in *2017 39th Annual International Conference of the IEEE Engineering in Medicine and Biology Society (EMBC)*, pp. 3248–3251, Jeju, Korea (South), July 2017.
- [13] M. Shabaz and U. Garg, "Predicting future diseases based on existing health status using link prediction," *World Journal of Engineering*, vol. 19, no. 1, pp. 29–32, 2021.
- [14] S. Reis, P. Gazinska, J. H. Hipwell et al., "Automated classification of breast cancer stroma maturity from histological images," *IEEE Transactions on Biomedical Engineering*, vol. 64, no. 10, pp. 2344–2352, 2017.
- [15] C. Wu, P. Lu, F. Xu, J. Duan, X. Hua, and M. Shabaz, "The prediction models of anaphylactic disease," *Informatics in Medicine Unlocked*, vol. 24, article 100535, 2021.
- [16] S. C. Hagness, A. Taflove, and J. E. Bridges, "Two-dimensional FDTD analysis of a pulsed microwave confocal system for breast cancer detection: fixed-focus and antenna-array sensors," *IEEE Transactions on Biomedical Engineering*, vol. 45, no. 12, pp. 1470–1479, 1998.
- [17] S. Chopra, G. Dhiman, A. Sharma, M. Shabaz, P. Shukla, and M. Arora, "Taxonomy of adaptive neuro-fuzzy inference system in modern engineering sciences," *Computational Intelligence and Neuroscience*, vol. 2021, Article ID 6455592, 4 pages, 2021.
- [18] T. Botterill, T. Lotz, A. Kashif, and J. G. Chase, "Reconstructing 3-D skin surface motion for the DIET breast cancer screening system," *IEEE Transactions on Medical Imaging*, vol. 33, no. 5, pp. 1109–1118, 2014.
- [19] Y. Hu, A. Sharma, G. Dhiman, and M. Shabaz, "The identification nanoparticle sensor using back propagation neural network optimized by genetic algorithm," *Journal of Sensors*, vol. 2021, Article ID 7548329, 12 pages, 2021.
- [20] N. Sharma and C. Chakraborty, "Evaluation of bioinspired algorithms for image optimization," *Journal of Electronic Imaging*, vol. 31, no. 4, article 041206, 2022.

## Retraction

# Retracted: The Optos 200Tx Scanning Laser Ophthalmoscope Application in Retinoblastoma Patients' Follow-Up

### BioMed Research International

Received 8 January 2024; Accepted 8 January 2024; Published 9 January 2024

Copyright © 2024 BioMed Research International. This is an open access article distributed under the Creative Commons Attribution License, which permits unrestricted use, distribution, and reproduction in any medium, provided the original work is properly cited.

This article has been retracted by Hindawi following an investigation undertaken by the publisher [1]. This investigation has uncovered evidence of one or more of the following indicators of systematic manipulation of the publication process:

- (1) Discrepancies in scope
- (2) Discrepancies in the description of the research reported
- (3) Discrepancies between the availability of data and the research described
- (4) Inappropriate citations
- (5) Incoherent, meaningless and/or irrelevant content included in the article
- (6) Manipulated or compromised peer review

The presence of these indicators undermines our confidence in the integrity of the article's content and we cannot, therefore, vouch for its reliability. Please note that this notice is intended solely to alert readers that the content of this article is unreliable. We have not investigated whether authors were aware of or involved in the systematic manipulation of the publication process.

Wiley and Hindawi regrets that the usual quality checks did not identify these issues before publication and have since put additional measures in place to safeguard research integrity.

We wish to credit our own Research Integrity and Research Publishing teams and anonymous and named external researchers and research integrity experts for contributing to this investigation.


The corresponding author, as the representative of all authors, has been given the opportunity to register their agreement or disagreement to this retraction. We have kept a record of any response received.

### References

- [1] X. Cui, X. Ji, Y. Shao, P. Zhao, and X. Li, "The Optos 200Tx Scanning Laser Ophthalmoscope Application in Retinoblastoma Patients' Follow-Up," *BioMed Research International*, vol. 2022, Article ID 5422360, 5 pages, 2022.

## Research Article

# The Optos 200Tx Scanning Laser Ophthalmoscope Application in Retinoblastoma Patients' Follow-Up

Xuehao Cui,<sup>1,2</sup> Xunda Ji,<sup>2</sup> Yan Shao,<sup>1</sup> Peiquan Zhao,<sup>2</sup> and Xiaorong Li<sup>1</sup> 

<sup>1</sup>Tianjin Key Laboratory of Retinal Functions and Diseases, Tianjin International Joint Research and Development Centre of Ophthalmology and Vision Science, Eye Institute and School of Optometry, Tianjin Medical University Eye Hospital, 300384, China  
<sup>2</sup>Xinhua Hospital Affiliated to Shanghai Jiaotong University School of Medicine 200092, Department of Ophthalmology, China

Correspondence should be addressed to Xiaorong Li; [prolixiaorong@163.com](mailto:prolixiaorong@163.com)

Received 23 May 2022; Accepted 22 July 2022; Published 11 August 2022

Academic Editor: Gaganpreet Kaur

Copyright © 2022 Xuehao Cui et al. This is an open access article distributed under the Creative Commons Attribution License, which permits unrestricted use, distribution, and reproduction in any medium, provided the original work is properly cited.

**Background and Objective.** Examination under general anesthesia is the conventional method of follow-up examination for retinoblastoma (RB) patients. As most of the RB patients are infants or children, general anesthesia for examination often put the children at great risk and affect their growth and development. This retrospective study was aimed at observing and evaluating the application value of Optos 200Tx scanning laser ophthalmoscope (Optomap 200Tx) in the long-term follow-up of patients with RB who achieves stable disease after treatment. **Methods.** A total of 1134 examinations with Optomap 200Tx were performed for 318 children who were clinically diagnosed with RB in the Ophthalmology Department of Tianjin Medical University Eye Hospital, China, between July 2015 and July 2017, and achieved stable disease lasting for more than 6 months after combined treatment. The children received examinations every 1-12 months (mean 4 months), initially at 31 months to 15 years of age (mean 51 months), and were given a full eye examination under anesthesia (EUA) immediately if recurrent tumor, recurrent vitreous seeding (VS), or recurrent subretinal seeding (SRS) was detected, or in the next follow-up visit if no abnormality was detected, and early treatment was performed when the lesion was confirmed. **Results.** Recurrence was detected in 4 children in the examination with Optomap 200Tx, including 2 cases of recurrent vitreous seeding (VS) and 2 cases of recurrent subretinal seeding (SRS), which were confirmed by EUA and well controlled after early treatment. **Conclusion.** The use of Optomap 200Tx in the long-term following up of patients with RB reduces the number of eye examinations under general anesthesia (EUA), increases the time between EUAs, and protects children from exposure to the adverse effects of general anesthetics. Optomap 200Tx can detect recurrent tumor and recurrent seeding, allowing for early treatment which produces better outcomes.

## 1. Introduction

Retinoblastoma (RB) is the most common primary malignant tumor seen in infants and children, with an incidence rate of one in 15-20000 children [1-5]. The strategy of using combined systemic chemotherapy, intra-arterial chemotherapy (IAC), and topical therapy has achieved a 5-year survival rate of 95% and partial vision reservation in pediatric patients with intraocular RB in recent years [6, 7]. Regular follow-up in the course of treatment is important for early detection of recurrent tumors and seeding. It also facilitates to understand the disease progression and evaluate the

effects of treatment, providing clinical basis for further treatment [7].

Examination under general anesthesia (EUA) is the conventional method for follow-up of RB patients [8]. As most of the RB patients are infants or children, general anesthesia may put the children at greater risk and affect their growth and development [8]. Backeljauw et al. [9] reported a control study involving 53 children who had received general anesthesia before 4 years of age and 53 who did not. Children in the experimental group scored lower in language development and listening comprehension ability than the control group and showed lower grey matter density in head

magnetic resonance imaging (MRI) [9]. The United States' Food and Drug Administration (FDA) issued a warning in December 2016 that repeated or long-time use of general anesthetics or sedative in women in the third trimester or in children under 3 years of age may compromise the brain development of the fetuses and children [10]. Recent studies on animals showed that exposure of developing brains to anesthetics may cause extensive neuron apoptosis and neurodegeneration leading to neuropsychological or behavioral developmental disorders [11].

Optomap 200Tx is an emerging funduscopy system, which has such advantages as a broader view, no needs for anesthesia, and increased convenience as compared to EUA. This study was aimed at observing and evaluating the application value of Optos 200Tx scanning laser ophthalmoscope (Optomap 200Tx) in the long-term follow-up of patients with RB who achieves stable disease after treatment.

## 2. Materials and Methods

**2.1. Study Subjects.** This retrospective study was performed on the data of 318 children who were clinically diagnosed with RB in the Ophthalmology Department of Tianjin Medical University Eye Hospital, China, between July 2015 and July 2017. Those patients who achieved stable disease lasting for more than 6 months after combined treatment and received examinations with Optomap 200Tx during their follow-ups were included in the study. Data of those patients who had incomplete information or missed the follow-up were excluded from the study. This study was approved by the ethics committee of the Tianjin Medical University Eye Hospital, China.

**2.2. Examination with Optomap 200Tx.** Prior to the examination with Optomap 200Tx, 5 images of the fundus (posterior pole, nasal, superior, inferior, and temporal side) were taken by a medical professional after the use of mydriatics in darkroom. The images were then sent to the information system of the hospital for reading and interpretation by doctors with specialization in RB, and the children's families were informed of the results. The RB staging was assigned according to the International Retinoblastoma Staging System as stage A–stage E.

**2.3. Statistical Analysis.** SPSS software (version 23.0) was used for data analysis in the study. The measurement data were expressed as Mean  $\pm$  SD. Count data were expressed as numbers or percentages.

## 3. Results

The data of 318 patients including 168 males and 150 females were analyzed. One hundred and two (102) children had unilateral and 216 children had bilateral tumors. According to the International Retinoblastoma Staging System, 35 cases were in stage A, 53 in stage B, 102 in stage C, 84 in stage D, and 44 in stage E. The children received a total of 1-8 (mean 3.57) examinations every 1-12 months

(mean 4 months). A total of 1134 examinations with Optomap 200Tx were performed for 318 children with RB.

During the examination with Optomap 200Tx, presence of recurrent tumor and seeding, which requires early treatment (Figures 1(a) and 1(b)); activity of vitreous or subretinal seeding (Figure 1(c)); extent of calcification of tumors and stability of fish-like tumors (Figure 1(d)); presence of new tumors in the contralateral eye of children with unilateral RB (Figures 1(e) and 1(f)); and presence of complications such as retinal detachment, fundus angiopathy, and choroidal atrophy (Figure 1(g)), was observed. The children were given EUA immediately if recurrence was detected in the examination with Optomap 200Tx, or in the next follow-up visit if no recurrence was detected, in order to confirm the lesion.

Recurrence was detected in 4 children, which were confirmed by EUA and well controlled after early treatment. Examination with Optomap 200Tx demonstrated inactive VS and SRS, stable fish-like tumor, which were confirmed by EUA in the next follow-up visit. New oncogenesis was not found in the examination of the contralateral eye of children with unilateral RB with Optomap 200Tx. Retinal detachment was observed in 1 child and was successfully restored after surgical treatment. According to Table 1, the sensitivity and specificity of Optomap 200Tx to recurrent VS and SRS was 100% and 100%, respectively. However, statistical analysis showed that there were few cases of recurrence. The reason for the low incidence of recurrence in follow-ups could be due to the fact that examination with Optomap 200Tx was performed for children who achieved stable disease lasting for more than 6 months (6-28 months, mean 14 months) after combined treatment.

## 4. Discussion

In recent years, Optomap 200Tx is widely used in the funduscopy of patients with various retinal diseases, including diabetic retinopathy [12], age-related macular degeneration [13], retinal pigment degeneration [14], and retinopathy in children [15], and is considered an effective means of examination. Compared with EUA, Optomap 200Tx is considered superior due to several reasons including its ultrawide field of view (200°) which is capable of photographing areas from the posterior pole to the peripheral areas. In addition, it allows clear display of tumors around the retina, such as recurrent tumor and seeding in the follow-up examination of RB patients. Moreover, there is no need of anesthesia, which avoids the risks caused by anesthesia and reduces the times of general anesthesia in the long-term follow-up and the adverse effect of general anesthesia on the growth and development of children. It is easier to operate than EUA and more suitable for long-term follow-up of patients. It has a wider angle in autofluorescence and fundus fluorescein angiography than conventional machines [8]. It takes only 0.3s to complete the photographing, which reduces the difficulties due to poor cooperation of young child with RB. It does not contact with the eyeball, which avoided infection, corneal injury, subconjunctival hemorrhage, and other complications of the eyes. It provides high-resolution

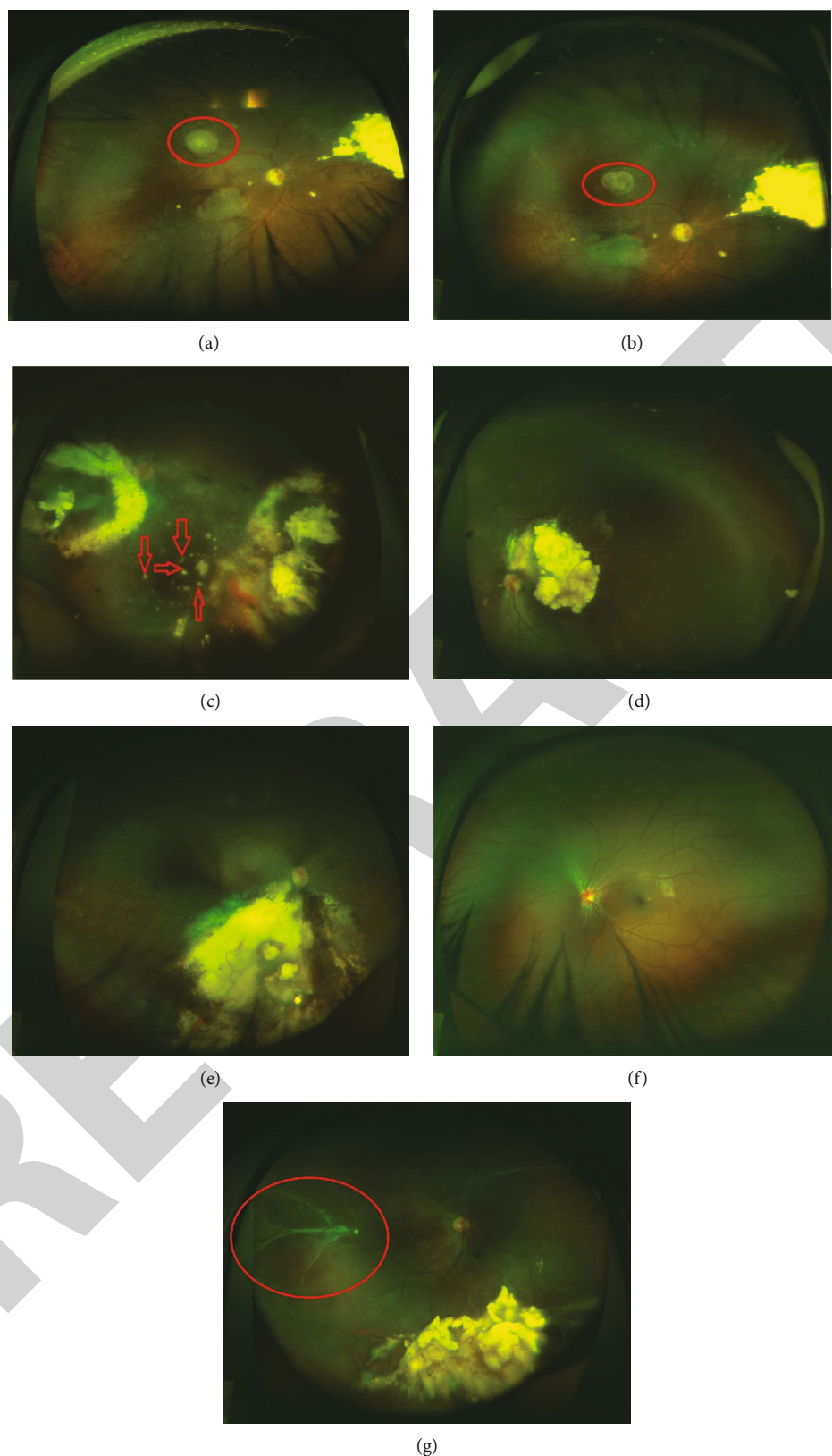


FIGURE 1: Examples of main observations in the examination with Optomap 200Tx. (a) Recurrent tumor above the macula lutea. (b) Significantly shrank recurrent tumor after a intra-arterial chemotherapy. (c) Large amount of inactive VS. (d) Partial calcification of the tumor beside the optic papilla, with neovascularization on the surface, which obscures the macular area. (e) Affected eye of child with unilateral RB. (f) Contralateral eye of child with unilateral RB without any abnormality. (g) Retinal detachment seen in the temporal side.

TABLE 1: Sensitivity and specificity of Optomap 200Tx to recurrent VS and SRS.

Examination methods	Optomap 200TX	EUA
VS	2	2
SRS	2	2
Recurrent tumor	0	0
Stable	1130	1130
Total	1134	1134

images, which increases the accuracy of the physician's judgement, and allows use in remote consultation and academic exchange. It is inexpensive and saves the expenses for anesthesia and related examinations, as well as the fasting before and after anesthesia. The examination is normally completed within 10 minutes.

Still, Optomap 200Tx has some limitations and shortcomings including extremely peripheral areas are difficult to photograph, for example, recurrence near the ora serrata cannot be seen. In addition, it is not effective in detecting some retinopathies. Mackenzie [16] found that Optomap 200Tx has a low sensitivity to disorders in pre-equatorial retina. It requires active cooperation of the children, and thus is not suitable for children under 3 years of age or uncooperative children. The quality of image will be poor when the children are not cooperative. In EUA, the operator may press the eyeball to view the extremely peripheral retina, and steadier photographing is obtained as the children are in general anesthesia, which is not possible in examination with Optomap 200Tx. Therefore, Optomap 200Tx cannot completely replace fundus under general anesthesia. Our strategy is to use Optomap 200Tx and EUA alternately. This study suggests that Optomap 200Tx can be used in the long-term following up of patients with RB who achieve stable disease, to effectively monitor changes in the fundus, detect recurrent tumors and fundus complications, increase the time between fundus examinations under general anesthesia, and reduce the adverse effect of anesthesia on the growth and development of THE children. However, Optomap 200Tx cannot completely replace EUA, but can be used as a supplementary of EUA in the long-term follow-up of children with RB.

## 5. Conclusion

Most of the RB patients are infants or children, and general anesthesia for examination often put the children at great risk and affect their growth and development. This retrospective study was aimed at observing and evaluating the application value of Optos 200Tx scanning laser ophthalmoscope (Optomap 200Tx) in the long-term follow-up of patients with RB who achieves stable disease after treatment. A total of 1134 examinations with Optomap 200Tx were performed for 318 children who were clinically diagnosed with RB and achieved stable disease lasting for more than 6 months after combined treatment. Recurrence was detected in 4 children in the examination with Optomap 200Tx, including 2 cases of recurrent vitreous seeding (VS)

and 2 cases of recurrent subretinal seeding (SRS), which were confirmed by EUA and well controlled after early treatment. The use of Optomap 200Tx in the long-term following up of patients with RB reduces the number of eye examinations under general anesthesia (EUA), increases the time between EUAs, and protects children from exposure to the adverse effects of general anesthetics. Optomap 200Tx can detect recurrent tumor and recurrent seeding, allowing for early treatment which produces better outcomes.

## Data Availability

Data will be provided upon reasonable request to the corresponding author.

## Ethical Approval

This study was approved by the ethics committee of the Tianjin Medical University Eye Hospital, China.

## Conflicts of Interest

The authors have no conflicts of interest.

## Acknowledgments

This study has been supported by the program on the therapeutic effect of MSC-exosome loaded with PEDF-34 on diabetic retinopathy and its underlying mechanisms, National Natural Science Foundation of China (no. 81870675), and the Natural Science Foundation of Tianjin (no. 19JCZDJC64000).

## References

- [1] A. N. Pandey, "Retinoblastoma: An overview," *Saudi Journal of Ophthalmology*, vol. 28, no. 4, pp. 310–315, 2014.
- [2] C. Rodriguez-Galindo, D. B. Orbach, and D. Vander Veen, "Retinoblastoma," *Pediatric Clinics*, vol. 62, no. 1, pp. 201–223, 2015.
- [3] D. H. Abramson, "Retinoblastoma: saving life with vision," *Annual Review of Medicine*, vol. 65, no. 1, pp. 171–184, 2014.
- [4] L. Asnaghi, A. Tripathy, Q. Yang et al., "Targeting Notch signaling as a novel therapy for retinoblastoma," *Oncotarget*, vol. 7, no. 43, pp. 70028–70044, 2016.
- [5] H. Dimaras, K. Kimani, E. A. Dimba et al., "Retinoblastoma," *The Lancet*, vol. 379, no. 9824, pp. 1436–1446, 2012.
- [6] M. Jehanne, H. Brisse, M. Gauthier-Villars, L. Lumbroso-le Rouic, P. Freneaux, and I. Aerts, "Le rétinoblastome : les avancées récentes," *Bulletin du Cancer*, vol. 101, no. 4, pp. 380–387, 2014.
- [7] A. Künkele, C. Jurklies, R. Wieland et al., "Chemoreduction improves eye retention in patients with retinoblastoma: a report from the German retinoblastoma reference centre," *The British Journal of Ophthalmology*, vol. 97, no. 10, pp. 1277–1283, 2013.
- [8] S. M. Hariprasad, R. D. Patel, and J. W. Kitchens, "The uncharted realm of the retinal periphery: how widefield imaging is launching a brand new field of study," *Retinal Physician*, vol. 2011, pp. 32–40, 2011.

## *Retraction*

# **Retracted: CNN-Based Cross-Modal Residual Network for Image Synthesis**

### **BioMed Research International**

Received 8 January 2024; Accepted 8 January 2024; Published 9 January 2024

Copyright © 2024 BioMed Research International. This is an open access article distributed under the Creative Commons Attribution License, which permits unrestricted use, distribution, and reproduction in any medium, provided the original work is properly cited.

This article has been retracted by Hindawi, as publisher, following an investigation undertaken by the publisher [1]. This investigation has uncovered evidence of systematic manipulation of the publication and peer-review process. We cannot, therefore, vouch for the reliability or integrity of this article.

Please note that this notice is intended solely to alert readers that the peer-review process of this article has been compromised.

Wiley and Hindawi regret that the usual quality checks did not identify these issues before publication and have since put additional measures in place to safeguard research integrity.

We wish to credit our Research Integrity and Research Publishing teams and anonymous and named external researchers and research integrity experts for contributing to this investigation.

The corresponding author, as the representative of all authors, has been given the opportunity to register their agreement or disagreement to this retraction. We have kept a record of any response received.

### **References**

- [1] R. Kumar, V. Bhatnagar, A. Jain, M. Singh, Z. H. Kareem, and R. Sugumar, "CNN-Based Cross-Modal Residual Network for Image Synthesis," *BioMed Research International*, vol. 2022, Article ID 6399730, 9 pages, 2022.



## Research Article

# CNN-Based Cross-Modal Residual Network for Image Synthesis

Rajeev Kumar <sup>1</sup>, Vaibhav Bhatnagar <sup>2</sup>, Amit Jain <sup>3</sup>, Mahesh Singh <sup>4</sup>, Z. H. Kareem <sup>5</sup>,  
and R. Sugumar <sup>6</sup>

<sup>1</sup>Department of MCA, Dewan Institute of Management Studies Meerut UP, India

<sup>2</sup>Department of Computer Applications, Manipal University Jaipur, India

<sup>3</sup>Department of Computer Science and Engineering, Guru Nanak Dev Engineering College, Ludhiana, Punjab, India

<sup>4</sup>Kebri Dehar University, Ethiopia

<sup>5</sup>Medical Instrumentation Techniques Engineering Department, Al-Mustaqbal University College, Babylon, Iraq

<sup>6</sup>Department of Computer Science & Engineering, Saveetha School of Engineering, Saveetha Institute of Medical and Technical Sciences, Chennai 602105, India

Correspondence should be addressed to Vaibhav Bhatnagar; [vaibhav.bhatnagar15@gmail.com](mailto:vaibhav.bhatnagar15@gmail.com) and Mahesh Singh; [drmaheshsingh@kdu.edu.et](mailto:drmaheshsingh@kdu.edu.et)

Received 12 June 2022; Revised 7 July 2022; Accepted 21 July 2022; Published 10 August 2022

Academic Editor: Gaganpreet Kaur

Copyright © 2022 Rajeev Kumar et al. This is an open access article distributed under the Creative Commons Attribution License, which permits unrestricted use, distribution, and reproduction in any medium, provided the original work is properly cited.

This study attempts to address the issue that present cross-modal image synthesis algorithms do not capture the spatial and structural information of human tissues effectively. As a consequence, the resulting photos include flaws including fuzzy edges and a poor signal-to-noise ratio. The authors offer a cross-sectional technique that combines residual modules with generative adversarial networks. The approach incorporates an enhanced residual initial module and attention mechanism into the generator network, reducing the number of parameters and improving the generator's feature learning capabilities. To boost discriminant performance, the discriminator employs a multiscale discriminator. A multilevel structural similarity loss is included in the loss function to improve picture contrast preservation. On the ADNI data set, the algorithm is compared to the mainstream algorithms. The experimental findings reveal that the synthetic PET image's MAE index has dropped while the SSIM and PSNR indexes have improved. The experimental findings suggest that the proposed model may maintain picture structural information while improving image quality in both visual and objective measures. The residue initial module and attention mechanism are employed to increase the generator's capacity for learning, while the multiscale discriminator is utilized to improve the model's discriminative performance. The enhanced method in this study can maintain the structure and contrast information of the picture, according to comparative experimental findings using the ADNI dataset. The produced picture is hence more aesthetically similar to the genuine print.

## 1. Introduction

With the development of science and technology, there are various ways of acquiring medical images, and different modalities of medical images have distinct advantages and disadvantages. For example, magnetic resonance imaging (MRI) has no radiation on the human body, the soft tissue structure is displayed, and rich diagnostic information can be obtained, but the acquisition time is extended, which is prone to artifacts; positron emission computed tomography (positron emission tomography (PET)) can make an early

diagnosis of the disease through the functional changes of the tissue in the diseased area, but it is expensive, and the image resolution is low. Furthermore, studies have shown that the morphological or functional abnormalities of the human body caused by diseases are often manifested in various aspects. Therefore, the information obtained by a single modality imaging device usually cannot fully reflect the complex characteristics of the disease [1]. Still, clinical medical images of different modalities are collected simultaneously. It requires a lot of time and financial resources. Therefore, how to use the medical images of the existing

modalities to accurately synthesize the pictures of the needed modalities through computer technology has been the research direction in recent years.

The majority of medical picture cross-modality synthesis techniques are based on deep learning, which may be classified as cross-modality synthesis methods based on paired data or cross-modality synthesis methods based on unpaired data depending on the kind of data employed. This work investigates cross-modal synthesis approaches based on paired data since cross-modal synthesis based on unpaired data cannot provide subject-specific visuals. PET scans (positron emission tomography scans) are frequently performed in combination with CT scans or MRI scans (magnetic resonance imaging scans). While CT and MRI scans provide images of the inside organs and tissues of your body, PET scans can provide your doctor with a glimpse of complicated systemic disorders because they highlight cellular concerns. PET scans employ positrons as opposed to MRIs. Your body is given an injection of a tracer that enables the radiologist to view the region being scanned. While PET scans are used to examine your body's function, an MRI scan may be utilized to determine the form of your organs or blood arteries. 3D CNN was utilized in the literature [2] to predict from MRI to PET. Each sample picture was broken into many image blocks in the experiment to maximize the quantity of sample data. The method created a PET picture with an excellent classification effect. A deep residual inception encoder-decoder neural network (RIED-Net) was suggested in the literature [3] to learn the mapping between pictures of various modalities and improve generation performance. CNN-based approaches outperform older methods because they can automatically and effectively learn and pick characteristics. The transfer learning of VGG16 with one retrained ConvLayer produces the best results, which are somewhat higher than the state-of-the-art result. The specified feature may learn from the new dataset using the unfrozen ConvLayer. As a result, the specific feature is an important aspect in improving accuracy; a model's strength of expression and overfitting must be balanced. A network that is too basic frequently cannot learn enough from the data and so cannot achieve high accuracy. An extremely complicated network, on the other hand, is difficult to train and soon overfits. As a result, precision remains poor. Only a network structure with the correct size and other efficient overfit prevention strategies, such as a proper dropout rate and data augmentation, will produce the best outcomes. However, due to time constraints, further research is required. Training a fine-tuned deep convolutional neural network with defrosted ConvLayers tends to overfit in transfer learning. Other more powerful CNN models, such as ResNetv2 and ensembles of multiple CNN models, have not been evaluated, but they may improve the results; visualization should be added to improve understanding and explanation of the CNN-based system's results, as these are required for the adaptation of a CNN-based system in real clinical applications. Literature [4] suggested a context-aware generative adversarial network that uses an artificial context model to get the high-accuracy and resilient mapping from MRI to CT (computed tomography) images. A multichannel generative adversarial network

was presented in the literature [5] to manufacture PET pictures. The experiment was carried out on 50 lung cancer patients' PET-CT data to produce more realistic PET pictures. To produce projected PET data with given CT data, literature [6] paired a fully convolutional network with a conditional generative adversarial network and obtained excellent results. In contrast to statistical parameter mapping analysis, literature [7] developed a 3D generative network model based on residual network to learn the mapping from MRI to FDG (fluorodeoxyglucose). Despite the excellent results of the above cross-modal synthesis approaches, owing to the complicated spatial structure of medical pictures, the above synthesis results still cannot accurately capture the edge information of human tissue, and there are issues such as poor signal-to-noise ratio and fuzzy edges. We present the Cross-Modal Contrastive Generative Adversarial Network (XMC-GAN) in "Cross-Modal Contrastive Learning for Text-to-Image Generation," which addresses text-to-image generation by learning to maximize the similarity matrix between text and image using intermodal (image-text) and intramodal (image-image) contrastive losses. This method assists the discriminator in learning more robust and discriminative features, making XMC-GAN less prone to mode collapse even with one-stage training. In comparison to earlier multistage or hierarchical techniques, XMC-GAN provides state-of-the-art performance with a simple one-stage generation. It is trainable from start to finish and simply requires image-text pairings (as opposed to labeled segmentation or bounding box data). Furthermore, the available public medical picture data collection has very little matched data. The majority of the data utilized in the aforementioned approaches are gathered by hand, which necessitates large personnel and material resources.

To summarize, this study presents a technique for the cross-modal synthesis of PET pictures from MRI images by combining residual modules and generative adversarial networks to enhance the synthesis of subject-specific PET images with little paired data. The three primary points of the main work are as follows: the generator now includes an enhanced residual initial module and an attention mechanism to completely extract the features of MRI pictures; the pix2pix network architecture has been upgraded, and the discriminator now uses a multiscale discriminator to increase discriminate performance and reduce loss; the function incorporates a multilevel structural similarity loss based on the classic adversarial loss and L1 loss, which improves picture contrast preservation.

*1.1. Advantages and Limitations of Medical Imaging.* The ability to promptly and precisely diagnose sickness and determine its severity or harmless nature is one of the potential advantages of imaging tests. It might not be essential to perform invasive diagnostic techniques such as exploratory surgery, angiography, or cardiac catheterization. Medical imaging is crucial when a person has a chronic illness or a kind of cancer, not only for the initial diagnosis but also for tracking how the illness is responding to therapy, determining whether the illness is advancing, and determining when treatment should be discontinued or changed.

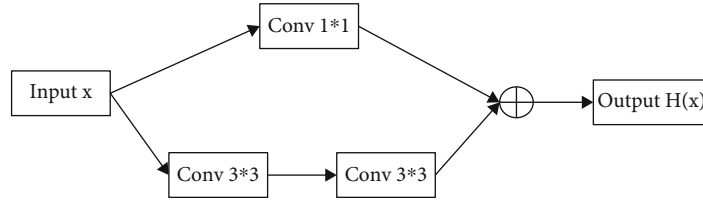


FIGURE 1: Residual initial module structure [3]

One of the drawbacks of medical imaging is that there is a slight increase in the likelihood that a person exposed to X-rays would acquire cancer later in life. Cataracts, skin reddening, and hair loss are all tissue consequences that occur at quite high levels of radiation exposure and are uncommon for many types of imaging tests.

## 2. Related Work

**2.1. Generative Adversarial Networks.** The fundamental generative adversarial networks (GAN) model consists of the input vector, generator, and discriminator. The generators and discriminators are both implicit function expressions that are often employed by deep neural networks. GAN can train the predictive model of any distribution of data using adversarial approaches and get great results. GAN's primary job is to train an adversarial generator and discriminator. The objective goal is either a stronger generator or a more sensitive discriminator, depending on the project's needs. Thus, generative adversarial networks are used in CNN-based cross-modal residual networks for image synthesis. Cross-modality image estimation includes creating pictures for one form of medical imaging from those for another. It has been demonstrated that convolutional neural networks (CNNs) are effective in recognizing, classifying, and extracting picture patterns. CNNs are used as generators in generative adversarial networks (GANs), and estimated pictures are classified as true or false based on a second network. In the context of the image estimating paradigm, CNNs and GANs may be seen more broadly as deep learning techniques since imaging data frequently have a large number of network weights. The CNN/GAN image estimate literature almost exclusively uses MRI data, with PET or CT being the two main modalities. Literature [8] created the first generative adversarial network (GAN) in 2014, which included a generator  $G$  and a discriminator  $D$ . The generator takes noise  $z$  from distribution as input, maps it to the data space, records the data distribution of the actual sample  $x$ , and creates a sample  $G(z)$  that looks like the original data. The produced samples and the real samples are sent to the discriminator, and the purpose is to categorize the generated samples  $G(z)$  as false and the actual samples as true. GAN is a process in which the generator and discriminator are always in conflict, playing a game of maximum and minimum values until they strike a dynamic equilibrium. GAN's goal function is as follows:

$$\min_G \max_D V(D, G) = E_{x \sim P_{\text{data}}(x)}[\ln D(x)] + E_{z \sim P_z(z)}[\ln(1 - D(G(z)))]. \quad (1)$$

Since the results generated by the unconditional generative adversarial network have great uncertainty, literature [9] proposed to add additional information  $y$  to the generator and discriminator as a condition to construct a conditional generative adversarial network (CGAN). The loss function of CGAN is defined as

$$L_{\text{CGAN}}(G, D) = E_{x,y}[\ln D(x, y)] + E_{x,z}[\ln(1 - D(x, G(x, y)))]. \quad (2)$$

The pix2pix network [10] is a type of CGAN for image translation. However, it no longer inputs noise but directly inputs the original image as a condition to the generator. The discriminator uses the target image and the true and false image pair composed of the generated image and the original image as input to judge the true and false.

**2.2. Residual Initial Block.** The structure of the initial residual block [3] is shown in Figure 1, including two paths. Among them, two  $3 \times 3$  convolution paths extract data features. A  $1 \times 1$  initial residual short-circuit connection can deepen (in the encoder) or reduce (in the decoder) the depth of the convolution kernel while solving the input. The problem is that feature maps and output feature maps have different channels, ensuring the fusion of input and output maps at the pixel level. Compared with the inception module, the initial residual block has fewer parameters and a more straightforward structure, which can solve the problems caused by the depth of the network.

**2.3. Attention Module.** [11] proposed an attention module for medical images; the structure is shown in Figure 2. The attention mechanism determines the attention coefficients of different regions on each input  $x^1$  by gating the signal  $g$ , allowing the network to focus on areas more relevant to the task and suppress irrelevant background regions. The neural network with the added attention module has higher sensitivity and accuracy

## 3. Proposed Algorithm

We have provided a generally and locally aware GAN framework for cross-modality transfer from MRI to PET in this research. To improve the quality of generated PET scans, the suggested multipath GAN architecture assists in simultaneously collecting both global structure and local texture. To assist the generative model in accurately learning the fundamental bimodal data distribution, the overall framework and the combined synthesis goal function were created. Experimental findings show that our methodology not only

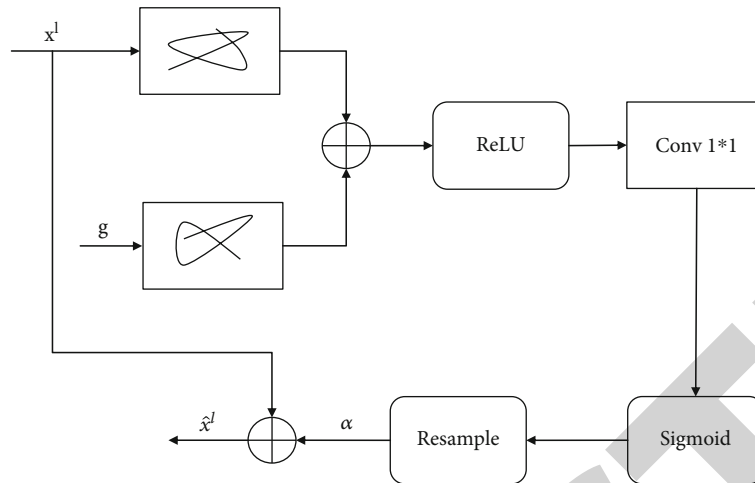


FIGURE 2: Attention module [5].

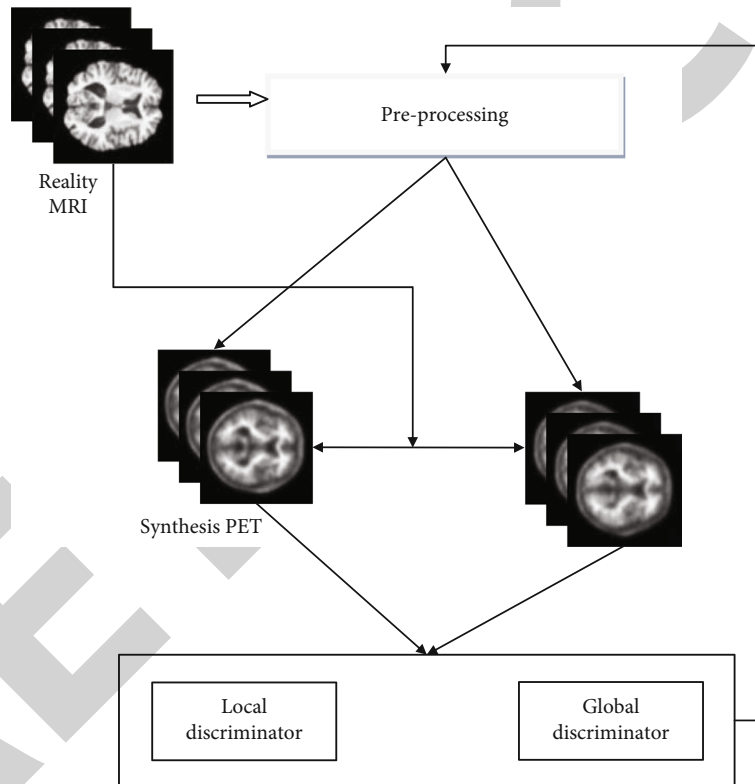


FIGURE 3: Proposed framework.

produces PET scans with higher-quality images. The model framework of the improved fusion residual module and generative adversarial network cross-modality PET image synthesis method is shown in Figure 3. The generator takes authentic MRI images as input, learns the feature mapping relationship between MRI and PET, and generates synthetic PET corresponding to accurate MRI synthesis.

PET and natural PET are spliced with accurate MRI to form a true and false image pair. Next, the two discriminators use the true and false image pairs as input to perform

true and false discrimination. Finally, the weighted average of the two discrimination results is used as the final result.

**3.1. Generator Network.** Due to its good performance and efficient use of memory, U-Net [12] is widely used in medical image segmentation tasks. Therefore, the algorithm in this paper uses U-Net as the generator.

The generator structure is shown in Figure 4, which consists of an encoding path and a decoding path. The encoding course consists of a series of  $3 \times 3$  convolutions,  $4 \times 4$

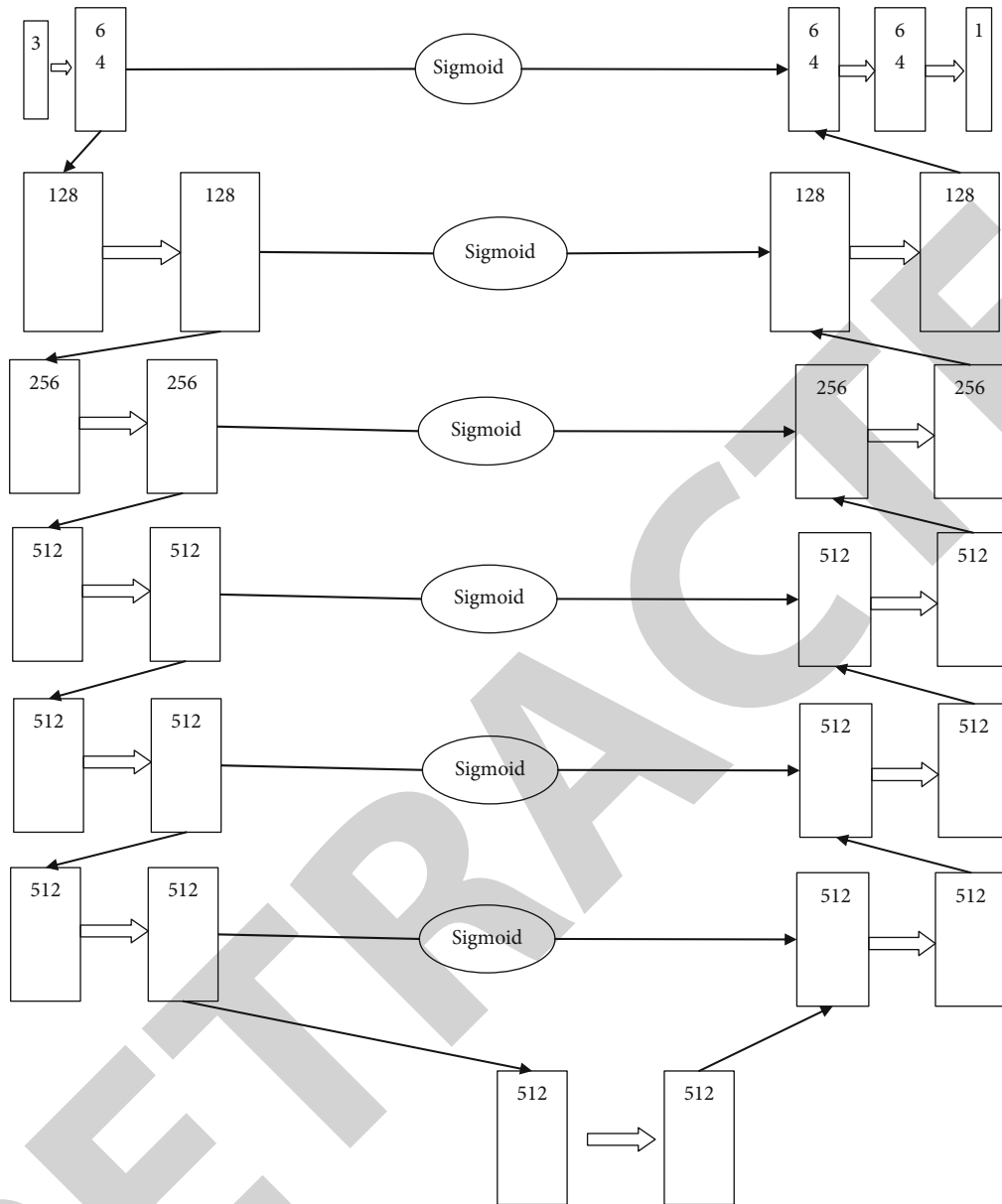


FIGURE 4: Generator structure.

convolutions, batch normalization, and activation layers. The algorithm replaces the top pooling layer in U-Net with a convolution layer, continuously extracts critical features of MRI images through convolution operations, and compresses the vital information extracted from soft layers to high layers. The decoding path consists of a series of  $3 \times 3$  convolutions,  $4 \times 4$  deconvolutions, batch normalization layers, and activation layers and reconstructs the final output from the feature maps compressed by the encoding path.

To better learn the pixel information in the image, the algorithm in this paper introduces the improved residual initial module into the encoding and decoding paths to ensure a better generation effect. Increasing the size of the convolution kernel in the neural network can expand the receptive field, but blindly increasing the convolution kernel will increase the network parameters and bring specific difficulties

to the training of the network. Therefore, the algorithm in this paper adds a  $3 \times 3$  convolution to the  $3 \times 3$  convolution path of the initial residual module, replaces the larger convolution kernel with 3 small convolution kernels, and reduces the receptive field as much as possible while expanding the receptive field—network parameters. In addition, the introduction of the initial residual module can also solve the problem of gradient disappearance caused by the depth of the network.

Since the structural information and spatial information of medical images are more complex than natural images, to better extract the critical structural features in MRI images, the algorithm in this paper sets the encoder-decoder path depth of the generator to 7 layers. However, considering the network complexity and memory consumption, the algorithm does not put the improved residual initial module in all convolutional layers of the encoding and decoding

paths but compares the generation effect through multiple experiments and finally puts the initial residual module in the middle four layers of the network; only two  $3 \times 3$  convolutions are used in the first 3 layers of the encoding path and the last 3 layers of the decoding path, which reduces network parameters and training time while improving the generation quality.

The skip connection in U-Net can capture the contextual features from the encoding path to the decoding path. The fusion of low-level features and high-level features can retain more detailed information of high-level feature maps, but it may also contain feature information irrelevant to the synthesis task. Therefore, to improve the synthesis quality, the algorithm in this paper introduces a self-attention mechanism in the skip connection path and combines the features extracted by the decoding path before the skip connection operation. The event features through the attention gate mechanism and further eliminates the skip connection.

The interference caused by irrelevant features and noise in the MRI images highlights the critical elements in the skip connections to capture the essential information of MRI images better.

In addition, to prevent the network from overfitting, the algorithm also introduces a dropout operation in the generator. Finally, the synthesized PET image is obtained through the Tanh activation function after encoding and decoding the feature information.

**3.2. Discriminator Network.** To better learn the local and global features of PET images, improve the game ability of the discriminator, and enable the generator to generate PET images that are more in line with the actual distribution, this paper adopts multiscale discriminators, namely, local discriminator and global discriminator. With two discriminators with different receptive fields ( $70 \times 70$  and  $128 \times 128$ ), the generator and discriminator can learn the relationship between the spatially shorter and longer distance pixels.

Based on the idea of patchGAN, the discriminator network first divides the image into  $N \times N$  blocks and then discriminates whether each subblock is true or false. The two discriminator networks are 5 layers and 7 layers, respectively, composed of convolution layers, batch normalization layers, and activation layers alternately. Finally, the weighted average of all results is used as the output of the discriminator.

**3.3. Loss Function.** This paper uses adversarial loss, L1 loss, and multiscale structural similarity loss (MS-SSIM) as loss functions.

**3.3.1. Adversarial Loss.** Adversarial loss can constrain the generated results to a certain extent, making the results closer to the actual distribution. The damaging loss is shown in

$$L_{\text{GAN}} = \frac{1}{N} \sum_{n=1}^N [-D(G(x, z))]. \quad (3)$$

**3.3.2. L1 Loss.** The L1 loss is passed through the generator to reduce the difference between natural and synthetic images. The L1 loss is shown in

$$L_{L1} = \frac{1}{N} \sum_{i=1}^N |x_i - y_i|. \quad (4)$$

**3.3.3. MS-SSIM Loss.** Structural similarity (SSIM) was initially described by literature [13] and proposed to measure the similarity of two images. The introduction of multiscale structural similarity loss into the loss function can better preserve the brightness and contrast information of the image.

The MS-SSIM loss is shown in equation

$$L_{\text{MS-SSIM}}(x, y) = [L_M(x, y)]^{\alpha_M} \prod_{j=1}^M [c_j(x, y)]^{\beta_j} [s_j(x, y)]^{\gamma_j}. \quad (5)$$

Among them,  $L_M(x, y)$ ,  $c_j(x, y)$ , and  $s_j(x, y)$  represent the brightness, contrast, and structural similarity of the image, respectively, and  $\alpha_M$ ,  $\beta_j$ , and  $\gamma_j$  represent the weights occupied by different parts, respectively.

The final loss function of the model is as follows:

$$L = \lambda_1 L_{\text{GAN}} + \lambda_2 L_{L1} + \lambda_3 L_{\text{MS-SSIM}}. \quad (6)$$

Among them,  $\lambda_i (i = 1, 2, 3)$  is the weight coefficient of each loss.

## 4. Experimental Results and Analysis

**4.1. Experimental Platform.** The experiments in this article are run using the PyTorch framework, with an Intel i7-6700 CPU and an NVIDIA GeForce GTX1080Ti GPU as the hardware setup. The software environment consists of Ubuntu 16.04, CUDA 9.0, cuDNN 7.6, PyTorch 1.1.0, and Python 3.7.

**4.2. Data Preparation and Parameter Setting.** The Alzheimer's disease neuroimaging initiative (ADNI) public dataset [14] was utilized, with 33 problems eliminated, to create paired MRI and PET scans of 716 Alzheimer's disease participants. Subjects' aberrant data were subsequently accepted, and 683 subjects' data were eventually utilized.

Before training, data is preprocessed. The FSL software [15] is utilized for data preparation in this research, with neck removal, skull stripping, and linear registration to MNI152 space among the processes. Three-dimensional data with a size of 9110991 is acquired after preprocessing. As model input, the 40th axial slice of the 3D data was collected and upsampled to a size of 128128. The experiment uses the 5-fold cross-validation approach to get more accurate experimental findings. All of the data is split into five groups at random, with four of them serving as the training set (547 slices) and the other serving as the test set (136 pieces).

The weight coefficients of the loss function are changed throughout the network training phase. Because the input image's pixel range is (0, 1), the resultant L1 loss is much less. When the MS-SSIM loss coefficient is more important, the brightness of the synthesized picture is higher, and when the volume is lower, it has a less significant influence on the outcome. As a result, the weight of each loss function is eventually adjusted to  $1 = 1$ ,  $2 = 100$ , and  $3 = 1$  after

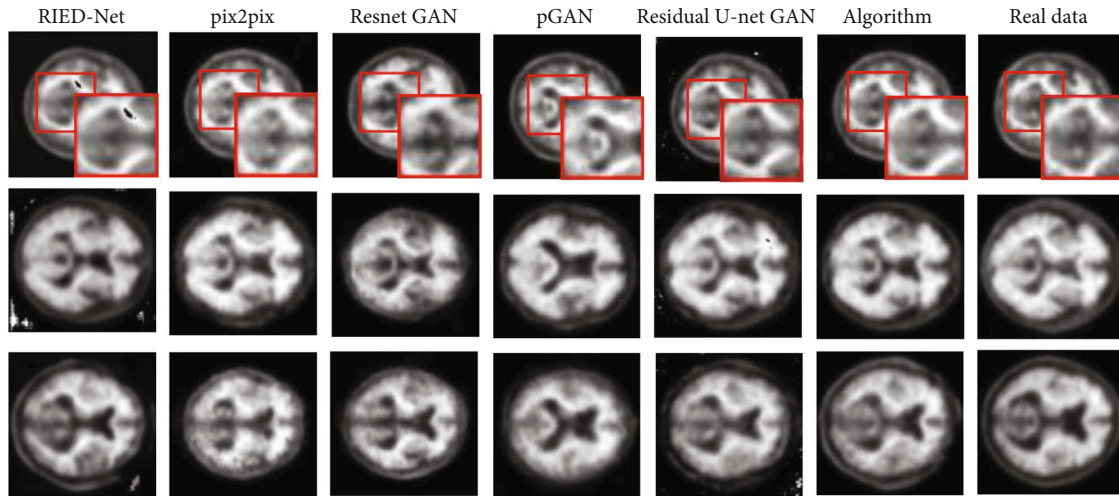


FIGURE 5: Comparative result.

numerous testing and troubleshooting. Furthermore, the batch size is set to 16, the initial learning rate is set at 0.0002, the network is optimized using the Adam optimizer, and 200 epochs are iteratively trained. The learning rate for the first 100 epochs remains intact, whereas the learning rate for the final 100 epochs is lowered linearly to zero.

**4.3. Experimental Results.** To verify the performance of the improved algorithm in this paper, this paper conducts experiments on the ADNI dataset. The algorithm uses the pix2pix model as the benchmark model and, at the same time, compares with RIED-Net, pGAN [16], and GAN with residual network [17] as the generator (ResnetGAN); the GAN model with residual U-Net as the generator [7] and other mainstream algorithms based on CNN and GAN are compared and evaluated from qualitative and quantitative aspects. A total of 5 sets of cross-experiments are carried out.

**4.3.1. Qualitative Evaluation.** The qualitative comparison between the generated results of the algorithm in this paper and the generated results of other algorithms is shown in Figure 5. As shown from the first row of Figure 5, compared with the actual image, different algorithms have the problem of significant deviation of results and speckle noise. The consequences of this algorithm are more complete. In addition, the structural edges of the results obtained by other algorithms look too smooth or blurred. In contrast, the results generated by the algorithm in this paper are relatively more precise. The difference is also improved to a certain extent, and the visual is closer to the actual image.

In addition, due to the different brain sizes of other subjects, there is still a specific deviation after linear registration to the standard space. As shown in the second and third rows of Figure 5, pix2pix and Resnet GAN cannot learn this mapping relationship well, and the generated images and size mapping confusion. Although other algorithms can learn the change of structure size, there is a lot of missing edge information, and there are still problems of noise and significant structural errors. In contrast, the results synthe-

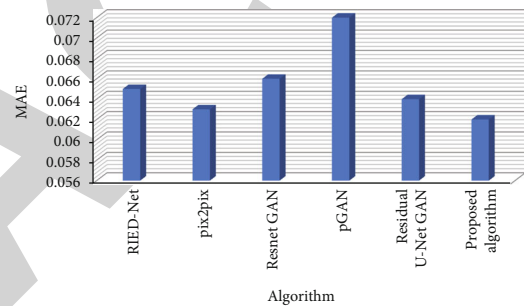


FIGURE 6: Quantitative evaluation of MAE.

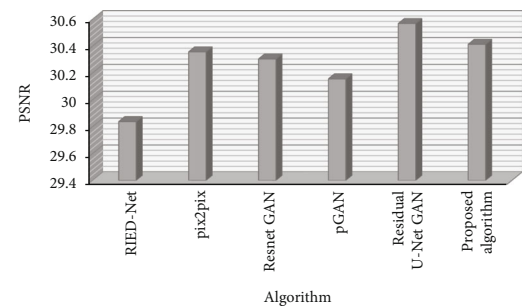


FIGURE 7: Quantitative evaluation of PSNR.

sized by the algorithm in this paper have better edge integrity and no noise speckles, which may be because the improved residual initial module is introduced in this paper, which improves the model performance. It can be seen that the results generated by the improved algorithm in this paper are more diverse and can preserve the edge structure of the image more thoroughly.

**4.3.2. Quantitative Evaluation.** In this paper, mean absolute error (MAE), peak signal-to-noise ratio (PSNR), and structural similarity index (SSIM) are used as evaluation indicators. Figure 6 shows the quantitative evaluation of MAE.

TABLE 1: Quantitative evaluation results of each algorithm.

Evaluation indicators	RIED-Net [5]	pix2pix [7]	Reset GAN [11]	pGAN [15]	Residual U-Net GAN [17]	Proposed algorithm
MAE	0.065 ± 0.030	0.063 ± 0.030	0.066 ± 0.030	0.072 ± 0.030	0.064 ± 0.030	0.062 ± 0.030
PSNR/dB	29.838 ± 0.815	30.357 ± 0.969	30.304 ± 0.642	30.156 ± 0.745	30.568 ± 1.056	30.413 ± 0.823
SIM	0.564 ± 0.133	0.637 ± 0.160	0.641 ± 0.736	0.630 ± 0.130	0.644 ± 0.150	0.670 ± 0.151

MAE [10] and PSNR [12] are calculated as

$$\text{MAE} = \frac{1}{n} \sum_{i=1}^n |y_i - x_i|, \quad (7)$$

$$\text{LGPSNR} = 10 * \lg \left( \frac{I_{\max}^2}{\text{MSE}} \right). \quad (8)$$

Among them, MSE is the mean square error of the two images, and  $I_{\max}$  represents the maximum value of the image color, which is expressed as 255 using 8-bit sampling points.

SSIM [15] is calculated as

$$\text{SSIM}(x, y) = \frac{(2\mu_x\mu_y + c_1)(2\sigma_{xy} + c_2)}{(\mu_x^2 + \mu_y^2 + c_1)(\sigma_x^2 + \sigma_y^2 + c_2)}. \quad (9)$$

Among them,  $\mu_x$ ,  $\mu_y$ ,  $\sigma_x^2$ ,  $\sigma_y^2$ , and  $\sigma_{xy}$  are the mean, variance, and covariance of the pictures  $x$  and  $y$ , respectively;  $c_1 = (k_1L)^2$  and  $c_2 = (k_2L)^2$  are two constants that prevent the denominator from being 0. Figure 7 shows the quantitative evaluation of PSNR.

Table 1 shows the quantitative indicators derived from the comparison experiments. The MAE indices of the results synthesized by the method in this research are all lowered when compared to previous algorithms, showing that the enhanced technique in this work is more stable. The SSIM values of the findings in this work are 0.106, 0.033, 0.029, 0.040, and 0.026, respectively, greater than those of previous techniques, demonstrating that the proposed approach may enhance the quality of synthetic pictures. The PSNR value of the technique in this research is significantly enhanced when compared to the MAE and SSIM indicators. The PSNR values of the method in this work have been improved by 0.575 dB, 0.056 dB, 0.109 dB, and 0.257 dB, respectively, in addition to the GAN model based on residual U-Net. The method may be observed to increase the quality of the synthetic picture to some degree. The PSNR value of the method generated in this research is lower than the GAN model based on residual U-Net. This might be because PSNR is an error-sensitive picture quality rating statistic that ignores the human eye's visual features. As a result, the picture quality it reflects does not always match the image quality witnessed and verified by the human eye. Figure 8 shows the quantitative evaluation of SSIM.

As a consequence, the method in this study may improve the quality of the synthesized image and increase the edge

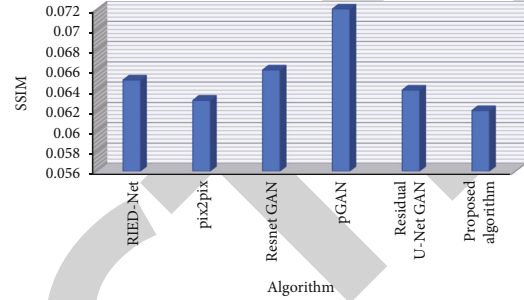


FIGURE 8: Quantitative evaluation of SSIM.

synthesis impact of the picture by integrating the qualitative and quantitative findings of the experiment.

## 5. Conclusion

Aiming at the problems of blurred edges and low signal-to-noise ratio of synthetic results in cross-modal synthesis tasks of medical images, this paper proposes a cross-modal PET image synthesis method that fuses initial residual modules and generative adversarial networks. The authors provide a cross-sectional method that combines generative adversarial networks with residual modules. The method reduces the number of parameters and enhances the generator's capacity for feature learning by incorporating an improved residual initial module and attention mechanism. The discriminator uses a multiscale discriminator to improve discriminant performance. To better preserve visual contrast, a multilevel structural similarity loss is incorporated into the loss function. The algorithm is contrasted with the common algorithms using the ADNI data set. The experimental results show that the MAE index of the synthetic PET picture has decreased while the SSIM and PSNR indexes have increased. The experimental results imply that the suggested approach could preserve picture structural information while enhancing image quality in both subjective and visual metrics. By introducing improvements in the generator, the residual initial module and attention mechanism are used to improve the learning ability of the generator, and the multiscale discriminator is used to enhance the discriminative performance of the model. The comparative experimental results under the ADNI dataset show that the improved algorithm in this paper can preserve the image's structural information and contrast information. As a result, the generated image is visually closer to the actual print. However, there are still some shortcomings in this paper. For example, the medical images collected by instruments with different parameters have certain deviations. Furthermore, this paper uses the



## *Retraction*

# **Retracted: Structural Modifications and Strategies for Native Starch for Applications in Advanced Drug Delivery**

### **BioMed Research International**

Received 12 December 2023; Accepted 12 December 2023; Published 13 December 2023

Copyright © 2023 BioMed Research International. This is an open access article distributed under the Creative Commons Attribution License, which permits unrestricted use, distribution, and reproduction in any medium, provided the original work is properly cited.

This article has been retracted by Hindawi, as publisher, following an investigation undertaken by the publisher [1]. This investigation has uncovered evidence of systematic manipulation of the publication and peer-review process. We cannot, therefore, vouch for the reliability or integrity of this article.

Please note that this notice is intended solely to alert readers that the peer-review process of this article has been compromised.

Wiley and Hindawi regret that the usual quality checks did not identify these issues before publication and have since put additional measures in place to safeguard research integrity.

We wish to credit our Research Integrity and Research Publishing teams and anonymous and named external researchers and research integrity experts for contributing to this investigation.

The corresponding author, as the representative of all authors, has been given the opportunity to register their agreement or disagreement to this retraction. We have kept a record of any response received.

### **References**

- [1] P. Bhatt, V. Kumar, R. Goel et al., "Structural Modifications and Strategies for Native Starch for Applications in Advanced Drug Delivery," *BioMed Research International*, vol. 2022, Article ID 2188940, 14 pages, 2022.

## Research Article

# Structural Modifications and Strategies for Native Starch for Applications in Advanced Drug Delivery

Pankaj Bhatt <sup>1,2</sup>, Vipin Kumar <sup>2</sup>, Richa Goel <sup>1</sup>, Somesh Kumar Sharma <sup>3</sup>,  
Shikha Kaushik <sup>1</sup>, Shivani Sharma <sup>4</sup>, Alankar Shrivastava <sup>1</sup>, and Mulugeta Tesema <sup>5</sup>

<sup>1</sup>KIET Group of Institutions (KIET School of Pharmacy), Delhi NCR, Muradnagar, Ghaziabad, India

<sup>2</sup>Department of Pharmaceutical Science, Gurukul Kangri (Deemed to Be University), Haridwar, Uttarakhand, India

<sup>3</sup>Department of Pharmaceutics, KIET Group of Institutions (KIET School of Pharmacy), Delhi NCR, Muradnagar, Ghaziabad, India

<sup>4</sup>School of Pharmacy and Research, Dev Bhoomi Uttarakhand University, Dehradun, Uttarakhand, India

<sup>5</sup>Department of Chemistry (Analytical), College of Natural and Computational Sciences, Dambi Dollo University, Dambi Dollo, Oromia Region, Ethiopia

Correspondence should be addressed to Mulugeta Tesema; [mulugeta@dadu.edu.et](mailto:mulugeta@dadu.edu.et)

Received 4 June 2022; Revised 12 July 2022; Accepted 22 July 2022; Published 10 August 2022

Academic Editor: Mukesh Soni

Copyright © 2022 Pankaj Bhatt et al. This is an open access article distributed under the Creative Commons Attribution License, which permits unrestricted use, distribution, and reproduction in any medium, provided the original work is properly cited.

Pharmaceutical excipients are compounds or substances other than API which are added to a dosage form, these excipients basically act as carriers, binders, bulk forming agents, colorants, and flavouring agents, and few excipients are even used to enhance the activity of active pharmaceutical ingredient (API) and various more properties. However, despite of these properties, there are problems with the synthetic excipients such as the possibility of causing toxicity, inflammation, autoimmune responses, lack of intrinsic bioactivity and biocompatibility, expensive procedures for synthesis, and water solubility. However, starch as an excipient can overcome all these problems in one go. It is inexpensive, there is no toxicity or immune response, and it is biocompatible in nature. It is very less used as an excipient because of its high digestibility and swelling index, high glycemic index, paste clarity, film-forming property, crystalline properties, etc. All these properties of starch can be altered by a few modification processes such as physical modification, genetic modification, and chemical modification, which can be used to reduce its digestibility and glycemic index of starch, improve its film-forming properties, and increase its paste clarity. Changes in some of the molecular bonds which improve its properties such as binding, crystalline structure, and retrogradation make starch perfect to be used as a pharmaceutical excipient. This research work provides the structural modifications of native starch which can be applicable in advanced drug delivery. The major contributions of the paper are advances in the modification of native starch molecules such as physically, chemically, enzymatically, and genetically traditional crop modification to yield a novel molecule with significant potential for use in the pharmaceutical industry for targeted drug delivery systems.

## 1. Introduction

Starch has been utilised in everyday life for centuries. Egyptians generally used cooked flour of various cereal pastes which was diluted with vinegar to prepare cement papyrus strips, although the early Chinese public covered the papers with starch which had less viscosity when gelatinized to avoid ink permeation. Carbohydrate chemists began synthesising several starch compounds in the 1930s, considerably expanding starch's utility. Starches are essential carbohy-

drates which are included in our nutritional intake and come from a variety of environmental sources which can be listed as such as rice, wheat, potato, maize and wheat, potato, rice, maize, and tropical plants. They have a wide variety of qualities that help to obtain the preferred quality of food products. Due to the limitations of raw starch obtained directly from natural sources, during processing, some of its characteristics being resistance to high temperature, viscosity, and thermal disintegration, the food industries have a preference for starches with superior behavioural qualities [1].

TABLE 1: Different physical modifications and properties changed after native starch modification.

Starch type	Technique(s)	Modification method	Properties changed	Reference
Rice starch	Heat and moisture treatment	It is performed at the moisture content of 25%, then allowed to stand at 4°C for 24 hrs, transferred to screw stainless steel nonstop, then heated with oil for 4 h at 110°C, and then dried at 40°C.	Digestibility, physiological index, nutritional content, biochemical indices	[30]
Potato starch	Osmotic-pressure treatment (OMT)	100 g of dry starch is suspended in Na <sub>2</sub> SO <sub>4</sub> solution, kept in the autoclave at 105°C and 120°C at 328 and 341 bar, respectively, kept for a particular period of time, and then cooled to room temperature; excess chemicals are removed by rinsing through distilled water, finally centrifuged, and then dried at 40°C.	Microscopy, thermal properties, particle size, pasting properties, viscosity, water holding strength,	[31]
Potato starch	Deep freezing	Starch which is dried through an oven is immersed in liquid N <sub>2</sub> kept in an open container for a particular period of time, then the nitrogen is allowed to evaporate, and the sample is allowed to warm up to the room temperature for a while.	Molecular structure, chemical composition, thermal properties, diffraction patterns, viscosity	[27]
Corn starch	Pulsed electric fields treatment	Deionized water is added to the suspension of native corn starch (8% w/w) along with KCl to maintain a 200 μS/cm electric conductivity. The sample is then exposed to different levels of PEF where it is filtered and dried at 40°C afterwards.	Particle size distribution, diffraction pattern, viscosity, granulation, size, denaturation, and molecular rearrangement	[32]
Waxy maize and potato starch	Thermally inhibited treatment (dry heating)	Firstly, starch is partially hydroxypropylated; then xanthan gum was added to water with constant stirring. The prepared gum solution is added to the starch, mechanically stirred for a specific period, and then dried in a hot air oven to maintain a moisture of <10%; then the mixture of starch and gum is heated at 130°C for 2-4 h.	Viscosity, pH of the mixture, pasting properties, light transmittance, paste clarity	[33]
Maize starch	Superheated starch	A mixture of demineralized water and starch in 5:1 is heated at the desired temperature in DSC with the rate of increase in temperature to be 10°C/min and cooled rapidly at a rate of decrease in temperature to be 200°C/min to 25°C	Physical characteristics, molecular characteristics, thermal properties, gelling properties,	[34]

Starches are carbohydrates composed of primarily of two components called amylopectin and amylose. This biodegradable and nontoxic biopolymer is abundant in nature and creates consistent pastes and gels when heated in the presence of adequate water. As a result, starch is widely considered as an industrial ingredient in large quantities in a wide range of industries including chemicals, petrochemicals, pharmaceuticals, bioethanol, food, feed, paper, cloth, laundry finishing, construction resources, and other decomposable products [2].

Free fatty acids and lipids present in the form of phospholipids in starch [3] and tend to form complexes with amylose and amylopectin and form starch granules with less solubility [4]. Their end products are opaque and low-viscosity pastes [5] which significantly reduces the property of the starch particles [6]. Hence, starch is considered as biocompatible and nontoxic, although LC50 is characterised as toxic when 50% embryos die at a conc. of 1 mg/ml equal to 1000 mg/l [7]. Excipients have traditionally been thought of as inactive chemicals that serve as binders, sweeteners, disintegrants, and adhesives in oral delivery systems [8].

In the past decades, to enhance patient amenability, biocompatibility, and effectiveness, more importance has been given to the effects of excipients on formulation and to the decrease in the use of synthetic/chemical grade excipients in pharmaceutical formulations [9].

Excipients have been proven in studies to change the rate at which the drugs are released from the formulations, hence changing the system's efficiency and the active pharmaceutical ingredients absorption. As a result, there is a growing trend in the direction of use of naturally obtained excipients, sometimes known as "herbal excipients" [10]. The extracts of the plant and their useful properties may prove helpful in pharmacological studies possessing large amounts of bioactive constituents, which can be used for the preparation of therapeutic and health promoting formulations which may provide future drugs for dreadful diseases [11]. Being biologically active, phytochemical constituents are natural compounds found in plants which protect them from diseases and damage [12].

Inappropriately, starches have limited functionality in their natural state, which can make them difficult to use.

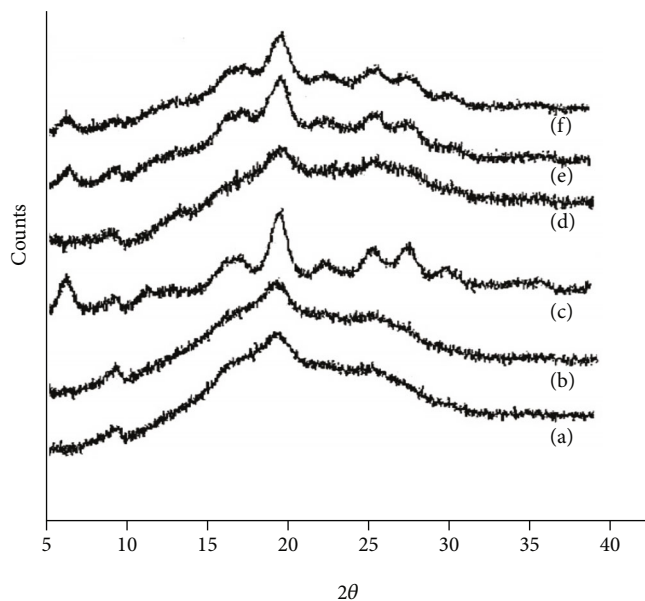


FIGURE 1: Models of X-ray diffraction of different starch samples: (a) frozen oven-dried. (b) Oven-dried and frozen without the use of water. (c) The ratio of water to oven-dried and frozen is 1:1.5 and 1:1. (d) Oven-dried and mixed only with water, but not frozen. (e) Dried and not frozen in the air. (f) Dried and frozen in the air [27].

The temperature of gelatinization, digestibility, rheological properties, crystalline quality, different amounts of water absorbed at different temperatures, pasting capability, and strength of the gel are only a few of the properties that each starch source has. Due to the paucity of economical sources, modified starches have been frequently prepared and used to improve quality and overcome various limitations of native starches, henceforth broadening their use in industry. Modification methods can alter a variety of features including gelatinization, swelling, solubility, pasting and retrogradation quality, digestibility, and rheological properties, among others [13]. As a result, many forms of starch alterations are used to enhance the structural, physical, and functional qualities for precise utilisation of starches.

Chemical alteration procedures are most commonly carried out in industry because they are efficient in cost and simple to use. The three accessible -OH functional groups (at C2, C3, and C6 positions) (at positions C2, C3, and C6) [14] of the molecular structure can be transformed with a few chemical modifications named etherification, esterification, and/or oxidation in the most widely used chemical procedures [15]. The amount of alteration in each of the three groups varies based on the genetic origin and synthesis conditions [16]. By modification of starch, gelatinization, swelling, solubility, pasting, and retrogradation are the few properties which are affected [13]. Compared to its natural form, these newly developed features allow the altered starch to be considered for use for pharmaceutical purposes, such as the use of it as an excipient. Demat form and screened starch is frequently used as a stabilizer in the wet gelation process, and it is an important component in the formation

of capsules, tablets, and other dry dosing schedules [17]. A disintegrant is a pharmaceutical excipient used to break down solid dose forms such as granules, tablets, or into smaller discrete particles. The origin or type of starch determines the degree of swelling, which is symptomatic of the relative contribution and structure of amylose and amylopectin in the particular starch [18, 19].

The weak associated interactions of starch can indicate its disintegrating ability [20], which is caused by the creation of holes via which liquids can permeate the dry active ingredient, enabling the medicine to dissolve. Starch absorbs moisture between 10 and 17 percent when acclimatised to typical ambient air due to its hygroscopic characteristics [21].

As a result, this paper examines the different processes to alter the various properties of the native starch. From the plant sources, native starch with minimal treatment was obtained [22]. Starch is constant in storage for longer periods [23]. Native as well as modified starches are used as pharmaceutical excipients because of their soft dryness, gelling, and viscosity providing properties [17].

## 2. Physical Modification

In the food industries, physical changes are applied since they do not require any chemical entity for reaction processes. Several new technologies have emerged in the physical modification of starch. Deep freezing, osmotic pressure treatment, and dry heating are few of the latest physical alterations that have been researched in the recent decade [24]. It does not cause the D-glucopyranosyl units of the starch molecules to be modified. Physical modifications simply modify the structural arrangement of starch molecules inside the granules and the complete arrangement of the granules. These alterations in granules have an impact on starch characteristics such as paste and gel properties and even digestibility [25] as presented in Table 1.

Miller and Huber [24] studied the results of three different studies and reported changes in the properties of starch which are affected by osmotic pressure treatment. These changes were due to the heating of the starch in an osmotic solution which reduces granule gelatinization and swelling; hence, osmotic pressure treatment is a type of hydrothermal treatment. Szymonska and Krok [26] and Szymonska and Wodnicka [27] reported that recurrent thawing and freezing of potato starch granules of 13% moisture resulted in surface erosion, increased surface area, mean pole diameter, and total micro- and mesovolume. Chiu et al. [28] heated starch with <15% moisture at a temperature of 100C and the temperature at which thermal degradation occurred, and it formed products with shear, acid, and temperature tolerances related to those of chemically cross-linked starches. The transformation was due to low moisture content and alkalinity. Fluidized bed is a way to heat starch, but this process has only been investigated with amaranth [29].

The changes in the molecular structure of starch samples have been studied through FT-IR, and X-ray diffraction results are shown in Figures 1 and 2. The results inferred

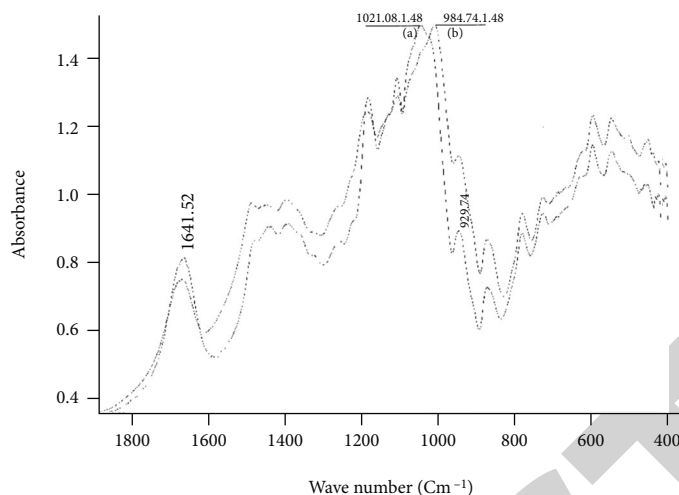


FIGURE 2: FT-IR absorption spectra of potato starch: (a) oven-dried and iced up with water in the ratio of 1 : 1.5; (b) oven-dried and not iced up [27].

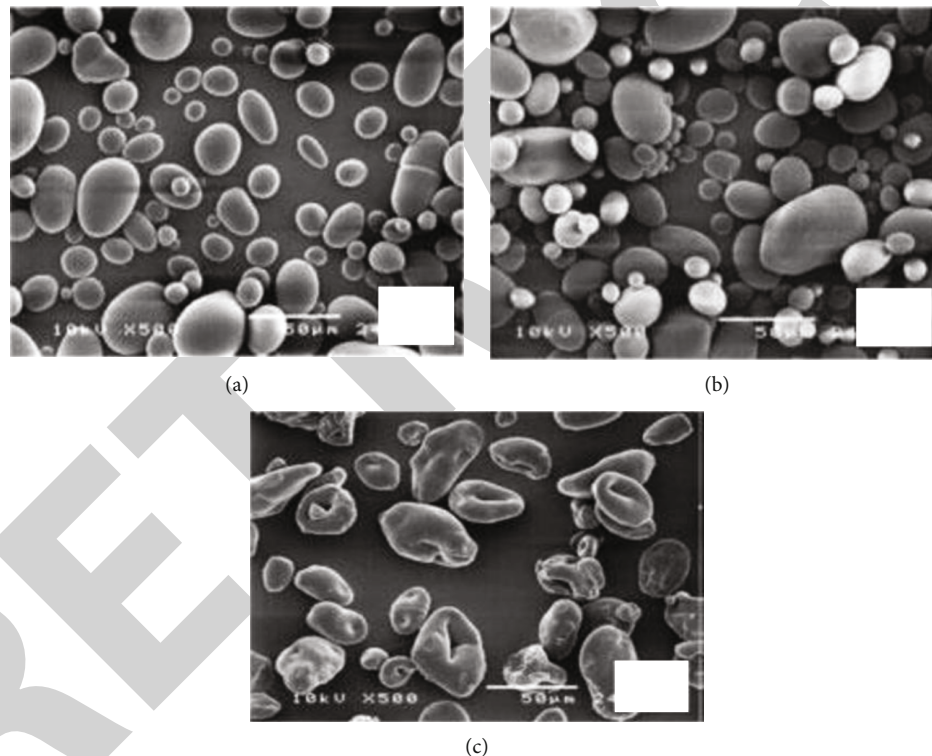


FIGURE 3: SEM of starch granules of potato. (a) Potato native starch. (b) Moisture heat treatment of starch sample (120°C, 60 min). (c) Osmotic pressure treatment with potato starch (120°C, 60 min) [31].

that the molecular structure of the starch is being changed and due to that the various properties of the native starch are also altered [27].

Pukkahuta et al. studied through SEM results (Figure 3) that there is no variance between native and heat moisture treated potato starch, but osmotic pressure-treated potato starch causes changes in the granular morphology of the pretentious granules, and these seem to have folded structures with their outermost side down inwards, looking like donut's shape. This transformed morphology of granules

are because of the effect of osmotic pressure treatment is called "plasmolysis" [31].

### 3. Enzymatic Modification

Hydrolysing enzymes have been widely used in enzymatic modifications [25]. The distribution of branch chain length, molecular mass of amylose/amylopectin, and percentage of amylose/amylopectin are the properties that are altered by the enzymatic modifications of natural starch. Designing a

TABLE 2: Enzymatic modifications and properties changed after native starch modification.

Starch type	Reagent used	Modification method	Properties changed	Reference
Corn starch	4- $\alpha$ -Glucotransferase	Cornstarch is prepared with pH 7.5, 50 mM Tris-HCl buffer solution (8% w/v), then heated in a water bath at 95°C for a particular period of time, and then the reagent is mixed to the mixture. It is incubated for different time intervals, then immediately kept in autoclave for 30 min. Then, ethanol is used to precipitate out the reagent, centrifuged, washed with the help of deionized water, and then freeze-dried.	Digestibility, amylose content, iodine binding, chain length distribution, molecular weight, structural properties	[41]
Rice starch	Pullulanase	A 20% suspension of native starch is treated with sodium acetate buffer, and then it is gelatinized in a boiling water bath for 30 min; pullulanase (20 U/g) is added and kept at 60°C for 6 h. After that, the mixture is kept in the boiling water bath for a while to stop the enzymatic reaction, and it is cooled at room temperature. Then, stored at 4°C for 24 h. the precipitate is centrifuged and dried in a blast drying oven.	Chain length distribution, surface holes, physiochemical properties, crystalline structure, swelling index, solubility, thermal properties, digestibility, rheological properties	[42]
Amylose starch	Glycogen branching enzyme in <i>Streptococcus mutans</i> (SmGBE)	A starch solution is prepared with 1 N NaOH followed by demineralized water and 200 mM buffer consisting of sodium acetate and the pH is raised to 5.0 using hydrochloric acid and then gelatinized and incubated for 1-24 h at 37°C in 6001 SmGBE, then three volumes of ethanol are added to and kept at 4°C for 1 h. and then ppt. Is centrifuged and washed with ethanol followed by vacuum drying.	Branch chain length, molecular weight, retrograde properties, digestibility	[43]
Maize starch	Maltogenic amylase	Starch sample is dispersed in sodium acetate buffer and then the mixture is heated at 90°C for a particular period of time, cooled to 50°C and hydrolysed by Maltogenic amylase at 50°C for the period of time then kept at 95°C for 15 min to finish the enzymatic reaction.	Molecular weight, chain length thermal properties, swelling index, digestibility, branched density.	[44]
Cassava starch	Fungal lipase	Palmitic acid and starch are taken in equal proportion and dissolved in solution (DMF). 200 mg lipase power is added and incubated in a water bath at 40°C for 4 hours; by adding alcohol the sample is precipitated and then is oven dried.	Thermostability, digestibility, swelling power, viscosity,	[45]
Rice starch	$\beta$ -Amylase	20% suspension is prepared with native starch and sodium acetate buffer and then allowed to be gelatinized on a water boiling bath for almost 30 min. And immediately kept in an autoclave at 121°C for an hour, then incubated with the $\beta$ -amylase at 55°C for 15 minutes. Then kept in a boiling water bath to inactivate the enzyme. Stored at 4°C for 24 hr. and ppt. Were separated through centrifugation and dried through blast drying oven	Crystalline properties, chain length distribution, amylose content, thermal properties, digestibility, solubility, swelling index,	[42]

starch with a specific and unique structure of starch can be processed by enzymatic reactions which occur when the gelatinized starch reacts with the provided enzyme to form upgraded starch. For enzymatic starch alterations, it is one

of the modification procedures as discussed in Table 2. For a variety of food and nonfood uses, these processes usually result in starch with modified physicochemical properties and structural qualities [35]. The less well-ordered

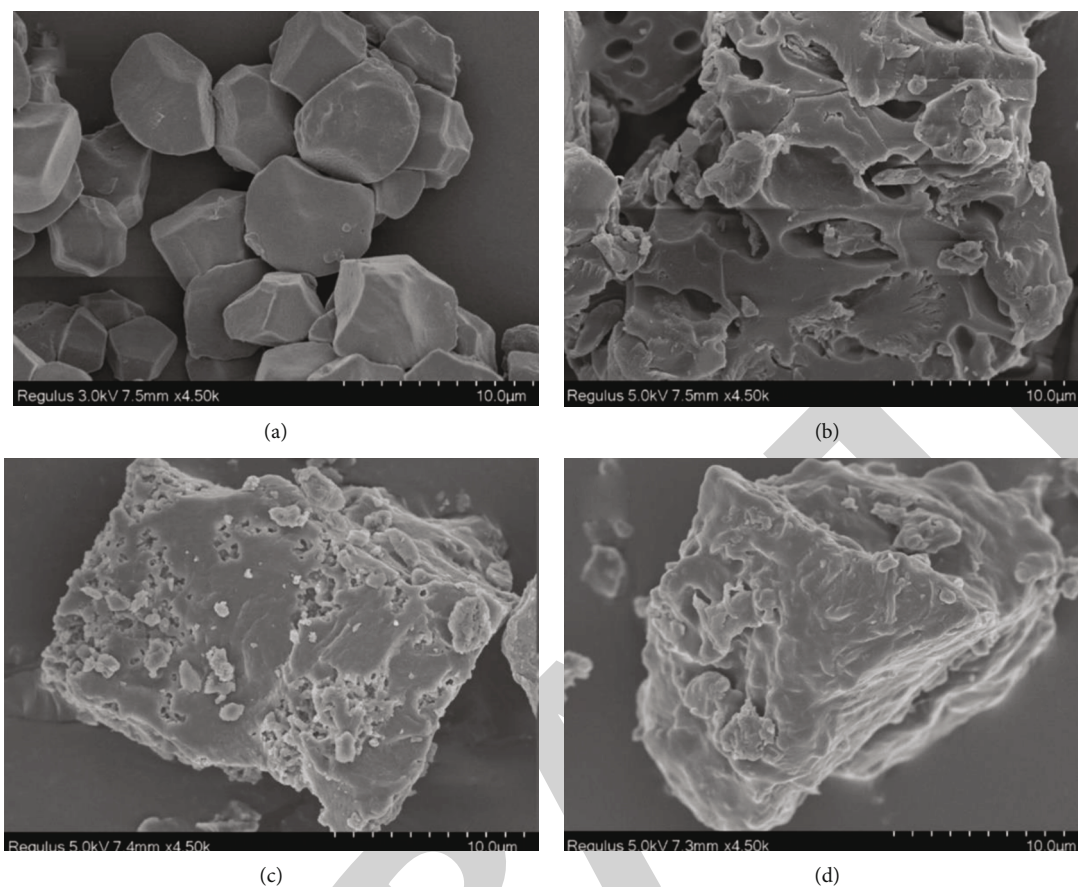


FIGURE 4: SEM results of (a) native rice starch (NRS), (b) autoclaved developed starch (A-MS), (c) autoclaved/pullulanase-changed starch (A/PUL-MS), and (d) autoclaved/sequential three enzymatic-modified starch (A/STE-MS) [42].

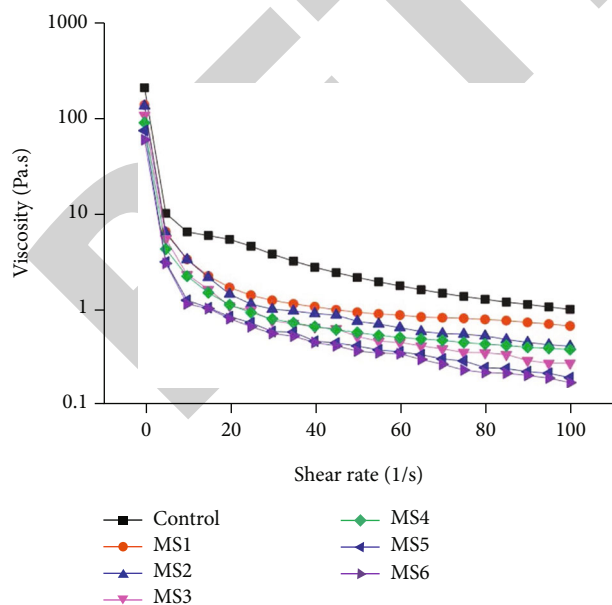


FIGURE 5: Viscosity of 4 $\alpha$ GT-treated starch with different concentrations of 4 $\alpha$ GT [41].

amorphous sections in the structure are more vulnerable to enzymatic replacement, but the most resistant part to enzymatic treatment is crystalline lamellae [36, 37].

Hydrolytic enzymes, also known as hydrolases, break different groups of biomolecules such as esters, glycosides, and peptides. They break down lipids, nucleic acids, proteins, carbohydrate, and fat molecules into their simplest units [38]. The proportion of different components of enzyme and the source of the enzyme influence the rate of enzymatic [39]. Lignocellulose enzymatic hydrolysis has long been studied as a method to depolymerize the biomass into fermentable sugars and conversion to biofuels and biochemicals [40]. Cellulose to glucose enzymatic hydrolysis has received increased interest over the last 10 years. The growing demand for economically sustainable biofuels specifies an urgent need for reducing the costs related to their production [35].

As per Li et al., native rice starch grains are polyhedral, angular, and irregular, and the surfaces are smooth with no cracks as displayed in Figure 4. Due to gelatinization and retrogradation of the modified starches, the granular structures get disappeared completely. A-MS has continuous irregular spongy structures with continuous network. These have pores and loose structure, but the structures of A/PUL-MS

TABLE 3: Oxidation of starch and properties changed modification.

Starch type	Reagent used	Modification method	Properties changed	Reference
Potato starch	Hydrogen peroxide (30%)	The starch is made with the help of distilled water and maintaining pH to 4 with the help of $\text{CH}_3\text{COOH}$ and then added $\text{H}_2\text{O}_2$ dropwise, left it for 8 h, and dried at $45^\circ\text{C}$ for 48 h in a hot air oven.	Viscosity, C-H bonds, crystalline properties, microstructure	[63]
Cassava starch	Ozonation by industrial oxygen	The starch is dispersed in water in 1 : 10 ratio mixture in a glass reactor; then ozone is produced by using ozone generator unit, ozone is passed through the sample and treated for 15-30 minutes.	Solubility, crystallinity, rigidity, tensile strength, opacity	[64]
Rice starch	13-Hydroperoxyoctadecadienoic acid	The 10 mg/ml rice starch mixture were incubated using a particular conc. of 13-HPODE at $25^\circ\text{C}$ for 24 h. Unreacted 13-HPODE is decanted, and modified rice starch is lyophilized in its place.	Solubility, oil holding ability, water holding ability, foaming ability, emulsification, foam stability, activity index, emulsification stability index	[65]
Arracacha starch	Ozonation	The ozone in ozone generator unit by the coronal discharge method passed through the starch solution with water kept in a glass reactor and dried in oven at $35^\circ\text{C}$	Paste clarity, particle size, viscosity, pasting properties, water solubility and absorption indexes, molecular size, apparent amylose content.	[66]
Potato starch	$\text{H}_2\text{O}_2$ with electrolytic cell	A 50 g starch and 150 ml of 0.1 mol/l $\text{Na}_2\text{SO}_4$ were taken in an electrolytic cell with magnetic force stirring and a boiling water bath. $\text{H}_2\text{O}_2$ is added and the current is allowed to flow for a particular period, temperature reduced to $25^\circ\text{C}$ and filtered through vacuum filtration.	Carboxyl content, thermal stability, crystalline properties, viscosity, and chemical bonds	[67]

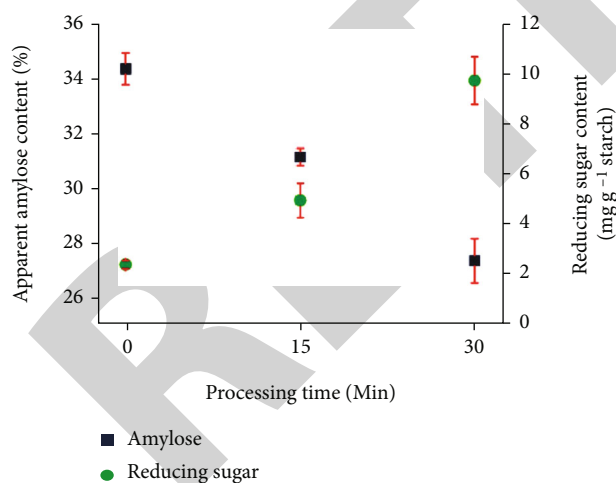


FIGURE 6: Apparent amylose and reducing sugar contents [66].

have fewer holes and small pore size and have dense layered structure compared to the A-MS, whereas A/STE-MS has no surface holes, and the granular structure is very dense which appears like a stone [42].

Jiang et al. have found the alteration in the rheological properties of normal starch and enzymatically modified starch as shown in Figure 5. The unmodified starches have

the greater viscosity compared to the modified one, and the viscosity of starch keeps on decreasing with the increase in the reaction time with 4 $\alpha$ GT [41].

#### 4. Genetic/Biotechnological Modification

The alteration in genetic material of the plant or biotechnological alteration of plant DNA is referred to as genetic modifications. The enzymes responsible for the production of starch are targeted by transgenic technology; thus, it is considered a genetic alteration technique which can also be done through traditional plant breeding techniques or biotechnology [46]. Plant biotechnology breakthroughs have created a good prospect to increase the quality of starch in various crops. Starch is not only a common dietary carbohydrate [47] but also a low-cost, renewable raw resource utilised to make varieties of vital products, e.g., paper, textiles, medications, construction materials, and nutraceuticals [48]. Multiple aspects of starch can be changed through genetic manipulation, including morphological characteristics, crystallinity, gelation temperature, amylopectin and amylose ratio, and the number of phospholipids. In general, there are three types of genetic alteration of crops that can be done, e.g., traditional crop modification, genetic engineering, and genome editing [49].

Plants generate a range of proteins, including mammalian antibodies, blood substitutes, vaccines, and some other



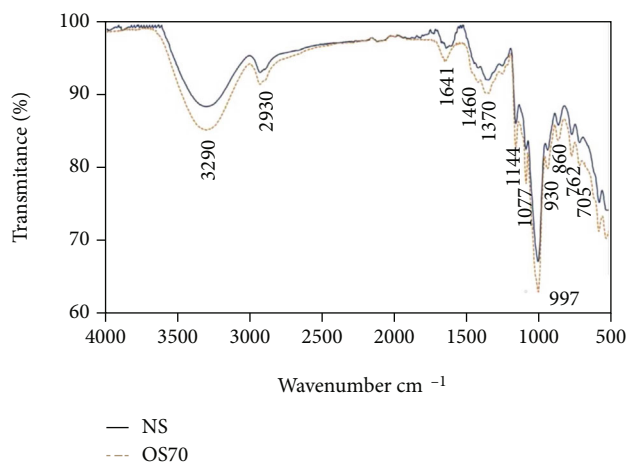


FIGURE 7: FT-IR of native and oxidised ( $H_2O_2$  treated) potato starch [53].

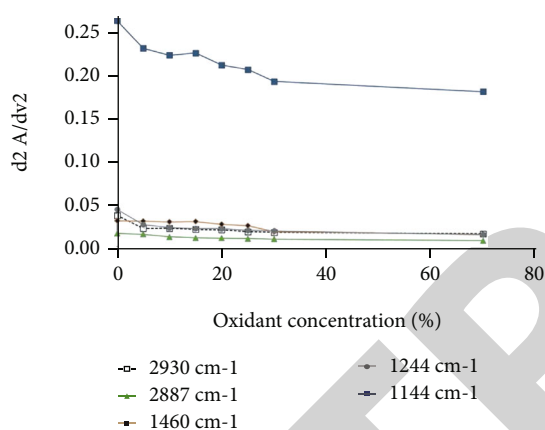


FIGURE 8: 2nd derivative FT-IR band behaviour as a function of the oxidant concentration [53].

therapeutic substances using gene editing, which has led to a renaissance of interest in getting novel pharmaceutical molecules from botanical extracts [23]. Foreign protein production from genetically engineered plants has recently emerged as a viable alternative to microbial fermentation or mammalian cell culture. Plants genetically engineered to function as bioreactors can create fusion proteins in larger numbers than mammalian cell systems [50]. Traditional therapeutic immunotherapies were produced in rodents by the body's immune system; however, these molecules were quickly detected as foreign, restricting the value of such inhibitors for therapeutic usage, especially with chronic exposure. Aside from the absence of anaphylaxis or serum sickness, the presence of neutralising antibodies that inactivate the medicine frequently precludes future therapeutic usage. While innovative technologies have enabled the replacement of murine antigens with substantially humanised or chimeric antigens and the synthesis of full human antigens [42], polio vaccines, like conventional food vaccines, employ whole, weakened microorganisms or semipurified substances to promote both systemic (Ig-G) and local mem-

brane (Ig-A) protection. Plant vaccines may produce complete proteins, but the use of DNA encoding just specific antigenic regions from bacteria, harmful viruses, and parasites has garnered a lot of interest [51].

## 5. Traditional Crop Modification

The traditional methods of modification of the plant such as selective breeding and cross-breeding are one of the processes in which plant breeding is used to selectively develop a particular phenotypic trait by selecting which male and females will reproduce and have offspring together.

**5.1. Genetic Engineering.** It is basically a method in which authorized experts copy a particular gene with a look for a trait from one plant and put it into the other plant in which the desired characteristics are incorporated, and it builds the scientific advantages through DNA technology.

**5.2. Genome Edition.** Genome edition is a novel approach that allows some researchers to generate new crop types in a more precise and targeted manner. The use of a genome editing tool makes modifications easy and efficient that were previously possible through traditional breeding [52].

## 6. Chemical Modification

It is done by attaching a functional group in to the molecular structure of starch in its natural state resulting in specific physicochemical properties for the starch molecule. These alterations influence the retro gradation, pasting ability, proximal composition, and gelatinization of unmodified starch granules [53]. At various sites and locations of unmodified starch, the stability of intra- and intermolecular interactions are increased due to these alterations which are carried out with the help of various chemicals. The other chemical and functional properties of altered starches are affected by the amount of starch supply, degree of substitution, synthesis environment, types of starch used, and the circulation of their placing agents throughout the starch molecule. The derivatization methods that are used for chemical alterations are oxidation, acetylation, cross-linking, acid hydrolysis, cationization, etc. [54].

The starch is recyclable and the existence of particular functional groups and the macroscopic structure of starch are all factors that influence its sensitivity towards modification. Furthermore, regarding chemical modifications subjected to the position of -OH group and alpha-1, 4-glycosidic bonds versus alpha-1,4-glycosidic bonds and alpha-1,6-glycosidic bonds in starch have different properties. Primary alcohols have a hydroxyl group at carbon C6, whereas secondary alcohols have a hydroxyl group at carbons C2 and C3. Unmodified starch is a triol compound which can be converted to hemiacetal whenever the glucose ring component -CHOH-CHOH- replaces the carbon atoms at C2 and C3 positions. The existence of three -OH groups in glucose renders it amenable to replacement processes allowing for a wide range of starch alterations. The reactivity of starch is also affected by its grain size. The susceptibility to modification increases with the size of the

TABLE 4: Esterification of starch and properties changed modification.

Starch type	Reagent used	Modification method	Properties changed	Reference
Maca starch	Citric acid	Citric acid and native starch are mixed and kept at room temperature for 16 h and dried in a hot air oven to obtain a moisture level of around 5-10%, afterwards, it is dried at 140°C for 4 h before being cleaned with distilled water multiple times to eliminate untreated citric acid.	Digestibility, microstructure, partial size, zeta potential value, stability	[71]
Waxy maize starch	Octenyl succinic anhydride (OSA)	The starch is suspended in purified water and the pH is brought to 8.5 with the help of NaOH, the required amount of OSA (0.5-3% starch) is added slowly and left for 6 hrs. At room temp. Then, the pH were maintained to 6.5 with HCl, then centrifuged, washed, and oven dried.	Digestibility, molecular structure, nutritional properties, swelling properties, solubility, gelatinization, retrogradation	[72]
Waxy corn starch	Dodecyl succinic anhydride (DDSA)	An emulsion of DDSA and MES prepared by distilled water, finished dried starch is suspended in water, pH is adjusted to 8.5 with NaOH and the emulsion mentioned above is added, after reaction pH is maintained at 6.5-7 by HCl, the mixture is centrifuged and dried in vacuum oven	Wettability, contact angle, water solubility, chemical bonds	[73]
Waxy maize starch	Citric acid	In a ratio of 5:2 w/w, starch and citric acid are dissolved in distilled water, respectively, pH is adjusted to 3.5 with NaOH and kept at normal temperature for 24 h, then esterified at 130-150°C for 3-5 h. it is washed with ethanol and dried.	Digestibility, gelatinization, particle size, microstructure, chemical bonds, clarity	[74]
Corn starch	Folic acid	Firstly, folic acid is reacted with N,N'-dicyclohexylcarbodiimide and dimethyl sulfoxide, then addition of starch to the reaction mixture and afterwards reacted in dark conditions for 24 h, then the product is washed with 0.1 N HCl, then the unreacted FA is washed out, the finished substance is lyophilized and powdered.	Mesoscopic structure, crystallinity, molecular packing, digestibility, solubility, wettability	[54]
Canna starch (RS4)	Citric acid	Citric acid is dissolved in water and the pH is adjusted to 3.0 with the help of NaOH, the solution is uniformly sprayed on canna starch and the mix is being packed and vacuum treated. The sample were kept in Petri dish and kept in microwave at 55°C for 4 min for microwave treatment, grind powder and IR treatment at 140°C for 1 h. after that, it is rinsed with purified water and then ethanol and in the end oven dried.	Digestibility, optical activity, pasting properties, thermal properties, particle size, and crystallinity.	[75]

grains. This is due to the fact that external influences have comparatively easier contact with larger grains. Modification is the procedure of altering normal properties through physical, chemical, or enzymatic processes [55].

## 7. Oxidation of Starch

The most commonly used alteration technique to obtain specific changes in molecular structure is the oxidation of starch. In this process, the primary and secondary -OH groups present in the glucose molecule led to the development of aldehyde or carboxyl groups. The efficiency of the oxidation reaction is determined by the nature of the oxidant, the biological origin of the starch, and the procedural parameters. Furthermore, the oxidation method can affect the intermolecular bonds and/or fractional depolymerisation

of polymer chains present in the starch molecule [55]. Typically, the properties of starch are altered by carrying out a reaction of the slurry of starch with an oxidising agent at a particular temperature and specified pH [56]. The three most accessible -OH groups react with the oxidising agents throughout the oxidative process to create new starch derivatives. The oxidative technique and reagents are considered a parameter to govern the type and quality of the oxidised starch derivative. As a result, the native starch-derived physicochemical properties are improved [57]. Table 3 shows the oxidation of starch and the change in its properties after modification. Oxidised starches are widely used in the paper industry to improve paper strength and processability. It is also used in the finishing, textile, laundry, construction materials, and culinary sectors. The major purpose of oxidised starch seems to be in the pulp and leather sectors;

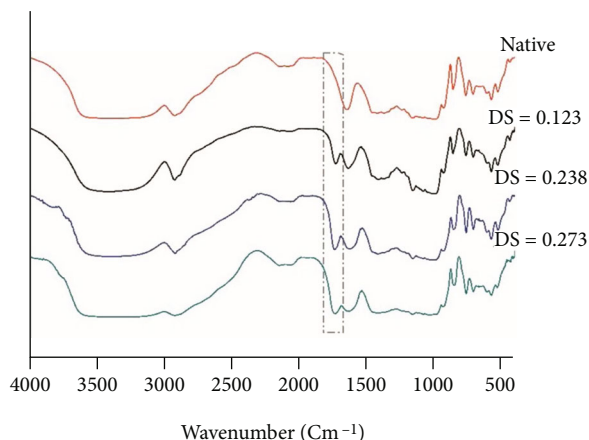


FIGURE 9: FT-IR spectra of native- as well as citric acid-treated starch [9].

nevertheless, due to its low viscosity and high stability, clarity, film forming, and bonding quality, which have been employed in food coatings, its usage inside the food sector is expanding. The oxidation approach for starch alteration is an essential procedure in which absorption bands such as carbonyl and carboxyl groups are inserted into the starch granules for depolymerization [54] despite the fact that proper conditions, such as temperature and pH, must be maintained during oxidation. The aggressive oxidants utilised are hydrogen peroxide, peracetic acid, potassium permanganate, sodium hypochlorite, chromic acid, and nitrogen dioxide [55, 56].

In recent years, oxidised starch has been widely used in the food sector to create adherent surfaces and coatings [57]. Because of partial macromolecule decomposition in oxidised starches, they have reduced hot paste viscosity, a lesser susceptibility to syneresis due to bulk carbonyl and carboxyl groups, whiter granules, and more translucent pastes [58]. Reagents that generate ether or ester linkages with hydrophilic groups in starch granules play an essential role in bridge starch [59]. This alteration increases the stiffness of the polymer by producing a three-dimensional web. Cross-linking increases the degree of polymerization and molecular mass in starch. Aside from the origin of the starch molecules, the methods and settings utilised for covalent modification have a considerable influence on the end product's quality. Cross-linking affects the paste clarity and swelling capacity [60, 61], because of the pastes' stabilising, hardening, purity, and thermal decomposition qualities. Crucifix starch is related to frozen pharmaceutical preparations in the food business, as well as being employed in other sectors such as polymers [62].

As reported by Lima et al. Figure 6 represents the amylose content in native and oxidised starch, and it gets reduced with the increase in the reduced sugar, and the amount of amylose present in the modified starch also depends on how long the starch is being treated with ozone [66].

According to Barbosa et al., there are structural changes in potato starch as presented in Figure 7 which are due to the

reduction in the basic viscosity of the starch as the amount of  $H_2O_2$  is increased, and it is significant if the molecular weight is reduced. It occurs due to breakage of glycosidic bonds during the reaction and consequently, due to modification. However, the oxidation reaction is not at all easy to identify due to bands' overlapping and suppression. Therefore, a 2nd derivative process is carried out on the spectra to develop the sensitivity for the possible changes in chemical structures which are changed during process. In Figure 8, the 2nd derivative values of band behaviour as a function of oxidant concentration have been shown for the wavenumbers 2930, 2887, 1460, 1244, and 1144  $cm^{-1}$  [53].

## 8. Esterification of Starch

It is a procedure in which three easily accessible -OH groups of starch molecules are converted to alkyl or aryl derivatives. This alteration process usually affects various properties, and one of the most important is its retro gradation ability resulting in reduced in-between amylase connections with the outside chain of amylopectin [68]. This category includes a number of techniques and acetylation in one of the techniques which is most frequently used. This technique is extensively employed in the biotechnology, food industry, and fabric sectors [69]. On the basis of the degree of substitution, acetylated starches are characterised into three different forms (DS), which are listed as low DS, medium DS, and high DS starches. Small degrees of substitution starch by acetyl group are the most prevalent type of acetylated modified starches. These low DS starches have a degree of substitution value of 0.01% to 0.2% and are cold water soluble [70]. Starches in medium DS are usually water-soluble at room temperature but not as much as low DS starches and have a degree of substitution of 0.3% to 1%. The solubility of high degree of substitution acetylated starches is not well in water but have a very good solubility in organic solvent, and the degree of substitution is 2% to 3%. The effectiveness and amount of acetylation are determined by the starch type's ultrastructure, which varies based on the botanical origin, as well as the reaction conditions. The changed properties after esterification of starch are shown in Table 4 [4]. Figure 9 shows the FT-IR spectra of citric acid and native starch FT-IR-treated starch.

Wu et al. reported that citrate-modified raw starch of canna is different from the citrate modified starch, because a new peak is observed by them in the modified starches at 1740  $cm^{-1}$ . This new absorption band is linked to the extending vibration of C=O bond of the carboxylic acid group. With the increase in the degree of substitution of citric acid, the peak at 1740  $cm^{-1}$  becomes stronger. These results confirm the esterification reaction carried out between canna starch molecules, and citric acid [75].

Lee and Chang reported that the shapes of maca starch granules as shown in Figure 10 are oval or round with being smooth in shape and are consistent with the previous studies. However, esterified maca starch with citric acid shows some of the irregular surfaces and some wrinkles and dents with irregular oval and doughnut shapes. They reported that

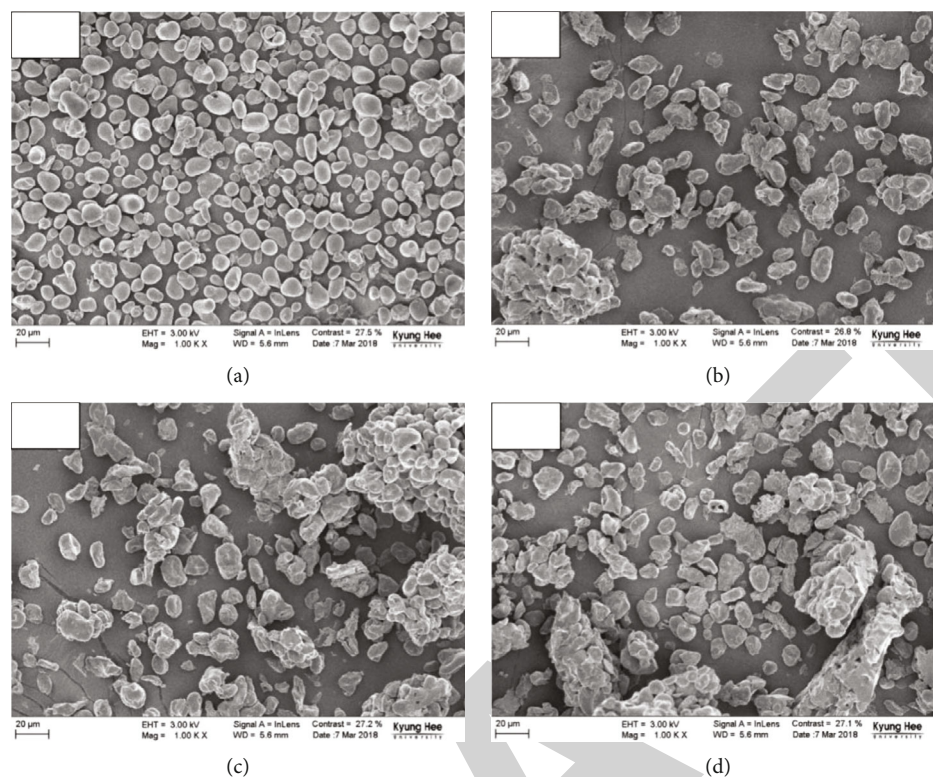


FIGURE 10: SEM of and esterified and native maca starch with citric acid [71].

the morphological properties of the esterified granules were almost the same in accordance to previous study [71].

## 9. Conclusion

However, these physical and chemical alterations may limit starch's utility in some formulations while enhancing its functional quality in others. Functionalizing delivery systems with these physicochemical features create new possibilities for enhancing the overall efficacy of starch related systems. The most common starch modification methods are chemical modification methods, which basically include esterification and oxidation and few other modification techniques. These are the modification methods which can alter various properties of starch like digestibility, chemical bonds, molecular structure, amylose, and amylopectin chain, and these can be altered according to the necessity of the properties which are required. In essence, physical modification shows that it significantly alters the physical properties of starch such as the morphology of granules or viscosity of the starch paste. Altering these properties can be beneficial for a targeted drug delivery systems. Genetic and enzymatic are other techniques which are also capable of altering the various properties of starch enzymatic modification and are also used to alter the nutritional content or gelatinization properties or granule morphology. Although enzymatic modifications which alter the properties in a similar fashion as chemical modifications but carrying out an enzymatic reaction is not feasible and cannot be performed without professionals, chemical modifications are preferred

over enzymatic modifications. The genetic modification alters with the plant genetic material and the properties of starch automatically get modified in its native form itself. Furthermore, this modified starch can be used in the formulation of novel drug delivery systems or in the preparation of various products according to the needs. If the chemical modifications were enhanced, novel drugs were isolated in the future having potential for use in the medical industry for a targeted drug delivery system.

## Data Availability

The data shall be made available on request.

## Conflicts of Interest

The authors declare that they have no conflict of interest.

## References

- [1] Y. F. Chen, L. Kaur, and J. Singh, *Chemical modification of starch*, Elsevier Ltd, 2018.
- [2] B. C. Maniglia, N. Castanha, P. Le-Bail, A. Le-Bail, and P. E. D. Augusto, "Starch modification through environmentally friendly alternatives: a review," *Critical Reviews in Food Science and Nutrition*, vol. 61, no. 15, pp. 2482–2505, 2021.
- [3] R. F. Tester, J. Karkalas, and X. Qi, "Starch—composition, fine structure and architecture," *Journal of Cereal Science*, vol. 39, no. 2, pp. 151–165, 2004.
- [4] W. R. Morrison, R. F. Tester, C. E. Snape, R. Law, and M. J. Gidley, "Swelling and gelatinization of cereal starches. IV.

- Some effects of lipid-complexed amylase and free amylase in waxy and normal barley starches," *Cereal Chemistry*, vol. 170, pp. 385–391, 1993.
- [5] S. A. S. Craig, C. C. Maningat, P. A. Seib, and R. C. Hosney, "Starch paste clarity," *Cereal Chemistry*, vol. 66, no. 3, pp. 173–182, 1989.
  - [6] S. C. Alcazar-Alay and M. A. A. Meireles, "Physicochemical properties, modifications and applications of starches from different botanical sources," *Journal of Food Science and Technology*, vol. 35, no. 2, pp. 215–236, 2015.
  - [7] H. Afidah, *Sintesis, pencirian dan penggunaan n-metilena fosfonik, oleoil dan oleoil metilena fosfonik kitosan sebagai penyerap minyak*, [Ph.D thesis], Fakulti Sains dan Teknologi, Universiti Kebangsaan Malaysia, 2014.
  - [8] P. Bhatt, S. Singh, S. Kumar Sharma, and S. Rabi, "Development and characterization of fast dissolving buccal strip of frovatriptan succinate monoydrate for buccal delivery," *International Journal of Pharmaceutical Investigation*, vol. 11, no. 1, pp. 69–75, 2021.
  - [9] J. Singh, L. Kaur, and O. J. McCarthy, "Factors influencing the physico-chemical, morphological, thermal and rheological properties of some chemically modified starches for food applications-a review," *Food Hydrocolloids*, vol. 21, no. 1, pp. 1–22, 2007.
  - [10] D. Ražem and B. Katušin-Ražem, "The effects of irradiation on controlled drug delivery/controlled drug release systems," *Radiation Physics and Chemistry*, vol. 77, no. 3, pp. 288–344, 2008.
  - [11] A. Hassan, U. Yaqoob, I. A. Nawchoo et al., "Conspectus of phytochemical constituents of *Euphorbia wallichii* Hook. F.: a review," *Research & Reviews: Journal of Botany*, vol. 5, pp. 24–31, 2016.
  - [12] S. Gulzar, A. Hassan, and I. A. Nawchoo, "Comparative analysis of the phytochemical constituents of two species of *Ajuga*," *International Journal of Research in Science and Engineering*, vol. 7, article 1116, 2018.
  - [13] R. N. Tharanathan, "Biodegradable films and composite coatings: past, present and future," *Trends in Food Science and Technology*, vol. 14, no. 3, pp. 71–78, 2003.
  - [14] A. Shrivastava, "Pulsatile drug delivery systems: a case of beta-blockers," *Asian Journal of Pharmaceutical and Clinical Research*, vol. 12, no. 3, pp. 16–22, 2019.
  - [15] J. Godara, R. Aron, and M. Shabaz, "Sentiment analysis and sarcasm detection from social network to train health-care professionals," *World Journal of Engineering*, vol. 19, no. 1, pp. 124–133, 2021.
  - [16] H. Pu, L. Chen, X. Li, F. Xie, L. Yu, and L. Li, "An oral colon-targeting controlled release system based on resistant starch acetate: synthesis, characterization, and preparation of film-coating pellets," *Journal of Agricultural and Food Chemistry*, vol. 59, no. 10, pp. 5738–5745, 2011.
  - [17] O. O. Kunle and A. B. Bangudu, "The effects of some starches on the properties of sulphadimidine tablets," *Pharmacy World Journal*, vol. 7, no. 1, pp. 26–31, 1990.
  - [18] H. T. Chan, R. Bhat, and I. Karim, "Physicochemical and functional properties of ozone-oxidized starch," *Journal of Agricultural and Food Chemistry*, vol. 57, no. 13, pp. 5965–5970, 2009.
  - [19] H. Kusumanyati, N. A. Handayani, and H. Santosa, "Swelling power and water solubility of cassava and sweet potatoes flour," *Procedia Environmental Sciences*, vol. 23, pp. 164–167, 2015.
  - [20] R. V. Manek, O. O. Kunle, M. O. Emeje et al., "Physical, thermal and sorption profile of starch obtained from *tacca leonpetaloides*," *Starch - Stärke*, vol. 57, no. 2, pp. 55–61, 2005.
  - [21] H. W. Leach, "Gelatinization of starch," in *Starch: Chemistry and Technology*, R. L. Whistler and E. F. Paschall, Eds., vol. 1, p. 20, Academic Press, New York, 1965.
  - [22] D. L. Madrigal-Aldana, B. Tovar-Gomez, M. M.-M. de Oca, S. G. Sayago-Ayerdi, F. Gutierrez-Meraz, and L. A. Bello-Pérez, "Isolation and characterization of Mexican jackfruit (*Artocarpus heterophyllus* L) seeds starch in two mature stages," *Starch - Stärke*, vol. 63, pp. 364–372, 2011.
  - [23] H. Daniell, S. J. Streatfield, and K. Wycoff, "Medical molecular farming: production of antibodies, biopharmaceuticals and edible vaccines in plants," *Trends in Plant Science*, vol. 6, no. 5, pp. 219–226, 2001.
  - [24] J. N. Bemiller and K. C. Huber, "Physical modification of food starch functionalities," *Annual Review of Food Science and Technology*, vol. 6, no. 1, pp. 19–69, 2015.
  - [25] B. Kaur, F. Ariffin, R. Bhat, and A. A. Karim, "Progress in starch modification in the last decade," *Food Hydrocolloids*, vol. 26, no. 2, pp. 398–404, 2012.
  - [26] J. Szymonska and F. Krok, "Potato starch granule nanostructure studied by high resolution non-contact AFM," *International Journal of Biological Macromolecules*, vol. 33, no. 1–3, pp. 1–7, 2003.
  - [27] J. Szymońska, F. Krok, and P. Tomasik, "Deep-freezing of potato starch," *International Journal of Biological Macromolecules*, vol. 27, no. 4, pp. 307–314, 2000.
  - [28] C. W. Chiu, E. Schiermeyer, D. J. Thomas, and M. B. Shah, "Thermally Inhibited Starches and Flours and Process for Their Production," 1998, US Patent 5,725,676.
  - [29] R. González, C. Carrara, E. Tosi, M. C. Añón, and A. Pilosof, "Amaranth starch-rich fraction properties modified by extrusion and fluidized bed heating," *Food Science and Technology*, vol. 40, no. 1, pp. 136–143, 2007.
  - [30] B. Zheng, H. Wang, W. Shang et al., "Understanding the digestibility and nutritional functions of rice starch subjected to heat-moisture treatment," *Journal of Functional Foods*, vol. 45, pp. 165–172, 2018.
  - [31] C. Pukkahuta, S. Shobngob, and S. Varavinit, "Effect of osmotic pressure on starch: new method of physical modification of starch," *Starch - Stärke*, vol. 59, no. 2, pp. 78–90, 2007.
  - [32] Z. Han, X.-a. Zeng, B.-s. Zhang, and S.-j. Yu, "Effects of pulsed electric fields (PEF) treatment on the properties of corn starch," *Journal of Food Engineering*, vol. 93, no. 3, pp. 318–323, 2009.
  - [33] S. T. Lim, J. A. Han, H. S. Lim, and J. N. BeMiller, "Modification of starch by dry heating with ionic gums," *Cereal Chemistry*, vol. 79, no. 5, pp. 601–606, 2002.
  - [34] P. A. M. Steeneken and A. J. J. Woortman, "Superheated starch: a novel approach towards spreadable particle gels," *Food Hydrocolloids*, vol. 23, no. 2, pp. 394–405, 2009.
  - [35] S. H. Park, Y. Na, J. Kim, S. D. Kang, and K. H. Park, "Properties and applications of starch modifying enzymes for use in the baking industry," *Food Science and Biotechnology*, vol. 27, no. 2, pp. 299–312, 2018.
  - [36] H. Z. Almarzouki, H. Alsulami, A. Rizwan, M. S. Basingab, H. Bukhari, and M. Shabaz, "An internet of medical things-based model for real-time monitoring and averting stroke sensors," *Journal of Healthcare Engineering*, vol. 2021, Article ID 1233166, 9 pages, 2021.

- [37] C. G. Oates and A. D. Powell, "Bioavailability of carbohydrate material stored in tropical fruit seeds," *Food Chemistry*, vol. 56, no. 4, pp. 405–414, 1996.
- [38] L. P. Walker and D. B. Wilson, "Enzymatic hydrolysis of cellulose—an overview," *Bioresource Technology*, vol. 36, no. 1, pp. 3–14, 1991.
- [39] D. B. Hodge, M. N. Karim, D. J. Schell, and J. D. McMillan, "Model-based fed-batch for high-solids enzymatic cellulose hydrolysis," *Applied Biochemistry and Biotechnology*, vol. 152, no. 1, pp. 88–107, 2009.
- [40] L. R. Lynd, M. S. Laser, D. Brandsby et al., "How biotech can transform biofuels," *Nature Biotechnology*, vol. 26, no. 2, pp. 169–172, 2008.
- [41] H. Jiang, M. Miao, F. Ye, B. Jiang, and T. Zhang, "Enzymatic modification of corn starch with 4- $\alpha$ -glucanotransferase results in increasing slow digestible and resistant starch," *International Journal of Biological Macromolecules*, vol. 65, pp. 208–214, 2014.
- [42] H. Li, Y. Gui, J. Li, Y. Zhu, B. Cui, and L. Guo, "Modification of rice starch using a combination of autoclaving and triple enzyme treatment: structural, physicochemical and digestibility properties," *International Journal of Biological Macromolecules*, vol. 144, pp. 500–508, 2020.
- [43] E. J. Kim, S. I. Ryu, H. A. Bae, N. T. Huong, and S. B. Lee, "Biochemical characterisation of a glycogen branching enzyme from *Streptococcus mutans*: enzymatic modification of starch," *Food Chemistry*, vol. 110, no. 4, pp. 979–984, 2008.
- [44] P. Liu, Y. Fang, X. Zhang et al., "Effects of multienzyme treatment on the physicochemical properties of maize starch-lauric acid complex," *Food Hydrocolloids*, vol. 107, article 105941, 2020.
- [45] A. Rajan, J. D. Sudha, and T. E. Abraham, "Enzymatic modification of cassava starch by fungal lipase," *Industrial Crops and Products*, vol. 27, no. 1, pp. 50–59, 2008.
- [46] M. Majzoobi and A. Farahnaky, "Granular cold-water swelling starch; properties, preparation and applications, a review," *Food Hydrocolloids*, vol. 111, article 106393, 2021.
- [47] A. Gaur, A. Mittal, D. Ghosh, and J. Sahoo, "Challenges in development of colon drug delivery system with respect to dissolution studies," *World Journal of Pharmaceutical Sciences*, vol. 8, no. 6, pp. 1465–1491, 2019.
- [48] J. Chen, E. Hawkins, and D. Seung, "Towards targeted starch modification in plants," *Current Opinion in Plant Biology*, vol. 60, article 102013, 2021.
- [49] A. Regina, Z. Li, M. K. Morell, and S. A. Jobling, "Genetically Modified Starch: State of Art and Perspectives," in *Starch Polymers*, Elsevier B.V, 2014.
- [50] F. C. Breedveld, "Therapeutic monoclonal antibodies," *The Lancet*, vol. 355, no. 9205, pp. 735–740, 2000.
- [51] B. R. Mahon, A. Moore, P. A. Johnson, and K. H. G. Mills, "Approaches to new vaccines," *Critical Reviews in Biotechnology*, vol. 18, no. 4, pp. 257–282, 1998.
- [52] U States Department of Health, H Services, U Food, and D Administration, "Types of genetic modification methods for crops traditional crop modification," 2020, <http://www.fda.gov/feedyourmind>.
- [53] J. V. Barbosa, J. Martins, L. Carvalho, M. M. S. M. Bastos, and F. D. Magalhães, "Effect of peroxide oxidation on the expansion of potato starch foam," *Industrial Crops and Products*, vol. 137, pp. 428–435, 2019.
- [54] H. X. Zia-ud-Din and P. Fei, "Physical and chemical modification of starches: a review," *Critical Reviews in Food Science and Nutrition*, vol. 57, no. 12, pp. 2691–2705, 2017.
- [55] K. Lewicka, P. Siemion, and P. Kurcok, "Chemical modifications of starch: microwave effect," *International Journal of Polymer Science*, vol. 2015, Article ID 867697, 10 pages, 2015.
- [56] B. Yaacob, M. C. I. M. Amin, K. Hashim, and B. A. Bakar, "Optimization of reaction conditions for carboxymethylated sago starch," *Iranian Polymer Journal*, vol. 20, no. 3, pp. 195–204, 2011.
- [57] K. Sangseethong, N. Termvejsayanon, and K. Siroth, "Characterization of physicochemical properties of hypochlorite- and peroxide-oxidized cassava starches," *Carbohydrate Polymers*, vol. 82, no. 2, pp. 446–453, 2010.
- [58] D. Kuakpetoon and Y. J. Wang, "Characterization of different starches oxidized by hypochlorite," *Starch-Starke*, vol. 53, no. 5, pp. 211–218, 2001.
- [59] M. M. Sánchez-Rivera, F. J. L. García-Suárez, M. Velázquez Del Valle, F. Guttierrez-Meraz, and L. A. Bello-Pérez, "Partial characterization of banana starches oxidized by different levels of sodium hypochlorite," *Carbohydrate Polymers*, vol. 62, no. 1, pp. 50–56, 2005.
- [60] Y. J. Wang and L. Wang, "Physicochemical properties of common and waxy corn starches oxidized by different levels of sodium hypochlorite," *Carbohydrate Polymers*, vol. 52, no. 3, pp. 207–217, 2003.
- [61] O. S. Lawal, K. O. Adebawale, B. M. Ogunsanwo, L. L. Barba, and N. S. Ilo, "Oxidized and acid thinned starch derivatives of hybrid maize: functional characteristics, wide-angle X-ray diffractometry and thermal properties," *International Journal of Biological Macromolecules*, vol. 35, pp. 71–79, 2005.
- [62] M. P. Cereda, O. Vilpoux, and I. M. Demiate, "Amidos modificados," in *Tecnologia, usos e potencialidades de tuberosas amiláceas latino americanas*, M. P. Cereda and O. F. Vilpoux, Eds., pp. 246–332, Fundação Cargill, São Paulo, 2003.
- [63] P. K. Borah, M. Rappolt, R. K. Duary, and A. Sarkar, "Structurally induced modulation of in vitro digestibility of amylopectin corn starch upon esterification with folic acid," *International Journal of Biological Macromolecules*, vol. 129, pp. 361–369, 2019.
- [64] C. I. A. La Fuente, A. T. de Souza, C. C. Tadini, and P. E. D. Augusto, "Ozonation of cassava starch to produce biodegradable films," *International Journal of Biological Macromolecules*, vol. 141, pp. 713–720, 2019.
- [65] X. Wu, F. Li, and W. Wu, "Effects of oxidative modification by 13-hydroperoxyoctadecadienoic acid on the structure and functional properties of rice protein," *Food Research International*, vol. 132, article 109096, 2020.
- [66] D. C. Lima, J. Villar, N. Castanha, B. C. Maniglia, M. D. Matta Junior, and P. E. Duarte Augusto, "Ozone modification of arracacha starch: effect on structure and functional properties," *Food Hydrocoll*, vol. 108, 2020.
- [67] X. Dang, H. Chen, Z. Shan, W. Zhen, and M. Yang, "The oxidation of potato starch by electro-Fenton system in the presence of Fe(II) ions," *International Journal of Biological Macromolecules*, vol. 121, pp. 113–119, 2019.
- [68] Y. S. Jeon, A. Viswanathan, and R. A. Gross, "Studies of starch esterification: reactions with alkenylsuccinates in aqueous slurry systems," *Starch/Staerke*, vol. 51, no. 2–3, pp. 90–93, 1999.

## Retraction

# Retracted: PSO-Based Evolutionary Approach to Optimize Head and Neck Biomedical Image to Detect Mesothelioma Cancer

### BioMed Research International

Received 8 January 2024; Accepted 8 January 2024; Published 9 January 2024

Copyright © 2024 BioMed Research International. This is an open access article distributed under the Creative Commons Attribution License, which permits unrestricted use, distribution, and reproduction in any medium, provided the original work is properly cited.

This article has been retracted by Hindawi following an investigation undertaken by the publisher [1]. This investigation has uncovered evidence of one or more of the following indicators of systematic manipulation of the publication process:

- (1) Discrepancies in scope
- (2) Discrepancies in the description of the research reported
- (3) Discrepancies between the availability of data and the research described
- (4) Inappropriate citations
- (5) Incoherent, meaningless and/or irrelevant content included in the article
- (6) Manipulated or compromised peer review

The presence of these indicators undermines our confidence in the integrity of the article's content and we cannot, therefore, vouch for its reliability. Please note that this notice is intended solely to alert readers that the content of this article is unreliable. We have not investigated whether authors were aware of or involved in the systematic manipulation of the publication process.

Wiley and Hindawi regrets that the usual quality checks did not identify these issues before publication and have since put additional measures in place to safeguard research integrity.

We wish to credit our own Research Integrity and Research Publishing teams and anonymous and named external researchers and research integrity experts for contributing to this investigation.

The corresponding author, as the representative of all authors, has been given the opportunity to register their agreement or disagreement to this retraction. We have kept a record of any response received.

### References

- [1] S. Praveen, N. Tyagi, B. Singh et al., "PSO-Based Evolutionary Approach to Optimize Head and Neck Biomedical Image to Detect Mesothelioma Cancer," *BioMed Research International*, vol. 2022, Article ID 3618197, 12 pages, 2022.

## Research Article

# PSO-Based Evolutionary Approach to Optimize Head and Neck Biomedical Image to Detect Mesothelioma Cancer

Sheeba Praveen <sup>1</sup>, Neha Tyagi <sup>2</sup>, Bhagwant Singh <sup>3</sup>, Girija Rani Karetla <sup>4</sup>,  
Meenakshi Anurag Thalor <sup>5</sup>, Kapil Joshi <sup>6</sup>, and Melkamu Tsegaye <sup>7</sup>

<sup>1</sup>Integral University Lucknow, India

<sup>2</sup>Department of IT, G.L Bajaj Institute of Technology & Management, Greater Noida, India

<sup>3</sup>Informatics Cluster, School of Computer Science, University of Petroleum and Energy Studies (UPES) Dehradun, Uttarakhand, 248007, India

<sup>4</sup>School of Computer, Data and Mathematical Sciences, Western Sydney University, Sydney, Australia

<sup>5</sup>Department of Information Technology, AISSMS Institute of Information Technology, India

<sup>6</sup>UIT, Uttarakhand University, India

<sup>7</sup>Wollo University, Dessie, Ethiopia

Correspondence should be addressed to Melkamu Tsegaye; [melkamu.tsegaye@wu.edu.et](mailto:melkamu.tsegaye@wu.edu.et)

Received 20 May 2022; Revised 30 June 2022; Accepted 21 July 2022; Published 5 August 2022

Academic Editor: Gaganpreet Kaur

Copyright © 2022 Sheeba Praveen et al. This is an open access article distributed under the Creative Commons Attribution License, which permits unrestricted use, distribution, and reproduction in any medium, provided the original work is properly cited.

Mesothelioma is a form of cancer that is aggressive and fatal. It is a thin layer of tissue that covers the majority of the patient's internal organs. The treatments are available; however, a cure is not attainable for the majority of patients. So, a lot of research is being done on detection of mesothelioma cancer using various different approaches; but this paper focuses on optimization techniques for optimizing the biomedical images to detect the cancer. With the restricted number of samples in the medical field, a Relief-PSO head and mesothelioma neck cancer pathological image feature selection approach is proposed. The approach reduces multilevel dimensionality. To begin, the relief technique picks different feature weights depending on the relationship between features and categories. Second, the hybrid binary particle swarm optimization (HBPSO) is suggested to automatically determine the optimum feature subset for candidate feature subsets. The technique outperforms seven other feature selection algorithms in terms of morphological feature screening, dimensionality reduction, and classification performance.

## 1. Introduction

Cancer, as one of the common diseases in the world, has a very high fatality rate, among which head and neck cancer (HNC) ranks first among systemic tumors due to its many primary sites and pathological types. At the same time, because the head and neck include most of the important organs and tissues of the human body, the anatomical relationship is complex, and the treatment of this type of cancer is particularly difficult. Therefore, accurate survival prediction of patients is the key to current cancer problems [1].

At present, most common survival predictions start from genomics data [2]. However, in addition to this, other cancer data such as pathological images and clinical information are also closely related to the survival prediction of head and neck cancer [3]. A large number of studies have shown that pathological images contain rich information related to cancer survival prediction, which can directly reflect the type of cancer and distinguish benign and malignant tumors and histopathological grades of tumors. This information is related to the prognosis of head and neck cancer, especially survival. It is directly related to the state of cancer [4] and plays a very important role in the prediction of cancer



survival [5, 6]. At present, some cancer survival prediction works based on pathological images have been successfully proposed. Yang et al. extracted 166 pathological image morphological features and used them for classification and survival prediction of non-small cell lung cancer [5]. After that, Dong et al. further used the literature [7] tool to extract 9879-dimensional features containing more comprehensive image information from 2186 lung cancer pathological images [6]. However, the image features extracted by the existing tools have the distinctive characteristics of high data dimension and small number of samples relative to the features. These data often contain irrelevant or redundant features [8], which affect the effect of existing machine learning algorithms on small sample high-dimensional data. Reducing the data dimension through feature selection is an effective way to solve this problem.

Histology is the study of how cells and tissues of living things look under a microscope. A thin slice (section) of tissue is looked at under a light (optical) or electron microscope to do a histological analysis. In the current research, looking at histology images is seen as the benchmark for clinically diagnosing cancer and figuring out how to treat it and what its prognosis will be [9]. Histopathology is the study of biopsies under a microscope to find and classify diseases. In histology image analysis for cancer detection, histopathologists visually inspect the regularities of cell shapes and tissue distributions, identify whether tissue regions are malignant, and assess the severity of malignancy. This type of histopathological examination has been widely utilized for cancer detection and grading applications, such as prostate, breast, cervical, and lung cancer grading, neuroblastoma categorization, and follicular lymphoma grading [10].

As a common dimensionality reduction method, feature selection can be divided into two categories [11]: correlation-based filtered feature selection and search-based heuristic feature selection. Correlation-based filtered feature selection evaluates the effect of feature subsets on classification targets through statistical properties of samples, thereby selecting optimal feature subsets. It does not incorporate any classifiers into the evaluation criteria and has strong independence from subsequent classification algorithms, which can avoid the higher operating costs of classification algorithms caused by high-dimensional data. But at the same time, this statistical method cannot preserve the influence of the correlation between features on the classification results. Common feature selection algorithms under this type include Relief [8], MRMR (minimum-redundancy maximum-relevancy) [11], Mitra feature selection based on feature similarity [12], CFS (completely fair schedule) [13], and FCBF (fast correlation-based filter) [14] and so on.

The other is the feature selection based on search. In this kind of algorithm, a heuristic search method is often used to find the optimal feature subset [15]. The feature subset selected in this way guarantees the common influence of the features on the classification target. However, search-based feature selection is affected by the search space and performs poorly on high-dimensional problems. In recent years, due to the excellent global search ability and versatility

of evolutionary algorithms, many researchers have focused on searching feature spaces by improving various evolutionary algorithms. Dökeroğlu et al. [15] applied the backbone particle swarm algorithm combined with the nearest neighbor algorithm to feature selection. Dökeroğlu et al. [15] used decision trees for feature selection and used genetic algorithms to find a set of feature subsets that minimized the classification error rate of decision trees. Liu et al. [16] introduced three new initialization mechanisms, individual and global optimal update mechanisms in particle swarm optimization, which improved both the number of features and the classification performance. A heuristic algorithm is one that prioritizes speed over accuracy, precision, or completeness in order to achieve better results faster than more traditional methods. The algorithms apart from heuristic search methods that can be involved for optimization of HNC are swarm intelligence algorithms [17], Tabu search [18], simulated annealing [19], genetic algorithms [20, 21], artificial neural networks [22], support vector machines [23], etc.

The objective of the paper is to target the problem of high-dimensional small samples that are generated after feature extraction of head and neck cancer pathological images. The paper is aimed at proposing a multilevel feature selection algorithm based on Relief-HBPSO.

- (1) To create a multilevel framework, the Relief-HBPSO method combines the filtering feature selection algorithm with the heuristic search algorithm. Due to the challenges of low screening accuracy and efficiency in the heuristic search algorithm in a high-dimensional environment, a filtering feature selection technique is presented to limit the search space, enhance the search accuracy, and reduce the algorithm's running time. The proposed model preprocesses the dataset in the initial stage and then the resulting dataset is fed as an input to Relief algorithm. After that HBPSO parameters are initialized and arranged in descending order as the fitness function. The first half OS sorted particles are retained to update the individual extreme position and global extreme position of the current iteration, and the remaining particles are mutated on the basis of the elite particles to generate new descendant particle swarms to participate in the global update optimal. This process is repeated until the iteration termination condition is satisfied, and the optimal feature subset is generated
- (2) Hybrid binary evolutionary particle swarm optimization (HBPSO) combines evolving neural strategies (ENS) with classic binary particle swarm optimization (BPSO) to enhance imaging characteristics in head and neck cancer. Binary PSO is a subset of PSO that applies to binary domains; however, it relies on continuous PSO's concepts of velocity and momentum. The standard PSO has some issues, resulting in slow convergence rates on various optimization tasks and hence resulting in BPSO. In HBPSO, the search space is represented as a

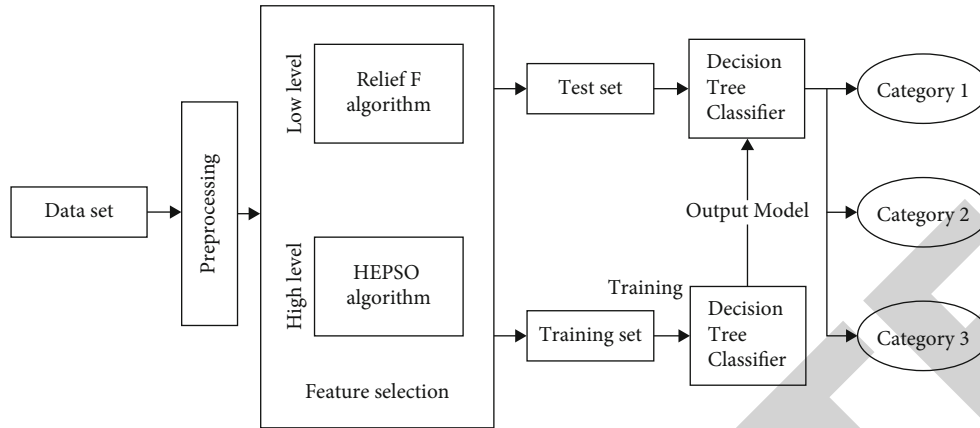


FIGURE 1: Multilevel pathological image feature selection algorithm flow.

hypercube. Within this hypercube, it is possible to observe a particle moving to more nearby or more distant corners of the hypercube depending on the number of bits that are inverted. The BPSO algorithm enhances/optimizes the image characteristics. The algorithm uses ENS to make particle mutations form a new particle population, enriching the variety of the population and allowing the program to escape the local optimal solution and boost search efficiency

- (3) HBPSO evaluates the efficiency of the ReliefF-HBPSO method on the head and neck cancer pathological image feature data by using the classification accuracy of the decision tree (DT) classifier as the algorithm’s objective function (i.e., the evaluation criteria). ReliefF-HBPSO is a quick technique that discovers a subset of problematic image features with excellent classification performance and a limited number of features

The organization of this paper is as follows: Section 2 is the premap of mammography images which is the preprocessing process; Section 3 introduces the framework of this method; Section 4 is divided into three parts: the first part introduces the nonsampling contour transformation method (NSCT) principle and its applications, Z-Moments are presented in part II, and the third part discusses the classification algorithm of SVM; Section 5 introduces the experimental dataset and presents the experimental results and analysis; and Section 6 presents the conclusion and scope for future work.

## 2. ReliefF-HBPSO Multilevel Pathological Image Feature Selection

This paper proposes a multilevel pathological image feature selection algorithm—ReliefF-HBPSO, which combines ReliefF and HBPSO. As shown in Figure 1, for the head and neck cancer data feature set, first use the average value of the corresponding features to complete the entire sample set, and input the dataset after data preprocessing into

ReliefF-HBPSO; secondly, extract the data through ReliefF. Low-dimensional features are used as the input of HBPSO, and the optimal feature subsets are obtained by continuous iteration; finally, the feature-selected dataset is divided into a test set and a training set, where the training set is used to train the relevant parameters of the decision tree classifier. The test set is then fed into a decision tree classification model with fixed parameters to obtain the classification results of head and neck cancer data.

**2.1. ReliefF Algorithm.** The ReliefF algorithm is a feature selection method based on random selection of feature weight search [8]. It gives different weights to features according to the correlation between a single feature and the data category and regards features that are higher than a specified threshold or meet certain judgment conditions as features. In the candidate subset, the remaining features are removed. The weights of the features are updated according to

$$w(k) = w(k) - \sum_{j=1}^p \frac{\text{diff}(k, R, H)}{M_p} + \sum_{C \neq \text{class}(R_i)} \frac{(P(C)/(1 - P(\text{class}(R_i)))) \times \sum_{j=1}^p \text{diff}(k, R, M(C))}{M_p}. \tag{1}$$

Among them,  $R_i$  is a sample randomly selected from the training sample set  $U$  each time,  $H$  and  $M(C)$  are the  $p$  nearest neighbors found in the same sample set of  $R_i$  and the sample set of different classes (set as class  $C$ ), respectively. In the samples, the selection of the number of neighbor samples  $p$  is determined by the actual situation of the dataset,  $p > 0$  and less than the minimum value in the class samples; in this paper,  $p \in [0, 14]$ , and  $P(C)$  is the number of class  $C$  samples in the total number of samples. The probability of  $M$  is the sampling times.

The patient’s case image features have both continuous and discrete values. When the attribute of the  $k$ th feature is a continuous value, the absolute difference between the sample  $R_a$  and the sample  $R_b$  on the  $k^{\text{th}}$  feature is calculated

according to

$$\text{diff}(k, R_a, R_b) = \frac{|\text{value}(k, R_a) - \text{value}(k, R_b)|}{\max k - \min k}. \quad (2)$$

When the attribute of the  $k^{\text{th}}$  feature is a discrete value, it is calculated according to

$$\text{diff}(k, R_a, R_b) = \begin{cases} 1, & \text{value}(k, R_a) \neq \text{value}(k, R_b). \\ 0, & \text{value}(k, R_a) = \text{value}(k, R_b). \end{cases} \quad (3)$$

If the distance between  $X_i$  and  $H_j$  on a feature is less than the distance between  $X_i$  and  $M_j(C)$ ,  $\text{diff}(k, R_i, H_j) < \text{diff}(k, R_i, M_j(C))$ , indicating that the feature pair distinguishes between the same and different class samples are beneficial, and the weight of this feature should be increased; otherwise, the weight of this feature should be decreased. Iterate  $m$  times to get the best weight of each feature.

The larger  $w(k)$  is, the stronger the classification ability of the feature is, and the feature weight is screened. If  $w(k) > \partial$ ,  $\partial$  is the feature threshold, and the  $k^{\text{th}}$  feature is reserved as a candidate feature; otherwise, the feature is deleted. Repeat this process until all  $i$  features are traversed.

**2.2. Binary Particle Swarm Optimization (BPSO).** An optimization method known as particle swarm optimization (PSO) uses a large number of candidate solutions (referred to as particles) that move about the search area in a swarm-like fashion to try to identify the optimum global solution [4]. At any given time, each particle has a location  $x$  and a velocity  $v$ . Particle velocity is changed using a velocity update algorithm that also takes account the best position the particle so far and the best location found by the entire swarm. When optimizing objective functions, this nature-inspired technique performs exceptionally well in a continuous search space. For feature selection, however, the binary version of this technique is needed. To summarize, the basic idea is that a complete solution for feature selection in a PSO technique can be readily described as a binary position vector, where the 1's represent feature selection and the 0's represent feature removal [24]. To find the average classification error given any binary vector reflecting the selection of a subset of features, we can use a good classifier like random forest. In this case, the objective function that needs to be minimized is this.

Zhang et al. [25, 26] introduced a discrete particle swarm optimization technique (BPSO) based on binary coding to satisfy the needs of discrete issues. The program maps the solution space of the issue to the flight space of birds, abstracting each bird as a particle to represent possible solutions, by replicating the foraging behavior of biological populations (birds).

For the high-dimensional feature selection problem, BPSO has two main deficiencies: First, the particles generated by each iteration in BPSO cannot be eliminated even if they are determined to be nonoptimal particles and still participate in the iterative process of the algorithm, which greatly increases the behavior. Second, the more optimal

particles in BPSO discard all valuable information at the end of each iteration and are randomly initialized again at the beginning of the next iteration, such behavior patterns and algorithms throughout the evolution. In the process, the goal of tracking the local optimum and the global optimum is always contradictory, which can easily make BPSO fall into a local minimum.

Therefore, this paper adopts the evolutionary neural strategy (ENS) to generate a new particle population through particle mutation to enrich the diversity of the population, while discarding the failed particles and reducing the time complexity of the algorithm.

### 3. Hybrid Binary Evolutionary Particle Swarm Optimization (HBPSO)

**3.1. Evolutionary Neural Strategies (ENS).** Evolutionary neural strategies (ENS) is an appropriate strategy learned in mathematical games by Chandrashekar and Sahin [27]. The strategy consists of  $m$  neural networks  $p_i (i = 1, 2, \dots, m)$ , each network has an adaptive parameter vector  $\sigma_i(j)$ , each component of  $\sigma_i(j)$  corresponds to a weight or bias set values, which govern the step size of searching for new mutated parameters of the neural network. Weights or bias values are generated by sampling from a uniform distribution over  $[-2, 2]$ .

For each parent  $p_i$ , the offspring  $p'_i (i = 1, 2, \dots, m)$  can be created by

$$\sigma'_i(j) = \sigma_i(j) \exp(\tau N_j(0, 1)), j = 1, 2, \dots, N_w, \quad (4)$$

$$w'_i(j) = w_j(j) + \sigma'_i N_j(0, 1), j = 1, 2, \dots, N_w, \quad (5)$$

where  $N_j(0, 1)$  is the standard normal distribution resampled for each  $j$ ,  $N_w$  represents the maximum number of weights and biases, and  $\tau = 1/\sqrt{2\sqrt{N_w}}$ .

**3.2. Improved Algorithm of BPSO HBPSO.** The position and velocity of each particle  $i$  in the  $K$ -dimensional space in the population of  $m$  particles can be represented as a vector.

The position vector  $X_i = \{X_{i1}, X_{i2}, \dots, X_{ik}\}$  represents the candidate feature subset, and  $X_{ik}$  represents the  $k$ th feature of the  $i$ th particle;

The velocity vector  $V_i = \{V_{i1}, V_{i2}, \dots, V_{ik}\}$  represents the probability of selecting this subset of features, i.e., the probability that the particle position  $X_i$  is assigned to 1.

In the HBPSO algorithm, the position vector and velocity vector of the particle are initialized randomly, and the velocity vector of the particle is updated according to formulas (6) and (7), and the position vector is updated according to

$$V_{ik}(n+1) = w \times V_{ik}(n) + c_1 \text{rand}() \times (\text{pbest}_{ik}(n) - X_{ik}(n)) + c_2 \text{rand}() \times (\text{pbest}_{ik}(n) - X_{ik}(n)), \quad (6)$$

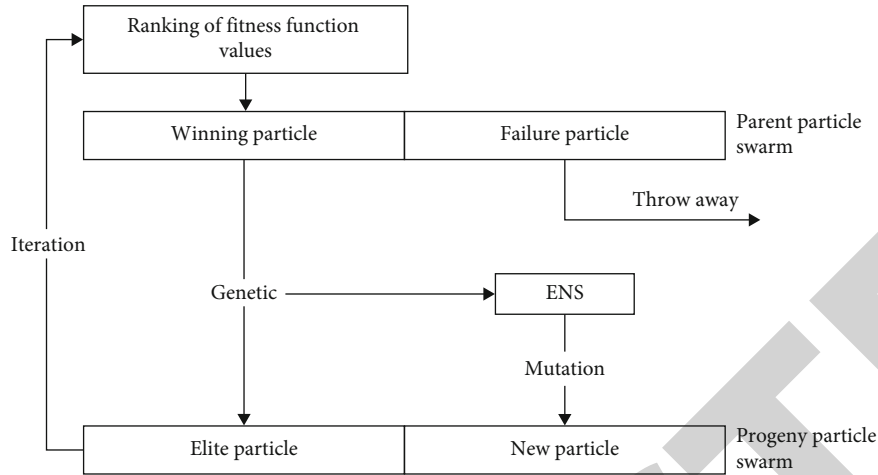


FIGURE 2: HBPSO particle mutation network.

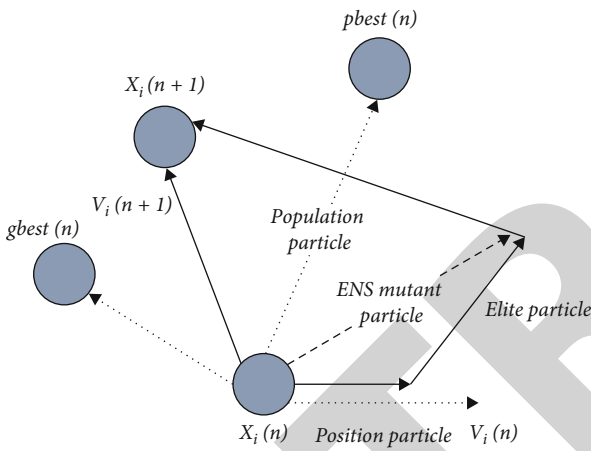


FIGURE 3: Particle evolution process in HBPSO.

$$\text{sig}(V_{ik}(n+1)) = \frac{1}{1 + \exp(-V_{ik}(n+1))}, k = 1, 2, \dots, K, \quad (7)$$

$$X_{ik}(n+1) = \begin{cases} 1, & \text{rand}() \leq \text{sig}(V_{ik}(n+1)), \\ 0, & \text{otherwise,} \end{cases} \quad (8)$$

$$f(p_i) = \frac{TP + TN}{F}. \quad (9)$$

Among them, TP (true positives) is the number of samples that are correctly classified as positive examples by the classifier, TN (true negatives) is the number of correctly classified as negative examples, and  $F$  is the total number of samples.

In this paper, the idea of feature selection is introduced into the optimization search algorithm, and the hybrid binary evolutionary particle swarm algorithm (HBPSO) is used, which combines BPSO and ENS to enrich the diversity of particle population through the mutation between the parent and the child in the iterative process. Collaboration and information sharing among individuals also enables better search for optimal feature sets.

As shown in Figure 2, at each iteration, the fitness function values are sorted, and the winning particles corresponding to the first half of the better fitness values are retained. The optimized individual (or solution) is directly inherited to the next generation and inherits all its information through BPSO regarded as elite particles. And the remaining failed particles with the lowest fitness function value will be discarded. On the basis of the winning particle, new particles are generated by mutation according to formulas (4) and (5) and combined with the elite particles in the original parent  $p_i$  to form a new population  $p'_i$  for the next iteration.

The evolution process of particle  $i$  in the HBPSO algorithm is shown in Figure 3.

The mutation feature in ENS is to help the particle population diversify by making particles “fly into” a new search space to achieve the purpose of enriching the population diversity and solve the local optimal solution problem generated by BPSO in the iterative process. At the same time, the same number of particles from the BPSO parent mutation will be used to fill the gaps of the discarded particles. These new particles inherit cognitive traits from their parents, which will in turn enhance the competitiveness and diversity of the ENS.

After the  $k + 1$ th particle state update is completed, the individual optimal value and the population optimal value of the particle are updated. The update methods of the local optimal  $pbest$  and the global optimal  $gbest$  are as follows

$$pbest_{ik}(n+1) = \begin{cases} X_{ik}(n), & f(X_{ik}(n)) < f(pbest_{ik}(n)), \\ pbest_{ik}(n), & f(X_{ik}(n)) \geq f(pbest_{ik}(n)), \end{cases}$$

$$gbest_n = pbest_{g,k},$$

$$g = \text{argmin}_{1 \leq n \leq M} [f(pbest_{n,k})]. \quad (10)$$

Step-1: randomly initialize the parameter PID of the HBPSO algorithm, including the number of particles  $m$ , the number of iterations  $n$ , the neighborhood size  $[-a, a]$ , constant parameters  $c_1, c_2$ , etc.

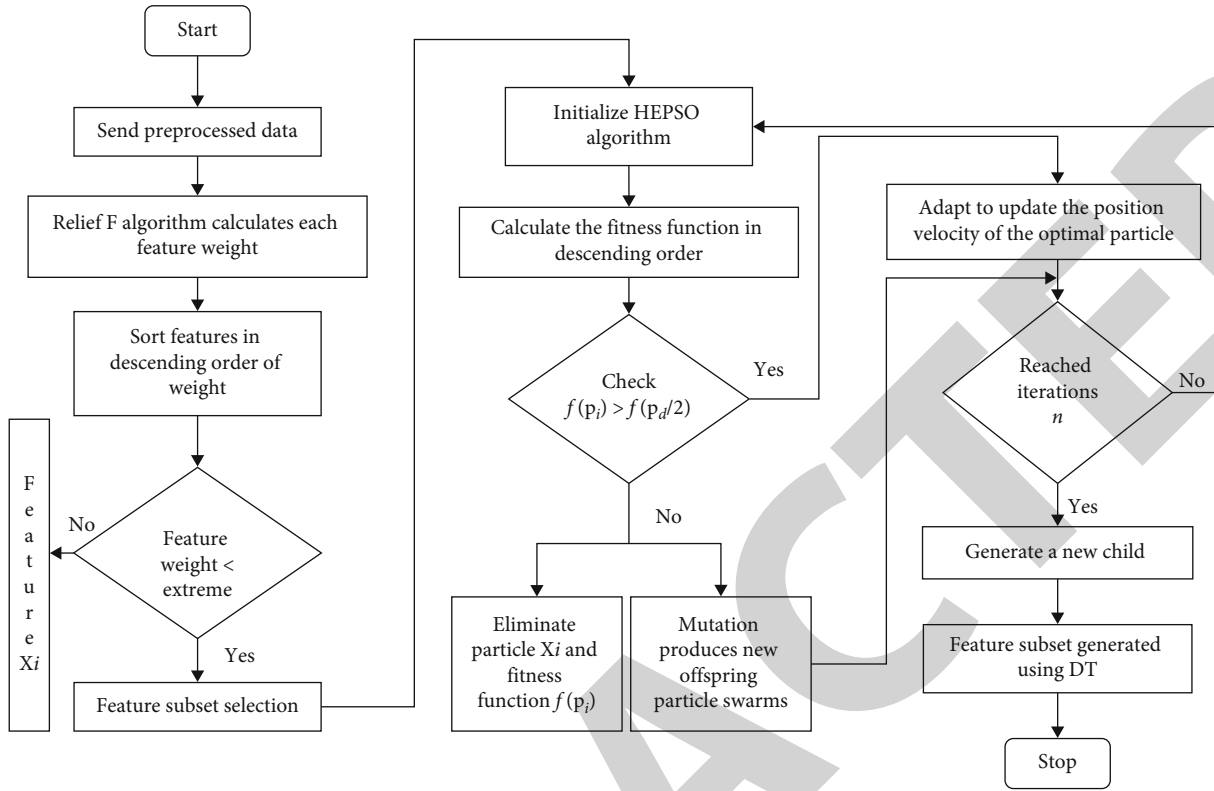


FIGURE 4: ReliefF-HBPSO multilevel pathological image feature selection algorithm.

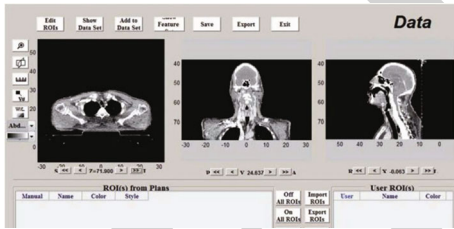


FIGURE 5: CT image display in Ibex.

Step-2: randomly select a set of particles and initialize the particle positions  $\text{random}(X_{ik}, V_{ik})$ , that is, randomly select feature vectors.

Step-3: calculate the fitness function  $f(p_i)$  of all particles according to formula (9).

Step-4: traverse all currently existing fitness functions  $f(p_i)$  and sort them in descending order. Simultaneously compute  $f(p_i)$  numbers  $d$ .

Step-5: if  $f(p_i) \geq f(p_{d/2})$ , keep all the information of the elite particle. Update the current particle optimal pbest and population optimal gbest.

Step-6: if  $f(p_i) < f(p_{d/2})$ , calculate the adaptive parameter  $\sigma'_i$  according to the formula (4) for each elite particle in step 5, and then calculate the position information of the new particle according to the formula (5). The fitness function  $f(p_i)$  corresponding to the elite particles remains unchanged, and new particles are obtained, the number of which is equal to the number of elite particles.

Step-7: update the position and velocity of elite particles according to equations (6) to (8), and combine the parent elite particles and mutant particles as the child particle swarm for the next iteration.

Step-8: if the current iteration number  $j \geq n$ , end the iteration loop and go to step 9; otherwise, go to step 3.

Step-9: output the optimal gbest of the population as the optimal solution of the problem and obtain the optimal feature set.

#### 4. ReliefF-HBPSO Multilevel Feature Selection Algorithm

The algorithm flow of the ReliefF-HBPSO multilevel feature selection algorithm is shown in Figure 4. First, the dataset is preprocessed, and the processed data is sent to the ReliefF algorithm. Large features serve as candidate feature subsets. Secondly, initialize the HBPSO parameters and sort them in descending order with the classification accuracy of the decision tree classifier as the fitness function. The first half of the sorted particles are retained as elite particles to update the individual extreme position and global extreme position of the current iteration, while the remaining particles are mutated on the basis of the elite particles to generate new descendant particle swarms to participate in the global update optimal. This process is repeated until the iteration termination condition is satisfied, and the optimal feature subset is generated.

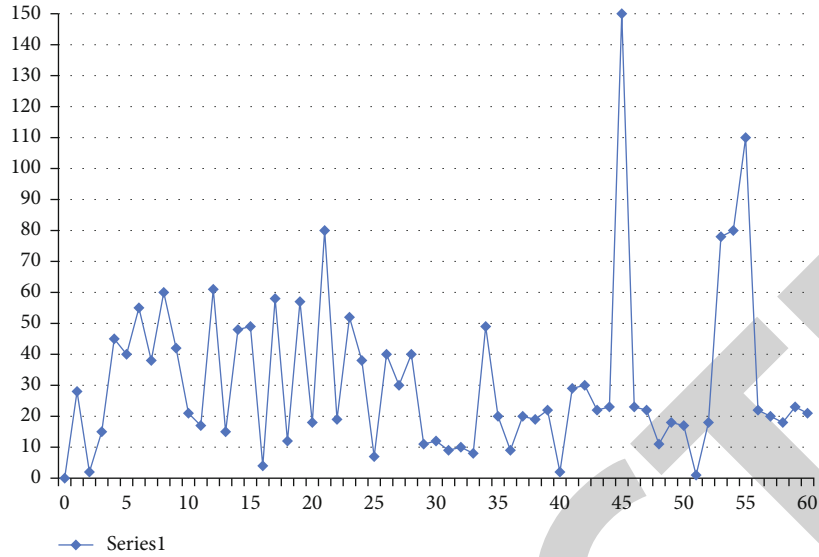


FIGURE 6: Label distribution of survival time.

Let the number of iterations of ReliefF-HBPSO be  $n$  and the number of particles to be  $m$ , where the total number of features of the ReliefF algorithm is  $N$ , the number of sampling times is  $M$ , and the number of selected neighbor samples is  $p$ , then the time complexity of executing the ReliefF algorithm is  $O(M \times \max(N \times p, N^2))$ . Assuming that the number of features retained after the ReliefF algorithm is executed is  $K_1$ , the time complexity of the HBPSO algorithm is  $O(n \times \max(m^2, mK_1/2))$ . The traditional BPSO algorithm does not need to sort the fitness function and mutate the new particles. If the number of features is  $K_2$ , the time complexity is  $O(n \times m \times K_2)$ . Since  $K_1$  in the HBPSO algorithm is selected by the ReliefF algorithm for low-dimensional feature selection, it is much lower than  $K_2$  using all features in BPSO, and  $m$  is usually smaller than  $K_1$  and  $K_2$ , so the time complexity of HBPSO is smaller than that of BPSO. At this point, the time complexity of ReliefF-HBPSO is

$$O\left(\max\left(M \times \max(N \times p, N^2), n \times \max\left(m^2, \frac{mK_1}{2}\right)\right)\right). \tag{11}$$

In terms of space complexity, the HBPSO of the ReliefF-HBPSO algorithm in this paper adds a constant order of intermediate variables in each iteration than the standard BPSO algorithm, such as  $\sigma_i(j)$  and  $\sigma'_i$  in equations (4) and (5) and the storage of related temporary variables, the space complexity has increased, but because the ReliefF algorithm is used before iteration to greatly reduce the length of the particle vector as input in the HBPSO algorithm, the storage space is reduced, so the space is complex. Compared with the standard BPSO algorithm, the degree is still lower.

### 5. Experimental Results

5.1. *Experimental Data.* The experimental data adopts the real patient dataset provided by the California hospital in

the United States, in which sensitive personal information about the patients has been removed, and the dataset is pre-processed before use. The original data is the RT pathological image of the patient, and the image format is the CT image of dicom, as shown in Figure 5. Text data in csv format with data shape [60, 1385] was extracted from CT images of patients by Ibex software [28]. Among them, 60 refer to a total of 60 patients as samples to participate in the prediction, and 1385 refer to the extracted image features with a total of 1385 dimensions.

Since the dataset is real case data, some information is missing, and the average value of the entire column of features is used for completion. For some feature attributes, in order to avoid some attributes with small values from being hidden and to improve the accuracy, the data is standardized.

The distribution of survival (in months) for the 60 patients given by the hospital's raw data is shown in Figure 6. According to the analysis of relevant medical literature and doctors' experience, the survival time of 60 patients was divided into 3 categories, which were denoted by 0, 1, and 2, respectively. Among them, 0~18 months is the first category, which is represented by 0, with a total of 24 people; 18~36 months is the second category, which is represented by 1, with a total of 15 people; 36~150 months is the third category, with 2 said, a total of 20 people. The proportion of each type of labels to the total is 41%, 25%, and 34%, respectively.

5.2. *Experimental Design.* The experimental environment of this paper is Windows 10 64-bit operating system, the processor is Intel i5-8250U, 2.6 GHz, and the installed memory RAM is 4.00 GB. Software environment pycharm compiler, python3.5.

In order to verify the effectiveness and superiority of the ReliefF-HBPSO algorithm in the feature selection of head and neck cancer pathological images, this paper compares the nondimensionality reduction and feature dimension

TABLE 1: Number of features under different algorithms.

Algorithm	Data dimension	Accuracy	Dimensionality reduction	Running time (s)
Not dimensionally reduced	1385	0.55	0	8.61
PCA	100	0.64	0.92	7.03
ReliefF	110	0.78	0.94	1.89
WOA-SA	595	0.71	0.59	51.04
BPSO	725	0.64	0.47	31.45
HBPSO	670	0.75	0.53	21.93
Relief-BPSO	40	0.86	0.93	17.08
Relief-HBPSO	24	0.87	0.98	11.06

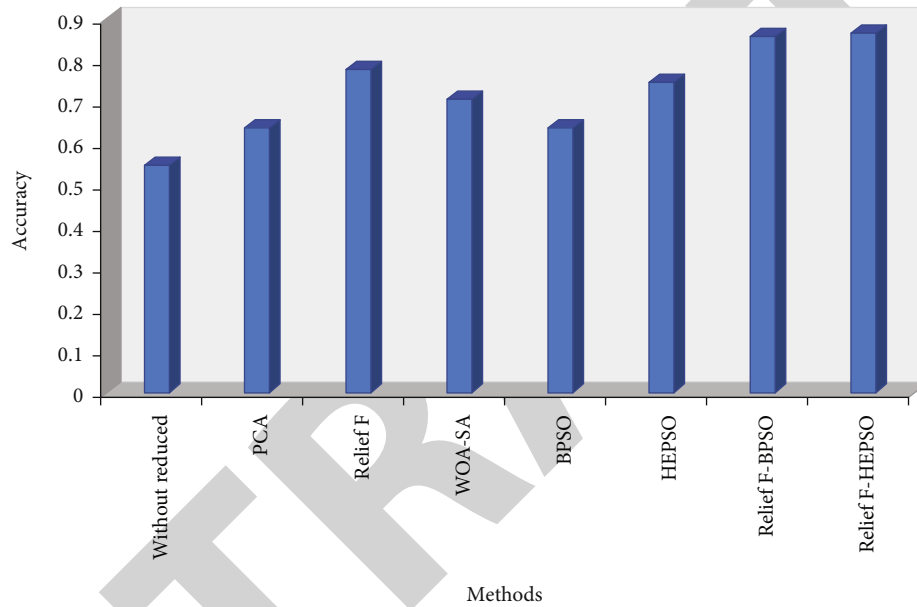


FIGURE 7: Comparative analysis over accuracy under different models for dimension reduction.

reduction methods—PCA [29], ReliefF algorithm [30], and whale optimization algorithm-simulate anneal, respectively, with, WOA-SA [31], binary particle swarm optimization (BPSO) [32, 33], hybrid binary evolutionary particle swarm optimization (HBPSO), and ReliefF-BPSO for comparative experiments.

Among them, the maximum number of iterations  $n$  of the five models of WOA-SA, BPSO, HBPSO, ReliefF-BPSO, and ReliefF-HBPSO is 100. Other parameters of the WOA-SA model are set according to the literature [34–36]. BPSO and HBPSO model parameter settings: population size  $m = 50$ , learning factor  $c_1 = c_2 = 0.5$ , inertia coefficient  $w = 2.5$ , maximum particle velocity  $V_{\max} = 4$ , and minimum velocity  $V_{\min} = -4$ . ReliefF-BPSO and ReliefF-HBPSO parameter settings: sampling times  $M = 5$ , threshold  $\partial = 30\,293.46$ , number of nearest neighbor samples  $p = 10$ , and other parameters are the same as BPSO and HBPSO models. ReliefF parameters: sampling times  $M = 5$ , threshold  $\partial = 50\,588.91$ , and number of nearest neighbor samples  $p = 10$ .

**5.3. Result Analysis.** For the head and neck cancer pathological image feature dataset extracted by Ibox software, the experiment uses the original data (that is, the dimensionality reduction data), PCA, ReliefF, WOA-SA, BPSO, HBPSO, ReliefF-BPSO, and ReliefF-HBPSO, a total of 8 models. The optimal feature sets under the real dataset are obtained, respectively, and the decision tree classification model is used as the classifier. The dimensionality-reduction technique, known as principal component analysis (PCA) [37], reduces the size of huge datasets by condensing the number of variables in the original dataset into a manageable number [38]. Dimensionality reduction algorithms compromises some accuracy in exchange for more simplicity, and this is the tradeoff that must be made when trying to reduce the size of a dataset. Since small datasets are easy to evaluate and visualize, they allow machine learning algorithms to handle data more quickly without having to deal with additional variables [39]. In this paper, the proposed algorithm is evaluated against this technique to prove its efficiency.

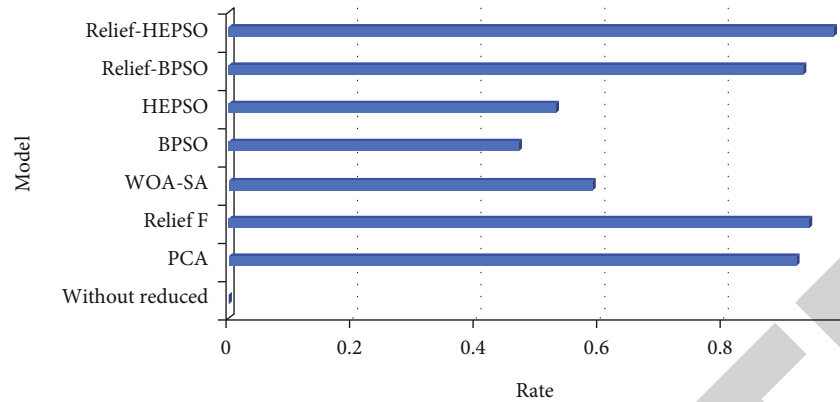


FIGURE 8: Comparative analysis over dimension reduction under different models for dimension reduction.

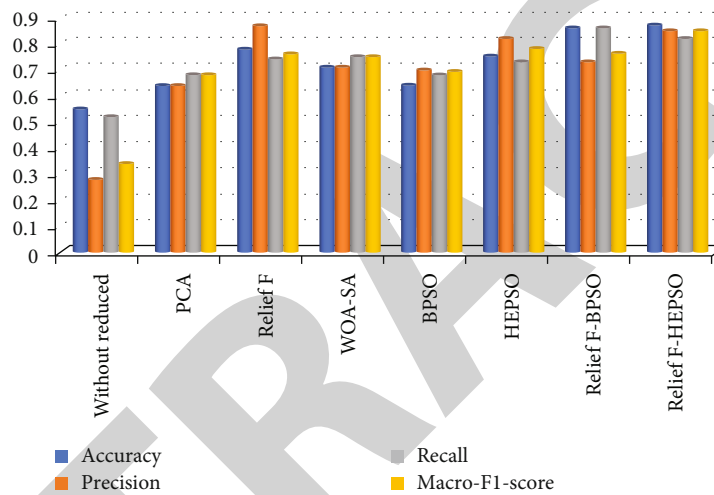


FIGURE 9: Comparison of classification performance of different feature selection and dimensionality reduction algorithms.

The test uses 5-fold cross-validation to calculate the accuracy, precision, recall,  $F1$ -score, and running time (unit: s) and compare the multiple items of the 8 models. The classification performance index and its feature subset size illustrate the ability of the algorithm in feature selection and classification prediction. It can be seen from Table 1 that the size of feature subsets selected by the PCA, ReliefF, WOA-SA, BPSO, HBPSO, ReliefF-BPSO, and ReliefF-HBPSO algorithms are reduced by 92%, 94%, 59%, 47%, 53%, 93% and 98%, respectively, compared with those before dimension reduction. And when the dimensionality reduction ratio is the lowest 98%, the ReliefF-HBPSO algorithm achieves the best classification effect of 87%.

When the dimensionality reduction rate of PCA and ReliefF algorithms are 92% and 94%, respectively, the classification accuracy rates on the dataset are 64% and 78%, respectively, and they are both better than the data before dimensionality reduction. Therefore, on the dataset of this paper, the classification performance obtained by using the feature selection algorithm is better.

Under the same iteration conditions, the classification accuracy of HBPSO is 75%, which is 11 percentage points higher than that of BPSO, and the dimensionality reduction

rate of features is also increased by 3 percentage points, and the number of features is reduced to 670 compared with 725 of BPSO. ReliefF-BPSO achieved 86% accuracy when the dimensionality reduction rate was 93%, and ReliefF-HBPSO achieved 87% accuracy when the dimensionality reduction rate was 98%, and the number of features was reduced by 51.8% compared to the 41% of Relief F-BPSO. Therefore, HBPSO performs better than traditional BPSO on this dataset and achieves better classification performance with a higher dimensionality reduction rate. Whether it is BPSO, Relief F-BPSO, or HBPSO, compared with ReliefF-HBPSO, the algorithm that uses the ReliefF algorithm to select low-dimensional features first can achieve better dimensionality reduction and improve classification accuracy. Figure 7 shows the comparative analysis over accuracy under different models for dimension reduction.

The WOA-SA algorithm is a heuristic algorithm proposed by Mafarja for feature selection in 2017, and it has a good performance in the UCI classic dataset. Under the same iterative conditions, it can be seen from Table 1 that WOA-SA has a dimensionality reduction rate and an accuracy rate of 59% and 71%, respectively. Although the performance is better than the traditional BPSO algorithm, it is



TABLE 2: Comparison of classification performance of different feature selection and dimensionality reduction algorithms.

Algorithm	Accuracy	Precision	Recall	Macro-F1 -score
Not dimensionally reduced	0.55	0.28	0.52	0.34
PCA	0.64	0.64	0.68	0.68
Relieff	0.78	0.87	0.74	0.76
WOA-SA	0.71	0.71	0.75	0.75
BPSO	0.64	0.70	0.68	0.69
HBPSO	0.75	0.82	0.73	0.78
Relief-BPSO	0.86	0.73	0.86	0.76
Relief-HBPSO	0.87	0.85	0.82	0.85

still inferior to the ReliefF-HBPSO algorithm proposed in this paper.

When the dimensionality reduction rates of BPSO, HBPSO, ReliefF-BPSO, and ReliefF-HBPSO are 47%, 53%, 93%, and 98%, respectively, the classification accuracies are 64%, 75%, 86%, and 87%. As the dimensionality reduction rate increases, the classification accuracy also increases. But, in WOA-SA, when the dimensionality reduction rate is 59%, the classification accuracy is only 71%. Therefore, the dimensionality reduction rate is proportional to the classification accuracy rate, which is only established within a certain interval. With the increase of the dimensionality reduction rate, the classification accuracy rate reaches the highest at a certain time, and then, there is a possibility of decreasing. Figure 8 shows the comparative analysis over dimension reduction under different models for dimension reduction.

From the perspective of running time, under the same number of iterations, the running times of BPSO, HBPSO, ReliefF-BPSO, and ReliefF-HBPSO are 31.79 s, 22.99 s, 16.63 s, and 10.84 s, respectively. The running times of ReliefF-BPSO and ReliefF-HBPSO are compared with BPSO and HBPSO, and it improves 15.16 s and 12.15 s, respectively, without reducing the classification performance. Compared with BPSO and Relief F BPSO, the running time of HBPSO and ReliefF-HBPSO is also improved. It can be seen that using the ReliefF algorithm to select low-dimensional features first can greatly reduce the computing time and maintain a good classification accuracy.

In summary, the ReliefF-HBPSO algorithm has excellent feature selection ability on the dataset of this paper, and can obtain a smaller proportion of feature subsets; and based on the original thousand-dimensional features, the algorithm only uses about 2% of the features. The best classification performance is achieved with the shortest running time. Therefore, the ReliefF-HBPSO algorithm can not only obtain a smaller scale of feature subsets, but also ensure the highest classification performance in a relatively short period of time. Figure 9 shows the comparison of classification performance of different feature selection and dimensionality reduction algorithms.

The classification performance of the eight algorithms under the multi-label classifier of decision tree is shown in Table 2. The parameters that are taken into consideration for evaluating the efficacy of the proposed methodology is accuracy, precision, recall, and *F1*-score. However, comparing with nondimensionality reduction, PCA, WOA-SA, BPSO, HBPSO, and ReliefF-BPSO algorithms, the ReliefF-HBPSO algorithm has greatly improved by achieving accuracy 87%, precision values obtained are 0.73 and 0.85, recall values are 0.86 and 0.82, and *F1*-score is 0.76 and 0.85, respectively. However, while comparing with the ReliefF-BPSO algorithm, ReliefF-HBPSO improves the classification accuracy, classification precision, and *F1* parameters and maintains a similar recall rate.

In summary, the ReliefF-HBPSO algorithm can effectively remove feature redundancy, obtain a smaller feature subset, and outperform similar algorithms in overall performance, and the output feature subset is more streamlined and effective. Therefore, this paper proposes the ReliefF-HBPSO multilevel feature selection algorithm, and it is feasible to apply it to the selection of head and neck cancer pathological image features. Pathological image features after feature selection can be used to design individualized radiation therapy to potentially improve clinical outcomes.

## 6. Conclusion

In this paper, the feature selection technique is used to investigate pathological imaging features of patients with head and neck cancer, and a multilevel feature selection method based on ReliefF-HBPSO is developed. The algorithm first uses the ReliefF algorithm to quickly reduce the dimensionality of the morphological features of the pathological image and then initializes the particle swarm with the feature candidate subset with larger feature weight, with the feature subset's evaluation being the classification accuracy of the decision tree classifier (DT). This function combines discrete binary particle swarm optimization (BPSO) with evolutionary neural strategy (ENS) across numerous iterations to get the optimum feature subset. Experiments show that the ReliefF-HBPSO technique outperforms the six models of PCA, ReliefF, WOA-SA, BPSO, HBPSO, and ReliefF-BPSO in removing redundant features and screening out highly linked pathological image morphological traits. A dimensionality reduction rate of 98 percent is achieved with 98 percent classification accuracy and a fast operating speed. The ReliefF-HBPSO approach provides a multilevel hybrid model that combines filtering and searching techniques to not only reduce data dimension quickly but also to automatically discover the optimal feature subset in a predetermined way. It is proposed in this paper that use of hybrid approach outperforms other techniques to identify cancer by deleting extraneous information from various models. There may be concerns with overfitting the training dataset if a large amount of data is used in this suggested approach. Deep learning and other forms of computational intelligence are both options that can be considered.

## Data Availability

The data shall be made available on request.

## Conflicts of Interest

The authors declare that they have no conflict of interest.

## References

- [1] E. Graf, C. Schmoor, W. Sauerbrei, and M. Schumacher, "Assessment and comparison of prognostic classification schemes for survival data," *Statistics in Medicine*, vol. 18, no. 17-18, pp. 2529-2545, 1999, PMID: 10474158.
- [2] C.-L. Chi, W. N. Street, and W. H. Wolberg, *Application of artificial neural network-based survival analysis on two breast cancer datasets. AMIA Annual Symposium Proceedings*, American Medical Informatics Association, 2007.
- [3] J. Quackenbush, "Data standards for 'omic' science," *Nature Biotechnology*, vol. 22, pp. 613-614, 2004, A short, incisive report that introduces some of the problems that the omics sciences face with regards to data quality and representation standards.
- [4] N. Sharma, C. Chakraborty, and R. Kumar, "Optimized multimedia data through computationally intelligent algorithms," *Multimedia Systems*, pp. 1-17, 2022.
- [5] W. Yang, J. Soares, P. Greninger et al., "Genomics of Drug Sensitivity in Cancer (GDSC): a resource for therapeutic biomarker discovery in cancer cells," *Nucleic Acids Research*, vol. 41, pp. D955-D961, 2013.
- [6] Z. Dong, N. Zhang, C. Li et al., "Anticancer drug sensitivity prediction in cell lines from baseline gene expression through recursive feature selection," *BMC Cancer*, vol. 15, no. 1, p. 489, 2015.
- [7] X. Chen, B. Ren, M. Chen, Q. Wang, L. Zhang, and G. Yan, "NLLSS: predicting synergistic drug combinations based on semi-supervised learning," *PLoS Computational Biology*, vol. 12, no. 7, article e1004975, 2016.
- [8] M. P. Menden, F. Iorio, M. Garnett et al., "Machine learning prediction of cancer cell sensitivity to drugs based on genomic and chemical properties," *PLoS One*, vol. 8, no. 4, article e61318, 2013.
- [9] S. Tang and M. Shabaz, "A new face image recognition algorithm based on cerebellum-basal ganglia mechanism," in *Journal of Healthcare Engineering (Vol. 2021, pp. 1-11)*, C. Chakraborty, Ed., Hindawi Limited, 2021.
- [10] C. Sharma, A. Bagga, R. Sobti, M. Shabaz, and R. Amin, "A robust image encrypted watermarking technique for neurodegenerative disorder diagnosis and its applications," in *Computational and Mathematical Methods in Medicine (Vol. 2021, pp. 1-14)*, D. Koundal, Ed., Hindawi Limited, 2021.
- [11] D. Schüssele, P. Haller, M. Haas, C. Hunter, K. Sporbeck, and T. Proikas-Cezanne, "Autophagy profiling in single cells with open source CellProfiler-based image analysis," *Autophagy*, pp. 1-14, 2022.
- [12] Z. Wanwan and M. Jin, "Improving the performance of feature selection methods with low-sample-size data," *The Computer Journal*, 2022.
- [13] J. Zhou and Z. Hua, "A correlation guided genetic algorithm and its application to feature selection," *Applied Soft Computing*, vol. 123, p. 108964.
- [14] R. J. Urbanowicz, M. Meeker, W. La Cava, R. S. Olson, and J. H. Moore, "Relief-based feature selection: introduction and review," *Journal of Biomedical Informatics*, vol. 85, pp. 189-203, 2018.
- [15] T. Dökeröglü, A. Deniz, and H. Kızılöz, "A comprehensive survey on recent metaheuristics for feature selection," *Neurocomputing*, vol. 494, pp. 269-296, 2022.
- [16] Y. Liu, H. Chen, T. Li, and W. Li, "A robust graph based multi-label feature selection considering feature-label dependency," *Applied Intelligence*, vol. 1-27, 2022.
- [17] N. Sharma and C. Chakraborty, "Evaluation of bioinspired algorithms for image optimization," *Journal of Electronic Imaging*, vol. 31, no. 4, article 041206, 2022.
- [18] Y. Sun, H. Li, M. Shabaz, and A. Sharma, "Research on building truss design based on particle swarm intelligence optimization algorithm," in *International Journal of System Assurance Engineering and Management*, Springer Science and Business Media LLC, 2022.
- [19] M. Shabaz and U. Garg, "Predicting future diseases based on existing health status using link prediction," in *World Journal of Engineering: Vol. ahead-of-print (issue ahead-of-print)*, Emerald, 2021.
- [20] S. Chaudhury, N. Shelke, K. Sau, B. Prasanalakshmi, and M. Shabaz, "A novel approach to classifying breast cancer histopathology biopsy images using bilateral knowledge distillation and label smoothing regularization," in *Computational and Mathematical Methods in Medicine (Vol. 2021, pp. 1-11)*, D. Koundal, Ed., Hindawi Limited, 2021.
- [21] A. Gupta and L. K. Awasthi, "Peer-to-peer networks and computation: current trends and future perspectives," *Computing and Informatics*, vol. 30, no. 3, pp. 559-594, 2011.
- [22] V. Jagota, M. Luthra, J. Bhola, A. Sharma, and M. Shabaz, "A secure energy-aware game theory (SEGaT) mechanism for coordination in WSANs," *International Journal of Swarm Intelligence Research*, vol. 13, no. 2, pp. 1-16, 2022.
- [23] N. Sharma and U. Batra, "A review on spatial domain technique based on image steganography," in *2017 International Conference on Computing and Communication Technologies for Smart Nation (IC3TSN)*, pp. 24-27, IEEE, Gurgaon, India, 2017, October.
- [24] Y. Lei, S. Vyas, S. Gupta, and M. Shabaz, "AI based study on product development and process design," *International Journal of Systems Assurance Engineering and Management*, vol. 13, no. 1, pp. 305-311, 2022.
- [25] Y.-D. Zhang, S. Wang, P. Phillips, and J. Genlin, "Binary PSO with mutation operator for feature selection using decision tree applied to spam detection," *Knowledge-Based Systems*, vol. 64, pp. 22-31, 2014.
- [26] B. Bakir-Gungor, H. Hacilar, A. Jabeer, O. Nalbantoglu, O. Aran, and M. Yousef, "Inflammatory bowel disease biomarkers of human gut microbiota selected via different feature selection methods," *PeerJ*, vol. 10, article e13205, 2022.
- [27] G. Chandrashekar and F. Sahin, "A survey on feature selection methods," *Computers and Electrical Engineering*, vol. 40, no. 1, pp. 16-28, 2014.
- [28] V. Bolón-Canedo and A. Alonso-Betanzos, "Ensembles for feature selection: a review and future trends," *Information Fusion*, vol. 52, pp. 1-12, 2019.
- [29] A. Gupta and L. K. Awasthi, "Peer enterprises: a viable alternative to cloud computing?," in *2009 IEEE International Conference on Internet Multimedia Services Architecture and Applications (IMSAA)*, Bangalore, India, 2009.

## *Retraction*

# **Retracted: Diagnostic Significance of 3D Automated Breast Volume Scanner in a Combination with Contrast-Enhanced Ultrasound for Breast Cancer**

### **BioMed Research International**

Received 8 January 2024; Accepted 8 January 2024; Published 9 January 2024

Copyright © 2024 BioMed Research International. This is an open access article distributed under the Creative Commons Attribution License, which permits unrestricted use, distribution, and reproduction in any medium, provided the original work is properly cited.

This article has been retracted by Hindawi following an investigation undertaken by the publisher [1]. This investigation has uncovered evidence of one or more of the following indicators of systematic manipulation of the publication process:

- (1) Discrepancies in scope
- (2) Discrepancies in the description of the research reported
- (3) Discrepancies between the availability of data and the research described
- (4) Inappropriate citations
- (5) Incoherent, meaningless and/or irrelevant content included in the article
- (6) Manipulated or compromised peer review

The presence of these indicators undermines our confidence in the integrity of the article's content and we cannot, therefore, vouch for its reliability. Please note that this notice is intended solely to alert readers that the content of this article is unreliable. We have not investigated whether authors were aware of or involved in the systematic manipulation of the publication process.

Wiley and Hindawi regrets that the usual quality checks did not identify these issues before publication and have since put additional measures in place to safeguard research integrity.

We wish to credit our own Research Integrity and Research Publishing teams and anonymous and named external researchers and research integrity experts for contributing to this investigation.

The corresponding author, as the representative of all authors, has been given the opportunity to register their agreement or disagreement to this retraction. We have kept a record of any response received.

### **References**

- [1] Q. Yuan, C. Song, Y. Tian et al., "Diagnostic Significance of 3D Automated Breast Volume Scanner in a Combination with Contrast-Enhanced Ultrasound for Breast Cancer," *BioMed Research International*, vol. 2022, Article ID 3199884, 8 pages, 2022.

## Research Article

# Diagnostic Significance of 3D Automated Breast Volume Scanner in a Combination with Contrast-Enhanced Ultrasound for Breast Cancer

Quan Yuan <sup>1</sup>, Canxu Song <sup>1</sup>, Yan Tian <sup>1</sup>, Nan Chen <sup>2</sup>, Xing He <sup>1</sup>, Ying Wang <sup>1</sup>, and Pihua Han <sup>2</sup>

<sup>1</sup>Department of Ultrasound, Shaanxi Provincial Cancer Hospital, Xi'an 710061, China

<sup>2</sup>Department of Breast Surgery, Shaanxi Provincial Cancer Hospital, Xi'an 710061, China

Correspondence should be addressed to Canxu Song; [songcanxu@mjc.edu.cn](mailto:songcanxu@mjc.edu.cn)

Received 20 May 2022; Revised 28 June 2022; Accepted 11 July 2022; Published 3 August 2022

Academic Editor: Gaganpreet Kaur

Copyright © 2022 Quan Yuan et al. This is an open access article distributed under the Creative Commons Attribution License, which permits unrestricted use, distribution, and reproduction in any medium, provided the original work is properly cited.

The incidence of cancer is increasing today, particularly lung and chest cancer. Employing novel methods to detect cancer in its earliest stages and discover painless, noninvasive treatments are urgently needed. The goal of the proposed study is to investigate the value of automated breast volume scanning (ABUS) in conjunction with contrast-enhanced ultrasonography (CEUS) in properly diagnosing breast cancer in its early stages and the effectiveness of neoadjuvant chemotherapy (NAC) in treating the disease. For the research study, information on 98 patients who had NAC and surgery in the breast surgery department of the Shaanxi Provincial Cancer Hospital has been gathered. All patients have received four cycles of NAC and underwent conventional ultrasound (HUS), CEUS, ABUS, and pathological examination. At the same time, receiver operating characteristic (ROC) curve analysis, single factor, multiple linear regression, and other methods have also been used to analyze the diagnostic efficacy of breast cancer and NAC efficacy evaluation results. The study of this paper is totally based on the data collected from Shaanxi Provincial Cancer Hospital. The statistical and computational analyses are performed on the data collected for drawing inferences. When the findings are compared to the results of the pathological examination, HUS has demonstrated a significant distinction between benign and malignant diagnoses with a statistical value of  $P < 0.05$ . ABUS combined with CEUS has shown no considerable differences in correlation study. Except for negative likelihood ratio, the diagnostic performance indexes of CEUS+ ABUS are substantially higher than HUS with  $P < 0.05$ . ROC curve analysis is also performed which shows that CEUS and ABUS combination has higher precision in the analysis of breast cancer. ABUS pooled with CEUS shows great application value in the judgment of breast cancer as per the results obtained from the statistical analysis on data of 98 patients.

## 1. Introduction

Epidemiological data show that there are about 12.7 million new cases of cancer worldwide each year and up to 7.6 million deaths from cancer. In terms of the incidence and mortality rates of all cancer cases, breast cancer ranks first among diseases that kill women, accounting for 23% and 14%, respectively. This proportion is relatively high, and it also shows an increasing trend year by year. In conclusion, breast cancer constitutes a serious threat to the health of women [1, 2]. Breast cancer develops slowly, and the majority of cases are found through routine screenings. The

following are signs of breast cancer: newly discovered lump or underarm bulge (armpit), swelling or thickening of a breast region, breast skin irritation, nipple pulling in or nipple region discomfort, bleeding from the breasts, in addition to breast milk and many more. Therefore, how to make early diagnosis of breast cancer and judge the therapeutic effect of tumor has become the main topic of clinical concern.

At present, the approaches for initial analysis of breast cancer include traditional ultrasound, magnetic resonance imaging (MRI), molybdenum target radiography (MTR), and positron emission tomography/computed tomography (PET/CT). Ultrasound is currently the most important

imaging method for clinical diagnosis of breast diseases [3–5]. Studies on the effectiveness of the ABUS in the prediction of breast cancer have been conducted in recent years. These results showed that the detection rate, sensitivity, and specificity of ABUS in the diagnosis of breast cancer are more than that of MTR, but whether it is higher than HHUS is still controversial [6–8]. Some studies showed that ABUS and HHUS did not show considerable differences in prediction of cancer in breast and specificity, detection rate, and sensitivity [9]. Neoadjuvant chemotherapy (NAC) is an important part of preoperative treatment of breast cancer, which is systemic therapy as the first step of breast cancer treatment [10–12]. Although NAC can prolong survival with tumor, drug resistance or tumor progression may occur during treatment, which may delay the timing of surgery. In addition, some reports indicated that there was no considerable variance in endurance rate between breast cancer patients with NAC and postoperative chemotherapy [13–16]. In general, there is still a great controversy about the efficacy of NAC [17]. The adjustment of the chemotherapeutic regimen and long-term prognosis depend greatly on the prompt and precise evaluation of the therapeutic efficacy of NAC.

The most crucial techniques for assessing NAC effectiveness at the moment are pathology and imaging practices. Pathology is still the benchmark for assessing the effectiveness of chemotherapy on tumors and its diagnostic accuracy is high. However, it has disadvantages such as invasiveness, the risk of needle metastasis caused by repeated puncture during chemotherapy, distant metastasis of tumor, and difficulty for patients to accept the disease. MRI is the gold standard for image evaluation, which can accurately observe lesions and have a good differentiation effect between lesions and normal primary tissues, as well as reflect the blood perfusion in lesions [18]. Pure blood pool imaging, or CEUS, is carried out by infusing a microbubble contrast dye into a peripheral venous mass to make the lesion tissue more visible. It visually displays the microperfusion of the lesion before and after chemotherapy. In addition, it has many advantages such as relatively low price, no nephrotoxicity, and repeatability [19].

In summary, ABUS and CEUS are favorable procedures for clinical finding of breast cancer and assessment of the efficacy of NAC. However, both methods have their own advantages, disadvantages, and indications. Hence, it was speculated that the combination of the two can improve the accuracy of diagnosis and efficacy judgment. Therefore, patients undergoing NAC and surgical treatment in the breast surgery department of Shaanxi Provincial Cancer Hospital were nominated as the research objects.

The main research highlights of the paper are as follows:

- (1) Conventional ultrasound (HUSS), CEUS, and ABUS were performed before NAC, at the 2nd and 4th cycles, and after the end of chemotherapy to check the efficacy of diagnostic method
- (2) The assessment of CEUS collective with ABUS in the analysis of breast cancer was explored, and the efficacy of NAC was evaluated to deliver allusion and

basis for clinical diagnosis and efficacy estimation of connected ailments

- (3) The three methods commonly used in clinical diagnosis of breast cancer and evaluation of NAC efficacy, namely, clinical evaluation, imaging evaluation, and pathological evaluation, are analyzed and compared for CEUS and ABUS

Rest of the paper is organized as follows: In Section 2, a detailed elaboration of the research object, imaging examination methods, treatment and pathological examination, diagnostic performance analysis, curative effect evaluation, and statistical methods is discussed. In Section 3, results and discussion on pathological examination results, maximum diameter assessment of the malignant tumor, evaluation of consistency for diagnosis of tumor, and NAC efficacy are elaborated. In Section 4, overall summary of the diagnostic significance of CEUS and ABUS is done. In Section 5, the research work is concluded.

## 2. Materials and Methods

**2.1. The Research Object.** From April 2021 to April 2022, 98 patients who underwent NAC and operation in breast surgery department of Shaanxi Provincial Cancer Hospital were designated as the research objects. All patients received HUSS, CEUS, ABUS, and pathological examination. Inclusion criteria are as follows: before NAC therapy, ultrasound-guided coarse needle biopsy was performed, which was pathologically confirmed as clear invasive breast cancer. NAC patients underwent HUSS, ABUS, and CEUS with complete pathological data. Exclusion criteria are as follows: early pregnancy with breast cancer; elderly and infirm patients with serious organic heart and lung diseases; patients who were unable to undergo CEUS or ultrasound imaging; patients with distant metastasis, preoperative treatment was rescue therapy rather than NAC; patients with swelling or skin ulceration that was difficult to measure; multifocal breast cancer; and Paget's disease. Informed consent was obtained for all studies in this work.

**2.2. Imaging Examination Methods.** HUSS: GE (General Electric) LOGICE9 color Doppler ultrasound diagnostic instrument was used, and the frequency was 9~15 Hz. The examination was performed by a sonographer with more than five years of experience. The patient was supine with both upper limbs raised, fully exposing the breasts. It was made easier for people to take the lateral decubitus position assessment if they had plump breasts and had trouble with the lateral image examination. The probe was applied to the breast surface with appropriate pressure and was scanned continuously perpendicular to the skin. The anatomical layers of the breast were observed, and the ultrasound instrument was adjusted according to the nature and location of the lesions that were available. The tissue surrounding the lesion can be clearly seen until the lesion is in the center of the screen, allowing for detailed description and recording of the lesion's location, size, morphology, internal echo properties and characteristics, boundary

properties, edge echo characteristics, and surrounding tissue conditions. The stone clock positioning method was used and the thoroughgoing span of the tumor in three quadrants and the distance from the nipple were measured on the maximum display section of the tumor. In addition, the maximum section blood flow state of the tumor should be observed and recorded under Doppler conditions.

CEUS: GE LOGICE9 color Doppler ultrasound diagnostic instrument was used at a frequency of 7-9 Hz. The patient was set up for intravenous access, and the position preparation was consistent with HUSS examination. SonoVue from Bracco was used as a contrast agent. The lesions were observed under two-dimensional conditions and the sections with abnormal blood supply or suspicious edge infiltration were selected as the contrast observation sections. Enough breast tissues were collected on both sides of the lesion for comparison. Meanwhile, the CEUS was switched to contrast mode. 5 mL contrast agent microbubble suspension was intravenously injected, and 5 mL normal saline was injected into the flushing tube. Doctors dynamically observed the enhancement characteristics of the lesion, including the enhancement mode of the tumor. The tumor's maximum diameter and image features were recorded, together with the distribution of the contrast agent in the area in front of the invasion of the tumor and the perfusion process. The angiography parameters and all imaging data were saved.

ABUS inspection: GE ABUS inspection system was employed. The ABUS workstation is an automatic image acquisition system, which can automatically adjust the depth and gain of the scan, and perform reconstruction work by itself. When evaluating patients with dense glandular breasts, automated breast ultrasound, or ABS, is a complementary ultrasound technique that is becoming more and more popular. Associated to individuals with fatty breasts, those with thick breasts have an upper chance of breast cancer. Additionally, mammography has a low sensitivity for finding breast tumors in this patient population, particularly if they are not accompanied with architectural deformation or calcifications. The ABUS is a standardized exam that has several benefits in both screening and diagnostic settings: it improves workflow, decreases examination time, and boosts the rate of breast cancer diagnosis.

Meanwhile, it can also obtain cross-sectional, sagittal, and coronal images. The volume of each scan was 15.4 cm × 17.0 cm × 5 cm, and the probe frequency was 6-14 MHz. All ABUS operators and analysts had received Food and Drug Administration- (FDA-) mandated training provided by GE and had been certified. Before examination, the physician chose the most appropriate scan mode according to the size of the breast. In general, the anterior and posterior positions, lateral positions, and medial positions of the mammary gland are examined, and the upper or lower positions were scanned if necessary. After the scan, the scan images were sent to the workstation and the ultrasound physicians with more than five years of working experience analyzed them in blind state, referring to the Bi-Rads standard developed by American College of Radiology (ACR). Detailed information of the lesion was recorded, including

number, maximum diameter, location, quadrant, distance, tumor morphology, tumor growth direction, tumor margin, echo characteristics, posterior echo characteristics, calcification and presence of structural distortion, catheter changes, skin changes, edema, and presence of convergence signs.

*2.3. Treatment and Pathological Examination.* NAC chemotherapy regimen: 1, TEC\*6 (docetaxel+pharmorubicin+cyclophosphamide); 2, EC\*4-TH\*4 (pharmorubicin+cyclophosphamide, continuation docetaxel+herceptin); and 3, TX\*3-ECX\*3 (docetaxel+tegafur, followed with pharmorubicin+cyclophosphamide+tegafur).

Operation and pathology: one week before chemotherapy, a coarse needle puncture biopsy (TSK 14G biopsy needle) was performed on the lesion and 6-8 effective tissues were taken out. Biopsy specimens were sent for examination to obtain pathological types and immunohistochemical indicators. Modified radical mastectomy or breast conserving surgery was performed within three weeks after the end of chemotherapy. The size of lesions and axillary lymph node metastasis were measured after gross specimens were submitted for examination and were compared with puncture specimens before chemotherapy for postoperative pathological MP grading. The specific and detailed pathological MP grades were shown in Table 1.

*2.4. Diagnostic Performance Analysis.* The ROC curve is mainly used to assess the classification/diagnosis effect of a certain index and to find the optimal index critical value to achieve the best classification effect. The 1-specificity is the abscissa of the curve, and the sensitivity is the ordinate. The sensitivity and 1-specificity corresponding to each truncated value constitute coordinate points. ROC is obtained when multiple coordinate points are connected. In this study, it was intended to use ROC curve to assess the analytic value of HUSS and CEUS+ ABUS for NAC, and the indexes were calculated to evaluate the diagnostic values. Sensitivity analysis, accuracy analysis, positive predictive value (PPV), and area under ROC curve (AUC) metrics are used to evaluate the efficacy of the combined methods used for the diagnosis and cure for breast cancer.

After the diagnostic efficacy of different imaging methods was evaluated by ROC curve, the diagnostic value was comprehensively evaluated by single factor and multiple linear regression.

*2.5. Curative Effect Evaluation.* Prior to and following chemotherapy, the tumor's largest diameter was measured by HUSS and assessed in accordance with the RECIST evaluation criteria. The efficacy evaluation was graded into progressed disease (PD), partial response (PR), complete response (CR), and stable disease (SD). CR and PR were effective, while SD and PD were ineffective. The details were shown in Table 2.

*2.6. Statistical Methods.* Statistical Package for Social Sciences 22.0 software was used, and the quantity data were articulated in rappers of mean ± standard deviation ( $\bar{x} \pm s$ ). *T*-test was used for assessment amongst groups. An intragroup comparison was made using analysis of variance.

TABLE 1: Pathological grading standards.

Grade	The symptom manifestations
1 <sup>st</sup> grade	The infiltrating cells did not change or only a few cells did, and the total number of cells remained the same.
2 <sup>nd</sup> grade	The amount of invasive cancer cells reduced somewhat, but the total amount of cancer cells remained high, with a reduction of no more than 30%.
3 <sup>rd</sup> grade	Between 30% and 90% fewer cancer cells were seen.
4 <sup>th</sup> grade	More than 90% of the cancer cells were eliminated, leaving only a few small clusters and solitary cells.
5 <sup>th</sup> grade	The main tumor bed lacked infiltrating cancer cells, yet there may be mammary carcinoma in situ.

TABLE 2: Efficacy evaluation criteria for solid tumors.

Grading of efficacy	Standard
CR	Entirely tumor lesions vanished
PR	Target lesions' longest diameters added together were decreased by 30%.
SD	The lesion changes were between PR and PD
PD	The development of new lesions, a 20% rise in the aggregate of the biggest widths of target lesions, or a clear development of nontarget lesions

Chi-square test was used for counting data.  $P < 0.05$  was statistically significant.

### 3. Results and Discussion

**3.1. Pathological Examination Results.** Pathological examination results of all patients are as shown in Figure 1. 100 breast masses in total, including 66 malignant tumors, were identified, as shown in Figure 1. There were 53 invasive ductal carcinoma cases, 5 ductal carcinomas in situ, 3 invasive lobular carcinoma cases, 3 mucinous carcinoma cases, and 2 malignant fluid tumor instances. There were 44 benign lesions including 19 fibroadenomas, 9 adenosis, 8 intraductal papilloma, 3 cysts, 2 benign lobular tumors, 2 inflammation, and 1 hamartoma.

**3.2. Comparison of Diagnostic Efficacy.** The diagnostic results of breast tumors by the two methods are as shown in Figure 2. According to Figure 2, the number of malignant and benign tumors diagnosed by pathology was 66 and 34, respectively. The number of malignant and benign tumors diagnosed by HHUS was 52 and 48, respectively. The number of malignant and benign tumors diagnosed by CEUS+ ABUS was 67 and 33, respectively. There was considerable difference between HHUS diagnosis results and pathological examination results,  $P < 0.05$ . There was no significant variance between pathological examination and CEUS+ ABUS for  $P < 0.05$ .

The diagnostic efficacy of the two methods for breast tumors and ROC breast analysis results are shown in Figure 3. According to Figure 3, the sensitivity, negative predictive value (NPV), accuracy, specificity, positive predictive value (PPV), positive likelihood ratio (PLR), and negative likelihood ratio (NLR) of HHUS in diagnosing breast tumors were 85.4%, 88.3%, 86.6%, 88.3%, 86.1%, 5.33, and 0.14, respectively. The sensitivity, NPV, accuracy, specificity, PPV, PLR, and NLR of HHUS in diagnosing breast tumors

were 97%, 96%, 98.3%, 95.7%, 94.8%, 31.6, and 0.08, respectively. Except for the negative likelihood ratio, CEUS+ ABUS were substantially higher than HHUS in all the diagnostic efficiency indicators of breast tumors. The analysis results under ROC curve of the two methods showed that the area under HHUS curve was 0.87 (97% CI: 0.9-0.8), and the area under CEUS+ ABUS curve was 0.981 (97% CI: 0.8-0.978), demonstrating that the accurateness of the two methods were high. The two methods were compared,  $P = 0.003$ , suggesting that the difference was statistically significant.

**3.3. Maximum Diameter Assessment of the Malignant Tumor.** The results of the maximum diameter of malignant tumor evaluated by the two examination methods are shown in Figure 4. Figure 4(a) depicts that the maximum diameter of tumor measured by HHUS and CEUS+ ABUS pathological tests were  $2.38 \pm 0.8$ ,  $2.73 \pm 1.01$ , and  $2.77 \pm 0.93$ , respectively. The maximum diameter of tumor measured by HHUS and pathological tests was substantially different ( $P < 0.05$ ). There was no considerable difference between CEUS+ ABUS and pathological examination. According to Figure 4(b), the number of accurate, large, and small tumors measured by HHUS was 32, 15, and 19, respectively, while the number of accurate, large, and small tumors measured by CEUS+ ABUS was 51, 8, and 7, respectively. Obviously, CEUS+ ABUS had substantially higher accuracy in tumor diameter measurement than HHUS,  $P < 0.05$ .

**3.4. Evaluation of Consistency for Diagnosis of Tumor.** The consistency evaluation results of the two methods for tumor diagnosis are as shown in Figure 5. In the consistency comparison of the tumor shape, direction, edge, border, internal echo characteristics, posterior echo characteristics, calcification, and BI-RADS grading indicators, Figure 5 shows that the  $K$  values of the two methods were, respectively, 0.53, 0.51, 0.66, 0.54, 0.62, 0.66, 0.57, and 0.63. It

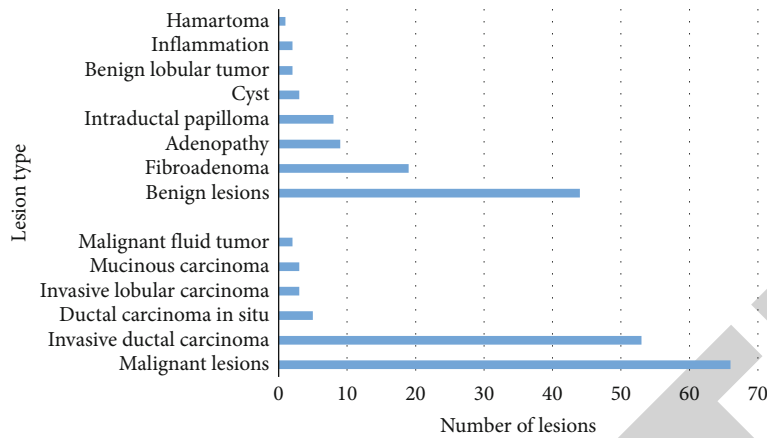


FIGURE 1: Pathological examination results.

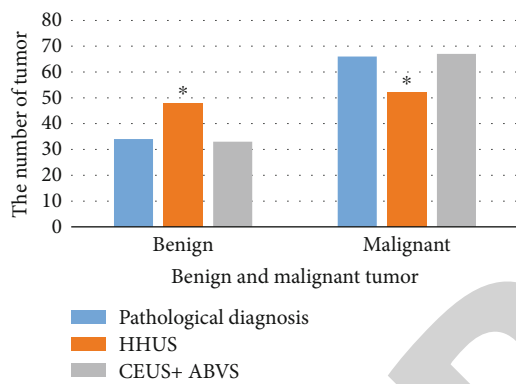


FIGURE 2: Diagnostic results of breast tumor by two methods. Note: compared with pathological examination, \* $P < 0.05$ .

was obvious that the two methods had good consistency in the above indications.

**3.5. NAC Efficacy.** The efficacy evaluation results of the two methods for NAC are as shown in Figure 6. Figure 6 show that the HHUS classified 76 cases as invalid and 22 cases as effective. By using CEUS+ ABUS, it was determined that 65 cases were invalid and 33 cases were effective. Pathological diagnosis determined 67 and 31 cases to be invalid and effective, respectively. There was considerable difference between HHUS evaluation results and the pathological diagnosis evaluation results,  $P < 0.05$ . However, there was little distinction between the outcomes of the CEUS+ ABUS analysis and the analysis of the pathological diagnosis.

#### 4. Discussion

Currently, breast cancer is the most prevalent and high female malignant tumor in the globe. It is also the most common cause of death for female malignant tumors. According to the latest *Global Cancer Report 2020* released by the *World Health Organization (WHO)*, breast cancer has become the number one cancer affecting women. At present, the incidence of new breast cancer in China is 59.0/100,000, which is the first in the incidence of female

malignant tumors in China and the mortality rate is the fourth. In China nowadays, breast cancer is the leading cause of cancer death among women over 45 [20].

At present, NAC is a very important component in the treatment of breast cancer. NAC refers to systemic cytotoxic drug therapy before surgery or radiotherapy for malignant tumors [20]. Studies by some scholars have shown that there is no considerable difference in the survival rate between NAC and postoperative chemotherapy for the breast cancer patients [21].

Currently, there are three methods commonly used in clinical diagnosis of breast cancer and evaluation of NAC efficacy, namely, clinical evaluation, imaging evaluation, and pathological evaluation [22]. Although MRI is now regarded as one of the most accurate method to assess the efficacy of NAC, it is expensive and prone to respiratory side effects despite having a high consistency with pathological testing. In addition, the contrast agent used has strong renal toxicity, so its clinical acceptance and promotion is not very high. Additionally, the shrinkage of microvessels is a key indicator that chemotherapy medications slow the rate at which tumor cells proliferate. [22]. Relevant clinical studies showed that the effective standard for breast cancer treatment is not only the death of tumor cells but also the reduction of blood perfusion [23]. The pathological results before and after NAC treatment showed that the internal microvessels of tumors were substantially reduced, indicating that chemotherapy drugs can reduce the blood perfusion of tumor tissues and kill tumor vascular endothelial cells at the same time. When compared to MRI, CEUS size measurement consistency, prediction accuracy, and pathological outcomes are essentially comparable [23]. Compared with HUSS technology, ABUS can continuously collect images, standardize ultrasonic examination, have high repeatability, and avoid interference of human factors [24]. Additionally, it can offer a transverse, sagittal, and coronal image that displays the tumor's size, shape, edge, growth direction, and internal echo in addition to two-dimensional information like structure distortion and three-dimensional reconstruction stereo diagnostic data to help with diagnosis [25]. In this work, patients with breast cancer who underwent NAC and surgical treatment were studied. All patients



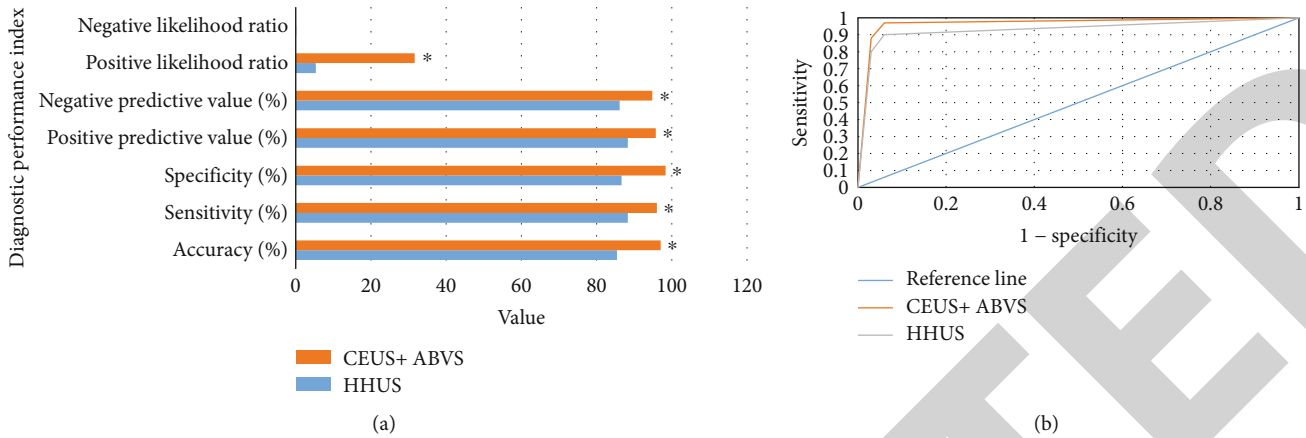


FIGURE 3: Comparison of diagnostic efficiency. Note: (a) diagnostic effectiveness and (b) the ROC curve; compared with HHUS, \* $P < 0.05$ .

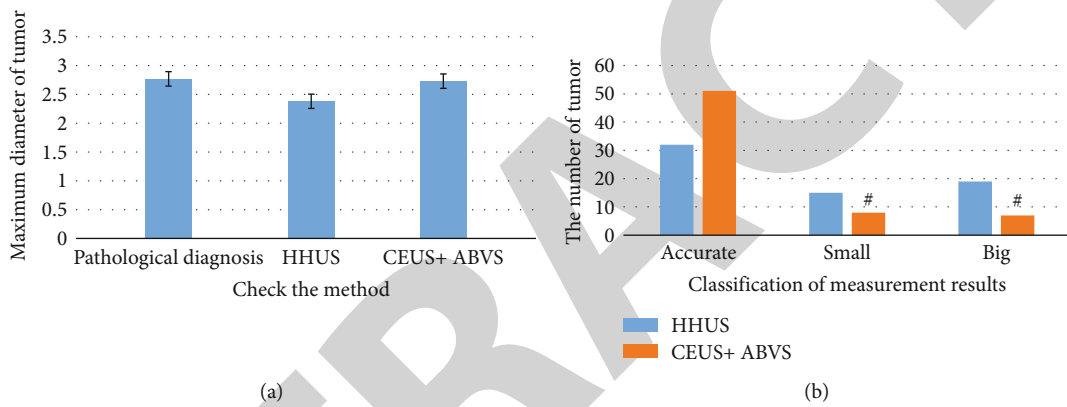


FIGURE 4: The maximum diameter of malignant tumor. Note: (a) maximum diameter of tumor and (b) accuracy of maximum diameter measurement; compared with pathological examination,  $P < 0.05$ ; compared with HHUS,  $P < 0.05$ .

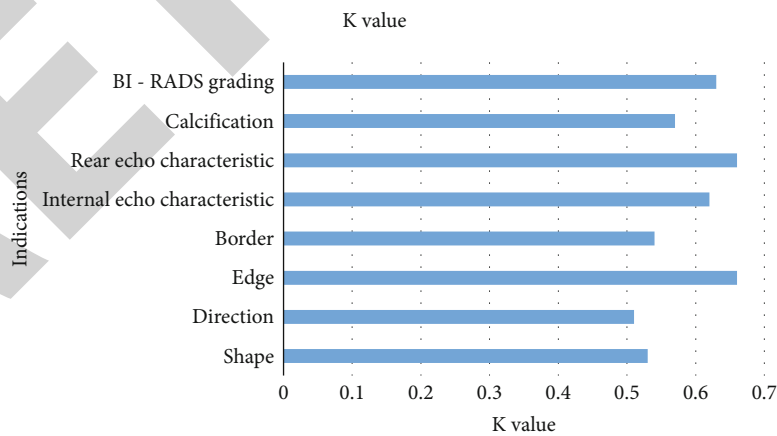


FIGURE 5: Consistency evaluation of the two methods for tumor diagnosis.

underwent pathological examination, HUSS, ABUS, and CEUS examination. At the same time, ROC curve analysis, single factor, multiple linear regressions, and other methods were used to examine and associate the analytic efficacy of each method in the diagnosis of breast cancer and the results of NAC treatment. The results showed that ABUS combined

with CEUS had the best efficacy in the judgment of breast cancer, and the results of diagnosis and efficacy evaluation of NAC were the most similar to the results of pathological examination. This indicates that ABUS combined with CEUS had a high application prospect in breast cancer diagnosis and NAC efficacy evaluation.

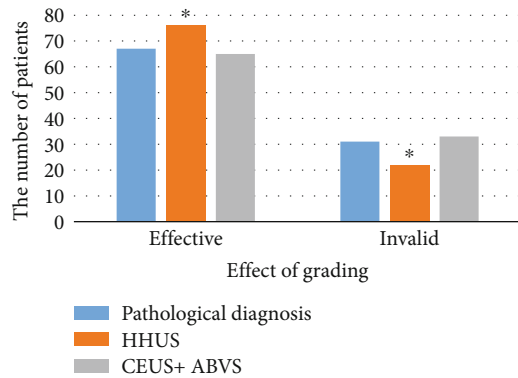


FIGURE 6: Efficacy evaluation results of NAC. Note: compared with pathological examination, \* $P < 0.05$ .

## 5. Conclusion

The data of 98 breast cancer patients who received NAC and surgical treatment were examined in this study. All the patients underwent pathological examination, HHUS, ABUS, and CEUS examination. At the same time, ROC curve analysis, single factor, multiple linear regressions, and other methods have been used to evaluate and relate the indicative usefulness of each method for the prediction of breast cancer as well as the results of NAC treatment. The results prove that ABUS combined with CEUS has the best efficacy in the diagnosis of breast cancer, and the results of diagnosis and efficacy evaluation of NAC are the most similar to the results of pathological examination. This indicates that ABUS combined with CEUS has a high application prospect in breast cancer diagnosis and NAC efficacy evaluation. In conclusion, this work provides a new idea and basis for clinical diagnosis of breast cancer at early stages and evaluation of the efficacy of NAC. Pathology identified 66 malignant tumors and 34 benign cancers, respectively. 52 aggressive tumors and 48 benign tumors, respectively, were identified by HHUS. The number of malignant and benign tumors diagnosed by CEUS+ ABUS was 67 and 33, respectively. However, due to the limited samples and space, this work still has some limitations. In the future study, we will include more samples to conclude the efficacy of the combined methods for the prognosis of breast cancer.

## Data Availability

The data is restricted to share as it is confidential data of Shaanxi Provincial Cancer Hospital.

## Conflicts of Interest

The authors have nothing to declare as conflicts of interest.

## Acknowledgments

The authors are thankful to the Shaanxi Provincial Health Research.

## References

- [1] R. Guo, G. Lu, B. Qin, and B. Fei, "Ultrasound imaging technologies for breast cancer detection and management: a review," *Ultrasound in Medicine & Biology*, vol. 44, no. 1, pp. 37–70, 2018.
- [2] R. M. Mann, C. K. Kuhl, and L. Moy, "Contrast-enhanced MRI for breast cancer screening," *Journal of Magnetic Resonance Imaging*, vol. 50, no. 2, pp. 377–390, 2019.
- [3] A. Rix, M. Piepenbrock, B. Flege et al., "Effects of contrast-enhanced ultrasound treatment on neoadjuvant chemotherapy in breast cancer," *Theranostics*, vol. 11, no. 19, pp. 9557–9570, 2021.
- [4] M. Kaur, S. R. Sakhare, K. Wanjale, and F. Akter, "Early stroke prediction methods for prevention of strokes," *Behavioural Neurology*, vol. 2022, Article ID 7725597, 9 pages, 2022.
- [5] M. B. Suter, F. Pesapane, G. M. Agazzi et al., "Diagnostic accuracy of contrast-enhanced spectral mammography for breast lesions: a systematic review and meta-analysis," *Breast*, vol. 53, pp. 8–17, 2020.
- [6] J. Sogani, V. L. Mango, D. Keating, J. S. Sung, and M. S. Jochelson, "Contrast-enhanced mammography: past, present, and future," *Clinical Imaging*, vol. 69, pp. 269–279, 2021.
- [7] J. Luo, L. Feng, Q. Zhou et al., "The value of contrast-enhanced ultrasound in determining the location of sentinel lymph nodes in breast cancer," *Cancer Imaging*, vol. 21, no. 1, p. 28, 2021.
- [8] A. Vourtsis and W. A. Berg, "Breast density implications and supplemental screening," *European Radiology*, vol. 29, no. 4, pp. 1762–1777, 2019.
- [9] N. M. Mule, D. D. Patil, and M. Kaur, "A comprehensive survey on investigation techniques of exhaled breath (EB) for diagnosis of diseases in human body," *Informatics in Medicine Unlocked*, vol. 26, article 100715, 2021.
- [10] M. E. Hatzipanagiotou, D. Huber, V. Gerthofer et al., "Feasibility of ABUS as an alternative to handheld ultrasound for response control in neoadjuvant breast cancer treatment," *Clinical Breast Cancer*, vol. 22, no. 2, pp. e142–e146, 2022.
- [11] D. L. Monticciolo, M. S. Newell, L. Moy, B. Niell, B. Monsees, and E. A. Sickles, "Breast cancer screening in women at higher-than-average risk: recommendations from the ACR," *Journal of the American College of Radiology*, vol. 15, no. 3, pp. 408–414, 2018.
- [12] I. Boca, A. I. Ciurea, C. A. Ciortea, and S. M. Ducea, "Pros and cons for automated breast ultrasound (ABUS): a narrative review," *Journal of Personalized Medicine*, vol. 11, no. 8, p. 703, 2021.
- [13] M. S. Jochelson and M. B. I. Lobbes, "Contrast-enhanced mammography: state of the art," *Radiology*, vol. 299, no. 1, pp. 36–48, 2021, Epub 2021 Mar 2.
- [14] S. Lin, Y. Cao, L. Chen, M. Chen, S. Zhang, and X. Jia, "Contrast-enhanced ultrasound of breast fibromatosis: a case report," *The Journal of International Medical Research*, vol. 49, no. 5, 2021.
- [15] R. K. Garg, J. Bhola, and S. K. Soni, "Healthcare monitoring of mountaineers by low power wireless sensor networks," *Informatics in Medicine Unlocked*, vol. 27, article 100775, 2021.
- [16] X. Liang, Z. Li, L. Zhang, D. Wang, and J. Tian, "Application of contrast-enhanced ultrasound in the differential diagnosis of different molecular subtypes of breast cancer," *Ultrasonic Imaging*, vol. 42, no. 6, pp. 261–270, 2020.

## *Retraction*

# **Retracted: Correlation-Based Mutual Information Model for Analysis of Lung Cancer CT Image**

### **BioMed Research International**

Received 8 January 2024; Accepted 8 January 2024; Published 9 January 2024

Copyright © 2024 BioMed Research International. This is an open access article distributed under the Creative Commons Attribution License, which permits unrestricted use, distribution, and reproduction in any medium, provided the original work is properly cited.

This article has been retracted by Hindawi, as publisher, following an investigation undertaken by the publisher [1]. This investigation has uncovered evidence of systematic manipulation of the publication and peer-review process. We cannot, therefore, vouch for the reliability or integrity of this article.

Please note that this notice is intended solely to alert readers that the peer-review process of this article has been compromised.

Wiley and Hindawi regret that the usual quality checks did not identify these issues before publication and have since put additional measures in place to safeguard research integrity.

We wish to credit our Research Integrity and Research Publishing teams and anonymous and named external researchers and research integrity experts for contributing to this investigation.

The corresponding author, as the representative of all authors, has been given the opportunity to register their agreement or disagreement to this retraction. We have kept a record of any response received.

### **References**

- [1] N. S. Vadivu, G. Gupta, Q. N. Naveed, T. Rasheed, S. K. Singh, and D. Dhabliya, "Correlation-Based Mutual Information Model for Analysis of Lung Cancer CT Image," *BioMed Research International*, vol. 2022, Article ID 6451770, 12 pages, 2022.

## Research Article

# Correlation-Based Mutual Information Model for Analysis of Lung Cancer CT Image

N. Shanmuga Vadivu <sup>1</sup>, Gauri Gupta <sup>2</sup>, Quadri Noorulhasan Naveed <sup>3</sup>,  
Tariq Rasheed <sup>4</sup>, Sitesh Kumar Singh <sup>5</sup> and Dharmesh Dhabliya <sup>6</sup>

<sup>1</sup>Department of Electronics and Communications Engineering, RVS College of Engineering and Technology, Coimbatore, India

<sup>2</sup>Department of Biomedical Engineering, SGSITS, Indore, India

<sup>3</sup>College of Computer Science, King Khalid University, Abha 61413, Saudi Arabia

<sup>4</sup>Department of English, College of Science and Humanities, Al-Kharj, Prince Sattam Bin Abdulaziz University, Al-Kharj 11942, Saudi Arabia

<sup>5</sup>Department of Civil Engineering, Wollega University, Nekemte, Oromia, Ethiopia

<sup>6</sup>Department of Information Technology, Vishwakarma Institute of Information Technology, Pune, Maharashtra, India

Correspondence should be addressed to Sitesh Kumar Singh; [sitesh@wollegauniversity.edu.et](mailto:sitesh@wollegauniversity.edu.et)

Received 30 May 2022; Revised 1 July 2022; Accepted 12 July 2022; Published 2 August 2022

Academic Editor: Gaganpreet Kaur

Copyright © 2022 N. Shanmuga Vadivu et al. This is an open access article distributed under the Creative Commons Attribution License, which permits unrestricted use, distribution, and reproduction in any medium, provided the original work is properly cited.

Most of the people all over the world pass away from complications related to lung cancer every single day. It is a deadly form of the disease. To improve a person's chances of survival, an early diagnosis is a necessary prerequisite. In this regard, the existing methods of tumour detection, such as CT scans, are most commonly used to recognize infected regions. Despite this, there are certain obstacles presented by CT imaging, so this paper proposes a novel model which is a correlation-based model designed for analysis of lung cancer. When registering pictures of thoracic and abdominal organs with slider motion, the total variation regularization term may correct the border discontinuous displacement field, but it cannot maintain the local characteristics of the image and loses the registration accuracy. The thin-plate spline energy operator and the total variation operator are spatially weighted via the spatial position weight of the pixel points to construct an adaptive thin-plate spline total variation regular term for lung image CT single-mode registration and CT/PET dual-mode registration. The regular term is then combined with the CRMI similarity measure and the L-BFGS optimization approach to create a nonrigid registration procedure. The proposed method assures the smoothness of interior of the picture while ensuring the discontinuous motion of the border and has greater registration accuracy, according to the experimental findings on the DIR-Lab 4D-CT public dataset and the CT/PET clinical dataset.

## 1. Introduction

Image registration is to find the optimal spatial transformation to make the floating image correspond to the reference image in a spatial position [1]. In clinical applications, medical image registration, especially multimodal image registration, can fuse image information from multiple modalities in the same image, enabling doctors to observe the structural information and functional metabolism information of human organs simultaneously. Lesion detection, disease tracking, and treatment plan formulation have improved the diagnostic efficiency and treatment level [2]. Therefore, accurate medical

image registration algorithms are essential. Since image registration is an ill-posed problem, a specific regular term is usually added to the measurement function of the registration algorithm to constrain the registration results. Different regularization terms have a significant influence on the image registration results. For the nonrigid registration algorithm of the image, the smooth regular representation based on the thin plate spline energy operator used by literature [3] is usually selected. The smooth regular term averages the displacement field of the registration image to make the displacement of adjacent structures. The field maintains continuous consistency, ensuring the smoothness of the registered image.

However, for particular thoracic and abdominal organs such as the lungs and liver, the breathing motion will cause them to slide and interact between the ribs, that is, sliding movement [4]. The adjacent organ structures form independent motion patterns. It leads to discontinuous motion in the displacement field of the adjoining structure boundary. The erratic movement of the boundary displacement field is a unique movement pattern caused by the phenomenon of human respiration. For this type of image, the original movement pattern should be kept as much as possible in boundary registration to avoid smooth operation. However, the smoothing effect of the standard smoothing regular term on the image boundary area cannot preserve this discontinuous displacement field, resulting in the loss of registration accuracy.

A class of methods is proposed to register organ images, such as lung and liver images. The method is an image segmentation method based on physiological characteristics. First, the parts with a continuous displacement field and a discontinuous displacement field in the image are divided. Then, the two parts of the divided images are independently registered. Finally, the registration results are combined. Literature [5] proposed a registration method based on a physiological motion model. First, a motion model was established by marking anatomical points on the image and extracting features. Then, regions with different motion patterns were segmented, and then, each part was registered separately. However, this method requires prior physiological knowledge to label feature points and complex segmentation registration. Another widely used way is to establish an appropriate regular term to constrain the measure function of the registration algorithm. Literature [6] used bilateral filtering instead of continuous Gaussian smoothing to deny the deformation field. Still, the paper did not systematically propose a regular term-based cost function sensitive to noise. Literature [7] used a diffusion regularization term based on the  $l_2$  norms, decomposed the deformation field into two directions, and only performed smooth constraints based on the diffusion model on the tangential component within the boundary. Literature [8, 9] and literature [10] introduced a total variation (TV) regularization term for the registration of thoracic and abdominal organ images. The TV operator spreads along the orthogonal direction of the gradient, which can effectively protect the discontinuous information at the edge of the image, thereby ensuring the discontinuity of the boundary displacement field. However, the above methods are only experimented with for single-mode image registration and do not consider the difference between organ boundaries and internal structures. Specifically, although the slip motion causes discontinuous boundary movement, the no boundary area inside the organ is not affected by the slip motion. If the global TV constraint is applied to the registration image, the registration accuracy and quality will still be affected. Aiming at the above problems, this paper proposes an adaptive thin-plate spline-based total variation (TPS-TV). The common term nonrigid registration method is mainly used in lung image CT single-mode registration and CT/PET dual-mode registration. The main idea of this regularization term is to obtain the pixel space position weight based on boundary segmentation and to establish a

regularization method for the adaptive pixel. The paper focuses on both CT single-mode registration [11] and CT/PET dual-mode registration [12] for calculating the spatial positions of the pixel. In the case of CT single-mode registration, the accuracy achieved is higher than that of the smooth ordinary time, and for CT/PET dual-mode registration, the registration accuracy of the worldwide TV standard term is lower than that of the smooth common term [13]. This shows that the global TV common term is more suitable for CT single-mode registration. However, the adaptive TPS-TV common term proposed in this paper has a good registration effect in CT single-mode registration and CT/PET dual-mode registration experiments [14].

The combination of positron emission tomography (PET) and computed tomography (CT), also known as PET/CT [15], has emerged as an important diagnostic technique for the early diagnosis of lung cancer. Imaging studies that were carried out for other reasons usually reveal the presence of insignificant pulmonary nodules as an accidental discovery [16]. Even while the majority of solitary pulmonary nodules are benign lesions, such as a granuloma or hamartoma, up to twenty percent of the time, they indicate a malignant tumour [17]. This is notably the case in elderly individuals and smokers. There is a possibility that these higher risk populations will have an incidence of cancer that is close to 70 percent [18]. Patients are referred to and handled by a multidisciplinary team to determine the nature of a nodule after it has been found in the body of the patient [19]. PET/CT plays a crucial role in helping to differentiate between benign and malignant lesions in suspicious lesions, with metabolically active lesions being more likely to indicate malignancy [20]. PET/CT results are used as a primary factor in the decision-making process to determine how to proceed with obtaining a tissue diagnosis [21].

The organization of this paper is as follows: Section 2 discusses the proposed methodology by illustrating the establishment of regular terms and optimization of the measure function; Section 3 discusses and analyzes the experimental results and discusses the DIR lab dataset and CT/PET clinical dataset; Section 4 presents the conclusion and scope for future work.

## 2. Methods

The reference image  $F(x)$  and the floating image  $M(x)$  are known,  $u(x, y, z; \phi)$  represents the deformation displacement field between the two images. Then, the image matching criterion is to find  $u$  that maximizes the matching degree between the reference image and the floating image. Therefore, the image registration problem can be equivalent to the minimization problem of the measure function  $C$  [22]:

$$C = D(F(x), M(u(x))) + \lambda R(u). \quad (1)$$

Among them,  $D$  represents the similarity measure function of registration,  $R$  represents the regular term, and  $\lambda$  represents the coefficient to adjust the regularization term.

In this paper, a B-spline-based Free-Form Deformation (FFD) model [23] is chosen to perform a nonrigid

transformation on the lung images to be registered. The similarity measurement function selects the CRMI algorithm proposed by Cai et al. [24], which combines mutual information (MI) and correlation ratio (CR). It adds the corresponding pixel grey level mapping based on the position information, which corrects the position deformation and makes up for the defect that MI only considers grayscale information and ignores pixel space information. As a result, CR is not sensitive to the calculated image size and noise. The specific expression of CRMI is as follows:

$$\text{CRMI}(M, F; \phi) = (2 - \text{MI}(M, F; \phi)) \cdot (1 - \text{CR}(M, F; \phi)). \quad (2)$$

To reduce the amount of registration calculation and reduce the registration time, Philippe proposed multiresolution Gaussian pyramid decomposition to improve the search efficiency.

*2.1. The Establishment of Regular Terms.* When the image registration problem is transformed into the solution of the minimization problem of the measure function, overfitting may occur, so a common term is usually introduced into the cost function to constrain it. The standard time is aimed at preventing overfitting, and its essence is to deny the optimization parameters [25]. A regular period is added to the measurement function of the registration algorithm, mainly to remove unnecessary or unreasonable solutions and ensure that the spatial variation between quasi-images approximates a one-to-one correspondence, which turns the nonrigid registration problem into an energy functional minimization problem. The TV regular term is a practical constraint method for the image registration problem with slip motion.

The TV regular term is a constraint method based on the gradient l1 norm, which is expressed explicitly as follows [10]:

$$R^{\text{TV}}(u) = \sum_{x \in \Omega} \sqrt{\left(\frac{du}{dx}\right)^2 + \left(\frac{du}{dy}\right)^2 + \left(\frac{du}{dz}\right)^2}. \quad (3)$$

The TV regular term has a smaller diffusion coefficient at the edge, so the diffusion speed of the edge area is slower, and the edge details of the image can be preserved [26]. However, the TV standard term usually produces a "staircase effect" in the smooth area, which cannot guarantee the image's smoothness [27]. For images of thoracic and abdominal organs with a sliding motion, such as the lung, the registration should keep the discontinuous displacement field of the image boundary and still carry out smooth constraints in the area that is not affected by the sliding motion. However, the conventional global TV regular term cannot achieve this goal. Therefore, based on the spatial position characteristics of the image, this paper introduces the thin-plate spline energy operator and the TV operator for spatial weighting to improve the conventional TV regular term. There is inapplicability in smooth regions. The thin-plate spline energy operator achieves the smoothness constraint effect by finding a smooth surface with minimal curvature passing through all control points, and the specific expression is

$$R^{\text{TPS}}(u) = \frac{1}{N} \sum_{x \in \Omega} \left[ \left(\frac{d^2u}{dx^2}\right)^2 + \left(\frac{d^2u}{dy^2}\right)^2 + \left(\frac{d^2u}{dz^2}\right)^2 + 2\left(\frac{d^2u}{dxdy}\right)^2 + 2\left(\frac{d^2u}{dxdz}\right)^2 + 2\left(\frac{d^2u}{dzdy}\right)^2 \right], \quad (4)$$

where  $N$  represents the image sample size.

According to the slip motion characteristics, the lung image's boundary displacement field discontinues while the internal displacement field still moves continuously. Therefore, the closer the pixel position of the image to be registered is to the boundary, the more pronounced the discontinuity of the displacement field; on the contrary, the farther the pixel position is from the edge, the more pronounced the smoothness of the displacement field. Therefore, taking the pixel position feature as the prior knowledge, by calculating the spatial position weight of the pixel, the TV operator and the thin-plate spline energy operator are combined to establish the thin-plate spline total variation regular term that is adaptive to the pixel position feature; the expression is as follows:

$$R^{\text{TPS-TV}}(u) = w(x)R^{\text{TV}}(u) + n(1 - w(x))R^{\text{TPS}}(u). \quad (5)$$

Among them,  $x$  represents the image domain,  $\eta$  is the empirical coefficient, and the function is to unify the range of the TV operator and the TPS operator.  $w(x)$  represents the weight of the spatial position of the pixel point, which is calculated by the relative distance from the pixel point to the boundary, which can mean the spatial position feature of the pixel point. First, based on the apparent advantages of the lung boundary, the level set algorithm is selected to realize the boundary detection and segmentation of the lung image, and the energy spectrum represents the relative distance from the pixel point to the boundary. Then, the method proposed by Sharma et al. in literature [17] is selected to calculate the spatial position weight  $w(x)$  of the pixel point based on the energy spectrum result. Its specific expression is as follows:

$$w(x) = 1 - \frac{1}{1 + c_1 \exp(-c_2 q(x)^2)}, \quad (6)$$

where  $c_1$  and  $c_2$  represent distance parameters and  $q(x)$  represents the level set split energy spectrum. The weight  $w(x) \in (0, 1)$ ; the closer  $w(x)$  is to 1, the closer the pixel position is to the boundary, and the TV operator in the common term has a noticeable effect; on the contrary, the closer it is to 0, the farther the pixel position is from the boundary; the TPS operator in the regular term plays a prominent role. In this paper,  $c_1$  is 200, and  $c_2$  is 0.45. Figures 1(a) and (b) are the lung boundary detection results of CT reference image and PET floating image. (c) and (d) represent the lung regions obtained after segmentation of the CT reference image and spatial location weights.

*2.2. Optimization of the Measure Function.* After the measure function is established, the next step is to select an appropriate

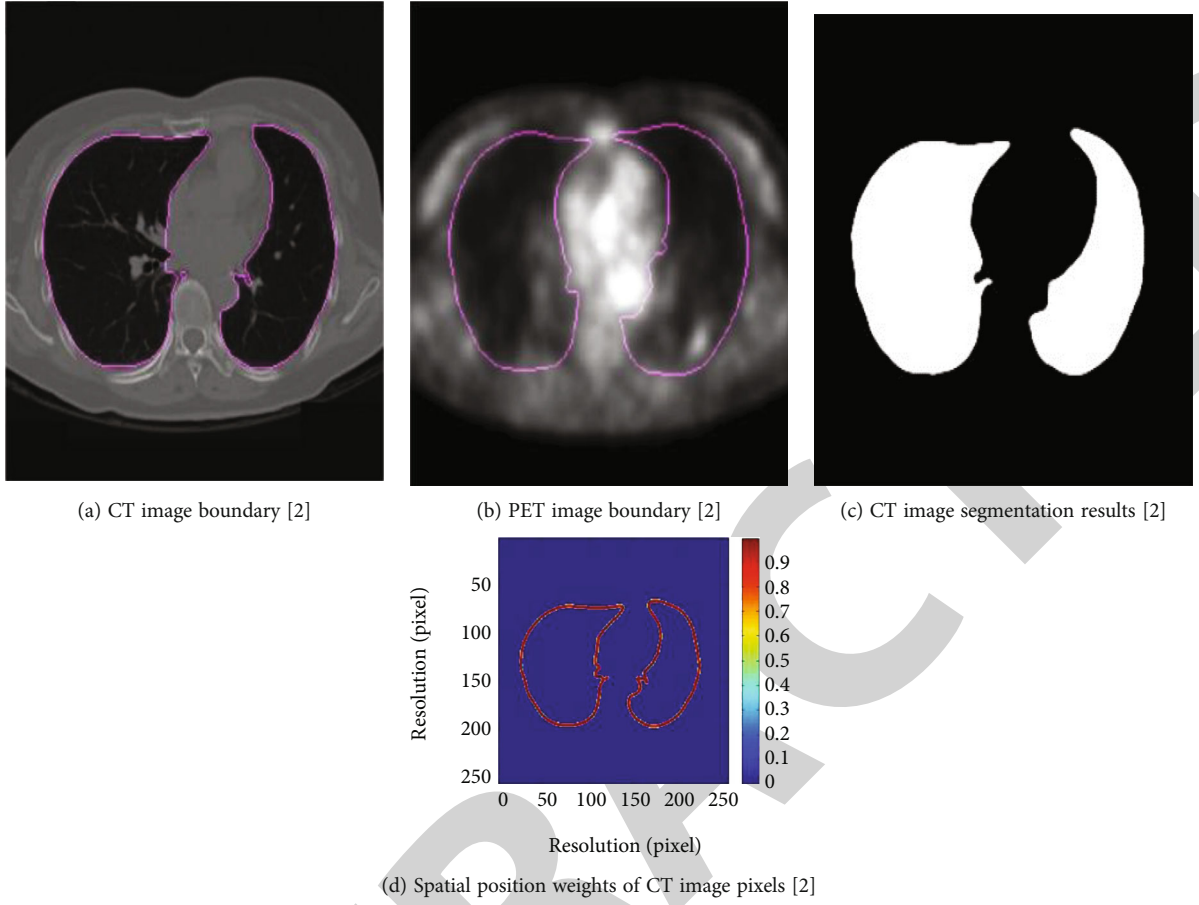


FIGURE 1: Boundary segmentation results of lung CT/PET images and spatial position weights of pixels.

optimization algorithm to optimize the measure function. The L-BFGS optimization algorithm is suitable for large-scale numerical calculation. It has the characteristics of fast convergence speed of Newton's method and does not need to store Hessian matrix like Newton's method, so it can save a lot of space and computing resources. Considering the large amount of experimental data in this paper, the L-BFGS algorithm is chosen as the optimizer. For the L-BFGS optimizer, the first derivative of the measure function for each grid control point  $\phi_{i,j,k}$  needs to be given, as follows:

$$\frac{dc}{d\phi_{i,j,k}} = \frac{d\text{CMRI}(M, F; \phi)}{d\phi_{i,j,k}} + \lambda \frac{dR^{\text{TPS-TV}}(u)}{d\phi_{i,j,k}}. \quad (7)$$

Among them, the derivative of the similarity measure function CRMI with respect to  $\phi_{i,j,k}$  has been introduced in detail in [8]. The following mainly introduces the derivation results of the regular term proposed in this paper as follows:

$$\frac{dR^{\text{TPS-TV}}(u)}{d\phi_{i,j,k}} = w(x) \frac{dR^{\text{TV}}(u)}{d\phi_{i,j,k}} + (1 - w(x)) \frac{dR^{\text{TPS}}(u)}{d\phi_{i,j,k}}. \quad (8)$$

The first derivatives of  $R^{\text{TV}}(u)$  and  $R^{\text{TPS}}(u)$  with respect to the grid control points  $\phi_{i,j,k}$  are calculated separately, and the results are as follows:

$$\left. \left\{ \begin{aligned} \frac{dR^{\text{TV}}(u)}{d\phi_{i,j,k}} &= \sum_{X \in \Omega} \frac{(du/dx) \left( (du/dx)/d\phi_{i,j,k} \right) + du/dy \left( (du/dy)/d\phi_{i,j,k} \right) + (du/dz) \left( (du/dz)/d\phi_{i,j,k} \right)}{\sqrt{(du/dx)^2 + (du/dy)^2 + (du/dz)^2}} \right\} \\ \frac{dR^{\text{TPS}}(u)}{d\phi_{i,j,k}} &= \frac{1}{N} \sum_{X \in \Omega} \left[ \begin{aligned} &2 \frac{d^2 u}{dx^2} \frac{d(d^2 u/dx^2)}{d\phi_{i,j,k}} + 2 \frac{d^2 u}{dy^2} \frac{d(d^2 u/dy^2)}{d\phi_{i,j,k}} + 2 \frac{d^2 u}{dz^2} \frac{d(d^2 u/dz^2)}{d\phi_{i,j,k}} + \\ &4 \frac{d^2 u}{dx dy} \frac{d(d^2 u/dx dy)}{d\phi_{i,j,k}} + 4 \frac{d^2 u}{dx dz} \frac{d(d^2 u/dx dz)}{d\phi_{i,j,k}} + 4 \frac{d^2 u}{dz dy} \frac{d(d^2 u/dz dy)}{d\phi_{i,j,k}} \end{aligned} \right] \end{aligned} \right\}. \quad (9)$$

Among them, the literature [10] introduces the derivation process and results of  $dR^{TV}(u)/d\phi_{i,j,k}$  in detail. For  $dR^{TPS}(u)/d\phi_{i,j,k}$ , first calculate the free deformation field  $u(x, y, z; \phi)$  of the second-order partial derivative; the result is as follows:

$$\left. \begin{aligned} \frac{d^2 u}{dx^2} &= \frac{1}{\delta^2} \sum_{l=0}^3 \sum_{m=0}^3 \sum_{n=0}^3 \frac{d^2 B_l u}{du^2} B_m(v) B_n(w) \phi_{p_x} + lp_y + mp_z + n \\ \frac{d^2 u}{dy^2} &= \frac{1}{\delta^2} \sum_{l=0}^3 \sum_{m=0}^3 \sum_{n=0}^3 B_l(u) \frac{d^2 B_m(v)}{dv^2} B_n(w) \phi_{p_x} + lp_y + mp_z + n \\ \frac{d^2 u}{dz^2} &= \frac{1}{\delta^2} \sum_{l=0}^3 \sum_{m=0}^3 \sum_{n=0}^3 B_l(u) B_m(v) \frac{d^2 B_n(w)}{dw^2} \phi_{p_x} + lp_y + mp_z + n \\ \frac{d^2 u}{dx dy} &= \frac{1}{\delta^2} \sum_{l=0}^3 \sum_{m=0}^3 \sum_{n=0}^3 \frac{dB_l(u)}{du} \frac{dB_m(v)}{dv} B_n(w) \phi_{p_x} + lp_y + mp_z + n \\ \frac{d^2 u}{dy dz} &= \frac{1}{\delta^2} \sum_{l=0}^3 \sum_{m=0}^3 \sum_{n=0}^3 B_l(u) \frac{dB_m(v)}{dv} \frac{dB_n(w)}{dw} \phi_{p_x} + lp_y + mp_z + n \\ \frac{d^2 u}{dx dz} &= \frac{1}{\delta^2} \sum_{l=0}^3 \sum_{m=0}^3 \sum_{n=0}^3 \frac{dB_l(u)}{du} B_m(v) \frac{dB_n(w)}{dw} \phi_{p_x} + lp_y + mp_z + n \end{aligned} \right\} \quad (10)$$

Among them,  $B_l, B_m, B_n$  represent B-spline basis functions;  $\{x \in \Omega \mid |x - \phi_{i,j,k}| \leq 2\delta\}$  represents the range of neighbouring pixels affected by the control point  $\phi_{i,j,k}$ , then the deformation. The first derivative of the second partial derivative of the field  $u$  concerning the control points  $\phi_{i,j,k}$  is

$$\left. \begin{aligned} \frac{d(d^2 u/dx^2)}{d\phi_{i,j,k}} &= \begin{cases} \frac{1}{\delta^2} \frac{dB_{l-p_x}(u)}{du} B_{j-p_y}(v) B_{k-p_z}(w), & |x - \phi_{i,j,k}| \leq 2\delta \\ 0, & |x - \phi_{i,j,k}| > 2\delta \end{cases} \\ \frac{d(d^2 u/dy^2)}{d\phi_{i,j,k}} &= \begin{cases} \frac{1}{\delta^2} B_{l-p_x}(u) \frac{dB_{m-p_y}(v)}{dv} B_{k-p_z}(w), & |x - \phi_{i,j,k}| \leq 2\delta \\ 0, & |x - \phi_{i,j,k}| > 2\delta \end{cases} \\ \frac{d(d^2 u/dz^2)}{d\phi_{i,j,k}} &= \begin{cases} \frac{1}{\delta^2} B_{l-p_x}(u) B_{j-p_y}(v) \frac{dB_{n-p_z}(w)}{dw}, & |x - \phi_{i,j,k}| \leq 2\delta \\ 0, & |x - \phi_{i,j,k}| > 2\delta \end{cases} \\ \frac{d(d^2 u/dx dy)}{d\phi_{i,j,k}} &= \begin{cases} \frac{1}{\delta^2} \frac{dB_{l-p_x}(u)}{du} \frac{dB_{m-p_y}(v)}{dv} B_{k-p_z}(w), & |x - \phi_{i,j,k}| \leq 2\delta \\ 0, & |x - \phi_{i,j,k}| > 2\delta \end{cases} \\ \frac{d(d^2 u/dx dz)}{d\phi_{i,j,k}} &= \begin{cases} \frac{1}{\delta^2} \frac{dB_{l-p_x}(u)}{du} B_{j-p_y}(v) \frac{dB_{n-p_z}(w)}{dw}, & |x - \phi_{i,j,k}| \leq 2\delta \\ 0, & |x - \phi_{i,j,k}| > 2\delta \end{cases} \\ \frac{d(d^2 u/dy dz)}{d\phi_{i,j,k}} &= \begin{cases} \frac{1}{\delta^2} B_{l-p_x}(u) \frac{dB_{m-p_y}(v)}{dv} \frac{dB_{n-p_z}(w)}{dw}, & |x - \phi_{i,j,k}| \leq 2\delta \\ 0, & |x - \phi_{i,j,k}| > 2\delta \end{cases} \end{aligned} \right\} \quad (11)$$

### 3. Experiments and Results

This paper selects two experimental data sets to verify the above algorithm. The first dataset is the DIR-Lab 4D-CT dataset, and ten groups of single-mode lung CT images in this dataset are selected. The second experimental dataset is from the clinical data of Huashan Hospital, and a total of 8 patients' lung CT images and lung PET images are obtained. CRMI is selected as the similarity measure function in the experiment, combined with the adaptive thin-plate spline total variation regular term and the L-BFGS optimization algorithm. In the investigation of the DIR-Lab dataset, the mesh size of the deformation model is [27]. In the clinical data experiments of CT/PET, the mesh size of the deformation model is. Therefore, the empirical coefficient  $\eta$  is selected as  $1.5 \times 10^4$ , and the common term coefficient  $\lambda$  is chosen as 0.01.

**3.1. DIR-Lab Dataset.** The ten sets of images in this dataset range in resolution from  $256 \times 256 \times 94$  to  $256 \times 256 \times 136$ , with an average voxel size of  $1 \text{ mm} \times 1 \text{ mm} \times 2.5 \text{ mm}$ . The standard smooth regular term based on the thin-plate spline and the registration method proposed for slip motion in literature [5, 6] and literature [10] is selected as the comparison algorithm. Since 300 anatomical points were marked in each group of images, the target registration error (TRE) was established. The mean value was calculated as a quantitative index to measure the registration accuracy. The smaller the TRE, the better the registration effect. The target registration error (TRE) is the distance after registration between matching points that were not included in the calculation of the registration transform. For the majority of registration jobs, the TRE is the most essential error metric to use. The usage of the word "target" gives the impression that the points are directly related to the purpose for which the registration was completed. In medical applications, these sites are often located within lesions that need to be resected during surgery or on the boundary of lesions that need to be inspected for diagnostic purposes. Additionally, they can be regions of functional activity that need to be examined [28].

The literature [10] only conducts experiments on the first five data groups in the DIR-Lab dataset, so only the mean of the first five groups is calculated in the table. This paper qualitatively analyzes the registration effect by comparing different algorithms' boundary displacement field change graphs. Table 1 shows TRE results after lung images are registered based on different constraints. Before registration, the average TRE of the 10 sets of data was 8.46 mm, and after registration, the average value decreased to 2.60 mm based on smooth regular terms. After several registration methods proposed for slip motion, the mean values were 1.95 mm, 1.87 mm, and 1.27 mm (the first five groups), and the TRE decreased further than the smooth regular term. After using the adaptive TPS-TV common term registration proposed in this paper, the average TRE is 1.47 mm, smaller than the average TRE of the above four algorithms, indicating that it is consistent with the standard smooth regular



TABLE 1: 10 groups of lung CT images after different registrations and their results after algorithm registration.

Group	Group	Group	Literature [4]	Literature [12]	Literature [6]	This article
1	3.84	1.25	1.06	1.375	1.166	0.95
2	5.12	1.18	1.07	1.298	1.177	0.94
3	7.68	1.26	1.5	1.386	1.65	1.25
4	11.52	1.98	1.9	1.98	1.88	1.35
5	8.96	1.99	1.95	1.88	1.97	1.45
Mean 1	7.424	1.532	1.496	1.5838	1.5686	1.188
6	10.7	2.45	2.205	1.9845		1.25
7	11.67	3.56	3.204	2.8836		1.4
8	15.45	5.56	5.004	4.5036		3.34
9	7.75	3.12	2.808	2.5272		1.35
10	7.86	2.27	2.043	1.8387		1.4
Mean 2	10.69	3.338	3.0528	2.74752		1.47

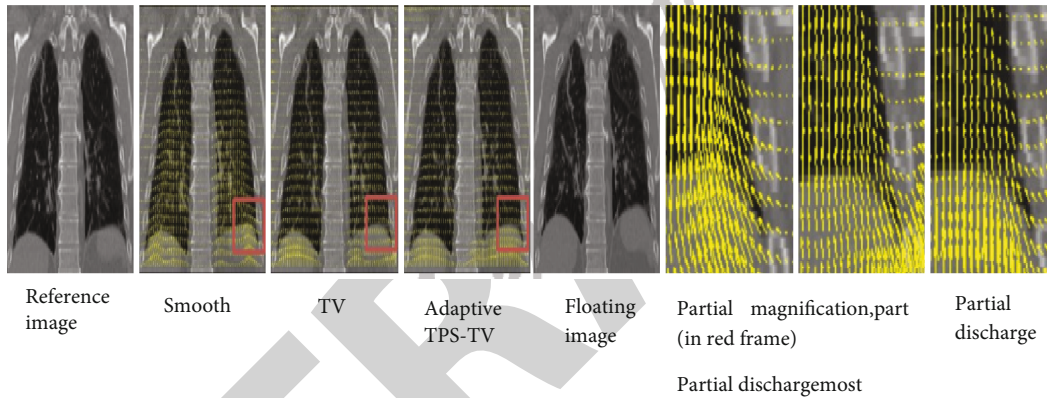


FIGURE 2: Variation diagram of displacement field after registration of floating image based on smooth TV and adaptive TPS-TV regular term.

term and the existing registration for slip motion. Compared with the method in this paper, the registration accuracy of the process in this paper is higher.

To more vividly show the constraining effect of different regular terms on the slip motion, the image displacement field change map after registration based on smoothing TV and adaptive TPS-TV regular terms is given, as shown in Figure 2 where (a) and (e) represent the reference image and the floating image, respectively. (b), (c), and (d) represent the image displacement field change map after registration based on smoothing TV and adaptive TPS-TV regular terms, respectively ((f), (g), and (h); table (b), (c), and (d) of the magnified part (in the red frame)). As shown in the figure, compared with the smooth regular term, the image production based on the registration of the adaptive TPS-TV, and the TV standard term, the generated displacement field spreads slowly at the boundary position, which better preserves the discontinuous feature of the image boundary. Since the weight of the TV operator in the adaptive TPS-TV regular term at the edge is close to 1, which is similar to the TV regular term, the difference between the two displacement fields is not evident in the figure. However, combined with quantitative index analysis, the TRE (1.19 mm) of

the method in this paper is smaller than the TRE (1.27 mm) of the TV regular term, indicating that its registration effect is better. The experimental results show that the adaptive TPS-TV regular term proposed in this paper has a better effect on nonrigid registration of single-mode CT lung images than the existing smooth regular term and TV regular term and other constraint methods for slip motion.

**3.2. CT/PET Clinical Dataset.** This dataset includes lung CT images and pulmonary PET images acquired with equipment from 8 patients. CT images are selected as reference images, and PET images are chosen as floating images. Since the resolution and signal-to-noise ratio of the two are different, they need to be preprocessed to eliminate the influence of unfavorable factors on the accuracy of the registration algorithm. First, the apparent background noise such as CT bed is removed by a threshold method. Then, adjust the resolution of the two images to keep them consistent, which is convenient for subsequent coordinate system mapping. The original key of PET images ranged from  $128 \times 128 \times 90$  to  $128 \times 128 \times 113$ , and the average voxel size was  $4.07 \text{ mm} \times 4.07 \text{ mm} \times 3 \text{ mm}$ . The original resolution of CT images ranges from  $512 \times 512 \times 54$  to  $512 \times 512 \times 62$ , and

TABLE 2: Eight groups of original lung CT/PET images, based on TV smoothing, and adaptive HD and M-HD results after TPS-TV regular term registration.

Group	Group		TV		Group		TPS-TV	
	M-HD	HD	M-HD	HD	M-HD	HD	M-HD	HD
1	4.2718	32.2558	3.9432	30.9838	3.4132	3.4132	3.4132	24.9842
2	9.3174	82.6906	5.0668	44.944	4.346	4.346	4.346	29.7224
3	10.6318	61.6814	6.784	44.5942	3.7842	3.7842	3.7842	29.839
4	8.1832	50.8164	3.9008	30.7718	3.4026	3.4026	3.4026	21.2212
5	9.8156	57.3142	5.9572	50.7104	4.7064	4.7064	4.7064	28.1324
6	6.0738	47.6046	4.4414	32.4042	3.8902	3.8902	3.8902	24.2104
7	3.6464	25.3022	3.3814	22.7476	2.7454	2.7454	2.7454	18.7302
8	5.9996	38.637	3.9962	24.9312	4.0068	4.0068	4.0068	23.9136
Mean	7.2398	49.5338	4.6852	35.2556	3.7842	29.2136	3.392	25.0902

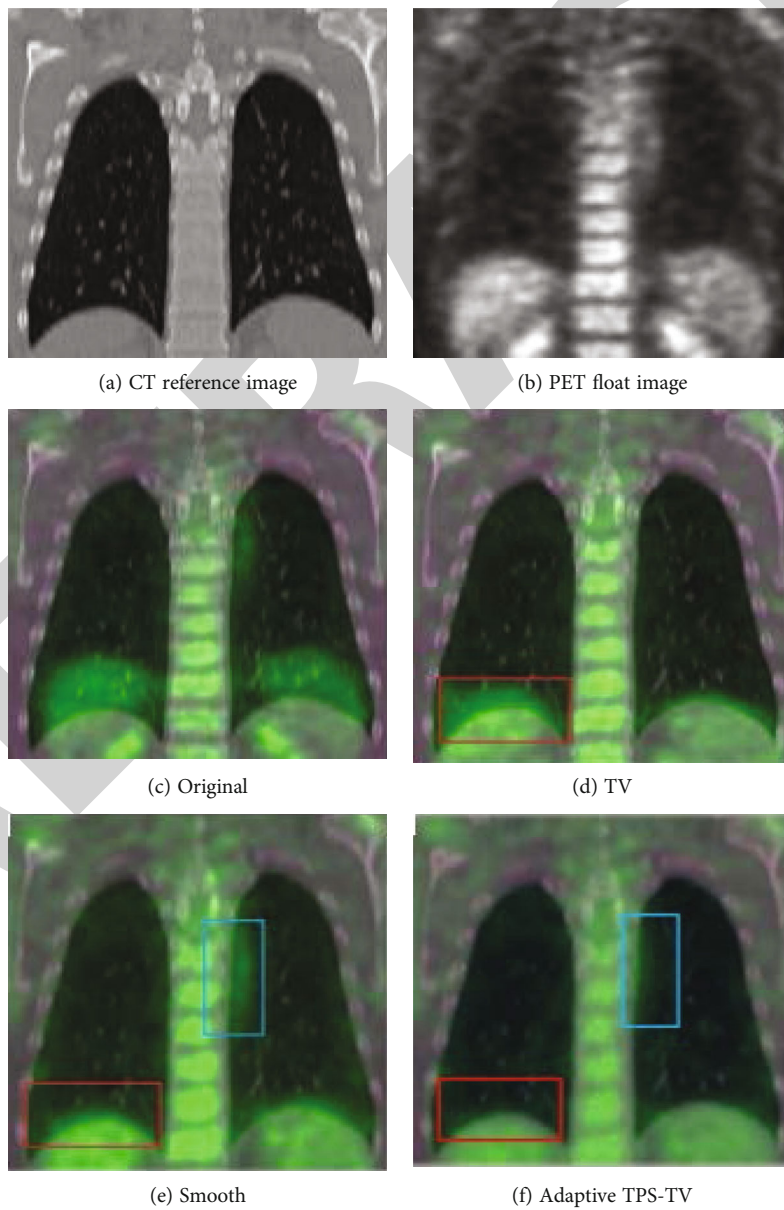


FIGURE 3: Reference image and original floating image and TV-based smooth fusion map of images after adaptive TPS-TV regular term registration.

TABLE 3: CT single-mode and CT/PET dual-mode registration based on different experiences. Experimental results of coefficients and regularization coefficients.

Regular coefficient	Single-mode TRE	Dual mode		Experience coefficient	Single-mode TRE	Dual mode	
		M-HD	HD			M-HD	HD
0.0005	1.4595	3.318	25.9245	5000	1.323	4.1265	20.4645
0.001	1.449	3.318	25.557	1000	1.3125	3.423	21.546
0.005	1.3755	3.276	23.415	12500	1.3335	3.3075	21.399
0.01	1.2915	3.003	21.021	15000	1.2915	3.003	21.021
0.03	1.491	3.2445	25.221	17500	1.344	3.2655	21.483
0.05	1.6275	3.2865	23.478	20000	1.365	3.213	21.609
0.08	1.974	4.389	35.3535	25000	1.3965	3.234	21.672
0.1	2.1105	5.0295	24.402	30000	1.428	3.276	21.819
0.5	3.0975	10.941	54.285	—	—	—	—

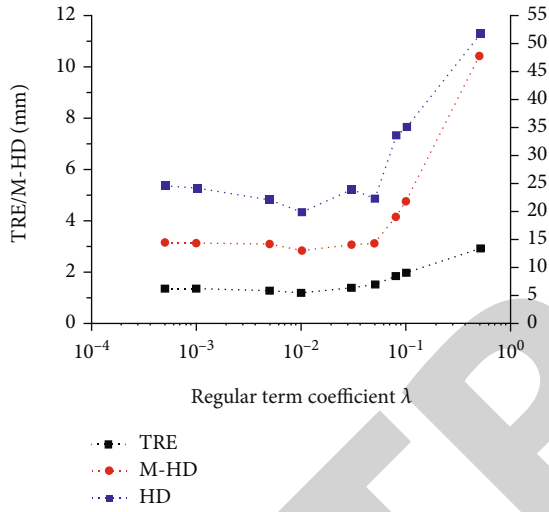


FIGURE 4: CT single-mode and CT/PET dual-mode registration results under different regularization coefficients.

the voxel size is  $0.75 \text{ mm} \times 0.75 \text{ mm} \times 5 \text{ mm}$ . Considering factors such as registration accuracy and registration time, the resolution range of CT and PET images was finally adjusted to  $256 \times 256 \times 90 \sim 256 \times 256 \times 113$ , with an average voxel size of  $1.5 \text{ mm} \times 1.5 \text{ mm} \times 3 \text{ mm}$ . Since this dataset does not label anatomical points, it is inconvenient to calculate TRE. However, the boundary pixel coordinates are obtained during boundary detection. Therefore, we choose to calculate the Hausdorff Distance (HD) and M-Hausdorff Distance (M-HD) of the boundary pixel set of the reference image and the floating image before and after registration [29] as a quantitative indicator. Due to the characteristics of PET images, a more appropriate pseudocolour fusion is selected, and the graph is used as a qualitative indicator to analyze the registration effect.

HD and M-HD are objective and accurate quantitative evaluation indexes. By calculating the spatial position deviation of the pixel points on the boundary of the two images, the quality of the registration results is expressed. The distance of a pair of pixels, M-HD, represents the average of the lengths of all pairs of pixels. Therefore, the smaller the HD and M-HD, the higher the registration accuracy. For

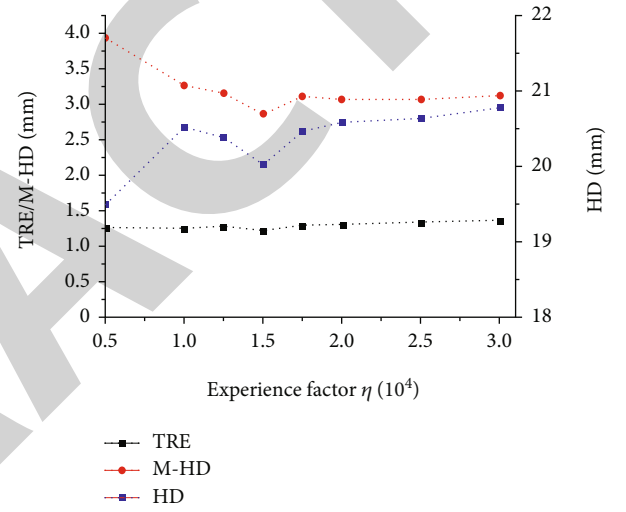


FIGURE 5: CT single-mode and CT/PET dual-mode registration results under different empirical coefficients.

the calculation of the 3D image HD, the set of boundary coordinates of the reference image and the floating image is known:

$$M = (m_1^x, m_1^y, m_1^z), (m_2^x, m_2^y, m_2^z), \dots, (m_I^x, m_I^y, m_I^z), \text{ and} \\ F = \{(f_1^x, f_1^y, f_1^z), (f_2^x, f_2^y, f_2^z), \dots, (f_J^x, f_J^y, f_J^z)\} \quad (12)$$

Among them,  $I$  and  $J$  represent the set size. The HD calculation based on Euclidean distance is as follows:

$$\text{HD}(M, F) = \max_{(m^x, m^y, m^z) \in M} D_F(m^x, m^y, m^z) \\ = \max_{(m^x, m^y, m^z) \in M} \left\{ \min_{(f^x, f^y, f^z) \in F} \|(m^x, m^y, m^z) - (f^x, f^y, f^z)\| \right\}. \quad (13)$$

Among them,  $D_F$  represents the minimum distance from the point  $(m^x, m^y, m^z)$  to the point set  $F$  and  $\|\cdot\|$

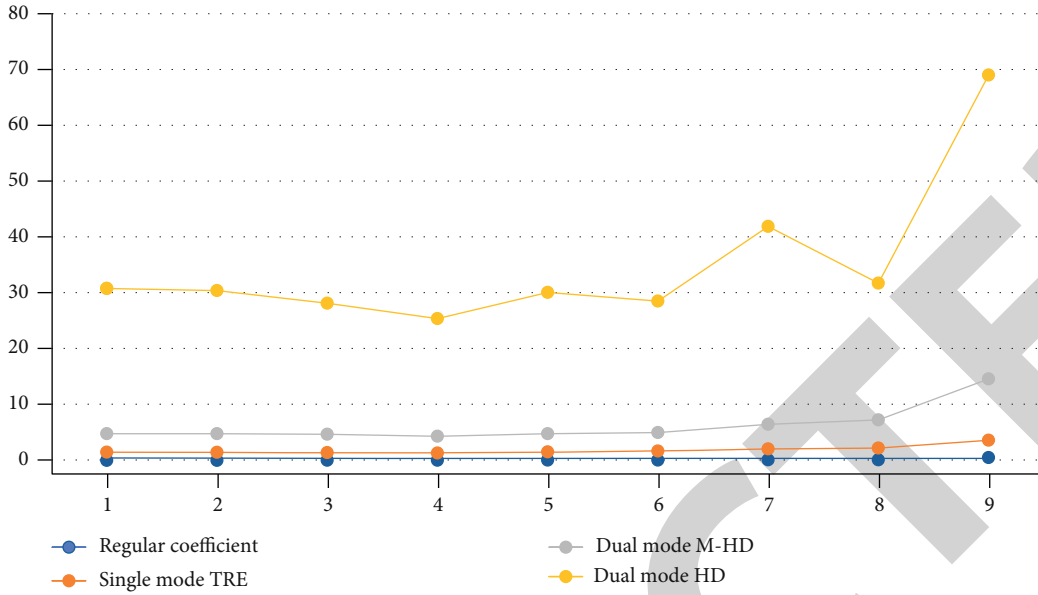


FIGURE 6: CT single-mode and CT/PET dual-mode registration.

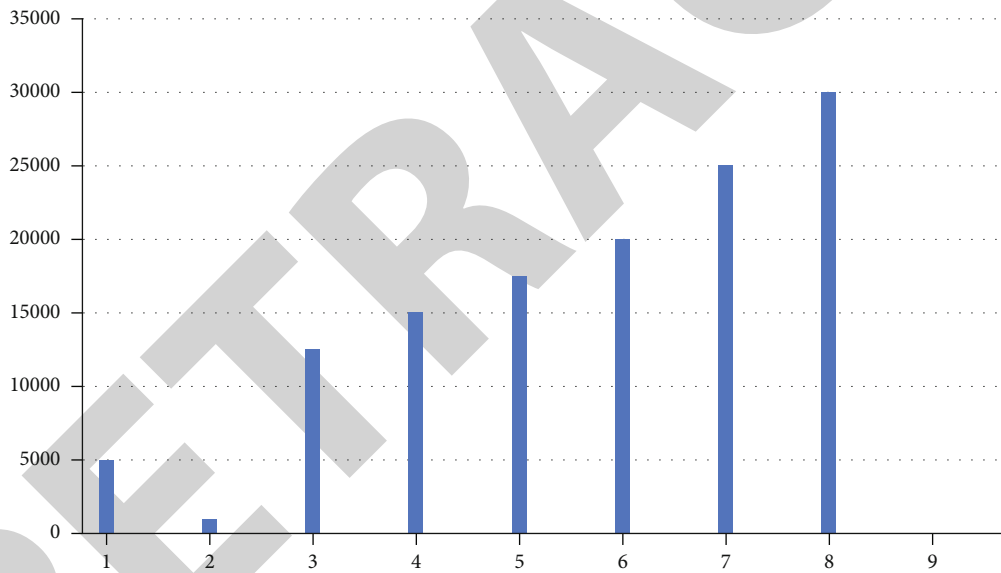


FIGURE 7: Experimental results of coefficients and regularization coefficients.

represents the two norms. Since HD is more sensitive to abnormal extreme values, a calculation method of M-HD based on statistical ideas is proposed in [30], which is expressed explicitly as follows:

$$\left. \begin{aligned}
 M - HD(M, F) &= \frac{1}{I} \sum_{(m^x, m^y, m^z) \in M} \rho(D_F(m^x, m^y, m^z)) \\
 \rho(x) &= \begin{cases} |x|, & |x| \leq OSP \\ |OSP|, & |x| > OSP \end{cases}
 \end{aligned} \right\} \quad (14)$$

OSP is a threshold parameter set to eliminate abnormal extreme values, and OSP is set to infinity in this paper.

Table 2 shows the computed results of HD and M-HD of CT images and PET images of 8 groups of lungs after registration based on different regularization terms. The table shows that the M-HD mean before registration was 6.83 mm and the HD mean 46.73 mm. After registration based on the smooth regular tour, M-HD is 3.57 mm, and HD is 27.56 mm. After registration based on TV standard terms, MHD is 4.42 mm, and HD is 33.26 mm. After registration based on the adaptive TPS-TV regular term, the M-HD is 3.20 mm, and the HD is 23.67 mm. Compared with the single-mode registration, the registration error of the TV standard term in the dual-mode registration is higher than that of the smooth standard term, and the registration accuracy decreases. However, the error of the adaptive TPS-TV standard term is lower than that of the smooth

standard term, and the registration accuracy remains the highest. The above results show that the smooth regularization term plays a more significant role in the CT/PET dual-mode registration of lung images than the TV regularization term. The adaptive TPS-TV regularization term combines the two constraints. Its registration accuracy is significantly higher than that of the TV regularization term.

Figure 3 shows the pseudocolour fusion map of the floating image and the reference image after registration based on different regularization items, which intuitively indicates the registration effect of the three regularization items on CT/PET dual-mode images. Among them, (a) represents the CT reference image, (b) represents the PET floating image, (c) represents the fusion map of the reference image and the original floating image, and (d), (e); and (f) represent the TV, smoothed, and self-fusion of the reference image and the floating image after the registration of the TPS-TV common term; blue and red mark its apparent differences. As shown in the figure, the part registered in the CT/PET image is mainly concentrated in the lower part of the lung and the boundary. After the TV regular item registration, the lower part of the lung is not accurately registered (marked in red). After the smooth regular term registration, its effect is slightly better than the TV standard term. However, the inner boundary is still not fully aligned, and some position errors are apparent (red and blue marks). After the adaptive TPS-TV standard term registration, the registration effect of its inner boundary is significantly improved. The above experimental results show that for the registration of dual-mode CT/PET images, the adaptive TPS-TV regular term can adapt the image features after spatially weighting the TV operator and the TPS operator, ensuring the registration of image boundaries and interiors. The results of quantitative indicators HD and M-HD also show that the algorithm in this paper has higher registration precision.

**3.3. Parameter Selection.** Regarding selecting the empirical coefficient  $\eta$  and the common term coefficient  $\lambda$ , the primary function of the empirical coefficient  $\eta$  is to unify the range of the TPS operator and the TV operator in the adaptive TPS-TV regular term. The standard term coefficient  $\lambda$ 's primary role is the weight of the standard adjustment term in the measure function. Table 3 shows the CT single-mode registration and the variation of the error measuring the registration accuracy in the CT/PET dual-mode registration experiment, using TRE for single mode and M-HD and HD for dual mode. Figure 4 shows the influence of different standard term coefficients  $\lambda$  on the registration results, and Figure 5 shows the impact of different empirical coefficients  $\eta$  on the registration results. The left vertical axis represents the TRE and M-HD ranges, and the right vertical axis represents the HD range.

It can be seen from Table 3 and results in the figure that for the regular term coefficient  $\lambda$ , TRE, M-HD, and HD decrease with the increase of the coefficient, and the registration accuracy increases, when  $\lambda$  reaches 0.01, when the coefficient increases, the error increases instead, and the accuracy declines. Therefore, in this paper, the coefficient  $\lambda$  of the regular term is chosen to be 0.01. For the Department of Experi-

ence, for the number  $\eta$  in CT single-mode registration, the registration accuracy as a function of empirical coefficients is not very obvious, but choosing  $1.5 \times 10^{-4}$  in  $\eta$  can be compared.

In CT/PET bimodal registration,  $\eta$  was chosen to be  $0.5 \times 10^{-4}$  for HD and M-HD, respectively, and  $1.5 \times 10^{-4}$  reached the minimum, but the change of HD under the two coefficients increased from 19.49 mm to 20.02 mm, and the change range is small. The M-HD is reduced from 3.93 mm to 2.86 mm, and the optimization range is more significant. To sum up, the empirical coefficient  $\eta$  of this paper is selected  $1.5 \times 10^{-4}$ . Figure 6 shows the CT single-mode and CT/PET dual-mode registration. The experimental results of coefficients and regularization coefficient are shown in Figure 7.

## 4. Conclusion

In this paper, for lung CT single-mode image registration and CT/PET dual-mode image registration with slip motion, the spatial position weights are calculated by the spatial position features of the pixels. Then, the thin-plate spline energy operator, the TV operator, is spatially processed—weighted establishment of a nonrigid registration algorithm based on an adaptive thin-plate spline total variation regular term. The experimental results on the DIR-lab public dataset and CT/PET clinical dataset show that the adaptive thin-plate spline whole variation regularization term combines the TV operator and the thin-plate spline energy operator based on the spatial position weights of the pixels, which can adapt to the local features of the image. During registration, it can retain the discontinuity of the image boundary displacement field and improve the boundary registration effect and ensure the smoothness of the internal displacement field of the image with higher registration accuracy.

In CT single-mode registration, the registration accuracy of the global TV regular term is significantly higher than that of the smooth ordinary time. In contrast, for CT/PET dual-mode registration, the registration accuracy of the worldwide TV standard term is lower than that of the smooth common term. This shows that the global TV common term is more suitable for CT single-mode registration. In contrast, the smooth regular time is more effective for CT/PET dual-mode registration, and their adaptability to single-mode and dual-mode registration is unstable. However, the adaptive TPS-TV common term proposed in this paper has a good registration effect in CT single-mode registration and CT/PET dual-mode registration experiments. Both have obtained the highest registration accuracy. The above results show that the algorithm in this paper applies to both CT single-mode registration and CT/PET dual-mode registration. Furthermore, the algorithm has more robust adaptability than the global TV regularization term and a smooth regularization term, and the registration accuracy can always keep the highest. This shows that the algorithm in this paper has strong stability.

## Data Availability

The data shall be made available on request.

## Conflicts of Interest

The authors declare that they have no conflict of interest.

## References

- [1] D. Rueckert, L. I. Sonoda, C. Hayes, D. L. G. Hill, M. O. Leach, and D. J. Hawkes, "Nonrigid registration using free-form deformations: application to breast MR images," *IEEE Transactions on Medical Imaging*, vol. 18, no. 8, pp. 712–721, 1999.
- [2] J. A. Schnabel, C. Tanner, A. D. Castellano-Smith et al., "Validation of nonrigid image registration using finite-element methods: application to breast MR images," *IEEE Transactions on Medical Imaging*, vol. 22, no. 2, pp. 238–247, 2003.
- [3] X. Wu, S. Xiao, and Y. Zhang, "Registration based super-resolution reconstruction for lung 4D-CT," in *2014 36th Annual International Conference of the IEEE Engineering in Medicine and Biology Society*, pp. 2444–2447, Chicago, IL, USA, 2014.
- [4] V. Gorbunova, S. Durrleman, P. Lo, X. Pennec, and M. de Bruijne, "Lung CT registration combining intensity, curves and surfaces," *IEEE International Symposium on Biomedical Imaging: From Nano to Macro*, vol. 2010, pp. 340–343, 2010.
- [5] D. Bystrov, T. Vik, H. Schulz, T. Klinder, and S. Schmidt, "Local motion analysis in 4D lung CT using fast groupwise registration," in *2009 16th IEEE International Conference on Image Processing (ICIP)*, pp. 1749–1752, Cairo, Egypt, 2009.
- [6] S. C. C. Coutre, M. W. Evens, S. G. Armato, and R. Orlandic, "Automatic radionuclide lung scan registration: a comparison of four methods," in *1999 IEEE Nuclear Science Symposium. Conference Record. 1999 Nuclear Science Symposium and Medical Imaging Conference (Cat. No.99CH37019)*, pp. 1033–1037, Seattle, WA, USA, 1999.
- [7] H. Haneishi, H. Ue, N. Takita et al., "Lung image segmentation and registration for quantitative image analysis," in *2001 IEEE Nuclear Science Symposium Conference Record (Cat. No.01CH37310)*, pp. 1390–1393, San Diego, CA, USA, 2001.
- [8] D. E. Hurtado, N. Villarroel, J. Retamal, G. Bugeado, and A. Bruhn, "Improving the accuracy of registration-based biomechanical analysis: a finite element approach to lung regional strain quantification," *IEEE Transactions on Medical Imaging*, vol. 35, no. 2, pp. 580–588, 2016.
- [9] K. Chaisaowong and M. Jiang, "An automated 3D-atlas-based registration towards the anatomical segmentation of pulmonary pleural surface," in *2018 International ECTI Northern Section Conference on Electrical, Electronics, Computer and Telecommunications Engineering (ECTI-NCON)*, pp. 85–88, Chiang Rai, Thailand, 2018.
- [10] A. Poreva, V. Vaityshyn, V. Timofeyev, and A. Honcharenko, "Improving of lung sounds registration device for further signal processing," in *2017 IEEE 37th International Conference on Electronics and Nanotechnology (ELNANO)*, pp. 329–332, Kyiv, Ukraine, 2017.
- [11] J. Chen, L. Chen, and M. Shabaz, "Image fusion algorithm at pixel level based on edge detection," *Journal of Healthcare Engineering*, vol. 2021, 10 pages, 2021.
- [12] C. Sharma, B. Amandeep, R. Sobti, T. K. Lohani, and M. Shabaz, "A secured frame selection based video watermarking technique to address quality loss of data: combining graph based transform, singular valued decomposition, and hyperchaotic encryption," *Security and Communication Networks*, vol. 2021, 19 pages, 2021.
- [13] Z. Yan, Y. Yu, and M. Shabaz, "Optimization research on deep learning and temporal segmentation algorithm of video shot in basketball games," *Computational Intelligence and Neuroscience*, vol. 2021, 10 pages, 2021.
- [14] J. Wang, C. Xia, A. Sharma, G. S. Gaba, and M. Shabaz, "Chest CT findings and differential diagnosis of mycoplasma pneumoniae pneumonia and mycoplasma pneumoniae combined with streptococcal pneumonia in children," *Journal of Healthcare Engineering*, vol. 2021, 10 pages, 2021.
- [15] N. Sharma and C. Chakraborty, "Evaluation of bioinspired algorithms for image optimization," *Journal of Electronic Imaging*, vol. 31, no. 4, article 41206, 2022.
- [16] T. Thakur, I. Batra, M. Luthra et al., "Gene expression-assisted cancer prediction techniques," *Journal of Healthcare Engineering*, vol. 2021, 9 pages, 2021.
- [17] N. Sharma, C. Chakraborty, and R. Kumar, "Optimized multimedia data through computationally intelligent algorithms," *Multimedia Systems*, pp. 1–17, 2022.
- [18] J. Bhola, M. Shabaz, G. Dhiman, S. Vimal, P. Subbulakshmi, and S. K. Soni, "Performance evaluation of multilayer clustering network using distributed energy efficient clustering with enhanced threshold protocol," in *In Wireless Personal Communications*, pp. 1–15, Springer Science and Business Media LLC, 2021.
- [19] N. Sharma and U. Batra, "An enhanced Huffman-PSO based image optimization algorithm for image steganography," *Genetic Programming and Evolvable Machines*, vol. 22, no. 2, pp. 189–205, 2021.
- [20] N. Sharma and U. Batra, "A review on spatial domain technique based on image steganography," in *In 2017 International Conference on Computing and Communication Technologies for Smart Nation (IC3TSN)*, pp. 24–27, Gurgaon, India, 2017.
- [21] A. Mehbodniya, I. Alam, S. Pande et al., "Financial fraud detection in healthcare using machine learning and deep learning techniques," *Security and Communication Networks*, vol. 2021, 8 pages, 2021.
- [22] H. Haneishi, N. Takita, D. Tsuchida, Y. Mori, H. Toyama, and T. Miyamoto, "Image registration between CT, SPECT and dose map images of lung and its application to image analysis in radiation therapy," in *2003 IEEE Nuclear Science Symposium. Conference Record (IEEE Cat. No.03CH37515)*, pp. 2946–2950, Portland, OR, USA, 2003.
- [23] J. Ehrhardt, R. Werner, A. Schmidt-Richberg, and H. Handels, "Statistical modeling of 4D respiratory lung motion using diffeomorphic image registration," *IEEE Transactions on Medical Imaging*, vol. 30, no. 2, pp. 251–265, 2011.
- [24] N. Cai, H. Chen, Y. Li, Y. Peng, and J. Li, "Adaptive weighting landmark-based group-wise registration on lung DCE-MRI images," *IEEE Transactions on Medical Imaging*, vol. 40, no. 2, pp. 673–687, 2021.
- [25] R. Hu, H. Wang, T. Ristaniemi, W. Zhu, and X. Sun, "Lung CT image registration through landmark-constrained learning with convolutional neural network," in *2020 42nd Annual International Conference of the IEEE Engineering in Medicine & Biology Society (EMBC)*, pp. 1368–1371, Montreal, QC, Canada, 2020.
- [26] S. Chopra, G. Dhiman, A. Sharma, M. Shabaz, P. Shukla, and M. Arora, "Taxonomy of adaptive neuro-fuzzy inference system in modern engineering sciences," *Computational Intelligence and Neuroscience*, vol. 2021, 14 pages, 2021.

## Retraction

# Retracted: Effects of Sacubitril/Valsartan on the Expression of CaMKII/Ca<sub>v</sub>1.2 in Atrial Fibrillation Stimulation Rabbit Model

### BioMed Research International

Received 8 January 2024; Accepted 8 January 2024; Published 9 January 2024

Copyright © 2024 BioMed Research International. This is an open access article distributed under the Creative Commons Attribution License, which permits unrestricted use, distribution, and reproduction in any medium, provided the original work is properly cited.

This article has been retracted by Hindawi following an investigation undertaken by the publisher [1]. This investigation has uncovered evidence of one or more of the following indicators of systematic manipulation of the publication process:

- (1) Discrepancies in scope
- (2) Discrepancies in the description of the research reported
- (3) Discrepancies between the availability of data and the research described
- (4) Inappropriate citations
- (5) Incoherent, meaningless and/or irrelevant content included in the article
- (6) Manipulated or compromised peer review

The presence of these indicators undermines our confidence in the integrity of the article's content and we cannot, therefore, vouch for its reliability. Please note that this notice is intended solely to alert readers that the content of this article is unreliable. We have not investigated whether authors were aware of or involved in the systematic manipulation of the publication process.

Wiley and Hindawi regrets that the usual quality checks did not identify these issues before publication and have since put additional measures in place to safeguard research integrity.

We wish to credit our own Research Integrity and Research Publishing teams and anonymous and named external researchers and research integrity experts for contributing to this investigation.

The corresponding author, as the representative of all authors, has been given the opportunity to register their agreement or disagreement to this retraction. We have kept a record of any response received.

### References

- [1] Q. Lou, L.-y.-f. Li, G.-z. Liu et al., "Effects of Sacubitril/Valsartan on the Expression of CaMKII/Ca<sub>v</sub>1.2 in Atrial Fibrillation Stimulation Rabbit Model," *BioMed Research International*, vol. 2022, Article ID 5832543, 8 pages, 2022.

## Research Article

# Effects of Sacubitril/Valsartan on the Expression of CaMKII/Ca<sub>v</sub>1.2 in Atrial Fibrillation Stimulation Rabbit Model

Qi Lou,<sup>1</sup> Lu-yi-fei Li,<sup>1</sup> Guang-zhong Liu,<sup>2</sup> Cheng-chuang Zhan,<sup>3</sup> Li Zhang,<sup>1</sup> Yan-xiang Zang,<sup>1</sup> and Wei-min Li<sup>1</sup> 

<sup>1</sup>Department of Cardiology, First Affiliated Hospital of Harbin Medical University, Harbin 150001, China

<sup>2</sup>Department of Cardiology, Shenzhen People's Hospital, Shenzhen 518020, China

<sup>3</sup>Department of Cardiology, First Affiliated Hospital of Soochow University, Soochow 215006, China

Correspondence should be addressed to Wei-min Li; [liweimin\\_2009@163.com](mailto:liweimin_2009@163.com)

Received 11 May 2022; Revised 22 June 2022; Accepted 18 July 2022; Published 28 July 2022

Academic Editor: Abolfazl Mehdodniya

Copyright © 2022 Qi Lou et al. This is an open access article distributed under the Creative Commons Attribution License, which permits unrestricted use, distribution, and reproduction in any medium, provided the original work is properly cited.

**Background and Objective.** Atrial fibrillation (AF) is linked to high morbidity and death rates throughout the world due to limited therapeutic options and thus presents a major challenge to the developed and developing countries. In this study, we aim to investigate the influence of sacubitril/valsartan (sac/val) treatment on the calmodulin-dependent protein kinase II (CaMKII)/Ca<sub>v</sub>1.2 expression in AF models. **Methods.** Overall, 18 rabbits were randomly divided into control, pacing (600 beats/min), and pacing+sac/val groups. The rabbits in the pacing+sac/val cohort received oral sac/val (10 mg/kg twice daily) across the 21-day investigation period. After three weeks, the atrial effective refractory period (AERP) and AF induction rate were compared. HL-1 cultures were exposed to fast pacing (24 h) with and without LBQ657 (active sacubitril form)/valsartan. Western blots were used for detecting Ca<sub>v</sub>1.2 and CaMKII expression within atrial muscles of the rabbits and HL-1 cultures of AF model. **Results.** In comparison to the sham cohort, the AF induction rate was markedly increased together with AERP reduction within pacing cohort. Such changes were markedly rescued through sac/val treatment in pacing+sac/val cohort. The proteomic expression profiles of CaMKII and Ca<sub>v</sub>1.2 showed that the CaMKII expression was markedly upregulated, while Ca<sub>v</sub>1.2 expression was downregulated in the pacing cohort. Importantly, these effects were absent in pacing+sac/val cohort. **Conclusion.** Results of this study show that sac/val treatment regulates the expression of CaMKII/Ca<sub>v</sub>1.2 and could alter this pathway in atrial rapid electrical stimulation models. Therefore, this investigation could contribute to a novel strategy in AF therapeutics in clinical settings.

## 1. Introduction

Atrial fibrillation (AF) is the most common long-lasting heart rhythm abnormality in people who have heart failure (HF) which is linked to high morbidity and death rates, thus being a major challenge for modern-day societies/economies [1, 2]. Heart failure often coexists with AF because they share some common pathophysiologic mechanisms and risk factors. Atrial electrical remodeling and structural remodeling, together with autonomic remodeling, are responsible for AF pathogenesis/prolonged establishment [3, 4]. Electrical remodeling is usually an early manifestation of atrial remodeling [5]. Electrical remodeling for the atrium is mainly related to changes in ion channels within atrial myo-

cytes, particularly the calcium channels. L-Type calcium channels (LTCCs) represent the most important pathway for extracellular calcium influx when cardiomyocytes are excited [6]. LTCCs have four subtypes including Ca<sub>v</sub>1.1, Ca<sub>v</sub>1.2, Ca<sub>v</sub>1.3, and Ca<sub>v</sub>1.4 where Ca<sub>v</sub>1.2 is present in the myocardium [7]. Ca<sub>v</sub>1.2 is the upstream protein that regulates L-type calcium current (ICaL). Ca<sub>v</sub>1.2 protein expression reduction results in a decrease in ICaL, which shortens action-potential duration (APD), eventually promoting the occurrence of arrhythmias such as AF [8].

Electrical remodeling caused by abnormal calcium regulation in atrial myocytes has a pivotal role in AF pathogenesis/establishment. CaMKII works as a serine/threonine kinase that can phosphorylate Ca<sub>v</sub>1.2 and induce abnormal



calcium regulation in myocardial cells, exacerbating AF pathogenesis [9]. Epidemiology-based investigations demonstrated that the prevalence of AF is increasing each year and causing reduced quality of life because of insufficient treatment options [10]. Therefore, strategies for effective regulation of CaMKII/Ca<sub>v</sub>1.2 signaling pathway are needed to prevent and correct the electrical remodeling in AF.

Some studies have confirmed that the natriuretic peptide (NP) family can improve electrical remodeling [11], but the specific mechanism is unclear. Experimental studies have shown that valsartan can improve atrial electrical remodeling in AF [12]. Sacubitril/valsartan (sac/val) is a combination of an angiotensin receptor–neprilysin inhibitor (ARNi) drugs, given orally for treating HF. This combination is composed of an enkephalinase (sacubitril) and angiotensin-receptor antagonist (valsartan) linked by hydrogen bonds at a molar ratio of 1 : 1. The drug has dual regulatory effects; i.e., it can inhibit the renin-angiotensin-aldosterone system (RAAS) via antagonism of angiotensin II receptor 1 (AT<sub>1</sub>R). On the other hand, it can simultaneously inhibit the degradation of NPs, such as A-type NPs (ANPs), B-type NPs (BNPs), and C-type NPs (CNPs) through enkephalinase leading to increased levels of cyclic guanosine monophosphate and reduced cardiac remodeling in patients with heart failure (HF) [13–17]. Clinical studies have shown that the sac/val treatment is more effective than enalapril for lowering all-cause/sudden cardiac-mortality rates in aggravated HF clinical cases having lowered ejection-fraction/s [18–20]. The sac/val combination is gaining wider research interests these days for various cardiac-related pathway regulation. In a recent study, it was shown to decrease AF susceptibility by inhibiting angiotensin II-induced AF through p-Smad2/3, p-JNK, and p-p38 signaling pathways [21]. In this study, we aim to validate sac/val influence on CaMKII/Ca<sub>v</sub>1.2 expression in rabbit model and HL-1 AF cultures.

## 2. Methods

**2.1. Animal Model of Fast Atrial Pacing.** This research was performed according to the directives of the Care and Use of Laboratory Animals (US National Institutes of Health; no. 85-23). The study protocol was approved by the Ethics Committee of Harbin Medical University. Healthy-adult, male New Zealand white rabbits (approximately 3 kg, four months old) were procured from the Experimental Animal Center affiliated with the First Affiliated Hospital of Harbin Medical University. All the animals were housed in a specialized, nonpathogenic laboratory animal center, in individual cages, and received *ad libitum* filtered water and diet. Rabbit-based models for rapid pacing were developed following previous research protocol [22, 23]. A surface electrocardiogram (ECG) was performed on the individual animal, whereby those animals that demonstrated baseline/normal sinus rhythm at investigation commencement were consequently anesthetized using xylazine (5 mg/kg, Sigma-Aldrich™, USA) and ketamine (35 mg/kg, Sigma-Aldrich™, USA). A pacemaker (Harbin Polytechnic University, Harbin, China) was placed within a subcutaneous (SC) pocket on the animal's dorsal region. A pacemaker electrode was stitched

onto the right atrium of the animal heart. Animals were confined for seven days postpacemaker implantation surgery for recovery, followed by randomization into three cohorts ( $n = 6/\text{cohort}$ ) including (1) control cohort (the rabbits underwent a sham operation, i.e., sutured electrode only) with no pacing, (2) pacing cohort (the rabbits received an electrode and underwent fast atrial pacing, i.e., 600 bpm/21 days), and (3) the pacing+sac/val cohort (the rabbits underwent fast atrial pacing, i.e., 600 bpm/21 days while receiving sacubitril/valsartan (Novartis Pharma Schweiz AG™, Switzerland) oral treatment of 10 mg/kg, twice daily for 21 days) [15].

**2.2. HL-1 Culture Model of High-Frequency Electrical Stimulation.** HL-1 cultures stemming from the murine atrial tumor (AT-1) cells are considered immortalized cultures. Differentiated HL-1 culture lines show cardiac morphological, biochemical, and electrophysiological functions similar to atrial cardiomyocytes [24, 25]. HL-1 cells were cultured in DMEM/low glucose (JRH Biosciences™, USA) augmented with 9% fetal calf serum and 0.9% penicillin-streptomycin solution (Gibco-BRL, Rockville, MD, USA). Six-well plates were used to culture HL-1 cultures ( $\geq 1,000,000$  myocytes), and YC-2 program-controlled stimulator (Chengdu™, China) was used for 24 hours [23] with a 1.5 V/cm pulse voltage, a 5-millisecond square wave width and duration, and a frequency of stimulation of 10 Hz. The necessary capture-effectiveness approximated 90% of all HL-1 cultures across a stimulatory timespan. HL-1 cultures were split into three cohorts: (1) control cohort (receiving no stimulatory/pharmacological treatments, with 24 h culturing time), (2) the pacing cohort (received high-frequency field-stimulation (24 h) as described previously), and (3) the pacing + sac/val cohort (treated with high-frequency field-stimulation (24 h) + LBQ657 and valsartan (both at 10  $\mu\text{mol/L}$ ; MedChem Express™, USA)) [26, 27].

**2.3. AERP/AF Induction Rate Determinations.** The rabbits' atrial electrophysiological analyses were conducted according to previously published literature [22, 23]. Within such rabbits, the AERPs were registered using baseline cycle lengths (150 milliseconds), whereby eight essential stimuli (S1) and a subsequent premature stimulus (S2) were applied. The S1–S2 interval was extended (5 ms) and consequently lowered (2 ms-steps) until S2 failed in catching depolarization and consequently deemed as AERP (determined across three technical replicates for a mean AERP assertion). Consequently, AF induction involved the application of 10s pacing (10 Hz, 2 ms) onto the atrium using a fourfold present threshold current [28], with individual animals treated 10 times. The AF induction rate was determined by dividing AF times by induction times in each cohort [29].

**2.4. Western Blot Assay.** Proteomic specimens from the left atrial tissues were collected through animal atria/HL-1 cultures. Proteomic content was transferred to polyvinylidene fluoride membranes and analyzed through a proteomic assay kit (Bio-Rad™, Canada) via Western blotting following previously published literature [30]. The antibodies included

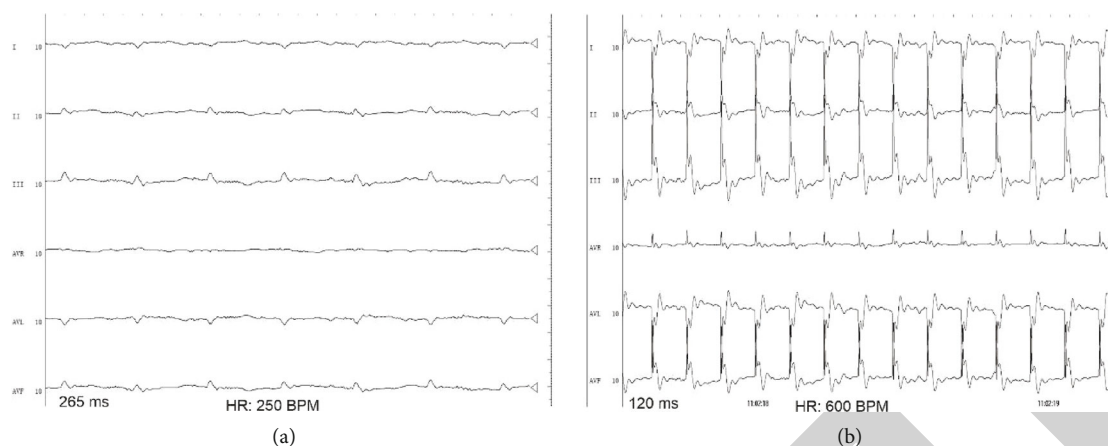


FIGURE 1: Comparison of the pacing of rabbits through electrocardiogram (ECG): (a) rabbits within the normal cohort and (b) rabbits within the pacing cohort.

CaMKII antibody (1:2000; Wanleibio, Shenyang, China),  $Ca_v1.2$  antibody (1:1000; Abcam™, China), and GAPDH antibody (1:10000; ZSGB-BIO™, China). Other antibodies were horseradish peroxidase-conjugated goat anti-rabbit (1:5000; ZSGB-BIO, China) and goat anti-mouse immunoglobulin G (1:3000; ZSGB-BIO™, China). The Western blot result bands were subjected to GAPDH-internal control normalization for comparison.

**2.5. Statistical Analysis.** SPSS® v.22.0 was used for all statistical analysis in this research.  $P < 0.05$  was considered a statistically significant difference between results. All quantitative data were presented as mean  $\pm$  standard error for mean, except for AF induction rate, which was presented as a percentage. The SNK-Q test based on one-way analysis of variance (ANOVA) was employed for the comparison of mean values.

### 3. Results

**3.1. Pacing Model Establishment in Rabbits with AF.** In this study, the pacing mode was AOO (atrium is paced at a set rate regardless of atrial activity) with 600 beats/min. The rabbits had a normal rhythm and pacing rhythm. The normal rhythm was regular, and the frequency was approximately  $250 \pm 15$  beats/min (Figure 1(a)). The pacing rhythm was irregular and fast, approximately  $600 \pm 23$  beats/min (Figure 1(b)).

Sac/val treatment effect upon AERP in rabbits was studied. The AERP<sub>150</sub> ms values of rabbits in the control cohort, pacing cohort, and sac/val+pacing cohort were identified. AERP<sub>150</sub> for the control cohort was 116 ms (Figure 2(a)). The AERP<sub>150</sub> for the pacing cohort was 64 ms (Figure 2(b)). The AERP<sub>150</sub> for pacing+sac/val cohort was 99 ms (Figure 2(c)). The AERP<sub>150</sub> values of the control cohort, pacing cohort, and pacing+sac/val cohort were statistically analyzed and compared. In comparison with the control cohort, AERP<sub>150</sub> was markedly decreased within the pacing cohort ( $P < 0.05$ ). In comparison with the pacing cohort, AERP<sub>150</sub> was markedly increased within the pacing

+sac/val cohort ( $P < 0.05$ ). AERP<sub>150</sub> was markedly reduced in the pacing cohort followed by the control cohort. Sac/val treatment rescued such reductions in AERP<sub>150</sub> (Figure 2(d)).

Sac/val therapeutic function upon inducibility rate for AF was studied. AF occurrences in rabbits of the control cohort, pacing cohort, and pacing+sac/val cohort were detected. According to our results, AF was not induced within the control cohort (Figure 3(a)) and induced within the pacing cohort (Figure 3(b)). Inducibility rates of AF within the control cohort, pacing cohort, and pacing+sac/val cohort were statistically analyzed and compared. In comparison to the control cohort, the AF inducibility rate was markedly increased in the pacing cohort ( $P < 0.05$ ). In comparison to the pacing cohort, the AF inducibility rate was markedly decreased in the pacing+sac/val cohort ( $P < 0.05$ ). The rabbits in the pacing cohort showed a stronger indication of AF than animals in the control cohort. However, in comparison with the pacing cohort, AF incidence was lowered within the sac/val-treated cohort (Figure 3(c)).

**3.2. Regulation for CaMKII/ $Ca_v1.2$  Signaling Pathway In Vivo and in a Rapid Electrical Stimulation Model In Vitro.** Sac/val regulated the CaMKII- $Ca_v1.2$  signaling pathway in rabbits' AF model. The CaMKII and  $Ca_v1.2$  protein levels in the control cohort, pacing cohort, and pacing+sac/val cohort were analyzed and compared. Our results showed that the  $Ca_v1.2$  protein level was markedly reduced whereas that of the CaMKII was strongly increased in the pacing cohort when compared with the control cohort ( $P < 0.05$ ). The proteomic levels of  $Ca_v1.2$  were markedly upregulated whereas the levels of CaMKII were downregulated in the pacing+sac/val cohort when compared with the pacing cohort ( $P < 0.05$ ), and sac/val reversed the changes of both proteins (Figures 4(a)–4(d)). Similarly, in the high-frequency electrical stimulation (pacing) model of HL-1 cultures, the  $Ca_v1.2$  expression was severely downregulated, whereas CaMKII levels were markedly upregulated in the pacing cohort in comparison with the control cohort ( $P < 0.05$ ). The proteomic expression of  $Ca_v1.2$  was markedly upregulated, while CaMKII was severely downregulated

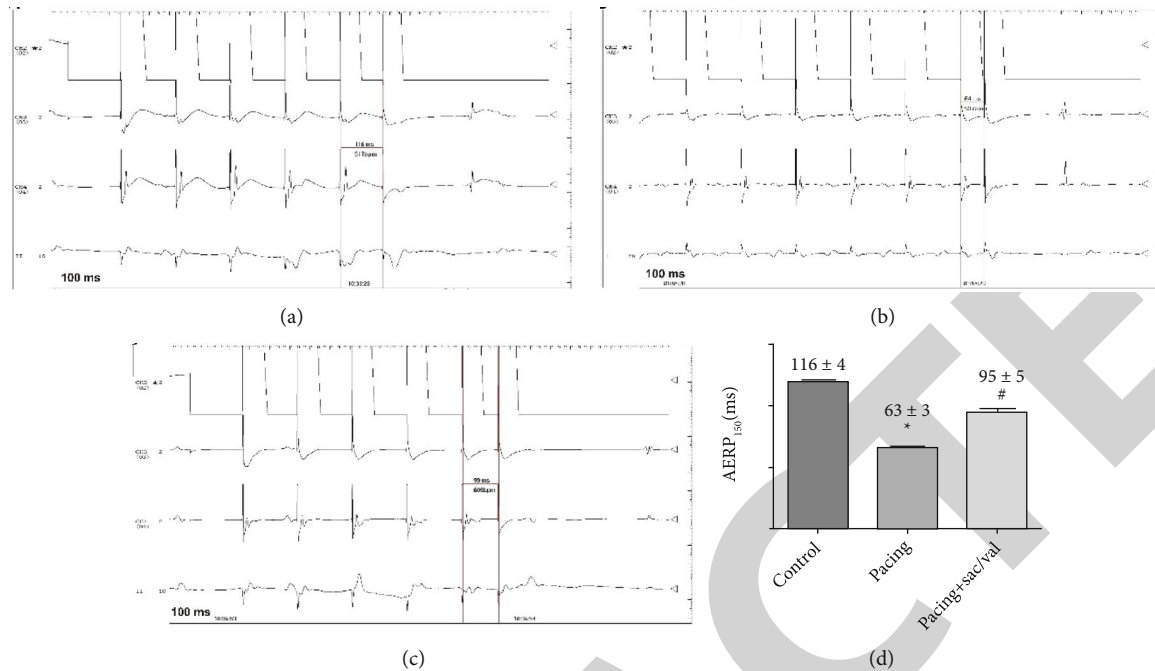


FIGURE 2: Representation of AERP<sub>150</sub> ms values for rabbits in (a) the control cohort (116 ms), (b) the pacing cohort (64 ms), (c) the pacing +sac/val cohort (99 ms), and (d) shows statistical analysis results for AERP<sub>150</sub> values of control cohort, pacing cohort, and pacing+sac/val cohort. \* $P < 0.05$  for comparison of pacing cohort with a control cohort. # $P < 0.05$  for comparison of pacing+sac/val cohort with pacing cohort.

in the pacing+sac/val cohort in comparison with the pacing cohort ( $P < 0.05$ ), and the changes were inhibited through LBQ657 and valsartan (Figures 4(e)–4(h)). Sac/val regulated the CaMKII/Ca<sub>v</sub>1.2 expression in HL-1 culture and rabbit models of rapid electrical stimulation.

#### 4. Discussion

This investigation demonstrated that sac/val regulated the CaMKII/Ca<sub>v</sub>1.2 signaling pathway in atrial rapid electrical stimulation models. Previous studies have shown that rapid atrial pacing can activate CaMKII, which modulates L-type calcium channel opening by enhanced phosphorylation of the Ca<sub>v</sub>1.2 channel and promotes AF atrial electrical remodeling [9], typically exhibiting atrial electrical remodeling through AERP reduction, as well as downregulation of Ca<sub>v</sub>1.2 protein expression, whereby lowering I<sub>CaL</sub> shortens the APD and finally promotes the occurrence of AF [8, 31, 32]. Previous studies have confirmed that the natriuretic peptide (NP) family can improve electrical remodeling in AF [11]. Sac/val attenuated AF electrical remodeling through lowering AF inducibility and circumventing diminished AERP, probably via the CaMKII/Ca<sub>v</sub>1.2 pathway. Such dataset outcomes corroborate with past results, discovering that sac/val alleviated these changes in AF models via the CaMKII/Ca<sub>v</sub>1.2 pathway.

**4.1. CaMKII/Ca<sub>v</sub>1.2 Signaling Pathway in AF.** A study of dementia showed that CaMKII and Ca<sub>v</sub>1.2 protein expression within CaMKII/Ca<sub>v</sub>1.2 signaling pathway exhibits an opposite trend in a mouse model [33]. However, there is

no evidence that the CaMKII/Ca<sub>v</sub>1.2 signaling pathway exists within the myocardium. A previous study showed proteomic levels for CaMKII and Ca<sub>v</sub>1.2 in the AF model with opposing trends [32] which was consistent with the trend of CaMKII and Ca<sub>v</sub>1.2 protein expression within the above research on dementia. Therefore, we speculate that the CaMKII/Ca<sub>v</sub>1.2 signaling pathway exists within the atrial myocardium.

**4.2. Role of the CaMKII/Ca<sub>v</sub>1.2 Pathway in Electrical Remodeling of AF.** Ca<sub>v</sub>1.2 is a subtype of LTCCs within the myocardium that has a pivotal role in action potential formation, triggering excitation/contraction in cardiomyocytes [34]. CaMKII is a serine/threonine kinase having a key role in multiple cardiac remodeling functions, such as ion-channel gene expression modulation [35, 36]. CaMKII, as an upstream protein regulating LTCCs, can phosphorylate Ca<sub>v</sub>1.2 and decrease its expression [9]. These changes lead to electrical reconfiguration, including the shortening of AERP, ultimately promoting the occurrence and maintenance of AF [37]. Therefore, we evaluated the AERP and CaMKII and Ca<sub>v</sub>1.2 protein levels. We found that the AF induction rate was markedly increased, the AERP was markedly reduced after 3 weeks' rapid pacing, CaMKII expression was increased, and Ca<sub>v</sub>1.2 expression was decreased. CaMKII expression was markedly upregulated while Ca<sub>v</sub>1.2 was markedly downregulated within HL-1 cultures.

**4.3. Sac/Val Regulated the CaMKII/Ca<sub>v</sub>1.2 Pathway in AF Electrical Stimulation Models.** Sac/val can inhibit the degradation of NPs and thus increase their levels. Past investigations

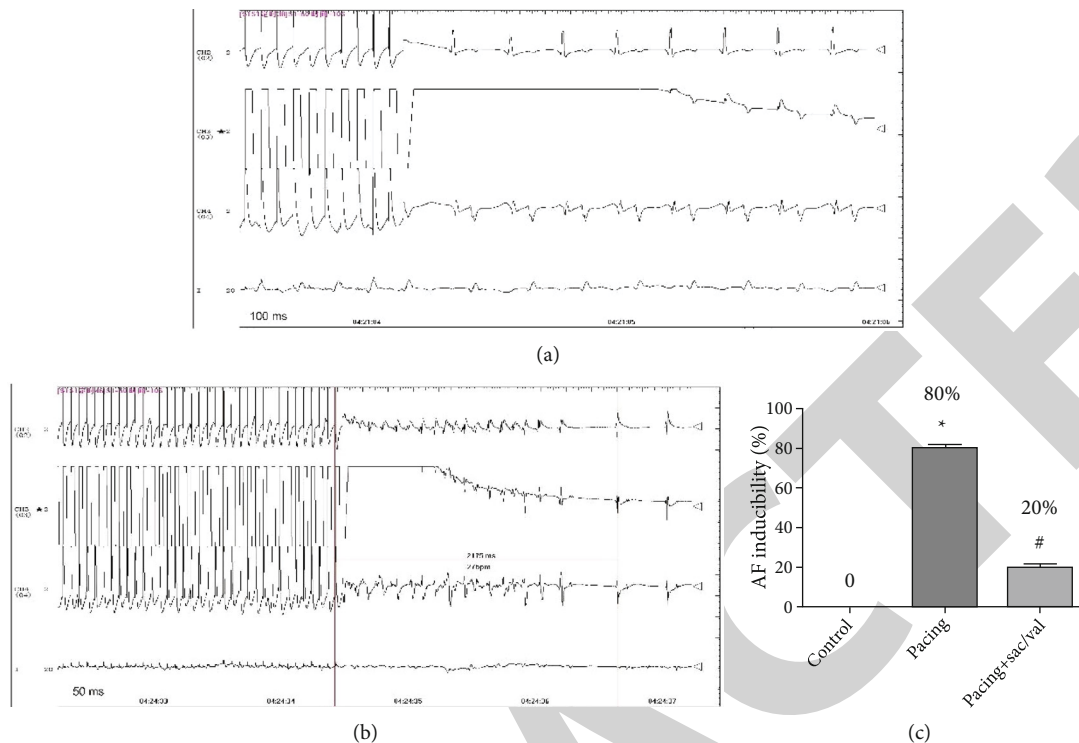


FIGURE 3: Representation of the typical ECG of animal (a) without AF induction, (b) ECG of animal with induced AF, and (c) comparison of AF inducibility between control cohort, pacing cohort, and pacing+sac/val cohort. \* $P < 0.05$  represents the comparison of the pacing cohort with the control cohort. # $P < 0.05$  represents the comparison of the pacing+sac/val cohort with the pacing cohort.

revealed that NPs attenuate atrial electrical remodeling in AF. Atrial myocytes express ANP genes [38], and mutant atrial NP (Mut-ANP) promotes ion channel remodeling in familial AF [39]. An investigation indicated Ang-(1–7) to prevent cardiac electrical remodeling induced by ARP in dogs by increasing ANP secretion [40]. Atrial myocytes also express B-type natriuretic peptide (BNP) genes, with atria being predominating sources for BNP in “lone AF” [41]. Long-term BNP therapeutics prevented atrial electrical remodeling in AF-rabbit models [11]. BNP and CNP can increase the  $ICaL$  of right atrial myocytes by activating NP receptors, thus increasing the spontaneous action potential frequency of isolated mouse cardiomyocytes [42]. The CNP level was markedly upregulated in AF cases [43]. The above results indicate that sac/val can reduce atrial electrical remodeling in AF cases by increasing the levels of NPs.

A previous study showed that treatment with valsartan can alleviate atrial electrical remodeling in AF [44]. Sac/val had increased effectiveness for ameliorating left atrial (LA)/LA appendage (LAA) activity, in comparison to ARBs (angiotensin receptor blockers) within humans/murines [45]. Other studies have shown that sac/val has a stronger effect than ACEIs or ARBs in myocardial infarction and HF [17, 18, 46, 47]. Our study found that sac/val regulated the CaMKII/ $Ca_v1.2$  pathway in atrial rapid electrical stimulation models, but additional research is required to validate increased effectiveness in comparison with valsartan.

Studies have shown that BNP can effectively improve atrial electrical remodeling in animal models of AF through the CaMKII pathway and reduce the incidence of AF [11].

Recent research demonstrated that sac/val can inhibit atrial remodeling in AF through the CaN/NFAT pathway [48]. Such an endpoint corroborated with this investigation’s dataset outcomes. We found that sac/val effectively regulated the CaMKII/ $Ca_v1.2$  expression and could alter this pathway in atrial rapid electrical stimulation models. Therefore, the above-described investigation could contribute to a novel strategy in AF therapeutics in clinical settings.

## 5. Study Limitations

First, our observations are derived from a rabbit model for AF driven through fast atrial pacing. However, clinical AF is often complicated by valvular/coronary heart disease/HF/hypertension, and solitary AF can also occur. This rabbit model simulates “lone AF” and does not fully reflect complex clinical spectra within human AF. Secondly, NPs have many physiological functions and can protect the heart through various mechanisms. Such an investigation was restricted to observing sac/val influence upon calcium regulation for the CaMKII/ $Ca_v1.2$  signaling pathway within the AF model and did not examine sac/val influence upon atrial electrical remodeling, structural and autonomic nerve remodeling, or AF-related intracellular calcium-handling remodeling. The lack of histological analyses is another limitation. Third, this study did not establish a rapid pacing + valsartan cohort and never compared sac/val and valsartan influence in AF. Fourth, the species used within *in vivo* assays varied from *in vitro* assays.

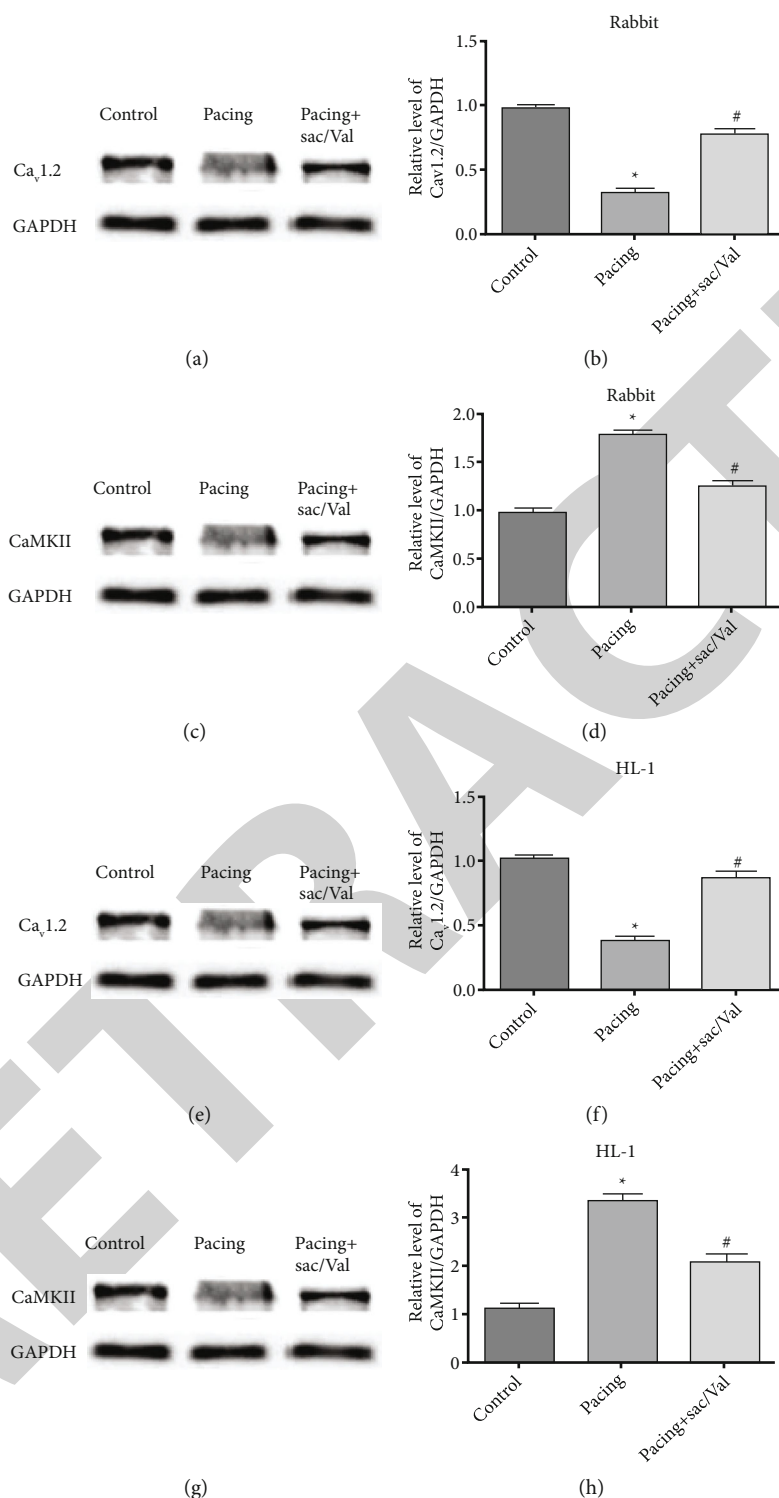


FIGURE 4: Representation of the changes in Ca<sub>v</sub>1.2 and CaMKII levels in rabbits and HL-1 cultures where (a) and (b) show the Ca<sub>v</sub>1.2 protein levels in rabbits of three cohorts. \* $P < 0.05$  represents the comparison of the pacing cohort with the control cohort. # $P < 0.05$  represents the comparison of the pacing+sac/val cohort with the pacing cohort. (c, d) The CaMKII protein levels in rabbits from the three cohorts. \* $P < 0.05$  for comparison of pacing cohort with a control cohort. # $P < 0.05$  for comparison of the pacing+sac/val cohort with the pacing cohort. (e, f) The Ca<sub>v</sub>1.2 protein levels in HL-1 cultures for three cohorts. \* $P < 0.05$  for comparison of pacing cohort with control cohort and # $P < 0.05$  for comparison of pacing+sac/val cohort with pacing cohort. (g, h) The CaMKII protein levels in HL-1 cultures for three cohorts. \* $P < 0.05$  for comparison of pacing cohort with a control cohort. # $P < 0.05$  for comparison of the pacing+sac/val cohort with the pacing cohort.

## 6. Conclusion

The sac/val is gaining wider research interests these days for various cardiac-related pathway regulation. This study was designed to validate sac/val influence on CaMKII/Ca<sub>v</sub>1.2 expression in rabbit model and HL-1 AF cultures. The AF induction rate was markedly increased together with AERP reduction in the pacing cohort. The sac/val treatment rescued such changes in pacing+sac/val cohort. The proteomic expression profiles of CaMKII and Ca<sub>v</sub>1.2 showed that the CaMKII expression was markedly upregulated, while Ca<sub>v</sub>1.2 expression was downregulated in the pacing cohort. These effects were absent in the pacing+sac/val cohort. Results of this study showed that sac/val can affect the CaMKII/Ca<sub>v</sub>1.2 expression and thus could lead to altering the CaMKII/Ca<sub>v</sub>1.2 signaling pathway in the atrial fibrillation stimulation rabbit model. In the future, further research is needed to establish and validate the role of sac/val on the CaMKII/Ca<sub>v</sub>1.2 pathway regulation to prevent and treat atrial fibrillation with sac/val.

## Data Availability

Data will be provided on request.

## Conflicts of Interest

The authors declare that they have no conflicts of interest.

## Authors' Contributions

All the authors participated in the conception and design of the work. All the authors believe that the manuscript represents valid work and have carefully read and fully approve of it.

## Acknowledgments

The authors are thankful to the Department of Cardiology, First Affiliated Hospital of Harbin Medical University, Harbin, China, for providing lab facilities.

## References

- [1] D. Calvo, D. Filgueiras-Rama, and J. Jalife, "Mechanisms and drug development in atrial fibrillation," *Pharmacological Reviews*, vol. 70, no. 3, pp. 505–525, 2018.
- [2] P. Poudel, Y. Xu, Z. Cui, D. Sharma, B. Tian, and S. Paudel, "Atrial fibrillation: recent advances in understanding the role of microRNAs in atrial remodeling with an electrophysiological overview," *Cardiology*, vol. 131, no. 1, pp. 58–67, 2015.
- [3] R. Pathak, D. H. Lau, R. Mahajan, and P. Sanders, "Structural and functional remodeling of the left atrium: clinical and therapeutic implications for atrial fibrillation," *Journal of Atrial Fibrillation*, vol. 6, no. 4, 2013.
- [4] J. Pellman and F. Sheikh, "Atrial fibrillation: mechanisms, therapeutics, and future directions," *Comprehensive Physiology*, vol. 5, no. 2, pp. 649–665, 2015.
- [5] T. Christ, P. Boknik, S. Wöhrle et al., "L-type Ca<sup>2+</sup> current downregulation in chronic human atrial fibrillation is associated with increased activity of protein phosphatases," *Circulation*, vol. 110, no. 17, pp. 2651–2657, 2004.
- [6] R. Treinys and J. Jurevičius, "L-type Ca<sup>2+</sup> channels in the heart: structure and regulation," *Medicina*, vol. 44, no. 7, pp. 491–499, 2008.
- [7] Z. Hu, M. C. Liang, and T. W. Soong, "Alternative splicing of L-type Ca<sub>v</sub>1.2 calcium channels: implications in cardiovascular diseases," *Genes*, vol. 8, no. 12, p. 344, 2017.
- [8] X. Y. Qi, Y. H. Yeh, L. Xiao et al., "Cellular signaling underlying atrial tachycardia remodeling of L-type calcium current," *Circulation Research*, vol. 103, no. 8, pp. 845–854, 2008.
- [9] A. G. Rokita and M. E. Anderson, "New therapeutic targets in cardiology," *Circulation*, vol. 126, no. 17, pp. 2125–2139, 2012.
- [10] Z. Wang, Z. Chen, X. Wang et al., "The disease burden of atrial fibrillation in China from a national cross-sectional survey," *The American Journal of Cardiology*, vol. 122, no. 5, pp. 793–798, 2018.
- [11] H. Zhao, T. Li, G. Liu et al., "Chronic B-type natriuretic peptide therapy prevents atrial electrical remodeling in a rabbit model of atrial fibrillation," *Journal of Cardiovascular Pharmacology and Therapeutics*, vol. 24, no. 6, pp. 575–585, 2019.
- [12] GISSI-AF Investigators, "Valsartan for prevention of recurrent atrial fibrillation," *New England Journal of Medicine*, vol. 360, no. 16, pp. 1606–1617, 2009.
- [13] A. A. Voors, B. Dorhout, and P. van der Meer, "The potential role of valsartan+ AHU377 (LCZ696) in the treatment of heart failure," *Expert Opinion on Investigational Drugs*, vol. 22, no. 8, pp. 1041–1047, 2013.
- [14] T. G. von Lueder, B. H. Wang, A. R. Kompa et al., "Angiotensin receptor neprilysin inhibitor LCZ696 attenuates cardiac remodeling and dysfunction after myocardial infarction by reducing cardiac fibrosis and hypertrophy," *Heart Failure*, vol. 8, no. 1, pp. 71–78, 2015.
- [15] J. Torrado, C. Cain, A. G. Mauro et al., "Sacubitril/valsartan averts adverse post-infarction ventricular remodeling and preserves systolic function in rabbits," *Journal of the American College of Cardiology*, vol. 72, no. 19, pp. 2342–2356, 2018.
- [16] R. M. Burke, J. K. Lighthouse, D. M. Mickelsen, and E. M. Small, "Sacubitril/valsartan decreases cardiac fibrosis in left ventricle pressure overload by restoring PKG signaling in cardiac fibroblasts," *Heart Failure*, vol. 12, no. 4, article e005565, 2019.
- [17] P. Martens, D. Nuyens, M. Rivero-Ayerza et al., "Sacubitril/valsartan reduces ventricular arrhythmias in parallel with left ventricular reverse remodeling in heart failure with reduced ejection fraction," *Clinical Research in Cardiology*, vol. 108, no. 10, pp. 1074–1082, 2019.
- [18] J. J. McMurray, M. Packer, A. S. Desai et al., "Dual angiotensin receptor and neprilysin inhibition as an alternative to angiotensin-converting enzyme inhibition in patients with chronic systolic heart failure: rationale for and design of the prospective comparison of ARNI with ACEI to determine impact on global mortality and morbidity in heart failure trial (PARADIGM-HF)," *European Journal of Heart Failure*, vol. 15, no. 9, pp. 1062–1073, 2013.
- [19] J. J. McMurray, M. Packer, A. S. Desai et al., "Angiotensin-neprilysin inhibition versus enalapril in heart failure," *The New England Journal of Medicine*, vol. 371, no. 11, pp. 993–1004, 2014.
- [20] E. J. Velazquez, D. A. Morrow, A. D. DeVore et al., "Angiotensin-neprilysin inhibition in acute decompensated heart

## *Retraction*

# **Retracted: Classification and Detection of Mesothelioma Cancer Using Feature Selection-Enabled Machine Learning Technique**

### **BioMed Research International**

Received 8 January 2024; Accepted 8 January 2024; Published 9 January 2024

Copyright © 2024 BioMed Research International. This is an open access article distributed under the Creative Commons Attribution License, which permits unrestricted use, distribution, and reproduction in any medium, provided the original work is properly cited.

This article has been retracted by Hindawi, as publisher, following an investigation undertaken by the publisher [1]. This investigation has uncovered evidence of systematic manipulation of the publication and peer-review process. We cannot, therefore, vouch for the reliability or integrity of this article.

Please note that this notice is intended solely to alert readers that the peer-review process of this article has been compromised.

Wiley and Hindawi regret that the usual quality checks did not identify these issues before publication and have since put additional measures in place to safeguard research integrity.

We wish to credit our Research Integrity and Research Publishing teams and anonymous and named external researchers and research integrity experts for contributing to this investigation.









The corresponding author, as the representative of all authors, has been given the opportunity to register their agreement or disagreement to this retraction. We have kept a record of any response received.

### **References**

- [1] M. Shobana, V. R. Balasrswathi, R. Radhika et al., "Classification and Detection of Mesothelioma Cancer Using Feature Selection-Enabled Machine Learning Technique," *BioMed Research International*, vol. 2022, Article ID 9900668, 6 pages, 2022.

## Research Article

# Classification and Detection of Mesothelioma Cancer Using Feature Selection-Enabled Machine Learning Technique

**M. Shobana** <sup>1</sup>, **V. R. Balasraswathi** <sup>2</sup>, **R. Radhika** <sup>2</sup>, **Ahmed Kareem Olewi** <sup>3</sup>,  
**Sushovan Chaudhury** <sup>4</sup>, **Ajay S. Ladkat** <sup>5</sup>, **Mohd Naved** <sup>6</sup>,  
**and Abdul Wahab Rahmani** <sup>7</sup>

<sup>1</sup>SRM Institute of Science and Technology, SRM Nagar, Kattankulathur, Kanchipuram, 603203, Chennai, India

<sup>2</sup>Department of Networking and Communications, School of Computing, SRM Institute of Science and Technology, Kattankulathur, India

<sup>3</sup>Department of Computer Technical Engineering, The Islamic University, 54001 Najaf, Iraq

<sup>4</sup>University of Engineering and Management, Kolkata, India

<sup>5</sup>Department of Instrumentation Engineering, Vishwakarma Institute of Technology, Pune, India

<sup>6</sup>Amity International Business School (AIBS), Amity University, Noida, India

<sup>7</sup>Isteqlal Institute of Higher Education, Kabul, Afghanistan

Correspondence should be addressed to Abdul Wahab Rahmani; [ab.wahab.professor@isteqlal.edu.af](mailto:ab.wahab.professor@isteqlal.edu.af)

Received 2 June 2022; Revised 30 June 2022; Accepted 14 July 2022; Published 27 July 2022

Academic Editor: Gaganpreet Kaur

Copyright © 2022 M. Shobana et al. This is an open access article distributed under the Creative Commons Attribution License, which permits unrestricted use, distribution, and reproduction in any medium, provided the original work is properly cited.

Cancer of the mesothelium, sometimes referred to as malignant mesothelioma (MM), is an extremely uncommon form of the illness that almost always results in death. Chemotherapy, surgery, radiation therapy, and immunotherapy are all potential treatments for multiple myeloma; however, the majority of patients are identified with the disease at an advanced stage, at which time it is resistant to these therapies. After obtaining a diagnosis of advanced multiple myeloma, the average length of time that a person lives is one year after hearing this news. There is a substantial link between asbestos exposure and mesothelioma (MM). Using an approach that enables feature selection and machine learning, this article proposes a classification and detection method for mesothelioma cancer. The CFS correlation-based feature selection approach is first used in the feature selection process. It acts as a filter, selecting just the traits that are relevant to the categorization. The accuracy of the categorization model is improved as a direct consequence of this. After that, classification is carried out with the help of naive Bayes, fuzzy SVM, and the ID3 algorithm. Various metrics have been utilized during the process of measuring the effectiveness of machine learning strategies. It has been discovered that the choice of features has a substantial influence on the accuracy of the categorization.

## 1. Introduction

Cancer of the mesothelium, often known as malignant mesothelioma (MM), is an exceedingly rare but fatal type of the disease. It is possible to treat multiple myeloma with chemotherapy, surgery, radiation therapy, and immunotherapy; however, the majority of patients are diagnosed with the illness at an advanced stage, at which point it is resistant to these therapies. The median amount of time someone survives after receiving a diagnosis of advanced multiple mye-

loma is one year. Asbestos, a substance that was used extensively around the world in the 1970s and 1980s, has a significant connection to mesothelioma (MM) [1, 2].

Due to the fact that multiple myeloma cases have continued to climb despite the fact that the use of asbestos has been prohibited ever since the turn of the twenty-first century, the disease's extended latency period is to blame [3]. The most important diagnostic technique for multiple myeloma is the histological investigation, which should also be supported by clinical and radiographic findings (MM). The



definite diagnosis of multiple myeloma (MM), which is required for the proper treatment of the disease, is crucial from both a medical and a legal aspect. The effective treatment of the illness is essential for survival. However, a precise diagnosis may be difficult to arrive at in the earlier stages of multiple myeloma [4, 5]. This is due to the fact that there is a great deal of variation between individual cases and traits that are shared with other malignancies or benign or reactive processes. In addition, as multiple myeloma has a very low prevalence, pathologists are often inexperienced with the illness and fail to recognize it due to this lack of familiarity [5].

CFS takes into account not only the unique ability of each characteristic but also the degree of overlap that occurs between those features in order to determine the worth of a certain collection of attributes. Examples of characteristics that are selected are those that have a high correlation with the class but a low intercorrelation with the other qualities [6].

This paper presents classification and detection of mesothelioma cancer using feature selection-enabled machine learning technique. First features are selected using CFS correlation-based feature selection method. It is a filter which selects relevant features for the classification. It results in improving the accuracy of classification model. Then, classification is performed using fuzzy SVM, naïve Bayes, and ID3 algorithm.

## 2. Literature Survey

In this article, a review of current research on feature selection, dimensionality reduction, and classification is offered. A variety of methodologies are now being used in an effort to assess cancer data in the most efficient manner feasible. It is challenging to create and assess prediction models due to the small sample size of the cancer data as well as the high complexity of the data.

According to Kar et al. [7], the adaptive  $K$ -Nearest Neighborhood- (KNN-) based gene selection approach and the PSO method were both suggested in order to choose just a limited group of relevant genes that are adequate for the intended classification purpose. Both of these approaches are based on the idea that the KNN is the neighborhood with the most similar genes. Chen et al. [8] presented the PSOC4.5 method, which combines PSO with C4.5-based feature selection. To test the effectiveness of this method, the researchers used 10 different datasets. You may pick from one of five subsets of the dataset that are all the same size but do not overlap with one another. During the evaluation phase, each subset is used only once, and the remaining four runs are put into the training process. After that, we proceed to get the averages from these results. The model's overall performance was evaluated based on how accurately it classified new data. The recommended method worked far better than the ones that were attempted before that were relevant to the problem at hand. When using the suggested models, using five folds and five runs resulted in an average accuracy of 97.52 percent for 11 tumors, 74 percent for 14, 74 percent for 9, and 56.34 percent for brain

tumor 1, 85.75 percent for brain tumor 2, and 100 percent for leukemia. The accuracy of the leukemia prediction was 100 percent, one hundred percent in the case of lung cancer, 92.49 percent in the case of SRBCT, 94.11 percent in the case of prostate cancer, and 91.88 percent in the case of DLBCL.

Garro et al. [9] came up with the notion that the artificial bee colony (ABC) feature selection approach is superior to other methods. They asserted that they designed this model utilizing the bee's hired bees, bystanders, and scouts based on the principles of the bee's division of labor. This was based on the fact that the bee has a division of labor. In order to train the algorithm, microarray datasets relating to ALL-AML leukemia, breast cancer, prostate, and diffuse large B cell leukemia are used (DLBCL). The model achieved a classification accuracy of 85.6 percent after training and testing on breast cancer with 0.1 thresholds, whereas the overall accuracy of the model was 65.3 percent. When the threshold value is increased from 0.1 to 0.5, the performance of the system is shown to rise to 84.2 percent during testing; but, during training, the performance is shown to decrease to 83.3 percent.

When it comes to classifying the information contained in microarrays, Nguyen and his colleagues [10] came up with a method of selecting genes collectively. The Analytic Hierarchy Process (AHP), in its modified form, is used as the foundation for gene selection. The modified AHP may be used to handle two-sample  $t$ -tests, entropy tests, receiver operating characteristic curves, Wilcoxon tests, and signal-to-noise ratios, among other statistical tests and analyses (MAHP). In the process of gene selection, a singular strategy is not optimal; hence, these researchers developed a way to address the problem of individual ranking approaches. Before being included in the final analysis, the method's top-ranking genes were put through a classification process that included the usage of SVM, MLP, KNN, LDA, and PNN. They train the model using LOOCV because it works well with very few samples and is thus more efficient. When attempting to measure performance, they make use of accuracy, sensitivity, and specificity.

Sasikala et al. [11] propose employing game theory in conjunction with an optimization strategy for the purpose of feature selection for supervised classification. The Shapely Value Embedded Genetic Algorithm (SVEGA) is a novel adaptive feature selector for multiclass classification that is based on game theory and optimization techniques. Its goal is to improve detection accuracy while also selecting the best possible subset of features. In order to determine whether or not there was a difference between the selected features and the original datasets, the recommended method for selecting features was put through its paces. SVEGA was evaluated in comparison to the SVM, NB, KNN, C4.5, and ANN classifiers, which are all quite prevalent.

Moayedikia et al. [12] presented the feature selection approach called SYMON, which employs symmetric uncertainty and harmony search, in order to solve the problem of classifying large dimensions of unbalanced class datasets. This approach was developed in order to solve the problem of classifying large dimensions of unbalanced class datasets. In order to overcome the difficulty of classifying the datasets,

this solution was implemented. They make use of a method that is referred to as “hold-out,” which gives them the ability to utilize samples that were not employed in the process of creating the model. Training, validation, and testing samples are the names given to the three separate subsets that make up the dataset. These subsets are referred to by their respective titles, using DNA microarrays to collect data and having eight distinct datasets. First, the cost of computation for SYMON is rather high, and second, the flexible subset properties of the method make it hard to find a solution that is optimal.

A mixture of Fuzzy Backward Feature Elimination (FBFE) and Independent Component Analysis (ICA) was utilized by Aziz et al. [13] to improve the accuracy of SVM and NB classifiers. This was accomplished by using both techniques. They combine the ICA and FBFE algorithms, both of which are extensions of the PCA, and use this combination for feature selection. After utilizing ICA to determine the most important traits beforehand, researchers then turn to FBFE and ICA to decide which genes should be included in the optimal subset.

Tabakhi et al. [14] used the Ant Colony Optimization (ACO) algorithm into the filter process in order to reduce the number of redundant genes and increase the number of genes that are relevant to the study. MGSACO is a technique of gene selection that does not involve any supervision. During the course of an iterative process for making improvements, a population of agents will choose a subset of genes at each stage of the process. The performance of the newly found subset of genes is evaluated with the use of a fitness function once this step has been completed. The final gene collection is composed of those genes that have consistently shown strong performance throughout all of the iterations. SVM, NB, and DT were the three different classifiers that were used in order to analyze and categorize the genes that were found. The error rate of their model was 1.4 for SVM, 2.0 for NB, and 1.5 for DT, respectively; the data suggest that error rate was utilized to evaluate model performance with relevant research. In the future, they suggest developing a metric for assessing the quantity of selected genes present in each individual ant, in addition to developing other fitness functions, in order to enhance the efficiency of the gene selection process.

Sreepada et al. [15] proposed for the use of a hybrid approach, which would combine filters and wrappers in order to take use of the most beneficial aspects of both approaches. The approach is put to the test using three different datasets: those pertaining to the colon, DLBCL, and leukemia, respectively.

Hesitant fuzzy sets (HFSs), as described by Ebrahimpour and Eftekhari [16], have the potential to be used as a feature selection technique for the purpose of the classification of data pertaining to cancer. They were driven to do the sequential forward search by the correlation-based feature selection (CFS). This research made use of a total of nine binary class microarray datasets, two of which were known as the Smk and Gli85 ovarian microarrays. This methodology may be broken down into a total of three stages. The first phase in the process of creating hesitant fuzzy sets is looking

for qualities that are redundant with one another by using similarity measures. In the second stage, ranker algorithms are used to quantitatively assess the importance of the relationships between the various features and class labels. The third stage of the method consists of the computer doing a sequential forward search for the subset of desired qualities.

Feature detection, classification, and performance evaluation are all components of a technique that may be broken down into three distinct phases, as stated by Al-Rajab et al. [17]. The model was validated using the dataset pertaining to colon cancer. First and foremost, we investigated the criteria that are used to pick and then categorize characteristics. In the third and final phase, you will engage in introspection and analysis. Information gain (IG), particle swarm optimization (PSO), and genetic algorithm (GA) were the algorithms that were used in the feature selection process (IG). It was decided to use SVM, naive Bayes, and GP as classifiers, while the Weka tool was used as a development aid. Utilizing the particle swarm optimization (PSO) approach proved to be the most effective method. Other algorithms were unable to compete with this combination (94 percent). It is feasible that the method developed by the authors might be used to the selection and classification of cancer datasets other than colon cancer.

A method to feature selection that is based on an adaptive genetic algorithm (AGA) and mutual information maximization (MIM) was developed by Lu et al. [18]. This technique is known as MIMAGA. The proposed model was verified by employing six different microarray cancer datasets, including leukemia, colon cancer, prostate cancer, lung cancer, and breast cancer, with the exception of SRBCT, which is a four-class dataset. These datasets were used to test the model's accuracy. The proposed model was evaluated with the assistance of four distinct classifiers, including the BPNN, SVM, ELM, and Regularized Extreme Learning Machine (RELM). The results obtained using the recommended approach were evaluated and contrasted with those obtained using more conventional feature reduction techniques such as information gain and principal component analysis (PCA).

Combining Artificial Intelligence (AI) with fuzzy logic allows one to take advantage of the distinct advantages offered by both AI and ANN classification capabilities. As a result, it is possible to develop an effective and precise hybrid classifier even in situations in which there is an insufficient amount of data. Because fuzzy parameters rather than crisp parameters are used in the training process of the proposed model, it requires fewer training samples than conventional nonfuzzy neural networks. As a result, it may learn better than the conventional neural network and provide more accurate results than the conventional neural network. Models such as LDA, QDA, *K*-Nearest Neighbor, and SVM, along with other statistically intelligent techniques and typical artificial neural networks, are compared to the one that was recommended (SVM). One component of the model is not hierarchical, whereas the other component of the model is hierarchical. The model consists of two components (hierarchical). The performance of the model yields a classification error rate that is 6.3 percent and 8.3 percent

for the training dataset and 3.7 percent and 4.4 percent for the testing dataset, respectively.

### 3. Methodology

This section presents classification and detection of mesothelioma cancer using feature selection-enabled machine learning technique. First, features are selected using CFS correlation-based feature selection method. It is a filter which selects relevant features for the classification. It results in improving the accuracy of classification model. Then, classification is performed using fuzzy SVM, naïve Bayes, and ID3 algorithm. The block diagram is shown in Figure 1.

CFS takes into account not only the unique ability of each characteristic but also the degree of overlap that occurs between those features in order to determine the worth of a certain collection of attributes [19]. Examples of characteristics that are selected are those that have a high correlation with the class but a low intercorrelation with the other qualities [20].

The categorizing approach may be used in either a supervised or particularly unsupervised manner, depending on the researcher's preference [21]. This is a truth that is well recognized. As a direct consequence of this, support vector networks are now considered to be machine learning standards that are being monitored. It is possible to utilize a support vector machine (SVM) to create feature points or attribute states by using nonlinear hyperplanes and planar projections [22]. The use of support vector machines is significantly influenced by the utilization of Gaussian kernels, the variance and standard deviation of the data, and the methods that were utilized to compute the kernels. You may train a machine learning model to recognize only one class at a time by using fuzzy support vector machines (fuzzy SVM). The SVM was unable to pinpoint any locations where eruptions were taking place. In this way, FSVM is being put to productive use. Data that are stochastic and probabilistic need to have prelearning data performed on them. The topic of discussion in this section is stochastic relationships.

The construction of metadata using these naïve Bayes classifiers makes use of both factual and probabilistic data. In this particular instance, the Bayes hypothesis (H) and predictions based on fundamental freedom are underlined. Since it was initially brought to light in the 1950s, a significant number of individuals have been paying attention to it ever since then. Research in the field of medical diagnostics, data on spatial imaging, and the organization of information are only some of its numerous uses [23]. This classifier contains a vast variety of customizable indicators and requires a wide variety of parameters to function properly [24].

ID3 is credited as being one of the people who first developed it. This was the very first strategy based on a decision tree that was ever developed [25]. In addition to the notion of entropy, this approach makes use of the idea of information gain. Calculating the functional characteristic entropy in an iterative manner requires us to begin with a nodule as our point of departure. In the context of entropy and information gain, split attributes are datasets that have

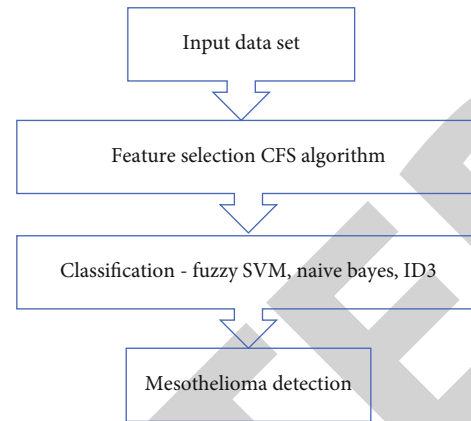


FIGURE 1: Classification and detection of mesothelioma cancer using feature selection-enabled machine learning technique.

been partitioned into subsets based on the error rate that is the lowest among them [26]. This is how the theory of split attributes proposes that split attributes should work (entropy). In the absence of a specific classification of the target classes, all the algorithm does is repeat through its own stages for each individual subset of data [27]. The nodes that are part of a branch but are not considered to be its terminal nodes are referred to as the branch's terminal nodes. The split attribute allows for the identification of nonterminal nodes in a tree, which is possible given that these nodes do in fact exist [6, 28].

### 4. Result Analysis and Discussion

Mesothelioma dataset [29] consists of 324 instances and 34 features. CFS feature selection algorithm is applied for feature selection. It selects 14 features. Then, machine learning algorithms like fuzzy SVM, naïve Bayes, and ID3 algorithm are applied to classify data. Accuracy, specificity, and sensitivity parameters are used to measure the performance of machine learning techniques for mesothelioma detection. Results are shown in Figures 2–4.

$$\text{Accuracy} = \frac{TP + TN}{TP + TN + FP + FN},$$

$$\text{Sensitivity} = \frac{TP}{TP + FN}, \quad (1)$$

$$\text{Specificity} = \frac{TN}{TN + FP},$$

where

$$\begin{aligned} TP &= \text{true positive,} \\ TN &= \text{true negative,} \\ FP &= \text{false positive,} \\ FN &= \text{false negative.} \end{aligned} \quad (2)$$

During the first phase of the feature selection process, the CFS correlation-based feature selection technique is

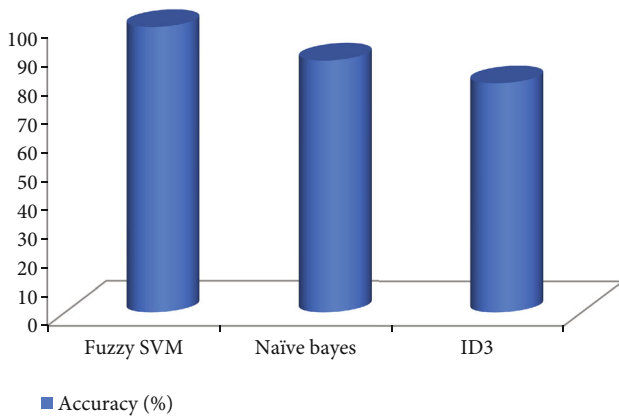


FIGURE 2: Accuracy of machine learning classifiers for mesothelioma detection.

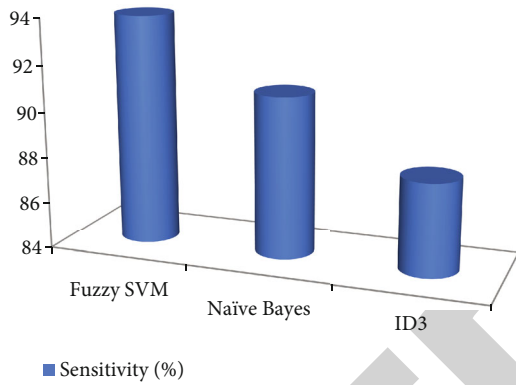


FIGURE 3: Sensitivity of machine learning classifiers for mesothelioma detection.

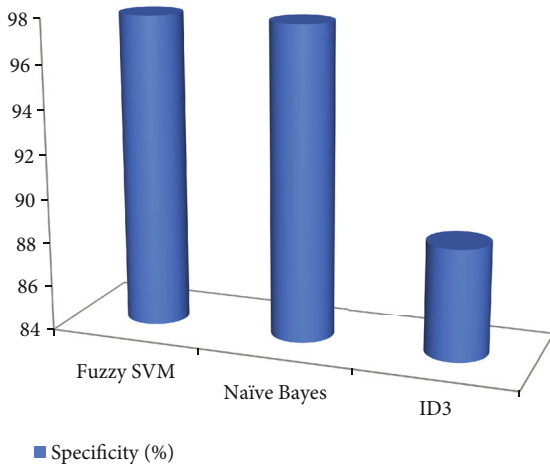


FIGURE 4: Specificity of machine learning classifiers for mesothelioma detection.

used. It performs the function of a filter, choosing just the characteristics that are pertinent to the categorization. As a direct result of this, the accuracy of the model used for categorizing data is much increased. Following that, classifica-

tion is performed with the assistance of naive Bayes, fuzzy support vector machines, and the ID3 method. During the process of determining how successful certain machine learning algorithms are, a number of different measures have been applied. It has been shown that the selection of characteristics has a significant impact on the precision of the classification process.

### 5. Conclusion

Cancer of the mesothelium, also known as malignant mesothelioma (MM), is a very rare type of the disease that nearly always ends in the patient’s death. Numerous myelomas have multiple possible treatments, including chemotherapy, surgery, radiation therapy, and immunotherapy; however, the majority of patients are diagnosed with the illness at an advanced stage, when it is resistant to these therapies. One year is the typical amount of time that a person has left to live after receiving the diagnosis that they have advanced multiple myeloma after they have received this information. The risk of developing mesothelioma is significantly increased when a person has been exposed to asbestos (MM). Using an approach that enables feature selection and machine learning, this article proposes a classification and detection method for mesothelioma cancer. The CFS correlation-based feature selection approach is first used in the feature selection process. It acts as a filter, selecting just the traits that are relevant to the categorization. The accuracy of the categorization model is improved as a direct consequence of this. After that, classification is carried out with the help of naive Bayes, fuzzy SVM, and the ID3 algorithm. Various metrics have been utilized during the process of measuring the effectiveness of machine learning strategies. It has been discovered that the choice of features has a substantial influence on the accuracy of the categorization.

### Data Availability

The data shall be made available on request.

### Conflicts of Interest

The authors declare that they have no conflict of interest.

### Acknowledgments

This research work is self-funded.

### References

- [1] J. Remon, N. Reguart, J. Corral, and P. Lianes, “Malignant pleural mesothelioma: new hope in the horizon with novel therapeutic strategies,” *Cancer Treatment Reviews*, vol. 41, no. 1, pp. 27–34, 2015.
- [2] V. Jasti, A. S. Zamani, K. Arumugam et al., “Computational technique based on machine learning and image processing for medical image analysis of breast cancer diagnosis,” *Security and Communication Networks*, vol. 2022, article 1918379, 7 pages, 2022.

## Retraction

# Retracted: Effect of Evodiamine on Collagen-Induced Platelet Activation and Thrombosis

### BioMed Research International

Received 8 January 2024; Accepted 8 January 2024; Published 9 January 2024

Copyright © 2024 BioMed Research International. This is an open access article distributed under the Creative Commons Attribution License, which permits unrestricted use, distribution, and reproduction in any medium, provided the original work is properly cited.

This article has been retracted by Hindawi following an investigation undertaken by the publisher [1]. This investigation has uncovered evidence of one or more of the following indicators of systematic manipulation of the publication process:

- (1) Discrepancies in scope
- (2) Discrepancies in the description of the research reported
- (3) Discrepancies between the availability of data and the research described
- (4) Inappropriate citations
- (5) Incoherent, meaningless and/or irrelevant content included in the article
- (6) Manipulated or compromised peer review

The presence of these indicators undermines our confidence in the integrity of the article's content and we cannot, therefore, vouch for its reliability. Please note that this notice is intended solely to alert readers that the content of this article is unreliable. We have not investigated whether authors were aware of or involved in the systematic manipulation of the publication process.

Wiley and Hindawi regrets that the usual quality checks did not identify these issues before publication and have since put additional measures in place to safeguard research integrity.

We wish to credit our own Research Integrity and Research Publishing teams and anonymous and named external researchers and research integrity experts for contributing to this investigation.

The corresponding author, as the representative of all authors, has been given the opportunity to register their agreement or disagreement to this retraction. We have kept a record of any response received.

### References

- [1] X. Yang, M. Leng, L. Yang et al., "Effect of Evodiamine on Collagen-Induced Platelet Activation and Thrombosis," *BioMed Research International*, vol. 2022, Article ID 4893859, 10 pages, 2022.

## Research Article

# Effect of Evodiamine on Collagen-Induced Platelet Activation and Thrombosis

Xiaona Yang, Min Leng, Lihong Yang, Yunzhu Peng, Jing Wang , Qian Wang, Kun Wu, Junhua Zou, Wen Wan, Longjun Li, Yujia Ye , and Zhaohui Meng 

Laboratory of Molecular Cardiology, Department of Cardiology, The First Affiliated Hospital of Kunming Medical University, Kunming, China

Correspondence should be addressed to Yujia Ye; [yeyj@ydy.cn](mailto:yeyj@ydy.cn) and Zhaohui Meng; [zhmeng@aliyun.com](mailto:zhmeng@aliyun.com)

Received 4 June 2022; Revised 2 July 2022; Accepted 5 July 2022; Published 27 July 2022

Academic Editor: Gaganpreet Kaur

Copyright © 2022 Xiaona Yang et al. This is an open access article distributed under the Creative Commons Attribution License, which permits unrestricted use, distribution, and reproduction in any medium, provided the original work is properly cited.

*Evodia rutaecarpa* has multiple pharmacological effects and is widely used in the prevention and treatment of migraine, diabetes, cardiovascular disease, cancer, and other chronic diseases; however, the pharmacological effects of its active compound evodiamine (Evo) have not been thoroughly investigated. The purpose of this study was to investigate the effects of Evo on antiplatelet activation and thrombosis. We discovered that Evo effectively inhibited collagen-induced platelet activation but had no effect on platelet aggregation caused by activators such as thrombin, ADP, and U46619. Second, we found that Evo effectively inhibited the release of platelet granules induced by collagen. Finally, evodiamine inhibits the transduction of the SFKs/Syk/Akt/PLC $\gamma$ 2 activation pathway in platelets. According to *in vivo* studies, Evo significantly prolonged the mesenteric thromboembolism induced by ferric chloride and had no discernible effect on the coagulation function of mice. In conclusion, the antiplatelet and thrombotic effects of Evo discovered in this study provide an experimental basis for the investigation of the pharmacological mechanisms of Evo and the development of antiplatelet drugs.

## 1. Introduction

Ischemic cardiomyopathy and ischemic stroke are the leading causes of death and disability in the world after cancer, accounting for approximately 17 million deaths annually [1–3]. Arterial thrombosis is the primary pathophysiological cause of ischemic cardiomyopathy and ischemic stroke. The primary pathological changes that lead to acute thrombosis are atherosclerotic plaque rupture or vascular endothelial cell injury. Platelets are small fragments of cytoplasm derived from mature megakaryocytes (without nuclei) in the bone marrow. In the resting state, platelets appear as double concave discs and do not interact with the intact vascular wall [4]. Blood clots are damaged during the circulation of blood and eventually form blood clots with blood matrix proteins [5]. Antiplatelet therapy is a crucial intervention for the clinical treatment and prevention of thrombosis [4].

After vascular wall injury, collagen and the von Willebrand factor (VWF) interact with platelets, and platelet mem-

brane complex glycoprotein (GP)Ib-V-IX mediates platelet acute adhesion to the injured surface of the vascular wall under high shear stress [6, 7]. Platelet membrane protein GPVI, integrin  $\alpha$ 2 $\beta$ 1, and integrin  $\alpha$ 5 $\beta$  are expressed following adhesion. The stable adhesion of platelets is mediated by the interaction between 1 and fibrinogen [7]. Platelets adhering to the damaged surface activate platelets further by releasing soluble activators such as ADP and thromboxane, which interact with platelet surface receptors such as thromboxane, purinoreceptors 1 and 12 (P2Y1 and P2Y12), and PAR1 or PAR4 [8–10]. Eventually, the conformation of GPIIb/IIIa, the primary platelet adhesion receptor, changes. GPIIb/IIIa binds to fibronectin with varying degrees of affinity, ultimately promoting stable platelet aggregation and thrombosis [11].

*Evodia rutaecarpa* [12] has been used in traditional Chinese medicine for hundreds of years. In addition to treating migraines, *Evodia rutaecarpa* is widely used in the treatment and prevention of chronic diseases such as diabetes,

cardiovascular disease, and cancer [13]. The main active components of *Evodia rutaecarpine* are *evodiamine* (Evo) and *rutaecarpine*, which have similar structures and functions [14, 15].

Recent studies have revealed that Evo has a variety of pharmacological effects, including anti-inflammatory [16], anticancer [17, 18], antimicrobial [19], neuroprotective [20], cardioprotective [21], and therapeutic protective [22, 23] activities. *Rutaecarpine* has antiplatelet activation and antithrombotic effects [15, 24, 25]. Recent research results suggest that *rutaecarpine* promotes PI3K/Akt/GSK3  $\beta$  signal-axis-inhibited collagen-induced platelet activation and inhibits the formation of mouse microvascular thrombosis [26]. Although the antithrombotic and antiplatelet effects of Evo have not been thoroughly investigated.

The current investigation into the antithrombotic and antiplatelet properties of Evo investigated the effects of Evo on platelet aggregation and release induced by various activators, as well as on bleeding and thrombosis in mice. Our findings showed that Evo has anticollagen-induced platelet activation ability as well as the ability to inhibit the collagen-mediated SFKs/Syk/Akt/PLC $\gamma$ 2 signal pathway. In vivo studies show that Evo has no effect on bleeding in mice, but it can significantly inhibit mesenteric thrombosis caused by ferric chloride. Our research indicates that Evo possesses antithrombotic and antiplatelet properties. Evo is anticipated to be effective as an antithrombotic and antiplatelet drug for the treatment and prevention of thrombotic diseases.

## 2. Results

**2.1. Evodiamine Selectively Inhibits Collagen-Induced Platelet Aggregation.** After the arterial endothelial injury, collagen and VWF under the endothelium are exposed to activated platelets in the blood circulation, where they induce platelet adhesion, aggregation, and activation and initiate platelet clot formation [4]. The effects of Evo on collagen-induced platelet aggregation were investigated. As shown in Figures 1(a) and 1(g), Evo inhibited collagen-induced platelet aggregation, as less than 10% platelet aggregation was observed at 50  $\mu$ M concentration, and the degree of inhibition was dose-dependent. After platelet aggregation, thrombin, ADP, and TXA2 were secreted and further activated platelets, thereby accelerating platelet aggregation and thrombosis in the blood circulation [27]. U46619, an activator of thrombin, ADP, and the TXA2 pathway, can also be used as platelet activators that act via various membrane receptors. The effects of Evo on the platelet aggregation induced by these activators were also investigated. Figures 1(b)–1(f) demonstrate that Evo had no discernible effect on the platelet aggregation induced by thrombin, ADP, or TXA2. As a result, we concluded that Evo primarily inhibits collagen-induced platelet aggregation.

**2.2. Study of the Toxicity of Evo to Platelets.** In recent years, it was discovered that Evo inhibits the metastasis of tumor cells, but recent studies have also revealed that it is toxic to cardiomyocytes [28]. LDH is a soluble substance that is

released into the periphery when cells are damaged and can effectively reflect the toxicity of substances to cells. As a positive control, LDH was effectively released when platelets were treated with the membrane detergent Triton X-100 [29]. We investigated the effects of various Evo concentrations on platelet LDH release. The results showed that, compared with DMSO treatment, Evo below 100  $\mu$ M did not significantly increase platelet LDH release within 1 hour, and 250  $\mu$ M Evo only slightly increased the release of platelet LDH (Figure 1(h)). Accordingly, we found that under the conditions of our experiments, Evo did not cause any observable toxicity to platelets.

**2.3. Evodiamine Inhibits Platelet Release of  $\alpha$ -Granules and Dense Granules.** After activation, platelets release dense granules and  $\alpha$ -granules. The release of particular dense granules, such as ATP/ADP, and the expression of CD63 or LAMP-2 are regarded as specific markers of platelet activation [30]. P-selectin on the surface of platelets was detected utilizing flow cytometry. The expression of ATP and the release of ATP were detected by chemiluminescence ( $\alpha$ -granules). As shown in Figure 2, collagen, ADP, U46619, and thrombin stimulated the release of granules by platelets. In comparison to DMSO treatment, Evo inhibited the release of ATP by collagen-stimulated platelets with less than 10% ATP released at 50  $\mu$ M (Figures 2(a) and 2(b)) and the expression of platelet P-selectin by collagen-stimulated platelets (Figures 2(d) and 2(e)). Furthermore, Evo had no significant effect on the expression of platelet P-selectin or release of ATP by ADP-, U46619-, and thrombin-stimulated platelets (Figures 2(c) and 2(f)). Thus, Evo can significantly inhibit the release of platelet granules induced by collagen.

**2.4. Evodiamine Inhibits Collagen-Induced SFKs/Syk/PLC $\gamma$ 2 Signal Transduction.** The preceding findings indicate that Evo significantly inhibits the aggregation and release of platelets induced by collagen. The major pathway for collagen-mediated platelet activation is ITAM signal transduction in platelets [31]. Therefore, we investigated the effect of Evo on platelet ITAM signaling molecules induced by Src, Syk, Akt, and PLC2 phosphorylation. The expression of immunoreceptor tyrosine-based activation motif (ITAM) signal pathway molecules in Evo-treated platelets did not differ significantly from the DMSO-treated group, as depicted in Figures 3(a) and 3(b). After collagen stimulation of platelets, the phosphorylation of ITAM signal molecules was significantly increased compared to the DMSO control group, and Evo significantly inhibited the phosphorylation of Src, Syk, Akt, and PLC following collagen activation (Figures 3(a) and 3(b)). Additionally, Evo affected the collagen-activated platelet Akt downstream signal molecule GSK-3 $\beta$ . Evo inhibited the GSK-3 $\beta$  phosphorylation process (Figure 3(c)). MAPKs consisted of the extracellular signal-regulated kinase (ERK)1/2, JNK1/2, and p38, which are also signaling molecules mediated by collagen GPVI. As depicted in Figures 3(d) and 3(e), collagen-stimulated platelet aggregation results in significant activation of JNK1/2 and p38, whereas Evo had no noticeable effect on the phosphorylation

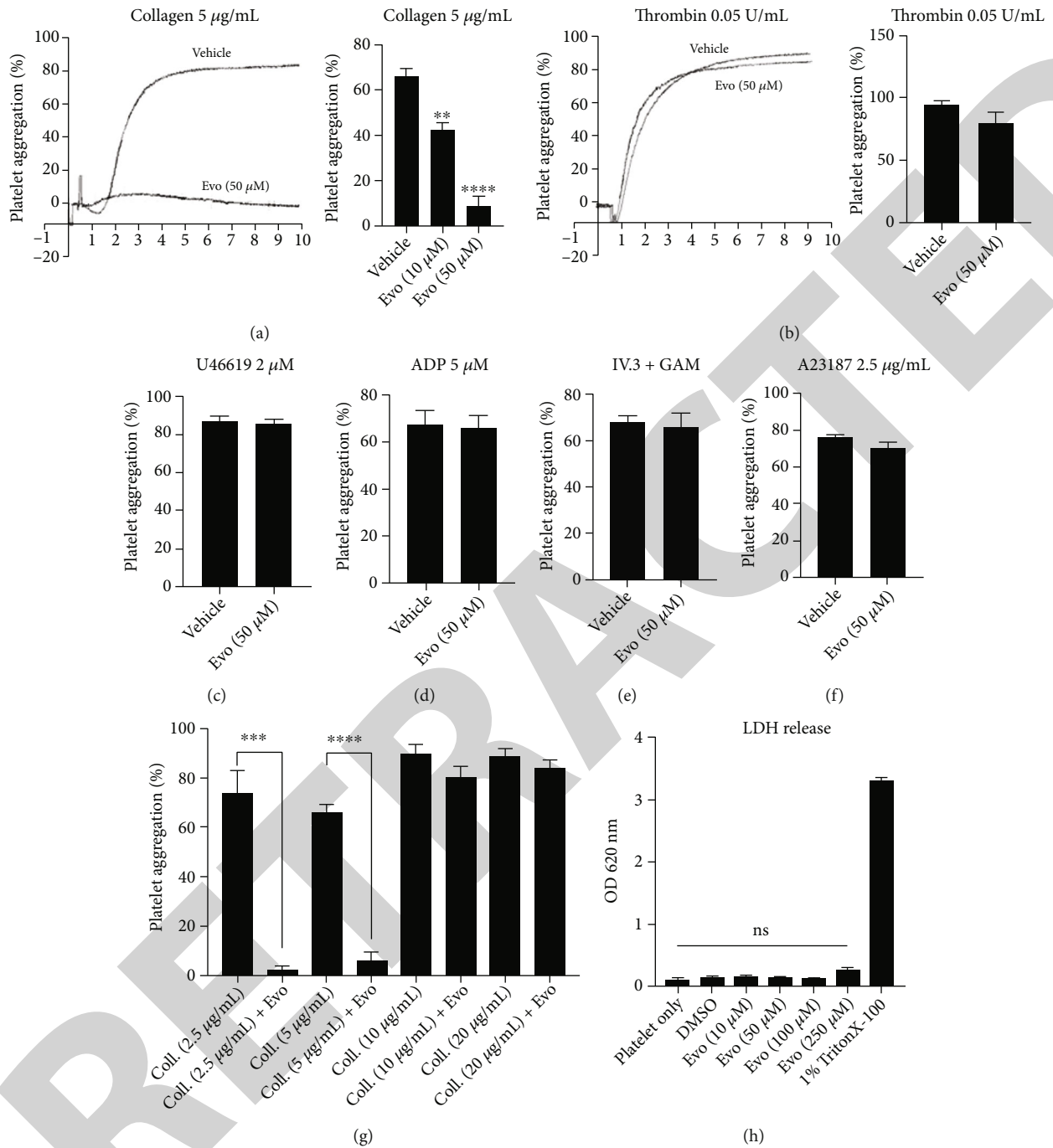


FIGURE 1: Evodiamine toxicity and effect on the aggregation of platelets caused through diverse activators.

of the aforementioned MAPKs. The results demonstrated that Evo inhibits collagen-induced activation of the SFKs/Syk/Akt/PLCγ2 signal pathway in platelets.

**2.5. Evodiamine Inhibits Mesenteric Artery Thrombosis In Vivo.** Experiments conducted in vitro revealed that Evo significantly inhibited collagen-induced platelet activation but had no significant effect on thrombin-, U46619-, or ADP-induced platelet activation. The effect of Evo on coagulation function in mice was then investigated. According to Figure 4(c), Evo had no significant prolongation effect on tail

hemorrhaging in mice, implying that Evo has little effect on the coagulation system under the conditions of this experiment. Subendothelial collagen and other matrix components are exposed to the blood during vascular endothelial injury. Platelet adhesion and aggregation on these matrix components are a critical step in the initiation of acute arterial thrombosis [32]. Therefore, we used ferric chloride to induce acute mesenteric endothelial injury and thrombosis in mice and then examined the effect of Evo on thrombosis in vivo. According to Figures 4(a) and 4(b), Evo significantly prolonged mesenteric artery embolization and inhibited



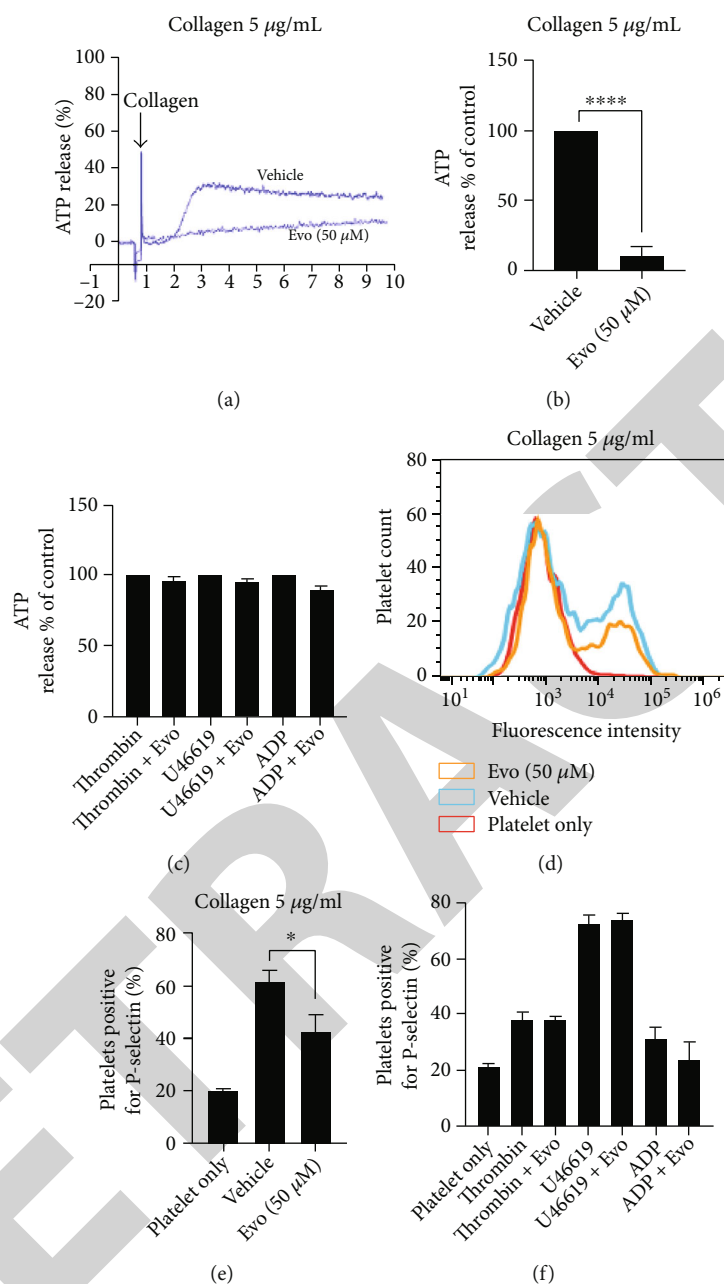


FIGURE 2: Influence of evodiamine on collagen-induced platelet dense granule and  $\alpha$ -granule release.

thrombus volume increase when compared to DMSO treatment. As a result, Evo not only had a negligible impact on the function of coagulation but also effectively inhibited thrombosis *in vivo*.

### 3. Material and Methods

**3.1. Chemicals and Reagents.** Biological materials and reagents were acquired as follows: antibodies against Src, phospho-Src (Tyr416), phospho-Akt (Thr308), Akt, Syk, phospho-Syk (Tyr525/526), GSK-3 $\beta$ , phospho-GSK-3 $\beta$  (Ser9), PLC $\gamma$ 2, phospho-JNK (Thr183/Tyr185), JNK, p38 MAPK, and phospho-p38 MAPK (Thr180/Tyr182) were purchased from Cell Signaling Technology Inc. (Danvers,

MA, USA). Phospho-PLC $\gamma$ 2 (Tyr 759) was acquired from GeneTex (Irvine, California, US). Peroxidase-labeled antibodies to rabbit IgG were obtained from SeraCare (Milford, MA, USA);  $\beta$ -actin was acquired from GeneTex (Irvine, CA, USA); PageRuler Prestained Protein Ladder from ThermoFisher Scientific (Shanghai, China); 5 $\times$  SDS-PAGE Sample Loading Buffer and BCA Protein Assay Kit from Biosharp (Hefei, Anhui, China); polyvinylidene difluoride (PVDF) membranes from MilliporeSigma (Burlington, MA, USA); and electrochemiluminescence (ECL) western blotting detection reagent, SDS-PAGE Gel Preparation Kit, Primary Antibody Dilution Buffer, Secondary Antibody Dilution Buffer, and Western Blocking Buffer from Beyotime Biotechnology (Shanghai, China).

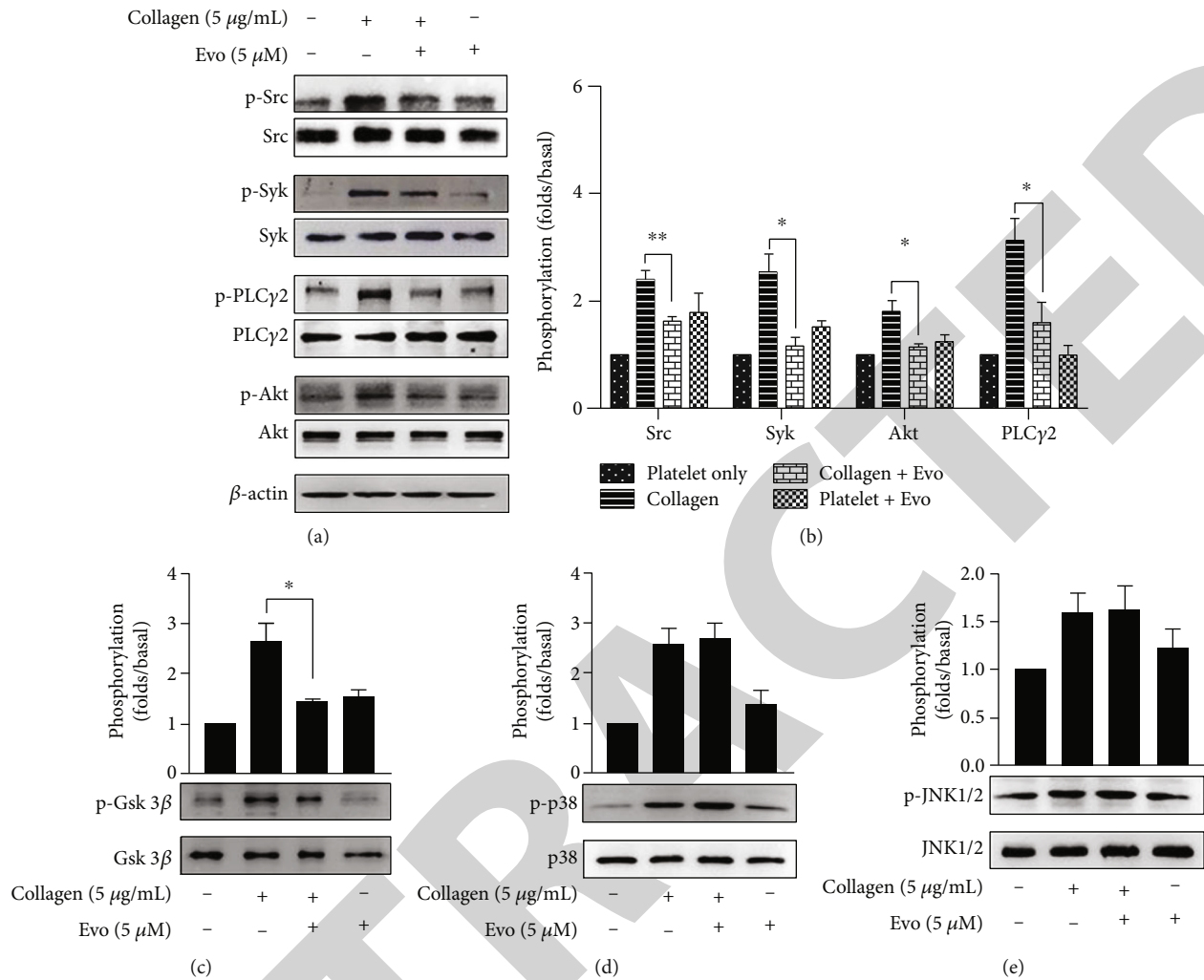


FIGURE 3: Influence of Evo on collagen-induced platelet ITAM-activation signal pathway.

**3.2. Study Protocol.** The study protocol was approved by the Ethics Committee of Kunming Medical University and the First Affiliated Hospital of Kunming Medical University (Kunming, China; Approval nos. 2021-737 and 2020-L-17).

**3.3. Platelet Aggregation and ATP Release Assay.** Human apheresis platelets were obtained from healthy individuals who had not taken medication within the previous 14 days. Blood was extracted from the elbow vein of all volunteers and anticoagulated with 3.8% sodium citrate in anticoagulant tube [33, 34]. The dilution ratio of anticoagulant to venous blood was 1 : 9. Platelet-rich plasma (PRP) was separated by centrifuging acquired venous blood at 100  $\times$  g for 10 minutes at room temperature. Platelet precipitation was obtained by adding PGE1 at a final concentration of 50 ng/ml and 5 mm EDTA to the PRP, which was then centrifuged at 2000  $\times$  g for 2 minutes. Platelets were precipitated by employing Tyrode's buffer (20 mm 4-(2-hydroxytyl)-1-piperazineethanesulfonic acid [HEPES], pH 7.4, 128 mM NaCl, 12 mm NaHCO $_3$ , 5 mm D-glucose, 0.4 mm NaH $_2$ PO $_4$ , 2.8 mM KCl, 0.25% bovine serum albumin [BSA]) with 50 ng/ml PGE1 and 5 mm EDTA. Platelets were resuspended

in Tyrode's buffer for 2 minutes to obtain washed platelets, and the platelet count was adjusted to 150 – 200  $\times$  10 $^9$  platelets/L with Tyrode's buffer. The platelet aggregation experiment was carried out using a Lumi aggregometer (Chrono Log Corp.), and 1 mM calcium chloride was added to the platelet suspension before the aggregation experiment. For Fc  $\gamma$  RIIa-mediated platelet aggregation, the washed platelets were first mixed with IV.3 (1.25  $\mu$ g/mL) while stirring at 1200 rpm per min for 1 minute, and then, 20  $\mu$ g/mL of GAM IgG F(ab') $_2$  antibody was added. Before the aggregation experiment, luciferin and D-luciferase were added to the platelet suspension to initiate the bioluminescence reaction [33]. The platelet activator was added after 2 minutes of incubation. The release of platelet ATP was observed using a Lumi aggregometer (Chrono Log Corp.).

**3.4. Platelet Cytotoxicity Assay.** The LDH cytotoxicity assay kit (Beyotime Biotechnology) was used to detect the platelet toxicity of Evo. First, wash platelets (200  $\times$  10 $^9$ /L) were incubated with various concentrations of Evo, DMSO, or 0.1% Triton X-100 (cell lysis buffer) at 37 $^{\circ}$ C for 30 minutes, followed by centrifugation at 2000  $\times$  g for 10 minutes to

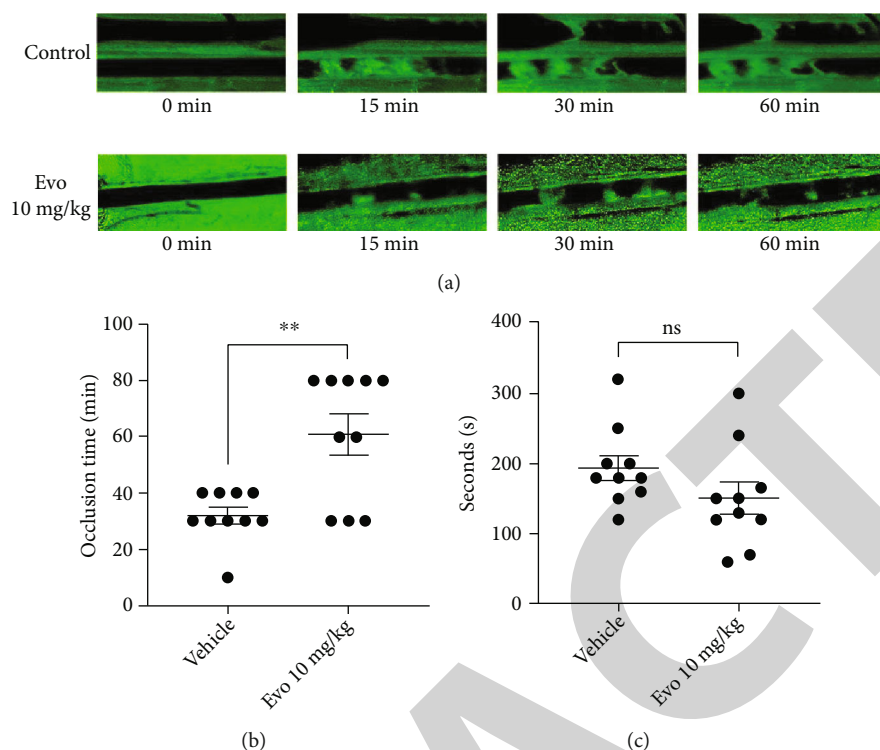


FIGURE 4: Influence of evodiamine on thrombosis and hemostatic function induced by ferric chloride.

obtain the supernatant. The supernatant was treated according to the instructions, and the absorbance value was measured at 490 nm using a Multiskan FC (ThermoFisher Scientific Inc., Waltham, MA, USA) spectrophotometer.

**3.5. Flow Cytometry.** Washed platelets ( $50 \times 10^7/L$ ) were incubated with various concentrations of Evo, DMSO, or PGE1 for 10 minutes at  $37^\circ C$ . Platelets were washed after incubation, 1 mM calcium chloride and platelet agonist were added, and 10 mM EDTA was added 30 minutes later to stop the reaction. Platelets were incubated with phycoerythrin (PE-) conjugated anti-cd62p (P-selectin) monoclonal antibody for 30 minutes, and then, the fluorescent-labeled platelets were detected by flow cytometry in a Facsanto II flow cytometer (BD Biosciences, San Diego, CA, USA).

**3.6. Western Blotting.** Platelets were resuspended in Tyrode's buffer B without 0.25% BSA and incubated at  $37^\circ C$  for 5 minutes with DMSO (vehicle group) or Evo. Processed platelets were stimulated with Evo before  $2 \times$  Triton X-100 cell lysis buffer (PBS, pH 7.4, comprising 10 mM EDTA, 145 mM NaCl,  $2 \times 0.5\%$  sodium dodecyl sulfate [SDS],  $2 \times 1\%$  deoxycholate,  $2 \times 1\%$  vol/vol Triton X-100,  $2 \times$  phosphatase, and proteinase inhibitors cocktails) was added for 60 seconds. The treated platelets were centrifuged at  $12000 \times g$  for 10 minutes, and the supernatant was retained. The concentration of the protein was measured by employing a BCA protein assay reagent after heating at  $100^\circ C$  for 10 minutes.  $5 \times$  SDS-PAGE sample loading buffer was added after protein quantification. The platelet lysate was loaded and separated using a 10% (wt/vol) sodium dodecyl

sulfate-polyacrylamide gel electrophoresis (SDS-PAGE) gel. The separated peptides were subsequently transferred onto PVDF membranes. Tris-buffered saline with Tween (TBST) containing 20 mM Tris, 137 mM NaCl, and 0.1% Tween-20 was used to rinse the membranes three times. After blocking the PVDF membranes with blocking buffer at  $4^\circ C$  for 1 hour and washing with TBST once, the membranes were incubated during the night hours at  $4^\circ C$  with primary antibodies diluted in primary antibody dilution buffer. Src, Syk, Akt, PLC $\gamma$ 2, GSK-3 $\beta$ phospho-Src, phospho-Syk, phospho-Akt, phosphor-PLC $\gamma$ 2, phosphor-GSK-3 $\beta$ , and  $\beta$ -actin were detected by implementing particular antibodies at a dilution ratio of 1 : 1000. Following rinsing with TBST three times, the membranes were incubated for 3 hours at  $4^\circ C$  with a peroxidase-labeled antibody to rabbit IgG, which was employed as a secondary antibody at a dilution ratio of 1 : 5000. The target protein bands were visualized using ECL after antibody incubation and three washes with TBST. The intensity of the target bands was assessed by ImageJ software.

**3.7. Mouse Tail Hemorrhage Experiment.** C57/b6l mice aged 6-8 weeks were anesthetized with sevoflurane. The coagulation time was then measured by placing a 5 mm sample of the mice's tails into normal saline at  $37^\circ C$ . Blood coagulation was assumed to have occurred when there was no blood flow for 60 s.

**3.8. Ferric Chloride-Induced Mesenteric Thrombosis in Mice.** C57/b6l mice aged 6-8 weeks were anesthetized by an intraperitoneal injection of pentobarbital (45 mg/kg). After the

mice were fixed in position, the neck hair was cut off, the neck skin was cut open, the jugular vein was found and catheterized, and rhodamine (5 mg/kg) was injected. The abdominal cavity was opened to expose the mesenteric vessels, and mesenteric arterioles with a diameter of about 60–80  $\mu\text{m}$  were selected under the microscope. Filter paper (approx. 5 mm long and 2 mm wide) soaked in 7.5%  $\text{FeCl}_3$  solution was placed on blood vessels for 2 minutes to induce vascular injury and thrombosis. Evo (10 mg/kg) or DMSO was injected into the jugular vein 30 minutes before thrombosis induction. Images were captured every 5 minutes using an MSHOT MD50 camera (Micro Shot Technology Ltd., Guangzhou, China) and an Olympus ix73 microscope (Olympus Corp., Shinjuku, Japan) during thrombosis. More than 90% of the blood vessels were considered completely occluded, and the longest observation time was 80 minutes.

**3.9. Statistical Analysis.** All experimental results were analyzed with GraphPad 5.0 Prism software and presented as the mean  $\pm$  standard error of the mean (SEM). A two-tailed unpaired comparison *t*-test was utilized for comparing differences between two experimental groups. To compare more than two groups, we used a one-way analysis of covariance (ANOVA). The significance level was considered at  $P < 0.05$ .

## 4. Discussion

*Evodia rutaecarpa* has multiple pharmacological effects and is widely used in the treatment and prevention of chronic diseases such as migraines, diabetes, cardiovascular disease, and cancer [35]. Although the antithrombotic and antiplatelet effects of Evo remain unclear. We discovered that Evo significantly inhibited the aggregation of collagen-activated platelets, but had no significant effect on platelet activation induced by other activators, including thrombin, ADP, and U46619. Furthermore, Evo had no significant toxic effects on platelets at the dose described in Figure 1. In addition, the  $\alpha$ -granule- and dense-granule-release experiments confirmed the selective inhibitory impact of Evo on collagen-induced platelet activation (Figure 2). According to the signal pathway analysis, Evo inhibited collagen-induced platelet ITAM-signal transduction (Figure 3). In vivo experiments also confirmed that our experimental dose of Evo did not significantly affect the bleeding time of mice, but it significantly prolonged the mesenteric thrombosis induced by ferric chloride (Figure 4). The results of the current study show that Evo can be used as an effective antiplatelet medication to inhibit platelet activation and thrombosis. Atherosclerotic plaque rupture or vascular endothelial cell injury is the main pathological change leading to acute thrombosis [36]. Following vascular wall injury caused by shear stress in the artery, collagen and VWF are exposed to the bloodstream and interact with platelets. The blood platelet membrane protein GPIIb/IIIa mediates acute adhesion of platelets to the injury surface [6]. The interaction between platelet membrane proteins and collagen performs an essential task in the formation of platelet clots on the damaged surface of the endothelium in the early stages of thrombosis

[37]. The results showed that Evo significantly inhibited the aggregation and release of collagen-induced platelets, but had no effect on the aggregation and release of ADP-, U46619-, and thrombin-induced platelets. As a result, we hypothesized that Evo exerts its inhibitory antiplatelet-aggregation function primarily through collagen-platelet interactions. According to several investigations, it has been found that the adhesion between platelets and collagen is dependent on the collagen receptors GPVI,  $\alpha_2\beta_1$ , and GPIIb-IX-V and that the activation process after platelet adhesion is mostly mediated through GPVI—an important collagen receptor of platelets [4, 37]. In the physiological state, GPVI and FcR $\gamma$  form a heterodimer, and GPVI uses the ITAM base sequence of FcR $\gamma$  to transduce intracellular activation signals [38].

We also discovered that Evo had a negligible effect on collagen receptor-mediated platelet aggregation induced by the GPVI-specific activator convulxin (results not shown). Although GPVI, as the primary receptor of collagen, mediates platelet activation and adhesion, platelet activation is mediated by a network of membrane receptors that interact with collagen in a vertically and horizontally intertwined activation network [37–39]. Therefore, Evo may act on receptors other than GPVI receptors, such as the  $\alpha_2\beta_1$  receptor, which mainly mediates the early activation of platelets. In combination with secondary activation receptors on platelets,  $\alpha_2\beta_1$  can further activate the main platelet collagen receptor GPVI. A monoclonal antibody that inhibited its effect significantly reduced the aggregation of collagen-induced platelets [40]. Consequently, based on current experimental findings, Evo may also influence  $\alpha_2\beta_1$ -mediated platelet activation function; however, the specific mechanism remains to be determined.

The tyrosine of the intracellular segment of FcR $\gamma$ 's ITAM sequence is phosphorylated when GPVI is activated by its ligand. This phosphorylated site can recruit and bind to the SH2 domain of Syk, which can then be activated by itself or SFKs [41, 42]. The activation of Syk triggers the phosphorylation of lat, a downstream signal-transduction member. After lat is activated, it can phosphorylate a variety of signal molecules, such as PI3K, SLP-76, Grb2, and SHC, which leads to PLC $\gamma$ 2 activation [43–45]. The activation of PI3K combined with lat acts on PIP2 and generates PIP3. PIP3 is enriched by Btk and Tec and activated by phosphorylated PLC $\gamma$ 2. Activated PLC $\gamma$ 2 decomposes phospholipids to produce the second messengers IP3 and DAG, which cause the increase of calcium from platelets and the activation of PKC [43, 45].

The analysis of signal transduction results revealed that Evo significantly inhibited the collagen-mediated platelet ITAM signal pathway molecules Src, Syk, and PLC  $\gamma$ 2 (Figures 3(a) and 3(b)). Based on the findings presented above, we have concluded that Evo exerts a significant inhibitory effect on collagen-mediated platelet activation and that its mechanism is primarily associated with the SFKs/Syk/PLC  $\gamma$ 2 signal pathway.

The serine/threonine kinase Akt is an important effector molecule of PI3K, and PI3K/Akt also performs an essential regulatory task in GPVI-mediated signal transduction. Akt-

knockout mice show defective platelet activation [46], and the Akt regulator GSK3  $\beta$  is also regarded as necessary for platelet activation [47]. Previously, it was discovered that the arterial thrombotic instability of platelet-specific PI3K- $\beta$ -deficient mice was superior to that of wild-type mice under conditions of high shear stress. This may be due to the inhibition of Akt and GSK3 functions during thrombotic enlargement [47]. According to the findings of this study, the degree of phosphorylation of Akt and GSK3  $\beta$ , which are activators of the PI3K signaling pathway, is very low in platelets when they are in their resting state (Figures 3(a)–3(c)). Following stimulation with collagen, there was a notable increase in the degree to which Akt and GSK3 $\beta$  were phosphorylated, and Evo was found to have a significant inhibitory effect on their phosphorylation (Figures 3(a)–3(c)).

The results of previous studies suggest that PI3K/Akt and MAPKs activate each other within platelets. MAPKs are comprised of a group of serine/threonine kinases that are capable of translating extracellular stimuli into cellular responses [48]. MAPK family members include ERK1/2, p38  $\alpha$ ,  $\beta$ ,  $\gamma$ , and  $\delta$ , JNK1/2/3, and big MAPK (ERK5). Several investigations employing MAPK-specific inhibitors or MAPK knockout in mice demonstrated that ERK1/2, JNK1/2, and p38 MAPK are present in platelet activation and thrombosis [48–50]. We found that Evo demonstrated no significant inhibitory impact on the phosphorylation of MAPK family molecules p38 and JNK1/2 (Figures 3(d) and 3(e)). Recent research results suggest that rutaecarpine, another extract of Evo, works through PI3K/Akt/GSK3 $\beta$  and the MAPK signal axis to inhibit collagen-induced platelet activation. The findings of this study indicate that Evo inhibits the collagen-induced SFKs/Syk/Akt/PLC $\gamma$ 2 inhibition of the platelet activation signal pathway. In conjunction with other research, the results of this investigation have led us to hypothesize that the effect of *Evodia rutaecarpa* extract on collagen-induced platelet activation is achieved through a combination of different signal transduction pathways.

One of the most important steps in the development of acute arterial thrombosis is the adhesion and aggregation of platelets, which takes place when platelets are subjected to a strong shearing force [27]. The mouse mesenteric thrombosis induced by ferric chloride mimics the pathophysiology of human atherosclerotic plaque rupture and thrombosis and is a widely used animal experimental model for evaluating platelet function and observing arterial thrombosis [51, 52]. Furthermore, blocking the collagen receptor GPVI with a monoclonal antibody can significantly reduce the mesenteric thrombosis induced by ferric chloride in mice [53, 54]. This model was chosen to examine the effect of Evo on thrombosis in vivo based on the in vitro experimental findings of the current work (Figures 4(a) and 4(b)). It was discovered that iron chloride significantly increased the bleeding time of Evo-treated mice. This experiment, however, had limitations. We did not observe thrombosis induction for a long time, and recent studies revealed that the mechanism of thrombosis in this mouse model is closely related to many factors, including ROS injury of

endothelial cells, erythrocyte adhesion, and the role of plasma proteins [55, 56]. To further investigate the mechanism of Evo's effect on thrombosis, fluorescent staining and microscopy are required to observe the interactions between cells during the thrombosis process.

Although this study suggests that the effects of Evo on platelets are linked to collagen, the platelet membrane proteins that interact with Evo were not identified. Evo inhibits collagen-induced platelet activation but has a negligible effect on GPVI-mediated platelet aggregation. These experimental results led us to suspect that Evo acts through other collagen receptors such as  $\alpha$ 2 $\beta$ 1 and GP Ib-V-IX, which may interact to play an antiplatelet role. To further investigate the effects of Evo on platelet  $\alpha$ 2 $\beta$ 1 and GPIb-V-IX function, it is necessary to improve this investigation of the adhesion between platelets and collagen subjected to static and high shear forces. Furthermore, Evo exhibits anti-inflammatory and antioxidant properties [57]. The effects of Evo on platelet activation, apoptosis, autophagy, and other functions under oxidative stress are also worthy of further investigation. In vitro studies demonstrated that Evo selectively inhibits collagen-induced human platelet activation. According to the in vivo findings, Evo significantly inhibited the thrombosis induced by ferric chloride while not significantly prolonging bleeding time. However, it is necessary to pay attention to the complex pathological processes of thrombosis, as well as the inhibitory effects of Evo on endothelial cells and neutrophils. It is still worthwhile to investigate whether Evo has significant inhibitory effects in several different types of pathological thrombosis, such as venous embolism and tumor embolism, and so on. As a Chinese patent medicine with multiple activities, Evo appears to have effects on platelets and thrombosis, and the current work has provided a novel experimental foundation for the investigation of the pharmacological mechanism of Evo and the development of antiplatelet and antithrombotic drugs.

In conclusion, the effects of Evo on antiplatelet activation and thrombosis were investigated in this study, and it was demonstrated that Evo effectively inhibited collagen-induced platelet activation but had no effect on platelet aggregation caused by activators such as thrombin, ADP, and U46619. In addition, the effect of Evo on the release of platelet granules was studied, and the results demonstrated that Evo can effectively inhibit the release of platelet granules induced by collagen. It can also significantly inhibit the collagen-mediated SFKs/Syk/Akt/PLC $\gamma$ 2 signal pathway. In vivo studies on the mesenteric artery, thrombosis revealed that the Evo has no effect on bleeding in mice, but it can significantly inhibit ferric chloride-induced mesenteric thrombosis. This study found that Evo has antithrombotic and antiplatelet properties and that it can be used effectively as an antithrombotic and antiplatelet drug for the treatment and prevention of thrombotic diseases.

## Data Availability

Data will be provided upon request to the authors.

## Conflicts of Interest

The authors declare that they have no conflicts of interest.

## Authors' Contributions

Xiaona Yang and Min Leng contributed equally to this works.

## Acknowledgments

This work was supported by the National Natural Science Foundation of China (no. 81860074), the Yunnan Fundamental Research Projects (no. 202101AU070105), the Education Department of Yunnan Province Natural Science Fund (no. 2021J0245), the Construction Program of Clinical Medical Center of Cardiovascular and Cerebrovascular Disease of Yunnan Province (no. ZX2019-03-01), the First Affiliated Hospital of Kunming Medical University Doctoral Research Fund Project (no. 2019BS012), and the Priority Union Foundation of Yunnan Provincial Science and Technology Department and Kunming Medical University (no. 202101AY070001-118).

## References

- [1] "Global, regional, and national age-sex specific mortality for 264 causes of death, 1980-2016: a systematic analysis for the global burden of disease study 2016," *Lancet*, vol. 390, no. 10100, pp. 1151-1210, 2017.
- [2] C. Dong, X. Bu, J. Liu, L. Wei, A. Ma, and T. Wang, "Cardiovascular disease burden attributable to dietary risk factors from 1990 to 2019: a systematic analysis of the global burden of disease study," *Nutrition, Metabolism, and Cardiovascular Diseases*, vol. 32, no. 4, pp. 897-907, 2022.
- [3] D. Zhao, J. Liu, M. Wang, X. Zhang, and M. Zhou, "Epidemiology of cardiovascular disease in China: current features and implications," *Nature Reviews. Cardiology*, vol. 16, no. 4, pp. 203-212, 2019.
- [4] P. E. J. van der Meijden and J. W. M. Heemskerk, "Platelet biology and functions: new concepts and clinical perspectives," *Nature Reviews. Cardiology*, vol. 16, no. 3, pp. 166-179, 2019.
- [5] Y. Sang, M. Roest, B. de Laat, P. G. de Groot, and D. Huskens, "Interplay between platelets and coagulation," *Blood Reviews*, vol. 46, article 100733, 2021.
- [6] E. Falk, "Plaque rupture with severe pre-existing stenosis precipitating coronary thrombosis. Characteristics of coronary atherosclerotic plaques underlying fatal occlusive thrombi," *British Heart Journal*, vol. 50, no. 2, pp. 127-134, 1983.
- [7] Z. M. Ruggeri, "Platelet adhesion under flow," *Microcirculation*, vol. 16, no. 1, pp. 58-83, 2009.
- [8] J. Jin, J. L. Daniel, and S. P. Kunapuli, "Molecular basis for ADP-induced platelet activation," *The Journal of Biological Chemistry*, vol. 273, no. 4, pp. 2030-2034, 1998.
- [9] J. S. Huang, S. K. Ramamurthy, X. Lin, and G. C. Le Breton, "Cell signalling through thromboxane A<sub>2</sub> receptors," *Cellular Signalling*, vol. 16, no. 5, pp. 521-533, 2004.
- [10] S. R. Coughlin, "How the protease thrombin talks to cells," *Proceedings of the National Academy of Sciences of the United States of America*, vol. 96, no. 20, pp. 11023-11027, 1999.
- [11] J. S. Bennett, "Structure and function of the platelet integrin alphaIIb beta3," *The Journal of Clinical Investigation*, vol. 115, no. 12, pp. 3363-3369, 2005.
- [12] Y. Xu, S. Wu, Y. Wu, M. Gong, and Z. Wang, "Recognition and optimization of ingredients treating nitroglycerin-induced migraine rats from Wuzhuyu decoction," *Evidence-based Complementary and Alternative Medicine*, vol. 2019, Article ID 6156754, 15 pages, 2019.
- [13] Q. Tan and J. Zhang, "Evodiamine and its role in chronic diseases," *Advances in Experimental Medicine and Biology*, vol. 929, 2016.
- [14] Q. Sun, L. Xie, J. Song, and X. Li, "Evodiamine: A review of its pharmacology, toxicity, pharmacokinetics and preparation researches," *Journal of Ethnopharmacology*, vol. 262, article 113164, 2020.
- [15] K. M. Tian, J. J. Li, and S. W. Xu, "Rutaecarpine: A promising cardiovascular protective alkaloid from *Evodia rutaecarpa* (Wu Zhu Yu)," *Pharmacological Research*, vol. 141, pp. 541-550, 2019.
- [16] T. Meng, S. Fu, D. He et al., "Evodiamine inhibits lipopolysaccharide (LPS)-induced inflammation in BV-2 cells via regulating AKT/Nrf2-HO-1/NF- $\kappa$ B signaling axis," *Cellular and Molecular Neurobiology*, vol. 41, no. 1, pp. 115-127, 2021.
- [17] Z. Hong, Z. Wang, B. Zhou et al., "Effects of evodiamine on PI3K/Akt and MAPK/ERK signaling pathways in pancreatic cancer cells," *International Journal of Oncology*, vol. 56, no. 3, pp. 783-793, 2020.
- [18] F. Liu, G. Lou, T. Zhang et al., "Anti-metastasis traditional Chinese medicine monomer screening system based on perinucleolar compartment analysis in hepatocellular carcinoma cells," *American Journal of Translational Research*, vol. 11, no. 6, pp. 3555-3566, 2019.
- [19] H. Zhang, L. Yin, M. Lu et al., "Evodiamine attenuates adjuvant-induced arthritis in rats by inhibiting synovial inflammation and restoring the Th17/Treg balance," *The Journal of Pharmacy and Pharmacology*, vol. 72, no. 6, pp. 798-806, 2020.
- [20] P. Wu and Y. Chen, "Evodiamine ameliorates paclitaxel-induced neuropathic pain by inhibiting inflammation and maintaining mitochondrial anti-oxidant functions," *Human Cell*, vol. 32, no. 3, pp. 251-259, 2019.
- [21] Q. Q. Wu, Y. Xiao, X. H. Jiang et al., "Evodiamine attenuates TGF- $\beta$ 1-induced fibroblast activation and endothelial to mesenchymal transition," *Molecular and Cellular Biochemistry*, vol. 430, no. 1-2, pp. 81-90, 2017.
- [22] F. S. Li, J. Huang, M. Z. Cui et al., "BMP9 mediates the anticancer activity of evodiamine through HIF-1 $\alpha$ /p53 in human colon cancer cells," *Oncology Reports*, vol. 43, no. 2, pp. 415-426, 2020.
- [23] E. Eraslan, A. Tanyeli, E. Polat, and Z. Yetim, "Evodiamine alleviates kidney ischemia reperfusion injury in rats: a biochemical and histopathological study," *Journal of Cellular Biochemistry*, vol. 120, no. 10, pp. 17159-17166, 2019.
- [24] J. R. Sheu, W. C. Hung, Y. M. Lee, and M. H. Yen, "Mechanism of inhibition of platelet aggregation by rutaecarpine, an alkaloid isolated from *Evodia rutaecarpa*," *European Journal of Pharmacology*, vol. 318, no. 2-3, pp. 469-475, 1996.
- [25] W. C. Huang, S. M. Hou, M. P. Wu et al., "Decreased human platelet activation and mouse pulmonary thrombosis by rutaecarpine and comparison of the relative effectiveness with

## *Retraction*

# **Retracted: Image Processing and Machine Learning-Based Classification and Detection of Liver Tumor**

### **BioMed Research International**

Received 12 December 2023; Accepted 12 December 2023; Published 13 December 2023

Copyright © 2023 BioMed Research International. This is an open access article distributed under the Creative Commons Attribution License, which permits unrestricted use, distribution, and reproduction in any medium, provided the original work is properly cited.

This article has been retracted by Hindawi, as publisher, following an investigation undertaken by the publisher [1]. This investigation has uncovered evidence of systematic manipulation of the publication and peer-review process. We cannot, therefore, vouch for the reliability or integrity of this article.

Please note that this notice is intended solely to alert readers that the peer-review process of this article has been compromised.

Wiley and Hindawi regret that the usual quality checks did not identify these issues before publication and have since put additional measures in place to safeguard research integrity.

We wish to credit our Research Integrity and Research Publishing teams and anonymous and named external researchers and research integrity experts for contributing to this investigation.

The corresponding author, as the representative of all authors, has been given the opportunity to register their agreement or disagreement to this retraction. We have kept a record of any response received.

### **References**

- [1] V. D. P. Jasti, E. Prasad, M. Sawale et al., "Image Processing and Machine Learning-Based Classification and Detection of Liver Tumor," *BioMed Research International*, vol. 2022, Article ID 3398156, 7 pages, 2022.

## Research Article

# Image Processing and Machine Learning-Based Classification and Detection of Liver Tumor

V. Durga Prasad Jasti <sup>1</sup>, Enagandula Prasad <sup>2</sup>, Manish Sawale <sup>3</sup>, Shivlal Mewada <sup>4</sup>,  
Manoj L. Bangare <sup>5</sup>, Pushpa M. Bangare <sup>6</sup>, Sunil L. Bangare <sup>7</sup>, and F. Sammy <sup>8</sup>

<sup>1</sup>CSE Department, VR Siddhartha Engineering College, Andhra Pradesh, India

<sup>2</sup>Department of Mathematics, Vallurupalli Nageswara Rao Vignana Jyothi Institute of Engineering & Technology, Vignana Jyothi Nagar, Pragathi Nagar, Nizampet, Hyderabad, Telangana, India

<sup>3</sup>Department of Electronics and Communication, Oriental Institute of Science and Technology, Bhopal, India

<sup>4</sup>Department of Computer Science, Government College, Makdona (Vikram University), Ujjain, India

<sup>5</sup>Department of Information Technology, Smt. Kashibai Navale College of Engineering, Savitribai Phule Pune University, Pune, India

<sup>6</sup>Department of E&TC, Sinhgad College of Engineering, Savitribai Phule Pune University, Pune, Maharashtra, India

<sup>7</sup>Department of Information Technology, Sinhgad Academy of Engineering, Savitribai Phule Pune University, Pune, India

<sup>8</sup>Department of Information Technology, Dambi Dollo University, Dembi Dolo, Welega, Ethiopia

Correspondence should be addressed to F. Sammy; sammy@dadu.edu.et

Received 26 May 2022; Revised 1 July 2022; Accepted 12 July 2022; Published 26 July 2022

Academic Editor: Mukesh Soni

Copyright © 2022 V. Durga Prasad Jasti et al. This is an open access article distributed under the Creative Commons Attribution License, which permits unrestricted use, distribution, and reproduction in any medium, provided the original work is properly cited.

The liver is in charge of a plethora of tasks that are critical to healthy health. One of these roles is the conversion of food into protein and bile, which are both needed for digestion. Inhaled and possibly harmful chemicals are flushed from the body. It destroys numerous nutrients acquired through the gastrointestinal system and limits the release of cholesterol by utilizing vitamins, carbohydrates, and minerals stored in the liver. The body's tissues are made up of tiny structures known as cells. Cells proliferate and divide in order to create new ones in the normal sequence of events. When an old or damaged cell has to be replaced, a new cell must be synthesized. In other circumstances, the procedure is a total and utter failure. If the tissues of dead or damaged cells that have been cleared from the body are not removed, they may give birth to nodules and tumors. The liver can produce two types of tumors: benign and malignant. Malignant tumors are more dangerous to one's health than benign tumors. This article presents a technique for the classification and identification of liver cancers that is based on image processing and machine learning. The approach may be found here. During the preprocessing stage of picture creation, the fuzzy histogram equalization method is applied in order to bring about a reduction in image noise. After that, the photographs are divided into many parts in order to zero down on the area of interest. For this particular classification task, the RBF-SVM approach, the ANN method, and the random forest method are all applied.

## 1. Introduction

The skin is the biggest organ in the human body; the liver is the second largest organ. The liver of an adult typically weighs about three pounds on average. The liver is located on the right side of the body, just behind the right lung, and is concealed by the rib cage. One lobe of the brain is located on either side of the median line that runs through

the centre of the head. It reminds me of a laboratory or a chemical facility. The liver is responsible for a multitude of functions that are essential to maintaining good health. One of these functions is the transformation of food into protein and bile, both of which are required for digestion. Ingested and potentially toxic substances are flushed out of the circulation. By using the vitamins, carbs, and minerals that are stored in the liver, it degrades various nutrients that



are absorbed through the gastrointestinal tract and controls the release of cholesterol. The tissues of the body are constructed from smaller structures known as cells. In the regular course of events, cells will multiply and divide in order to make new ones. When an older cell or one that has been damaged needs to be replaced, a new cell must be synthesized. In other cases, the procedure ends up being a complete and utter disaster. The tissues of dead or damaged cells that have been eliminated from the body might give rise to nodules and tumors if they are not eliminated. There are two types of tumors that can develop in the liver: benign and malignant. Malignant tumors provide a greater risk to one's health than benign tumors [1]. Liver CT scan image is shown in Figure 1.

According to the World Health Organization (WHO), liver cancer is the third most common cause of death in the world today. Cancer, in general, is one of the top causes of death. It would be helpful for oncologists to be able to segment liver tumors in order to check that there have been any changes in the size of the tumor. These data might be used to evaluate how effective the treatment is working for the patient and to determine whether or not any modifications are necessary. The categorizing of medical images is one of the most essential components of a well-developed system for the retrieval of medical pictures. When working with a significant volume of medical image data, it is very necessary to make use of the appropriate classification models. Computer tomography is utilized in the clinical identification process to provide assistance to radiologists in the detection of aberrant changes. CT imaging can give information that assists in medical diagnosis by allowing different types of tissues to be identified depending on the grey levels of the picture [2, 3].

Cancer is frequently the main cause of death in countries with high standards of living. The classification of cancer in clinical practice is dependent on clinical and histological data, both of which have the potential to provide erroneous or incomplete findings. The liver, which is located in the upper abdomen, is an organ that processes food and removes waste from the bloodstream. It is responsible for digesting. If there are an abnormally high number of cells that need to be eliminated in the liver, a growth or tumor may develop in that organ. Since benign tumors do not develop into cancer, medical professionals remove them. After being medically removed, benign tumors almost never return to their original location [4, 5].

When the blood vessels contained inside a haemangioma become deformed and obstructed with blood, the condition is referred to be a tumor. Cancer is a progressive disease that destroys cells throughout the body. Cells are its primary target. Hepatocytes, which are liver cells and the most common starting point for primary liver cancer, are responsible for the development of the vast majority of these tumors. The most common starting point for primary liver cancer is in the hepatocytes. Hepatocellular carcinoma, also known as malignant hematoma, is a kind of cancer that may emerge in the liver. This type of cancer is also known as hepatocarcinoma.

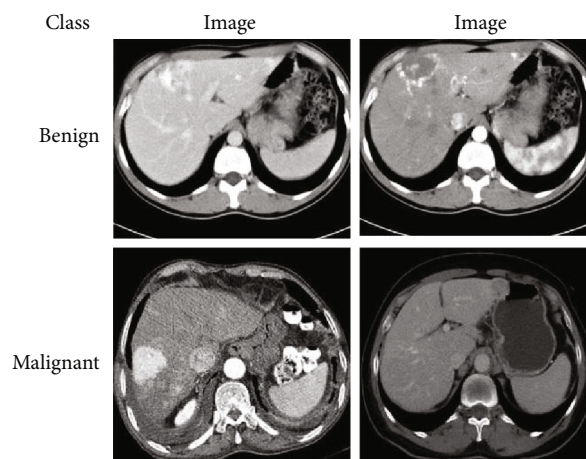


FIGURE 1: Liver CT scan images.

Ultrasonography (US), computed tomography (CT), and magnetic resonance imaging (MRI) are the medical imaging investigations that are utilized the most frequently for the early detection and diagnosis of liver cancers (MRI). Because a clinician can use the CT picture to confirm the presence of a tumor as well as evaluate its size, precise position, and the degree to which the tumor interacts with the other tissue that is adjacent, CT is the tool that is most commonly used and preferred for detecting many different types of cancers, including colon cancer. Biopsies are an example of a minimally invasive operation that may be guided by CT scans. CT scans can also be used to plan and carry out radiation treatments for cancer, as well as plan and carry out other procedures [6].

In image processing, one of the most important steps is known as "smoothing out the picture." This phase makes it easier to extract features and classify them. The analysis of biological images consequently necessitates the use of an appropriate filtering approach. It is necessary to choose the most effective liver tumor picture denoising algorithm if one wants to get outstanding results. It is possible to employ segmentation algorithms in order to eliminate unwanted elements from images of the liver. Following the steps of pre-processing and segmentation comes the step of feature extraction, which is then followed by the step of feature selection. After they have been selected, they will immediately go through the process of being categorized as quickly as possible. Denoising, segmenting, feature selection, and prediction algorithm selection are all aspects of liver tumor pictures that require more research and development [7].

Literature survey section contains review of exiting methods for cancer detection. Methodology section contains a classification and detection method for liver tumors that is based on image processing and machine learning. The fuzzy histogram equalization technique is utilized during the pre-processing of images in order to reduce noise. Following that, the photos are split in order to locate the region of interest. The RBF-SVM, ANN, and random forest method are utilized here for the classification process. Results and Discussion contains the discussion related to experimental setup and various results achieved.

## 2. Literature Survey

The interpretation of medical images has been significantly impacted by both artificial intelligence and technological advancements in medical imaging processing [8]. CAD systems, which make use of computer technology to detect and categorize abnormalities in medical photos, are a popular topic of research right now and for good reason. CAD systems make use of computer technology to identify and classify anomalies in medical pictures. It is utilized by radiologists in order to identify lesions, determine the severity of a disease, and arrive at diagnostic conclusions utilizing computerized image analysis. In order to resolve a variety of diagnostic problems, computer-aided design (CAD) systems have been developed for use with digital images obtained from a variety of imaging modalities. These imaging modalities include computed tomography (CT), magnetic resonance imaging (MRI), and ultrasound.

The quality of the image is improved by the employment of techniques such as noise reduction, boosting, and standardizing during the preprocessing stage of the picture. Therefore, preprocessing is required since the quality of the input photographs will determine the effectiveness of following operations such as the determination of the ROI and the extraction of features. Prior to continuing with image processing tasks such as edge detection, segmentation, or compression, it is essential to first do noise reduction in order to significantly improve the quality of an image for display (keeping diagnostic features).

With the use of a mean filter, it is feasible to give each pixel in a picture the same value as the average of the intensities that surround it [9]. It is easy to deploy and bring the diversity in a localized region down to a lower level. Gaussian noise, also known as mean square error (MSE), is perfect for this approach since it generates pictures that are both smooth and blurry. The adaptive mean filters adjust themselves locally to the characteristics of the picture in order to selectively minimize noise. They use local image statistics like the mean, variance, and spatial correlation in order to reliably detect and keep edges and other properties. This allows them to maintain the integrity of the data. Following this, a number known as the local mean is substituted for the noisy data in order to remove any lingering artefacts. Compared to its more conventional equivalents, adaptive mean filters are superior in their ability to reduce noise while simultaneously preserving the sharp edges of the signal.

When it comes to reducing noise in the probability density function that has a long tail, order-statistic filters perform exceptionally well. The median filter is part of the order-statistic filter family [10]. It blurs the image less than the average filter while maintaining the crispness of the edges. It works really well, particularly in situations where an image has granular noise.

Edge detection is utilized in the process of adjusting the direction and magnitude of the effect of the adaptive filter known as nonlinear diffusion. It may quiet the background while simultaneously bringing out the details in the edges. To remove the speckles from the image, a partial differential equation is solved, and the results are applied. Anisotropic

diffusion fares exceptionally well when confronted to additive Gaussian noise. When attempting to estimate the edges of the image by using the gradient operator, it is challenging to cope with several noisy photos at the same time. To compensate for this shortcoming, a technique known as speckle reduction anisotropic diffusion [11] is utilized. In general, the values are greater near the margins, while the values are lower in areas that are more consistent. As a consequence of this, it maintains the mean in areas that are relatively consistent while simultaneously amplifying and preserving the edges in areas that are quite distinct.

The pixel values in a region are changed as a result of the repetitive application of the nonlinear geometric filter (GF), which modifies them based on their locations in relation to one another [12]. During the process of picture processing, GF not only successfully eliminates noise but also preserves important details. An adaptive method that was developed and given the name aggressive region growing filtering locates a filtering region in an image by using a homogeneity threshold for region expanding that has been correctly identified. The nonlinear median filter is used to smooth out pixels closer to the edges, whereas the arithmetic mean filter is used to smooth out parts of the image that are homogenous.

You may use something called the discrete wavelet transform if you want to clean up a picture that has a lot of noise in it (DWT). Because of the wavelet transform's superior ability to compress energy, small coefficients are more likely to reflect background noise, whereas large coefficients are more likely to reflect information that is essential to understanding the image. It would appear that the coefficients that indicate qualities have a tendency to be spatially connected to one another and persist across all of the scales. Because of these qualities, DWT is an excellent candidate for denoising [13]. Wavelet shrinkage, wavelet despeckling within a Bayesian framework, wavelet filtering, and diffusion are examples of denoising algorithms that are based on wavelets.

A curvelet transform is quite similar to the wavelet transform in that it comprises frame components that are indexed by scale and position. The wavelet transform does not have these qualities, despite the fact that the curvelet pyramid does include directional parameters and a high degree of directional specificity. The use of curvelets can help minimize the amount of noise in medical photographs. Wavelets, which may be regarded of as wave atoms due to the fact that they follow the parabolic scaling of curvelets, might be utilized to perform excellent denoising on medical images [14].

In order to extract features from medical photographs, one must first recognize and choose a group of distinguishable and pertinent traits from inside the pictures. Extraction of spectral as well as spatial features, for instance, is a possibility. Following the extraction of features, it is essential to pick or reduce to a subset of the most distinguishing traits in order to maximize the accuracy of the classification while simultaneously reducing the total complexity.

During the process of classification, the extracted, selected, or reduced feature subsets are given a suspicious or not suspicious label depending on the results. The

collection of qualities that a classification system contains can determine whether the classification process is supervised or unsupervised. The classification of data can be done in one of two ways: supervised or unsupervised.

For instance, [15] created a hierarchical classifier called the decision tree classifier. In this classifier, attributes are compared to the data. A decision tree is a structure similar to a tree in which the nonterminal nodes indicate different attributes and the terminal nodes represent different choice outcomes. The data is partitioned into the descendants of each nonterminal node using a threshold that is associated with one or more attributes. The method is finished when each terminal node has only one class of data connected with it. The decision tree may be used as a classification tool after the thresholds have been established during the training phase. The decision tree method is noticeably less complicated and more efficient than the neural network approach. Nevertheless, the construction of classification algorithms and the determination of threshold values for each nonterminal node are of utmost significance.

There are mathematical models that can imitate the massively parallel architecture of the brain in terms of how it processes information and how it learns to adapt biologically. Artificial neural networks are the name given to these types of models (ANNs). During the learning phase, the system will adjust its configuration in response to new information that comes from either the outside or the inside and is sent over the network. An ANN could contain one, two, or even many hidden layers depending on the circumstances. Each layer is composed of neuronal cells. A wide variety of ANN classifiers are utilized for the purpose of medical picture analysis [16].

Nonlinear transfer functions in the neurons of the hidden layer of a multilayer perceptron (MLP) [17] are a special kind of feed-forward network that consists of three or more layers. MLPs allow for the linking of data that is not capable of being separated linearly to training patterns. Feed-forward networks are best suited for medical imaging applications that make use of numerical inputs and outputs and pairs of input/output vectors that provide a clear basis for supervised training.

An RBF network [18] is a three-layer supervised feed-forward network that uses a nonlinear transfer function for the hidden neurons and a linear transfer function for the output neurons. To calculate a radial function of the distance between each pattern vector and each hidden unit weight vector, a Gaussian function is applied to the net input of each neuron. This is done so that the function may be determined. RBF networks are a great option for a broad variety of circumstances due to their inherent flexibility in terms of both their size and their topology.

The support vector machine [19] is a supervised learning approach that seeks to determine the hyperplane that differentiates two groups of data most effectively. This is accomplished by first transforming the input data into a feature space with a higher dimension by utilizing kernel functions and then finding an optimum hyperplane inside the feature space with a higher dimension that most effectively isolates the data from one another.

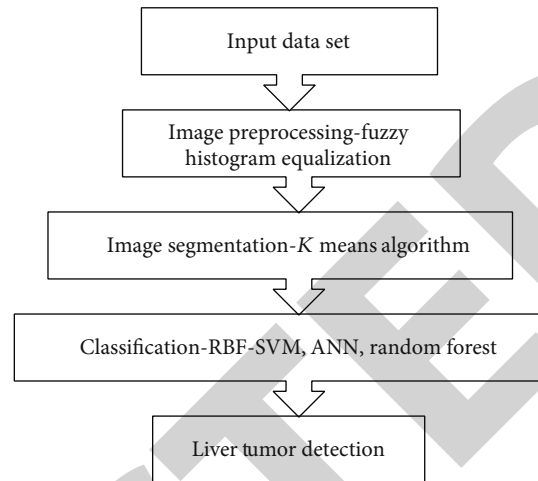


FIGURE 2: Methodology for classification and detection of liver tumor.

### 3. Methodology

This section presents image processing and machine learning-based classification and detection of liver tumor (Figure 2). Images are preprocessed to remove noise by fuzzy histogram equalization technique. Then, images are segmented to identify region of interest. Classification is performed by RBF-SVM, ANN, and random forest algorithm.

Images are filtered in order to increase the amount of information that may be reflected or comprehended by people. This is accomplished by removing unnecessary details. When the histogram of the input picture is equalized, the outcome is an intensity distribution that is compatible with a histogram that is constant. This tactic increases the image's overall contrast on a consistent basis, particularly when the image's underlying data is already rather high contrast. This method has the potential to evenly distribute the intensity across the histogram. This is beneficial for areas with a low contrast. Equalization of histograms results in a more uniform distribution of the intensities that occur most often [20].

Before the image is segmented to acquire the desired ROI, dynamic fuzzy histogram equalization is applied to the image in order to increase its quality. They proceed to isolate the qualities that are most important from each of these components. It is the process of determining and organizing the components of a picture that are connected to one another. There are methods of segmentation that are based on the regions and edges of the data. By analyzing the intensity patterns that are surrounded by a cluster of surrounding pixels, it is feasible to discover anatomical or functional elements.

Within the context of this investigation, region-based segmentation was utilized to categorize the ROI according to its texture or pattern. The local mean is utilized as a cluster pattern in the technique known as  $k$ -means clustering. This technique divides the data into  $k$  separate clusters. The sum of the individual values obtained from each group is what will be used for this method. It uses squared

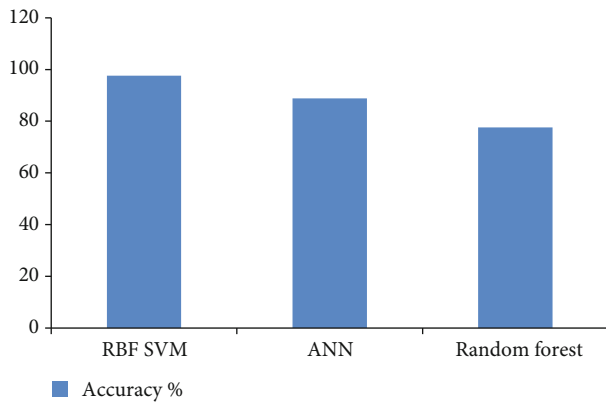


FIGURE 3: Accuracy of classifiers for classification of liver tumor images.

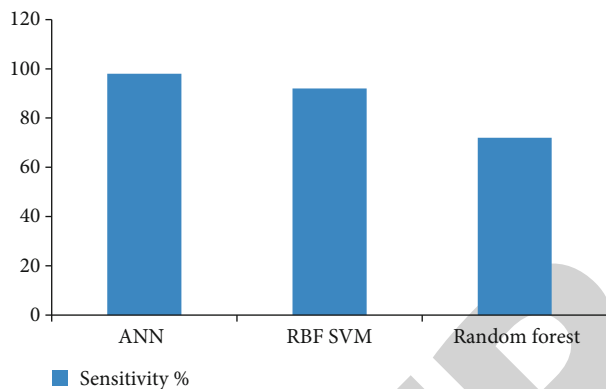


FIGURE 4: Sensitivity of classifiers for classification of liver tumor images.

Euclidean distances in order to identify the data that is the most nearby. In this procedure, the attributes that are presented are evaluated, and a single  $k$  group is designated to each data point based on those evaluations [21].

This algorithm, known as random forest, is superior to all others. It enables precise classification of enormous volumes of data, which was previously impossible. It is a technique to group learning, and it is utilized in the context of classification and regression (also known as a closest neighbor predictor). During the process of learning, it constructs a huge number of decision trees and makes use of each one to provide output for the many classes contained in the model. It is possible to make predictions about all of the trees in a forest by employing a combination of different predictor trees, each of which is dependent on a random vector sample that has the same distribution on each tree. There is a significant amount of both variation and bias inside a single tree. The problem of excessive variance and high bias may be reduced with the help of random forest, which makes averages and seeks for a natural equilibrium between two extremes. This method is both quicker and more effective than others when it comes to categorizing [22].

Using mathematical models, it is feasible to create a simulation of the massively parallel architecture of the brain in

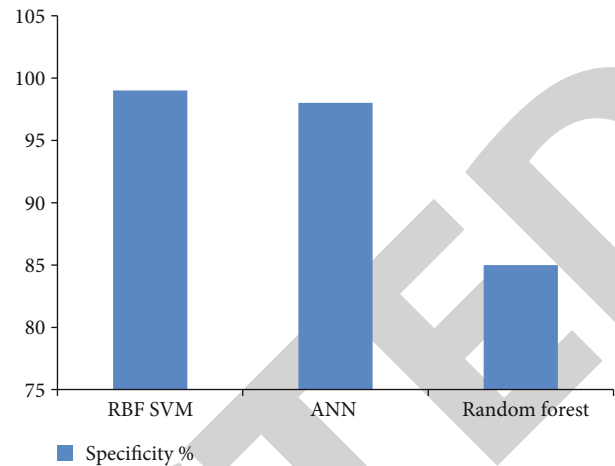


FIGURE 5: Specificity of classifiers for classification of liver tumor images.

terms of the information processing it is capable of as well as how it learns to adapt physically. Artificial neural networks are the name given to these types of models (ANNs). During the process of learning, the configuration of the system is continually modified whenever new data from within or outside the system is obtained over the network. This process occurs constantly. This type of education is known as iterative learning. Depending on the circumstances, an ANN might have anywhere from one to multiple secret levels. The exact number of these layers is never revealed. The components of each stratum are neuronal cells. In the field of medical image analysis, there is a wide variety of ANN classifiers that are employed [18].

According to [19], the objective of the support vector machine is to locate the hyperplane that differentiates two sets of data in the most effective manner. A kernel function is utilized to first transform the input data into a feature space that possesses a higher dimension and then to locate an ideal hyperplane within the feature space that possesses a higher dimension that most effectively isolates the data from one another. This procedure is repeated until the desired results are achieved. The RBF kernel function works very well with SVMs due to its adaptability.

#### 4. Results and Discussion

A standard for the segmentation of liver tumors known as LiTS17 has been created [23]. The data and segmentation are made available by a number of clinical locations spread out over the world. The test data set has seventy CT scans, whereas the training data set contains one hundred thirty CT scans.

In this study, the performance of a number of different algorithms is analyzed and compared based on three criteria: accuracy, sensitivity, and specificity. The results of the classifiers may be seen in Figures 3–5. When it comes to the classification of liver tumors, the accuracy and specificity of the SVM RBF algorithm are unmatched. The sensitivity of ANNs is significantly higher than that of other approaches.

$$\text{Accuracy} = \frac{\text{TP} + \text{TN}}{\text{TP} + \text{TN} + \text{FP} + \text{FN}},$$

$$\text{Sensitivity} = \frac{\text{TP}}{\text{TP} + \text{FN}}, \quad (1)$$

$$\text{Specificity} = \frac{\text{TN}}{\text{TN} + \text{FP}},$$

where TP is true positive, TN is true negative, FP is false positive, and FN is false negative.

## 5. Conclusion

The liver is responsible for a wide variety of functions that are essential to maintaining good health. One of these functions is the transformation of food into protein as well as bile, both of which are essential for the digestive process. The elimination of substances can be inhaled by humans and that may be hazardous to the body. It does this by metabolizing the vitamins, carbs, and minerals that are stored in the liver, which results in the destruction of a large number of nutrients that were absorbed via the digestive system. Additionally, this process inhibits the production of cholesterol. The term “cell” refers to the very small structures that make up the body’s tissues. In the natural order of things, cells must first reproduce and then divide before they can start producing new cells. When an older cell or one that has been damaged needs to be replaced, a new cell must be synthesized to take its place. In other contexts, the process is a complete and utter bust and should not be attempted. If the tissues of the cells that have died or been damaged and have been removed from the body are not eliminated, they have the potential to give rise to nodules and tumors. There are two distinct kinds of tumors that can develop in the liver: benign and malignant. The health risks posed by malignant tumors are far higher than those posed by benign tumors. This article presents a technique for the classification and identification of liver tumors that is based on image processing and machine learning. The approach may be found here. During the preprocessing stage of picture creation, a method known as fuzzy histogram equalization is utilized in order to cut down on image noise. After that, the photographs are divided into many parts in order to zero down on the area of interest. In this particular instance, the classification procedure makes use of the RBF-SVM, the ANN, and the random forest approach. When it comes to the classification of liver tumors, the accuracy and specificity of the SVM RBF algorithm are unmatched. The sensitivity of ANNs is significantly higher than that of other approaches.

## Data Availability

The data shall be made available on request.

## Conflicts of Interest

The authors declare that they have no conflict of interest.

## References

- [1] C. Cassinotto, A. Denys, F. Gay et al., “Radiofrequency ablation of liver tumors: no difference in the ablation zone volume between cirrhotic and healthy liver,” *Cardiovascular and Interventional Radiology*, vol. 41, no. 6, pp. 905–911, 2018.
- [2] Y. Sun, N. Zhang, Y. L. Ding et al., “Effect of lipid metabolism disorder on liver function in patients with malignant tumors after chemotherapy: a case-control study,” *Lipids in Health and Disease*, vol. 18, no. 1, p. 108, 2019.
- [3] M. Kaur and D. Singh, “Multiobjective evolutionary optimization techniques based hyperchaotic map and their applications in image encryption,” *Multidimensional Systems and Signal Processing*, vol. 32, no. 1, pp. 281–301, 2021.
- [4] C. Bhardwaj, S. Jain, and M. Sood, “Hierarchical severity grade classification of non-proliferative diabetic retinopathy,” *Journal of Ambient Intelligence and Humanized Computing*, vol. 12, no. 2, pp. 2649–2670, 2020.
- [5] J. Shindoh, Y. Nishioka, and M. Hashimoto, “Bilateral anatomic resection of the ventral parts of the paramedian sectors of the liver with total caudate lobectomy for deeply/centrally located liver tumors: a new technique maximizing both oncological and surgical safety,” *Journal of Hepato-Biliary-Pancreatic Sciences*, vol. 24, no. 12, pp. E10–E16, 2017.
- [6] V. Jasti, A. Zamani, K. Arumugam et al., “Computational technique based on machine learning and image processing for medical image analysis of breast cancer diagnosis,” *Security And Communication Networks*, vol. 2022, 7 pages, 2022.
- [7] S. Chaudhury, A. N. Krishna, S. Gupta et al., “Effective image processing and segmentation-based machine learning techniques for diagnosis of breast cancer,” *Computational and Mathematical Methods in Medicine*, vol. 2022, Article ID 6841334, 6 pages, 2022.
- [8] E. S. Berner and M. J. Ball, *Clinical Decision Support Systems: Theory and Practice*, Springer-Verlag, New York, NY, USA, 1998.
- [9] P. B. Caliope, F. N. S. Medeiros, R. C. P. Marques, and R. C. S. Costa, “A comparison of filters for ultrasound images,” *Telecommunications and Networking*, vol. 3124, pp. 1035–1040, 2004.
- [10] C. Ning, S. Liu, and M. Qu, “Research on removing noise in medical image based on median filter method,” in *2009 IEEE International Symposium on IT in Medicine & Education. Education (ITIME)*, pp. 384–388, Jinan, China, 2009.
- [11] Y. Yu and S. T. Acton, “Speckle reducing anisotropic diffusion,” *IEEE Transactions on Image Processing*, vol. 11, no. 11, pp. 1260–1270, 2002.
- [12] S. Sharma, P. Rattan, A. Sharma, and M. Shabaz, “Voice activity detection using optimal window overlapping especially over health-care infrastructure,” *World Journal of Engineering*, vol. 19, no. 1, pp. 118–123, 2022.
- [13] A. Pizurica, A. M. Wink, E. Vansteenkiste, W. Philips, and J. B. T. Roerdink, “A review of wavelet denoising in MRI and ultrasound brain imaging,” *Current Medical Imaging Reviews*, vol. 2, no. 2, pp. 247–260, 2006.
- [14] J. Godara, R. Aron, and M. Shabaz, “Sentiment analysis and sarcasm detection from social network to train health-care professionals,” *World Journal of Engineering*, vol. 19, no. 1, pp. 124–133, 2022.
- [15] C. Y. Fan, P. C. Chang, J. J. Lin, and J. C. Hsieh, “A hybrid model combining case-based reasoning and fuzzy decision tree

## Retraction

# Retracted: Detection of Pancreatic Cancer in CT Scan Images Using PSO SVM and Image Processing

### BioMed Research International

Received 8 January 2024; Accepted 8 January 2024; Published 9 January 2024

Copyright © 2024 BioMed Research International. This is an open access article distributed under the Creative Commons Attribution License, which permits unrestricted use, distribution, and reproduction in any medium, provided the original work is properly cited.

This article has been retracted by Hindawi following an investigation undertaken by the publisher [1]. This investigation has uncovered evidence of one or more of the following indicators of systematic manipulation of the publication process:

- (1) Discrepancies in scope
- (2) Discrepancies in the description of the research reported
- (3) Discrepancies between the availability of data and the research described
- (4) Inappropriate citations
- (5) Incoherent, meaningless and/or irrelevant content included in the article
- (6) Manipulated or compromised peer review

The presence of these indicators undermines our confidence in the integrity of the article's content and we cannot, therefore, vouch for its reliability. Please note that this notice is intended solely to alert readers that the content of this article is unreliable. We have not investigated whether authors were aware of or involved in the systematic manipulation of the publication process.

Wiley and Hindawi regrets that the usual quality checks did not identify these issues before publication and have since put additional measures in place to safeguard research integrity.

We wish to credit our own Research Integrity and Research Publishing teams and anonymous and named external researchers and research integrity experts for contributing to this investigation.

The corresponding author, as the representative of all authors, has been given the opportunity to register their agreement or disagreement to this retraction. We have kept a record of any response received.

### References

- [1] A. S. Ansari, A. S. Zamani, M. S. Mohammadi et al., "Detection of Pancreatic Cancer in CT Scan Images Using PSO SVM and Image Processing," *BioMed Research International*, vol. 2022, Article ID 8544337, 7 pages, 2022.

## Research Article

# Detection of Pancreatic Cancer in CT Scan Images Using PSO SVM and Image Processing

Arshiya S. Ansari <sup>1</sup>, Abu Sarwar Zamani <sup>2</sup>, Mohammad Sajid Mohammadi <sup>3</sup>,  
Meenakshi <sup>4</sup>, Mahyudin Ritonga <sup>5</sup>, Syed Sohail Ahmed <sup>6</sup>, Devabalan Pounraj <sup>7</sup>,  
and Karthikeyan Kaliyaperumal <sup>8</sup>

<sup>1</sup>Department of Information Technology, College of Computer and Information Sciences, Majmaah University, Al-Majmaah 11952, Saudi Arabia

<sup>2</sup>Department of Computer and Self Development, Preparatory Year Deanship, Prince Sattam Bin Abdulaziz University, Al-Kharj, Saudi Arabia

<sup>3</sup>Department of Information Technology, College of Computer, Qassim University, Buraydah, Saudi Arabia

<sup>4</sup>GD Goenka University Sohna Haryana, India

<sup>5</sup>Universitas Muhammadiyah Sumatera Barat, Indonesia

<sup>6</sup>Department of Computer Engineering, Qassim University, Buraydah, Saudi Arabia

<sup>7</sup>BVC Engineering College (Autonomous), Odalarevu, Allavaram Mandal, East-Godhavari District, Andhra Pradesh, India

<sup>8</sup>IT @ IoT-HH Campus, Ambo University, Ethiopia

Correspondence should be addressed to Karthikeyan Kaliyaperumal; [karthikeyan@ambou.edu.et](mailto:karthikeyan@ambou.edu.et)

Received 4 June 2022; Revised 30 June 2022; Accepted 11 July 2022; Published 26 July 2022

Academic Editor: Gaganpreet Kaur

Copyright © 2022 Arshiya S. Ansari et al. This is an open access article distributed under the Creative Commons Attribution License, which permits unrestricted use, distribution, and reproduction in any medium, provided the original work is properly cited.

A diagnosis of pancreatic cancer is one of the worst cancers that may be received anywhere in the world; the five-year survival rate is very less. The majority of cases of this condition may be traced back to pancreatic cancer. Due to medical image scans, a significant number of cancer patients are able to identify abnormalities at an earlier stage. The expensive cost of the necessary gear and infrastructure makes it difficult to disseminate the technology, putting it out of the reach of a lot of people. This article presents detection of pancreatic cancer in CT scan images using machine PSO SVM and image processing. The Gaussian elimination filter is utilized during the image preprocessing stage of the removal of noise from images. The  $K$  means algorithm uses a partitioning technique to separate the image into its component parts. The process of identifying objects in an image and determining the regions of interest is aided by image segmentation. The PCA method is used to extract important information from digital photographs. PSO SVM, naive Bayes, and AdaBoost are the algorithms that are used to perform the classification. Accuracy, sensitivity, and specificity of the PSO SVM algorithm are better.

## 1. Introduction

A diagnosis of pancreatic cancer is one of the worst cancers that may be received anywhere in the world; the five-year survival rate is only 9.3 percent. The majority of cases of this condition may be traced back to pancreatic cancer (American Cancer Society, 2017). One of these organs is the pancreas, which is the organ that comes after the liver in the digestive system. There are a few species of fish that have heads, bodies,

and tails that are all deceptively similar to one another in appearance. Even after it is grown to adult size, the width is just around 5 centimeters (about 2 inches) [1, 2].

It is possible for a condition known as pancreatic adenocarcinoma to develop when exocrine cells in the pancreas grow in an uncontrolled manner. This particular form of pancreatic cancer occurs the most frequently. Exocrine cells are what make up the ducts and glands that are known as exocrine organs. These organs are located in the pancreas

and are responsible for the secretion of fluid. These glands, which are known as exocrine glands and can be found in the digestive tract, are responsible for the production of enzymes that are of assistance in the digestion of food [3].

The pancreatic duct is the ultimate resting place for enzymes after they have been secreted into ducts, which are very thin tubes. The bile that is produced by the liver is expelled into the ampulla of the Vater during the digestive process. This occurs after the bile has passed through the regular bile conduit. The pancreatic duct eventually makes its way into the ordinary bile conduit and joins it there. Endocrine cells, which are a smaller percentage of the cells that make up the organ but produce essential hormones such as insulin and glucagon, which regulate and release blood sugar levels directly into the circulation, are the cells in the pancreas that are responsible for the development of the pancreatic tumor. These cells are responsible for the growth of the pancreatic tumor [4], despite the fact that they make up a lesser percentage of the cells that make up the organ.

Even though the vast majority of pancreatic growths are benign, which means they do not cause cancer, there are some of them that have the potential to develop into cancer if they are not treated. These growths are known as precancers. Imaging tools like as magnetic resonance imaging (MRI), computed tomography (CT), ultrasound, positron emission tomography (PET), and positron emission tomography combined with computed tomography (PET/CT) scans are helpful in the detection of certain pancreatic [5]. One image showing pancreatic cancer is shown in Figure 1

Since image processing and computer modelling are the most common techniques used in medical imaging, biomedical imaging has attracted a diverse variety of imaging technologies. Researchers of biological and microbiological data still rely heavily on the participation of humans in a huge majority of their studies. Inherent in physical processes are the human propensity for biased interpretations of those processes, the unpredictability that exists among human specialists, as well as lengthy and expensive procedures. In order to carry out an analysis that is both objective and recursive, accurate quantitative measurements, the examination of huge datasets, and the use of technologies that are automated are necessary [6, 7].

There is also the possibility for cancer burden reduction to be achieved through early detection and treatment options. If many cancerous growths are found at an early stage and given appropriate treatment, there is a good possibility that all of them can be eliminated. It is necessary for the World Health Organization (WHO) to make an effort in order to close the discovery gap in this situation and progress the process of early identification of cancerous development. Recent changes and upgrades have been made to the infrastructure of the research facilities. The development and widespread use of novel approaches to the early detection of cancer are now underway. The identification of people who seek medical attention for cancer-related symptoms and are ultimately given a cancer diagnosis has been the focus of recent efforts. On the other hand, a significant number of people who have cancer go undiagnosed or are only diagnosed and treated after significant delays.

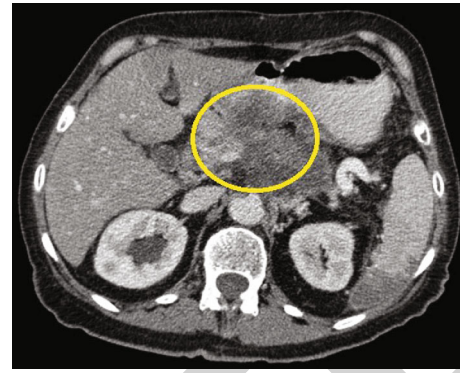


FIGURE 1: CT scan image of pancreatic cancer tissue.

Due to medical image scans, a significant number of cancer patients are able to identify abnormalities at an earlier stage. The expensive cost of the necessary gear and infrastructure makes it difficult to disseminate the technology, putting it out of the reach of a lot of people. As a result, heavy-duty radiography of expert quality and in-depth analysis are not readily available. Because of this, and concerns about the low accuracy of image-based cancer diagnosis as well as significant intra- and interreader variability, earlier WHO guidelines for resource-limited settings emphasized that medical scan pictures should be used primarily when cancer is not proven with lab tests and biopsies. This recommendation was made in light of the fact that medical scan pictures should be used [8].

Radiologists rely on computer-aided diagnostic tools to assist them in interpreting the images of patients' medical conditions. Using image processing and machine learning algorithms applied to CT scans, it is possible to identify pancreatic cancer at an earlier stage.

Literature survey contains a review of existing work in the field of pancreatic cancer detection and classification. Methodology contains proposed methodology. The Gaussian elimination filter is utilized during the image preprocessing stage of the removal of noise from images. The  $K$ -means algorithm uses a partitioning technique to separate the image into its component parts. The process of identifying objects in an image and determining the regions of interest is aided by image segmentation. The PCA method is used to extract important information from digital photographs. PSO SVM, naive Bayes, and AdaBoost are the algorithms that are used to perform the classification. Result Analysis contains experimental results. Accuracy, sensitivity, and specificity of PSO SVM algorithm are better.

*1.1. Literature Survey.* Suhas and Venugopal [9] employed a technique that included median and mean filtering in order to remove noise from medical images. This strategy was part of their overall approach. It has been suggested that an innovative technique be used that makes use of linear as well as nonlinear filters. The median and mean filter values are utilized in order to obtain a more accurate reading of each pixel in an image that contains noise. A comparison was made between the recommended method and filters based on the mean, the median, and the halfway using numerical metrics



such as PSNR, SNR, and RMSE. The results of this comparison were compared to the typical pattern of sounds. It has been proved that the structural details of a medical picture may be kept when using this technology, while at the same time, the image noise can be significantly decreased. When using this experimental method, MRI photos will have a higher degree of precision.

Denosing medical images required the application of the median and Wiener filters, as stated in Anitha et al. [10]. The median filter is a type of image filter that, like the mean filter, is used to reduce the amount of noise in a picture. However, unlike the mean filter, the median filter does so without affecting the image's fine details. When the median filter is applied to a specific pixel, an intensity level will have its value changed to be the median of the other neighboring intensity levels. Pixels that have had their quality reduced might always be substituted for those that are considered to be good. The amount of noise that the Wiener filter eliminates from an audio stream is determined by first doing an analysis of what the sound of a signal that is free of noise should be like. The only method to ascertain the answer is through the use of statistical analysis. In order to arrive at this conclusion, the pixel size and clarity of a picture are assessed and compared to a conventional noise pattern. In terms of filtering and overall performance, the median filter was the clear winner over the other filters. Photos filtered using the median have a higher pixel quality than images filtered with the Wiener filter.

Lakshmi and colleagues [11] have developed a preprocessing method that is based on soft computing techniques for the purpose of functional MRI data segmentation. Image denoising that is based on the curvelet transform is a very effective method for getting rid of noise. Quantitative testing will need to be increased since further clinical scans and realistic phantoms are going to be required in order to validate the method's precision and consistency.

An improvement has been made to a technique that was created by Rong and Yong [12] in order to remove salt and pepper noise from an image. Visual noise is identified using Median Filter 2.0, which then generates a noise-marked matrix that takes into consideration the characteristics of the found noise. In this particular instance, the processing skips over the pixel that has been determined to be a signal. On the other hand, the median filter is the one that is used the most frequently since it has a fantastic ability to get rid of background noise and a wonderful efficiency when it comes to computing. The task of the median filter is to replace the grey value of each pixel with the median value of its neighbors. When there is a significant quantity of noise, image features become obscured. The author came up with an improved method for median filtering by making use of local histograms. This method is able to keep the image's finer details intact. The histogram is utilized to determine which noise pixels have a significant amount of impulsivity. The histogram provides a visual representation of the number of noise detections that occurred for each conceivable value of the grey scale in pixels. A significant increase in the peak value of the histogram provides irrefutable evidence of the presence of impulse noise. The performance of enhanced median filters has been

examined by subjecting them to testing with various noise densities ranging from 10% to 50% with an increase of 10% in each step. These performance metrics demonstrate that the technique that was advised is more effective in cutting down on background noise. According to the findings of the experiment, not only does it a better job of preserving the picture's details but it is also more suited for the routine denoising of images on computers.

In this particular study, it was Gao and colleagues [13] that investigated the segmentation of 4D CT scans for nodules (taken at different points in time). It has been recommended that this criterion, which takes into account the degree to which the images of the different phases are similar to one another, be added into the graph cut approach in order to reduce the size of the energy function. This strategy has the downside of requiring manual segmentation to be performed in the very beginning of the process.

Ju et al. came up with a different strategy that is based on the graph cut [14]. This approach, which takes use of the data obtained from CT and PET imaging, can have its accuracy improved by the application of cosegmentation. This approach uses a random walk algorithm in order to generate the starting seeds for the graph cut technique. Graph cut is a technique for cutting graphs. This strategy makes use of two subgraphs: one for PET pictures and one for CT images. Both of these subgraphs are connected to one another via a particular connection that penalizes the difference in segmentation that results from using the two different modalities. The next step in lowering the energy function is to increase the flow while simultaneously minimizing the cuts.

In the hybrid cost function that Mukherjee and his colleagues created, deep learning and domain-specific knowledge are integrated [15]. The second set of authors proposes a strategy that begins with graph cut segmentation and then concludes with CNN. The use of convolutional neural networks (CNN) as a filter to eliminate false positives is at the heart of this methodology.

Lee and colleagues [16] developed a color image segmentation algorithm that is based on particle swarm optimization and takes saliency into consideration (PSO). When computing the saliency map, spatiotemporal feature maps are put to use. This map is then put to use to guide the area merging process, which is carried out with a modified PSO and an image segmentation hybrid fitness function for color.

Akila and Sumathy [17] proposed an innovative method for the segmentation of color images by combining local histogram equalization (LHE) with  $K$ -means clustering. LHE is a method for enhancing color photographs that works by changing pixels and making use of the information contained inside the image. In the end, a color picture is segmented by the use of the  $K$ -means clustering approach. After that, this method is contrasted with some other tried-and-true approaches, such as the subtractive clustering, fuzzy  $C$ -means, and  $K$ -means approaches.

The paper [18] devised a method for segmenting medical images using principal component analysis (PCA) and  $K$ -means clustering. This method isolates the areas of the image that are most pertinent to the study.  $K$ -means is the process of clustering is one method that may be utilized to

single out significant aspects of an image. Increasing the use of principal component analysis (PCA) in the process of feature extraction and determining the optimal number of clusters is one way to enhance accuracy. A novel approach was developed in order to increase the reliability of illness diagnosis through the use of MRI image segmentation.

Surlakar conducted a quick comparison of the segmentation techniques of  $K$ -means and  $K$ -nearest neighbor in the field of medicine [19]. These algorithms have been tested using cells derived from tumors. It has been demonstrated that the  $K$ -nearest neighbor approach is more effective in the process of picture segmentation based on mutual assessment criteria. The  $K$ -means approach produced satisfactory segmentation outcomes for  $k$  values that were lower than 1. The segmentation, on the other hand, gets progressively coarse as  $k$  increases, which results in a scattering of clusters over the images.

An ANN-based image classifier was utilized by Arunkumar and Murthi [20] for the purpose of performing early identification of pancreatic tumors. The fact that an abdominal ultrasound does not offer information on the stage of the tumor and does not capture the microscopic tumors that are picked up by an MRI or CT scan is a significant disadvantage. They utilized a neural network-based image classifier in order to increase the percentage of patients who make a full recovery and detect pancreatic tumors at an earlier stage utilizing PET scan images.

Using an artificial neural network model that Olufemi and his colleagues created, it is feasible to diagnose pancreatic cancer. The Levenberg-Marquardt back propagation technique was utilized throughout the training process of the network. Utilizing this approach, we were able to diagnose pancreatic cancer at a variety of stages. The results demonstrated an accuracy rate of 87 percent, which demonstrates the advantages of utilizing an ANN model [21].

Only MRI photos are capable of identifying the tumorous region due to image processing, which employs  $K$ -means segmentation and image preprocessing. Adaptive brain tumor detection was proposed by Swapnil et al. [22]. In order to make this system more flexible, an unsupervised SVM (support vector machine) was used to build and store the pattern for later application. This was done to make the system more versatile. Finding a feature that can be used to train SVM on is an issue that patterns face as well. Because of this, they have conducted an analysis of the area's texture as well as its color. It is anticipated that the results of the experiments conducted using the proposed system would be superior to those conducted using competing systems.

A comparison was made between the modified self-organizing map (SOM) network and the conventional SOM network for the purpose of medical picture analysis [23]. During the analysis of the dataset, thirty ultrasound photographs of the breast, ten images of the brain obtained from an MRI scan, and one image of the skull obtained from a CT scan were seen. The input feature space of the network is built with the help of a DWT, which stands for discrete wavelet transform. The filtering features of the network contribute in many different ways to the reduction of visual noise. The Jaccard index, the Rogers index, and the Tanimoto index all agree that the strategy that has been recom-

mended provides more accurate results than the SOM-based network method.

Hashem and his colleagues [24] came up with several ideas automating the classification of mammograms, and they presented those ideas. First, the image is described with the help of feature extraction techniques, and then, it is categorized with the assistance of machine learning algorithms. Texture descriptors from the first and second orders of statistics were utilized in order to provide an analysis of mammography images. A decision tree (DT), a random forest (RF), a naive Bayes (NB) algorithm, a C4.5 algorithm, and a multilayer perceptron (MLP) algorithm were employed to identify the pictures (DT). Their ultimate goal is to determine the optimal combination of feature extraction and classification algorithms that will result in precise mammogram classifications. This will allow them to achieve their target. It was determined that the most successful method for classifying mammography images was to use a mix of second-order statistics and random forest.

The accuracy of a machine learning algorithm's cancer prediction is dependent on the data collection and the characteristics of the data [25]. There are a variety of methods that are utilized to classify data, including support vector machines, random forests, naive Bayes, decision trees,  $K$ -nearest neighbors, artificial neural networks, fuzzy neural networks, RBFN, shuffled frog leaping with levy flights, particle swarm optimization, back propagation neural networks, multilayered perceptron, and SVM recursive feature elimination. According to the findings of this research, the support vector machine (SVM) method of machine learning is the most effective method for predicting cancer sickness from a given dataset.

*1.2. Methodology.* This section presents detection of pancreatic cancer in CT scan images using machine PSO SVM and image processing. To remove noise from images, image preprocessing is performed by Gaussian elimination filter. Image is partitioned in to segments by  $K$ -means algorithm. Image segmentation helps in object identification and deciding region of interest. Relevant features from images are extracted using PCA algorithm. Classification is performed by PSO SVM, naive Bayes, and AdaBoost algorithm. This is shown below in Figure 2.

There are several different morphological activities that may be taken to lessen or eliminate background noise. The median filtering technique may be used to adjust the brightness of the pixels, while the Gaussian filtering technique can be used to smooth out the images. Both techniques can be combined. In this particular instance, the Gaussian filter was used to achieve noise reduction (GF). The properties of the picture are preserved by the application of a weighted average of the intensities of neighboring pixels; nevertheless, the importance of the intensity at each pixel is changed. Using this technology, it is feasible to smooth photos while maintaining the borders of the images. Smoothing is done to the picture using Gaussian kernels by applying accumulative standard deviation [26].

$K$ -means clustering is a kind of pattern that divides the many interpretations into  $k$  different clusters, each of which is connected to a different cluster that has the local mean.

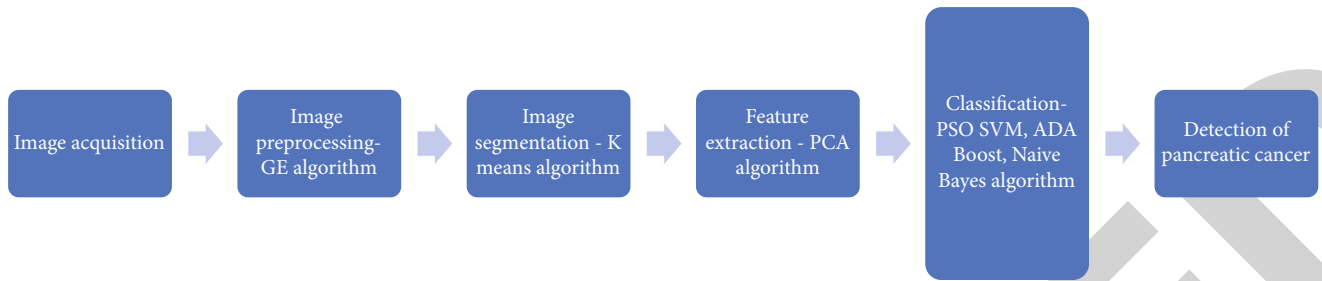


FIGURE 2: Detection of pancreatic cancer in CT scan images using machine PSO SVM and image processing.

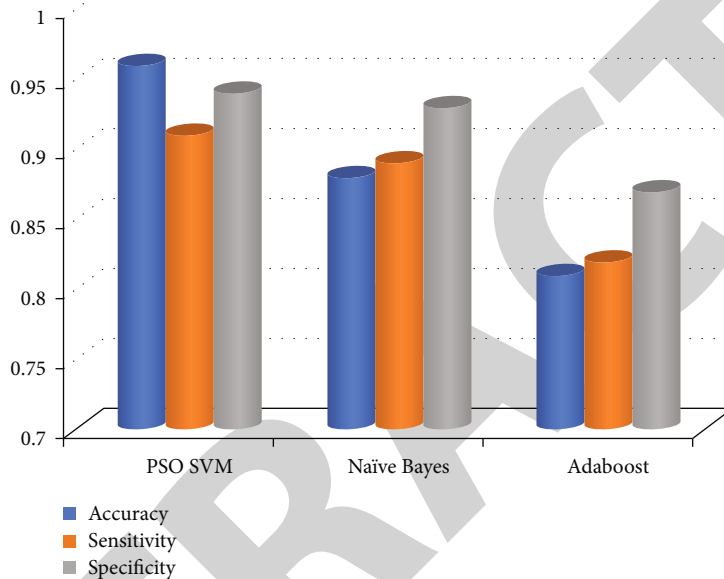


FIGURE 3: Result comparison of machine learning for pancreatic cancer detection.

The approach makes advantage of the total number of groups that are represented by  $k$  in order to locate groups within a dataset. It determines the closest data points by using squared Euclidean distances in its calculations. In accordance with the characteristics that were selected, each data point was put into one of the  $k$  different categories. The data points are categorized according to how closely their characteristics align with one another [27].

The approach known as principal component analysis (PCA) is used to carry out the process of feature extraction. It is possible that the linear technique of principal component analysis (PCA) to dimensionality reduction may be helpful in the process of data analysis and compression [28]. It is possible to combine a large number of uncorrelated characteristics by using this strategy, which involves finding orthogonal linear combinations of the characteristics that were originally included in the dataset.

For nonprobabilistic binary linear classification, the best method is the particle swarm optimization support vector machine. “Particle swarm optimization” is what “PSO-SVM” stands for as an acronym. Because of its ease of use and broad applicability, the PSO (particle swarm optimization) method has been effectively used in the cancer classification process. This method allows for the separation of samples into a single

target class as well as into a large number of target classes. Every bit of information is represented by a single point in this chart. It continues to become broader as a result of the significant distinctions that exist between each successive group. Depending on which side of the gap new instances land on, the target classes of newly created instances may be remapped. It is feasible to do nonlinear classification when the datasets being inputted are not labelled. In order to classify the data, the support vector machine makes use of an unsupervised learning strategy. This is necessary due to the fact that the instances cannot be assigned to target classes. After the formation of the clusters based on functions, further instances are added to the database. Evidence suggests that a nonlinear support vector machine recommendation system is in operation. When it comes to dealing with unlabeled data, the nonlinear support vector machine technique is the one that is used most often [29].

Bayes’ theorem provides the foundation for the Bayesian classification system and serves as its basis. These naive Bayesian classification techniques, when applied to a large database, are able to characterize simple bases in a manner that is analogous to the classification of end trees and selected networks. The naive Bayes classification is able to represent a restricted number of dependent qualities because to this feature. Using this technique, an estimate can be

made for the probability  $P(x|c)$  for each class. The classes that were found in this research to have the greatest probability served as the basis for the prediction of the results [30].

$$P(c|x) = \frac{P(x|c)P(c)}{P(x)}, \quad (1)$$

where the  $P(c|x)$  posterior probability of each class given diabetes  $x$  attribute,  $P(x|c)$  is the likelihood value,  $P(c)$  is the prior probability of diabetes class, and  $P(x)$  is the prior probability of predictor.

Each attribute conditionally forgives the subset class.

In AdaBoost decision tree, a different base classification has a weighted dataset if the weight of a single instance in the dataset depends on the previous base classifier results for each of these instances [31]. If they misunderstand an instance, the weight of that instance will increase in future models, and if the classification is correct, the weight will remain the same [31].

**1.3. Result Analysis.** The medical segmentation decathlon (MSD) dataset [32] has 420 abdomen CT scans of patients with different pancreatic tumors. 280 images were used for training and remaining 140 images are used for testing of model. To remove noise from images, image preprocessing is performed by Gaussian elimination filter. Image is partitioned in to segments by  $K$ -means algorithm. Image segmentation helps in object identification and deciding region of interest. Relevant features from images are extracted using PCA algorithm. Classification is performed by PSO SVM, naïve Bayes, and AdaBoost algorithm. Three parameters accuracy, sensitivity, and specificity are used in this study to compare performance of different algorithms. Accuracy, sensitivity, and specificity of PSO-SVM, naïve Bayes, and AdaBoost classifiers for pancreatic cancer tissue detection are shown below in Figure 3.

$$\text{Accuracy} = \frac{TP + TN}{(TP + TN + FP + FN)}, \quad (2)$$

$$\text{Sensitivity} = \frac{TP}{TP + FN}, \quad (3)$$

$$\text{Specificity} = \frac{TN}{TN + FP}, \quad (4)$$

where TP indicates true positive, TN indicates true negative, FP indicates false positive, and FN indicates false negative.

## 2. Conclusion

It is one of the worst diseases that may be diagnosed anywhere in the world; the five-year survival rate is quite low. Pancreatic cancer is one of the worst tumors that can be diagnosed. One of the most common causes of this syndrome is pancreatic cancer, which accounts for the majority of cases. A sizeable percentage of cancer patients are now able to detect anomalies at earlier stages because to the increased availability of medical imaging scans. It is difficult

to propagate the technology because of the high cost of the necessary gear and infrastructure, which puts it out of reach for a significant number of people. This article discusses the use of machine PSO SVM and image processing for the purpose of detecting pancreatic cancer in CT scan pictures. The CLAHE method is applied during image preprocessing in order to clean up photos that have noise. The  $K$ -means method uses a partitioning technique to separate the image into its component parts. The process of identifying objects in an image and determining the regions of interest is aided by image segmentation. The PCA method is used to extract important information from digital photographs. PSO SVM, AdaBoost, and C4.5 are the algorithms that are utilized for the classification process.

## Data Availability

The data shall be made available on request.

## Conflicts of Interest

The authors declare that they have no conflict of interest.

## References

- [1] G. Suman, A. Patra, P. Korfiatis et al., "Quality gaps in public pancreas imaging datasets: implications & challenges for AI applications," *Pancreatology*, vol. 21, no. 5, pp. 1001–1008, 2021.
- [2] P. T. Chen, D. Chang, H. Yen et al., "Radiomic features at CT can distinguish pancreatic cancer from noncancerous pancreas," *Radiol Imaging Cancer*, vol. 3, no. 4, article e210010, 2021.
- [3] G. Suman, A. Panda, P. Korfiatis, and A. H. Goenka, "Convolutional neural network for the detection of pancreatic cancer on CT scans," *The Lancet Digital Health*, vol. 2, no. 9, article e453, 2020.
- [4] V. Jasti, A. Zamani, K. Arumugam et al., "Computational technique based on machine learning and image processing for medical image analysis of breast cancer diagnosis," *Security And Communication Networks*, vol. 2022, Article ID 1918379, 7 pages, 2022.
- [5] D. P. Ryan, T. S. Hong, and N. Bardeesy, "Pancreatic adenocarcinoma," *The New England Journal of Medicine*, vol. 371, no. 11, pp. 1039–1049, 2014.
- [6] B. Kenner, S. T. Chari, D. Kelsen et al., "Artificial intelligence and early detection of pancreatic cancer," *Pancreas*, vol. 50, no. 3, pp. 251–279, 2021.
- [7] S. Chaudhury, A. N. Krishna, S. Gupta et al., "Effective image processing and segmentation-based machine learning techniques for diagnosis of breast cancer," *Computational and Mathematical Methods in Medicine*, vol. 2022, Article ID 6841334, 6 pages, 2022.
- [8] A. S. Zamani, L. Anand, K. P. Rane et al., "Performance of machine learning and image processing in plant leaf disease detection," *Journal of Food Quality*, vol. 2022, Article ID 1598796, 7 pages, 2022.
- [9] S. Suhas and C. R. Venugopal, "An efficient MRI noise removal technique using linear and nonlinear filters," *International Journal of Computer Applications*, vol. 179, no. 15, pp. 17–20, 2018.

## Retraction

# Retracted: Prognostic Diagnosis for Breast Cancer Patients Using Probabilistic Bayesian Classification

### BioMed Research International

Received 8 January 2024; Accepted 8 January 2024; Published 9 January 2024

Copyright © 2024 BioMed Research International. This is an open access article distributed under the Creative Commons Attribution License, which permits unrestricted use, distribution, and reproduction in any medium, provided the original work is properly cited.

This article has been retracted by Hindawi following an investigation undertaken by the publisher [1]. This investigation has uncovered evidence of one or more of the following indicators of systematic manipulation of the publication process:

- (1) Discrepancies in scope
- (2) Discrepancies in the description of the research reported
- (3) Discrepancies between the availability of data and the research described
- (4) Inappropriate citations
- (5) Incoherent, meaningless and/or irrelevant content included in the article
- (6) Manipulated or compromised peer review

The presence of these indicators undermines our confidence in the integrity of the article's content and we cannot, therefore, vouch for its reliability. Please note that this notice is intended solely to alert readers that the content of this article is unreliable. We have not investigated whether authors were aware of or involved in the systematic manipulation of the publication process.

Wiley and Hindawi regrets that the usual quality checks did not identify these issues before publication and have since put additional measures in place to safeguard research integrity.

We wish to credit our own Research Integrity and Research Publishing teams and anonymous and named external researchers and research integrity experts for contributing to this investigation.

The corresponding author, as the representative of all authors, has been given the opportunity to register their agreement or disagreement to this retraction. We have kept a record of any response received.

### References

- [1] N. Junath, A. Bharadwaj, S. Tyagi, K. Sengar, M. N. S. Hasan, and M. Jayasudha, "Prognostic Diagnosis for Breast Cancer Patients Using Probabilistic Bayesian Classification," *BioMed Research International*, vol. 2022, Article ID 1859222, 10 pages, 2022.

## Research Article

# Prognostic Diagnosis for Breast Cancer Patients Using Probabilistic Bayesian Classification

**N. Junath** <sup>1</sup>, **Alok Bharadwaj** <sup>2</sup>, **Sachin Tyagi** <sup>3</sup>, **Kalpna Sengar** <sup>4</sup>,  
**Mohammad Najmus Saquib Hasan** <sup>5</sup> and **M. Jayasudha** <sup>6</sup>

<sup>1</sup>The University of Technology and Applied Science Ibri Sultanate of Oman, Oman

<sup>2</sup>Department of Biotechnology, GLA University, Mathura, India

<sup>3</sup>Bharat Institute of Technology, School of Pharmacy Meerut, India

<sup>4</sup>Biosense Lifecare Research and Development Laboratory, Kalphelix Biotechnologies, Kanpur 208011, India

<sup>5</sup>Wollega University, Nek'emtē, Ethiopia

<sup>6</sup>School of Computer Science and Engineering, Vellore Institute of Technology, Chennai, India

Correspondence should be addressed to Mohammad Najmus Saquib Hasan; mohammadk@wollegauniversity.edu.et

Received 6 June 2022; Revised 6 July 2022; Accepted 15 July 2022; Published 25 July 2022

Academic Editor: Gaganpreet Kaur

Copyright © 2022 N. Junath et al. This is an open access article distributed under the Creative Commons Attribution License, which permits unrestricted use, distribution, and reproduction in any medium, provided the original work is properly cited.

The diagnosis and treatment of patients in the healthcare industry are greatly aided by data analytics. Massive amounts of data should be handled using machine learning approaches to provide tools for prediction and categorization to support practitioner decision-making. Based on the kind of tumor, disorders like breast cancer can be categorized. The difficulties associated with evaluating vast amounts of data should be overcome by discovering an efficient method for categorization. Based on the Bayesian method, we analyzed the influence of clinic pathological indicators on the prognosis and survival rate of breast cancer patients and compared the local resection value directly using the lymph node ratio (LNR) and the overall value using the LNR differences in effect between estimates. Logistic regression was used to estimate the overall LNR of patients. After that, a probabilistic Bayesian classifier-based dynamic regression model for prognosis analysis is built to capture the dynamic effect of multiple clinic pathological markers on patient prognosis. The dynamic regression model employing the total estimated value of LNR had the best fitting impact on the data, according to the simulation findings. In comparison to other models, this model has the greatest overall survival forecast accuracy. These prognostic techniques shed light on the nodal survival and status particular to the patient. Additionally, the framework is flexible and may be used with various cancer types and datasets.

## 1. Introduction

Breast cancer is the one of most common malignant tumors in women in my nation and the sixth-largest cause of cancer-related mortality [1]. Breast cancer incidence and death among Chinese women have been rising fast in recent years, with certain places seeing considerable and rapid increases [2, 3]. To minimize patient mortality, researchers must study and select more effective treatment plans, or design specific treatment plans for patients, both of which rely on accurate prognostic analysis and patient survival prediction.

Based on one or more predictor variables, the logistic method is used to predict the class (or category) of persons ( $x$ ). It is used to simulate a binary result, or a variable with only two potential values, such as 0 or 1, yes or no, or sick or not. The main goal of using logistic regression analysis is to make sure that it is the best analytical form that can assign data to groups when the dependent variable in various scientific domains has two or more levels and the control variables are both discontinuous and continuous. Whereas by microscopic inspection of suspicious tissue that has been removed via biopsy or surgical resection, the histological type is identified. If the tissue under examination

exhibits a different histological type than what is typically seen there, it may indicate that the cancer is spreading there from a primary location. Medical students benefit much from studying histology in a variety of ways. It aids students in comprehending how tissues and cells are arranged in a typical organ system. Additionally, it links the development of different tissues to each function, which links structure to function.

In the study of the prognostic factors of cancer, the researchers found that there are many factors affecting the prognostic level of patients, and they can be roughly divided into the following three categories: First, the demographic and genetic characteristics of patients, such as the incidence of patients' age and whether they carry breast cancer susceptibility genes; second, disease characteristics, such as tumor location, size, and histological grade; third, treatment options, such as chemotherapy and immunotherapy [4]. At present, a large number of statistical methods have been analyzed and studied on the above factors, to quantify the influence of these factors on the prognosis of patients [5, 6]. The Bayesian method gives no instructions on how to choose a precedent. The selection of a previous can be done in any method. The ability to convert irrational prior beliefs into mathematically specified prior is necessary for Bayesian findings. Without exercising caution, you might produce false findings. It may result in posterior distributions with strong previous impact. Practically speaking, it could occasionally be challenging to persuade subject-matter experts who disagree with the accuracy of the selected prior. It frequently has a significant computational cost, particularly in models with several parameter choices. In addition, if a different random seed is used, simulations provide somewhat different results. It should be noted that minor deviations in simulation results do not refute the initial assertion that Bayesian judgments are precise. Given the log-likelihood and the priors, the posterior distributions of a parameter are accurate; however, simulation-based estimations of the posterior numbers might vary depending on the random number employed in the methods.

The first step in the prognostic analysis is to determine which factors have the most significant effect. Among the various factors listed above, some factors are highly correlated or even redundant and cannot provide more information. Since the follow-up investigation of the patient's prognosis requires a lot of time and economic cost, the first step in establishing a survival prediction model is to select significant prediction features to make the prediction model as concise as possible, that is, under the premise of obtaining almost the same amount of information, select the model with the least amount of features. At present, the commonly used feature selection methods include forward feature selection, reverse feature selection, or the use regression model for univariate analysis to select features with greater influence weights. In this paper, after referring to a large number of literature and comparing the advantages and disadvantages of various feature selection methods [7, 8], the commonly used reverse feature selection method is selected, and the most significant factors are selected for prognostic analysis, of which LNR is one of the most significant

disease-characterizing factors. Recent research suggests that LNR, as opposed to the number of positive nodes alone, is better good at predicting overall survival and relapse survival rate. It is regarded as a significant prognostic factor in the gastrointestinal system, breast, bladder, and pancreatic cancers. LNR has been found to have a stronger predictive value than the lymph node phase. Due to its simplicity and repeatability, LNR can be used in the follow-up of many cancers. There has not been established a unified and widely accepted appropriate cut-point for LNR despite numerous studies on epithelial malignancies. Divergences may be caused by variations in sample sizes, inclusion requirements, disease kinds, assessment criteria, and statistical techniques.

LNR is one of the most important variables in cancer prognosis analysis, especially for recurrence risk. This trait improves cancer prognosis and survival rate. Author [9] discovered that the metastatic lymph node ratio predicts survival in cervical squamous cell carcinoma patients. The author used LNR and other parameters to use the standard Bayesian model to predict pancreatic cancer patient's survival rate and survival rate [4]. The author analyzed 2591 Sun Yat-sen University Cancer Center medical data from 1998 to 2007 using a standard regression model and found that breast cancer patients with lower LNR levels were more likely to have breast cancer. LNR predicts overall, disease-free, and metastasis-free survival [10].

LNR utilizes the number of positive lymph nodes on a slide divided by the total number seen. The test's LNR result may differ greatly from the patient's real LNR. Total lymph nodes in the test sample are simply a local observation. This causes a substantial difference between the experimental LNR and the patient's real LNR. More lymph nodes identified during slice identification means a more accurate LNR value. The LNR test result obtained from total identified lymph nodes and positive lymph nodes is an approximation of the patient's genuine LNR [4]. In this work, extra pathological characteristics were incorporated to enhance LNR estimation accuracy, and the LNR value was calculated using the logistic regression technique to provide a closer assessment of the patient's total LNR. In this paper's simulation, the overall LNR estimate based on logistic regression and the LNR local cutoff value were compared on prognostic analysis.

As mentioned previously, the overall estimates of LNR based on logistic regression models are important clinical features for prognostic analysis. At present, the classical regression model is widely used in prognostic analysis to predict the survival rate of patients. This model was proposed by a British statistician in 1972 [11], and its basic idea is to express the survival rate of patients as a risk function, that is, the probability of death of an individual in a certain unit of time during the survival process. The regression model is a semiparametric survival analysis model [12].

Compared with the parametric model [13], its conditions are more relaxed, and the survival data does not need to meet a certain distribution in advance. Compared with the parametric model, its test efficiency is relatively higher, and the survival function and the benchmark risk function can be obtained at the same time when the survival

distribution and benchmark risk function of the data are unknown. It is these advantages that make the classic regression model popular and widely used in the decades after it was proposed. However, in a classic regression model, the covariate coefficients are always constant and cannot reflect the dynamic effects of predictors on survival over time [14]. By combining the prior knowledge of each parameter and the observation data, the posterior distribution of the parameters was inferred and continuously updated, to better capture the prediction variables in different time intervals' effect on survival.

Figure 1 shows this study's flowchart. First, SEER samples were selected (The Surveillance, Epidemiology, and End Results). 20-80-year-old women with breast cancer and at least one lymph node diagnosed between 2010 and 2012. Due to differences in overall survival rates across breast cancer subtypes [15], this investigation included only "Her2-/HR+" patients. 4,402 samples were obtained after screening. Table 1 lists the samples. The leftover features are utilized for survival analysis after LNR features are chosen via reverse feature selection. Total lymph nodes, number of positive lymph nodes, M stage, and N stage have the greatest relationship with LNR, according to the Akaike Information Criterion (AIC) index. These are utilized to train a logistic regression model and estimate the LNR value. In the prognostic study, a dynamic Bayesian regression model was created to predict patient survival using overall LNR estimates as well as patient age, tumor size, and T stage.

**1.1. Implications of Machine Learning in Breast Cancer Detection.** Cancer has been described as a diverse illness with a wide range of subgroups. Early cancer diagnosis and prognosis are essential for clinical patient treatment, which has become a requirement in cancer research. Numerous research teams from the biomedical and bioinformatics fields have studied the use of machine learning (ML) techniques due to the significance of classifying cancer sufferers into high- or low-risk categories. These methods have been applied to stimulate the development and management of malignant diseases.

Furthermore, their significance is demonstrated by the fact that ML algorithms can recognize important characteristics in complicated datasets. Artificial Neural Networks (ANNs), Bayesian Networks (BNs), Support Vector Machines (SVMs), and Decision Trees (DTs) are a few of the methods that have been widely used in cancer research to construct prediction models that enable precise and effective decision-making. Although using ML techniques can enhance our comprehension of how cancer progresses, further validation is required before these techniques can be used in routine clinical practice. The author et al. did a comparative analysis of breast cancer detection using machine learning and biosensors. They found that automation is required since ML and biosensors are required to detect tumors from microscopic pictures. The goal of ML is to help computers learn for themselves. It is built on pattern recognition in observed data and creating models to anticipate outcomes rather than depending on specific pre-programmed rules and models [16]. The author et al. con-

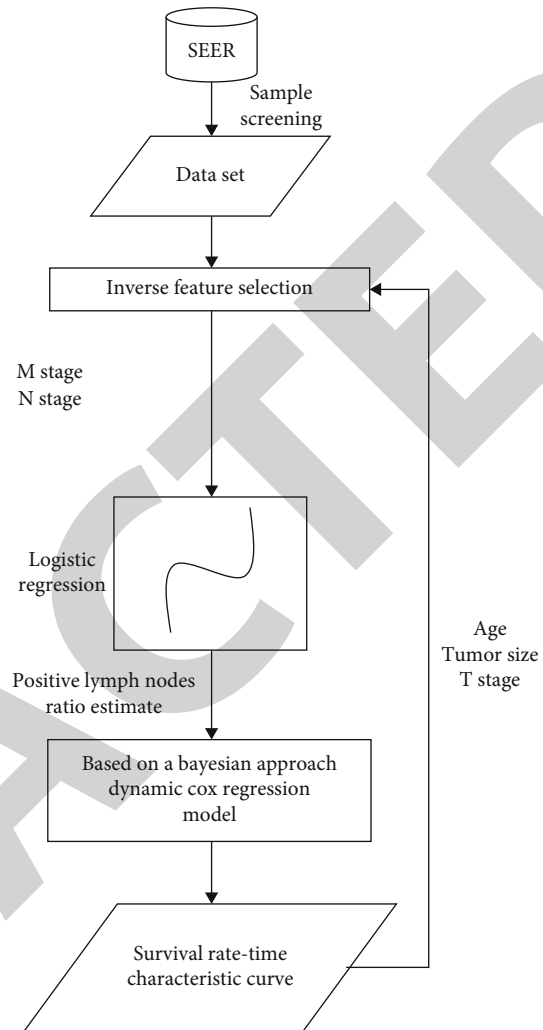


FIGURE 1: Overall flowchart.

cluded that the most effective algorithm for detecting breast cancer is XGboost, which has a 98.24 percent effectiveness rate. The dataset must first be processed, though, before the method can be executed [17].

## 2. Data and Methods

**2.1. LNR Estimation Based on Logistic Regression Model.** LNR is computed by dividing the number of positive lymph nodes on a slice by the total number of lymph nodes. In reality, it is difficult to adequately depict the patient's total LNR by the LNR local resection value. This research evaluated additional relevant pathological information of LNR patients and used a logistic regression model to predict total LNR values. First, the LNR local cut value is used as the response feature, and the relevant pathological features are selected as input features through reverse feature selection. Then, the covariate coefficient is calculated by fitting the logistic regression model, and the patient's overall LNR is estimated using the covariate coefficient value.

The logistic regression model is a commonly used machine learning model, its form is relatively simple and



TABLE 1: Dataset sample characteristics.

Feature name	Value	Number of samples (percentage)	Mean
Track time	0~59	4405 (100)	37.89
State	Die	160 (3.8)	
	Survive	4250 (95.69)	
Total number of lymph nodes	1~84	4405 (100)	12.68
Number of positive lymph nodes	1~82	4405 (100)	4.71
	20~80	4405 (100)	57.12
Age at diagnosis	[20,30)	48 (1.3)	
	[30,40)	334 (8.6)	
	[40,50)	951 (26.34)	
	[50,60)	1064 (28.26)	
	[60,70)	975 (25.18)	
	[70,80]	520 (13.25)	
		T0	78 (1.9)
T stage	T1	1028 (32.8)	
	T2	1766 (40.4)	
	T3	600 (13.8)	
	T4	235 (5.6)	
	TX adjusted	58 (1.4)	
	Others	240 (5.5)	
		M0	4112 (94.12)
M stage	M1	240 (5.6)	
	M2	53 (1.4)	
	N1	2870 (65.4)	
N stage	N2	889 (20.11)	
	N3	588 (13.6)	
	NX adjusted	58 (1.2)	

intuitive, and it has good interpretability. In this paper, the regression analysis is performed using the range of the logistic regression model in the range of [0,1] to estimate the overall value of LNR within the same range. In this study, the basic form of the logistic regression model is as follows: for sample I, its response value, that is, the LNR value is  $Y_i$ ; 4 pathological features related to LNR are screened out through reverse feature selection as input features, which are positive lymph nodes, respectively. The number  $X_1$  is the total number of lymph nodes  $X_2$ , the M stage  $X_3$ , and the N stage  $X_4$ . According to the logistic regression model, the relationship between the LNR value  $Y_i$  of sample I and its corresponding predicted feature  $X_i$  is:

$$y_i = \frac{1}{1 + \exp[-(\beta_0 + \beta_1 X_{i,1} + \dots + \beta_4 X_{i,4})]} = \frac{1}{1 + \exp(-\beta^T X_i)}. \quad (1)$$

Among them,  $\beta_0$  is a constant term,  $\beta_1$ ,  $\beta_2$ ,  $\beta_3$ , and  $\beta_4$  are the covariate coefficients corresponding to each prediction feature, and  $\beta$  is a vector composed of the above covariate coefficients.  $X_{i,1}$ ,  $X_{i,2}$ ,  $X_{i,3}$ , and  $X_{i,4}$  are the four predic-

eigenvalues sample m IIe I, and  $X_i$  is a vector composed of the above pride eigenvalues. After fitting the logistic regression model with the training set data, the covariate coefficients  $\beta$  corresponding to all the predicted features are obtained. After that, according to the coefficient  $\beta$  and the prediction feature  $X_i$ , substituting Equation (1) can get the overall estimated value of LNR.

*2.2. Probabilistic Bayesian-Based Dynamic Regression Model.*  
The basic form of the classic regression model is:

$$\lambda(t | Z) = \lambda_0(t) \exp \{Z^T \beta_s\}. \quad (2)$$

The covariate coefficients in a standard regression model stay constant across time points. In practice, however, the effect of each predictor on patient survival is frequently time-varying. To this aim, the Bayesian dynamic regression model encodes the covariate coefficients at different time points as  $s(t)$ , and the posterior distribution is calculated using the Bayesian approach and the survival data. Wang et al. devised this approach, which is only briefly described in this work.

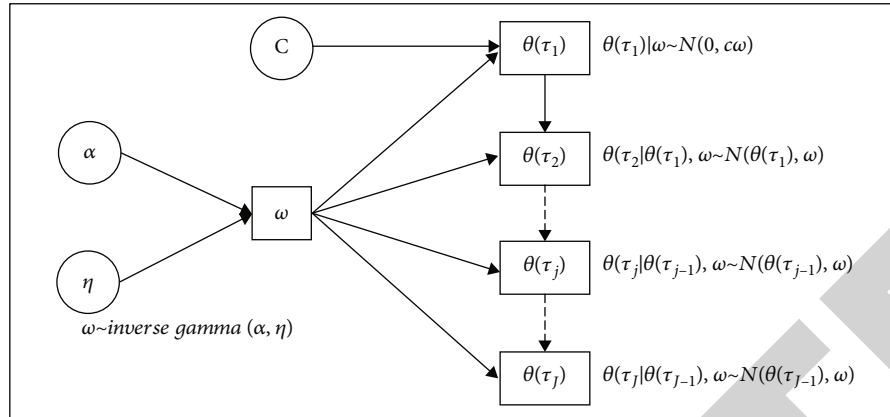


FIGURE 2: Prerelationship between parameters.

The dynamic regression model based on the Bayesian technique takes the following basic form:

$$\lambda(t | Z) = \lambda_0(t) \exp \{Z^T \beta_s(t)\}, \quad (3)$$

where  $Z$  is the matrix of predictors for all samples,  $\lambda_0(t)$  is the baseline risk at time  $t$ , and  $\beta_s(t)$  is the vector of covariate coefficients at time  $t$ . In this dynamic model, both  $\lambda_0(t)$  and  $\beta_s(t)$  are assumed to be left-continuous step functions. The reference risk function must be estimated in the model  $\lambda_0(t)$  and the covariate coefficient vector  $\beta_s(t)$  specific step times and corresponding step values and step time points to accomplish the goal of dynamic parameter estimation Let:  $\Theta = \{\ln \lambda_0(t), \beta_s(t); t > 0\}$ , All unknown parameters are included in the set., use  $\theta(t)$  to refer to  $\ln \lambda_0(t)$  or  $\beta_s(t)$  in an amount.

All unknown parameters are estimated from data samples. For sample  $i(i = 1, 2, \dots, n)$ , let  $T_i$  denote the time at which the event “patient death” occurred. If  $T_i$  is known, the sample data is complete survival data. If only  $T_i \in [L_i, R_i)$  can be determined and  $R_i$  is a finite value, the sample data is interval-censored; if  $R_i = \infty$ , the sample data is right-censored. Let  $\Delta k = SK - SK_{-1}$  represent the width of the  $k^{\text{th}}$  grid interval, and count  $\lambda_k = \lambda_0(SK), \beta_k = \beta(SK)$ . Finally, let  $Dobs = \{Ti \in [Li, Ri), Zi; i = 1, 2, \dots, n\}$ ; this set represents the survival information of all samples and the information of the predictor variables related to the survival analysis.

In dynamic models, a Bayesian approach as:

$$(o | x) = p(o) \frac{p(x | o)}{p(x)} \propto p(o)L(x | o). \quad (4)$$

This formula says that the posterior distribution of the parameters is proportional to the product of the joint prior distribution  $p(o)$  of the parameters and the sample likelihood  $L(x | o)$ . Among them, the sample likelihood  $L(x | o)$  can be expressed as

TABLE 2: Coefficients of some predictors.

Predictor variable	Estimated value	Standard deviation
Intercept	0.227	0.084
Total number of lymph nodes	-0.183	0.015
Number of positive lymph nodes	0.367	0.029
M1	0.589	0.248
MX	-0.148	1.245
N2	0.505	0.141
N3	0.531	0.248
NX adjusted	0.298	0.173

$$(x | o) = \prod_{i=1}^N \Pr(T_i \in [L_i, R_i) | o, xZ_i), \quad (5)$$

where  $n$  is the total number of samples. The likelihood contribution of any one of the samples  $i$  is:

$$\Pr(T_i \in [L_i, R_i) | o, x_i) = \Pr(T_i > L_i | o, x_i) - \Pr(T_i > R_i | o, x_i). \quad (6)$$

In

$$\Pr(T_i > t | o, x_i) = \exp \left\{ - \sum_{k=1}^K I(s_k < t) \Delta_k \lambda_k \exp(x_i^T B_k) \right\}, \quad (7)$$

$I(\bullet)$  is the indicator function in the preceding formula; if  $\bullet$  is true,  $I(\bullet) = 1$ , else  $I(\bullet) = 0$ .

$$\begin{cases} \theta(\tau_1) | \omega \sim N(0, c\omega) \\ \theta(\tau_j | \theta(\tau_{j-1}), \omega \sim N(\theta(\tau_{j-1}), \omega), j = 2, 3, \dots, J \\ \omega \sim \text{Inverse Gamma}(\alpha, \eta) \end{cases} \quad (8)$$

The prior distribution hypothesis for that parameter at the preceding time interval is connected to the prior

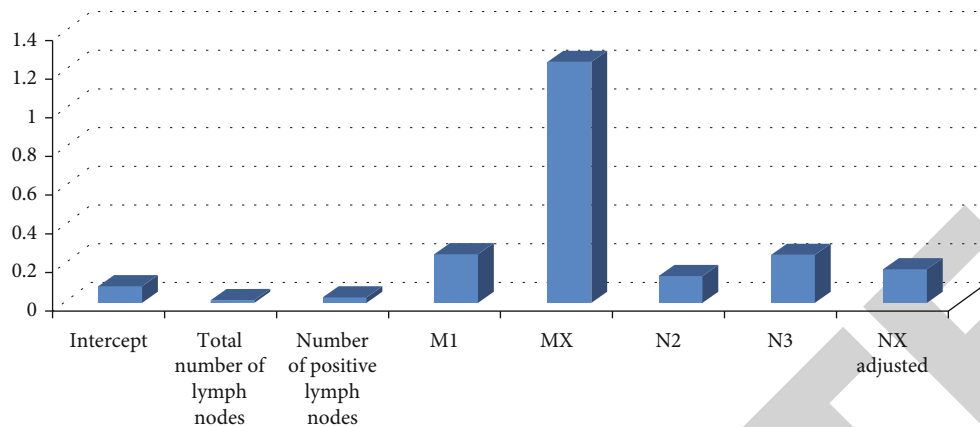


FIGURE 3: Predicted training and test set standard deviation coefficients.

distribution hypothesis for the covariate coefficients for each period. The link between the previous distribution assumptions for the parameters is shown in Figure 2. The circular box’s parameters are predetermined constants, and the box’s parameters only know which distribution they follow; therefore, the particular value must be approximated.

The joint prior distribution of  $\theta(t)$  and  $\omega$ ,  $\pi(\theta(t), \omega)$  is proportional to the following formula, according to the dynamic prior connection of the Bayesian framework and parameters given earlier: The joint prior distribution of  $\theta(t)$  and  $\omega$ ,  $\pi(\theta(t), \omega)$  is proportional to the following formula: dynamic prior connection of the Bayesian framework and parameters indicated earlier.

$$\text{alaomegala} \frac{\eta^\alpha}{\Gamma(\alpha)} \omega^{-\alpha-1} \exp\left(-\frac{\eta}{\omega}\right) \omega^{-j/2} \exp\left\{-\frac{\theta\tau_1^2}{2c\omega}\right\} \prod_{j>2} \exp\left\{-\frac{[\theta(\tau_j) - \theta(\tau_{j-1})]^2}{2\omega}\right\}. \quad (9)$$

$(\eta^\alpha/\Gamma(\alpha))\omega^{-\alpha-1} \exp(-\eta/\omega)$  is the probability density function of  $\omega$ , where the remainder is the product of the probability density functions of  $\theta(\tau_1), \theta(\tau_2), \dots, \theta(\tau_J)$ . For each  $\theta(t)$ , there is its corresponding  $\omega$ . The joint probability density of  $\Theta$  and  $\omega$  can be obtained by multiplying  $p + 1$  by Equation (9). Equations (5), (8), and (9) may be used to compute the posterior component of all parameters (9). The posterior distribution, however, cannot be determined directly owing to the complicated shape of the joint probability density  $\Theta$  and  $\omega$ . The posterior distribution is calculated using Gibbs Sampling for this purpose.

### 3. Simulation Results

For data processing and analysis, R Studio 1.0.143 was utilized, and the R language version used was 3.4.4, with 4402 samples screened in SEER. These samples are randomly separated into training and test sets throughout the simulation. The test set has 1402 samples, whereas the training set contains 3000 samples.

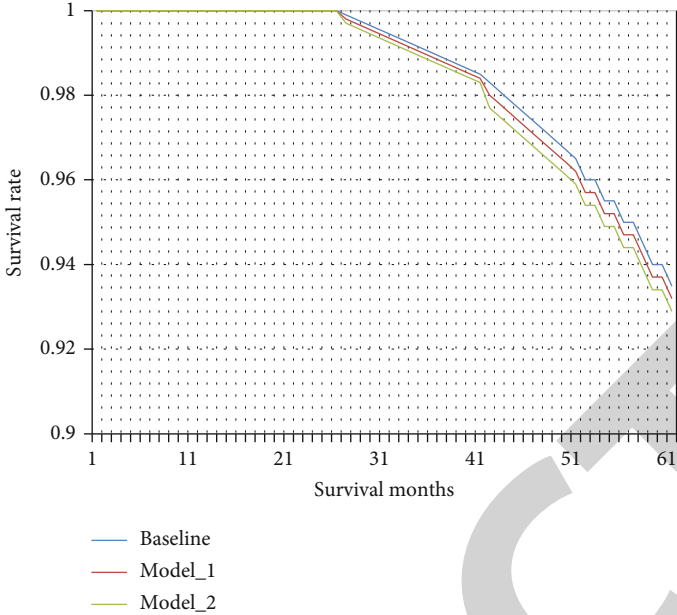
TABLE 3: Model features.

Name	LNR data	Survival analysis model	LPML
Model_1	Local cut value	Standard model	-719.45
Model_2	Overall estimate	Standard model	-705.81
Model_3	Local cut value	Dynamic model	-703.11
Model_4	Overall estimate	Dynamic model	-694.43

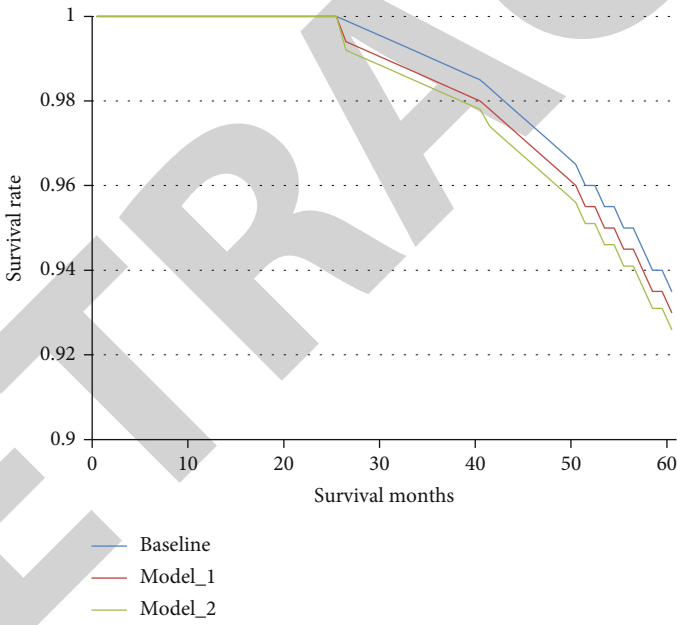
3.1. *LNR Estimation.* The number of positive lymph nodes, the total number of lymph nodes, the M stage, and the N stage were all utilized to determine the LNR value after reverse feature selection. The logistic regression model obtained the lowest AIC value in 1968 when these four characteristics were used. A low AIC score means the model can fit the data well with fewer parameters. Table 2 shows the covariate coefficients of certain predicted characteristics after logistic regression model training. The standard deviation of the two characteristics of a total number of lymph nodes and several positive lymph nodes is the lowest in the table, suggesting that these two characteristics have the strongest link with LNR.

To judge whether there is an overfitting problem, the MSE of the training set and the test set data after fitting the logistic probability regression model are calculated, respectively. After calculation, the MSE value of the training set data after fitting the model is 0.019, and the MSE value of the test set data is 0.021. The two are on the same order of magnitude and the gap is small. According to this judgment, the logistic probability regression model after training has no overfitting phenomenon. In the subsequent calculation process, it is feasible to use the LNR value estimated by this model. Figure 3 shows the predicted training and test set standard deviation coefficients.

3.2. *Subsistence Analysis.* To test the predictive effect of the overall estimate of LNR on patient survival, two datasets were used in this study in the survival analysis section. Both contain patient survival information, T and N stage information, age at diagnosis, and tumor size; the only difference is that dataset 1 uses LNR local resection values and dataset 2 uses LNR overall estimates. Furthermore, so that the

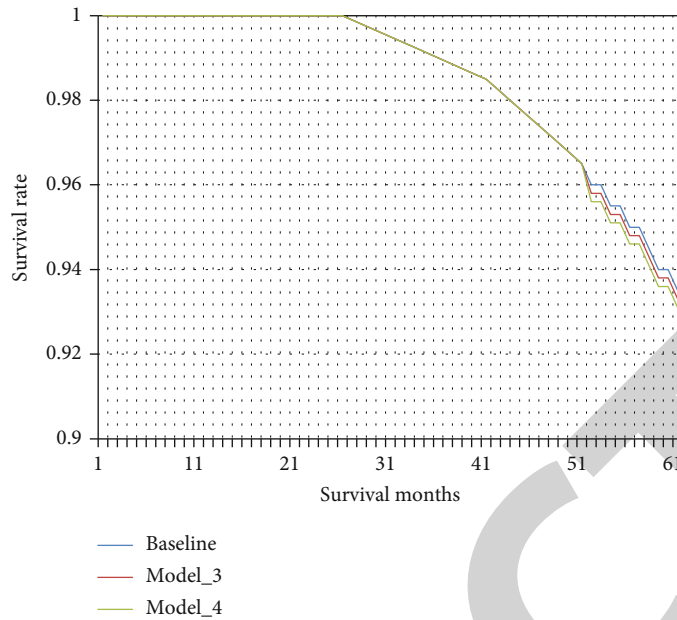


(a) Comparison of Model\_1 and Model\_2 predicted training set curves and actual curves

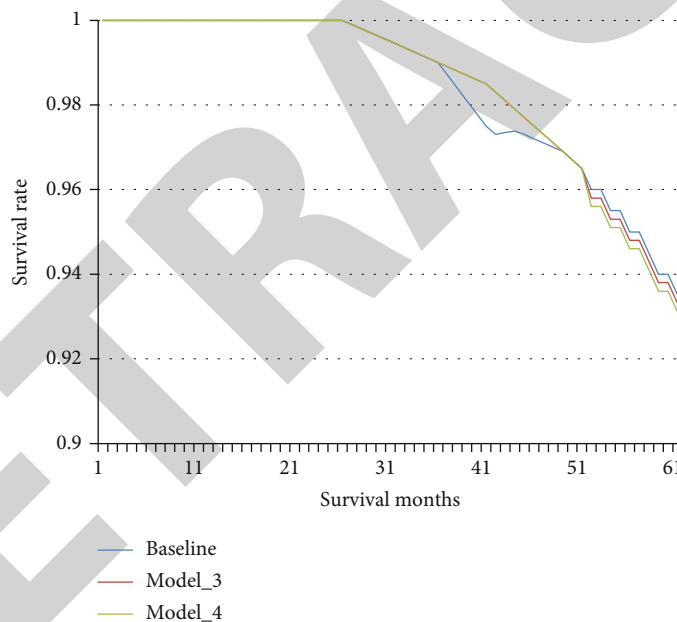


(b) Comparison of the predicted test set curves of Model\_1 and Model\_2 with the actual curves

FIGURE 4: Continued.



(c) Comparison of Model\_3 and Model\_4 predicted training set curves and actual curves



(d) Comparison of the predicted test set curves of Model\_3 and Model\_4 with the actual curves

FIGURE 4: Predicted training and test set survival-time curves.

dynamic regression model based on the Bayesian method can better reflect the influence of predictors on the survival rate of patients at different time stages, this paper uses the classical regression model and the dynamic regression model, respectively. Therefore, different datasets were paired with different survival analysis models, resulting in a total of 4 model models to compare the difference in results between them. The main features of the four models are shown in Table 3. All models were set to 500 Gibbs samples.

In this paper, the Log Pseudo Marginal Likelihood (LPML) is used as the evaluation index of the survival analysis model. For the model, the larger the value of this indica-

tor is, the more the sample supports the model. The LPML values of the four models are -719.45, -705.81, -703.11, and -694.43. As shown in Table 3, the LPML value of Model\_2 is larger than that of Model\_1. Likewise, the LPML value of Model\_4 is greater than the LPML value of Model\_3. Based on this numerical comparison, it can be seen that using the LNR overall estimate has a relatively good model fit. Also, the LPML values of Model\_3 and Model\_4 are higher than those of Model\_1 and Model\_2. This result shows that the dynamic regression model based on the Bayesian method can better fit the survival data than the classical regression model.

To judge the effect of the model more intuitively, the overall survival rate-time curves obtained by analyzing the training set and test set data of the four models were drawn. In comparison, the overall survival rate-time curve of patients was drawn using the Kaplan-Meier method (hereinafter referred to as the KM method). It is closer to the KM curve, indicating that the prediction effect of the model is relatively better. Shown in Figure 4 are the survival-time curves for the training and test set data predicted by the four models. As can be seen from the figure, Model\_1 and Model\_2 using the classical regression model perform worse than Model\_3 and Model\_4 using the dynamic model on both the training set and the test set. The overall survival-time curve predicted by the dynamic model is closer to reality. In addition, the curves obtained by Model\_3 and Model\_4 on the training set and test set are relatively close, but it can still be seen that the Model\_4 curve has a relatively good prediction effect, and Model\_4 has a lower LPML value. This suggests that the survival-time characteristic curve can be more accurately predicted using the overall estimate of LNR.

#### 4. Conclusion

This paper points out two important problems in breast cancer prognosis analysis and proposes corresponding solutions: one is that the LNR value obtained by the experimental detection is greatly affected by the observation error, which has deviations in the subsequent survival analysis process; regression models were unable to capture the dynamic effects of cancer-related factors on patient survival across time intervals. For the first question, this study first used logistic regression to estimate the LNR population value and then used the LNR population estimate value with other predictor variable information and survival data to fit a Bayesian method-based dynamic regression model. Compared with the use of LNR local cutoff values, the use of estimated values reduces the effect of the smaller total number of lymph node tests on the LNR value, as well as the effect of individual differences between patients on the LNR value. For the second problem, using the dynamic regression model based on the Bayesian method can better capture the impact of different time stages and predict the impact of characteristics on the survival rate of patients; The Bayesian method of the empirical distribution predicts the parameters more accurate.

The data set used in this article is part of the data of female breast cancer patients in SEER, and the algorithm is implemented using R language. To verify the performance of the method described in the paper, LPML values are used as a measure of model performance. Simulation results show that the model using the LNR estimate and the Bayesian-based dynamic regression method has the highest LPML value, indicating that the data best supports the model. In addition, to verify the prediction effect of the model, the survival rate-time curve of the test set data was calculated using the KM method and used as a benchmark, which was compared with that predicted by the logistic regression model to estimate LNR and the dynamic survival analysis model based on the Bayesian method. Survival-time curves were

compared. The results show that the two curves have many overlaps, and the trends are consistent. In future research, we can continue to explore the predictive effect of LNR on the survival rate of cancer patients, and try to use other machine learning methods, such as decision trees and random forests, to estimate the LNR value. The predictive value of the lymph node ratio (LNR), which is measured as the percentage of positive nodes tested, has attracted attention more lately. However, there are not enough statistical techniques to model LNR and its impact on cancer survival together. T and M stages as well as histologic grade were significantly predictive of LNR status. Age, gender, marital status, grade, histology, T and M stages, tumor size, and radiation treatment were all significant predictors of survival. An extremely significant, nonlinear influence of LNR on survival was discovered. Furthermore, the survival model's prediction ability outperformed that of studies using predictors with more customized and uniform patient populations. The understanding and management of illness rely heavily on prognostic models. These prognostic techniques shed light on the nodal survival and status particular to the patient. Additionally, the framework is flexible and may be used with various cancer types and datasets.

The probabilistic technique has the benefit of allowing current models to be expanded with previous information. This may be done at both the structural and parameter levels. This will have an effect on the variables that appear in the Markov blanket, resulting in an attribute selection approach based on data and previous biological knowledge, with automated tweaking of the data-prior knowledge balance. Furthermore, because Bayesian networks are not tailored for classification and instead provide a more generic framework by modeling a multidimensional probability distribution; the claimed performance may be improved by employing more traditional classifiers. We are now researching the usage of Bayesian networks as feature selectors, accompanied by Least Squares Support Vector Machines for classification.

#### Data Availability

The data shall be made available on request.

#### Conflicts of Interest

The authors declare that they have no conflict of interest.

#### References

- [1] American Cancer Society, *Global Cancer Facts & Figures 4th Edition*, American Cancer Society, Atlanta, 2018.
- [2] Z.-G. Yu, C.-X. Jia, L.-Y. Liu et al., "The prevalence and correlates of breast cancer among women in Eastern China," *PLoS One*, vol. 7, no. 6, article e37784, 2012.
- [3] N. Howlader, A. M. Noone, M. Krapcho et al., *SEER Cancer Statistics Review 1975-2014*, H. S. Chen, E. J. Feuer, and K. A. Cronin, Eds., National Cancer Institute, Bethesda, MD, 2017, [https://seer.cancer.gov/csr/1975\\_2014/](https://seer.cancer.gov/csr/1975_2014/) November 2016 SEER.
- [4] J. Teng, A. Abdygametova, J. Du et al., "Bayesian inference of lymph node ratio estimation and survival prognosis for breast

## Retraction

# Retracted: Cyclic GAN Model to Classify Breast Cancer Data for Pathological Healthcare Task

### BioMed Research International

Received 8 January 2024; Accepted 8 January 2024; Published 9 January 2024

Copyright © 2024 BioMed Research International. This is an open access article distributed under the Creative Commons Attribution License, which permits unrestricted use, distribution, and reproduction in any medium, provided the original work is properly cited.

This article has been retracted by Hindawi following an investigation undertaken by the publisher [1]. This investigation has uncovered evidence of one or more of the following indicators of systematic manipulation of the publication process:

- (1) Discrepancies in scope
- (2) Discrepancies in the description of the research reported
- (3) Discrepancies between the availability of data and the research described
- (4) Inappropriate citations
- (5) Incoherent, meaningless and/or irrelevant content included in the article
- (6) Manipulated or compromised peer review

The presence of these indicators undermines our confidence in the integrity of the article's content and we cannot, therefore, vouch for its reliability. Please note that this notice is intended solely to alert readers that the content of this article is unreliable. We have not investigated whether authors were aware of or involved in the systematic manipulation of the publication process.

Wiley and Hindawi regrets that the usual quality checks did not identify these issues before publication and have since put additional measures in place to safeguard research integrity.

We wish to credit our own Research Integrity and Research Publishing teams and anonymous and named external researchers and research integrity experts for contributing to this investigation.

The corresponding author, as the representative of all authors, has been given the opportunity to register their agreement or disagreement to this retraction. We have kept a record of any response received.

### References

- [1] P. Chopra, N. Junath, S. K. Singh, S. Khan, R. Sugumar, and M. Bhowmick, "Cyclic GAN Model to Classify Breast Cancer Data for Pathological Healthcare Task," *BioMed Research International*, vol. 2022, Article ID 6336700, 12 pages, 2022.

## Research Article

# Cyclic GAN Model to Classify Breast Cancer Data for Pathological Healthcare Task

Pooja Chopra <sup>1</sup>, N. Junath <sup>2</sup>, Sitesh Kumar Singh <sup>3</sup>, Shakir Khan <sup>4</sup>, R. Sugumar <sup>5</sup>, and Mithun Bhowmick <sup>6</sup>

<sup>1</sup>School of Computer Applications, Lovely Professional University, Phagwara, Punjab, India

<sup>2</sup>University of Technology and Applied Science Ibri, Oman

<sup>3</sup>Department of Civil Engineering, Wollega University, Nekemte, Oromia, Ethiopia

<sup>4</sup>College of Computer and Information Sciences, Imam Mohammad Ibn Saud Islamic University (IMSIU), Riyadh, Saudi Arabia

<sup>5</sup>Department of Computer Science and Engineering, Saveetha School of Engineering, Saveetha Institute of Medical and Technical Sciences, Chennai 601205, India

<sup>6</sup>Bengal College of Pharmaceutical Sciences and Research, Durgapur, West Bengal, India

Correspondence should be addressed to Sitesh Kumar Singh; [sitesh@wollegauniversity.edu.et](mailto:sitesh@wollegauniversity.edu.et)

Received 19 May 2022; Revised 25 June 2022; Accepted 4 July 2022; Published 21 July 2022

Academic Editor: Gaganpreet Kaur

Copyright © 2022 Pooja Chopra et al. This is an open access article distributed under the Creative Commons Attribution License, which permits unrestricted use, distribution, and reproduction in any medium, provided the original work is properly cited.

An algorithm framework based on CycleGAN and an upgraded dual-path network (DPN) is suggested to address the difficulties of uneven staining in pathological pictures and difficulty of discriminating benign from malignant cells. CycleGAN is used for color normalization in pathological pictures to tackle the problem of uneven staining. However, the resultant detection model is ineffective. By overlapping the images, the DPN uses the addition of small convolution, deconvolution, and attention mechanisms to enhance the model's ability to classify the texture features of pathological images on the BreakHis dataset. The parameters that are taken into consideration for measuring the accuracy of the proposed model are false-positive rate, false-negative rate, recall, precision, and F1 score. Several experiments are carried out over the selected parameters, such as making comparisons between benign and malignant classification accuracy under different normalization methods, comparison of accuracy of image level and patient level using different CNN models, correlating the correctness of DPN68-A network with different deep learning models and other classification algorithms at all magnifications. The results thus obtained have proved that the proposed model DPN68-A network can effectively classify the benign and malignant breast cancer pathological images at various magnifications. The proposed model also is able to better assist the pathologists in diagnosing the patients by synthesizing the images of different magnifications in the clinical stage.

## 1. Introduction

The most definitive criterion for detecting breast disorders is a histological examination of breast tissue [1]. To aid pathologists in diagnosis, the traditional auxiliary diagnostics employ edge detection to segment cell nuclei [2]. Support vector machines [3], random forest [4], and other machine learning-based approaches employ artificially derived features for modelling and classification [5, 6]. The classification accuracy is low because pathological pictures typically have considerable differences [7], feature extraction relies on high professional expertise, and comprehensive feature

extraction is challenging. Deep learning can overcome the limits of manual feature extraction and extract complicated nonlinear characteristics automatically, which has become increasingly popular in the categorization of diseased pictures [8]. In literature [9] on the BreakHis dataset, the classification accuracy of the patient-level and image-level classifications was 90 percent and 85.6 percent, respectively, based on the AlexNet model paired with the maximum fusion approach for classification. Literature [10] used a single-task CNN model to train two CNN (convolutional neural network). Breast cancer can occur in two different categories [22–24], namely, benign [25] and malignant



[26], and is a difficult task for pathologists to identify the type of cancer. Benign tumors are not cancerous, but on the other hand, malignant tumors are cancerous. A benign tumor [27] can be formed anywhere on or in the patient's body when cells multiply more than they should or they do not die when they should [30, 31]. Therefore, different machine learning techniques like logistic regression, naïve Bayes, and SVM [28, 29] and deep learning techniques like CNN, RNN, and neural networks [32, 33] are used in the field of healthcare for the detection purposes [34, 35]. Multitask CNN is utilized to predict malignant subtypes in breast cancer tumors, and the accuracy rates of binary and quaternary classification at the patient level are 83.25 percent and 82.13 percent, respectively. Literature [11] calculated that the average accuracy of binary classification at the patient level is 91 percent, according to GoogLeNet's fine-tuning learning process. Literature [12] introduced the msSE-ResNet (multiscale channel squeeze and excitation) multiscale channel recalibration model, which has 88.87 percent classification accuracy for benign and malignant tumors. Literature [13] created the BN-Inception (batch normalization-inception) model, which ignores magnification during training and achieves an accuracy rate of 87.79 percent on 40 diseased images. Literature [14] extracted characteristics using frequency domain information and classified them using long short-term memory (LSTM) and gated recurrent unit (GRU), with a classification accuracy of 93.01 percent. These findings show that deep learning-based approaches for pathological picture categorization are successful.

Inconsistency in staining is a common concern with different batches of pathology pictures. The classification accuracy will be reduced if these samples are used to train the classification model. Pathological pictures include rich textural characteristics and little semantic information. To increase classification accuracy, additional medium- and low-level characteristics must be extracted. To address the aforementioned issues, this research provides an approach based on CycleGAN and an upgraded DPN, as well as a color normalizing technique based on CycleGAN, to mitigate the influence of dyeing issues on classification accuracy. The DPN is used to extract and classify features automatically. To increase the picture classification accuracy, we use improvement methods including tiny convolution, deconvolution layer, and attention mechanism, as well as a discriminating approach based on confidence rate and voting mechanism.

The next section of the paper discussed some of the related work, followed by the algorithm description used in the research. Later on, the experiments involved in the research have been analyzed and finally conclusion has been discussed.

## 2. Related Work

**2.1. CycleGAN Structure.** In image generation, the generative adversarial network (GAN) [15] is commonly utilized. A generator and a discriminator form the foundation of the system. The loss function is continuously optimized to generate actual data, which is extremely close to pseudodata, through the game between the generator and the discrimina-

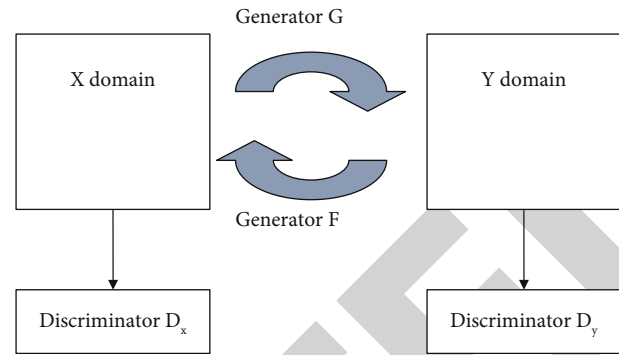


FIGURE 1: CycleGAN structure.

tor. The CycleGAN presented in literature [16] is a ring network structure based on GAN that can realize style transfer between unpaired images and ensure that the generated image's color changes while remaining consistent with the source image. The specifics have not changed.

Two generators and two discriminators make up CycleGAN. Figure 1 depicts the CycleGAN model structure. The generator is one of them, since it is used to create Y domain style images from the X domain, and the generator will create the Y domain image. Restore the image of the X domain [36]. The discriminator is used to make the image generated by the generator as close to the image of the Y domain style as possible, and the discriminator is used to make the image generated by the generator as close to the original image of the original X domain as possible so that when the image style is transferred, the features of the original image in the original X domain remain. Cycle consistency allows the CycleGAN to create more accurate and dependable pictures. The CNN classifier can also assist the producer in concentrating on lesion regions and obtaining prediction results. The differentiator and classification can help the generator perform accurate and dependable generating operations [37]. The advantage of cyclic GAN is that this model is faster than CNN as the model is more realistic in operation [38, 39]. Another benefit is that it does not require more preprocessing but suffers from time and space complexity like CNN and RNN [40]. The sigmoid loss function has been considered in the research. The loss function for the overall training of  $L_{GAN}(F, D_X, Y, X)$  CycleGAN consists of the following 3 parts.

- (1) The loss of X domain GAN, where the discriminator is  $D_X$  and the generator is  $F$
- (2) The loss of Y domain GAN, where the discriminator is  $D_Y$  and the generator is  $G$
- (3) Reconstruction error:  $L_{cyc} = L_{cyc}^X + L_{cyc}^Y$

The total loss of CycleGAN is

$$L(G, F, D_X, D_Y) = L_{GAN}(G, D_Y, X, Y) + L_{GAN}(F, D_X, Y, X) + \lambda L_{cyc}(G, F). \quad (1)$$

In the formula,  $\lambda$  is the weight coefficient.

- (1)  $L_{GAN}(G, D_Y, X, Y)$ : input the original  $X$  domain slice “ $a$ ” into the generator to generate slice  $a'$  with  $Y$  domain color features, and the discriminator judges whether slice  $a'$  belongs to the  $Y$  domain. The loss of the  $X$  domain GAN is

$$L_{GAN}(G, D_Y, X, Y) = E_{y \sim p_{data}(y)} [\log_2 D_Y(y)] + E_{x \sim p_{data}(x)} [\log_2 (1 - D_Y(G(x)))],$$

$$\min_G \max_{D_Y} L_{GAN}(G, D_Y, X, Y). \quad (2)$$

- (2)  $L_{GAN}(F, D_X, Y, X)$ : the original  $Y$  domain slice  $b$  is input to the generator to generate slice  $b'$  with  $X$  domain color features, and the discriminator judges whether slice  $b'$  belongs to the  $X$  domain. The loss of the  $Y$  domain GAN for

$$L_{GAN}(G, D_X, X, Y) = E_{x \sim p_{data}(x)} [\log_2 D_X(x)] + E_{y \sim p_{data}(y)} [\log_2 (1 - D_X(F(y)))], \quad (3)$$

where  $F$  represents the generator from the  $Y$  domain to the  $X$  domain,  $D_X$  is the discriminator, and  $F(y)$  is the generated false sample in the  $X$  domain. The goal of the generator  $F$  is to minimize  $L_{GAN}(F, D_X, Y, X)$ , and the objective of discriminator  $D_X$  is to maximize it, so the objective function is

$$\min_F \max_{D_X} L_{GAN}(F, D_X, Y, X). \quad (4)$$

- (3)  $cyc(G; F)$ : ideally, the original slice “ $a$ ” of the  $X$  domain and the restored slice  $a''$  of the  $X$  domain should be the same, but in fact, there is a difference between  $a$  and  $a''$ , and the difference between slice  $a$  and slice  $a''$  is counted as  $L_{cyc}^{X \rightarrow X}$ . In the original  $Y$  domain, the difference between slice  $b$  and restored slice  $b''$  in the  $Y$  domain is calculated as  $L_{cyc}^Y$

**2.2. DPN68 Network Structure.** DPN is a dual-path structure network based on ResNeXt and DenseNet [17]. It combines the advantages of ResNeXt and DenseNet and changes the output of each layer in addition to parallel so that each layer can directly obtain all previous. The output of the layer makes the model more fully utilize the features.

The DPN68 network structure is shown in Table 1. After a  $3 \times 3$  convolution operation and then a  $3 \times 3$  maximum pooling operation, it enters the block operation (the content of [a] in Table 1). Among them,  $\times 3$  means 3 cycles, the block of this parameter,  $G$ , refers to how many paths (i.e., the number of groups) are divided in a block of ResNeXt, and +16 represents the number of channels added each time in a block in DenseNet. The original DPN68 network goes through Conv3, Conv4, and Conv5, and softmax is used for multiclassification.

TABLE 1: DPN68 network structure.

Layer	DPN68 network structure
Conv1	$3 \times 3, 10, \text{stride } 2$
	$3 \times 3 \text{ max pool, stride } 2$
Conv2	$\begin{bmatrix} 1 \times 1, & 128 \\ 3 \times 3, & 128, G = 32 \\ 1 \times 1, & 256(+16) \end{bmatrix} \times 3$
Conv3	$\begin{bmatrix} 1 \times 1, & 256 \\ 3 \times 3, & 256, G = 32 \\ 1 \times 1, & 512(+32) \end{bmatrix} \times 4$
Conv4	$\begin{bmatrix} 1 \times 1, & 512 \\ 3 \times 3, & 512, G = 32 \\ 1 \times 1, & 1024(+32) \end{bmatrix} \times 12$
Conv5	$\begin{bmatrix} 1 \times 1, & 1024 \\ 3 \times 3, & 1024, G = 32 \\ 1 \times 1, & 2048(+32) \end{bmatrix} \times 3$
	Global average pooling layer, 1000-dimensional fully connected layer, softmax classifier

Figure 2 depicts the block structure of the DPN. The ResNeXt channel is on the top, and the DenseNet channel is on the bottom. Following the addition of the upper and lower channels, a 33% convolution and an 11% dimension transformation are performed. The output is separated, the upper path is combined with the upper path’s original input, and the lower path is merged with the lower path’s original input, generating a DPN block.

**2.3. Attention Model.** The study of human eyesight led to the discovery of the attention mechanism. Humans must choose certain portions to focus on to devote limited visual information processing resources to life. Attention may be applied to the input picture in neural networks. To increase the categorization accuracy of benign and malignant tumors, we partially assign different weights [18]. Figure 3 depicts the structure of the attention layer.

Adding attention layers is achieved through 3 operations named squeeze, excitation, and scale [19].

**2.3.1. Squeeze Operation.** Squeeze operation achieves feature compression for each channel through global pooling operation. The number of channels  $C$  remains unchanged so that the original size of the feature map of  $H \times W \times C$  becomes  $1 \times 1 \times C$ . The formula is as follows:

$$z_C = F_{sq}(u_C) = \frac{1}{H \times W} \sum_{i=1}^H \sum_{j=1}^W u_C(i, j). \quad (5)$$

In the formula,  $u_C(i, j)$  is the element of the  $i$ -th row and the  $j$ -th column of the two-dimensional matrix output by the deconvolution operation.

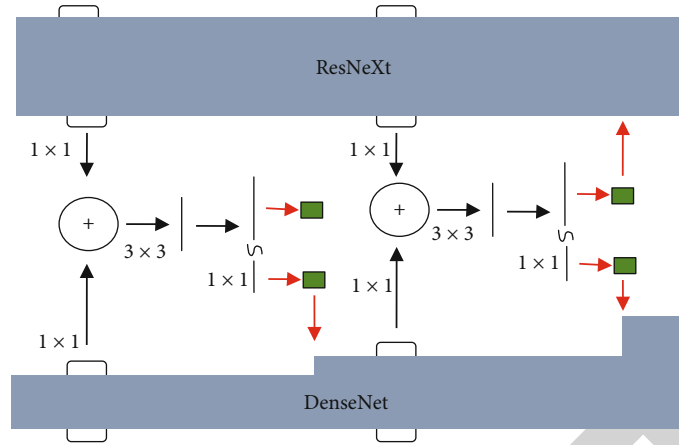


FIGURE 2: Block structure of DPN.

**2.3.2. Excitation Operation.** The excitation operation reduces the feature dimension to the original  $1/n$  through the fully connected layer, and after the activation of the ReLU function layer, it is restored to the original number of channels  $C$  through the fully connected layer, and the sigmoid function is used to generate the normalization weights.

$$s_C = F_{\text{ex}}(z_C, W_1, W_2) = \sigma(W_2 \delta(W_1 z_C)). \quad (6)$$

In the formula,  $0 < s_C < 1.0$ ;  $\sigma$  represents the sigmoid function;  $\delta$  represents the ReLU function, and the output is positive;  $W_1$  and  $W_2$  are the weight matrices of the two fully connected layers, respectively.

**2.3.3. Scale Operation.** The scale operation introduces an attention mechanism by weighting the normalized weight  $s_C$  to the features of each channel; that is, the channel input is multiplied by the weight coefficient and assigns different weights to the features of different dimensions. The weighting process formula is as follows:

$$F_{\text{scale}}(u_C, s_C) = s_C u_C. \quad (7)$$

### 3. Algorithm Description

To better enhance the pathological image classification accuracy, a model structure based on CycleGAN and DPN for image classification of pathological image is proposed, as shown in Figure 4.

The CycleGAN is used for color normalization of pathological images, that is, to convert pathological images of different colors to the same color to reduce the impact of color on classification. The DPN uses a 68-layer DPN model with an attention mechanism, which enhances the ability to classify pathological images.

- (1) Perform overlapping slice processing on the pathological images with the original size of  $700 \times 460$  pixels in the BreakHis dataset. Each original image is converted into 12 pathological image slices with the size of  $224 \times 224$  pixels

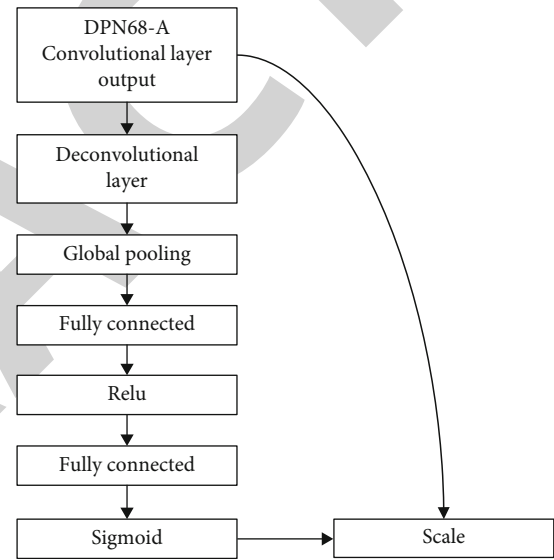


FIGURE 3: Attention mechanism structure.

- (2) According to the different colors of the pathological images in the dataset, a target color is selected, and the remaining color images are converted into target colors based on the CycleGAN to achieve color normalization
- (3) Data enhancement is carried out for the problem of unbalanced data. Data augmentation is carried out by flipping, rotating, fine-tuning, brightness, and contrast [20] so that the number of benign slices and the number of malignant slices reach a basic balance
- (4) Based on the DPN68 network, improve the classification accuracy by adding small convolution and deconvolution and introducing attention mechanism

**3.1. Color Normalization of Pathological Images Based on CycleGAN.** Due to the different doses of different doctors when dyeing pathological images, it is easy to cause different shades of stained pathological images, especially pathological

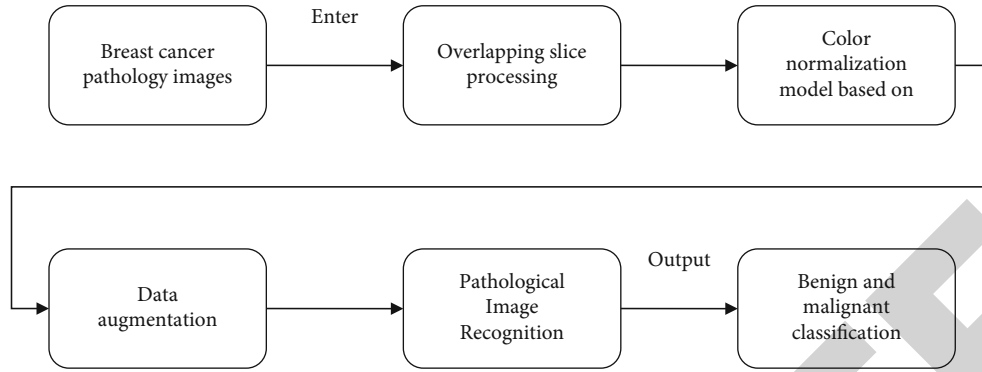


FIGURE 4: CycleGAN and DPN model.

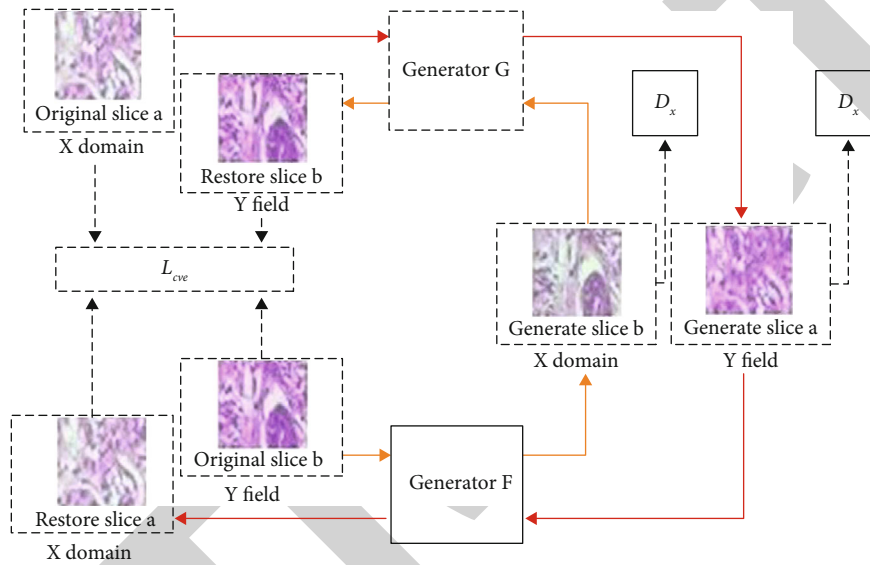


FIGURE 5: CycleGAN pathological image color normalization model.

TABLE 2: DPN68-A network structure.

Layer	DPN68 network structure
Conv1	1 × 1, 10, stride 1 3 × 3, 10, stride 2
Conv2~Conv5	Same as DPN68
Deconvolution layer	Deconv
Attenuation layer	Global pooling, fc, ReLu, fc, sigmoid, scale

TABLE 3: Number of benign and malignant tumor images with different magnifications.

A	$N_{ib}$	$N_{im}$	$N_i$
50	645	1365	1986
150	654	1498	2048
250	687	1354	2035
500	535	1289	1868

images of different periods, which are very different, such as original slice  $a$  and original slice  $b$  in Figure 5. The training and modeling of pathological images with different staining will lead to a decrease in the accuracy of the model, so it is necessary to perform color normalization on pathological images. The red arrows in Figure 5 indicate cycle loss, yellow arrows indicate GAN loss, and dotted arrows indicate  $L_{cyc}$ .

The generators  $G$  and  $F$  in CycleGAN have the same structure, which consists of three parts: encoder, converter, and decoder. The structures of discriminator  $D_x$  and discriminator  $D_y$  are the same, and they are composed of 5-layer convolutional neural networks.

The pathological image slices in the dataset are classified by color, and one of them is used as the  $Y$  domain image (target color image), and the rest of the color categories are used as the  $X$  domain image. The model framework of the pathological image color normalization based on CycleGAN is shown in Figure 5, the input is the  $X$  domain slice, and the output is the generated  $Y$  domain slice.

As shown in Figure 5, the input  $X$  domain slice  $a$  pass through the generator  $G$  to generate slice  $a'$  with the  $Y$  domain coloring feature, and the generator  $G$  continuously competes with the discriminator  $D_y$  to make the generated slice color as close to the  $Y$  domain as possible. Then input

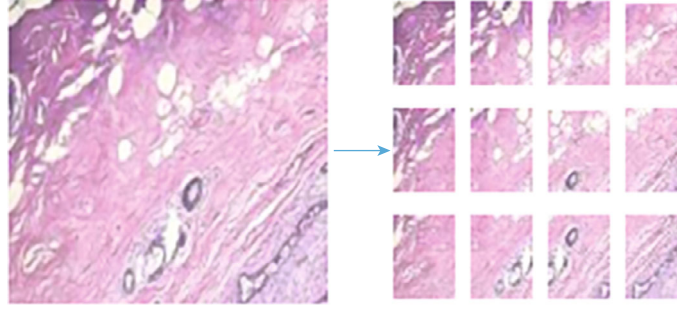


FIGURE 6: Overlapping cutting of pathological images.

TABLE 4: Benign and malignant section distribution.

$A$	$N_{ib}$	$N_{im}$	$N_i$
Data1	23564	22789	46218
Data2	16658	22351	38451
Data3	17894	20846	38165

to the generator  $F$ , a restored slice  $a''$  dyed in the  $X$  domain is generated. In theory, the restored slice and the original slice should be the same, and the error between them is  $L_{cyc}$ .  $B$   $m$ ,  $y$  continuously optimized  $L_{cyc}$ , the texture features during color conversion are guaranteed. The same is true from the  $Y$  domain to the  $X$  domain, as shown in the inner circle structure in Figure 5.

The trained CycleGAN model can color-normalize the input raw slices of different colors, while keeping the texture features unchanged. After color-normalizing all pathological image slices, the classification results can be prevented from being affected by factor effects of uneven dyeing.

**3.2. Improved DPN68-A Pathological Image Classification Model.** The proposed improved DPN68-A network structure is shown in Table 2. The improved network adds a  $1 \times 1$  small convolution in the Conv1 layer and introduces a deconvolution layer and an attention layer in the original DPN-68 network.

In the classification of pathological images, different from image classification tasks such as people, plants, and animals, it is necessary to extract high-level features for classification. Because the texture features of pathological images are more complex, it is more beneficial to use neural networks to extract the middle- and low-level features of pathological images. In the convolutional neural network, the size of the receptive field of a single node is affected by convolution kernel size in the feature map. The greater the convolution kernel, the more will be receptive field corresponding to a single node, the more abstract the extracted features, and the more difficult it is to focus on the image in the image. Detailed features: it is proposed to use a  $1 \times 1$  small convolution in the Conv1 layer to transform the original image to obtain a new image; by connecting the ReLU activation function on the premise of keeping the size of the feature map (feature map) unchanged, the front the learning representation of one layer adds a nonlinear excita-

tion, which allows the network to learn more complex non-linear expressions, improves generalization ability, and reduces overfitting. Extracting more texture features from the original image enhances the expressive ability of the neural network.

Considering that the size of the feature map extracted from the input image after passing through the convolutional neural network is usually small, the deconvolution operation can enlarge the feature map, which helps the subsequent classifier to make a better judgment, so the deconvolution layer is added after Conv5.

Due to the different focus of distinguishing benign and malignant diseases in pathological images, it is necessary to assign different classification weights to different features and introduce an attention mechanism into the model. Through the three operations of squeeze, excitation, and scale in the attention layer, the normalization can be the weights are weighted to the features of each channel of the output of the deconvolution layer so that more classification weights are assigned to important features such as blood vessels, glands, and nuclei during classification, and less important features such as bubbles are assigned less classification weights.

**3.3. Discrimination Strategy.** When the image slice is used as the classification unit, a discriminative strategy combining confidence rate and majority vote is adopted. The classification results of multiple slices are integrated to obtain the final classification result of the image, which improves the classification accuracy of the pathological image in the network.

For the  $k$  slices of each pathological image, let the number of slices classified as malignant be  $k_{nm}$ , and the sum of confidence rates be CRM; the number of slices classified as benign is  $k_{nb}$ , and the sum of confidence rates is CRB. The final classification result  $T$  is

$$T = \begin{cases} 1, & k_{nb} > \frac{k}{2}, \\ 0, & k_{nm} > \frac{k}{2}. \end{cases} \quad (8)$$

The result that takes the majority of slices is the final result of the patient. If the number of benign slices in the classification result is equal to the number of malignant

TABLE 5: Benign and malignant classification comparison.

Method	FPR	FNR	Recall	Precision	F1 score	I
No normalization	23.9	9.2	91.21	79.12	84.35	84.22
Normalization by Vahadane's method	14.5	5.3	96.14	88.64	92.41	92.38
CycleGAN normalization	11.7	4.6	95.37	89.83	93.71	93.16

TABLE 6: Accuracy comparison of different CNN models.

Model	FPR	FNR	Recall	Precision
VGG16	37.11	8.19	80.25	83.01
AlexNet	30.59	12.60	83.49	85.81
GoogLeNet	31.78	11.04	84.71	84.48
ResNet34	20.98	8.97	88.91	91.41
ResNet101	21.81	9.10	87.46	88.94

slices, the larger sum of confidence rates is taken as the final classification result of the image.

$$T = \begin{cases} 1, & \text{CRB} > \text{CRM}, \\ 0, & \text{CRM} > \text{CRB}. \end{cases} \quad (9)$$

**3.4. Algorithm Process.** The proposed algorithm based on CycleGAN and improved DPN68-A network is as follows.

- (1) The original breast cancer pathological image ( $700 \times 460$  pixels) is processed by overlapping slices, and each pathological image corresponds to 12 pathological image slices with a size of  $224 \times 224$  pixels
- (2) Pick out 2 pathological image slices of different colors in the pathological image slices, in which the X domain images are pathological image slices of different colors and the Y domain images are all pathological image slices of the target color
- (3) Train the CycleGAN model so that the model can output pathological image slices of different inputs as the same color. All data are color-normalized
- (4) Train and optimize the DPN68-A network
- (5) In the test phase, a fusion strategy combining majority voting and confidence rate is adopted, and the classification result of 12 slices corresponds to one image
- (6) Output the benign and malignant classification results of the image

## 4. Experimental Results and Analysis

### 4.1. Experimental Environment and Evaluation Indicators

**4.1.1. Experimental Environment.** The following is a list of the hardware utilized in the experiment. The CPU is Intel Core i7-9750H@2.6 GHz; the memory is 16 GB; the operating system is 64-bit Windows10; the operating environment

is Python 3.6; the GPU is NVIDIA GeForce GTX 1660Ti; and the hard drive capacity is 1 TB.

**4.1.2. Dataset and Data Processing.** The breast cancer pathological image data collection BreakHis was employed, which contains 7909 labelled breast cancer pathological pictures from 82 individuals with breast illness. 700 RGB three-channel pictures make up the data format. A total of 24 bits of color are used in the 460-pixel picture, with 8 bits in each channel. Table 3 shows the particular distribution of pictures of benign and malignant tumors at various magnifications. The total number of images is divided by the number of cancerous images. Each picture is magnified five times: 50, 150, 250, and 500 times. The number of photos under 50x is 1986, 2048 for images under 150x, 2035 for images under 250x, and 1868 for images under 500x.

Since the size of the input image required by the neural network is  $224 \times 224$  pixels, the pathological image of breast cancer is sliced and segmented. Considering that many breast cancer pathological images contain a large number of bubbles, the image is displayed as white. If the nonoverlapping cutting method is used when classifying, it is easy to mistake such sliced images with a large proportion of white areas as normal images, reducing the accuracy of classification. Each image of  $700 \times 460$  pixels is cut into 12 image slices of  $224 \times 224$  pixels; as shown in Figure 6, by overlapping cutting, the same lesion area under different fields of view is repeatedly predicted to avoid false detection in the above situation.

In the BreakHis dataset, the number of malignant patients and the number of malignant images are much higher than those of benign. The number of images is different for different patients, and the number of images between different disease categories varies greatly. To balance the data, 40x slice images are augmented. Augmentation methods include rotation, flipping, and fine-tuning contrast.

In the current research, there are usually two ways to establish datasets: dividing the dataset without isolating patients and dividing the dataset with isolated patients. The former does not consider patients and randomly divides the pathological image data into training set and test set, which will lead to pathological images of a certain patient may exist in both the training set and the test set. The model classification accuracy of this type of method is usually high, but its application value in specific clinical settings is limited. The latter isolates patients when dividing to ensure training data and testing data. The data is completely independent at the patient level, and the classification model established in this way has better practical application. Isolate patients and divide them into threefold. Table 4 shows the specific distribution of benign and malignant sections.

TABLE 7: Accuracy comparison of improved classification using DPN68 network.

The Internet	FPR	FNR	Recall	Precision	F1 score	I	R	AUC
DPN68	13.84	7.1	94.12	95.15	94.02	92.15	91.94	94.12
DPN68+small convolution	9.98	6.8	92.94	93.64	93.87	91.94	92.48	93.96
DPN68-A	8.10	5.9	93.45	95.89	95.64	93.18	93.74	95.03

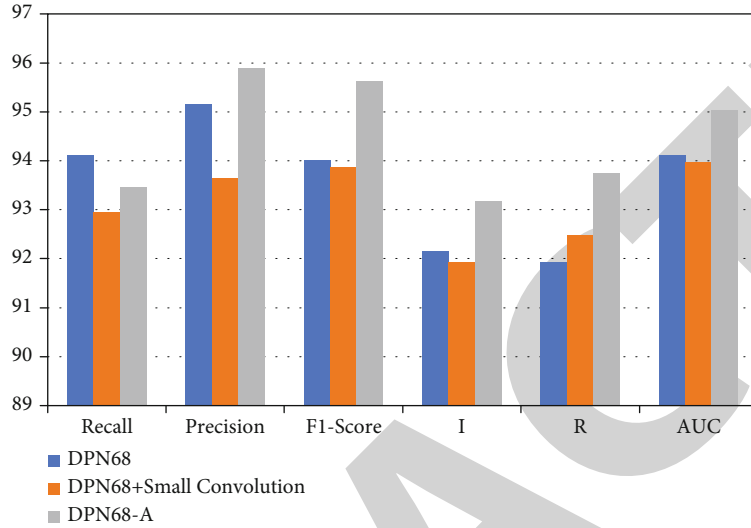


FIGURE 7: Accuracy comparison of improved classification using DPN68 network.

(1) Image-Level Accuracy.

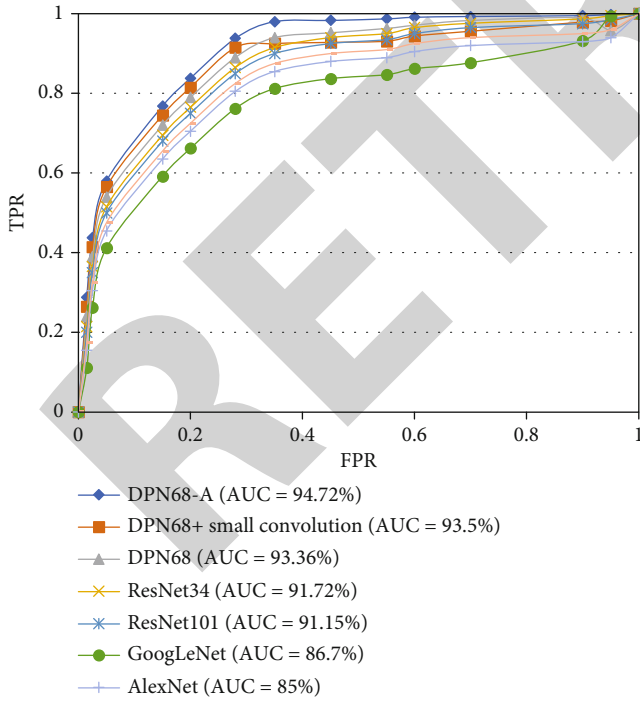


FIGURE 8: ROC curves of network.

$$I = \frac{N_r}{N_{all}}, \tag{10}$$

where  $N_{all}$  is the number of pathological images in the validation set and test set and  $N_r$  is the number of images that is correctly classified.

The false detection rate is also known as type I error which is the probability that a false alarm will be raised; that is, the positive result will be given when the true value is negative.

$$FPR = \frac{FP}{FP + TN} = \frac{FP}{N_b}. \tag{11}$$

The missed detection rate is also known as type II error which is the probability that a true positive will be missed by the test.

$$FNR = \frac{FN}{TP + FN} = \frac{FN}{N_m}. \tag{12}$$

Recall rate:

$$Recall = \frac{TP}{TP + FN} = \frac{TP}{N_m}. \tag{13}$$

4.1.3. Evaluation Criteria. The classification performance of the model was evaluated from two aspects: patient level and image level.

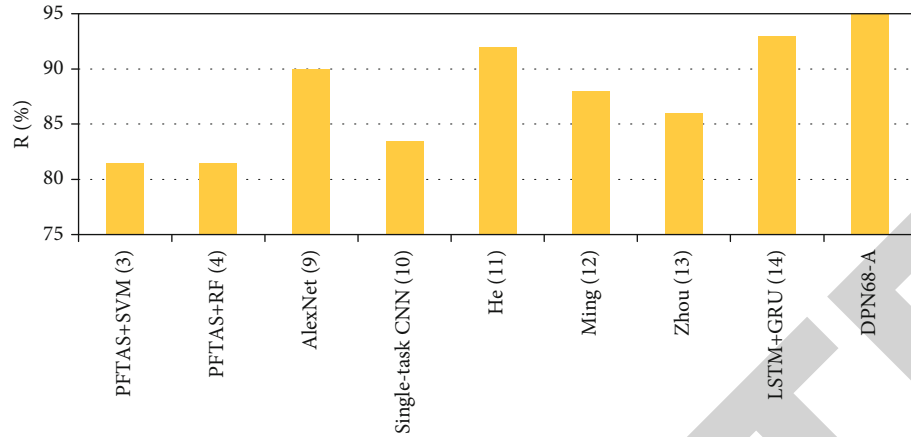


FIGURE 9: Comparison results of DPN68-A and other classification algorithms.

The accuracy is

$$\text{Precision} = \frac{\text{TP}}{\text{TP} + \text{FP}}. \quad (14)$$

F1 score is

$$\text{F1 score} = \frac{2 \times \text{Precision} \times \text{Recall}}{\text{Precision} + \text{Recall}}. \quad (15)$$

(2) Patient-Level Accuracy.

$$R = \frac{\sum P_s}{N_p}. \quad (16)$$

In the formula,  $P_s$  is the classification accuracy rate of each patient,  $P_s = N_{rp}/N_{np}$ , where  $N_{np}$  is the number of pathological images of each patient and  $N_{rp}$  is the number of correctly classified images of each patient;  $\sum P_s$  is the classification accuracy of all patients is the sum of the rates;  $N_p$  is the total number of patients.

## 4.2. Experiment and Result Analysis

**4.2.1. Experiment 1: Color Normalization Comparison Experiment.** This experiment compares the impacts of two distinct color normalizing techniques and is used to verify the usefulness of the suggested color normalization approach. In the color normalization comparison experiment, 300 benign and 300 malignant photos from the pathological image 40 dataset were chosen at random as the experimental data. The training and test sets were built in a 7:3 ratio, with no crossover between the patient samples in the training and test sets. We examined the effects of color normalization without color normalization, color normalization with the Vahadane technique [21], and color normalization with the CycleGAN model on detection accuracy via tests. For parameter fine-tuning, the detection model uses DPN68-A, which was introduced in this publication and is based on ImageNet-5K pretraining. For 100 iterations, the pretraining parameter transfer learning is applied, and the final accuracy is computed

TABLE 8: DPN68-A results at all magnifications.

A	FPR%	FNR%	Recall%	Precision%	F1 score%	I%	R%
50	8.10	7.15	94.41	97.87	95.74	94.11	95.11
150	7.05	5.65	95.01	98.61	97.21	93.94	95.31
250	8.16	3.45	94.89	95.94	96.48	94.12	95.17
500	7.95	5.59	93.47	98.10	95.32	95.01	94.67

as the evaluation index. Table 5 shows the outcomes of the experiment.

The experimental results show that after the pathological images are color normalized, the classification accuracy improves significantly, indicating that uneven color affects the deep learning model for pathological image classification, because normalization eliminates the interference of different colors on the classification results. The CycleGAN model's data classification accuracy rate is 10% higher than without the normalization approach, and the false detection rate is 14.4 percent lower, the missed detection rate is 5.6 percent lower, and the accuracy rate is increased. The classification accuracy is increased by 2.22 percent, the false detection rate is lowered by 3.3 percent, the missed detection rate is reduced by 1.1 percent, and the accuracy is improved by 2.22 percent when compared to the Vahadane technique. It is clear that the color normalization strategy for the pathological pictures described in this study, based on CycleGAN, is successful.

**4.2.2. Experiment 2: Comparison of Different CNN Models.** To verify the effectiveness of different CNN models, GoogLeNet, VGG16, ResNet34, ResNet101, and AlexNet were compared. The experiment was carried out based on Data1, Data2, and Data3, and the results are as follows and shown in Table 6.

It can be analyzed from the experimental results that the ResNet34 and ResNet101 models based on residual structure have significantly higher classification accuracy than GG16, AlexNet, and GoogLeNet at both the image level and the patient level. Among them, the best performing ResNet34 network is accurate at the image level compared with



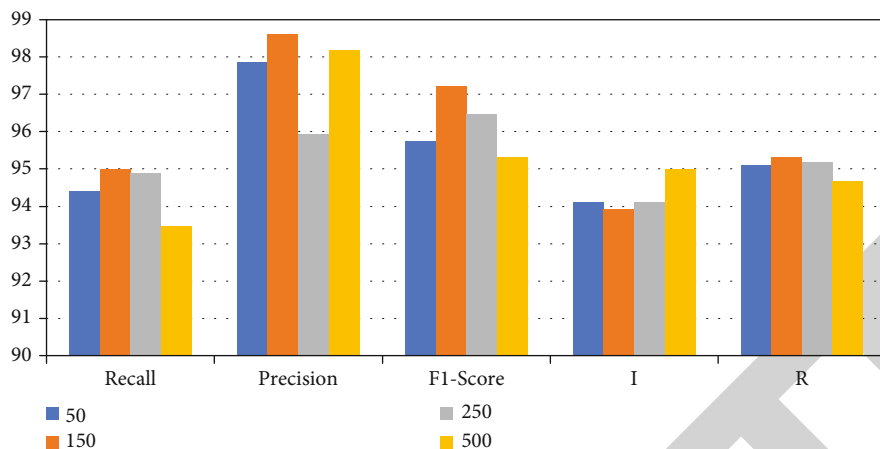


FIGURE 10: Comparison results of DPN68.

VGG16, the rate is improved by 5.42%, the false detection rate is reduced by 16.98%, the missed detection rate is reduced by 0.18%, and the patient-level classification accuracy rate is improved by 8.21%. Compared with the ResNet101 network with deeper network layers, the image-level classification accuracy rate increases 0.6% and 1.71% increase in the patient-level classification accuracy. The residual structure is more suitable for the classification of pathological images, but the more layers of the network, the better the performance is not necessary.

**4.2.3. Experiment 3: DPN68 Network Improvement Ablation Experiment.** This experiment is used to verify the effectiveness of the proposed DPN68-A model. The experiment adopts the form of ablation experiment, comparing the original DPN68 network and DPN68 network adding small convolution and DPN68 adding results of small convolution, deconvolution, and attention layers. The experiments are carried out based on Data1, Data2, and Data3, and the results are shown in Table 7 and Figure 7. In Table 7, AUC is the area under the ROC curve.

It can be seen from the experimental results that, compared with the original DPN68 network, the DPN68 network with a small convolutional layer has an increase of 0.96% in patient-level classification accuracy, 0.95% in image-level classification accuracy, 1.9% in false detection rate, and 1.9% in missed detection. Compared with the DPN68 network, the improved DPN68-A model has a 1.92% improvement in patient-level classification accuracy and a 2.2% improvement in image-level classification rate, the false detection rate is reduced 5.26%, and the missed detection rate is reduced by 0.5%. It can be seen that the improved model has greatly improved the classification accuracy at both the patient level and the image level, effectively improving the performance of the classification model. The ROC curve is shown in Figure 8. The AUC metric of the improved DPN68-A model is 1.36% higher than that of the DPN.

**4.2.4. Experiment 4: Comparison Experiment of DPN68-A Model with Different Deep Learning Methods.** Single-task

CNN method [10], improved deep convolutional neural network model [11], multiscale recalibration model [12], BN-Inception classification model [13], and the LSTM+GRU classification model [14] for comparison and the accuracy results at the patient level are shown in Figure 9.

The detection accuracy of the approach in this study is superior to other machine learning and deep learning methods at the patient level, as shown by the comparative findings. There is a 3.68 percent improvement, a 5.81 percent increase, a 6.89 percent improvement, and a 1.67 percent improvement over the Ming algorithm, Zhou method, and LSTM+GRU algorithm.

**4.2.5. Experiment 5: Test Experiments of DPN68-A at All Magnifications.** To prove that the proposed DPN68-A model is also applicable at other magnifications, the  $\times 100$ ,  $\times 200$ , and  $\times 400$  data were color-normalized, respectively. The model is trained and the classification accuracy is tested. The experimental results are shown in Table 8 and Figure 10.

According to the experimental results, it can be seen that DPN68-A has a good detection effect on pathological images of various magnifications and can better assist pathologists in diagnosing patients by synthesizing images of different magnifications in the clinical stage.

## 5. Conclusion

Aiming at the problem of high-precision detection of breast cancer pathological images, this paper proposes a color normalization method for pathological image slices based on CycleGAN, which reduces the influence of uneven staining on the classification of pathological images. It is proposed to use DPN to establish a detection model. A  $1 \times 1$  small convolution is added to the network structure to enhance the nonlinear expression ability of the network and better capture the texture features of pathological images. By adding a deconvolution layer and an attention mechanism, the model can better allocate the intermediate features. The weight of the network improves the classification accuracy of breast pathological images. A discriminant strategy

combining confidence rate and voting mechanism is proposed to improve the classification accuracy of patient-level lesions. Experiments show that the proposed DPN68-A network can classify benign and malignant breast pathological images. It has a good effect and has certain clinical application value. In the future, the segmentation network will be combined to accurately label malignant areas on the basis of correctly classifying malignant images, to achieve more accurate clinical auxiliary judgments.

## Data Availability

The data shall be made available on request.

## Conflicts of Interest

The authors declare that they have no conflict of interest.

## References

- [1] P. Mathur, K. Sathishkumar, M. Chaturvedi et al., "Cancer Statistics, 2020: Report From National Cancer Registry Programme, India. In JCO Global Oncology," *American Society of Clinical Oncology*, no. 6, pp. 1063–1075, 2020.
- [2] A. Marciniak, A. Obuchowicz, A. Monczak, and M. Kolodziński, "Cytomorphometry of fine needle biopsy material from the breast cancer," in *Advances in Soft Computing*, pp. 603–609, Springer-Verlag, Berlin, Heidelberg.
- [3] J. Pereira, R. Barata, and P. Furtado, "Experiments on automatic classification of tissue malignancy in the field of digital pathology," in *Proc. SPIE 10443, Second International Workshop on Pattern Recognition*, vol. 1044312, pp. 188–194, 2017.
- [4] V. Roulliera, O. Lezoraya, V.-T. Tab, and A. Elmoataza, "Multi-resolution graph-based analysis of histopathological whole slide images: application to mitotic cell extraction and visualization," *Computerized Medical Imaging and Graphics*, vol. 35, no. 7-8, pp. 603–615, 2011.
- [5] M. Veta, J. P. Pluim, P. J. Van Diest, and M. A. Viergever, "Breast cancer histopathology image analysis: a review," *IEEE Transactions on Biomedical Engineering*, vol. 61, no. 5, pp. 1400–1411, 2014.
- [6] T. Araújo, G. Aresta, E. Castro et al., "Classification of breast cancer histology images using convolutional neural networks," *PLoS One*, vol. 12, no. 6, p. 0177544, 2017.
- [7] C. Zhu, F. Song, Y. Wang, H. Dong, Y. Guo, and J. Liu, "Breast cancer histopathology image classification through assembling multiple compact CNNs," *BMC Medical Informatics and Decision Making*, vol. 19, no. 1, p. 198, 2019.
- [8] R. Yan, F. Ren, Z. Wang et al., "Breast cancer histopathological image classification using a hybrid deep neural network," *Methods*, vol. 173, pp. 52–60, 2020.
- [9] L. G. Hafemann, L. S. Oliveira, and P. Cavalin, "Forest species recognition using deep convolutional neural networks," in *International Conference on Pattern Recognition*, pp. 1103–1107, 2014.
- [10] A. Cruz-Roa, J. Arevalo Ovalle, A. Madabhushi, and F. A. Gonzalez Osorio, "A deep learning architecture for image representation visual interpretability and automated basal-cell carcinoma cancer detection," in *Medical Image Computing and Computer-Assisted Intervention-MICCAI 2013 ser*, vol. 8150, pp. 403–410, Berlin Heidelberg, 2013.
- [11] S. Tang and M. Shabaz, "A new face image recognition algorithm based on cerebellum-basal ganglia mechanism," *Journal of Healthcare Engineering*, C. Chakraborty, Ed., vol. 2021, 11 pages, 2021.
- [12] G. Litjens, C. I. Sánchez, N. Timofeeva et al., "Deep learning as a tool for increased accuracy and efficiency of histopathological diagnosis," *Scientific Reports*, vol. 6, no. 1, p. 26286, 2016.
- [13] H. Z. Almarzouki, H. Alsulami, A. Rizwan, M. S. Basingab, H. Bukhari, and M. Shabaz, "An Internet of medical things-based model for real-time monitoring and averting stroke sensors," *Journal of Healthcare Engineering*, C. Chakraborty, Ed., vol. 2021, 9 pages, 2021.
- [14] S. Roy, S. R. Dubey, S. Chatterjee, and B. Chaudhuri, "FuSE-Net: fused squeeze-and-excitation network for spectral-spatial hyperspectral image classification," *IET Image Processing*, vol. 14, no. 8, pp. 1653–1661, 2020.
- [15] A. Tiwari, V. Dhiman, M. A. M. Iesa, H. Alsarhan, A. Mehbodniya, and M. Shabaz, "Patient behavioral analysis with smart healthcare and IoT," *Behavioural Neurology*, H. Lin, Ed., vol. 2021, 9 pages, 2021.
- [16] N. Bayramoglu, J. Kannala, and J. Heikkilä, "Deep learning for magnification independent breast cancer histopathology image classification," in *Pattern Recognition (ICPR), 2016 23rd International Conference Onpp*. 2440–2445, Cancun, 2016.
- [17] T. Thakur, I. Batra, M. Luthra et al., "Gene expression-assisted cancer prediction techniques," vol. 2021, pp. 1–9, 2021.
- [18] L. Sui, D. Bosheng, M. Zhang, and K. Sun, "A new variable selection algorithm for LSTM neural network," in *Data Driven Control and Learning Systems Conference (DDCLS) 2021 IEEE 10th*, pp. 571–576, 2021.
- [19] S. Chaudhury, N. Shelke, K. Sau, B. Prasanalakshmi, and M. Shabaz, "A novel approach to classifying breast cancer histopathology biopsy images using bilateral knowledge distillation and label smoothing regularization," *Computational and Mathematical Methods in Medicine*, D. Koundal, Ed., vol. 2021, 11 pages, 2021.
- [20] A. Aggarwal, M. Mittal, and G. Battineni, "Generative adversarial network: an overview of theory and applications," *International Journal of Information Management Data Insights*, vol. 1, no. 1, p. 100004, 2021.
- [21] G. K. Saini, H. Chouhan, S. Kori et al., "Recognition of human sentiment from image using machine learning," *Annals of the Romanian Society for Cell Biology*, vol. 25, no. 5, pp. 1802–1808, 2021.
- [22] P. Isola, J.-Y. Zhu, T. Zhou, and A. A. Efros, "Image-to-image translation with conditional adversarial networks," in *CVPR*, 2017.
- [23] M. Sanaullah Chowdhury, F. R. Taimy, N. Sikder, and A.-A. Nahid, "Diabetic retinopathy classification with a light convolutional neural network," in *Computer Communication Chemical Materials and Electronic Engineering (ICAME2) 2019 International Conference on*, pp. 1–4, 2019.
- [24] M. A. Haq, "IoT based secured UAV system. UASG 2021," in *2nd INTERNATIONAL CONFERENCE ON UNMANNED AERIAL SYSTEMS IN GEOMATICS*, 2021 <https://www.iitr.ac.in/uasg2021/>.
- [25] S. Deshmukh, K. Thirupathi Rao, and M. Shabaz, "Collaborative Learning Based Straggler Prevention in Large-Scale Distributed Computing Framework," *Security and Communication Networks*, M. Kaur, Ed., vol. 2021, 9 pages, 2021.

## *Retraction*

# **Retracted: Principal Component and Path Analysis for Trait Selection Based on the Assessment of Diverse Lentil Populations Developed by Gamma-Irradiated Physical Mutation**

### **BioMed Research International**

Received 8 January 2024; Accepted 8 January 2024; Published 9 January 2024

Copyright © 2024 BioMed Research International. This is an open access article distributed under the Creative Commons Attribution License, which permits unrestricted use, distribution, and reproduction in any medium, provided the original work is properly cited.

This article has been retracted by Hindawi following an investigation undertaken by the publisher [1]. This investigation has uncovered evidence of one or more of the following indicators of systematic manipulation of the publication process:

- (1) Discrepancies in scope
- (2) Discrepancies in the description of the research reported
- (3) Discrepancies between the availability of data and the research described
- (4) Inappropriate citations
- (5) Incoherent, meaningless and/or irrelevant content included in the article
- (6) Manipulated or compromised peer review

The presence of these indicators undermines our confidence in the integrity of the article's content and we cannot, therefore, vouch for its reliability. Please note that this notice is intended solely to alert readers that the content of this article is unreliable. We have not investigated whether authors were aware of or involved in the systematic manipulation of the publication process.

Wiley and Hindawi regrets that the usual quality checks did not identify these issues before publication and have since put additional measures in place to safeguard research integrity.

We wish to credit our own Research Integrity and Research Publishing teams and anonymous and named external researchers and research integrity experts for contributing to this investigation.

The corresponding author, as the representative of all authors, has been given the opportunity to register their agreement or disagreement to this retraction. We have kept a record of any response received.

### **References**

- [1] S. Debnath, A. Sarkar, K. Perveen et al., "Principal Component and Path Analysis for Trait Selection Based on the Assessment of Diverse Lentil Populations Developed by Gamma-Irradiated Physical Mutation," *BioMed Research International*, vol. 2022, Article ID 9679181, 14 pages, 2022.

## Research Article

# Principal Component and Path Analysis for Trait Selection Based on the Assessment of Diverse Lentil Populations Developed by Gamma-Irradiated Physical Mutation

Sandip Debnath <sup>1</sup>, Abhik Sarkar <sup>1</sup>, Kahkashan Perveen <sup>2</sup>, Najat A. Bukhari <sup>2</sup>,  
Kavindra Kumar Kesari <sup>3</sup>, Amit Verma <sup>4</sup>, Nihar Ranjan Chakraborty <sup>1</sup>,  
and Mulugeta Tesema <sup>5</sup>

<sup>1</sup>Department of Genetics and Plant Breeding, Institute of Agriculture, Visva-Bharati University, Sriniketan, PIN-731236 West Bengal, India

<sup>2</sup>Department of Botany & Microbiology, College of Science, King Saud University, Riyadh 11495, Saudi Arabia

<sup>3</sup>Department of Bioproducts and Biosystems, Aalto University, Espoo, P.O. Box 11000, Otakaari 1B, Finland

<sup>4</sup>University Centre for Research & Development & Department of Computer Science & Engineering, Chandigarh University, Gharuan, Mohali, Punjab, India

<sup>5</sup>Department of Chemistry (Analytical), College of Natural and Computational Sciences, DambiDollo University, Dambi Dollo, Oromia Region, Ethiopia

Correspondence should be addressed to Sandip Debnath; [sandip.debnath@visva-bharati.ac.in](mailto:sandip.debnath@visva-bharati.ac.in) and Mulugeta Tesema; [mulugeta@dadu.edu.et](mailto:mulugeta@dadu.edu.et)

Received 4 June 2022; Revised 19 June 2022; Accepted 25 June 2022; Published 18 July 2022

Academic Editor: Gaganpreet Kaur

Copyright © 2022 Sandip Debnath et al. This is an open access article distributed under the Creative Commons Attribution License, which permits unrestricted use, distribution, and reproduction in any medium, provided the original work is properly cited.

Lentil is a notable legume crop valued for its high protein, vitamin, mineral, and amino acid (lysine and tryptophan) content. This crop has a narrow genetic base due to the formation of gene pool barriers during interspecific hybridization within and across species. Mutagenesis may be seen as a novel and alternative breeding technique for the production of new diversity. For the identification of new alleles, the creation of mutants followed by selection in subsequent generations would be necessary. Induction of mutation in lentil cv. *Moitree* by gamma rays therefore produced high variation for the majority of quantitative measures examined. Henceforth, principal component analysis (PCA) and path coefficient analysis were conducted to identify and exclude redundant mutant genotypes with similar traits as the success of breeding is dependent on understanding the relationship between morpho-agronomic traits and seed yield. As shown by the findings of this research, the total quantity of pods per mutant plant should be given considerable priority. The identified mutant genotypes, such as lines 24, 43, 28, 33, and 10, may be used as parents in future breeding or released directly following trials.

## 1. Introduction

In India, lentils (*Lens culinaris* Medik) are an important pulse crop. It belongs to the *Fabaceae* family and contains 14 chromosomes ( $2n = 2x$ ). [1]. It is an annual edible legume with pods and seeds shaped like lenses and purses [2]. This is the oldest known legume [3]. Its grains contain necessary amino acids like lysine and tryptophan [4]. Currently, pulses, their significance in food and nutrition security,

and sustainable agriculture are receiving more worldwide attention than ever before. Legumes are included among high-protein plant foods. It is spectacular to note that protein-rich meals are advised to consume regularly by mesothelioma patients whose appetites may be affected by chemotherapy, and nutritious diets give energy and help preserve muscular mass. Mesothelioma patients generally eat too little protein and calories to promote healing, boost immunity, and fight tiredness. A healthy mesothelioma diet

may reduce stress, maintain weight and energy, combat infection, and control treatment-related side effects. Improving the quality of the high-protein legume “lentil” employing novel crop improvement techniques might thus play a significant role. Systematized evaluation is required for the genetic and agronomic improvement of lentil. It will remain the major objective of all breeding initiatives. Frequent use of conventional breeding techniques has decreased genetic diversity, which is a primary need for crop improvement projects. To achieve the aim of increasing genetic variability, new breeding procedures, such as induced mutagenesis, are necessary. In addition to genetic diversity, induced mutagenesis allows for the improvement of a specific trait without affecting the genetic composition as a whole [5, 6]. The “day-length bottleneck” constrained the flow of lentil germplasm into the *Indo-Gangetic* plain due to its narrow genetic base, which is less sensitive to photoperiod and more sensitive to temperature than landraces from West Asia, despite the fact that South Asia is home to half of the world’s lentil cultivation [7]. In addition, the tiny and fragile flowers reduced the success rate of artificial hybridization by 20–50% due to the problems of emasculation and pollination, which resulted in mutant plant damage. As a result, cross-pollination of lentils has become a time-consuming procedure [8]. In addition, *Lens* was known for the formation of cross ability barriers during interspecific hybridization within and across species [9]. The interspecific hybridization is a technique of intercrossing two different species which have the same genus. This technique is useful for exploiting useful genes from raw species to improve the cultivated species. Eventually, these events resulted in the narrow genetic foundation of lentils. Several researchers have already recognized this narrow genetic base as the fundamental constraint on lentil yield [10]. In addition, adaptive specificity and recurrent failures to use several unproductive wild germplasms contribute to the failure of lentil genetic advancement [11]. Given the aforementioned conditions, mutagenesis may be viewed as a unique and supplemental breeding approach. It is capable of producing variants that does not exist in the genetic background of the organism. Consequently, mutagenesis may be exploited to improve a multitude of desirable traits in a mutant plant species [12, 13]. The development of mutants followed by selection in the next generations would be essential for the discovery of novel alleles and might be released directly as varieties or prebreeding material in the near future if proved to be commercially viable and agronomically advantageous [14]. Nonetheless, crop yield in general is a complex process arising from the interplay of several genes with diverse environmental implications that impact a wide range of phenotypes [15]. Successful mutant plant selection during breeding requires knowledge of the link between morpho-agronomic parameters and seed yield [16]. A path coefficient analysis was conducted to determine the nature of the link between yield and other variables, as well as the direct and indirect effects of different factors on yield. PCA is a statistical technique used to identify and eliminate duplicate genotypes with similar characteristics [17]. It allows for the natural classification of genotypes and gives an accurate indication of genotypic differences.

The primary benefit of PCA is that each genotype may be assigned to only one group [18]. In addition, this test is used to categorize a large number of variables into important components and assess their contribution to the total variance [19]. So, PCA was done to determine how the various attributes were connected and to identify the traits that cosegregated. This enabled for the identification of the characteristics so that the selected  $M_4$  mutants could be utilized for crop development. Having in mind the limitations on lentil yield and the importance of optimizing physical mutagen, a multiyear-induced mutagenesis field experiment was conducted from 2017 to 2021 to increase the genetic diversity and yielding potential of lentil cultivars.

## 2. Materials and Methods

Approximately 5000 healthy seeds of lentil (Cultivar: *Moitree*), were irradiated with 250 Gy of gamma rays because the  $GR_{50}$  value for *Moitree* (published elsewhere) was calculated to be 217.2 Gy. The irradiation was applied at the RNARC, BCKV, West Bengal, India, where gamma chamber (GC-6000) was utilized. Using the mutant plant-to-progeny method, in 2018-2019, seeds from the  $M_1$  generation were sown in the next generation to grow the  $M_2$  population in the field mentioned above. To investigate the mutagenic impact of the previously delivered gamma irradiation doses, individual mutant plants were picked across the field based on their chlorophyll content and a variety of morphological traits. After ten days of germination, the potential mutants were tagged and recorded correctly. In 2019–2020, 433 agro-morphologically superior mutants with high production potential were chosen and produced in the  $M_3$  generation using the bulk breeding technique to reap the benefits of natural selection. The  $M_4$  generation was made up of 62 types of economically superior mutant types that were obtained from 433  $M_3$  populations in 2020–21.

These 62 lentil mutant types were grown at the institutional agricultural farm during winters of 2020-2021, using a RCBD design with three replications. Apparently healthy and competitive five mutant plants were randomly selected from each plot, and data were obtained on fourteen distinct traits defined by Satpathy and colleagues [20]. Dewey and Lu’s path coefficient analysis was used to examine the direct and indirect impacts of a variety of independent factors on seed yield. [21]. Windostat version 9.2 was applied for statistical studies involving correlation, route analysis, and PCA. Following the formula presented by Allard (1960), different genetic parameters were determined [22].

## 3. Results

Recent research on the genetic diversity of 50 distinct lentil germplasms, as well as the identification of the best heritable attributes from our laboratory, was published [20]. Examining the direct and indirect impacts of numerous characteristics on seed yield, as well as analyzing the pattern of variation in characters, classifying the traits, and exploring novel mutants, was the objective of this research.

**3.1. Principal Component Analysis.** PCA was used to evaluate the diversity of 14 traits. Table 1 illustrates, based on the variable factor loadings, that the eight PC aspects explained 78.21 percent of the total variance.

Each principal component analysis shows the central variability of all attributes. 14.11 percent of the total variation was explained by the first main component (PC1). The factors with the largest loading on PC1 were grain yield/mutant plant, days to fifty percent blooming, harvest index, and mutant plant height. 12.54 percent of the variation was explained by the second main component (PC2). The variables mutant plant height, days to fifty percent flowering, days to fifty percent pod maturity, seeds/mutant plant, biomass/mutant plant, and weight of 100 seeds showed high positive support, whereas the remaining variables revealed substantial negative involvement. The third main component (PC3) accounted for 11.30 percent of the variance. The remaining five PCs explained just 9.91, 8.88, 7.99, 7.33, and 6.11 percent of the variance, respectively. A scree plot depicted the proportion of variation attributable to eigenvalues and principal components for each graphed PC (Figure 1).

PC 1 had the largest variance with an eigenvalue of 1.97, whereas the variance of the remaining principal components gradually declined. After the fourth PC, the line begins to straighten out, with minor differences across PCs. It is obvious from the graph that PC1 had the highest variance compared to the other four PCs; therefore, it may be advantageous to select lines for characters with a positive impact under PC1. The PC score for each component contains both positive and negative values. These scores may be employed to develop precise selection indices whose strength is dictated by the variation explained by each basic component [23]. A high PC score for a certain genotype in a specific component suggests that the mutant's variables have high values. We acquired the PCA scores (Table 2) for 62 lentil mutant variants in the first three principal components and referred to them as axes X vector (PCA-1), Y vector (PCA-2), and Z vector (PCA-3).

The squared distance of each genotype from these three axes was also calculated there. These PCA scores for mutant lineages were graphed to create a three-dimensional scatter picture (Figure 2).

Examining these findings indicated eight distinct clusters by Tocher method (Figure 3). Four of these clusters were shown to be mono-genotypic. The distribution pattern of mutants in these clusters was discovered to be random, with no agro-morphological diversity serving as a reference. Mutants with a more phenotypic variability were clustered in both the same and distinct classes.

**3.2. Genetic Variability of the Mutant Population.** Studies of the coefficient of variation revealed that the phenotypic coefficient variation (PCV) values were greater than those of the genotypic coefficient variation (GCV) for the majority of the traits, indicating that the environment influences these traits to some extent during both the vegetative and reproductive stages (Table 3). Secondary branches (number) per plant had the largest phenotypic coefficient variation (PCV) and

genotypic coefficient variation (GCV) according to the research (70.85 percent and 60.32 percent, respectively). Biomass/mutant plant (57.21 percent) was followed by number of major branches (36.69 percent), seeds/pod (36.17 percent), seeds/mutant plant (35.25 percent), and pods/mutant plant (33.44 percent). Characters with a high GCV include biomass/mutant plant (24.3 percent), pods/mutant plant (21.86 percent), seeds/pod (20 percent), and mutant plant height (21.0 percent). The high values of PCV above GCV for the aforementioned features imply strong environmental influences; hence, when establishing a breeding program using this material, additional attention should be placed on these traits. The secondary branches (number) exhibited the highest heritability and genetic advance as a percentage of the mean (72.47 percent and 105.79 percent, respectively), and the other traits in which high heritability and high genetic advance were observed were weight of 100 seeds, harvest index, and pods/mutant plant, indicating that these traits are less influenced by the environment and are more stable and governed by additive gene action. Consequently, the easy selection process affords these characters a larger potential for advancement.

**3.3. Path Analysis.** The correlation coefficients between genotypic and phenotypic characteristics for fourteen traits are provided in (Tables 4 and 5). Days for pod initiation and pods/mutant plant (0.221\*\* and 0.404\*\*) and number of main branches (0.155\*), root length (0.149\*), seeds/pod (0.159\*), and harvest index (0.155\*) are significantly and positively linked with grain production per plant at both levels, respectively. Secondary branches (number) (0.43\*\*) and biomass/mutant plant (0.144\*) were shown to be substantially and adversely associated to grain production per plant. The phenotypic analysis indicated only a significant and positive connection between grain yield and pods/mutant plant (0.246\*\*), seeds/mutant plant (0.399\*\*), and biomass/mutant plant (0.306\*\*). The correlation study demonstrated the link between the features; hence, the relationship between the numerous lentil traits will establish their relative importance for yield enhancement.

Path analysis based on phenotypic correlations found that all variables had direct positive impacts on grain production per mutant plant, except for number of main and secondary branches, days for pod initiation, root length, and harvest index, which had direct negative effects. The number of main and secondary branches, pods per plant, and harvest index demonstrated favorable indirect impacts of mutant plant height on grain yield (Table 6). The number of main branches had favorable indirect impacts on the secondary branches (number), days to 50% blooming and pod initiation, pods per plant, root length, seeds per pod, and biomass/mutant plant. The secondary branches (number) had both direct and indirect negative impacts on mutant plant height, days to 50% blooming and pod maturity, root length, seeds per pod, and seed weight per 100 seeds. Days to 50% blooming have negative indirect impacts on grain production via solely mutant plant height, main branch number, and root length. The days to 50 percent blooming, the days for pod initiation, the weight of 100

TABLE 1: Eigenvalues for the first five principal components of various Lentil mutant characteristics.

	PC-1	PC-2	PC-3	PC-4	PC-5	PC-6	PC-7	PC-8
Eigenvalue	1.97542	1.75629	1.58303	1.3886	1.2444	1.11867	1.02712	0.85597
% variability explained	14.11013	12.5449	11.30738	9.91859	8.88858	7.99046	7.33658	6.11404
Cumulative variability explained	14.11013	26.65503	37.96241	47.881	56.76958	64.76005	72.09662	78.21066
Characters								
Mutant plant height (cm)	0.25048	0.38142	0.23943	0.35319	0.10706	0.23783	0.014	0.05966
Primary branches (number)	0.20003	-0.10371	-0.45645	0.03086	-0.04338	-0.27438	-0.45303	-0.28496
Secondary branches (number)	-0.42991	-0.36133	0.12583	0.21243	-0.12712	0.06455	-0.1351	-0.21038
Days for fifty percent flowering	0.33698	0.2377	-0.19927	-0.04982	-0.20773	-0.12079	-0.03962	-0.24344
Days for pod initiation	0.18892	-0.04746	0.05889	0.1501	-0.30677	0.08208	0.66552	-0.53522
Days for fifty percent pod maturity	-0.22596	0.21722	-0.18955	-0.00637	0.53665	-0.34055	0.12435	-0.43063
Pods/mutant plant	0.17953	-0.42745	-0.36813	0.02671	-0.3105	-0.13369	0.16883	0.26938
Root length (cm)	-0.20586	-0.03981	-0.32296	0.3199	0.24083	-0.27468	0.42932	0.28707
Seeds/pod	-0.09768	-0.29664	0.12013	-0.50335	0.28993	0.0991	0.20353	-0.01967
Seeds/mutant plant	0.05965	0.10157	0.36315	-0.22488	-0.21891	-0.64245	0.14612	0.23137
Biomass/mutant plant (g)	-0.28123	0.18136	-0.43314	-0.23535	-0.17822	0.42124	0.14436	0.06376
100 seed weight (g)	-0.22237	0.53104	-0.20035	-0.23379	-0.22218	-0.04262	0.06298	0.17617
Harvest index (%)	0.28529	-0.06901	-0.00689	-0.52825	0.13598	0.07246	0.05908	-0.13679
Grain yield/mutant plant (g)	0.46312	-0.07071	-0.15954	0.08975	0.39904	0.16212	0.1117	0.27769

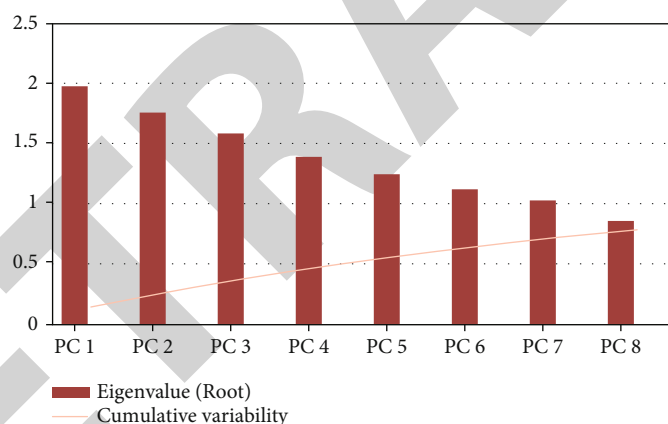


FIGURE 1: Scree plot of eigenvalues and cumulative variability against different principal components in lentil mutants.

seeds, and the harvest index are all negatively impacted by the days for pod initiation. Days for 50% pod maturity has a positive indirect influence on the number of main and secondary branches, days to 50% blooming and pod maturity, seeds per plant, and 100 seed weight. Pods per plant, on the other hand, have a negative indirect influence through just the number of main and secondary branches, days for pod initiation and 50% maturity, and seeds per pod. Through the secondary branches (number), pods per plant, root length, seeds per pod, biomass/mutant plant, and 100 seed weight, root length has a negative indirect effect. Seeds per pod have a positive indirect influence on secondary branch number, days to 50% blooming, root length, seeds per pod, seeds per plant, and biomass/mutant plant. Through mutant plant height, secondary branches (number), days for pod initiation, root length, and harvest index,

seeds per plant have a negative indirect influence. Biomass/mutant plant has a negative indirect influence on mutant plant height, the number of main and secondary branches, the number of days before pod initiation, and pod maturity at 50 percent. There is a positive indirect impact of 100 seed weight on all variables except mutant plant height and seeds/pod. The harvest index has a favorable indirect impact via the secondary branches (number), days for 50% pod maturity, root length, seeds per pod, and seeds per plant.

Path analysis based on genotypic correlations revealed direct positive effects of mutant plant height, days to 50 percent pod maturity, pods/mutant plant, seeds/pod, biomass/mutant plant, and direct negative effects of primary branches (number), secondary branches (number), and days to 50 percent flowering, days for pod initiation, root length, seeds/mutant plant, 100 seed weight, and harvest index on

TABLE 2: PCA scores of 62 lentil mutants shown as three axes X vector (PCA-1), Y vector (PCA-2), and Z vector (PCA-3).

Mutant types	PCA I <i>X vector</i>	PCA II <i>Y vector</i>	PCA III <i>Z vector</i>
1   1	-1.253	3.83	-4.81
2   2	-2.892	6.217	-4.34
3   3	0.173	5.999	-4.008
4   4	-0.26	7.368	-4.691
5   5	-0.077	8.372	-6.995
6   7	0.588	6.867	-5.029
7   13	-0.458	8.087	-5.493
8   14	-1.032	6.472	-5.597
9   23	-1.141	5.997	-5.395
10   25	0.223	6.772	-5.717
11   28	-1.393	6.023	-4.889
12   31	-0.641	6.329	-5.094
13   32	-1.49	9.11	-5.856
14   33	-0.31	7.795	-5.538
15   34	-1.247	7.855	-5.326
16   35	-1.05	7.798	-6.284
17   36	-1.013	7.083	-5.151
18   37	0.758	6.742	-5.443
19   38	1.296	6.264	-4.003
20   39	0.882	7.196	-5.277
21   40	0.117	8.701	-4.767
22   42	-0.12	6.11	-6.36
23   44	-0.401	6.081	-5.307
24   45	2.196	6.896	-4.829
25   47	-1.564	6.088	-4.856
26   51	-1.386	5.34	-4.572
27   52	-2.497	5.039	-5.712
28   59	1.275	6.306	-4.928
29   61	-1.038	5.948	-5.32
30   62	-1.195	5.985	-5.731
31   66	-1.172	4.713	-4.153
32   67	-1.217	7.502	-6.095
33   72	1.036	6.306	-5.251
34   76	0.057	5.592	-6.419
35   77	-1.16	5.831	-5.019
36   82	-0.029	7.121	-5.657
37   86	-0.982	6.165	-4.892
38   87	0.554	6.387	-6.6
39   88	-0.649	6.086	-5.168
40   89	-1.567	6.463	-5.268
41   91	0.326	4.788	-6.247
42   93	-0.109	5.682	-6.327
43   96	1.433	6.006	-5.533
44   97	0.44	6.565	-4.699
45   101	0.192	6.662	-5.335
46   103	-0.139	4.931	-3.679
47   104	-0.675	4.892	-5.731

TABLE 2: Continued.

	PCA I	PCA II	PCA III
48   105	-0.12	6.756	-6.362
49   107	0.069	6.586	-4.807
50   111	0.64	5.456	-5.767
51   114	-0.04	4.967	-5.511
52   115	-0.283	6.154	-6.45
53   116	0.934	4.987	-5.037
54   117	0.575	4.123	-5.015
55   127	-0.26	5.489	-5.362
56   128	-0.509	7.381	-5.841
57   133	0.819	5.802	-6.377
58   137	0.533	5.674	-5.441
59   138	-0.278	6.376	-5.838
60   142	0.35	6.519	-4.07
61   150	-0.303	6.729	-4.883
62   152	-0.761	6.008	-5.518

grain yield (Table 7). The mutant plant height had favorable indirect impacts on grain production via the number of main branches, the secondary branches (number), the number of seeds per plant, the weight of 100 seeds, and the harvest index. Number of main branches had favorable indirect impacts via secondary branches (number), days for pod initiation, days for 50% pod maturity, pods per plant, root length, biomass/mutant plant, and 100 seed weight. The secondary branches (number) had negative direct and indirect impacts on mutant plant height, days to 50 percent pod maturity, root length, seeds per pod, and seeds per plant. Days to 50% blooming have indirect favorable benefits on grain output via mutant plant height, secondary branches (number), pods per plant, and root length. Days for pod initiation has a negative indirect influence on grain yield through days to 50% blooming, seeds per pod, seeds per plant, and harvest index. The secondary branches (number), the number of days to 50 percent blooming, the number of seeds per pod, and the number of seeds per plant have a positive indirect influence on the days to 50 percent pod maturity. In contrast, pods per plant have a beneficial indirect benefit through biomass/mutant plant and hundred seed weight. Root length has a negative indirect influence through the amount of secondary branches, seeds per pod, seeds per plant, and weight per 100 seeds. Seeds per pod have a negative indirect influence on three traits: mutant plant height, pods per plant, and harvest index. Through pods/mutant plant, seeds/pod, and biomass/mutant plant, seeds/mutant plant have a positive indirect impact. The days to 50% blooming, pods/mutant plant, seeds/pod, and harvest index indicate a favorable indirect influence of biomass/mutant plant. 100 seed weight demonstrates a beneficial indirect impact via the number of main and secondary branches, days for pod initiation and 50% pod maturity, biomass/mutant plant, and harvest index. The harvest index demonstrates a negative indirect influence via mutant plant height, number of main branches, days to 50% blooming and pod



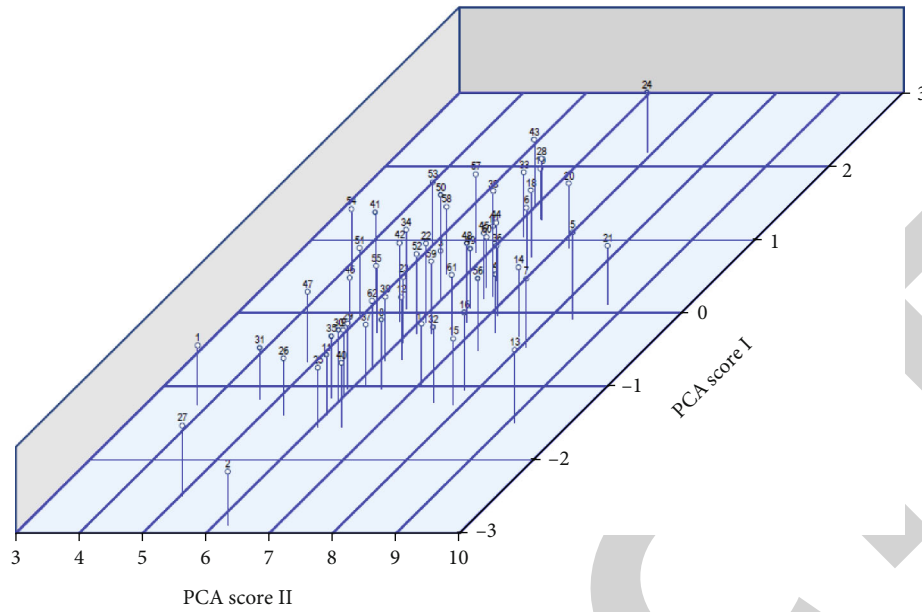


FIGURE 2: 3-D scatter diagram of PCA scores for mutant lines.

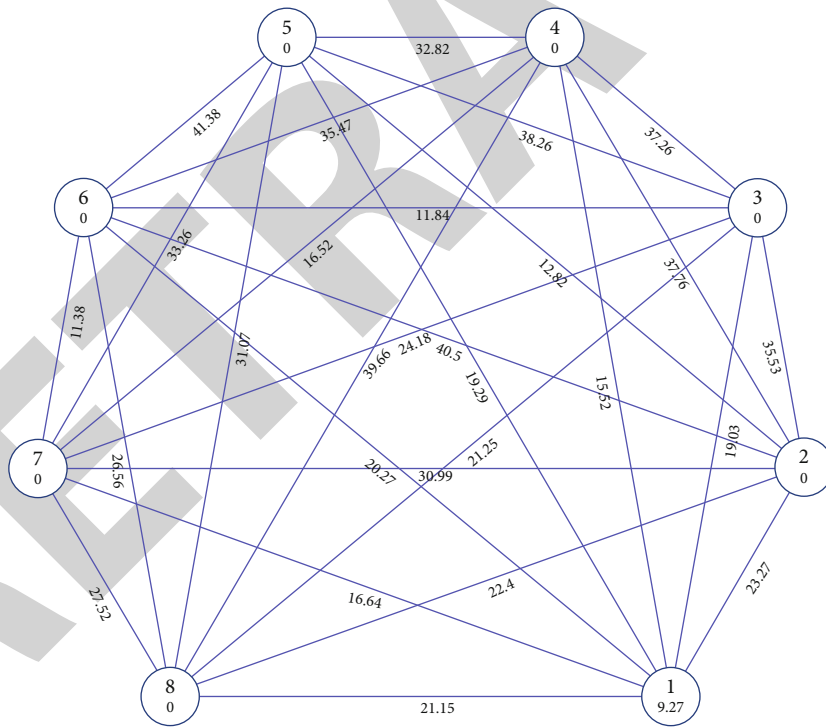


FIGURE 3: Distribution pattern of mutants in eight clusters by Tocher method.

commencement, seeds/mutant plant, and biomass/mutant plant.

#### 4. Discussion

It is suggested that PCA is useful for selecting agronomically superior mutant lines for breeding endeavors [24]. In multivariate analysis, PCA is the major selection method as well

clustering using the Tocher technique separated the mutagenic populations in the current research, demonstrating that mutagenic treatments created diverse populations. Because analyzing several phenotypic traits is a time-consuming and error-prone procedure that might hamper selection; consequently, multivariate analysis is essential for accurate selection [25]. It also facilitates the reduction of complicated data and improves breeding accuracy. Within the various clusters,

TABLE 3: Parameters related to genetic variability showing high influence of environment to most of the traits throughout both the vegetative and reproductive phases.

Genetic parameters	Mutant plant height (cm)	Main branches (number)	Secondary branches (number)	Days for 50% flowering	Days for pod initiation	Days for 50% pod maturity	Pods/ mutant plant	Root length (cm)	Seeds/ pod	Seeds/ mutant plant	Biomass/ mutant plant (g)	100 seed weight (g)	Harvest index (%)	Grain yield/ mutant plant (g)
Heritability (%)	40.133	20.383	72.475	16.04	26.397	40.155	42.762	17.61	33.344	24.311	18.042	71.391	56.285	20.459
Genotypic coefficient of variations (GCV)	20.046	16.569	60.323	5.637	2.503	2.76	21.868	12.584	20.887	17.382	24.301	21.431	10.958	19.507
Phenotypic coefficient of variations (PCV)	31.642	36.699	70.858	14.075	4.872	4.355	33.441	29.988	36.171	35.253	57.21	25.364	14.607	43.127
Genetic advance	3.607	0.217	2.067	2.362	1.846	3.092	1.354	0.511	0.367	1.036	0.03	0.333	6.321	0.009
Genetic advance as % means	26.16	15.409	105.79	4.651	2.649	3.602	29.458	10.879	24.845	17.655	21.263	37.301	16.936	18.176

TABLE 4: Genotypic correlation coefficients between all investigated traits over 62 novel mutant types.

Traits	Mutant plant height (cm)	Main branches (number)	Secondary branches (number)	Days for 50% flowering	Days for pod initiation	Days for 50% pod maturity	Pods/ mutant plant	Root length (cm)	Seeds/ pod	Seeds/ mutant plant	Biomass/ mutant plant (g)	100 seed weight (g)	Harvest index (%)
Mutant plant height (cm)													
Main branches (number)	-0.392**												
Secondary branches (number)	-0.213**	-0.118 <sup>NS</sup>											
Days for 50% flowering	0.162*	0.360**	-0.242**										
Days for pod initiation	0.193**	-0.196**	-0.253**	0.128 <sup>NS</sup>									
Days for 50% pod maturity	-0.035 <sup>NS</sup>	0.055 <sup>NS</sup>	-0.222**	-0.078 <sup>NS</sup>	0.033 <sup>NS</sup>								
Pods/mutant plant	-0.247**	0.504**	0.007 <sup>NS</sup>	0.266**	0.195**	-0.383**							
Root length (cm)	0.080 <sup>NS</sup>	-0.144*	0.172*	-0.021 <sup>NS</sup>	-0.081 <sup>NS</sup>	0.508**	0.244**						
Seeds/pod	-0.213**	-0.329**	-0.069 <sup>NS</sup>	-0.078 <sup>NS</sup>	-0.053 <sup>NS</sup>	0.111 <sup>NS</sup>	-0.321**	-0.346**					
Seeds/mutant plant	-0.375**	0.030 <sup>NS</sup>	0.141 <sup>NS</sup>	0.003 <sup>NS</sup>	0.157*	-0.178*	0.441**	0.153*	0.107 <sup>NS</sup>				
Biomass/ mutant plant (g)	-0.497**	0.107 <sup>NS</sup>	0.108 <sup>NS</sup>	-0.030 <sup>NS</sup>	0.130 <sup>NS</sup>	-0.287**	0.285**	0.128 <sup>NS</sup>	0.259**	0.114 <sup>NS</sup>			
100 seed weight (g)	-0.052 <sup>NS</sup>	-0.104 <sup>NS</sup>	-0.136 <sup>NS</sup>	0.221**	-0.139 <sup>NS</sup>	0.164*	-0.108 <sup>NS</sup>	0.081 <sup>NS</sup>	-0.095 <sup>NS</sup>	0.065 <sup>NS</sup>	0.667**		
Harvest index (%)	-0.080 <sup>NS</sup>	0.126 <sup>NS</sup>	-0.294**	0.100 <sup>NS</sup>	0.101 <sup>NS</sup>	0.139 <sup>NS</sup>	0.036 <sup>NS</sup>	-0.291**	0.378**	0.113 <sup>NS</sup>	-0.043 <sup>NS</sup>	-0.218**	
Grain yield/ plant (g)	0.102 <sup>NS</sup>	0.155*	-0.430**	0.049 <sup>NS</sup>	0.221**	-0.052 <sup>NS</sup>	0.404**	0.149*	0.159*	0.075 <sup>NS</sup>	-0.144*	0.005 <sup>NS</sup>	0.155*

\* = significant at 5 percent level; \*\* = significant at 1 percent level; NS = Non-Significant.

TABLE 5: Phenotypic correlation coefficients between all investigated traits over 62 novel mutant types.

Traits	Mutant plant height (cm)	Main branches (number)	Secondary branches (number)	Days for 50% flowering	Days for pod initiation	Days for 50% pod maturity	Pods/ mutant plant	Root length (cm)	Seeds/ pod	Seeds/ mutant plant	Biomass/ mutant plant (g)	100 seed weight (g)	Harvest index (%)
Mutant plant height (cm)	-0.179*												
Main branches (number)	-0.051 <sup>NS</sup>	-0.006 <sup>NS</sup>											
Secondary branches (number)	-0.005 <sup>NS</sup>	0.016 <sup>NS</sup>	-0.065 <sup>NS</sup>										
Days for 50% flowering	0.067 <sup>NS</sup>	-0.076 <sup>NS</sup>	-0.147*	-0.079 <sup>NS</sup>									
Days for pod initiation	-0.019 <sup>NS</sup>	-0.121 <sup>NS</sup>	-0.159*	0.028 <sup>NS</sup>	0.094 <sup>NS</sup>								
Days for 50% pod maturity	0.031 <sup>NS</sup>	0.108 <sup>NS</sup>	0.026 <sup>NS</sup>	0.127 <sup>NS</sup>	0.037 <sup>NS</sup>	-0.100 <sup>NS</sup>							
Pods/mutant plant	0.018 <sup>NS</sup>	-0.059 <sup>NS</sup>	0.060 <sup>NS</sup>	0.105 <sup>NS</sup>	-0.003 <sup>NS</sup>	0.111 <sup>NS</sup>	-0.002 <sup>NS</sup>						
Root length (cm)	-0.087 <sup>NS</sup>	0.011 <sup>NS</sup>	-0.053 <sup>NS</sup>	0.014 <sup>NS</sup>	0.060 <sup>NS</sup>	-0.024 <sup>NS</sup>	-0.292**	-0.083 <sup>NS</sup>					
Seeds/pod	-0.069 <sup>NS</sup>	-0.025 <sup>NS</sup>	0.115 <sup>NS</sup>	0.047 <sup>NS</sup>	0.045 <sup>NS</sup>	0.009 <sup>NS</sup>	0.389**	0.078 <sup>NS</sup>	0.052 <sup>NS</sup>				
Seeds/mutant plant	-0.010 <sup>NS</sup>	0.012 <sup>NS</sup>	0.101 <sup>NS</sup>	0.040 <sup>NS</sup>	0.030 <sup>NS</sup>	-0.059 <sup>NS</sup>	0.297**	-0.125 <sup>NS</sup>	0.153*	0.462**			
Biomass/ mutant plant (g)	-0.045 <sup>NS</sup>	-0.077 <sup>NS</sup>	-0.080 <sup>NS</sup>	0.089 <sup>NS</sup>	-0.062 <sup>NS</sup>	0.077 <sup>NS</sup>	0.016 <sup>NS</sup>	-0.055 <sup>NS</sup>	-0.048 <sup>NS</sup>	0.111 <sup>NS</sup>	0.336**		
100 seed weight (g)	-0.092 <sup>NS</sup>	0.058 <sup>NS</sup>	-0.206**	-0.027 <sup>NS</sup>	0.118 <sup>NS</sup>	0.190**	-0.008 <sup>NS</sup>	-0.132 <sup>NS</sup>	0.164*	0.039 <sup>NS</sup>	-0.114 <sup>NS</sup>	-0.166*	
Harvest index (%)	0.073 <sup>NS</sup>	-0.046 <sup>NS</sup>	-0.101 <sup>NS</sup>	0.045 <sup>NS</sup>	0.053 <sup>NS</sup>	0.046 <sup>NS</sup>	0.246**	-0.036 <sup>NS</sup>	0.049 <sup>NS</sup>	0.399**	0.306**	0.111 <sup>NS</sup>	0.023 <sup>NS</sup>

\* = significant at 5 percent level; \*\* = significant at 1 percent level; NS = Non-Significant.

TABLE 6: Phenotypic path matrix based on phenotypic correlations for all the variables to reveal direct as well as indirect impacts on grain yield per mutant plant.

Phenotypic path matrix	Mutant plant height (cm)	Main branches (number)	Secondary branches (number)	Days for 50% flowering	Days for pod initiation	Days for 50% pod maturity	Pods/ mutant plant	Root length (cm)	Seeds/ pod	Seeds/ mutant plant	Biomass/ mutant plant (g)	100 seed weight (g)	Harvest index (%)	Grain yield/ plant (g) correlations
Mutant plant height (cm)	0.40412	0.17438	0.06296	-0.02478	-0.05976	-0.02712	-0.34366	-0.05008	-0.05916	0.01869	-0.01555	0.00212	0.01956	0.102 <sup>NS</sup>
Main branches (number)	-0.15849	-0.44463	0.03484	-0.05519	0.06077	0.04291	0.7006	0.0905	-0.09137	-0.00148	0.00336	0.00428	-0.03089	0.155 *
Secondary branches (number)	-0.08597	0.05234	-0.29594	0.03709	0.07828	-0.17306	0.00956	-0.10776	-0.01903	-0.00703	0.00339	0.00563	0.07209	-0.430 **
Days for 50% flowering	0.06541	-0.16024	0.07168	-0.15313	-0.03973	-0.061	0.36962	0.01306	-0.02156	-0.00015	-0.00095	-0.00913	-0.02456	0.049 <sup>NS</sup>
Days for pod initiation	0.07805	0.08734	0.07488	-0.01967	-0.3094	0.02587	0.27033	0.05086	-0.01482	-0.0078	0.00406	0.00572	-0.02481	0.221 **
Days for 50% pod maturity	-0.01405	-0.02446	0.06565	0.01198	-0.01026	0.78004	-0.53172	-0.31886	0.03084	0.00888	-0.00898	-0.00674	-0.03401	-0.052 <sup>NS</sup>
Pods/mutant plant	-0.09994	-0.22417	-0.00204	-0.04073	-0.06019	-0.29847	1.38963	-0.15324	-0.08911	-0.02197	0.00891	0.00445	-0.0089	0.404 **
Root length (cm)	0.03222	0.06406	-0.05077	0.00318	0.02505	0.39598	0.33903	-0.62812	-0.09612	-0.00763	0.004	-0.00335	0.07146	0.149 *
Seeds/pod	-0.08607	0.14627	0.02028	0.01188	0.01651	0.08662	-0.44584	0.21737	0.27776	-0.00532	0.0081	0.00393	-0.09285	0.159 *
Seeds/ mutant plant	-0.15162	-0.01318	-0.04179	-0.00045	-0.04844	-0.13908	0.61281	-0.09618	0.02966	-0.04982	0.00356	-0.00269	-0.02779	0.075 <sup>NS</sup>
Biomass/ mutant plant (g)	-0.20088	-0.04774	-0.03208	0.00463	-0.0402	-0.22381	0.3956	-0.08034	0.07194	-0.00567	0.03128	-0.02748	0.01066	-0.144 *
100 seed weight (g)	-0.02082	0.04617	0.04039	-0.0339	0.04291	0.12755	-0.14996	-0.05098	-0.02651	-0.00325	0.02086	-0.04122	0.05343	0.005 <sup>NS</sup>
Harvest index (%)	-0.03222	-0.05598	0.08695	-0.01533	-0.03129	0.10811	0.05038	0.18296	0.10511	-0.00564	-0.00136	0.00898	-0.24535	0.155 *

\* = significant at 5 percent level; \*\* =significant at 1 percent level; NS = Non-Significant.

TABLE 7: Genotypic path matrix based on genotypic correlations for all the variables to reveal direct as well as indirect impacts on grain yield per mutant plant.

Genotypic path matrix	Mutant plant height (cm)	Main branches (number)	Secondary branches (number)	Days for 50% flowering	Days for pod initiation	Days for 50% pod maturity	Pods/ mutant plant	Root length (cm)	Seeds/ pod	Seeds/ mutant plant	Biomass/ mutant plant (g)	100 seed weight (g)	Harvest index (%)	Grain yield/ plant (g) correlations
Mutant plant height (cm)	0.08526	0.007	0.00012	-0.00002	-0.00012	-0.00081	0.00329	-0.00076	-0.00389	-0.02223	-0.00122	-0.00073	0.00107	0.073 <sup>NS</sup>
Main branches (number)	-0.0153	0.00077	0.00014	0.00007	0.00014	-0.00527	0.01129	0.00251	0.00051	-0.00809	0.00149	-0.00125	-0.00068	-0.046 <sup>NS</sup>
Secondary branches (number)	-0.00431	-0.13852	0.00027	-0.00027	0.00027	-0.00689	0.00276	-0.00257	-0.00237	0.03698	0.01274	-0.0013	0.00239	-0.101 <sup>NS</sup>
Days for 50% flowering	-0.00047	0.00901	0.00014	0.0042	0.00014	0.00122	0.01333	-0.0045	0.00061	0.01513	0.005	0.00145	0.00032	0.045 <sup>NS</sup>
Days for pod initiation	0.00574	0.02042	-0.00033	-0.00018	-0.0018	0.00409	0.00384	0.00013	0.00269	0.01441	0.00379	-0.00101	-0.00138	0.053 <sup>NS</sup>
Days for 50% pod maturity	-0.0016	0.02196	0.00012	0.00012	-0.00017	0.04347	-0.01051	-0.00475	-0.00108	0.00287	-0.00741	0.00125	-0.00221	0.046 <sup>NS</sup>
Pods/mutant plant	0.00267	-0.00364	0.00053	-0.00007	-0.00007	-0.00435	0.10493	0.00009	-0.01306	0.12471	0.03723	0.00025	0.00009	0.246 **
Root length (cm)	0.00151	-0.0083	0.00044	0.00001	0.00001	0.00481	-0.00022	-0.04292	-0.00372	0.02511	-0.01568	-0.00089	0.00153	-0.036 <sup>NS</sup>
Seeds/pod	-0.00741	0.00733	0.00006	-0.00011	-0.00011	-0.00104	-0.03061	0.00357	0.04476	0.01676	0.01923	-0.00077	-0.00191	0.049 <sup>NS</sup>
Seeds/ mutant plant	-0.00591	-0.01598	0.0002	-0.00008	-0.00008	0.00039	0.04083	-0.00336	0.00234	0.32051	0.05799	0.0018	-0.00045	0.399 **
Biomass/ mutant plant (g)	-0.00083	-0.01405	0.00017	-0.00005	-0.00005	-0.00257	0.03112	0.00536	0.00686	0.14807	0.12553	0.00546	0.00132	0.306 **
100 seed weight (g)	-0.00383	0.01111	0.00038	0.00011	0.00011	0.00336	0.00165	0.00237	-0.00214	0.03552	0.04222	0.01622	0.00194	0.111 <sup>NS</sup>
Harvest index (%)	-0.00783	-0.00189	0.02847	-0.00011	-0.00021	0.00826	-0.00081	0.00565	0.00733	0.01236	-0.01426	-0.0027	-0.01165	0.023 <sup>NS</sup>

\* = significant at 5 percent level; \*\* =significant at 1 percent level; NS = Non-Significant.

genetically distinct groups were categorized. In lentil improvement projects focused at promoting genetic variability, mutants selected from distinct clusters might thus be advanced to next generations [26]. Positive correlations were found between the first principal component and grain yield/mutant plant, days to fifty percent flowering, harvest index, mutant plant height, main branches (number), days for pod initiation, pods/mutant plant, and seeds/mutant plant, indicating that these variables fluctuate in the same direction. Therefore, the property of the high-yield mutant plant-1 is related to yield attribute traits and blooming traits. The PCA analysis demonstrated that yield contributed the most to population divergence, indicating that yield favorably responded to mutagenic treatments for the prospective selection of high-yield mutants. Similar modifications were applied to the second primary component, an evaluation of the architectural and floral aspects of mutant plants. The third key element emphasized the correlation between mutant plant morphology and its relationship. The first five PCs in our analysis explained 56.76 percent of the total variance. The pattern of distribution also suggested that the mutant group exhibited a high degree of quantitative trait variation [27]. The yield-related properties of the  $M_4$  populations were characterized using principal component analysis in order to explain their phenotypes and identify superior high-yield mutant plants for multiplication. The number of uncorrelated variables have decreased due to the linear adjustment of the original variables. Yield per mutant plant and harvest index are major contributions to genetic divergence; selecting these traits in the following generation might result in mutants with more distinctive yield characteristics [23, 24]. The three-dimensional scatter plot illustrates the second component with the first. Mutant-24, Mutant-43, and Mutant-28 have high values for the first component; thus, we presume that they also have high values for the characteristics that are closely related to it. Therefore, mutant plants from this diverse blend of mutant lines associated with certain traits may be used as breeding parents to generate better lentil varieties [17].

Surprisingly substantial environmental influence was observed for almost all traits, which is rare when genetic variability parameters are assessed on extant cultivars that are assumed to be acclimatized and adaptable in their optimal agro-climatic zones [37]. These results pointed to the genetic uniqueness of the newly created mutant types, which must be acclimatized by determining their ideal growth circumstances and particular agronomic practices. Yield is a polygenic trait with a complicated mode of inheritance, and direct selection for yield is seldom successful. Therefore, correlations between quantitative characteristics are influenced by the small cumulative effects of numerous genes governing trait expression. In fact, in mutant breeding initiatives, correlation analysis between character combinations is crucial for assessing the impact of yield characteristics on overall yield [28]. So, it is essential to prioritize indirect selection, concentrating on yield-altering traits. A thorough understanding of the relationship between yield and yield characteristics is effectively understood from path analysis. By splitting the correlation coefficient into direct and indirect effects, path analysis provides more comprehensive informa-

tion on the interrelationships of complex traits; hence, it has been used to define the selection criteria for genetic improvement. The nature of the relationship between yield and its associated characteristics would decide which attribute will be used in indirect selection to increase lentil production. According to the scale supplied by Lenka and Mishra, the major direct influences on grain yield were seeds/mutant plant, followed by biomass/mutant plant and pods/mutant plant [29]. The major difference in correlation and path analysis may be attributable to the fact that correlation simply calculates mutual association without addressing causes, while path analysis detects causes and evaluates their relative significance. Therefore, correlation and path analysis must be investigated to determine the precise relationship between attributes. Similar patterns were seen in terms of days to fifty percent blossom [30], pods per mutant plant [31], branches per mutant plant [32], seeds per mutant plant [33], and biomass/mutant plant [34]. The disparity between direct impacts and genotypic correlations of traits revealed that the relationship was mostly the result of indirect effects of characteristics through other component variables. Therefore, indirect selection of the previously indicated feature is typically advantageous. By assigning correlations, previous research [35] differentiates between direct and indirect effects for a more exact evaluation of the cause-and-effect association. Several vegetative, yield, and yield-contributing factors have a high association, according to a recent study. These parameters have both direct and indirect impacts on pod yield and its contributing characteristics due to their interaction [36].

Therefore, it was discovered that mutation induction by gamma rays was useful for establishing new sources of variability in lentils and avoiding breeding limitations. The induction of mutation in cv. *Moitree* by 250 Gy of gamma rays resulted in considerable variance for the vast majority of quantitative parameters examined. Due to its significant connection with and direct impacts on seed yield per mutant plant, both PCA and path analysis suggested that selection should place a significant emphasis on the total number of pods per mutant plant. The findings of cluster analysis revealed that there are genetic differences among mutant families [37]. The found mutant genotypes, such as lines 24, 43, 28, 33, and 10, maybe employed as parents for future breeding.

## 5. Conclusion

Selecting superior crop genotypes requires genetic diversity. Artificial selection has reduced allelic diversity since time immemorial. So, extending genetic diversity in a crop species may improve breeding effectiveness. Mutagenesis may be introduced directly to elite cultivars without being disturbed by the circumstances of linkage drag. Therefore, a popular lentil cultivar was irradiated for this study. This approach uses irradiation to create diversity while retaining fertility. Consequently, this research helped to the discovery of significant variables that directly or indirectly affect lentil yields. The highlighted traits may serve as selection criteria for hybridization and continuous selection-based lentil yield

enhancement programs. In addition, the researchers identified a number of lines with diverse sets of traits that may be used to create superior kinds. Induced mutations at loci controlling commercially relevant features in chosen high-yielding mutants have efficiently contributed to diversifying the existing lentil genetic base and will be of invaluable use for future lentil breeding programs. In the coming days, Targeting Induced Local Lesions in Genomes (TILLING) might be used to confirm the mutants generated by this study at the genomic level.

## Data Availability

The data shall be made available on request to the corresponding authors.

## Conflicts of Interest

The authors declare that they have no conflict of interest.

## Acknowledgments

This research article is the part of Mr. Abhik Sarkar's M.Sc. (Ag.) in GPB research program in 2022, which was supervised by Sandip Debnath at Visva-Bharati University, West Bengal, India and the study was self-funded. The authors would also like to acknowledge Researchers Supporting Project Number (RSP-2021/358), King Saud University, Riyadh, Saudi Arabia.

## References

- [1] S. K. Sharma, M. R. Knox, and T. H. N. Ellis, "AFLP analysis of the diversity and phylogeny of *Lens* and its comparison with RAPD analysis," *Theoretical and Applied Genetics*, vol. 93, no. 5-6, pp. 751-758, 1996.
- [2] M. C. Saxena, "Mutant plant morphology, anatomy and growth habit," in *The Lentil: Botany, Production and Uses. Advances in Mutant Plant Breeding Strategies: Legumes*, W. Erskine, F. J. Muehlbauer, A. Sarker, and B. Sharma, Eds., pp. 34-46, British Library, London, UK, 2009.
- [3] P. N. Bahl, S. Lal, and B. M. Sharma, "An overview of the production and problems in Southeast Asia," in *Lentil in South Asia, Proceedings of the seminar on lentils in south Asia*, pp. 1-10, Aleppo, Syria, 1993.
- [4] G. P. Savage, "The composition and nutritive value of lentils (*Lens culinaris*)," *Nutrition Abstracts and Reviews (Series A)*, vol. 58, pp. 320-343, 1988.
- [5] F. Maghuly, S. Pabinger, J. Krainer, and M. Laimer, "The pattern and distribution of induced mutations in *J. curcas* using reduced representation sequencing," *Frontiers in Plant Science*, vol. 9, no. 524, 2018.
- [6] R. W. Allard, *Principles of Plant Breeding*, John Wiley and Sons Inc, New York, NY, 1960.
- [7] M. Materne and D. L. McNeil, "Breeding methods and achievements," in *Lentil: An Ancient Crop for Modern Times*, S. S. Yadav, D. L. McNeil, and P. C. Stevenson, Eds., pp. 241-253, Springer, Dordrecht, The Netherlands, 2007.
- [8] R. A. Laskar, S. Khan, C. R. Deb et al., *Advances in Mutant plant Breeding Strategies: Legumes*, J. Al-Khayri, S. Jain, and D. Johnson, Eds., Springer, Cham, 2019.
- [9] M. E. Ferguson, N. Maxted, M. Van Slageren, and L. D. Robertson, "A re-assessment of the taxonomy of *Lens* mill. (Leguminosae, Papilionoideae, Viciae)," *Botanical Journal of the Linnean Society*, vol. 133, no. 1, pp. 41-59, 2000.
- [10] R. Amin, R. A. Laskar, and S. Khan, "Assessment of genetic response and character association for yield and yield components in lentil (*Lens culinaris* L.) population developed through chemical mutagenesis," *Cogent Food & Agriculture*, vol. 1, no. 1, article 1000715, 2015.
- [11] J. A. F. Ali, M. Arian, and N. Shaikh, "Genetic manipulation of lentil through induced mutations," *Pakistan Journal of Botany*, vol. 42, pp. 3449-3455, 2010.
- [12] K. Phasinam, T. Kassanuk, and M. Shabaz, "Applicability of internet of things in smart farming," *Journal of Food Quality*, vol. 2022, 7 pages, 2022.
- [13] A. J. Parry, P. J. Madgwick, C. Bayon et al., "Mutation discovery for crop improvement," *Journal of Experimental Botany*, vol. 60, no. 10, pp. 2817-2825, 2009.
- [14] S. Debnath and S. Guha, "Breeding methods for quality improvement in horticultural crops," in *Value Addition of Horticultural Crops: Recent Trends and Future Directions*, pp. 201-211, Springer, New Delhi, 2015.
- [15] S. Mohanasundaram, E. Ramirez-Asis, A. Quispe-Talla, M. W. Bhatt, and M. Shabaz, "Experimental replacement of hops by mango in beer: production and comparison of total phenolics, flavonoids, minerals, carbohydrates, proteins and toxic substances," *International Journal of System Assurance Engineering and Management*, vol. 13, no. S1, pp. 132-145, 2022.
- [16] S. Satpathy and S. Debnath, "Genetic analysis of yield and its attributing traits in lentil," *Journal of Pharmacognosy and Phytochemistry*, vol. 9, no. 2, pp. 713-718, 2020.
- [17] S. Singh, A. Prakash, N. R. Chakraborty, C. Wheeler, P. K. Agarwal, and A. Ghosh, "Trait selection by path and principal component analysis in *Jatropha curcas* for enhanced oil yield," *Industrial Crops and Products*, vol. 86, pp. 173-179, 2016.
- [18] M. Khodadadi, M. H. Fotokian, and M. Miransari, "Genetic diversity of wheat (*Triticum aestivum* L.) genotypes based on cluster and principal component analyses for breeding strategies," *Australian Journal of Crop Science*, vol. 5, no. 1, pp. 17-24, 2011.
- [19] I. B. Holme, P. L. Gregersen, and H. Brinch-Pedersen, "Induced genetic variation in crop plants by random or targeted mutagenesis: convergence and differences," *Frontiers in Plant Science*, vol. 10, p. 1468, 2019.
- [20] S. Satpathy, S. Debnath, and A. Mishra, "Study on character association in *Lens culinaris* medik," *Electronic Journal of Plant Breeding*, vol. 12, no. 1, pp. 58-65, 2021.
- [21] D. R. Dewey and K. H. Lu, "A correlation and path analysis of components of crested wheat grass seed production," *Agronomy Journal*, vol. 51, pp. 513-518, 1959.
- [22] K. C. Muduli and R. C. Misra, "Genetic divergence analysis among micromutant lines in finger millet (*Eleusinecoracana* G.)," *Journal of Crop Science and Biotechnology*, vol. 11, pp. 63-68, 2008.
- [23] R. Amin Laskar, M. R. Wani, A. Raina, R. Amin, and S. Khan, "Morphological characterization of gamma rays induced multipodding mutant (mp) in lentil cultivar Pant L 406," *International Journal of Radiation Biology*, vol. 94, no. 11, pp. 1049-1053, 2018.



## Retraction

# Retracted: Identification and Classification of Prostate Cancer Identification and Classification Based on Improved Convolution Neural Network

### BioMed Research International

Received 26 September 2023; Accepted 26 September 2023; Published 27 September 2023

Copyright © 2023 BioMed Research International. This is an open access article distributed under the Creative Commons Attribution License, which permits unrestricted use, distribution, and reproduction in any medium, provided the original work is properly cited.

This article has been retracted by Hindawi following an investigation undertaken by the publisher [1]. This investigation has uncovered evidence of one or more of the following indicators of systematic manipulation of the publication process:

- (1) Discrepancies in scope
- (2) Discrepancies in the description of the research reported
- (3) Discrepancies between the availability of data and the research described
- (4) Inappropriate citations
- (5) Incoherent, meaningless and/or irrelevant content included in the article
- (6) Peer-review manipulation

The presence of these indicators undermines our confidence in the integrity of the article's content and we cannot, therefore, vouch for its reliability. Please note that this notice is intended solely to alert readers that the content of this article is unreliable. We have not investigated whether authors were aware of or involved in the systematic manipulation of the publication process.

Wiley and Hindawi regrets that the usual quality checks did not identify these issues before publication and have since put additional measures in place to safeguard research integrity.

We wish to credit our own Research Integrity and Research Publishing teams and anonymous and named external researchers and research integrity experts for contributing to this investigation.

The corresponding author, as the representative of all authors, has been given the opportunity to register their agreement or disagreement to this retraction. We have kept a record of any response received.

### References

- [1] S. Tyagi, N. Tyagi, A. Choudhury, G. Gupta, M. M. A. Zahra, and S. A. Rahin, "Identification and Classification of Prostate Cancer Identification and Classification Based on Improved Convolution Neural Network," *Bio Med Research International*, vol. 2022, Article ID 9112587, 10 pages, 2022.

## Research Article

# Identification and Classification of Prostate Cancer Identification and Classification Based on Improved Convolution Neural Network

Shobha Tyagi <sup>1</sup>, Neha Tyagi <sup>2</sup>, Amarendranath Choudhury <sup>3</sup>, Gauri Gupta <sup>4</sup>,  
Musaddak Maher Abdul Zahra <sup>5</sup> and Saima Ahmed Rahin <sup>6</sup>

<sup>1</sup>Computer Science & Engineering, Manav Rachna International Institute of Research and Studies, Faridabad, 121001 Haryana, India

<sup>2</sup>Department of IT, G.L Bajaj Institute of Technology & Management, Greater Noida, India

<sup>3</sup>Department of Zoology, Patharkandi College, 788724, Karimganj, Assam, India

<sup>4</sup>Department of Biomedical Engineering, SGSITS, Indore, India

<sup>5</sup>United International University, Dhaka, Bangladesh

<sup>6</sup>Computer Techniques Engineering Department, Al-Mustaqbal University College, Hillah, 51001, Iraq

Correspondence should be addressed to Saima Ahmed Rahin; [srahin213012@mscse.uui.ac.bd](mailto:srahin213012@mscse.uui.ac.bd)

Received 26 May 2022; Revised 23 June 2022; Accepted 28 June 2022; Published 18 July 2022

Academic Editor: Gaganpreet Kaur

Copyright © 2022 Shobha Tyagi et al. This is an open access article distributed under the Creative Commons Attribution License, which permits unrestricted use, distribution, and reproduction in any medium, provided the original work is properly cited.

Prostate cancer is one of the most common cancers in men worldwide, second only to lung cancer. The most common method used in diagnosing prostate cancer is the microscopic observation of stained biopsies by a pathologist and the Gleason score of the tissue microarray images. However, scoring prostate cancer tissue microarrays by pathologists using Gleason mode under many tissue microarray images is time-consuming, susceptible to subjective factors between different observers, and has low reproducibility. We have used the two most common technologies, deep learning, and computer vision, in this research, as the development of deep learning and computer vision has made pathology computer-aided diagnosis systems more objective and repeatable. Furthermore, the U-Net network, which is used in our study, is the most extensively used network in medical image segmentation. Unlike the classifiers used in previous studies, a region segmentation model based on an improved U-Net network is proposed in our research, which fuses deep and shallow layers through densely connected blocks. At the same time, the features of each scale are supervised. As an outcome of the research, the network parameters can be reduced, the computational efficiency can be improved, and the method's effectiveness is verified on a fully annotated dataset.

## 1. Introduction

Most common among male cases in the latest global cancer statistics is lung cancer (14.5%), followed by prostate cancer (13.5%), the incidence of cancer in men, with the highest disease which is prostate cancer in more than 100 countries [1]. In the biography during the traditional diagnosis of prostate cancer, pathologists using needle biopsy to obtain case samples were obtained, pathological images were obtained after H&E staining, and microscopy was performed. To observe the tissue morphological pattern of the

cells, it is necessary to confirm whether there is cancer in the tissue exists and is Gleason rated [2].

The Gleason grading model is a widely accepted and recognized standard in the evaluation of prostate cancer tissue microarrays [3]. It has been developed since 1966 and has been revised many times by the International Society of Urology and has been used in clinical practice. This stage is not only a pathological evaluation index, but also provides a reliable basis for doctors to diagnose in clinical diagnosis [4]. Sections containing biopsies can show the morphological organization of the glandular structures of the prostate.

In low-grade tumors, the epithelial cells remain glandular structures, whereas in high-grade tumors, glandular structures are eventually lost. Prostate cancer's microarray tissue is divided into 5 growth patterns, 1 to 5, corresponding to different cell tissue morphology with better prognosis. Basically, there is no difference between normal tissue and poor prognosis. According to the proportion of the growth pattern, the growth pattern of a pathological section is divided into primary structure and secondary structure. The final score is obtained by adding the primary structure and secondary structure and classified into different prognosis groups according to the different scores, when not more than 6 points usually have better prognostic results. As shown in Table 1, five different prognostic groups were classified in the latest modified Gleason grading model: G1 when the score is not higher than 3+3; G2 for 3+4; G3 for 4+3; G4 for 3+5, 5+3, and 4+4; and G5 for higher scores. As shown in Figure 1, they represent benign Gleason scores of 6, 8, and 10, respectively.

The commonly used method in the Gleason automatic grading system for prostate cancer is to extract the feature organization and then classify the selected features using such as SVM (support vector machine), random forest, or Bayesian classifier. In these three methods, SVM is a supervised machine learning algorithm, whereas Bayesian classifier is an analytical paradigm that describes probability values as logics based on conditions conditional logic rather than long-run frequency range, and random forest is a supervised learning classification method and regression that randomly uses subsets of data and is inherently suitable for multiclass concerns. All of them can be employed in the classification of features in general. Reference uses ResNet18 as the basic model and believes that neural networks can be divided into distinguishing networks and generating networks [4].

The discriminative network adopts a classification model. This study first uses the texture features of glands to identify the presence of individual glandular structures; then, the texture features and morphometric obtained from glandular units are applied to the classification stage, and finally the images are labeled as grades 1 to 5 [5]. The literature shows that the texture features of the image are represented according to the different power spectra of the image [6].

Classifiers assign different Gleason scores. In addition to this, another method is based on deep learning, especially convolutional neural networks (convolutional neural networks), and neural network (CNN), which can perform both feature learning and classification steps in one framework and achieve better results when the training data reaches a certain size, without being overly dependent on manual annotation [7]. The development of deep learning and computer vision has made CAD (computer auxiliary diagnostic systems) that are used in medical clinical treatments [8, 9]. The study used inceptionv3 to train 120,000 images and reached the expert level of dermatologists through the classification algorithm [10]. This study used a deep network classifier to predict the probability of diagnosis and referral after training tens of thousands of scans on histo-

TABLE 1: Gleason rating prognostic group distribution.

Prognostic group	G1	G2	G3	G4	G5
				3+5	4+5
Score	<3+3	3+4	4+3	5+3	5+4
				4+4	5+5

grams with confirmed diagnosis and optimal referral [11]. Convolutional neural networks (CNN) notably uses both feature learning and classification processes in a single framework and produces better results when this technique is employed over images that are obtained using various scanning techniques like MRI and PET scans and thus helps in better prediction and diagnosis of prostate cancer. Compared with the fully convolutional neural network (FCN), U-Net has more advantages in medical image processing as it has its roots in the convolutional network. It was developed for the segmentation of biomedical images with its vast application in the segmentation of brain site prediction in protein binding, liver, and biomedical image reconstruction. Its design was improved and expanded so that it could operate with less trained images to provide a more detailed segmentation method. Both share a classic idea, encoding and decoding (encoder-decoder); U-Net's network architecture is completely symmetrical on both sides and uses concatenation, which is different from FCN in that FCN uses summation [12, 13]. Fully convolutional networks are a type of structure commonly employed for feature extraction, also known as classification problems. The only locally linked layers of FCN are used that constitutes of convolution, filtering and data augmentation. There are fewer variables because dense layers are not utilized that can make networks faster to train. Due to the fact that all connections are local, an FCN can manage a broad set of image dimensions for providing assistance in feature extraction.

Due to being easily affected by subjective factors among pathology expert observers, manual viewing is labor-intensive, time-consuming, and inefficient, and there are differences in the ratings of the same slice among different observers [14]. With the aging of the population, the number of prostate cancer patients is increasing year by year, and the number of people who need biopsy is also increasing; the observation range of CAD tools is all areas of the slice, and the advantage of CAD tools is to avoid missed inspections caused by manual observation; and CAD tools are only compatible with internal algorithms [15]. It has nothing to do with labor intensity and time and can reuse computer resources to provide reproducible results, which can greatly improve the efficiency of diagnosis and treatment and ease the tension between doctors and patients [16, 17].

Different from the classifier algorithm, this paper proposes a Gleason grading study of prostate cancer tissue microarray region segmentation based on convolutional neural network, as shown in Figure 2, which has great clinical significance in the diagnosis and treatment of prostate cancer. Many studies have shown that region segmentation can be successfully applied in clinical trials [18, 19]. Most

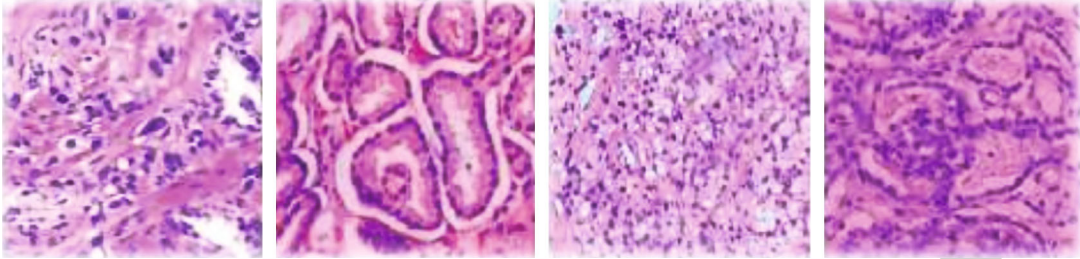


FIGURE 1: Gleason rating prognostic group distribution.

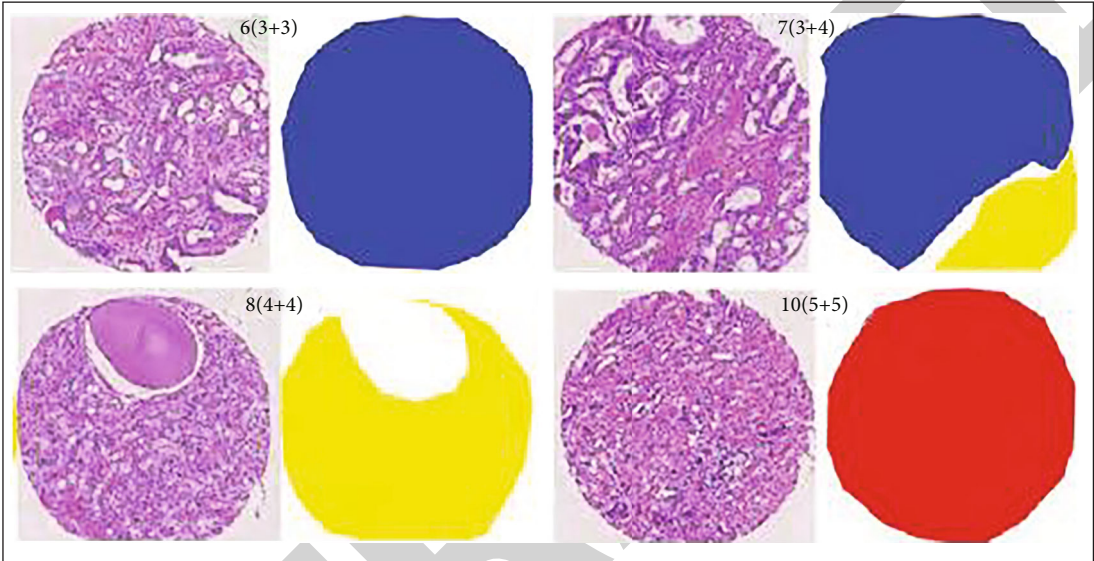


FIGURE 2: Gleason classification based on region segmentation.

TABLE 2: Distribution of Gleason scores in training, testing, and validation sets.

Test group	Total number of cases	Benign	G = 1	G = 2	G = 3	G = 4	G = 5
Test set	245	12	75	32	27	86	13
Training set	641	103	193	62	26	133	124
Validation set	135	3	42	31	24	14	21
Total	1021	118	310	125	77	233	158

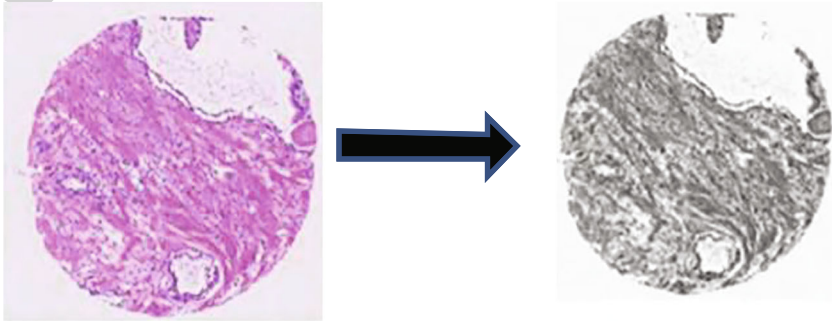


FIGURE 3: Gray processing of microarray histopathological sections.

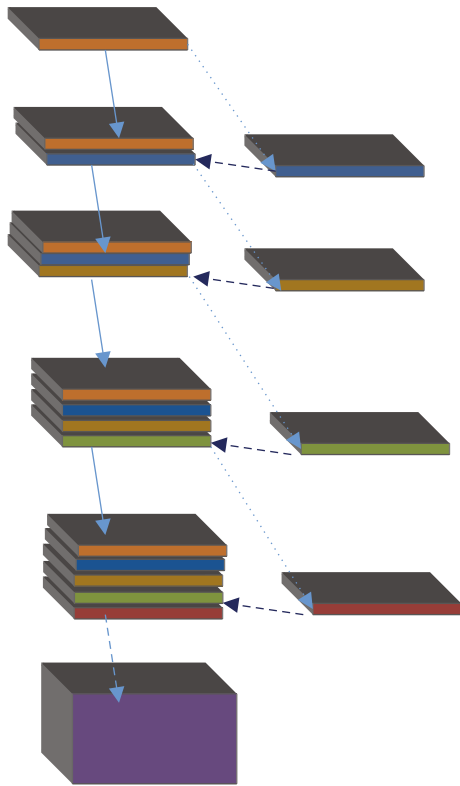


FIGURE 4: Densely connected blocks.

studies only focus on the distinction between Gleason 3 and Gleason 4. The research scope of this paper covers all types of benign and Gleason 1~5, and the scope is wider [18]. The difference from the segmentation of MR images and X-ray images is that the segmentation of tissue microarray images is based on cell morphological tissue and the difficulty coefficient of identifying growth patterns between different cell tissue morphologies, especially Gleason grades 3 and 4, is high, in the presence of cancer, particularly prostate [19, 20]. Furthermore, X-ray images vary from histopathology in that histology images possess a high amount of items of interest like cell features, e.g., nuclei that are widely distributed and accompanied by tissue and organs. X-ray image processing, on either hand, focuses primarily on a few tissues in the image that are more reliable in their location. Histology pictures, on either hand, are typically taken at a much lower incredible characteristics; the histology magnification extent is sufficient to allow some assessment at the cell level, such as nucleus measuring and identifier of gross malformations in the nucleoplasm; the lower magnifying level enables evaluation at the tissue level; therefore, due to these features possessed in the images provided by the histology, medical field is much reliable in this technique for the detection and investigation of malfunctioned cells that may be cancerous for the further prevention of fatal diseases.

The proportion of cancerous tissue cells in the biopsy is not more than 1%, and the evaluation steps of the biopsy are cumbersome and error-prone, which will lead to the inability to give the correct Gleason rating in the process of prostate cancer detection [21, 22]. This research offers the

YOLOv5x-CG real-time lesion diagnosis model to improve the lesion identification rate of colorectal cancer patients dealing with lung, breast, and prostate [23]. This research proposes an improved AlexNet-based image categorization model, with two specified block structures that are added to Alex-Net to extract specification of diseased images [24]. The novelty of this study is that a region segmentation model based on an improved U-Net network is proposed, which fuses deep and shallow layers through densely connected blocks. At the same time, the features of each scale are supervised. As an outcome of the research, the network parameters can be reduced, the computational efficiency can be improved, and the method's effectiveness is verified on a fully annotated dataset that is obtained for prostate cancer detection and investigation. However, this paper advances on the basis of the original U-Net improvements that were made to increase densely connected blocks, and after merging feature maps. The gradient path is added to make the calculation between the layers tend to be balanced, which not only improves the gradient of the original U-Net progress on the basis after the feature map is merged.

The network adds a gradient path so that the calculation between each layer tends to be balanced, which not only improves the gradient of the original U-Net network and the problem of low model feature utilization and prevents excessively repetitive information flow from occupying the memory flow. Training and testing are carried out on public datasets, and patients are diagnosed in Haikou People's Hospital. The verification is carried out on the existing prostate cancer pathological images of the Science Department, which makes the experimental results more realistic and reliable.

Organization: The paper is structured into several sections where the Introduction is the initial section followed by the second section which states the proposed methodology of the study. The 3rd module describes the experiment and result analysis followed by the last module conclusion.

## 2. Proposed Method

*2.1. Data Preprocessing.* The prostate tissue microarray images used in this study consist of two parts: The first part comes from a total of 886 public databases with detailed pathology expert annotations; the other part comes from the pathological sections of existing prostate cancer in the Department of Pathology, Haikou People's Hospital images, from which 135 were screened. These image data are divided into three groups: training group, validation group, and test group. The details of each group are shown in Table 2.

In histopathology, scanned samples usually have megapixels, and the current memory and video memory limit the training of the entire image, as shown in Figure 3; the original image size is  $3,100 \times 3,100$  RGB images, to obtain the optimal experimental results; in this paper, for the obtained original prostate cancer tissue microarray images, firstly use the original grayscale processing of all image data used for testing, training, and verification, and then grayscale each original image. And the label map is divided into

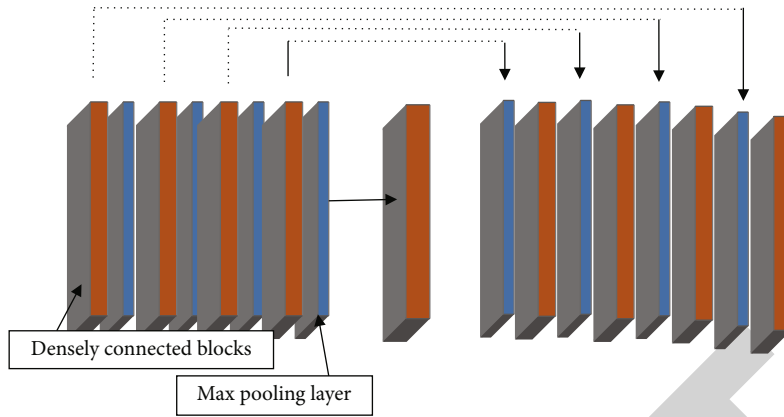


FIGURE 5: Improved network architecture.

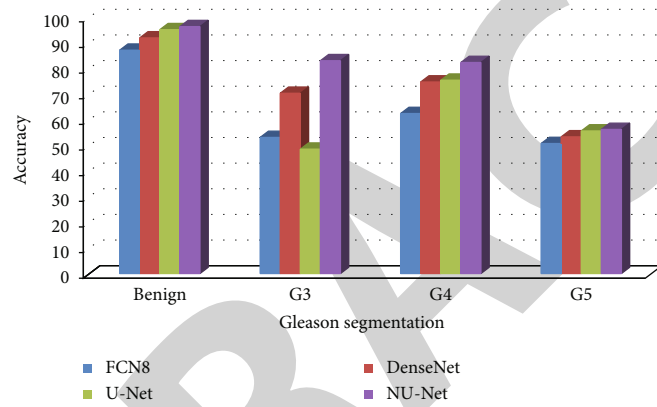


FIGURE 6: Accuracy of Gleason segmentation results.

100 nonoverlapping parts according to the corresponding order, and the size is  $256 \times 256$ .

**2.2. Network Model.** In the field of medical image segmentation, the commonly used network models are fully convolutional neural network (FCN), DenseNet, and U-Net. The U-Net network architecture can perform model training on the basis of insufficient datasets and can combine low-level information with high-level information. The original U-Net network model passes from the beginning to the end of the network stage in an end-to-end mode. Feature map integrates to solve the deformability of the gradient. After 4 times of down sampling, a total of 16 times, the corresponding up sampling is performed 4 times, and the feature information obtained in the down sampling process is restored to the same size as the original image. The corresponding stage adopts skip links so that the feature map can integrate the underlying information, making the segmentation and prediction results more accurate.

In a segmentation network, it can be described as an encoding stage  $U$  followed by a decoding operation  $R$ . When the input image is  $x$ , the model can be represented by  $g(x)$ , and the formula is as follows:

$$g(x) = R(U(x)). \quad (1)$$

$U$  means to reduce the dimension of the input image  $x$  and encode the image content and  $R$  to reconstruct the obtained feature information back to the pixel space. The goal of the network architecture is to first down sample the input image and then up sample and finally performs the regression operation in the U-Net architecture. The previous layer needs to pass the learned feature information to the next layer through the convolution operation, but the connection between each layer is sparse. To make full use of the feature information of each layer of the network, dense connections are used to transfer information between layers, and the last layer can obtain rich feature information to realize feature information reuse. Concatenation of dimensions makes the total number of parameters smaller than traditional structures.

In this paper, part of the dense link module and part of the transition layer are added to the U-Net architecture. As shown in Figure 4, the underlying feature map is passed through part of the dense link block, and the new feature map fuses the output of the previous layer as the input of the next module. After each dense connection block, two convolution and feature fusion operations will be performed. The improved network architecture is shown in Figure 5. To improve the performance of the network and avoid the problems of overfitting and regular parameter selection, a BN layer and a ReLu activation layer are added after the

TABLE 3: Parameter settings of each layer of the network model.

Parameter	Feature map size	Step size
Enter	256 * 256	—
Densely connected blocks	256 * 256	[3 × 3 Conv – 64] × 2
Max pooling layer	128 * 128	2 × 2/2
Densely connected blocks	128 * 128	[3 × 3 Conv – 128] × 2
Max pooling layer	64 * 64	2 × 2/2
Densely connected blocks	64 * 64	[3 × 3 Conv – 256] × 2
Max pooling layer	32 * 32	2 × 2/2
Densely connected blocks	32 * 32	[3 × 3 Conv – 512] × 2
Max pooling layer	16 * 16	2 × 2/2
Densely connected blocks	16 * 16	[3 × 3 Conv – 1024] × 2
Deconvolution layer	32 * 32	2 × 2/2
Densely connected blocks	32 * 32	[3 × 3 Conv – 512] × 2
Deconvolution layer	64 * 64	2 × 2/2
Densely connected blocks	64 * 64	[3 × 3 Conv – 256] × 2
Deconvolution layer	128 * 128	2 × 2/2
Densely connected blocks	128 * 128	[3 × 3 Conv – 128] × 2
Deconvolution layer	256 * 256	2 × 2/2
Densely connected blocks	256 * 256	[3 × 3 Conv – 64] × 2
Convolutional layer	256 * 256	1 × 1 conv

TABLE 4: Comparison of accuracy of Gleason segmentation results of different models, %.

Model	Benign	G3	G4	G5
FCN8	<b>87.1</b>	<b>53.08</b>	<b>62.4</b>	<b>50.7</b>
DenseNet	<b>91.9</b>	<b>70.3</b>	<b>74.7</b>	<b>53.3</b>
U-Net	<b>95.1</b>	<b>48.5</b>	<b>75.4</b>	<b>55.6</b>
NU-Net	<b>96.3</b>	<b>83</b>	<b>82.3</b>	<b>56.2</b>

TABLE 5: Comparison of F1 score of Gleason segmentation results of different models %.

Model	Benign	G3	G4	G5
FCN8	87.19	53.13	62.46	50.75
DenseNet	91.99	70.37	74.77	53.35
U-Net	95.20	48.55	75.48	55.66
NU-Net	96.40	83.08	82.38	56.26

TABLE 6: Comparison of precision of Gleason segmentation results of different models %.

Model	Benign	G3	G4	G5
FCN8	68.01	41.44	48.72	39.59
DenseNet	71.75	54.89	58.32	41.62
U-Net	74.25	37.87	58.87	43.41
NU-Net	75.19	64.80	64.26	43.88

convolutional layer. The ReLU layer can alleviate the problem of gradient disappearance and can train a deeper network than sigmoid, with high speed and low computational cost. Transformation and reconstruction can restore the influence of the normalization operation of this layer on the existing feature information. After introducing learnable reconstruction parameters, the BN layer is defined as follows:

$$\mu_B = \frac{1}{m} \sum_{i=1}^m x_i, \quad (2)$$

$$\sigma_B^2 = \frac{1}{m} \sum_{i=1}^m (x_i - \mu_B)^2, \quad (3)$$

$$x_i = \frac{x_i - \mu_B}{\sqrt{\sigma_B^2 + \epsilon}}, \quad (4)$$

$$y_i = \gamma x_i + \beta = BN_{\gamma, \beta(x_i)}, \quad (5)$$

where  $\mu$  is the translation parameter,  $\sigma$  is the scaling function,  $m$  is the size of the block, and  $\gamma$  and  $\beta$  are the reconstruction parameters. The calculation results of the above formulas are the mean, standard deviation, normalization, and reconstruction transformation, respectively.

**2.3. Loss Function.** This paper optimizes the objective function by defining loss. The goal of the network architecture model design is to minimize the prime loss between the trained labels and the output layer of the network model. In the training process of this paper, sigmoid is used as the activation function of neurons, and each training label is independent. In the binary classification task, the binary cross entropy loss function is often used. The formula is as follows:

$$BCE = \frac{1}{n} \sum_i^n (y_i \ln y_i) + (1 - y_i) \ln (1 - y_i), \quad (6)$$

Among them,  $y_i$  is the prediction result of the pixel point, and  $y_i$  is the real classification of the pixel point. Suppose that when the label is 1 and the prediction result is larger, the loss is smaller. In an ideal case, the prediction result is 1, and the returned loss is 0; otherwise, when the prediction result is 0, the smaller the prediction result, the smaller the loss. As shown in Figure 6, the prediction result has a good calculation effect when the data distribution is relatively balanced and has an adverse effect on the back

TABLE 7: Comparison of recall of Gleason segmentation results of different models %.

Model	Benign	G3	G4	G5
FCN8	68.35	41.65	48.96	39.78
DenseNet	72.11	55.16	58.62	41.82
U-Net	74.62	38.06	59.17	43.63
NU-Net	75.57	65.13	64.58	44.10

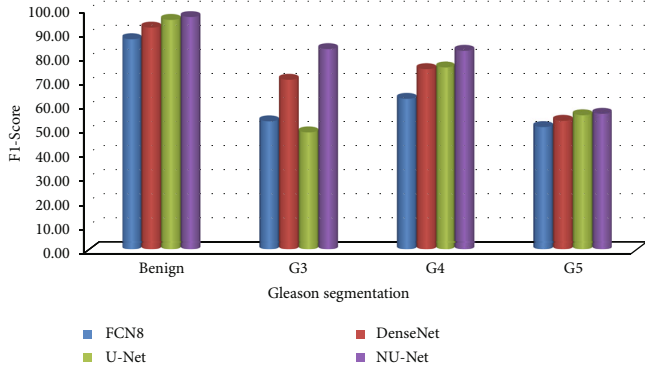


FIGURE 7: F1 score of Gleason segmentation results.

propagation, which is easy to make the training unstable. In view of the obvious imbalance of pixel categories in this study, the use of binary cross-entropy loss function will be dominated by the class with more pixels. In previous experiments, when the loss function used binary cross-entropy as the loss function, the test set predicted the image results and not ideal.

The Dice function was originally proposed in V-Net [25]. It is more effective for the problem of unbalanced categories and is often used to calculate the similarity between two samples, with a value ranging from 0 to 1. Assuming that A and B represent the same set of pixels in the two contour regions, and then Dice is defined as follows:

$$Dice(A, B) = 2 \frac{|A \cap B|}{|A| + |B|}, \quad (7)$$

It can also be expressed as

$$Dice = 1 - \frac{2 \sum_i^n y_i \hat{y}_i}{\sum_i^n y_i + \sum_i^n \hat{y}_i}, \quad (8)$$

When the target value and the predicted value are too small, the gradient will change drastically, which is not conducive to model training.

This paper combines the binary cross entropy loss function, and Dice BCE\_Dice\_loss is used as the loss function of this experiment, and the formula is as follows:

$$L = \gamma Dice + (1 - \gamma) BCE, \quad (9)$$

### 3. Experiment and Result Analysis

**3.1. Dataset.** In this study, each trained object  $x$  must have a corresponding label  $y$ , and the label image with the same height and width as the input and output is selected to complete the semantic segmentation task. Semantic segmentation performed by convolutional neural networks is based on pixel level. Unlike classification algorithms, the output is a labeled image with a fixed value for each pixel. A total of 641 detailed annotated prostate cancer pathological slices were used for training the model, and 245 digital pathological slices were used for training, and a certain number were randomly selected in the validation set for evaluation. The test set was annotated by two pathology experts. Due to the large size of the original pathological slices, Matlab was used to grayscale each image, and then each image was divided into 100 nonoverlapping images of the same size. The image dataset after segmentation was expanded by 100 times. There are 88,600 pieces of data in the test set and the test set. Then, set the size to  $256 \times 256$ , rename each image from 0 codes in the order of position, and then send the preprocessed image data into the model. To better represent the performance of this study, several images were randomly selected from the validation cohort for prediction, and the results were compared with the ground truth.

**3.2. Parameter Settings.** In the training process of this paper, Adam optimizer is used for optimization, the learning rate (lr) is 0.001, and BCE\_Dice\_loss is selected as the objective function. On the test set, a mixture matrix and Cohen's Kappa metric are used. Table 3 shows the parameter settings of each layer in the improved U-Net model.

**3.3. Experiments and Results.** This paper uses the Kappa coefficient to predict the results of the NU-Net model test consistency check with expert manual annotation results, the formula is as follows:

$$Kappa = 1 - \frac{\sum_{i,j} w_{i,j} O_{i,j}}{\sum_{i,j} w_{i,j} E_{i,j}}, \quad (10)$$

$$w_{i,j} = \frac{(i-j)^2}{(M-1)^2}, \quad (11)$$

Among them,  $M$  is the number of images.  $i$  and  $j$  represent different image categories:  $1 \leq i, j \leq M$ , and  $O_i$ ;  $j$  is classified as  $i$  by the first rater and classified as  $j$  by the second rater number.  $E_i$  refers to the expected number of images that the first rater is expected to label as class  $i$  and the second rater is expected to label images as class  $j$ .

To compare the performance of U-Net model with FCN and DenseNet before and after improvement, this paper trains and tests the above four models on the same training set and test set. FCN8 is based on a pretrained VGG16 model with a stride of 8; DenseNet is tested on the ImageNet dataset with a stride of 2; the U-Net model is based on a standard configuration; NU-Net adds a dense connection module.



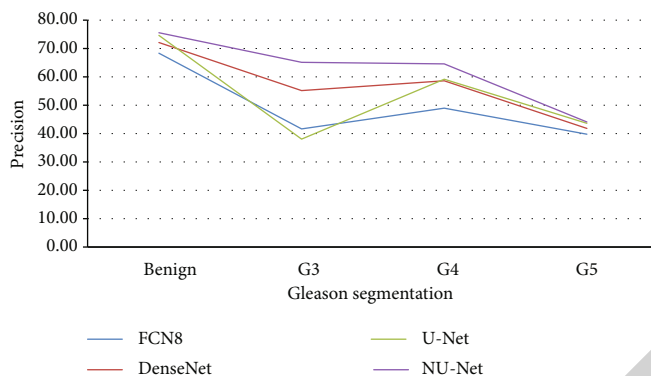


FIGURE 8: Precision of Gleason segmentation results.

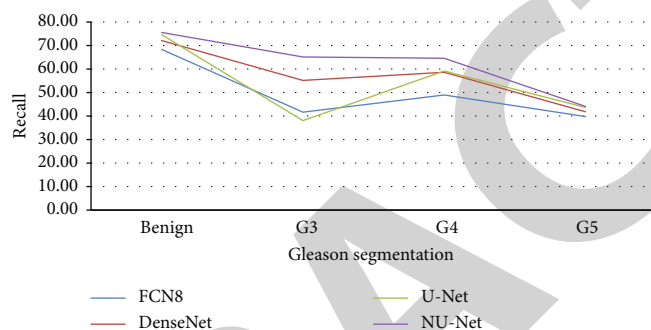


FIGURE 9: Recall of Gleason segmentation results.

In this study, 886 and 135 prostate cancer microarray tissue images were selected from the public dataset and the Radiology Department of Haikou People's Hospital, respectively, for preprocessing, with good pathologist annotations, which is divided into three parts: training set, test set, and validation set; the images in each dataset are independent and non-repeating. Through the pretrained FCN8 DenseNet, the original U-Net model, and the improved NU-Net model, 80 images randomly selected in the validation set are compared in the experiment, and the results are shown in Tables 4–7, and Figures 6–9.

Compared with the original U-Net model and the mainstream models in the other two segmentation algorithms, the improved NU-Net model shows good performance in different levels of Gleason pattern recognition, among which the original U-Net and DenseNet are in the recognition of the L averages of benign tissue and G3, G4, and G5 are 62.46% and 75.44%, respectively. The results show that the performance of the DenseNet model is better than that of U-Net on the dataset of this paper, and the worst performance is the FCN8 model. The L average value of the U-Net model with densely connected blocks has reached 78.71%, and the segmentation performance of Gleasons 3, 4, and 5 is improved to varying degrees compared with the original U-Net model.

To calculate the consistency between the experimental results of the improved NU-Net model and the ground truth of the manual viewing annotation results, this paper conducts experiments on the test set and uses the Kappa indica-

tor for evaluation, and the model prediction results are consistent with the ground truth annotation results. The comparison between the model prediction and the ground truth is shown in Figure 9. The first row is the original image of the prostate cancer microarray tissue, the middle is the ground truth, and the last row is the prediction result of the improved NU-Net model in this study. From the perspective of sorting and segmentation effects, the segmentation results of NU-Net are roughly comparable to the ground truth. To better show the experimental results, label map according to different.

#### 4. Conclusion

In this paper, an improved U-Net model is proposed to grade prostate cancer microarray tissue. The experimental results show that in the test set and the validation set, under the same evaluation reference standard, the experimental results of the model are in good agreement with the manual annotation results of pathologist's high similarity. In this paper, four different networks are tested on the validation set, and the results show that the improved NU-Net has the best segmentation effect in benign G3, G4, and G5, with an L mean of 77.73%. The segmentation results of the NU-Net model on the test set are in good agreement with the pathologist's manual annotation results in different ratings such as benign, G1, and G2, with a Kappa value of 0.797. Previous research focused on the area divided into G3 and G4, Gleason's rating in this paper covers G1~G5,

and the research is more comprehensive. The present study could be improved in several ways: First, it does not take into account for the most common pathologist errors in clinical diagnosis; the model focuses on prostate cancer microarray tissue grading, but other types of cell tissue may be present in biopsy results for a future perspective; and second, it does not account for the most common pathologist errors in clinical diagnosis experimental. The image data utilized in the dyeing is complete, with high definition and good image quality. Ideally, the system should be able to dye and process at the same time. External technological issues such as scanner calibration caused differences; each biopsy in this study was conducted separately by pathologists and deep learning models. Multiple biopsies are required in clinical practice in the future; also, the data used in the study were based on biopsies rather than patients, which could contribute to an overestimation of the new dimensions. From the patient's perspective, the learning model should be based on several needle biopsies and predict the Gleason grade.

### Data Availability

The data shall be made available on request.

### Conflicts of Interest

The authors declare that they have no conflict of interest.

### References

- [1] J. Silva-Rodríguez, A. Colomer, and V. Naranjo, "WeGleNet: a weakly-supervised convolutional neural network for the semantic segmentation of Gleason grades in prostate histology images," *Computerized Medical Imaging and Graphics*, vol. 88, article 101846, 2021.
- [2] Y. Li, N. He, S. Peng, K. Ma, and Y. Zheng, "Medical Image Computing and Computer Assisted Intervention," *MICCAI*, vol. 12908, article 487, 2021.
- [3] H.-C. Lu, E.-W. Loh, and S. C. Huang, "The classification of mammogram using convolutional neural network with specific image preprocessing for breast cancer detection 2nd international conference on artificial intelligence and big data (ICAIBD)," in *2019 2nd International Conference on Artificial Intelligence and Big Data (ICAIBD)*, Chengdu, China, May 2019.
- [4] M. Li, "Research on the detection method of breast cancer deep convolutional neural network based on computer aid," 2021, <https://arxiv.org/abs/2104.11551>.
- [5] N. Mohanapriya, B. Kalaavathi, and T. Kuamr, "Lung tumor classification and detection from CT scan images using deep convolutional neural networks (DCNN)," in *2019 International Conference on Computational Intelligence and Knowledge Economy (ICCIKE)*, pp. 800–805, Dubai, December 2019.
- [6] R. Zhang, "Melanoma detection using convolutional neural network," in *2021 IEEE International Conference on Consumer Electronics and Computer Engineering (ICCECE)*, Guangzhou, China, January 2021.
- [7] G. Polat, Y. D. Serinagaoglu, and U. Halici, "Effect of input size on the classification of lung nodules using convolutional neural networks," 2021, <https://arxiv.org/abs/2107.05085>.
- [8] W. Abdul, "An automatic lung cancer detection and classification (ALCDC) system using convolutional neural network," in *2020 13th International Conference on Developments in eSystems Engineering (DeSE)*, pp. 443–446, United Kingdom, December 2020.
- [9] C. Muramatsu, Y. Hiramatsu, H. Fujita, and H. Kobayashi, "Mass detection on automated breast ultrasound volume scans using convolutional neural network," in *2018 International Workshop on Advanced Image Technology (IWAIT)*, Chiang Mai, Thailand, January 2018.
- [10] N. Khuriwal and N. Mishra, "Breast cancer detection from histopathological images using deep learning," in *2018 3rd International Conference and Workshops on Recent Advances and Innovations in Engineering (ICRAIE)*, Jaipur, India, November 2018.
- [11] B. Kaur, K. S. Mann, and M. K. Grewal, "Ovarian cancer stage based detection on convolutional neural network," in *2017 2nd International Conference on Communication and Electronics Systems (ICCES)*, Coimbatore, India, October 2017.
- [12] P. Moradi and M. Jamzad, "Detecting lung cancer lesions in CT images using 3D convolutional neural networks," in *2019 4th International Conference on Pattern Recognition and Image Analysis (IPRIA)*, Tehran, Iran, March 2019.
- [13] R. Nimje, "Disease diagnostic system using deep learning," *International Journal for Research in Applied Science and Engineering Technology*, vol. 9, no. 10, pp. 1664–1673, 2021.
- [14] T. Thakur, I. Batra, M. Luthra et al., "Gene expression-assisted cancer prediction techniques," *Journal of Healthcare Engineering*, vol. 2021, Article ID 4242646, 9 pages, 2021.
- [15] B. Goswami, J. Chatterjee, R. R. Paul, M. Pal, and R. Patra, "Classification of oral submucous fibrosis using convolutional neural network," in *2020 National Conference on Emerging Trends on Sustainable Technology and Engineering Applications (NCETSTEA)*, Durgapur, India, February 2020.
- [16] B. N. Narayanan, V. Krishnaraja, and R. Ali, "Convolutional neural network for classification of histopathology images for breast cancer detection," in *2019 IEEE National Aerospace and electronics conference (NAECON)*, Dayton, USA, April 2019.
- [17] S. Chaudhury, N. Shelke, K. Sau, B. Prasanalakshmi, and M. Shabaz, "A novel approach to classifying breast cancer histopathology biopsy images using bilateral knowledge distillation and label smoothing regularization," *Computational and Mathematical Methods in Medicine*, vol. 2021, Article ID 4019358, 11 pages, 2021.
- [18] A. Gupta and L. K. Awasthi, "Secure thyself: securing individual peers in collaborative peer-to-peer environments," in *Proceedings of the 2008 International Conference on Grid Computing & Applications, GCA 2008*, H. R. Arabnia, Ed., pp. 140–146, CSREA Press, Las Vegas, Nevada, USA, 2008.
- [19] M. Thachayani and S. Kurian, "AI based classification framework for cancer detection using brain MRI images," in *2021 International Conference on System, Computation, Automation and Networking (ICSCAN)*, Puducherry, India, July 2021.
- [20] S. Chopra, G. Dhiman, A. Sharma, M. Shabaz, P. Shukla, and M. Arora, "Taxonomy of adaptive neuro-fuzzy inference system in modern engineering sciences," *Computational Intelligence and Neuroscience*, vol. 2021, Article ID 6455592, 14 pages, 2021.
- [21] S. R. Qureshi and A. Gupta, "Towards efficient big data and data analytics: a review. 2014," in *2014 Conference on IT in*

## *Retraction*

# **Retracted: Image Super-Resolution Reconstruction Method for Lung Cancer CT-Scanned Images Based on Neural Network**

### **BioMed Research International**

Received 8 January 2024; Accepted 8 January 2024; Published 9 January 2024

Copyright © 2024 BioMed Research International. This is an open access article distributed under the Creative Commons Attribution License, which permits unrestricted use, distribution, and reproduction in any medium, provided the original work is properly cited.

This article has been retracted by Hindawi, as publisher, following an investigation undertaken by the publisher [1]. This investigation has uncovered evidence of systematic manipulation of the publication and peer-review process. We cannot, therefore, vouch for the reliability or integrity of this article.

Please note that this notice is intended solely to alert readers that the peer-review process of this article has been compromised.

Wiley and Hindawi regret that the usual quality checks did not identify these issues before publication and have since put additional measures in place to safeguard research integrity.

We wish to credit our Research Integrity and Research Publishing teams and anonymous and named external researchers and research integrity experts for contributing to this investigation.

The corresponding author, as the representative of all authors, has been given the opportunity to register their agreement or disagreement to this retraction. We have kept a record of any response received.

### **References**

- [1] J. Xu, W. Liu, Y. Qin, and G. Xu, "Image Super-Resolution Reconstruction Method for Lung Cancer CT-Scanned Images Based on Neural Network," *BioMed Research International*, vol. 2022, Article ID 3543531, 10 pages, 2022.

## Research Article

# Image Super-Resolution Reconstruction Method for Lung Cancer CT-Scanned Images Based on Neural Network

Jianming Xu , Weichun Liu, Yang Qin, and Guangrong Xu

Provincial Key Laboratory of Informational Service for Rural Area of Southwestern Hunan, Shaoyang University, Shaoyang, 422000 Hunan, China

Correspondence should be addressed to Jianming Xu; 2598@hnsyu.edu.cn

Received 8 May 2022; Revised 10 June 2022; Accepted 20 June 2022; Published 18 July 2022

Academic Editor: Gaganpreet Kaur

Copyright © 2022 Jianming Xu et al. This is an open access article distributed under the Creative Commons Attribution License, which permits unrestricted use, distribution, and reproduction in any medium, provided the original work is properly cited.

The super-resolution (SR) reconstruction of a single image is an important image synthesis task especially for medical applications. This paper is studying the application of image segmentation for lung cancer images. This research work is utilizing the power of deep learning for resolution reconstruction for lung cancer-based images. At present, the neural networks utilized for image segmentation and classification are suffering from the loss of information where information passes through one layer to another deep layer. The commonly used loss functions include content-based reconstruction loss and generative confrontation network. The sparse coding single-image super-resolution reconstruction algorithm can easily lead to the phenomenon of incorrect geometric structure in the reconstructed image. In order to solve the problem of excessive smoothness and blurring of the reconstructed image edges caused by the introduction of this self-similarity constraint, a two-layer reconstruction framework based on a smooth layer and a texture layer is proposed for a medical application of lung cancer. This method uses a global nonzero gradient number constrained reconstruction model to reconstruct the smooth layer. The proposed sparse coding method is used to reconstruct high-resolution texture images. Finally, a global and local optimization models are used to further improve the quality of the reconstructed image. An adaptive multiscale remote sensing image super-division reconstruction network is designed. The selective core network and adaptive gating unit are integrated to extract and fuse features to obtain a preliminary reconstruction. Through the proposed dual-drive module, the feature prior drive loss and task drive loss are transmitted to the super-resolution network. The proposed work not only improves the subjective visual effect but the robustness has also been enhanced with more accurate construction of edges. The statistical evaluators are used to test the viability of the proposed scheme.

## 1. Introduction

At present, there is an increasing demand for high-resolution images in various fields such as medicine, security, and entertainment [1]. Medical science is the field where images play very important role in diagnosis of the diseases where images are supplied as inputs and output is achieved in terms of identification of the diseases based on images [2]. For example, doctors attempt to identify diseases through high-resolution CT images; diseases are identified through high-resolution surveillance images where similar images can mislead [3]. It is expected that through high-resolution video, healthcare practitioners can obtain more realistic and detailed visual effects to diagnose the diseases and ailments

in a detailed manner [4, 5]. The most direct way to increase the resolution is to increase the hardware resolution of the digital image acquisition system [6]. However, high costs and technical bottlenecks often make this method difficult to achieve, and it is not feasible for healthcare practitioners to devise these computational methods to enhance the quality of the images of patients [7]. Therefore, obtaining high-resolution images under unified hardware conditions is the focus of super-resolution reconstruction technology [8]. Super-resolution reconstruction technology provides an effective way to solve this problem. Spatially modulated full-polarization imaging technology is following the traditional methods to fetch the information from the image [9]. A new system of polarization imaging technology has been

evolved from the time-sharing and simultaneous polarization imaging technology [10]. Under the new imaging system, the system uses the Savart polarizer to modulate the four Stokes vectors of the detected target in the same interference image, so as to pass a single image as an input [11].

The complete polarization information can be obtained by acquisition [12]. The system has gradually become a research hotspot due to its advantages of obtaining multiple Stokes vectors at the same time, simple structure, and easy implementation with respect to dynamic targets [13]. A direct mapping function is established between the sensor pixels and the scene to obtain enhanced images with the new computational imaging system [14]. The feature extraction and image reconstruction as a whole is devised using the adaptive and the latest methods. The newer systems can use high-performance computing power and global information processing capabilities to enhance the resolution of the images and to extract the relevant information from the images [15, 16]. It plays a role in applications such as ultra-diffraction-limit imaging, high resolution (HR) imaging with a large field of view, and clear imaging through scattering media [17]. Single-image super-resolution technology uses a single degraded low-resolution image to reconstruct a high-resolution image [18]. High-resolution images have more details, and these details are of great significance in practical applications such as diagnosis of diseases [19]. Image super-resolution technology has always been a research hotspot in aerospace, remote sensing, target recognition, and other fields [20]. Image super-resolution (SR) technology has been widely applied, with high practical value in medical imaging, face recognition, high-definition audio, video, and other fields. Until now, medical imaging has played an important role in the medical field. High-resolution medical images can improve the work efficiency of doctors and reduce the rate of missed diagnosis. CT images are often used in guided radiotherapy, so it is of great significance to obtain high-resolution CT images.

In [2], authors have proposed super-resolution technology for the first time. At present, super-resolution technology is divided into three categories: interpolation-based methods, reconstruction-based methods, and learning-based methods. The learning-based method can introduce more high-frequency information than the other two types of methods and can obtain better robustness to noise. In [3], optical remote sensing image super-resolution reconstruction technology is used that processes one or more low-resolution optical remote sensing images with complementary information to obtain high-resolution optical remote sensing images. Optical remote sensing image is the data support and application basis of remote sensing image target detection, providing rich information for monitoring the images to extract the hidden information. Therefore, it is of great significance to improve the resolution of remote sensing images. Optical remote sensing image reconstruction algorithms are divided into two categories; one is human-centered methods, and the other is machine-centered methods. Human-centered methods often use PSNR (peak signal-to-noise ratio) and SSIM (structural similarity) as evaluation indicators and generate visually satisfactory pictures for recognition. Usually this

type of method ignores the follow-up due to the particularity of computer vision tasks (such as target detection and classification). The machine-centric method has many options, and the machine learning-based algorithms enhance the quality of the image for drawing useful information from the images by training the algorithm on huge data set of images.

The newly developed methods take the execution result of the computer vision task as an optimization index and evaluate the reconstruction performance of the algorithm through the input of images and their respective outputs. The super-resolution reconstruction task is regarded as a preprocessing step for processing the images where the resolution of the images is improved before applying any feature extraction algorithms and classification algorithms [21, 22]. The design principle focuses on learning the resolution invariance of a special task to process multiscale targets in a remote sensing image, so as to facilitate higher-level computer vision task processing and analysis. In the early days, most of the models for SR tasks have been implemented based on interpolation methods, and the most representative of them is the model based on sparse representation [14–16]. These types of models assume that any natural image can be sparsely represented by elements in the image dictionary. Then the model can reconstruct the high-resolution images based on the image dictionary. However, this type of method is computationally complex and requires a lot of computing resources, and this type of method does not perform well in restoring the details of the image. With the development of deep learning, deep neural networks have been introduced into the SR task. SR tasks based on neural networks are implemented in a supervised learning manner. From the perspective of neural networks, it is necessary to establish a pixel-level mapping from low-resolution images to high-resolution images [17]. From a statistical point of view, this process can be considered to establish a conditional probability  $p(y|x)$ , where  $x$  is the input low-resolution image and  $y$  is the corresponding high-resolution image. Through training, the neural network can learn to obtain the statistical characteristics of low-resolution images and restore high-resolution images accordingly, that is, generalize from the training data set to the test data set [18–20]. Image super-resolution reconstruction based on deep neural networks can be roughly divided into two research directions. In order to solve the above problems and generate sharper images, this paper designs a stable and effective energy-based counter-assistance loss based on the commonly used VGG reconstruction loss. Super-resolution (SR) image reconstruction is a technique used to recover a high-resolution image using the cumulative information provided by several low-resolution images. Super-resolution reconstruction of sequence remote sensing image is a technology which handles multiple low-resolution images to provide a better quality image irrespective of the underlying hardware. This technology works purely independently without the involvement of hardware support, and once the low-resolution images are enhanced by using this super-resolution technology, the images can be used on any machine; they will be classified in an accurate manner irrespective of the hardware configuration of the machine.

The advantage of using an energy function as a discriminator to replace the traditional discriminator is that the process of encoding data into energy takes into account the volatility of the neural network itself, and after the energy flow of the data is constructed, the generator can be used to track the energy flow. Another advantage of tracking the energy flow of data is that when the energy approaches 0, the discriminator no longer generates additional gradients, so the energy-based confrontation generation network is relatively stable. In order to construct a relatively stable auxiliary energy loss, this article draws on the concept of Boltzmann distribution in statistical mechanics and the energy-based GAN model [19]; the Boltzmann distribution establishes the relationship between energy and probability. According to this distribution, the lower the energy, the greater the probability of the corresponding sample to find a matching image. When the loss function converges, the curve tends to be flat. The corresponding probability distribution can be considered as the distribution  $P_{data}$  of real data. Therefore, it is assumed that samples that obey the data distribution have low energy. Then when the energy of the sample that passed to the discriminator is low enough, it can be considered that the sample obeys the data distribution and the generated confrontation network can be regarded as the energy flow of tracking the data using the model distribution.

For spatially modulated computational imaging, the image degradation process not only includes the direct mapping model between the sensor pixel and the scene in the traditional imaging method, and the mapping relationship corresponds to the interference fringe intensity image on the CCD of the spatially modulated full-polarization computational imaging; it also includes the use of two-dimensional discrete Fourier transform to transform the spatial domain interference fringe information into the frequency domain computational imaging and the use of low-pass filter calculation to obtain the target's Stokes vector information spatial modulation process [2]. At the same time, in the hyperspectral full polarization imaging system, in addition to obtaining the polarization information of the detection target, it is also very important to obtain the Hyperspectral Information and high-resolution visible panchromatic image of the target. These heterogeneous redundant hyperspectral and visible light images are the low resolution of the same target scene. The polarized image SR method provides additional target scene priors. Interpolation-based methods for super resolutions are also explored by the researchers in the existing literature. These methods use the pixel values of adjacent pixels in the image space domain to determine the pixel values of the points to be interpolated. The most common ones are the nearest neighbor interpolation, bilinear interpolation, and bicubic interpolation. The existing literature proposes spatial nonlinear interpolation algorithms, wavelet-based algorithms, and bilinear interpolation-based methods [10–12] as interpolation-based image super-resolution reconstruction method is easy to process, but due to the lack of sufficient prior knowledge and image observation model, the reconstructed image has blurred edges and poor overall visual effect.

In recent years, transfer learning methods [15, 16] have provided ideas and technical means for using scene priors to perform SR. The representative method is to use HR RGB image prior information to enhance hyperspectral image SR [17–19]. In actual imaging detection, hyperspectral imaging systems often sacrifice time and spatial resolution in order to achieve high spectral resolution, while visible light (or multispectral) cameras integrate radiation with a wide wavelength range, which can easily capture high spatial resolution in real-time images. Inspired by this, this article focuses on the spatial modulation type computational imaging degradation process for lung cancer images. The characteristics of the imaging system are utilized for preparing the model. The convolutional neural networks (CNNs) are utilized with new architecture in the proposed framework where the hybrid mechanism is used by fusion of spatial modulation-based computational imaging method based on scene feature migration.

In order to solve the problem of excessive smoothness and blurring of the reconstructed image edges caused by the introduction of this self-similarity constraint, a two-layer reconstruction framework based on a smooth layer and a texture layer is proposed for a medical application of lung cancer. This method uses a global nonzero gradient number constrained reconstruction model to reconstruct the smooth layer. The proposed sparse coding method is used to reconstruct high-resolution texture images. Finally, a global and local optimization models are used to further improve the quality of the reconstructed image.

The dual-drive adaptive remote sensing image for target detection is based on the characteristics of optical remote sensing images. An adaptive multiscale remote sensing image super-division reconstruction network is designed. The adaptive feature terminology is used as a flexible feature of the proposed approach which works well on all type of low-resolution images by employing super-resolution technology without caring about the hardware and software details. Any images can be supplied as input images, and the adaptive feature technology is able to extract the features from the image to assist in enhancement of its resolution and to assist in classifying the image more accurately. The selective core network and adaptive gating unit are integrated to extract and fuse features to obtain a preliminary reconstruction. Through the proposed dual-drive module, the feature prior drive loss and task drive loss are transmitted to the super-resolution network. Due to the precision of the remote sensing image target detection task, the super-division network can better serve the target detection task and improve the performance of target detection for serious diseases like lung cancer from the available images. The proposed work not only improves the subjective visual effect, but the robustness has also been enhanced with more accurate construction of edges.

## 2. Existing Frameworks

*2.1. Spatial Modulation Type Hyperspectral Full-Polarization System.* Spatial modulation type full-polarization imaging is a new type of polarization imaging systems developed next

to the traditional time-sharing and simultaneous polarization imaging systems. Figure 1 shows a 2-channel hyperspectral full-polarization simultaneous imager. The system is mainly composed of pre-expanded optic devices (beam expander optics (BEO)), half-wave plate front surface aperture diaphragm (S), Savart polariscope (SP), liquid crystal tuning filter (P), computing imaging system (CIS), and CCD. Among them, the area array detector has a resolution of  $2048 \times 2048$  in the visible near infrared band and a pixel size of  $12 \mu\text{m}$ ; the short-wave infrared band has a resolution of  $640 \times 512$  and a pixel size of  $20 \mu\text{m}$ .

The imaging system adopts the principle of spatial modulation of Stokes vectors and modulates 4 Stokes vectors (S03~S) in the same image at the same time. One acquisition can obtain modulation information containing the 4 Stokes vectors of the target. Based on this, it can be parsed out. The realization of hyperspectrum can quickly switch the band through the liquid crystal tuning filter and realize the rapid measurement of the complete polarization state of the target which can reflect the scene and target information from different angles.

**2.2. Image Degradation Model.** Let  $\{g_1, g_2, \dots, g_n\}$  be  $n$  frames of low-resolution images collected by existing hardware devices, and  $f$  is the high-resolution image to be reconstructed. As shown in Figure 2, the high-resolution image in Figure 2(a) is transformed into the result in Figure 2(b) after geometric transformation  $T_k$ , and then Figures 2(a) and 2(b) are, respectively, blurred (point spread function  $H_k$  and downsampling  $D$ ); add noise to get Figures 2(c) and 2(d). Consistent with literature [11], the image degradation model is expressed as:

$$g_k = DH_k T_k f + \eta_k, k = 1, 2, \dots, n. \quad (1)$$

In Equation (1),  $T_k$  is the geometric transformation,  $H_k$  is the point spread function,  $D$  is the downsampling operator, and  $\eta_k$  is the noise signal. In this paper,  $4 \times 4$  times reconstruction is considered, so the downsampling operator  $D$  is 4:1 sampling.

In order to obtain a more accurate degradation model, it is necessary to study the corresponding relationship between the high-resolution coordinate system and the low-resolution coordinate system. For this reason, it is specified that the upper left corner of the image is the origin of the coordinate, the right is the positive direction of the  $x$ -axis, and the downward is the positive direction of the  $y$ -axis. The positions of the pixels indicated by the dots in Figures 2(a), 2(b), and 2(d) in the corresponding coordinate system are shown in Figures 2(a), 2(b), and 2(d). Figure 2(d) is the positional relationship of the pixels shown by the dots in Figure 2(d) in the low-resolution coordinate system, and its coordinates are  $(s, t)$ ; Figure 2(b) is the position of the dots in Figure 2(b) shows the positional relationship of the pixel in the high-resolution coordinate system. Its coordinates are  $(x_0, y_0)$ . After downsampling,  $(x_0, y_0)$  becomes  $(s, t)$ , which is the gray value of  $(s, t)$ . It is determined by the blur of the point spread function  $H_k$  at  $(x_0, y_0)$ ; Figure 2(a) is the positional relationship of the pixel shown

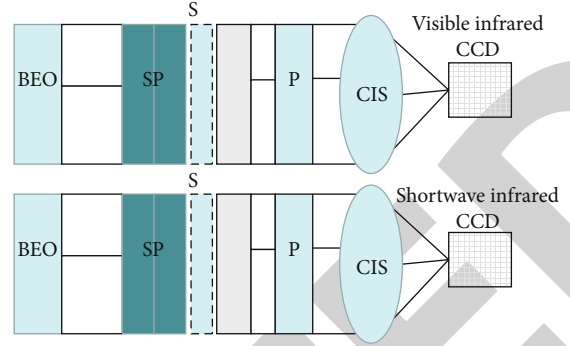


FIGURE 1: Depicting the basic composition of a full-polarization imager.

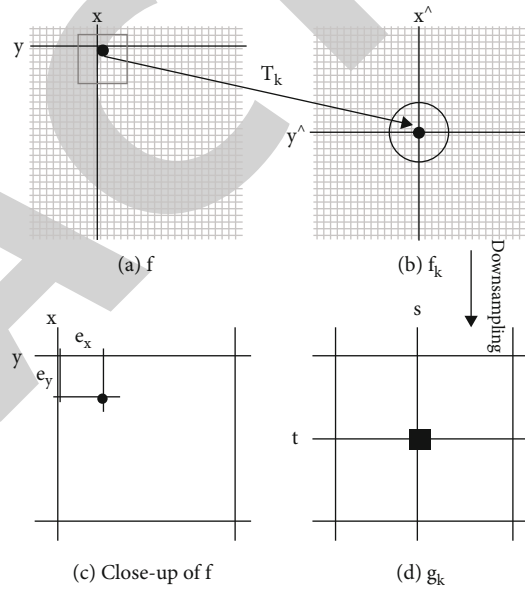


FIGURE 2: Correspondence between high- and low-resolution coordinate systems.

by the dot in Figure 1 in the high-resolution coordinate system, and its coordinates are  $(x + e_x, y + e_y)$ ; after the transformation  $f_k = T_k f$ , it becomes  $(x_0, y_0)$ ; Figure 2(c) is a partial enlarged view of the box part in Figure 2(a), and the errors in the  $x$  and  $y$  directions are respectively. In addition, since the point spread function  $H_k$  does not change the positional relationship of the coordinates, the process from Figures 2(b) to 2(d) does not reflect  $H_k$ .

Therefore, the accurate degradation process can be described as

$$g_k(s, t) = H_k T_k f(x + e_x, y + e_y) + \eta_k. \quad (2)$$

In Equation (2),  $(s, t) = DT_k(x + e_x, y + e_y)$ . Here, the gray value at the position  $(s, t)$  in the low-resolution grid is not only determined by the high-resolution grid  $(x + e_x, y + e_y)$  but is determined by the position and the surrounding pixels. The determination method depends on the point spread function  $H_k$ . Considering that the

acquisition process of low-resolution images is the overall acquisition of the same scene; it may be assumed that the transformation  $T_k$  is an overall transformation. In addition, assuming that the point spread function  $H_k$  has translation invariance, then the resolution is represented by

$$H_k T_k(x', y') = H_k f(x + e_x, y + e_y). \quad (3)$$

Considering that  $f_k = T_k f$ , thus forming

$$g_k(s, t) = H_k f(x + e_x, y + e_y) + \eta_k. \quad (4)$$

Since  $|e_x|$  and  $|e_y|$  will not exceed half a pixel unit, the above model is usually approximated by

$$g_k(s, t) \approx H_k f(x, y) + \eta_k. \quad (5)$$

Assuming that the point spread function remains unchanged during the image degradation process, and the filter  $h$  is approximated instead, two image degradation models in the spatial domain can be obtained:

$$g_k(s, t) = h * f(x + e_x, y + e_y) + \eta_k, \quad (6)$$

$$g_k(s, t) \approx h * f(x, y) + \eta_k. \quad (7)$$

In Equations (6) and (7), “ $*$ ” is convolution,  $(s, t) = DT_k(x + e_x, y + e_y) \approx DT_k(x, y)$ . Equation (5) retains sub-pixel information, and Equation (6) is approximated by rounding. Ignore this information. In the process of super-resolution reconstruction, literature [11–14] all use Equation (6) as the image degradation model, directly discarding the subpixel information which will inevitably affect the accuracy of the reconstruction model. This paper tries to base on the degradation model (5) which establishes a super-resolution reconstruction model based on subpixel displacement to improve the accuracy of the reconstruction model.

### 3. Model Building Using the CNN-Based Hybrid Mechanism

**3.1. Sparse Coding Model.** This paper proposes a dual-drive adaptive multiscale super-division reconstruction algorithm for target detection which mainly utilizes an adaptive multiscale super-division reconstruction method for enhancing the image quality of the degraded images of lung cancers. The specific structure is shown in Figure 3. The low-resolution remote sensing (ILR) image first obtains the reconstructed super-division image ISR through the adaptive multiscale method specially designed for remote sensing images. This module contains the adaptive multiscale feature extraction block and integrates the optional multiscale. The feature extraction and feature gating units can flexibly fuse the multiscale features of remote sensing images and enhance the target features. Then the super-division image ISR and the original high-resolution image IHR are sent to the feature-driven prior module for feature alignment, and the feature-driven loss is passed into the super-division

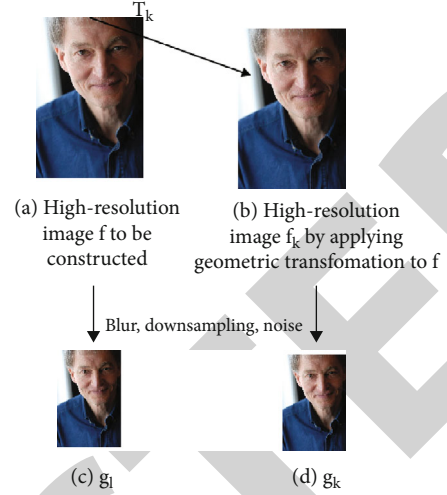


FIGURE 3: Correspondence between high- and low-resolution coordinate systems.

reconstruction network to guide the generation of super-divisions that are more suitable for target detection of remote sensing images. Then, considering the particularity of the subsequent target task, send the super-divided optical remote sensing image to the task driving module, that is, the target detection module, and pass the task driving loss to the previous super-dividing network to obtain the final remote sensing images detection result. The overall structure is shown in Figure 4 with lung cancer image of CT scan.

**3.2. Sparse Coding Unit.** Recent studies have shown that the traditional sparse coding considering the geometric structure of the image in sparse coding improves the sparse coding ability [15]. A priori condition for image geometric structure is that the natural images often contain repeated structural blocks. However, due to the potential instability of sparse coding methods, image blocks with similar geometric structures often have different sparse coefficients, resulting in flaws in the reconstruction results which can be eliminated by proposing more potential solutions. Therefore, it is necessary to use the nonlocal self-similarity of the image to stabilize the sparse coding. Rahman et al. [16] have proposed a hypothesis based on nonlocal self-similarity; if in a nonlocal neighborhood, the image block  $\times j$  is the  $j$ th of the  $k$  most similar to the image block  $\times j$ , then in the same the nonlocal neighborhood corresponding to the sparsity coefficient,  $S_j$  is also the  $j$ th most similar sparsity of  $S_j$ . This nonlocal self-similar prior condition is defined:

$$\varepsilon_1 = \sum_{i=1}^n \left\| s_i - \sum_j \omega_{ji} s_j \right\|_2^2 = \|S - SW\|_2^2, \quad (8)$$

where  $\omega_{ji}$  is the self-similar weight of  $\times j$  relative to  $\times j$ , in  $\omega_{ji} = \omega_{ji} = c_i \cdot e^{-((\|x_i - x_j\|^2)/(h_j))}$  definition,  $h_j$  is a smoothing parameter, and  $c_j$  is a normalized parameter.



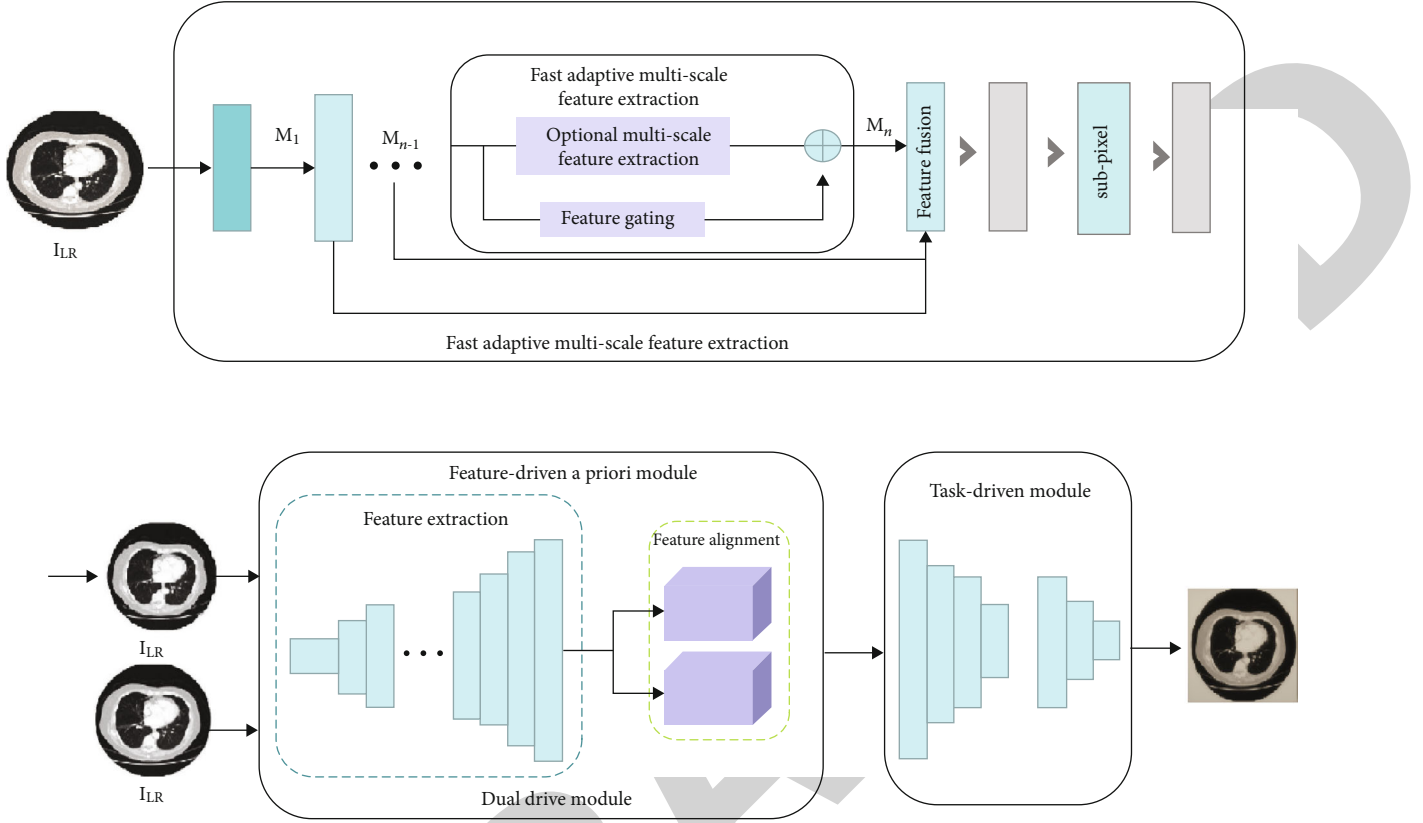


FIGURE 4: Overall CNN-based network structure for lung cancer-based CT scan images.

$$W_{ji} = \begin{cases} \omega_{ji}, \\ 0, \text{ otherwise.} \end{cases} \quad (9)$$

If  $x_j$  belongs to the  $k$  blocks most similar to  $x_j$ , combine Equation (8) with the traditional sparse coding model in Equation (9) to obtain a nonlocal self-similar sparse coding model as shown:

$$\arg \min_{D,S} \|X - DS\|_F^2 + \lambda \sum_{i=1}^n \|s_i\|_1 + \lambda_1 \|S - SW\|_2^2, \quad (10)$$

where  $s.t. \|d_i\|^2 \leq c, i = 1, 2, \dots, k$ .

The sparse coding model pays attention to the sparse coefficient space, uses the self-similarity of sparse coefficients to reduce the error of sparse representation, and protects the geometric structure of the image but does not pay attention to the choice of dictionary training. A good training dictionary can reduce rebuild defects and improve the quality of reconstructed images. The dictionaries obtained by training the sparse coding model of Equations (9) and (10) lack orthogonality and have redundancy which weakens the effectiveness and stability of the dictionary. It also reduces the reconstruction efficiency and reconstruction accuracy and easily leads to the inaccuracy of the reconstructed geometric structure. It is necessary to introduce the noncorrelation constraint of the dictionary to reduce the inaccuracy of the reconstructed geometric structure

and improve the quality of the reconstruction result. This nonrelevance constraint is defined as follows:

$$\varepsilon_2 = \|D^T D - I\|_2^2. \quad (11)$$

In Equation (11),  $I \in Rk \times k$  is the identity matrix, and  $D^T$  is the transposed matrix of dictionary  $D$ . When any two atoms in the dictionary are orthogonal,  $\varepsilon_2 = 0$ , at this time, the noncorrelation of the dictionary is the highest. Introducing Equations (8) and (11) into the traditional sparse coding model, the resulting sparse coding model is shown as

$$\arg \min_D \|X - DS\|_F^2 + \lambda_2. \quad (12)$$

The solution of Equation (12) is divided into two parts: fixed dictionary  $D$  to solve the sparse coefficient  $S$  and fixed sparse coefficient  $S$  to solve the dictionary  $D$ . Fixed dictionary  $D$  solves the sparse coefficient  $S$ ; Equation (12) becomes the following formula as shown.

$$\arg \min_S \|X - DS\|_F^2 + \lambda \sum_{i=1}^n \|s_i\|_1 + \lambda_1 \|s - sw\|_2^2. \quad (13)$$

Use feature search algorithm to update  $s_j$  one by one. The fixed sparse coefficient  $S$  is used to solve the dictionary  $D$  with a fixed sparse coefficient  $S$ , and Equation (13) leads to the following equation:

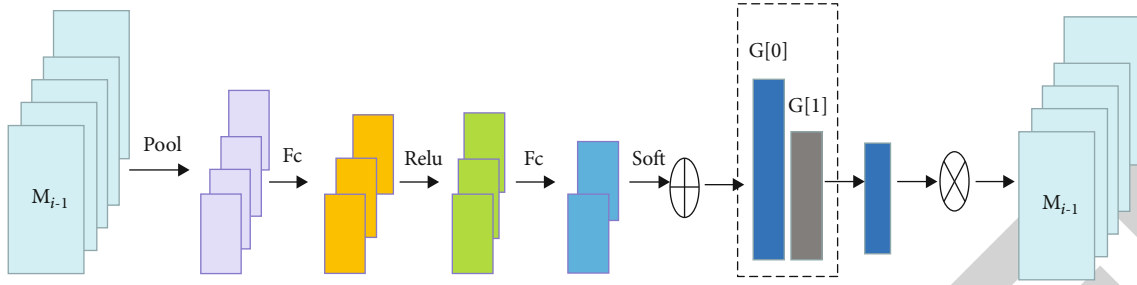


FIGURE 5: Adaptive feature gating structure diagram.

$$\arg \min_D \|X - DS\|_F^2 + \lambda_2 \|D^T D - I\|_2^2. \quad (14)$$

**3.3. Adaptive Feature Gating.** In order to obtain a better reconstruction effect and reduce calculations, it is necessary to add an adaptive gating unit between the selectable multiscale feature extraction layers to adapt to the complex nonlinear mapping relationship during remote sensing image reconstruction which reduces the redundant information. Therefore, in the process of feature transfer, we adopt a simple adaptive gating mechanism to solve the redundant information in the process of feature transfer and increase the flexibility of the network. The adaptive feature gating unit is shown in Figure 5. The key to adaptive feature gating is to adaptively obtain the gate control score of the input feature map  $M_{i-1}$ . When the gate control score ( $M_{i-1}$ ) is determined, it provides detail on how much feature information needs to be retained. The characteristic information is retained as

$$M'_{i-1} = M_{i-1} * \text{Score}(M_{i-1}). \quad (15)$$

In order to calculate the gating score, we first use the global average pooling operation to reduce the dimensionality of the feature map and then add two full connections connected to BN as a simple nonlinear mapping function, and a ReLU function is utilized to capture the dependence between channels. Finally after the Softmax operation, the vector  $G$  containing two elements is output. The element with a larger value is recorded as the gated score of the feature map  $M_{i-1}$ .

**3.4. Dual-Drive Module.** We know that the quality of optical remote sensing image target detection results depends largely on the clear image and sufficient texture information to extract specific feature information. Therefore, a dual-drive module (DDM) is proposed, and feature priority drive (FPD) and task drive (TD) are added to reduce the feature gap between super-resolution images and real high-resolution images. We combine the target detection network and the super-division reconstruction network for joint training to make the super-division reconstruction model more suitable for target detection and provide a solution for the remote sensing image super-division reconstruction method for target detection. The dual-drive module consists of two parts, a characteristic a priori-driven part and a task-

driven part. In order to reduce the feature gap between the super-resolution image and the real high-resolution image, we first add the feature prior drive and use the trained mask R-CNN with ResNet50-C4 [15] as the feature extractor since mask R-CNN introduces mask reflection and it has no transitional coupling with subsequent detectors which helps to improve the usability of the generated image in other detection networks. After feature alignment, the loss is passed to the previous super-division reconstruction network to constrain the characteristics of the super-division reconstruction image to be as similar as possible to the characteristics of the real image.

Then, it is observed that the feature gap between the super remote sensing image and the real high-resolution image is reduced. The feature prior drive is a result of relying on empirical selection but lacks flexibility and adaptability. Therefore, in order to fully explore the interaction between the super-division network and target detection, we also add task driving to jointly train the target detection network and the adaptive multiscale super-division reconstruction network. Explicitly include the task driving loss  $L_{\text{task}}$  in the training of the adaptive multiscale super-division reconstruction network.

## 4. Experimental Outcome

**4.1. Comparative Experiment.** The comparative study is made in order to evaluate the results of the proposed approach with the existing methods. We have selected several mainstream representative super-division reconstruction methods and magnified the image by 2 times for comparison experiments. The detection performance of these super-reconstructed images is tested on the UCAS-AOD data set, and then in second phase, these are tested on the lung cancer data set taken from the Zhongnan University Xiangya Medical College. The detection networks selected by the comparison method are the same as this method, and all use the Faster R-CNN network with FPN. Table 1 shows the PSNR values of optical remote sensing images reconstructed by different methods and the results of the detection performance AP (average precision) of these images. APS, APM, and APL represent the detection performance of small, medium, and large-scale targets, respectively.

As shown in Table 1 in case of double downsampling, the AP decreases from 47.6% to 22.14%. It can be seen that the performance of the super-resolution reconstruction

TABLE 1: The experimental results of our method for mAP and PSNR with other methods on NWPU VHR-10 data set.

Method	PSNR	mAP
Bicubic	24.74	47.44
MSRN	26.89	57.78
AMFFN	27	58.2
VDSR	26.7	62.85
FDSR	26.84	63.72
Proposed	28.46	68.49

TABLE 2: The experimental results are shown for mAP (mean average precision) and PSNR (peak signal-to-noise ratio).

Method	PSNR	mAP
Bicubic	25.83	48.73
MSRN	27.43	58.85
AMFFN	27.44	59.11
VDSR	26.31	62.84
FDSR	26.53	63.86
Proposed	28.63	69.55

network has a great impact on the detection results of the target detection network Faster R-CNN. Small-scale and mesoscale targets are greatly affected. The APS is reduced from 21.5% to 6.71%, and the APM is reduced from 48.5% to 23.46%, respectively. According to the analysis, this is caused by the loss of multiscale information and the limitation of downstream target detection tasks. We have utilized an adaptive multiscale super-division reconstruction module and a dual-driver module to reconstruct the multi-scale information of the image and also to significantly improve the performance of remote sensing image target detection. Our method has an AP value of 44.89% and the original high resolution. The image detection result is only 2.71% which shows the effectiveness of our method. The detection effect of small-scale targets is improved more obviously, and the APS is increased from 6.71% to 20.3%.

It can be seen from Tables 1–2 that both MSRN and AMFFN use multiscale methods to reconstruct super-resolution remote sensing images, but their multiscale networks are fixed which cannot guarantee the extraction of the multi-scale information of optical remote sensing images. The subsequent target detection task is difficult; hence, there are serious shortcomings in both the results of reconstruction effect and the target detection effect. The results are evaluated on two data sets as mentioned in the tabular results. Our method has an average increase of 1.38 dB and 1.67 dB, respectively, in resolution, and mAP increased by 10.67% and 10.3% on an average, respectively, which shows the effectiveness of the adaptive multiscale super-division reconstruction module and the dual-drive module for improving the quality of the images. VDSR uses the loss of the detection network to optimize the previous super-resolution network D-DBPN to improve the performance of target detection, but the deep VDSR network

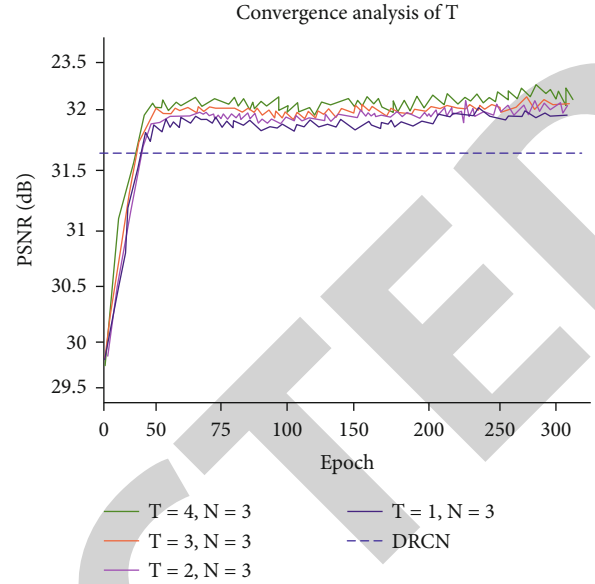


FIGURE 6: Convergence curve comparison diagram of different feedback times  $T$ .

structure may cause problems such as the disappearance of the gradient. FDSR only uses the feature extractor to align the original image features with the reconstructed image features and then transfers the alignment loss to the previous D-DBPN network. This method has great limitations. The detection accuracy of the above two methods is a little higher than that of the conventional super-resolution method. However, the above two methods do not take into account the characteristics of optical remote sensing images, so the reconstruction effect is general. On the above two data sets, the average detection accuracy mAP of these methods is 62.96% and 63.91%, but the PSNR is only 26.62 dB and 26.80 dB. Taking into account the advantages and disadvantages of these two methods, we have introduced dual-drive modules, combined with feature prior drive and task drive. In proposed method, the PSNR reached to 28.75 dB and 28.58 dB on the UCAS-AOD data set and lung cancer data set, respectively. VDSR and FDSR are 2 dB higher on average, and the target detection accuracy mAP is improved more obviously reaching 69.67% and 68.61% which shows that our method has greatly improved the reconstruction effect and detection accuracy.

In order to better verify the superiority of our method, we also selected representative test results on the UCAS-AOD and lung cancer data sets for visual display. In the test result, the red box indicates missed inspection, and the yellow box indicates the wrong test result. It can be seen from the Figure 5 that other methods have error detection and missed detection to varying degrees, and our method has good detection results. In summary, our method has the best overall performance. It not only has a better reconstruction effect on optical remote sensing images with diverse scales, but also has a great improvement in detection accuracy.

4.2. *Convergence Curve Comparison.* In order to verify the effectiveness of the key components of the proposed

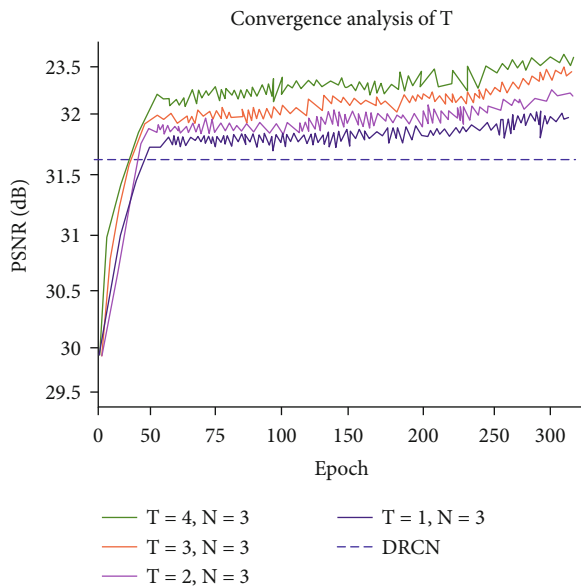


FIGURE 7: Convergence curve comparison diagram of different MRB module number  $N$ .

algorithm model, this section conducts sufficient ablation experiments. The first is to discuss the impact of the number of feedback loops, that is, the number of recursive DCB modules  $T$  and the number of MRB modules  $N$  in the DCB module on performance and then the impact of global feature fusion (GFF) and multicore fusion module (MKFB) on performance in structural design. It should be noted that in order to speed up the training process and ensure the fairness of the result comparison, all ablation experiments in this section only use the DIV2K data set as the training set, the Set5 data set as the test set, and the magnification factor is 4.

(1) In the analysis of the number of feedback  $T$  and the number of MRB modules  $N$ , Figures 6 and 7, respectively, show the PSNR index of the reconstruction result of the proposed algorithm under different  $T$  or  $N$  conditions, and the result of the DRCN algorithm is used as the benchmark reference value. It can be observed that the larger  $T$  and  $N$ , the better the performance of the algorithms.

## 5. Conclusion

In order to solve the problem of excessive smoothness and blurring of the reconstructed image edges caused by the introduction of self-similarity constraints in medical images, this paper proposes a two-layer reconstruction framework based on a smooth layer and a texture layer for providing smooth CT images of lung cancer for better diagnosis. First, in the smooth layer reconstruction, the proposed global non-zero gradient number constrained reconstruction model is used to sharpen the edge of the images and obtain an ideal smooth layer image. The generative model which takes low-resolution images as input, train on ImageNet as the feature extractor, extracts the features of high-resolution images and then builds content-based images. The energy function is utilized for compensating the confrontation loss

in the neural network which makes the model more stable and allows the model to generate clear and sharp high-resolution images. The experimental part of this article verifies the effectiveness of the proposed algorithm. The proposed work has achieved mAP (mean average precision) and PSNR (peak signal-to-noise ratio) better than the existing schemes as shown in the result section. The conversion analysis is also optimal as shown in the result section. The algorithm proposed in this article is attempting to reduce the noise and enhance the image quality for better diagnosis and it can be experimented with more data sets to prove its viability and versatility.

## Abbreviations

PSNR: Peak signal-to-noise ratio  
 AP: Average precision  
 mAP: Mean average precision  
 MSRN: Multiscale residual network  
 VSDR: Very deep super resolution  
 FDSR: Fuzzy discriminative sparse representation.

## Data Availability

The data presented in this work can be accessed through PubMed or corresponding author.

## Conflicts of Interest

The authors declare no conflict of interest.

## References

- [1] L. Zhenghao and L. Cong, "Multi-scale feature multiplexing hybrid attention network image reconstruction," *Chinese Journal of Image and Graphics*, vol. 26, no. 11, pp. 2645–2658, 2021.
- [2] D. Ling, D. Shifei, Z. Jian, and Z. Zichen, "Single image super-resolution reconstruction using VGG energy loss," *Journal of Software*, vol. 32, no. 11, pp. 3659–3668, 2021.
- [3] L. Zunxiong, Z. Chengjia, H. Ji, and C. Tijian, "Image super-resolution reconstruction of multi-hop connection residual attention network," *Computer Science*, vol. 48, no. 11, pp. 258–267, 2021.
- [4] C. Shengdi, "Medical image super-resolution reconstruction based on generative confrontation network," *Computer Times*, vol. 10, pp. 15–19, 2021.
- [5] S. Lei, Z. Hongmeng, M. Xiuqing, G. Song, and H. Yongjin, "Strongly compressed deep forged video detection based on super-resolution reconstruction," *Journal of Electronics and Information*, vol. 43, no. 10, pp. 2967–2975, 2021.
- [6] D. Glasner, S. Bagon, and M. Irani, "Super-resolution from a single image," in *2009 IEEE 12th International Conference on Computer Vision*, pp. 349–356, Kyoto, Japan, 2009.
- [7] B. Yuyang, Z. Fuzhen, and W. Hong, "Improved super-resolution reconstruction of remote sensing images in densely connected networks," *High-tech Communications*, vol. 31, no. 10, pp. 1037–1043, 2021.
- [8] Z. Du, J. Liu, J. Tang, and G. Wu, "Two strategies toward light-weight image super-resolution," in *ICASSP 2022 - 2022 IEEE*

## *Retraction*

# **Retracted: Groundwater Suitability Evaluation Using Entropy Weightage Quality Index (EWQI) Model and Human Health Cancer Risk Assessment of Heavy Metal in Eastern India**

### **BioMed Research International**

Received 8 January 2024; Accepted 8 January 2024; Published 9 January 2024

Copyright © 2024 BioMed Research International. This is an open access article distributed under the Creative Commons Attribution License, which permits unrestricted use, distribution, and reproduction in any medium, provided the original work is properly cited.

This article has been retracted by Hindawi following an investigation undertaken by the publisher [1]. This investigation has uncovered evidence of one or more of the following indicators of systematic manipulation of the publication process:

- (1) Discrepancies in scope
- (2) Discrepancies in the description of the research reported
- (3) Discrepancies between the availability of data and the research described
- (4) Inappropriate citations
- (5) Incoherent, meaningless and/or irrelevant content included in the article
- (6) Manipulated or compromised peer review

The presence of these indicators undermines our confidence in the integrity of the article's content and we cannot, therefore, vouch for its reliability. Please note that this notice is intended solely to alert readers that the content of this article is unreliable. We have not investigated whether authors were aware of or involved in the systematic manipulation of the publication process.

Wiley and Hindawi regrets that the usual quality checks did not identify these issues before publication and have since put additional measures in place to safeguard research integrity.

We wish to credit our own Research Integrity and Research Publishing teams and anonymous and named external researchers and research integrity experts for contributing to this investigation.

The corresponding author, as the representative of all authors, has been given the opportunity to register their agreement or disagreement to this retraction. We have kept a record of any response received.

### **References**

- [1] S. Saw, P. K. Singh, J. K. Mahato, R. Patel, D. N. Dhopte, and E. Asenso, "Groundwater Suitability Evaluation Using Entropy Weightage Quality Index (EWQI) Model and Human Health Cancer Risk Assessment of Heavy Metal in Eastern India," *BioMed Research International*, vol. 2022, Article ID 2476126, 14 pages, 2022.

## Research Article

# Groundwater Suitability Evaluation Using Entropy Weightage Quality Index (EWQI) Model and Human Health Cancer Risk Assessment of Heavy Metal in Eastern India

Shivam Saw <sup>1</sup>, Prasoon Kumar Singh <sup>1</sup>, Jaydev Kumar Mahato <sup>1</sup>, Rohit Patel <sup>1</sup>,  
Deepak Naresh Dhopte <sup>1</sup>, and Evans Asenso <sup>2</sup>

<sup>1</sup>Department of Environmental Science and Engineering, IIT (ISM), Dhanbad, Jharkhand, India

<sup>2</sup>Department of Agricultural Engineering, University of Ghana, Ghana

Correspondence should be addressed to Prasoon Kumar Singh; pks0506@iitism.ac.in and Evans Asenso; easenso@ug.edu.gh

Received 26 May 2022; Revised 17 June 2022; Accepted 23 June 2022; Published 12 July 2022

Academic Editor: Gaganpreet Kaur

Copyright © 2022 Shivam Saw et al. This is an open access article distributed under the Creative Commons Attribution License, which permits unrestricted use, distribution, and reproduction in any medium, provided the original work is properly cited.

This study evaluated the groundwater using the Entropy Weightage Quality Index model (EWQI). Eighteen samples were taken from the different wellbores during premonsoon seasons in 2021. The present study is aimed at developing a comprehensive approach for groundwater quality assessment and associated health risk along with the cancer risk due to the presence of heavy metals. The water quality of Ranchi city was found to be better except in the western zone. Principal component analysis (PCA) revealed that arsenic (As) was the most influencing element that deteriorated the potability of water which supports our study. The study looked at cancer and noncancer health hazards connected with heavy metal music. The value of hazardous quotient (HQ) was observed to be relatively higher in As ( $HQ > 1$ ) and Ni, followed by  $Mn > Fe > Zn > Cu$ . Also, the children were at higher risk than adults. The cancer risk associated with arsenic was investigated and found that the northern part and southeast-west (lapung block) of the study are at higher risk. Prolonged ingestion of As causes diseases like arsenicosis that leads to enhanced chances of cancer risk. This research provides an immense research database to assess the potability of drinking water in a similar city like Ranchi.

## 1. Introduction

Globally, it has been considered that groundwater is an essential natural reserve for the existence of life, and approx. two billion people worldwide rely on it [1]. India is heavily reliant (25%) on groundwater resources, followed by the United States (11%) and China (11%). Among all the consumption activities, nearly 85% of the supply is consumed for drinking purposes and 60% for the agricultural activities [2]. During 2013-14 to 2019-20, the Indian government has launched a potable water supply and cleanliness program for low-income states, such as Jharkhand in association with the world bank. The wells and bore wells are vital resources for drinking water in a rural area of this state. Contamination and degradation of groundwater can occur naturally by the interlinkage of hazardous materials found in topsoil and rocks beneath the earth's surface, and contamination can

occur artificially by the activity of poor drainage systems, agriculture, discharge of untreated sewage, and industrial water [3, 4]. This contamination mechanism in groundwater varies widely on the basis of landuse pattern, lithological characteristics water-rock-soil interrelation, physicochemical excellence, microbial and mineral existence, and other factors [5]. Land use and lithological characteristics interrupt groundwater resources through changes in recharge and by altering demands for water. Inappropriate land use, primarily poor land management, causes chronic groundwater quality problems. Human health is jeopardized by the presence of harmful elements in groundwater sources. These elements are nonbiodegradable, immobile, poisonous, and bioaccumulative, with a thousand-year residence duration. Recently, there has been a lot of focus on evaluating the chemical parameters of potable water and the related health problem linked with nitrate ( $\text{NO}_3^-$ ) and fluoride ( $\text{F}^-$ ), which

are considered to be the most prevalent chemical elements and also found to be most toxic [6–8]. Li et al. [9] investigated the groundwater quality and its risks posed by pollutants such as nitrate and fluoride ions in an arid climate zone near northwest China, and the study reported that responsible pollutants emerge from industrial, agricultural, and geogenic sources. They also discovered that adults are not as vulnerable to health risks as children and girls. The hazard in respect of both carcinogenic and noncarcinogenic impacts can be assessed using human health risk assessment [10]. Kaur et al. [11] investigated the impact of human interventions on drinking water in Panipat, India, and the subsequent impact on the health of the exposed people, finding that kids are at a higher danger as compared to men and women cases of non-carcinogenic risk. The application of entropy approaches to the weighting of each assessment index is a very relative technique that successfully removes human prejudices. In India, various studies evaluate the quality of drinking water for irrigation and consumption in Andhra Pradesh (Subba Rao et al. [4]), Chandigarh (Rahman et al. [12]), and various parts of the country. Water polluted with As (arsenic) has caused major chronic human ailments such as dermatological disorders, arsenicosis, keratosis, and cancer all over the world [12]. In 2005, the National Metallurgical Laboratory in collaboration with United Nations International Children's Emergency Fund (UNICEF) confirmed the existence of arsenic in Sahibganj [13].

Ranchi, the state capital of Jharkhand, is emerging as a major educational and industrial center. Because of the reason of involuntary development, movement of people from rural to urban areas, insufficient drainage systems, and inefficient sewage disposal services in various major and small-size companies, and periurban accumulation are deteriorating in most Indian towns [14]. As a result, strong water management is essential to meeting basic water needs; otherwise, substantial environmental and health costs will be incurred. Efficient water management requires accurate assessment and investigation of drinking water quality. Several indices of water quality can aid in handling enormous volumes of water quality data because they are an excellent method for condensing huge quantities of data into a single numeric number allowing for a simple and easy explanation of the observed data [15]. Conducted a study for evaluation of only the quality of groundwater resources in Zanjan Plain using EWQI. Adimalla [16] conducted a study in the rural area of Telangana state, India, to assess the groundwater quality using EWQI and pollution index. Kumar and Augustine [17] carried out the assessment of groundwater quality of Odai Sub-Basin, South India. Such previous studies were limited to the assessment of groundwater quality incorporating EWQI approach, but the present study comprises of comprehensive approach for groundwater quality assessment and associated health risk along with the cancer risk due to presence of heavy metals in eastern India.

The goal of this work was to assess (i) spatial distribution analysis to determine the overall acceptability of groundwater quality using an entropy-weighted water quality index (EWWQI), (ii) hazard index (HI), to carry out the risk associated with drinking water for the residents who are using extremely contaminated groundwater for drinking purposes,

(iii) the carcinogenic risk assessment of arsenic, and (iv) principal component analysis (PCA) and hierarchical cluster analysis of the study area. This research contributes to the identification of the intensity of distinct zone of vulnerability at a particular location to adopt effective methods to enhance groundwater quality.

## 2. Materials and Methods

**2.1. Location Map of Study Area.** In present study, all the samples were collected from Ranchi, Jharkhand, during April-May month of 2021. It is situated at 23.37°N latitude and 85.35°E longitude, and its height is about 2300 feet above sea level. According to the census of Ranchi Municipal Corporation (RMC) 2011, it has a total population of around 1,073,440. The average annual rainfall of Ranchi is 1394 mm. The water sample was collected from the 18 defined groundwater wells of Ranchi city. The location sites were selected at random based on the availability of wells (Figure 1). ArcGIS, version 10.3, was used to create the sampling sites and spatial distribution maps. The methodology involved in the present study is shown in the form of flow diagram in Figure 2.

**2.2. Computational Methods.** The physicochemical properties of groundwater samples were calculated in their entirety as per the standards protocol of APHA [18]. The value of pH and electrical conductivity (EC) was evaluated on the site using water quality multimeter (Model No. Hach HQ430d). Cations ( $\text{Na}^+$ ,  $\text{K}^+$ ,  $\text{Ca}^{2+}$ ) were analyzed by using flame photometry (Model 1385), while the anions i.e., sulfate ( $\text{SO}_4^{2-}$ ), chloride ( $\text{Cl}^-$ ), and fluoride ( $\text{F}^-$ ) are done by using the turbidimetric method, argentometric method, and SPADNS methods, respectively. The heavy metal concentration was analyzed by atomic absorption spectrophotometry (AAS) (REF-3000AA, Refinement). In this case, the widespread use of AAS across the globe is ascribed to its acceptance, recognizability, usability, and affordability when compared to other fundamental approaches like inductively coupled plasma. Additionally, AAS is a sensitive technique that may identify elements at quantities as low as ng/mL, particularly when using the graphite furnace mode for atomization. Due to the use of a selective irradiation source, AAS also benefits from good selectivity. Excel 2019 and Origin software version 20 were used to conduct the statistical analysis.

**2.3. Entropy-Weighted Water Quality Index (EWWQI).** The EWWQI is a scientific tool for determining quality for drinking purposes and other domestic uses [19, 20]. The calculation procedures of EWWQI consist of 5 different steps [21, 22] which are as follows.

The matrix ( $A$ ) is an eigenvalue matrix connected with water quality information for “ $m$ ” no. of various samples and “ $n$ ” no. of physicochemical parameters during the first step (Eq. (1)).

$$A = \begin{vmatrix} a_{11} & a_{12} & \cdots & a_{1n} \\ a_{21} & a_{22} & \cdots & a_{2n} \\ \vdots & \vdots & \ddots & \vdots \\ a_{m1} & a_{m2} & \cdots & a_{mn} \end{vmatrix}. \quad (1)$$

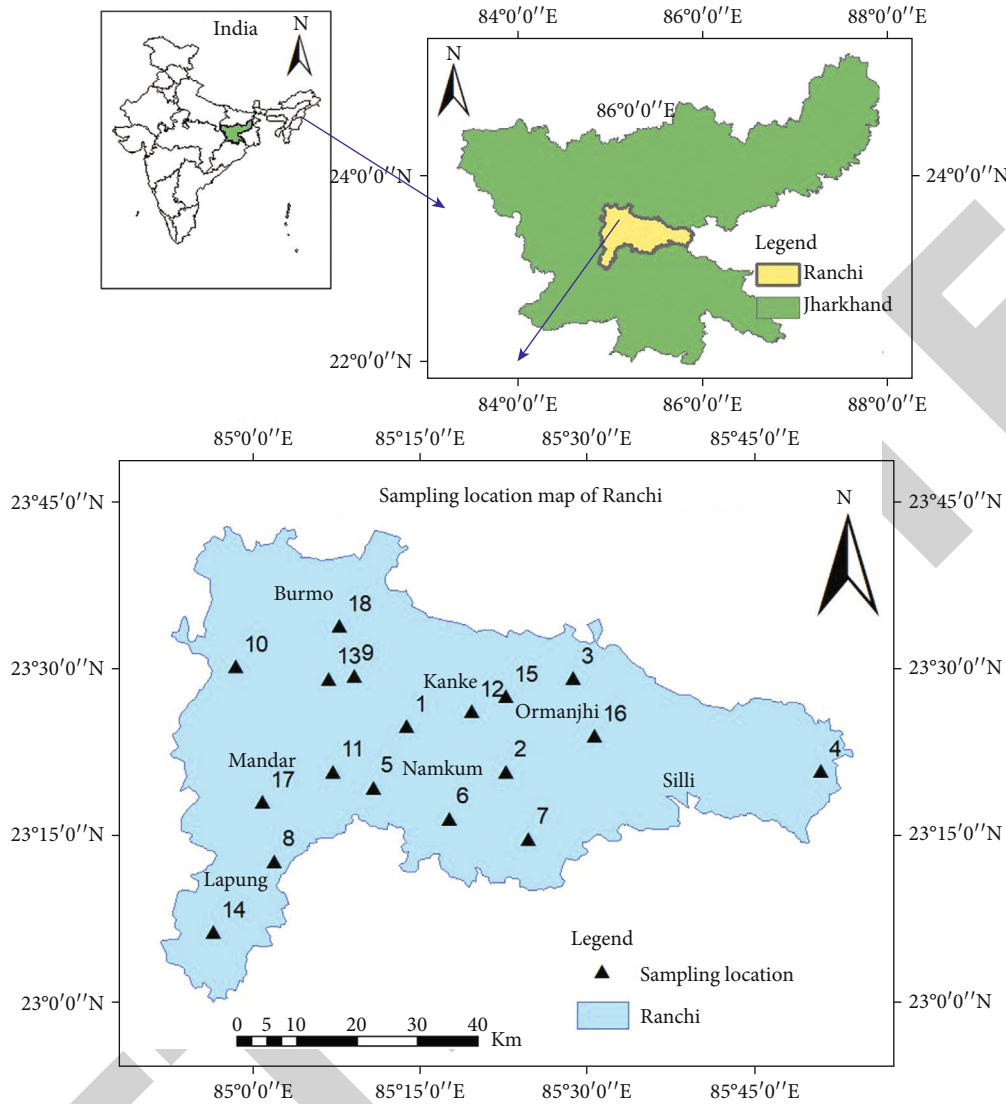


FIGURE 1: Sampling location of the study area.

The above matrix (*A*) was modified into a new-grade matrix (*B*) in the second stage, using Equations (2) and (3).

$$b_{ij} = \frac{a_{ij} - (a_{ij})_{\min}}{(a_{ij})_{\max} - (a_{ij})_{\min}}, \quad (2)$$

$$B = \begin{vmatrix} b_{11} & b_{12} & \dots & b_{1n} \\ b_{21} & b_{22} & \dots & b_{2n} \\ \vdots & \vdots & \ddots & \vdots \\ b_{m1} & b_{m2} & \dots & b_{mn} \end{vmatrix}. \quad (3)$$

The information entropy (*e<sub>j</sub>*) was calculated in the third stage, using Equations (4) and (5).

$$e_j = -\frac{1}{\ln m} \sum_{i=1}^m P_{ij} \ln P_{ij}, \quad (4)$$

$$P_{ij} = \frac{(1 + b_{ij})}{\sum_{i=1}^m (1 + b_{ij})}. \quad (5)$$

Using Equations (6) and (7), the weight of entropy (*w<sub>j</sub>*) and the rating scale (*q<sub>j</sub>*) were evaluated in the fourth step.

$$w_j = \frac{(1 - e_j)}{\sum_{i=1}^m (1 - e_j)}, \quad (6)$$

$$q_j = \frac{C_j}{S_j} \times 100. \quad (7)$$

According to WHO [23] and BIS [24], *C<sub>j</sub>* is the physico-chemical parameter (*j*) content (mg/L), and *S<sub>j</sub>* is the



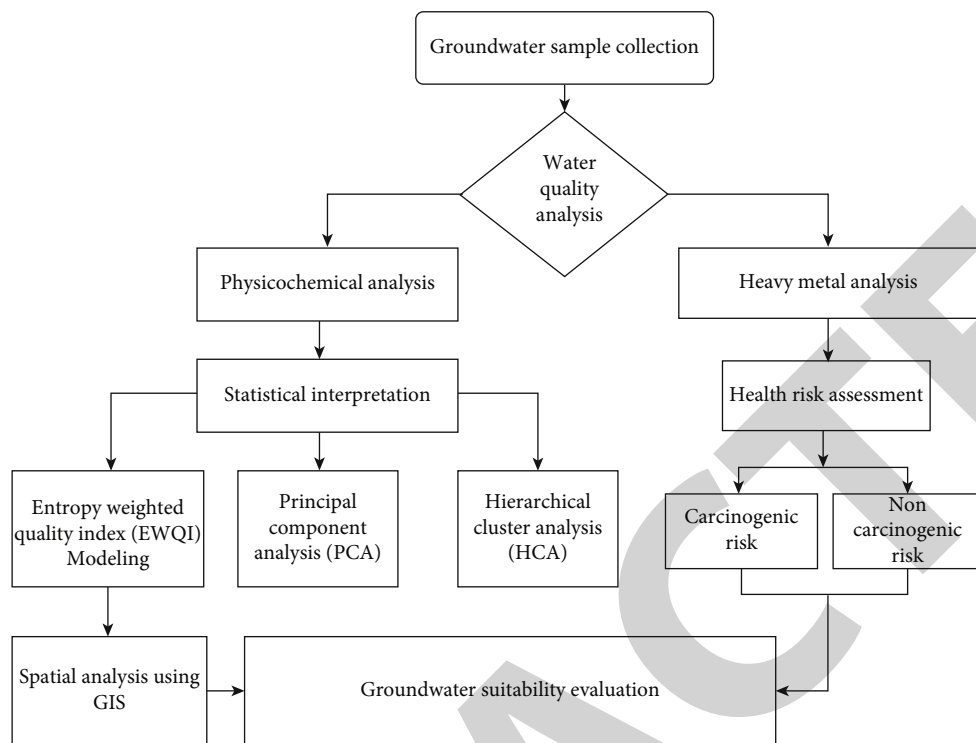


FIGURE 2: Schematic layout of methodology involved in present study.

standard desired limit of the physicochemical parameter ( $j$ ) given in mg/L. Finally, EWWQI was calculated with the help of equation (8).

$$EWWQI = \sum_{j=1}^m w_j q_j. \quad (8)$$

With the help of EWQI modeling approach different categories are assigned corresponding to EWQI range, excellent quality has been assigned to the EWQI if it is below 25, the good quality between 25 and 50, medium quality between 50 and 100, poor quality between 100 and 150, and unfit for drinking if it is above 150. Additionally, Table 1 presents the EWQI rankings and classification for groundwater quality [25].

**2.4. Health Risk Assessments of Heavy Metals.** The noncarcinogenic human health risk due to the oral exposure associated with the heavy metals present in groundwater was evaluated by the computation of total hazard index (HI) given by methods (Eq. (9)). The noncancer risks were characterization as hazard quotient (HQ) (Eq. (10)). It is the ratio of individual element exposure levels to the reference dose (RfD) of the corresponding element. The RfD values of various heavy metals are based on the hazard index (HI) value, which is the ratio of multiple substance/unit-exposure pathways and can be expressed as the sum of all HQ values (Eq. (11)).

$$ADD = (C_w \times I_r \times F_R \times E_D) / (W_b \times T_m), \quad (9)$$

TABLE 1: Classification standards of groundwater quality according to Entropy Weighted Water Quality Index (EWQI).

Sl no.	Range of EWQI	Category
01	<25	Excellent
02	25-50	Good
03	50-100	Medium
04	100-150	Poor
05	>150	Unfit

TABLE 2: Carcinogenic risk level scale [26].

Risk level	HQ/HI	Occurrence of cancer	Carcinogenic risk
1	<0.1	<1 per 10 lakh inhabitants	Very low
2	$\geq 0.1 < 1$	> 1 per 10 lakh inhabitants <1 per 1 lakh inhabitants	Low
3	$\geq 1 < 4$	> 1 per 1 lakh inhabitants <1 per 10 thousand inhabitants	Medium
4	$\geq 4$	> 1 per 10 thousand inhabitants <1 per inhabitants	High

$$HQ = \text{exposure level} \frac{(ADD)}{RfD}, \quad (10)$$

$$HI = \sum HQ. \quad (11)$$

Here, ADD is the mean daily dose of heavy metals (mg/kg/day),  $C_w$  is the concentration of heavy metals (mg/l) in the

TABLE 3: The analyzed data of groundwater quality variables.

Parameters	Min	Max	Avg	SD	BIS [24]
pH	7	8.1	7.55	0.31	6.5–8.5
EC	236	1369	554.72	333.57	—
TDS	236	1168	573.05	273.59	500-2000
F <sup>-</sup>	0.21	0.96	0.55	0.25	1-1.5
Cl <sup>-</sup>	31.12	228.3	91.46	59.32	250-1000
HCO <sub>3</sub> <sup>-</sup>	89	536	222.93	107.31	200-600
SO <sub>4</sub> <sup>-2</sup>	12.6	85.3	42.33	21.83	200-400
NO <sub>3</sub> <sup>-</sup>	4.1	65.7	24.95	18.10	45
Ca <sup>2+</sup>	22.6	130.6	70.66	30.63	75-200
Mg <sup>2+</sup>	11.8	60.5	33.40	14.35	30-100
Na <sup>+</sup>	12.5	42.3	25.68	9.51	200
K <sup>+</sup>	3.6	18.6	8.46	4.33	12
Total hardness	105.66	578.58	307.54	121.71	200–600

All parameters are in mg/l, except EC( $\mu$ S/cm) and pH has no unit.

water samples,  $I_r$  is the rate of ingestion (3 l/day for adults),  $F_R$  is the frequency of exposure (days/year),  $E_D$  is the total duration of exposure (years),  $W_b$  is the average weight of (60.5 kg in adults) [10], and  $T_m$  is the meantime (days).

The product of ADD (mg/kg/day) and SF (mg/kg/day)<sup>-1</sup> was used to determine the carcinogenic hazard. The characterization scale was derived using Table 2 as a guide [26].

### 3. Result and Discussion

**3.1. Physicochemical and Hydrogeochemical Characterization of Groundwater.** Table 3 shows the summary data regarding the physicochemical quality of groundwater in Ranchi. The pH value was observed mostly basic in nature that varied from (7 to 8.1). The measured value of electrical conductivity (EC) in the study area varies from 236 to 1369  $\mu$ S/cm. The chemistry of cations in the study has the dominancy of calcium (Ca<sup>2+</sup>) > magnesium (Mg<sup>2+</sup>) > sodium (Na<sup>+</sup>) and > (potassium) K<sup>+</sup>. In contrast, the observed seasonal value of anions was the highest in bicarbonate (HCO<sub>3</sub><sup>-</sup>) and lowest in fluoride (F<sup>-</sup>). The geochemical processes and interactions of numerous minerals and organic materials are the fundamental causes of variation in groundwater composition.

**3.2. EWQI Modeling.** This study computed the suitability of physicochemical quality with the help of the entropy-weighted water quality index (EWWQI) model [25]. They ranged from 39.8 to 138.3 with average of 85.4 shown in Table 4. The descriptive table shows categories of water with its rank that helps to identify the suitability for drinking or domestic purposes. This whole study area belongings to three categories, viz., good (25-50), medium (50-100), and poor (100-150). It has been observed that only one sample found to be in good category of water for drinking. The medium type of category is unfit for drinking purposes while it can be fit for domestic purposes; on other hand, the poor category is neither good for drinking nor for domestic pur-

TABLE 4: Categorization of EWQI and its suitability.

Sampling no.	EWQI	Category	RANK	Suitability for drinking purposes	Suitability of domestic purpose
1	39.8	G	2	Fit	Yes
2	45.9	M	3	Unfit	Yes
3	64.9	M	3	Unfit	Yes
4	82.7	M	3	Unfit	Yes
5	61.7	M	3	Unfit	Yes
6	85.4	M	3	Unfit	Yes
7	91.1	M	3	Unfit	Yes
8	134.1	P	4	Unfit	NO
9	138.3	P	4	Unfit	NO
10	107.0	P	4	Unfit	NO
11	74.6	M	3	Unfit	Yes
12	90.5	M	3	Unfit	Yes
13	103.7	P	4	Unfit	NO
14	84.7	M	3	Unfit	Yes
15	73.5	M	3	Unfit	Yes
16	84.2	M	3	Unfit	Yes
17	75.4	M	3	Unfit	Yes
18	99.6	M	3	Unfit	Yes

G: good; M: medium; P: poor.

poses. As illustrated in Figure 2, the 72% of the samples was found in medium category, ranked as 3, 22% of the samples was under poor category, ranked as 4, and only 6% of sample was fall in good category, ranked as 2. The spatial map of EWQI value shown in Figure 3, this picture, clearly shows that the good (EWQI < 50) and medium (EWQI ranged 50-100) quality of water was identified in the center of the research area while the poor (EWQI > 100) quality of water in the eastern part. Figure 4 shows the percentage of groundwater samples in different category.

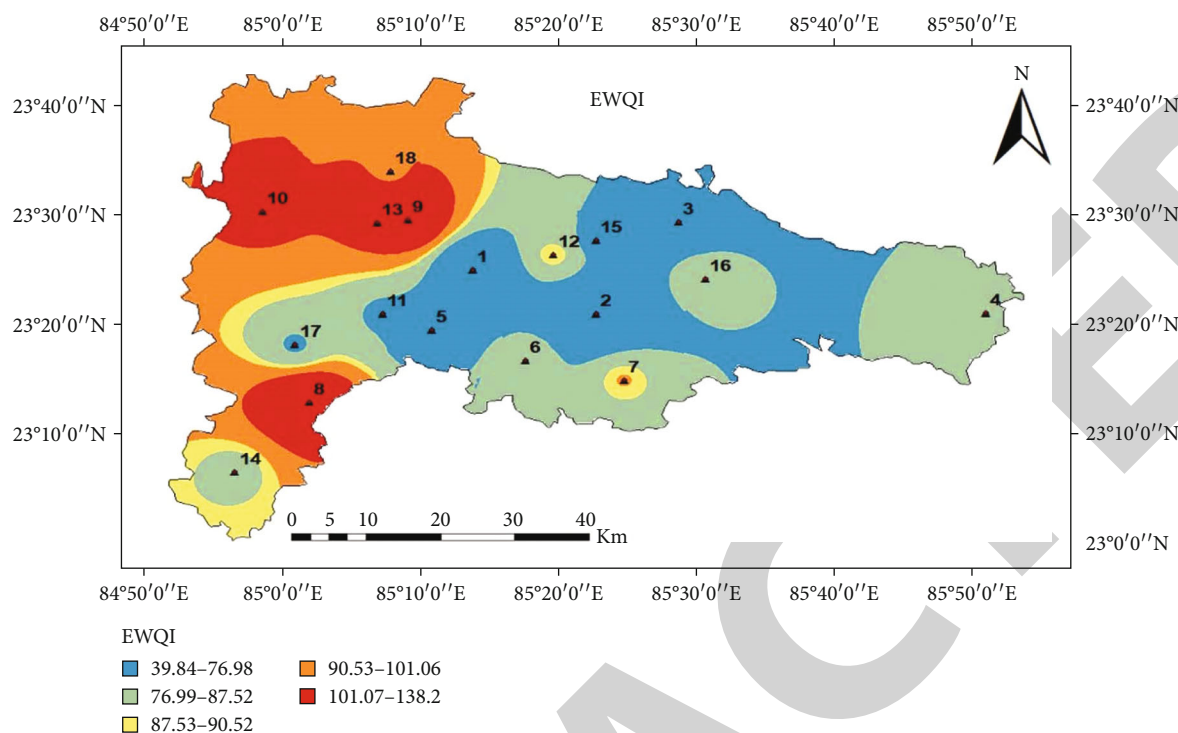


FIGURE 3: Spatial distribution of the EWQI model.

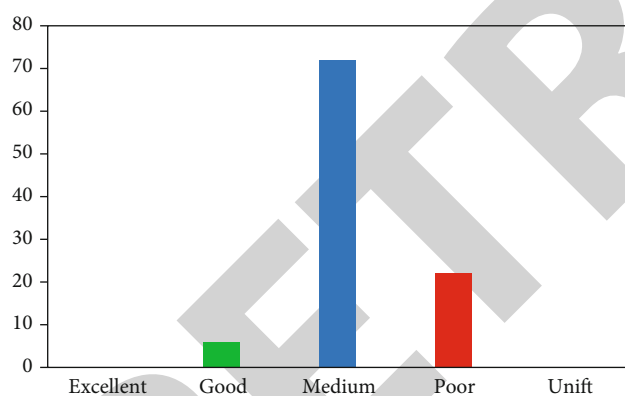
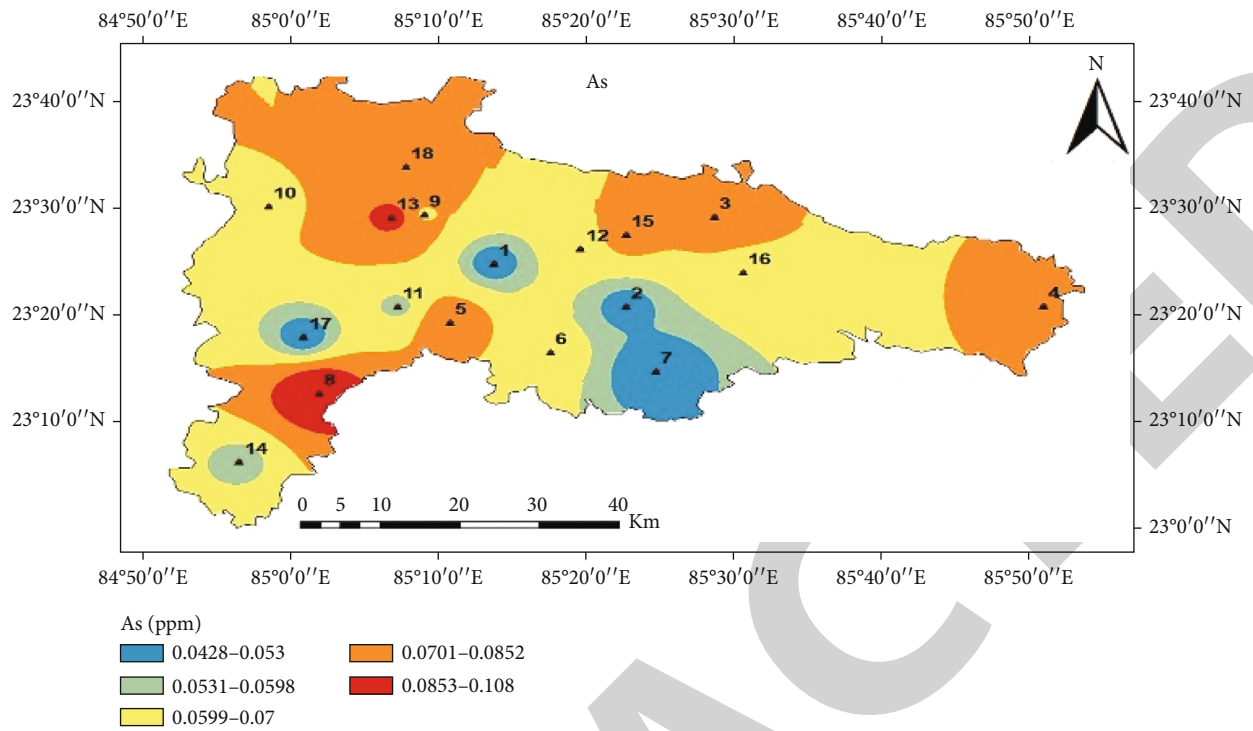


FIGURE 4: Percentage of groundwater samples in different categories.

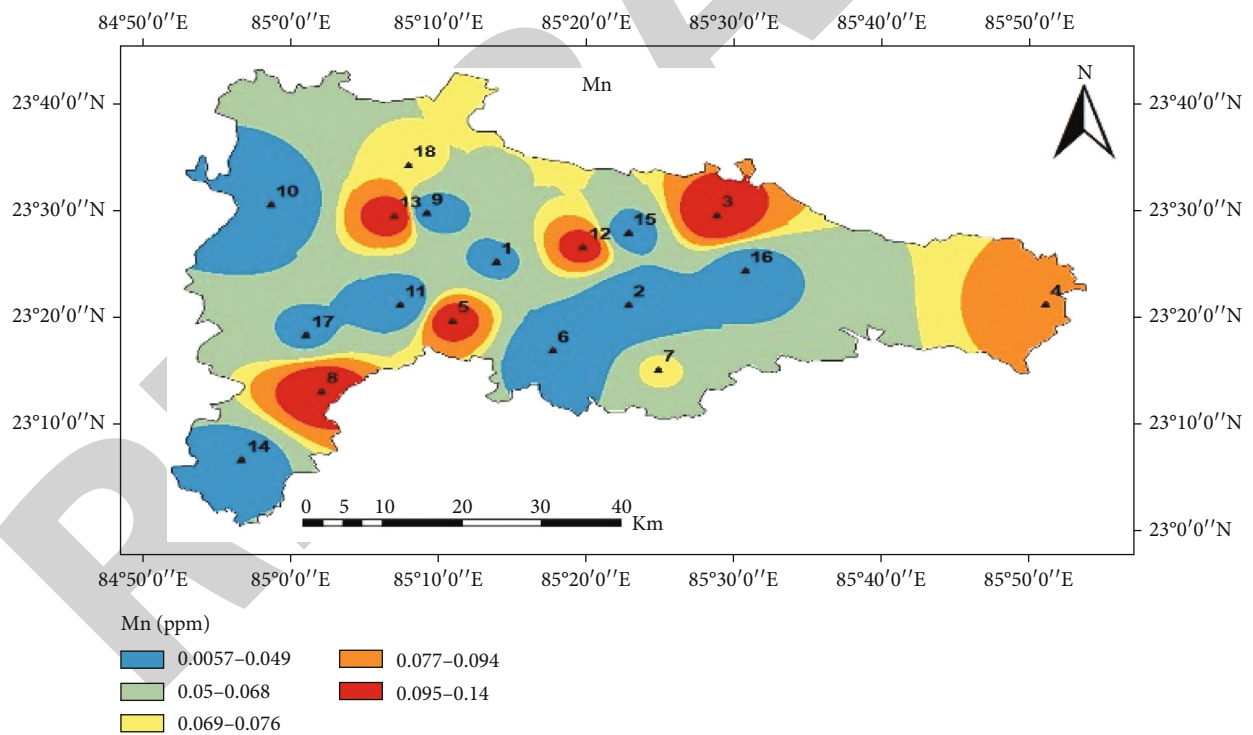
**3.3. Spatial Distribution Map of Heavy Metal.** The concentration levels of heavy metals in the region differ significantly. The higher concentration range of manganese (0.0057- 0.14 ppm) was reported in the study area, followed by iron concentration range of (0.0036-00.53 ppm) and arsenic (0.042-0.108), which exceeded the permissible limit prescribed given by the World Health Organization [23]. Figures 5(a)–5(f) represent spatial distribution map of GIS-based inverse distance weightage (IDW) technique for the pattern of arsenic (As), copper (Cu), manganese (Mn), nickel (Ni), lead (Pb), and iron (Fe). Except in the southeastern and northern zone, the amount of arsenic was found to be dominant across the field of study. The greater level of arsenic in this region could be owing to industrial wastewa-

ter discharge into the open ground, contaminating groundwater through infiltration [27]. Furthermore, as a result of chemical weathering, archaic consolidated granite-gneiss rocks of Chotanagpur, which are made up of quartzite and schist, might be the sources of As in this area's groundwater aquifers. Only the research area's southeastern corner is within the arsenic safe contamination zone (Figure 5(a)). Iron (Fe) and manganese (Mn) are naturally available in the earth's crust, and if they exceed the recommended limit, they can cause a variety of issues in groundwater [28]. The map shows the concentration of Fe more in the center and southern parts of the studied region (Figure 5(b)). The Fe contour map in this place can be linked to the earth's crust and the research area's geological development [29]. Mn is an essential element that plays a role in a number of important component [30]. The higher value of Mn was found in some locations of the northern and southern region of study area (Figure 5(c)). The map of Ni, Pb, and Cu demonstrated that throughout the area of research, all three elements are typically within the safe drinking zone (Figures 5(d)–5(f)).

**3.4. Assessment of Human Health Risks.** Oral intake was utilized to determine the health risk of heavy metals in groundwater at all 18 locations. Furthermore, the HI value ranges from 10 to 25 for the study area. Its value is greater than unity because of the major contribution of As, which indicates a very high chronic risk. In contrast, the carcinogenic risk associated with As was found to be  $<0.1$ , which indicates less carcinogenic risk. According to the spatial map of HI, the majority of the study region are at a noncarcinogenic risk that might cause significant health problems (Figure 6). The

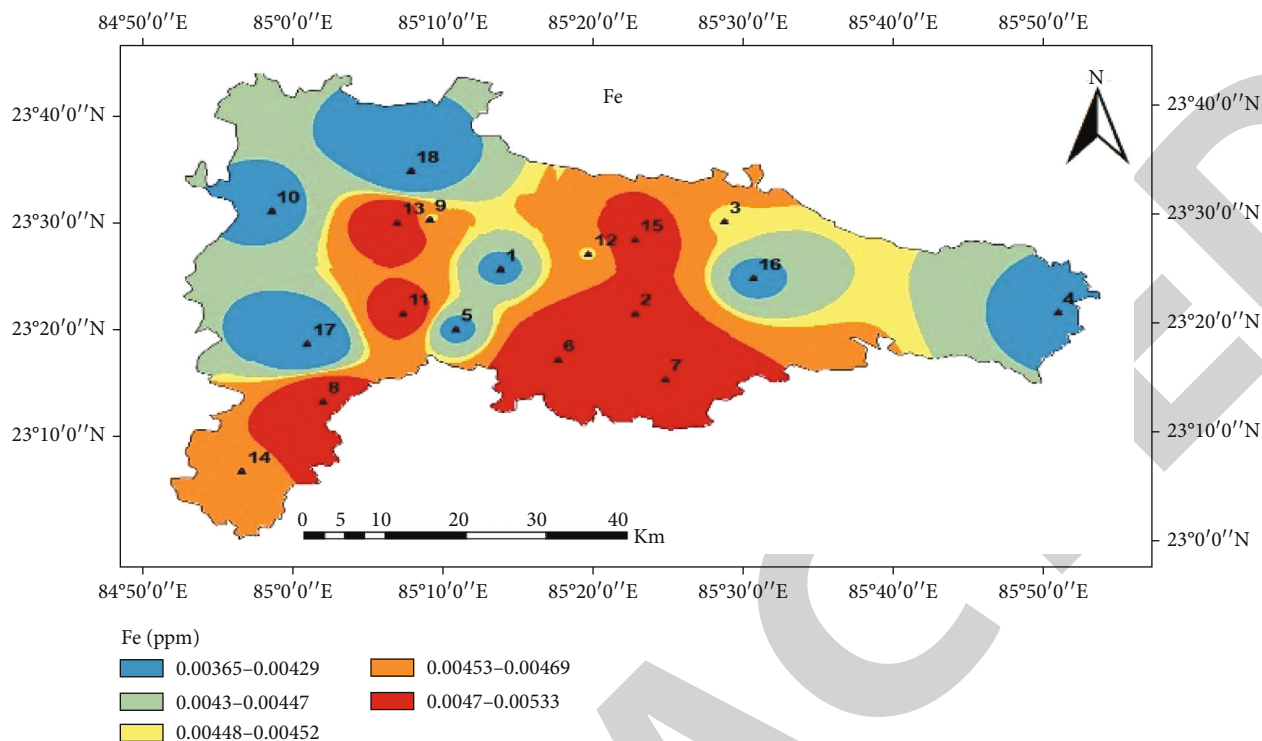


(a)

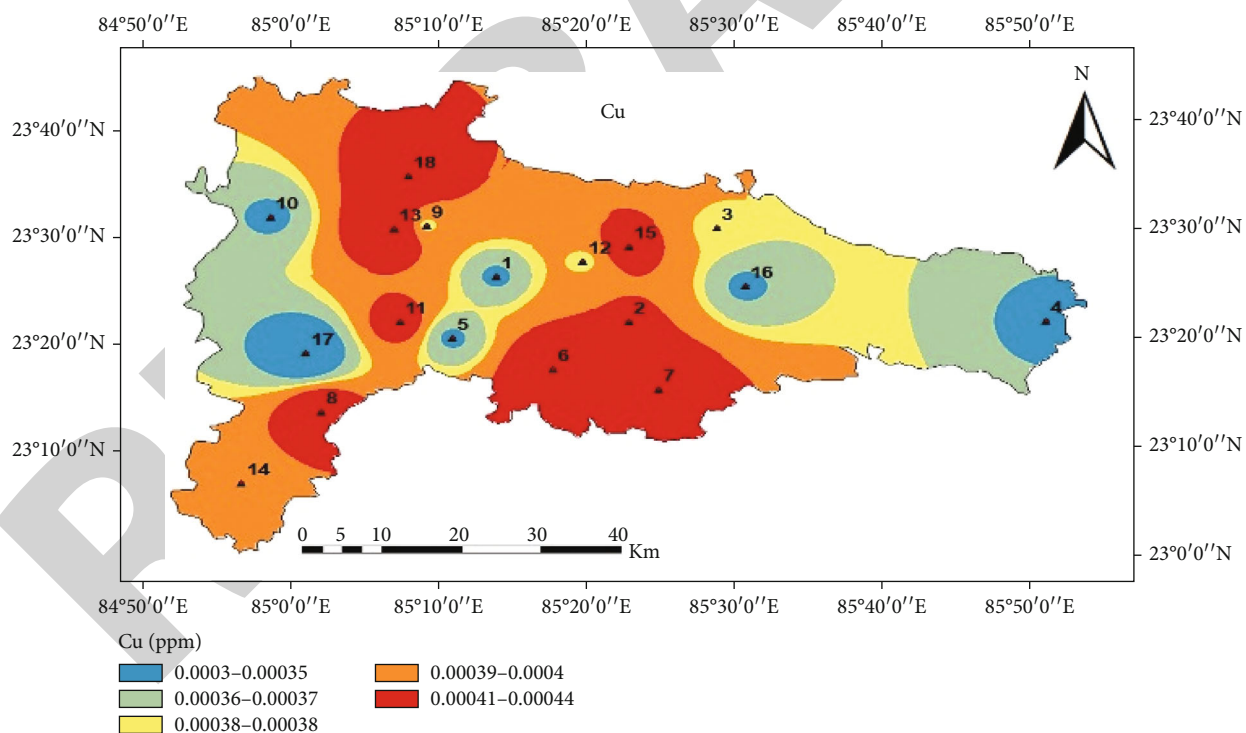


(b)

FIGURE 5: Continued.



(c)



(d)

FIGURE 5: Continued.

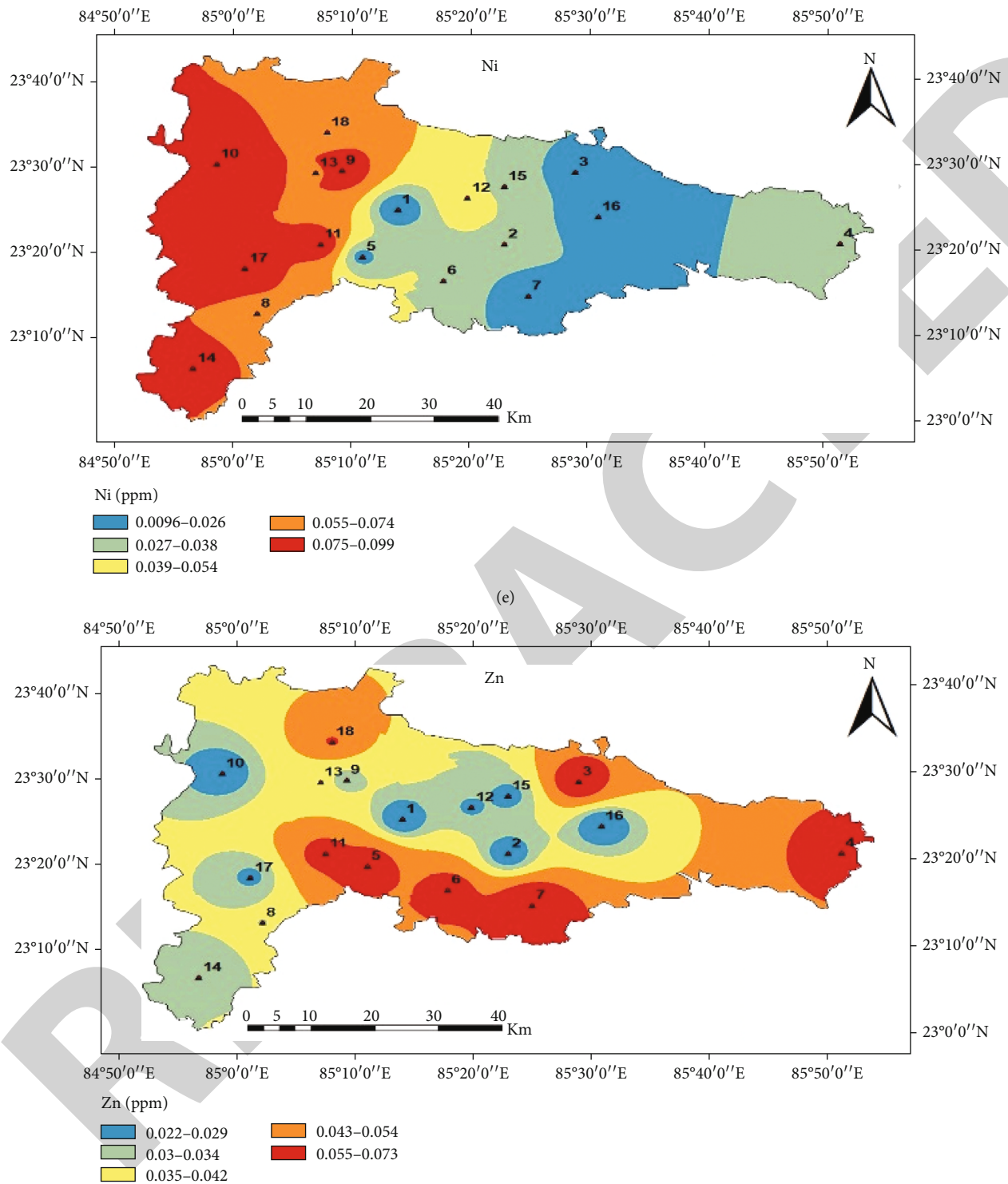


FIGURE 5: (a)–(f) Spatial distribution map of concentration of heavy metal: (a) As, (b) Mn, (c) Fe, (d) Cu, (e) Ni, and (f) Zn.

only section of the study area where health risks are minimal is the southeast. It has also been revealed that students are more vulnerable than adults to the danger of heavy metals when consumed orally (Table 5).

The average arsenic concentration was found to be 42.8 ppb to 108 ppb, the carcinogenic risk value shown in

Table 6. The concentration of arsenic was found higher in the northern part of the study area which might be due to anthropogenic sources like mining, use of pesticides, and industries located nearby. The excess of arsenic present in groundwater causes arsenicosis diseases as shown in Figure 7 which is now a days very serious issues. Also, it

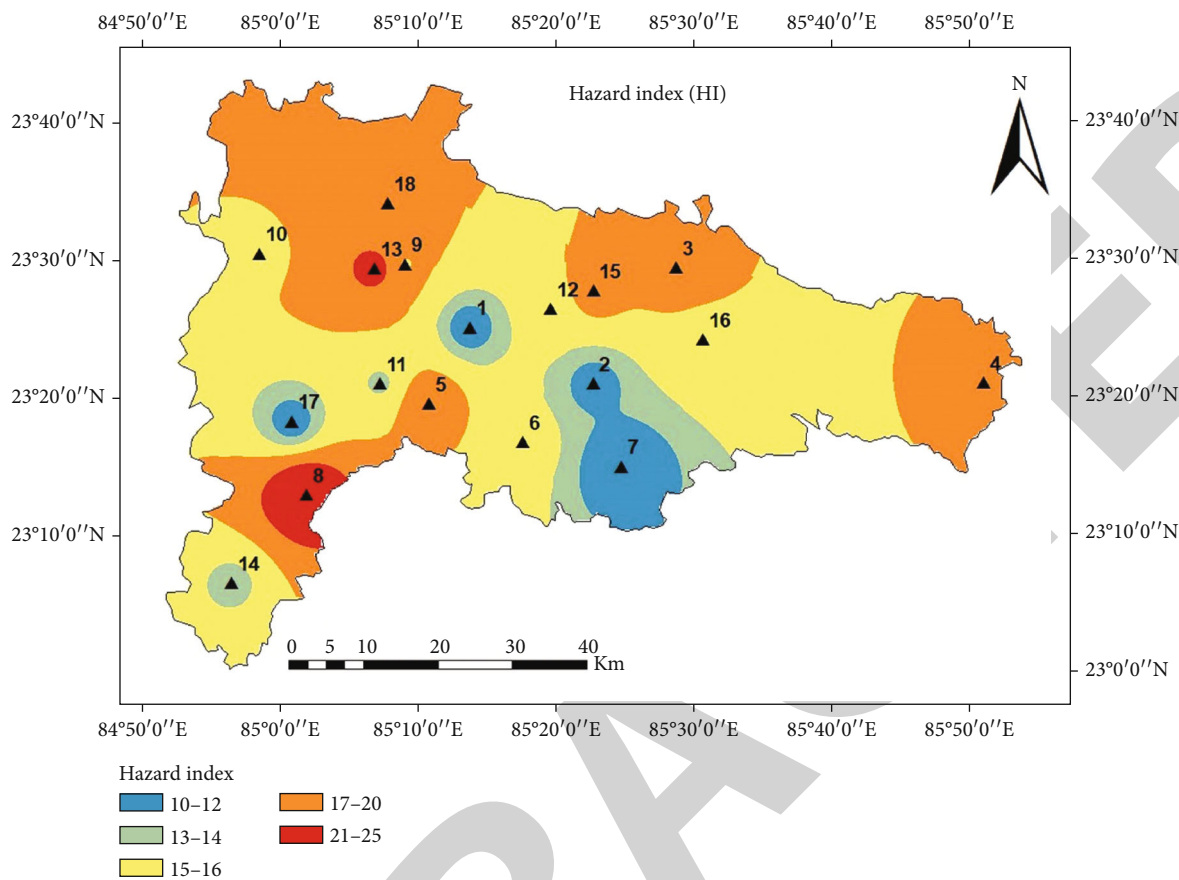


FIGURE 6: Spatial distribution map of hazard index (HI).

TABLE 5: HQ value of noncarcinogenic risk of heavy metal.

Sl. no.	AS (xE+01)		NI (xE-02)		Mn (xE-02)		Fe (xE-04)		Zn (E03)		Cu (xE-04)		HI (xE+01)	
	A	C	A	C	A	C	A	C	A	C	A	C	A	C
1	0.98	1.08	2.8	3.3	1.64	1.95	3.46	4.11	4.20	4.99	5.03	5.98	0.93	1.08
2	0.93	1.11	10.9	12.9	0.33	0.39	4.02	4.77	4.56	5.41	5.84	6.93	0.94	1.12
3	1.55	1.84	4.8	5.8	5.72	6.79	3.74	4.44	12.76	15.15	5.44	6.45	1.561	1.85
4	1.45	1.72	9.8	11.6	3.54	4.20	3.46	4.11	11.28	13.38	5.03	5.98	1.47	1.74
5	1.59	1.89	6.2	7.4	5.03	5.97	3.46	4.11	12.80	15.19	5.03	5.98	1.60	1.90
6	1.29	1.53	10.9	12.9	0.50	0.59	4.43	5.26	11.83	14.04	6.44	7.65	1.30	1.54
7	0.83	0.98	3.2	3.8	3.04	3.61	4.29	5.10	14.09	16.72	6.24	7.41	0.83	0.99
8	2.10	2.49	20.4	24.2	5.64	6.70	4.29	5.10	6.62	7.86	6.24	7.41	2.12	2.52
9	1.33	1.58	27.6	32.8	0.60	0.71	3.74	4.44	6.17	7.33	5.44	6.45	1.36	1.62
10	1.30	1.55	28.9	34.3	0.24	0.28	3.46	4.11	4.78	5.68	5.03	5.98	1.33	1.58
11	1.12	1.33	25.8	30.6	0.51	0.61	4.15	4.93	11.60	13.77	6.04	7.17	1.14	1.36
12	1.22	1.45	15.6	18.5	4.96	5.89	3.74	4.44	5.49	6.52	5.44	6.45	1.24	1.47
13	1.79	2.12	20.6	24.5	5.74	6.81	4.43	5.26	6.82	8.09	6.44	7.65	1.82	2.16
14	1.11	1.32	22.8	27.0	1.31	1.55	3.88	4.60	5.85	6.94	5.64	6.69	1.14	1.35
15	1.51	1.79	9.6	11.4	1.13	1.34	4.15	4.93	5.27	6.25	6.04	7.17	1.52	1.80
16	1.31	1.56	3.9	4.6	1.09	1.29	3.46	4.11	4.33	5.14	5.03	5.98	1.32	1.56
17	0.913	1.08	25.1	29.8	1.65	1.96	3.05	3.62	5.43	6.44	4.43	5.26	0.94	1.12
18	1.40	1.66	18.1	21.5	3.15	3.74	3.03	3.60	10.57	12.55	6.14	7.29	1.42	1.69

TABLE 6: The carcinogenic risk value of arsenic(As).

Sample no.	Carcinogenic risk value (adult) (E-03)	Carcinogenic risk value (child) (E-03)
1	4.09	4.85
2	4.20	4.99
3	6.97	8.27
4	6.53	7.75
5	7.15	8.49
6	5.79	6.87
7	3.74	4.44
8	9.44	11.20
9	6.01	7.13
10	5.86	6.96
11	5.02	5.96
12	5.50	6.52
13	8.06	9.56
14	5.00	5.94
15	6.79	8.06
16	5.90	7.01
17	4.11	4.88
18	6.29	7.47



FIGURE 7: Effect of arsenic in human body parts.

was found that children are at more prone than adult as cancer risk value was higher.

3.5. *PCA Analysis.* The link between the parameters and the principal components was determined using principal component analysis (PCA). The primary components were restricted when the eigenvalue was more significant than 1. Figure 8 shows a scree plot of the PCA. As a result of the investigation, two major components were identified. These two variables accounted for a maximum of the variance in the data. Arsenic explains the most variation among the

metal characteristics, accounting for 37%, while nickel and manganese account for 23% and 20.8 percent of the overall variation. Cu and Fe showed the strongest positive ties to PC1, while Ni had the strongest negative ties to PC1. Cu and Fe exhibited the strongest positive relationship in PC1 and PC2, while Mn and Zn had the most negative relationship. In PC1 and PC2, the relationship between the parameters revealed that  $Cu > Fe > As > Mn > Zn > Ni$  and  $Fe > Cu > Ni > As > Zn > Mn$  evolved from very positive to strongly negative. Furthermore, a scree plot graph was produced between eigenvalue and principal component number



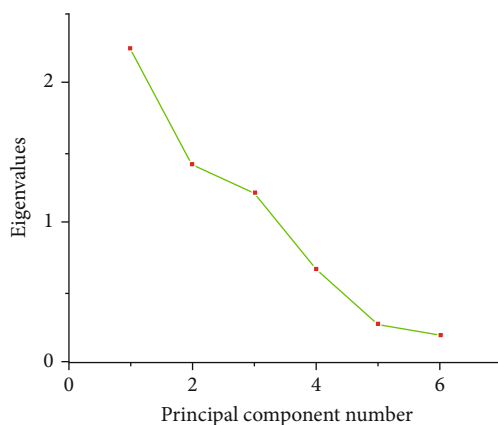


FIGURE 8: Scree plot of PCA.

TABLE 7: PCA analysis of heavy metal concentration.

Parameter	Coefficients of PC1	Coefficients of PC2	Eigenvalue	Percentage of variance	Cumulative variance
As	0.42454	-0.18525	2.24	37.48	37.4
Ni	-0.1321	0.42347	1.40	23.47	60.9
Mn	0.40861	-0.53642	1.21	20.23	81.1
Fe	0.48102	0.47852	0.66	11.14	92.3
Zn	0.35787	-0.28842	0.27	4.51	96.8
Cu	0.52527	0.4318	0.19	3.18	100.0

and demonstrated that As (2.24) had the highest eigenvalue while cu had the lowest (0.19). Similar trends of the percentage of variance are shown as eigenvalue. Table 7 depicts the PCA analysis of metal parameters.

**3.6. HCA Analysis.** Based on metal values, hierarchical cluster analysis was utilized to analyze the closeness and homogeneity inside the sampling sites. The mean correlation resulted in the dendrogram displayed in Figure 9. There are four types of clusters majorly divided shown in different colors, viz., red (Nos. 1,2,6,15, and 16), green (Nos. 9,10,11,14, and 17), blue [6, 14, 18, 31], and cyan (Nos. 4,7, and 18). Furthermore, the red and green sampling locations formed a subcluster linked with the subcluster of green and cyan to complete the dendrogram linkage. It was also discovered that there was a high correlation between 6, 10, and 12 sampling stations. The 6, 11, and 7 sampling stations revealed significant diversity in which each station exhibited a shaky connection on its own.

**3.7. Strategy Requires for Groundwater Management.** The management of groundwater deals with the complex interaction between the physical environment and human activities. It possesses an extremely difficult challenge for solving the benefit of all parties involved. The rapid urbanization and growing population results in the exploitation of underground water pockets. Consequently, there are rivalries between the exploiters without care about management programs. The management strategies for groundwater management are as follows:

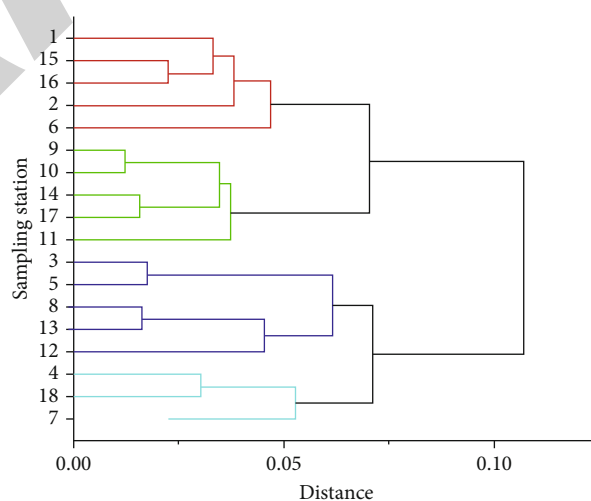


FIGURE 9: Dendrogram of HCA.

- (i) Groundwater management awareness for beneficiaries
- (ii) Limit the exposition according with monitoring results
- (iii) Enhancement in the ground water recharge from other sources
- (iv) Maintain and avoidance of the degradation of groundwater quality
- (v) Maintaining the minimum level of groundwater especially in unconfined aquifers

#### 4. Conclusion

EWQI modeling and hydrogeochemical evaluation could help to evaluate factors controlling chemistry and suitability of groundwater for drinking purposes in Ranchi city. Only 6% of the sample is good quality, while the rest ranges from medium (72%) to poor (3.22%). The concentration level of Mn (0.0057-0.14 ppm), Fe (0.0036-0.053 ppm), and As (0.042-0.108 ppm) exceeds the prescribed guideline by WHO. Through oral intake, children are more susceptible to the risk than adults. Hydrogeochemical processes of groundwater were dominated by reverse ion exchange. The arsenic was the most influencing parameter among all other metals, as its value of HQ > 1. The cluster analysis identified four clusters based on groundwater quality data sets. The study is helpful to avoid the possibility of increasing contamination of groundwater and in ensuring public safety. Since numerous factories are located in this region, carcinogenic risk assessment the other heavy metal that leading to carcinogenic risk must be examined to understand the better influencing heavy metals.

#### Data Availability

All the data will be made available on request.

#### Conflicts of Interest

There is no conflict of interest.

#### Acknowledgments

The authors are very much grateful to the Department of Environmental Science and Engineering, IIT (ISM), Dhanbad.

#### References

- [1] P. Li, H. Qian, and J. Wu, "Conjunctive use of groundwater and surface water to reduce soil salinization in the Yinchuan Plain, North-West China," *International Journal of Water Resources Development*, vol. 34, no. 3, pp. 337–353, 2018.
- [2] R. P. Sishodia, S. Shukla, W. D. Graham, S. P. Wani, and K. K. Garg, "Bi-decadal groundwater level trends in a semi-arid south indian region: declines, causes and management," *Journal of Hydrology: Regional Studies*, vol. 8, pp. 43–58, 2016.
- [3] M. B. Alaya, S. Saidi, T. Zemni, and F. Zargouni, "Suitability assessment of deep groundwater for drinking and irrigation use in the Djeffara aquifers (northern Gabes, South-Eastern Tunisia)," *Environmental Earth Sciences*, vol. 71, no. 8, pp. 3387–3421, 2014.
- [4] N. Subba Rao and M. Chaudhary, "Hydrogeochemical processes regulating the spatial distribution of groundwater contamination, using pollution index of groundwater (PIG) and hierarchical cluster analysis (HCA): a case study," *Groundwater for Sustainable Development*, vol. 9, p. 100238, 2019.
- [5] A. O. Sojobi, "Evaluation of groundwater quality in a rural community in north central of Nigeria," *Environmental Monitoring and Assessment*, vol. 188, no. 3, pp. 188–192, 2016.
- [6] P. Li, J. Wu, H. Qian, X. Lyu, and H. Liu, "Origin and assessment of groundwater pollution and associated health risk: a case study in an industrial park, Northwest China," *Environmental Geochemistry and Health*, vol. 36, no. 4, pp. 693–712, 2014.
- [7] M. Qasemi, M. Afsharnia, M. Farhang, A. Bakhshizadeh, M. Allahdadi, and A. Zarei, "Health risk assessment of nitrate exposure in groundwater of rural areas of Gonabad and Bajestan, Iran," *Environmental Earth Sciences*, vol. 77, no. 15, p. 551, 2018.
- [8] Z. Tahernezhad, Z. Zabihollah Yousefi, and N. Mousavinasab, "A survey on fluoride, nitrate, iron, manganese and total hardness in drinking water of Fereydoonkenar city during 2008–2013," *Journal of Advances in Environmental Health Research*, vol. 4, pp. 102–112, 2016.
- [9] P. Li, X. Li, X. Meng, M. Li, and Y. Zhang, "Appraising groundwater quality and health risks from contamination in a semi-arid region of Northwest China," *Exposure and Health*, vol. 8, no. 3, pp. 361–379, 2016.
- [10] USEPA (US Environmental Protection Agency), *National Primary/Secondary and Drinking Water Regulations*, Washington, D.C., 2009.
- [11] L. Kaur, M. S. Rishi, and A. U. Siddiqui, *Deterministic and Probabilistic Health Risk Assessment Techniques to Evaluate Non-carcinogenic Human Health Risk (NHHR) Due to Fluoride and Nitrate in Groundwater of Panipat, Haryana, India*, Environmental Pollution, 2020.
- [12] M. Rahman, M. Vahter, M. A. Wahed et al., "Prevalence of arsenic exposure and skin lesions. A population-based survey in Matlab, Bangladesh," *Journal of Epidemiology and Community Health*, vol. 60, no. 3, pp. 242–248, 2006.
- [13] R. Nickson, C. Sengupta, P. Mitra et al., "Current knowledge on the distribution of arsenic in groundwater in five states of India," *Journal of Environmental Science and Health. Part A, Toxic/Hazardous Substances & Environmental Engineering*, vol. 42, no. 12, pp. 1707–1718, 2007.
- [14] P. Bhattacharya, O. Sracek, B. Eldvall et al., "Hydrogeochemical study on the contamination of water resources in a part of Tarkwa mining area, Western Ghana," *Journal of African Earth Sciences*, vol. 66–67, pp. 72–84, 2012.
- [15] P. Tirkey, T. Bhattacharya, and S. Chakraborty, "Water quality indices – important tools for water quality assessment: a review," *International Journal of Advances in Chemistry*, vol. 1, no. 1, pp. 15–28, 2013.
- [16] N. Adimalla, "Application of the entropy weighted water quality index (EWQI) and the pollution index of groundwater (PIG) to assess groundwater quality for drinking purposes: a case study in a rural area of Telangana state, India," *Archives of Environmental Contamination and Toxicology*, vol. 80, no. 1, pp. 31–40, 2021.
- [17] P. J. Kumar and C. M. Augustine, "Entropy-weighted water quality index (EWQI) modeling of groundwater quality and spatial mapping in Uppar Odai Sub-Basin, South India," *Modeling Earth Systems and Environment*, vol. 8, no. 1, pp. 911–924, 2022.
- [18] APHA, *Standard Methods for the Examination of Water and Wastewater*, American Public Health Association, Washington, DC, 22nd edition, 2012.
- [19] H. Su, W. Kang, Y. Xu, and J. Wang, "Assessing groundwater quality and health risks of nitrogen pollution in the Shenfu mining area of Shaanxi Province, Northwest China," *Exposure and Health*, vol. 10, no. 2, pp. 77–97, 2018.
- [20] Y. Zhou, A. Wei, J. Li, L. Yan, and J. Li, "Groundwater quality evaluation and health risk assessment in the Yinchuan Region,

## *Retraction*

# **Retracted: Appropriate Supervised Machine Learning Techniques for Mesothelioma Detection and Cure**

### **BioMed Research International**

Received 8 January 2024; Accepted 8 January 2024; Published 9 January 2024

Copyright © 2024 BioMed Research International. This is an open access article distributed under the Creative Commons Attribution License, which permits unrestricted use, distribution, and reproduction in any medium, provided the original work is properly cited.

This article has been retracted by Hindawi, as publisher, following an investigation undertaken by the publisher [1]. This investigation has uncovered evidence of systematic manipulation of the publication and peer-review process. We cannot, therefore, vouch for the reliability or integrity of this article.

Please note that this notice is intended solely to alert readers that the peer-review process of this article has been compromised.

Wiley and Hindawi regret that the usual quality checks did not identify these issues before publication and have since put additional measures in place to safeguard research integrity.

We wish to credit our Research Integrity and Research Publishing teams and anonymous and named external researchers and research integrity experts for contributing to this investigation.








The corresponding author, as the representative of all authors, has been given the opportunity to register their agreement or disagreement to this retraction. We have kept a record of any response received.

### **References**

- [1] K. Saxena, A. S. Zamani, R. Bhavani et al., “Appropriate Supervised Machine Learning Techniques for Mesothelioma Detection and Cure,” *BioMed Research International*, vol. 2022, Article ID 2318101, 11 pages, 2022.

## Research Article

# Appropriate Supervised Machine Learning Techniques for Mesothelioma Detection and Cure

**Komal Saxena** <sup>1</sup>, **Abu Sarwar Zamani** <sup>2</sup>, **R. Bhavani** <sup>3</sup>, **K. V. Daya Sagar** <sup>4</sup>,  
**Pushpa M. Bangare** <sup>5</sup>, **S. Ashwini** <sup>6</sup>, and **Saima Ahmed Rahin** <sup>7</sup>

<sup>1</sup>Amity Institute of Information Technology, Amity University, Noida, Uttar Pradesh, India

<sup>2</sup>Department of Computer and Self Development, Preparatory Year Deanship, Prince Sattam Bin Abdulaziz University, Al-Kharj, Saudi Arabia

<sup>3</sup>Institute of Computer Science and Engineering, Saveetha School of Engineering, Saveetha Institute of Medical and Technical Sciences, Chennai 600124, India

<sup>4</sup>Electronics and Computer Science, Koneru Lakshmaiah Education Foundation, Vaddeswaram, Guntur, Andhra Pradesh, India

<sup>5</sup>Department of E&TC, Sinhgad College of Engineering, Savitribai Phule Pune University, Pune, India

<sup>6</sup>Computer Science and Engineering, Saveetha School of Engineering, Saveetha Institute of Medical and Technical Sciences, Tamilnadu, India

<sup>7</sup>United International University, Dhaka, Bangladesh

Correspondence should be addressed to Saima Ahmed Rahin; [srahin213012@mscse.uui.ac.bd](mailto:srahin213012@mscse.uui.ac.bd)

Received 18 May 2022; Accepted 20 June 2022; Published 7 July 2022

Academic Editor: Gaganpreet Kaur

Copyright © 2022 Komal Saxena et al. This is an open access article distributed under the Creative Commons Attribution License, which permits unrestricted use, distribution, and reproduction in any medium, provided the original work is properly cited.

Mesothelioma is a dangerous, violent cancer, which forms a protecting layer around inner tissues such as the lungs, stomach, and heart. We investigate numerous AI methodologies and consider the exact DM conclusion outcomes in this study, which focuses on DM determination. K-nearest neighborhood, linear-discriminant analysis, Naive Bayes, decision-tree, random forest, support vector machine, and logistic regression analyses have been used in clinical decision support systems in the detection of mesothelioma. To test the accuracy of the evaluated categorizers, the researchers used a dataset of 350 instances with 35 highlights and six execution measures. LDA, NB, KNN, SVM, DT, LogR, and RF have precisions of 65%, 70%, 92%, 100%, 100%, and 100%, correspondingly. In count, the calculated complication of individual approaches has been evaluated. Every process is chosen on the basis of its characterization, exactness, and calculated complications. SVM, DT, LogR, and RF outclass the others and, unexpectedly, earlier research.

## 1. Introduction

Dangerous mesothelioma (DM) is a cancer that develops within the inside layer of the vital organ likely to be in the lungs. Peritoneum mesothelioma occurs in the abdomen, and hardly, pericardial mesothelioma happens in the heart and the layer of the testicles. The occurrence of several types of DM in serous layers is seen in Figure 1 which portrays the three subtypes of mesothelioma cancer where the internal layer of the lungs can cater dangerous mesothelioma, the internal layer of the heart can be effected by pericardial mesothelioma, and the abdominal inside tissue can be prompted by

peritoneum mesothelioma. The occurrence of several types of DM in serous layers is seen in Figure 1. Dangerous mesothelioma accounts for 68-72% of all DM cases, peritoneal mesothelioma for 30%, and pericardial mesothelioma for 2-3%. “Contact with asbestos” is the most significant risk factor for DM; prolonged exposure increases the danger of getting affected [1]. Another prospect of dangers, like inherited characteristics along with contamination through simian virus-40, as well induces it. Even though DM had been formerly unusual, now this becomes more widespread because asbestos usage has increased, especially in developed countries. Chest pain, difficulty breathing, windedness, and difficulty gulping

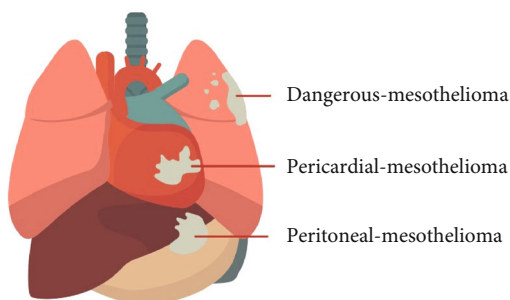


FIGURE 1: Existence of mesothelioma.

are all adverse symptoms of DM. DM progresses fast, with side symptoms appearing gradually [2].

To detect and restrict the existence of DM, imaging techniques like ultrasound, upper body radiography (called X-beam), and processed tomography (PT) have been employed. For confirming DM aetiology, cytopathology (testing of the liquid specimen) and histology (biopsy of studied tissues) tests have also been used. DM's findings on several imaging modalities are shown in Figure 2. Apart from decreasing contact with asbestos, DM initial phase discovery can also be critical for obtaining a feasible therapy on time.

Many studies have sought to integrate updated methodologies in addition to conventional procedures. Computerized analysis frameworks (CAF) have made significant contributions to clinical applications and research due to continuous cutting-edge improvements [3]. CAFs may provide valuable, accurate, and dependable results. On structured clinical data, CAFs solely used AI algorithms likely to be ANN, SVM, LDA, KNN, NB, LogR, deep learning, and ensemble learning. DM conclusion, like many other clinical informatics systems, has a setup problem. Different tactics usually criticize the various arrangement exactnesses based on the data.

In this regard, it is critical to seek out feasible and viable AI solutions that provide great accuracy.

Few experts have shown interest in using AI to automate the grouping of DM illnesses. Author proposed the planned sequence of mesothelioma sickness, as well as provided a publicly available dataset [4, 5]. Two types of brain structures are employed as ML strategies for ordering between mesothelioma and ordinary illnesses: PNN (probabilistic neural networks) and MLNN (multilayer learning neural network). PNN has a higher accuracy rate of 96.22 percent than MLNN (95%). These were investigated using various data mining methods, including Bayesian network, J50 choice structures, successive negligible streamlining (SNS) to prepare support vector machine, logistic prototype tree, multiclass categorizer, arbitrary CoDMittee, PARTS, and neural network, for distinguishing among ordinary mesothelioma as well as dangerous mesothelioma; furthermore, it achieves 88 percent and 89.2 percent; it concludes ANN as the top categorizer which identifies hazardous mesothelioma based on the supplied correctnesses. It recently used SVM categorizer to introduce the mesothelioma sickness location, and it achieves 97.20% along with 98.90% correctness, correspondingly.

To organically order the DM illness, we use seven AI approaches in this paper: SVM, LDA, KNN, DT, RF, NB, and LogR. Their results are examined and processed using six execution gauges. Similarly, the handling season of each categorizer is calculated to determine the calculation difficulty. Finally, the correctnesses attained by the evaluated procedures are compared to the present tactics. DT, SVM, LogR, and RF surpass the active techniques by providing exactly one hundred percent precision, in accordance with the correlation. Because of their excellent accuracy and ease of use, doctors may utilize them as emotionally supportive networks of choice in the detection of DM illness [5]. As our investigation is proposed in this study, K-nearest neighborhood, linear-discriminant analysis, Naive Bayes, decision tree, random forest, support vector machine, and logistic regression analyses have been used in clinical decision support systems in the detection of mesothelioma. We have tested the accuracy of the evaluated categorizers and used a dataset of 350 instances with 35 highlights and six execution measures. We have investigated that LDA, NB, KNN, SVM, DT, LogR, and RF have precisions of 65%, 70%, 92%, 100%, 100%, 100%, and 100%, correspondingly. In count, the calculated complication of individual approaches has been evaluated. Every process is chosen on the basis of its characterization exactness and calculated complication. SVM, DT, LogR, and RF outclass the others and, unexpectedly, earlier research.

This study is organized as follows: Section 1 discusses the introduction part, and in the Section 2, the representation of the dataset along with the review procedure has been presented. Section 3 depicts exploratory outcomes, correlation, and dialogues. Section 4 is where we put the finishing touches.

*1.1. Machine Learning.* ML has a vast range of applications like IT, statistical analysis, possibility, AI, and neurology, along with a variety of various fields. ML makes it simple to address problems by creating a prototype which is a fine demonstration concerning a given set of information. ML progressed to imitate a person's mind when compared earlier to observing PC on a comprehensive subject that generates fundamental statistical computational theories of learning processes [6, 7]. The goal of machine learning is to develop an algorithm that allows computers to learn. Learning has been the discovery with concern to the statistical uniformity either erstwhile data models. ML algorithms have been designed for mimicking the human method of learning a new skill [8]. These algorithms can also provide information on the relative difficulty of learning in various situations.

Machine learning is not what it is used to be, because of the latest computing advancement capabilities with concern to immense datasets. Lots of ML processes have been invented, reorganized, and enhanced recently, and the latest development in machine learning is obtaining faster calculations because of the capability of executing numerous sophisticated statistical computations arbitrarily for an abundance of information, ensuring the significantly faster computation [9, 10].

Adaptive programming is a popular choice. This has been utilized in ML; here, applications might mark layouts,

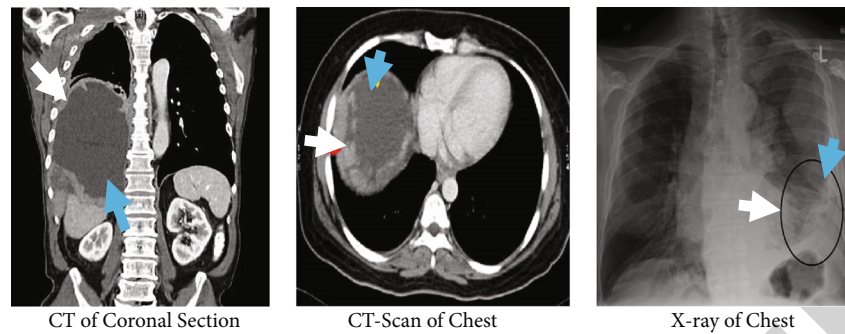


FIGURE 2: Mesothelioma with various scanning modes indicated by the marks arrows.

understand better through its errors from the dataset, extract the latest details, and enhance the accurateness along with the effectiveness of the outcome and processing [11]. ML methods have also been used for working with complex information that has been seen in numerous apps. Depending upon the required outcome of the program, ML program has been categorized into subsequent types:

**Supervised learning:** a function is generated by various algorithms that map feed-in for the required productivity. The general issue in SL is the difficulty of categorization; here, the apprentice has to be trained (for approximate behavior) for the task which measures the vector in various categories only through looking at numerous input/output function tests [12]

**Unsupervised learning:** prototype input sets without the use of labeled exemplars

**Semisupervised learning:** combines labeled along with unlabeled cases for producing a useful categorizer

**Reinforcement learning:** the algorithm develops a policy for how to act based on a world observation. Each deed affects the surroundings, and we can get feedback to the learning algorithm from these surroundings [13]

**Transduction:** just like SL, but instead of openly constructing a function, it attempts for predicting fresh outputs using training inputs, training outputs, and the latest inputs

**Learning to learn:** the program learns by its reasonable prejudice from previous experiences

Apart from those subsets, ML programs have been classified into two categories: supervised learning and unsupervised learning.

The classifications in the supervised program have been preset. Those categories have been established in a definite group, determined with the help of humans, and this means that a specific section of information would be labeled by these categorizations [14]. ML program's job is to look for a pattern as well as to build a statistical model with the employment of these techniques, thus assisting in examining the datasets using several machine learning programs. The visionary ability of these prototypes is then calculated by estimates of deviation in information, thereby declaring the issues and ailments if found in these datasets to predict the disease at early stages and take necessary precautions in its prevention and cure.

It is also important to differentiate between the two types of supervised prototypes: categorizer prototypes along with regression prototypes. The input space is mapped into an

actual value field by regression prototype. Categorizers divide the input space into categories. SVM assessment structures, potential reviews, arithmetical calculations, and more options exist for representing categorizers. Classification, together with degeneration and also with possibility assessment, has been the utmost researched prototype and arguably the most realistic. Progress in categorization has a large influence upon different areas in cooperation with inside data mining as well as its functions; therefore, the potential benefits are enormous [15, 16].

Unsupervised learning processes, on the other hand, are not given classification. Unsupervised learning was aimed at developing classification labels automatically. All of these programs are looking for resemblances between pieces of information to see where they can be put in a class or into the group. Clusters are these groups, and they constitute a complete variety of machine learning clustering approaches. The machine does not know how the clusters are categorized in this unsupervised categorization. Here, there is a greater chance of astonishing us when we use an assessment of clusters. Hence, cluster analysis is a potential approach for examining links between multiple works [17].

**1.1.1. Supervised Learning.** Training and testing are the two processes in a simple machine learning prototype's learning process. In the preparation procedure, the sample from the preparation information is used as feed-in data, and the learning program else apprentice learns the features and furthermore builds a learning model [18]. A learning model makes a forecast for the test or production data using the execution engine during the testing phase. The final prediction of classing data is labeled information, which is the learning model outcome.

Because the aim has generally been for encouraging devices to grasp a categorization method like which we have constructed, SL (Figure 3) is the most prevalent technique used in classification challenges. The figure depicts certain steps that are being followed in supervised learning where the initial step is the training information which is treated as feed-in data over which ML technique is being used incorporated with the new information block to add the additional information which is being further processed in the categorizer step in which data is being categorized into several data types before producing the output in the form of labels and features.

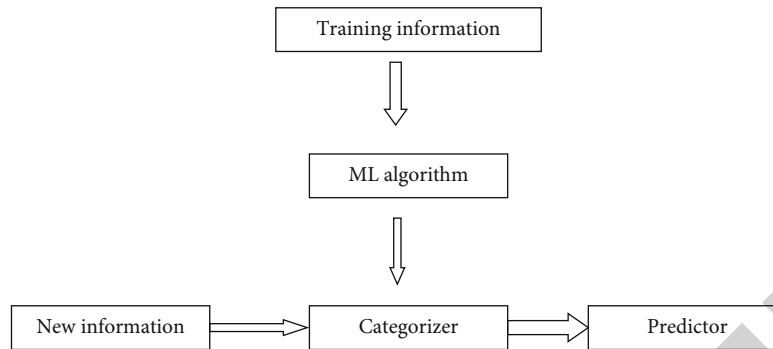


FIGURE 3: Supervised learning.

In most cases, SL provides a possibility aimed at feed-in data unspecified, like the feed-in data with known predicted output. This procedure generates a dataset with labels and features. The main goal is to build an estimator that can guess a substance's tag based on a feature set [19]. The learning program is then given the collection of features along with the right outputs as inputs; also, it learns by comparing its real output with the corrected outputs to discover faults. The prototype is then adjusted as required. For the time when feed-in data have been available, a prototype that is generated is not required; although when few feed-in data figures have been missed, no inferences about the outputs can be made [20, 21].

Training neutral system, as well as conclusion composition using SL, is the most popular method. Both rely upon the details provided through the preset categorization. Here, that method has been also employed in applications where past data is used to forecast likely feature events. Here, there have been other applications with regard to learning like this, such as the one that guesses the species of iris based on a collection of flower measurements. The two types of supervised learning tasks are classification and regression, as previously indicated. The label is discrete in classification and continuous in regression.

The method distinguishes between two types of data, an observed data  $X$  and a training data, which is usually structured data specified prototype throughout the procedure of the training, as shown in Figure 4. SL program is used to create the predictive prototype throughout this phase [22]. The fixed prototype will then try for predicting probable marks of the fresh sample group  $X$  within the test group once it has been trained. Supervised learning can be characterized according to the type of the target  $y$ :

- (i) Classification is the task of predicting  $y$  when  $y$  has rated in a preset group with regard to category outcome (integer)
- (ii) Regression is an assignment of predicting “ $y$ ” when “ $y$ ” has floating point values [23]

*1.1.2. In View.* Dangerous mesothelioma (DM) is a malignancy of mesothelial cells that is linked to previous asbestos exposure [24]. Mesothelioma growths are divided into three

histological categories by the World Health Organization in 2015: (a) epithelioid, (b) biphasic, and (c) sarcomatoid MM. Despite the availability of chemotherapy and a wide range of clinical tests, physicians and patients have been concerned about the accuracy of DM forecasting. DM is a very extraordinary affliction [25]. Its organizational structure results in a perplexing Ly recognized proof cycle, and the varied science prevents precise forecasting. DM has an annual impact of around 2 people per million in an all-inclusive community. Furthermore, industrialised zones are severely damaged by DM due to increased exposure to asbestos. It has been estimated as the numerous people expiring in Western Europe because of mesothelioma would increase approximately two-fold after some time [26]. Around 9000 passings were estimated in 2018, with a prediction of a quarter of a million passings by 2029. Mesothelioma has been categorized into four stages: stage 1, stage 2, stage 3, and stage 4 (malignant growth) [27]. Dry hacking, dyspnea, respiratory complications, chest or stomach pain, fever, dangerous emissions, weariness, and muscle weakness are all stage 1 and stage 2 DM side symptoms that are very ineffective markers of mesothelioma [28]. Patients are less likely to be connected with mesothelioma because it is fascinating. Furthermore, DM's underlying side symptoms in stages 1 and 2 are similar to common conditions including pneumonia and irritable bowel syndrome [29]. DM may also be misinterpreted as adenocarcinoma, which is nonterminal cellular disintegration in the lungs. If mesothelioma is not diagnosed and treated properly in its early stages, it may swiftly progress to stage 3 or stage 4 illness. Unfortunately, the survival rate after being diagnosed with late-stage mesothelioma is usually about a year. An early conclusion is recommended to treat mesothelioma [30]. Mesothelioma is a difficult disease to diagnose, and the expense of detecting it may rapidly mount [31]. Since the primary procedure for diagnosing mesothelioma is ruling out other probable illnesses, various tests may be performed that are not specific to mesothelioma but are all things considered, for prior issues. Furthermore, hearing a second opinion is usually suggested, as is repeating a large number of symptomatic tests. Analytic expenditures for mesothelioma are mounting even before the necessary treatment begins because of this wide range of causes. Finding mesothelioma requires imaging sweeps of growth, examination of a sample of illness tissue, and blood testing [32].

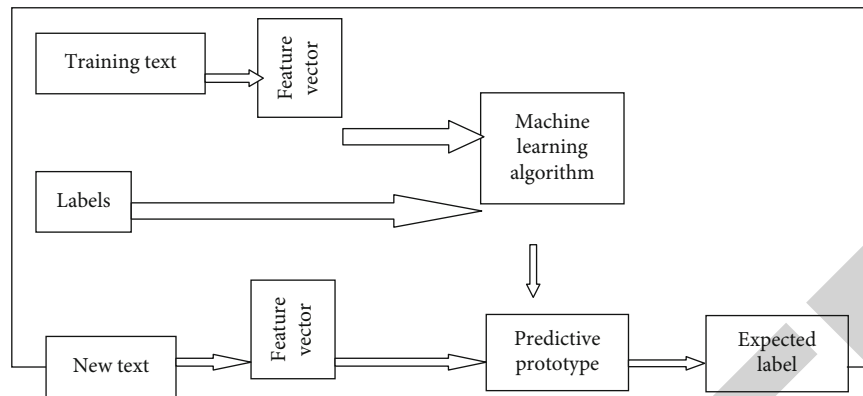


FIGURE 4: Supervised machine learning prototype.

Currently used imaging techniques for mesothelioma detection include X-rays, CT scans, MRI, and PET sweep, all of which are expensive. Both the initial purchase and ongoing maintenance of the imaging equipment are costly [24]. This equipment needs to be used by well-trained professionals to ensure the device's proper operation. A patient should expect to pay between \$850 and \$1,650 for a single CT, MRI, or PET scan. Furthermore, several sweeps may be anticipated throughout the completion, which might quickly increase overall costs [33].

Biopsy has been regarded as the most reliable noninvasive procedure for confirming mesothelioma among all existing methods for diagnosis. Expulsion of liquid or tissue testing from the growth or illness location and inspection under a magnifying device is part of a plan [34]. There are several approaches to obtaining a biopsy, and which one should be used depends on the suspected cancer's location. Some biopsies need an entrance site and embedding procedure to get a sample of the growing cell, while others just require the use of a needle. The cost of a needle biopsy may range from \$550 to 750 dollars, \$3,650 to \$5100 for pleuroscopy (lungs) or laparoscopy (midsection), and \$7,850 to \$7,950 for thoracotomy (lung) or laparotomy (midsection) (midregion). Biopsies, like other suggestive methods, may be performed at various periods, increasing the overall cost of discovery. Specialists also look for biomarkers that indicate mesothelioma using a variety of blood tests such as MESOMARK, SOMAmer, and human MPF [35]. Regardless, no blood tests are yet accurate enough to confirm a conclusion on their own [36].

We primarily concentrated on the investigation of malignant mesothelioma susceptibility variables. The use of data for mesothelioma sufferers was used to identify the clinical manifestations. The database, meanwhile, had included healthy and mesothelioma individuals [37]. The goal of this work was to create a deep learning system for diagnosing malignant mesothelioma reliably. A prospective assessment was done on 324 respondents who had or did not have MM. In MATLAB environment, important characteristics were extracted using an evolutionary algorithms (GA) or a relief technique [38].

Dangerous mesothelioma (MDM) is a dangerous cancer that may lead to sickness and affect the patient's health. DM,

like any other fatal condition, needs early diagnosis and effective treatment [39]. Nonetheless, effective termination techniques like thoracotomy and pleuroscopy are costly and unlikely to be affordable for many individuals. Furthermore, around 66 percent of the world's population lacks access to projected breakthroughs, expensive imaging equipment, and master experts [40]. There has been some research that has used computerized reasoning calculations to differentiate DM, including but not limited to a decision tree, arbitrary woodland, support vector machine, and counterfeit brain structures, but only within specified boundaries [41]. Choice tree prototypes, such as arbitrary timberland, are prone to overfitting, fail to generate 100 percent accuracy, and may also fail to connect a large dataset [42]. Figure 5 shows the applied strategy.

## 2. Process Applied

**2.1. Table of Contents.** This research relies on the open dataset "mesothelioma disease" commencing the UCI-AI datasets. Dataset has been organized with the use of clinical information from total-324 patient case, including normal-228 along with MM-96 patient case; furthermore, it is divided in two categories, as shown in Table 1. There are 34 distinct features that distinguish ordinary and MM infection. Table 2 shows the criteria that are utilized to distinguish between ordinary and infectious [43].

**2.2. Philosophy.** Figure 3 depicts the planned study's nonexclusive engineering. There are three main stages: (1) data segmentation, (2) AI prototype training, and (3) assessing the produced prototypes with the fresh information coming out of the experimenting dataset. Following the completion of the three essential steps, we record the presentation of each prototype and compare it to one another.

**2.2.1. Dataset Partitioning and Use.** The first dataset is a  $350 \times 35$  layered MM infection dataset. In an arbitrary 78-22 split, it is divided into preparation and testing datasets. It is important to notice that the same information is not confined to both the preparation and testing sets. The datasets are not connected. Table 3 categorizes the information segments and uses. The prototypes will be prepared using



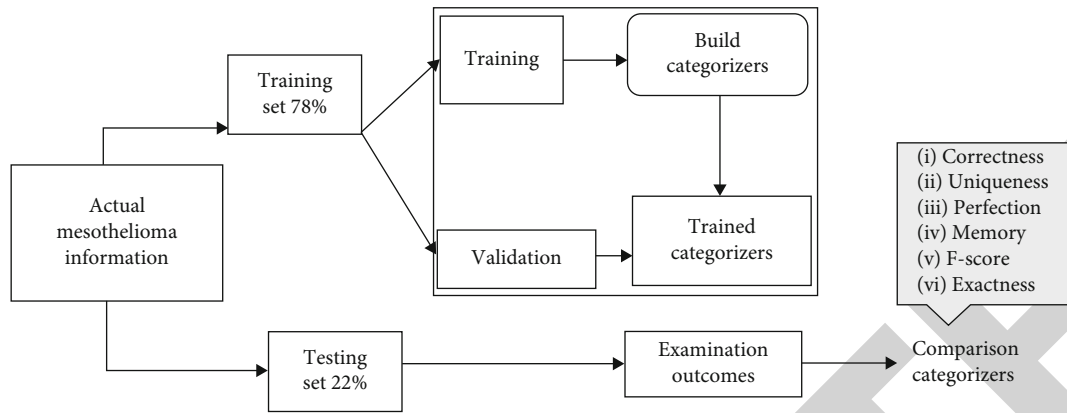


FIGURE 5: Applied strategy.

TABLE 1: Table of contents.

	Total	Normal	Dangerous mesothelioma
Number of instances	350	228	96
Number of attribute	35 features		
Classification category	Normal or dangerous		

the information gathered throughout the preparation process. The testing dataset, on the other hand, will be used to evaluate the created prototypes' presentation on fresh data.

**2.2.2. Machine Learning Prototype Construction.** The majority of MM infection characterization has been based on SVM and brain organizations up till now. In MM determination, there are currently no jobless AI approaches. It is possible that a different comparative determination process might provide almost comparable or superior results. In this vein, if an instance of MM determination occurs, it is critical to analyze the performance of the remaining methods. The techniques are mostly chosen which are still not tested upon a MM dataset. This study focuses on seven AI approaches, including KNN, LDA, SVM, LogR, RF, DT, and NB. SVM is also reused and investigated. It is important to highlight that the purpose of using several categorizers and also then using SVM again is for studying the exact progress concerning MM determination remaining uninfluenced by these causes for instance exploratory setup deviations, information consumption deviation, and so on.

(1) *Linear-Discriminant Analysis.* The LDA categorizer has an easy as well as an efficient approach for characterization. This categorizes information depending on the possibility which has been included in every class. The class which has the maximum possibility determines the class of outcome. The Bayes Theorem has been used for determining the probability recommended for curious readers.

(2) *Naive Bayes.* The NB categorizer is another Bayes Theorem-based probabilistic AI approach. It learns and describes information based on probability. Every single

highlight is completely self-contained. The information appropriated was analyzed by NB, and the class which has the maximum possibility was chosen similarly to an example's expected group having further information.

(3) *K-Nearest Neighborhood.* The KNN categorizer is also known as a nonparametric categorizer that ignores the distribution of observational data. In light of the highlights, it intends for predicting a class concerning incoming example information after looking for the recognized information from the closest neighbor of the class. The closest class has been identified depending upon a highlighted comparability that is known as "distance." The Euclidean distance, Manhattan distance, Minkowski distance, and Pearson relationship may all be used to record distance measurements and describe the complexity of KNN.

(4) *Support Vector Machine.* The universally practiced AI approaches are SVM categorizers. They are capable of dealing with both direct and indirect characterization and relapse concerns. It creates an isolating line across information classes, with the line attempting to emphasize the edge between the classes. It will most likely discover the finest procession, as well recognized by the ideal superplane, which may effectively categorize it. SVMs are not limited to becoming straight categorizer; this has been its primary advantage that they may handle nonstraight characterization challenges through offering component deceives such as direct pieces, quadratic parts, or outspread premise work bits, among other things.

(5) *Decision Structures.* The decision structure (DT) is a rule-depending characterization tool that is widely used. It uses a tree structure to construct learning prototypes. This splits a dataset in tiny sections, whereas it progressively increases a linked DR. Every component with regard to the information collection has been referred to as a root (choice) hub, whereas the leaf hubs deal with characterization options. The outcome depends upon the declination of entropy and the data that expand with the segments.

(6) *Logistic Regression.* The LogR categorizer is likely to be a common as well as efficient AI strategy for predicting parallel

TABLE 2: Functionalities summary.

No.	Attribute description	No.	Attribute description
1.	Oldness	2.	Blood platelets counts
3.	M/F	4.	Deposit
5.	Town	6.	BLD
7.	Asbestos contact	8.	High pH phosphatize
9.	Kind of DM	10.	Albumen
11.	Interval of asbestos experience	12.	Glucose contents
13.	Analysis process	14.	PLD
15.	Preserve apart	16.	Whole protein
17.	Analysis	18.	Tubercular protein
19.	Interval of signs	20.	Tubercular albumen
21.	Dyspnea	22.	Tubercular glucose
23.	Upper body aches	24.	Lifeless or not
25.	Faintness	26.	Tubercular outpouring
27.	Addiction to smoking	28.	The tubercular breadth on imaging
29.	Routine grade	30.	Tubercular near of bitterness
31.	Counts of WBCs	32.	CRP
33.	Hb	34.	Tubercular albumen
35.	Body cholesterol		

TABLE 3: Information usage in the investigations.

Information	Exercise	Challenging	Overall
Regular	175	55	230
Dangerous mesothelioma	72	30	102
Overall	245	83	328

characterization challenges (1 or 0, yes or no, and valid or misleading). It employs a computed capability to estimate the probabilities and trace out the link between the information highlighted and the mark. The probabilities are then converted into parallel structures to make a characterization decision.

(7) *Random Forest*. The random forest (RF) has been the collection of choice structures which includes the sacking provided by “Ho” along with an “arbitrary changeable determination” of Breiman. RF theory has been creating alternative DTs from a learning dataset using randomized bootstrapped tests along with arbitrarily opting for a particle in preparation of information. At last, RF adds up all expectations from all decision structures by casting a vote.

(8) *Using Fresh Information to Test the Prepared Prototypes*. After the prototypes are ready, we may use them to predict fresh information coming out of the experimenting dataset, just like as shown beneath.

- Input: information for testing
- Stage 1: loading prototype that has been prepared
- Stage 2: using the developed prototypes, forecast fresh information
- Gain: estimated gain (either ordinary or MM infection)

TABLE 4: Quantitative aftereffects of various categorizers.

DM	Supervised machine learning prototypes						
	LDA	NB	SVM	KNN	DT	LogR	RF
Resp	85%	88%	100%	97%	100%	100%	100%
Exp	18%	33%	100%	83%	100%	100%	100%
Corr	68%	72%	100%	92%	100%	100%	100%
Review	85%	87%	100%	97%	100%	100%	100%
F-score	75%	78%	100%	94%	100%	100%	100%
Exact	62%	68%	100%	92%	100%	100%	100%

TABLE 5: Investigation of computational intricacy.

S. no.	Categorizers	Calculation time (seconds)
I	LDA	.74 s
II	NB	.68 s
III	KNN	.88 s
IV	SVM	.89 s
V	DT	.92 s
VI	LogR	.66 s
VII	RF	.82 s

### 3. Results

This research was accomplished within the MATLAB location using a PC having an Intel-Core i9 processor running at 48-54GHz and 32 GB of RAM. In this research, we employ 7 AI approaches to intuitively classify the dangerous mesothelioma illness, and we utilized SVM, LDA, KNN, DT, RF, NB, and LogR that are six operational gauges to assess

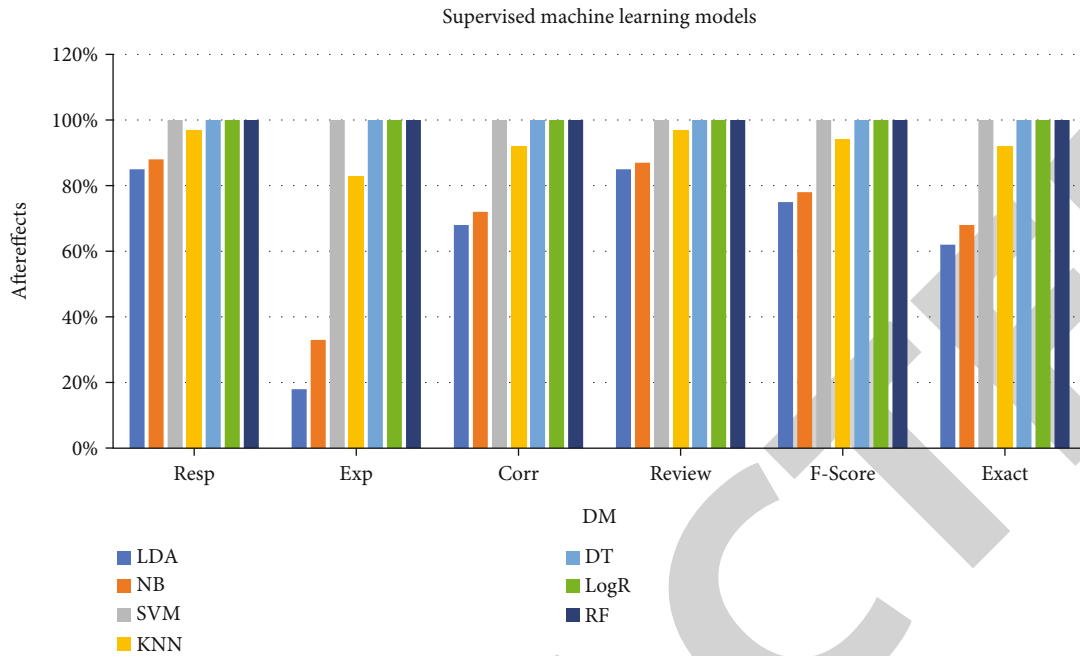


FIGURE 6: Quantitative aftereffects of various categorizers.

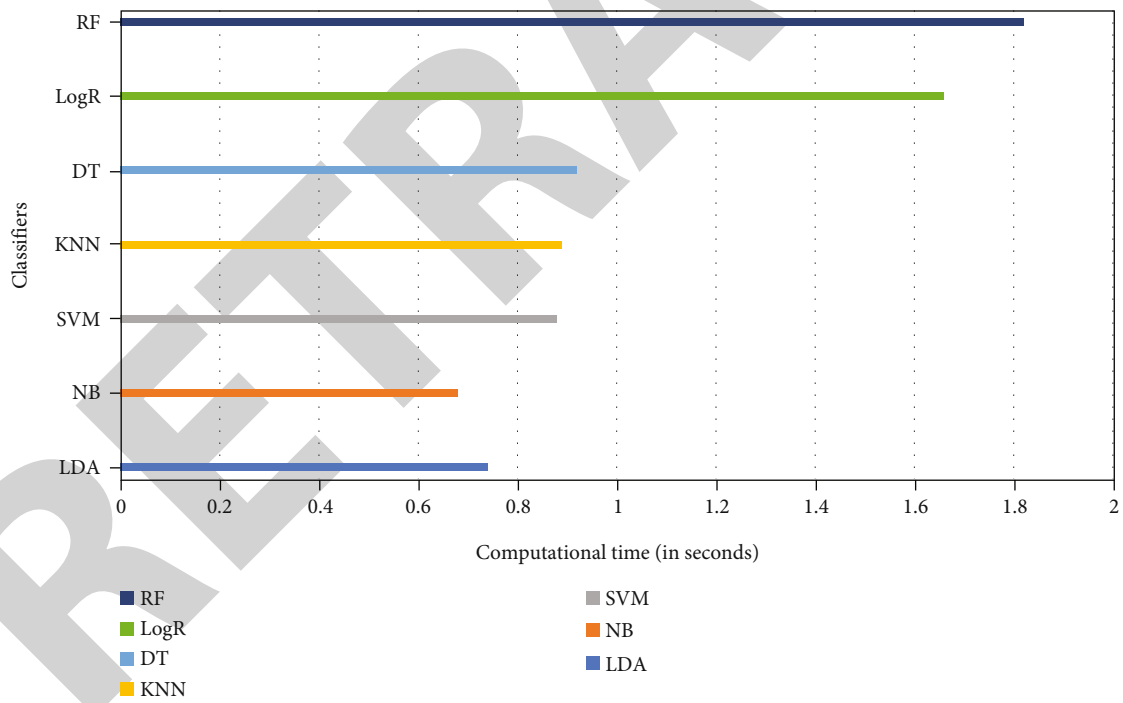


FIGURE 7: Investigation of computational intricacy.

and evaluate their findings. Consequently, each categorizer’s handling season is determined to estimate the computation difficulty. Finally, the assessed procedures’ correctnesses are compared to the current tactics’ correctnesses. As per association, DT, SVM, LogR, and RF surpass active techniques by providing exact one hundred percent precision. Professionals may deploy them as intellectually supportive networks of preference in the screening of DM ailment owing

to its high efficiency and ease of use. Moreover, the study has been dependent on the “mesothelioma disease” dataset, which has 350 components with 35 characteristics and is available online. Then, as described in segment B.1, a unique dataset containing  $350 \times 35$  layered information is arbitrarily divided into preparation and testing sets in a 78-22 percent proportion. We developed seven administered AI prototypes using the preparation dataset: LDA, NB, KNN, SVM, DT,

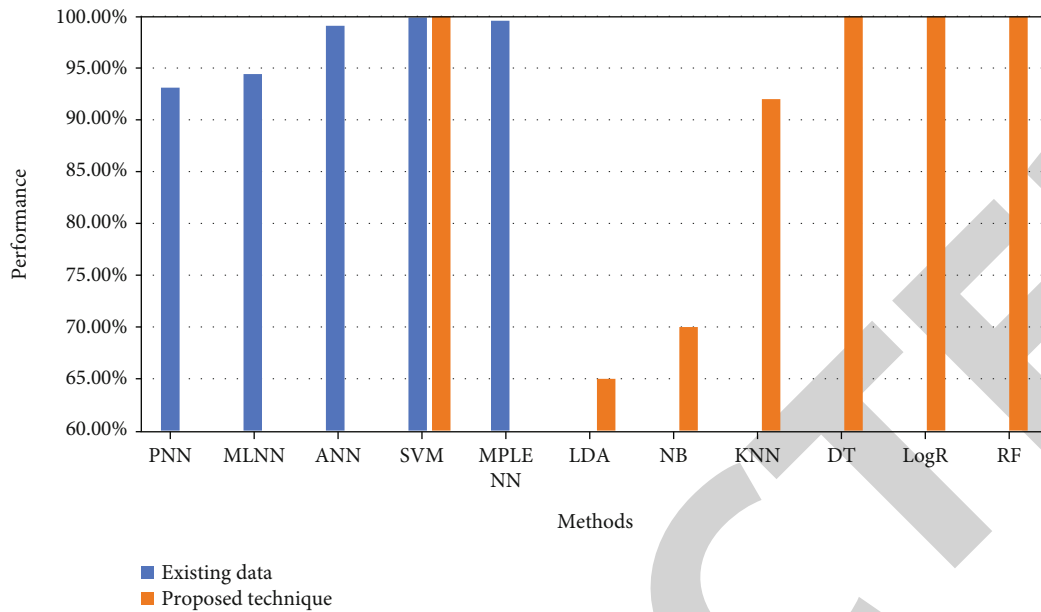


FIGURE 8: Correlation of correctnesses acquired through the proposed technique and existing strategies.

TABLE 6: Correlation of correctnesses acquired through the proposed technique and existing strategies.

Techniques	Methods	Performance
Existing data	PNN	93.1%
	MLNN	94.41%
	ANN	99.07%
	SVM	99.87%
	MLPE NN	99.56%
Proposed technique	LDA	65%
	NB	70%
	KNN	92%
	SVM	100%
	DT	100%
	LogR	100%
	RF	100%

SVM and DT, which have equal exactness rates. Furthermore, we compared and contrasted our completed results with those obtained via linked writing projects. Figure 8 and Table 6 introduce the quantitative examination. The investigation reveals that four prototypes which have been under consideration have been better than earlier efforts in terms of accuracy.

### 4. Conclusion

We suggested using AI techniques to computerize the detection of dangerous mesothelioma in this research. NB, KNN, LDA, SVM, DT, LogR, and RF have been the seven machine learning algorithms considered to distinguish between ordinary and dangerous mesothelioma, and then, the presentation remains related via noting the exactness besides the calculated complications. LDA = 65%, NB = 70%, LR = 100%, KNN = 92%, SVM = 100%, DT = 100%, LogR = 100%, and RF = 100% are the usual precisions supplied. Individually, the calculation times are 0.74 s, 0.68 s, 0.88 s, 0.89 s, 0.92 s, 1.66 s, and 1.82 s. The attained outcomes remain likewise equated to the results obtained from earlier training. This was discovered as noted strategies, RF, SVM, LogR, and DT, are likely to be greater than earlier research in terms of precision. These procedures may be used as an option emotionally supporting networks for specialists in the diagnosis of MM infection because of their high accuracy and simplicity. We will next test the evaluated strategies on a larger dataset to confirm their viability. Furthermore, effective information grouping mechanisms are still required.

LogR, and RF. After the prototypes have been created, all of them can be practiced for predicting fresh data from a testing dataset. Six evaluation metrics (EM) are used to evaluate the presentation of the focused methodologies, including responsiveness, explicitness, correctness, review, F-score, and exactness. Tables 4 and 5 and Figure 6 show the results of the exploratory research. Four prototypes, SVM, DT, LogR, and RF, resulting from seven AI approaches, achieved 100% accuracy. Every categorizer’s computational season is also recorded to analyze its complexity. Every categorizer’s handling season is shown in Table 5 and Figure 7.

Although NB and LDA have a reasonably fast computation time, their accuracy is not guaranteed for everyday usage. LogR and RF require longer to calculate than the other two algorithms that achieve 100 percent accuracy. In this regard, they are less convincing than the other two,

### Data Availability

The data shall be made available on request.

## Conflicts of Interest

The authors declare that they have no conflict of interest.

## References

- [1] S. A. T. Ahmed and S. Ishtiaq, "Malignant mesothelioma," *Pakistan journal of medical sciences*, vol. 29, no. 6, pp. 1433–1438, 2013.
- [2] P. S. Adusumilli, L. Cherkassky, J. Villena-Vargas et al., "Regional delivery of mesothelin-targeted CAR T cell therapy generates potent and long-lasting CD4-dependent tumor immunity," in *Science Translational Medicine*, vol. 6, no. 261, 2014 American Association for the Advancement of Science (AAAS), 2014.
- [3] A. Ahamad, C. Stevens, W. Smythe et al., "Intensity-modulated radiation therapy: a novel approach to the management of malignant pleural mesothelioma," *International Journal of Radiation Oncology • Biology • Physics*, vol. 55, no. 3, pp. 768–775, 2003.
- [4] G. Ak, S. C. Tomaszek, F. Kosari et al., "MicroRNA and mRNA features of malignant pleural mesothelioma and benign asbestos-related pleural effusion," *BioMed Research International*, vol. 2015, Article ID 635748, 8 pages, 2015.
- [5] E. W. Alley, L. R. Molife, A. Santoro et al., "Clinical safety and efficacy of pembrolizumab (MK-3475) in patients with malignant pleural mesothelioma: preliminary results from KEY-NOTE-028," *Cancer Research*, vol. 75, 15\_Supplement, 2015.
- [6] H. Benjamin, D. Lebanony, S. Rosenwald et al., "A diagnostic assay based on microRNA expression accurately identifies malignant pleural mesothelioma," vol. 12, no. 6, pp. 771–779, 2010.
- [7] F. Brims and N. Maskell, "Prognostic factors for malignant pleural mesothelioma," *Current Respiratory Care Reports*, vol. 2, no. 2, pp. 100–108, 2013.
- [8] W. A. Buikhuisen, J. A. Burgers, A. D. Vincent et al., "Thalidomide versus active supportive care for maintenance in patients with malignant mesothelioma after first-line chemotherapy (NVALT 5): an open-label, multicentre, randomised phase 3 study," *The Lancet Oncology*, vol. 14, no. 6, pp. 543–551, 2013.
- [9] W. A. Buikhuisen, M. Scharpfenecker, A. W. Griffioen, C. M. Korse, H. van Tinteren, and P. Baas, "A randomized phase II study adding axitinib to pemetrexed-cisplatin in patients with malignant pleural mesothelioma: a single-center trial combining clinical and translational outcomes," *Journal of Thoracic Oncology*, vol. 11, no. 5, pp. 758–768, 2016.
- [10] L. Calabrò, A. Morra, E. Fonsatti et al., "Tremelimumab for patients with chemotherapy-resistant advanced malignant mesothelioma: an open-label, single-arm, phase 2 trial," *The Lancet Oncology*, vol. 14, no. 11, pp. 1104–1111, 2013.
- [11] L. Calabrò, A. Morra, E. Fonsatti et al., "Efficacy and safety of an intensified schedule of tremelimumab for chemotherapy-resistant malignant mesothelioma: an open-label, single-arm, phase 2 study," *The Lancet Respiratory Medicine*, vol. 3, no. 4, pp. 301–309, 2015.
- [12] B. Castagneto, S. Zai, D. Dongiovanni et al., "Cisplatin and gemcitabine in malignant pleural mesothelioma: a phase II study," *American journal of clinical oncology*, vol. 28, no. 3, pp. 223–226, 2005.
- [13] G. Ceresoli, B. Castagneto, P. Zucali et al., "Pemetrexed plus carboplatin in elderly patients with malignant pleural mesothelioma: combined analysis of two phase II trials," *British Journal of Cancer*, vol. 99, no. 1, pp. 51–56, 2008.
- [14] G. L. Ceresoli, P. A. Zucali, F. De Vincenzo et al., "Retreatment with pemetrexed-based chemotherapy in patients with malignant pleural mesothelioma," *Lung cancer*, vol. 72, no. 1, pp. 73–77, 2011.
- [15] G. L. Ceresoli, P. A. Zucali, A. G. Favaretto et al., "Phase II study of pemetrexed plus carboplatin in malignant pleural mesothelioma," *Journal of Clinical Oncology*, vol. 24, no. 9, pp. 1443–1448, 2006.
- [16] J. Creaney, I. M. Dick, T. M. Meniawy et al., "Comparison of fibulin-3 and mesothelin as markers in malignant mesothelioma," *Thorax*, vol. 69, no. 10, pp. 895–902, 2014.
- [17] J. Creaney, D. Yeoman, Y. Demelker et al., "Comparison of osteopontin, megakaryocyte potentiating factor, and mesothelin proteins as markers in the serum of patients with malignant mesothelioma," *Journal of Thoracic Oncology*, vol. 3, no. 8, pp. 851–857, 2008.
- [18] A. Dejmeek and A. Hjerpe, "Reactivity of six antibodies in effusions of mesothelioma, adenocarcinoma and mesotheliosis: stepwise logistic regression analysis," *Cytopathology*, vol. 11, no. 1, pp. 8–17, 2000.
- [19] B. W. Robinson, A. W. Musk, and R. A. Lake, "Malignant mesothelioma," *The Lancet*, vol. 366, no. 9483, pp. 397–408, 2005.
- [20] S. Kondola, D. Manners, and A. K. Nowak, "Malignant Pleural Mesothelioma: An Update on Diagnosis and Treatment Options," *Therapeutic advances in respiratory disease*, vol. 10, no. 3, pp. 275–288, 2016.
- [21] O. Er, A. C. Tanrikulu, A. Abakay, and F. Temurtas, "An approach based on probabilistic neural network for diagnosis of Mesothelioma's disease," *Computers & Electrical Engineering*, vol. 38, no. 1, pp. 75–81, 2012.
- [22] Q. Yao, M. Shabaz, T. K. Lohani, M. Wasim Bhatt, G. S. Panesar, and R. K. Singh, "3D modelling and visualization for vision-based vibration signal processing and measurement," *Journal of Intelligent Systems*, vol. 30, no. 1, pp. 541–553, 2021.
- [23] S. N. Khan, G. Sikander, S. Anwar, and M. T. Khan, "Classification of malignant mesothelioma cancer using support vector machine," in *2018 International Conference on Computing, Mathematics and Engineering Technologies (iCoMET)*, Sukkur, Pakistan, 2018.
- [24] T. Thakur, I. Batra, M. Luthra et al., "Gene Expression-Assisted Cancer Prediction Techniques," *Journal of Healthcare Engineering*, vol. 2021, Article ID 4242646, 9 pages, 2021.
- [25] S. Mukherjee, "Malignant mesothelioma disease diagnosis using data mining techniques," *Applied Artificial Intelligence*, vol. 32, no. 3, pp. 293–308, 2018.
- [26] M. A. Haq, "SMOTEDNN: a novel model for air pollution forecasting and AQI classification," *Computers Materials and Continua*, vol. 71, no. 1, pp. 1403–1425, 2021.
- [27] R. Caruana and A. Niculescu-Mizil, "An empirical comparison of supervised learning algorithms," in *Proceedings of the 23rd international conference on Machine learning*, Pittsburgh, Pennsylvania, USA, 2006.
- [28] S. Chaudhury, N. Shelke, K. Sau, B. Prasanalakshmi, and M. Shabaz, "A Novel Approach to Classifying Breast Cancer Histopathology Biopsy Images Using Bilateral Knowledge Distillation and Label Smoothing Regularization," *Computational and Mathematical Methods in Medicine*, vol. 2021, Article ID 4019358, 11 pages, 2021.

## *Retraction*

# **Retracted: ML-Based Texture and Wavelet Features Extraction Technique to Predict Gastric Mesothelioma Cancer**

### **BioMed Research International**

Received 8 January 2024; Accepted 8 January 2024; Published 9 January 2024

Copyright © 2024 BioMed Research International. This is an open access article distributed under the Creative Commons Attribution License, which permits unrestricted use, distribution, and reproduction in any medium, provided the original work is properly cited.

This article has been retracted by Hindawi, as publisher, following an investigation undertaken by the publisher [1]. This investigation has uncovered evidence of systematic manipulation of the publication and peer-review process. We cannot, therefore, vouch for the reliability or integrity of this article.

Please note that this notice is intended solely to alert readers that the peer-review process of this article has been compromised.

Wiley and Hindawi regret that the usual quality checks did not identify these issues before publication and have since put additional measures in place to safeguard research integrity.

We wish to credit our Research Integrity and Research Publishing teams and anonymous and named external researchers and research integrity experts for contributing to this investigation.

The corresponding author, as the representative of all authors, has been given the opportunity to register their agreement or disagreement to this retraction. We have kept a record of any response received.

### **References**

- [1] N. Garg, D. Sinha, B. Yadav, B. Gupta, S. Gupta, and S. Miah, "ML-Based Texture and Wavelet Features Extraction Technique to Predict Gastric Mesothelioma Cancer," *BioMed Research International*, vol. 2022, Article ID 1012684, 9 pages, 2022.

## Research Article

# ML-Based Texture and Wavelet Features Extraction Technique to Predict Gastric Mesothelioma Cancer

Neeraj Garg <sup>1</sup>, Divyanshu Sinha <sup>2</sup>, Babita Yadav <sup>3</sup>, Bhoomi Gupta <sup>4</sup>, Sachin Gupta <sup>3</sup>, and Shahajan Miah <sup>5</sup>

<sup>1</sup>Department of Computer Science and Engineering, Maharaja Agrasen Institute of Technology, Delhi, India

<sup>2</sup>Department of Computer Science, Sushant University, India

<sup>3</sup>School of Engineering and Technology, MVN University, India

<sup>4</sup>Department of Information Technology, Maharaja Agrasen Institute of Technology, Delhi, India

<sup>5</sup>Department of EEE, Bangladesh University of Business and Technology (BUBT), Dhaka, Bangladesh

Correspondence should be addressed to Shahajan Miah; [miahbubt@bubt.edu.bd](mailto:miahbubt@bubt.edu.bd)

Received 18 May 2022; Accepted 23 June 2022; Published 4 July 2022

Academic Editor: Gaganpreet Kaur

Copyright © 2022 Neeraj Garg et al. This is an open access article distributed under the Creative Commons Attribution License, which permits unrestricted use, distribution, and reproduction in any medium, provided the original work is properly cited.

Microsatellites are small, repetitive sequences found all across the human genome. Microsatellite instability is the phenomenon of variations in the length of microsatellites induced by the insertion or deletion of repeat units in tumor tissue (MSI). MSI-type stomach malignancy has distinct genetic phenotypes and clinic pathological characteristics, and the stability of microsatellites influences whether or not patients with gastric mesothelioma react to immunotherapy. As a result, determining MSI status prior to surgery is critical for developing treatment options for individuals with gastric cancer. Traditional MSI detection approaches need immunological histochemistry and genetic analysis, which adds to the expense and makes it difficult to apply to every patient in clinical practice. In this study, to predict the MSI status of gastric cancer patients, researchers used image feature extraction technology and a machine learning algorithm to evaluate high-resolution histopathology pictures of patients. 279 cases of raw data were obtained from the TCGA database, 442 samples were obtained after preprocessing and upsampling, and 445 quantitative image features, including first-order statistics of impressions, texture features, and wavelet features, were extracted from the histopathological images of each sample. To filter the characteristics and provide a prediction label (risk score) for MSI status of gastric cancer, Lasso regression was utilized. The predictive label's classification performance was evaluated using a logistic classification model, which was then coupled with the clinical data of each patient to create a customized nomogram for MSI status prediction using multivariate analysis.

## 1. Introduction

Gastric cancer is one of the most common malignant tumors in the world. There were 1,033,701 new cancer cases, accounting for 5.7% of the global new cancer cases, and 782,685 deaths, accounting for 8.2% of global cancer deaths. It ranks fifth in cancer incidence and third in mortality, and there is no decreasing trend in the incidence rate [1]. The heterogeneity of cancer, the appearance of gastric cancer, and the complex and diverse cancer types make the diagnosis and treatment of cancer more difficult. Microsatellite instability results from an impaired DNA mismatch repair, and a specific cancer phenotype is characterized by hyper-

variability of short repeats in the genome, a form characterized by DNA polymerase slippage and single nucleotides [2]. Extensive lengths of the microsatellite repeats are due to increased frequency of variants (SNVs). Polymorphism studies have shown that MSI-type gastric cancer accounts for about 15% of gastric cancer patients; these patients are more likely to benefit from immunotherapy [3]. MSI-type gastric cancer patients have their unique clinical features, such as the diffuse cancer tissue genome which is less stable, the disease site which is often distal to the tumor tissue, and the tumor types which are mostly type 3; MSI-type gastric cancer patients usually have a good overall long-term prognosis, compared with the contemporary MSS-type gastric

cancer patients; for MSI-type gastric cancer, the survival rate of patients is high [4]. From precancer to onset, MSI gradually accumulates and increases, and therefore, MSI detection for early diagnosis and screening of gastric cancer is prolonged [5]. The prognosis of gastric cancer patients and the clinical decision-making of adjuvant gastric cancer treatment are of great significance. There are two main methods of MSI detection: immunohistochemistry (Immunohistochemistry, IHC) and polymerase chain reaction (PCR). IHC responds to MSI by detecting the expression of mismatch repair gene state; PCR is carried out through a specific single-nucleotide site gene tagging genetic analysis; however, both IHC and PCR testing methods need to be large-capacity tertiary medical center and require high economic and time cost; it is difficult to extend to every patient in clinical practice [6]. Therefore, none provides timely immune screening for a large number of potential immunotherapy-sensitive patients with point inhibitor therapy, thereby losing the chance to control the disease [7].

Histopathology is an essential tool for cancer diagnosis and prediction, and its type reflects the combined effects of molecular changes on cancer cell behavior. Assessing disease progression provides a direct visualization tool. A group of histopathologists can assess cell density, tissue structure, and histological filamentous features such as cleft status which were used to classify lesions. Along with advances in microscopy, imaging technology, and computer technology based on pathological pictures, auxiliary diagnostic models are developing rapidly. Among them, image texture analysis is used for pathology. Image texture feature extraction for cancer grading, Classification and predict for example, the author [8]. For extracting tissue disease from breast cancer patients, the grayscale co-occurrence matrix (GLCM) and the graph run-length matrix (GRLM) of the image is used. Euler number and other texture features, using Linear Discriminant Classifier (LDA) are used to map histological images, malignant and non-malignant histopathology Image, and the classification accuracy was 80% and 100%, respectively. The researcher in this study has done extracting three sets of texture features of soft tissue sarcoma: gray level cooccurrence matrix (GLCM), gray-level run-length matrix (GLRLM), and local binary modulus texture analysis using the LBP method to achieve the metastases and lesions of soft tissue sarcoma's death prediction [9]. Author has trained a deep convolutional neural network; two subtypes of lung cancer can be accurately distinguished from histopathological images: lung adenocarcinoma (LUAD) and lung squamous cell carcinoma (LUSC). Mutation status of six genes is associated with lung cancer. In this study, tumors, malignancy of the lymph node is a predictor that has consequences for the degree of lymph dissection. Numerous nodal units are engaged in the capillary permeability of the stomach, each with a variable risk of malignancy. This study aimed to construct a deep network system for predicting lymph cancer in numerous nodal sites in individuals with gastric cancer using preoperative CT data. ML techniques are employed for the examination of these CT scans for the investigation of any changes if occurred to predict the ailments and recommend precautions for better curability

[10]. The focus of this research was to see if radiomic evaluation employing spectroscopic micro-CT-enhanced nanoparticle contrast enhancing may help distinguish tumors dependent on the amount of malignant cell lymphocytes [11]. In this research to improve survival prognosis, we offer a unique combined multitask system with multilayer characteristics that predicts clinical tumor and metastasis stages simultaneously to detect gastric cancer [12]. This paper can establish to fuse the statistical model of multiple residual networks; it can be obtained from a standard hematoxylin and accurate prediction of prostate cancer patients in histopathological images after eosin staining the mutation status of the speckle-type POZ gene [13].

This paper proposes gastric cancer based on the texture features of histopathological images. Authors in this research have forecasted MSI prediction method that targets tumor heterogeneity in gastric cancer histopathology, where researchers have used image feature extraction technology and a machine learning algorithm to evaluate high-resolution histopathology pictures of the patients. 279 cases of raw data were obtained from the TCGA database, out of which 442 samples were acquired after preprocessing and upsampling, and 445 quantitative image features, including first-order statistics of impressions, texture features, and wavelet features, were extracted from the histopathological images of each sample. To filter the characteristics and provide a prediction label (risk score) for MSI status of gastric cancer, Lasso regression was employed. Furthermore, the predictive label's classification performance was evaluated using a logistic classification model, which was then coupled with the clinical data of each patient to create a customized nomogram for MSI status prediction using multivariate analysis as an achievement of the research.

*1.1. Organization.* The paper is outlined in several sections where the starting section is the introduction part followed by the second section which discusses the data and methods employed in the study. The third section defines the analysis of experimental results, followed by the penultimate section that states about discussions and findings, and the ultimate section is the conclusion of the study.

In the representation of Figure 1 as depicted below, the extracted quantitative image features from images have been acquired, and the use of Lasso regression to construct the prediction has targeted a signature, and using the predictive signature as an independent predictor to be combined with the patient's clinical features has been opted, additionally the multivariate analysis by logistic regression to build a predictive model has been obtained; at last the prediction tool is being drawn termed as nomogram of personality that provides a powerful instrument for MSI prediction in gastric cancer patients. The method of flow is shown in the figure below.

## 2. Data and Methods

*2.1. Patient Data.* This paper's histopathological images of gastric cancer are from the TCGA data library. In addition, the MSI status of gastric cancer patients was analyzed to



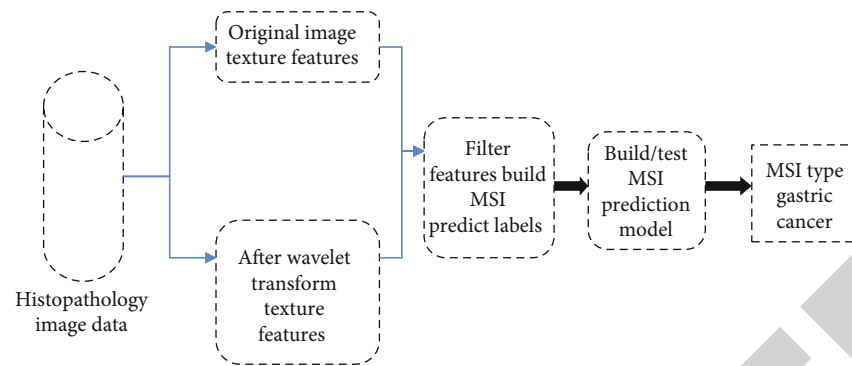


FIGURE 1: Construction process of MSI prediction model for gastric cancer.

use the obtained data effectively. This study established three inclusion criteria for the collected data: (1) Pathological images showing uniform staining, precise imaging and no tissue adhesion; (2) uniformly complete personal basic information and clinical characteristics; (3) have clear MSI status information. After screening, 277 case samples were eligible for the inclusion standard.

**2.2. Data Preprocessing.** To ensure the validity of the experiment and obtain valuable results, it is necessary to solve the problem of sample imbalance. Augment the minority class by sampling. For MSI-type cases, histopathological images for each patient is considered. Select multiple ROIs, each ROI as an independent sample, upsampled. The dataset has a total of 442 pieces. The obtained models are randomly divided into a training set and a validation set: There are 313 samples in the training set, of which 156 are of MSI type. There are 157 cases of MSS type; there are 129 samples in the validation set, of which 64 cases are of MSI type, for example, 65 cases of MSS type.

**2.3. Image Segmentation.** The histopathological image needs to be processed before image feature extraction to ensure the accuracy of the resulting image features and reduce the computational complexity degree segmentation. To obtain the most representative lesion area, under the guidance of a chief physician with experience in histopathological image detection, the tumor area was annotated and examined the marked lesion area by another expert. Finally, the ROI of all histopathological images was obtained by segmentation.

**2.4. Feature Extraction.** In this study, the original image of the ROI is obtained from the segmentation and the processed wavelet. A total of 445 image features are extracted from the filtered image, which can be divided into two classes, six groups per class: first-order statistics and gray-level cooccurrence matrix (GLCM), gray-level size zone matrix (GLSZM), gray-level run-length matrix (GLRLM), neighboring gray tone difference matrix (NGTDM), and gray-level dependence matrix (GLDM).

First-order statistics describe interest through common statistical indicators pixel intensity distribution within the region of interest. GLCM describes the grayscale of an image

and the second-order joint probability function of the spatial correlation characteristics obtained by calculating GLCM using the partial eigenvalues of the matrix to represent the texture features of the image, which can give the comprehensive information about the direction, adjacent interval and changing amplitude of the grayscale of the response image [14]. GLSZM is used to quantify the gray-level area in the image; the gray-level area domain is defined as the number of connected pixels that share the same gray-level intensity. GLRLM is used to quantify grayscale runs, which are defined as the length of consecutive pixels of the same gray value. In NGTDM through grayscale, the sum of absolute differences reflects the difference between the average gray values of adjacent pixels different. GLDM can quantify the grayscale dependence in images; grayscale dependence is defined as the number of connected pixels within a distance  $\delta$  that depends on the center pixel [15].

This study extracted 18 features from first-order statistics, mainly including entropy, total energy, mean absolute deviation, and skewness; from GLCM, 22 kinds of features are extracted, mainly including autocorrelation, joint average, clustering shading, and cluster tendency; 16 features were extracted from GLSZM, mainly including grayscale uneven normalization, uneven area size, and area percentage size area nonuniformity normalization; 16 were extracted from GLRLM features, including run entropy, run difference, gray variance, and run nonuniformity uniform standardization; 5 kinds of features are extracted from NGTDM, mainly including roughness, contrast, complexity, and intensity; 14 were extracted from GLDM features, mainly including dependence entropy, dependence nonuniformity, dependence nonuniformity standard standardization, and dependent variance.

**2.5. Feature Selection.** To reduce the complexity of the model and prevent overfitting, before modeling, this paper, features are selected using the lasso method [16]. Lasso improves the traditional, linear regression method provides a new perspective on the general linear regression algorithm on the basis of adding the L1 penalty term, the linear regression parameters have sparsity from the resulting model which has good predictability, and the selected features are related to the prediction. The test label is more relevant. For the

feature vector  $x_i (i = 1, 2, \dots, N)$  of a given sample,  $x_i \in R^n$ . The objective function of Lasso regression is

$$L(\alpha, \gamma) = \sum_{i=1}^N \left( y_i - \sum_j x_{ij} a_j \right)^2 + \gamma \sum_{j=1}^p |a_j|, \quad (1)$$

where  $y$  is the label of the sample and  $\alpha = \{a_j\}$  is the regression parameter to get the most optimal regression parameters and transform the objective function minimization problem into the following subproblems:

$$a_j^{(k+1)} = \operatorname{argmin} \frac{L}{2} \|a - z_j\|_2^2 + \gamma \|a\|_1 \quad (2)$$

In:

$$z_j = a_j^{(k)} - \frac{1}{L} \nabla f(a_j^{(k)}), \quad (3)$$

$$\nabla f(a_j^{(k)}) = 2 \sum_{i=1}^N \left[ x_{ij} \left( \sum_{s=1}^p x_{is} a_s^{(k)} - y_i \right) \right]. \quad (4)$$

Using proximal gradient descent [17], the algorithm iteratively solves Equation (3) and uses the soft domain function to solve Equation (2); the final solution is as follows:

$$a_j^{(k+1)} = \begin{cases} z_j - (\gamma/L), z_j > (\gamma/L), \\ 0, |z_j| \leq \frac{\gamma}{L}, \\ z_j + \frac{\gamma}{L}, z_j < -\frac{\gamma}{L}. \end{cases} \quad (5)$$

Through the above algorithm, the sparse feature matrix is finally obtained, which is used to build a classification model.

**2.6. Predictive Label Construction.** In this study, the sparse eigenvalues and their regression coefficients were used to construct a sample. Table 1 shows the risk score of the proposed model over the number of features and log variance. In the predicted label of Ben, the formula is as follows:

$$\text{Risk score} = \sum_{i=1}^n \text{Feature}_i \times \alpha_i. \quad (6)$$

Among them, feature is the  $i^{\text{th}}$  eigenvalue of the sample feature vector, and  $\alpha_i$  is the regression coefficient corresponding to the eigenvalue. Table 2 shows the risk coefficient of the proposed model over the number of feature and log variance.

Using risk score as an independent predictor and the clinical samples, combine features to build logistic regression models and draw personalized nomogram picture and through C index, AUC value, calibration curve, and decision curve evaluation predictive performance of the model [18].

TABLE 1: Risk score of the proposed model over the number of features and log variance.

Log $\gamma$	Binomial deviance	Number of features
-2	1.4	2
-4	1.35	5
-6	1.3	5
-8	1.25	9
-10	1.2	12

TABLE 2: Risk coefficient of the proposed model over number of feature and log variance.

Log $\gamma$	Coefficients	Number of features
-2	10	12
-4	5	11
-6	3	8
-8	2.5	11
-10	5	12

TABLE 3: Clinical characteristics of the patients.

Feature item	Classification	MSI (n = 55)	MSS (n = 222)	P value
Age	Mean	70.91	63.74	<0.001***
	Range	46~90	36~90	
Gender	Male	35 (54.5%)	157 (71.2%)	<0.001***
	Female	25 (45.5%)	64 (28.8%)	
TNM stage	I	12 (21.8%)	25 (11.3%)	<0.001***
	II	20 (36.4%)	67 (30.1%)	
	III	19 (34.5%)	106 (47.7%)	
	IV	4 (7.3%)	24 (10.8%)	

### 3. Analysis of Experimental Results

**3.1. Clinical Features.** The histopathological images used in this study were obtained from 277 gastric cancer patients, including 55 patients with MSI-type gastric cancer and 222 patients with MSS-type gastric cancer. Among them, there were 188 male patients and 89 female patients, with a median age of 67.64 years (33-90 years old), and the prevalence of MSI was 19.85% (55/277). According to gastric cancer, patients were divided into two groups by MSI status. There are differences in gender, age, and TNM staging between patients and MSS patients. The clinical characteristics of the patients are shown in Table 3.

**3.2. Image Feature Screening and Predicted Label Construction.** Based on the MSI status, Lasso regression is applied on the training set, features are filtered, and Figure 2(a) shows the binomial error classification points with log  $\gamma$ , where the least binomial error classification point represents the most retained. The best number of features fit the model. Based on the minimum criterion and 1 standard error standard, with 10-fold cross-validation, draw the

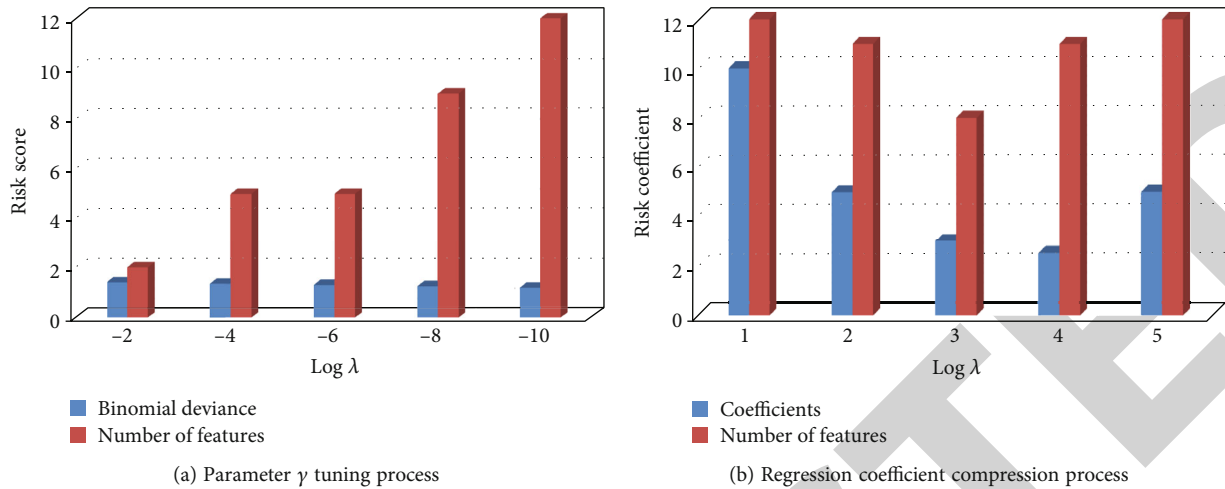


FIGURE 2: Lasso regression process.

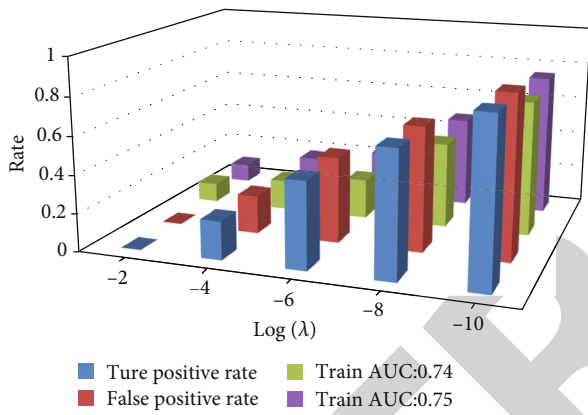


FIGURE 3: ROC curves of training set and test set.

dashed vertical with the best  $\gamma$  value wire. Figure 3(b) shows the lasso coefficient curve of the image features [19].

The results of lasso regression are shown in Tables 4, and 9 lines were finally screened nonzero number of features, including 4 image features based on the original image and based on 5 image features after wavelet filtering. Calculate the sample by Formula (6) Ben’s risk score. Single-factorial correlation of 9 image features with MSI status and prime variance analysis shows that the  $P$  values were all less than 0.001, indicating that the characteristics obtained from the screening were closely related to gastric MSI status of cancer patients and was significantly correlated.

**3.3. Prediction Accuracy Verification.** Based on the selected image texture features and logistic regression training, a predictive classification model for MSI was constructed. As shown in Figure 3, the ROC curve in line analysis, the AUC value was 0.75. Then apply that model to the validation set which can effectively predict MSI status in ROC curve analysis, AUC. The value is 0.74. Therefore, 9 features constituting the model associated with gastric cancer histopathological image features associated with patients’ MSI status. Table 5 gives the results of each evaluation index of the classification model [20].

TABLE 4: Lasso regression results.

Feature name	Regression coefficients	$P$ value
original_firstorder_10Percentile	0.212 204	<0.001***
original_firstorder_90Percentile	0.404 922	<0.001***
original_firstorder_Median	6.118 815	<0.001***
original_firstorder_Skewness		
wavelet-		
HL_glcm_Imc2 wavelet-	-0.817 240	<0.001***
LL_firstorder_10Percentile		
wavelet-		
LL_firstorder_Median wavelet-	0.490 395	<0.001***
LL_glcm_ClusterShade wavelet-	-5.750 580	<0.001***
LL_glrm_GrayLevelEmphasis	1.133 542	<0.001***
	-0.254 150	<0.001***

TABLE 5: Each evaluation index of the classification model.

Log $\gamma$	True positive rate	False positive rate	Train Auc:0.74	Train Auc:0.75
-2	0	0	0.1	0.1
-4	0.2	0.2	0.16	0.18
-6	0.45	0.45	0.21	0.25
-8	0.65	0.65	0.45	0.48
-10	0.85	0.85	0.71	0.75

**3.4. Construction and Evaluation of Monogram.** To reflect the clinical value of the predictive model, this study used all datasets. Table 6 and Figure 4 show the model evaluation results.

The Nomo-gram based on clinical characteristics were constructed using Risk Score. The latter nomogram was used to predict the MSI status of gastric cancer patients, as shown in Tables 7 and 8.

The nomogram includes gender, age, TNM stage, and risk score, which allows users to obtain MSI status

TABLE 6: Model evaluation results.

Dataset	Precision	Recall	F1 value	AUC value
Training set	0.68	0.73	0.72	0.75
Validation set	0.65	0.67	0.67	0.74

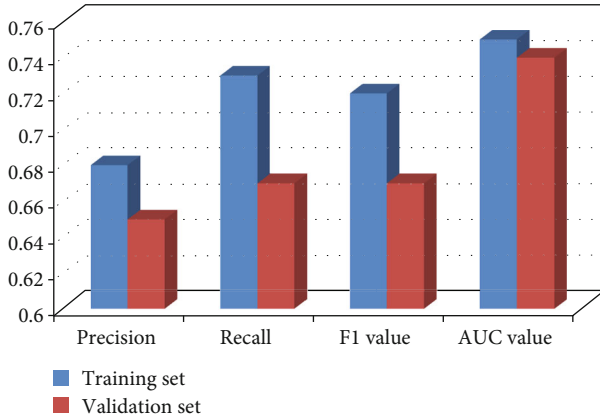


FIGURE 4: Model evaluation results.

TABLE 7: Evaluation results of model (before joining risk score).

Points	0-100
Gender	0 or 1
Age	30-90
TNM stage	01-Apr
Total point	0-180
Linear predictor	[-2.5,2.5]
Risk of MSI	0.1-0.9

TABLE 8: Evaluation results of model (after adding risk score).

Points	0-100
Gender	0 or 1
Age	30-90
TNM stage	01-Apr
Risk score	[-3.5,3.0]
Total point	0-130
Linear predictor	[-4,3]
Risk of MSI	0.1-0.9

predictions corresponding to patient covariate combination probability. For example, locate the patient's TNM stage axis; draw a line on that axis a vertical line to determine the predicted score corresponding to that TNM stage. For each variable, repeat this process and add the scores for each covariate to make the total score corresponding to get the predicted probability to achieve the MSI status of gastric cancer patients predict.

Apply the index of concordance (C-index), respectively, AUC, and calibration curve to evaluate the predictive performance of the nomogram. AUC values before and after adding risk score were 0.696 and 0.802; the consistency index is shown in Table 9; after adding risk score, the value of C-

TABLE 9: C-index evaluation of prediction model.

Predictive model	C-index	95% CI
Before joining risk score	0.7	0.64~0.74
After joining risk score	0.8	0.76~0.84

index is improved from 0.69. The calibration curve is shown in Figure 5. The dotted line represents the ideal prediction state. The results show that the calibration curve fits better after adding the prediction label constructed in this study. Table 10 shows the Calibration Curve Comparisons.

To further validate the clinical utility of the predictive model, a decision curve line analysis to quantify the net gain to evaluate columns based on texture features of pathological images was done. As shown in Figure 6, in the entire risk threshold area during the period, the predictive model after adding risk score achieved a larger net income beneficial. Table 11 shows the decision curve comparison.

This result shows that adding the risk score nomogram has a greater bed application potential.

**3.5. Comparison with Other MSI Prediction Studies.** To further verify the performance of the model, other studies on MSI prediction were compared, and the comparison results shown in Table 12 developed three prediction models for MSI prediction by extracting the morphology, texture, Gabor wavelet, and other radiomic features of CT images, combined with clinical features, using Lasso and Naive Bayes classifiers, and using clinical features alone [21]. The AUC value of the model with radiomic features was 0.598, the AUC value of the model using radiomic features alone was 0.688, and the AUC value of the model combining radiomic and clinical features was 0.752, which has a large gap with the classification performance of the proposed MSI prediction model.

We trained a ResNet-18 network through the slices of histopathological images to obtain the likelihood distribution of the patient's MSI status, generated the plaque likelihood histogram feature, and used the XGBoost classifier to predict the patient's MSI status [22]. The model has an AUC value of 0.93 on the training set and 0.73 on the test set, indicating obvious overfitting.

## 4. Discussion and Findings

This paper proposes a texture feature based on histopathological images of gastric cancer. The MSI prediction method of sign was used to extract the texture features such as GLCM, GLSZM, GLSZM, and GLRLM. In these texture features, after wavelet transformation sign, we have employed Lasso regression for feature selection, and lastly the texture features most relevant to the MSI state of the user are constructed based on these texture features. The MSI prediction labels of gastric cancer were obtained, and the predictions were compared on the training and validation sets. The label classification performance is verified, and the AUC values obtained are 0.75 and 0.74, respectively. The results show that the proposed predictive signature has a better effect on

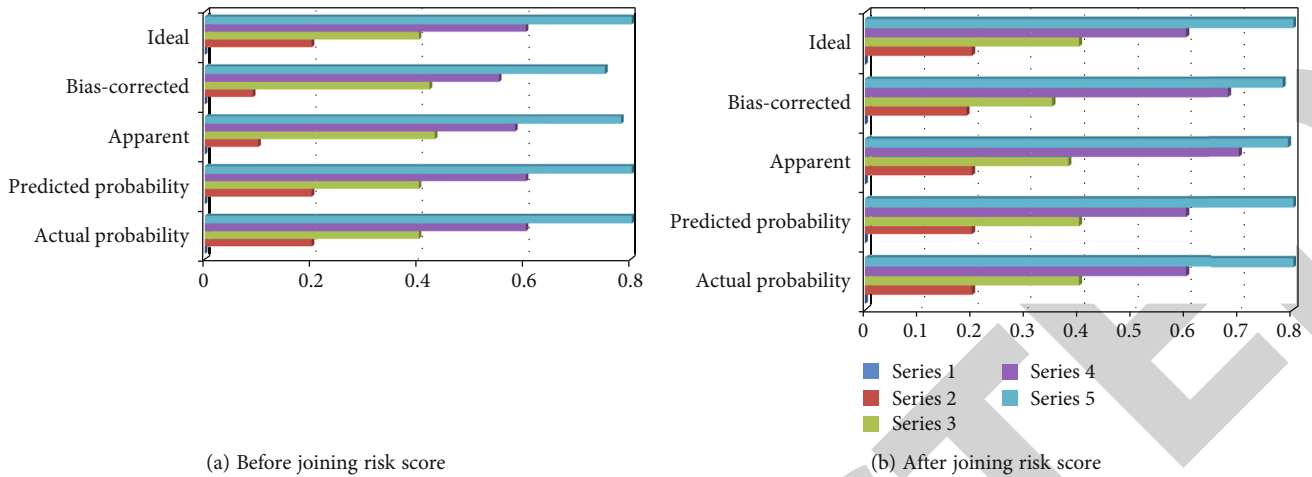


FIGURE 5: Calibration curve comparisons.

TABLE 10: Calibration curve comparisons.

(a) Before joining risk score

Actual probability	Predicted probability	Apparent	Bias-corrected	Ideal
0	0	0	0	0
0.2	0.2	0.1	0.09	0.2
0.4	0.4	0.43	0.42	0.4
0.6	0.6	0.58	0.55	0.6
0.8	0.8	0.78	0.75	0.8

(b) After joining risk score

Actual probability	Predicted probability	Apparent	Bias-corrected	Ideal
0	0	0	0	0
0.2	0.2	0.2	0.19	0.2
0.4	0.4	0.38	0.35	0.4
0.6	0.6	0.7	0.68	0.6
0.8	0.8	0.79	0.78	0.8

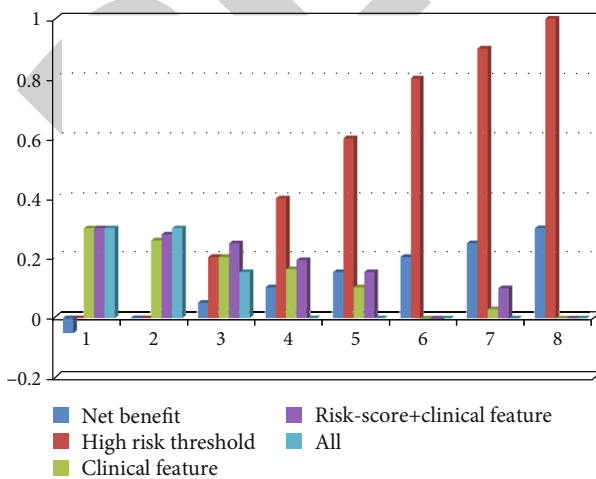


FIGURE 6: Decision curve comparison.

TABLE 11: Decision curve comparison.

Net benefit	High-risk threshold	Clinical feature	Risk score + clinical feature	ALL
-0.05	0	0.3	0.3	0.3
0	0	0.26	0.28	0.3
0.05	0.2	0.2	0.25	0.15
0.1	0.4	0.16	0.19	0
0.15	0.6	0.1	0.15	0
0.2	0.8	-0.01	-0.01	0
0.25	0.9	0.03	0.1	0
0.3	1	0	0	0

the MSI status of gastric cancer patients compared with the traditional MSI detection methods initially opted, using machine learning technology based on direct prediction of MSI in gastric cancer patients on the basis of readily available histopathological image status, without the need for

TABLE 12: Performance comparison of MSI prediction models.

Method	Type of data	Image features	Clinical features	Joint model
Win	Histopathological images	0.74	—	—
Nano	CT image	0.68	0.599	0.755
Proposed model	Histopathological images	0.75	0.697	0.801

additional laboratories for genetic testing and immunohistochemistry analysis; the prediction of MSI status can be achieved at a lower cost. Hence, this method when compared to computer-aided MSI prediction methods based on CT images outperforms, because the reproducibility of radiology features considering different scanners and imaging protocols and the potential differences in terms of the formation of H&E-stained histopathological images are less stable comparing to the performance of the MSI prediction model proposed in this paper. Therefore, this investigation proposes and confirms a strategy for predicting MSI in gastric cancer based on histopathological pictures that may accurately predict the MSI status of patients with gastric cancer, allowing for universal MSI screening and benefiting more gastric cancer patients to be investigated in a significant manner.

## 5. Conclusion

This study proposes and validates a method for predicting MSI in gastric cancer based on histopathological images, which can effectively predict the MSI status of patients with gastric cancer, hence providing a possibility for universal screening of MSI, and is expected to benefit more gastric cancer patients. Immunotherapy by combining the clinical features with predictive labels is proposed in this paper to construct gastric cancer MSI prediction models, as compared with prediction models based on clinical characteristics; after entering the predicted labels that are proposed in this paper, the AUC value of the model is improved from 0.696 to 0.802. To further verify the validity of the predicted labels, the clinical value of sex and predictive models, respectively, before and after adding predictive labels are analyzed. The prediction model was evaluated by calibration curves, C-index values, and decision curves. The results show that after adding the predicted labels proposed in this paper, the C-index value and the calibration performance of the quasi-curve are significantly improved, and the decision curve analysis has also demonstrated a greater net income.

## Data Availability

The data shall be made available on request.

## Conflicts of Interest

The authors declare that they have no conflict of interest.

## References

- [1] Y. Deng, J. Lan, Y. Huang et al., "Predicting differentiation degree of gastric cancer pathology images based on mask attention R-CNN," in *2nd International Conference on Computer Engineering and Intelligent Control (ICCEIC)*, Chongqing, China, 2021.
- [2] Y. Li, X. Li, X. Xie, and L. Shen, "Deep learning based gastric cancer identification," *IEEE 15th International Symposium on Biomedical Imaging (ISBI 2018)*, 2018, Washington, DC, USA, 2018, 2018.
- [3] S. Luo, H. Liu, H. Zhao, X. An, H. Xie, and L. Huo, "Gastric and colon cancer imaging with swept source optical coherence tomography," in *Conference on Lasers and Electro-Optics Pacific Rim (CLEO-PR)*, Singapore, 2017.
- [4] L. Li, M. Chen, Y. Zhou, J. Wang, and D. Wang, "Research of deep learning on gastric cancer diagnosis," in *Cross Strait Radio Science & Wireless Technology Conference (CSRSWTC)*, Fuzhou, China, 2020.
- [5] A. Yahata, H. Takemura, T. Takamatsu et al., "Wavelength selection of near-infrared hyperspectral imaging for gastric cancer detection," in *6th International Conference on Intelligent Informatics and Biomedical Sciences (ICIIBMS)*, Oita, Japan, 2021.
- [6] N.-y. Xiong, J.-h. Zhou, X.-b. Zhou, J. Zhang, and C.-y. Zhang, Eds., "Meta-analysis of association between dietary factors and gastric cancer in China," in *International Conference on Future BioMedical Information Engineering (FBIE)*, Sanya, China, 2009.
- [7] R. Caprara, K. L. Obstein, G. Scozzarro et al., "A platform for gastric cancer screening in low- and middle-income countries," *IEEE Transactions on Biomedical Engineering*, vol. 62, no. 5, pp. 1324–1332, 2015.
- [8] B. Gulzar and A. Gupta, "DAM: a theoretical framework for SensorSecurity in IoT applications," *International Journal of Next-Generation Computing*, vol. 12, no. 3, p. 10.47164/ijngc.v12i3.830, 2021.
- [9] Q. Yao, M. Shabaz, T. K. Lohani, B. M. Wasim, G. S. Panesar, and R. K. Singh, "3D modelling and visualization for vision-based vibration signal processing and measurement," *Journal of Intelligent Systems*, vol. 30, no. 1, pp. 541–553, 2021.
- [10] C. Jin, Y. Jiang, H. Yu et al., "Deep learning analysis of the primary tumour and the prediction of lymph node metastases in gastric cancer," *British Journal of Surgery*, vol. 108, no. 5, pp. 542–549, 2021.
- [11] A. J. Allphin, Y. Mowery, K. J. Lafata et al., "Spectral micro-CT and radiomic analysis for classification of tumors based on lymphocytic burden in cancer therapy studies," *Medical Imaging 2022: Biomedical Applications in Molecular, Structural, and Functional Imaging*, vol. 12036, 2022.
- [12] L. Zhang, D. Dong, Z. Liu, J. Zhou, and J. Tian, "Joint multi-task learning for survival prediction of gastric cancer patients

## *Retraction*

# **Retracted: Attention Layer-Based Multidimensional Feature Extraction for Diagnosis of Lung Cancer**

### **BioMed Research International**

Received 8 January 2024; Accepted 8 January 2024; Published 9 January 2024

Copyright © 2024 BioMed Research International. This is an open access article distributed under the Creative Commons Attribution License, which permits unrestricted use, distribution, and reproduction in any medium, provided the original work is properly cited.

This article has been retracted by Hindawi, as publisher, following an investigation undertaken by the publisher [1]. This investigation has uncovered evidence of systematic manipulation of the publication and peer-review process. We cannot, therefore, vouch for the reliability or integrity of this article.

Please note that this notice is intended solely to alert readers that the peer-review process of this article has been compromised.

Wiley and Hindawi regret that the usual quality checks did not identify these issues before publication and have since put additional measures in place to safeguard research integrity.

We wish to credit our Research Integrity and Research Publishing teams and anonymous and named external researchers and research integrity experts for contributing to this investigation.

The corresponding author, as the representative of all authors, has been given the opportunity to register their agreement or disagreement to this retraction. We have kept a record of any response received.

### **References**

- [1] M. Bhende, A. Thakare, V. Saravanan, K. Anbazhagan, H. N. Patel, and A. Kumar, "Attention Layer-Based Multidimensional Feature Extraction for Diagnosis of Lung Cancer," *BioMed Research International*, vol. 2022, Article ID 3947434, 11 pages, 2022.

## Research Article

# Attention Layer-Based Multidimensional Feature Extraction for Diagnosis of Lung Cancer

**Manisha Bhende** <sup>1</sup>, **Anuradha Thakare** <sup>2</sup>, **V. Saravanan** <sup>3</sup>, **K. Anbazhagan** <sup>4</sup>,  
**Hemant N. Patel** <sup>5</sup> and **Ashok Kumar** <sup>6</sup>

<sup>1</sup>Marathwada Mitra Mandal's Institute of Technology, Pune, India

<sup>2</sup>Department of Computer Engineering, Pimpri Chinchwad College of Engineering, Pune, India

<sup>3</sup>Dambi Dollo University, Ethiopia

<sup>4</sup>Department of Computer Science and Engineering, Saveetha School of Engineering, SIMATS, Chennai, India

<sup>5</sup>Computer Engineering, Sankalchand Patel College of Engineering, India

<sup>6</sup>Department of Computer Science, Banasthali Vidyapith, Banasthali-304022 (Rajasthan), India

Correspondence should be addressed to V. Saravanan; saravanan@dadu.edu.et

Received 16 May 2022; Accepted 20 June 2022; Published 4 July 2022

Academic Editor: Gaganpreet Kaur

Copyright © 2022 Manisha Bhende et al. This is an open access article distributed under the Creative Commons Attribution License, which permits unrestricted use, distribution, and reproduction in any medium, provided the original work is properly cited.

At present, early lung cancer screening is mainly based on radiologists' experience in diagnosing benign and malignant pulmonary nodules by lung CT images. On the other hand, intraoperative rapid freezing pathology needs to analyse the invasive adenocarcinoma nodules with the worst recovery in adenocarcinoma. Moreover, rapid freezing pathology has a low diagnostic accuracy for small-diameter nodules. Because of the above problems, an algorithm for diagnosing invasive adenocarcinoma nodules in ground-glass pulmonary nodules is based on CT images. According to the nodule space information and plane features, sample data of different dimensions are designed, namely, 3D space and 2D plane feature samples. The network structure is designed based on the attention mechanism and residual learning unit; 2D and 3D neural networks are along built. By fusing the feature vectors extracted from networks of different dimensions, the diagnosis results of invasive adenocarcinoma nodules are finally obtained. The algorithm was studied on 1760 ground-glass nodules with 5-20 mm diameter collected from a city chest hospital with surgical and pathological results. There were 340 nodules with invasive adenocarcinoma and 340 with noninvasive adenocarcinoma. A total of 1420 invasive nodule samples were cross-validated on this example dataset. The classification accuracy of the algorithm was 82.7%, the sensitivity was 82.9%, and the specificity was 82.6%.

## 1. Introduction

Lung cancer has recently emerged as a malignancy that poses a major threat to human health as one of its symptoms [1]. When opposed to other tumors, lung cancer has no symptoms in the early stages. Many patients have progressed to the point where they are inoperable or have metastasized, and patients in the middle and late stages have poor surgical outcomes [2, 3]. Lung cancer screening with low-dose helical CT is critical for early diagnosis of lung cancer, with reliable diagnostic results increasing the likelihood of a patient's capacity to be cured [4]. According to the statistics of the NLST study in the United States, in the lungs with suspected

imaging in 20% of cancer cases, the final surgical pathology is not lung cancer. For lung adenocarcinoma, its subpathological type dramatically affects the surgical approach. The surgical medium-fast frozen pathology is accurate in diagnosing whether small diameter tumors are invasive, and the accuracy rate is low [5]. Therefore, for early lung cancer nodules with similar shape characteristics, the diagnosis of subpathological type of nodules, tiny nodules of lung adenocarcinoma, is based only on subjective diagnosis by radiologists which will have certain limitations and preoperative. The ability to more accurately confirm the subpathological type is also essential for the formulation of the surgical plan to have greater significance.



At present, increasing scholars are studying the use of lung CT images to perform intelligent diagnosis of pulmonary nodules to assist radiologists and improve nodules' efficiency and accuracy of diagnosis [6]. Authors have adopted a multi-input 2D convolutional net network; the input of its network is designed to contain modules, no modules, and only packets [7]. There are three different views of the same nodule object with nodule images in the common open dataset LIDC-IDRI (Lung Image Database Consortium image collection) for benign and malignant prediction of pulmonary nodules [8]. Literature medical feature parameters were extracted from CT images of 87 patients with adenocarcinoma and used different machine learning models for its invasive and noninvasive classification of gonadal carcinoma. Literature introduces center crop operation to improve the 3D DenseNet network enhancing the classification accuracy of the algorithm [9]. Literature has combined the morphological description of medical knowledge and the deep features extracted from 2D network models. Pulmonary nodules were classified using SVM (Support Vector Machine) [10]. In this study by extracting nodule morphological features and intensity characteristics to describe the nodule characteristics combined with the log, it boosts a classifier for lung cancer diagnosis [11]. Literature proposed designing a multilevel 2D cross-convolution. A residual network was utilized to predict the malignancy of the nodule [12]. Literature uses a deep residual network combined with transfer learning to compare nodular and nonnodal samples, section samples are effectively classified [13]. Literature by penetrating a comparative analysis of the lesion characteristics of adenocarcinoma and noninvasive adenocarcinoma confirmed that the average diameter and shape of the lesions could provide a good reference for the construction of diagnostic models [14]. In literature, a multidimensional convolutional neural network is designed using three-dimensional images and two-dimensional multiscale images of nodules which are trained and classified, and the two classification results of the class network are weighted and fused to classify pulmonary nodules [15]. The essential benefit of CNN over its counterparts will be that it discovers essential qualities but without human intervention. Despite a big number of photos of dogs, it can learn distinct features for each category on its own. In contrast, CNN is computationally efficient. Along with some of its drawbacks such as the location of an object are not represented by CNN [16]. Inability to be substantially invariant when coping with incoming information and it is essential to collect a high volume of data [17].

Most of the current research is to design a 2D or 3D network as a classification algorithm for pulmonary nodules alone or to use machine learning algorithms for classification based on nodule feature parameters. The fusion in multidimensional convolutional neural network of authors combines the classification results of 2D and 3D networks [18]. However, like many existing networks, only the original image information of nodules is learned, which is different from medical research. Prior knowledge is less combined. Due to the lack of datasets of pulmonary nodules, it cannot reach more than 10,000 cases like other large data-

sets, and fewer studies are using deep learning to classify invasive adenocarcinoma nodules and noninvasive nodules. Provide adequate diagnostic help in preoperative preparation. For author survey classification of invasive adenocarcinoma, they used the random forest method to achieve an accuracy of 86.7% with a sensitivity of 66.7% and a specificity of 100%, but the total number of samples in their study was only 87%. For example, the classification accuracy has a significant chance, and an enormous sacrifice has been made in the diagnosis accuracy of malignant samples. An elevated sensing layer relying on dual-template biochemically functional monomer was devised and extensively utilized to detect CEA and AFP as lung cancer diagnostics one at a moment. The authors have proposed the specific 3D model for lung nodule extraction of CT images which provides the learning algorithm through many sizes and integrates elements in a lowest part hierarchical manner for investigation purpose.

In our proposed study, the network design includes an attention mechanism and a residual learning module. The 2D and 3D convolutional networks are trained separately initially, followed by the extraction of the two sets of network outputs. The eigenvectors are concatenated into new eigenvectors, and the classifier is retrained with XGBoost to improve its accuracy even more. The spatial and planar features of nodules have been thoroughly investigated in our study. The results showed that the different feature vectors extracted under the dimension are fused and reclassified. The classification result is better than the results of 2D network or 3D network classification alone and can be used in the accuracy, sensitivity, and specificity which can achieve a reasonable level. Hence, in this study, we investigated invasive adenocarcinoma nodules in ground-glass nodules during surgery. The previous diagnosis, different from the public dataset LIDC-IDRI samples from the subjective judgment of the existence of multiple radiologists, is different; this paper collects from Shanghai Chest Hospital with the gold standard, that is, with postoperative pathological support 1760 CT samples of ground-glass pulmonary nodules with invasive adenocarcinoma 340 nodules and 1420 noninvasive nodules in each CT sample containing 20 CT slices with a continuous slice thickness of 1 mm. For lungs in different samples due to the significant difference in nodule size and attention mechanism-based residual differential network model, using the designed 3D convolutional network and 2D convolutional network, respectively, the network extracts different feature information, removing the features from the other dimension networks. Finally, the vectors are concatenated into a new feature vector, and XGBoost is used for training analysis. The classification and diagnosis of invasive adenocarcinoma in pulmonary nodules were finally completed.

*1.1. Organization.* The paper has been organized as follows. Section 1 describes the introduction of the problem statement followed by Section 2 which elucidates the method description. Section 3 talks about the application and analysis followed by Section 4 which states the conclusion obtained from the strategy.

## 2. Method Description

As shown in Figure 1, the different dimensions of the attention mechanism proposed in this paper and the degree of network extraction feature fusion model AFCNN (Attention Fusion, implementation of Convolutional Neural Network) are mainly divided into the following: image preprocessing, data enhancement, and classifier structure construction.

The original dataset is an image preprocessed to generate good 2D and 3D images; the initial dataset was used for classification of 2D data to represent lung nodule center information such as texture features and contour features of layers and 3D data to express lung nodules. All the steps are depicted in Figure 1, where the various aspects of the attention mechanism have been presented, as well as the degree of network extraction feature fusion model AFCNN, which are largely split into the following parts such as picture preprocessing where preprocessed feature extraction of images is being done followed by data augmentation, and the creation of a classifier structure construction has been represented.

Spatial feature information of CT images uses 2D data for random plane cropping, rotation, 2D cutmix, and other data enhancement methods. 3D data is spatially randomized. Data enhancement methods for extraction of spatial feature information of CT images are being employed which include cropping, spatial flipping, 3D cutmix, etc. and are being generated with 2D and 3D datasets which were trained by the network; using the proposed fusion combined model for classification, all these methods are used for preprocessing the image features to investigate lung nodule internal information in order to predict certain ailments if any. The AFCNN fusing framework has two parts: 2D ACNN (2D Attention Convolutional Neural Network) for training to extract feature vectors from 2D datasets and 3D ACNN for training to extract feature vectors from 3D datasets; the framework is being used to extract 2D features. The vectors and 3D feature vectors are converted to one-dimensional vectors and coupled to create a new feature vector that fully expresses the spatial and plane feature information of pulmonary nodules. Then, the XGBoost algorithm is used for training classification, with more accurate classification results.

### 2.1. Image Preprocessing and Data Enhancement

**2.1.1. Image Preprocessing.** Image preprocessing on the original CT dataset is shown in Figure 2; there are two main parts: lung parenchyma extraction and lung nodule data extraction.

The lung parenchyma is extracted because the lung parenchyma is removed from the lung CT image. In addition, there is also information such as the thorax and ribs. The pixel information of these positions is for the pathological nature of pulmonary nodules and has no effect but will affect the study of nodule characteristics. Learning to cause interference and extracting lung parenchyma can strengthen the network with valuable learning features. Lung parenchyma extraction is mainly based on different pixel values

in different parts to get a rough lung parenchyma outline using the threshold method to extract the lung parenchyma roughly. Then, use morphological operations and other practices to make up for the location in the lungs. In lung nodules with incorrectly cropped parenchymal margins for more accurate lung parenchyma round the contour, the contour information was used to obtain the lung parenchyma from the original CT image points and remove redundant information such as the thorax.

Pulmonary nodule data extraction uses CT images extracted from the lung parenchyma. Generate 3D image data and 2D feature image counts for each lung nodule sample according to the location information used to remove pulmonary nodules which were obtained by manual annotation. Tightly frame the nodule on the CT slice where the geometric center of the nodule is located position, mark the part of the central slice, and record the contiguous CT slice occupied by the nodule layers to mark.

Take the marked nodule center layer as the center, according to the marked nodule center layer nodule position box, and then, take the thin layers of the CT image before and after the central layer, align the crop and stitch into 3D data of size  $N_x \times N_y \times N_z$ ;  $N_x$  and  $N_y$  represent the number of pixels on the CT image in the dataset.  $N_z$  denotes the number of CT slices, the size of which is instantiated as  $32 \times 32 \times 9$  in this study. 3D image data is used to express the spatial image information of the nodule and its surroundings. The 2D feature image data is generated from the nodule central layer image, which contains components: nodule central layer image, LBP (Local Binary Patterns), feature image, and contour feature image. 2D feature images are not in the depth direction; it is position invariant. The nodule center layer image in the component image is consistent with the image of the 3D data center layer; in this case, the image is  $32 \times 32$  in size and converted to grayscale. The LBP feature image is mainly used to express the texture information of lung nodules, centered at each pixel; the value of the pixel covered by the window is compared with the value of the center point, according to the value of the center point and surrounding points' small relation to represent the value of the center pixel, as shown in

$$\text{LBP}(x_0, y_0) = \sum_{i=0}^n \varepsilon(v_0 - v_i) 2^i, \varepsilon(t) = \begin{cases} 0, & t > 0, \\ 1, & t \leq 0. \end{cases} \quad (1)$$

Among them,  $\text{LBP}(x_0, y_0)$ , represents the LBP eigenvalue calculated at this point,  $n$  indicates the number of pixels covered by the edge of the window, which is taken as 8 in this example,  $v_i$  and  $v_0$  represent the pixel value of the center point and the center of the edge pixel of the  $i$ -th window, respectively.

The contour feature image is used to express the contour information of the nodule. In the CT image, the edges of ground-glass nodules are blurred, and operations such as Gaussian filtering are not required to work; directly use the Sobel operator to calculate the gradient of each position, to represent information on the borders of lung nodules. Each component image of the 2D feature image is, according to

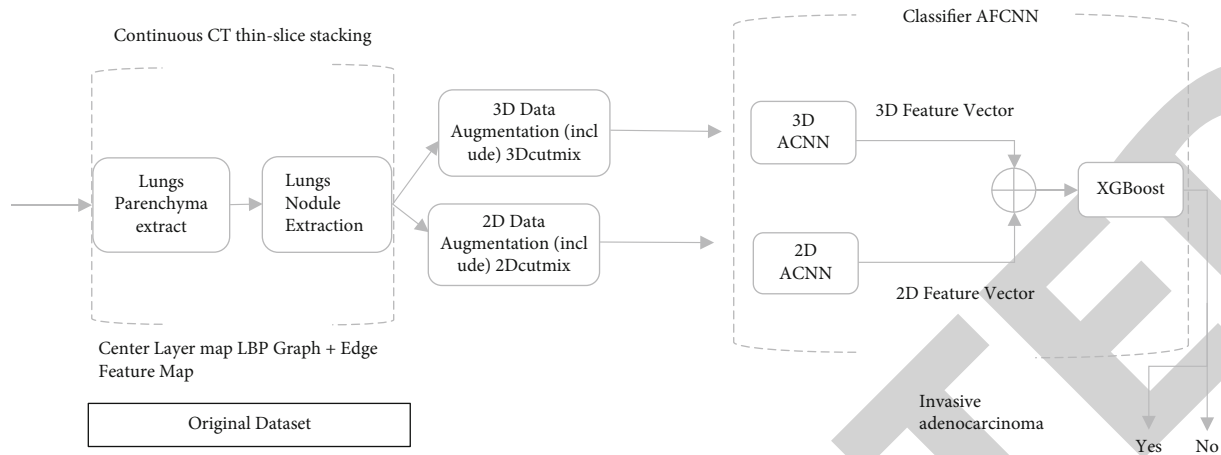


FIGURE 1: Model implementation process.

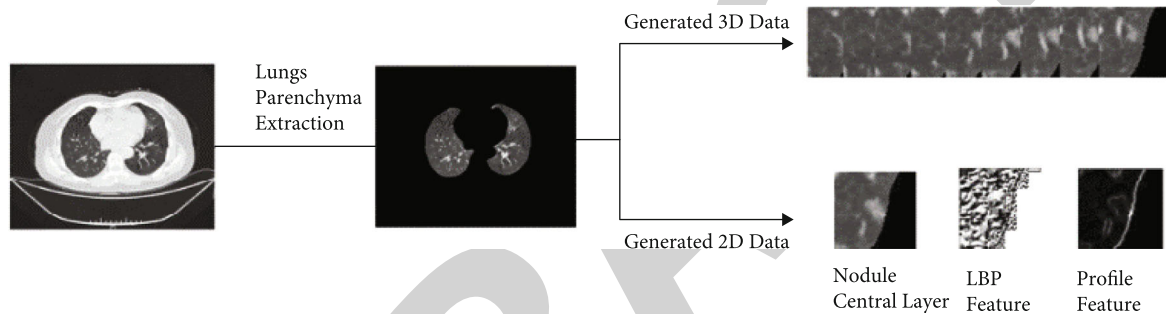


FIGURE 2: Image preprocessing.

the image generation of the central layer of the nodule, its corresponding actual CT image. The position information is the same, and the size is  $N_x \times N_y$ , in the example of this paper  $32 \times 32$ .

**2.1.2. Data Augmentation.** Common data with respective dimensions for 2D and 3D dataset augmentation methods as well as the cut mix algorithm. Common data augmentation methods can be used, for example: image rotation in plane direction (such as  $90^\circ$ ,  $180^\circ$ , and  $270^\circ$ ), plane transpose in the direction, add Gaussian noise, etc. In particular for 2D data random cropping on the row plane, in-space random cropping of 3D data, clipping, and flipping up and down in the depth direction, enhances 2D and 3D data. The generalization performance of the set supports the training of the classifier network parameters. Due to medical, image sample collection cost is high, and the cut mix algorithm is also used in this example. Enhance the learning ability of the network for local features of lung nodules. The algorithm is right, part of the data in the sample is randomly cropped, another sample is randomly taken, and the corresponding data part is combined with the remaining part of the original sample to form a new sample, the label of the new sample is in the data of the new sample according to the two sets of samples. The proportion of the heart is combined. 2Dcutmix on the 2D dataset, i.e., perform random cropping and samples at any position and two-dimensional size on the plane fusion, perform 3Dcutmix on 3D data, that is, perform arbitrary

random cropping of positions and arbitrary 3D sizes and sample fusion pass the feature fusion of different dimensions is performed on the original data, which improves the sample quality. Diversity and can enhance the ability of networks of different dimensions to local feature study.

## 2.2. Network Classifier with Attention Mechanism and Classification Training

**2.2.1. Design of Residual Learning Module with Attention Mechanism.** The pathological diagnosis of pulmonary nodules is mainly based on partial images of pulmonary nodules, while information such as other lung parenchyma contributes to the pathological diagnosis. For ground-glass hyaluronid nodules, the proportion of images of pulmonary nodules in the acquired data sample images; the size of pulmonary nodules in different samples varies greatly. Book diameter of ground-glass pulmonary nodules in the study varied widely, which may be helpful for 5 mm to 20 mm. Due to the pixel size in CT images and the real, physical size of the lung in the physical space has a unique correspondence, and the lung scaling nodules will destroy the correspondence between the image and the physical size, loss of actual size information of lung nodules. For lung nodules of different sizes in the nodule samples, the classification of the network can be more based on the lung nodule part image information, and less reference to the image information of the lung parenchyma, so to introduce the attention

mechanism when designing the network module, that is, through different channels comparison of the expression intensity of the feature images, according to the expression intensity of the feature images different to assign the corresponding feature weight to the channel.

As shown in Figure 3, a residual learning module with attention mechanism is designed. Leveraging the attention mechanism to learn to optimize the feature maps in the network during the training phase, the weight of each channel can learn the characteristics of the image that are important for classification feature, to extract important image features in the test set. This mechanism can make the network pay more attention to the information of the lung nodules, thereby improving the network classification ability of the network on this dataset. To reduce the network depth due to excessive gradient caused by the large disappears, and the residual learning module is designed to better combine the image features extracted make the extracted feature images more good participation in network classification.

In the residual learning module with attention mechanism as shown in Figure 3, the convolution transformation part consists of a convolution layer and a ReLU layer, which are used to extract the upper network feature images with the output, while the shortcut connections are made by convolution of size 1 layer composition, directly connecting the output with the upper layer network, so that the high-dimensional feature image combines better with low-dimensional feature images. The attention mechanism can be used to strengthen the weight of the important features in the convolutional transformation part.

Weight calculation of different feature channels for the attention mechanism in the module, it consists of two parts, which are the mean value and the maximum value of the characteristic images of each channel value. Let  $X_i$  denote the set of values of the feature image on channel  $i$ ; then, the realization of the attention mechanism can be expressed by

$$X_{inew} = \{f_1[\max(X_i)] + f_2[\text{avg}(X_i)]\}X_i. \quad (2)$$

Among them,  $X_{inew}$  represents the set of weighted feature images on channel  $i$ ,  $\max$  represents the maximum value in the feature image,  $\text{avg}$  represents the average value of the feature image mean,  $f_1$  represents the convolution transformation and activation function ReLU with a convolution kernel of 1 transformation combination which is  $\text{Conv}(1 \times 1) - \text{ReLU}$ , the convolution with the convolution kernel of 1 the operation is used to integrate the weight information on different channels, ReLU's the effect is to enhance the nonlinearity in the attention transition.  $f_2$ 's is and the same convolutional transform structure as  $f_1$ ,  $f_2$ , and  $f_1$  are trained separately.  $f_1$  is according to the feature image processed by the maximum value, the corresponding value of different channels is determined. Weight  $f_2$  is determined according to the average value of the processed feature images which are the corresponding weights of the channel. The weights obtained after training the two sets of attention mechanisms, results are added together, and differ-

ent weights are attached to each channel of the feature image, through training, important feature channels can have greater weights, learning important features of classification significance in the image.

The essence of this mechanism is the convolutional transformation part of the module. First, each feature channel is weighted, and through the training of the above weights, the feature image with a more apparent feature expression is obtained, as shown in

$$X = \sum_{i=1}^c X_{inew}, \quad (3)$$

where  $c$  is the number of channels of the feature map and  $X$  is the feature map of each track, like the output total feature image after the weight coefficients are superimposed.

After the feature image after the convolution transformation is weighted, the shortcut connection part uses a convolution transformation with a convolution kernel of 1 to integrate information. Finally, the divided feature images are superimposed to better integrate low-dimensional and high-dimensional features. The signature information is provided as the output of this module to the following parts of the network for training to learn.

**2.2.2. 2D ACNN Network Structure.** 2D ACNN is used to learn the plane features of lung nodules, such as edge features and texture features. The network model is designed based on the residual learning module with an attention mechanism. The detailed structure is shown in Figure 4. The network contains three residual learning modules with an attention mechanism, where Conv2D is represented by the convolutional layer, batch normalization layer, and activation layer, that is, the composite operation of  $\text{Conv}(k_s \times k_s) - \text{BN} - \text{ReLU}$ , where  $k_s$  represents the purpose of adding batch normalisation to the size of the convolution kernel is to make the input of the activation function conform to its numerical sensitive range, thereby reducing the phenomenon of gradient disappearance, increasing the convergence ability of the network, and speeding up the training of network parameters. Avg-Max attention represents the attention mentioned above module realized by the average value and the maximum value, that is, on each channel. The relationship between input and output is  $\text{Out}_i = \{f_1[\max(X_i)] + f_2[\text{avg}(X_i)]\}\text{In}_i$ . The subscript  $i$  represents the component of the feature image on the  $i$ -th channel; in the 2D network, the feature component is two-dimensional, and the transformation is denoted as  $g$ . With the attention machine, the output of the residual learning module is controlled by the attention module, and the convolution kernel is 1. The block outputs are added together, i.e.,  $X_{out} = g(X_{in}) + h(X_{in})$ ,  $X_{in}$  is the input of this learning module, and  $X_{in}$  is the input of the attention module by  $X_{in}$ . After two Conv2D module operations,  $h$  represents the convolution kernel with 1 Conv2D transformation. The convolution kernel setting for the input layer Conv2D of this network is 7; to increase the receptive field of the upper layer of the network, MaxPool means the most. A large pooling operation reduces the number of

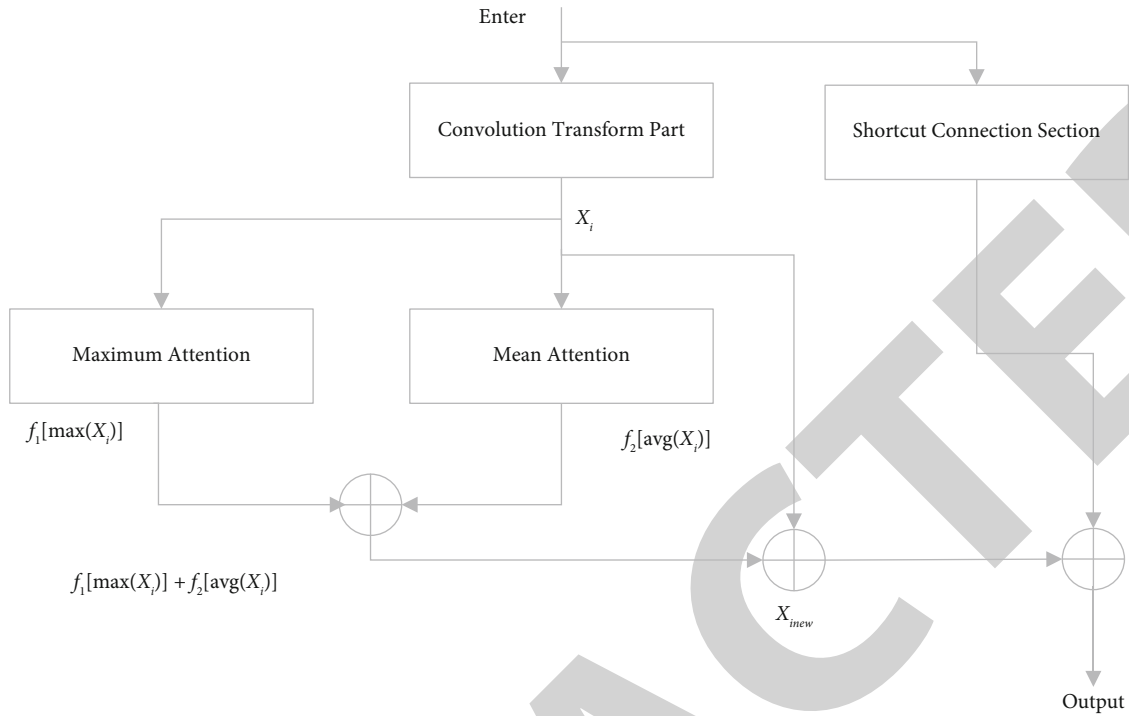


FIGURE 3: Network module with attention mechanism.

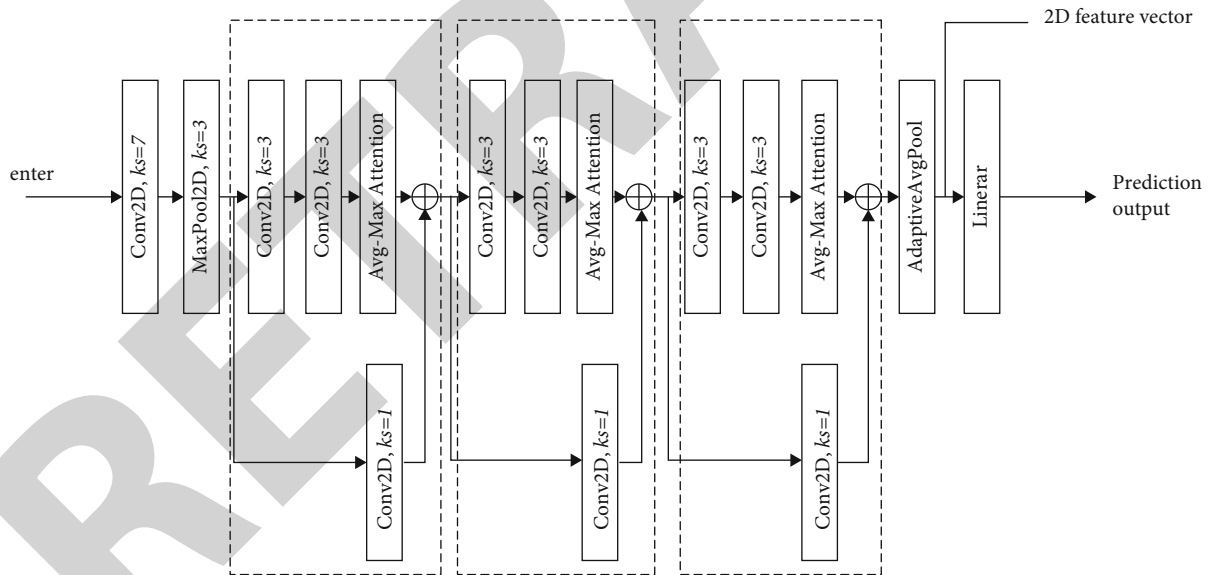


FIGURE 4: 2D ACNN network structure.

parameters the network needs to train. Adaptive Avg Pool represents a global average pooling operation for each channel. The feature images are globally pooled, and the average value is used to describe the channel’s eigenvalues. Output the 2D feature vector after global pooling, through the full convolution linear layer for classification.

**2.2.3. 3DACNN Network Structure.** 3D ACNN is used to learn the spatial information of pulmonary nodules. The Spatial features are invariant in the depth direction, so the

3D network structure is designed to the structure to understand contextual information from lung nodule data. To reduce network requirements with the number of parameters to be trained, the network model mainly has three machines’ attention. The detailed structure of the residual learning module is shown in Figure 5. Conv3D representation is implemented by a convolutional layer, batch normalization layer, and activation layer, namely, Conv ( $k_s \times k_s \times k_s$ )—composite operation of BN-ReLU, where  $k_s$  represents the volume in this case, the size of the kernel, the length, width, and depth

of the kernel. The size remains the same; Avg-Max attention is the average and maximum value. The current attention module is  $\text{Out}_i = \{f_1[\max(X_i)] + f_2[\text{avg}(X_i)]\} \text{In}_i$ . In a 3D network, the feature components on channel  $i$  are three-dimensional, and the transformation is denoted by  $a$  for  $g$ . The output of the residual learning module with the attention mechanism is  $X_{\text{out}} = g(X_{\text{in}}) + h(X_{\text{in}})$ , where  $X_{\text{in}}$  passed through the Conv3D module twice by  $X_{\text{in}}$ . The operation is obtained;  $h$  represents the Conv3D transform with a convolution kernel of 1 in the network.

The convolution kernels of the Conv3D are all set to 3, reducing the need for training the network—the number of parameters to exercise. Adaptive AvgPool represents the global average pooling operation to global pooling on the 3D feature images on each channel, using the flat mean to represent the eigenvalues of the channel. Output 3D features after the global pooling A vector is classified by a fully convolutional linear layer.

**2.2.4. Classification Objective Function and Feature Fusion.** The 2D network and 3D network are trained separately, and the goal of network optimization is to minimize the loss function. Because of the binary classification problem to be solved in the research, the loss function is selected as a binary cross-entropy function, and a regularization term is added, as shown in

$$\text{Loss} = -\frac{1}{n} \sum_{i=1}^n (y_i \ln y_e + (1 - y_i) \ln (1 - y_e)) + \alpha \sum \|w_i\|_2^2. \quad (4)$$

Among them,  $y_i$  is the label of sample  $i$ ,  $y_e$  is the classifier's prediction for the sample  $i$  label,  $n$  is the total number of samples,  $\alpha \sum \|w_i\|_2^2$  is the regularisation term, and  $\alpha$  is positive. The normalisation coefficient is generally a small positive number, and  $\|w_i\|_2^2$  is the weight coefficient in the network, which is the second norm of a number. L2 regularization controls the value of the objective function by optimizing the size of the weight parameters in the network, reducing the complexity of the network, and reducing the network overload fit.

After the two groups of networks are trained separately, take the output of the 2D network in Figure 4. The 2D feature vector and the 3D feature vector output by the 3D network in line feature fusion, because the 2D feature vector and the 3D feature vector are the corresponding feature vector extracted by the network for binary classification so that it can express 3D spatial features and 2D plane features, the implementation method of feature fusion is to combine the network. The 2D feature vector and 3D feature vector output by the network are converted into one-dimensional amount make the connection, that is  $v_{\text{new}} = [v_{3D}^1, v_{3D}^2, v_{3D}^3 \cdots, v_{3D}^k, v_{2D}^1, v_{2D}^2, \cdots, v_{2D}^k]$ , where  $v_{3D}^1$  represents the vector of the 1st channel in the 3D feature vector and the  $v_{2D}^1$  table shows the vector of the 1st channel in the 2D feature vector. Therefore,  $k$  represents the total number of channels of the 3D feature vector, and  $t$  is the total number of channels of the 2D fea-

ture vector number. Take new as the new feature vector of the sample and use XGBoost to calculate the method to classify and learn the new feature vector; the obtained classification result is the final classification result of this classifier. In the experiment, XGBoost chooses every. The second tree-based model is iterated, the iteration weight eta is designed to be 0.1, and the tree. The maximum depth of 5 is designed to avoid overfitting, the goal of the XGBoost model. The optimization function is consistent with formula (4).

### 3. Example Application and Analysis

The datasets used in this paper are from Shanghai Chest Hospital all over the years. Cases with accurate pathology after surgery, between 5 mm and 20 mm in diameter ground-glass pulmonary nodule samples a total of 1760 cases, invasive 340 samples of adenocarcinoma nodules and 1420 samples of noninvasive adenocarcinoma nodules examples. In noninvasive nodule samples microinvasive adenocarcinoma, primary adenocarcinoma, and other benign nodules each case data contains a slice thickness of 20 consecutive CT thin-slice images of 1 mm. Compared to most research papers, the LIDC-IDRI public dataset of this research, the dataset of this research has the gold standard, the public dataset of benign and malignant nodule samples was determined by four radiologists. The doctors independently marked the pulmonary nodules into five grades from 1 to 5 according to the degree of malignancy, with 5 representing the highest degree of malignancy and 1 representing a benign nodule. However, the doctor's diagnosis is subjective; in the diagnosis of 1 187 cases of nodules, four doctors, only 571 nodules were diagnosed as valid if the difference between the judging results of the judging results was less than 1. Unfortunately, the difference between the diagnoses of different doctors in the rest of the samples was large. Therefore, the annotation of the public dataset cannot be used as actual pulmonary nodule pathology, and the dataset contains different types of nodules, such as ground-glass nodules and solid nodules—classification of invasive adenocarcinoma.

The configuration of the experimental platform running in this article is an Intel Core i9-9900 processor, NVIDIA GeForce RTX 2080Ti discrete graphics card, and 32 GB memory. The experiment's data processing and model building are based on the thepython3.7, mainly based on PyTorch's deep learning framework. In the experiment, the parameters in the network are initialized using the Keming method.

The proposed algorithm was verified using five-fold cross-validation to make the network thoroughly trained and reduce the training results by chance. The original dataset was randomly divided into five independent parts of the same size. Sixty-eight samples contained invasive adenocarcinoma nodules and noninvasive adenocarcinoma 284 cancer nodules samples. In the  $i$ -th verification, select the  $i$ -th sample as the test set, the remaining four samples are used as the training set for training, that is, each activity. The ratio of the training set to test set in practice is 4 : 1. Initial training set: A total of 1 408 samples were collected, including 272

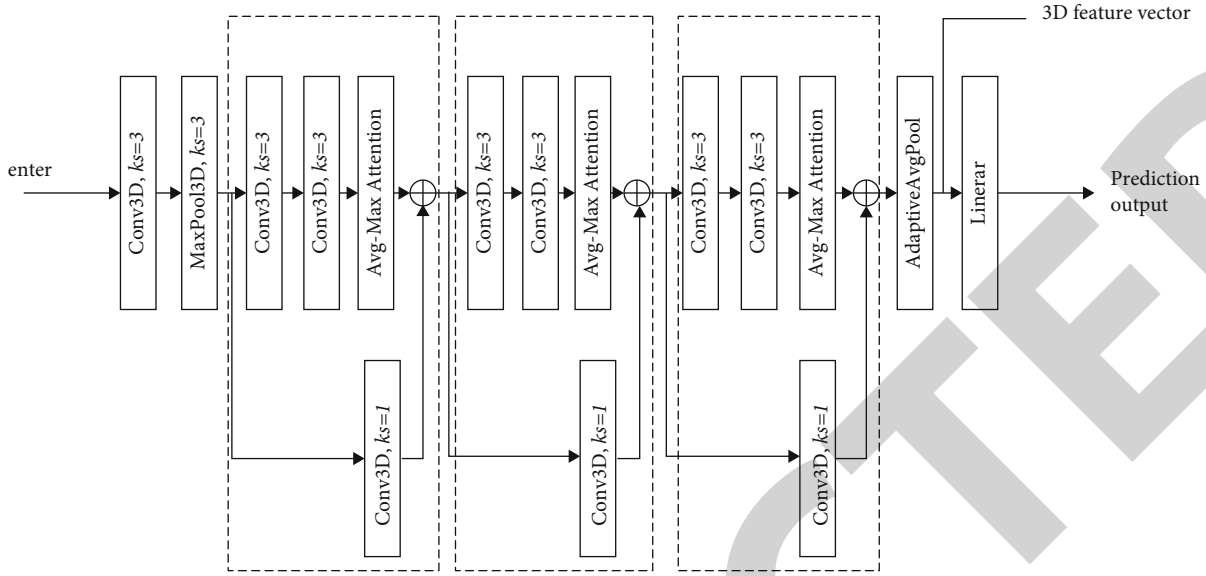


FIGURE 5: 3D ACNN network structure.

TABLE 1: Experimental result of 2D and 3D networks with different learning rates.

Learning rate	Accuracy		Sensitivity		Specificity	
	2D	3D	2D	3D	2D	3D
0.3	0.844	0.904	0.835	0.889	0.846	0.91
0.03	0.85	0.921	0.889	0.909	0.843	0.924
0.003	0.722	0.927	0.835	0.85	0.818	0.945

invasive adenocarcinoma nodules and 272 noninvasive adenocarcinoma nodules. One thousand one hundred thirty-six samples of invasive adenocarcinoma nodules. Data augmentation during training Strong augmented the training set to 84 224, in which invasive adenocarcinoma samples and noninvasive adenocarcinoma samples were 1 : 1.

Five experiments were conducted to train and verify the two networks, respectively. Record the results, fuse the training results of the two networks, and record their development. The size of the 2D samples in the experiment is instantiated as  $32 \times 32$ , and the 3D sample size of a is instantiated as  $32 \times 32 \times 9$ , the regularization coefficient  $\alpha$  is taken as 0.000 01; in this paper, the SGD optimizer is used for optimization, and the initial learning of the training network is the learning rate is designed to be 0.02, the momentum parameter is set to 0.9, and the learning rate is set to 10 times line attenuation. The selection of the initial learning rate is based on the experimental results in Table 1.

In network training, it will not be easy to converge if the learning rate is set too high. On the other hand, if the habit rate is too low, it will be trapped in local maxima. In this experiment, according to the table the results in 1 show that when the initial learning rate is 0.02, it can be achieved without sacrificing sensitivity and specificity and have higher accuracy, so the initial learning rate in this order of magnitude is 0.02. The regularization coefficient should not be

too high large; it will hinder network training, so taking a smaller value of  $10E-5$  can prevent overfitting. However, it plays a specific limiting role, and the fluctuation of this value will affect the experimental results with little noise.

This experiment used three accuracies, sensitivity, and specificity methods, respectively. Metrics evaluate the performance of the model. The definition of the indicator is shown in [18]

$$\begin{cases} \text{Accuracy} = \frac{TP + TN}{TP + TN + FP + FN}, \\ \text{Sensitivity} = \frac{TP}{TP + FN}, \\ \text{Specificity} = \frac{TN}{TN + FP}. \end{cases} \quad (5)$$

Among them, TP represents the sample whose correct category and prediction result are positive quantities. TN means the number of pieces whose right category and predicted result are negative quantities. FP represents the number of samples whose actual class is negative and expected to be positive. FN indicates the number of samples where the actual class is positive, and the prediction is negative. In this instance, the sensitivity indicates that the class of invasive adenocarcinoma is correctly predicted. The specificity represents the proportion of samples classified as noninvasive predicting the correct proportion [18].

As shown in Figure 6, some lung nodules on the test set are classified by the model in this paper—class error visualization results—box-select three of the noninvasive adenocarcinoma nodules. The actual pathology of the nodules in the group was noninvasive, but they were diagnosed as invasive nodules. The corresponding percentages are the probability of a diagnosis of an invasive nodule. Boxed in dip the actual pathology of the three groups of nodules of invasive adenocarcinoma was invasive nodules. Still, the model,

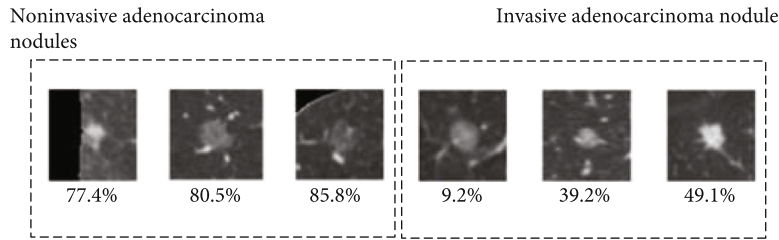


FIGURE 6: Some samples of the wrong classification of the model.

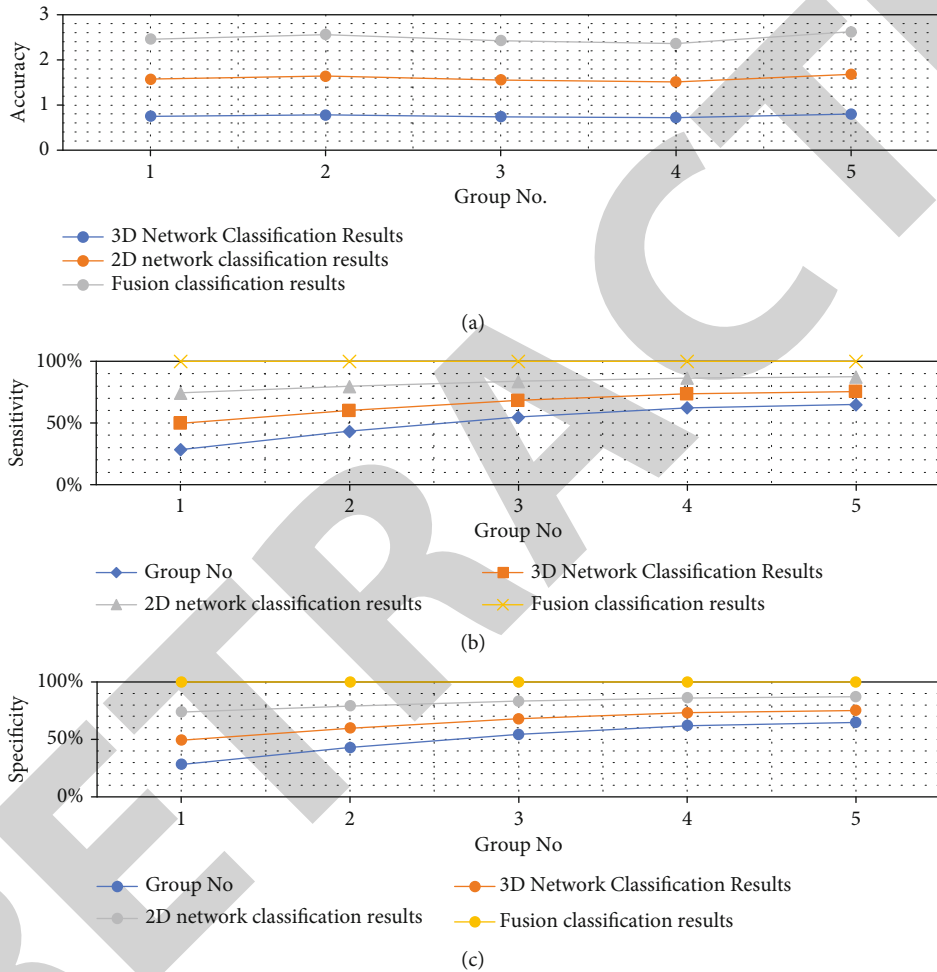


FIGURE 7: Accuracy, sensitivity, and specificity of five-fold cross-validation.

probability of predicting it as an invasive nodule is shallow, so the final classification the result is a noninvasive nodule. In the figure, the similarity between the two groups of pulmonary nodules is very high. The first two groups of nodules in invasive adenocarcinoma were regular in shape. They had regular density value and rhythm, while the noninvasive clusters of nodules were irregular in shape, leading to type produced misjudgment.

The results of the five-fold cross-validation are shown in Figure 7, which, respectively, represent the five experimental groups. The accuracy sensitivity and specificity of the test results, the Abscissa in the graph both represents the experimental group number, and the ordinate represents the

accuracy and sensitivity values, respectively. Specificity values, the three curves in each graph represent the 3D network classification results, 2D network classification results alone, and the classification result after feature fusion. For example, Figure 7(a) shows the three methods in five accuracy results on the group test set; 2d networks generally perform across groups. Poor, with an average accuracy of 0.753, the 3D network outperformed each group's 2D network with an average accuracy of 0.814; since the 3D dataset has more, the dataset is more informative, and the spatial characteristics of the modules are more effective for the classification results. Flat features have a more substantial effect. The fusion classification result combines 2D network, the



TABLE 2: (A) Accuracy of five-fold cross-validation. (B) Sensitivity of five-fold cross-validation. (C) Specificity of five-fold cross-validation.

(a)

Group no.	3D network classification results	2D network classification results	Fusion classification results
1	0.75	0.825	0.885
2	0.78	0.858	0.9204
3	0.74	0.814	0.8732
4	0.72	0.792	0.8496
5	0.8	0.88	0.944

(b)

Group no.	3D network classification results	2D network classification results	Fusion classification results
1	0.75	0.87	0.9
2	0.78	0.9048	0.936
3	0.74	0.8584	0.888
4	0.72	0.8352	0.864
5	0.8	0.928	0.96

(c)

Group no.	3D network classification results	2D network classification results	Fusion classification results
1	0.75	0.87	0.93
2	0.78	0.9048	0.9672
3	0.74	0.8584	0.9176
4	0.72	0.8352	0.8928
5	0.8	0.928	0.992

extracted feature vectors, and the feature vectors extracted by the 3D network, so you can combine spatial features and plane features to get better classification accuracy, the average. The accuracy is 0.827. Figure 7(b) shows the sensitivity results of the three methods results, classification results of 2D network and 3D network on different sets of datasets.

There is no clear distinction between superiority and inferiority, as sensitivity is shown in invasive adenocarcinoma. The raw data volume is small when it is diagnosed with the correct scale, so the 2D network is similar. There is no noticeable difference in the classification results of the 3D network [3, 19]. The fusion classification is after spatial features and planar features; there is no improvement in the fourth set of experiments [1, 20]. The rest, sensitivity of fusion classification in the group, has been dramatically improved. Figure 7(c) shows the specificity results of the three methods were compared, and the specificity of the 2D network was significantly lower than 3D networks, which is consistent with the experimental results on the

accuracy; the 3D network can learn more information by merging features of different dimensions, it can make the specificity been improved to a certain extent. Table 2 shows the accuracy, sensitivity, and specificity of five-fold cross-validation.

The study of the classification of invasive adenocarcinoma in this paper is based on the gold standard. A total of 1 187 samples were obtained. To compare the manual diagnosis of invasive adenocarcinoma nodules, 20 samples were randomly selected from the dataset, and one a doctor with many years of experience made a diagnosis. The doctor's diagnosis accuracy is 70%. As shown in Figure 7, the algorithm's accuracy proposed in this paper is 0.827, the sensitivity was 0.829, and the specificity was 0.826. Visible relative to physician experience, it can be concluded that the method in this paper can significantly improve the misdiagnosis rate in the diagnosis of invasive adenocarcinoma nodules and noninvasive nodules. It shows that the model in this paper can pass the pulmonary nodules. It can learn the image information of nodules and obtain good diagnostic ability of invasive nodules High accuracy without sacrificing classification sensitivity and specificity.

#### 4. Conclusion

Small nodules in invasive adenocarcinoma could well be diagnosed using the proposed method in this research. In this approach the attention process supports the multidimensional and multifeature fusion classification model; initially, lung parenchyma was extracted from the original CT picture to remove interfering information like thorax interest. The 2D lung nodule samples in the output of the model in the design are central layer images, LBP features, and round, to improve the model's learning of lung nodule features. The 3D lung nodule sample is made up of many CT slices. In this study the application of traditional data enhancement methods and the cut-mix algorithm to enhance the generalizability of the dataset can improve the ability of the network to learn valuable features for pulmonary nodules on the web, given the characteristics of the dataset, which include a small sample size and unbalanced samples. The network design includes an attention mechanism and a residual learning module. The 2D and 3D convolutional networks are trained separately initially, followed by the extraction of the two sets of network outputs. The eigenvectors are concatenated into new eigenvectors, and the classifier is retrained with XGBoost to improve its accuracy even more. The spatial and planar features of nodules have been thoroughly investigated in our study. The results showed that the different feature vector extracted under the dimension is fused and reclassified. The classification result is better than the results of 2D network or 3D network classification alone and can be used in the accuracy, sensitivity, and specificity can achieve a reasonable level. The technique was applied to nodules with a diameter of 5-20 mm that were gathered from Shanghai Chest Hospital. There were 340 invasive adenocarcinoma nodule samples and 1420 noninvasive adenocarcinoma samples. The nodule samples were examined, and cross-validation revealed that

## Retraction

# Retracted: Deep Learning-Based Real-Time Discriminate Correlation Analysis for Breast Cancer Detection

### BioMed Research International

Received 8 January 2024; Accepted 8 January 2024; Published 9 January 2024

Copyright © 2024 BioMed Research International. This is an open access article distributed under the Creative Commons Attribution License, which permits unrestricted use, distribution, and reproduction in any medium, provided the original work is properly cited.

This article has been retracted by Hindawi following an investigation undertaken by the publisher [1]. This investigation has uncovered evidence of one or more of the following indicators of systematic manipulation of the publication process:

- (1) Discrepancies in scope
- (2) Discrepancies in the description of the research reported
- (3) Discrepancies between the availability of data and the research described
- (4) Inappropriate citations
- (5) Incoherent, meaningless and/or irrelevant content included in the article
- (6) Manipulated or compromised peer review

The presence of these indicators undermines our confidence in the integrity of the article's content and we cannot, therefore, vouch for its reliability. Please note that this notice is intended solely to alert readers that the content of this article is unreliable. We have not investigated whether authors were aware of or involved in the systematic manipulation of the publication process.

Wiley and Hindawi regrets that the usual quality checks did not identify these issues before publication and have since put additional measures in place to safeguard research integrity.

We wish to credit our own Research Integrity and Research Publishing teams and anonymous and named external researchers and research integrity experts for contributing to this investigation.

The corresponding author, as the representative of all authors, has been given the opportunity to register their agreement or disagreement to this retraction. We have kept a record of any response received.

### References

- [1] M. Bhende, A. Thakare, B. Pant, P. Singhal, S. Shinde, and V. Saravanan, "Deep Learning-Based Real-Time Discriminate Correlation Analysis for Breast Cancer Detection," *BioMed Research International*, vol. 2022, Article ID 4609625, 12 pages, 2022.

## Research Article

# Deep Learning-Based Real-Time Discriminate Correlation Analysis for Breast Cancer Detection

Manisha Bhende <sup>1</sup>, Anuradha Thakare <sup>2</sup>, Bhasker Pant <sup>3</sup>, Piyush Singhal <sup>4</sup>,  
Swati Shinde <sup>5</sup> and V. Saravanan <sup>6</sup>

<sup>1</sup>Marathwada Mitra Mandal's Institute of Technology, Pune, India

<sup>2</sup>Pimpri Chinchwad College of Engineering, Pune, India

<sup>3</sup>Department of Computer Science & Engineering, Graphic Era Deemed to Be University, Dehradun, Uttarakhand 248002, India

<sup>4</sup>Department of Mechanical Engineering, GLA University, Mathura 281406, India

<sup>5</sup>Department of Computer Engineering, Pimpri Chinchwad College of Engineering, Pune, India

<sup>6</sup>Department of Computer Science, College of Engineering and Technology, Dambi Dollo University, Dambi Dollo, Oromia Region, Ethiopia

Correspondence should be addressed to V. Saravanan; saravanan@dadu.edu.et

Received 5 May 2022; Revised 28 May 2022; Accepted 11 June 2022; Published 28 June 2022

Academic Editor: Gaganpreet Kaur

Copyright © 2022 Manisha Bhende et al. This is an open access article distributed under the Creative Commons Attribution License, which permits unrestricted use, distribution, and reproduction in any medium, provided the original work is properly cited.

Breast cancer is the most common cancer in women, and the breast mass recognition model can effectively assist doctors in clinical diagnosis. However, the scarcity of medical image samples makes the recognition model prone to overfitting. A breast mass recognition model integrated with deep pathological information mining is proposed: constructing a sample selection strategy, screening high-quality samples across different mammography image datasets, and dealing with the scarcity of medical image samples from the perspective of data enhancement; mining the pathology contained in limited labeled models from shallow to deep information; and dealing with the shortage of medical image samples from the perspective of feature optimization. The multiview effective region gene optimization (MvERGS) algorithm is designed to refine the original image features, improve the feature discriminate and compress the feature dimension, better match the number of samples, and perform discriminate correlation analysis (DCA) on the advanced new features; in-depth cross-modal correlation between heterogeneous elements, that is, the deep pathological information, can be mined to describe the breast mass lesion area accurately. Based on deep pathological information and traditional classifiers, an efficient breast mass recognition model is trained to complete the classification of mammography images. Experiments show that the key technical indicators of the recognition model, including accuracy and AUC, are better than the mainstream baselines, and the overfitting problem caused by the scarcity of samples is alleviated.

## 1. Introduction

Authoritative reports show that breast cancer is the most common cancer in women and the second most deadly disease [1]. Therefore, breast lumps are a worrying breast abnormality, and about 90% of breast lumps are cancerous. Breast lumps are primarily hidden in breast tissue with unclear edges. Therefore, doctors must combine solid professional knowledge and rich diagnostic experience to complete accurate manual screening. However, doctors' diagnostic

level is uneven, and manual screening is cumbersome and subjective, which can easily lead to a high rate of misdiagnosis or missed diagnosis. The computer-aided breast mass recognition model can effectively assist doctors in clinical diagnosis. However, as we all know, the vast majority of medical image processing applications are faced with the problem of sample scarcity. The main factors that cause this problem are as follows: (1) the cost of labeling medical images is too high, and it takes a lot of human resources and material resources to obtain a certain amount of high-quality samples;

(2) due to the ethical clauses involved, a large number of medical image samples have personal privacy and cannot be obtained typically, which significantly limits the number of available samples; (3) due to the significant differences in the professional backgrounds involved, there is a particular “gap” between (medical) engineering (computer) cooperation, which in turn restricts the generation of high-quality samples. The scarcity of medical image samples can easily lead to fitting of the recognition model. In summary, how to deal with the shortage of medical image samples has become particularly important [2, 3]. In response to this problem, some scholars proposed to use the GAN (generative adversarial networks) model to generate new samples to expand the dataset, but the authenticity of the new selections was questioned; some scholars built a multitask learning framework (such as compound segmentation and recognition), that is, to deal with the scarcity of samples through information sharing between different tasks. Still, the design and training of multitask learning frameworks is complex [4, 5].

We are focusing on deep pathological information, which is a low-dimensional feature that has been mined numerous times, to fill the study gap. It has a lower dimension and is more discriminatory. It can better match the number of samples, lower the danger of model overfitting, and respond to medical imaging to a limited extent due to sample scarcity. It does not require the generation of new samples, and the model training is not complex, so the “cost-effectiveness” is higher than the other two approaches. As a result, we propose the “Breast Mass Recognition Model Integrated with Deep Pathological Information Mining” as a research topic. The deep pathological information in restricted labeled samples is mined from shallow to deep for training a high-quality and accurate model. Based on sample selection, the deep pathological information in limited labeled samples is mined from shallow through deep for training a high-quality and efficient breast mass recognition model. This paper contributes the following:

- (a) Design a sample selection algorithm, select high-quality samples across different mammography image datasets, lay a data foundation for training a robust breast mass recognition model, and deal with the problem of sample scarcity from the perspective of data enhancement
- (b) Design a multiview efficient range-based gene selection (MvERGS) algorithm, refine the original image features, and perform discriminate real time correlation analysis (DCA) to obtain the parts between the components [6]. The cross-modal correlation of the model is more discriminative. It has a lower dimension to match the number of samples, reduce the risk of model over fitting, and then deal with the problem of sample scarcity

The paper is organized into several sections where the first section states about the introduction of the problem followed by the second module, that is, the related work. The third section discusses about the proposed model

framework, followed by the fourth section which states about the experiment and analysis. Finally, the end module discusses the conclusion of the work.

## 2. Related Work

*2.1. Image Feature Learning.* Image features are an essential prerequisite for breast mass recognition. Features such as scale-invariant feature transform (SIFT) and histogram of oriented gradients (HOG) have played an essential role in breast mass recognition [7, 8]. Literature extracted the image’s interior and edge texture primitives and used linear discriminate analysis (LDA) to complete breast mass identification [9]. Literature optimized the critical features based on the mutual information model and used a support vector machine (SVM) to train the breast mass recognition model [9]. In addition, features such as complete local binary pattern (CLBP), grey-level cooccurrence matrix (GLCM), and other features have also been used for breast mass recognition [10, 11].

*2.2. Feature Optimization.* Because the feature dimension is high and contains noise, it is necessary to optimize the original image features to improve its discriminability and compress the feature dimension to better match the number of medical image samples. Feature optimization methods are divided into single-modal feature optimization and multimodal feature optimization as follows:

- (a) Single-modal feature optimization literature extracted optical coefficients from optical tomography images as features and optimized features based on maximum correlation and minimum redundancy algorithms to complete rheumatoid arthritis detection [12]. Literature used a spatial grey difference feature extraction algorithm and correlation-based feature selection method to complete brain image classification [13]. Literature performed feature optimization based on particle swarm optimization (PSO) algorithm [14]. Literature improved the lion algorithm to select subsets of features such as texture, intensity histogram, and shape of breast images [15]. Literature combined LDA and local-preserving projection methods to optimize neuroimaging features [16]. The single-modal feature optimization method can refine the original features and improve the recognition accuracy
- (b) Multimodal features preferably include positron emission tomography (PET), magnetic resonance imaging (MRI), computed tomography (CT), and other images so that they can surround them and expand multimodal feature optimization. Literature proposed a multimodal multitask learning framework to achieve multimodal feature fusion and complete diagnosis of Alzheimer’s disease (AD) [17]. Literature performed latent feature learning for different modalities and mapped the features to the label space to complete AD diagnosis [18]. Literature used a sparse deep polynomial network

(S-DPN) to complete multimodal data fusion to obtain new features with more robust discrimination [19]. Some scholars also use hypergraphs to complete high-order correlation analysis between multimodal data and generate high-quality features [20, 21]. The multimodal feature optimization method makes full use of the complementarity between features to improve the recognition accuracy

**2.3. Breast Mass Recognition.** In recent years, deep learning models have played an essential role in breast mass recognition. Mammograms are the most well-known tool for recognizing cancer in the breast at the initial stage. This cancer, which manifests itself mostly as mass, is hard to ascertain and diagnose because mass can be covered by normal breast tissue in breast density. Detection with the help of computers (CAD) is a method for avoiding mistakes in cancer screening of the breast, and its utility has been proven. Related work for breast mass recognition can be divided into four categories: fine-tuning model methods, ensemble deep learning methods, transfer learning methods, and multitask collaborative learning methods [22, 23]. The fine-tuning model method fine-tunes the pretrained convolutional neural network (CNN) to complete the recognition task. This method is simple and easy to use but is limited by the number of samples [24]. Literature connected the fully connected layer of the pretrained AlexNet model to the SVM to train the recognition model; the integrated deep learning method uses the complementarity between multiple models to improve recognition accuracy; this method requires a lot of computing resources [25]. Literature used DCNN (deep convolutional neural network) and deep belief network (DBN) to construct two prediction models, respectively and then integrated their results to realize breast mass recognition; the transfer learning method realizes recognition through a knowledge transfer task [26]. Literature used pretrained GoogLeNet, VGGNet, and ResNet models to extract image features, access the features to fully connected layers, pool them, and complete breast mass classification [27]. Literature first trained a patch-level recognition model, removed the fully connected layer, and added a new convolutional layer to train a recognition model for the entire angiographic image [28]. The multitask collaborative learning method refers to the diagnosis model including multiple related subtasks, such as lesion segmentation, tumor identification, and lesion localization, which complement each other, improve the recognition accuracy through collaborative learning, and reduce the dependence on the number of samples [29]. In summary, the lack of mammography images makes breast mass recognition more challenging [30]. The feature optimization algorithm can refine the original image features, better match the number of samples, and improve the model recognition performance. This paper proposes a “breast mass recognition model incorporating deep pathological information mining” to actively deal with the scarcity of medical image samples from multiple perspectives:

(a) Select high-quality samples across different mammography image datasets, laying the foundation for training a robust recognition model database

(b) Fully excavate the deep pathological information in the limited labeled samples to further alleviate the problem of model fitting; design the MvERGS algorithm to reduce noise interference and improve feature discrimination; in-depth analysis of the typical correlation between features, using cross-modal features to delineate the lesion area

To sum up, the model in this paper is called RMD, “R” stands for sample refinement, “M” stands for feature optimization algorithm MvERGS, and “D” stands for cross-modal analysis DCA. They are organically combined to improve breast mass recognition performance.

### 3. RMD Model Framework

The framework of the RMD model is shown in Figure 1, including sample selection, feature selection, cross-modal analysis, and breast mass recognition [31]. First, a sample selection strategy is designed to screen high-quality mammography image samples; second, SIFT (S), Gist (G), HOG (H), LBP (L), and DENSENET161 (D) are extracted from the perspectives of shape, texture, deep learning, etc., RESNET50(R) and VGG16(V) features. Third, consider feature diversity and complementarity, and lay the foundation for feature optimization and cross-modal analysis; design the feature optimization algorithm MvERGS to refine the original features and improve their discriminativeness, using  $\tilde{S}$ ,  $\tilde{G}$ ,  $\tilde{H}$ ,  $\tilde{L}$ ,  $\tilde{D}$ ,  $\tilde{R}$ , and  $\tilde{V}$ , respectively; represent the new features after feature optimization; use the DCA method to analyze the cross-modal correlation between the new features; and generate cross-modal features, which are represented by “~SG,” “~SH,” “~SV,” “~GV,” etc. For example, “~SG” represents the cross-modal correlation between  $\tilde{S}$  and  $\tilde{G}$ ; the breast mass recognition model is trained based on cross-modal features and standard classifiers and outputs “0” and “1,” indicating negative and positive, respectively [32]. Furthermore, there may arise some drawbacks which emerge at reasonably high doses of radiation absorption such as tissue damage that include conjunctivitis, facial reddening, and baldness and are uncommon for several sorts of imaging methods.

**3.1. Image Feature Extraction.** Breast mass recognition necessitates the use of image feature extraction. Breast mass detection has relied heavily on features such the scale-invariant feature transform and the histogram of oriented gradient. The interior and edge texture primitives of the image were recovered, and linear discriminate analysis was employed to complete breast mass identification. Hence, this feature extraction plays a significant role in carcinoma detection where on the basis of ML techniques, essential features can be chosen based on the breast mass identification model. Image features should accurately describe the visual characteristics of breast mass and consider complementarily preparing for cross-modal analysis. For example, SIFT locates the variable shape of the mass; Gist depicts the texture characteristics of the mass from a global perspective; HOG captures the edge information of the mass to describe the

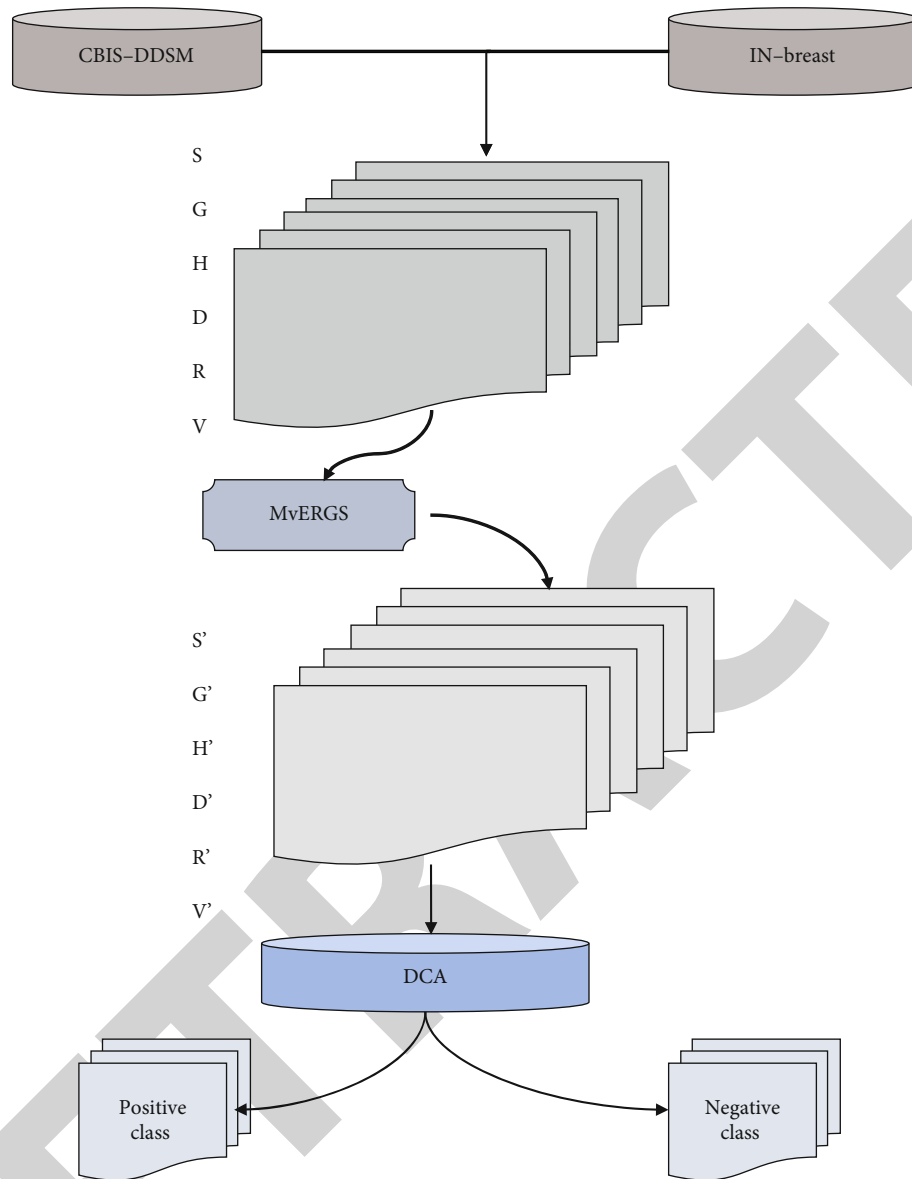


FIGURE 1: Proposed model.

appearance and shape of the mass; LBP depicts the texture changes of the mass from a local perspective. Deep learning features such as DENSENET161, RESNET50, and VGG16 are valuable supplements to standard components. The homologous network structure of the deep learning model was tried in the experiment, but the effect was slightly worse.

**3.2. Sample Selection ( $R$ ).** Breast mass recognition faces the problem of sample scarcity. Considering that randomly selecting samples to expand the dataset will introduce more noise information, which will affect the recognition performance of the model, try to choose samples with high confidence to expand the existing dataset, and reduce the impact of noise on recognition. Therefore, this paper designs a more targeted sample selection strategy, which spans different mammography image datasets, selects high-quality samples (confidence by a set of classifiers), and makes full use of

the pathological knowledge contained in new instances [33, 34] to train a more effective and robust recognition model. To sum up, in the RMD model, the basic idea of the sample selection algorithm is to select a set of classifiers with the best performance and use a complex voting mechanism to choose samples from the source dataset; that is, the source dataset can be correctly classified by this set of classifiers. Finally, the pieces are selected and merged with the target dataset to train a new classification model. The idea is simple and easy to implement. It not only focuses on source samples with higher confidence but also makes full use of the complementarity of different classifiers in decision-making and finally lays a data foundation for training high-quality classification models.

**3.3. Feature Optimization ( $M$ ).** The selected samples in Section 3.2 are minimal and affected by individual differences.

TABLE 1: Detail description of dataset.

Dataset	After preprocessing size/pixel	Negative samples/frame	Positive samples/frame	Train-test ratio
CBIS-DDSM	1152 × 896	1434	1347	70%-30%
INbreast	2500 × 3300	287	100	

Fully mining the pathological information in tiny labeled pieces is a more effective method to deal with the problem of sample scarcity. This section scoops the pathological features of mammography images from the perspective of feature selection. The original image features have high dimensions and noise, which will affect the recognition accuracy and restrict the recognition efficiency. The MvERGS algorithm is designed to refine the original parts from two perspectives and improve their discriminativeness to deal with the model fitting problem caused by the scarcity of samples (the dimension will be significantly reduced after feature optimization to better match the number of pieces). At the same time, the algorithm has good expansibility. It can introduce more perspectives to more comprehensively and carefully describe the lesion area in the mammography image from a complementary perspective, improve the feature representation, and continuously enhance the discrimination of features, thereby improving the model recognition accuracy. Second, the algorithm is robust to a certain extent; it only processes the lowest-level feature components and does not depend on the visual content described by the features.

**3.4. Cross-Modal Correlation Mining (D).** The MvERGS algorithm refines the original features, and the generated new features Fns contain shallow pathological information, which should further extract the deep pathological information in the labeled samples to better cope with the scarcity of samples. The texture, shape, color, edge, and other visual representations of similar breast masses point to the same or similar lesion area. The image features contain rich cross-modal correlation, which is of great significance for improving the recognition performance. Therefore, based on MvERGS feature optimization, we explore the cross-modal correlation between new features and continuously optimize the recognition accuracy.

## 4. Experiment and Analysis

### 4.1. Experimental Setup

**4.1.1. Dataset.** Select public datasets CBIS-DDSM (<https://wiki.cancerimagingarchive.net/display/Public/CBIS-DDSM>) and breast ([http://medicalresearch.inesporto.pt/breastresearch/index.php/Get\\_INbreast\\_Database](http://medicalresearch.inesporto.pt/breastresearch/index.php/Get_INbreast_Database)) for experimental comparison, and their related information is shown in Table 1. For the breast dataset [35], images labeled 1 and 2 in BI-RADS are classified as negative samples, and images labeled 4, 5, and 6 are classified as positive samples. The PCA algorithm reduces SIFT and HOG to 500 and 300 dimensions. When extracting deep learning features, due to the large resolution, a significant cropping operation is performed on the image to make the input image 224 × 224. VGG16

selects the first fully connected layer with a feature dimension of 4096. Both DENSENET161 and RESNET50 select the last average pooling layer with feature dimensions of 2 208 and 2 048, respectively.

**4.1.2. Benchmark Algorithm.** RMD models include RMD-KNN, RMD-LR, RMD-RF, RMD-DT, RMD-SVM, RMD-NB, RMD-Adaboost, RMD-GBDT, and RMD-XGBoost. There are five categories of comparison baselines, as follows:

- (a) Mainstream feature optimization algorithms: GS-XGBoost, ERGS, Fisher Score, PSO, and HGSCCA [36]
- (b) Recognition model based on MvERGS algorithm (M): M-KNN, M-LR, M-RF, M-DT, M-SVM, M-NB, M-Adaboost, M-GBDT, and M-XGBoost
- (c) Identification models based on MvERGS algorithm (M) and cross-modal correlation mining (D): MD-KNN, MD-LR, MD-RF, MDDT, MD-SVM, MD-NB, MD-Adaboost, MD-GBDT, and MD-XGBoost
- (d) Transfer learning class models: the models of DenseNet121, ResNet152, VGG16, and Literature [37]
- (e) Recognition models based on regions of interest (ROI): the model of literature, the model of literature, the model of Zhu et al., the model of literature, and the model of literature [38]

The experimental results of (2) and (3) baselines can be regarded as performing ablation analysis on the RMD model. Since the category (5) baselines are based on ROI, indirect comparisons are made with these models. The performance of breast mass recognition was evaluated by indicators such as accuracy (Accuracy, Acc), AUC, sensitivity (Sensitivity, Sen), specificity (Specificity, Spe), and accuracy (Precision, Pre). The higher the accuracy and AUC, the better the recognition effect; the higher the sensitivity, the lower the false-negative rate, and the less missed diagnosis; the higher the specificity, the lower the false-positive rate, and the higher the diagnosis probability.

**4.1.3. Feature Robustness of MvERGS Algorithm.** Extract the single category features “S,” “G,” “H,” “L,” “D,” “R,” and “V,” and complete the identification task based on the traditional classifier. Take the best results of each feature on the classifier for display and experimental results, as shown in Table 2. In the CBIS-DDSM dataset, the S feature performs well, with a false-positive rate of only 1.39%. The S feature can reduce the noise caused by changes in morphology and viewing angle and help the model lock the breast mass’s shape accurately. Second, G features capture abnormally textured breast masses from a global perspective. In TP “TN,”

TABLE 2: Performance evaluation over original image feature.

	Feature	Accuracy	Predicted positive	Predicted negative	Sensitivity	Specificity	AUC
CBIS-DDSM	S	82.56	74.56	64.62	60.28	89.56	95.52
	G	75.23	72.54	61.45	58.26	84.26	85.63
	H	70.26	68.26	60.84	54.56	82.51	74.26
	L	68.36	62.48	57.36	52.24	80.59	64.56
	D	65.26	59.23	55.62	50.68	80.24	56.34
	R	64.25	58.42	52.6	49.52	78.56	55.28
	V	59.56	52.56	50.85	48.56	76.85	50.28
INbreast	S	80.26	78.56	68.65	69.26	94.65	92.58
	G	74.26	74.52	65.25	68.45	92.68	90.86
	H	72.28	72.58	64.86	67.28	90.84	76.25
	L	65.78	68.48	59.62	61.24	88.63	69.25
	D	60.86	64.26	54.26	58.67	86.54	58.26
	R	59.56	59.85	52.26	56.95	84.68	55.28
	V	55.68	54.87	51.25	55.28	82.98	51.45

the model is prone to overfitting. In the breast dataset, D features and V features outperform. The number of positive predictive samples is much smaller than the number of negative predictive samples (TP+FP “TN”+FN), or the predictive probability of positive samples is 0 (PrePos=0), and the recognition model has serious overfitting, and the scarcity of samples is the cause of this and is the most important factor in the results [39]. Therefore, using high-dimensional original features for breast mass recognition, the overall recognition performance is not good due to overfitting. This requires fully excavating the low-dimensional and deep pathological information contained in the original image, features, more accurately depicting the lesion area of the mammography image, and matching the number of samples to reduce the risk of model overfitting [40]. Therefore, the RMD model proposed in this paper can mine valuable pathological information from shallow to deep, thereby improving the recognition performance and actively dealing with the problem of sample scarcity. Based on the MvERGS algorithm, feature optimization is performed on the original image features such as “S,” “G,” “H,” “L,” “D,” “R,” and “V” in Table 2, and new features “ $\tilde{S}$ ,” “ $\tilde{G}$ ,” and “ $\tilde{H}$ ” are generated [41]. “ $\tilde{L}$ ,” “ $\tilde{D}$ ,” “ $\tilde{R}$ ,” and “ $\tilde{V}$ ” compare fairly and fully verify the importance of the feature optimization algorithm, the common classifier is still selected to complete the breast mass recognition, and the optimal result of each feature is displayed on the classifier. This demonstrates the MvERGS algorithm’s scalability, implying that additional views can be absorbed into it to boost its efficiency, even more. Second, it only works with certain types of data. The bottom has components and is independent of the top, including the visual material to a high degree. This demonstrates the system’s sturdiness and MvERGS algorithm, demonstrating that it is capable of high performance computing any feature in any field of investigation. As a consequence, the MvERGS numerous subsequent scientific disciplines can benefit from the algorithm that necessitates elaborate features. The experimental results are shown in Table 3, and “ $\uparrow$ ” indicates an

improvement compared to the results in Table 2. Avg1 represents the mean value of all indicators of the original image features on the CBIS-DDSM dataset (calculated based on Table 2), Avg2 represents the mean value of all indicators of the new features on the CBIS-DDSM dataset, and Avg3 represents the original image features on the breast dataset [42]. The mean of all indicators (calculated based on Table 2) and Avg4 represents the mean of all indicators of new features on the breast dataset (calculated based on Table 3). Calculating these quantities can better judge the merits of the MvERGS algorithm. Figures 2 and 3 show the accuracy and productivity over robustness feature. Figure 4 shows the confusion element over robustness feature.

In the CBIS-DDSM dataset, (1) after feature optimization, the recognition performance of other new features has been improved except for the “ $\tilde{G}$ ” feature, among which the “ $\tilde{L}$ ” feature acc has the most significant improvement (10.53 percentage points), and its AUC has also improved effective (13.67 percentage points). The MvERGS algorithm refines the original features and enhances their discriminativeness. (2) The S feature is the best before the MvERGS algorithm is implemented, and the “ $\tilde{S}$ ” feature is still the best after the feature is optimized, the false-positive rate is reduced to 0.93%, 2.47 percentage points increase the AUC value, and the practicability of the model is continuously improved. The MvERGS algorithm is effective, and it preserves the core components of the original features to the greatest extent. This shows that fully mining the deep pathological information in the limited labeled samples can improve the model recognition performance. (3) From the perspective of mean value, all indicators have been improved after feature optimization. AUC and ACC have improved significantly, reaching 3.01 percentage points and 2.51 percentage points, respectively. The overall recognition performance of the model is better, indicating that the MvERGS algorithm is robust. More importantly, TP is gradually increasing, FN is slowly decreasing, and the overfitting



TABLE 3: Performance evaluation over MvERGS algorithm.

	Feature	Accuracy	Predicted positive	Predicted negative	Sensitivity	Specificity	AUC
CBIS-DDSM	S	80.91	73.81	62.04	54.85	84.19	94.56
	G	73.73	71.81	58.99	53.02	79.20	84.77
	H	68.85	67.58	58.41	49.65	77.56	73.52
	L	66.99	61.86	55.07	47.54	75.75	63.91
	D	63.95	58.64	53.40	46.12	75.43	55.78
	R	62.97	57.84	50.50	45.06	73.85	54.73
	V	58.37	52.03	48.82	44.19	72.24	49.78
INbreast	S	78.65	77.77	65.90	63.03	88.97	91.65
	G	72.77	73.77	62.64	62.29	87.12	89.95
	H	70.83	71.85	62.27	61.22	85.39	75.49
	L	64.46	67.80	57.24	55.73	83.31	68.56
	D	59.64	63.62	52.09	53.39	81.35	57.68
	R	58.37	59.25	50.17	51.82	79.60	54.73
	V	54.57	54.32	49.20	50.30	78.00	50.94

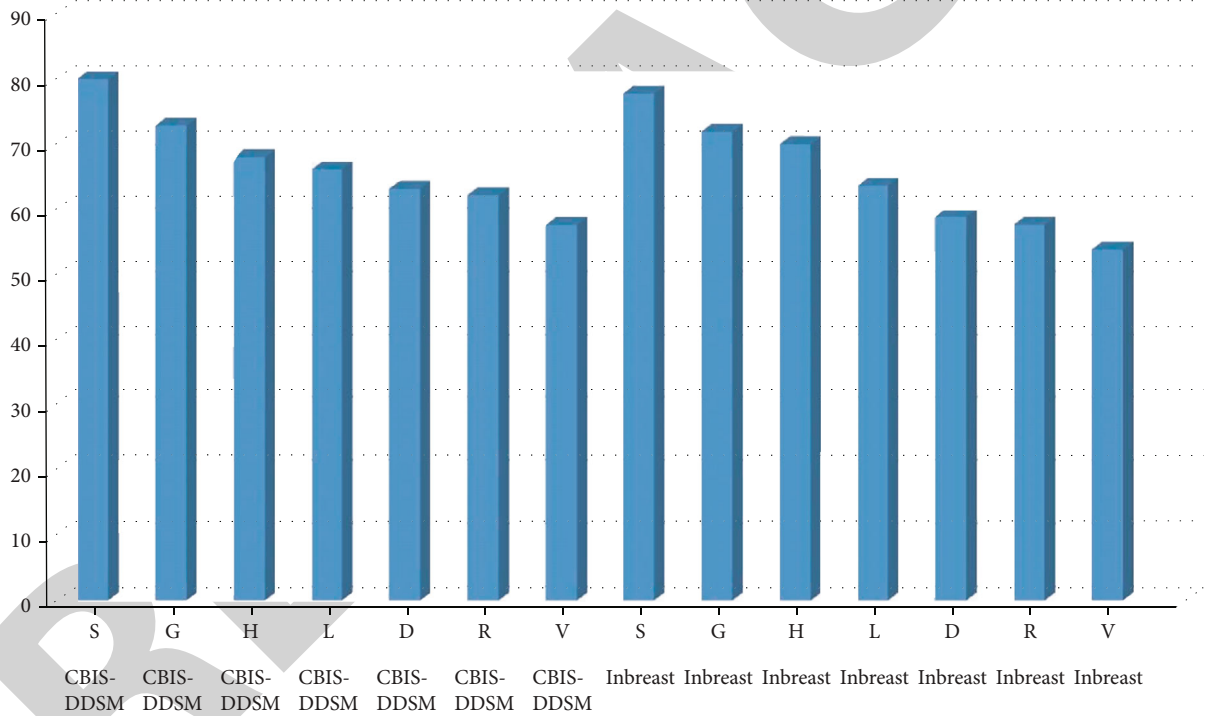


FIGURE 2: Accuracy over robustness feature.

tendency of the breast mass recognition model has been corrected to a certain extent; that is, new features with more compact dimensions can better match the number of training samples to cope with the scarcity of pieces. In summary, the MvERGS algorithm is effective on the CBIS-DDSM dataset, which verifies the integrity of the valuable information in the FN feature from another aspect. Figures 5 and 6 show the accuracy and productivity over MvERGS algorithm. The confusion element over MvERGS algorithm is shown in Figure 7.

In the breast dataset, (1) after feature optimization, all feature recognition performances have been improved, among which the “R” feature acc has improved significantly (4.31 percentage points), and its AUC value has been dramatically improved (22.49 percentage points). In terms of AUC improvement, the breast dataset performs better. Since the mammography images of the breast are more precise, the MvERGS algorithm can better refine the original features, thus laying an essential foundation for training an excellent recognition model. (2) After feature optimization,

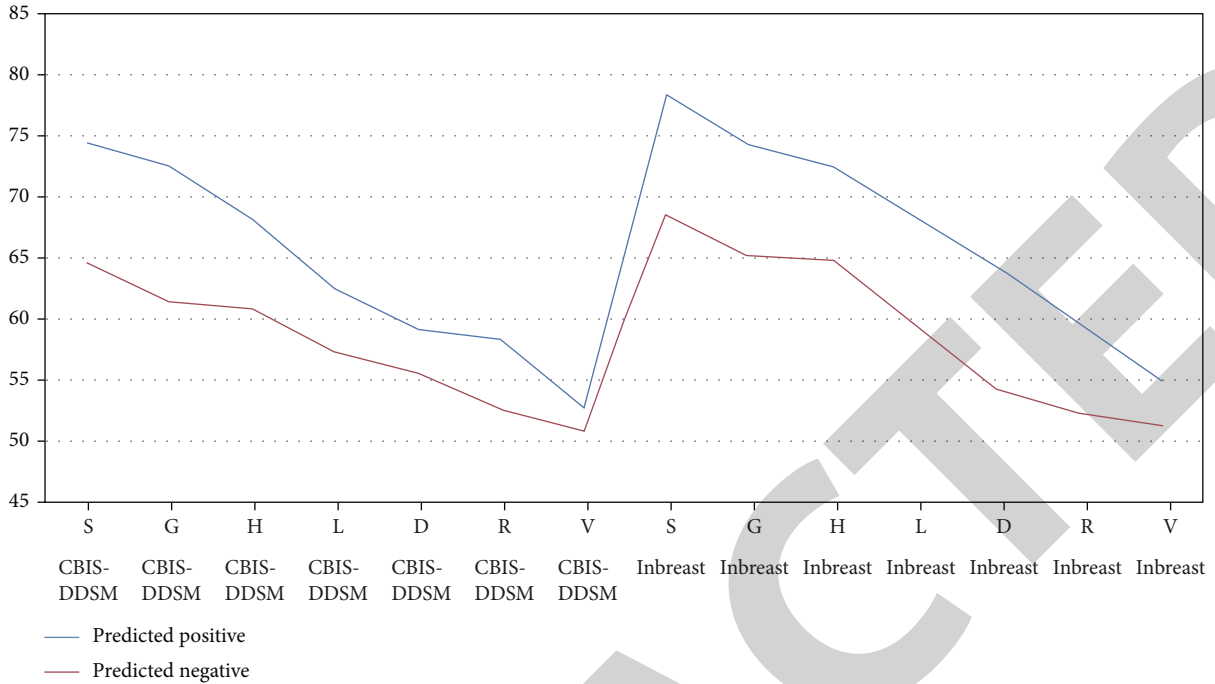


FIGURE 3: Productivity over robustness feature.

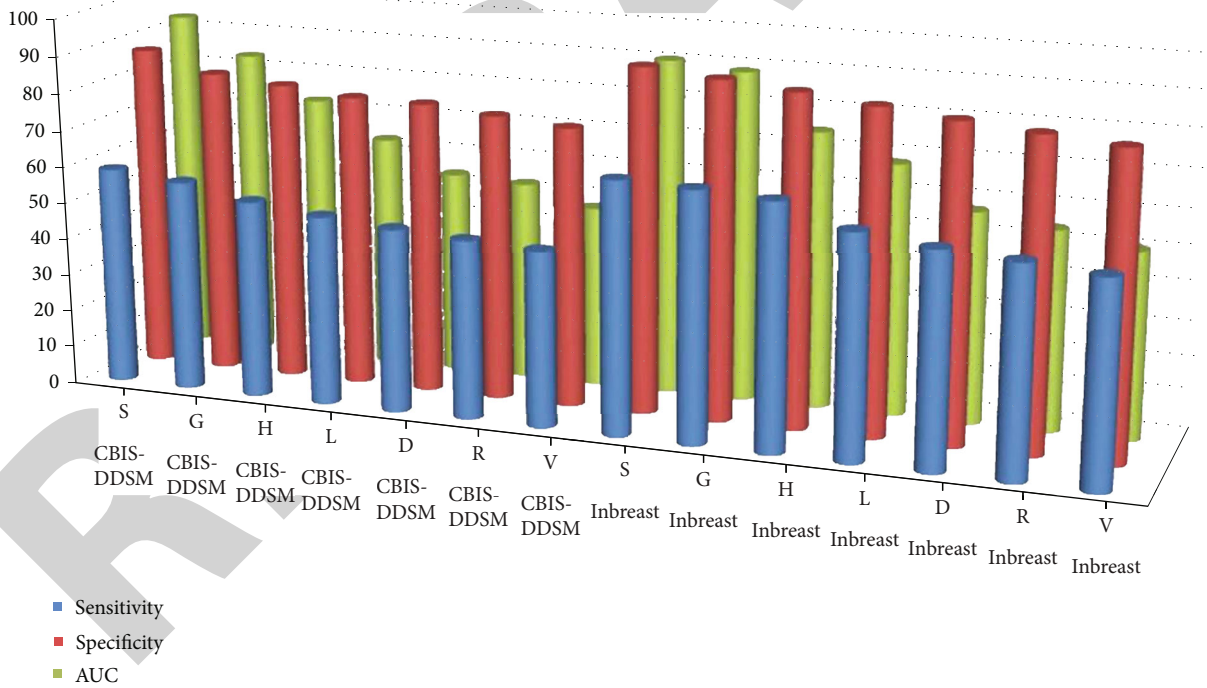


FIGURE 4: Confusion element over robustness feature.

“n” “S” has the best overall performance, and 6.37 percentage points increase its AUC value. This shows that the noise information is indeed less after feature optimization, and the new features can more accurately describe the visual characteristics of the image. (3) The overfitting of the model is alleviated to a certain extent. The number of samples in the breast dataset is small and unbalanced, and many original

features are overfitted. After implementing the feature optimization based on the MvERGS algorithm, the discriminative of new features is enhanced, the TP, FN, and other indicators are significantly improved, the number of misclassified samples is continuously reduced, and the tendency of overfitting is alleviated. (4) Measured from the mean point of view, most of the indicators have been improved

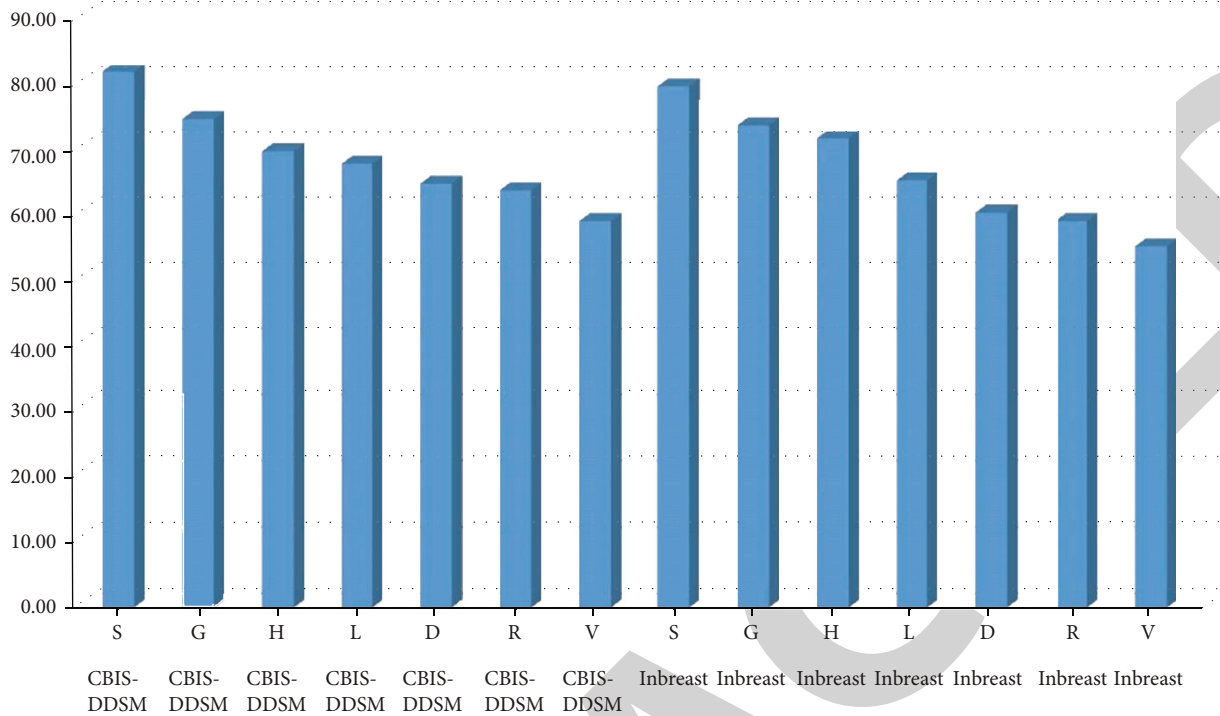


FIGURE 5: Accuracy over MvERGS algorithm.

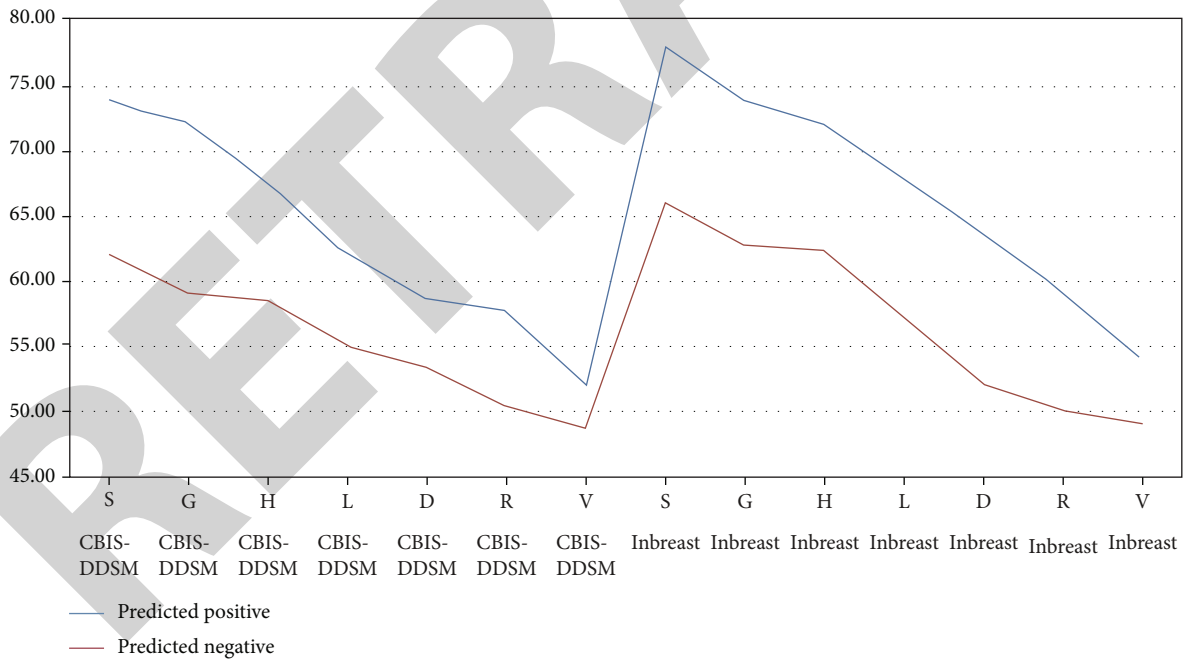


FIGURE 6: Predictively over MvERGS algorithm.

after feature optimization (compared to the CBIS-DDSM dataset, three indicators have not been improved, and the breast dataset is more challenging, which also shows that data scarcity affects the identification of impact), such as PrePos, Sen, and AUC, and the improvement of the PrePos indicator is also a vital sign that the overfitting problem is alleviated. To sum up, the MvERGS algorithm is

also effective on the breast dataset, which verifies the integrity of the valuable information in the FN features from another aspect. To sum up, after MvERGS feature optimization, the recognition performance on both datasets has been improved. The overfitting has been alleviated to a certain extent. Of course, the indicators such as sensitivity and accuracy on the two datasets are still low. It is

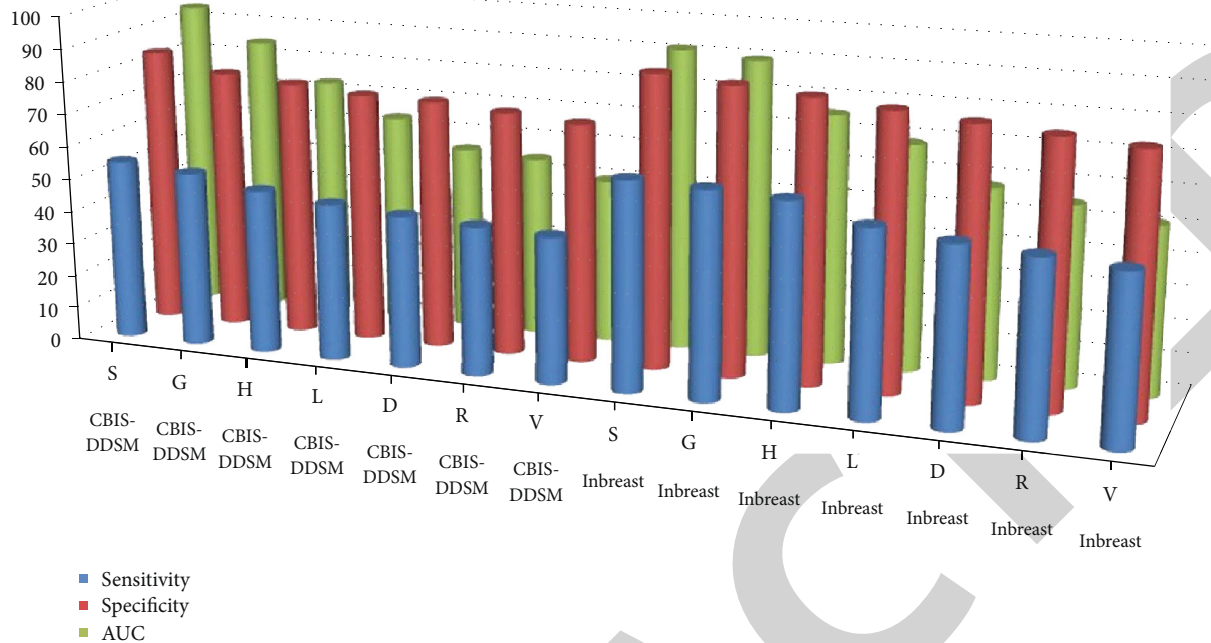


FIGURE 7: Confusion element over MvERGS algorithm.

necessary to continue performing cross-modal correlation mining to improve these indicators.

**4.1.4. Essential Indicators of the RMD Model.** In clinical diagnosis, specificity and sensitivity are also essential. The higher the specificity, the lower the false-positive rate, and the higher the probability of diagnosis; the higher the sensitivity, the lower the false-negative rate, the less missed diagnosis, and the actual patients can be treated in time. Specificity and sensitivity assess model utility from different perspectives. Draw the change graph of the specific mean and sensitivity mean of the RMD model as shown in Figure 4. The orange column represents the increase, the green column represents the decrease, and the blue column represents the mean. If the orange column is included, the blue column, the sum of the height of the orange bar, is the mean value of the corresponding indicator. The blue column represents the mean value of the corresponding index after introducing the sample selection strategy.

Selecting the mean can discover the real trend from a statistical point of view. “breast→DDSM” indicates the direction of sample selection, that is, selecting samples from the breast dataset to supplement the DDSM dataset. “DDSM →breast” means just the opposite. On the CBIS-DDSM dataset, cross-modal features containing “ $\tilde{S}$ ” have higher specificity. This means that the number of misdiagnosed patients is decreasing, which can ease the psychological burden of patients. After implementing the sample selection strategy, the specificity of 10 sets of cross-modal features was improved, of which “ $\sim SH$ ” and “ $\sim LD$ ” improved significantly. This shows that the features such as “ $\tilde{D}$ ” and “ $\tilde{L}$ ” of the samples selected from the breast can better explain the samples in CBIS-DDSM,

thereby improving the model specificity. On the breast dataset, the specificity improvement was not significant, and after implementing the sample selection strategy, the specificity of the five cross-modal features was improved. After all, there are specific differences between the individuals corresponding to the two types of samples, CBIS-DDSM and breast, and the image resolution and clarity are also different. On the CBIS-DDSM dataset, cross-modal features containing “ $\tilde{S}$ ” have higher sensitivity. After implementing the sample selection strategy, the sensitivity of 6 groups of cross-modal features is improved, of which “ $\sim GD$ ” and “ $\sim HD$ ” are significantly improved, and the deep learning feature “ $\tilde{D}$ ” plays an important role. This shows that the features such as “ $\tilde{D}$ ” and “ $\tilde{L}$ ” of the selected samples from the breast are beneficial supplements to the CBIS-DDSM dataset, which is consistent with the conclusion in Figure 4. The “ $\tilde{D}$ ” feature has strong robustness. On the breast dataset, most cross-modal features show better sensitivity. The cross-modal features containing “ $\tilde{S}$ ” and “ $\tilde{R}$ ” perform the best. After implementing the sample selection strategy, the sensitivity of the 13 groups of cross-modal features was improved. The sensitivity of the breast dataset is significantly enhanced. The pathological knowledge extracted from CBIS-DDSM can better describe the visual characteristics of negative samples, the false-negative rate is reduced, and the sensitivity is improved, which helps reduce the phenomenon of missed diagnosis and reduce the actual cost.

In summary, for a dataset with more balanced samples, the RMD model can obtain better specificity, which helps to reduce the false-positive rate of diagnosis and improve the diagnosis rate. On the other hand, for datasets with relatively low samples, the RMD model can obtain better

sensitivity, which helps to reduce the phenomenon of missed diagnosis and reduce the cost to patients. Clearly, after introducing the sample selection strategy, the specificity and sensitivity of the recognition model show positive changes, which enhance the practicability of the model to a certain extent.

## 5. Conclusion

In this work, we propose a breast mass recognition model RMD that is coupled with deep pathological information mining in this paper. Because the breast mass recognition model would aid doctors in clinical diagnosis, but there are not enough samples, the recognition accuracy will be limited, limiting the model's applicability. As a result, from the perspectives of sample selection, feature selection, and cross-modal correlation mining, this work actively reacts to the challenge of sample scarcity. Experiments indicate that the RMD model optimizes the recognition accuracy on two general mammography picture datasets, and that each component of the model (R, M, D) is useful. The most notable feature of the RMD model is to perform multistage, layer-by-layer feature selection to gain new features with stronger discriminative and lower dimensions. Of course, the RMD model is not end-to-end. As a result of this model, a web-based breast cancer diagnosis platform was created and internal testing was completed. Feature extraction, sample selection, feature optimization, and cross-modal correlation mining are all included in the platform. The technology is expected to speed up the model's actual landing, allowing doctors to make better clinical diagnoses. The nonlocal block model will be offered in the future to complete the localization of breast mass based on mass breast identification; additionally, the RMD model is likely to be used to detect new coronary pneumonia.

## Data Availability

The data shall be made available on request.

## Conflicts of Interest

The authors declare that they have no conflict of interest.

## Acknowledgments

This research work is self-funded.

## References

- [1] V. E. Orel, O. Rykhalskyi, L. Syvak et al., "Computer-assisted inductive moderate hyperthermia planning for breast cancer patients," *2020, IEEE 40th International Conference on Electronics and Nanotechnology (ELNANO)*, 2020, Kyiv, Ukraine, April 2020, 2020.
- [2] V. Burriel, O. Pastor, M. Peña-Chilet, M. T. Martínez, and G. Ribas, "Conceptual schema of miRNA's expression: using efficient information systems practices to manage and analyse data about miRNA expression studies in breast cancer," *2016 IEEE Tenth International Conference on Research Challenges in Information Science (RCIS)*, 2016, Grenoble, France, June 2016, 2016.
- [3] V. Burriel, O. Pastor, M. Peña-Chilet, M. T. Martínez, and G. Ribas, "Conceptual schema of miRNA's expression: using efficient information systems practices to manage and analyse data about miRNA expression studies in breast cancer," in *IEEE Tenth International Conference on Research Challenges in Information Science (RCIS)*, pp. 1-2, Grenoble, France, 2016.
- [4] B. Bilgic, "Comparison of breast cancer and skin cancer diagnoses using deep learning method," in *2021 29th Signal Processing and Communications Applications Conference (SIU)*, Istanbul, Turkey, June 2021.
- [5] K. Park, W. Chen, M. A. Chekmareva, D. J. Foran, and J. P. Desai, "Electromechanical coupling factor of breast tissue as a biomarker for breast cancer," *IEEE Transactions on Biomedical Engineering*, vol. 65, no. 1, pp. 96–103, 2018.
- [6] A. Easson, A. Pandya, J. Pasternak, N. Mohammed, and A. Douplik, "Improving the patient cancer experience: multispectral (white light/autofluorescence/Raman) needle endoscopy for cancer diagnostics in breast and thyroid," *2020, Photonics North (PN)*, 2020, Niagara Falls, ON, Canada, May 2020, 2020.
- [7] M. Mahrooghy, A. B. Ashraf, D. Daye et al., "Pharmacokinetic tumor heterogeneity as a prognostic biomarker for classifying breast cancer recurrence risk," *IEEE Transactions on Biomedical Engineering*, vol. 62, no. 6, pp. 1585–1594, 2015.
- [8] C. Keatmanee, S. S. Makhanov, K. Kotani, W. Lohitvisate, and S. S. Thongvigitmanee, "Automatic initialization of active contour model in breast cancer detection utilizing conventional ultrasound and Color Doppler," in *2017 39th Annual International Conference of the IEEE Engineering in Medicine and Biology Society (EMBC)*, Jeju, Korea (South), July 2017.
- [9] Q. Li, X. Xiao, L. Wang et al., "Direct extraction of tumor response based on ensemble empirical mode decomposition for image reconstruction of early breast cancer detection by UWB," *IEEE Transactions on Biomedical Circuits and Systems*, vol. 9, no. 5, pp. 710–724, 2015.
- [10] A. Tripathi and K. Misra, "Stilbene analogues as inhibitors of breast cancer stem cells through P-glycoprotein efflux; A 3D quantitative structure-activity relationship study (inhibitory activity of stilbenes analogues on breast cancer stem cells)," in *2016 International Conference on Bioinformatics and Systems Biology (BSB)*, Allahabad, India, March 2016.
- [11] Y. Amkrane, M. El Adoui, and M. Benjelloun, "Towards breast cancer response prediction using artificial intelligence and radiomics," in *2020 5th International Conference on Cloud Computing and Artificial Intelligence: Technologies and Applications (CloudTech)*, Marrakesh, Morocco, November 2020.
- [12] N. Aibe, K. Karasawa, M. Aoki et al., "Results of a nationwide survey on Japanese clinical practice in breast-conserving radiotherapy for breast cancer," *Journal of Radiation Research*, vol. 60, no. 1, pp. 142–149, 2019.
- [13] M. Li, "Research on the detection method of breast cancer deep convolutional neural network based on computer aid," in *2021 IEEE Asia-Pacific Conference on Image Processing, Electronics and Computers (IPEC)*, Dalian, China, April 2021.
- [14] S. C. Hagness, A. Taflove, and J. E. Bridges, "Two-dimensional FDTD analysis of a pulsed microwave confocal system for breast cancer detection: fixed-focus and antenna array sensors," *IEEE Transactions on Biomedical Engineering*, vol. 45, no. 12, pp. 1470–1479, 1998.

## Retraction

# Retracted: Prediction Performance of Deep Learning for Colon Cancer Survival Prediction on SEER Data

### BioMed Research International

Received 1 August 2023; Accepted 1 August 2023; Published 2 August 2023

Copyright © 2023 BioMed Research International. This is an open access article distributed under the Creative Commons Attribution License, which permits unrestricted use, distribution, and reproduction in any medium, provided the original work is properly cited.

This article has been retracted by Hindawi following an investigation undertaken by the publisher [1]. This investigation has uncovered evidence of one or more of the following indicators of systematic manipulation of the publication process:

- (1) Discrepancies in scope
- (2) Discrepancies in the description of the research reported
- (3) Discrepancies between the availability of data and the research described
- (4) Inappropriate citations
- (5) Incoherent, meaningless and/or irrelevant content included in the article
- (6) Peer-review manipulation

The presence of these indicators undermines our confidence in the integrity of the article's content and we cannot, therefore, vouch for its reliability. Please note that this notice is intended solely to alert readers that the content of this article is unreliable. We have not investigated whether authors were aware of or involved in the systematic manipulation of the publication process.

In addition, our investigation has also shown that one or more of the following human-subject reporting requirements has not been met in this article: ethical approval by an Institutional Review Board (IRB) committee or equivalent, patient/participant consent to participate, and/or agreement to publish patient/participant details (where relevant).

Wiley and Hindawi regrets that the usual quality checks did not identify these issues before publication

and have since put additional measures in place to safeguard research integrity.

We wish to credit our own Research Integrity and Research Publishing teams and anonymous and named external researchers and research integrity experts for contributing to this investigation.

The corresponding author, as the representative of all authors, has been given the opportunity to register their agreement or disagreement to this retraction. We have kept a record of any response received.

### References

- [1] S. Gupta, S. Kalaivani, A. Rajasundaram, G. K. Ameta, A. K. Oleiwi, and B. N. Dugbaki, "Prediction Performance of Deep Learning for Colon Cancer Survival Prediction on SEER Data," *BioMed Research International*, vol. 2022, Article ID 1467070, 12 pages, 2022.

## Research Article

# Prediction Performance of Deep Learning for Colon Cancer Survival Prediction on SEER Data

Surbhi Gupta <sup>1</sup>, S. Kalaivani <sup>2</sup>, Archana Rajasundaram <sup>3</sup>, Gaurav Kumar Ameta <sup>4</sup>,  
Ahmed Kareem Oleiwi <sup>5</sup> and Betty Nokobi Dugbaki <sup>6</sup>

<sup>1</sup>Model Institute of Engineering & Technology, Jammu, J&K, India

<sup>2</sup>School of Information Technology and Engineering, Vellore Institute of Technology (VIT), Vellore, Tamil Nadu, India

<sup>3</sup>Department of Anatomy, Sree Balaji Medical College and Hospital, Chennai, Tamil Nadu, India

<sup>4</sup>Department of Computer Engineering, Indus Institute of Technology & Engineering, Indus University, Ahmedabad, Gujarat, India

<sup>5</sup>Department of Computer Technical Engineering, The Islamic University, 54001 Najaf, Iraq

<sup>6</sup>Department of Chemical Engineering, Kwame Nkrumah University of Science and Technology (KNUST), Ghana

Correspondence should be addressed to Surbhi Gupta; [sur7312@gmail.com](mailto:sur7312@gmail.com)  
and Betty Nokobi Dugbaki; [bdnokobi@st.knust.edu.gh](mailto:bdnokobi@st.knust.edu.gh)

Received 4 May 2022; Revised 21 May 2022; Accepted 25 May 2022; Published 16 June 2022

Academic Editor: Gaganpreet Kaur

Copyright © 2022 Surbhi Gupta et al. This is an open access article distributed under the Creative Commons Attribution License, which permits unrestricted use, distribution, and reproduction in any medium, provided the original work is properly cited.

Colon and rectal cancers are the most common kinds of cancer globally. Colon cancer is more prevalent in men than in women. Early detection increases the likelihood of survival, and treatment significantly increases the likelihood of eradicating the disease. The Surveillance, Epidemiology, and End Results (SEER) programme is an excellent source of domestic cancer statistics. SEER includes nearly 30% of the United States population, covering various races and geographic locations. The data are made public via the SEER website when a SEER limited-use data agreement form is submitted and approved. We investigate data from the SEER programme, specifically colon cancer statistics, in this study. Our objective is to create reliable colon cancer survival and conditional survival prediction algorithms. In this study, we have presented an overview of cancer diagnosis methods and the treatments used to cure cancer. This paper presents an analysis of prediction performance of multiple deep learning approaches. The performance of multiple deep learning models is thoroughly examined to discover which algorithm surpasses the others, followed by an investigation of the network's prediction accuracy. The simulation outcomes indicate that automated prediction models can predict colon cancer patient survival. Deep autoencoders displayed the best performance outcomes attaining 97% accuracy and 95% area under curve-receiver operating characteristic (AUC-ROC).

## 1. Introduction

Cancer prediction and diagnosis is a complex subject that has piqued the interest of researchers worldwide due to the disease's high morbidity and mortality [1, 2]. Furthermore, cancer has been regarded as a multifaceted disease with several subtypes. Early diagnosis and prognosis of a cancer type has become a requirement in cancer research since it can aid in patient clinical therapy [3, 4]. Early cancer detection increases the chances of a successful therapy. The two components of cancer early detection are early diagnosis (or downstaging) and screening. Initial diagnosis is concerned with finding problematic patients as soon as possible,

whereas screening is concerned with examining healthy persons to detect cancers before symptoms appear. Screening programmes should be implemented only after their efficacy has been demonstrated, when resources (people, equipment, etc.) are sufficient to cover pretty much the entire target group, and when facilities for clarifying diagnoses, treatment, and follow-up of those with abnormal results have become available. One of the most effective means of treating cancer has been early detection and rigorous application of curative methods. To date, approaches to early detection of cancer have included endoscopic diagnosis, imaging diagnosis, tumor marker diagnosis, endoscopic ultrasonography, and histopathological diagnosis [5]. High tumor marker

levels can indicate cancer. Tumor marker testing, when combined with other tests, can assist doctors in detecting and treating specific types of cancer. Tumor marker tests are not optimal. They are not usually specific for cancer, and they may be ineffective at detecting a recurrence. The presence of tumor markers alone cannot be used to diagnose cancer. Other tests are very definitely needed to learn more about a possible malignancy or recurrence. However, these methods also have significant shortcomings: common shortcomings include time-consuming procedures, invasive examination methods (such as for histopathological diagnoses), analytical requirements, and a high need for very specialized training and knowledge that not even all medical professionals might have [6]. Even imaging-based methods of diagnosis are not always able to adequately analyze early examples. While tumor markers used for evaluation are available, they are not always effective and cannot always be identified early enough to provide treatment in a timely manner, thus creating further need for the development of an accurate and rapid method for the early diagnosis of cancer [7]. Moreover, artificial intelligence may be able to identify and diagnose colorectal cancer as well as or better to pathologists by reviewing tissue images. Artificial intelligence might assist pathologists in meeting the growing demand for their services. According to experts, early cancer detection focuses on recognising symptomatic individuals as soon as possible so that they have the highest chance of a successful therapy. When cancer therapy is delayed or unavailable, there is a reduced likelihood of survival, an increase in treatment complications, and an increase in treatment expenses [8, 9]. Cancers are definitely more effectively treated in the early stages, resulting in less physical, mental, and financial misery. Cancer is also one of those medical disorders that has no evident indications or indicators and hence can go unnoticed for a long period within the body [10, 11]. Spatial data from testing can be acquired by utilizing fluorescence hyperspectral imaging (FHSI), which makes it to map out images at the pixel level and makes it possible for researchers to work at capacities that cannot be accomplished utilizing the more customary optical imaging strategies. While these strategies still come with restrictions, there are also promising insights. Machine learning approaches are classified into three types: supervised, unsupervised, and semisupervised. The labelled training data is transferred to the intended output in supervised learning. Unsupervised learning uses unlabelled training data to identify patterns. Using the provided genes, comparable results were obtained. However, only labelled data is used in most cancer prediction studies, whereas large amounts of unlabelled data are excluded. In practice, the label information is usually difficult to get since labelling is expensive, time-consuming, and error-prone. However, the shallow nature of the most commonly used dimension reduction methods outlined above limits the capacity to automatically obtain important high-level information from input data. Deep learning is regarded as a significant achievement in machine learning compared to traditional machine learning methods.

Accurate early prediction is crucial for effective therapy and can enhance cancer outcomes [12]. Scientists employed

a variety of methods, including early-stage screening, to discover cancer forms before they developed symptoms. They have also developed new methods for forecasting cancer therapy results in the early stages [13, 14]. Large volumes of cancer data have been collected and made available to the medical research community as a result of the introduction of new medical technology. On the other hand, accurately predicting the fate of an illness is one of the most interesting and difficult undertakings for clinicians [15, 16]. Over the last few decades, similar technologies have seen increased application in a variety of clinical imaging domains, including endoscopy [17], pathology, and CT imaging. Such instruments, for example, can make endoscopic decisions that include the extraction of image highlights, potentially leading to the early detection of malignant growth, the recognition of precancerous conditions, the improvement of amplifying endoscopy with restricted band imaging, and the use or even advancement of Raman endoscopy [18]. These finding methods include the programmed distinguishing proof of malignancy and the discovery of diseases via slide imaging, just as CT conclusions can also zero in on and identify preoperative peritoneal metastasis. As a result, we may argue that computerised reasoning, such as AI, plays an important role in detecting, and hence treating, malignant development that would otherwise result in terminal cancer.

## 2. Background Study

The TNM system is a classification tool used to describe various levels of cancer. Here, T stands for tumor, N stands for node, and M stands for metastasis. Using the TNM system, the “T” plus a letter or number (0 to 4) is used to show how far up or away from its original starting point the tumor has grown, and in the case of cancers, this means how far into the wall of the stomach. The TNM system’s numerical classifications are as follows [19–21]:

- (i) Tis: tumor “in situ” that is caught very early and has not grown beyond stomach lining
- (ii) T1: tumor has grown through lining and into connective tissue
- (iii) T2: tumor has grown into thick inner muscle
- (iv) T3: tumor has spread through outer lining but not to any nearby organs or tissues
- (v) T4: tumor has spread into nearby tissues or organs

Meanwhile, the “N” denotes lymph nodes, which are small, bean-shaped organs that assist with combatting disease. The general forecast for patients with malignancy depends on its territorial lymph nodes, which can indicate how far the disease has progressed. The levels of this subsystem are as follows:

- (i) N0: no nodes
- (ii) N1: 1 to 6 nodes



(iii) N2: 7 to 15 nodes

(iv) N3: >15 nodes

Finally, the “M” indicates whether the tumor has extended to other parts of the patient’s body, in the process also known as differential metastasis. This part of the system only comes in two parts, which are as follows:

(i) M0: no metastasis

(ii) M1: metastasis

Using these three substages, doctors assign the stage of a patient’s cancer by combining the T, N, and M classifications in overall stages [22–24]. The combinations for cancer specifically are outlined here.

(i) Stage 0 (carcinoma in situ): surgery usually cures this stage, as doctors remove that part of the stomach as well as nearby lymph nodes

(ii) Stage I: in stage IA, cancer spreads into the submucosa (layer next to the mucosa) of the stomach wall, but not yet to any lymph hubs or other organs (T1, N0, and M0). Meanwhile, stage IB signifies that the cancer has grown into the interior levels of the stomach wall and extended to 1 or 2 lymph nodes but not any further (T1, N2, and M0). This IB stage cancer may have also spread into the exterior muscular layers of the stomach wall but not yet to the lymph nodes or other organs (T2, N0, and M0)

(iii) Stage II: surgery to remove that portion of the stomach and/or nearby lymph nodes is still the main treatment, though it is compulsory to receive chemotherapy (“chemo”) or chemo radiation treatments beforehand. In stage IIA, malignant growths expand into the inside layer of the stomach divider and have also spread to between 3 and 6 lymph hubs (T1, N2, and M0). Likewise, cancer in this stage spreads to the outside layers such as the stomach divider, and to 1 to 2 lymph nodes there (T2, N1, and M0), or just to the connective tissue outside the stomach but not the peritoneal coating, serosa, or any lymph nodes (T3, N0, and M0). However, in stage IIB, malignant growths expand into the internal layers and outside solid layers of the stomach divider just as its connective tissue which stretches out either to the peritoneal covering or serosa. This stage may also spread into 7 to 15 lymph nodes (T1, N3a, and M0), 3 to 6 lymph nodes (T2, N2, and M0), 1 to 2 lymph nodes (T3, N1, and M0), or no lymph nodes at all (T4a, N0, and M0)

(iv) Stage III: in stage IIIA, cancer spread deep into the external strong layers of the stomach divider as well as 7 to 15 lymph hubs (T2, N3a, and M0). Moreover, this malignant growth expands into all the levels of the muscle and the stomach’s connective tissue, but not the peritoneal coating or serosa. It

may also have spread into 3 to 6 lymph nodes (T3, N2, and M0), 1 to 2 lymph nodes (T4a, N1, and M0), or, more rarely, not into any lymph nodes or other organs hubs or far off pieces of the body (T4b, N0, and M0). However, in stage IIIB, cancer has spread into the nearby organs, which may include the spleen, colon, liver, pancreas, kidneys, adrenal organs, or small digestive tract. Here, stage IIIB cancer also expands into the innermost mass of the stomach, the external solid levels of the stomach divider, and at least 16 lymph hubs (T1 or T2, N3b, and M0). Moreover, this cancer grows into the muscular layer and/or the stomach’s connective tissue but not to the peritoneal lining or serosa; it may also spread to 7 to 15 lymph nodes (T3, N3a, and M0) or grow into the peritoneal lining or serosa (T4a, N3a, and M0). In other substages, such as T4b, N1 or N2, and M0, the cancer might or might not spread into 1 to 6 lymph nodes excluding different parts of the body. However, in stage IIIC, cancer grows to all muscular layers of the connective tissue found outside the stomach, its peritoneal lining, and its serosa as well as to nearby organs. It may also spread to 16 (T3 or T4a, N3b, and M0), 7, or more lymph instead of other parts of the body (T4b, N3a or N3b, and M0)

(v) Stage IV: stage IV tumors of any size have spread to different parts of the body as well as surrounding areas of the stomach. Stage 4 cancer is usually referred to as metastatic cancer since it indicates that the illness has spread from its original place to other parts of the body. This stage may be identified years after the initial cancer scare and/or after the primary tumor has been treated

*2.1. Cancer Diagnosis.* Medical experts use various diagnostic tools to search for, detect, and examine threats of cancer, as well as its spread to other parts of the body in metastasis. For example, imaging diagnostics can reveal whether the infection has extended, but there are also a range of other options available for diagnosing risk. The diagnosis techniques [25–28] are listed below.

(i) Biopsy: this is the expulsion of a limited quantity of cells for assessment under magnification. Depending on a variety of circumstances—including technician experience, skill levels, and equipment—biopsies can result in different, and sometimes inaccurate, diagnoses, and the method is not infallible

(ii) Molecular testing of the tumor: for malignancies, testing might be accomplished for PD-L1 and high microsatellite unsteadiness (MSI-H), which may also be known as a bungle fix lack. Likewise, testing should be able to decide whether the tumor is making an over-the-top protein called human epidermal development factor receptor 2 (HER2), especially if the disease is further developed

- (iii) Endoscopy: in this method, medical experts look inside the body with a slim, versatile pipe called a gastro degree. The chamber in patient is implanted through the mouth down the throat as well as in to the stomach and little entrail. The expert can kill tissues and detects its signs of infection
- (iv) Endoscopic ultrasound: in some ways, this method resembles the endoscopy previously mentioned. However, it comes with the addition of a little ultrasound test on the end, one whose function is to form an image of internal organs. The stomach divider's ultrasound image is intended to help medical experts assess how far the danger has extended
- (v) Computed tomography (CT) scan: this test utilizes x-rays taken from various points to examine specific internal areas of the body, which are consolidated into a three-dimensional image that shows any variations from the norm, such as tumors. Because of this, a CT sweep can be utilized to gauge the existence, location, and/or size of tumors
- (vi) Magnetic resonance imaging (MRI): it is based on the magnetic field that produces relevant pictures of the body and is used to calculate the size of a tumor. Contrast medium, which is a special dye, is provided to the patient before the scan in order to produce a clear image and is also incorporated into the patients' veins
- (vii) Positron emission tomography: is normally combined with a CT check and sometimes additionally with a PET-CT filter. A PET output consists of images of cells that are present internally in the body. To obtain these, a limited quantity of a radioactive material is infused into the body. At that point, a scanner can distinguish liquid to deliver internal images of the human body [29]
- (viii) Laparoscopy: in this approach, specialist embeds a small cylinder called a laparoscope in to the stomach depression. This device is utilized to see whether the disease has spread to or beyond the coating of the stomach hole or liver [30]. A laparoscope is a modified keyhole surgical endoscope (also known as laparoscopic surgery). Laparoscopic surgery, which requires just a small incision, can be used to perform appendectomies (removal of both the appendix), hysterectomies (removal of the uterus), and prostatectomies (removal of prostate tissue)
- (ix) Blood tests: blood tests that gauge organ capacity can demonstrate whether different organs in the body, for example, the liver, might be influenced by malignant growths such as gastric cancer
- 2.2. *Treatments of Cancer.* The multiple cancer treatment techniques used to cure cancer are listed below [31–33]:
- (i) Surgery: options may include the removal of the piece of stomach directly influenced by malignant growths during subtotal gastrectomy or removal of the whole stomach during complete gastrectomy. In this situation, the throat is connected straightforwardly to the small digestive system to permit the food to travel through the stomach-related framework, and evacuation of lymph nodes in the mid-section is prioritized as needed
- (ii) Endoscopic mucosal resection (EMR): EMR is accomplished with the use of a long, thin cylinder loaded with a light, camcorder, and many tools. During EMR of the upper stomach-related area, the cylinder is passed down the patient's throat to arrive at an irregularity in the throat, stomach, or upper piece of the small digestive tract. This particular treatment comes with dangers including narrowing of the throat, cuts, and so forth, even extending to death. Endoscopy has advanced in recent years, allowing a variety of surgeries to be done using a modified endoscope. As a consequence, the procedure is less disruptive. Gallbladder removal, fallopian tube sealing and tying, and excision of small tumors from the gastrointestinal process or lungs are all becoming routine treatments
- (iii) Chemo treatment: can be utilized to decimate any disease symptoms that remain after another medical procedure or used to slow the tumor's development or decrease malignant growth-related side effects. The greater part of its use against cancer in particular depends on the specific mix of accompanying medications, which may include cisplatin (accessible as a conventional medication), oxaliplatin (Eloxatin), and/or fluoruracil (5-FU, Efudex). Likewise, the efficacy of these treatments may rely upon the individual being treated and the portion utilized, but as a general rule, chemotherapy can incorporate exhaustion, danger of contamination, queasiness, regurgitating, balding, loss of hunger, and the run
- (iv) Radiation therapy: likewise, radiation treatment can be utilized after a medical procedure in order to get rid of any smaller patches of ill tissue or cells that may remain or for particularly malignant growths that cannot be treated with other medical treatments. Radiation therapy (also known as radiotherapy) is a treat symptoms and diseases dose of radiation to eliminate cancer cells and shrink tumors. Radiation is used in x-rays at low doses to see inside your body, such as for teeth or damaged bones. Procedure does not quickly destroy cancer cells. It might take days or weeks of treatment to break the DNA of cancer cells enough to destroy them. Cancer cells continue to die after radiation therapy for weeks or months

- (v) Targeted therapy: a medical specialist may test the malignancy of particular cells to see which focused treatments will work best against them. Directed treatment of malignant growths in the specific region may incorporate specific types
- (vi) Immunotherapy: this is a medication therapy that encourages safe frameworks as a means of battling malignant growth. The body's own infection-battling frameworks sometimes do not attach certain diseases on the grounds that the malignant cells produce proteins that make it hard for the resistant framework cells to perceive the disease cells as risky. Immunotherapy and similar treatments work by meddling with that cycle [34]
- (vii) Palliative care: consideration experts work with the individual, their family, and their PCPs to provide an additional layer of help that supplements the ongoing care. Palliative consideration can be utilized while going through other more forceful therapies, such as medical procedures, chemo treatment, and radiation treatment. Palliative consideration is provided by a group of specialists, medical attendants, and other exceptionally prepared experts [35]. Palliative consideration groups are meant to improve personal wellbeing and satisfaction for patients and their families, alongside other forms of treatment or healing the individual might be undergoing

### 3. Literature Survey

In 2020, [36] analyzed a neural network (NN) structure validated using 10-fold cross-validation. The neural networks and ensemble learning approach attained higher accurateness as compared to other techniques. Also, the models were validated on a mesothelioma dataset. The greater availability and integration of many data types, such as genomic, transcriptomic, and histopathology data, is allowing cancer therapy to shift toward precision medicine. The use and interpretation of a range of high-dimensional data types requires a significant amount of time and knowledge for translational research or therapeutic operations. Furthermore, merging many data types necessitates more resources than understanding individual data types, as well as modeling algorithms capable of learning from a large number of complex elements [37, 38]. An experimental work [39] in 2021 was carried out on three real datasets (diabetes, heart, and cancer) derived from the UCI repository. This study suggested a neural network-based ensemble learning methodology for the classification of diseases. The computational model achieved appreciable accurateness of 98.5, 99, and 100% on the diabetes dataset, heart dataset, and cancer dataset, respectively. Another recent study [40] in 2021 put forward a CNN algorithm to predict the metastasis status of prostate cancer patients. The classification approach presented favorable outcomes. The mean AUROC achieved by the neural model is 68%. CNNs established their significance classification performance in another latest study [41] car-

ried out in 2021 as well. This study employed CNNs to predict lung cancer. The dataset used in the study was a real-time dataset embracing 311 cancer patients. CNNs were used to derive the important feature, and further, ML models like SVM and KNN was used for the classification of cancer. The classification models performed well and achieved a 71% AUC score. Another efficient hybrid deep learning model was proposed in 2021 [42] to diagnose prostate cancer using histopathological images. A novel image segmentation technique, named RINGS (Rapid Identification of Glandular Structures), was in this article. This method achieved 90% accurateness and outperformed all the state-of-the-art methods. Firstly, a deep learning technique was employed to extract the regions with higher mitosis activity. Then, SVM model predicted the final tumor proliferation. The projected scheme achieved a 74% accuracy and outperformed all previous approaches significantly [43].

In 2021, a remarkable research [44] was conducted to analyze skin lesion images for skin cancer prediction. The research study conducted an in-depth analysis and identified the major encounters in skin cancer detection. This study also analyzed the performance of the conventional models and proposed the ensemble-based deep learning models for improved prediction performance. Another article in 2021 [45] focused on breast cancer prediction by SEER dataset using ANN approaches. This study disclosed that preprocessing methods can improve the cancer prediction outcomes. In 2021, [46] constructed an ensemble learning model to predict cervical malignancy. The dataset used in the study was derived from the UCI repository. This study used KNN imputations to fill the missing data and also employed data balancing techniques. The dataset was an imbalanced one; hence, data was balanced using the over-sampling technique. Random forest feature selection derived the most significant risk factors. The ensemble architecture suggested in the study performed significantly and achieved a 99% AUC score. An *empirical study* was carried out in 2021 [47] which offered a novel classification approach based on ensemble learning. The ensemble algorithm was evaluated on five benchmark datasets from the UCI repository. The model was further compared with 13 classification approaches. The ensemble algorithm achieved an AUC score of 98%, 93%, 99%, 97%, and 99.8% on the cervical cancer dataset, mesothelioma dataset, breast cancer dataset, prostate cancer dataset, and hepatitis C virus, respectively.

### 4. Proposed Architecture

Several strategies for gene selection in cancer categorization have been proposed in prior studies. Deep learning has had a significant impact on a wide range of machine learning applications and research. Technology is crucial for rapidly identifying cancer, and different researchers have presented their findings in a variety of ways. To solve this issue, numerous computer-aided diagnostic (CAD) approaches and systems have been proposed, developed, and implemented. Few of such studies are described in this section. The work flow used for classification of cancer data is shown in Figure 1.

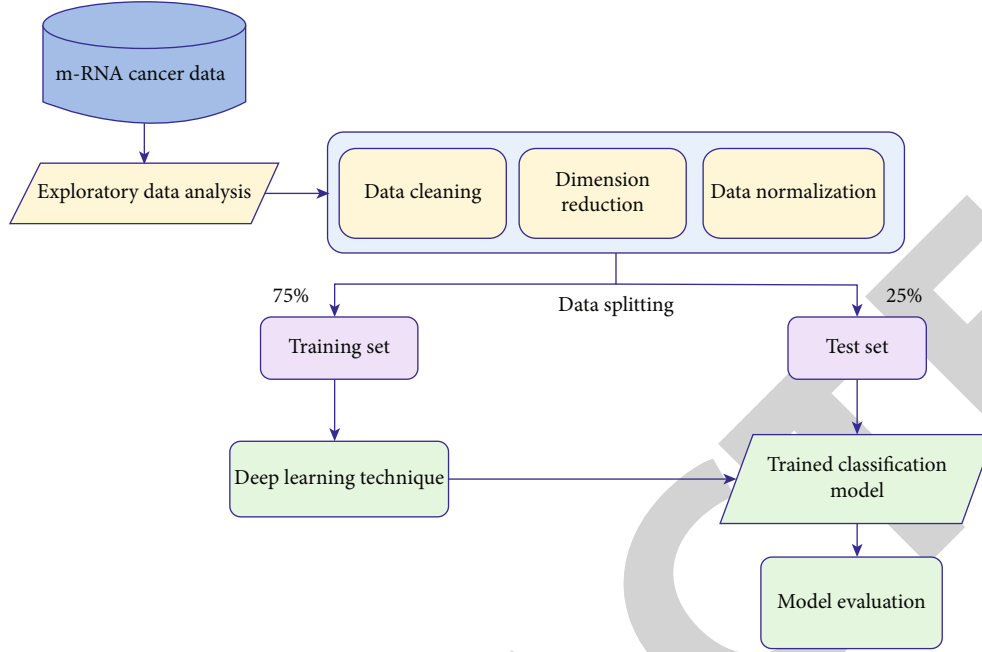


FIGURE 1: Deep learning for cancer classification.

Initially, the exploration of data is done and termed as “exploratory data analysis.” Further, data preprocessing steps are used like cleaning data, reducing dimension (feature reduction), and normalizing the data. Further the pre-processed data in the next stage is divided into training and testing set. The deep learning classification algorithm is trained on the training set for classification of data. The trained classification model is further evaluated on the test set. The evaluation of the data can express the accurateness of the model.

**4.1. Deep Learning Algorithms.** This study proposes to use numerous deep learning algorithms to predict the survivability of colon cancer patient. The research’s deep learning methodologies are discussed below.

**4.1.1. Artificial Neural Networks.** ANN is a method for neural/deep learning inspired by the notion of the human brain. ANN was developed to replicate the functioning of the human brain [48]. The operation of ANNs is somewhat similar to that of biological neural networks. The graphic representation of an ANN is given in Figure 2.

The artificial neural network (ANN) algorithm is only capable of processing numeric and structured data. Perceptrons are single-layer neural networks, whereas ANN comprise of multilayer perceptrons. A neural network may include several layers. Each layer contains one or more neurons or units. Each neuron in the system is linked to every other neuron. Each layer might be assigned a different activation function. Each neuron in layer ( $l$ ) executes the mathematical operation specified in

$$y_k^{[l]} = q_k^t \cdot a^{[l-1]} + b_i a_k^{[l]} = g^{[l]}(z_i^{[l]}). \quad (1)$$

The  $b_i$  and  $t$  signify the bias and *activation function*, respectively. The two phases of ANN are forward propagation and reverse propagation. Thus, forward propagation’s primary purpose is to multiply weights and add bias, then apply an activation function to the inputs, and propagate it forward. The process of layer updating is given in

$$y_1^{[2]} = q_1^t \cdot a^{[1]} + b_1 a_1^{[2]} = g^{[2]}(z_1^{[2]}), \quad (2)$$

$$y_2^{[2]} = q_2^t \cdot t^{[1]} + b_2 t_2^{[2]} = g^{[2]}(z_2^{[2]}), \quad (3)$$

$$y_3^{[2]} = q_3^t \cdot t^{[1]} + b_3 t_3^{[2]} = g^{[2]}(z_3^{[2]}), \quad (4)$$

$$y_4^{[2]} = q_4^t \cdot t^{[1]} + b_4 t_4^{[2]} = g^{[2]}(z_4^{[2]}), \quad (5)$$

$$y_5^{[2]} = q_5^t \cdot t^{[1]} + b_5 t_5^{[2]} = g^{[2]}(z_5^{[2]}), \quad (6)$$

$$y_6^{[2]} = q_6^t \cdot t^{[1]} + b_6 t_6^{[2]} = g^{[2]}(z_6^{[2]}). \quad (7)$$

By modifying the activation functions of the output layers, ANNs may be employed for regression and classification problem. The sigmoid activation function used for construction of CNN is given in

$$g(y) = \frac{1}{1 + e^{-y}}. \quad (8)$$

The most critical stage is backpropagation, which involves identifying the model’s optimum parameters via backpropagating the neural network layers. Backpropagation requires an optimization function to determine the optimal weights for the model.

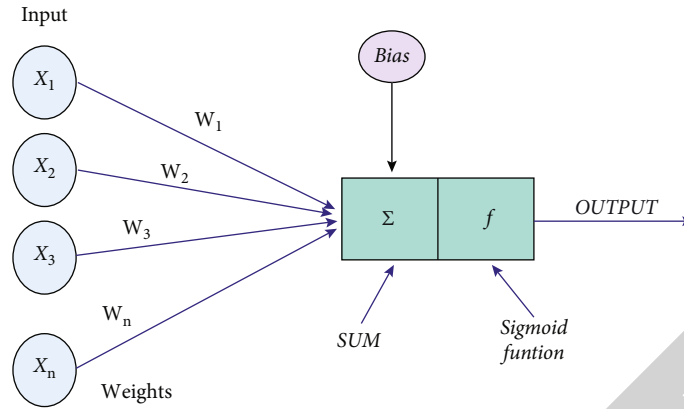


FIGURE 2: Artificial neural network (ANN) basic architecture.

4.1.2. *Convolutional Neural Networks (CNN)*. A CNN is distinct from a standard neural network in that it operates over a large number of inputs. Each layer searches for patterns or uses data included within the data [49]. Convolutional neural networks (CNNs), a form of artificial neural network prominent in computer vision, are finding traction in a variety of sectors, including radiology. CNN employs various building elements, including convolution layers, pooling layers, and fully connected layers, to learn geographical information hierarchies instantly and adaptively via back-propagation. The basic CNN architecture is depicted in Figure 3.

Each Conv layer comprises several planes, which enables the generation of multiple feature maps at every location using

$$L[m, n] = (a * b)[m, n] = \sum_i \sum_j b[i, j]a[m - i, n - j], \quad (9)$$

where  $a$  and  $b$  denote the input and  $[m, n]$  is the [row, column] index of the resultant matrix.

We used the CONV1D model to predict cancer patient survival. The model is optimized using the root mean square propagation algorithm. A CNN receives text in the form of a sequence. The embedding layer takes as an input the embedding matrix. Each remark is exposed to a combination of five different filter sizes and GlobalMaxPooling1D layers. After that, all outputs are pooled.

4.1.3. *Restriction Boltzmann Machine (RBM)*. The Boltzmann machine is a technique for unsupervised modelling. This technique employs probability-based prediction [50]. Figure 4 depicts the structure of a restricted Boltzmann machine.

RBM is a probabilistic, generative technique that is undirected. Since RBM comprises an input layer and a hidden layer, it is also an asymmetrical bipartite graph. Each visible node is associated with each hidden node. This approach was aimed at determining the joint probability distribution that maximizes the logarithmic-likelihood function. The

probability distribution is specified in

$$C(v_i = 1 | Y) = \frac{1}{1 + e^{-x}} \left( \sum_j w_{ij} Y_j + p_i \right), \quad (10)$$

$$D(Y_i = 1 | Y) = \frac{1}{1 + e^{-x}} \left( \sum_i w_{ij} v_i + q_j \right). \quad (11)$$

$C$  and  $D$  represent the vectors for the layers with no intralayer connection. Due to the undirected nature of RBMs, the weights are changed through a process called contrastive divergence. At the first step, the weight distribution for input layer nodes is produced arbitrarily and used for the nodes in the hidden layer.

Additionally, the hidden layer's nodes reproduce visible nodes by applying the same weights. Due to their isolation, the formed nodes are not identical. An RBM contains an asymmetric bipartite graph devoid of links between units belonging to the same group.

4.1.4. *Autoencoders with a Deep Learning Algorithm*. The autoencoder architecture is designed to provide encoding and decoding. Autoencoders function in a compression and decompression fashion [51]. Figure 5 illustrates the construction of a deep autoencoder, which includes the input, hidden, and output layers.

The encoder uses the concept of dimensionality reduction. The loss is calculated using the function "binary cross-entropy." Equation (12) is used to calculate the cross-entropy (CE).

$$CE = \frac{1}{j} \sum_{i=1}^j P_i \log(L_i) + (1 - P_i)(\log(1 - L_i)). \quad (12)$$

The word  $L_i$  reflects the probability associated with the  $i^{\text{th}}$  instance, and  $P_i$  represents all of the truth values associated with the  $j^{\text{th}}$  occurrence. The activation function employed in deep autoencoders, namely, "RELU," is

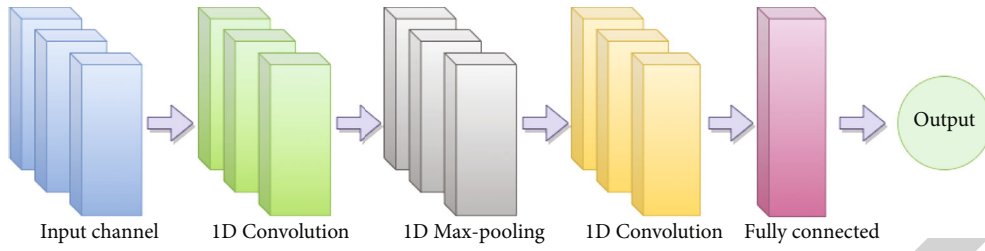


FIGURE 3: Framework for CNN.

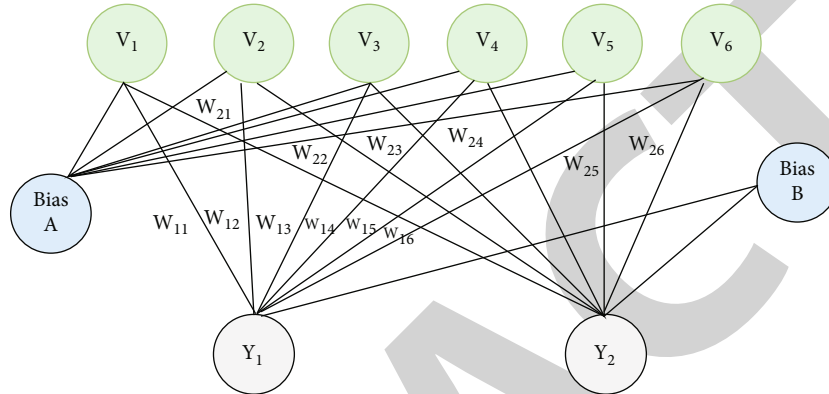


FIGURE 4: Model representation of RBM.

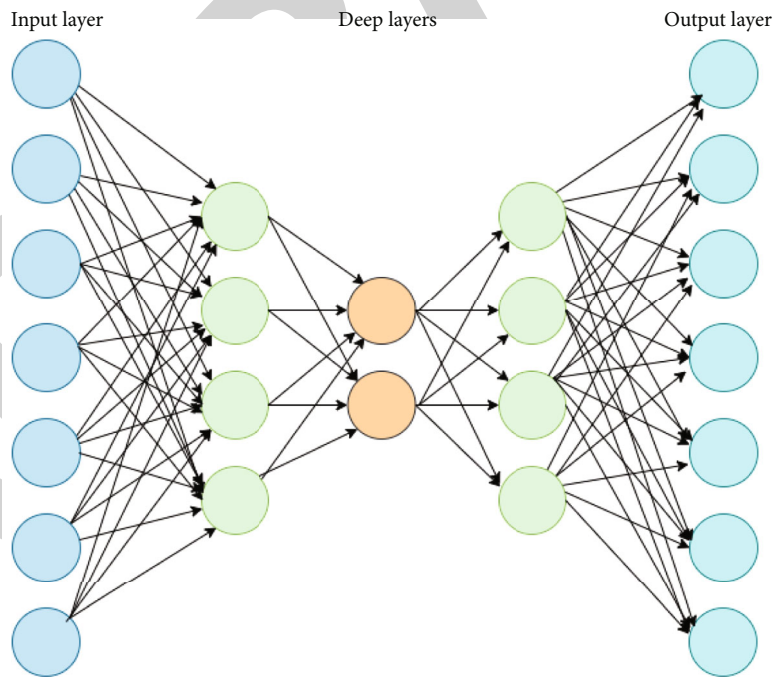


FIGURE 5: Deep autoencoders.

presented in

$$f(y) = \max(0, y). \tag{13}$$

$y$  is the input in this case. Additionally, we optimized the method using the “root mean square propagation”

optimizer. The root mean square error (RMSE) is determined using

$$RMSE = \sqrt{\sum_{i=1}^n \frac{(\alpha_i - \beta_i)^2}{n}}, \tag{14}$$

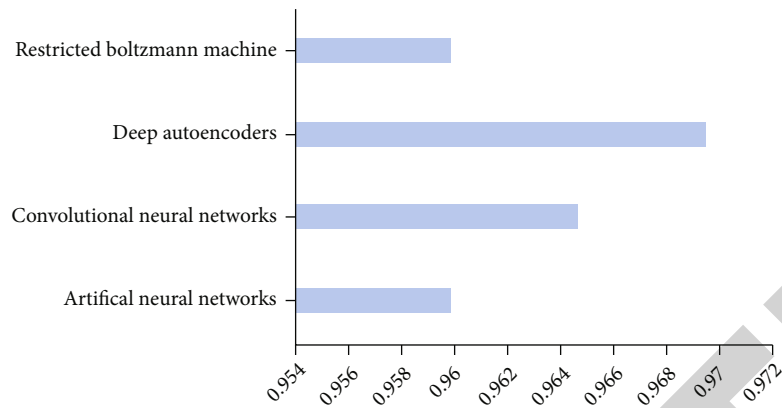


FIGURE 6: Accuracy scores.

where  $\alpha_1, \alpha_2, \alpha_3, \dots, \alpha_n$  are the predicted values,  $\beta_1, \beta_2, \beta_3, \dots, \beta_n$  are the observed values, and  $n$  denotes the number of observations.

The downside of this strategy is that compressed data cannot be organized in its compressed form. To be clear, the encoder does not remove any constraints.

## 5. Results

The prediction outcomes achieved by different learning approaches are presented below in this section. Multiple parameters have been used to assess the performance of ANN, CNN, Deep AE, RBM.

**5.1. Model Evaluation on Basis of Accuracy.** The accuracy scores attained by models are depicted in Figure 6.

The results shown in Figure 6 depict that all the neural learning approaches have shown great performance; the best accuracy score is obtained by deep autoencoder model.

**5.2. Model Evaluation on the Basis of AUC Scores.** The AUC scores attained by models are depicted in Figure 7.

As per Figure 7, deep autoencoder model has attained the highest AUC score (0.95) followed by RBM.

**5.3. Model Evaluation on the Basis of F1-Score.** The F1-scores accomplished by deep learning approaches are depicted in Figure 8.

The highest F1-score is attained by RBM model and the lowest F1-score is attained by artificial neural networks.

**5.4. Model Evaluation on the Basis of Recall.** Figure 9 illustrates the sensitivity (recall) scores attained by deep learning algorithms. The highest recall score is achieved using deep AE and lowest score is attained by CNN.

From Figures 6, 7, 8, and 9, it is clear that these methods have shown great success in detection of early cancer. One can say that deep learning technologies play an important role in detecting, and hence treating, malignant development that would otherwise result in terminal cancer. Deep learning, unlike typical machine learning methods, can detect intricate patterns underneath data

and give critical evidence. The performance of different deep learning models is extensively studied to determine which method outperforms the others, and then, the network's prediction accuracy is investigated.

## 6. Discussion

Experiment results show that deep learning-based models perform quiet well. Practically, there exists small amount of labelled data. The little labelled data may not provide enough information to forecast models. Assume we can include high-dimensional data, allowing for the discovery of critical and essential information while avoiding duplication. As a result, the following categorization approach produces more accurate and efficient results.

Multiple deep learning approaches were used to compare the proposed strategy. AEs have identical network topologies as stacked sparse autoencoders except for the lack of a pretraining phase and the sparse restriction. Section 5 provides the simulation results and reveals that AEs outperform the other three models in terms of accuracy, AUC, and recall scores. In terms of F1-score, RBM displayed the best results followed by autoencoders. This is because these two deep learning algorithms have deep architectures. Unlike traditional machine learning methodologies, deep learning can automatically identify complex patterns beneath data and provide crucial evidence that may be acquired, and discriminative qualities might be studied. Prediction performance is improved by both the recovered information and the underlying structure of the data.

Furthermore, we discover that the AE model beats the other prediction models. The global fine-tuning procedure then optimizes and specifies the entire model's parameters, making classification prediction easier. Furthermore, AEs learn more abstract and representational properties rather than just reconstructing the inputs, making them more successful than AEs for high-dimensional data and categorization. The simulation results show that automated prediction models can accurately estimate the survival of colon cancer patients. Deep autoencoders had the best performance, with a 97 percent accuracy and a 95 percent

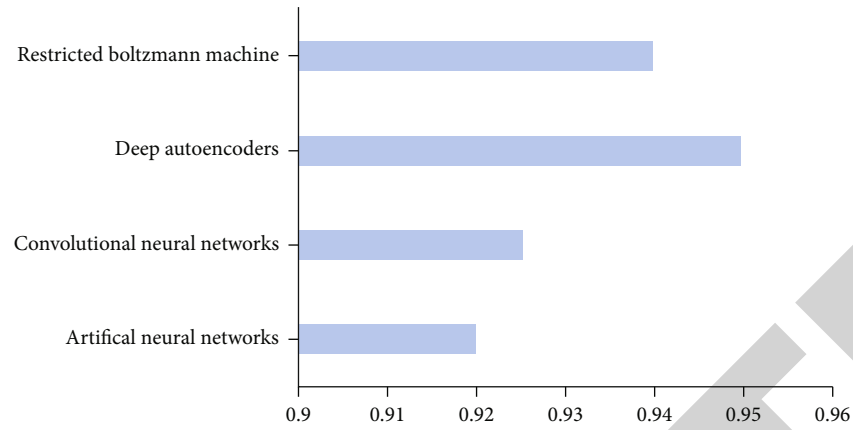


FIGURE 7: AUC scores.

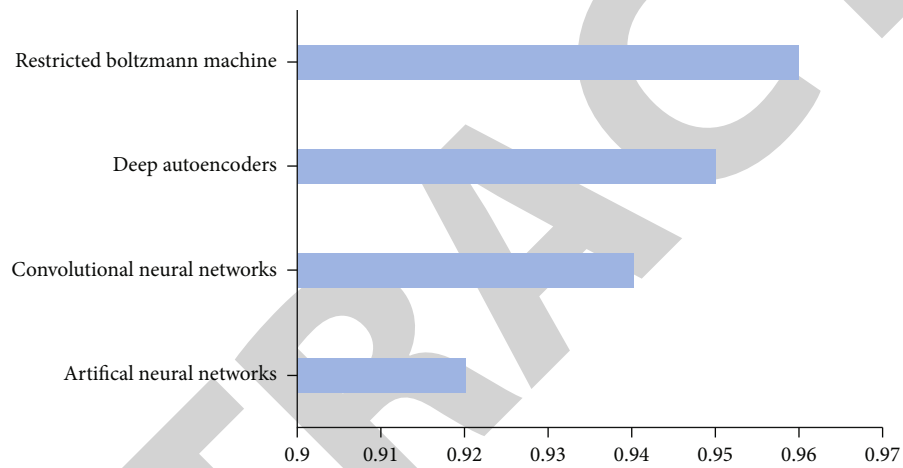


FIGURE 8: F1-score.

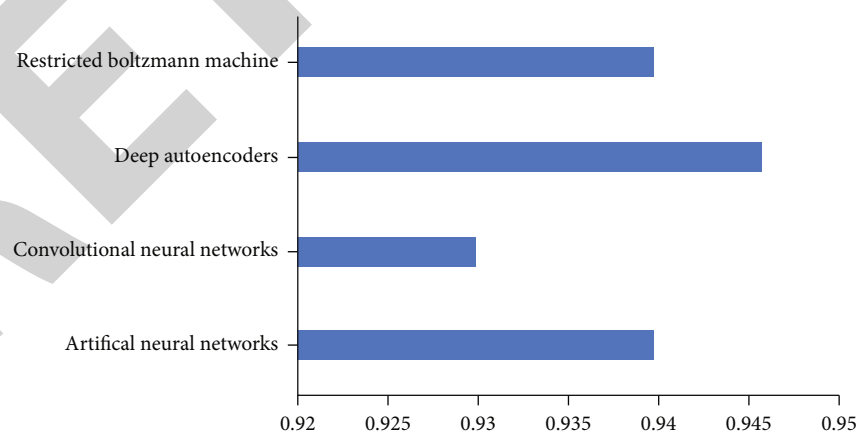


FIGURE 9: Recall score.

AUC-ROC (area under curve-receiver operating characteristic). As a result, we might conclude that computerised thinking, such as AI, plays a critical role in recognising and so treating malignant growth that would otherwise lead to fatal cancer.

## 7. Conclusion

Colon cancer is a type of cancer that begins in the large intestine. Cancer prediction and diagnosis is a complicated issue that has aroused international attention due to the



disease's high morbidity and fatality rates. Early accurate prognosis is critical for successful treatment and can improve cancer outcomes. Early identification and strict implementation of curative procedures have been two of the most successful approaches to treating cancer. Also, predicting the outcomes of treatments post cancer like therapies (chemotherapy, immunotherapy, and other related therapies) is very important for estimating the survivability of cancer patients. In this study, we evaluated colon cancer data from the SEER programme to generate reliable colon cancer survival prediction models. We compared several categorization methods to determine the risk of death five years following diagnosis. Our study discovered that the deep autoencoder model provided the most significant prediction performance in terms of accuracy and area under the receiver operating characteristic curve. According to the study, detecting and controlling cancer immunotherapy toxicities will be a critical component of treatment efficacy in the future. Personalised combination therapies that employ novel ways to address each patient's disease biology will be the most promising cancer therapy strategies.

## Data Availability

Data are available from the corresponding author upon request.

## Conflicts of Interest

There is no conflict of interest.

## References

- [1] A. Sharma and R. Rani, "A systematic review of applications of machine learning in cancer prediction and diagnosis," *Archives of Computational Methods in Engineering*, vol. 28, no. 7, pp. 4875–4896, 2021.
- [2] S. Gupta, A. Gupta, and Y. Kumar, "Artificial intelligence techniques in Cancer research: Opportunities and challenges," in *2021 International Conference on Technological Advancements and Innovations (ICTAI)*, pp. 411–416, Tashkent, Uzbekistan, November 2021.
- [3] J. Gu, R. Chen, S. M. Wang et al., "Prediction models for gastric cancer risk in the general population: a systematic review," *Cancer Prevention Research*, vol. 15, no. 5, pp. 309–318, 2022.
- [4] G. Kaur, H. Hitashi, and G. Singh, "Performance evaluation of image quality based on fractal image compression," *International Journal of Computers & Technology*, vol. 2, no. 1, pp. 20–27, 2012.
- [5] T. Thakur, I. Batra, M. Luthra et al., "Gene expression-assisted cancer prediction techniques," *Journal of Healthcare Engineering*, vol. 2021, 9 pages, 2021.
- [6] T. A. Qureshi, S. Javed, T. Sarmadi, S. J. Pandol, and D. Li, "Artificial intelligence and imaging for risk prediction of pancreatic cancer: a narrative review," *Chinese Clinical Oncology*, vol. 11, no. 1, p. 1, 2022.
- [7] A. Gupta, S. Gupta, and Y. Kumar, "A review on recent deep learning techniques, challenges and its applications for medical healthcare system," *Journal of Healthcare Engineering*, vol. 2021, Article ID 4242646, 648 pages, 2021.
- [8] G. K. Saini, H. Chouhan, S. Kori et al., "Recognition of human sentiment from image using machine learning," *Annals of the Romanian Society for Cell Biology*, vol. 25, no. 5, pp. 1802–1808, 2021.
- [9] M. Shabaz and A. Kumar, "SA sorting: a novel sorting technique for large-scale data," *Journal of Computer Networks and Communications*, vol. 2019, Article ID 3027578, 7 pages, 2019.
- [10] R. K. Garg, J. Bhola, and S. K. Soni, "Healthcare monitoring of mountaineers by low power wireless sensor networks," *Informatics in Medicine Unlocked*, vol. 27, article 100775, 2021.
- [11] S. Kaur and G. Kaur, "Content based image retrieval and classification using image features and deep neural network," *International Research Journal of Engineering and Technology (IRJET)*, vol. 3, no. 9, 2016.
- [12] S. Gupta and Y. Kumar, "Cancer prognosis using artificial intelligence-based techniques," *SN Computer Science*, vol. 3, no. 1, pp. 1–8, 2022.
- [13] S. N. H. Bukhari, A. Jain, E. Haq et al., "Machine learning-based ensemble model for Zika virus T-cell epitope prediction," *Journal of Healthcare Engineering*, vol. 2021, 10 pages, 2021.
- [14] G. Murugesan, T. I. Ahmed, J. Bhola et al., "Fuzzy logic-based systems for the diagnosis of chronic kidney disease," *BioMed Research International*, vol. 2022, Article ID 2653665, 15 pages, 2022.
- [15] A. Malik, G. Vaidya, V. Jagota et al., "Design and evaluation of a hybrid technique for detecting sunflower leaf disease using deep learning approach," *Journal of Food Quality*, vol. 2022, Article ID 9211700, 12 pages, 2022.
- [16] G. Murugesan, T. I. Ahmed, M. Shabaz et al., "Assessment of mental workload by visual motor activity among control group and patient suffering from depressive disorder," *Computational Intelligence and Neuroscience*, vol. 2022, Article ID 8555489, 10 pages, 2022.
- [17] J. Arai, T. Aoki, M. Sato et al., "Machine learning-based personalized prediction of gastric cancer incidence using the endoscopic and histologic findings at the initial endoscopy," *Gastrointestinal Endoscopy*, vol. 95, no. 5, pp. 864–872, 2022.
- [18] Z. Liu and L. Guo, "Comments on: 'Endoscopic prediction of submucosal invasion in Barrett's cancer with the use of artificial intelligence: a pilot study'," *Endoscopy*, vol. 54, no. 2, pp. 224–224, 2022.
- [19] F. Speichinger, M. P. Dragomir, S. Schallenberg et al., "Rethinking the TNM classification regarding direct lymph node invasion in pancreatic ductal adenocarcinoma," *Cancers*, vol. 14, no. 1, p. 201, 2022.
- [20] A. S. O'Shea, "Clinical staging of ovarian cancer," in *Ovarian Cancer*, pp. 3–10, Humana, New York, NY, 2022.
- [21] Q. Zhang, P. Chen, R. Tian, J. He, Q. Han, and L. Fan, "Metabolic syndrome is an independent risk factor for Fuhrman grade and TNM stage of renal clear cell carcinoma," *International Journal of General Medicine*, vol. Volume 15, pp. 143–150, 2022.
- [22] A. Gokce, M. Hatipoglu, S. A. Akboga, A. I. Sezen, Y. Akkas, and B. Kocer, "Critical care for lung cancer patients: surgical treatment during COVID-19 pandemic," *Bratislavske Lekarske Listy*, vol. 123, no. 2, pp. 125–128, 2022.
- [23] A. A. Javed, D. Ding, E. Baig et al., "Accurate nodal staging in pancreatic cancer in the era of neoadjuvant therapy," *World Journal of Surgery*, vol. 46, no. 3, pp. 667–677, 2022.

## *Retraction*

# **Retracted: Dynamic Data Infrastructure Security for Interoperable e-Healthcare Systems: A Semantic Feature-Driven NoSQL Intrusion Attack Detection Model**

### **BioMed Research International**

Received 8 January 2024; Accepted 8 January 2024; Published 12 February 2024

Copyright © 2024 BioMed Research International. This is an open access article distributed under the Creative Commons Attribution License, which permits unrestricted use, distribution, and reproduction in any medium, provided the original work is properly cited.

This article has been retracted by Hindawi following an investigation undertaken by the publisher [1]. This investigation has uncovered evidence of one or more of the following indicators of systematic manipulation of the publication process:

- (1) Discrepancies in scope
- (2) Discrepancies in the description of the research reported
- (3) Discrepancies between the availability of data and the research described
- (4) Inappropriate citations
- (5) Incoherent, meaningless and/or irrelevant content included in the article
- (6) Manipulated or compromised peer review

The presence of these indicators undermines our confidence in the integrity of the article's content and we cannot, therefore, vouch for its reliability. Please note that this notice is intended solely to alert readers that the content of this article is unreliable. We have not investigated whether authors were aware of or involved in the systematic manipulation of the publication process.

Wiley and Hindawi regrets that the usual quality checks did not identify these issues before publication and have since put additional measures in place to safeguard research integrity.

We wish to credit our own Research Integrity and Research Publishing teams and anonymous and named external researchers and research integrity experts for contributing to this investigation.

The corresponding author, as the representative of all authors, has been given the opportunity to register their agreement or disagreement to this retraction. We have kept a record of any response received.

### **References**

- [1] R. Sreejith and S. Senthil, "Dynamic Data Infrastructure Security for Interoperable e-Healthcare Systems: A Semantic Feature-Driven NoSQL Intrusion Attack Detection Model," *BioMed Research International*, vol. 2022, Article ID 4080199, 26 pages, 2022.

## Research Article

# Dynamic Data Infrastructure Security for Interoperable e-Healthcare Systems: A Semantic Feature-Driven NoSQL Intrusion Attack Detection Model

R. Sreejith <sup>1</sup> and S. Senthil<sup>2</sup>

<sup>1</sup>School of Computing and Information Technology, REVA University, Bangalore, India

<sup>2</sup>School of Computer Science and Applications, REVA University, Bangalore, India

Correspondence should be addressed to R. Sreejith; [r\\_sreejith@hotmail.com](mailto:r_sreejith@hotmail.com)

Received 4 May 2022; Revised 18 May 2022; Accepted 24 May 2022; Published 10 June 2022

Academic Editor: Gaganpreet Kaur

Copyright © 2022 R. Sreejith and S. Senthil. This is an open access article distributed under the Creative Commons Attribution License, which permits unrestricted use, distribution, and reproduction in any medium, provided the original work is properly cited.

The exponential rise in advanced software computing and low-cost hardware has broadened the horizon for the Internet of Medical Things (IoMT), interoperable e-Healthcare systems serving varied purposes including electronic healthcare records (EHRs) and telemedicine. However, being heterogeneous and dynamic in nature, their database security remains a challenge forever. Numerous intrusion attacks including bot-attack and malware have confined major classical databases towards e-Healthcare. Despite the robustness of NoSQL over the structured query language databases, the dynamic data nature over a heterogeneous environment makes it vulnerable to intrusion attacks, especially over interoperable e-Healthcare systems. Considering these challenges, this work proposed a first of its kind semantic feature-driven NoSQL intrusion attack (NoSQL-IA) detection model for interoperable e-Healthcare systems. This work assessed the efficacy of the different semantic feature-extraction methods like Word2Vec, Continuous Bag of Words, N-Skip Gram (SKG), Count Vectorizer, TF-IDF, and GLOVE towards NoSQL-IA prediction. Subsequently, to minimize computational exhaustion, different feature selection methods including Wilcoxon Rank Sum Test (WRST), significant predictor test, principal component analysis, Select K-Best, and variance threshold feature selection algorithms were employed. To alleviate the data imbalance problem, it applied different resampling methods including upsampling, downsampling, and synthetic minority oversampling technique (SMOTE) over the selected features. Later, Min-Max normalization was performed over the input feature vectors to alleviate any possibility of overfitting. Towards NoSQL-IA prediction, different machine learning methods like Multinomial Naïve Bayes, decision tree, logistic regression, support vector machine, k-NN, AdaBoost, Extra Tree Classifier, random forest ensemble, and XG-Boost were applied, which classified each input query as the regular query or the NoSQL-IA attack query. The depth performance assessment revealed that the use of Word2Vec features SKG in sync with VTFS feature selection and SMOTE resampling processed with the bootstrapped random forest classifier can provide the best performance in terms of high accuracy (98.86%), F-Measure (0.974), and area under the curve (AUC) (0.981), thus enabling it suitable for interoperable e-Healthcare database security.

## 1. Introduction

The high-pace rise in technologies, especially software computing, cloud computing, and low-cost hardware technologies, has broadened the horizon for the different applications to make timely, decentralized, and accurate decisions. It has helped almost every socioeconomic and industrial segment to exploit aforesaid technologies towards

optimal decision-making in query-driven services in business communication, industrial monitoring and control, finance, healthcare, science and technologies, education, entertainment, etc. The Healthcare sector has always remained a quality-concerned vertical demanding seamless communication to serve telemedicine, EHRs, e-medical, computer-aided diagnosis (CAD), health insurance services, etc. [1]. The benefits of online in healthcare involve

unequalled speed and information availability, which can assist in overcoming the challenges that leading companies and patients confront. The cloud may aid in clinical trial governance and knowledge exchange, and this cutting-edge technology has altered the scope of clinical research [2, 3]. e-Health technologies comprise varied practices like sensory data collection and logging, electronic computer-aided diagnosis (e-CAD) and detail sharing, cloud data upload and decentralized data access for telemedicine, etc. [1, 4]. Noticeably, the aforesaid tasks often involve data communication and data logging to the decentralized cloud or central warehouses or databases [5, 6]. In today's healthcare system, there is a significant danger of data misinterpretation and inaccuracy. It is also inconvenient and takes time. As the number of patient and healthcare institutions has grown, traditional management practices have gone out of favor. As a result, a comprehensive healthcare management system has grown increasingly important over time [7, 8]. To cope up with e-Health demands, interoperable systems provide a platform(s) for multiple stakeholders like patients, doctors, hospital management, lab technicians, nurses, and guardians with their corresponding roles, rights, and access provision [9, 10]. In this manner, the different users can have other notions, intends, intelligible inputs, and distinct writing structures, giving rise to a heterogeneous data environment with the databases. Under such a complex data environment identifying a malicious intruder turns out to be a challenge [5, 6]. Despite the fact that providing an interoperable framework can provide "Fit-To-All" solution for e-Healthcare, however, guaranteeing data security would always remain a challenge [5]. The recent events of unauthorized data breaches caused billions of dollars due to unauthorized insurance claims and patients' personal details for the different monetary benefits [5]. It has alarmed industries to ensure healthcare data security. Towards healthcare data security, different methods like steganography, cryptosystems, and blockchain have been proposed [1, 4]; however, the recent attacks like brute force, smart card loss, and impersonation have confined major solutions [10, 11]. Most of the existing methods have focused on encryption; however, very few efforts are made towards "data infrastructure security" [11]. Though different databases or allied data infrastructures employ gate-level access control using certain authentication methods, however, the nature of intrusion attacks often makes them inferior (see Section 2). This is because the hackers often intrude inside databases by mimicking genuine data structures or injecting malicious codes at the place of query variables [12–15].

e-Health makes use of a number of digital technologies. Users of e-Health can use the Internet to communicate with healthcare workers over e-mail, access medical records, research health information, and share text, audio, video, and other data [16, 17]. Polycom, or mobile TV, facilitates audio and video communications between two or more individuals in two or more locations. Kiosks in e-Health are self-contained devices (usually PCs) that provide interactive information to users [18, 19]. Interoperable e-Healthcare services apply databases in the form of local data warehouses or cloud storage to enable decentralized query-driven deci-

sion support [5, 6]. The intrusion risk turns out to be more severe with dynamic data storage and access ecosystem where the different users of the different types may use it for real-time decision-making [5]. In sync with EHRs or the patient's healthcare records (PHRs), the different users can make an access request or data log or even online computation on the same data infrastructure. The processes involve data feed, query-driven data retrieval, and online computation and update, hence, making them dynamic in nature. Moreover, there can be different e-Healthcare terminals like wireless body area networks, wearable healthcare devices, quantified-self devices, and web-based applications where the data can be logged or updated dynamically [4]. Most of the classical databases use certain relational database management approaches, which are often characterized in terms of their fixed or static schema, vertical scalability, etc. (i.e., SQL). However, being vertical in nature, the classical SQL-driven relational databases struggle in delivering fast responses especially over large inputs [5, 6]. To cope with time-efficient and interoperable system demands, NoSQL databases, which are often characterized in the form of their robust dynamic structure, hierarchical data storage, and vertical scalability, have gained widespread attention [9, 10]. Their efficacy in coping with more complex queries to serve real-time EHRs or telemedicine purposes makes them suitable for interoperable e-Healthcare [13]. NoSQL databases like MongoDB and CouchDB, Key-value: Redis and DynamoDB, Wide-column: Cassandra and HBase, and Graph: Neo4j and Amazon Neptune are found more efficient in terms of availability, credibility, identification, and automatic functional capabilities [13]. Such robustness makes NoSQL a suitable database candidate for a time-efficient and scalable solution towards interoperable e-Healthcare [11]. Despite all these advantages, the possibility and challenges of infiltration attacks in NoSQL cannot be ruled out [11]. Being an interoperable e-Healthcare system with multiple stakeholders, the data input and allied characteristics can be different that consequently making classical intrusion detection methods inappropriate [13, 14]. The classical term-matching-based intrusion detection methods might fail in detecting the malicious user or query [12–14]. Miscalculation towards the wrongly classified queries can force the model to under false-positive performance and hence can impact reliability. Noticeably, so far almost all existing intrusion detection systems focused on SLI-intrusion attack (SQLIA) detection, and no significant effort has been made toward intrusion detection in NoSQL databases [14]. This, as a result, broadens the gaps for academia industries to develop a robust intrusion detection system for NoSQL dynamic datasets for e-Healthcare systems [12, 14]. An intrusion detection system (IDS) is a software application that detects network intrusions using machine learning algorithms. IDS monitors a network or system for malicious behavior and protects against unauthorized access from users, including insiders [15, 20].

Considering at hand solutions, merely syntactic analysis and term-matching cannot be suitable for NoSQL-IA prediction. It can give rise to false-positive performance with reduced reliability. Classical manual testing methods are

limited to identifying intrusion attacks in large databases with multiple stakeholders over interoperable designs [11]. To cope with intrusion detection demands over the heterogeneous and dynamic data-based e-Healthcare system, developing a universal query learning and decision system (UQLDS) can be vital. Moreover, applying machine intelligence to understand each query from multiple sources is a must, and therefore, this problem can be well solved using natural learning programming. NLP can help understand different kinds of queries with varied structures or schema. However, unlike SQLIA, the efficacy of the NoSQL-IA detection model would mainly depend on the efficacy of the features being learnt and the algorithms being applied [14]. In addition to the suitable set of features, it also requires identifying the set of robust computational ecosystems armored with information-rich feature extraction method(s), computation-centric feature selection followed by highly efficient classification to perform reliable intrusion detection [5]. Unlike classical SQLIA methods employing query mapping and structural analysis, NoSQL-IA detection requires semantic feature learning ability [10]. Extracting semantic features from dynamic queries (at both gate level as well as within database transactions), one can apply machine learning models to identify the intrusion attack. However, identifying the optimal set of algorithms, including feature engineering and classification is a must for NoSQL-IA prediction [10]. In addition to the semantic feature need, NoSQL-IA detection model requires addressing the class-imbalance problem as well. This is because the number of intrusions in a real-time environment is always smaller in volume in the minority and therefore training a machine learning over the majority class can skew the prediction results (i.e., false-positive result). Though different machine learning algorithms have been applied towards intrusion detection, yet generalizing one's superiority is difficult due to diversity in their performance over the different test cases. Therefore, it is vital to assess varied machine learning methods and identify the best approach for the NoSQL-IA model. Generally, the telemedicine ecosystem is heterogeneous concerning data, storage, and data transfer methods. Intrusion detection models are typically deployed at the application level, which gives the privilege of scalability and context switching concerning the application environment. The proposed model focuses on constructing a semantic feature-driven intrusion detection system exploring the possibility of natural language processing, text mining, and machine learning. It is always possible to switch to a model trained with SQLIA dataset, which makes the system to adapt the heterogeneity of the telemedicine application environment.

In sync with above discussed key challenges and allied scopes, in this paper, a robust NoSQL-IA detection model is developed for interoperable e-Healthcare systems. The proposed NoSQL-IA detection focuses on improving feature superiority and computing robustness to achieve optimal performance. The proposed model applies different semantic feature extraction methods like Word2Vec, Continuous Bag of Word (CBOW), GLOVE, Skip-N-Gram (SKG), and Count Vectorizer (COUTV) towards their suitability for

the NoSQL-IA model. Once extracting these semantic features, different feature selection methods were applied, including WRST, significant predictor test (SPT), principal component analysis (PCA), Select K-Best (SKB), and variance threshold feature selection (VTFS) algorithms. Here, the key motive was to assess which specific feature and allied feature selection method is effective for NoSQL-IA prediction. The bootstrap method is a common resampling technique that uses replacement sampling to estimate statistics on a population. If the data contains a small number of extreme values, bootstrapping will undervalue these observations as bias correction is not performed. Bootstrap will not be very accurate if the samples are not representative of the entire population. Instead of duplicate data points, SMOTE creates synthetic data points that deviate slightly from the original data points. This method creates a representative sample from the minority group. As the data cannot fully represent the population in the research scenario, the proposed method is applied to alleviate the class-imbalance problem. Subsequently, the selected features were processed for Min-Max normalization to alleviate the overfitting problem. The relationship between the original data values is preserved with Min-Max normalization. In our scenario, we use Min-Max normalization as there is a high chance the data distribution may not be Gaussian, and the feature always falls within a bounded interval. Finally, the input features were processed for two-class classification using different algorithms including Multinomial Naïve Bayes (MNB), decision tree (DT), logistic regression (LOGR), AdaBoost (ADAB), Extra Tree Classifier (ETC), random forest (RF), and XG-Boost classifier. Here, the key motive was to identify the best performing classifier for NoSQL-IA prediction. The overall proposed model was assessed over NoSQL (MongoDB database retrieved from interoperable system design), and data revealed that the proposed NoSQL-IA model exhibits superior performance in terms of accuracy, F-Measure, and area under the curve (AUC) results. Some of the key contributions of this research are given as follows:

Key Contributions:

- (i) This work is the first of its kind effort towards intrusion detection in dynamic data structures like NoSQL for interoperable e-Healthcare services. Unlike classical SQLIA detection methods, especially term-matching or structural analysis approaches, NoSQL-IA model exploited semantic features derived from input queries to train the model that enabling it to achieve higher accuracy and reliability even under dynamic data structures. Here, semantic feature learning helped in coping with the dynamic data structure
- (ii) Realizing “query-driven features” as the backbone towards intrusion prediction, this work applied advanced feature engineering methods including semantic feature extraction, feature selection, data resampling, and normalization, along with state-of-the-art novel heterogeneous ensemble classification. This cumulative solution helped accomplish a reliable and highly accurate model for NoSQL-ID detection

- (iii) Though there are numerous feature extraction methods and hence to identify the optimally performing features, four different feature extraction methods like Word2Vec, CBOW, N-Skip Gram, Count Vectorizer, GLOVE, and TF-IDF were applied. Here, the key purpose was to identify the best performing feature towards NoSQL-IA detection
- (iv) In sync with time and computation efficient NoSQL-IA detection, the proposed model applied different feature selection methods including PCA, WRST, VTFS, and SKB heuristic algorithms. Similar to the feature extraction methods, this work examines the relative efficacy of the different feature selection methods towards NoSQL-IA detection
- (v) Unlike major existing injection attack detection approaches which often ignore the class-imbalance problem in intrusion detection, this work exploited multiple resampling techniques including UPS, DPS, and SMOTE to assess their efficacy to achieve superior NoSQL-IA detection
- (vi) In the real-time dynamic data structure, especially under interoperable e-Healthcare systems operating environment, the nonlinearity of the input data might force machine learning algorithm(s) to undergo convergence and overfitting problems. To alleviate these problems, the proposed model performs Min-Max normalization over the inputs (i.e., selected resampled features). It helps achieve better computation with superior learning
- (vii) The proposed NoSQL-IA model assessed different machine learning classifiers to identify the best suitable model for NoSQL-IA prediction
- (viii) Finally, the overall proposed model identifies the set of the best performing feature extraction, feature selection, resampling, and machine learning methods towards NoSQL-IA prediction. Thus, the eventual model provides a robust computing environment for NoSQL-IA prediction, which can be applied for intrusion detection at both “gate-level” security as well as “within data infrastructure” security
- (ix) Amongst the different sets of features and allied computing environment, this research identified that word-embedding methods like Word2Vec and SKG could be vital with WRST feature selection, SMOTE resampling, and RF classifier. This eventual set of the computing environment can be vital towards NoSQL-IA prediction

The other sections of this manuscript are divided as follows. Section 2 discusses the background of the interoperable e-Healthcare system and intrusion scopes. Section 3 presents the related works, followed by research questions and problem formulation in Section 4. Section 5 presents the proposed model implementation, which is followed by

results and discussion in Section 6. Section 7 presents the conclusion. References used in this manuscript are given at the end of the manuscript.

## 2. NoSQL Injection Threat in Interoperable e-Healthcare Systems

In the majority of the interoperable services including the e-Healthcare, humongous amount of data is generated from the different users having different purposes, intends, and taxonomies. Such systems often give rise to or undergo heterogeneous data environments where the applications often intend to provide query-driven analytics support swiftly with high intelligibility and accuracy. To cope up with such demands, NoSQL databases have gained widespread attention serving a large amount of cloud-based or even ERP-driven solutions serving numerous industrial verticals. Unlike classical SQL databases, NoSQL or not only SQL databases are characterized in the form of horizontal structure with superior time efficiency, availability, and high scalability. Such robustness makes it suitable towards interoperable services like e-Healthcare software systems or services. However, unlike SQL query structure which is fixed in nature, the dynamic nature of NoSQL makes it more vulnerable towards intrusion attacks. Similar to the other databases, NoSQL too undergoes allied functions like data creation, update, reading, and deletion. In the case of interoperable e-Healthcare services or software as well, the different stakeholders including patients, doctors, attendants, laboratory staff, and even insurance agents can have access to their respective data for real-time decision-making. To perform their respective job(s), the stakeholders often employ a function called a query. For query-driven tasks, databases provide a dedicated input box that enables different users to input the intended or expected data, details, etc. These input queries can be for both data retrieval as well as upload or update and hence undergoes continuous transaction during the operating period. While developing the system, the interoperable systems or allied functions store the inputs and allied variables used in the query. These input variables can be numbers, letters, data sequences containing notations, etc., in each query (say, query statement). These variables are employed to execute certain predefined tasks or functions. However, in case such variables are not assessed before executing any task, it can cause disaster in the form of intrusion attacks, manipulations, data deletion, etc. Here, the key threat is that the intruder or the malicious code would be executed once the query is running. Such intrusion can cause data manipulation, data bypass, data deletion, and sometimes encryption to cause ransomware attacks. Therefore, any possibility of such intrusion can be dangerous for databases including NoSQL, which itself is dynamic and heterogeneous in nature under interoperable applications. Same as SQL statement segmentation, intrusion, or malicious codes can change the functions in NoSQL databases like MongoDB. An illustration of the query statements in the SQL and NoSQL (MongoDB) database is depicted in Figure 1. This query intends to retrieve patient-related information.

Observing Figure 1, it can be easily found that the intruders or hackers might write and execute malicious codes and maybe feed them to the query's input boxes to get executed. This process is often called intrusion. Though attackers cannot inject complete arbitrary code, they can still set up attacks by injecting unvalidated inputs and using a small set of functions.

For example, the code below fetches the record with the name (attribute) 'Mr.Bean' using the \$where query operator.

Secure Coding Practices, Least Privilege Policy, and Input Validation are the most common techniques to prevent NoSQL injections in practice. Along with Input Validation, the proposed NoSQL-IA model enables application-level security to avoid data breaches and access breaches. Since overcomplex and multistakeholder driven interoperable models like e-Healthcare systems, the intrusion query or malicious code can be put into the condition statement directly, it becomes easier for hackers to retrieve information by executing injection easily (say, successfully). The severity of such intrusion can be higher in the case of interoperable e-Healthcare systems where the query elements or variables by the different users can be different from each other. For instance, a doctor writes a prescription or diagnosis decisions in the different medicine-related taxonomy or words; on the contrary, a patient with average language ability can feed any comfortable word(s) to state its condition or query. Such heterogeneity might broaden the gap for hackers to intrude or inject intrusion attacks successfully. This, as a result, makes the overall database system vulnerable, and, therefore, there is the need for a robust NoSQL-IA detection model which could have the ability to learn to intend, scope and highly intrinsic information from each query to detect an attack or allied malicious code. It can be considered as the key driving force behind this study.

### 3. Related Work

A major fraction of the recently developed machine learning-driven intrusion detection models has focused on SQL intrusion attack (SQLIA) detection. For instance, SEPTIC, a machine learning-driven SQLIA model, was developed in [21], yet it underwent high false positive due to a low feature quotient in structural information used for training. Despite exploiting deep features in [22–24], the authors failed to achieve efficient performance towards intrusion detection. The key limitation of this approach was the lack of ability to address the class imbalance and heterogeneous data processing (ability). Deep learning and allied features were applied in [21] as well towards SQLIA. Authors [25] inferred that under dynamic data conditions, intrusion detection could be solved as an NLP problem rather than syntax matching or term-matching stereotypes. To improve feature efficiency, the authors [26] suggested using Word2-Vec word-embedding concept for injection detection in databases. Authors [27] made an effort to improve feature information as well as learning by means of an adaptive deep-forest model; however, in addition to the increased computational complexity and exhaustion, AdaBoost-based classifier could exhibit low accuracy (near 90%), signifying

```
SQL: "SELECT * FROM users WHERE (Patient =
'+ PatLD +');"
MongoDB: db.collection.find((Patient: PatLD))
```

FIGURE 1: Permissions for the killing process.

high false-positive results. Despite an effort towards a multi-level regular expression paradigm to perform SQLIA prediction, authors [28] failed to achieve higher accuracy over dynamic data. Moreover, this approach was suitable mainly for static databases like SQL or XML. Authors in [29, 30] developed a penetrating testing-driven attack detection or intrusion detection model. However, its ability towards non-linear, heterogeneous traffic remains suspicious. Authors in [31] revealed that the inferior SQL query's structural information forces machine learning models to undergo increased false positive, especially under dynamic databases like a web-interfaced database. Similar inferences can be observed towards (SQL) query-manipulation detection-based methods, especially under dynamic run-time systems [32]. Though, in [22, 33], the authors suggested exploiting high-dimensional features extracted from the SQL queries to perform SQLIA, yet, their relevance towards NoSQL databases remains an unexplored domain. Despite a vital effort towards SQLIA prediction, authors failed to address their suitability over dynamic data structures such as NoSQL datasets, especially under heterogeneous data inputs. In [34], recently, authors developed a semantic feature-driven consensus-based learning environment for SQLIA prediction; however, it failed to address heterogeneous and distributed dynamic data learning, which is quite more complex than the classical static databases like SQL. The model trained with static database structure like SQL cannot be generalized over distributed dynamic databases like NoSQL [12–14]. The authors proposed case-based reasoning (CBR) engine equipped with learning and adaptation capacity for SQLIA. However, the accuracy of 93.8% doesn't guarantee its suitability with dynamic data because of its higher reliance on the predefined structural information-driven learning ability. Moreover, the lack of class-imbalance solutions in major machine learning-driven methods like [35] results in reduced and nongeneralizable outcomes [36]. Author [37] applied syntax-structure learning concept towards injection detection; however, lower computational efficiency (accuracy 83.1%) confines it is more limited for NoSQL databases. Noticeably, these approaches cannot be suitable for NoSQL databases due to dynamic data in nature and different data structures [38]. Authors in [39] applied Two-Class SVM (TC SVM) and Two-Class LR (TC LR) towards injection attack detection using Microsoft Azure Machine Learning (MAML) in online systems. Naïve Bayes (NB) algorithm was applied in [39] to perform a role-based access control and injection attack. Recently, authors [40] found that for dynamic data analysis and allied intrusion prediction, semantic features such as SKG can be of vital significance. Despite numerous efforts, above stated methods are assessed with fixed data structure, and hence, their suitability towards heterogeneous, nonlinear data

```

    Db.Collection.find({$where:function(){Return(this.name=='Mr.Bean')}});
    Through the variable $userData, an attacker can introduce unfiltered user input.
    Db.Collection.find({$where:function(){Return(this.name==$userData)}});
    If the injection worked, an attacker might put the string 'a'; sleep (10000) into the variable $userData. The injected code would tell the
    server to wait for 10 seconds, giving the intruder enough time to do what he wanted.
    Db.Collection.find({$where:function(){Return(this.name== 'a'; sleep (10000)}});

```

CODE 1

(say, dynamic data structure) seems limited. However, the key suggestions or allied inferences obtained from these intrusion detection methods indicate that the use of semantic features can be more effective, while addressing key challenges like class imbalance and data heterogeneity can help achieve superior performance towards intrusion detection in real-time databases.

Unlike SQLIA, recently, a few efforts were made toward NoSQL intrusion detection. For instance, authors [41] developed an intrusion detection model for MongoDB and CouchDB, which are well-known and highly used NoSQL databases. Authors [42] applied One-class SVM (OC-SVM) to perform intrusion detection over NoSQL databases. However, neither it could exploit semantic feature efficacy nor even address computational improvement as a goal toward generalizable performance. Similar to [43], authors in [42] developed a Bayesian network as a K2 algorithm for intrusion detection in MongoDB NoSQL-IA detection. However, the basic computational environment broadens the horizon for further study and innovation. In [43], the authors applied different machine learning methods for intrusion detection in MongoDB databases. Despite multiple machine learning models, this study inferred that the random forest method could be superior to classical k-NN, DT, and Naïve Bayes (NB) algorithms. Despite RF-based classification, this approach failed to address semantic feature significance, class-imbalance problems, etc., which can limit its efficacy towards real-time interoperable system design [44, 45]. Authors [41] found that the major interoperable systems developed onto JavaScript development platforms (specially designed with MongoDB databases) are susceptible to intrusion attacks; however, merely applying syntax features and code review cannot yield an optimal detection solution. Authors in [46] developed Diglossia, a sophisticated tool for intrusion attack detection over SQL and NoSQL queries. In order to detect intrusion attacks, their proposed model parses the inputs or queries and assesses whether the two parse trees are syntactically isomorphic. In [47], the authors developed an intrusion detection system for two well-known NoSQL datasets, Cassandra and MongoDB. Yet, their efficacy remained limited to real-time interoperable system designs. Authors in [48] discussed security concerns, especially over decentralized Hadoop has driven NoSQL databases and stated that to cope with the different intrusion attack detection demands, developing a query-learning concept can be vital rather than predefined rule-based methods. Authors in [49] suggested a reversible watermarking-based security model for NoSQL data security. However, it merely focuses on data security based on unique embedding fea-

tures and does not guarantee any intrusion-related attack scenario. Though authors in [50] developed a NoSQL intrusion detection method, yet it failed to exploit semantic features and advanced computing methods for NoSQL-IA detection. The depth assessment of the different existing approaches reveals that towards intrusion detection, merely applying syntactic information or structural rule learning cannot yield reliable intrusion detection in a real-time system, and hence, semantic features can yield more superior performance towards intrusion attack detection in databases [34, 39–41, 43]. Moreover, in addition to semantic feature learning, improving the computational environment with advanced feature selection, resampling, and classification is a must. Moreover, assessing the suitability of the aforesaid methods also needed to be tested with dynamic distributed data with interoperable heterogeneous query elements [51–53]. These key factors can be considered the key driving forces behind this study.

#### 4. Problem Formulation

The key challenge in an interoperable system e-Healthcare system is data security and reliability. In such an interoperable system, there can be multiple user types with distinct roles, rights, and access credentials. In such systems, the data patterns can be heterogeneous and can be more severe with e-Healthcare systems [5, 6, 9–12]. Under such a heterogeneous and complex working environment, assessing each input query or allied appropriateness is challenging. Considering such adversity and allied scopes, different intruders often make use of intrusion attacks to get access to the databases to perform data manipulation, alteration, deletion, etc. In addition to these, the cases of ransomware attacks to being witnessed globally, where an intruder mimics the normal queries and enters the database to manipulate access or data sources. In classical SQL databases, which are static, identifying intrusion is relatively easier due to the static query nature and syntactic comparison ability. However, almost all major SQL-driven databases are time-consuming and hence undergo delay over real-time interoperable system demands. Moreover, merely applying query-matching or syntactic analysis cannot guarantee intrusion detection because the recent intrusion efforts have been applying sophisticatedly designed bots that mimic the original queries and hence detecting them based on structure or syntax turns out to be infeasible. It infers that both the classical SQL data structures and allied intrusion detection models are limited to addressing contemporary attack scenarios, malicious code, or bot-driven attacks. To alleviate these problems,



dynamic data structures such as NoSQL have gained widespread attention [12–14]. Their dynamic data structure and interoperable characteristics make the system have superior availability, credibility, and time efficiency. Such robustness can help e-Healthcare systems, especially EHRs and telemedicine, to serve real-time demands. To be noted, being interoperable, the likelihood of attacks increases significantly over distributed dynamic data structures where the different users can input the different inputs having diverse intentions, terms, and meanings. In such a case, most of the existing intrusion detection methods can be limited due to low perceptibility and lack of universal intelligibility. Despite the robustness of NoSQL data structures towards interoperable data services, the attack likelihood remains the same with NoSQL distributed data structure and hence requires a robust intrusion detection model which could identify the attacker query at both “at the gateway” as well as “within humongous database.” To achieve it, unlike classical text mining approaches, syntax matching, and keyword search methods, there is the need to upgrade the intelligibility of the detection model with more semantic information capacity. In other words, improving intrusion detection systems with more diverse semantic and latent information and allied traceability can help identify or classify intrusion queries accurately. Moreover, towards a large distributed framework like “interoperable e-Healthcare system,” applying manual testing approaches cannot be effective, and hence, it requires certain artificial intelligence-driven analytics solutions which could exploit the different distributed data structures and allied queries to build a superior intelligible knowledge bank for real-time intrusion tracking. To achieve it, unlike term frequency matching or syntactic analysis, semantic feature-driven machine learning models specially designed in sync with the natural language programming (NLP) paradigm can be vital [34, 54]. In sync with aforesaid semantic features, the use of machine learning model(s) can be vital to perform automatic intrusion detection in NoSQL distributed data structures toward secure, interoperable e-Healthcare systems. The proposed work is a kind of industry-level semantic feature-driven IDS focusing on NoSQL-IA for telemedicine applications. Additionally, the model of IDA shall be added to the existing telemedicine application server to enhance security at the application level. Also, the model can be considered as a security layer to the newly designed telemedicine framework.

Considering above stated research goals and allied scopes, in this paper, a first of its kind NoSQL-IA detection model is developed for distributed data structures to be used for interoperable e-Healthcare systems. The overall proposed model has been designed as an NLP problem where at first semantic features have been extracted from queries originating from the different interoperable sources (or stakeholders). Realizing the diversity of performance by the different feature extraction models, in this paper, four well-known semantic feature extraction methods named Word2Vec, CBOW, SKG, TF-IDF, Count Vectorizer, and GLOVE were applied that generate features distinctly. Subsequently, realizing the computational efficiency, the proposed model applies four different feature selection methods, including

significant predictor test, WRST, PCA, VTFS, and SKB methods. Noticeably, these different feature selection algorithms are applied distinctly over the different features to assess the suitability of the dominant feature for NoSQL-IA prediction. Unlike major existing machine learning-based intrusion prediction models that often fail in addressing class-imbalance problems, the proposed model applies different resampling concepts to prepare feature vectors that sufficiently distribute minority as well as majority class data or events. It can help provide sufficiently large heterogeneous features to perform accurate NoSQL-IA prediction. Thus, once resampling input (selected) features, the proposed model applies Min–Max normalization to alleviate any possible overfitting or convergence problem. Finally, the normalized features were processed for classification using several state-of-the-art robust classifiers such as Multinomial Naïve Bayes, logistic regression, k-NN, decision tree, AdaBoost, Extra Tree Classifier, random forest, and XGBoost classifiers. Here, the key motive was to identify the best performing machine learning environment for NoSQL-IA prediction. Thus, applying above stated approach, the proposed model intends to perform “gate-level” as well “within database” intrusion detection to ensure the safety and security of the interoperable e-Healthcare systems for seamless decision-making. The overall research intends to achieve answer(s) for the following key research questions:

RQ1: Can the use of semantic features enable intrusion detection and classification in distributed data structures like NoSQL for interoperable e-Healthcare services?

RQ2: Which semantic feature extraction model be an optimally effective approach toward NoSQL-IA prediction in interoperable e-Healthcare services?

RQ3: Which feature resampling model be an optimally effective approach towards NoSQL-IA prediction in interoperable e-Healthcare services?

RQ4: Which machine learning model is optimally effective towards NoSQL-IA prediction in distributed data structures based on interoperable e-Healthcare services?

RQ5: What should be the set of a computing environment including feature extraction, selection, sampling, and classification to yield optimally accurate and reliable NoSQL-IA prediction for interoperable e-Healthcare services?

## 5. System Model

As discussed in the previous sections, the proposed NoSQL-IA prediction model is developed as an NLP problem where the key motive is to exploit semantic features from each query of the data entry and learn over a highly robust computing environment to classify it as normal or the NoSQL-IA attack query class. To achieve it, the proposed model applies phased implementation encompassing the following steps:

- (1) Data acquisition and preprocessing
- (2) Semantic feature extraction

- (3) Feature selection
- (4) Feature resampling
- (5) Feature normalization
- (6) NoSQL-IA classification

A detailed discussion of these key methods is given in the subsequent sections.

*5.1. Data Acquisition and Preprocessing.* In sync with the targeted interoperable e-Healthcare services using NoSQL databases and allied infrastructure security, the proposed model was specially designed for NoSQL databases. Undeniably, the majority of the interoperable e-Healthcare services and allied databases can be characterized in terms of heterogeneity and dynamic nature that makes intrusion detection a challenging task. On the other hand, the efficacy of intrusion detection models primarily depends on feature information and allied statistical characteristics (of the training datasets). Exploring in-depth, we observed that though a few benchmark datasets are available for SQL intrusion attack detection; however, there is no benchmark available for NoSQL-IA detection. Moreover, attack-annotation is a challenge in NoSQL-IA prediction. Considering this fact, we prepared our training dataset to validate the efficacy of the proposed NoSQL-IA prediction model toward interoperable e-Healthcare services. The considered data environment was distributed dynamically in nature with data heterogeneity, which is generated by the multiple users with different roles, meanings, and terminologies; a dynamic application was created. In the considered interoperable system environment, multiple users could interact with each other as well as with the system. In addition, the deployed system environment inculcated a static application as well, which does not possess any user and executes a static process each time to introduce a query to the system's database. This model of query execution was applied to introduce attack traces inside the database. A snippet of the data synthesis model developed is given in Figure 2.

Being distributed dynamically in nature, the proposed data environment resembles MongoDB and CouchDB, which can be characterized in the form of a NoSQL-Map database. For the proposed distributed dynamic data synthesis, the experimental setup discussed in Figure 2 was applied. The deployed approach enabled the generation of the different queries or traces towards NoSQL-IA prediction. The NoSQL-IA system has two significant entities, the trigger model and the serving infrastructure. As the system uses the containership concept of serving the model, the system is highly scalable concerning model upgradation and architecture expansion. When the telemedicine application scales up, the NoSQL-IA IDA shall have multiple containers synchronizing with any container orchestration tool of that particular server environment. The container is a lightweight virtualization technology similar to VM for creating isolated environments. Docker virtualizes applications, decouples them from their underlying devices, and allows them to be deployed and migrated between physical devices with ease.

The proposed research uses Docker containers to simulate multiple instances and construct an isolated environment for model deployment. Kubernetes orchestration methods are explored to run the Docker containers. To alleviate any possibility of interferences over the interoperable framework (amongst the different users), a Docker container was deployed that was running over the MongoDB server in conjunction with a virtual machine setup (see VM1 in Figure 2). As depicted in Figure 2, Sysdig is executed within a kernel space and is functional towards call traces retrieval where the call traces are being generated by the running container. Here, in order to inculcate dynamic behavior with heterogeneous inputs (amongst the different interoperable users concurrently), the proposed model sent requests to the container by means of VM1 (Figure 2). To achieve this, the Apache JMeter workload generator tool was applied. Though a simple HTTP sampler of Apache JMeter can be applied on CouchDB to enable web traffic simulating different users, the study explores the possibility of Nmap and Metasploit tools for intrusion-related traces executed by VM2. In this work, JMeter with JSR223 sampler was applied to generate the traffic traces from the different users. Functionally, web requests were transmitted to the server to initiate the database functions. In sync with interoperable (system) functionality, for each application, two threads (i.e., Thread-1 and Thread-2 in JMeter) were deployed to send a request to the server simulation and post the data values concurrently. In the deployed platform, Thread-1 encompassed a total of 100 users that performed simultaneous document queries (say, enquiry) and (basic) data feed over the execution period. Similarly, Thread-2 encompassed four users (here, we hypothesized them to be doctors, hospital management, assistants, and lab technicians) having the right to create, update, and delete the database(s). Noticeably, in the deployed framework, as Apache JMeter generates the dynamic data traffic, Sysdig (Figure 2) performs monitoring of the queries or calls of the server, signifying the normal traces. In this work, we generated a total of 4000 traces with 347 intrusion traffic traces. Thus, collecting this database, we deployed it for feature engineering for further NoSQL-IA prediction tasks. Towards preprocessing task, the proposed model applied tokenization of the input queries, followed by stemming and stopping word's removal from making data suitable for feature generation. Once obtaining the token information for each query, the extracted data or tokens (per query) were processed for semantic feature extraction. The details of the proposed feature engineering model are given in the subsequent sections.

*5.2. Semantic Feature Extraction.* Being heterogeneous in nature, the collected query traces possessed varied tokens, operators, structural indexes, literals, punctuations, and identifiers. In addition, unlike classical structural query languages, the proposed dynamic distributed data NoSQL traces contains different clauses, predicates, and expressions. In such dynamic data structure and allied representation, assessing the hidden embedding information and allied semantic features can be of great significance towards NoSQL-IA prediction. In the input queries, the aforesaid

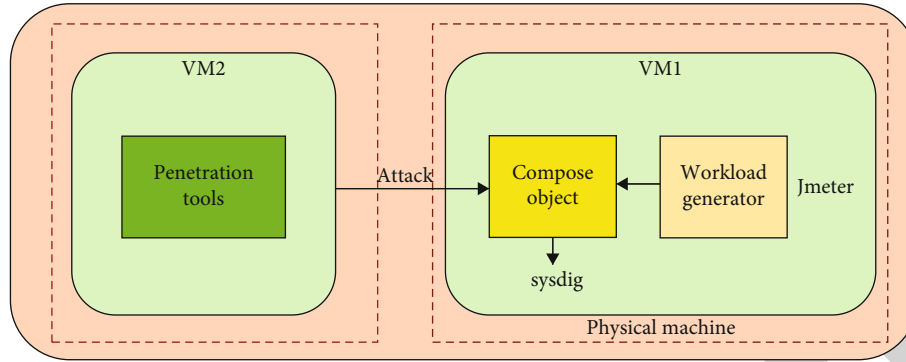


FIGURE 2: Setup for normal and intrusion transaction trace(s) generation towards distributed dynamic database generation and NoSQL-IA prediction.

clause, predicate, and expressions are employed to characterize a query to make further real-time NoSQL-IA predictions. Any intruding query can be strategically designed to mimic and penetrate normal NoSQL data structure in certain tautological types to retrieve outputs from a database far beyond the developer’s intention. In NoSQL-IA, the sophisticatedly designed attackers identify the poorly coupled clauses, predicates, and expressions due to dynamic structure to intrude inside. Though such specific structural features can be applied to static SQLIA; however, their generalization over dynamic data structure seems unrealistic. In the targeted distributed dynamic structure models, the specially designed bots can mimic the original query, and hence, intrusion becomes easier over dynamic (and heterogeneous) databases. Therefore, unlike classical structural features or syntax characteristics, this research work proposes to exploit semantic (or latent) features for the NoSQL-IA prediction task. Despite the fact that the semantic features can provide superior learning over classical structure-learning-based methods, different algorithms claim their superiority over others. Considering this motive, four different kinds of semantic feature extraction algorithms have been applied. These algorithms are:

- (1) Word2Vec word-embedding
- (2) N-Skip Gram method
- (3) Continuous Bag of Words (CBOW),
- (4) Count Vectorizer
- (5) GLOVE
- (6) TF-IDF

In the proposed work, the input queries or data samples are in the form of textual data, which is required to be encoded into relevant numeric vectors toward the corresponding feature representation. Considering this motive, the proposed model applied the concept of word-embedding that transforms input tokens or queries into related numeric (high-dimensional) feature presentations. This work applied the Word2Vec word-embedding concept that hypothesizes that the contexts in the natural presenta-

tion or language possess high correlation, and hence, the tokens (or words) can be vectorized as per the corresponding context. Subsequently, the word vector can be retrieved from the training corpus so as to measure the semantic similarity between different words (present in the natural language). In the proposed work, each processed token was converted into a numeric feature representation called a feature vector. Here, the Gensim Word2Vec model was designed with a double-layered neural network possessing two hidden layers, which helped to retain more sparse and significantly important features. Though Word2Vec is realized in two distinct configurations, CBOW and SKG, we applied these two methods to extract semantic features distinctly. A snippet of these algorithms is given as follows.

5.2.1. *N-Skip Gram (SKG)*. Let the total set of words be  $\{1, \dots, W\}$ . Then for a given NoSQL query set, the proposed Word2Vec N-Skip Gram method performs learning over the vector representation of each encompassing token  $w$ . In this manner, the obtained feature representations are processed for training to identify the words having a higher probability of taking place within the context window of a particular center word. In this manner, with the extracted input tokens from the query corpus  $(w_1, \dots, w_T)$ , the proposed model improves the probability of the context word in sync with the center word. Here, the prime motive was defined as

$$\sum_{t=1}^T \sum_{c \in C_t} \log p(w_c | w_t). \tag{1}$$

In (1),  $C_t$  represents the factor called context window, which is decided around the centre token  $w_t$ . In this manner, the probability of occurrence of the context word near the center word  $w_t$  is obtained as per the Softmax over the function defined in

$$p(w_c | w_t) = \frac{e^{s(w_c | w_t)}}{\sum_{j=1}^W e^{s(w_t, j)}}. \tag{2}$$

In (2), the parameter  $s$  signifies the scoring function representing the convolution of the centre word  $w_t$  and the

corresponding context word. In this manner, an objective function  $J_\theta$  (3) which is supposed to be reduced over training is defined.

$$J_\theta = - \sum_{w_i \in V} \log \frac{p(w_i | c)}{p(w_i | c) + kQ(w_i)} + \sum_{j=1}^k \log \frac{p(\bar{w}_i | c)}{p(\bar{w}_{ij} | c) + kQ(\bar{w}_{ij})}. \quad (3)$$

In (3),  $Q$  states the noise distributions to be used for generating  $k$ -noise samples. The proposed work employed the embedding matrices obtained in reference to each  $n$ -gram in  $n$ -gram vocabulary to retrieve context words. In addition, we applied a token-only embedding matrix configured with  $n = 1$ , the window size of five long with the Skip Gram size of one. In our proposed model, each batch of input corpus, along with the labels passed over each run, transforms allied mapping output to the  $n$ -gram. It helped estimate the embedding vectors that eventually constitute required word vector representations. These word vectors were transformed to the loss function in which it applied SGDM (stochastic gradient descent model) to update embedding metrics. Updated embedding metrics were obtained as a feature vector for further processing.

**5.2.2. Word2Vec CBOW.** A few existing pieces of literature criticize that N-Skip Gram methods often generate high-dimensional features increasing the computational complexity of the system. Unlike the N-Skip Gram method, CBOW Word2Vec methods provide more significant semantic features than NLP methods. In the CBOW method, the context token is predicted on the basis of the neighboring context-window. Now, let  $W_{i-1}$ ,  $W_{i-2}$ ,  $W_{i+1}$ ,  $W_{i+2}$  be the context word or corpus obtained from each NoSQL query, and then the proposed method predicts  $W_i$  that possesses a higher correlation with the other tokens in the corpus or query. The two distinct word-embedding sets of the native CBOW method are the source and target sides, signifying  $v_w, v'_w \in \mathbb{R}^d$  for each token of the NoSQL query (i.e.,  $w \in V$ ). In this manner, a text-window can have the centre word  $w_0$  and the corresponding context words  $w_1, \dots, w_C$ . Thus, for a predefined text-window representing a NoSQL query, we defined CBOW loss as

$$v_c = \frac{1}{C} \sum_{j=1}^C v_{w_j}, \quad (4)$$

$$\mathcal{L} = - \log \sigma \left( v'_{w_0} T_{v_c} \right) - \sum_{i=1}^k \log \sigma \left( -v'_{n_i} T_{v_c} \right). \quad (5)$$

In (5), the variable  $n_1 \dots n_k \in V$  be the negative samples retrieved from the noise-distribution  $P_n$  over query corpus  $V$ . In (5), the gradient of  $\mathcal{L}$  in reference to the different components like the expected value  $v'_{w_0}$ , a negative target sample  $v'_{n_i}$  and average context source ( $v_c$ ) are represented

as per ((6)–(8)), respectively.

$$\frac{\partial \mathcal{L}}{\partial v'_{w_0}} = \left( \sigma \left( v'_{w_0} T_{v_c} \right) - 1 \right) v_c, \quad (6)$$

$$\frac{\partial \mathcal{L}}{\partial v'_{n_i}} = \left( \sigma \left( v'_{n_i} T_{v_c} \right) - 1 \right) v_c, \quad (7)$$

$$\frac{\partial \mathcal{L}}{\partial v_c} = \left( \sigma \left( v'_{w_0} T_{v_c} \right) - 1 \right) v'_{w_0} + \sum_{i=1}^k \left( \sigma \left( v'_{n_i} T_{v_c} \right) - 1 \right) v'_{n_i}. \quad (8)$$

In this manner, employing the concept of chain rule with respect to the source context embedding, we obtained the feature vector as output (9).

$$\frac{\partial \mathcal{L}}{\partial v_{w_j}} = \frac{1}{C} \left[ \left( \sigma \left( v'_{w_0} T_{v_c} \right) - 1 \right) v'_{w_0} + \sum_{i=1}^k \left( \sigma \left( v'_{n_i} T_{v_c} \right) - 1 \right) v'_{n_i} \right]. \quad (9)$$

Thus, for a given context window, say bag-of-words, it generates embedding metrics representing the semantically connected probable words, which are used for further training. In the CBOW feature extraction method, a key challenge is an incorrect update in the context vector, and, therefore, to alleviate it, we performed context word normalization. For context word normalization, we resampled the width of the context window randomly in the range of 1 to  $C_{\max}$  for each target word. It broadened the context-embedding over the wider context window and provided more significant features for training.

**5.2.3. GLOVE.** Different kinds of literature reveal that a superior word-embedding requires representing the words in such a manner that two distinct tokens or words possessing the same semantic inference or significance would have the same vector representations. In this manner, one can preserve the other linguistic associations amongst the varied words for better training. Similar to the above discussed Word2Vec word-embedding method(s), the approach called Global Vectors (GLOVE) is also a statistical unsupervised learning concept. However, unlike aforesaid methods, GLOVE exploits cooccurrence metrics to generate the numerical vector-space representation. In practice, it is accomplished by estimating how frequently the different words cooccur within a defined context window in a given query corpus. Subsequently, it applies the dimensional-reduction method over the cooccurrence matrix. Noticeably, based on the size of corpus employed for training, GLOVE method might demand significantly large memory, which can later make feature extraction and allied classification more exhaustive. However, to assess relative performance towards NoSQL-IA prediction, we employed the GLOVE method as one of the semantic feature extraction tools. To implement it, we employed a pretrained GLOVE model, which has been trained over the data corpora from Wikipedia and Gigaword. The pretrained model was prepared over

the dataset encompassing a total of six billion tokens with a total vocabulary of 400,000 distinct words. In our proposed model, we considered the length of the vectorized word representation as 100, which helped reduce computational exhaustion in comparison to TF-IDF or classical Count Vectorizer.

**5.2.4. TF-IDF.** Similar to the above-discussed GLOVE model, the TF-IDF method calculates the total number of the frequently occurred word identified based on the (frequent) occurrence of the words in a corpus. In our proposed NoSQL-IA detection model, TF-IDF was applied as a feature extraction model where it estimated the frequency of the term(s) within each query or input corpus. In the proposed feature extraction model, term frequency (TF) provides the total number of repeats that a specific word undergoes in the provided query or input corpus. It estimated the total number of repeats that a specific word does (within a provided input corpus) than the total number of tokens or words available in the input corpus. TF is estimated as per

$$tf_{i,j} = \frac{n_{ij}}{\sum_k n_{ik}}. \quad (10)$$

In inverse data frequency (IDF), it calculated the number of occurrences of a unique token across the input corpus. Noticeably, tokens with very rare presence over an input corpus used to have larger IDF, which is obtained using

$$df(w) = \log \left( \frac{N}{df_i} \right). \quad (11)$$

In this manner, applying the score over (10) and (11), scores, TF-IDF estimated a cumulative score value ( $w$ ) for a token within an input query or allied corpus, using

$$w_{i,j} = tf_{i,j} \times \log \left( \frac{N}{df_i} \right). \quad (12)$$

In (12),  $tf_{i,j}$  represents the total number of occurrences of  $i$ -token in  $j$ th corpus. On the contrary, the number of queries possessing  $i$ -token is  $df_i$ . Here,  $N$  represents the total number of queries. Once obtaining the TF-IDF score for each input token, the proposed model performed text-to-sequence conversion and thus estimated an equivalent sequence of words or values for further learning towards NoSQL-IA prediction.

In addition to the above-discussed feature extraction methods, we also applied Count Vectorizer (COUTV) using SciKit Learn Library in Python to extract features from the input queries. However, due to space constraints, a detailed discussion of COUTV is not given in this manuscript. The details of COUTV can be found in [49, 50].

**5.3. Feature Selection.** This is a matter of the fact that the above-stated word-embedding methods obtain high-dimensional information-rich feature sets for better learning, however, at the cost of increased search (or data) space and hence higher computational cost. In sync with real-time

NoSQL-IA prediction demands, to alleviate this problem, in this paper, feature selection was performed. Here, the key motive was to reduce the insignificant or relatively low significant features to improve computational efficiency as well as better training. Different researches advocate different feature selection methods and, therefore, to identify the optimally performing feature set towards NoSQL-IA prediction. In this reference, the proposed model applies four different types of feature selection methods, including the following:

- (1) Select K-Best
- (2) Principal component analysis
- (3) Wilcoxon Rank Sum Test (WRST)
- (4) Variance threshold method

The detailed discussion of the overall proposed feature selection method is given as follows:

**5.3.1. Select K-Best Feature Selection.** In this work, we applied SKB feature selection method that estimates the top-k most significant features. In our proposed Select K-Best-based feature selection, we applied the chi-squared method which helped in estimating the set of most significant features. A snippet of the proposed chi-squared SKB feature selection method is given as follows:

(1) *Univariate Chi-Squared Test.* The univariate chi-squared approach applies a criteria-driven feature selection concept where it estimates the vitality of a feature element by estimating  $\chi^2$  statistics in reference to the target class. Here, each feature is examined for its vitality distinctly to assess the corresponding relationship to the target variable. It functions as a key nonparametric test approach to compare multiple variables for randomly selected data. Being a kind of the independence-test method, the proposed model enabled identifying the disparity and independence amongst multiple random variables. In this manner, it estimated a value based on the relationship between the feature instance and the class it should belong. For the out value 0, it states that there is no relationship between the feature element and the class. The higher association value shows a stronger relationship between the feature element and the class it should belong. Here, we employed the chi-squared concept towards initial feature estimation using SciKit Learn Library. Functionally, the chi-square's statistics approach is applied as per the information-theoretic feature selection paradigm. In this approach, it tries to assess the intuition that the term  $t_k$  for a specific label or class  $c_i$  is the one distributed amongst the set of positive and negative examples. Mathematically, the chi-squared test is defined as

$$Chi - Square(t_k, c_i) = \frac{N(AD - CB)^2}{(A + C)(B + D)(C + D)}. \quad (13)$$

In (13),  $N$  states the total number of feature elements in the corpus, while  $A$  states the elements in class  $c_i$

encompassing  $t_k$ . The number of feature elements containing  $t_k$  in other classes is given by  $B$ , while the number of feature elements in class  $c_i$  which do not have any terms of  $t_k$  be  $C$ . The other parameter  $D$  states the number of feature elements having no term  $t_k$  in other classes. In this manner, applying (13), the proposed approach assigned a score for each feature towards each class (here, normal query or the NoSQL-IA query). Finally, the total scores are combined to give rise a final score, defined as

$$\max (\text{Chi-Square}(t_k, c_i)). \quad (14)$$

Thus, applying above method, we obtained the set of most significant features for further NoSQL-IA prediction task.

**5.3.2. Principal component analysis.** To implement PCA, we calculated the principal component and eigenvalues of the covariance or correlation for each feature element. The distance between each feature element from the average principal component (here, 0.5) is considered here. Thus, those feature elements fulfilling this condition were retained for further computing. The selected feature elements were hypothesized to have a higher impact on prediction results. Those feature elements with a distance lower than the average principal component value of 0.5 were dropped from the further computation. In this manner, it helped retain only statistically significant feature elements to perform better learning and reduce redundant processing costs. The finally selected feature elements were used for further resampling and NoSQL-IA prediction or allied classification.

**5.3.3. Wilcoxon Mann-Whitney Test.** This method is also called the significant predictor test. Wilcoxon Mann-Whitney Test also called Wilcoxon Rank Sum Test (WRST) is a kind of nonparametric test with independent samples. It assesses the correlation between the feature elements and their likelihood of NoSQL-IA prediction accuracy. Here, WRST was applied to estimate the correlation between the feature elements and allied corresponding class labels to perform NoSQL-IA prediction. The extracted feature elements are hypothesized to be the independent variable; on the contrary, the likelihood of NoSQL-IA is taken as the dependent variable. This approach enabled estimating the  $p$  value for each data element with respect to the corresponding significance towards NoSQL-IA probability, and therefore, employing the  $p$  value of each feature element, it labeled each data element as significant or insignificant. It helped identify a set of samples having an impact on NoSQL-IA probability and allied accuracy. It helped retain only those significant feature elements which had a significant impact on NoSQL-IA prediction.

**5.3.4. Variance Threshold Feature Selection.** The variance threshold method is a baseline concept for feature selection. The ability to eliminate those feature elements whose variance does not fulfill some predefined or expected threshold makes it a goal-oriented feature selection approach. It

assumes that the feature elements with high variance can have more significant information to make prediction. In this reference, in our work, the variance threshold method dropped all zero-variance feature elements (the feature elements with the same value in all samples). Unlike correlation test-based methods, the employed variance threshold method does not consider any correlation or relationship between features. We considered variance threshold as 0, signifying features with zero-variance, and therefore, identifying the feature elements with zero-variance, it dropped those specific feature elements and retained the set of feature elements with nonzero variance for further processing. Thus, applying these four feature selection methods, the suitable set of feature elements was retained for further computation.

**5.4. Feature Resampling.** This is a matter of the fact that the above-stated feature selection methods retained the optimal set of (distinct) features for NoSQL-IA training; however, the fact that the likelihood of NoSQL-IA intrusion query would be significantly lower than the normal query cannot be denied. In other words, in real-time NoSQL-IA data traces, the fraction of intrusion query is significantly lower than the normal queries, signifying the inevitable probability of class imbalance (or skewed data). Training a machine learning model over the skewed data or the class-imbalance training dataset can force the model to exhibit false-positive or skewed performance. To alleviate this problem, feature resampling can be of great significance. Towards feature resampling, the key methods used are random sampling, upsampling and downsampling. However, these methods have their own strengths as well as limitations. For instance, in random sampling, the samples from the minority class are selected arbitrarily and added to the original sample to increase the minority sample in the training set. Similarly, in UPS methods, the minority samples are increased using a certain method to reach uniform sample distribution. On the contrary, in DPS, the majority of samples are reduced to make minority samples sufficient for training. However, these approaches often give rise to the unbalanced data condition, which can impact NoSQL-IA prediction results. In this work, we performed resampling in such a manner that the minority samples are augmented with 95% of a confidence interval. We performed random duplication of the observations taken from the minority class that helped reinforce their respective values. However, such methods with sample duplication can give rise to iterative overfitting problems, and hence, we applied sampling strategy (SS), also called threshold adaptive sampling, to resample the input features. We applied  $SS=0.5$ . In this case, for a case of 500 majority class samples and 50 minority samples, it inculcated 250 minority samples to the original feature set. Here, our key motive was to increase the number of minority class samples to provide fairly sufficient examples for training. To further improve the performance and data efficacy, we applied SMOTE as one of the resampling methods. We generated synthetic positive samples using the k-NN algorithm. We applied 5-nearest neighborhood to the minority "NoSQL-IA" class, which was followed by equalization of the samples in such a manner that it yields

the number of the majority class same as the number of the minority class. Thus, in this work, a total of three resampling methods, including upsampling, downsampling, and SMOTE sampling, were applied distinctly over the selected features to assess the suitability of the best performance sampling method. The resampled outputs were processed for normalization so as to alleviate any possibility of overfitting.

**5.5. Feature Normalization.** In this paper, we applied Min-Max normalization over each feature set that mapped each input value to the scale of 0 to 1. Here, the Min-Max normalization algorithm, as defined in (15), mapped each data element in the range of [0-1]. It was achieved by transforming input features into the range of 0-1, linearly. The input data element  $x_i$  from feature element  $X$  was mapped to achieve the normalized value  $x'_i$  using (15). Here,  $\min(X)$  and  $\max(X)$  represents the minimum and maximum values of  $X$ , correspondingly.

$$Norm(x_i) = x'_i = \frac{x_i - \min(X)}{\max(X) - \min(X)}. \quad (15)$$

As depicted in Table 1, post normalization, a total of 12 feature sets were obtained with respect to the different input features. These features were processed for two-class classification using the different machine learning methods. The details of the classification methods used in this work are given as follows:

**5.6. NoSQL-IA Classification.** Unlike classical standalone classifier-based learning, in this work, we applied an ensemble learning-assisted consensus-based classification model. Being a two-class classification problem, each classifier classifies the data and labels it as 1 or 0, signifying NoSQL-IA query and normal query, respectively. In this work, a total of seven well-known machine learning classifiers were used to perform NoSQL-IA prediction or allied classification. These machine learning models are:

- (1) Naïve Bayes Algorithm (NB)
- (2) Support vector machine (SVM)
- (3) Decision tree (DT)
- (4) Logistic regression (LOGR)
- (5) k-NN (KN)
- (6) AdaBoost (ADAB)
- (7) Random forest (RF)
- (8) Extra Tree Ensemble Classifier (ETC)
- (9) XGBoost (XGB)

A brief of these machine learning classifiers is given in the subsequent sections.

**5.6.1. Naïve Bayes Algorithm.** Naïve Bayes is one of the predominantly used probabilistic classification approaches that apply Bayes' rules with autonomous assumptions to classify

input patterns. Being a probabilistic approach, it is also stated as an "independent feature model" which assumes that all allied features are independent and do not impact result decisively. It assumes that the existence of a particular feature in a class is not related to the presence of another feature. Functionally, the NB algorithm allocates an object  $x$  to the class  $e^* = \text{argmax}_d P(d|x)$  as per the Bayes' rule.

$$P(d|x) = \frac{P(x|d)P(d)}{P(x)}. \quad (16)$$

In (16),  $P(d)$  refers to the class-prior probability of  $c$ . The other parameter  $P(d|x)$  states the likelihood of  $x$  data element, while  $P(x)$  states the predictor prior probability and is defined as

$$P(x|d) = \prod_{i=1}^m P(x_i|d). \quad (17)$$

We applied a multinomial NB algorithm that, unlike Gaussian NB, learns on the basis of the count's frequency, signifying the number of times  $x_i$  occurs over  $n$  trails. Here, feature vectors state the frequency with which a specific event is caused by a multinomial function. NB algorithms classify each query as a normal query or NoSQL-IA query and label it as "0" and "1," respectively.

**5.6.2. Support Vector Machine (SVM).** SVM represents a kind of supervised learning approach for pattern mining and classification. The ability to learn and categorize input patterns based on the hyperplane makes it one of the most suitable algorithms for text classification, image processing, etc. Functionally, it learns over the input features and functions as nonprobabilistic binary classifier. To perform NoSQL-IA prediction, SVM reduces the generalization error over the unobserved input patterns, often called instances. To achieve it, it applied a structural risk reduction method. In this approach, support vector refers the training instances or the set of training data that calculates the hyperplane between the two or multiple types of data patterns to perform classification. To achieve it, it employs

$$Y' = w * \phi(x) + b. \quad (18)$$

In (18),  $\phi(x)$  states the nonlinear transform where it focuses on assigning the suitable values of the weight  $w$  and the bias  $b$  values to perform classification. The output  $Y'$  is estimated by reducing the regression-risk parameter, given as

$$R_{reg}(Y') = C * \sum_{i=0}^l \gamma(Y'_i - Y_i) + \frac{1}{2} * \|w\|^2. \quad (19)$$

In equation (19),  $C$  presents the penalty factor, while the

TABLE 1: Training data structure.

Input feature	Resampling	Normalized feature
<i>Feat_Word2Vec_NNNorm</i>	<i>(Feat_Word2Vec_NNNorm)_UpSampling</i>	<i>Norm(Feat_Word2Vec_NNNorm)_UpSampling</i>
	<i>(Feat_Word2Vec_NNNorm)_DownSampling</i>	<i>Norm(Feat_Word2Vec_NNNorm)_DownSampling</i>
	<i>(Feat_Word2Vec_NNNorm)_SMOTESampling</i>	<i>Norm(Feat_Word2Vec_NNNorm)_SMOTESampling</i>
<i>Feat_Word2Vec_CBOW</i>	<i>(Feat_Word2Vec_CBOW)_UpSampling</i>	<i>Norm(Feat_Word2Vec_CBOW)_UpSampling</i>
	<i>(Feat_Word2Vec_CBOW)_DownSampling</i>	<i>Norm(Feat_Word2Vec_CBOW)_DownSampling</i>
	<i>(Feat_Word2Vec_CBOW)_SMOTESampling</i>	<i>Norm(Feat_Word2Vec_CBOW)_SMOTESampling</i>
<i>Feat_GLOVE</i>	<i>(Feat_GLOVE)_UpSampling</i>	<i>Norm(Feat_GLOVE)_UpSampling</i>
	<i>(Feat_GLOVE)_DownSampling</i>	<i>Norm(Feat_GLOVE)_DownSampling</i>
	<i>(Feat_GLOVE)_SMOTESampling</i>	<i>Norm(Feat_GLOVE)_SMOTESampling</i>
<i>Feat_TF-IDF</i>	<i>(Feat_TF-IDF)_UpSampling</i>	<i>Norm(Feat_TF-IDF)_UpSampling</i>
	<i>(Feat_TF-IDF)_DownSampling</i>	<i>Norm(Feat_TF-IDF)_DownSampling</i>
	<i>(Feat_TF-IDF)_SMOTESampling</i>	<i>Norm(Feat_TF-IDF)_SMOTESampling</i>
<i>Feat_W2V</i>	<i>(Feat_W2V)_UpSampling</i>	<i>Norm(Feat_W2V)_UpSampling</i>
	<i>(Feat_W2V)_DownSampling</i>	<i>Norm(Feat_W2V)_DownSampling</i>
	<i>(Feat_W2V)_SMOTESampling</i>	<i>Norm(Feat_W2V)_SMOTESampling</i>
<i>Feat_COUTV</i>	<i>(Feat_COUTV)_UpSampling</i>	<i>Norm(Feat_COUTV)_UpSampling</i>
	<i>(Feat_COUTV)_DownSampling</i>	<i>Norm(Feat_COUTV)_DownSampling</i>
	<i>(Feat_COUTV)_SMOTESampling</i>	<i>Norm(Feat_COUTV)_SMOTESampling</i>

cost function is  $\gamma$ . We estimated the weight value using

$$w = \sum_{j=1}^l (\alpha_j - \alpha_j^*) \phi(x_j). \quad (20)$$

In (20), the parameter  $\alpha$  and  $\alpha^*$  represent the nonzero value, often called Lagrange relaxation factor. Thus, the eventual output is obtained as

$$Y' = \sum_{j=1}^l (\alpha_j - \alpha_j^*) \phi(x_j) * \phi(x) + b = \sum_{j=1}^l (\alpha_j - \alpha_j^*) * K(x_j, x) + b. \quad (21)$$

Here,  $K(x_j, x)$  states the kernel function. In our proposed model, we applied the RBF kernel function to perform NoSQL-IA prediction or allied two-class (normal query and NoSQL-IA query) classification.

**5.6.3. Decision Tree (DT).** Decision tree (DT) being one of the most used association mining-based classifiers has evolved over the period due to its increasing significance and efficacy. It has emerged from the CART, ID3, C4.5, and C5.0 association rule mining models to serve classification tasks. Functionally, it originates at the root node, where applying the association rule in between the split condition, it divides the input features into multiple branches at each node of the tree. Subsequently, DT applies a factor called information gain ratio (IGR) for an individual branch of the tree. Functionally, once dividing the input data into mul-

iple branches, it generates other nodes that subsequently branch-off into other nodes with corresponding instances. Thus, it resembles a tree structure with multiple branches. In other words, it resembles a binary tree with a parent node and multiple children's nodes, possessing left child and right child. Let the parent node, left child, and right child be  $LC_d$  and  $RC_d$ , respectively. Now, with input feature  $x$ , the impurity measures  $I$ ; we estimate the total samples in  $P_d$ ,  $LC_d$ , and  $RC_d$ ; and decision tree method intends to enhance information gain using

$$Information\ Gain(P_d x) = I(P_d) - \frac{LC_n}{P_n} I(L.C_d) - \frac{RC_n}{P_n} I(R.C_d). \quad (22)$$

In this method, the impurity measure  $I$  is calculated by applying three distinct approaches named, Gini-Index  $I_G$ , Entropy  $I_H$ , and classification error  $I_E$ . These methods are mathematically defined as

$$I_H(n) = - \sum_{i=1}^c p(c|n) \log_2 p(c|n), \quad (23)$$

$$I_G(n) = 1 - \sum_{i=1}^c p(c|n)^2, \quad (24)$$

$$I_E(n) = 1 - \max \{p(c|n)\}. \quad (25)$$

In the above equations (23)–(24), the parameter  $c$  states the class(es), while a node is indicated by the term  $n$ . The



ratio of  $c$  to  $n$  is given by  $p(c|n)$ . In this manner, the proposed decision tree model labels each query as the normal query and NoSQL-IA query and labels each with “0” and “1,” respectively.

**5.6.4. Logistic Regression.** In the at-hand two-class classification problem, the logistic regression (LOGR) algorithm performs regression over the input features by retaining feature instances as the independent variable while assigning their corresponding SQLIA probability as the dependent variable. To achieve it, we executed regression .

$$\text{logit}[\pi(x)] = \beta_0 + \beta_1 X_1 + \beta_2 X_2 + \dots + \beta_m X_m. \quad (26)$$

In (26), the function  $\text{logit}[\pi(x)]$  signifies the dependent variable while  $x_i$  states the independent variable. This function helped in transforming the dichotomous outputs by logit function resulting into varying  $\pi(x)$  in the range of 0 to 1 to  $-\infty$  to  $+\infty$ . In (24), the parameter  $m$  states the total number of independent variables, while the NoSQL-IA probability is given by  $\pi$ . It estimated the probability of NoSQL-IA using

$$\pi(x) = \frac{e^{\beta_0 + \beta_1 X_1 + \beta_2 X_2 + \dots + \beta_m X_m}}{1 + e^{\beta_0 + \beta_1 X_1 + \beta_2 X_2 + \dots + \beta_m X_m}}. \quad (27)$$

**5.6.5. k-NN Algorithm.** k-NN (k-nearest neighbor) is one of the most popular models that classify unlabeled observations or patterns by assigning it the class of the most similar labeled examples. The ease of implementation of k-NN makes it one of the most used classifiers for the different data mining and regression predictive tasks. Typically, k-NN algorithm applies Euclidean distance to estimate interattribute distance using

$$D(p, q) = \sqrt{(p_1 - q_1)^2 + (p_2 - q_2)^2 + \dots + (p_n - q_n)^2}. \quad (28)$$

In (28),  $p$  and  $q$  are subjected to be compared with  $n$  features.

The efficiency of the k-NN algorithm depends on the value of  $k$  that decides how many neighbours can be selected for classification. Selection of an optimal  $k$  value helps achieve better performance. The large value of  $k$  minimizes the effect of a variance imposed by random error and forces it to be used with a low number of samples. The force maintaining an optimal balance between performance and computation (by selecting the optimal  $k$  value) depends on maintaining a better balance between overfitting and underfitting. In most of the existing methods, authors assigned the value of  $k$  as the square root of the number of instances in the training data; however, its efficacy for large-scale data with varying patterns cannot be guaranteed. In some works,  $k$  is assigned on the basis of the sample size by employing the cross-validation concept, however, at the cost of increased computation and time. To alleviate such problems, in this paper, a concept called  $kTree$  learning was applied, which helped us learn different  $k$  values for the different training samples. For training,  $kTree$  at first performs learning the

optimal value of  $k$  for all data samples by applying the sparse reconstruction method. Subsequently, it constructs a decision tree (here we call  $kTree$ ) using training samples and the learned optimal  $k$  values. During testing,  $kTree$  model outputs the value of  $k$  swiftly for each data (testing data) sample, which is then followed by  $k-NN$  classification using learned optimal  $k$  value and data training. Eventually, the proposed  $k-NN$  model classifies each query as a NoSQL-IA query and normal query and labels them with 1 and 0, respectively.

**5.6.6. AdaBoost.** AdaBoost falls under the category of ensemble learning method designed as an adaptive bootstrap classifier. As the name indicates, it is called adaptive boosting as the learning weight parameters are reinforced for each instance, where it assigns higher weights to the wrongly classified data elements or instances. Functionally, being a meta-estimator, it is initiated by fitting a classifier deployed over the original datasets. Subsequently, it fits supplementary replicas of the classifiers on the same data but in that it adjusts the weights of the wrongly classified instances. In this manner, the replicated classifiers focus more on complex classification cases. In this manner, a number of weak learners are transformed into the stronger learner and hence achieves more accurate performance than the classical standalone classifier. In this work, AdaBoost classifies each input query into two classes, NoSQL-IA query and the normal query, and assigns a label to each with 1 and 0, correspondingly.

**5.6.7. Random Forest (RF) Algorithm.** Similar to the AdaBoost classifier, random forest (RF) algorithm is a kind of ensemble learning method. It embodies multiple tree-structured learners giving rise to a new ensemble learning environment. In the constituted tree-structures, each tree performs classification distinctly over the input instances and labels data with a vote of class category. In the case of data classes be  $N$ , then it selects a sample containing  $N$  cases arbitrarily from the input feature vector. The selected sample is later employed as the training set to form a tree. With  $M$  input instances, it divides the input instances  $m$  to split the node, where the value of  $m$  remains fixed throughout the forest development. In this manner, each tree develops a large tree structure with multiple branches and subtrees. Typically, RF needs lower tuning parameters that make it superior to other methods like Naïve Bayes, k-NN, and DT. RF, being the bootstrapped learning model, is mathematically derived as

$$\{h(x, \theta_k), k = 1, 2, \dots, i \dots\}. \quad (29)$$

In (29),  $h$  states the RF classifier, while  $\{\theta_k\}$  is the arbitrary vector distributed uniformly where each tree provides a vote for the high likelihood class for an input instance  $x$ . The size of  $\theta$  often depends on its use towards tree formation. RF algorithm employs a bootstrapped subset of training samples which helps to perform training over each tree throughout the forest. This process applies almost 70% of the training data, while the remaining data is applied as the out-of-bag (OOB) samples. The OOB samples are

employed to perform cross-validation that helps achieve higher accuracy [30]. As stated, functionally, RF as an ensemble model houses  $T$  trees, and thus, during training, the DTs are independently formed onto the bootstrap training set by applying randomly selected data. Noticeably, this approach applies feature selection methods like bagging and random subspace algorithm. In the proposed RF model, DT is constituted by using the following approach.

- (i) Choose the training sample by replacing it from the original training data  $S$ . In this work, OOB samples (30%), which are except the bootstrapped sample, are applied to estimate the misclassification error
- (ii) Select  $M \leq D$  features randomly and select the best split by applying Gini-Index method
- (iii) Develop tree to the highest depth

Over the classification process, the input data  $x$  is classified by traversing each tree until it reaches the leaf-node. Subsequently, it results in the classification output with the decision function  $h$ , which is deployed to each leaf node. In this manner, the final class label  $y$  is obtained by choosing the class having the highest rank or the votes. The final output is defined as

$$y = \underset{c \in \{1, 2, \dots, C\}}{\operatorname{argm}} \sum_{t: h_t(x)=c}^T 1. \quad (30)$$

**5.6.8. Extra Tree Classifier (ETC).** Similar to the above-discussed AdaBoost and RF ensemble methods, ETC forms a set of unpruned DTs by applying top-down concept. However, unlike RF it applies random instance as well as cut-point selection when performing tree-split. ETC distinguishes itself from other tree-based ensemble learning algorithms in reference to two factors. The first is that it divides nodes by choosing cut-points arbitrarily and by using the complete training sample. To be noted, unlike ETC, RF algorithm applies a bootstrap replica of the DT to form tree structure. The second distinguishing fact is that the classified results of all the encompassing trees are joined together to yield the final prediction result by applying the maximum voting ensemble (MVE) concept. The prime motive behind ETC is that the overall randomization of the cut-point and instances with ensemble averaging minimizes the variance in comparison to the weaker randomization methods, as applied in other ensemble approaches like RF and AdaBoost. In addition, the use of original training data rather than the bootstrap replicas alleviates the likelihood of any probable classification bias. Consequently, it helps ETC to achieve higher accuracy.

Thus, the proposed model applied these algorithms distinctly toward two-class classification to classify each input query as a NoSQL-IA query and normal query and labels them as 1 and 0, respectively. Here, our key motive was to identify the best set of feature engineering methods and the classifier performing the best performance towards NoSQL-IA intrusion prediction for Interoperable e-

Healthcare Infrastructure security. A detailed discussion of the overall simulation results and allied inferences is given in the subsequent section.

## 6. Results and Discussion

This research work mainly focused on developing a robust and highly efficient NoSQL-IA prediction model for interoperable e-Healthcare systems to support seamless and reliable services. Unlike SQLIA methods which are often developed based on certain predefined syntax structure learning or term-matching concepts, this model considered distributed dynamic data structure resembling NoSQL databases where the data can be in heterogeneous data format. The likelihood of data heterogeneity and unstructuredness can be severe in the case of interoperable e-Healthcare systems that often support NoSQL database systems or infrastructures. In such a complex operating environment, the likelihood of intrusion attacks can be more probable, which can cause data breaches, manipulation, and even ransomware kinds of attacks. On the other hand, detecting aforesaid adversaries over interoperable e-Healthcare infrastructures with the large number of users can be highly complex and almost infeasible with manual test approaches or classical black-box techniques. To address these challenges, it was inevitable to exploit the maximum possible latent or semantic information from queries for highly advanced machine learning-based prediction. Considering the aforesaid challenges and allied scope, in this work, we formulated NoSQL-IA prediction as a semantic feature learning and natural language programming (NLP) problem. In addition, recalling the fact that the efficacy of any machine learning-driven NLP model(s) depends on the feature superiority and classification (computing) environment, we focused our effort on improving features as well as the overall computing environment. Our overall research intended to identify the optimal set of features and allied computing environment that could provide optimal performance toward NoSQL-IA prediction. Though there is no significant effort made so far towards NoSQL-IA prediction; however, for different intrusion detection or allied NLP problem, authors have claimed different features and allied computing environments to have better performance. However, no effort is available which could generalize the optimal feature and allied computing models towards NoSQL-IA or other intrusion detection or prediction systems. Considering this fact, we applied multiple semantic feature extraction methods along with the different feature selection, resampling, and classification models. Here, the prime motive was to identify the best performing feature and corresponding computing environment (such as feature selection method, resampling method, and classification model) so as to provide an optimal NoSQL-IA prediction solution which would perform gate-level intrusion detection as well as within-database intrusion identification and classification.

To achieve it, at first, we prepared our own synthetic data in sync with a real-time interoperable e-Healthcare system. The prepared data comprised a total of 14454 queries or transaction traces with almost 1400 intrusion queries.

Once collecting the raw heterogeneous input data, we processed for preprocessing by applying tokenization followed by stopping words removal. Subsequently, unlike classical SQL-IA methods that often use structural or syntax information to perform intrusion detection, we applied the well-known word-embedding concepts to extract semantic features from each query. Here, we employed a total of five different semantic feature extraction methods, including Count Vectorizer, TF-IDF, Word2Vec, CBOW, Skip Gram, and GLOVE. Here, our key motive was to identify the best performing feature which could enable more efficient and reliable NoSQL-IA prediction. Undeniably, aforesaid methods yield high-dimensional semantic features towards learning, however, at the cost of increased computation. To alleviate this problem, we applied five different kinds of feature selection methods, including Select-K-Best (SKB), PCA, WRST, VTFS, and combined hybrid feature (AF). Here, we intended to assess with what specific feature selection model the optimal set of feature vectors could be obtained to perform NoSQL-IA prediction. To be noted, the intrusion queries are merely 9.7% of the total queries or data size. In other words, in the considered dataset, almost 92.3% of the samples or feature instances are majority class (i.e., normal query), while merely 9.7% of the samples are intrusion queries (say, minority class). This, as a result, shows the case of the imbalanced dataset and hence directly training a machine learning model with this data can force machine learning to undergo skewed performance or false-positive outputs. To alleviate this problem, we performed a resampling method, where we applied three different kinds of resampling methods, including downsampling (DNS), upsampling (UPS), and SMOTE sampling. Thus, once resampling the input features, it applied Min-Max normalization that mapped each input feature element in the range of 0-1 and thus helped in alleviating any possibility of overfitting or convergence. Once normalizing the inputs (from each feature sets over varied feature selection and resampling), each feature vector was processed for two-class classification using different machine learning models that classify each input query as the normal query or NoSQL-IA query and label them with 0 and 1, respectively. More specifically, we applied Naïve Bayes (with multinomial kernel function) classifier, k-NN, logistic regression (LOGR), decision tree (DT), support vector machine (with radial basis function kernel SVMR), AdaBoost (ADAB), random forest (RF), Extra Tree Classifier (ETC), and XGBoost (XGB). To assess relative performance towards NoSQL-IA prediction, we estimated confusion matrix and measured classification accuracy, F-Measure and AUC performance for each input feature, feature selection methods, resampling methods, and eventual classification models. The key motive was to identify the best performing feature and corresponding computing environment for the NoSQL-IA system to be used for interoperable e-Healthcare services or systems. The overall proposed model was developed using the Anaconda Spark development platform, where the programs were developed in Python language and simulated over Microsoft Windows operating system, armored with 8 GB RAM and a 2.82 GHz processor. To assess efficacy of the overall proposed model,

the performance characterization is done in two phases: intramodel characterization and intermodel characterization. The detailed discussion of the results obtained is given as follows:

*6.1. Intramodel Characterization.* The performance assessment for the simulated results and allied inferences for the different features, feature selection methods, resampling approaches, and classifiers is discussed in intramodel characterization. Here, we intended to identify the best set of semantic features and allied computing environments (i.e., feature selection, resampling, and classification method(s)) for the NoSQL-IA prediction task.

*6.1.1. Assessing Semantic Feature Efficacy.* Since different feature extraction methods claim their superiority over others in analytics or even in intrusion detection systems, we examined the relative efficacy of the different feature extraction methods toward NoSQL-IA prediction. As already discussed in the previous section, this work employed a total of six different word-embedding concepts, including Count Vectorizer (COUTV), TF-IDF, CBOW, SKG, Word2Vec (W2V), and GLOVE. A confusion matrix is an  $n \times n$  matrix; each row reflects the true classification of observation, and each column represents the anticipated classification (or vice versa). When looking at a confusion matrix, the number of correct classifications may be determined by looking at the values on the diagonal; a successful model will have high counts (diagonal) and low counts off the diagonal. Furthermore, analyzing the highest count, not on the diagonal, can reveal the model's struggle. These evaluations are used to find scenarios when the model's accuracy is high, yet it consistently misclassifies the same data. The ratio of accurately anticipated positive observations to the predicted positive observations is called "precision." The ratio of accurately predicted positive observations to all positive observations in the actual positive class is called "recall." The weighted average of precision and recall is the F1-Measure. As a result, this score considers both false positives and false negatives. Although it is not as intuitive as accuracy, F1 is frequently more advantageous than accuracy, especially if the class distribution is unequal. When false positives and false negatives have equivalent costs, accuracy works well. It is the best to look at precision and recall if false positives and false negatives are considerably different. These different semantic algorithms have distinct computing or feature vector representation and hence can have different efficacies towards NoSQL-IA prediction. Figures 3–5 present the prediction accuracy (%), F-Measure, and AUC performance by these feature extraction methods, respectively.

Observing Figure 3, it can easily be found that N-Skip Gram method and CBOW algorithm exhibits superior accuracy to other semantic approaches. More specifically, N-Skip Gram features exhibited an accuracy of 97.63%, followed by the CBOW feature (96.41%), Gensim Word2Vec (96.2%), COUTV (94.7%), TF-IDF (94.2%), and GLOVE (88.68%). This result reveals that being distributed and significantly heterogeneous (dynamic in nature) in nature, approaches such as TF-IDF and Count Vectorizer (COUTV) are less

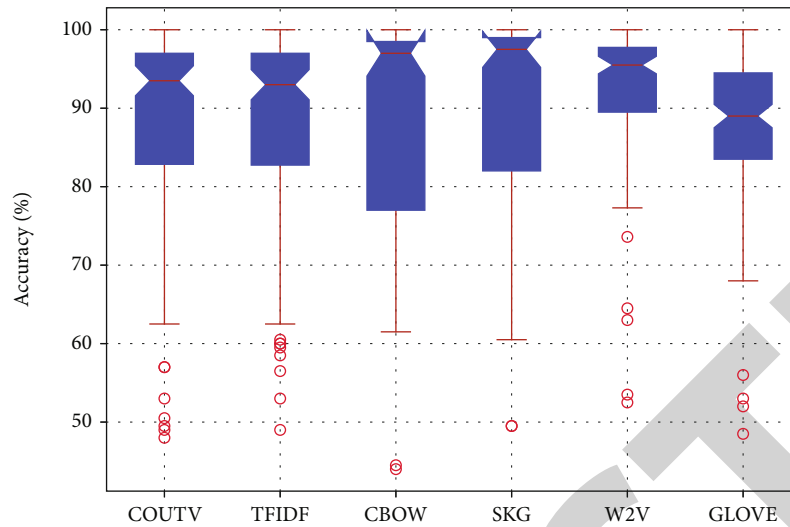


FIGURE 3: Accuracy of the different semantic features towards NoSQL-IA prediction.

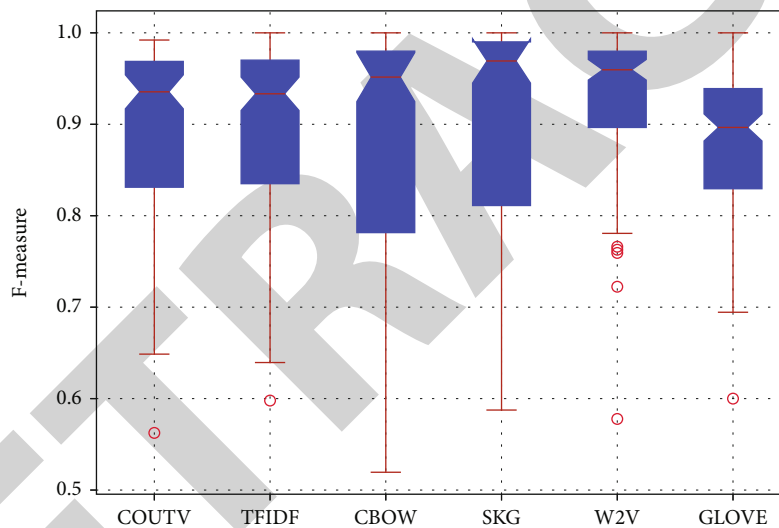


FIGURE 4: F-Measure of the different semantic features towards NoSQL-IA prediction.

significant as these methods often exploit the number of occurrences of the tokens rather than the allied latent information. On the contrary, Word2Vec (W2V), N-Skip Gram (SKG), and CBOW exploit interconnected semantic feature information to derive numerous (feature-vector) representations. In this manner, these methods do not lose feature information that helps better training and hence higher accuracy (Figure 3). GLOVE, a Wikipedia-driven pretrained feature set too, has been found limited over the proposed synthetic data environment, where the data queries were obtained from the varied users with autonomous query feeds and entries. The disparity of trained feature elements and input query variables has resulted in reduced performance for GLOVE, affirming the fact that a pretrained model like GLOVE or even W2V is required to be properly trained with the input data rather than generic dictionary variables or tokens.

Figure 4 presents the F-Measure performance of the different feature extraction methods. Similar to the accuracy performance, as discussed above (Figure 3), SKG, W2V, and CBOW features have shown superior F-score or F-Measure, signifying efficient performance in terms of sensitivity (recall) and precision. It affirms their suitability for the NoSQL-IA prediction task, which can undergo class-imbalance conditions. These features (i.e., SKG, W2V, and CBOW) can perform reliably without undergoing any false-positive or skewed performance. Noticeably, F-Measure with SKG feature was observed as 0.962, followed by W2V (0.957), CBOW (0.949), TF-IDF (0.936), COUTV (0.933), and GLOVE (0.904). Similar to accuracy performance (Figure 3), GLOVE exhibited the minimal F-Measure performance, signifying its inferiority over the other word-embedding methods like SKG, W2V, and CBOW. Figure 5 depicts AUC performance, where SKG

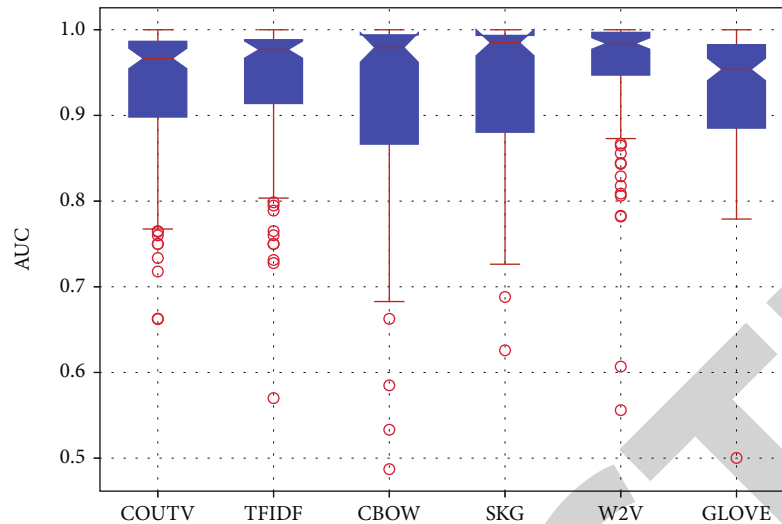


FIGURE 5: AUC of the different semantic features towards NoSQL-IA prediction.

has been found superior over the other methods or features with its AUC value of 0.976, though other word-embedding methods like W2V and CBOW too exhibited AUC of 0.973, and 0.971, respectively. TF-IDF feature exhibited an AUC of 0.969, followed by COUTV (0.951) and GLOVE (0.947).

An interesting fact is that amongst all six different features, SKG and Word2Vec semantic features exhibited a minimum outlier or deviation in performance than other approaches and hence can be stated as the superior method towards reliable NoSQL-IA prediction tasks. Therefore, either of SKG or Word2Vec method can be applied towards semantic feature-driven NoSQL-IA prediction task.

**6.1.2. Assessing Feature Selection Efficacy.** In this work, we applied four different kinds of feature selection methods named Significant K-Best (SKB), principal component analysis (PCA), Wilcoxon Rank Sum Test (WRST), and variance threshold feature selection (VTFS). In addition to these, we merged different features (i.e., COUTV, TF-IDF, CBOW, SKG, W2V, and GLOVE) together to generate a hybrid feature set named all features (AF). For these different selected features, the performance was characterized in terms of accuracy (Figure 6), F-measure (Figure 7), and AUC (Figure 8). Figure 6 reveals that amongst the different feature selection methods, WRST exhibits the superior accuracy performance (accuracy 95.7%). The other methods like VTFS and PCA feature too exhibit the accuracy of 95.2% and 94.6%, respectively. Significant predictor test (SKB), which exploits interelement correlation towards prediction, could achieve the accuracy of 92.7%, while the hybrid feature (say, AF) performed poor with the classification accuracy of merely 87.8%. This can be mainly because of feature heterogeneity and ambiguity over learning a gigantic feature element together. This result (Figure 6) reveals that WRST (and VTFS as well) can be well-suited for feature selection in NLP-driven NoSQL-IA prediction tasks.

Figure 7 shows F-Measure performance by the different feature selection methods. As depicted, similar to Figure 6, WRST, VTFS, and PCA have exhibited superior perfor-

mance (WRST (0.956), PCA (0.951), and VTFS (0.948)) over other methods like SKB (0.927). It also confirms that the amalgamation of the different features together can force the model to undergo convergence or overfitting and hence can result in poor performance (AF-0.86).

Considering AUC performance over the different feature selection methods, the result (Figure 8) exhibits that the WRST method yields higher AUC (0.984) than other methods like (PCA (0.978), SKB (0.977), VTFS (0.972), and AF (0.941)). Noticeably, higher AUC affirms robustness of the method(s) towards prediction over nonlinear, heterogeneous, and imbalanced data environment like NoSQL-IA prediction system. It affirms that WRST feature selection can be a superior solution towards NoSQL-IA prediction.

**6.1.3. Assessing Feature Resampling.** As already stated, the current NoSQL-IA prediction problem undergoes class imbalance, and hence, to alleviate it, we employed three different kinds of resampling methods: SMOTE, upsampling (UPS), and downsampling (DNS). The accuracy performance, as depicted in Figure 9, reveals that SMOTE sampling performs an accuracy of 96.4%, which is almost the same as UPS which exhibited a prediction accuracy of 96.32%, though DNS underwent reduced performance with an accuracy of 88.96%.

Considering F-Measure performance, the result (Figure 10) reveals that UPS and SMOTE perform similar approximate performance (F-measure 0.952), which is higher than the downsampling method DNS (0.875). A similar performance can be observed in Figure 11 as well, where UPS exhibited superior AUC (0.988) followed by SMOTE (0.983) and DNS (0.879). Noticeably, though upsampling (UPS) method has exhibited relatively better performance; however, the allied probability of skewed data cannot be universally eliminated. High upsampling might even skew the data and hence can give rise to the data imbalance. Therefore, in comparison to UPS, SMOTE sampling can be a better alternative for NoSQL-IA prediction.

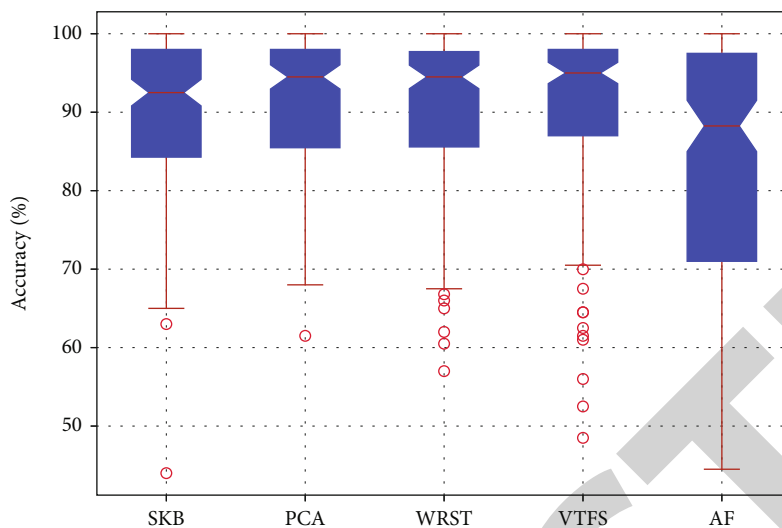


FIGURE 6: Accuracy with the different features selection methods towards NoSQL-IA prediction.

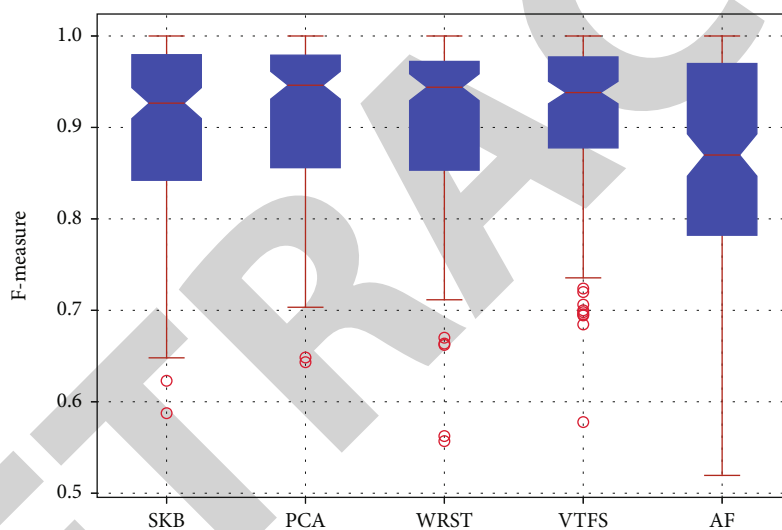


FIGURE 7: F-Measure with the different features selection methods towards NoSQL-IA prediction.

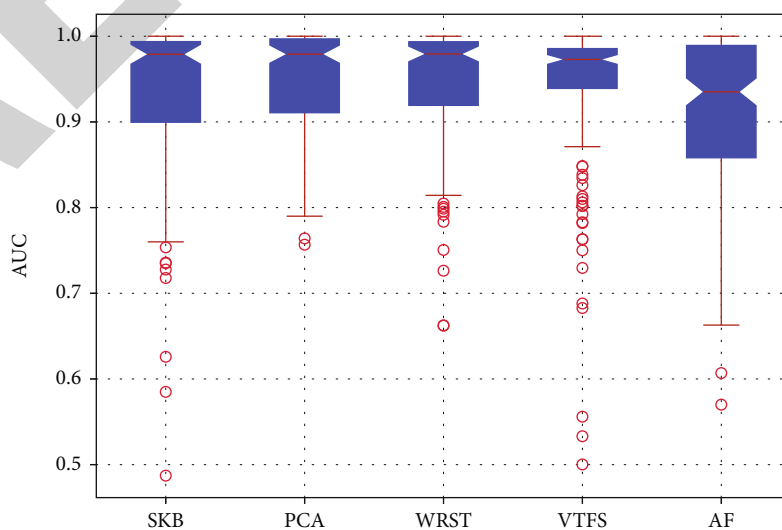


FIGURE 8: AUC with the different features selection methods towards NoSQL-IA prediction.

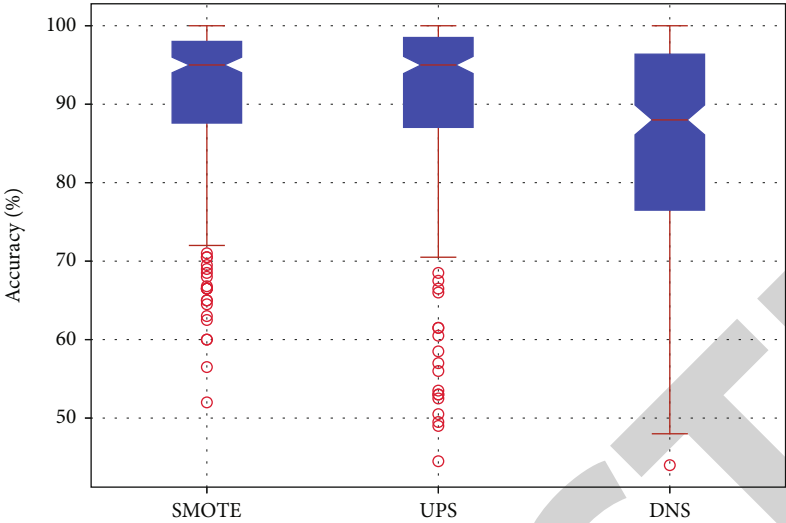


FIGURE 9: Accuracy (%) with the different features resampling methods towards NoSQL-IA prediction.

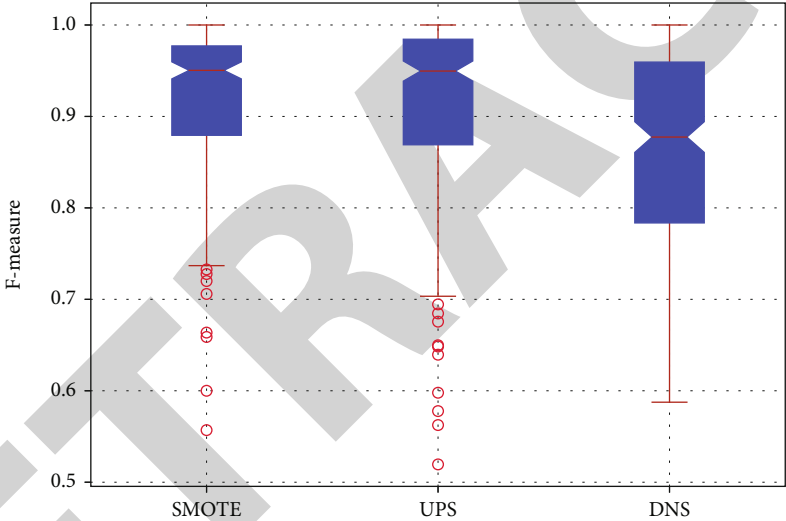


FIGURE 10: F-Measure with the different features resampling methods towards NoSQL-IA prediction.

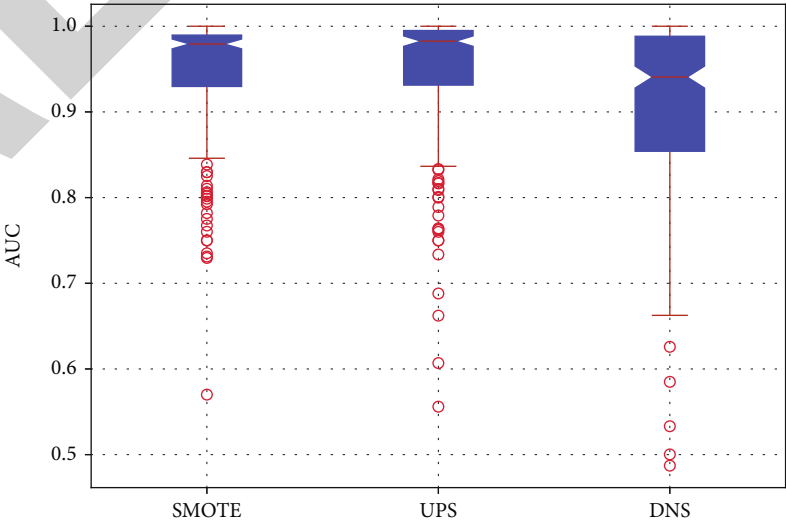


FIGURE 11: AUC with the different features resampling methods towards NoSQL-IA prediction.

*6.1.4. Assessing NoSQL-IA Classification.* In this work, we exploited the relative performance of the different machine learning algorithms toward NoSQL-IA prediction. The relative performance outputs by the different machine learning algorithms are given in Figures 12–14. The depth assessment revealed that the average accuracy by Naïve Bayes (multinomial kernel function) method was 96.98%, while k-NN could achieve the average accuracy of 74.37%. The other methods like DT, LOGR, SVM, ADAB, RF, ETC, and XGB exhibited the prediction accuracy of 87.61%, 92.37%, 88.04%, 91.50%, 98.86%, 89.51%, and 93.47%, respectively. The performance assessment reveals that amongst the different machine learning models, the random forest (RF) method exhibited superior performance with the highest accuracy of 98.86%.

The average F-Measure performance by the different machine learning classifiers exhibited that similar to the accuracy output (Figure 12), the RF classifier exhibited the highest F-Measure of 0.974. The other methods like NB, k-NN, DT, LOGR, SVM, ADAB, ETC, and XGB could exhibit the average F-Measure of 0.89, 0.794, 0.90, 0.933, 0.888, 0.936, 0.867, and 0.911, respectively. Though the F-Measure performance by these algorithms is higher than the hypothetical scale of 0.6; however, the results (Figures 12 and 13) affirm that RF method can be vital towards NoSQL-IA prediction system, where it can yield higher accuracy than the other standalone methods. To be noted, RF being the bootstrapped decision tree has confirmed its superiority over the standalone DT method and hence performs in sync with the development goal (i.e., to achieve better performance than the classical or standalone DT algorithm).

Figure 14 shows AUC performance by the different machine learning classifiers towards NoSQL-IA prediction. The average AUC by NB, k-NN, DT, LOGR, SVMR, ADAB, RF, ETC, and XGB was obtained as 0.958, 0.846, 0.923, 0.956, 0.905, 0.975, 0.987, 0.920, and 0.954, respectively. Observing result, it can be found that the RF algorithm performs better AUC (0.987) than other methods toward NoSQL-IA prediction.

Similar to the above statement, the majority of NLP problems or classification problems hypothesize that a model with AUC of more than 0.66 (sometime 0.6) is supposed to be efficient towards analytics problems; though all classifiers have achieved higher AUC, and it can be used for real-time computation, the relative performance confirms the robustness of RF over other methods. The overall classification or allied prediction results (Figures 12–14) confirm that RF can be a superior ensemble learning model for NoSQL-IA prediction.

Considering overall performance, it can easily be found that towards NoSQL-IA prediction task, the use of word-embedding methods like N-Skip Gram and Word2Vec can be a suitable semantic feature, while WRST can be a suitable and lightweight feature selection approach. WRST can not only retain significant features, but can also reduce data search space so as to improve overall NoSQL-IA prediction. It makes it suitable towards real-time applications demanding a swift and reliable analytics platform for intrusion detection. Similarly, in sync with aforesaid Word2Vec

(word-embedding) features and corresponding WRST feature selection, the use of SMOTE sampling can help alleviate any possible data-imbalance problem. It can help improve overall accuracy and reliability even under class-imbalanced conditions. Finally, the SMOTE resampled feature vector (post-normalization) can be classified using the RF algorithm, a bootstrapped ensemble learning classifier to yield optimal and most efficient (say, reliable and highly accurate) NoSQL-IA prediction model for real-time intrusion detection in interoperable e-Healthcare system of services.

*6.2. Intermodel Characterization.* In this section, the relative performance assessment is done with reference to the existing methods. This is the matter of fact that a few efforts have been made towards NoSQL-IA detection; however, the extensive survey and analysis identified a few recent works including the efforts in [41, 42]. Authors in [41] focused on intrusion detection in distributed dynamic datasets with multiple users. The data construction proposed in [41] was followed in this work, where considering heterogeneous data nature and distributed dynamically in nature MongoDB database was considered. To be noted, amongst NoSQL databases, MongoDB is a kind of document-based database, while other NoSQL databases like Couchbase, Dynamo, Redis, Riak, and OrientDB store data in the form of keys and values. Similarly, Cassandra, HBase, vertical stores data in column-oriented architecture, Neo4J, Allegro Graph, and Stardog are also the kind of NoSQL databases that store data in the form of graphs. Considering the heterogeneous nature of interoperable healthcare datasets and allied characteristics [44], we considered MongoDB as the test dataset, where the data is in the form of a document and hence applying word-embedding was easier over the continuous documents or allied corpus. Thus, considering the similarity of data and motive, we compared the performance of our proposed NoSQL-IA prediction model with [41, 42]. Comparison model one [41] has applied One-class SVM (OC-SVM), whereas model two [42] has applied the Bayesian network as K2 algorithm (simulated onto WEKA tool) for intrusion detection over NoSQL data. Noticeably, both these datasets employed MongoDB data structure which is quite common in interoperable system designs. The relative performance assessment revealed that the average AUC performance in [41] was 0.959, which is lower in comparison to our proposed NoSQL-IA prediction model, which exhibited an average AUC of 0.981 with RF classifier. Interestingly, with an SVM classifier, our proposed NoSQL-IA model could achieve the average AUC of 0.905, which is lower than both our proposed RF-based prediction as well as the existing OC-SVM-based intrusion detection model [41]. It signifies that the use of ensemble learning methods like RF, XGB, and ETC can be superior to the standalone classifier for NoSQL intrusion detection and classification. Authors in [42] applied the K2 algorithm for intrusion detection, where the different NoSQL datasets like KDD99, DARPA1998, and DARPA1999 were applied as input data for intrusion detection. Though aforesaid datasets belong to NoSQL category, however, it differs from the real-time intrusion cases like



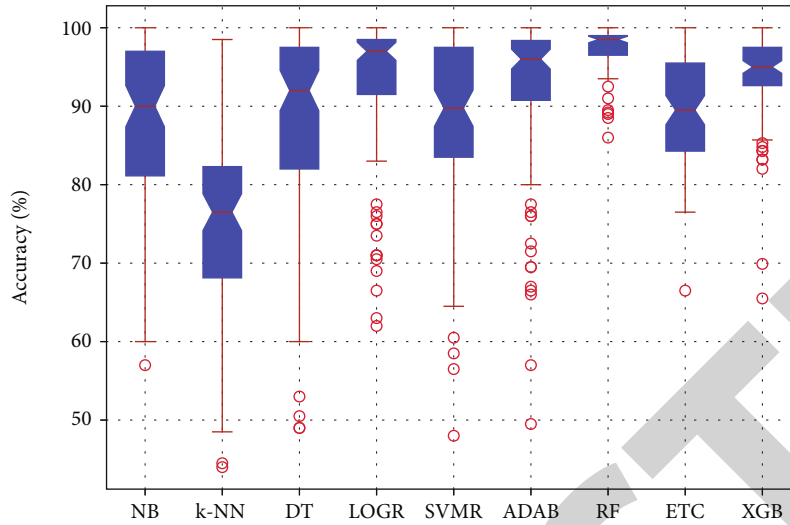


FIGURE 12: Accuracy with the different classifiers towards NoSQL-IA prediction.

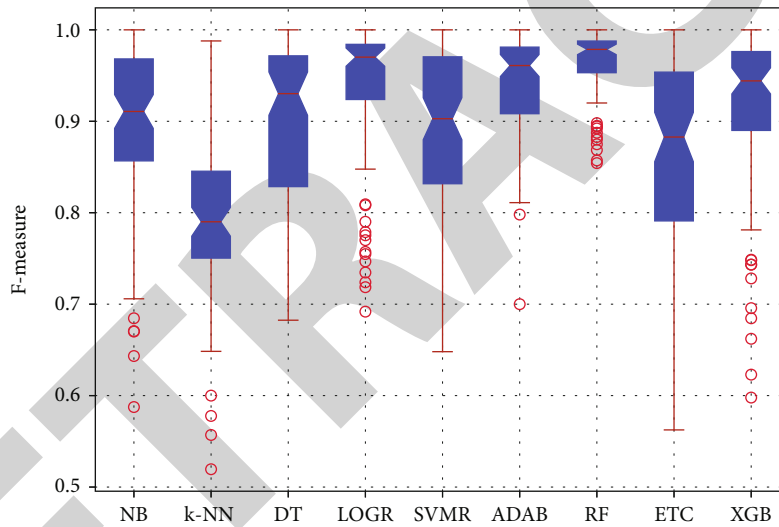


FIGURE 13: F-Measure with the different classifiers towards NoSQL-IA prediction.

camouflage query-driven attack, bots driven attack, mimicking attacks, etc. To represent their model as a NoSQL system, the authors merged aforesaid datasets (i.e., KDD99, DARPA1998, and DARPA1999) to generate a MongoDB dataset for further analysis. To improve feature efficiency, authors [42] applied factorial multiple correspondence analysis (FMCA) method. On the contrary, in our proposed model, we employed multiple highly robust statistical analysis approaches to retain the most significant features while guaranteeing their semantic feature retention. The data considered in [42] encompassed multiple datasets and hence possessed different attack conditions. Considering this fact, we averaged the accuracy performance of [42] and found that the average intrusion detection accuracy of their model was 92.37%. On the contrary, the average NoSQL-IA prediction accuracy by our proposed model (with RF classifier) is 98.86%. The relative performance with the existing methods [41, 42] reveals that the proposed NoSQL-IA prediction

approach with Word2Vec word-embedding (semantic) features processed with WTFS feature selection, SMOTE sampling, Min-Max normalization, and RF classification yields better performance than any other existing NoSQL-IA prediction or classification approaches. Authors in [43] applied different machine learning methods towards intrusion detection in MongoDB-driven analytics. The recall and precision performance revealed that the highest recall or sensitivity with RF was 0.9137, followed by k-NN (0.8756), DT (0.8725), and Naïve Bayes (NB) (0.8720). Similar simulation results were obtained in the form of precision parameters. However, it indicates lower performance than the proposed NoSQL-IA prediction model. Recall and precision are the key driving elements of F-score or F-Measure, and therefore, higher value of F-Measure (0.937) of the proposed model indicates the higher value of precision and recall. It indicates superior performance by our proposed RF-driven NoSQL-IA prediction performance. Thus, observing overall results

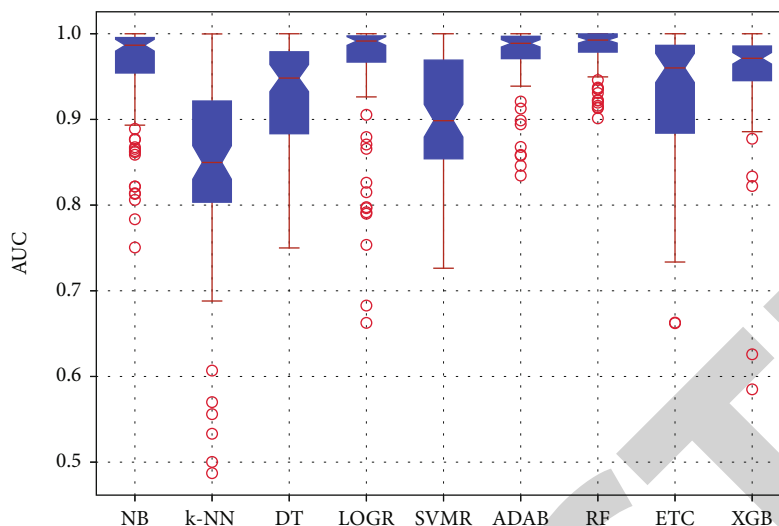


FIGURE 14: AUC with the different classifiers towards NoSQL-IA prediction.

and allied inferences, it can be stated that the proposed NoSQL-IA model exhibits superior performance to the other state-of-the-art methods. The research conclusion and allied inferences are given in the subsequent section.

## 7. Conclusion

This paper mainly focused on achieving an optimal set of computing environments for highly efficient intrusion detection systems for interoperable e-Healthcare systems. In sync with the aforesaid motive, this research made an effort to address the key real-time problems, including data heterogeneity, minimal intelligibility over interoperable systems having multiple stakeholders, class imbalance, and diversified performance by the different machine learning models towards intrusion detection (and classification) in dynamic data structures or NoSQL databases. The research is limited to constructing the optimized semantic feature-based IDS model as part of NoSQL-IA. The study can be further extended to explore the possibility of keeping the model optimal with periodic retraining. The case of asynchronous IDA execution can be considered at the server level. Summarily, this work contributed a first of its kind NoSQL-IA detection and classification system to be used for interoperable e-Healthcare services. To address data heterogeneity over an interoperable multistakeholder environment, the proposed model employed the semantic feature learning concept BERT (Bidirectional Encoder Representations from Transformers) which is an open-source machine learning framework for natural language processing (NLP) that uses surrounding text to establish context to help computers learn the meaning of ambiguous language in the text data. There is a possibility of exploring the BERT pretrained framework for text classification considering the deployment environment and model serving the architecture as future scope of work. Since different algorithms claim their superiority over others in semantic feature retention, this work applied four different well-known algorithms, including Word2Vec, GLOVE, TF-IDF, and CBOW, for feature

extraction. Here, the motive was to identify the best performing semantic features for NoSQL-IA attack detection. The topic model Latent Dirichlet Allocation (LDA) is used to classify text in a document to a particular topic. It creates a Dirichlet distribution-based topic per document and word per topic model. The author in [55] discussed LDA and Word2Vec as a hybrid document feature extraction method. They obtain an F1 score of 0.8 for a topic of 250. Our input data is not of abstract group nature, and hence, this method shall not fit into the study's scope. Applying the aforesaid semantic feature extraction method imposes data search space to reduce computational overheads in real-time; the proposed model applied feature selection methods like PCA, WRST significant predictor test, Select-K-Best, and VTFS algorithms over the extracted features. The purpose of these feature selection methods was to reduce computational overhead so as to cope with the run-time demands. Subsequently, it applied resampling methods, which helped in alleviating any class-imbalance problem that can impose any machine learning model to undergo false-positive or skewed performance. More specifically, this work applied upsampling, random sampling, and SMOTE-ENN methods. Moreover, the use of Min-Max normalization helped alleviate the overfitting problem to support better training. The proposed model was trained over each input query and allied label, which helped in performing two-class classification, where it predicts each input query as a normal query or intrusion (or NoSQL-IA attack). To identify the best classification environment towards NoSQL-IA prediction, this work employed Naïve Bayes, decision tree, k-NN, gradient boosting, random forest, and XG-Boost algorithms. The depth performance assessment of the developed NoSQL-IA model revealed that the use of SKG, Word2Vec word-embedding features, followed by SMOTE resampling, and Random Forest classification can yield the most accurate and reliable performance towards intrusion prediction under heterogeneous interoperable e-Healthcare systems. The overall performance reveals that the proposed SKG semantic feature-driven model with WRST feature selection,

SMOTE resampling, Min–Max normalization, and RF classifier-based prediction yields a superior accuracy of 98.86%, F-Measure of 0.936, and AUC of 0.987. The aforesaid feature (i.e., SKG word-embedding or Word2Vec) with a computational environment (WRST as feature selection, SMOTE as resampling method, and Min–Max normalization followed by Random Forest ensemble classification) can yield optimal performance towards NoSQL-IA prediction in interoperable e-Healthcare systems. Since the proposed model was designed especially in sync with heterogeneous input queries and semantic features, its intelligibility affirms its suitability for real-time intrusion detection in e-Healthcare services.

## Data Availability

Data will be made available on request from the corresponding author.

## Conflicts of Interest

The authors declare that they have no conflicts of interest.

## Acknowledgments

Authors are thankful to the REVA University for the facilities provided to carry out the research.

## References

- [1] S. Srinivasan, "Compromises in healthcare privacy due to data breaches," *European Scientific Journal*, vol. 12, no. 10, pp. 91–98, 2016.
- [2] P. Dwivedi and M. K. Singha, "IoT based wearable healthcare system: post COVID-19," in *The Impact of the COVID-19 Pandemic on Green Societies*, pp. 305–321, Springer, Cham, 2021.
- [3] R. K. Garg, J. Bhola, and S. K. Soni, "Healthcare monitoring of mountaineers by low power wireless sensor networks," *Informatics in Medicine Unlocked*, vol. 27, article 100775, 2021.
- [4] M. Elhoseny, G. Ramírez-González, O. M. Abu-Elnasr, S. A. Shawkat, N. Arunkumar, and A. Farouk, "Secure medical data transmission model for IoT-based healthcare systems," *IEEE Access*, vol. 6, pp. 20596–20608, 2018.
- [5] A. Omotosho and J. Emuoyibofarhe, "A criticism of the current security, privacy and accountability issues in electronic health records," *International Journal of Applied Info.Systems*, vol. 7, no. 8, pp. 11–18, 2014.
- [6] R. Carroll, "Aspen Valley Hospital accused of patient-privacy breach," <http://www.aspentimes.com/news/22463520-113/aspen-valley-hospital-accused-of-patient-privacy-breach>.
- [7] M. Singh and G. Kaur, "A surveys of attacks in MANET," *International Journal of Advanced Research in Computer Science and Software Engineering*, vol. 3, no. 6, pp. 1631–1636, 2013.
- [8] A. Mehbodniya, I. Alam, S. Pande et al., "Financial fraud detection in healthcare using machine learning and deep learning techniques," *Security and Communication Networks*, vol. 2021, Article ID 9293877, 8 pages, 2021.
- [9] S. H. El-Sappagh and S. El-Masri, "A distributed clinical decision support system architecture," *Journal of King Saud University-Computer and Information Sciences*, vol. 26, no. 1, pp. 69–78, 2014.
- [10] O. Iroju, A. Soriyan, I. Gambo, and J. Olaleke, "Interoperability in healthcare: benefits, challenges and resolutions," *International Journal of Innovative and Applied Studies*, vol. 3, no. 1, pp. 262–270, 2013.
- [11] D. Kalra and B. G. Blobel, "Semantic interoperability of EHR systems," *Studies in Health Technology and Informatics*, vol. 127, pp. 231–245, 2007.
- [12] J. A. Kassem, C. De Laat, A. Taal, and P. Grosso, "The epi framework: a dynamic data sharing framework for healthcare use cases," *IEEE Access*, vol. 8, pp. 179909–179920, 2020.
- [13] M. U. Bokhari and A. Khan, "Critical Review on Threat Model of Various NoSQL Databases," in *International Conference on Computing for Sustainable Global Development*, pp. 5021–5028, Vidyapeeth's Institute of Computer Applications and Management (BVICAM), New Delhi (INDIA), 2017.
- [14] K. A. ElDahshan, A. A. AlHabsby, and G. E. Abutaleb, "Data in the time of COVID-19: a general methodology to select and secure a NoSQL DBMS for medical data," *PeerJ Computer Science*, vol. 6, article e297, 2020.
- [15] G. Kaur, S. Kaur, and A. Kaur, "Plant disease detection: a review of current trends," *International Journal of Engineering & Technology*, vol. 7, no. 3.34, pp. 874–881, 2018.
- [16] G. Murugesan, T. I. Ahmed, J. Bhola et al., "Fuzzy logic-based systems for the diagnosis of chronic kidney disease," *BioMed Research International*, vol. 2022, Article ID 2653665, 15 pages, 2022.
- [17] M. Shabaz and A. Kumar, "SA sorting: a novel sorting technique for large-scale data," *Journal of Computer Networks and Communications*, vol. 2019, Article ID 3027578, 7 pages, 2019.
- [18] L. Wang, P. Kumar, M. E. Makhatha, and V. Jagota, "Numerical Simulation of Air Distribution for Monitoring the Central Air Conditioning in Large Atrium," *International Journal of System Assurance Engineering and Management*, vol. 13, no. 1, pp. 340–352, 2021.
- [19] S. Sanobar, I. Alam, S. Pande et al., "An enhanced secure deep learning algorithm for fraud detection in wireless communication," *Wireless Communications and Mobile Computing*, vol. 2021, Article ID 6079582, 14 pages, 2021.
- [20] F. Ajaz, M. Naseem, S. Sharma, M. Shabaz, and G. Dhiman, "COVID-19: challenges and its technological solutions using IoT," *Current Medical Imaging*, vol. 18, no. 2, pp. 113–123, 2022.
- [21] I. Medeiros, M. Beatriz, N. Neves, and M. Correia, "SEPTIC: detecting injection attacks and vulnerabilities inside the DBMS," *IEEE Transactions on Reliability*, vol. 68, no. 3, pp. 1168–1188, 2017.
- [22] Q. Li, F. Wang, J. Wang, and W. Li, "LSTM-based SQL injection detection method for intelligent transportation system," *IEEE Transactions on Vehicular Technology*, vol. 68, no. 5, pp. 1–4191, 2019.
- [23] S. V. Shanmuganeethi, S. C. E. Shyni, and S. Swamynathan, "SBSQLID: Securing web applications with service based SQL injection detection," in *2009 International Conference on Advances in Computing, Control, and Telecommunication Technologies*, pp. 702–704, Trivandrum, Kerala, 2009.
- [24] A. Luo, W. Huang, and W. Fan, "A CNN-Based Approach to the Detection of SQL Injection Attacks," in *2019 IEEE/ACIS 18th International Conference on Computer and Information Science (ICIS)*, pp. 320–324, Beijing, China, 2019.